OUTLOOK
Cannabis

nature

THE INTERNATIONAL WEEKLY JOURNAL OF SCIENCE

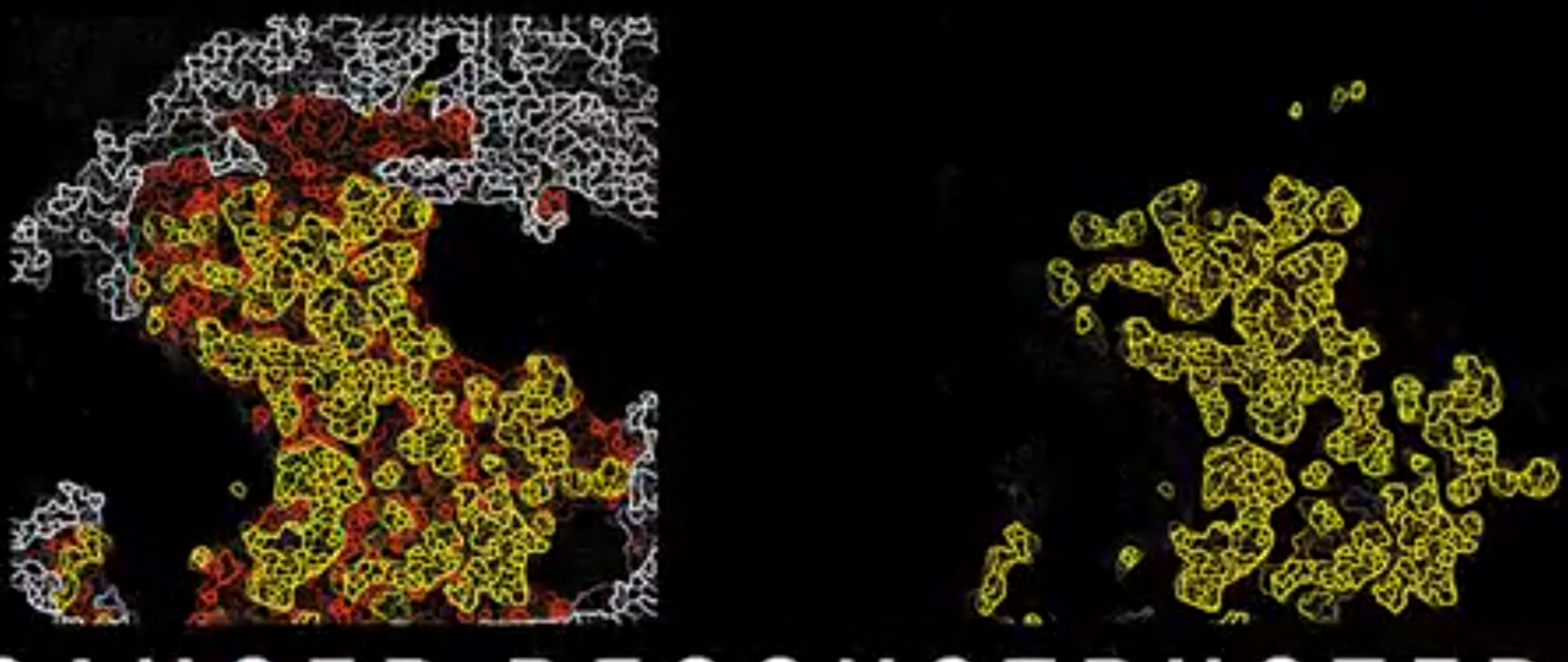

CANCER DECONSTRUCTED

Fluorescent labelling reveals the changing cellular environment of early-stage metastasis

PAGES 589 & 603

NATURE.COM
29 August 2019
Vol. 572, No. 7771

THIS WEEK

EDITORIALS

FACE TIME Moratorium needed on technologies that identify individuals **p.565**

HEART OF THE MATTER Falling cardiovascular death rates start to stall **p.567**

MIT FUNDING Links to sex offender Jeffrey Epstein to be investigated **p.568**

Italy must keep its funding pledges

The collapse of Italy's coalition government has left researchers vulnerable. The incoming administration must keep a longstanding promise to end austerity in funding.

Last week, Italy's coalition government ended abruptly, when the nationalist Lega party of deputy prime minister Matteo Salvini announced that it was walking away from its turbulent coalition with the anti-establishment M5S party, known as the Five Star Movement. The collapse is of great concern: a much-delayed funding increase is now on hold, and the political uncertainty adds further threat.

What will happen now is unclear. One of the coalition partners could form a government with others in parliament, or an election might be needed if an agreement cannot be reached. Italy's head of state, President Sergio Mattarella, will oversee the process. He needs to use his discussions with party leaders to remind them of the coalition's promise to the nation's scholars: that austerity in research funding would come to an end.

The challenge for whoever takes office is that Italy's economy has been mostly stagnant for a decade. It also has high levels of debt and could be on the brink of a recession. And as Italy, like other European countries, aimed to shrink its budget deficit after the 2008–09 financial crisis, funding for universities took a hit.

The coalition government had promised to return funding for universities to 2009 levels of around €7.5 billion (US$8.3 billion). It had also vowed to increase a smaller fund for research institutes, known as the FOE, which has consistently been cut since 2013. These increases, although modest, would have provided welcome relief for a system in which most of the funding from the government is currently used to pay for salaries and fixed costs, such as utility bills.

Furthermore, there is a possibility that indirect taxation — value-added tax (VAT) — will need to rise, from 22% to 25%. Italy has exceeded European Union limits on the size of its borrowing, and if the government cannot cut €23 billion from public spending, it will need to raise VAT. That will put even more pressure on research budgets.

Money is not the only issue. Lega was responsible for running the interior ministry, and ministers clashed with scientists on the party's policies towards refugees and asylum-seekers — including an indefensible law that imposes a €1-million fine on humanitarian ships patrolling the Mediterranean looking to save people in distress. Academic independence is also a concern. At the Ministry of Education, University and Research — also the responsibility of Lega — there is evidence that inspectors have been monitoring the teaching of political science in schools. In some classes, they have been discussing whether today's government policies echo Italy's Mussolini-era past. This has unsettled teachers.

And although Italy's spending on research and development — at around 1.3% of its gross domestic product — sits well below the EU average of 2%, its research performance continues to improve. Between 2000 and 2016, Italy's share of published scientific papers increased from 3.2% to 4% and the number of publications as a fraction of spending on research is comfortably above the EU average.

In his resignation speech to Italy's senate, prime minister Giuseppe Conte from the Five Star movement spoke about the need to invest more in research and to establish a national agency for research — such words are welcome, but not enough, and he must uphold his earlier promises if his party returns to power.

After a decade of austerity, Italy's researchers and research leaders will need to dig deep yet again and find ways to hold the next government accountable for these promises. Mattarella, a former education minister, can and should also play a vital supporting part. As the head of state, he has no executive authority, but he does have moral authority. He needs to use it so that promised funds and scholarly autonomy are protected in the next administration. ■

Paying the price

Universities must see that inadequate support of early-career researchers has consequences.

Letters from research funders to university leaders rarely raise eyebrows. But a letter sent this month by the heads of the United Kingdom's three largest medical-research funders did just that.

It says that some types of funding could be withheld unless universities provide better support for early- and mid-career staff — particularly women and trainees. And it warns that institutions could be prevented from bidding for funded posts unless they change their ways. The letter is signed by the heads of the Medical Research Council, the National Institute for Health Research (NIHR) and Wellcome.

What has sparked funder frustration is the fact that universities promise to look after new researchers when applying for grants — making pledges including the provision of quality mentoring, or a path to promotion. But in some cases these commitments are ignored once grant money is banked — sometimes in violation of contracts.

No institutions are named in the letter, a copy of which has been seen by *Nature*, but it points to "some very large and well-established Universities and Medical Schools".

One of the signatories — the NIHR — was an early adopter of tough measures in support of advancing women's careers. In 2011, it made grants conditional on medical schools achieving a gold or silver in the Athena SWAN Charter, a scheme designed to improve women's career prospects that has also raised awareness of the structural barriers to gender equality in universities.

Athena SWAN has enabled many universities to take positive action to advance equality and diversity. But when it comes to the needs of early- and mid-career clinical researchers, the NIHR and the other medical-research funders are right to challenge universities that are not doing enough. A strongly worded letter warning universities that they could be sanctioned unless they change is a necessary step. ■

Regulate facial-recognition technology

Until appropriate safeguards are in place, we need a moratorium on biometric technology that identifies individuals, says **Kate Crawford**.

Earlier this month, Ohio became the latest of several state and local governments in the United States to stop law-enforcement officers from using facial-recognition databases. The move followed reports that the Immigration and Customs Enforcement agency had been scanning millions of photos in state driver's licence databases, data that could be used to target and deport undocumented immigrants. Researchers at Georgetown University in Washington DC used public-record requests to reveal this previously secret operation, which was running without the consent of individuals or authorization from state or federal lawmakers.

It is not the only such project. Customs and Border Protection is using something similar at airports, creating a record of every passenger's departure. The technology giant Amazon is building partnerships with more than 200 police departments to promote its Ring home-security cameras across the United States. Amazon gets ongoing access to video footage; police get kickbacks on technology products.

Facial-recognition technology is not ready for this kind of deployment, nor are governments ready to keep it from causing harm. Stronger regulatory safeguards are urgently needed, and so is a wider public debate about the impact it is already having. Comprehensive legislation must guarantee restrictions on its use, as well as transparency, due process and other basic rights. Until those safeguards are in place, we need a moratorium on the use of this technology in public spaces.

There is little evidence that biometric technology can identify suspects quickly or in real time. No peer-reviewed studies have shown convincing data that the technology has sufficient accuracy to meet the US constitutional standards of due process, probable cause and equal protection that are required for searches and arrests.

Even the world's largest corporate supplier of police body cameras — Axon in Scottsdale, Arizona — announced this year that it would not deploy facial-recognition technology in any of its products because it was too unreliable for police work and "could exacerbate existing inequities in policing, for example by penalizing black or LGBTQ communities". Three cities in the United States have banned the use of facial recognition by law-enforcement agencies, citing bias concerns.

They are right to be worried. These tools generate many of the same biases as human law-enforcement officers, but with the false patina of technical neutrality. The researchers Joy Buolamwini at Massachusetts Institute of Technology in Cambridge and Timnit Gebru, then at Microsoft Research in New York City, showed that some of the most advanced facial-recognition software failed to accurately identify dark-skinned women 35% of the time, compared to a 1% error rate for white men. Separate work showed that these technologies mismatched 28 US members of Congress to a database of mugshots, with a nearly 40% error rate for members of colour. Researchers at the University of Essex in Colchester, UK, tested a facial-recognition technology used by London's Metropolitan Police, and found it made just 8 correct matches out of a series of 42, an error rate they suspect would not be found lawful in court. Subsequently, a parliamentary committee called for trials of facial-recognition technology to be halted until a legal framework could be established.

But we should not imagine that the most we can hope for is technical parity for the surveillance armoury. Much more than technical improvements are needed. These tools are dangerous when they fail and harmful when they work. We need legal guard rails for all biometric surveillance systems, particularly as they improve in accuracy and invasiveness. Accordingly, the AI Now Institute that I co-founded at New York University has crafted four principles for a protective framework.

First, given the costly errors, discrimination and privacy invasions associated with facial-recognition systems, policymakers should not fund or deploy them until they have been vetted and strong protections have been put in place. That includes prohibiting links between private and government databases.

THESE TOOLS ARE DANGEROUS WHEN THEY FAIL AND HARMFUL WHEN THEY WORK.

Second, legislation should require that public agencies rigorously review biometric technologies for bias, privacy and civil-rights concerns, as well as solicit public input before they are used. Agencies that want to deploy these technologies should be required to carry out a formal algorithmic impact assessment (AIA). Modelled after impact-assessment frameworks for human rights, environmental protection and data protection, AIAs help governments to evaluate artificial-intelligence systems and guarantee public input.

Third, governments should require corporations to waive any legal restrictions on researching or overseeing these systems. As we outlined in the AI Now Report 2018, tech companies are currently able to use trade-secrecy laws to shield themselves from public scrutiny. This creates a legal 'black box' that is just as opaque as any algorithmic 'black box', and serves to shut down investigations into the social implications of these systems.

Finally, we need greater whistle-blower protections for technology-company employees to ensure that the three other principles are working. Tech workers themselves have emerged as a powerful force of accountability: for example, whistle-blowers revealed Google's work on a censored search engine in China. Without greater protections, they are in danger of retaliation.

Scholars have been pointing to the technical and social risks of facial recognition for years. Greater accuracy is not the point. We need strong legal safeguards that guarantee civil rights, fairness and accountability. Otherwise, this technology will make all of us less free. ■

Kate Crawford *is a distinguished research professor and co-director of the AI Now Institute at New York University, and a principal researcher at Microsoft Research in New York City.*
Twitter: @katecrawford

SEVEN DAYS *The news in brief*

INSTITUTIONS

Alaska funding

Tenured faculty members in the University of Alaska (UA) system no longer face the possibility of being laid off with 60 days' notice. UA's governing board voted unanimously on 20 August to reverse its declaration of "financial exigency", which it made in July in response to an unprecedented US$135-million cut to state funding for the university system. Financial exigency grants the board extraordinary powers to reduce costs, including the ability to fire faculty members and end academic programmes. But the budget crisis eased on 13 August, when Alaska's governor Michael Dunleavy and UA administrators agreed to a smaller, $25-million cut this year. The UA governing board will meet in early September to discuss how to distribute this year's cut, and a proposal to consolidate the system's three main branches — in Anchorage, Fairbanks and Juneau — into one accredited institution.

MIT inquiry

The Massachusetts Institute of Technology (MIT) is launching an investigation into its interactions with sex offender and alleged sex trafficker Jeffrey Epstein. The university, in Cambridge, Massachusetts, received about US$800,000 in donations from the disgraced financier over two decades, MIT president Rafael Reif said on 22 August. All of Epstein's donations went to either the MIT Media Lab or to physics professor Seth Lloyd. "In this instance, we made a mistake of judgment," Reif said. Lloyd and MIT Media Lab director Joichi Ito have issued public apologies for their dealings with Epstein. The MIT announcement came days after two researchers cut ties with the Media Lab because of the university's interactions with Epstein.

DALE OMORI/CLEVELAND MUS. NAT. HIST.

3.8-million-year-old skull discovered

Scientists have discovered a 3.8-million-year-old hominin skull (pictured) in Ethiopia that could help to clarify the origins of Lucy, our famous forerunner. The specimen suggests that Lucy's species coexisted with an ancestor in the ancient Ethiopian landscape. Most researchers think that Lucy's species, *Australopithecus afarensis*, falls on the same branch of the evolutionary tree as an earlier species called *Australopithecus anamensis*. The idea is that *A. anamensis* gradually morphed into *A. afarensis*, implying that the two species never coexisted. The skull, described this week in *Nature*, suggests otherwise. The fossil's facial features indicate that it belongs to *A. anamensis*, and strengthens the case that a previously discovered fossil, a 3.9-million-year-old face fragment found in the 1980s, belongs to *A. afarensis*. This suggests that the two species coexisted, after all. *A. afarensis* may have evolved from a small *A. anamensis* group before gradually outcompeting the wider *A. anamensis* population.

HEALTH

Polio milestone

Polio is no longer endemic in Nigeria, the World Health Organization (WHO) said on 21 August, as the country marked three years without any new cases of the paralysing disease. Nigeria is the last country in Africa in which polio has circulated in the wild; now, the entire continent could be declared polio-free next year. The WHO, private donors and governments have led a multibillion-dollar global campaign to eradicate polio. The number of new infections has fallen globally, from roughly 350,000 in 1988 to 33 in 2018.

POLICY

UK immigration

The UK government has said that freedom of movement as it currently stands for European Union citizens will end as soon as the country leaves the bloc on 31 October. This means that EU scientists coming to work in the United Kingdom after this date would be subject to new immigration arrangements, which the government promised to publish "shortly" in an announcement on 19 August. The previous government's policy would have left the rights of EU citizens coming to study or work in the United Kingdom essentially unchanged at least until the

end of next year. Experts have questioned whether it is possible to implement a new immigration policy without a way of distinguishing between existing EU migrants, whose rights remain unchanged, and those arriving in the United Kingdom soon after the Brexit date. Science organizations have expressed concern at the move, which they say creates uncertainty among employers.

ENVIRONMENT

Trump lawsuit

A coalition of environmental groups filed a lawsuit against the administration of US President Donald Trump on 21 August to block a rule that weakens protections for threatened species. The changes — finalized on 12 August by the Fish and Wildlife Service and the National Marine Fisheries Service — affect how the Endangered Species Act is applied, and constitute some of the most significant alterations to the law since it was enacted in 1973. The revisions remove blanket protections for animals and plants that are listed as threatened, a category for organisms at risk of becoming endangered. The changes also allow federal agencies to conduct economic analyses when deciding whether to protect a species.

GIULIO ORIGLIA/GETTY

Giraffe protections

Nations have agreed to regulate trade in giraffes (**pictured**) for the first time. The decision — which is expected to be finalized this week — was made at a meeting of parties to the Convention on International Trade in Endangered Species (CITES) in Geneva, Switzerland. Nine giraffe species will be protected under Appendix II of the convention, which protects species that could have faced extinction had trade restrictions not been implemented. Countries also voted to protect 18 shark and ray species — many of which are hunted for their meat and fins — under Appendix II. But the parties stopped short of approving amendments to shut down all domestic ivory markets.

Amazon funds

Brazil has rejected an offer from the world's seven largest economies (G7) to provide US$22 million in immediate funding to help put out fires in the Amazon (see 'Trend watch'). The fund was put together by France's President Emmanuel Macron and pledged at the G7 annual meeting in Biarritz, France, on 26 August. After initially accepting the funding, the Brazilian government declined the offer. Earlier, Macron's decision to put the Amazon on the G7 agenda angered Brazil's President Jair Bolsonaro, who accused France of acting in a colonial way. Bolsonaro said that he is mobilizing Brazil's military to drop water on burning regions, and that Amazon countries should be able to deal with the issue without outside help. The G7 meeting had a strong focus on the environment and development, and also produced an agreement between the European Union, the G7 and international funding agencies to provide more support for the countries of the Sahel.

SPACE

Moon mission

India's Chandrayaan-2 spacecraft entered the Moon's orbit on 20 August, says the nation's space agency. The event is a milestone in the country's second mission to the Moon: it will be its first attempt at a 'soft' landing on the lunar surface. Early next week, the lander will separate from the orbiter, which will continue to circle the Moon for another year. The lander, which carries a six-wheeled rover called Pragyan, is due to touch down near the south pole on 7 September. If the landing is successful, India's will be the fourth space agency, after those of the United States, the Soviet Union and China, to perform a soft landing.

TREND WATCH

The Brazilian Amazon is burning, and the world is taking notice. So far this year, more than 80,000 wildfires have burnt in Brazil — the majority in the Amazon — amounting to an increase of roughly 80% over the same period last year, according to the country's National Institute for Space Research (INPE).

The Amazon is the world's largest rainforest and it contains several million plant, animal and insect species. It also acts as a huge carbon sink that helps to cool global temperatures. The wildfire data, which INPE released on 20 August, have prompted an international outcry. In a tweet on 22 August, French President Emmanuel Macron called for discussion of the fires at the G7 summit he was hosting in Biarritz from 24 to 26 August. German Chancellor Angela Merkel backed Macron's call. But Brazilian President Jair Bolsonaro hit back, tweeting that Macron was using the situation for his own political gain. Critics of Bolsonaro say that his push to make the Amazon more accessible to industries such as logging and agriculture is partly responsible for the rise in the number of fires.

RECORD BURN

Brazil's space-agency satellites have detected hotspots — fires with a front at least 30 metres long — in record numbers this year. Most fires are burning in the country's Amazon rainforest.

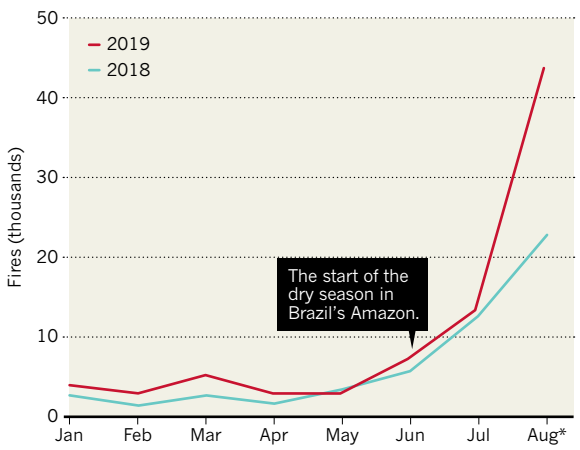

*Data current as of 26 August.

SOURCE: INPE

NEWS IN FOCUS

DAVID SOLM

The University of Adelaide suspended Alan Cooper as leader of the prestigious Australian Centre for DNA following an investigation.

RESEARCH CULTURE

Anxiety mixed with great science in troubled DNA lab

Researchers say lab leader Alan Cooper, who was suspended last week, bullied them.

BY DYANI LEWIS

The University of Adelaide has suspended the leader of its ancient-DNA centre, Alan Cooper, following an investigation into the 'culture' at the Australian laboratory. The university has not given a reason for its decision, but current and former co-workers of Cooper — an award-winning evolutionary biologist who specializes in human migration — have told *Nature* that he bullied them and others.

Their accounts paint a picture of a lab that was exciting scientifically — but that had a toxic work environment. Former student Nic Rawlence says he was bullied while at the Australian Centre for Ancient DNA (ACAD) and developed stress-induced health issues. Another former student, Dean Male, says he left the lab as a result of Cooper's bullying. "I couldn't get out of there fast enough," he says.

Nature interviewed nine of Cooper's current and former co-workers. Four — including one current team member — say that he bullied them; four more, two of whom still work at the centre, say that they observed him bullying team members. Most of those people requested anonymity for fear of damaging their academic careers. Three of those who allege that Cooper bullied them gave evidence to the investigation, as did two of those who say they observed it.

Another former colleague, Paul Brotherton, told *Nature* that although Cooper is brash, he is not a bully. Cooper could be disdainful towards someone and their work if it wasn't ▶

going to lead to a high-profile publication, he says. "Perhaps he's not very good at disguising his impatience and his lack of interest."

Some of the people *Nature* spoke to say they had complained before but that things did not change. Others say they did not make formal complaints for fear that Cooper would find out and the bullying would get worse.

Rawlence says he's "cautiously optimistic" that the university's decision to suspend one of its most prominent scientists is a sign that the allegations against Cooper are being taken seriously. But others are sceptical that the university will take further action or that the situation will improve, citing the funding that Cooper brings in, and the fact that previous complaints seem to have had little effect. In 2016, Cooper was named South Australian Scientist of the Year. He has also been awarded millions of dollars in highly competitive grants from the Australian Research Council.

Several of the researchers say that the university should permanently remove Cooper as leader of ACAD, which has about 36 staff and students, according to its website. "He is just going to tear up lives as long as he's in that role," says one former student.

At the time of publication, Cooper had not responded to *Nature*'s request for comment.

Cooper is a pioneer of ancient-DNA research, and his work to improve extraction techniques in the mid-1990s transformed the field. In 2001, he sequenced the first full mitochondrial genome from an extinct animal, two species of the New Zealand moa (*Emeus crassus* and *Dinornis giganteus*; A. Cooper *et al. Nature* **409**, 704–707; 2001). He has also characterized plaque on ancient teeth to understand changes in early-human diet across Europe (C. J. Adler *et al. Nature Genet.* **45**, 450–455; 2013). A project he leads to sequence the genomes of Indigenous Australian groups was awarded a prestigious Australian Museum Eureka Prize in 2017.

NIGHTMARE LAB

Cooper's suspension comes after the university engaged SAE Consulting in Adelaide to conduct a 'culture check' of ACAD in July. Cooper was not named as a focus of the probe, and the university did not say what prompted it, but on 19 August, ACAD students and staff were notified of Cooper's suspension. "Following on from the information provided, the University has decided to take further action," a spokesperson for the university told *Nature*. Cooper will remain suspended pending "the outcome of further processes", the statement read.

Rawlence was at ACAD from 2006 to 2013 and gave evidence to the investigation. He says Cooper would yell at him, sometimes in front of colleagues, and criticize his work. "It was pretty much an everyday occurrence," says Rawlence, who now leads a lab at the University of Otago in Dunedin, New Zealand.

Male, who was a senior researcher at ACAD from 2006 to 2007 and did not give evidence to the investigation, says his experience of working in the world-class lab was marred by Cooper's bullying. "It was fantastic science, really breathtaking, cutting-edge stuff," he said. Cooper often targeted the most vulnerable people in the lab, according to Male, who still works in research but has left academia.

KEN MILLER

Nic Rawlence alleges that Alan Cooper bullied him at ACAD.

Male recalls hearing Cooper's shouting from behind his closed office door, and was himself yelled at several times. "He'd kind of stalk and walk a bit, warming up, and then the door would close and he'd be behind you and it was actually quite intimidating, and then the shouting and yelling would start," he says.

"It was fantastic science, really breathtaking, cutting-edge stuff."

Cooper's criticisms of students' work were unconstructive and tinged with personal insults, according to a former ACAD student who witnessed Cooper bullying others. "It borders on cruel because it's just so relentless and not everyone is subjected to it," they say.

The current ACAD student who accuses Cooper of bullying them and who gave evidence to the investigation told *Nature* in an e-mail that they were surprised when they came out of a meeting unscathed. "I was frequently paralysed by anxiety and feelings of inadequacy."

Some students say Cooper took an unusually long time to read their papers and theses — sometimes several months — and was slow to sign paperwork that allowed them to graduate.

Rawlence says he had to lodge a formal complaint to the then-dean of graduate studies, Richard Russell, to get Cooper to read his PhD thesis so that he could complete his studies. Rawlence says Cooper then complied.

Rawlence and another former student who alleges they were bullied say they told their postgraduate coordinator about Cooper, and were informed that the university was aware of problems with his behaviour. They also say they complained to the university's management. The university did not indicate to them whether any steps had been taken to address the grievances, they say.

Another former student says they left without completing their studies partly owing to Cooper's behaviour.

But Brotherton, who worked as a postdoc with Cooper at the University of Oxford, UK, and later at ACAD, doesn't think Cooper is a bully. In his opinion, many of the alleged incidents are about personality differences. "[Alan] won't win empathetic boss of the year competition, but he's not a savage bully," says Brotherton, who no longer works in academia. He does say, however, that Cooper can be "quite abrasive and in-your-face", and that behaviours such as taking less interest in some people's projects are sins of "omission rather than commission".

AIRING GRIEVANCES

Most of the people whom *Nature* interviewed say that they were relieved when the university launched the culture check. But some have also questioned whether the scope of the investigation was too narrow. Rawlence and several other former students say that, initially, only current students were asked to participate.

Rawlence ended up participating only because colleagues currently at the centre alerted some former students to the probe, which prompted him and some others, he says, to contact the consultant leading the investigation, SAE Consulting's Sophie Rayner. But because the university didn't initially approach former students, some of the students worry that the probe might have missed accounts from past members of the lab.

Others complain that they could not give anonymous accounts to the investigation. One former student says Rayner told them that the university did not want anonymous accounts, and so decided against giving their account of witnessing bullying behaviour. SAE Consulting principal Sallie Emmett says the firm does not comment on matters relating to clients.

The university declined to comment when asked about the investigation and its handling of previous complaints against Cooper. ■

BIOMEDICAL RESEARCH

Huge US government study will offer genetic counselling

The National Institutes of Health has hired a firm to help participants cope with results.

BY JONATHAN LAMBERT

HYDROMET/GETTY

Researchers running a genetic-sequencing project in the United States aim to recruit one million people.

A US government project that aims to sequence the genomes of one million volunteers will partner with a genetic-counselling company to help participants understand their results. It will be the largest US government study to provide such a service.

The National Institutes of Health (NIH) in Bethesda, Maryland, is leading the project, called All of Us. And on 21 August, the agency announced the award of a US$4.6-million, 5-year grant to Color.

The firm, in Burlingame, California, will counsel every study participant with a genetic variant that could have serious health implications — such as *BRCA* mutations associated with breast cancer — when they receive their results. Color will also develop educational materials for all study participants, and will offer telephone consultations to those who wish to discuss their results with a counsellor.

"This is a really responsible and more equitable way of communicating the results of research to all participants," says Bartha Knoppers, the director of the Centre of Genomics and Policy at McGill University in Montreal, Canada. "They're laying the foundations for building good bridges between the findings and the people."

The All of Us study, which launched in May 2018, aims to enrol at least one million people. Participants will be asked to provide a host of health information, including electronic health records, genomic data and blood and urine samples. Study researchers also plan to collect data recorded by personal activity trackers, such as those found on smartphones. They will store the information in an online database that outside scientists can access with permission from the programme.

Enrolling participants from ethnic and socio-economic groups that are typically under-represented in biomedical research is a priority for the study's organizers. Most genomic research until now has been conducted on non-Hispanic white people. One recent review found that as of 2018, 78% of people included in genomic studies of disease were of European descent (G. Sirugo *et al. Cell* **177**, 26–31; 2019). That bias narrows the applicability of conclusions from genetic-testing studies, and can lead to misleading or dangerous interpretations of genetic variants found in other populations.

The All of Us study has enrolled 175,000 people around the United States so far. About 50% are people of colour, and 80% are from groups that have historically been under-represented in biomedical research. The study's scientists have yet to sequence any genomes, but they hope to provide participants with results in the first half of 2020, says Stephanie Devaney, the deputy director of All of Us.

To generate the kind of long-term data set necessary for breakthroughs in precision medicine — which uses genomic, physiological and other data to tailor treatments to individuals — All of Us must retain these participants, ideally throughout their lives. That's where genetic counselling comes in.

"It's imperative to our mission that we return value to our participants, that we communicate back the results of [our] research," says Devaney.

WORKING OUT THE DETAILS

This is a step in the right direction, says Amy McGuire, a bioethicist at Baylor College of Medicine in Houston, Texas. But "the devil is in the details", she adds.

And Devaney and her colleagues need to work out a lot of details — including what the programme will tell participants about their own genomes, and how. A genetic counsellor will give people information on genetic variants that have clear, actionable consequences for health, such as those in the *BRCA* gene. But study organizers are still discussing how much to tell participants about genetic variants that don't have such an explicit link to illness.

Their task is complicated by the fact that knowledge about genetic variants can change over time. A mutation that researchers now think is benign could one day be considered an indication of increased cancer risk. All of Us participants are told that the implications of their genetic-test results could change as scientists learn more about certain mutations, says Brad Ozenberger, genomics programme director at All of Us. But he and his colleagues are still working out how frequently to notify participants of such developments.

The effects of a genetic variant can also depend on ethnicity. Certain genetic tests that physicians use to help determine whether someone with cancer should undergo chemotherapy have been tested only in white Europeans. It's unclear whether these are accurate for people of colour. All of Us and Color say that they are working out the best way to communicate such uncertainties to study participants.

But the company says that it's prepared to have those conversations. "We've worked with a lot of diverse communities," says Alicia Zhou, vice-president of research and scientific affairs at Color. These include technology and manufacturing companies, railway workers in Alaska and residents of Trinidad and Tobago, she adds. ■

BIOMATERIALS

CRISPR turns gels into biological watchdogs

Gene-editing tool used to trigger smart materials that can deliver drugs and sense biological signals.

BY EWEN CALLAWAY

Is there anything CRISPR can't do? Scientists have wielded the gene-editing tool to make scores of genetically modified organisms, as well as to track animal development, detect diseases and control pests. Now, they have found yet another application for it: using CRISPR to create smart materials that change their form on command.

The shape-shifting materials could be used to deliver small molecules, and to create sentinels for almost any biological signal, researchers reported on 22 August (M. A. English *et al. Science* **365**, 780–785; 2019). The study was led by James Collins, a bioengineer at the Massachusetts Institute of Technology in Cambridge.

Collins's team worked with water-filled polymers that are held together by strands of DNA, known as DNA hydrogels. To alter the properties of these materials, Collins and his team turned to a form of CRISPR that uses a DNA-snipping enzyme called Cas12a. (The gene editor CRISPR–Cas9 uses the Cas9 enzyme to snip a DNA sequence at the desired point.) The Cas12a enzyme can be programmed to recognize a specific DNA sequence. The enzyme cuts its target DNA strand, then severs single strands of DNA nearby.

This property allowed the researchers to build a series of CRISPR-controlled hydrogels containing a target DNA sequence and single strands of DNA, which break up after Cas12a recognizes the target sequence in a stimulus. The break-up of the single DNA strands triggers the hydrogels to change shape or, in some cases, completely dissolve, releasing a payload (see 'CRISPR-controlled gel').

SMART OBJECTIVES

The team created hydrogels programmed to release enzymes, small molecules and even human cells — for instance, as part of a therapy — in response to stimuli. Collins hopes that the gels could be used to make smart therapeutics that release, for example, cancer drugs in the presence of a tumour, or antibiotics around an infection.

The researchers also integrated CRISPR-controlled hydrogels into electronic circuits. In one approach, they placed hydrogels inside a small chip-like device called a microfluidic chamber that was linked to an electronic circuit. The circuit switched off in response to the detection of genetic material from pathogens including the Ebola virus and methicillin-resistant *Staphylococcus aureus* (MRSA). The team even used the hydrogels to develop a prototype diagnostic tool that sends a wireless signal when it recognizes genetic material from Ebola in lab samples.

Dan Luo, a bioengineer at Cornell University in Ithaca, New York, says that the CRISPR hydrogels are an improvement on other responsive hydrogels because scientists can easily determine what triggers a change in the material.

"We're in the CRISPR age right now," Collins says. "It's taken over biology and biotechnology. We've shown that it can make inroads into materials and bio-materials." ■

CRISPR-CONTROLLED GEL

Researchers have created a smart hydrogel material that is held together by DNA. The CRISPR–Cas12a protein cuts the DNA strands, changing the gel's shape, which can be controlled to release drugs, particles or even switch an electronic circuit.

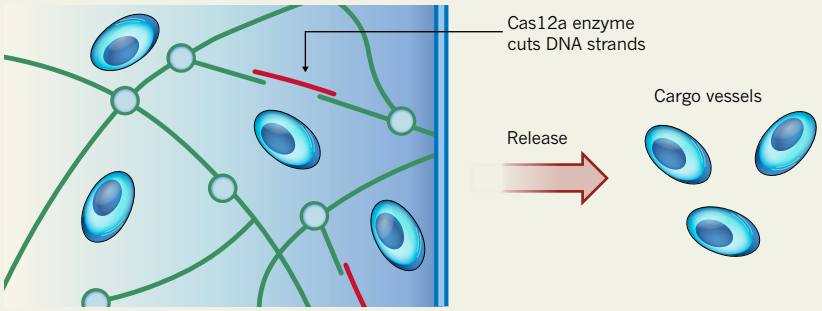

DENMARK

Geologist's sacking prompts outcry

Tenured professor dismissed from University of Copenhagen.

BY QUIRIN SCHIERMEIER

For the second time in three years, geoscientists are protesting against the dismissal of a geologist from the University of Copenhagen.

The management of the university's science faculty dismissed Irina Artemieva, a tenured professor and internationally esteemed specialist in lithospheric geophysics, on 29 July — saying that she has repeatedly failed to fulfil various administrative and teaching duties. They allege that she has failed to use the appropriate calendar to plan holidays; travelled to conferences without approval; and caused inconvenience to examination and teaching schedules. "Your actions and behaviour have had a negative impact on the performance of your duties relating to teaching and research activities in overall terms," the faculty told Artemieva in the July letter informing her of her dismissal.

Artemieva denies the accusations, and defended herself in a 128-page document sent to the faculty of science after the management informed her in May that it was contemplating her dismissal. She says that all her external work activities, including field trips, conference attendance and editorial work, are standard professional undertakings that she has documented as required by the university's rules.

An international group of 32 geoscientists says that the university's action is problematic because the reasons given do not warrant the dismissal of a tenured professor, by international academic standards. This — combined

IRINA ARTEMIEVA

Irina Artemieva is a specialist in lithospheric geophysics.

with the similar dismissal of another geologist three years ago from the same faculty, which geoscientists also protested about — threatens the reputation of the University of Copenhagen and the Danish university system, they say in a July letter sent to the university after it had told Artemieva that it was considering her dismissal.

In 2016, the faculty's management sacked Hans Thybo, a prominent geologist who was, at the time, president of the European Geosciences Union, over his use of a private e-mail account for work purposes. A group of geoscientists similarly criticized that sacking, and urged the university to reconsider its decision. Thybo, now a researcher at the University of Oslo, appealed against the sacking, and received a settlement of six months' salary after arbitration discussions between the university and a trade union representing academic employees — but he was not reinstated to his post.

PERSONAL DISAGREEMENTS

"Throughout most of the developed world, a tenured professor can only be dismissed for gross misconduct or criminal activity," the group of geoscientists wrote. "Professor Artemieva's dismissal appears to be based on personal disagreements between her and the management of the department," the scientists wrote. "At least on these occasions, the University of Copenhagen is not adhering to the international standards of academic freedom and the rights of its employees."

"This new dismissal will damage the reputation of the university system and the country's scientific community even more than the earlier case," they wrote.

"Irina is an outstanding researcher, adviser and geoscience community member," says Seth Stein, an Earth scientist at Northwestern University in Evanston, Illinois, who organized the protest letter to the university. "Losing her would be a great loss to the geophysics programme at the University of Copenhagen."

The University of Copenhagen declined *Nature*'s request for comment on the dismissal, saying that it does not discuss matters concerning individual employees. The Danish ministry for science and education also declined to comment on the case, or on the suggestion that the dismissal would harm Danish universities' reputations.

Artemieva says that her treatment has amounted to discrimination — complaints that the university says, in its letters to her, are unsubstantiated. The researcher, who is originally from Russia and was the only female professor in her department, says that she was consistently made to feel unwelcome after gaining her tenured position through an open call for applications. "No matter what I would do, I was facing professional enmity here from the very start," she says.

In Artemieva's dismissal letter, the department's dean, John Renner Hansen, says that the faculty of science "does not recognize the picture of [Artemieva] having been exposed to 'harassment', 'bullying' and 'discrimination' since you were appointed professor". It adds: "Your actions have been confrontational and conflict-escalating … Rather than responding to the critique raised, you continue to make accusations against different management members." ■

FUNDING

Brazil budget cuts threaten 80,000 science scholarships

The country's main research-funding agency could stop payments as soon as September.

BY RODRIGO DE OLIVEIRA ANDRADE

Brazil's main science-funding agency will have to suspend more than 80,000 scholarships to postdoctoral researchers and graduate and undergraduate students starting in September unless it receives additional cash from the government.

The National Council for Scientific and Technological Development (CNPq) announced the impending cancellations on 15 August. The CNPq also won't be offering new scholarships, according to the statement. Brazil's government hasn't released the 330 million reais (US$89 million) that it froze in the CNPq's budget as part of broader spending cuts in March. If President Jair Bolsonaro's administration doesn't release some of the money soon, the CNPq's scholarship fund will run out of cash by next month.

"Government is jeopardizing the future of a whole generation of Brazilian scientists," says Paulo Artaxo, a physicist at the University of São Paulo. Cancelling the scholarships will have a devastating impact on Brazilian science, which depends on these young researchers, he says.

Not supporting students in research programmes "is like shooting oneself in the foot", says Alexander Turra, an oceanographer at the Oceanographic Institute of the University of São Paulo.

A MATTER OF SURVIVAL

Biologist Nicole Malinconico is one of many graduate students who might have to leave research if the CNPq scholarships fall through. She moved to São Paulo in January and has applied to the doctorate programme at the Oceanographic Institute.

"Now, even if I enter the doctorate [programme], without the scholarship I won't be able to keep myself in São Paulo," says Malinconico. She plans to apply for a scholarship offered by the São Paulo Research Foundation, a local science-funding agency. But the competition for alternative sources of money has grown stiff, she says. Malinconico fears that she will have to give up her research career to look for a job outside academia, as many of her friends are doing.

"For many students, a scholarship is much more than research support, it is a salary that they use to live, to eat and to pay their bills," ▶

EVARISTO SA/AFP/GETTY

Students in Brazil's capital protested against cuts to education and science funding earlier this year.

says Daniel Martins-de-Souza, a biochemist at the University of Campinas in Brazil. Without that support, lots of researchers will be out of work, which could shift Brazil's overall unemployment figures, he says.

The Brazilian Society for the Advancement of Science, based in São Paulo, along with 97 other research and academic institutions in the country, launched an online petition on 13 August demanding that the government help the CNPq meet its funding commitments. As of 27 August, it has more than 900,000 signatures.

GOING BACKWARDS

Researchers in Brazil have been working under a cloud of uncertainty since March, when Bolsonaro's administration announced that it would freeze 42% of the budget of the science and communications ministry (MCTIC). This included the freeze in the budget of the CNPq, which is an agency within the MCTIC. Around that time, the government also announced that it would cut 30% of the funds that it gives to federal universities.

Many researchers left Brazil for better situations abroad, and those who stayed have struggled to keep their laboratories functioning.

"Science is walking backwards in Brazil," says Marcos Buckeridge, the director of the National Institute of Bioethanol Science and Technology.

The institute includes 31 laboratories in 5 Brazilian states that develop technology to produce biofuels using materials such as plants or animal waste. Buckeridge fears that if the CNPq stops funding student and post-doctoral scholarships, in the next few months the institute won't have enough researchers to run experiments.

The CNPq and the MCTIC are in negotiations with the Ministry of Economy for more money by the end of the year so that the agency can support scholarships, says CNPq spokesperson Mariana Galiza de Oliveira. But it's unclear whether the agency will receive the money in time to avoid an interruption to payments for current scholarship holders, she says. ■

POLICING SELF-CITATIONS

Some top academics cite themselves heavily, and researchers are debating what to do about it.

BY RICHARD VAN NOORDEN AND DALMEET SINGH CHAWLA

The world's most-cited researchers, according to newly released data, are a curiously eclectic bunch. Nobel laureates and eminent polymaths rub shoulders with less familiar names, such as Sundarapandian Vaidyanathan from Chennai in India. What leaps out about Vaidyanathan and hundreds of other researchers is that many of the citations to their work come from their own papers, or those of their co-authors.

Vaidyanathan, a computer scientist at the Vel Tech R&D Institute of Technology, a privately run institute, is an extreme example: he has received 94% of his citations from himself or his co-authors up to 2017, according to a study in *PLoS Biology* this month[1]. He is not alone. The data set, which lists around 100,000 researchers, shows that at least 250 scientists have amassed more than 50% of their citations from themselves or their co-authors, whereas the median self-citation rate is 12.7%.

The study could help to flag potential extreme self-promoters, and possibly 'citation farms', in which clusters of scientists massively cite each other, say the researchers. "I think that self-citation farms are far more common than we believe," says John Ioannidis, a physician at Stanford University in California who led the work and specializes in meta-science — the study of how science is done. "Those with greater than 25% self-citation are not necessarily engaging in unethical behaviour, but closer scrutiny may be needed," he says.

The data are by far the largest collection of self-citation metrics ever published. And they arrive at a time when funding agencies, journals and others are focusing more on the potential problems caused by excessive self-citation. In July, the Committee on Publication Ethics (COPE), a publisher-advisory body in London, highlighted extreme self-citation as one of the main forms of citation manipulation. This issue fits into broader concerns about an over-reliance on citation metrics when making decisions about hiring, promotions and research funding.

"When we link professional advancement and pay attention too strongly to citation-based metrics, we incentivize self-citation," says psychologist Sanjay Srivastava at the University of Oregon in Eugene.

Although many scientists agree that excessive self-citation is a problem, there is little consensus on how much is too much or on what to do about the issue. In part, this is because researchers have many legitimate reasons to cite their own work or that of colleagues. Ioannidis cautions that his study should not lead to the vilification of particular researchers for their self-citation rates, not least because these can vary between disciplines and career stages. "It just offers complete, transparent information. It should not be used for verdicts such as deciding that too high self-citation equates to a bad scientist," he says.

DATA DRIVE

Ioannidis and his co-authors didn't publish their data to focus on self-citation. That's just one part of their study, which includes a host of standardized citation-based metrics for the most-cited 100,000 or so researchers over the past 2 decades across 176 scientific sub-fields. He compiled the data together with Richard Klavans and Kevin Boyack at analytics firm SciTech Strategies in Albuquerque, New Mexico, and Jeroen Baas, director of analytics at the Amsterdam-based publisher Elsevier; the data all come from Elsevier's proprietary Scopus database. The team hopes that its work will make it possible to identify factors that might be driving citations.

But the most eye-catching part of the data set is the self-citation metrics. It is already possible to see how many times an author has cited their own work by looking up their citation record in subscription databases such as Scopus and Web of Science. But without a view across research fields and career stages, it's difficult to put these figures into context.

Vaidyanathan's record stands out as one of the most extreme — and it has brought certain rewards. Last year, he won a 20,000-rupee (US$280) award for being among the nation's top researchers by measures of productivity and citation metrics. Vaidyanathan did not reply to *Nature*'s request for comment, but he has previously defended his citation record in reply to questions about Vel Tech posted on Quora, the online question-and-answer platform. In 2017, he wrote that because research is a continuous process, "the next work cannot be carried on without referring to previous work", and that self-citing wasn't done with the intention of misleading others.

Two other researchers who have gained plaudits and cite themselves heavily are Theodore Simos, a mathematician whose website lists affiliations at King Saud University in Riyadh, Ural Federal University in Yekaterinburg, Russia, and the Democritus University of Thrace in Komotini, Greece; and Claudiu Supuran, a chemist at the University of Florence, Italy, who also lists an affiliation at King Saud University. Both Simos, who amassed around 76% of his citations from himself or his co-authors, and Supuran (62%) were last year

COUNTRY BY COUNTRY

Authors in Russia and Ukraine have the highest self-citation rates*.

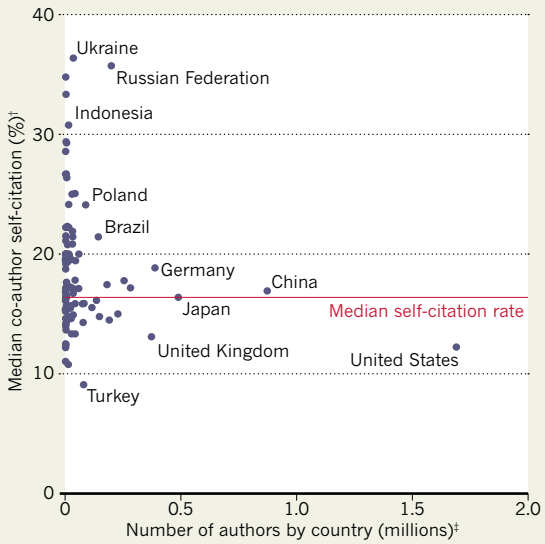

*From unpublished analysis of 7 million authors (with >5 papers) in Scopus data set.
†Co-author self-citation: self-citations to a paper by any co-author are counted as self-citations in each co-author's record.
‡Only countries with >1,000 such authors shown.

SOURCE: JEROEN BAAS, UNPUBLISHED ANALYSIS OF SCOPUS DATABASE

named on a list of 6,000 "world-class researchers selected for their exceptional research performance" produced by Clarivate Analytics, an information-services firm in Philadelphia, Pennsylvania, which owns Web of Science. Neither Simos nor Supuran replied to *Nature*'s requests for comment; Clarivate said that it was aware of the issue of unusual self-citation patterns and that the methodology used to calculate its list might change.

WHAT TO DO ABOUT SELF-CITATIONS?

In the past few years, researchers have been paying closer attention to self-citation. A 2016 preprint, for instance, suggested that male academics cite their own papers, on average, 56% more than female academics do[2], although a replication analysis last year suggested that this might be an effect of higher self-citation among productive authors of any gender, who have more past work to cite[3]. In 2017, a study showed that scientists in Italy began citing themselves more heavily after a controversial 2010 policy was introduced that required academics to meet productivity thresholds to be eligible for promotion[4]. And last year, Indonesia's research ministry, which uses a citation-based formula to allocate funding for research and scholarship, said some researchers had gamed their scores using unethical practices, including excessive self-citations and groups of academics citing each other. The ministry said that it had stopped funding 15 researchers and planned to exclude self-citations from its formula, although researchers tell *Nature* that this hasn't yet happened.

But the idea of publicly listing individuals' self-citation rates, or evaluating them on the basis of metrics corrected for self-citation, is highly contentious. For instance, in a discussion document issued last month[5], COPE argued against excluding self-citations from metrics because, it said, this "doesn't permit a nuanced understanding of when self-citation makes good scholarly sense". (See go.nature.com/2z3uomu for a survey.)

In 2017, Justin Flatt, a biologist then at the University of Zurich in Switzerland, called for more clarity around scientists' self-citation records[6]. Flatt, who is now at the University of Helsinki, suggested publishing a self-citation index, or *s*-index, along the lines of the *h*-index productivity indicator used by many researchers. An *h*-index of 20 indicates that a researcher has published 20 papers with at least 20 citations; likewise, an *s*-index of 10 would mean a researcher had published 10 papers that had each received at least 10 self-citations.

Flatt, who has received a grant to collate data for the *s*-index, agrees with Ioannidis that the focus of this kind of work shouldn't be about establishing thresholds for acceptable scores, or shaming high self-citers. "It's never been about criminalizing self-citations," he says. But as long as academics continue to promote themselves using the *h*-index, there's a case for including the *s*-index for context, he argues.

PHYSICS ENVY?

Because particle physics and astrophysics have big consortia that publish multi-authored papers which cite each other, they have the highest (co-author) self-citation rates*.

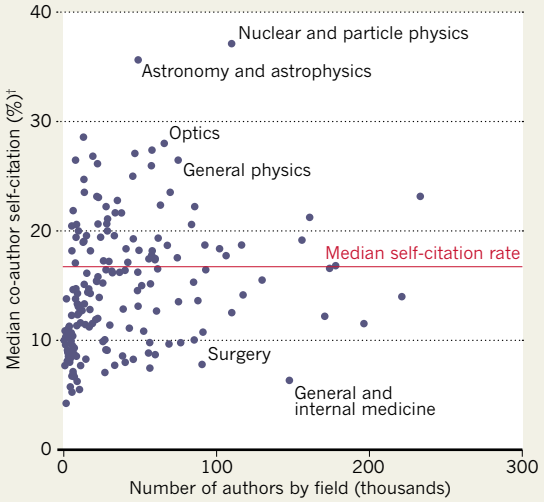

*From unpublished analysis of 7 million authors (with >5 papers) in Scopus data set, divided into 176 fields.
†Co-author self-citation: self-citations to a paper by any co-author are counted as self-citations in each co-author's record.

SOURCE: JEROEN BAAS, UNPUBLISHED ANALYSIS OF SCOPUS DATABASE

CONTEXT MATTERS

An unusual feature of Ioannidis's study is its wide definition of self-citation, which includes citations by co-authors. This is intended to catch possible instances of citation farming; however, it does inflate self-citation scores, says Marco Seeber, a sociologist at Ghent University in Belgium. Particle physics and astronomy, for example, often have papers with hundreds or even thousands of co-authors, and that raises the self-citation average across the field.

Ioannidis says that it's possible to account for some systematic differences by comparing researchers with the average for their country, career stage and discipline. But more generally, he says, the list is drawing attention to cases that deserve a closer look. In unpublished work, Elsevier's Baas says that he has applied a similar analysis to a much larger data set of 7 million scientists: that is, all authors listed in Scopus who have published more than 5 papers. In this data set, Baas says, the median self-citation rate is 15.5%, but as many as 7% of authors have rates above 40%. This proportion is much higher than among the top-cited scientists, because many of the 7 million researchers have only a few citations overall or are at the start of their careers. Early-career scientists tend to have higher self-citation rates because their papers haven't had time to amass many citations from others.

According to Baas's data, Russia and Ukraine stand out as having high median self-citation rates (see 'Country by country'). His analysis also shows that some fields stick out — such as nuclear and particle physics, and astronomy and astrophysics — owing to their many multi-authored papers (see 'Physics envy?'). Baas says he has no plans to publish his data set, however.

NOT GOOD FOR SCIENCE?

Although the *PLoS Biology* study identifies some extreme self-citers and suggests ways to look for others, some researchers say they aren't convinced that the self-citation data set will be helpful, in part because this metric varies so much by research discipline and career stage. "Self-citation is much more complex than it seems," says Vincent Larivière, an information scientist at the University of Montreal in Canada.

Srivastava adds that the best way to tackle excessive self-citing — and other gaming of citation-based indicators — isn't necessarily to publish ever-more-detailed metrics to compare researchers against each other. These might have their own flaws, he says, and such an approach risks sucking scientists even further into a world of evaluation by individual-level metrics, the very problem that incentivizes gaming in the first place.

"We should ask editors and reviewers to look out for unjustified self-citations," says Srivastava. "And maybe some of these rough metrics have utility as a flag of where to look more closely. But, ultimately, the solution needs to be to realign professional evaluation with expert peer judgement, not to double down on metrics." Cassidy Sugimoto, an information scientist at Indiana University Bloomington, agrees that more metrics might not be the answer: "Ranking scientists is not good for science."

Ioannidis, however, says his work is needed. "People already rely heavily on individual-level metrics anyhow. The question is how to make sure that the information is as accurate and as carefully, systematically compiled as possible," he says. "Citation metrics cannot and should not disappear. We should make the best use of them, fully acknowledging their many limitations." ■

Richard Van Noorden *is a features editor with* Nature *in London.* **Dalmeet Singh Chawla** *is a freelance science journalist in London.*

1. Ioannidis, J. P. A., Baas, J., Klavans, R. & Boyack, K. W. *PLoS Biol.* **17**, e3000384 (2019).
2. King, M. M., Bergstrom, C. T., Correll, S. J., Jacquet, J. & West, J. D. *Socius* https://doi.org/10.1177/2378023117738903 (2017).
3. Mishra, S., Fegley, B. D., Diesner, J. & Torvik, V. I. *PLoS ONE* **13**, e0195773 (2018).
4. Seeber, M., Cattaneo, M., Meoli, M. & Malighetti, P. *Res. Policy* **48**, 478–491 (2019).
5. COPE Council. *COPE Discussion Document: Citation Manipulation* (COPE, 2019).
6. Flatt, J. W., Blasimme, A. & Vayena, E. *Publications* **5**, 20 (2017).

COMMENT

RONALDO SCHEMIDT/AFP/GETTY

An archaeologist works on the osteological collection at the Anthropology National Museum in Mexico City.

Use ancient remains more wisely

Researchers rushing to apply powerful sequencing techniques to ancient-human remains must think harder about safeguarding, urge **Keolu Fox** and **John Hawks**.

The study of ancient-human populations and our now-extinct close relatives has thrived over the past decade, as genetic material is examined with cheaper and more sophisticated sequencing technologies. Only nine years ago, the partial sequencing of a Neanderthal genome was a major scientific achievement[1]. Today, researchers are pursuing what many have termed a factory-like approach to analysing ancient DNA[2], with the processing of hundreds of samples.

As a result, we have a much better understanding of (among other things) which human populations interbred with Neanderthals, and which didn't[3]; how people dispersed across Europe during the Bronze Age[4]; and how pastoralism developed in Africa[5].

But such progress comes at a price.

Extracting the best-quality DNA from ancient remains requires the partial destruction of those specimens. And once bones, teeth, hair and so on are ground ▶

into dust, future opportunities for using them to understand our past are lost.

We recognize the enormous potential of ancient DNA to help reveal human history. In fact, as long as interested parties give their consent, we are hoping to apply genomics to the remains of Hawaiian men and women who lived hundreds to thousands of years ago. (Our aim is to understand how the introduction of leprosy, smallpox, syphilis and other diseases from European colonialists in the eighteenth century have shaped the genomes of Native Hawaiians today.) We also recognize that some leading labs are taking steps to reduce the destructiveness of sampling, for instance by developing techniques that allow ancient-DNA sequences and radiocarbon dates to be obtained from the same sample instead of from multiple ones[6].

Yet we are becoming increasingly concerned. To our knowledge, no one currently has a full list of all the samples from ancient humans and closely related species examined so far (meaning samples ranging from hundreds to tens of thousands of years old). No one is tracking the success rate of data recovery across laboratories and samples. And no one knows how many specimens are left.

With such a rapid scale up in analytical capacity, the diverse stakeholders involved (archaeologists, molecular biologists and bioinformaticians; editors and journalists; museum curators; and the descendants of the populations being studied) must talk. They need to establish how to balance discovery now with the need to safeguard cultural remains in the long term.

Unless some ground rules are established, future scientists, armed with better, potentially less-invasive methods for extracting DNA from ancient samples[7] could well look back on this era as a time of heedless destruction, fuelled by the relentless pressure to publish — or what one anthropologist has described as an "impetuous anxiety for discovery"[8].

HOW BAD IS IT?

Over the past ten years, there have been tremendous successes in education and engagement efforts that aim to bring a broader range of people (including those with interests and responsibilities as descendants of particular ancient communities) into consultations about genetic research. For instance, since 2011, a growing consortium of genomicists, now in North America, Hawaii, Finland, New Zealand and Australia, have helped to guide summer training programmes for Indigenous people. These educate students about the potential uses and misuses of genomics, including ancient genomics, as well as how to sequence DNA.

Yet irrevocable decisions continue to be made about the sampling of ancient specimens, guided by the immediate research interests of a few.

As an example, many researchers focus their sampling effort on the petrous bone, the hard portion of the temporal bone at the base of the skull, which houses the intricate structures of the inner ear. This dense bone contains a high concentration of endogenous DNA.

Last year, a team looking at the morphology of the inner ear noted that researchers were breaking open bony labyrinths and drilling into hundreds of petrous bones for DNA without first taking photographs, or using scanning techniques such as micro computed tomography (microCT) to make morphological records[9].

Petrous bone could contain uniquely high concentrations of other potentially informative biomolecules, such as protein or lipid biomarkers[10]. Also, because it contains the structures of the inner ear, including the semicircular canals and cochlea, intact bone could reveal insights about an individual's balance or hearing.

"Genomic research on ancient-human populations could hit a ceiling within decades."

Some laboratories have used microCT scanning, both to preserve data from petrous bone, and to guide their drilling to minimize destruction of the specimen[11]. Unfortunately, such methods have not been adopted as a standard, partly because individual groups tend to focus on their own research agenda rather than on the bigger picture.

Destruction of fragments of ancient bones or teeth is key to many techniques used in palaeoanthropology — including ancient proteomics, radiocarbon analysis, electron-spin resonance dating, stable-isotope sampling, dental-calculus sampling to assess what food people ate, and the sectioning of teeth for studies of growth. But so far, investigators and commentators have begun to routinely apply the terms 'DNA factory' or 'industrial-scale' only to ancient genomics (whether in publications, at conferences or on social media).

BONE BONANZA

The number of ancient samples used in DNA analyses has soared in recent years.

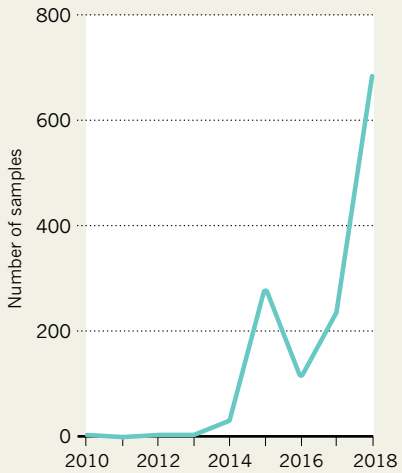

SOURCES: E CALLAWAY *NATURE* **555**, 573–576 (2018); DAVID REICH

Most of these other techniques are applied to tens of samples in any one study, occasionally to a single sample. Ancient genomics stands apart because the decreased cost of sequencing and the rapid acceleration of technologies have enabled some laboratories to pursue projects involving hundreds of samples. The publication of such large-scale studies has put pressure on others to use similarly impressive sample sizes. What's more, analysing the movement and evolution of ancient populations requires researchers to compare the genome of any one sample with those of as many of the individual's ancient contemporaries as possible. Thus, studies involving bigger sample sizes provide more reference data for other investigators to draw on, creating a feedback loop.

RETHINK PERSPECTIVE

In our view, two changes need to be implemented in ancient genomics research.

Give diverse stakeholders a say. Currently, a patchwork of regulations and institutions determines whether destructive research on ancient human remains can proceed. In some jurisdictions, Indigenous communities are formally involved in decision-making for research that involves the bones of their ancestors. In others, the decision could rest in the hands of a single curator.

But on its current trajectory (see 'Bone bonanza'), genomic research on ancient-human populations, or on close extinct relatives, could hit a ceiling within decades because of the scarcity of ancient remains. It is therefore urgent that, rather than sequencing an ancient genome in the hope that something interesting will emerge, researchers state up front what question they are seeking to answer — and that people with diverse perspectives evaluate their goals. Because human remains have intrinsic value and a role in the beliefs and cultures of many peoples of the world, as well as scientific value, decisions about whether or how to use them for research should be governed by a broad group, from researchers to the descendants of the populations being studied. For instance, if only three samples of a given ancient human population exist in the world, how many is it reasonable to destroy to answer a specific question about human migration?

JAMES KING-HOLMES/SPL

The petrous part of the temporal bone is used for radiocarbon dating.

This 'question-led' approach would enable people to consider the trade-off between collecting ancient DNA data today and waiting for future sequencing methods, which could potentially yield more information less expensively and less destructively[7]. (Sequencing DNA from ancient samples was much more hit and miss before the emergence in the mid- to late 2000s of targeted-capture next-generation sequencing, which enables researchers to separate endogenous from contaminant DNA, and then amplify it.) Also, greater engagement from more diverse stakeholders on how to handle scarce ancient remains as new technologies emerge will inspire conversations that bridge disciplines, lead to more accurate models and hypotheses and help form lasting partnerships. In our view, such an approach is crucial for fostering trust in a field in which, historically, the decisions of archaeologists and geneticists have led to deep distrust in many communities[12].

Create accountability. Just as timber and minerals are meticulously tracked at truck weighing stations and other venues to discourage the illegal acquisition of resources, curators, researchers and others must openly document the passage of ancient remains from one institution to another — and everything that happens to those remains along the way. With such a record, all ancient remains would be audited and people would know which specimens were ground into dust, but did not generate useful data, and which efforts generated data but did not result in a publication, and so on[13].

In the United States, the National Science Foundation (NSF) could take the lead on establishing such a database. Or grass-roots initiatives at museums, such as the Smithsonian Museum of Natural History in Washington DC or the Bernice Pauahi Bishop Museum in Honolulu, Hawaii, could help to shift practice. Buy-in from the research community could easily be obtained if referees and grantors required declaration of all sampling information. Importantly, such a decentralized approach would help to ensure that knowledge about ancient samples is not limited to a few groups[13].

WASTED RESOURCES

Many of the great archaeological sites of prehistory are now empty thanks to early archaeologists — sometimes little more than treasure-hunters — commanding armies of unskilled workers to scoop up the contents of caves, tombs and burial grounds. When so little was known, the bar was low; any discovery was interesting, and little or nothing was left for future generations. In fact, even as late as the 1990s, large sections of ancient human skeletons were destroyed for radiocarbon and other analyses that can now be accomplished using much smaller portions of bone.

Rather than repeat the mistakes of the past, future generations of scientists — from all countries of the world and from all sectors of society — must be given the opportunity to interpret our shared history. ■

Keolu Fox *is an assistant professor of biological anthropology at the University of California, San Diego.* **John Hawks** *is the Vilas-Borghesi Distinguished Achievement Professor of Anthropology at the University of Wisconsin–Madison.*
e-mails: pkfox@ucsd.edu; jhawks@wisc.edu

1. Green, R. E. *et al. Science* **328**, 710–722 (2010).
2. Reich, D. *Who We Are and How We Got Here: Ancient DNA and the New Science of the Human Past* (Oxford Univ. Press, 2018).
3. Wall, J. D. *et al. Genetics* **194**, 199–209 (2013).
4. Allentoft, M. E. *et al. Nature* **522**, 167–172 (2015).
5. Prendergast, M. E. *et al. Science* **365**, eeaw6275 (2019).
6. Korlević, P., Talamo, S. & Meyer, M. *Sci. Rep.* **8**, 4127 (2018).
7. McGrath, K. *et al. Sci. Rep.* **9**, 11027 (2019).
8. Kolodny, A. *In Search of First Contact: The Vikings of Vinland, the Peoples of the Dawnland, and the Anglo-American Anxiety of Discovery* (Duke Univ. Press, 2012).
9. Ponce de León, M. S. *et al. Proc. Natl Acad. Sci. USA* **115**, 4128–4133 (2018).
10. Collins, M. J. *et al. Archaeometry* **44**, 383–394 (2002).
11. Douka, K. *et al. J. Hum. Evol.* **107**, 86–93 (2017).
12. Claw, K. *et al. Hum Biol.* **89**, 177–180 (2017).
13. Casey, M. J. & Vigna, P. *The Truth Machine: The Blockchain and the Future of Everything* (St Martin's Press, 2018).

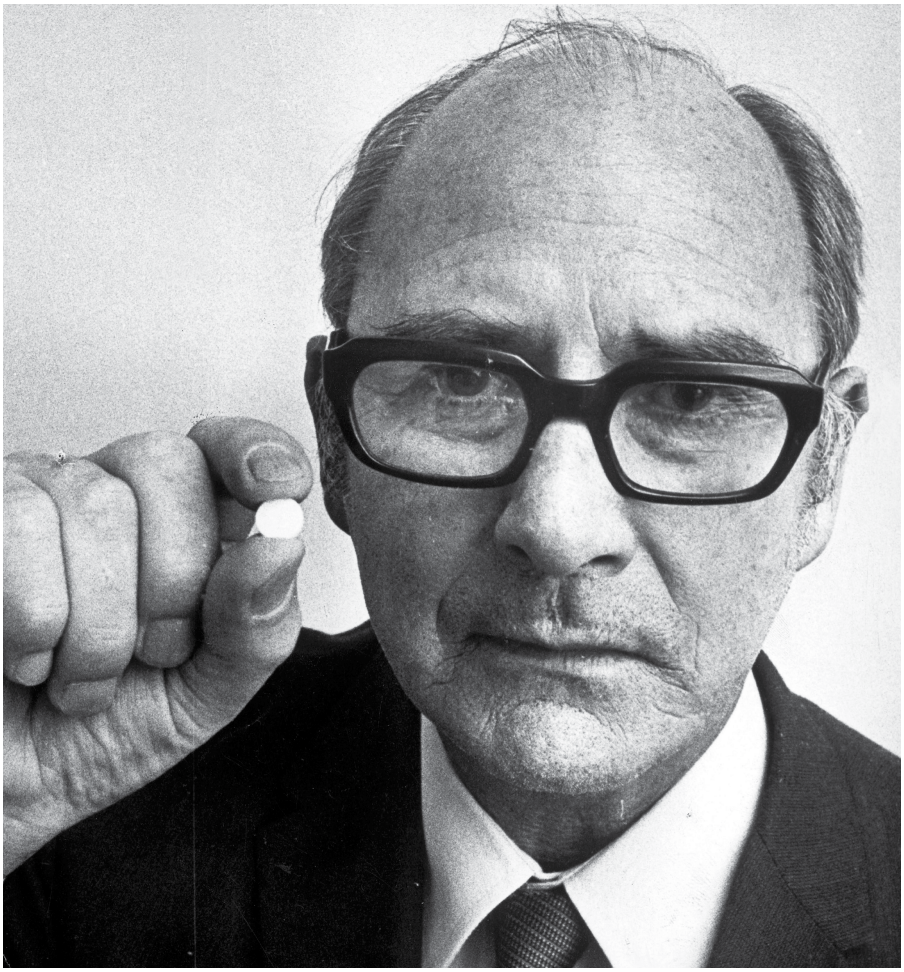

NEWS LTD/NEWSPIX

John Cade, pictured in 1974, was the first person to test lithium as a treatment for biopolar disorder.

PHARMACOLOGY

The serendipitous story of lithium

Douwe Draaisma praises a gripping history of psychiatry's most consistently effective medicine.

Some 70 years ago, John Cade, an Australian psychiatrist, discovered a medication for bipolar disorder that helped many patients to regain stability swiftly. Lithium is now the standard treatment for the condition, and one of the most consistently effective medicines in psychiatry. But its rise was riddled with obstacles. The intertwined story of Cade and his momentous finding is told in *Lithium*, a compelling book by US psychiatrist Walter Brown.

Bipolar disorder, labelled manic-depressive illness until 1980, affects around 1 in 100 people globally. Without treatment, it can become a relentless cycle of emotional highs and lows. Suicide rates for untreated people are 10–20 times those in the general population. Fortunately, lithium carbonate — derived from the light, silvery metal lithium — can reduce that figure tenfold.

Brown's telling of Cade's eventful life covers much of the same ground as *Finding Sanity* (2016), a rather hagiographic biography by Greg de Moore and Ann Westmore. What Brown does superbly well is to show that Cade made his discovery without access to advances in technology or to modern facilities — and almost despite them. His finding was the happy result of being forced to work with the simplest of means.

During the Second World War, Cade was interred for more than three years in the notorious Japanese prisoner-of-war camp at Changi in Singapore. He was put in charge of the psychiatric section, where he began to note the decisive link between certain food deficiencies and diseases in his fellow prisoners. A lack of B vitamins, for instance, caused beriberi and pellagra.

After the war, he pursued his investigations. Working from an abandoned pantry in Bundoora Repatriation Mental Hospital near Melbourne, Australia, he began to collect urine samples from people with depression, mania and schizophrenia, aiming to discover whether some secretion in their urine could be correlated to their symptoms. With no access to sophisticated chemical analysis and largely unguided by theory, Cade injected the urine into the abdominal cavities of guinea pigs, raising the dose until they died. The urine of people with mania proved especially lethal to the animals.

In further experiments at Bundoora, Cade found that lithium carbonate — which had been used to treat conditions such as gout since the nineteenth century — reduced the toxicity of patients' urine. Cade also noticed that a large dose of the medication tended to calm the guinea pigs. He could turn them on their backs, and the normally restive rodents would gaze placidly back at him. He wondered whether lithium could have the same tranquillizing effect on his patients. After trying it out on himself to establish a safe dose, Cade began treating ten people with mania. In September 1949, he reported fast and dramatic improvements in all of them in the *Medical Journal of Australia* (J. F. J. Cade *Med. J. Aus.* **2**, 349–351; 1949). The majority of these patients had been in and out of Bundoora for years; now, five had improved enough to return to their homes and families.

Cade's paper went largely unnoticed at the time. Soon, moving along the rows of the periodic table like a beachcomber on a shore, Cade began to experiment with salts of rubidium, cerium and strontium. None proved therapeutic. In 1950, he also abandoned his experiments with lithium. The therapeutic dose of lithium is dangerously close to a toxic dose, and that year one of his patients — "W.B.", a man with a 30-year history of bipolar disorder — appeared in the coroner's records as having died from lithium poisoning.

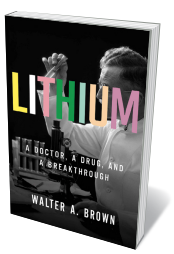

Lithium: A Doctor, a Drug, and a Breakthrough
WALTER A. BROWN
Liveright (2019)

Brown also weaves in the story of Mogens Schou. The Danish psychiatrist was as much a hero as Cade, fighting long and hard to get lithium accepted as a treatment for

bipolar disorder. He knew the condition intimately, because his brother had it. Starting in the 1950s, Schou teamed up with fellow psychiatrist Poul Baastrup to conduct a series of lithium experiments with ever stricter conditions, culminating in a double-blind, placebo-controlled clinical trial. Published in 1970 in *The Lancet*, this established beyond doubt that lithium was effective for most people with bipolar disorder, including Schou's brother (P. C. Baastrup *et al*. *Lancet* **296**, 326–330; 1970).

Today, lithium helps to stabilize the moods of millions of people with the condition, although the dose must be carefully controlled and it can have unpleasant side effects, such as nausea and trembling. Its mechanism is still something of a mystery. Most research targets the delicate chemistry supporting the functioning of neurotransmitters; but as yet, definitive results are lacking. Nor has the cause of the disorder been established. It is clear that there is a genetic component: if one of a pair of monozygotic twins (who share all their genetic material) has the disorder, there is around a 60% chance that the other will have it. In dizygotic twins, the figure is 10%.

"It is unlikely that a present-day researcher would get permission for experiments like Cade's."

Finishing *Lithium*, readers are left with a sense of paradox. The drug that set off the 'psychopharmacological revolution' of the 1950s, with antipsychotics and antidepressants arriving in its wake, is in many ways a stunning success. Yet it was developed in a ramshackle pantry, and the bottled urine samples were stored in the Cade family refrigerator. Moreover, in retrospect, the discovery of lithium seems in part related to an erroneous interpretation on Cade's part. The 'tranquillized' guinea pigs were probably showing the first symptoms of lithium poisoning: lethargy is still a warning sign of an overdose. And the step from guinea pigs to humans was a "conceptual leap", as Brown kindly puts it — hardly a deduction from sound theory. It is unlikely that a modern researcher would get permission for experiments such as Cade's.

Cade's findings could easily have foundered if Schou and others, such as US medical researcher John Talbott, hadn't followed up on his 1949 paper. Thus, hailing Cade as a trailblazer is valid — but without Schou and the rest, there would be no trail. Thanks to them all, this ubiquitous element, easily manufactured and never patented by pharmaceutical companies, remains both cheap and invaluable as a treatment for a troubling disorder. ■

Douwe Draaisma *is professor of the history of psychology at the University of Groningen in the Netherlands, and author of* Disturbances of the Mind.
e-mail: d.draaisma@rug.nl

Books in brief

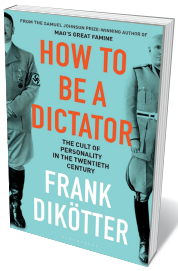

How to Be a Dictator
Frank Dikötter BLOOMSBURY *(2019)*
For this magisterial study on the misuse of power, historian Frank Dikötter analysed the strategies of eight brutal twentieth-century dictators. The result reveals how weak, largely unelectable men such as Adolf Hitler and Joseph Stalin maintained cults of personality through tireless self-glorification, aided by propaganda and the illusion of popular consent. Dikötter's insights into their modus operandi — "to sow confusion, to destroy common sense, to enforce obedience, to isolate individuals and crush their dignity" — make for salutary reading at a time of persistent attacks on democracy.

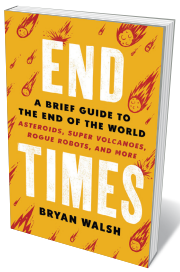

End Times
Bryan Walsh HACHETTE *(2019)*
In this sweeping "brief guide to the end of the world", journalist Bryan Walsh details the science on existential risks, from supervolcanoes to global war — many of them amplified by chaotic governance. He explores United Nations climate conferences, synthetic-biology labs and the US nuclear command-and-control system. He disentangles the maths of asteroid strikes and the complexities of gene editing. And, as billionaires focus on escape (boltholes in New Zealand, space colonization), Walsh envisions survival for the rest of us — a scenario of subterranean refugees subsisting on insects, fungi and rats.

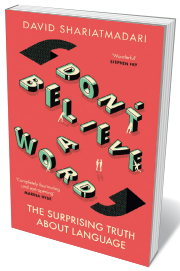

Don't Believe a Word
David Shariatmadari WEIDENFELD & NICOLSON *(2019)*
Language, notes writer David Shariatmadari, is a hall of mirrors: we can understand it only through language itself. His assured tour takes in the origins of language (he argues for nurture over nature) and deconstructs a plethora of myths. These include the supposed demise of linguistic standards, the question of animal communication, the vagaries of translation and the comparative richness of vocabularies. Insights abound, from the blurred boundary between Hindi and Urdu, to Australian languages in which the grammar changes when the speaker's mother-in-law is present.

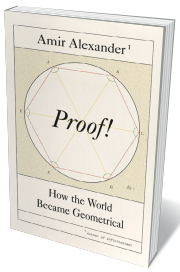

Proof!
Amir Alexander FARRAR, STRAUS AND GIROUX *(2019)*
In his opus *Elements*, fourth-century BC Greek mathematician Euclid created a "complete world of mathematical truths". Yet, as historian Amir Alexander's subtle chronicle shows, Euclid's ideas really blossomed only in the Renaissance. Then, luminaries such as Leon Battista Alberti codified what they saw as the hidden geometries of the Universe, including the rules of perspective. The geometric imperative went on to shape the French monarchy's rigidly hierarchical world view, symbolized by the formal gardens of Versailles, before emerging in the architecture of power from New Delhi to Washington DC.

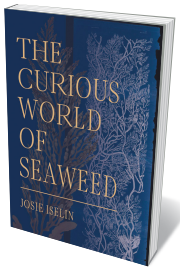

The Curious World of Seaweed
Josie Iselin HEYDAY *(2019)*
From the silken greens of *Ulva fenestrata* to the bulbous glories of *Botryocladia pseudodichotoma*, seaweeds are stars of the intertidal zone. This paean by Josie Iselin, a fine-art photographer, and writer celebrates both their remarkable morphology and tactility ("smooth and slimey and tough and stretchy"), and the history of phycology. Iselin studs her evocative text with exquisite 'portraits' of algal species — a mix of archival illustrations, snaps of historical specimens and luminous shots taken using a flatbed scanner. A mesmerizing swim through a liminal world. **Barbara Kiser**

Correspondence

Funding open-access papers after 2024

Several publishers are concerned about the timeline for implementing Plan S, the European initiative that will make all research papers free to access (see *Nature* **561**, 17–18; 2018). Their main concern is whether their markets will be ready for a 'pay to publish' model by 2024, when funders' support for transformative agreements ends. As co-chairs of the implementation task force of the international research-funder consortium cOAlition S (see www.coalition-s.org), we wish to clarify our position with regard to financially supporting the important transition to full open access after 2024.

We recommend that open-access publication fees should be covered by funders or research institutions, not by individual researchers (see go.nature.com/33rdttn). Our 2019 guidelines for implementing Plan S indicate how we, as funders, intend to help finance full and immediate open-access publication until 2024 (see *Nature* https://doi.org/gf3x2r; 2019).

After 2024, we will be encouraging institutional libraries and large consortia to switch from 'read and publish' agreements with publishers to 'pure publish' deals for portfolios of subscription journals that have become open-access journals. The cOAlition S funders will contribute to financing such deals, which will be more cost-effective and have fewer transaction costs than a single-paper charging system. The financial transaction would then no longer be between the author and the editor or journal, removing any concerns about perverse incentives for lax quality control.

We look forward to working with publishers who demonstrate leadership in this important new era of research reporting.

John-Arne Røttingen *Research Council of Norway, Oslo, Norway.*
David Sweeney *Research England, UK Research and Innovation, London, UK.*
jro@forskningsradet.no

Ditch mouse swim test for depression

Having practised psychiatry for 24 years, I was pleased to see that the value of the mouse 'forced-swim test' is being called into question by researchers studying human depression (*Nature* **571**, 456–457; 2019). Besides being shockingly cruel, this behavioural test misses the mark in approximating clinical depression in people.

Physical and emotional abuse (such as that associated with the test) is likely to induce hopelessness in humans and animals alike. In my experience, however, hopelessness is just one symptom of clinical depression in humans; abused people do not always meet the full criteria for major depressive disorder; and most individuals with the disorder are not currently being abused.

In my view, the complexity of human-brain function means that interpretations based on simplistic animal-behavioural testing are questionable. Data from clinical studies and from technologies that use human induced pluripotent stem cells offer a more rational approach for research into mental health.

Jaymie Shanker *Shaker Heights, Ohio, USA.*
jaymieshanker@gmail.com

Enable accreditation of scientific software

We would see improvements in the long-term accuracy and reliability of academic open-source software if journals required submitted software to be accredited, and if funders were to establish a mechanism for accrediting it (see *Nature* **571**, 133–134; 2019).

Funding bodies could improve the quality and reproducibility of scientific software by creating a software-engineering task force that would cover code reviews, training workshops and standards development, for example.

A software-standards accreditation scheme from large funding organizations would carry considerable clout and help to usher in cultural change. The scheme would ensure minimum standards in reproducibility, documentation and security. Different aspects such as code coverage (the proportion of code that is automatically tested) could be evaluated using automated metrics and tests.

Public parts of code would be subject to automated vulnerability testing for common security issues. They would also need to have basic application-programming-interface documentation, which describes how programmers can use each software function and how other code can interface with it.

Alexander L. R. Lubbock *Vanderbilt University, Nashville, Tennessee, USA.*
alex.lubbock@vanderbilt.edu

Keep a close eye on the tiger

The good news that India's wild tiger numbers have been increasing by 6% annually since 2006 is offset by reported declines in their habitat (see go.nature.com/2tig959). Habitat loss is a particular concern for the genetically unique populations in the northeast of the country. Conservation efforts must now focus on protecting those areas and improving the connectivity of the habitat corridors that are crucial for the animals' dispersal.

Tiger surveys, produced in conjunction with the Wildlife Institute of India, are run every four years by the Indian government. The 2018 survey was unprecedented in intensity and scale, with 77,000 tiger photographs taken from motion-triggered camera pairs placed in 27,000 locations. Together with some 35 million photos, it identified more than 80% of the country's 3,000 tigers.

Surveys on this scale entail sifting through tens of millions of wildlife photos, of which only a tiny fraction are of tigers. Research teams in India and elsewhere are developing artificial-intelligence tools to automate the process. This will improve conservation efforts worldwide by teaching us more about the effects of human pressures on the abundance and distribution of wildlife.

Chris Carbone *Zoological Society of London, UK.*
Matt Hayward *University of Newcastle, Australia.*
Joseph Bump *University of Minnesota, USA.*
chris.carbone@ioz.ac.uk
C.C., M.H. and J.B. declare competing interests; see go.nature.com/2z6tbiv.

Testing the impacts of sea-bed mining

Our DISCOL experiment of 1989 was intended to explore some of the environmental impacts of sea-bed mining (see *Nature* **571**, 465–468; 2019). It did not 'simulate' industrial mining of the deep sea as you imply, because it did not cause the type and extent of sea-floor disruption and habitat destruction that would be associated with commercial extraction processes. We simply provoked a mechanical disturbance of the sea floor and studied the recolonization and restoration of the disturbed area over a seven-year period.

Until industry has developed a test system for extracting metalliferous nodules from the sea floor, it will not be possible to simulate the actual impacts of mining or to monitor its effects on sediments and communities. It will then take time to do the environmental investigations and evaluations that are required before commercial mining can proceed.

Hjalmar Thiel, Gerd Schriever *Hamburg, Germany.*
hjalmar.thiel@hamburg.de

ELECTRONICS

Nanotube computer scaled up

Electronic devices that are based on carbon nanotubes have the potential to be more energy efficient than their silicon counterparts, but have been restricted in functionality. This limitation has now been overcome. SEE ARTICLE P.595

FRANZ KREUPL

For many decades, progress in electronics has been driven by a gradual reduction in the size of silicon transistors (electronic switches). However, this scaling is becoming increasingly difficult and is now yielding diminishing returns. Transistors based on semiconducting carbon nanotubes are clear front runners as replacements for silicon transistors in advanced microelectronic devices. But imperfections inherent in carbon nanotubes, and challenges in handling these tiny objects, have prevented their use in real-world microelectronic applications. On page 595, Hills *et al.*[1] report a major advance in this field: a 16-bit computer that is built entirely from carbon-nanotube transistors.

To achieve this milestone, the authors needed to develop a viable nanotube-transistor technology that provides two kinds of transistor: p-type metal–oxide–semiconductor (PMOS) and n-type metal–oxide–semiconductor (NMOS). In digital electronics, a computation is divided into a sequence of elementary (logic) operations that are carried out by components called logic circuits. The present design of these circuits in the electronics industry is based on complementary metal–oxide–semiconductor (CMOS) technology, which requires both PMOS and NMOS transistors.

A PMOS (or NMOS) transistor is switched on when a negative (or positive) voltage is applied to an electrode known as the gate. This electrode controls the conductivity of the channel (in this case, formed by carbon nanotubes) between two other electrodes (the source and the drain). When a PMOS transistor and an NMOS transistor are interconnected in series, the result is an element called an inverter (Fig. 1). If a low voltage is applied to such an inverter, the output voltage will be high, and vice versa. This element is the basic ingredient of all the logic circuits used in Hills and colleagues' computer.

The authors made their transistors by forming a network of randomly distributed, high-purity (99.99%) semiconducting nanotubes on a substrate. The formation process resembles pouring a bowl of cooked spaghetti onto a surface and then removing all the strands that are not in direct contact with the surface. The result is a substrate covered with roughly a single-layer of randomly oriented nanotubes.

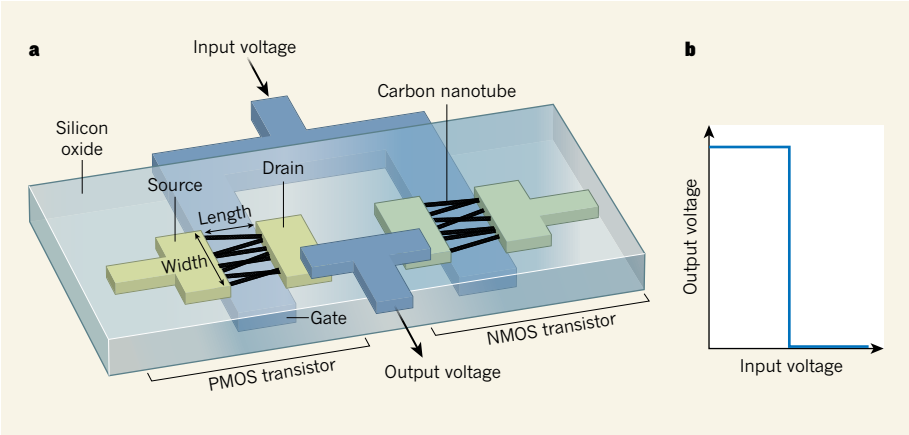

Figure 1 | A carbon-nanotube inverter. a, Hills *et al.*[1] demonstrate a computer that uses basic elements called inverters. Each of these inverters contains two kinds of transistor (electronic switch): a p-type metal–oxide–semiconductor (PMOS) transistor and an n-type metal–oxide–semiconductor (NMOS) transistor. These transistors are interconnected in series and are formed on a silicon oxide substrate. Each transistor consists of three electrodes known as the source, the gate and the drain; the source and the drain are separated by a channel that is formed of semiconducting carbon nanotubes. The micrometre-scale width and length of a channel are indicated. **b,** If a low voltage is applied to the inverter, the output voltage will be high, and vice versa.

Hills *et al.* then deposited metal on the nanotubes to connect them to the source and the drain. The work function of this metal (the energy needed to remove an electron from its surface) depended on whether the device was a PMOS or an NMOS transistor. The authors covered the rest of each nanotube with carefully selected and trimmed oxide materials, to isolate the nanotubes from their surroundings and to adjust their properties. In principle, the substrate does not need to be made of silicon; it simply needs to be flat. Moreover, the processing happens at relatively low temperatures (about 200–325 °C), so that stacking of further functional layers would easily be possible.

Contemporary computer design is based on libraries of standard cells — sets of logic operations that can be interconnected for greater functionality. Hills and colleagues devised all the standard cells required to make their computer's architecture using commercially available, conventional design tools. Because the semiconducting nanotubes had a purity of 99.99%, about 0.01% of them were metallic (non-semiconducting) and could have jeopardized the circuits. However, certain combinations of standard cells are more vulnerable to the presence of metallic nanotubes than are others. The authors therefore enforced modified design rules that excluded such vulnerable combinations. Equipped with these tools, they were able to design, fabricate and test their computer by letting it execute 'Hello, World' — a simple program that outputs the message "Hello, World" when run.

Hills and colleagues' nanotube computer is based on CMOS technology, runs 32-bit instructions on 16-bit data and has a transistor-channel length of roughly 1.5 micrometres. It can therefore be compared to the silicon-based Intel 80386 processor, which was introduced in 1985 and had similar specifications. The early 80386 could process its instructions at a frequency of 16 megahertz (see go.nature.com/33clr1a), whereas the nanotube computer has a maximum processing frequency of about 1 MHz. The reason for this difference lies in the capacitances (charge-storage abilities) of the electronic components, and in the amount of current that the smallest transistor can deliver.

Digital logic simply involves charging and discharging the transistor gates and the

interconnects. The speed of charging and discharging depends on the amount of current that a transistor can provide, which is related to the width and length of the transistor. A well-designed silicon transistor can deliver roughly one milliampere of current per micrometre of width (1 mA μm^{-1}) (see go.nature.com/2z4wjda). By contrast, the typical nanotube transistors used by Hills *et al.* can provide only about 6 $\mu A\ \mu m^{-1}$. This is the main feature that will need improvement in future versions of the computer.

The first step for increasing the electric current is to reduce the transistor-channel length. It has already been demonstrated[2] that the channel lengths of nanotube transistors can be scaled down to 5 nm. The second step is to increase the density of nanotubes in each channel from as little as 10 nanotubes per micrometre to 500 nanotubes per micrometre. For these networks of randomly distributed nanotubes, there might be an upper limit on the achievable density, but a deposition technique has been shown[3] to boost the current in such networks to 1.7 mA μm^{-1}. The third step is to decrease the width of the transistors, and thereby the widths of the source and the drain, which would allow these electrodes to be charged and discharged more quickly[4]. These scaled-down transistors are essential for nanotube-based CMOS technology that operates at gigahertz frequencies[5].

Hills and colleagues' achievement is based on averaging the performances of several nanotubes in each transistor channel. In the large-scale nanotube computer of the distant future, the PMOS and NMOS transistors will contain only one nanotube. These nanotubes will need to be semiconducting: no design trick will provide a workaround if one of the two nanotubes in an inverter is metallic.

The authors' work is a great accomplishment that touches on many research topics — from materials science to processing technology, and from circuit design to electrical testing. However, more effort is required before the team will need a sales department. ■

Franz Kreupl *is in the Department of Hybrid Electronic Systems, Technical University of Munich, 80333 Munich, Germany.*
e-mail: franz.kreupl@tum.de

1. Hills, G. *et al. Nature* **572**, 595–602 (2019).
2. Qiu, C. *et al. Science* **355**, 271–276 (2017).
3. Zhong, D., Xiao, M., Zhang, Z. & Peng, L.-M. *2017 IEEE Int. Electron Devices Meet.* 5.6.1–5.6.4 (2017).
4. Cao, Q., Tersoff, J., Farmer, D. B., Zhu, Y. & Han, S.-J. *Science* **356**, 1369–1372 (2017).
5. Han, S.-J. *et al. Nature Nanotechnol.* **12**, 861–865 (2017).

TUMOUR BIOLOGY

Cells tagged near an early spread of cancer

Cancer cells that travel to a distant site can prompt the normal neighbouring cells at that location to create a tumour-promoting microenvironment. A tool that identifies these normal cells offers a way to study this process. SEE ARTICLE P.603

MARIE-LIESSE ASSELIN-LABAT

Most types of cancer are lethal after tumour cells have left their primary site of growth and moved to colonize a distant organ through a process termed metastasis. Whether a cancer cell will metastasize is determined not only by the cell itself, but also by the microenvironment of that far-away site called the metastatic niche[1]. Only a small number of the cells that reach such a new location will successfully establish a presence there and proliferate[2]. The early processes that aid cancer-cell growth at secondary locations remain poorly understood, partly because of a scarcity of suitable tools with which to analyse these events. On page 603, Ombrato *et al.*[3] describe an innovative *in vivo* method for identifying and isolating the rare normal cells that are in close contact with cancer cells that have just migrated to a secondary site. This approach should help to clarify the early direct interactions between metastatic cells and neighbouring normal cells that help to shape the formation of a metastatic niche.

Ombrato and colleagues engineered mouse breast cancer cells to express a fluorescent protein containing a region of amino-acid residues that make it permeable to lipids (Fig. 1); this feature enabled the protein to be released from the cancer cell in a soluble form that could be taken up by neighbouring cells. The authors studied a model of metastasis in which mouse breast cancer cells that expressed this protein, plus a different fluorescent protein that could be used to specifically monitor cancer cells, were injected into the mouse tail vein and subsequently colonized the lung.

Analysis of lung tissue revealed that healthy cells located within a distance of five cell layers from cancer cells took up the protein, enabling the specific analysis of healthy cells in close contact with an emerging site of tumour growth. Ombrato *et al.* noted a direct correlation between the number of cancer cells in the lung and the number of neighbouring cells that took up the protein. These neighbouring cells included immune cells, which are known[4] to aid the colonization of the lung by breast cancer cells.

Previous studies have used other techniques to identify cells in the vicinity of malignant tumours, by, for example, tagging the cells that specifically receive vesicles released from tumour cells[5]. The advantage of Ombrato and colleagues' technique is that it offers a way to tag probably any type of cell present in the vicinity of a metastatic site.

The lipid-permeable fluorescent protein is

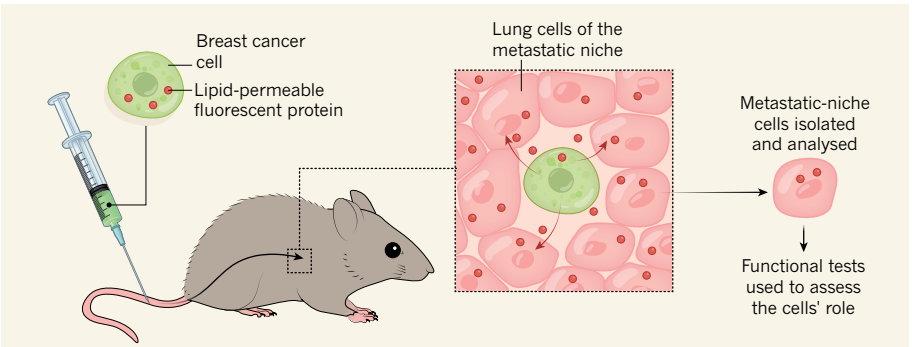

Figure 1 | A tool for identifying healthy cells in the vicinity of cancer cells. Ombrato *et al.*[3] engineered a fluorescent protein to contain amino-acid residues conferring lipid permeability, which enables the protein to enter cells. The authors engineered mouse breast cancer cells to express this protein, and injected the cells into the tail veins of mice. The cancer cells then colonized lung tissue at a site that is termed a metastatic niche. The fluorescent protein released there from tumour cells was taken up by the neighbouring healthy lung cells. The authors carried out direct *in situ* analysis, using approaches such as microscopy, to assess these healthy cells of the metastatic niche. The lung tissue was then removed, and the presence of the lipid-permeable fluorescent protein permitted the isolation and molecular characterization of these cells. This information allowed the authors to carry out functional tests *in vitro* to study how this type of healthy cell affects tumour growth.

stable in recipient cells for only approximately 48 hours. Thus, the authors' method allows an evaluation of the initial changes that occur at metastatic sites through time, but is not suitable for long-term tracking.

Cancer cells can alter their local environment to promote tumour growth through processes such as driving blood-vessel formation to increase nutrient supply, or causing changes that protect the tumour against immune attack[6]. The rare cancer cells that successfully thrive at a distant site usually alter the microenvironment there to promote their growth by, for example, starving normal cells of metabolite molecules to increase nutrient availability[7], or preparing a microenvironment that promotes tumour growth[8,9]. Ombrato and colleagues used their tool to identify and isolate healthy cells for molecular analysis by methods that included RNA sequencing, to track changes that might promote the formation of the metastatic niche.

The authors showed that normal lung cells (of a type called an epithelial cell) that surrounded invading breast cancer cells belonged to a cell lineage known as alveolar type 2 (AT2) cells. Metastasizing cells benefited from this type of microenvironment, as demonstrated by Ombrato and colleagues' observation that cancer cells grown with lung epithelial cells *in vitro* had a high proliferation rate.

The AT2 cells that the authors identified in the vicinity of the invading cancer cells also had characteristics of a comparatively undifferentiated sort of lung cell — a stem cell[10–14]. In the lung, most AT2 cells are fully differentiated, with only a small subset behaving like stem cells[15]. Do these cancer cells prefer to locate near lung stem cells, or do they drive the recruitment of such cells to their vicinity? Alternatively, might the cancer cells drive neighbouring differentiated AT2 cells to take on a stem-cell-like fate?

To investigate these possibilities, Ombrato and colleagues studied cancer cells grown *in vitro* with AT2 cells. This revealed that the presence of the cancer cells boosted the capacity of AT2 cells to act as stem cells and to give rise to various types of differentiated lung cell, compared with AT2 cells grown in the absence of cancer cells.

Future *in vivo* studies combining Ombrato and colleagues' labelling approach with other methods for tracing the lineage of lung stem cells will undoubtedly help to resolve how metastatic breast cancer cells create a microenvironment that nurtures tumour cells in the lung. The observation that breast cancer cells form a metastatic niche near lung stem cells is reminiscent of a previous observation: when prostate cancer cells metastasize to the bone, they settle near stem cells in the bone marrow, which helps to provide an environment that supports tumour growth[16].

Ombrato and colleagues' method holds great promise for addressing why a given type of cancer cell preferentially migrates to a particular initial secondary site, such as the bone marrow or lung. This key question has not been fully answered. Using the authors' technique to study breast cancer cell lines that have distinct organ preferences for their secondary sites[17] should provide insight about the mechanisms underlying such preferences.

It will be important to determine whether the authors' findings in mice are relevant for human cancer. In samples of human lung tissue containing metastatic breast cancer cells, Ombrato *et al.* found that lung epithelial cells neighbouring the tumour expressed a higher level of a protein associated with proliferation than did lung epithelial cells located farther away from the site of tumour invasion. Analyses to understand how this type of dividing cell supports breast cancer growth are essential areas for future studies.

If migrating tumour cells could be prevented from lodging in distant organs, this would have a major positive clinical impact. Because cancer cells often have a high level of genomic alteration, focusing instead on their neighbouring cells, which are genetically more stable, might be an effective strategy for targeting a metastatic niche. The complexity of the microenvironment at such sites, in which components such as immune and non-immune cells affect the settlement of cancer cells, will need to be characterized in depth to test whether manipulation of such regions is a potential therapeutic strategy. Ombrato and colleagues' method provides a crucial way forward for such endeavours. ■

Marie-Liesse Asselin-Labat *is in the Personalised Oncology Division, Walter and Eliza Hall Institute of Medical Research, University of Melbourne, Parkville 3052, Australia, and in the Cancer Early Detection and Advanced Research Centre, Knight Cancer Institute, Oregon Health and Science University, Portland, Oregon, USA.*
e-mail: labat@wehi.edu.au

1. Quail, D. F. & Joyce, J. A. *Nature Med.* **19**, 1423–1437 (2013).
2. Obenauf, A. C. & Massagué, J. *Trends Cancer* **1**, 76–91 (2015).
3. Ombrato, L. *et al. Nature* **572**, 603–608 (2019).
4. Wculek, S. K. & Malanchi, I. *Nature* **528**, 413–417 (2015).
5. Zomer, A. *et al. Cell* **161**, 1046–1057 (2015).
6. Hanahan, D. & Weinberg, R. A. *Cell* **144**, 647–674 (2011).
7. Fong, M. Y. *et al. Nature Cell Biol.* **17**, 183–194 (2015).
8. Lee, J. W. *et al. Nature* **567**, 249–252 (2019).
9. Liu, Y. *et al. Cancer Cell* **30**, 243–256 (2016).
10. McQualter, J. L., Yuen, K., Williams, B. & Bertoncello, I. *Proc. Natl Acad. Sci. USA* **107**, 1414–1419 (2010).
11. Kim, C. F. B. *et al. Cell* **121**, 823–835 (2005).
12. Zacharias, W. J. *et al. Nature* **555**, 251–255 (2018).
13. Chapman, H. A. *et al. J. Clin. Invest.* **121**, 2855–2862 (2011).
14. Treutlein, B. *et al. Nature* **509**, 371–375 (2014).
15. Nabhan, A. N., Brownfield, D. G., Harbury, P. B., Krasnow, M. A. & Desai, T. J. *Science* **359**, 1118–1123 (2018).
16. Shiozawa, Y. *et al. J. Clin. Invest.* **121**, 1298–1312 (2011).
17. Aslakson, C. J. & Miller, F. R. *Cancer Res.* **52**, 1399–1405 (1992).

ARTHRITIS

An immune-cell barrier protects joints

Inflammation and the repair of damaged tissues are regulated by immune cells called macrophages. The finding that they form a layer that shields mouse joints from damage has implications for the treatment of arthritis. SEE LETTER P.670

CHRISTOPHER D. BUCKLEY

Immune cells called macrophages commonly function as scavenger-like (phagocytic) cells that ingest and remove damaged cells. Culemann *et al.*[1] report on page 670 that the macrophages present in joints also fulfil an unexpectedly different role.

Macrophages derive from two main cellular lineages[2]. One lineage arises from bone-marrow-derived immune cells called monocytes. The other lineage is monocyte independent, and is derived from cells that disperse into the tissues during embryonic development[2]. The tissue-resident macrophages in this lineage have distinctive gene-expression profiles[3,4] that depend on the particular tissue in which they reside.

Rheumatoid arthritis is an immune-mediated disease associated with inflammation and the destruction of the cartilage and bone in joints, and macrophages have a key role in the initiation of this condition. However, little is known about the relative contribution of the two lineages of macrophages to the development and function of joints in health and disease. To add to the complexity, macrophages exist as various subsets, some of which are pro-inflammatory, whereas others are anti-inflammatory and aid tissue repair[5].

To study macrophages, the authors began by focusing on a protein called CX3CR1, which is expressed on monocytes and macrophages. The authors engineered CX3CR1-expressing

cells in mice to make a red fluorescent protein so that the cells could be tracked *in vivo*. These cells were monitored in knee joints using an approach called 3D light-sheet fluorescence microscopy, and the joint tissue was treated using a technique that enabled the authors to obtain 'optical clearance', which improves the visualization of internal structures[6].

Unexpectedly, the authors' observations revealed that CX3CR1-expressing macrophages exist as a layer of cells that forms a barrier, similar to a thin protective membrane, in the healthy joint (Fig. 1). This barrier forms as an outer layer of cells in the synovium, a region of the tissue that lines the joint. The barrier layer forms in a part of the synovium called the lining layer, and it physically separates the synovial fluid (which bathes the joint) from the sublining layers of the synovium. The CX3CR1-expressing barrier-forming macrophages are found adjacent to a layer of cells called fibroblasts in the lining layer.

The authors carried out RNA sequencing, including single-cell sequencing, to profile the barrier macrophages. These cells express genes typically associated with barrier formation in a type of non-immune cell called an epithelial cell. For example, the macrophage profile included genes that encode proteins associated with the formation of a structure called a tight junction that connects epithelial cells by forming a 'seal' between adjacent epithelial cells. This is surprising, because macrophages are usually thought of as having a signalling or scavenging role, rather than having a structural, barrier-like function.

Using a mouse model of arthritis in which macrophages could be tracked by engineering them to be fluorescent, the authors observed that the barrier layer was highly dynamic. When arthritis was induced, the layer underwent active remodelling that loosened the physical interactions between barrier macrophages and lining-layer fibroblasts. Like other types of tissue-resident macrophage, the barrier macrophages can ingest and remove inflammatory immune cells called neutrophils that accumulate and die in the synovial fluid in arthritis.

When the authors induced arthritis in mice at the same time as they disrupted the barrier-forming layer of macrophages through genetic or pharmacological manipulation, arthritis was more severe than in animals in which the layer was intact. It would be interesting to test whether transferring barrier macrophages directly into mouse joints could suppress arthritis.

To explore the origin of the barrier-forming, CX3CR1-expressing macrophages, the authors used intricate fate-mapping experiments, which revealed that these cells are not derived from monocytes. They also found that monocytes did not give rise to the other type of macrophage that resides in the joint, termed an interstitial synovial macrophage, which populates the sublining layer. The authors' data are consistent with a model in which interstitial macrophages give rise to barrier macrophages.

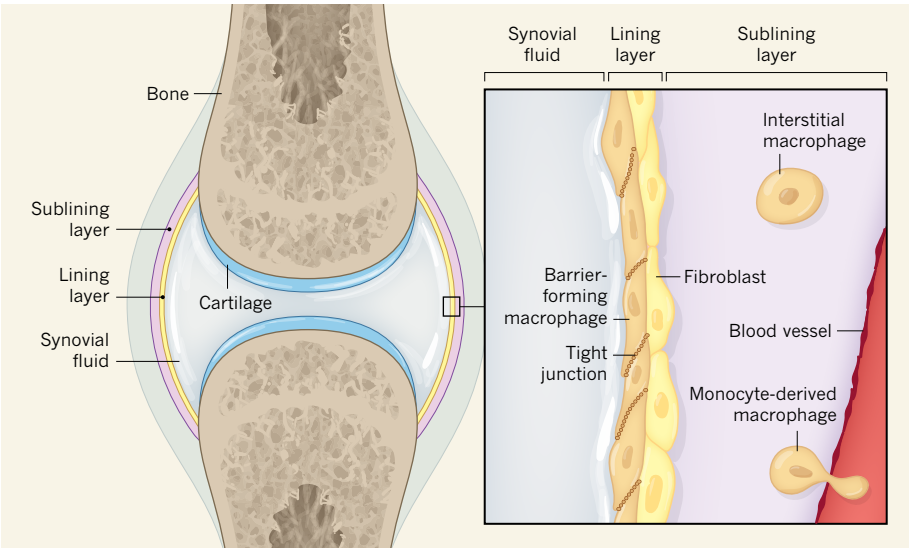

Figure 1 | Barrier macrophages in the joint. Culemann *et al.*[1] studied immune cells called macrophages in mouse and human joints. Joints are surrounded by a tissue called the synovium, which is formed from layers of cells called the lining and the sublining layers. The authors discovered that certain macrophages form a cell layer that protects joints from the inflammatory immune-cell attacks on bone and cartilage that are associated with arthritis. This barrier is formed in the lining layer, adjacent to a layer of cells called fibroblasts. The barrier-forming macrophages express proteins associated with a type of barrier-forming cell called an epithelial cell, and these proteins form structures called tight junctions that 'seal' cells together. Barrier-forming macrophages arise from a type of macrophage called an interstitial macrophage, which resides in the sublining layer. By contrast, non-resident macrophages enter the joint from blood vessels. These cells, which can drive inflammation, arise from immune cells called monocytes.

RNA-sequencing experiments revealed that interstitial macrophages can be divided into two groups. One group expresses the gene *Retnla*, whereas the other has a high level of expression of the genes that encode the proteins MHC class II and aquaporin. Cells of the latter group divide and differentiate to form either barrier macrophages, or interstitial macrophages that express *Retnla*.

To analyse the macrophage subsets that arise as arthritis develops, compared with those present in an uninflamed joint, the authors carried out further single-cell RNA sequencing. As expected from previous work[7], monocyte-derived macrophages that produce pro-inflammatory molecules accumulated in the arthritic joint. They are recruited into the joint from the bloodstream, exiting blood vessels to enter the sublining layer. During the influx of these pro-inflammatory macrophages, the barrier macrophages maintained their anti-inflammatory role, expressing the proteins needed for them to remove dead neutrophils from the joint.

When the authors compared their single-cell RNA data from mice with similar data sets[8] available from an analysis of the joints of people with rheumatoid arthritis, the gene-expression profiles of the macrophage subsets matched up between the two species. This suggests that cells similar to the barrier and interstitial macrophages in mice might also exist in humans, and thus be relevant to human disease.

The authors found that barrier macrophages were almost totally absent in synovial samples from people with active rheumatoid arthritis, whereas they made up 10% of the macrophage population in samples from people who have osteoarthritis, a type of arthritis that is not associated with inflammation. It would be interesting to learn whether the population of barrier macrophages is restored in people whose rheumatoid arthritis is being successfully treated and is in remission.

Culemann and colleagues' work adds to studies[3,4,9] showing that macrophages are exquisitely adapted to the functions they perform in the tissues in which they reside. Barrier macrophages join a growing list of types of macrophage that shield tissues from damage caused by infection, inflammation or cancer. Tissue-resident macrophages can prevent neutrophil-mediated inflammatory damage by physically shielding damaged tissue from neutrophils[10]. Furthermore, in large body cavities, such as those surrounding the gut, heart and lungs, specialized macrophages have been described that are thought to repair mechanical damage[3,9]. These findings also complement the discovery of distinct subsets of fibroblasts, located in the sublining or lining regions of the joint, which, respectively, drive either inflammation or bone damage in arthritis[11]. The challenge that lies ahead will be to develop ways of specifically targeting subsets of macrophages and fibroblasts with the ultimate goal of developing new treatments for people with arthritis. ■

50 Years Ago

Medical geography could soon benefit considerably from computer graphics … Medical geography is concerned with variations in the incidence of disease in different areas and the link with possible causes connected with elements of the physical, biological and sociocultural environment. As such it is a topic in which maps should be valuable, but they are often of little use because of the time taken for such lengthy and repetitive processes as the calculation and statistical testing of attack rates, fatality rates, standardized mortality ratios and other disease indices. And it takes a long time to represent these indices in cartographic form. Computer graphics — the construction of maps and diagrams using the electronic computer — could have considerable potential in medical geography. They may, by the speed, efficiency and reliability of processing and mapping medical data, lead to a more effective use of maps.

From *Nature* 30 August 1969

100 Years Ago

The Medical Research Committee has issued a report … on the influence of alcohol on manual work and neuromuscular co-ordination. Accuracy and speed in typewriting and in using an adding machine, and accuracy in hitting spots on a target, were used as tests, and both pure alcohol and alcohol in the form of wine and spirit were employed. There was no distinct difference between the two forms of alcohol, and when very dilute (5 per cent.) the effect was about three-fourths as great as when taken strong (37–40 per cent.) for the same amount of alcohol … The degree of effect depended largely on whether the alcohol was taken on an empty stomach or with food; on an average it was twice as toxic under the former condition.

From *Nature* 28 August 1919

Christopher D. Buckley *is at the Institute for Inflammation and Ageing, College of Medical and Dental Sciences, University of Birmingham, Queen Elizabeth Hospital, Birmingham B15 2WD, UK, and at the Kennedy Institute of Rheumatology, University of Oxford, Oxford, UK.*
e-mail: c.d.buckley@bham.ac.uk

1. Culemann, S. *et al. Nature* **572**, 670–675 (2019).
2. Davies, L. C., Jenkins, S. J., Allen, J. E. & Taylor, P. R. *Nature Immunol.* **14**, 986–995 (2013).
3. Buechler, M. B. *et al. Immunity* **51**, 119–130 (2019).
4. Lavin, Y. *et al. Cell* **159**, 1312–1326 (2014).
5. Udalova, I. A., Mantovani, A. & Feldmann, M. *Nature Rev. Rheumatol.* **12**, 472–485 (2016).
6. Tainaka, K., Kuno, A., Kubota, S. I., Murakami, T. & Ueda, H. R. *Annu. Rev. Cell Dev. Biol.* **32**, 713–741 (2016).
7. Misharin, A. V. *et al. Cell Rep.* **9**, 591–604 (2014).
8. Zhang, F. *et al. Nature Immunol.* **20**, 928–942 (2019).
9. Wang, J. & Kubes, P. *Cell* **165**, 668–678 (2016).
10. Uderhardt, S., Martins, A. J., Tsang, J. S., Lammermann, T. & Germain, R. N. *Cell* **177**, 541–555 (2019).
11. Croft, A. P. *et al. Nature* **570**, 246–251 (2019).

This article was published online on 7 August 2019.

CONDENSED-MATTER PHYSICS

Superconductivity seen in a nickel oxide

Magnetism alone was thought to be responsible for superconductivity in copper oxides. The finding of superconductivity in a non-magnetic compound that is structurally similar to these copper oxides challenges this view. SEE LETTER P.624

GEORGE A. SAWATZKY

In 1986, scientists unexpectedly discovered that a lanthanum barium copper oxide, $La_{1.85}Ba_{0.15}CuO_4$, becomes a superconductor (has zero electrical resistance) below a relatively high temperature[1] of 35 kelvin. This result triggered one of the most intense experimental and theoretical research efforts in condensed-matter physics. Soon afterwards, many other copper oxides (cuprates) were found to superconduct at temperatures[2] of up to 133.5 K. However, after more than 30 years, there is no consensus regarding the underlying mechanism of cuprate superconductivity. On page 624, Li *et al.*[3] report that a neodymium strontium nickel oxide, $Nd_{0.8}Sr_{0.2}NiO_2$, superconducts below 9–15 K. This material has a similar crystal structure to that of the cuprate superconductors, suggesting that the authors' discovery could lead to a better understanding of superconductivity in these systems.

Superconductivity can occur in a metallic material if the usual repulsive interaction between electrons turns into an attractive one. In this scenario, the response of surrounding atoms to the charge and spin (magnetic moment) of electrons indirectly leads to electron pairing. At a low enough temperature, these paired electrons condense to form a superfluid (a state of matter that flows without friction), which exhibits zero electrical resistance[4]. The key to understanding superconductivity in a given material is to identify the mechanism that provides the 'pairing glue'.

In the conventional mechanism, the spatial displacement of atoms close to an electron forms an attractive region for another electron[4]. An analogy is that of two heavy balls on a spring mattress, whereby the indentation in the mattress made by one of the balls produces an attractive region for the other ball. However, some theoretical work has suggested that this effect is too small to account for the high-temperature superconductivity of the cuprates.

Researchers have therefore considered that the spins of moving electrons might cause deviations in the magnetic order (the ordered pattern of atomic spins) in the cuprates. With respect to the mattress analogy, these deviations represent mattress indentations, and the strong interactions between the spins of neighbouring Cu^{2+} ions represent the mattress springs. To understand how this mechanism works, consider the cuprate superconductor $La_{1.85}Ba_{0.15}CuO_4$, which is obtained from the compound La_2CuO_4 by replacing some lanthanum atoms with barium.

In La_2CuO_4, the electrons of a particular Cu^{2+} ion are prevented from moving by their strong repulsion to the electrons of surrounding Cu^{2+} ions. As a result, the material is an electrical insulator[5]. Each Cu^{2+} ion has an odd number of electrons and a net spin of 1/2. The ions have strong antiferromagnetic order, which means that the spins of neighbouring ions point in opposite directions.

When lanthanum in La_2CuO_4 is partially replaced with barium, electron vacancies called holes are introduced into the system in a process known as doping. These holes migrate to the planes of CuO_2 in the material. If their density is low enough, they act as freely moving charge carriers, resulting in metallic behaviour. The combination of a Cu^{2+} ion and a doped hole has an even number of electrons and a net spin of 0, which causes a severe disturbance in the spin directions of surrounding

Cu^{2+} ions. It is this change in the magnetic background associated with hole doping that leads to pairing.

Over the past 30 years or so, researchers have looked for superconductivity in other compounds that have planes containing spin-1/2 ions. Examples of such compounds are $LaNiO_2$ and $NdNiO_2$, which comprise alternating planes of lanthanum or neodymium and NiO_2. Ni^{1+} ions in these materials could have the same role in inducing superconductivity as do Cu^{2+} ions in $La_{1.85}Ba_{0.15}CuO_4$. Several groups have prepared $LaNiO_2$ and $NdNiO_2$ in both powder and thin-film form (see, for example, refs 6–8). However, no superconductivity (but also no sign of magnetic order) has been found.

Enter Li and colleagues. The authors grew a thin film of $NdNiO_2$ and then hole-doped this film by replacing some Nd^{3+} ions with Sr^{2+} ions. They found that the resulting material, $Nd_{0.8}Sr_{0.2}NiO_2$, superconducts at temperatures of up to 15 K. After some 30 years of trying, scientists have finally found a non-cuprate compound that has a cuprate-like structure and that exhibits superconductivity at surprisingly high temperatures. But, unlike in the cuprates, there is no sign of magnetic order in $NdNiO_2$ down to a temperature[8] of 1.7 K. The authors' discovery might therefore indicate that magnetism is not exclusively responsible for cuprate superconductivity.

However, this conclusion is based on the assumption that the cuprates and hole-doped $NdNiO_2$ have similar electronic structures. There are three reasons why this assumption might not be valid. First, in the cuprates, the holes reside mainly in the 2*p* electron orbitals of oxygen atoms. The spins of these holes couple antiferromagnetically to the spins of neighbouring Cu^{2+} ions, producing a net spin of 0. By contrast, in hole-doped $NdNiO_2$, the holes reside mostly in Ni^{1+} ions and result in Ni^{2+} ions that, in conventional oxides, have a spin of 1 (ref. 9). But perhaps the situation here is different from that of conventional oxides. X-ray spectroscopy could determine whether this is the case, if good enough samples are available.

Second, the antiferromagnetic coupling between spins might be substantially stronger in the cuprates than in $NdNiO_2$. This difference would be consistent with the absence of magnetic order in $NdNiO_2$. And third, a theoretical study[10] suggests that 5*d* electron orbitals of lanthanum atoms in $LaNiO_2$ and of neodymium atoms in $NdNiO_2$ are involved in electrical transport. If confirmed, this result could change the picture completely. In particular, local spins would be affected by being coupled to delocalized conducting electrons, as in compounds called Kondo systems[11]. Such systems exhibit a minimum in a plot of resistivity against temperature, which is observed by Li *et al.* for $NdNiO_2$.

There are therefore many issues to address before it can be concluded that the electronic structures of the cuprates and of hole-doped $NdNiO_2$ are similar. Future work should check that the nickel ions in $NdNiO_2$ are Ni^{1+} ions, determine the local symmetry and spin of the hole-doped states and explore how the temperature at which the material becomes superconducting varies with hole doping. The chemical composition of the material also needs to be verified, because unwanted hydrides or hydroxides might have formed. Nevertheless, Li and colleagues' work could become a game changer for our understanding of superconductivity in cuprates and cuprate-like systems, perhaps leading to new high-temperature superconductors. ■

George A. Sawatzky *is at the Stewart Blusson Quantum Matter Institute and in the Department of Physics and Astronomy, University of British Columbia, Vancouver, British Columbia V6T 1Z1, Canada.*
e-mail: sawatzky@physics.ubc.ca

1. Bednorz, J. G. & Müller, K. A. *Z. Phys. B* **64**, 189–193 (1986).
2. Schilling, A., Cantoni, M., Guo, J. D. & Ott, H. R. *Nature* **363**, 56–58 (1993).
3. Li, D. *et al. Nature* **572**, 624–627 (2019).
4. Bardeen, J., Cooper, L. N. & Schrieffer, J. R. *Phys. Rev.* **106**, 162–164 (1957).
5. Mott, N. F. & Peierls, R. *Proc. Phys. Soc.* **49**, 72–73 (1937).
6. Crespin, M., Levitz, P. & Gatineau, L. J. *Chem. Soc. Faraday Trans. 2* **79**, 1181–1194 (1983).
7. Hayward, M. A., Green, M. A., Rosseinsky, M. J. & Sloan, J. *J. Am. Chem. Soc.* **121**, 8843–8854 (1999).
8. Hayward, M. A. & Rosseinsky, M. *J. Solid State Sci.* **5**, 839–850 (2003).
9. Zaanen, J., Sawatzky, G. A. & Allen, J. W. *Phys. Res. Lett.* **55**, 418–421 (1985).
10. Lee, K.-W. & Pickett, W. E. *Phys. Rev. B* **70**, 165109 (2004).
11. Kondo, J. *Prog. Theor. Phys.* **32**, 37–49 (1964).

REGENERATIVE BIOLOGY

What makes flatworms go to pieces

Flatworms called planarians can break off fragments of themselves that regenerate to form new, complete worms. The molecular cues that regulate the frequency of such fission events have been revealed. SEE LETTER P.655

THOMAS W. HOLSTEIN

Understanding how tissues and organs can regenerate requires an appreciation of the mechanisms and factors that organize cells and tissues, both in space and through time. Planarian flatworms are a widely used model for studying such pattern formation because pieces of these animals that are cut off can regrow missing body parts and form complete worms. Planarians also have a self-scission behaviour called fission — they stretch and contract their tail tissue, which leads to detachment of parts of their posterior body that then grow into clones. Whether or not fission occurs depends on the size of the parent worm, but the underlying molecular and cellular processes have not been well understood. On page 655, Arnold *et al.*[1] establish a method to reliably induce fission in the planarian *Schmidtea mediterranea*, and show that cell-signalling pathways involving the proteins Wnt and transforming growth factor-β (TGF-β) are key regulators of this process.

Wnt signalling has a decisive role in development and cell differentiation and is involved in many diseases[2]. The Wnt proteins are highly diverse, are found only in animals and are usually attached to a lipid chain and secreted by cells. They bind to receptor proteins of different families to activate various downstream cell-signalling cascades that regulate the levels of cytoplasmic factors — molecules that control gene expression and, thus, cell function[2,3]. Although our knowledge of the influence of Wnt signalling on tissue-pattern formation has advanced greatly in the past few years, how such patterning might be linked to specific tissue functions is still unknown.

Previous studies[4–6] in planarians have characterized a molecular framework in which self-organized gradients of Wnt proteins regulate patterning along the length of the animal (that is, along the anterior–posterior axis), and in which a gradient of TGF-β regulates patterning from its topside to its underside (along the dorsal–ventral axis). It has been suggested[7] that planarian fission is regulated by gradients in metabolic activity, molecular positional cues or neurohormone molecules along the anterior–posterior body axis. One study indicated that fission might be inhibited by the front part of the nervous system[7], and another examined the biomechanical forces and tissue properties that enable it to occur[8].

Unlike regeneration, which can be induced experimentally by cutting planarian worms into pieces, fission has been difficult to induce reliably, limiting studies on this process. However, Arnold *et al.* found that transferring worms to cultures in which food was limited and water was stagnant induced fissioning in worms longer than about 4 or 5 millimetres

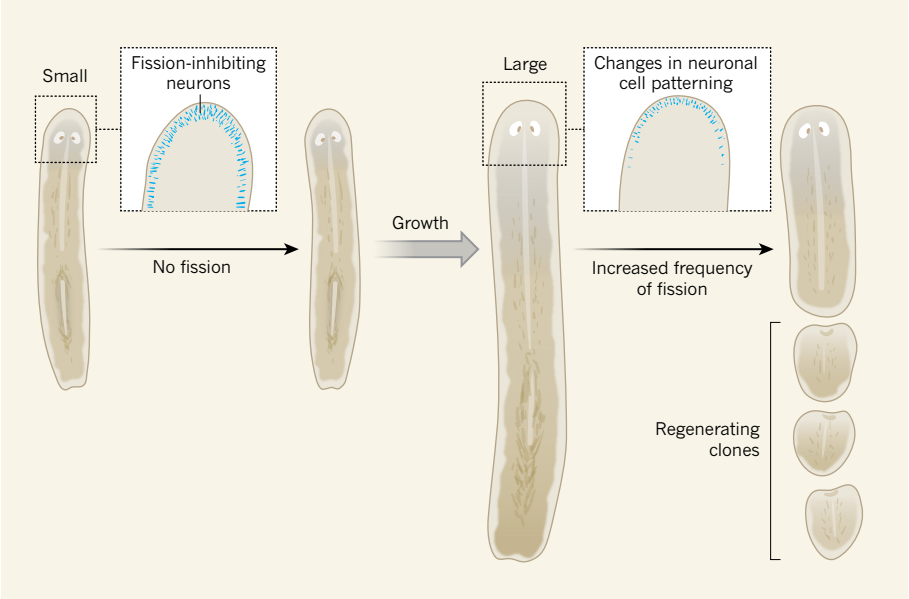

Figure 1 | Size-dependent fission behaviour in planarian flatworms. Planarian flatworms can reproduce through a process called fission. In this process, a worm breaks off a portion of tissue from the back end of its body, and this portion regenerates to form a complete worm. Arnold *et al.*[1] examined the molecular and cellular underpinnings of this fission process. They found that the frequency of fission events correlated with the size of the parent animal. Experimental disruptions of the expression of certain proteins involved in the Wnt signalling pathway (not shown), which controls tissue patterning along the length of planarians[4,5], did not affect the positioning of fission planes along the body, but did increase or reduce the frequency of fission events. The authors showed that Wnt signalling regulates the fine-scale patterning of a population of neuronal cells at the front of the worm (boxes) that inhibit fission behaviour, and showed that the patterning of these neurons changes with animal size.

(Fig. 1). By analysing image recordings, the researchers discovered that fission events take about 30 minutes and result in fragments that are about 1 mm long, and that the frequency of fission events correlates with the size of the parent. Arnold *et al.* also found that, when they applied pressure to a cover glass placed on top of a worm in normal culture, the worm would break apart into multiple, regularly spaced fragments along its entire anterior–posterior axis. This suggests that, in adult worms, there are pre-established fission planes that scale in number with the animal's size, and that a hidden, segmented structure underlies this size control.

Using both the starvation and compression methods to induce fission, the authors tested which molecular cues are required to induce size-dependent fissioning. They carried out a screen in which they used different RNA molecules to selectively inhibit the expression of various proteins involved in patterning, including those in the Wnt and TGF-β cell-signalling pathways[4,6,9,10]. These targeted disruptions affected fission frequency; for example, blocking the expression of APC, a protein that suppresses the Wnt signalling pathway, roughly doubled the frequency of sequential fission attempts in which the animals showed their characteristic stretching behaviour. However, interfering with these signalling pathways did not affect the positioning of fission planes along the body axis. Thus, Wnt and TGF-β signalling seem to regulate fission behaviour independently of their function in axial patterning.

A previous gene-expression analysis[11] revealed that genes encoding proteins involved in Wnt and TGF-β signalling are co-expressed with genes expressed by cells in the central nervous system (CNS). In Arnold and colleagues' study, removing the front part of the worm that contained the cephalic ganglia (two clusters of neurons that together comprise the planarian brain) delayed the onset of fission behaviour. The authors saw a similar effect in worms in which the expression of a neuronal transcription-factor protein that was previously shown to be required for CNS patterning[12] was suppressed.

Arnold *et al.* found that a set of neuronal cells that are sensitive to mechanical stimuli act downstream of Wnt and TGF-β signalling to inhibit fission behaviour. The authors demonstrated that Wnt and TGF-β signalling together regulate the patterning of these and other specific populations of neurons (Fig. 1). It will be exciting to examine how these key regulators of axial patterning control the fine patterning of the planarian nervous system[13] — one of the big questions about the patterning of different types of cell is how these signalling pathways are integrated by progenitor cells to induce the generation of specific neuronal cell types.

Although Arnold *et al.* focused their analysis on the induction of fission, even less is known about how the released tissue fragments form complete animals. For example, it is unclear whether these worms regenerate after fission in the same way that they regrow after being cut into pieces. In both cases, populations of stem cells called neoblasts cluster to form a mass called a blastema at the wound site in the tissue fragment, which in turn can regenerate different organs and tissues[14]. But how the information concerning the position of the cut or fission plane is transmitted to neoblasts is not clear.

Asexual reproduction through fission is a major strategy for increasing population size, not only in planarians, but also in other worm-like creatures (including acoels[15] and other acoelomorph flatworms[16], and annelids[17]) in which fission occurs at the posterior end of the animal. Sea anemones can also propagate asexually through fission[18], and budding — a fission-related strategy for asexual reproduction — has been well characterized in the freshwater animal *Hydra*[19] and is strongly related to regeneration[20].

Detailed investigation of fission and budding in different model organisms will be important because, in these processes, pattern formation is induced without injury, and therefore might be different from regeneration after injury. If the processes that enable regeneration in planarians after fission and after cutting are indeed the same, future research should determine the mechanisms that compensate for the lack of an injury signal in fissioning tissue. Such research will be crucial for understanding how injury and patterning signals converge to initiate the regeneration process. ■

Thomas W. Holstein *is in the Department of Molecular Evolution and Genomics, Centre for Organismal Studies, Heidelberg University, 69120 Heidelberg, Germany.*
e-mail: thomas.holstein@cos.uni-heidelberg.de

1. Arnold, C. P., Benham-Pyle, B. W., Lange, J. J., Wood, C. J. & Sánchez Alvarado, A. *Nature* **572**, 655–659 (2019).
2. Steinhart, Z. & Angers, S. *Development* **145**, dev146589 (2018).
3. Wiese, K. E., Nusse, R. & van Amerongen, R. *Development* **145**, dev165902 (2018).
4. Gurley, K. A., Rink, J. C. & Sánchez Alvarado, A. *Science* **319**, 323–327 (2008).
5. Niehrs, C. *Development* **137**, 845–857 (2010).
6. Stuckemann, T. *et al. Dev. Cell* **40**, 248–263 (2017).
7. Best, J. B., Goodman, A. B. & Pigon, A. *Science* **164**, 565–566 (1969).
8. Malinowski, P. T. *et al. Proc. Natl Acad. Sci. USA* **114**, 10888–10893 (2017).
9. Petersen, C. P. & Reddien, P. W. *Cell* **139**, 1056–1068 (2009).
10. Molina, M. D., Salo, E. & Cebria, F. *Dev. Biol.* **311**, 79–94 (2007).
11. Collins, J. J. III *et al. PLoS Biol.* **8**, e1000509 (2010).
12. Cowles, M. W., Omuro, K. C., Stanley, B. N., Quintanilla, C. G. & Zayas, R. M. *PLoS Genet.* **10**, e1004746 (2014).
13. Kobayashi, C., Saito, Y., Ogawa, K. & Agata, K. *Dev. Biol.* **306**, 714–724 (2007).
14. Reddien, P. W. *Cell* **175**, 327–345 (2018).
15. Sikes, J. M. & Bely, A. E. *Dev. Biol.* **338**, 86–97 (2010).
16. Cannon, J. T. *et al. Nature* **530**, 89–93 (2016).
17. Zattara, E. E. & Bely, A. E. *Evol. Dev.* **13**, 80–95 (2011).
18. Burton, P. M. & Finnerty, J. R. *Dev. Genes Evol.* **219**, 79–87 (2009).
19. Chapman, J. A. *et al. Nature* **464**, 592–596 (2010).
20. Petersen, H. O. *et al. Mol. Biol. Evol.* **32**, 1928–1947 (2015).

This article was published online on 14 August 2019.

ARTICLE

https://doi.org/10.1038/s41586-019-1493-8

Modern microprocessor built from complementary carbon nanotube transistors

Gage Hills[1,3], Christian Lau[1,3], Andrew Wright[1], Samuel Fuller[2], Mindy D. Bishop[1], Tathagata Srimani[1], Pritpal Kanhaiya[1], Rebecca Ho[1], Aya Amer[1], Yosi Stein[2], Denis Murphy[2], Arvind[1], Anantha Chandrakasan[1] & Max M. Shulaker[1]*

Electronics is approaching a major paradigm shift because silicon transistor scaling no longer yields historical energy–efficiency benefits, spurring research towards beyond–silicon nanotechnologies. In particular, carbon nanotube field–effect transistor (CNFET)–based digital circuits promise substantial energy–efficiency benefits, but the inability to perfectly control intrinsic nanoscale defects and variability in carbon nanotubes has precluded the realization of very–large–scale integrated systems. Here we overcome these challenges to demonstrate a beyond–silicon microprocessor built entirely from CNFETs. This 16–bit microprocessor is based on the RISC–V instruction set, runs standard 32–bit instructions on 16–bit data and addresses, comprises more than 14,000 complementary metal–oxide–semiconductor CNFETs and is designed and fabricated using industry–standard design flows and processes. We propose a manufacturing methodology for carbon nanotubes, a set of combined processing and design techniques for overcoming nanoscale imperfections at macroscopic scales across full wafer substrates. This work experimentally validates a promising path towards practical beyond–silicon electronic systems.

With diminishing returns of silicon field-effect transistor (FET) scaling[1], the need for FETs leveraging nanotechnologies has been steadily increasing. Carbon nanotubes (CNTs, nanoscale cylinders made of a single sheet of carbon atoms with diameters of approximately 10–20 Å) are prominent among a variety of nanotechnologies that are being considered for next-generation energy-efficient electronic systems[2–4]. Owing to the nanoscale dimensions and simultaneously high carrier transport of CNTs[5,6], digital systems built from FETs fabricated with CNTs as the transistor channel (that is, CNFETs) are projected to improve the energy efficiency of today's silicon-based technologies by an order of magnitude[3,7,8].

Over the past decade, CNT technology has matured: from single CNFETs[9] to individual digital logic gates[10,11] to small-scale digital circuits and systems[7,12–16]. In 2013, this progress led to the demonstration of a complete digital system: a miniature computer[2] comprising 178 CNFETs that implemented only a single instruction operating on only a single bit of data (see Supplementary Information for a full discussion of previous work). However, as with all emerging nanotechnologies, there remained a substantial disconnect between these small-scale demonstrations and modern systems comprising tens of thousands of FETs (for example, microprocessors) to billions of FETs (for example, high-performance computing servers). Perpetuating this divide is the inability to achieve perfect atomic-level control of nanomaterials at macroscopic scales (for example, yielding CNTs of consistent 10-Å diameter uniformly across industry-standard wafer substrates of diameter 150–300 mm). The resulting intrinsic defects and variations have made the realization of such modern systems infeasible. For CNTs, there are three major intrinsic challenges: material defects, manufacturing defects and variability.

(1) Material defects. Although semiconducting CNTs form energy-efficient FET channels, the inability to precisely control CNT diameter and chirality results in every CNT synthesis containing some percentage of metallic CNTs. Metallic CNTs have little to no bandgap and therefore their conductance cannot be sufficiently modulated by the CNFET gate, resulting in high leakage current and potentially incorrect logic functionality[17].

(2) Manufacturing defects. During wafer fabrication, CNTs inherently 'bundle' together, forming thick CNT aggregates[18,19]. These aggregates result in CNFET failure (reducing CNFET circuit yield), as well as prohibitively high particle contamination rates for very-large-scale integration (VLSI) manufacturing.

(3) Variability. Energy-efficient complementary metal–oxide–semiconductor (CMOS)[20] digital logic requires the ability to fabricate CNFETs of complementary polarities (p-CNFETs and n-CNFETs) with well-controlled characteristics (for example, tunable and uniform threshold voltages, and p- and n-CNFETs with matching on- and off-state current). Previous techniques for realizing CNT CMOS have relied on either extremely reactive, non-air-stable, non-silicon CMOS-compatible materials[21–25] or have lacked tunability, robustness and reproducibility[26]. This has severely limited the complexity of CNT CMOS demonstrations (a complete CNT CMOS digital system has not yet been fabricated).

Although much previous work has focused on overcoming these challenges, none meets all of the strict requirements for realizing VLSI systems. In this work, we overcome the intrinsic CNT defects and variations to enable a demonstration of a beyond-silicon modern microprocessor: RV16X-NANO, designed and fabricated entirely using CNFETs. RV16X-NANO is a 16-bit microprocessor based on the open-source and commercially available RISC-V instruction set processor, running standard RISC-V 32-bit instructions on 16-bit data and addresses. It integrates >14,000 CMOS CNFETs, and operates as modern microprocessors do today (for example, it can run compiled programs; in addition, we demonstrate its functionality by executing all types and formats of instructions in the RISC-V instruction-set architecture). This is made possible by our manufacturing methodology for CNTs (MMC)—a set of original processing and circuit design techniques that are combined to overcome the intrinsic CNT challenges. The key elements of MMC are:

[1]Department of Electrical Engineering and Computer Science, Massachusetts Institute of Technology (MIT), Cambridge, MA, USA. [2]Analog Devices, Inc. (ADI), Wilmington, MA, USA. [3]These authors contributed equally: Gage Hills, Christian Lau. *e-mail: shulaker@mit.edu

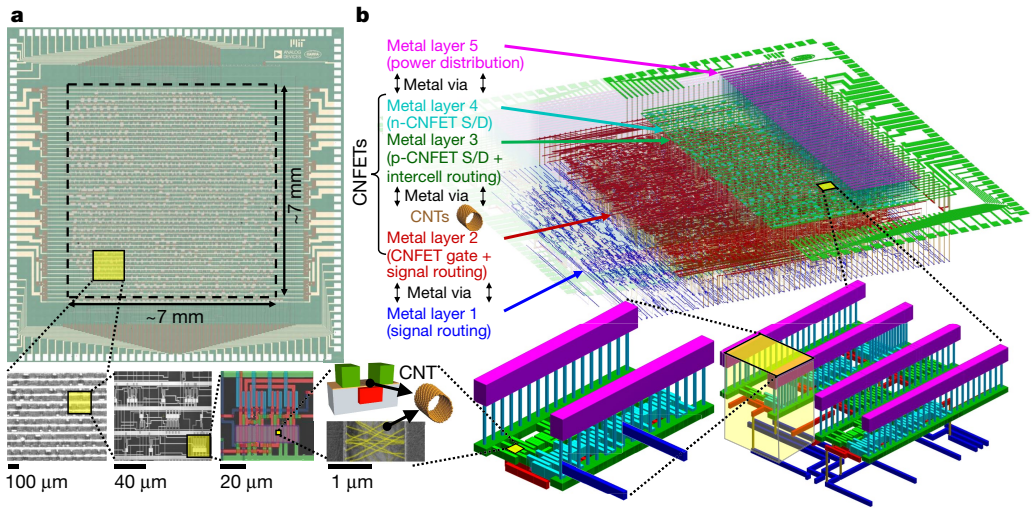

Fig. 1 | RV16X-NANO. a, Image of a fabricated RV16X-NANO chip. The die area is 6.912 mm × 6.912 mm, with input/output pads placed around the periphery. Scanning electron microscopy images with increasing magnification are shown below (one image is false-coloured to match the colouring in the schematic in **b**). RV16X-NANO is fabricated entirely from CNFET CMOS, in a wafer-scalable, VLSI-compatible, and silicon-CMOS compatible fashion. **b**, Three-dimensional to-scale rendered schematic of the RV16X-NANO physical layout (all dimensions are to scale except for the *z* axis, which is magnified to clarify each individual vertical layer). RV16X-NANO leverages a new three-dimensional (3D) physical architecture in which the CNFETs are physically located in the middle of the stack, with metal routing both above and below.

(1) RINSE (removal of incubated nanotubes through selective exfoliation). We propose a method of removing CNT aggregate defects through a selective mechanical exfoliation process. RINSE reduces CNT aggregate defect density by >250× without affecting non-aggregated CNTs or degrading CNFET performance.

(2) MIXED (metal interface engineering crossed with electrostatic doping). Our combined CNT doping process leverages both metal contact work function engineering as well as electrostatic doping to realize a robust wafer-scale CNFET CMOS process. We experimentally yield entire dies with >10,000 CNFET CMOS digital logic gates (2-input

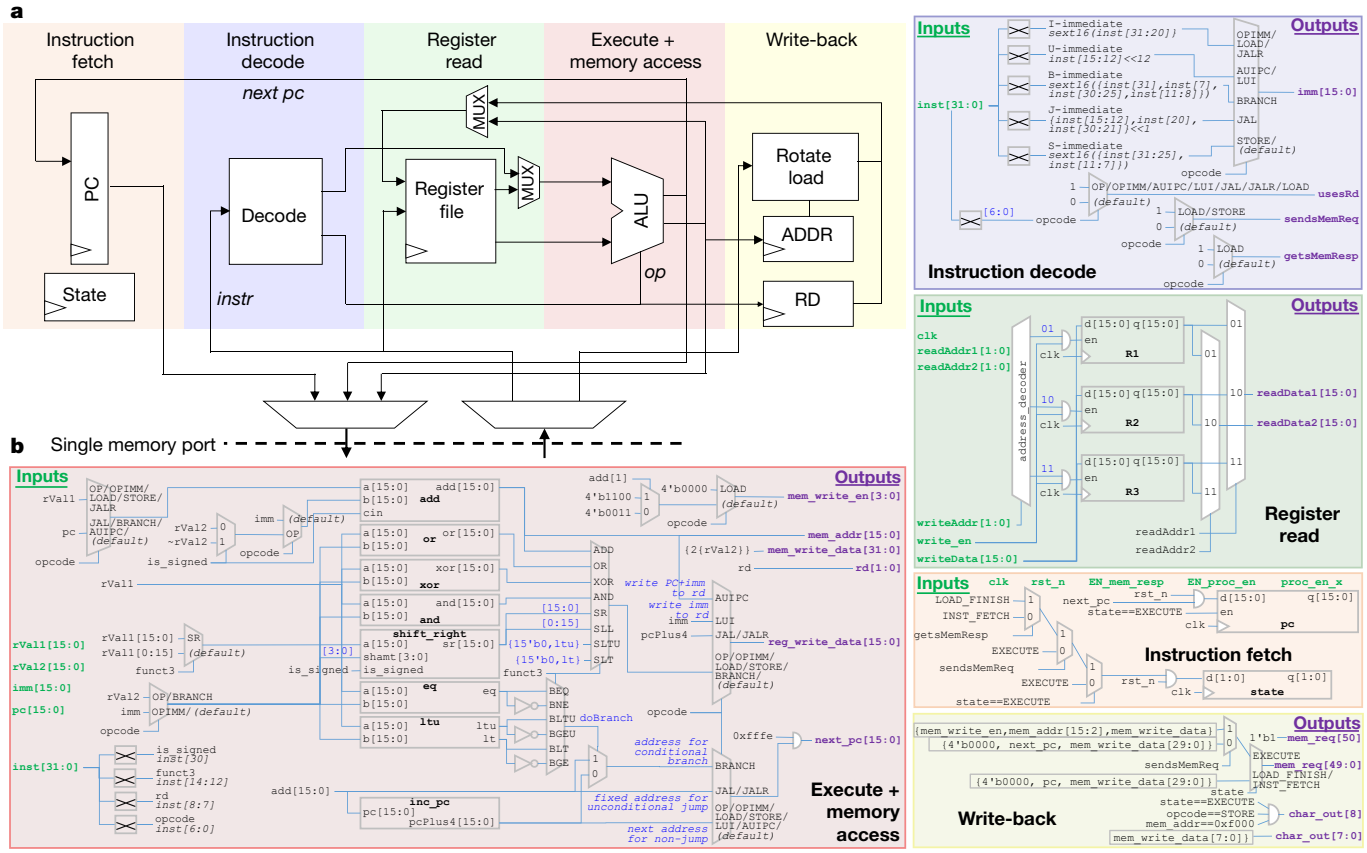

Fig. 2 | Architecture and design of RV16X-NANO. a, Block diagram showing the organization of RV16X-NANO, including the instruction fetch, instruction decode, register read, execute + memory access, and write-back stages. See Supplementary Information section 'RISC-V: Operational Details' for definitions of terms. **b**, Schematics describing the high-level register transfer level (RTL) description of each stage, including inputs, outputs and signal connections. Additional information on the RV16X-NANO is in the Supplementary Information.

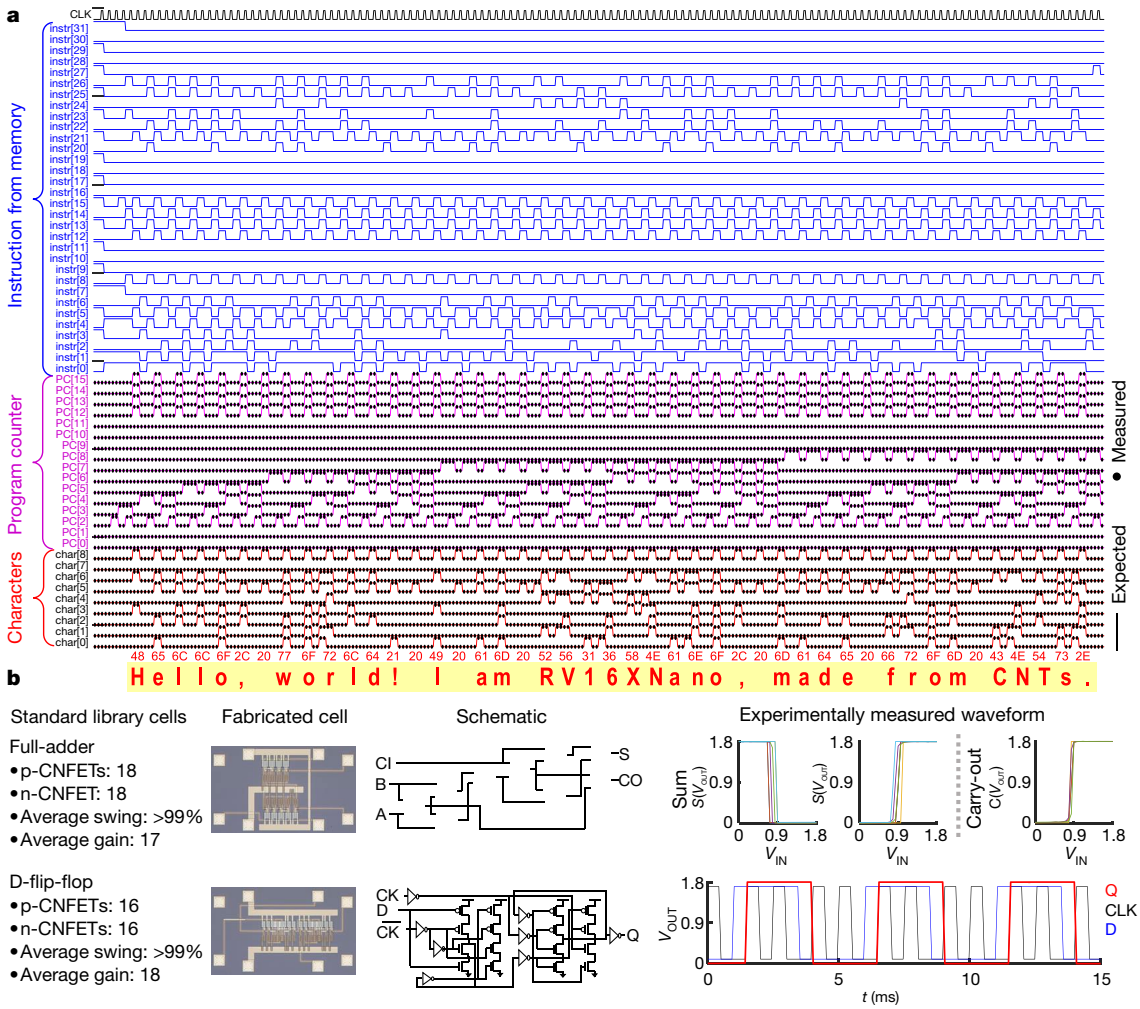

Fig. 3 | RV16X-NANO experimental results. a, Experimentally measured waveform from RV16X-NANO, executing the famous 'Hello, World' program. The waveform shows the 32-bit instruction fetched from memory, the program counter stored in RV16X-NANO, as well as the character output from RV16X-NANO. Below the waveform, we convert the binary output (shown in red in hexadecimal code) to their ASCII characters to their ASCII characters, showing RV16X-NANO printing out "Hello, world! I am RV16XNano, made from CNTs." In addition to this program, we test functionality by executing all of the 31 instructions within RV32E (see Supplementary Information). **b**, RV16X-NANO is designed using conventional electronic design automation (EDA) tools, leveraging our CNT process design kit and CNT CMOS standard cell library. An example combinational cell (full-adder) and example sequential cell (D-flip-flop) are shown alongside an optical microscopy image of the fabricated cells, their schematics, as well as their experimentally measured waveforms. For the full-adder, we show the outputs (sum and carry-out outputs) for all possible biasing conditions in which sweeping the voltage of input (from 0 to V_{DD}) causes a change in the logical state of the output (that is, for the full adder, with $C_{OUT} = A*B + B*C_{IN} + A*C_{IN}$, with A = logical '0' and B = logical '1', then sweeping C_{IN} from '0' to '1' causes C_{OUT} to change from logical '0' to logical '1'). (CI indicates C_{IN} and CO indicates C_{OUT}.) For the sum output $S(V_{OUT})$, there are 12 such conditions: six where V_{OUT} has the same polarity as the swept input (positive unate) and six where V_{OUT} has the opposite polarity to the swept input (negative unate). For the carry-out output $C(V_{OUT})$ there are six such conditions (all positive unate); the measurements are overlaid over one another in **b**). Gain for all transitions is >15, with output voltage swing >99%. The D-flip-flop waveform (voltage versus time) illustrates correct functionality of the positive edge-triggered D-flip-flop (output state Q shows correct functionality based on data input D and clock input CLK). CK and $\overline{CK}$ are the clock input and the inverse of the clock input, respectively.

'not-or' gates with functional yield 14,400/14,400, comprising 57,600 total CNFETs), and present a wafer-scale CNFET CMOS uniformity characterization across 150-mm wafers (such as analysing the yield for more than 100 million possible combinations of cascaded logic gate pairs).

(3) DREAM (designing resiliency against metallic CNTs). This technique overcomes the presence of metallic CNTs entirely through circuit design. DREAM relaxes the requirement on metallic CNT purity by about 10,000× (relaxed from a semiconducting CNT purity requirement of 99.999999% to 99.99%), without imposing any additional processing steps or redundancy. DREAM is implemented using standard electronic design automation (EDA) tools, has minimal cost, and enables digital VLSI systems with CNT purities that are available commercially today.

Importantly, the entire MMC is wafer-scale, VLSI-compatible and is seamlessly integrated within existing infrastructures for silicon CMOS—both in terms of design and of processing. Specifically, RV16X-NANO is designed with standard EDA tools, and leverages only materials and processes that are compatible with and exist within commercial silicon CMOS manufacturing facilities. Together, these contributions establish a robust CNT CMOS technology and represent a major milestone in the development of beyond-silicon electronics.

RV16X-NANO

Figure 1 shows an optical microscopy image of a fabricated RV16X-NANO die alongside three-dimensional to-scale rendered schematics of the physical layout. It is the largest CMOS electronic system

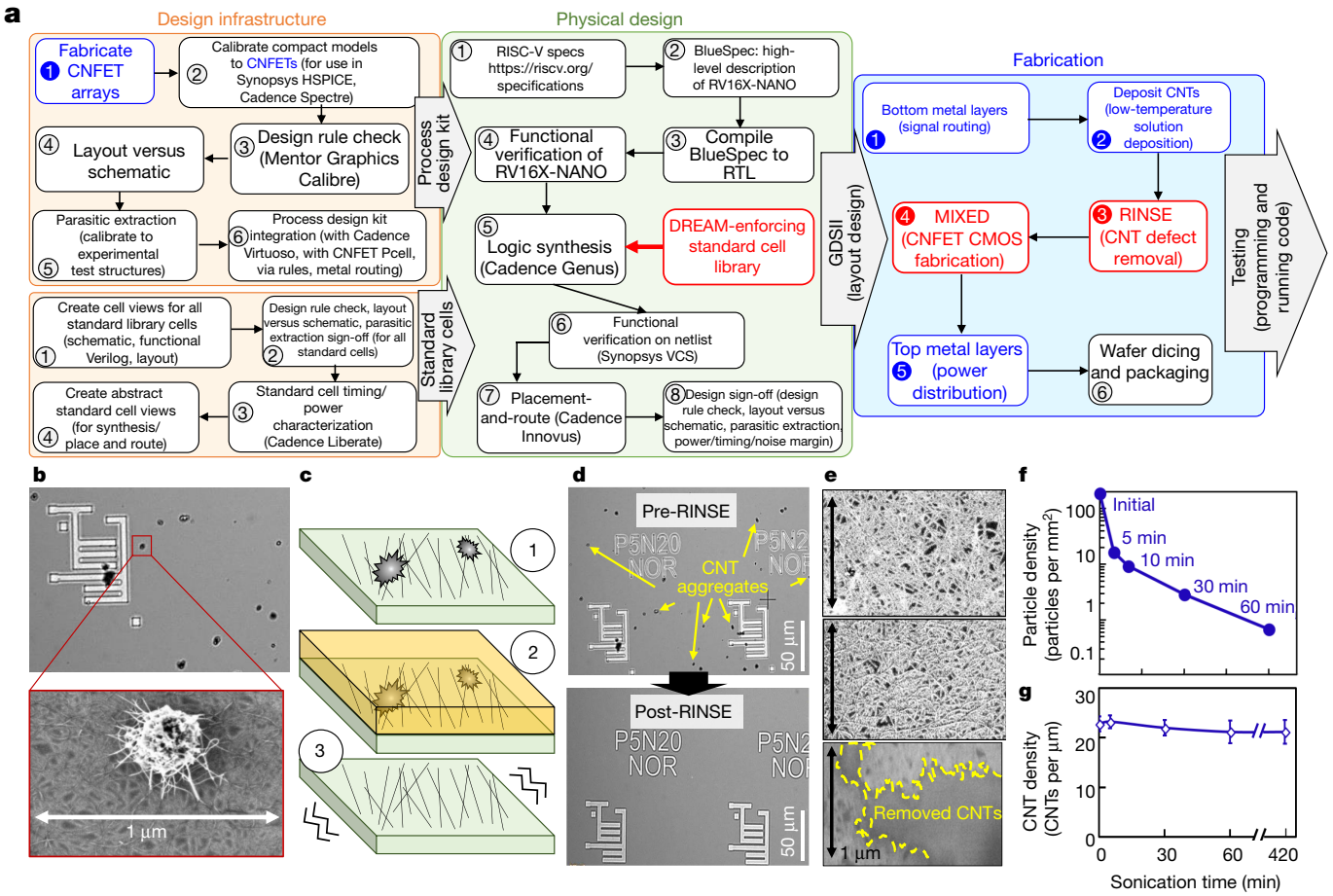

Fig. 4 | MMC. a, Design and manufacturing flow for RV16X-NANO, illustrating how MMC seamlessly integrates within conventional silicon-based EDA tools. Black boxes show conventional steps in silicon-CMOS design flows. Blue text indicates steps that are adjusted for CNTs instead of silicon, and red text represents the additions needed to implement the MMC. RV16X-NANO is the first hardware demonstration of a beyond-silicon emerging nanotechnology leveraging a complete RTL-to-GDS physical design flow that uses only conventional EDA tools. Software packages are from Synopsys (https://www.synopsys.com/), Cadence (https://www.cadence.com/) and Mentor Graphics (https://www.mentor.com/). **b**, RINSE. As shown in the scanning electron microscopy images, CNTs inherently bundle together, forming thick CNT aggregates. These aggregates result in CNFET failure (reduced CNFET yield) as well as prohibitive particle contamination for VLSI manufacturing. **c**, The RINSE process steps: (1) CNT incubation, (2) adhesion coating, (3) mechanical exfoliation (see text for details). **d**, **e**, RINSE results. After performing RINSE, CNT aggregates are removed from the wafer (as shown in **d**). Importantly, the individual CNTs not in aggregates are not removed from the wafer, while without RINSE, sonication inadvertently removes large areas of all CNTs from the wafer (in **e**, where the top shows CNT incubation pre-RINSE, the middle shows CNTs left on the wafer post-RINSE, and the bottom shows CNTs inadvertently removed from the wafer after sonicating a wafer to remove CNT aggregates without performing the critical adhesion-coating step in RINSE). **f**, Particle contamination reduction due to RINSE: RINSE decreases particle density by >250×. **g**, Ideally, individual CNTs are not inadvertently removed during RINSE; increasing the time of step 3 (sonication time) to over 7 h results in no change in CNT density across the wafer.

realized using beyond-silicon nanotechnologies: comprising 3,762 CMOS digital logic stages, totalling 14,702 CNFETs containing more than 10 million CNTs, and includes logic paths comprising up to 86 stages of cascaded logic between flip-flops (that is, that must evaluate sequentially in a single clock cycle). It operates with supply voltage (V_{DD}) of 1.8 V, receives an external referenced clock (generating local clock signals internally), receives inputs (instructions and data) from and writes directly to an off-chip main memory (dynamic random-access memory, DRAM), and stores data on-chip in a register file. No other external biasing or control signals are supplied. Furthermore, RV16X-NANO has a three-dimensional (3D) physical architecture, as the metal interconnect layers are fabricated both above and below the layer of CNFETs; this is in contrast to silicon-based systems in which all metal routing can only be fabricated above the bottom layer of silicon FETs (see Methods). In RV16X-NANO, the metal layers below the CNFETs are primarily used for signal routing, while the metal layers above the CNFETs are primarily used for power distribution (Fig. 1c, d). The fabrication process implements five metal layers and includes more than 100 individual processing steps (see Methods and section 'MMC' for details). This 3D layout, with routing above and below the FETs promises improved routing congestion (a major challenge for today's systems[27]), and is uniquely enabled by CNTs (owing to their low-temperature fabrication; see Methods).

Physical design

The design flow of RV16X-NANO leverages only industry-standard tools and techniques: we create a standard process design kit (PDK) for CNFETs as well as a library of standard cells for CNFETs that is compatible with existing EDA tools and infrastructure without modification. Our CNFET process design kit includes a compact model for circuit simulations that is experimentally calibrated to our fabricated CNFETs. The standard cell library comprises 63 unique cells, and includes both combinational and sequential circuit elements implemented with both static CMOS and complementary transmission-gate digital logic circuit topologies (see Supplementary Information for a full list of standard library cells, including circuit schematics and physical layouts). We use the CNFET process design kit to characterize the timing and power for all of the library cells, which we experimentally validate by fabricating and measuring all cells individually (see Supplementary Information for full description and experimental characterization of the standard

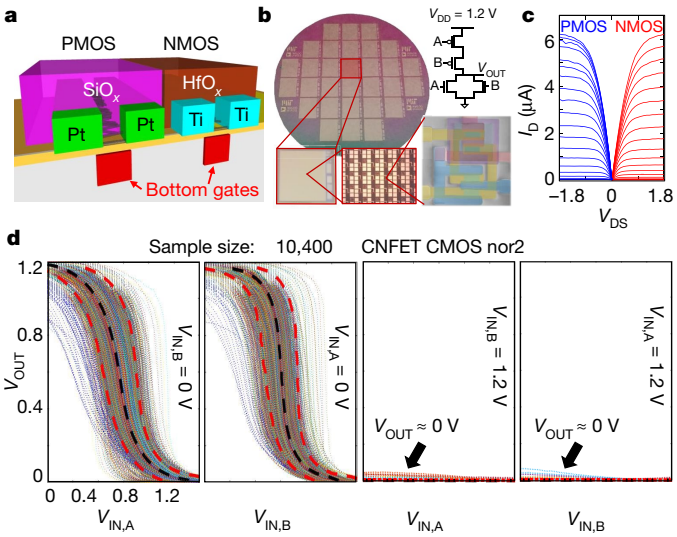

Fig. 5 | MIXED. a, Schematic of CNFET CMOS fabricated using MIXED. MIXED is a combined doping process that leverages both metal contact work-function engineering as well as electrostatic doping to realize a robust wafer-scale CNFET CMOS process. We use platinum contacts and SiO_x passivation for p-CNFETs, and titanium contacts and HfO_x passivation for n-CNFETs (see Methods for details). To characterize MIXED, we fabricated dies with 10,400 CNFET CMOS digital logic gates across 150-mm wafers (**b**). **c**, **d**, Experimental results. **c**, I_D versus V_{DS} characteristics showing p-CNFETs and n-CNFETs that exhibit similar I_D–V_{DS} characteristics (for opposite polarity of input bias conditions, for example, $V_{DS,P} = -V_{DS,N}$), achieved with MIXED. The gate-to-source voltage V_{GS} is swept from $-V_{DD}$ to V_{DD} in increments of 0.1 V. See Supplementary Information for I_D–V_{GS} and additional CNFET characteristics. **d**, Output voltage transfer curves (VTCs, V_{OUT} vs V_{IN}) for all 10,400 CNT CMOS logic gates (nor2) within a single die. Each VTC illustrates V_{OUT} as a function of the input voltage of one input (V_{IN}), while the other input is held constant. For each nor2 logic gate (with logical function OUT = !(IN_A|IN_B), we measure the VTC for each of two cases: V_{OUT} versus $V_{IN,A}$ with $V_{IN,B} = 0$ V and V_{OUT} versus $V_{IN,B}$ with $V_{IN,A} = 0$ V). All 10,400/10,400 exhibit correct functionality (which we define as having output voltage swing >70%). The black dotted line represents the average VTC (average V_{IN} across all measured VTC for each value of V_{OUT}), while the red dotted line represents the boundary of ±3 standard deviations (again, across all V_{IN} values for each value of V_{OUT}). See Supplementary Information for extracted distributions of key metrics from these experimental measurements (gain, output voltage swing and SNM analysing >100 million possible cascaded logic gates pairs formed from these 10,400 samples), as well as uniformity characterization across the 150-mm wafer. Importantly, despite the high yield and robust CNFET CMOS enabled by MIXED and RINSE, we note that there are outlier gates with degraded output swing (the blue lines in **d**). These outliers are caused by CNT CMOS logic gates that contain metallic CNTs; the third component of the MMC (DREAM; see Fig. 6), is a design technique that is essential for overcoming the presence of these metallic CNTs.

cell library). A full description of our industry-practice VLSI design methodology, including how we implement DREAM during logic synthesis and place-and-route, is provided in the Methods.

Computer architecture

Figure 2 illustrates the architecture of RV16X-NANO, which follows conventional microprocessor design (implementing instruction fetch, instruction decode, register read, execute/memory access, and write-back stages). It is designed from RISC-V, a standard open instruction-set architecture used in commercial products today and gaining widespread popularity in both academia and industry[28,29]; see https://riscv.org/wp-content/uploads/2017/05/Tue1345pm-NVIDIA-Sijstermans.pdf and https://www.westerndigital.com/company/innovations/risc-v). RV16X-NANO is derived from a full 32-bit RISC-V microprocessor supporting the RV32E instruction set (31 different 32-bit instructions, see Supplementary Information), while truncating the data path width from 32 bits to 16 bits, and reducing the number of registers from 16 to 4. It is designed using the publicly available software Bluespec (https://bluespec.com/), and is verified using a Satisfiability Modulo Theories (SMT)-based bounded model checking against a formal specification of the RISC-V instruction-set architecture (see Supplementary Information). To demonstrate the correct functionality of the microprocessor, we experimentally run and validate correct functionality of all types and formats of instructions on the fabricated RV16X-NANO. Figure 3 shows the first program executed on RV16X-NANO: the famous 'Hello, World'. See Methods and Supplementary Information for schematics, operational details and experimental measurements.

MMC

Here we describe our MMC—a set of combined processing and design techniques that are the foundation for enabling the realization of RV16X-NANO (Fig. 4a). All design and fabrication processes are wafer-scale and VLSI-compatible, not requiring any per-unit customization or redundancy.

RINSE

The CNFET fabrication process begins by depositing CNTs uniformly over the wafer. 150-mm-diameter wafers (with the bottom metal signal routing layers and gate stack of the CNFET already fabricated for the 3D design) are submerged in solutions containing dispersed CNTs (Methods). Although CNTs are uniformly deposited over the wafer, the CNT deposition also inherently results in manufacturing defects: CNT aggregates deposited randomly across the wafer (Fig. 4b). These CNT aggregates act as particle contamination, reducing die yield. Several existing techniques have attempted to remove these aggregates before CNT deposition, but none is sufficient to meet wafer-level yield requirements for VLSI systems: (1) excessive high-power sonication for dispersing aggregates in solution damages CNTs, which results in degraded CNFET performance and does not disperse all CNTs; (2) centrifugation, which does not remove all smaller aggregates (and aggregates can re-form post-centrifugation), (3) excessive filtering, which removes both aggregates and the CNTs themselves from the solution, and (4) etching the aggregates, which is not feasible owing to lack of selectivity versus the underlying CNTs themselves. Instead, to remove these aggregates, we developed a process that we call RINSE, consisting of three steps (Fig. 4c):

(1) CNT incubation. Solution-based CNTs are deposited on wafers pre-treated with a CNT adhesion promoter (hexamethyldisilazane, bis(trimethylsilyl)amine).

(2) Adhesion coating. A standard photoresist (polymethylglutarimide) is spin-coated onto the wafer and cured at about 200 °C.

(3) Mechanical exfoliation. The wafer is placed in solvent (*N*-methylpyrrolidone) and sonicated.

The key to RINSE is the adhesion coating (step 2): without it, sonicating the wafer inadvertently removes sections of CNTs in addition to the aggregates (Fig. 4d). The adhesion coating leaves an atomic layer of carbon that remains after step 3, which exerts sufficient force to adhere the CNTs to the wafer surface while still allowing for the removal of the aggregates. Experimental results for RINSE are shown in Fig. 4d–g; by optimizing the adhesion-coating cure temperature and time as well as the sonication power and time, RINSE reduces the CNT aggregate density by >250× (quantified by the number of CNT aggregates per unit area) without damaging the CNTs or affecting CNFET performance (see Supplementary Information).

MIXED

After using RINSE to overcome intrinsic CNT manufacturing defects, CNFET circuit fabrication continues. Unfortunately, while energy-efficient CMOS logic requires both p-CNFETs and n-CNFETs with controlled and tunable properties (such as threshold voltage), techniques for realizing CNT CMOS today result in large FET-to-FET

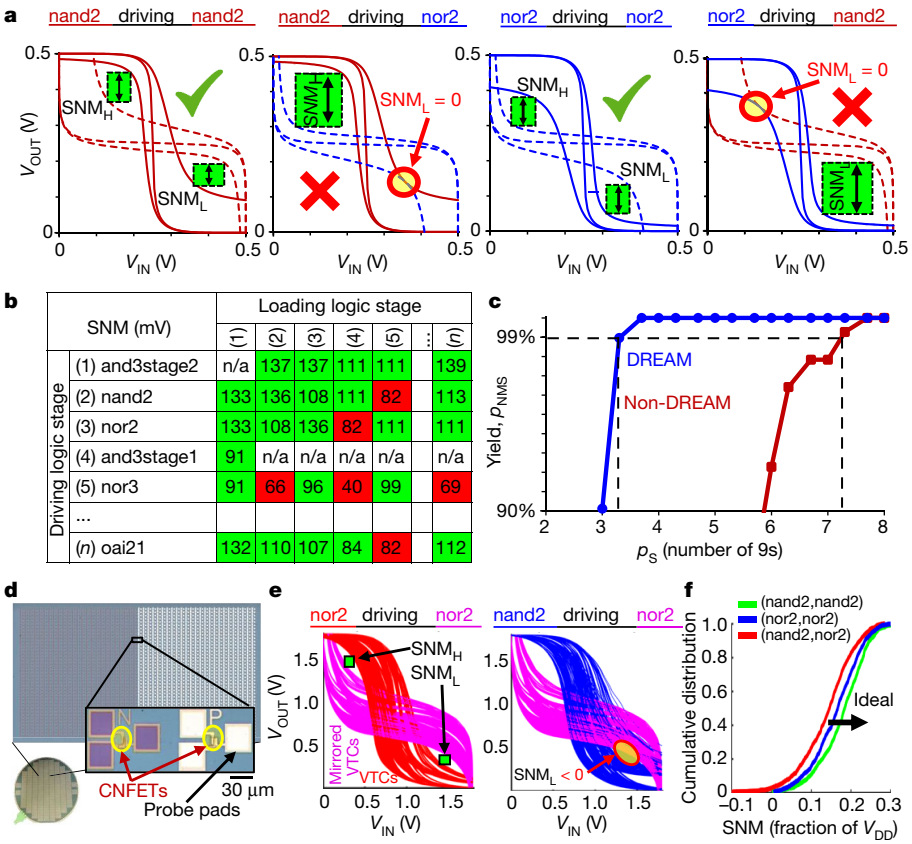

Fig. 6 | DREAM. DREAM overcomes the presence of metallic CNTs entirely through circuit design, and is the final component of the MMC. DREAM relaxes the requirement on metallic CNT purity by about 10,000×, without imposing any additional processing steps or redundancy. DREAM is implemented using standard EDA tools, has minimal cost (≤10% energy, ≤ 10% delay and ≤ 20% area), and enables digital VLSI systems with CNT purities that are available commercially today (99.99% semiconducting CNT purity). **a**, VTCs for driving logic stages and mirrored VTCs for loading logic stages, showing SNM simulated for 4 different logic stage pairs (SNM is defined in the Supplementary Information), with up to two metallic CNTs in all CNFETs. The logic stage pairs: (nand2, nand2) and (nor2, nor2) have better SNM than do (nand2, nor2) and (nor2, nand2) despite all logic stages having exactly the same VTCs. We note that we distinguish logic stages (for example, an inverter) from logic gates (for example, a buffer, by cascading two inverters); a logic gate can comprise multiple logic stages. **b**, Example DREAM SNM table (see Methods for details, analysed for a projected 7-nm node with a scaled V_{DD} of 500 mV), which shows the minimum SNM for each pair of connected logic stages. As an example, values less than 83 mV are highlighted in red, indicating that these combinations would not be permitted during design, to reduce overall susceptibility to noise at the VLSI circuit level. **c**, Yield (p_{NMS}) versus semiconducting CNT purity for a required SNM level (SNM_R) of $SNM_R = V_{DD}/5$, shown for the OpenSparc 'dec' module designed using the 7-nm node CNFET standard library cells derived from the ASAP7 process design kit with a scaled V_{DD} of 500 mV (details in Methods). **d**, Fabricated CNT CMOS die, comprising 1,000 NMOS CNFETs and 1,000 PMOS CNFETs. Semiconducting CNT purity is $p_S \approx 99.99\%$, with around 15–25 CNTs per CNFET. **e**, **f**, Experimental demonstration of DREAM. VTCs for nand2 and nor2 generated by randomly selecting two NMOS and two PMOS CNFETs from **d** (some of which contain metallic CNTs). This is repeated to form 1,000 unique nor2 and nand2 VTCs. We then analyse the SNM for over one million logic stage pairs (shown in **f**), corresponding to all combinations of 1,000 VTCs for the driving logic stage and 1,000 VTCs for the loading logic stage. **e**, A subset of these logic stage pairs; the (nor2, nor2) maintains minimum SNM > 0, while (nand2, nor2) suffers from minimum SNM < 0 in the presence of metallic CNTs; >99.99% of (nor2, nor2) and (nand2, nand2) logic stage pairs achieve SNM > 0 V, while only about 97% of (nand2, nor2) achieve SNM > 0 V. **f**, Cumulative distributions of SNM over one million logic stage pairs.

variability that has made the realization of large-scale CNFET CMOS systems infeasible. Moreover, the vast majority of existing techniques are not air-stable (for example, they use materials that are extremely reactive in air[23]), are not uniform or robust (for example, they do not always successfully realize CMOS[22]), or rely on materials not compatible with conventional silicon CMOS processing (for example, molecular dopants that contain ionic salts prohibited in commercial fabrication facilities[24,25]).

These challenges are overcome by our processing technique, MIXED, described in Fig. 5. The key to MIXED is a combined doping approach that engineers both the oxide deposited over the CNTs to encapsulate the CNFET as well as the metal contact to the CNTs[30]. First, we encapsulate the CNFETs in oxide (deposited by atomic-layer deposition) to isolate them from their surroundings. By leveraging the atomic-layer control of atomic-layer deposition, we also engineer the precise stoichiometry of this oxide encapsulating the CNTs, which enables us to simultaneously electrostatically dope the CNTs (the stoichiometry dictates both the amount of redox reaction at the oxide–CNT interface and the fixed charge in the oxide). In addition, we engineer the metal source/drain contacts to the CNTs to further optimize the p- and n-CNFETs. We use a lower-work-function metal (titanium) for the contacts to n-CNFETs and a higher-work-function metal for the contacts to p-CNFETs (platinum), improving the on-state drive current of both (for a given off-state leakage current). In contrast to previous approaches, MIXED has the following key advantages: it leverages only silicon CMOS-compatible materials, it allows for precise threshold voltage tuning through controlling the stoichiometry of the atomic-layer deposition doping oxide, and it is robust owing to tight process control by using atomic-layer deposition and only air-stable materials.

Figure 5c shows the current–voltage (I–V) characteristics of p-CNFETs and n-CNFETs, demonstrating well-matched characteristics (such as on- and off-state currents). To demonstrate the reproducibility of MIXED at the wafer scale, Fig. 5 shows measurements from 10,400/10,400 correctly functioning 2-input 'not-or' (nor2) CNFET

logic gates within a single die, and 1,000/1,000 correctly functioning nor2 gates randomly selected from across a 150-mm wafer. Additional characterization results (including output voltage swing, gain, and SNM for >100 million possible combinations of cascaded logic gate pairs), are in Supplementary Information. This demonstrates solid-state, air-stable, VLSI- and silicon-CMOS compatible CNFET CMOS at the wafer scale.

DREAM

Despite the robust CNFET CMOS enabled by RINSE and MIXED, a small percentage (around 0.01%) of CNTs are metallic CNTs. Unfortunately, a metallic CNT fraction of 0.01% can be prohibitively large for VLSI-scale systems, owing to two major challenges—increased leakage power, which degrades energy-delay product (EDP) benefits, and degraded noise immunity, which potentially results in incorrect logic functionality. To quantify the noise immunity of digital logic, we extract the static noise margin (SNM) for each pair of connected logic stages, using the voltage transfer curves (VTCs) of each stage (details in Extended Data Fig. 8). The probability that all connected logic stages meet a minimum SNM requirement (SNM_R, typically chosen by the designer as a fraction of V_{DD}, for example, $SNM_R = V_{DD}/4$) is p_{NMS}: the probability that all noise margin constraints are satisfied (Methods). Although previous works have set requirements on semiconducting-CNT purity (p_S) based on limiting metallic-CNT-induced leakage power, no existing works have provided VLSI circuit-level guidelines for p_S based on both increased leakage and the resulting degraded SNM. Although p_S of 99.999% is sufficient to limit EDP degradation to ≤5%, SNM imposes far stricter requirements on purity: p_S must be about 99.999999% to achieve $p_{NMS} \geq 99\%$ (analysed for 1 million gate circuits, Supplementary Information).

Unfortunately, typical CNT synthesis today achieves a p_S value of only about 66%. While many different techniques have been proposed to overcome the presence of metallic CNTs (Supplementary Information), the highest reported purity is a p_S of about 99.99%: this is 10,000× below the requirement for VLSI circuits[31–33]. Moreover, these techniques have substantial cost, requiring either additional processing steps (for example, applying high voltages for electrical 'breakdown' of metallic CNTs during fabrication[10]) or redundancy (incurring substantial energy-efficiency penalties[34]). Here we present and experimentally validate a new technique, DREAM, that overcomes the presence of metallic CNTs entirely through circuit design. The key contribution of DREAM is that it reduces the required p_S by around 10,000×, allowing 99% p_{NMS} with $p_S = 99.99\%$ (for circuits with one million logic gates). This enables digital VLSI circuits to use CNT processing available today: $p_S = 99.99\%$ is already commercially available (and can also be achieved through several means, including solution-based sorting, which we use in our process for fabricating RV16X-NANO; see Methods).

The key insight for DREAM is that metallic CNTs affect different pairs of logic stages uniquely depending on how the logic stages are implemented (considering both the schematic and physical layout). As a result, the SNM of specific combinations of logic stages is more susceptible to metallic CNTs. To improve overall p_{NMS} for a digital VLSI circuit, DREAM applies a logic transformation during logic synthesis to achieve the same circuit functionality, while prohibiting the use of specific logic stage pairs whose SNM is most susceptible to metallic CNTs. As an example, let (G_D, G_L) be a logic stage pair with driving logic stage G_D and loading logic stage G_L. Figure 6 shows that some logic stage pairs have better SNM in the presence of metallic CNTs than others, despite using exactly the same VTCs for the logic stages comprising the circuit (in this instance, logic stage pairs (nand2, nand2) and (nor2, nor2) have better SNM than (nand2, nor2) or (nor2, nand2)). Thus, a designer can improve p_{NMS} by prohibiting the use of logic stage pairs that are more susceptible to metallic CNTs, while permitting logic stage pairs that maintain better SNM despite the presence of metallic CNTs.

Beyond this simple example to illustrate DREAM, we also quantify the benefit of DREAM using both simulation and experimental analysis for VLSI-scale circuits; in simulation, we leverage a compact model for CNFETs (derived from ref. [8]), which accounts for both semiconducting CNTs and metallic CNTs, to analyse the effect of metallic CNTs on the leakage power, energy consumption, speed and noise susceptibility of physical designs of VLSI-scale circuits at a 7-nm technology node designed using standard EDA tools, with and without DREAM (results are shown in Fig. 6; see additional discussion in Supplementary Information). Experimentally, we fabricate and characterize 2,000 CMOS CNFETs fabricated with MIXED (1,000 p-type metal-oxide-semiconductor (PMOS) and 1,000 n-type metal-oxide-semiconductor (NMOS) CNFETs; see Fig. 6). Using I–V measurements from these 2,000 CNFETs, we analyse one million combinations of CNFET digital logic gates (whose electrical characteristics are solved using the I–V characteristics of the measured CNFETs; Extended Data Fig. 8) to show the benefits of DREAM in reducing circuit susceptibility to noise. In the Methods, we provide extensive details of these analyses and the implementation of DREAM for arbitrary digital VLSI circuits, including how to implement DREAM using standard industry-practice physical design flows, how we implement DREAM for RV16X-NANO, and an efficient algorithm to satisfy target p_{NMS} constraints (such as $p_{NMS} \geq 99\%$), while minimizing energy, delay and area costs.

Outlook

These combined processing and design techniques overcome the major intrinsic CNT challenges. Our complete manufacturing methodology for CNTs (MMC) enables a demonstration of a beyond-silicon modern microprocessor fabricated from CNTs, RV16X-NANO. In addition to demonstrating the RV16X-NANO microprocessor, we thoroughly characterize and analyse all facets of MMC, illustrating the feasibility of our approach and more broadly of a future CNT technology. This work is a major advance for CNTs, paving the way for next-generation beyond-silicon electronic systems.

Online content

Any methods, additional references, Nature Research reporting summaries, source data, extended data, Supplementary Information, acknowledgements, peer review information; details of author contributions and competing interests; and statements of data and code availability are available at https://doi.org/10.1038/s41586-019-1493-8.

Received: 16 January 2019; Accepted: 3 July 2019;
Published online 28 August 2019.

1. Khan, H. N., Hounshell, D. A. & Fuchs, E. R. H. Science and research policy at the end of Moore's law. *Nat. Electron.* **1**, 14–21 (2018).
2. Shulaker, M. et al. Carbon nanotube computer. *Nature* **501**, 526–530 (2013).
3. Hills, G. et al. Understanding energy efficiency benefits of carbon nanotube field-effect transistors for digital VLSI. *IEEE Trans. NanoTechnol.* **17**, 1259–1269 (2018).
4. Franklin, A. et al. Sub-10 nm carbon nanotube transistor. *Nano Lett.* **12**, 758–762 (2012).
5. Brady, G. J. et al. Quasi-ballistic carbon nanotube array transistors with current density exceeding Si and GaAs. *Science* **2**, e1601240 (2016).
6. Javey, A., Guo, J., Wang, Q., Lundstrom, M. & Dai, H. Ballistic carbon nanotube field-effect transistors. *Nature* **424**, 654–657 (2003).
7. Aly, M. M. S. et al. Energy-efficient abundant-data computing: the N3XT approach to energy-efficient abundant-data computing. *Proc. IEEE* **107**, 19–48 (2019).
8. Lee, C.-S., Pop, E., Franklin, A. D., Haensch, W. & Wong, H.-S. P. A compact virtual-source model for carbon nanotube FETs in the sub-10-nm regime-Part I: Intrinsic elements. *IEEE Trans. Electron Devices* 62.9 3061-3069 (2015).
9. Tans, S. J., Verschueren, A. R. M. & Dekker, C. Room-temperature transistor based on a single carbon nanotube. *Nature* **393**, 49–52 (1998).
10. Patil, N. et al. VMR: VLSI-compatible metallic carbon nanotube removal for imperfection-immune cascaded multi-stage digital logic circuits using carbon nanotube FETs. In *IEEE Int. Electron Devices Meet.* https://doi.org/10.1109/IEDM.2009.5424295 (IEEE, 2009).
11. Cao, Q., Kim, H., Pimparkar, N., Kulkarni, J. & Wang, C. Medium-scale carbon nanotube thin-film integrated circuits on flexible plastic substrates. *Nature* **454**, 495–500 (2008).
12. Shulaker, M., Saraswat, K., Wong, H. & Mitra, S. Monolithic three-dimensional integration of carbon nanotube FETs with silicon CMOS. In *Symp. VLSI Technology Digest Tech. Pap.* https://doi.org/10.1109/VLSIT.2014.6894422 (IEEE, 2014).
13. Shulaker, M. et al. Carbon nanotube circuit integration up to sub-20 nm channel lengths. *ACS Nano.* **8**, 3434–3443 (2014).
14. Shulaker, M. et al. Experimental demonstration of a fully digital capacitive sensor interface built entirely using carbon-nanotube FETs. In *IEEE Int. Solid-State Circuits Conf. Digest Tech. Pap.* https://doi.org/10.1109/ISSCC.2013.6487660 (IEEE, 2013).

15. Shulaker, M. et al. Sensor-to-digital interface built entirely with carbon nanotube FETs. *IEEE J. Solid-State Circ.* **41**, https://doi.org/10.1109/JSSC.2013.2282092 (2014).
16. Ding, L. et al. CMOS-based carbon nanotube pass-transistor logic integrated circuits. *Nat. Commun.* **3**, 677 (2012).
17. Shulaker, M. et al. Efficient metallic carbon nanotube removal for highly-scaled technologies. *In IEEE Int. Electron Devices Meet.* https://doi.org/10.1109/IEDM.2015.7409815 (IEEE, 2015).
18. Shulaker, M., Wei, H., Patil, N., Provine, J. & Chen, H. Linear increases in carbon nanotube density through multiple transfer technique. *Nano Lett.* **11**, 1881–1886 (2011).
19. Won, Y. et al. Zipping, entanglement, and the elastic modulus of aligned single-walled carbon nanotube films. *Proc. Natl Acad. Sci. USA* **110**, 20426–20430 (2013).
20. Kang, S.-M. & Leblebici, Y. *CMOS Digital Integrated Circuits* (Tata McGraw-Hill Education, 2003).
21. Zhang, Z. et al. Doping-free fabrication of carbon nanotube based ballistic CMOS devices and circuits. *Nano Lett.* **7**, 3603–3607 (2007).
22. Shahrjerdi, D. et al. High-performance air-stable n-type carbon nanotube transistors with erbium contacts. *ACS Nano* **7**, 8303–8308 (2013).
23. Ding, L. et al. Y-contacted high-performance n-type single-walled carbon nanotube field-effect transistors: scaling and comparison with Sc-contacted devices. *Nano Lett.* **9**, 4209–4214 (2009).
24. Xu, J.-L. et al. Efficient and reversible electron doping of semiconductor-enriched single-walled carbon nanotubes by using decamethylcobaltocene. *Sci. Rep.* **7**, 6751 (2017).
25. Geier, M. L., Moudgil, K., Barlow, S., Marder, S. R. & Hersam, M. C. Controlled n-type doping of carbon nanotube transistors by an organorhodium dimer. *Nano Lett.* **16**, 4329–4334 (2016).
26. Zhang, J., Wang, C., Fu, Y., Che, Y. & Zhou, C. Air-stable conversion of separated carbon nanotube thin-film transistors from p-type to n-type using atomic layer deposition of high-κ oxide and its application in CMOS logic circuits. *ACS Nano* **5**, 3284–3292 (2011).
27. Markov, I. L., Hu, J. & Kim, M.-C. Progress and challenges in VLSI placement research. *Proc. IEEE* **103**, 1985–2003 (2015).
28. Celio, C., Patterson, D. A. & Asanovic, K. The Berkeley Out-Of-Order Machine (BOOM): an Industry-Competitive, Synthesizable, Parameterized RISC-V Processor. Technical Report No. UCB/EECS-2015-167 (University of California at Berkeley, 2015); http://www2.eecs.berkeley.edu/Pubs/TechRpts/2015/EECS-2015-167.pdf.
29. Patterson, D. 50 Years of computer architecture: From the mainframe CPU to the domain-specific tpu and the open RISC-V instruction set. In *IEEE Int. Solid-State Circuits Conf.* (IEEE, 2018).
30. Lau, C., Srimani, T., Bishop, M. D., Hills, G. & Shulaker, M. M. Tunable n-type doping of carbon nanotubes through engineered atomic layer deposition HfO_x films. *ACS Nano* **12**, 10924–10931 (2018).
31. Brady, G. et al. Polyfluorene-sorted, carbon nanotube array field-effect transistors with increased current density and high on/off ratio. *ACS Nano* **8**, 11614–11621 (2014).
32. Wang, J. et al. Growing highly pure semiconducting carbon nanotubes by electrotwisting the helicity. *Nat. Catal.* **1**, 326–331 (2018).
33. Si, J. et al. Scalable preparation of high-density semiconducting carbon nanotube arrays for high-performance field-effect transistors. *ACS Nano* **12**, 627–634 (2018).
34. Lin, A., Patil, N., Wei, H., Mitra, S. & Wong, H.-S. P. ACCNT—A metallic-CNT-tolerant design methodology for carbon-nanotube VLSI: concepts and experimental demonstration. *IEEE Trans. Electron Dev.* **56**, 2969–2978 (2009).

METHODS

Fabrication process. The fabrication process is shown in Extended Data Fig. 1, and a final fabricated 150-mm wafer is shown in Extended Data Fig. 4. It uses five metal layers and over 100 individual processing steps.

Bottom metal routing layers. The starting substrate is a 150-mm silicon wafer with 800-nm-thick thermal oxide for isolation. The bottom metal wire layers are defined using conventional processing (for example, lithographic patterning, metal deposition, etching, and so on). After the first metal layer is patterned (Extended Data Fig. 1a), an oxide spacer (300 °C) is deposited to separate this first metal layer from the subsequent second metal layer (Extended Data Fig. 1b). To produce interlayer vias between the first and second metal layer, vias are lithographically patterned and etched through this spacer dielectric using dry reactive ion etching (RIE) that stops on the bottom metal layer (Extended Data Fig. 1c). The second metal layer is then defined lithographically and deposited. The vias are formed simultaneously with the second metal wire layer, because the vias are filled during the metal deposition (Extended Data Fig. 1d). RV16X-NANO has two bottom metal layers, which are used for signal routing. The second metal layer also acts as the bottom gate for the CNFETs.

Bottom gate CNFETs. The second metal layer (Extended Data Fig. 1d) provides both signal routing (local interconnect) as well as the bottom gate for the CNFETs. To fabricate the remaining bottom gate CNFET structure, a high-k (k is the dielectric constant) gate dielectric (a dual-stack of AlO_2 and HfO_2) is deposited through atomic layer deposition (at 300 °C) over the bottom metal gates (Extended Data Fig. 1e). The HfO_2 is used for the majority of the dielectric stack owing to its high-k dielectric constant, while the AlO_2 is used for its improved seeding and increased dielectric breakdown voltage. Following gate dielectric deposition, contact vias through the gate dielectric are patterned, and again RIE is used to etch the contact vias, stopping on the local bottom gates (Extended Data Fig. 1f). These contact vias are used by the top metal wiring to contact and route to the bottom gates and bottom metal routing layers. Post-etch, the surface is cleaned with both a solvent rinse as well as oxygen plasma, in preparation for the CNT deposition. Before CNT deposition, the surface is treated with hexamethyldisilazane, a common photoresist adhesion promoter, which improves the CNT deposition (both density and uniformity) over the high-k gate dielectric. The 150-mm wafer is then submerged in a toluene-based solution of purified CNTs (similar to the commercial Isosol-100 available from NanoIntegris; http://nanointegris.com/), containing approximately 99.99% semiconducting-CNTs. The amount of time the wafer incubates in the solution, as well as the concentration of the CNT solution, both affect the final CNT density; this process is optimized to achieve approximately 40–60 CNTs per linear micrometre (Extended Data Fig. 1g). Immediately before CNT incubation, the CNT solution is diluted to the target concentration and is horn-sonicated briefly to maximize CNT suspension (importantly, some CNT aggregates will always remain). Post-CNT deposition, we perform the RINSE method (the first step of our MMC) to remove CNT aggregates that deposit on the wafer, leaving CNTs uniformly deposited across the 150-mm wafer. Importantly, RINSE does not degrade the remaining CNTs or remove the non-aggregated CNTs on the wafer (Extended Data Fig. 5). After CNT incubation, we perform the CNT active etch in order to remove CNTs outside the active region of the CNFETs (that is, the channel region of the CNFETs). To do so, we lithographically pattern the active region of the CNFETs (protecting CNTs in these regions with photoresist), and etch all CNTs outside these regions in oxygen plasma. The photoresist is then stripped in a solvent rinse, leaving CNTs patterned only in the intended locations (that is, in the channel regions of the CNFETs) on the wafer (Extended Data Fig. 1h). We use solution-based CNTs here, but an alternative method for depositing CNTs on the substrate is aligned growth of CNTs on a crystalline substrate followed by transfer of the CNTs onto the wafer used for circuit fabrication; both methods have shown the ability to achieve high-drive-current CNFETs[5,17].

MIXED method for CNT CMOS. After the active etch of the CNTs (described in the paragraph above), the p-CNFET source and drain metal contacts are lithographically patterned and defined. We deposit the p-CNFET contacts (0.6-nm-thick titanium for adhesion followed by 85-nm-thick platinum) using electron-beam evaporation, and the contacts are patterned through a dual-layer lift-off process (Extended Data Fig. 1i). This third metal layer acts as both the p-CNFET source contact and the p-CNFET drain contact, as well as the local interconnect. After establishing the p-CNFET source and drain contacts, we passivate the p-CNFETs by depositing 100-nm-thick SiO_2 over only the p-CNFETs (Extended Data Fig. 1j). Following p-CNFET passivation, the wafer undergoes an oxide densification anneal in forming gas (dilute H_2 in N_2) at 250 °C for 5 min. This concludes the p-CNFET fabrication. To fabricate the n-CNFETs, the fourth metal layer (100-nm-thick titanium, n-CNFET source and drain contacts) are defined (Extended Data Fig. 1k, similar to the p-CNFET source and drain contact definition). For the electrostatic doping, nonstoichiometric HfO_x is deposited through atomic-layer deposition at 200 °C uniformly over the wafer. Finally, we lithographically pattern and etch contact vias (Extended Data Fig. 1m) through the HfO_x for metal contacts to the bottom metal layers, and then etch the HfO_x covering the p-CNFETs (the p-CNFETs are protected during this etch by the SiO_2 passivation oxide deposited previously). Additional experimental characterization of the MIXED method (step two of our MMC) is shown in Extended Data Fig. 6.

Back-end-of-line metal routing. Following the CNT CMOS fabrication, conventional back-end-of-line metallization is used to define additional metal layers over the CNFETs (for example, for power distribution and signal routing). As the metal layers below the CNFETs are primarily used for signal routing, we use the top (fifth) metal layer in the process for power distribution (Extended Data Fig. 1n). Additional metal can be deposited over the input/output pads for wire bonding and packaging. At the end of the process, the wafer undergoes a final anneal in forming gas at 325 °C. The finished wafer is diced into chips, and each chip can be packaged for testing or probed for standard cell library characterization.

This 3D physical architecture (with metal routing below and above the CNFETs) is uniquely enabled by the low-temperature processing of the CNFETs. The solution-based deposition of the CNTs decouples the high-temperature CNT synthesis from the wafer, enabling the entire CNFET to be fabricated with a maximum processing temperature below 325 °C. This enables metal layers and the gate stack to be fabricated before the CNFET fabrication takes place. This is in contrast to silicon CMOS, which requires high-temperature processing (for example, >1,000 °C) for steps such as doping activation annealing. This prohibits the fabrication of silicon CMOS over pre-fabricated metal wires, as the high-temperature silicon CMOS processing would damage or destroy these bottom metal layers[35,36].

Experimental measurements. A supply voltage (V_{DD}) of 1.8 V is chosen to maximize the noise resilience of the CNT CMOS digital logic, given the experimentally measured transfer characteristics of the fabricated CNFETs (noise resilience is quantified by the SNM metric (see main-text section 'DREAM'). To interface with each RV16X-NANO chip, we use a high channel count data acquisition system (120 channels) that offers a maximum clock frequency of 10 kHz while simultaneously sampling all channels. This limits the frequency we run RV16X-NANO at to 10 kHz, at which the power consumption is 969 μW (dominated by leakage current). However, this is not the maximum clock speed of RV16X-NANO; during physical design, using an experimentally calibrated CNFET compact model and process design kit in an industry-practice VLSI design flow, the maximum reported clock frequency is 1.19 MHz, reported by Cadence Innovus following placement-and-routing of all logic gates. Future work may improve CNFET-level metrics (for example, improvements in contact resistance, gate stack engineering, CNT density and CNT alignment to increase CNFET on-current) to further speed up clock frequency.

VLSI design methodology. The design flow of RV16X-NANO leverages only industry-standard tools and techniques. We have created a standard process design kit for CNFETs as well as a library of standard cells for CNFETs that is compatible with existing EDA tools and infrastructure without modification. This enables us to leverage decades of existing EDA tools and infrastructure to design, implement, analyse and test arbitrary circuits using CNFETs, which is important to enable CNFET circuits to be widely adopted in the mainstream. This is the first experimental demonstration of a complete process design kit and library for an emerging beyond-silicon nanotechnology.

A high-level description of RISC-V implementation is written in Bluespec and then compiled into a standard RTL hardware description language: Verilog. Bluespec enables testing of all instructions (listed in Extended Data Table 1) written in assembly code (for example, using the assembly language commands) to verify proper functionality of the RV16X-NANO. The functional tests for each instruction are also compiled into waveforms and tested on the RTL generated by Bluespec, they are verified using Verilator to verify proper functionality of the RTL (inputs and outputs are recorded and analysed as value change dump (.vcd) files). RTL descriptions of each module are shown in Fig. 2.

Next is the physical design of RV16X-NANO, including logic synthesis with a DREAM-enforcing standard cell library (see Methods section 'DREAM method implementation'), placement and routing, parasitic extraction, and design sign-off (that is, design rule check, layout versus schematic, verification of the final Graphic Database System, GDSII), as shown in Fig. 4. The RTL is synthesized into digital logic gates using Cadence Genus, using the following components of the CNFET process design kit and standard cell library: the LIBERTY file (.lib) containing power/timing information for all standard library cells, the cell macro library exchange format file (.macro.lef) containing abstract views of all standard library cells (for example, signal/power pin locations and routing blockage information), the technology library exchange format file (.tech.lef) containing metal routing layer information (for example, metal/via width/spacing), and the back-end-of-line parasitic information (.qrcTech file). To enforce DREAM, we use a subset of library cells in the standard cell library, including cells with inverter- and nand2-based logic stages (for combinational logic), and logic stages using tri-state inverters (for sequential logic), as well as fill cells (to connect power rails) and decap cells (to increase capacitance between power rails V_{DD} and V_{SS}); specifically, these 23 cells comprise (see Extended Data Fig. 3): and2_x1, buf_x1, buf_x2, buf_x4, buf_x8, decap_x3, decap_x4, decap_x5, decap_x6, decap_x8, dff2xdlh_x1, fand2stk_x1,

inv_x1, inv_x2, inv_x4, inv_x8, inv_x16, mux2nd2_x1, nand2_x1, nor2nd2_x1, or2nd2_x1, xnor2nd2_x1 and xor2nd2_x1. During synthesis, all output pads are buffered with library cell buf_x8 to drive the output pad so that no signal simultaneously drives an output pad as well as another logic stage to prevent excessive capacitive loading in the core. Also, to minimize routing congestion in preparation for place-and-route, the register file (containing four registers, as described in Fig. 2) is directly synthesized from the Verilog hardware description language (instead of being designed 'by hand' or using a memory compiler) so that the D-flip-flops (dff2xdlh_x1: Extended Data Fig. 3) comprising the state elements (registers) can be dispersed throughout the chip to lower the overall total wire length. The final netlist is flattened so there is no hierarchy, and so logic can be optimized across module boundaries, and is then exported for place and route.

Placement-and-routing is performed using Cadence Innovus, loading the synthesized netlist output from Cadence Genus. The core floorplan for standard library cells is defined as 6.912 mm × 6.912 mm. Given the standard cell library and logic gate counts from synthesis (and2_x1: 188, buf_x1: 3, buf_x8: 82, buf_x16: 25, dff2xdlh_x1: 68, fand2stk_x1: 15, inv_x1: 75, inv_x2: 15, inv_x4: 10, inv_x8: 27, mux2nd2_x1: 189, nand2_x1: 625, nor2nd2_x1: 27, or2nd2_x1: 211, xnor2nd2_x1: 14 and xor2nd2_x1: 8), the resulting standard cell placement utilization is 40%. The pad ring for input/output is defined as another cell with 160 pads: 40 on each side, with minimum width 170 μm and minimum spacing 80 μm, totalling pitch 250 μm. Inputs are primarily towards the top of the chip, outputs are primarily on the bottom, and power/ground (V_{DD}/V_{SS}) pads are on the sides (Fig. 1). 1. In addition to the core area, an additional boundary of 640 μm is permitted for signal routing around the core area (containing all standard library cells), for example, for relatively long global routing signals. Placement is performed while optimizing for uniform cell density and low routing congestion. The power grid is defined on top of the core area using the fifth metal layer (as shown in Fig. 1), while not consuming any additional routing resources within the metal layers for signal routing. The clock tree is implemented as a single high-fanout net loaded by all 68 D-flip-flops (for each of CLK and the inverted clock: CLKN), which is directly connected to an input pad, to minimize clock skew variations between registers. All routing signals and vias are defined on a grid, with routing jogs enabled on each metal layer to enable optimization targeting maximum spacing between adjacent metal traces. After this stage of routing, incremental placement is performed to further optimize congestion, and then filler cells and decap cells are inserted to connect the power rails between adjacent library cells and to increase capacitance between V_{DD} and V_{SS} to improve signal integrity. After this incremental placement, the final routing takes place, reconnecting all the signals and routing to the pads, including detailed routing to fix all design rule check violations (for example, metal shorts and spacing violations). Finally, parasitic resistance and capacitances are extracted to finalize the power/timing analysis, and the final netlist is output to quantify the SNM for all pairs of connected logic stages. The GDSII is streamed out from Cadence Innovus and is imported into Cadence Virtuoso for final design rule check and layout versus schematic, using the standard verification rule format files with Mentor Graphics Calibre. The synthesized netlist is again used in the RTL functional simulation environment to verify proper functionality of all instructions, using Synopsys VCS, with waveforms for each test stored in a value change dump (.vcd) file. We note that these waveforms constitute the input waveforms to test the final fabricated CNFET RV16X-NANO, as well as the expected waveforms output from the core, as shown in Fig. 3.

Once the GDSII for the core is complete, it is instantiated in a full die, which contains the core in the middle, alignment marks and test structures (including all standard library cells, CNFETs and test structures to extract wire/via parasitic resistance and capacitance) around the outside of the core as shown in Extended Data Fig. 2. This die (2 cm × 2 cm) is then tiled onto a 150-mm wafer, each of which comprises 32 dies (6 × 6 array of dies minus 4 dies in the corners). Each layer in the GDS is flattened for the entire wafer and then released for fabrication.
DREAM method implementation. To implement DREAM:

1) Generate the DREAM SNM table—for each pair of logic stages in the standard cell library, quantify the susceptibility of the pair to metallic CNTs as follows: use the variation-aware CNFET SNM model (Extended Data Fig. 9) to compute SNM for all possible combinations of whether or not each CNFET comprises an metallic CNT (for example, in a (nand2, nor2) logic stage pair, there are 256 such combinations because there are 8 total CNFETs ($2^8 = 256$)). Record the minimum computed SNM in the DREAM SNM table (Fig. 6b, Extended Data Fig. 9).

2) Determine prohibited logic stage pairs—choose an SNM cut-off value (SNM_C), such that all logic stage pairs whose SNM in the DREAM SNM table is less than SNM_C are prohibited during physical design (see example in Fig. 6b: green entries satisfy SNM_C whereas red entries prohibited cascaded logic gate pairs). The method of choosing SNM_C is described below.

3) Physical design—use industry-practice design flows and EDA tools to implement VLSI circuits without using the prohibited logic stage pairs. Ideally, EDA tools will enable designers to set which logic stage pairs to prohibit during power/timing/area optimization, but this is currently not a supported feature. To demonstrate DREAM in this work, we create a DREAM-enforcing library that comprises a subset of library cells such that no possible combination of cells can be connected to form a prohibited logic stage pair.

To choose SNM_C, we use a bisection search. A larger SNM_C prohibits more logic stage pairs, resulting in better p_{NMS} with higher energy/delay/area cost (and vice versa). To satisfy target p_{NMS} constraints (for example, $p_{NMS} \geq 99\%$), while minimizing cost, we optimize SNM_C as follows. Step 1: Initialize a lower bound L and upper bound U for SNM_C. $L = 0$, and U is the maximum value of SNM_C that enables EDA tools to synthesize arbitrary logic functions (for example, prohibiting all logic stage pairs except (inv, inv) would be insufficient). Step 2: Find p_{NMS} using $SNM_C = (L + U)/2$, using the design flow in Extended Data Fig. 9. Record the set of prohibited logic stage pairs, as well as the circuit physical design, p_{NMS}, energy, delay and area. Step 3: If p_{NMS} satisfies the target constraint (for example, $p_{NMS} \geq 99\%$), set $U = SNM_C$. Otherwise set $L = SNM_C$. Step 4: Set $SNM_C = (L + U)/2$. If p_{NMS} has already been analysed for the resulting set of prohibited logic stage pairs, terminate. Otherwise, return to step 2.

For all physical designs recorded in step 2 we choose the physical design that satisfies the target p_{NMS} constraint with minimum energy/delay/area cost. Importantly, the cost of implementing DREAM is ≤10% energy, ≤10% delay and ≤20% area. To integrate DREAM within EDA tools—enabling p_{NMS} optimization simultaneously with power/timing/area optimization—is a goal for future work on improving p_s versus power/timing/area trade-offs. The effect that the remaining metallic CNTs have on EDP is shown in Extended Data Fig. 7.

Data availability

The data that supports the findings of this study are shown in Figs. 1–6, Extended Data Figs. 1–9, and Extended Data Table 1, and are available from the corresponding author on reasonable request.

35. Batude, P. et al. Advances, challenges and opportunities in 3D CMOS sequential integration. *In IEEE Int. Electron Devices Meet.* https://doi.org/10.1109/IEDM.2011.6131506 (IEEE, 2011).
36. Shulaker, M. et al. Monolithic 3D integration of logic and memory: Carbon nanotube FETs, resistive RAM, and silicon FETs. In *IEEE Int. Electron Devices Meet.* https://doi.org/10.1109/IEDM.2014.7047120 (IEEE, 2014).
37. Clark, L. T. et al. ASAP7: A 7-nm finFET predictive process design kit. *Microelectron. J.* **53**, 105–115 (2016).
38. Zhang, J. et al. Carbon nanotube correlation: promising opportunity for CNFET circuit yield enhancement. In *Proc. 47th Design Autom. Conf.* https://doi.org/10.1145/1837274.1837497 (IEEE, 2010).
39. Sherazi, S. M. et al. Track height reduction for standard-cell in below 5nm node: how low can you go? In *Design-Process-Technology Co-optimization for Manufacturability XII* **10588** 1058809 (International Society for Optics and Photonics, 2018).
40. Hills, G. et al. Rapid co-optimization of processing and circuit design to overcome carbon nanotube variations. *IEEE Trans. Comput.-Aided Des. Integr. Circuits Syst.* **34**, 1082–1095 (2015).

Acknowledgements We acknowledge Analog Devices, Inc. (ADI), the Defence Advanced Research Projects Agency (DARPA) Three-Dimensional System-on-Chip (3DSoC) program, the National Science Foundation and the Air Force Research Laboratory for support. We thank S. Feindt, A. Olney, T. O'Dwyer, S. Gupta and S. Knepper (all at ADI), and Dimitri Antoniadis and Utsav Banerjee (both at MIT) for collaborations.

Author contributions G.H. performed all VLSI design aspects of this project (developing and analysing DREAM, creating the CNFET process design kit and designing all standard cells in the CNFET library; he performed the entire RV16X-NANO RTL-to-GDS physical design and led experimental calibration and testing). C.L. performed all fabrication aspects of this project (developing and experimentally demonstrating RINSE, developing, experimentally demonstrating and characterizing MIXED; he developed the fabrication process, and fabricated all of the RV16X-NANO wafers and their subsequent packaging to chips). A.W. led the architectural definition of RV16X-NANO (including Bluespec, the Verilog hardware description language and the instruction-set architecture; he also wrote the test programs). S.F. contributed to the architectural definition, system design and implementation. M.D.B., T.S., P.K. and R.H. contributed to developing the fabrication process and establishing the CNFET fabrication flow. A.A. contributed to circuit design. Y.S. and D.M. contributed to project development. A., A.C. and M.M.S. were in charge, advised, and led on all aspects of the project.

Competing interests A.C. is a board member at Analog Devices, Inc., and this work was sponsored in part by Analog Devices, Inc.

Additional information
Supplementary information is available for this paper at https://doi.org/10.1038/s41586-019-1493-8.
Correspondence and requests for materials should be addressed to M.M.S.
Peer review information *Nature* thanks Marko Radosavljevic and the other, anonymous, reviewer(s) for their contribution to the peer review of this work.
Reprints and permissions information is available at http://www.nature.com/reprints.

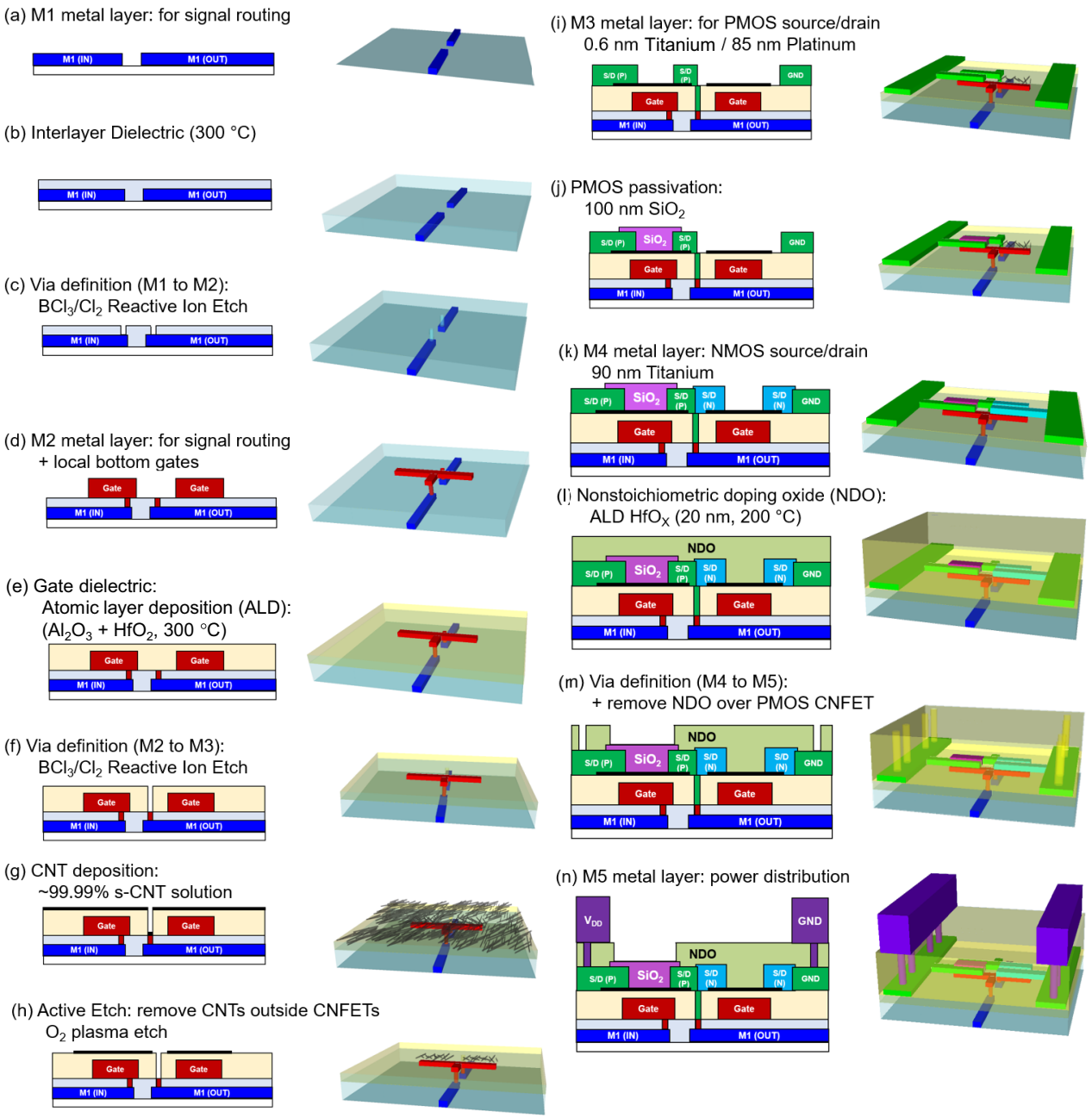

Extended Data Fig. 1 | Fabrication process flow for RV16X-NANO. The fabrication process is a 5-metal-layer (M1 to M5) process and involves >100 individual process steps. s-CNT, semiconducting CNT; S/D, source/drain.

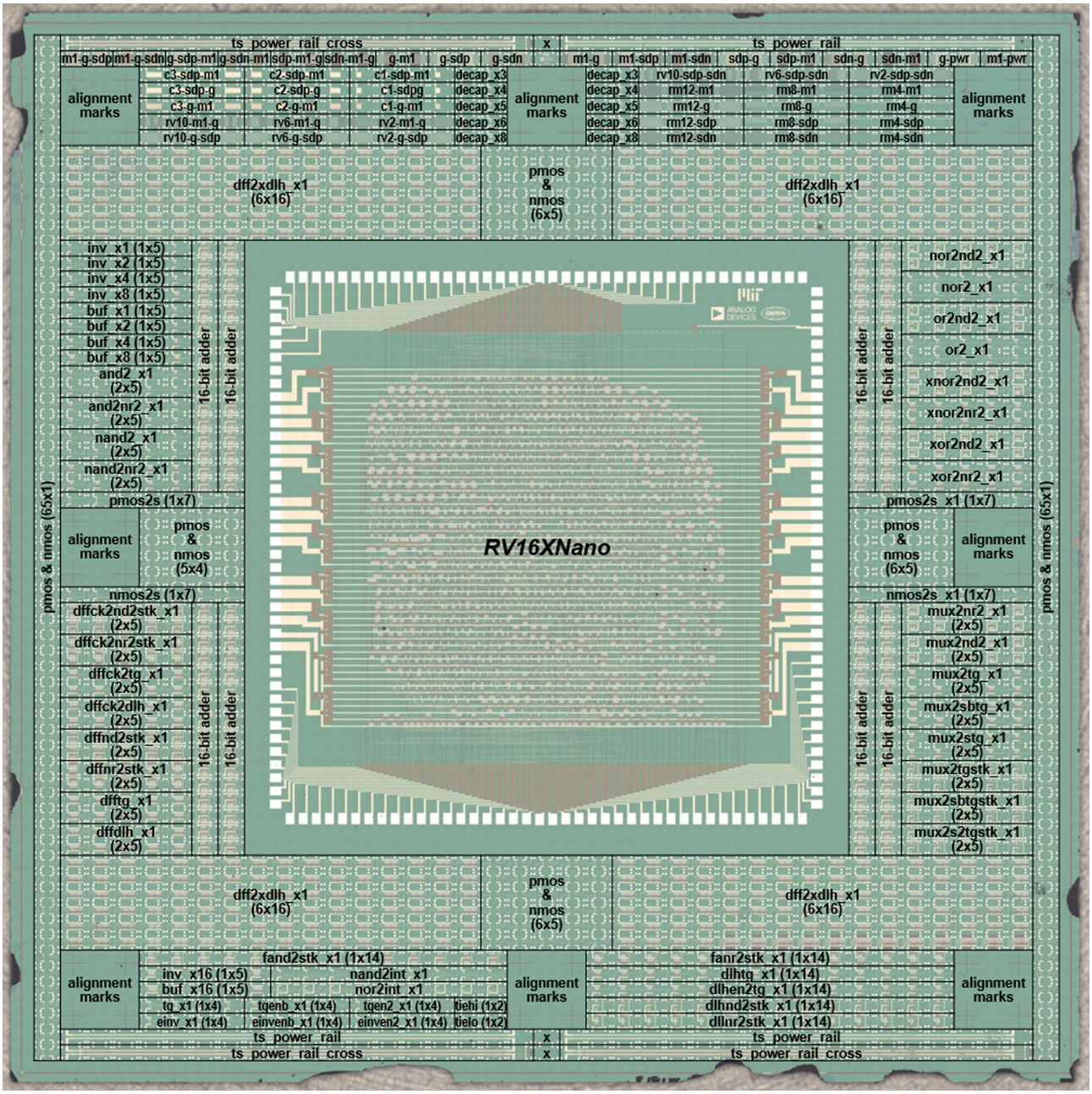

Extended Data Fig. 2 | Microscopy image of a full fabricated RV16X-NANO die. The processor core is in the middle of the die, with test circuitry surrounding the perimeter (when the RV16X-NANO is diced for packaging, these test structures are removed). The test structures include test structures for monitoring fabrication, as well as for measuring and characterizing all of the 63 standard cells in our standard cell library.

library cell (63)	description
and2_x1	2-input AND
and2nr2_x1	2-input AND (comprising nor2/inv logic stages)
buf_x1	buffer, drive strength 1x
buf_x2	buffer, drive strength 2x
buf_x4	buffer, drive strength 4x
buf_x8	buffer, drive strength 8x
buf_x16	buffer, drive strength 16x
decap_x3	capacitance between power rails, size 1x
decap_x4	capacitance between power rails, size 2x
decap_x5	capacitance between power rails, size 4x
decap_x6	capacitance between power rails, size 8x
decap_x8	capacitance between power rails, size 16x
dff2xdlh_x1	positive edge-triggered D-flip-flop (comprising 2x D-latches), input separate clocks for master/slave
dffck2dlh_x1	positive edge-triggered D-flip-flop (comprising 2x D-latches), input clock and inverted clock
dffck2nd2stk_x1	positive edge-triggered D-flip-flop (comprising nand2/inv logic stages), input clock and inverted clock, 2x cell height
dffck2nr2stk_x1	positive edge-triggered D-flip-flop (comprising nor2/inv logic stages), input clock and inverted clock, 2x cell height
dffck2tg_x1	positive edge-triggered D-flip-flop (comprising D-latch and transmission gate), input clock and inverted clock
dffdlh_x1	positive edge-triggered D-flip-flop (comprising 2x D-latches), inverted clock generated locally
dffnd2stk_x1	positive edge-triggered D-flip-flop (comprising nand2/inv logic stages), 2x cell height
dffnr2stk_x1	positive edge-triggered D-flip-flop (comprising nand2/inv logic stages), 2x cell height
dfftg_x1	positive edge-triggered D-flip-flop (comprising D-latch and transmission gate), inverted clock generated internally
dlhen2tg_x1	high-enable D-latch (comprising transmission gates), input enable and inverted enable
dlhnd2stk_x1	high-enable D-latch (comprising nand2/inv logic stages)
dlhtg_x1	high-enable D-latch (comprising transmission gates), inverted enable generated internally
dllnr2stk_x1	high-enable D-latch (comprising nor2/inv logic stages)
einv_x1	tri-state inverter, inverted enable generated internally
einven2_x1	tri-state inverter, input enable and inverted enable
einvenb_x1	tri-state inverter, enable (and inverted enable) buffered internally
fand2stk_x1	full-adder (comprising nand2/inv logic stages)
fanr2stk_x1	full-adder (comprising nor2/inv logic stages)
fill_x1	fill cell (extends power rails), size 1x
fill_x2	fill cell (extends power rails), size 2x
fill_x4	fill cell (extends power rails), size 4x
fill_x8	fill cell (extends power rails), size 8x
fill_x16	fill cell (extends power rails), size 16x
inv_x1	inverter, drive strength 1x
inv_x2	inverter, drive strength 2x
inv_x4	inverter, drive strength 4x
inv_x8	inverter, drive strength 8x
inv_x16	inverter, drive strength 16x
mux2nd2_x1	2-input multiplexer (comprising nand2/inv logic stages)
mux2nr2_x1	2-input multiplexer (comprising nor2/inv logic stages)
mux2s2tg_x1	2-input multiplexer (comprising transmission gates), input select and inverted select
mux2s2tgstk_x1	2-input multiplexer (comprising transmission gates), input selected and inverted select, 2x cell height
mux2sbtg_x1	2-input multiplexer (comprising transmission gates), select (and inverted select) buffered internally
mux2sbtgstk_x1	2-input multiplexer (comprising transmission gates), select (and inverted select) buffered internally, 2x cell height
mux2tg_x1	2-input multiplexer (comprising transmission gates), inverted select generated internally
mux2tgstk_x1	2-input multiplexer (comprising transmission gates), inverted select generated internally, 2x cell height
nand2_x1	2-input NOT-AND
nand2nr2_x1	2-input NOT-AND (comprising nor2/inv logic stages)
nor2_x1	2-input NOT-OR
nor2nd2_x1	2-input NOT-OR (comprising nand2/inv logic stages)
or2_x1	2-input OR
or2nd2_x1	2-input OR (comprising nand2/inv logic stages)
tg_x1	transmission gate, inverted enable generated internally
tgen2_x1	transmission gate, input enable and inverted enable
tgenb_x1	transmission gate, enable (and inverted enable) buffered internally
tiehi_x2	output is tied high (to VDD)
tielo_x2	output is tied low (to VSS)
xnor2nd2_x1	2-input EXCLUSIVE-NOT-OR (comprising nand2/inv logic stages)
xnor2nr2_x1	2-input EXCLUSIVE-NOT-OR (comprising nor2/inv logic stages)
xor2nd2_x1	2-input EXCLUSIVE-OR (comprising nand2/inv logic stages)
xor2nr2_x1	2-input EXCLUSIVE-OR (comprising nor2/inv logic stages)

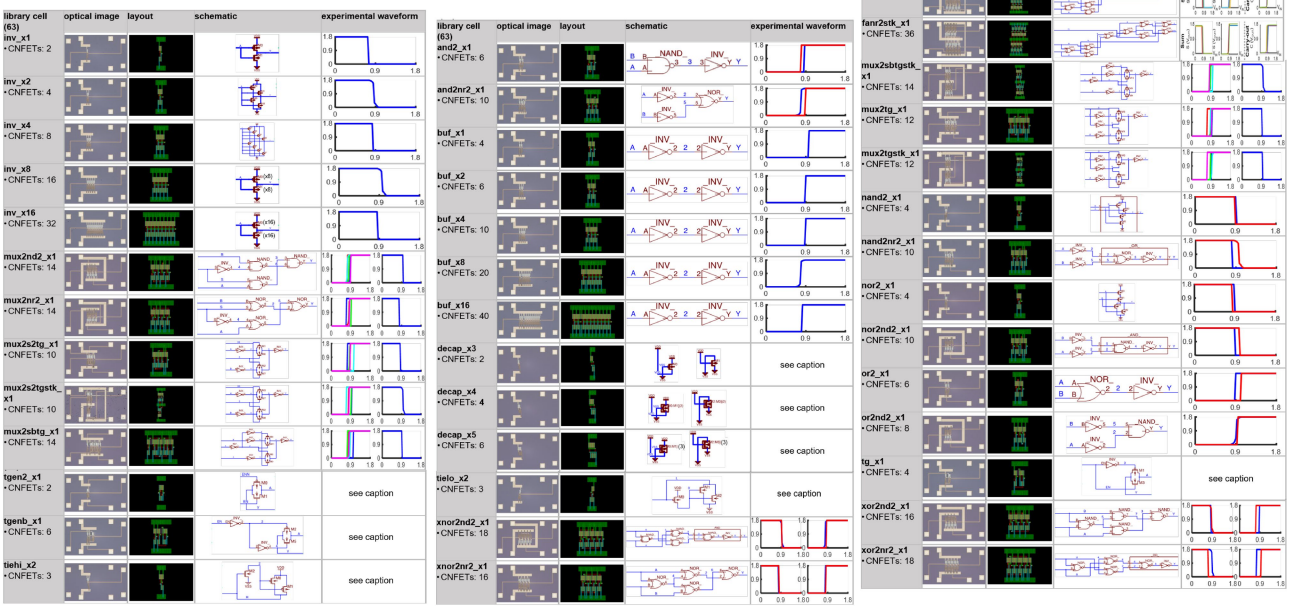

Extended Data Fig. 3 | CNFET standard cell library. List of all of the standard cells comprising our standard cell library, along with a microscopy image of each fabricated standard cell, the schematic of each cell, and a typical measured waveform from each fabricated cell. As expected for static CMOS logic stages, the CNFET logic stages exhibit output voltage swing exceeding 99% of V_{DD}, and achieve gain of >15. Experimental waveforms are not shown for cells whose functionality is not demonstrated by output voltage as a function of either input voltage or time; for example, for cells without outputs (for example, fill cells: cell names that start with 'fill_' or decap cells: cell names that start with 'decap_'), for cells whose output is constant (tied high/low: cell names that start with 'tie_'), or for transmission gates (cell names that start with 'tg_').

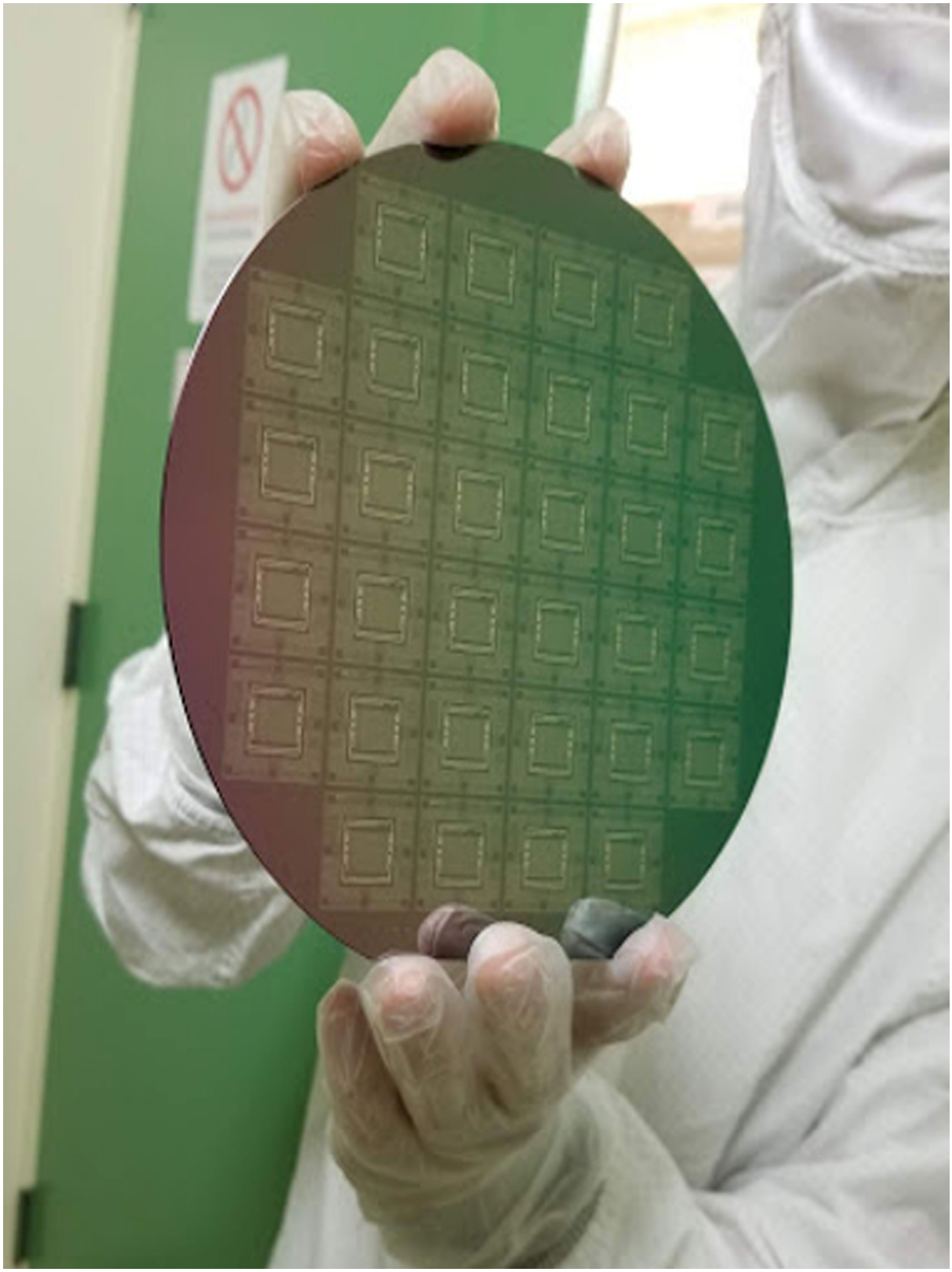

Extended Data Fig. 4 | Image of a completed RV16X-NANO 150-mm wafer. Each wafer includes 32 dies (single die shown in Extended Data Fig. 2).

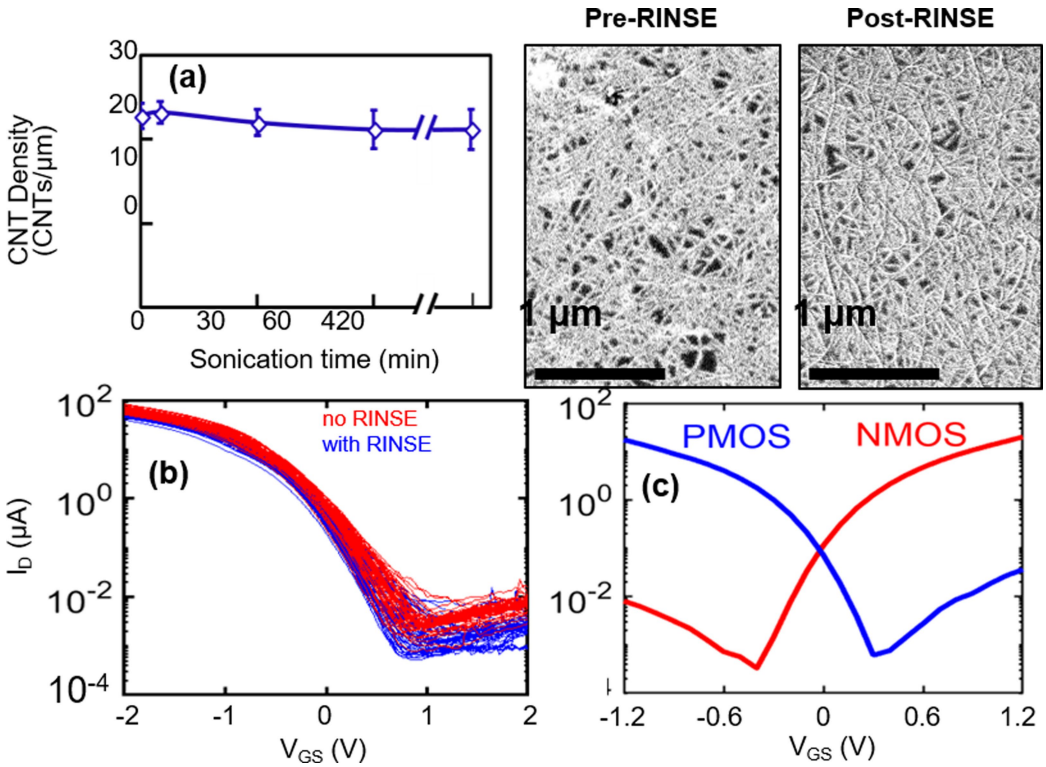

Extended Data Fig. 5 | Negligible effect of RINSE on CNTs and CNFETs. **a**, CNT density is the same pre- versus post-RINSE. **b**, CNFET I_D–V_{GS} exhibit minimal change for sets of CNFETs fabricated with and without RINSE ($V_{DS} = -1.8$ V for all measurements shown). Both samples came from the same wafer, which was diced after the CNT deposition but before the RINSE process. One sample underwent RINSE while the other sample did not. **c**, CNFETs can still be doped NMOS after the RINSE process, leveraging our MIXED process ($V_{DS} = -1.2$ V for all measurements shown).

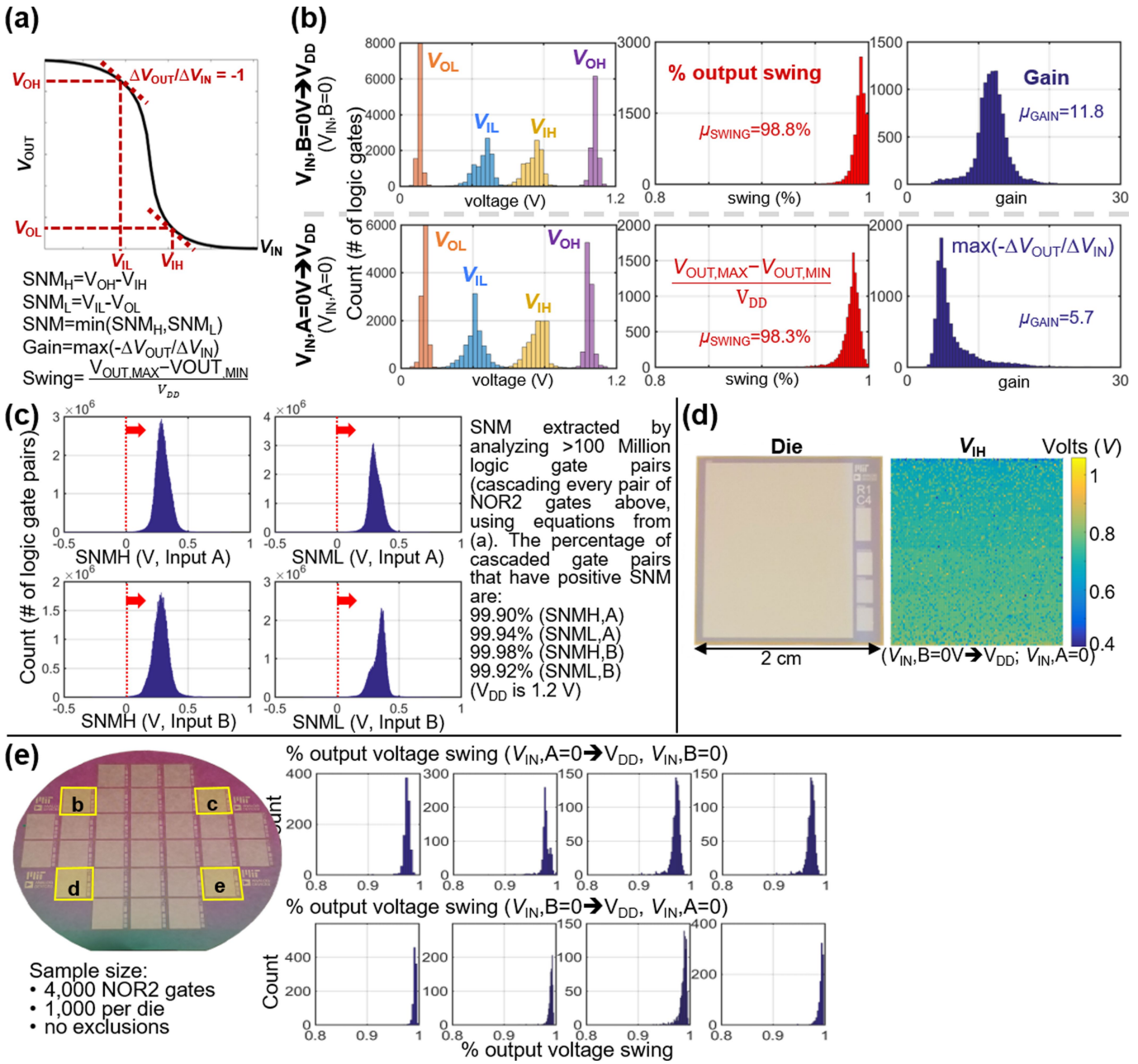

Extended Data Fig. 6 | MIXED CNFET CMOS characterization. **a**, Definitions of key metrics for characterizing logic gates, including SNM, gain and swing. V_{OH}, V_{IH}, V_{IL} and V_{IL} (labelled on the VTCs in **a**, where (V_{IL}, V_{OH}) and (V_{IH}, V_{OL}) are the points on the VTC where $\Delta V_{OUT}/\Delta V_{IN} = -1$) are used to extract the noise margin: SNM = min(SNM_H, SNM_L). **b**, Key metrics extracted for the 10,400 CNFET CMOS nor2 logic gates measured in Fig. 5 (metrics defined in **a**). This is the largest CNT CMOS demonstration to date, to our knowledge. V_{DD} is 1.2 V. **c**, SNM is extracted based on the distributions from **b**. We analyse >100 million logic gate pairs based on these experimental results. **d**, Spatial dependence of V_{IH} (as an example parameter to compute SNM). Each pixel represents the V_{IH} of the nor2 at that location in the die. Importantly, V_{IH} increases across the die (from top to bottom). The change in V_{IH} corresponds with slight changes in CNFET threshold voltage. The fact that the threshold voltage variations are not independently and identically distributed (i.i.d.), but rather have spatial dependence, illustrates that a portion of the threshold voltage variations (and therefore variation in SNM) is due to wafer-level processing-related variations (CNT deposition is more uniform across the 150-mm wafer). Future work should optimize processing steps, for example, increasing the uniformity of the atomic-layer-deposition oxide deposition used for electrostatic doping to further improve SNM for realizing VLSI circuits. **e**, Wafer-scale CNFET CMOS characterization. Measurements from 4 dies across 150-mm wafer (1,000 CNFET CMOS nor2 logic gates are sampled randomly from the 10,400 such logic gates in each die). No outliers are excluded. Yield and performance variations are negligible across the wafer, illustrated by the distribution of the output voltage swing.

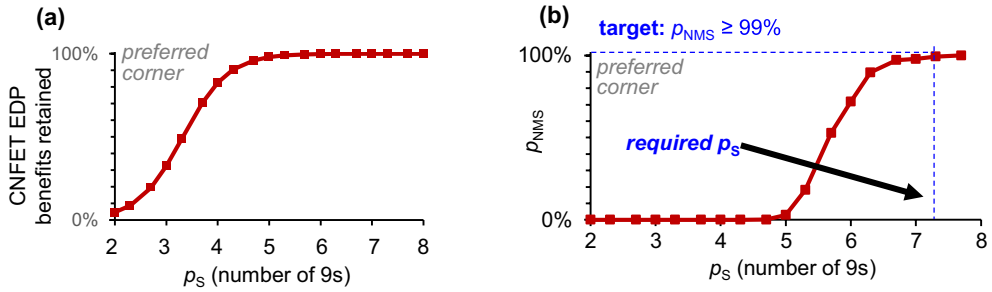

Extended Data Fig. 7 | Effect of metallic CNTs on digital VLSI circuits. **a**, Reduction in CNFET EDP benefits versus p_S (metallic CNTs increase I_{OFF}, degrading EDP). $p_S \approx 99.999\%$, sufficient to minimize EDP cost due to metallic CNTs to $\leq 5\%$. **b**, p_{NMS} versus p_S (metallic CNTs degrade SNM), (shown for $SNM_R = V_{DD}/5$, and for a circuit of one million logic gates). Although 99.999% p_S is sufficient to limit EDP degradation to $\leq 5\%$, panel **b** shows that SNM imposes far stricter requirements on purity: $p_S \approx 99.999999\%$ (that is, number of 9s is 8) to achieve $p_{NMS} \geq 99\%$ (number of 9s is 2). Results in panels **a** and **b** are simulated for VLSI circuit modules from a 7-nm node processor core (see Supplementary Information and Methods for additional details).

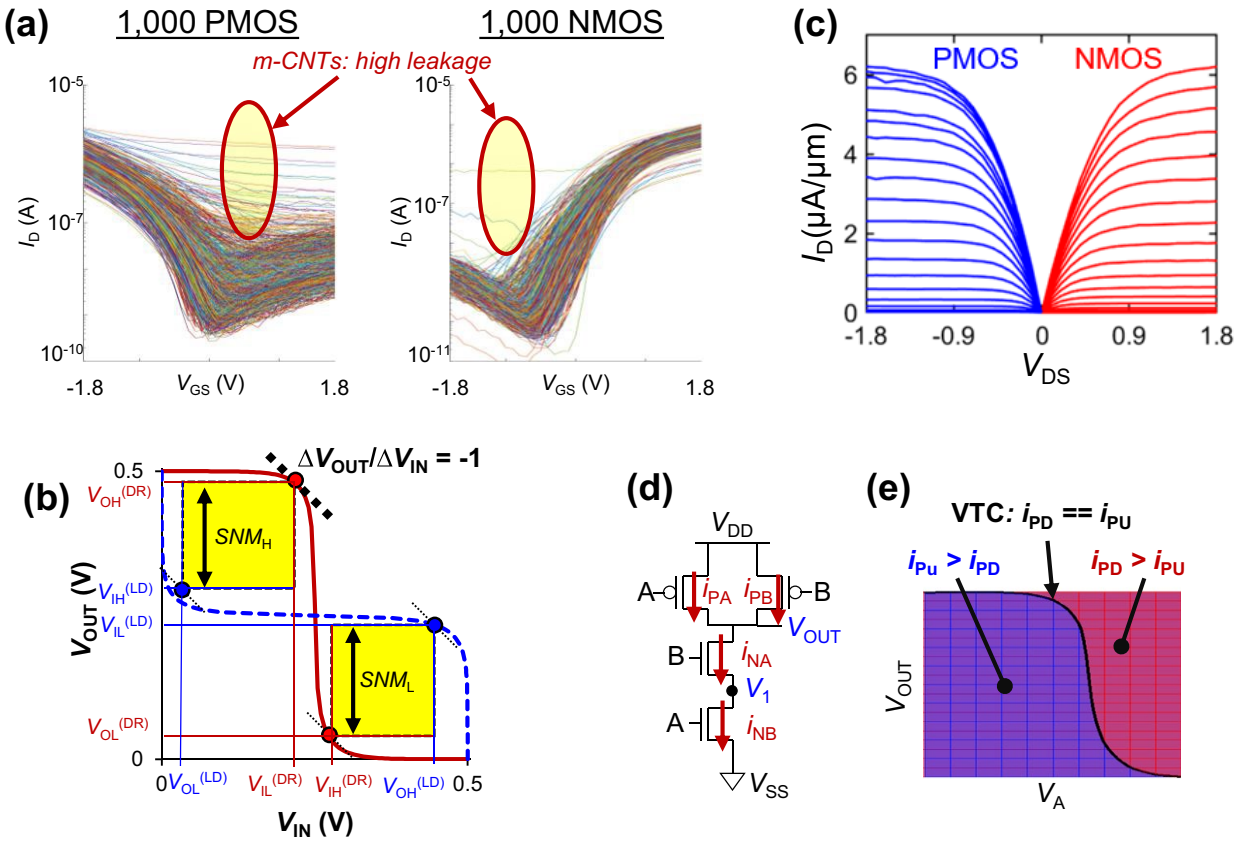

Extended Data Fig. 8 | Methodology to solve VTCs using CNFET *I–V* measurements. a, Experimentally measured I_D versus V_{GS} for all 1,000 NMOS (V_{DS} = 1.8 V) and 1,000 PMOS CNFETs (V_{DS} = −1.8 V), with no CNFETs omitted. Metallic CNTs (m-CNTs) present in some CNFETs result in high off-state leakage current ($I_{OFF} = I_D$ at V_{GS} = 0 V). **b**, VTC and SNM parameter definitions, for example, for (nand2, nor2). DR is the driving logic stage; LD is the loading logic stage. SNM = min(SNM$_H$, SNM$_L$), where SNM$_H$ = $V_{OH}^{(DR)} - V_{IH}^{(LD)}$ and SNM$_L$ = $V_{IL}^{(LD)} - V_{OL}^{(DR)}$. **c–e**, Methodology to solve VTCs (for example, for nand2) using experimentally measured CNFET *I–V* curves. **c**, Example I_D versus V_{DS} for NMOS and PMOS CNFETs (V_{GS} is swept from −1.8 V to 1.8 V in 0.1-V increments). **d**, Schematic. To solve a *V*TC (for example, V_{OUT} versus V_A with $V_B = V_{DD}$): for each V_A, find V_1 and V_{OUT} such that $i_{PA} + i_{PB} = i_{NA} = i_{NB}$ (DC, direct current, convergence). **e**, Current in the pull-up network (i_{PU}, where $i_{PU} = i_{PA} + i_{PB}$, and i_{PA} and i_{PB} are the labelled drain currents of the PMOS FETs gated by A and B, respectively) and current in the pull-down network (i_{PD}, where $i_{PD} = i_{NA} = i_{NB}$, and i_{NA} and i_{NB} are the labelled drain currents of the NMOS FETs gated by A and B, respectively) versus V_{OUT} and V_A. The VTC *is* seen where these currents intersect. CNFETs are fabricated at a ~1 μm technology node, and the CNFET width is 19 μm in panel **a**.

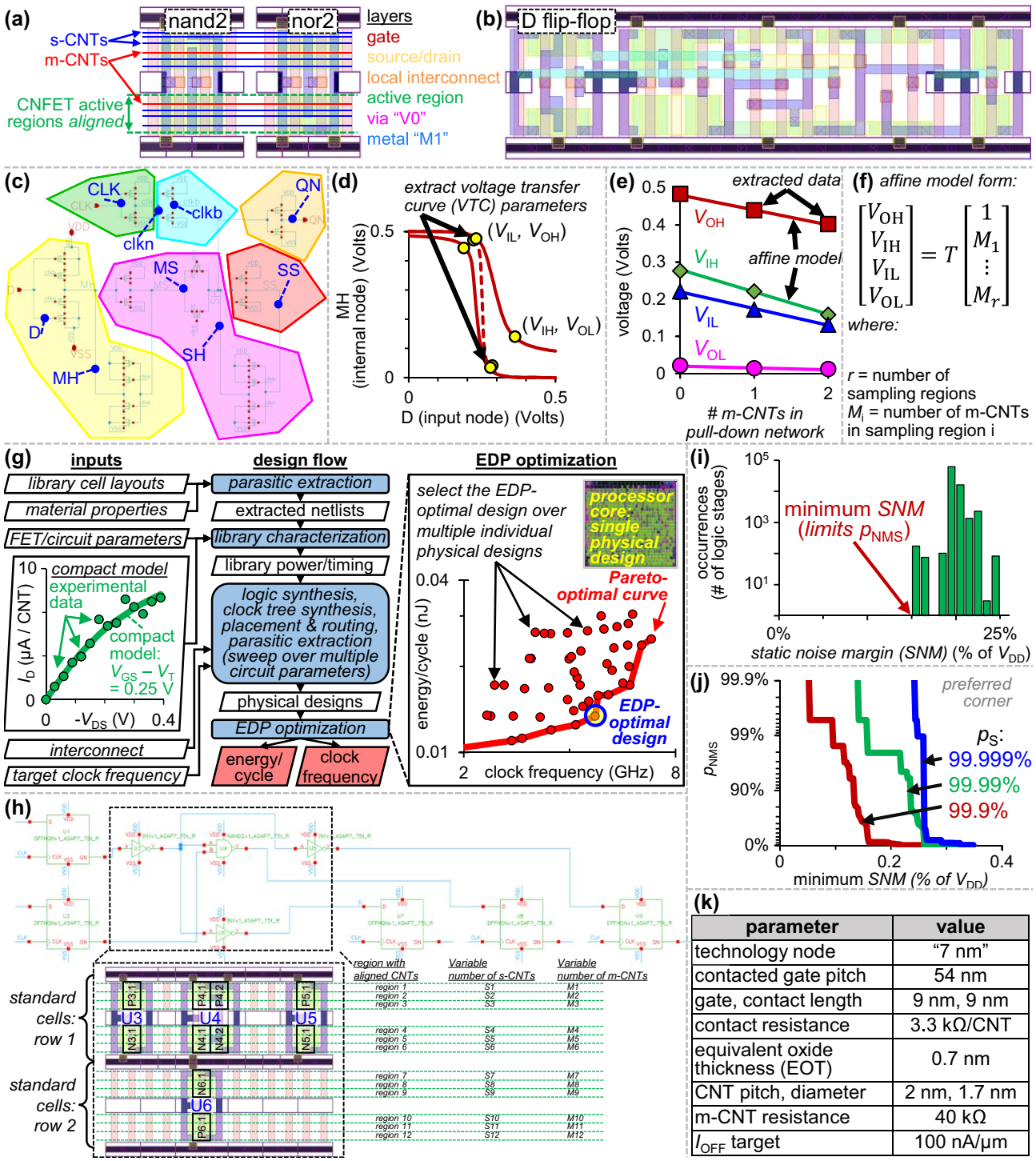

(k)

parameter	value
technology node	"7 nm"
contacted gate pitch	54 nm
gate, contact length	9 nm, 9 nm
contact resistance	3.3 kΩ/CNT
equivalent oxide thickness (EOT)	0.7 nm
CNT pitch, diameter	2 nm, 1.7 nm
m-CNT resistance	40 kΩ
I_{OFF} target	100 nA/μm

Extended Data Fig. 9 | See next page for caption.

Extended Data Fig. 9 | DREAM implementation and methodology. **a,** Standard cell layouts (derived using the 'asap7sc7p5t' standard cell library[37]), illustrating the importance of CNT correlation: because the length of CNTs (which can be of the order of hundreds of micrometres) is typically much longer compared with the CNFET contacted gate pitch (CGP, for example about 42–54 nm for a 7-nm node[37]), the number of s-CNTs and m-CNTs in CNFETs can be uncorrelated or highly correlated depending on the relative physical placement of CNFET active regions[38]. For many CMOS standard cell libraries at sub-10-nm nodes (for example refs [37,39]), the active regions of FETs are highly aligned, resulting in highly correlated number of m-CNTs among CNFETs in library cells, further degrading VTCs (because one m-CNT can affect multiple CNFETs simultaneously). **b**–**f**, Generating a variation-aware CNFET SNM model, shown for a D-flip-flop (dff) derived from the asap7sc7p5t standard cell library[37]. **b**, Layout used to extract netlists for each logic stage. **c**, Schematic: CNFETs are grouped by logic stage (with nodes arbitrarily labelled 'D', 'MH', 'MS', 'SH', 'SS', 'CLK', 'clkn', 'clkb' and 'QN' for ease of reference). **d**, For each extracted netlist, there can be multiple VTCs: for each logic stage output, a logic stage input is sensitized if the output state (0 or 1) depends on the state of that input (given the states of all the other inputs). For example, for a logic stage with Boolean function: Y = !(A*B+C), C is sensitized when (A, B) = (0, 0), (0, 1) or (1, 0). We simulate all possible VTCs (over all logic stage outputs and sensitized inputs), and also in the presence of m-CNTs. For example, panel **d** shows a subset of the VTCs for the logic stage in panel **b** with output node 'MH' (labelled in panel **c**), and sensitized input 'D' (with labelled nodes ('clkb', 'clkn', 'MS') = (0, 1, 0)). The dashed line indicates VTC with no m-CNTs, and the solid lines are example VTCs in the presence of m-CNTs (including the effect of CNT correlation). In each case, we model V_{OH}, V_{IH}, V_{IL} and V_{OL} as affine functions of the number of m-CNTs (M_i) in each of r regions (M_1, ..., M_r), with calibration parameters in the static noise margin (SNM) model matrix T (shown in panel **f**). **e**, Example calibration of the SNM model matrix T for the VTC parameters extracted in panel **d**; the symbols are VTC parameters extracted from circuit simulations (using Cadence Spectre), and solid lines are the calibrated model. **f**, Affine model form. **g**–**j**, VLSI design and analysis methodology. **g**, Industry-practice physical design flow to optimize energy and delay of CNFET digital VLSI circuits, including: (1) library power/timing characterization (using Cadence Liberate) across multiple V_{DD} and using parasitics extracted from standard cell layouts (derived from the asap7sc7p5t standard cell library), in conjunction with a CNFET compact model[8]. (2) Synthesis (using Cadence Genus), place-and-route (using Cadence Innovus) with back-end-of-line (BEOL) wire parasitics from the ASAP7 process design kit (PDK). (3) Circuit EDP optimization: we sweep both V_{DD} and target clock frequency (during synthesis/place-and-route) to create multiple physical designs. The one with best EDP is used to compare design options (for example, DREAM versus baseline). **h**, Subset of logic gates in an example circuit module, showing the effect of CNT correlation at the circuit level (for example, the m-CNT counts of CNFETs P3,1 and P5,1 are both equal to $M_1 + M_2 + M_3$)[40]. **i**, Distribution of SNM over all connected logic stage pairs, for a single sample of the circuit m-CNT counts. The minimum SNM for each trial limits the probability that all noise margin constraints in the circuit are satisfied (p_{NMS}). **j**, Cumulative distribution of minimum SNM over 10,000 Monte Carlo trials, shown for multiple target p_S values, where p_S is the probability that a given CNT is a semiconducting CNT. These results are used to find p_{NMS} versus p_S for a target SNM requirement (SNM_R), where p_{NMS} is the fraction of trials that meet the SNM requirement for all logic stage pairs. We note that p_{NMS} can then be exponentiated to adjust for various circuit sizes based on the number of logic gates. **k**, CNFET compact model parameters (for example, 7-nm node).

Extended Data Table 1 | RISC-V instruction set architecture implementation details

inst	category	summary	assembly
addi	register-immediate arithmetic	add constant, no overflow exception	addi rd, rs1, imm
add	register-register arithmetic	addition with 3 GPRs, no overflow exception	add rd, rs1, rs2
andi	register-immediate arithmetic	bitwise AND with constant	andi rd, rs1, imm
and	register-register arithmetic	bitwise AND with 3 GPRs	and rd, rs1, rs2
auipc	register-immediate arithmetic	load (pc + constant) into GPR	auipc rd, imm
beq	conditional branch	branch if 2 GPRs are equal	beq rs1, rs2, imm
bgeu	conditional branch	branch based on unsigned comparison of 2 GPRs	bgeu rs1, rs2, imm
bltu	conditional branch	branch based on unsigned comparison of 2 GPRs	bltu rs1, rs2, imm
bge	conditional branch	branch based on signed comparison of 2 GPRs	bge rs1, rs2, imm
blt	conditional branch	branch based on signed comparison of 2 GPRs	blt rs1, rs2, imm
bne	conditional branch	branch if 2 GPRs are not equal	bne rs1, rs2, imm
jalr	unconditional jump	jump to relative address, place return address in GPR	jalr rd, rs1, imm
jal	unconditional jump	jump to address, place return address in GPR	jal rd, imm
lh	memory instruction	load short from memory into GPR	lh rd, imm(rs1)
lui	register-immediate arithmetic	load upper bits of constant into GPR	lui rd, imm
ori	register-immediate arithmetic	bitwise OR with constant	ori rd, rs1, imm
or	register-register arithmetic	bitwise OR with 3 GPRs	or rd, rs1, rs2
sh	memory instruction	store short into memory	sh rs2, imm(rs1)
slli	register-immediate arithmetic	shift left logical by constant	slli rd, rs1, imm
sll	register-register arithmetic	shift left logical by GPR value	sll rd, rs1, rs2
sltiu	register-immediate arithmetic	set GPR based on unsigned comparison of GPR and constant	sltiu rd, rs1, imm
slti	register-immediate arithmetic	set GPR based on signed comparison of GPR and constant	slti rd, rs1, imm
sltu	register-register arithmetic	set GPR based on unsigned comparison of 2 GPRs	sltu rd, rs1, rs2
slt	register-register arithmetic	set GPR based on signed comparison of 2 GPRs	slt rd, rs1, rs2
srai	register-immediate arithmetic	shift right arithmetic by constant	srai rd, rs1, imm
sra	register-register arithmetic	shift right arithmetic by GPR value	sra rd, rs1, rs2
srli	register-immediate arithmetic	shift right logical by constant	srli rd, rs1, imm
srl	register-register arithmetic	shift right logical by GPR value	srl rd, rs1, rs2
sub	register-register arithmetic	subtraction with 3 GPRs, no overflow exception	sub rd, rs1, rs2
xori	register-immediate arithmetic	bitwise XOR with constant	xori rd, rs1, rs2
xor	register-register arithmetic	bitwise XOR with 3 GPRs	xor rd, rs1, rs2

inst	format (type-imm)	instruction format 31 30 29 28 27 26 25 24 23 22 21 20 19 18 17 16 15 14 13 12 11 10 09 08 07 06 05 04 03 02 01 00
addi	I-I	imm[11:0] rs1[4:2] rs1 funct3=ADD ~~rd[4:2]~~ rd opcode=OPIMM
add	R	0 0 0 0 0 0 0 ~~rs2[4:2]~~ rs2 ~~rs1[4:2]~~ rs1 funct3=ADD ~~rd[4:2]~~ rd opcode=OP
andi	I-I	imm[11:0] ~~rs1[4:2]~~ rs1 funct3=AND ~~rd[4:2]~~ rd opcode=OPIMM
and	R	0 0 0 0 0 0 0 ~~rs2[4:2]~~ rs2 ~~rs1[4:2]~~ rs1 funct3=AND ~~rd[4:2]~~ rd opcode=OP
auipc	I-U	~~imm[31:16]~~ imm[15:12] ~~rd[4:2]~~ rd opcode=AUIPC
beq	S-B	imm[10:5] ~~rs2[4:2]~~ rs2 ~~rs1[4:2]~~ rs1 funct3=BEQ imm[4:1] opcode=BRANCH
bgeu	S-B	imm[10:5] ~~rs2[4:2]~~ rs2 ~~rs1[4:2]~~ rs1 funct3=BGEU imm[4:1] opcode=BRANCH
bltu	S-B	imm[10:5] ~~rs2[4:2]~~ rs2 ~~rs1[4:2]~~ rs1 funct3=BLTU imm[4:1] opcode=BRANCH
bge	S-B	imm[10:5] ~~rs2[4:2]~~ rs2 ~~rs1[4:2]~~ rs1 funct3=BGE imm[4:1] opcode=BRANCH
blt	S-B	imm[10:5] ~~rs2[4:2]~~ rs2 ~~rs1[4:2]~~ rs1 funct3=BLT imm[4:1] opcode=BRANCH
bne	S-B	imm[10:5] ~~rs2[4:2]~~ rs2 ~~rs1[4:2]~~ rs1 funct3=BNE imm[4:1] opcode=BRANCH
jalr	I-I	imm[11:0] ~~rs1[4:2]~~ rs1 0 0 0 ~~rd[4:2]~~ rd opcode=JALR
jal	U-J	imm[10:1] ~~imm[19:16]~~ imm[15:12] ~~rd[4:2]~~ rd opcode=JAL
lh	I-I	imm[11:0] ~~rs1[4:2]~~ rs1 funct3=LH ~~rd[4:2]~~ rd opcode=LOAD
lui	I-U	~~imm[31:16]~~ imm[15:12] ~~rd[4:2]~~ rd opcode=LUI
ori	I-I	imm[11:0] ~~rs1[4:2]~~ rs1 funct3=OR ~~rd[4:2]~~ rd opcode=OPIMM
or	R	0 0 0 0 0 0 0 ~~rs2[4:2]~~ rs2 ~~rs1[4:2]~~ rs1 funct3=OR ~~rd[4:2]~~ rd opcode=OP
sh	S-S	imm[11:5] ~~rs2[4:2]~~ rs2 ~~rs1[4:2]~~ rs1 funct3=SH imm[4:0] opcode=STORE
slli	I-I	0 0 0 0 0 0 0 imm[3:0] ~~rs1[4:2]~~ rs1 funct3=SLL ~~rd[4:2]~~ rd opcode=OPIMM
sll	R	0 0 0 0 0 0 0 ~~rs2[4:2]~~ rs2 ~~rs1[4:2]~~ rs1 funct3=SLL ~~rd[4:2]~~ rd opcode=OP
sltiu	I-I	imm[11:0] ~~rs1[4:2]~~ rs1 funct3=SLTU ~~rd[4:2]~~ rd opcode=OPIMM
slti	I-I	imm[11:0] ~~rs1[4:2]~~ rs1 funct3=SLT ~~rd[4:2]~~ rd opcode=OPIMM
sltu	R	0 0 0 0 0 0 0 ~~rs2[4:2]~~ rs2 ~~rs1[4:2]~~ rs1 funct3=SLTU ~~rd[4:2]~~ rd opcode=OP
slt	R	0 0 0 0 0 0 0 ~~rs2[4:2]~~ rs2 ~~rs1[4:2]~~ rs1 funct3=SLT ~~rd[4:2]~~ rd opcode=OP
srai	I-I	0 1 0 0 0 0 0 imm[3:0] ~~rs1[4:2]~~ rs1 funct3=SR ~~rd[4:2]~~ rd opcode=OPIMM
sra	R	0 1 0 0 0 0 0 ~~rs2[4:2]~~ rs2 ~~rs1[4:2]~~ rs1 funct3=SR ~~rd[4:2]~~ rd opcode=OP
srli	I-I	0 0 0 0 0 0 0 imm[3:0] ~~rs1[4:2]~~ rs1 funct3=SR ~~rd[4:2]~~ rd opcode=OPIMM
srl	R	0 0 0 0 0 0 0 ~~rs2[4:2]~~ rs2 ~~rs1[4:2]~~ rs1 funct3=SR ~~rd[4:2]~~ rd opcode=OP
sub	R	0 1 0 0 0 0 0 ~~rs2[4:2]~~ rs2 ~~rs1[4:2]~~ rs1 funct3=ADD ~~rd[4:2]~~ rd opcode=OP
xori	I-I	imm[11:0] ~~rs1[4:2]~~ rs1 funct3=XOR ~~rd[4:2]~~ rd opcode=OPIMM
xor	R	0 0 0 0 0 0 0 ~~rs2[4:2]~~ rs2 ~~rs1[4:2]~~ rs1 funct3=XOR ~~rd[4:2]~~ rd opcode=OP

The top panel shows all supported instructions implemented in RV16X-NANO, adhering to RISC-V format specifications for RV32E, with high-level description summary for each. Each instruction is categorized into one of six formats, including instruction type (R-type, I-type, S-type, U-type) and immediate variant (I-immediate, U-immediate, B-immediate, J-immediate, S-immediate), forming one of six formats (type immediate): R, I-I, I-U, S-B, S-S, U-J (shown in the bottom panel). For the assembly code, 'rd' is the destination register, 'rs1' is the source register 1, 'rs2' is the source register 2, 'imm' is immediate. The bottom panel shows the bit-level description of each instruction format. The bottom 7 bits (inst[6:0]) are always the OPCODE, and then the remaining bits are decoded depending on the instruction format (determined by the OPCODE). Values that are crossed out indicate bits that are not used for the 16-bit data path implementation (RV16E) with four registers, instead of 32-bit data path implementation (RV32E) with 16 registers. For example, for instruction 'auipc', only 2 of the 5 reserved bits for 'rd' are required to address the register file for register 'rd' (because there are only $2^2 = 4$ registers instead of $2^5 = 32$), and also the upper 16 bits of the 32-bit immediate (that is, imm[31:16]) are not used because the data path is truncated to 16 bits.

ARTICLE

https://doi.org/10.1038/s41586-019-1487-6

Metastatic-niche labelling reveals parenchymal cells with stem features

Luigi Ombrato[1], Emma Nolan[1], Ivana Kurelac[1,2], Antranik Mavousian[3], Victoria Louise Bridgeman[1], Ivonne Heinze[4], Probir Chakravarty[5], Stuart Horswell[5], Estela Gonzalez-Gualda[1], Giulia Matacchione[1], Anne Weston[6], Joanna Kirkpatrick[4], Ehab Husain[7], Valerie Speirs[8], Lucy Collinson[6], Alessandro Ori[4], Joo-Hyeon Lee[3,9]* & Ilaria Malanchi[1]*

Direct investigation of the early cellular changes induced by metastatic cells within the surrounding tissue remains a challenge. Here we present a system in which metastatic cancer cells release a cell-penetrating fluorescent protein, which is taken up by neighbouring cells and enables spatial identification of the local metastatic cellular environment. Using this system, tissue cells with low representation in the metastatic niche can be identified and characterized within the bulk tissue. To highlight its potential, we applied this strategy to study the cellular environment of metastatic breast cancer cells in the lung. We report the presence of cancer-associated parenchymal cells, which exhibit stem-cell-like features, expression of lung progenitor markers, multi-lineage differentiation potential and self-renewal activity. In ex vivo assays, lung epithelial cells acquire a cancer-associated parenchymal-cell-like phenotype when co-cultured with cancer cells and support their growth. These results highlight the potential of this method as a platform for new discoveries.

Cancer cell behaviour is strongly influenced by the surrounding cells in the tumour microenvironment (TME). Various cell types in the TME are known to influence cancer cell behaviour, including mesenchymal cells such as activated fibroblasts, pericytes and endothelial cells, as well as different types of inflammatory cells[1].

During the early phase of metastatic growth, cancer cells generate a local TME (metastatic niche), which is distinct from the normal tissue structure and key for supporting metastatic outgrowth[2]. However, detailed analysis of the cellular composition of the metastatic niche, especially at early stages, is constrained by the difficulty of spatially discriminating the metastatic-niche cells within the bulk tissue. This hampers the identification of cells that might respond to early colonization by cancer cells but remain low in number as metastases grow.

In this study, we present a strategy in which metastatic cancer cells mark their neighbouring cells, thereby identifying them in the tissue and overcoming these limitations. We have applied this system to interrogate the early metastatic environment of breast cancer cells in the lung. We confirm that the system enables us to quantitatively and qualitatively distinguish known metastatic-niche cells within the tissue, and identify lung epithelial cells, in which a regenerative-like program is activated, as a component of the metastatic TME. We show that these epithelial cells acquire multi-lineage differentiation potential when co-cultured with cancer cells and support their growth. These results support the notion that, in addition to the well-characterized stromal activation, a parenchymal response might contribute to creating the metastatic microenvironment.

The mCherry niche-labelling system

To develop a labelling system that uses metastatic cancer cells to directly identify their neighbouring cells in vivo, we generated a secreted fluorescent mCherry protein containing a modified lipid-permeable transactivator of transcription (TATk) peptide[3,4] (sLP–mCherry) (Fig. 1a and Extended Data Fig. 1a). We engineered 4T1 breast cancer cells to co-express the sLP–mCherry and GFP; we refer to these cells as labelling-4T1 cells. In vitro, sLP–mCherry protein secreted by labelling-4T1 cells re-enters the cells, as indicated by changes in the intracellular localization of the red fluorescence (Extended Data Fig. 1b, c). sLP–mCherry protein is also taken up by unlabelled cells, both in co-culture with labelling-4T1 cells (Fig. 1b–d) and when cultured in medium conditioned by labelling-4T1 cells (LCM) (Extended Data Fig. 1d, e). Upon uptake into a cell, sLP–mCherry fluorescence has an intracellular half-life of 43 h (Extended Data Fig. 1f) and is localized in $CD63^+$ multi-lamellar bodies (lysosomal-like structures) where, owing to its high photostability[5], it retains high fluorescence intensity (Extended Data Fig. 1g, h). Fractionation of LCM shows that only the soluble fraction retains labelling activity, whereas the extracellular vesicles, a proportion of which contain sLP–mCherry, do not show labelling activity in vitro (Extended Data Fig. 1i–k).

In vivo, intravenous injection of labelling-4T1 cells ($GFP^+mCherry^+$) into syngeneic BALB/c mice to induce lung metastases efficiently labels surrounding host tissue cells ($GFP^-mCherry^+$), penetrating approximately five cell layers (Fig. 1e–g and Extended Data Fig. 2a, b). This enables specific discrimination of host cells in close proximity to cancer cells from distal lung cells ($GFP^-mCherry^-$) using fluorescence-activated cell sorting (FACS) (Fig. 1f). Notably, when micro-metastases grow larger, the number of $mCherry^+$-niche cells in the tissue remains proportional to the number of metastatic cells (Extended Data Fig. 2c). We detected no adaptive immunogenicity against sLP–mCherry and the local increase of $CD45^+$ immune cells within the mCherry population was observed specifically as a response to cancer cells (Extended Data Fig. 2d–f). Thus, this mCherry-niche-marking strategy enables spatial reconstitution of the local metastatic niche within the tissue. This permits functional identification of labelled cells and direct comparison with unlabelled cells within the same lung.

Tissue spatial resolution

To demonstrate the utility of the mCherry-niche strategy to specifically interrogate the local early changes induced by cancer cells, we

[1]Tumour-Host Interaction Laboratory, The Francis Crick Institute, London, UK. [2]Dipartimento di Scienze Mediche e Chirurgiche, Università di Bologna, Bologna, Italy. [3]Wellcome—MRC Cambridge Stem Cell Institute, University of Cambridge, Cambridge, UK. [4]Proteomics of Aging, Leibniz Institute on Aging, Fritz Lipmann Institute (FLI), Jena, Germany. [5]Bioinformatics and Biostatistics Unit, The Francis Crick Institute, London, UK. [6]Electron Microscopy Unit, The Francis Crick Institute, London, UK. [7]Department of Pathology, Aberdeen Royal Infirmary, Aberdeen, UK. [8]Institute of Medical Sciences, University of Aberdeen, Aberdeen, UK. [9]Department of Physiology, Development and Neuroscience, University of Cambridge, Cambridge, UK. *e-mail: jhl62@cam.ac.uk; Ilaria.Malanchi@crick.ac.uk

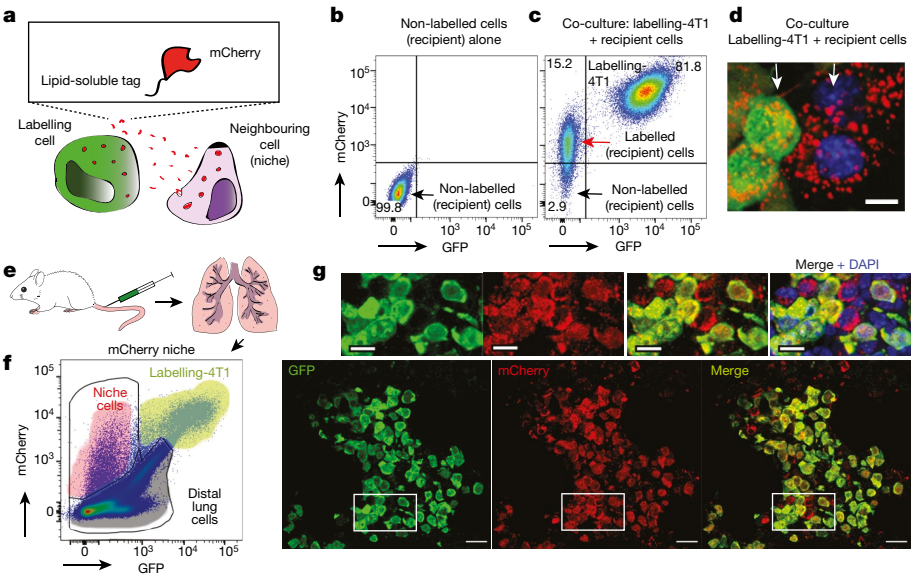

Fig. 1 | The mCherry-niche labelling strategy. **a**, Label design. Labelling-4T1 cells co-express the lipid-soluble cell-penetrating mCherry-fusion protein label and GFP. **b**, **c**, Representative FACS plots of naive 4T1 cells cultured alone (**b**) or co-cultured with labelling-4T1 cells (**c**). Numbers indicate the percentage of cells in the respective quadrant. **d**, Fluorescence image from co-cultures (scale bar, 10 μm). Data representative of two independent experiments (**b**–**d**). **e**–**g**, In vivo labelling. **e**, Schematic of the experiment[6]: labelling-4T1 cells are injected into mice; these cells metastasize in the lung and label nearby cells in the TME (niche) with mCherry. **f**, Representative FACS plot of a metastatic lung, $n = 50$ mice. **g**, Representative immunofluorescence images of labelling-4T1 cell metastasis ($n = 8$ mice). Labelling-4T1 cells are positive for both GFP and mCherry, whereas metastatic niche cells are positive for mCherry only. Blue, DAPI. Scale bars: main panels, 20 μm; enlarged insets, 10 μm. For gating strategy see Supplementary Information.

seeded 4T1-labelling cells in the lung via tail-vein injection. Lung tissue distant from micro-metastases remained unperturbed by primary-tumour-derived systemic changes[7]. To validate the mCherry-niche strategy, we first examined components known to be involved in metastatic-niche formation. CD45$^+$ immune cells were very abundant in the mCherry$^+$ niche and nearly exclusively derived from the myeloid lineage (CD11b$^+$) (Extended Data Figs. 2d, 3a). Lung neutrophils have been reported to enhance metastatic growth of cancer cells[8,9], and were indeed detected in the mCherry$^+$ niche (Extended Data Fig. 3b). Because abnormalities in lung neutrophils are often associated with cancer[10], we isolated mCherry$^+$-niche neutrophils (Ly6G$^+$) and compared their proteome to that of unlabelled neutrophils from the same lungs (Fig. 2a). The sub-pool of mCherry$^+$-niche neutrophils exhibited an increase in translation, oxidative phosphorylation and intracellular reactive oxygen species (ROS) levels relative to unlabelled neutrophils, as determined by FACS analysis (Fig. 2b, Extended Data Fig. 3c–f and Supplementary Data). To validate the functional relevance of specific features identified in mCherry$^+$-niche cells, we developed a 3D-scaffold co-culture system that mimics complex tissue-like cell–cell interactions. We found that lung neutrophils increased growth of actin–GFP$^+$ mouse mammary tumour virus (MMTV)–polyoma virus middle T antigen (PyMT) breast cancer cells in a ROS-dependent manner (Fig. 2c–e and Extended Data Fig. 3g, h). Collectively, these data highlight the potential of our strategy to detect in vivo changes that are spatially restricted to the metastatic environment.

The non-immune mCherry$^+$-niche signature

Whereas the contribution of immune cells to metastatic outgrowth has been widely investigated[11], less is known about the role of other TME cell types during metastatic nesting. Notably, the mCherry-labelling strategy can be used to provide spatiotemporal information by applying it to different stages of metastatic progression. We generated the gene-expression profile of non-immune (CD45$^-$) mCherry$^+$-niche cells at the time point immediately preceding micro-metastases as well as at an advanced metastatic stage (Fig. 3a, b). The majority of alterations were detected at the early stage, but additional changes subsequently discriminated the niche of macro-metastases (Fig. 3c and Extended Data Fig. 4a, b), confirming the evolution of the metastatic TME over time. MetaCore dataset enrichment and gene-set enrichment analysis (GSEA) highlighted changes in pathways related to proliferation, inflammation and tissue remodelling (Extended Data Fig. 4b, c). We next focused on the upregulated (more than twofold) genes encoding soluble factors in the mCherry$^+$ niche at both time

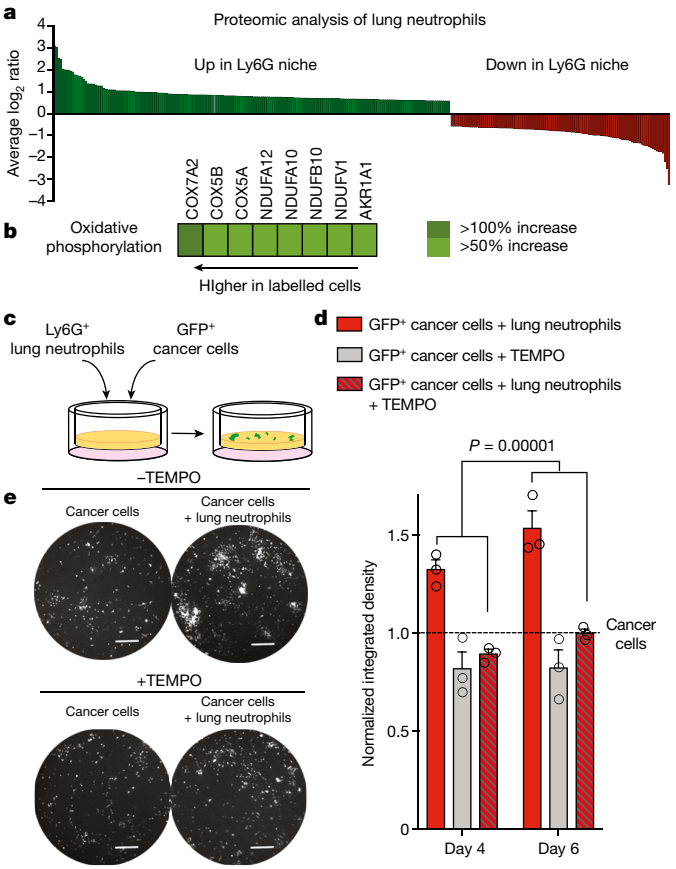

Fig. 2 | The mCherry-niche strategy enables characterization of metastatic-niche neutrophils. **a**, **b**, Proteomic analysis of FACS-sorted Ly6G$^+$ cells: all differentially detected proteins (**a**) and proteins associated with oxidative phosphorylation (**b**). **c**–**e**, Three-dimensional co-culture, with or without the ROS inhibitor TEMPO, of GFP$^+$ MMTV–PyMT cancer cells and Ly6G$^+$ cells sorted by magnetic-activated cell sorting (MACS). **c**, The co-culture scheme. **d**, Quantification of GFP signal ($n = 3$ independent experiments, each with 3 to 10 technical replicates). Data are normalized to cancer cell growth and represented as mean ± s.e.m. Statistical analysis of biological replicates by two-way ANOVA. **e**, Representative images from three independent experiments (day 6; scale bar, 400 μm).

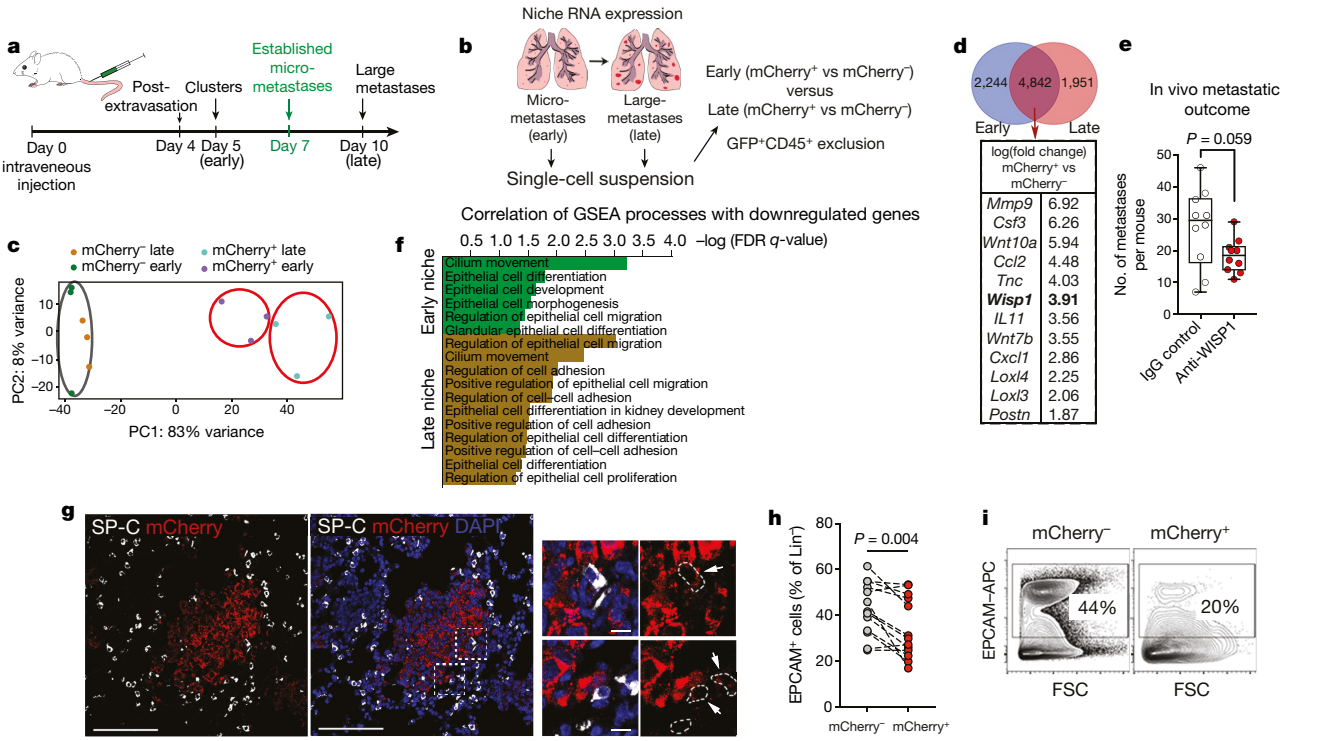

Fig. 3 | The mCherry-niche strategy identifies an epithelial component of metastatic TME. a, Schematic of metastatic progression using labelling-4T1 cells[6]. **b**, Experimental design for RNA-seq experiments[6]. **c**, Principal component analysis (PCA) of CD45$^-$Ter119$^-$ cell signatures from metastatic lungs at early ($n = 3$, 10 mice each) and late ($n = 3$, 5 mice each) time points. The black oval encloses the distal lung samples; red ovals enclose the mCherry$^+$-niche samples to highlight their similarity in the PCA plot. **d**, Venn diagram of differentially expressed genes in the mCherry$^+$ niche and selected factors that are common at early and late stages. *Wisp1* is also known as *Ccn4*. **e**, WISP1-blocking antibody treatment in vivo ($n = 10$, 2 independent experiments). Box edges represent 25th and 75th percentiles, the horizontal bar is the median and the whiskers show the range of values. **f**, GSEA correlation from RNA-seq data comparing early ($n = 3$) or late ($n = 3$) mCherry$^+$ samples with their respective mCherry$^-$ controls. **g**, Left, representative immunofluorescence images of lung tissue ($n = 3$ mice) showing mCherry-labelled micro-metastasis (red), SP-C (white) and DAPI (blue, middle). Right, enlarged view of areas indicated with dashed outlines. Scale bars: main panel, 100 μm; enlarged insets, 10 μm (white arrows and dashed outlines, mCherry-labelled SP-C$^+$ cells). **h**, EPCAM$^+$ cell frequency among Lin$^-$ (CD45$^-$CD31$^-$Ter119$^-$) cells in distal lung (mCherry$^-$) and mCherry$^+$ cells estimated by FACS ($n = 13$ mice). **i**, Representative FACS plots from **h**. Numbers indicate the percentage of cells in the respective quadrant. Statistical analysis by unpaired two-tailed *t*-test with Welch's correction (**e**), weighted Kolmogorov–Smirnov-like statistic with Benjamini–Hochberg correction (**f**) and paired two-tailed *t*-test (**h**).

points (Fig. 3d and Supplementary Data). We found many previously reported tumour-promoting factors[12–19], further validating the ability of our labelling system to faithfully capture the in vivo metastatic niche. We also found WNT1-induced protein (WISP1)—which has been suggested to act as an oncogene in breast cancer[20]—to be widely expressed in the mCherry$^+$ niche (Fig. 3d). Indeed, we detected upregulation of WISP1 in both cancer and metastatic-niche cells and confirmed its pro-metastatic activity by exogenous inhibition in vivo (Fig. 3e and Extended Data Fig. 5a–e).

We next probed the TME for other non-immune cell types, which might be difficult to resolve by standard techniques owing to their small numbers. Of note, we found pathways associated with lung epithelial cells in the metastatic-niche signature (Fig. 3f). Micro-metastases grow embedded within the alveolar compartment of the lung, and we found alveolar type II cells (AT2) expressing surfactant protein C (SP-C, encoded by *Sftpc*) in the metastatic niche (Fig. 3g). We also found mCherry$^+$-niche cells expressing the epithelial cell adhesion marker EPCAM, further supporting the presence of cells of lung parenchymal origin (Fig. 3h, i).

Cancer-associated parenchymal cells

We found mCherry$^+$-niche epithelial cells to have a higher proliferative activity compared to their normal lung counterparts (Fig. 4a). Concordantly, we detected alveolar cell clusters with increased proliferative activity at the metastatic borders of human breast cancer lung metastases, suggesting that a lung parenchymal response to metastatic growth may occur in both mouse and human (Extended Data Fig. 6a–f). Cancer cells benefit from the presence of a lung parenchymal response, as freshly isolated EPCAM$^+$ cells from naive lungs supported the growth of actin–GFP$^+$ MMTV–PyMT tumour cells in our 3D-scaffold co-culture system (Fig. 4b–d). Moreover, in line with the results shown in Fig. 2c–e, the presence of both lung neutrophils and epithelial cells further enhanced tumour growth (Extended Data Fig. 7a–d), highlighting the cellular complexity of the metastatic niche.

We next aimed to better define the perturbation occurring in lung epithelial cells in the proximity of cancer cells. To contextualize their presence among the other cellular components of the metastatic niche, we performed single-cell RNA sequencing (scRNA-seq) of CD45$^-$ cells. *t*-Distributed stochastic neighbour embedding (*t*-SNE) analysis of mCherry$^+$-niche cells identified a large stromal cluster in which different stromal cells could be distinguished (Fig. 4e and Extended Data Fig. 8a–c). This is in agreement with the various known mesenchymal cell components of the TME, as well as the characterization of different fibroblast subsets[21–24]. Notably, specifically in the mCherry$^+$ niche, *Epcam*-expressing epithelial cells are distributed in two clusters distinguished by the expression of E-cadherin (*Cdh1*) (Fig. 4e). We found that only mCherry$^+$-niche *Epcam*$^+$*Cdh1*$^+$ cells shared the expression of alveolar genes[25] with unlabelled distant lung *Epcam*$^+$ cells (Fig. 4f, g). Conversely, mCherry$^+$-niche *Epcam*$^+$*Cdh1*$^-$ cells expressed both the progenitor markers SCA1 (encoded by *Ly6a*) and *Tm4sf1*[26–28] (Fig. 4g). As validation of this de-differentiated signature observed in the majority of epithelial cells in the metastatic niche, reverse transcription with quantitative PCR (RT–qPCR) of EPCAM-sorted mCherry$^+$-niche cells also showed an overall reduction in expression of alveolar lineage

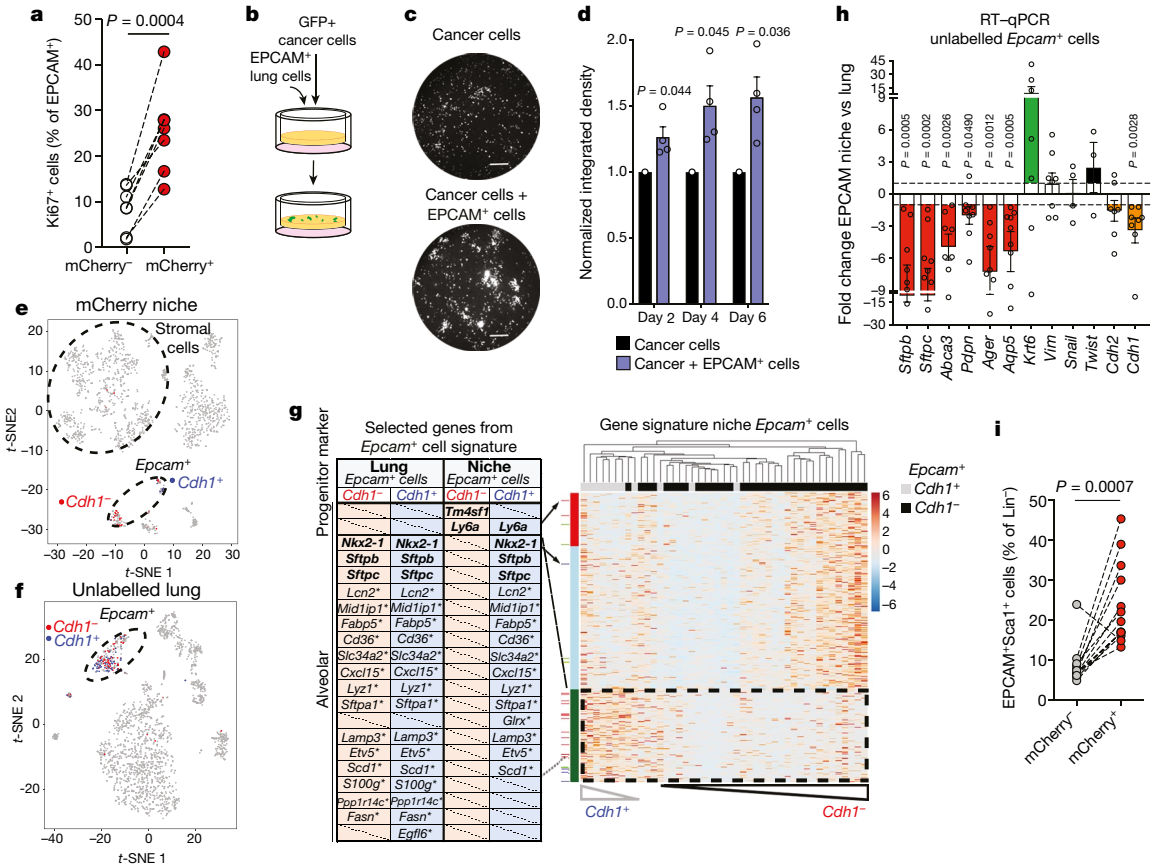

Fig. 4 | Lung epithelial cells in the metastatic niche display a progenitor phenotype. a, Ki67 staining in FACS-sorted mCherry$^-$ and mCherry$^+$ EPCAM$^+$ cells ($n = 7$ independent sorts). **b**–**d**, GFP$^+$ MMTV–PyMT cancer cell growth in 3D co-culture with MACS-sorted EPCAM$^+$ cells. **b**, The co-culture scheme. **c**, Representative images from 4 independent experiments (day 6; scale bar, 400 μm). **d**, Quantification of GFP signal ($n = 4$, each with 3 technical replicates, statistical analysis of biological replicates). Data are normalized to cancer cell growth. **e**–**g**, scRNA-seq analysis; *t*-SNE plots of CD45$^-$ cells from the mCherry$^+$ niche (**e**; $n = 1{,}473$) or distal lung (**f**; $n = 1{,}996$). **g**, Right, heat map of mCherry$^+$-niche EPCAM$^+$ cells (ordered genes in rows and hierarchically clustered cells in columns); left, table shows established lineage markers (bold); asterisks indicate putative alveolar markers[25]. **h**, RT–qPCR analysis of EPCAM$^+$ FACS-sorted cells (*Sftpc*, *Aqp5*, $n = 9$; *Sftpb*, *Abca3*, *Pdpn*, *Ager*, *Vim*, *Cdh1*, $n = 8$; *Krt6*, *Cdh2*, $n = 7$; *Snai1*, $n = 4$; *Twist*, $n = 3$). Data represented as fold change relative to mCherry$^-$ lung EPCAM$^+$ cells (statistical analysis on the ΔC_t values). **i**, EPCAM$^+$SCA1$^+$ cell frequency among Lin$^-$ (CD45$^-$CD31$^-$Ter119$^-$) cells, determined by FACS ($n = 13$ mice). Statistical analysis by paired two-tailed *t*-test (**a**, **h**, **i**), one-sample two-tailed *t*-test (**d**). Data represented as mean ± s.e.m.

markers (Fig. 4h). Moreover, the enrichment of EPCAM$^+$SCA1$^+$ cells in the mCherry$^+$ niche of different metastatic cell types was confirmed by FACS analysis (Fig. 4i and Extended Data Fig. 9a–c). Similarly, the presence of epithelial cells expressing another lung progenitor marker, integrin β4 (also known as CD104)[29], was increased in the mCherry$^+$-niche and in ex vivo co-cultures (Extended Data Fig. 9d–i).

In summary, we describe a parenchymal response to lung metastasis involving de-differentiated pools of epithelial cells in the niche, which we define as cancer-associated parenchymal cells (CAPs).

CAPs are activated AT2 cells

To functionally characterize CAPs, we tested their lineage differentiation potential ex vivo using a 3D Matrigel-based organoid co-culture system[27] (Fig. 5a). Unlabelled resident lung EPCAM$^+$ cells are predominantly alveolar[27], and formed mainly alveolar organoids when co-cultured with CD31$^+$ cells (Fig. 5b–d). mCherry$^+$-niche EPCAM$^+$ cells favoured the bronchiolar lineage and showed a remarkable capacity to generate multi-lineage bronchioalveolar organoids (Fig. 5d). Despite the bias in organoid formation towards the bronchial lineage, we did not detect mCherry-labelled cells expressing bronchial markers in vivo (Extended Data Fig. 10a). CAPs also retained high self-renewal capacity over multiple passages (Fig. 5e).

Next, we tested whether tumour cells could directly induce the CAP phenotype. When EPCAM$^+$ cells from unlabelled distal micro-metastatic lungs or naive lungs were co-cultured with metastatic cells, they generated a higher proportion of bronchiolar and bronchioalveolar organoids (Fig. 5f–h and Extended Data Fig. 10b, c). Similar alterations were induced by cancer cells when the assay was performed using mouse lung fibroblasts (MLg cells) instead of CD31$^+$ cells (Extended Data Fig. 10b, c).

Although lung EPCAM$^+$ cells are predominantly alveolar, they also contain epithelial progenitors that could be enriched by cancer cells to generate increased plasticity[27,30]. Therefore, we performed organoid cultures using lineage-labelled AT2 (*Sftpc*-lineage) cells. *Sftpc*-lineage cells, which show no plasticity in co-culture with CD31$^+$ cells, generated multi-lineage bronchioalveolar organoids when exposed to cancer cells, supporting the idea of a reprogramming activity driven by cancer-cell-derived factors ex vivo (Fig. 5i, j). Despite the potential of cancer cells to modulate the organoid formation ability of lineage-labelled club cells (*Scgb1a1* lineage), only rare single *Scgb1a1*-lineage cells were found in proximity to lung metastases (Extended Data Fig. 10d–f). Conversely, metastases growing in *Sftpc*-lineage lungs demonstrated the alveolar (AT2) origin of the CAPs (Fig. 5k).

Recently, a rare population of AT2 cells expressing *Axin2* with stem cell and repair activity (AT2 stem cells), was described in the lung alveoli[31]. Whereas a small proportion of *Axin2*-expressing cells was found in the unlabelled epithelial cluster, *Axin2* was undetectable in the mCherry$^+$-niche EPCAM clusters (data not shown). Therefore, even if cancer cell seeding could trigger lung injury, this phenomenon

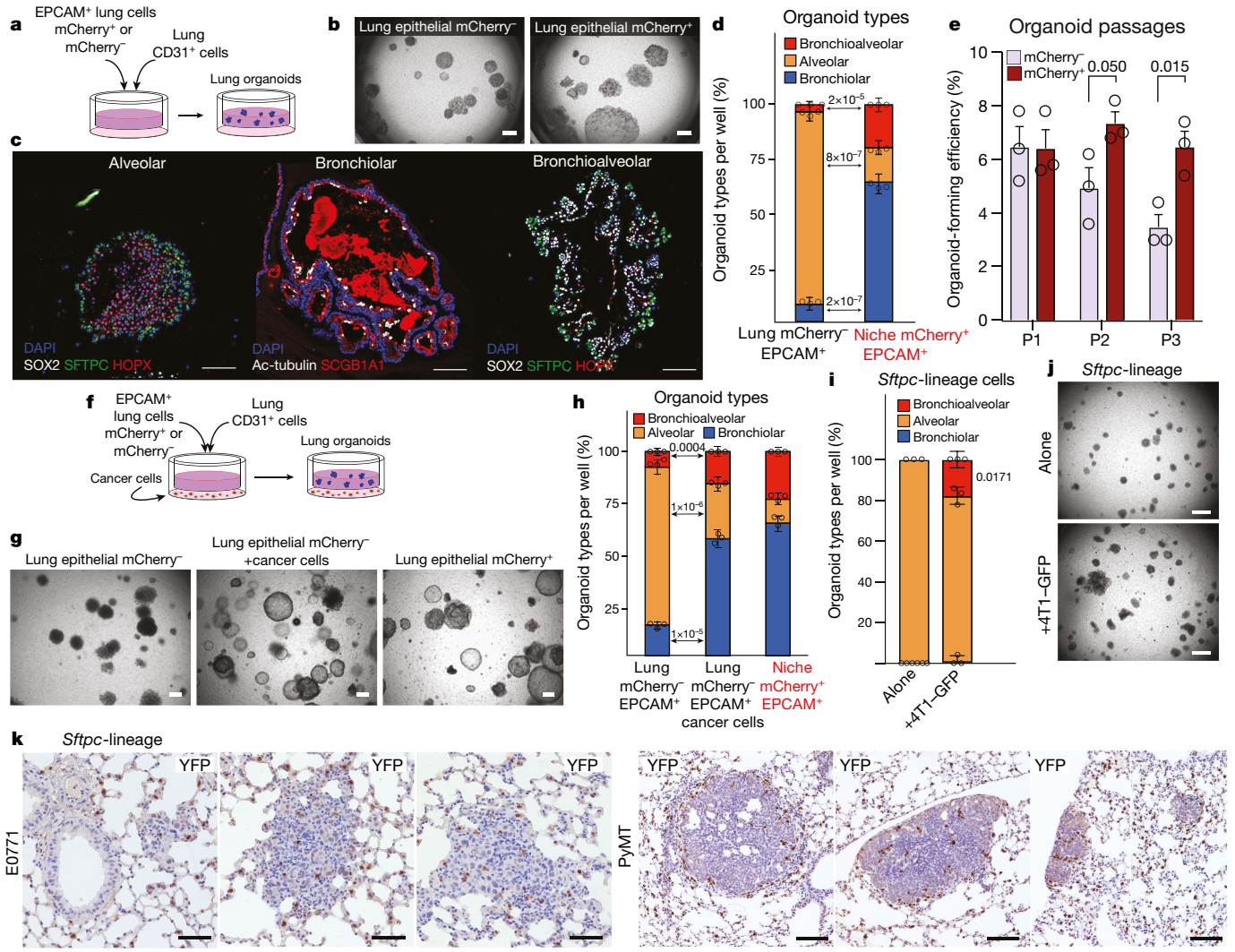

Fig. 5 | CAPs show multi-lineage differentiation potential. a–e, Lung organoids: co-culture scheme (**a**); representative bright-field images (**b**; scale bar, 100 μm); representative immunofluorescence of organoid sections stained with the indicated markers (**c**; scale bar, 50 μm); quantification (**d**) and organoid formation efficiency after passaging (**e**). Ac-tubulin, acetyl tubulin. **f–h**, Lung organoid cultures with or without labelling-4T1 cells: co-culture scheme (**f**); representative bright-field images (**g**; scale bar, 100 μm) and quantification (**h**). **i**, **j**, Lung organoids with *Sftpc-Cre*^{ERT2} lineage cells with or without non-labelling 4T1-GFP cells: quantification (**i**) and representative bright-field images (**j**; scale bar, 150 μm). Images are representative of six (**b**, **c**, **g**) or three (**j**) organoid cultures. Data generated from independent sorts (**d**, **h**, **i**) and represented as cumulative percentage using the mean ± s.d. of three co-cultures per sorting. **k**, Representative staining of lineage cells in metastatic lungs from *Sftpc-Cre*^{ERT2} mice injected with E0771 ($n = 3$; scale bar, 50 μm) or MMTV–PyMT ($n = 3$; scale bar, 100 μm) cancer cells. Statistical analysis by unpaired two-tailed *t*-test (**d**, **e**, **h**) and one-sample two-tailed *t*-test (**i**) on original non-cumulative values.

does not appear to specifically maintain an *Axin2*$^{+}$ AT2 population in the metastatic niche.

Collectively, these data demonstrate the alveolar origin of CAPs and the ability of cancer cells to induce multi-lineage differentiation potential of epithelial cells ex vivo.

Discussion

This study introduces the mCherry-niche labelling system and demonstrates its ability to resolve the host tissue cellular environment in regions surrounding cancer cells. We report the presence of a lung epithelial compartment within the metastatic niche, which originates from AT2 cells. We define this TME component as CAPs and describe their activated regenerative state by showing their de-differentiated signature, tissue stem-cell-like features, multi-lineage differentiation potential and increased self-renewal activity.

Parenchymal cells have been described as triggering a tissue-wide pro-tumorigenic inflammatory response to systemic primary tumour signals[32,33]. In addition to these systemic effects, we here show that a regenerative-like activation in the lung parenchyma occurs as a direct local response during breast cancer metastasis. This parenchymal response, combined with the stromal activation, is potentially a key orchestrator of tumour-niche formation.

Together these results consolidate the mCherry-niche system as a platform for discoveries with the potential to identify, isolate and functionally test cells from the metastatic niche with high spatial resolution.

Online content

Any methods, additional references, Nature Research reporting summaries, source data, extended data, supplementary information, acknowledgements, peer review information; details of author contributions and competing interests; and statements of data and code availability are available at https://doi.org/10.1038/s41586-019-1487-6.

Received: 12 July 2018; Accepted: 12 July 2019;
Published online 28 August 2019.

1. Hanahan, D. & Coussens, L. M. Accessories to the crime: functions of cells recruited to the tumor microenvironment. *Cancer Cell* **21**, 309–322 (2012).
2. Quail, D. F. & Joyce, J. A. Microenvironmental regulation of tumor progression and metastasis. *Nat. Med.* **19**, 1423–1437 (2013).

3. Barash, S., Wang, W. & Shi, Y. Human secretory signal peptide description by hidden Markov model and generation of a strong artificial signal peptide for secreted protein expression. *Biochem. Biophys. Res. Commun.* **294**, 835–842 (2002).
4. Flinterman, M. et al. Delivery of therapeutic proteins as secretable TAT fusion products. *Mol. Ther.* **17**, 334–342 (2009).
5. Shaner, N. C., Steinbach, P. A. & Tsien, R. Y. A guide to choosing fluorescent proteins. *Nat. Methods* **2**, 905–909 (2005).
6. del Pozo Martin, Y. et al. Mesenchymal cancer cell-stroma crosstalk promotes niche activation, epithelial reversion, and metastatic colonization. *Cell Rep.* **13**, 2456–2469 (2015).
7. Peinado, H. et al. Pre-metastatic niches: organ-specific homes for metastases. *Nat. Rev. Cancer* **17**, 302–317 (2017).
8. Wculek, S. K. & Malanchi, I. Neutrophils support lung colonization of metastasis-initiating breast cancer cells. *Nature* **528**, 413–417 (2015).
9. Coffelt, S. B., Wellenstein, M. D. & de Visser, K. E. Neutrophils in cancer: neutral no more. *Nat. Rev. Cancer* **16**, 431–446 (2016).
10. Singhal, S. et al. Origin and role of a subset of tumor-associated neutrophils with antigen-presenting cell features in early-stage human lung cancer. *Cancer Cell* **30**, 120–135 (2016).
11. Blomberg, O. S., Spagnuolo, L. & de Visser, K. E. Immune regulation of metastasis: mechanistic insights and therapeutic opportunities. *Dis. Model. Mech.* **11**, dmm036236 (2018).
12. Kessenbrock, K., Plaks, V. & Werb, Z. Matrix metalloproteinases: regulators of the tumor microenvironment. *Cell* **141**, 52–67 (2010).
13. Kowanetz, M. et al. Granulocyte-colony stimulating factor promotes lung metastasis through mobilization of Ly6G+Ly6C+ granulocytes. *Proc. Natl Acad. Sci. USA* **107**, 21248–21255 (2010).
14. Qian, B.-Z. et al. CCL2 recruits inflammatory monocytes to facilitate breast-tumour metastasis. *Nature* **475**, 222–225 (2011).
15. Acharyya, S. et al. A CXCL1 paracrine network links cancer chemoresistance and metastasis. *Cell* **150**, 165–178 (2012).
16. Oskarsson, T. et al. Breast cancer cells produce tenascin C as a metastatic niche component to colonize the lungs. *Nat. Med.* **17**, 867–874 (2011).
17. Erez, N. Cancer: Opening LOX to metastasis. *Nature* **522**, 41–42 (2015).
18. Onnis, B., Fer, N., Rapisarda, A., Perez, V. S. & Melillo, G. Autocrine production of IL-11 mediates tumorigenicity in hypoxic cancer cells. *J. Clin. Invest.* **123**, 1615–1629 (2013).
19. Malanchi, I. et al. Interactions between cancer stem cells and their niche govern metastatic colonization. *Nature* **481**, 85–89 (2012).
20. Su, F., Overholtzer, M., Besser, D. & Levine, A. J. WISP-1 attenuates p53-mediated apoptosis in response to DNA damage through activation of the Akt kinase. *Genes Dev.* **16**, 46–57 (2002).
21. Costa, A. et al. Fibroblast heterogeneity and immunosuppressive environment in human breast cancer. *Cancer Cell* **33**, 463–479 (2018).
22. Karnoub, A. E. et al. Mesenchymal stem cells within tumour stroma promote breast cancer metastasis. *Nature* **449**, 557–563 (2007).
23. Hosaka, K. et al. Pericyte-fibroblast transition promotes tumor growth and metastasis. *Proc. Natl Acad. Sci. USA* **113**, E5618–E5627 (2016).
24. Murgai, M. et al. KLF4-dependent perivascular cell plasticity mediates pre-metastatic niche formation and metastasis. *Nat. Med.* **23**, 1176–1190 (2017).
25. Treutlein, B. et al. Reconstructing lineage hierarchies of the distal lung epithelium using single-cell RNA-seq. *Nature* **509**, 371–375 (2014).
26. Kim, C. F. B. et al. Identification of bronchioalveolar stem cells in normal lung and lung cancer. *Cell* **121**, 823–835 (2005).
27. Lee, J.-H. et al. Lung stem cell differentiation in mice directed by endothelial cells via a BMP4–NFATc1–thrombospondin-1 axis. *Cell* **156**, 440–455 (2014).
28. Zacharias, W. J. et al. Regeneration of the lung alveolus by an evolutionarily conserved epithelial progenitor. *Nature* **555**, 251–255 (2018).
29. Chapman, H. A. et al. Integrin $\alpha 6\beta 4$ identifies an adult distal lung epithelial population with regenerative potential in mice. *J. Clin. Invest.* **121**, 2855–2862 (2011).
30. McQualter, J. L., Yuen, K., Williams, B. & Bertoncello, I. Evidence of an epithelial stem/progenitor cell hierarchy in the adult mouse lung. *Proc. Natl Acad. Sci. USA* **107**, 1414–1419 (2010).
31. Nabhan, A. N., Brownfield, D. G., Harbury, P. B., Krasnow, M. A. & Desai, T. J. Single-cell Wnt signaling niches maintain stemness of alveolar type 2 cells. *Science* **359**, 1118–1123 (2018).
32. Liu, Y. et al. Tumor exosomal RNAs promote lung pre-metastatic niche formation by activating alveolar epithelial TLR3 to recruit neutrophils. *Cancer Cell* **30**, 243–256 (2016).
33. Lee, J. W. et al. Hepatocytes direct the formation of a pro-metastatic niche in the liver. *Nature* **567**, 249–252 (2019).

METHODS

Sample sizes were estimated based on previous experiments conducted in our laboratory, providing sufficient numbers of mice in each group to yield a two-sided statistical test, with the potential to reject the null hypothesis with a power $(1-\beta)$ of 80%, subject to $\alpha = 0.05$. No further statistical methods were used to predetermine sample size. Most experiments were not randomized: only the experiment involving treatment was randomized. Whenever possible, investigators were blinded to allocation during outcome assessment.

Statistical analysis. Statistical analyses were performed using Prism v.7.0c (GraphPad Software). *P* values were obtained from two-tailed Student's *t*-tests with paired or unpaired adjustment. When needed, unpaired *t*-tests were adjusted using Welch's correction for unequal variance. In one instance (Fig. 4i), data in one of the groups did not pass the D'Agostino and Pearson normality test, therefore a Wilcoxon matched-pairs signed-rank test was performed. Single-sample tests were also used for comparisons of co-cultured cancer cell growth on scaffolds to the normalized value of cancer cells alone. For comparisons between two scaffold conditions of growth over time or to perform multiple analysis between experimental groups, two-way ANOVA was used.

Mouse strains. All mice used are available from the Jackson Laboratory. MMTV–PyMT mice[34] are on a FVB and C57BL/6 background, actin–GFP mice[35] and Rag1 KO mice are on the FVB background (gift from J. Huelsken laboratory (EPFL, Lausanne, Switzerland)). *Sftpc-Cre*^{ERT2}[36], *Rosa26R-YFP*[37] (*Sftpc-Cre*^{ERT2}*;R26R-YFP*) mice are on a C57BL/6 background. BALB/cJ mice and the above-mentioned lines were bred and maintained under specific-pathogen-free conditions by The Francis Crick Biological Research Facility and female mice were used between 6 and 10 weeks of age. Breeding and all animal procedures were performed at the Francis Crick Institute in accordance with UK Home Office regulations under project license P83B37B3C.

For ex vivo organoid lineage-tracing experiments, *Scgb1a1-Cre*^{ERT2} and *Rosa26R-fGFP*[38], *Sftpc-Cre*^{ERT2} (*Sftpc-Cre*^{ERT2}*;R26R-fGFP* and *Scgb1a1-Cre*^{ERT2}*;R26R-fGFP*) mice on a C57BL/6 background were bred and maintained under specific-pathogen-free conditions at the Gurdon Institute of the University of Cambridge in accordance with UK Home Office project licence PC7F8AE82. All animal work was conducted under UK Home Office regulations, project licenses P83B37B3C and PC7F8AE82.

Tamoxifen administration. Tamoxifen (Merck Sigma-Aldrich) was dissolved in Mazola corn oil (Merck Sigma-Aldrich) in a 20 mg ml^{-1} stock solution. Two doses of tamoxifen (0.2 mg per g body weight) were given via oral gavage every other day and lung tissues were collected two days after tamoxifen administration to isolate cells for lung organoids. For in vivo lineage tracing three doses of tamoxifen (0.2 mg per g body weight) were given via oral gavage over consecutive days and mice were injected two weeks later.

Cells. MLg cells were purchased from ATCC. Cancer-associated fibroblasts (CAFs) isolated from MMTV–PyMT tumours and human normal fibroblasts (hNLFs) were a gift from E. Sahai. MMTV–PyMT cells were isolated from MMTV–PyMT tumours as previously described[19]. All other cell lines were provided by the Cell Services Unit of The Francis Crick Institute. All cell lines were authenticated and tested for mycoplasma by the Cell Services Unit of The Francis Crick Institute. MMTV–PyMT cells were cultured on collagen-solution-coated dishes in DMEM/F12 (Thermo Fisher Scientific) with 2% fetal bovine serum (FBS; Labtech), 100 U ml^{-1} penicillin–streptomycin (Thermo Fisher Scientific), 20 ng ml^{-1} EGF (Thermo Fisher Scientific) and 10 μg ml^{-1} insulin (Merck Sigma-Aldrich). The collagen solution was made with 30 μg ml^{-1} PureCol collagen (Advanced Biomatrix), 0.1% bovine serum albumin (BSA), 20 mM HEPES in HBSS (Thermo Fisher Scientific). HC11 cells were cultured in RPMI (Thermo Fisher Scientific) supplemented with 10% FBS, 100 U ml^{-1} penicillin–streptomycin, 10 ng ml^{-1} EGF (Thermo Fisher Scientific) and 5 μg ml^{-1} insulin. All other cell lines were cultured in DMEM (Thermo Fisher Scientific) supplemented with 10% FBS and 100 U ml^{-1} penicillin–streptomycin. All cells were cultured at 37 °C and 5% CO_2.

Human samples. Human pulmonary breast cancer metastases from independent patients were obtained from the Grampian Biorepository, Aberdeen Royal Infirmary (REC approval: 16/NS/0055). Four samples were stained by immunohistochemistry and immunofluorescence and proliferation of epithelial cells was quantified. Further information about the human samples used is provided in the Supplementary Information.

Labelling system. A soluble peptide (SP)[3] and a modified TAT peptide[4] were cloned upstream of the mCherry cDNA, under the control of a mouse PGK promoter (sLP–mCherry). The sLP–mCherry sequence was cloned into a pRRL lentiviral backbone. 4T1, Renca, CT26 and HC11 cells were stably infected with sLP–mCherry and pLentiGFP lentiviral particles and subsequently sorted to isolate mCherry^{+}GFP^{+} cells.

Induction of experimental metastases. Procedures were performed at the Francis Crick Institute in accordance with UK Home Office regulations under project license P83B37B3C. Cancer cells were injected intravenously to generate metastases in the lung: 4T1 (1,000,000), Renca (500,000) or CT26 (200,000) cells were resuspended in 100 μl PBS and injected into the tail vein of BALB/cJ mice. Mice were euthanized on the basis of a time period rather than on the basis of their clinical signs. Therefore, the experimental end point (time controlled, seven days unless otherwise specified) most likely occurred before a humane end point (as determined by deterioration of heath conditions). All animals were monitored daily for unexpected clinical signs following the P83B37B3C licence guidelines and the principles set out in the NCRI Guidelines for the Welfare and Use of Animals in Cancer Research (UK). Deterioration of health conditions—such as reduction in food and water consumption, changes in the general appearance of the animal, or weight loss of 10% over a 24-h period—would result in animals being euthanized before the experimental end point.

In vivo lineage-tracing experiments. *Sftpc-Cre*^{ERT2} and *Scgb1a1-Cre*^{ERT2} mice on a C57BL/6 background were injected into the tail vein with 175,000 MMTV–PyMT C57BL/6 cells and lungs were collected 4 weeks later, or with 700,000 E0771 cells and lungs were collected 12 days later.

Tissue digestion for cell isolation or analysis. Lung tissues were dissociated as previously described[19]. In brief, lungs were removed at day 7 after tumour cell injection (unless otherwise specified), minced manually and then digested for 30 min in a shaker at 37 °C with a mixture of DNase I (Merck Sigma-Aldrich) and Liberase TM and TH (Roche Diagnostics) in HBSS solution. Samples were then washed, passed through a 100-μm filter and incubated in Red Blood Cell Lysis buffer (Miltenyi Biotec) for 3–5 min at room temperature. After a wash with MACS buffer (0.5% BSA and 250 mM EDTA in PBS), samples were passed through a 40-μm filter and a 20-μm strainer-capped flow cytometry tube to generate a single-cell suspension to use for flow cytometric analysis or further purification.

FACS analysis and cell sorting. Prepared single-cell suspensions of mouse lung tissues and in vitro cell lines were incubated with mouse FcR Blocking Reagent (Miltenyi Biotec) for 10 min at 4 °C followed by an incubation with a mix of pre-labelled antibodies (antibody information is provided in the Supplementary Information) for 30 min at 4 °C. After two washes with MACS buffer, dead cells were stained with DAPI. Flow cytometry analyses were carried out on a BD LSR-Fortessa (BD Biosciences) and FlowJo v.10.4.2 (FlowJo, LCC 2006-2018) was used for further analysis. All cell-sorting experiments were carried out using a BD Influx cell sorter (BD Biosciences).

Tissue digestion and FACS analysis in ex-vivo lineage-tracing experiments. Lung tissues were dissociated with a collagenase–dispase solution as previously described[27]. In brief, after lungs were cleared by perfusion with cold PBS through the right ventricle, 2 ml dispase (50 U ml^{-1}, BD Biosciences) was instilled into the lungs through the trachea until the lungs inflated, followed by instillation of 1% low melting agarose (Bio-Rad Laboratories) through the trachea to prevent leakage of dispase. Each lobe was dissected and minced into small pieces in a conical tube containing 3 ml PBS, 60 μl collagenase–dispase (Roche) and 7.5 μl of 1% DNase I (Merck Sigma-Aldrich) followed by rotating incubation for 45 min at 37 °C. The cells were then filtered sequentially through 100- and 40-μm strainers and centrifuged at 1,000 r.p.m. for 5 min at 4 °C. The cell pellet was resuspended in 1 ml of ACK lysis buffer (0.15 M NH_4Cl, 10 mM $KHCO_3$, 0.1 mM EDTA) and lysed for 90 s at room temperature. Six millilitres of basic F12 medium (Thermo Fisher Scientific) was added and 500 μl FBS (Fisher Scientific) was slowly added in the bottom of the tube. Cells were centrifuged at 1,000 r.p.m. for 5 min at 4 °C. The cell pellet was resuspended in PF10 buffer (PBS with 10% FBS) for further staining. The antibodies used were as follows: CD45 (30-F11)–APC (BD Biosciences), CD31 (MEC13.3)–APC (BD Biosciences) and EPCAM (G8.8)–PE-Cy7 (BioLegend). For antibody list see Supplementary Information. The MOFLO system (Beckman Coulter) was used for the sorting at Wellcome–MRC Stem Cell Institute Flow Cytometry Facility.

Lung organoid assay. Lung organoid co-culture assays were previously reported[27,39]. In brief, freshly sorted epithelial cells (EPCAM^{+}CD45^{-}CD31^{-}Ter119^{-}GFP^{-}) from either the metastatic niche or the distal lung were resuspended in 3D basic medium (DMEM/F12, supplemented with 10% FBS, penicillin–streptomycin, 1 mM HEPES and insulin–transferrin–selenium (ITS) (Merck Sigma-Aldrich), and mixed with MACS-sorted CD31^{+} lung stromal cells or MLg cells followed by resuspension in growth factor-reduced (GFR) Matrigel (BD Biosciences) at a ratio of 1:1. One hundred microlitres of mixture was then placed in a 24-well transwell insert with a 0.4-μm pore (Corning). Distal lung or niche epithelial cells (10^3 to 2.5×10^3 cells) and 25,000 CD31^{+} or MLg cells were seeded in each insert. Five hundred microlitres of 3D basic medium was placed in the lower chamber and medium was changed every other day. In addition, freshly sorted *Scgb1a1*-lineage labelled cells or *Sftpc*-lineage labelled cells were resuspended in 3D basic medium followed by mixing with GFR Matrigel retaining CD31^{+} stromal cells as described above. For co-culture of lung epithelial cells with tumour cells, a mixture of 10^3 to 2.5×10^3 distal lung epithelial cells and 25,000

$CD31^+$ cells in Matrigel was placed in the Transwell insert, and 2,000 tumour cells were FACS-sorted from metastatic lungs and seeded in the lower chamber. Plates were scored for colony number after 14 days. Organoid-forming efficiency was calculated as the number of organoids formed per number of cells plated per well as a percentage. Quantification of distinct types of differentiated organoids was performed by scoring the organoids expressing SOX2 or SP-C and HOPX by immunofluorescence from at least five step sections (20 μm apart) per individual well. Bright-field images were acquired after 14 days using an EVOS microscope (Thermo Fisher Scientific).

3D cell culture. Primary MMTV–PyMT actin–GFP cells were seeded at a density of 5,000 cells per well in a collagen-solution-coated Alvetex Scaffold 96-well plate (ReproCELL). The following day, $Ly6G^+$ lung cells and/or $Epcam^+$ lung epithelial cells were sorted by MACS and seeded on top of the cancer cells at a density of 50,000 cells per well. In selected experiments, wells were supplemented with 4-hydroxy-TEMPO (200 μM, Merck Sigma-Aldrich) or mouse WISP1 antibody (250 ng ml^{-1}, MAB1680, R&D Systems). The growth of GFP^+ cells was monitored daily for 6 days using the SteREO LumarV12 stereomicroscope (Zeiss), and images were quantified using ImageJ (NIH). For quantification, the Li's minimum cross entropy thresholding algorithm was performed on the stacked images.

For the CD104 staining experiment, $EPCAM^+$ lung cells were sorted from mouse lung tissues by MACS and seeded at a density of 1,500,000 cells per well on collagen-solution-coated Alvetex Scaffold 12-well inserts. After 48 h, MMTV–PyMT actin–GFP cells were seeded on top of the $EPCAM^+$ cells at a density of 2,000 cells per scaffold insert.

Immunofluorescence and immunohistochemistry. Mouse lungs were fixed in 4% PFA in PBS for 24 h and embedded in paraffin blocks. Four-micrometre-thick tissue sections were cut, deparaffinized and rehydrated using standard methods. After heat-mediated antigen retrieval in citrate buffer (unless stated otherwise), sections were blocked with a solution of 1% BSA, 10% donkey serum in PBS. For antibody list, see Supplementary Information.

mCherry and GFP staining. An overnight incubation at 4 °C with goat GFP and rabbit mCherry antibodies was followed by 1 h incubation at room temperature with anti-goat Alexa Fluor 488- and anti-rabbit Alexa Fluor 555-conjugated antibodies (1:400; Thermo Fisher Scientific). Next, the slides were incubated with Sudan Black B for 20 min and mounted with Vectashield mounting medium with DAPI (Vector Laboratories).

Lineage staining. An overnight incubation at 4 °C with goat GFP antibody was followed by 45-min incubation at room temperature with secondary biotinylated antibodies. Next, the Vectastain Elite ABC kit (Vector Laboratories) was used according to the manufacturer's instructions. Cell nuclei were visualized with haematoxylin and analysis was performed on a Nikon Eclipse 90i light microscope and with NIS-elements software (Nikon).

WISP1 staining. An overnight incubation at 4 °C with goat GFP and rabbit WISP1 antibodies was followed by 30-min incubation at room temperature with anti-goat Alexa Fluor 488 and anti-rabbit Alexa Fluor 555 (1:500; Thermo Fisher Scientific). Next, the slides were incubated with Sudan Black B for 20 min and mounted with Vectashield mounting medium with DAPI (Vector Laboratories).

Ki67 staining. $EPCAM^+CD45^-CD31^-Ter119^-GFP^-$ cells were sorted from lung suspensions, plated on polylysine-coated glass coverslips for 15 min at room temperature and fixed in 4% PFA in PBS for 10 min. After fixation, cells were permeabilized with 0.1% Triton X-100 in PBS for 5 min and incubated with a blocking solution (1% BSA, 10% goat serum, 0.3 M glycine and 0.1% Tween-20 in PBS) for 1 h at room temperature. Next, cells were incubated overnight with a rabbit Ki67 antibody diluted in blocking solution followed by a 1 h incubation with a goat anti-rabbit Alexa Fluor 488 antibody (1:500; Thermo Fisher Scientific). Finally, cells were mounted with Vectashield mounting medium with DAPI for imaging.

E-cadherin staining. $CD49f^+CD104^+CD45^-CD31^-Ter119^-GFP^-$ cells were sorted from lung suspensions, cytospun on glass slides and fixed in 4% PFA in PBS for 10 min. Next, cells were permeabilized with 0.5% Triton X-100 for 30 min and incubated in blocking solution (4% BSA, 0.05% Tween-20 in PBS) for 45 min at room temperature. Then, cells were incubated with a rat E-cadherin antibody in blocking solution overnight at 4 °C followed by an incubation with a goat anti-rat Alexa Fluor 647 antibody (1:500; Thermo Fisher Scientific). Finally, cells were mounted with Vectashield mounting medium with DAPI for imaging.

CD104 staining. $EPCAM^+$ cells were sorted by MACS and plated on Alvetex scaffold inserts as described above. Seven days after plating the whole scaffold was collected, washed with PBS and incubated in blocking solution (10% goat serum in PBS) for 1 h at room temperature. Next, the samples were incubated with a conjugated CD104–eFluor660 antibody (1:100 in PBS with 1:10 FcR blocking (Miltenyi Biotec)) for 1 h at room temperature. Then, the samples were fixed with 4% PFA in PBS for 10 min and mounted with Vectashield mounting medium with DAPI. Images were captured with the Axio Scan.Z1 slide scanner (Zeiss, Germany).

Lung organoid staining. Cultured organoids were fixed with 4% PFA in PBS for 2–4 h at room temperature followed by immobilization with Histogel (Thermo Fisher Scientific) for paraffin embedding. At least five step sections (20 μm apart) per individual well were stained. Fluorescence images were acquired using a confocal microscope Leica TCS SP5 (Leica Microsystems). All the images were further processed with Fiji software.

TTF1 and Ki67 co-staining. Target retrieval solution pH 9 (Agilent DAKO) was used for antigen retrieval. For histology, 1-h incubation at room temperature with mouse TTF1 antibody was followed by 45-min incubation at room temperature with secondary biotinylated antibodies. Next, the Vectastain Elite ABC kit (Vector Laboratories) was used according to the manufacturer's instructions. Cell nuclei were visualized with haematoxylin and analysis was performed on a Nikon Eclipse 90i light microscope and with NIS-elements software (Nikon). For immunofluorescence, 1 h incubation at room temperature with mouse TTF1 and rabbit Ki67 antibodies was followed by 45 min incubation at room temperature with anti-mouse Alexa Fluor 555 and anti-rabbit Alexa Fluor 488 (1:250; Thermo Fisher Scientific). Next, the slides were incubated with Sudan Black B for 20 min and mounted with Vectashield mounting medium with DAPI (Vector Laboratories).

All images were captured with a Zeiss Upright710 confocal microscope or a Zeiss Upright780 confocal microscope unless otherwise stated.

RT–qPCR. RNA preparation was performed using the MagMax-96 Total RNA Isolation Kit (Thermo Fisher Scientific). cDNA synthesis was performed using a SuperScript III First-Strand Synthesis System (Thermo Fisher Scientific) according to the manufacturer's protocol. Quantitative real-time PCR samples were prepared with 50–100 ng total cDNA for each PCR reaction. The PCR, data collection and data analysis were performed on a 7500 FAST Real-Time PCR System (Thermo Fisher Scientific). Glyceraldehyde 3-phosphate dehydrogenase (GAPDH) was used as an internal expression reference. A list of primers used can be found in the Supplementary Information.

Anti-WISP1 treatment in vivo. BALB/cJ female mice (6–8 weeks old) were administered with WISP1 antibody or a control-IgG antibody (5 μg AF1680 and 5 μg MAB1680, R&D Systems) via intra-tracheal injection (50 μl per mouse). The following day, mice were intravenously injected with 250,000 4T1 cells. Anti-WISP1 or control-IgG treatment was repeated daily via a second intra-tracheal injection on day 4 and intra-peritoneal injections on days 2, 3, 5 and 6. Mice were collected 7 days after the first treatment and lungs were embedded, cut and stained with haemotoxylin and eosin (H&E). The lung metastatic burden was assessed by counting the number of metastases on four levels (100-μm intervals) from two lung lobes ($n = 10$ per group).

EdU in vitro proliferation assay. MMTV–PyMT actin–GFP cells were seeded at a density of 10,000 cells per well into collagen-solution-coated six-well plates. The following day, $Ly6G^+$ lung cells and/or $EPCAM^+$ lung cells were sorted by MACS and added to the wells at a density of 100,000 cells per well. After 60 h, wells were supplemented with 20 μM EdU (5-ethynyl-2′-deoxyuridine). Cells were collected 6 h later and EdU incorporation was assessed using the Click-iT Plus EdU Flow Cytometry Assay Kit (Thermo Fisher Scientific), according to the manufacturer's instructions. Sample data were acquired on a BD LSR-Fortessa flow cytometer and analysed using FlowJo 10 software.

Conditioned medium preparation and vesicle isolation. Labelling-4T1 cells were plated on 10-cm Petri dishes. When cells were 80% confluent, 10 ml DMEM with 10% FCS was added to be conditioned for 48 h. The conditioned medium preparation and vesicle isolation were performed as previously described[40]. In brief, the medium was collected and spun at 300*g* for 10 min. Next, the supernatant was collected and spun at 2,000*g* for 10 min. The supernatant after this second centrifugation was collected and used as conditioned medium. For vesicle isolation, the conditioned medium was subsequently ultracentrifuged at 10,000*g* for 30 min and at 100,000*g* for 70 min. The vesicle pellet at this stage was washed with PBS, spun at 100,000*g* for 70 min and resuspended again in PBS for in vitro uptake experiments.

ImageStream analysis. Image stream analyses were carried out on an ImageStream Mark X II Imaging Flow Cytometer (Amnis Merck). The acquired data were analysed using IDEA software (Amnis Merck).

Electron microscopy. Experiments were performed on glass bottom dishes with a numbered grid (MatTek) to enable subsequent location of the same cell imaged by confocal microscopy. After confocal imaging, cells were fixed in 8% formaldehyde in 0.1 M phosphate buffer (pH 7.4) added in equal quantities to cell medium for 15 min and then further fixed in 2.5% glutaraldehyde and 4% formaldehyde in 0.1 M phosphate buffer (pH 7.4) for 1 h and then processed using the National Center for Microscopy and Imaging Research protocol[41]. For transmission electron microscopy, 70-nm serial sections were cut using a UC6 ultramicrotome (Leica Microsystems) and collected on formvar-coated slot grids.

No post-staining was required owing to the density of metal deposited using the NCMIR protocol. Images were acquired using a 120-kV Tecnai G2 Spirit transmission electron microscope (FEI Company Thermo Fisher Scientific) and an Orius CCD camera (Gatan).

RNA sequencing sample preparation. *Bulk RNA sequencing.* CD45$^-$Ter119$^-$ (CD45$^-$) cells were sorted from single-cell suspensions of metastatic lungs stained with anti-mouse CD45 and Ter119 antibodies and DAPI. RNA isolation was performed using the MagMax-96 Total RNA Isolation Kit (Thermo Fisher Scientific), which enables high-quality RNA extraction from samples with low cell numbers (<10,000 cells). RNA quality for each sample was assessed using the Agilent RNA 6000 Pico Kit (Agilent Technologies). RNA was amplified and analysed at the Barts and London Genome Centre.

Single-cell RNA sequencing. CD45$^-$Ter119$^-$ cells were sorted from single-cell suspensions of metastatic lungs stained with anti-mouse CD45 and Ter119 antibodies and DAPI. Library generation for 10x Genomics analysis were performed following the Chromium Single Cell 3′ Reagents Kits (10x Genomics) and sequenced on an Hiseq4000 (Illumina), to achieve an average of 50,000 reads per cell.

Determination of intracellular ROS levels. Single-cell suspensions from mouse lungs were incubated with mouse FcR blocking reagent for 5 min on ice and subsequently incubated with CellROX Deep Red Reagent (Thermo Fisher Scientific) for 30 min at 37 °C following the manufacturer's recommendations. Next, cells were washed twice with MACS buffer, stained with DAPI and analysed by flow cytometry.

Quantitative proteomic analysis of Ly6G cells. Neutrophils were sorted by FACS from single-cell suspensions of metastatic lungs stained with a conjugated anti-mouse Ly6G–APC antibody (three samples from independent sorts). Ly6G cells from the metastatic niche (mCherry$^+$) and the distal lung (mCherry$^-$) were digested into peptides using a previously described protocol[42] and analysed by data-independent acquisition mass spectrometry[43] on a Orbitrap Fusion Lumos instrument (Thermo Fisher Scientific). A hybrid spectral library was generated using the search engine Pulsar in Spectronaut Professional+ (v.11.0.15038, Biognosys) by combing data-dependent acquisition runs obtained from a pooled sample of Ly6G cells, and the data-independent acquisition data. Data analysis and differential protein expression was performed using Spectronaut Professional+. A detailed description of sample processing, data acquisition and processing can be provided on request from the corresponding authors.

Bioinformatics analysis. *Bulk RNA sequencing.* The sequencing was performed on biological triplicates for each condition, generating approximately 35 million 76-bp paired-end reads. The RSEM package[44] (v.1.2.29) and Bowtie2 were used to align reads to the mouse mm10 transcriptome, taken from the known-gene reference table available from University of California Santa Cruz (https://genome.ucsc.edu/). For RSEM, all parameters were run as default except "–forward-prob" which was set to 0.5. Differential-expression analysis was carried out with DESeq2 package[45] (v.1.12.4) in R v.3.3.1 (https://www.r-project.org/). Genes were considered to be differentially expressed if the adjusted *P* was less than 0.05. Differentially expressed genes were taken forward and their pathway and process enrichments were analysed using Metacore (https://portal.genego.com). Hypergeometric test was used to determine statistical enriched pathways and processes and the associated *P*-value was corrected using the Benjamini–Hochberg method. GSEA (v.2.2.3)[46,47] was carried out using ranked gene lists using the Wald statistic and the gene sets of C2 canonical pathways and C5 biological processes. All parameters were kept as default except for enrichment statistic (classic) and maximum size, which was changed to 5,000. Gene signatures with FDR *q*-value equal to or less than 0.05 were considered statistically significant. A weighted Kolmogorov–Smirnov-like statistic was derived and the associated *P*-value was corrected with the Benjamini–Hochberg method.

Single-cell RNA sequencing. Raw reads were initially processed by the Cell Ranger v.2.1.1 pipeline, which deconvolved reads to their cell of origin using the UMI tags, aligned these to the mm10 transcriptome using STAR (v.2.5.1b) and reported cell-specific gene expression count estimates. All subsequent analyses were performed in R v.3.4.1 using the cellrangerRkit, monocle and pheatmap packages. Genes were considered to be 'expressed' if the estimated ($\log_{10}$) count was at least 0.1. Primary filtering was then performed by removing from consideration: genes expressed in fewer than 20 cells; cells expressing fewer than 50 genes; cells for which the total yield (that is, sum of expression across all genes) was more than two standard deviations from the mean across all cells in that sample; and cells for which mitochondrial genes made up greater than 10% of all expressed genes. PCA decomposition was performed and, after consideration of the eigenvalue 'elbow-plots', the first 25 components were used to construct *t*-SNE plots for both samples. Niche cells expressing *Epcam* were subdivided into those also expressing *Cdh1* and those not expressing *Cdh1*. Other genes expressed in at least 50% of cells in a given group were said to be co-expressed and the set of genes co-expressed in one or more groups was presented as a heat map, with the columns (cells) clustered using the standard Euclidean hierarchical method.

Reporting summary. Further information on research design is available in the Nature Research Reporting Summary linked to this paper.

Data availability

The RNA-sequencing datasets have been deposited in the Gene Expression Omnibus with accession number GSE117930; the single-cell RNA-sequencing datasets have been deposited with accession number GEO13150. The proteomic datasets have been deposited in the Proteomics Identifications Database with accession number PXD010597.

34. Guy, C. T., Cardiff, R. D. & Muller, W. J. Induction of mammary tumors by expression of polyomavirus middle T oncogene: a transgenic mouse model for metastatic disease. *Mol. Cell. Biol.* **12**, 954–961 (1992).
35. Okabe, M., Ikawa, M., Kominami, K., Nakanishi, T. & Nishimune, Y. 'Green mice' as a source of ubiquitous green cells. *FEBS Lett.* **407**, 313–319 (1997).
36. Rock, J. R. et al. Multiple stromal populations contribute to pulmonary fibrosis without evidence for epithelial to mesenchymal transition. *Proc. Natl Acad. Sci. USA* **108**, E1475–E1483 (2011).
37. Srinivas, S. et al. Cre reporter strains produced by targeted insertion of *EYFP* and *ECFP* into the *ROSA26* locus. *BMC Dev. Biol.* **1**, 4 (2001).
38. Rawlins, E. L. et al. The role of Scgb1a1$^+$ Clara cells in the long-term maintenance and repair of lung airway, but not alveolar, epithelium. *Cell Stem Cell* **4**, 525–534 (2009).
39. Lee, J.-H. et al. Anatomically and functionally distinct lung mesenchymal populations marked by Lgr5 and Lgr6. *Cell* **170**, 1149–1163 (2017).
40. Théry, C., Amigorena, S., Raposo, G. & Clayton, A. Isolation and characterization of exosomes from cell culture supernatants and biological fluids. *Curr. Protoc. Cell Biol.* **30**, 3.22.1–3.22.29 (2006).
41. Deerink, T. J. et al. NCMIR methods for 3D EM: a new protocol for preparation of biological specimens for serial block face scanning electron microscopy. *National Center for Microscopy and Imaging Research* https://ncmir.ucsd.edu/sbem-protocol (2010).
42. Heinze, I. et al. Species comparison of liver proteomes reveals links to naked mole-rat longevity and human aging. *BMC Biol.* **16**, 82 (2018).
43. Bruderer, R. et al. Optimization of experimental parameters in data-independent mass spectrometry significantly increases depth and reproducibility of results. *Mol. Cell. Proteomics* **16**, 2296–2309 (2017).
44. Li, B. & Dewey, C. N. RSEM: accurate transcript quantification from RNA-seq data with or without a reference genome. *BMC Bioinformatics* **12**, 323 (2011).
45. Love, M. I., Huber, W. & Anders, S. Moderated estimation of fold change and dispersion for RNA-seq data with DESeq2. *Genome Biol.* **15**, 550 (2014).
46. Subramanian, A. et al. Gene set enrichment analysis: a knowledge-based approach for interpreting genome-wide expression profiles. *Proc. Natl Acad. Sci. USA* **102**, 15545–15550 (2005).
47. Mootha, V. K. et al. PGC-1α-responsive genes involved in oxidative phosphorylation are coordinately downregulated in human diabetes. *Nat. Genet.* **34**, 267–273 (2003).

Acknowledgements We thank E. Sahai, P. Scaffidi (The Francis Crick Institute) and V. Sanz-Moreno (Barts Cancer Institute) for scientific discussions, critical reading of the manuscript and sharing cell lines and mouse strains; M. Izquierdo (CSIC, Madrid) for sharing the CD63–GFP plasmid; E. Nye and the pathologists G. Stamp and E. Herbert from the Experimental Histopathology Unit at the Francis Crick Institute for histological processing and analysis support; J. Bee from the Biological Resources Unit at the Francis Crick Institute for technical support with mice and mouse tissues; R. Goldstone and A. Edwards from the Advanced Sequencing Facility at the Francis Crick Institute for technical support; M. Llorian-Sopena from the Bioinformatics and Biostatistics Unit at the Francis Crick Institute for helping with the RNA sequencing analysis; the Flow Cytometry Unit at the Francis Crick Institute, particularly S. Purewal and J. Cerveira, for invaluable technical help; the Cell Services Unit at the Francis Crick Institute; C. Moore (The Francis Crick Institute) for intra-tracheal injections; and I. Pshenichnaya, P. Humphreys, S. McCallum and Cambridge Stem Cell Institute core facilities for technical assistance. We acknowledge support from the FLI Core Facility Proteomics, which is a member of the Leibniz Association and is financially supported by the Federal Government of Germany and the State of Thuringia. This work was supported by the Francis Crick Institute, which receives its core funding from Cancer Research UK (FC001112), the UK Medical Research Council (FC001112), and the Wellcome Trust (FC001112) and the European Research Council grant (ERC CoG-H2020-725492); and by the Wellcome Trust—MRC Stem Cell Institute, which receives funding from the Sir Henry Dale Fellowship from Wellcome, the Royal Society (107633/Z/15/Z) and the European Research Council Starting Grant (679411).

Author contributions L.O. designed and performed most of the experiments, analysed and interpreted the data and contributed to the manuscript preparation. E.N. assisted with data collection, performed all the 3D-scaffold co-culture experiments, the in vivo WISP1 experiments and the scRNA sequencing, and interpreted and analysed the data and contributed to the manuscript preparation. I.K. performed the RT–qPCR analysis, some of the tissue immunofluorescence staining and analysed the data. A.M. and J.-H.L. performed some of the tissue immunofluorescence staining and all the lung organoid experiments, and interpreted and analysed the data. V.B. performed some of

the tissue immunofluorescence staining. P.C. and S.H. performed bioinformatics analysis. I.H., J.K. and A.O. performed the proteomics and analysed the data. E.G.-G. helped with the collection of $Ly6G^+$ cells for proteomics. G.M. performed the 3D-scaffold co-culture to analyse $CD104^+$ cells. A.W. and L.C. performed the electron microscopy experiments. E.H. and V.S. provided human samples. L.O., E.N., I.K., V.B. and J.-H.L. critically reviewed the manuscript. J.-H.L. supervised the lung organoid experiments. I.M. designed and supervised the study, interpreted the data and wrote the manuscript.

Competing interests The authors declare no competing interests.

Additional information

Supplementary information is available for this paper at https://doi.org/10.1038/s41586-019-1487-6.

Correspondence and requests for materials should be addressed to J.-H.L. or I.M.

Peer review information *Nature* thanks Marie-Liesse Asselin-Labat, Thomas Tüting and the other, anonymous, reviewer(s) for their contribution to the peer review of this work.

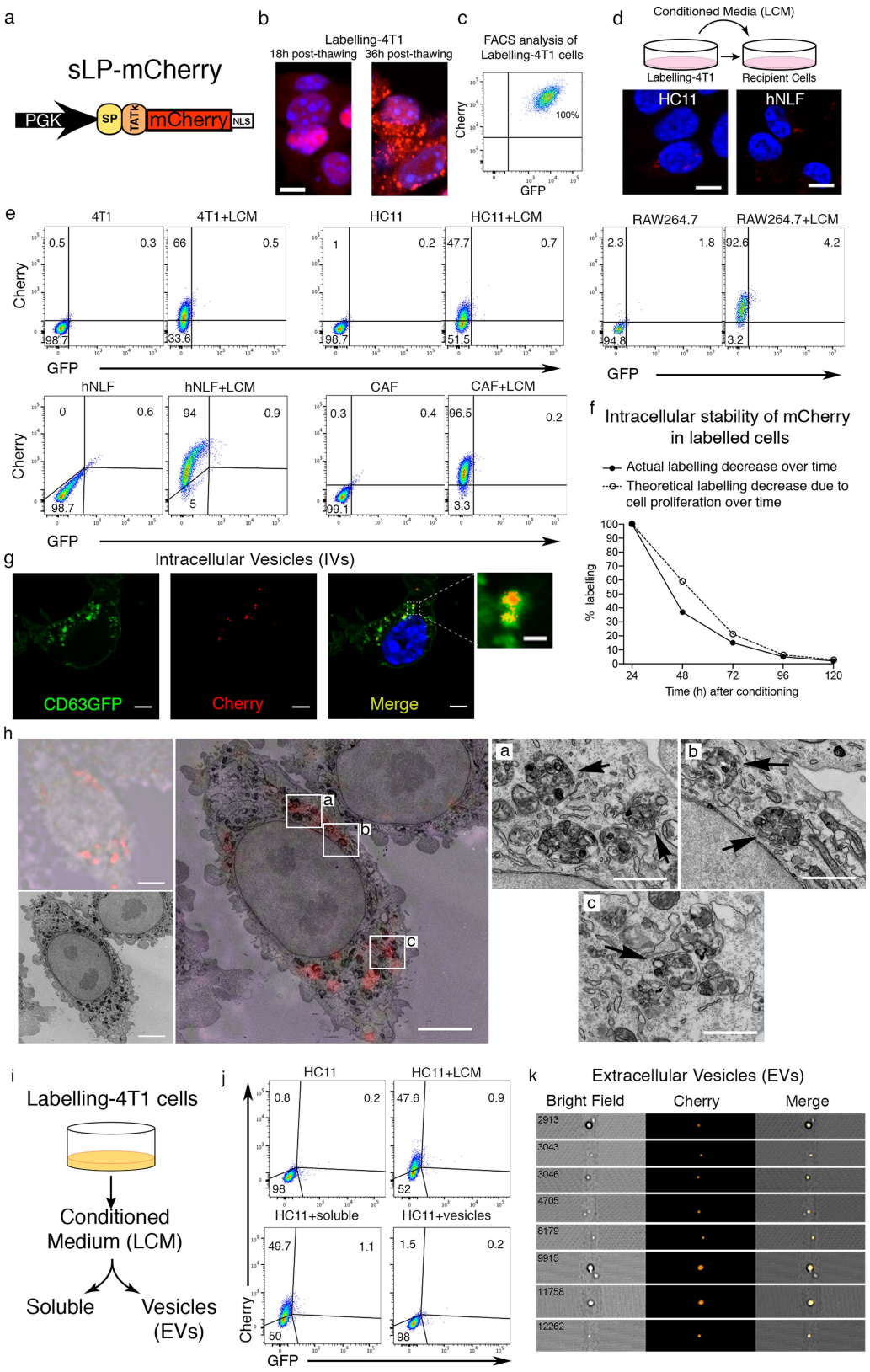

Extended Data Fig. 1 | See next page for caption.

Extended Data Fig. 1 | The mCherry-niche system in vitro. a, sLP–mCherry design. **b**, Fluorescence images of labelling-4T1 cells after thawing. Scale bar, 10 μm. **c**, Representative FACS plot of labelling-4T1 cells. **d**, In vitro cultures of the indicated cell types with LCM: culture scheme and representative fluorescence images of HC11 (mouse mammary epithelial cells) and hNLF (human normal lung fibroblasts) with LCM (scale bar, 10 μm). **e**, FACS plots of 4T1, HC11, RAW264.7 (mouse macrophages), hNLF and mouse breast CAFs cultured with LCM. **f**, FACS analysis of 293T cells cultured with LCM, at different time points after LCM removal (black dots); white dots show the theoretical decrease considering the cell proliferation rate only (the amount of 293T cells labelled with mCherry after 24 h incubation with LCM was set to 100%). **g**, Representative fluorescence image of 4T1-CD63–GFP cells cultured with LCM. Scale bars: main panels, 5 μm; enlarged region, 1 μm. **h**, Representative correlative light and electron microscopy of labelling-4T1 cells showing re-uptake of sLP–mCherry ($n = 5$ different cells analysed). Top left, bright-field image overlaid with mCherry immunofluorescence (~700 nm optical section). Bottom left, electron microscopy of the same cell (~70-nm section thickness). Centre, best approximation of immunofluorescence–bright-field–electron microscopy overlay (scale bar, 5 μm). Right, electron microscopy of the outlined regions (centre, labelled a–c) (black arrows point at vesicular structures containing mCherry; scale bar, 1 μm). **i**, **j**, Analysis of in vitro labelling potential of soluble fraction and extracellular vesicles isolated from LCM by FACS. **i**, Schematic representation of LCM fractionation. **j**, HC11 cells cultured with either LCM, soluble fraction after depletion of extracellular vesicles (soluble) or purified extracellular vesicles. **k**, ImageStream analysis of $mCherry^+$ extracellular vesicles in LCM (16% of total extracellular vesicles are $mCherry^+$). Data are representative of three (**b**), ten (**c**) or two (**d**–**g**, **j**, **k**) independent experiments.

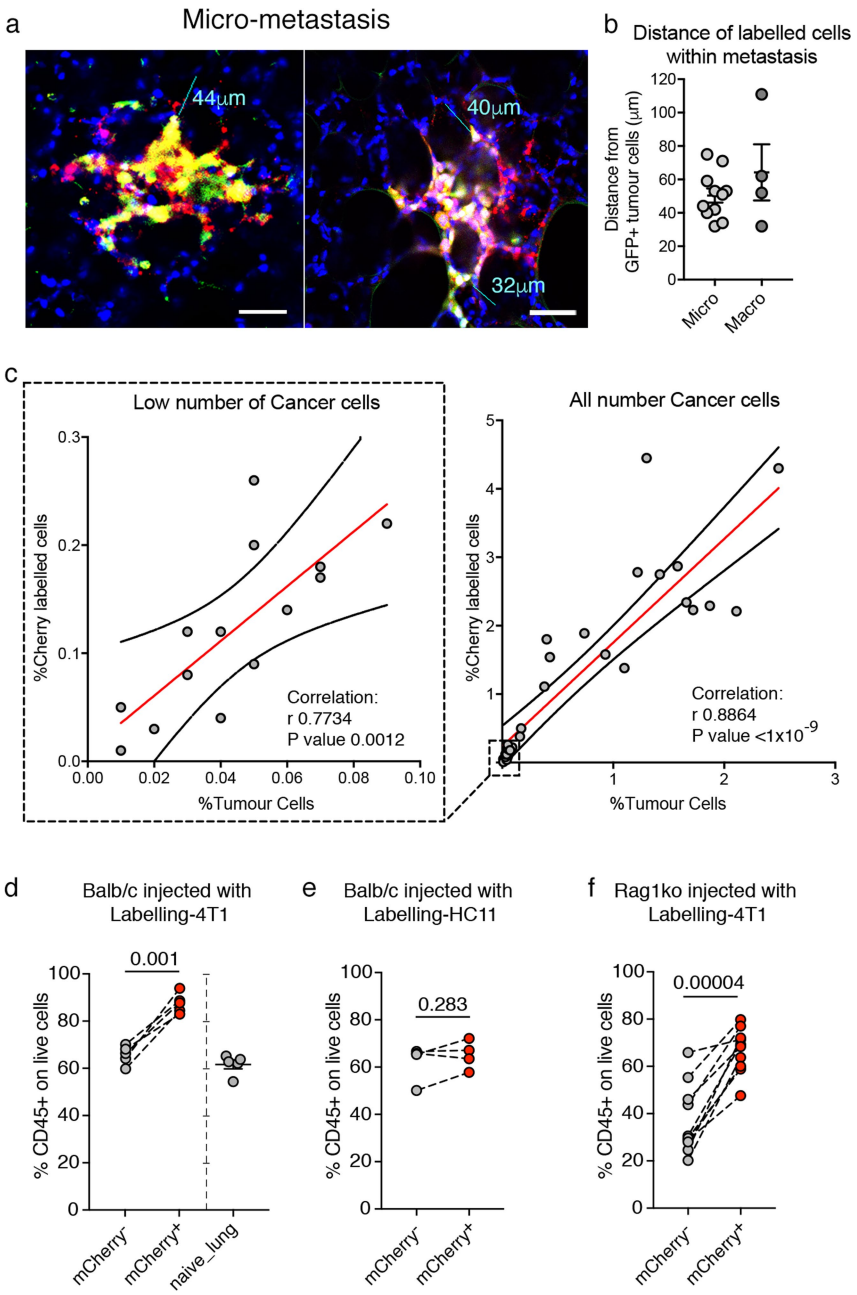

Extended Data Fig. 2 | The mCherry-niche system in vivo. a, **b**, Distance of labelled cells within metastases. **a**, Representative fluorescence images (lines measure the maximum distance of labelled cells (mCherry$^+$) from labelling-4T1 cells (mCherry$^+$GFP$^+$); scale bar, 50 μm). **b**, Quantification of labelling distance in micro-metastases ($n = 11$) and macro-metastases ($n = 4$). **c**, Correlation between the percentage of mCherry-labelled niche cells and the percentage of cancer cells in metastatic lungs analysed by FACS. Left, analysis of lungs with a small number of cancer cells ($n = 14$ mice). Right, analysis with all cancer cell frequencies ($n = 31$ mice). Statistical analysis by Pearson correlation. **d**–**f**, CD45$^+$ cell frequency on live cells in distal lung, mCherry$^+$ niche and not-injected naive lungs by FACS. **d**, BALB/c mice injected with labelling-4T1 cells ($n = 5$ mice per group). **e**, BALB/c mice injected with labelling-HC11 cells ($n = 4$ mice). **f**, RAG1-knockout mice injected with labelling-4T1 cells ($n = 10$ mice). Statistical analysis by paired two-tailed *t*-test. Data are represented as mean ± s.e.m.

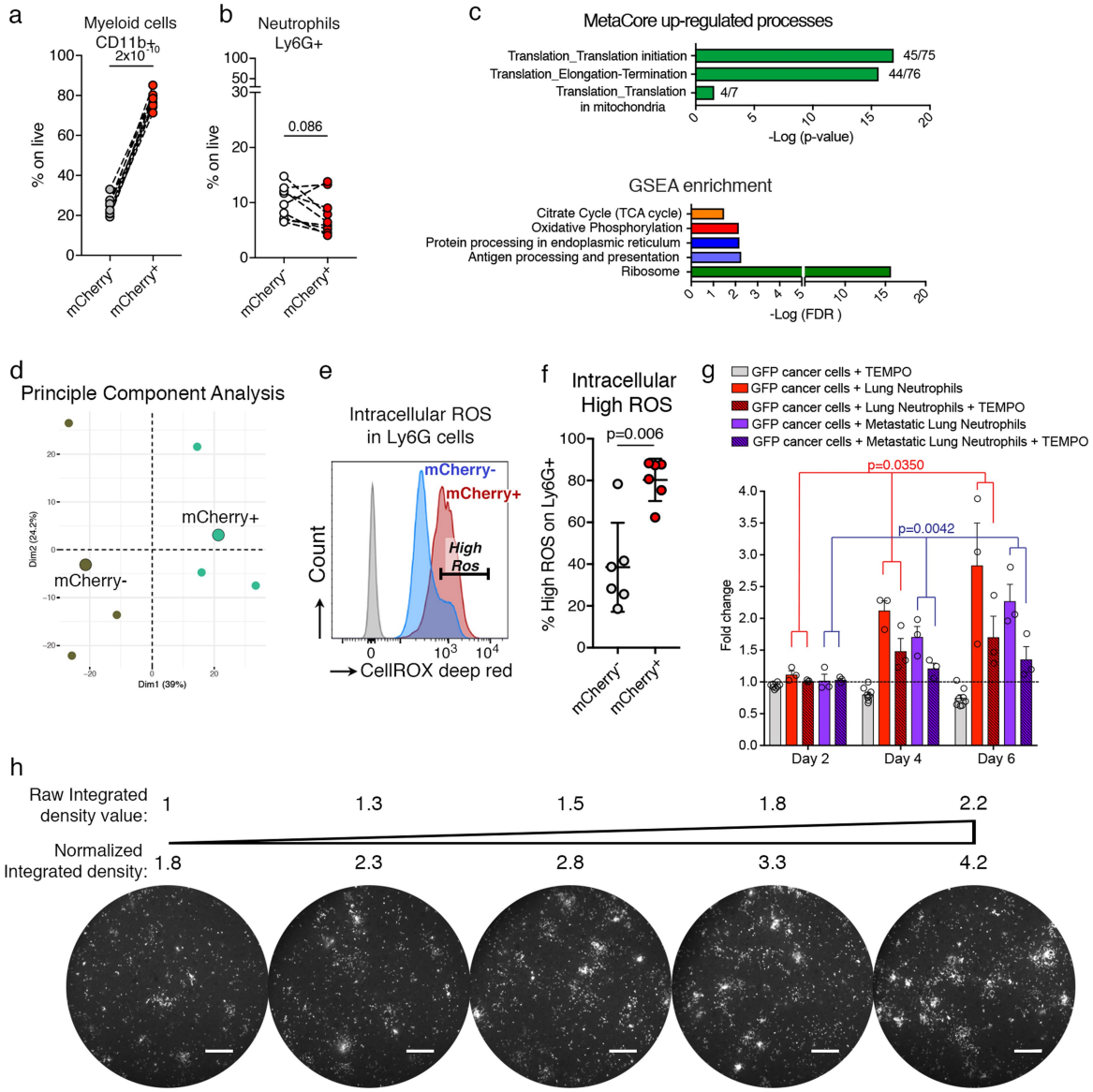

Extended Data Fig. 3 | mCherry$^+$-niche neutrophils increase ROS production. a, **b**, CD11b$^+$ (**a**) and Ly6G$^+$ (**b**) cell frequencies among live cells in distal lung and mCherry$^+$ niche by FACS ($n = 9$ mice per group). **c**, Enriched processes by MetaCore analysis and GSEA based on proteomic data by comparing mCherry$^+$-niche ($n = 3$) and distal lung ($n = 3$) neutrophils; dominant mCherry$^+$-niche proteins were obtained by using WebGestalt (http://www.webgestalt.org/option.php). **d**, PCA of proteins found in unlabelled or mCherry$^+$-niche neutrophils ($n = 3$, each with 10 mice, small circles; large circles represent the average of the triplicates). **e**, **f**, Representative FACS plot (**e**) and scatter plot (**f**) of intrinsic ROS in Ly6G$^+$ cells ($n = 6$ mice). **g**, GFP signal quantification of 3D co-culture with GFP$^+$ MMTV–PyMT cancer cells and MACS-sorted Ly6G$^+$ cells from either naive or metastatic lungs with or without the ROS inhibitor TEMPO ($n = 3$, each with 3 technical replicates). Data are normalized to cancer cell growth (statistical analysis on biological replicates). **h**, Representative cancer cell growth on the scaffold (from 14 independent experiments): integrated density of the GFP signal was measured on the scaffold using ImageJ and the corresponding fluorescent image of GFP$^+$ cancer cell growth (scale bar, 400 μm). Statistical analysis by paired two-tailed *t*-test (**a**, **b**, **f**), hypergeometric test with Benjamini–Hochberg correction (**c**, Metacore), weighted Kolmogorov–Smirnov-like statistic with Benjamini–Hochberg correction (**c**, GSEA) and two-way ANOVA (**g**). Data are presented as mean ± s.d. (**f**) and mean ± s.e.m. (**g**).

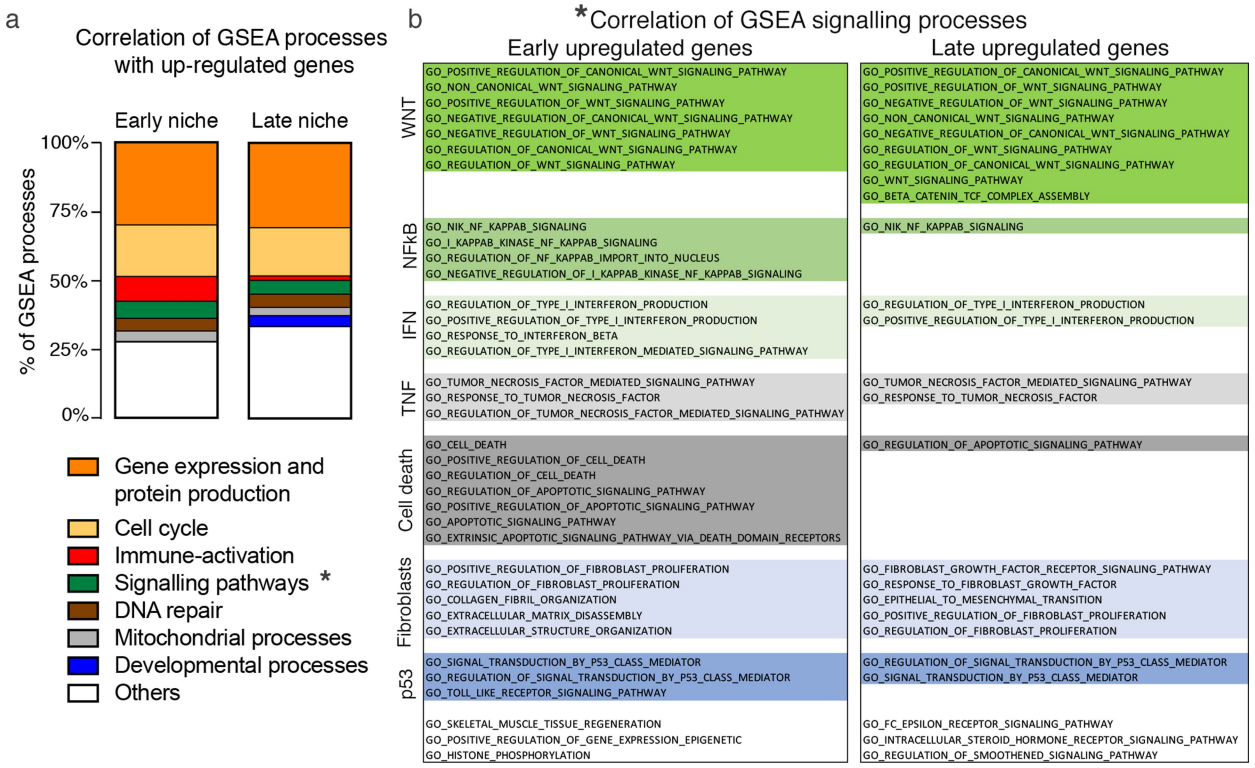

Extended Data Fig. 4 | RNA sequencing of non-immune mCherry$^+$-niche cells. a, **b**, GSEA of upregulated genes in mCherry$^+$-niche cells. **a**, Percentage of correlating processes related to the indicated activity. **b**, Specific signalling pathways (indicated by the ∗ in **a**) at early or late time point. **c**, MetaCore analysis of genes differentially expressed in RNA-seq data, comparing early ($n = 3$) or late ($n = 3$) mCherry$^+$ samples versus the respective mCherry$^-$ samples (see Fig. 3a, b). Statistical analysis by hypergeometric test with Benjamini–Hochberg correction.

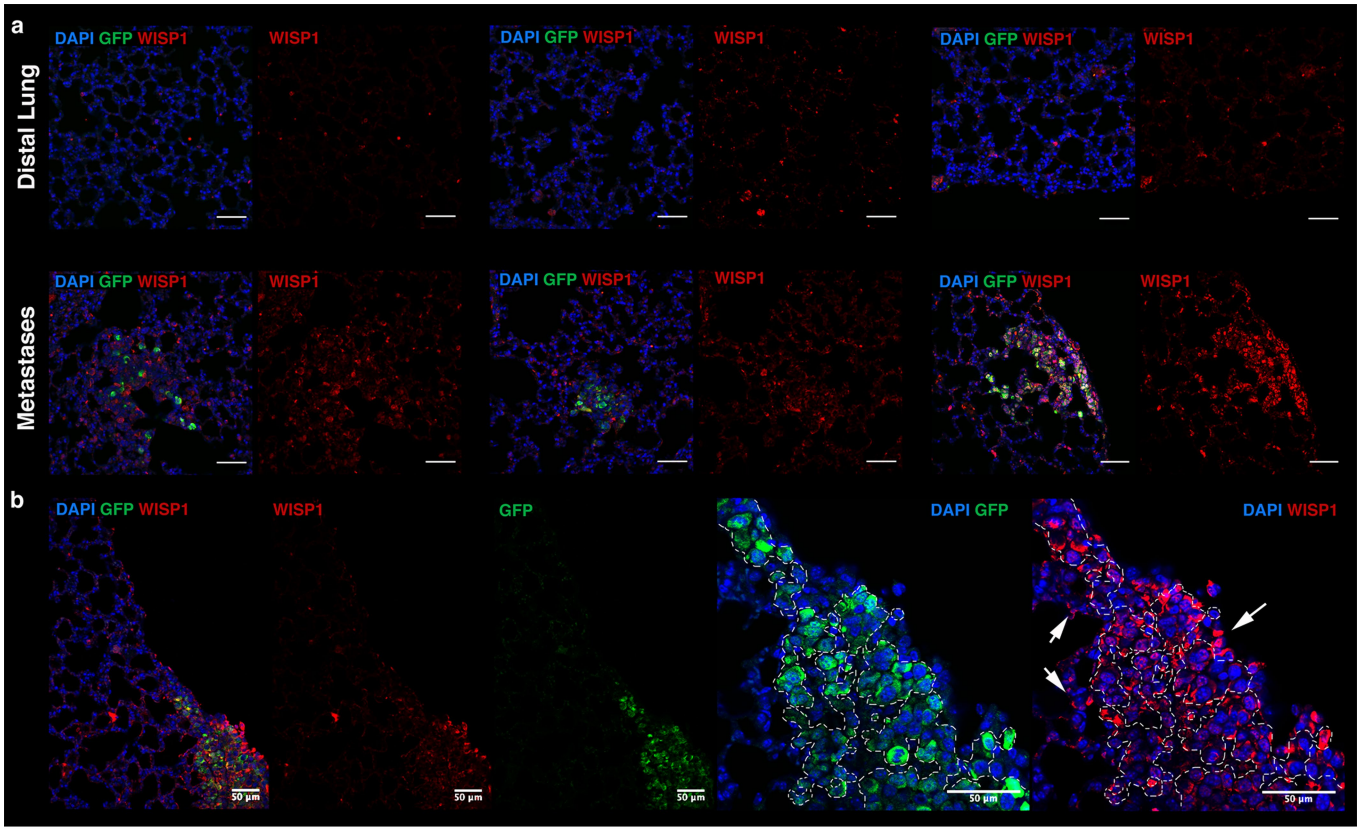

Extended Data Fig. 5 | WISP1 supports metastatic growth. **a**, **b**, Representative immunofluorescence images of lung metastatic tissues ($n = 2$ mice) stained for GFP (green) to detect labelling-4T1 cells, WISP1 (red) and DAPI (blue), showing distal lung and metastatic areas (**a**; scale bar, 50 µm), and a representative image showing the enrichment of WISP1^{+} cells within lung metastasis including niche cells (white arrows) (**b**; scale bar, 50 µm). **c**–**e**, WISP1-blocking antibody treatment in vivo. **c**, Experimental design (IT, intratracheal injection; IP, intraperitoneal injection). **d**, Metastatic outcome measured as the percentage of lung area covered by metastases (quantification was performed on two lung levels 100 µm apart). **e**, Representative H&E staining ($n = 5$ mice per group; black arrows show metastatic foci). Scale bar, 500 µm. Two experiments with lower overall metastatic frequency are quantified in Fig. 3e. Statistical analysis by two-way ANOVA (**d**). Data are presented as mean ± s.e.m.

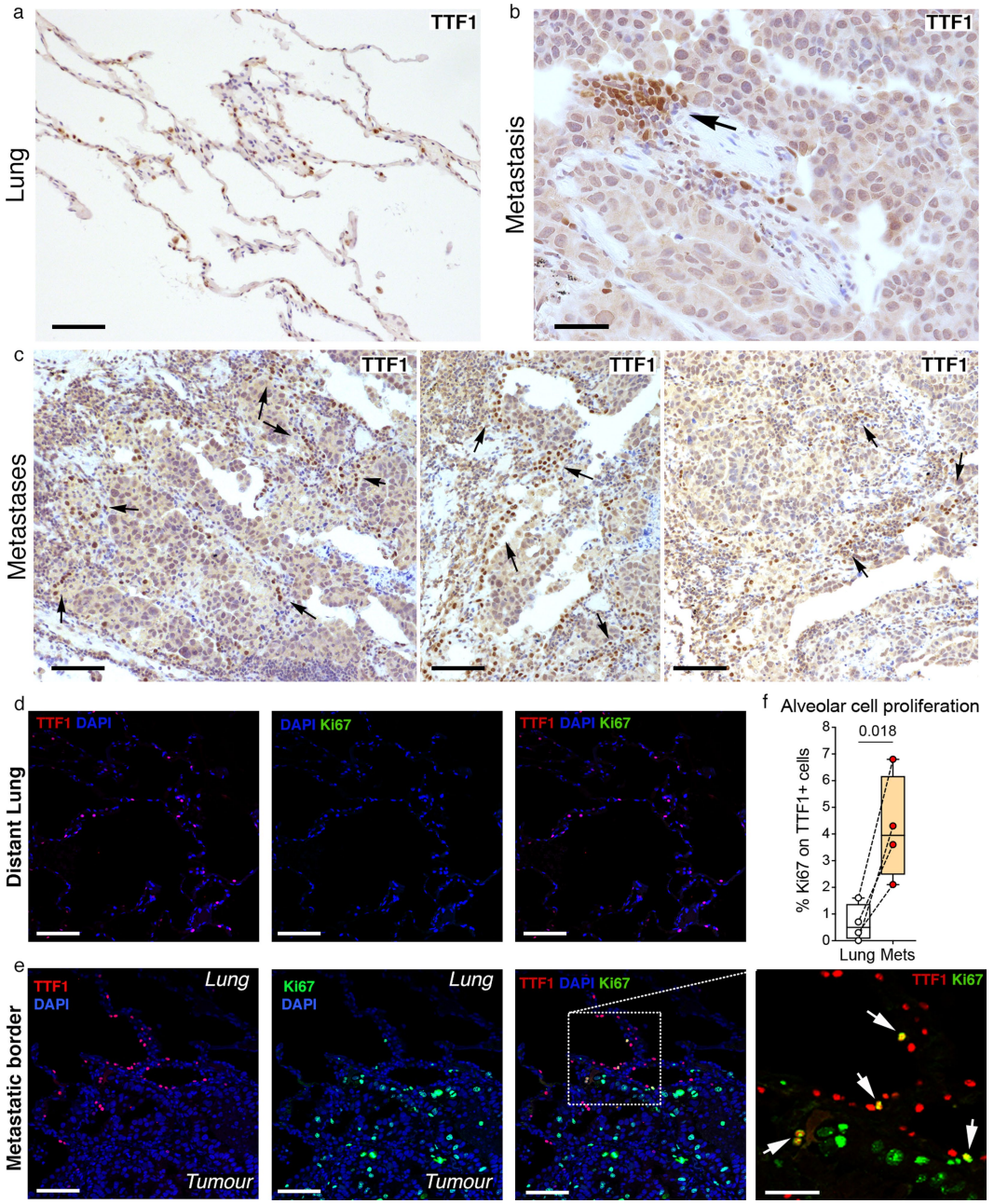

Extended Data Fig. 6 | Lung pneumocytes react to cancer cells in human breast pulmonary metastases. a–c, Histology of sections of human breast tumour lung metastases. **a**, Representative image of distal lung (scale bar, 100 μm). **b**, Image from the tumour–lung interface showing expression of the pneumocyte marker thyroid transcription factor 1 (TTF1) (scale bar, 50 μm). **c**, Representative histology of the metastatic border (scale bar, 100 μm). **d–f**, Alveolar cell proliferation in human breast tumour lung metastases analysed by immunofluorescence. Representative images from distal lung (**d**) and metastatic border (**e**) showing TTF1 (red), Ki67 (green) and DAPI (blue). Scale bars: all 100 μm, except **e** (far right), 50 μm. **f**, Quantification of alveolar proliferation. Box edges show 25th and 75th percentiles, the horizontal line shows the median and whiskers show the range of values. Statistical analysis by paired two-tailed *t*-test. Tissue sections from $n = 4$ independent patients were analysed.

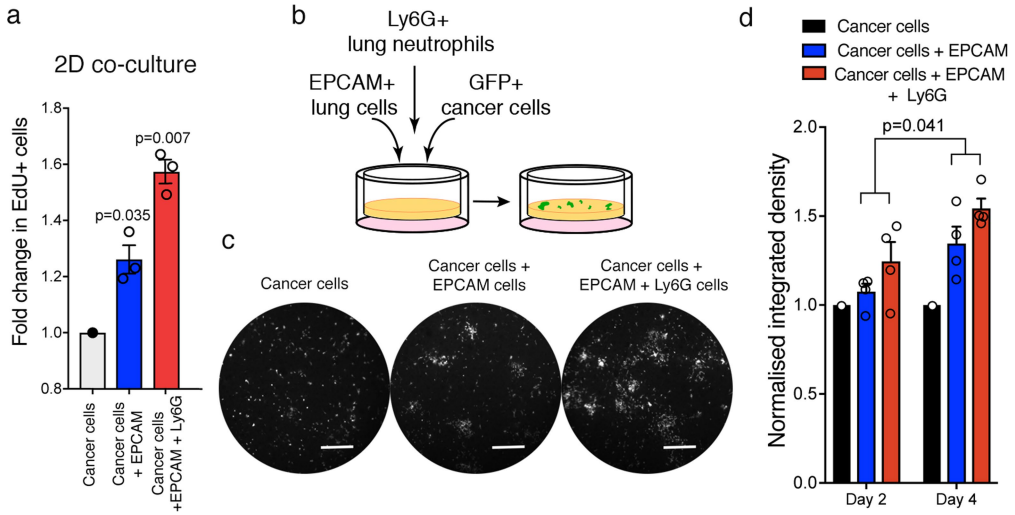

Extended Data Fig. 7 | Epithelial cells support cancer cell growth ex vivo. a, GFP$^+$ MMTV–PyMT cancer cell proliferation in 2D co-culture with MACS-sorted EPCAM$^+$ and Ly6G$^+$ cells stained with EdU and analysed by FACS ($n = 3$ independent experiments). Data are normalized to cancer cell proliferation. **b**–**d**, Three dimensional co-culture of GFP$^+$ MMTV-PyMT cancer cells with MACS-sorted EPCAM$^+$ and Ly6G$^+$ cells. **b**, Co-culture scheme. **c**, Representative images from four independent experiments (day 4; scale bar, 400 μm). **d**, Quantification of GFP signal. Data are normalized to cancer cell growth ($n = 4$ independent experiments (dots), each with 3–4 technical replicates). Statistical analysis of biological replicates by one-sample two-tailed *t*-test (**a**) and two-way ANOVA (**d**). Data are represented as mean ± s.e.m.

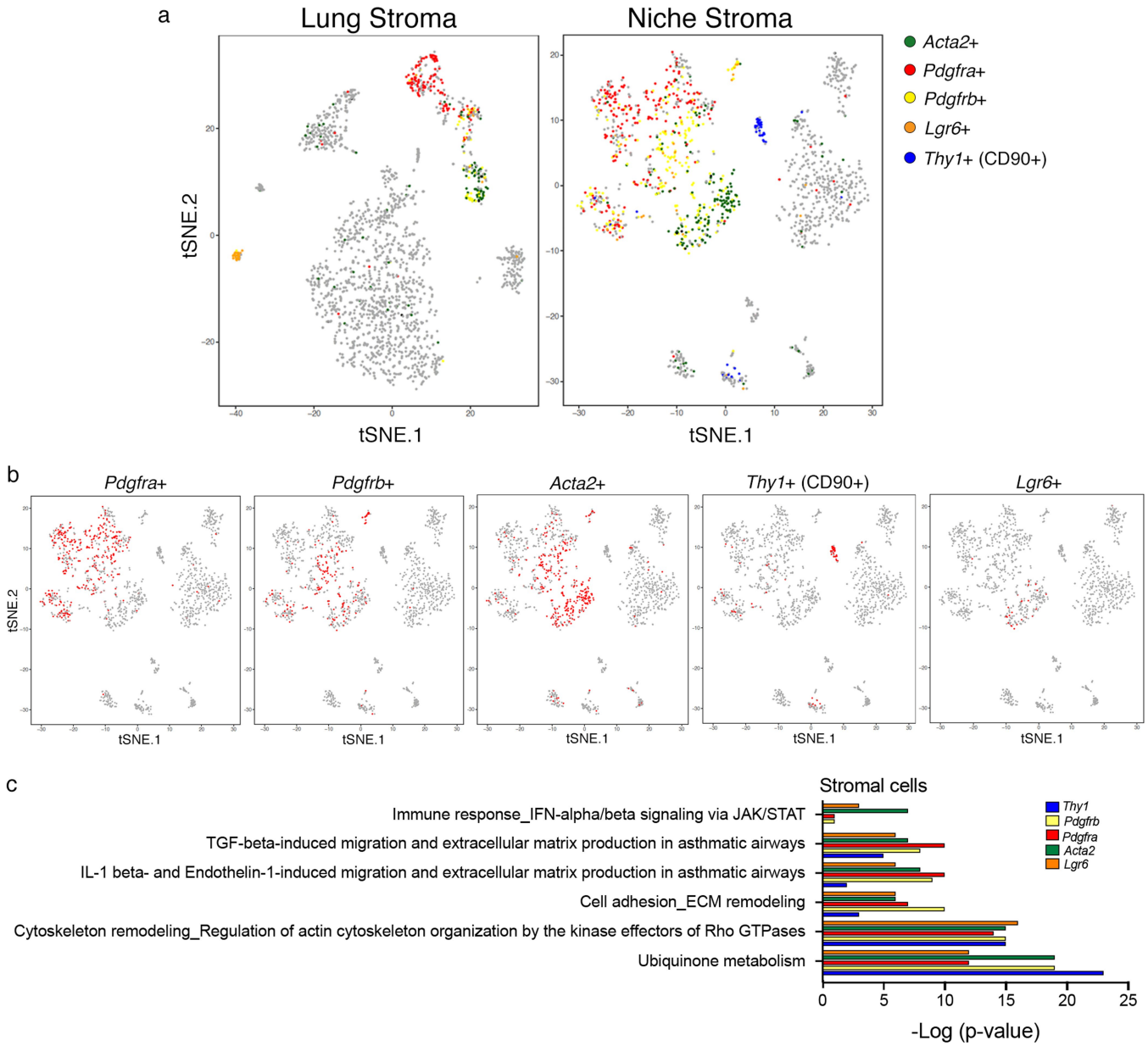

Extended Data Fig. 8 | scRNA-seq analysis reveals different sub-pools of stromal cells in the niche. a, *t*-SNE plots of CD45$^-$ cells isolated from distal lung ($n = 1{,}996$) or mCherry$^+$ niche ($n = 1{,}473$) after scRNA-seq analysis. Stromal cells are coloured on the basis of expression levels of the indicated genes. **b**, *t*-SNE niche plots from data in **a**; each plot shows (in red) the cells expressing the indicated stromal marker. **c**, MetaCore pathway enrichment analysis using the list of genes detected in at least 50% of the indicated marker-defined cells ($n = 66$ THY1$^+$ cells, $n = 175$ PDGFRB1$^+$ cells, $n = 322$ PDGFRA$^+$ cells, $n = 330$ ACTA2$^+$ cells, $n = 25$ LGR6$^+$ cells). Statistical analysis by hypergeometric test with Benjamini–Hochberg correction.

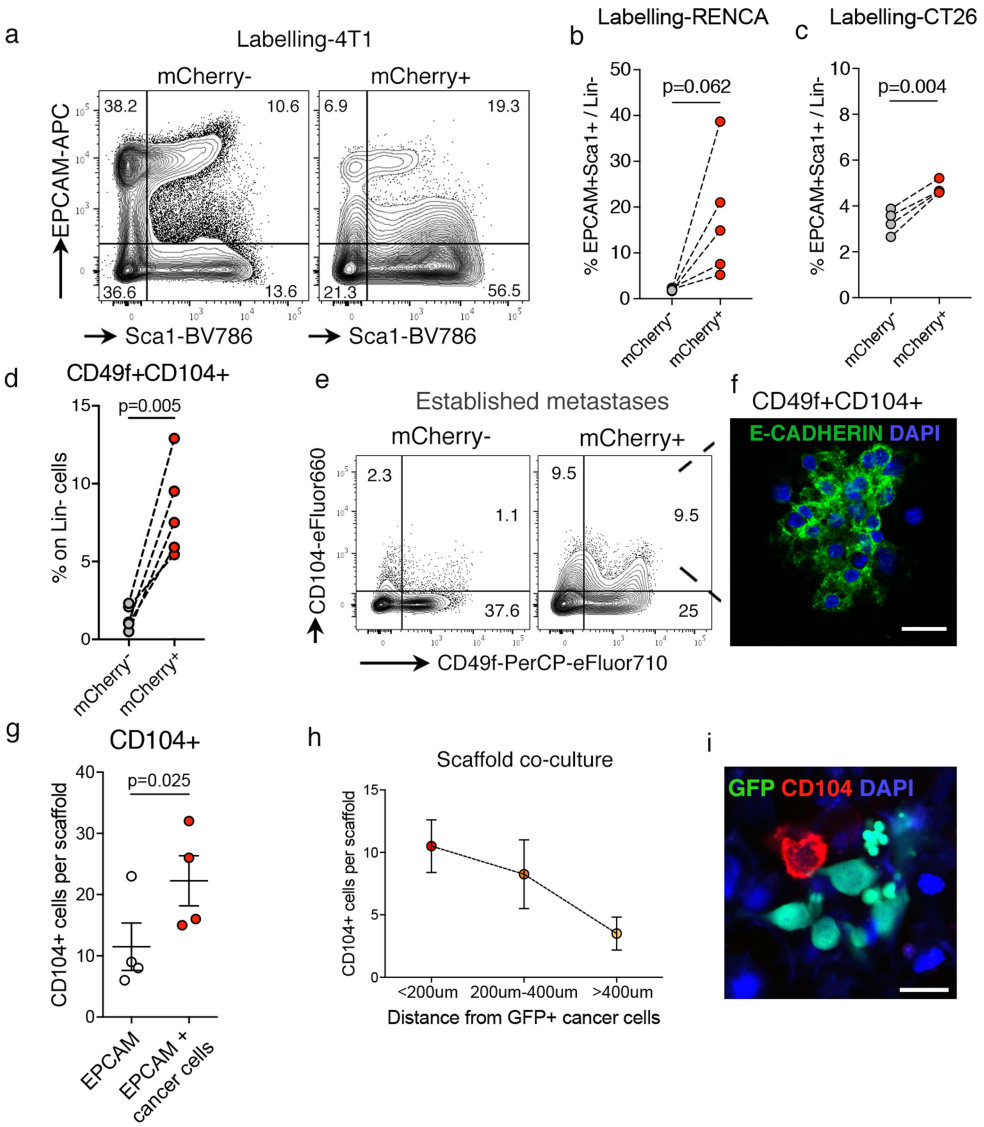

Extended Data Fig. 9 | mCherry$^+$-niche epithelial cells are enriched for stem cell markers. a, Representative FACS plots showing Lin$^-$ (CD45$^-$CD31$^-$Ter119$^-$) cells in distal lung and mCherry$^+$ niche from labelling-4T1-injected mice (quantification in Fig. 4i). **b**, **c**, Scatter plots showing FACS quantification of EPCAM$^+$SCA1$^+$ cell frequency on Lin$^-$ (CD45$^-$CD31$^-$Ter119$^-$) cells in distal lung and mCherry$^+$ niche with injection of labelling-RENCA (**b**; $n = 5$ mice) and labelling-CT26 (**c**; $n = 4$ mice). **d**–**f**, Scatter plot of CD49f$^+$CD104$^+$ cell frequency among Lin$^-$ (CD45$^-$CD31$^-$Ter119$^-$) cells in distal lung and mCherry$^+$ niche detected by FACS (**d**; $n = 5$ mice), representative FACS plots (**e**) and representative immunofluorescence image of FACS-sorted mCherry$^+$-niche CD49f$^+$CD104$^+$ cells stained for E-cadherin (green) and with DAPI (blue) (**f**; scale bar, 20 μm). **g**–**i**, Three-dimensional co-culture of GFP$^+$ MMTV–PyMT cancer cells with MACS-sorted EPCAM$^+$ cells. **g**, Quantification of integrin β4 (CD104) expression on EPCAM$^+$ cells. **h**, Number of CD104$^+$ cells proximal to cancer cells ($n = 4$ from three independent sorts). **i**, Representative immunofluorescence image from the co-culture stained for CD104 (red), GFP$^+$ cancer cells (green) and with DAPI (blue). Scale bar, 20 μm. Statistical analysis of biological replicates by paired two-tailed *t*-test (**b**–**d**, **g**). Data are presented as mean ± s.e.m.

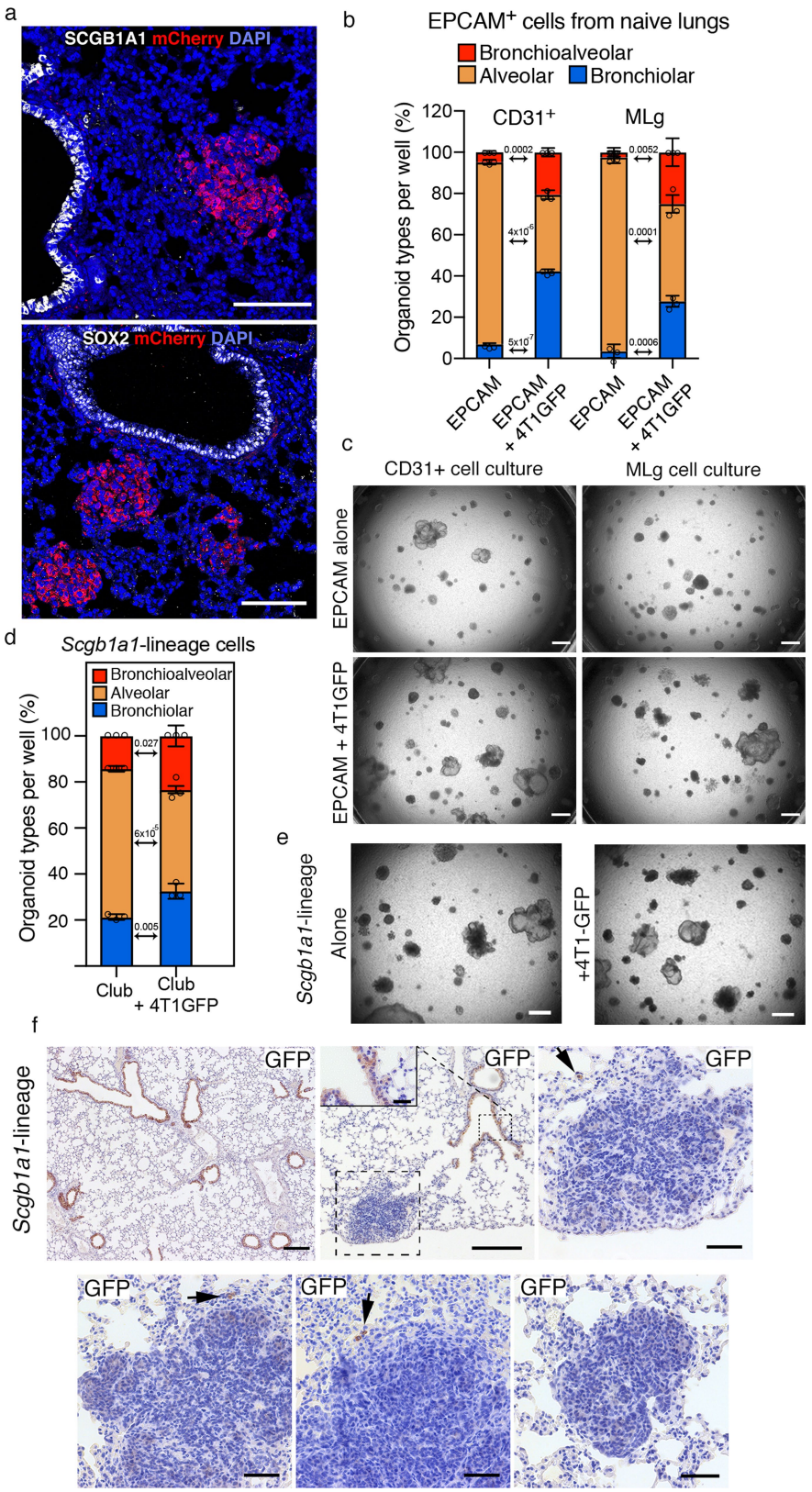

Extended Data Fig. 10 | See next page for caption.

Extended Data Fig. 10 | Cancer cells change lung epithelial cell-lineage commitment ex vivo. a, Representative immunofluorescence images of lung metastatic sections ($n = 3$ mice) co-stained for an airway marker (SCGB1A1 (top; white) or SOX2 (bottom; white)) and mCherry (red), and with DAPI (blue). Scale bar, 100 μm. **b**, **c**, Lung organoids from EPCAM$^+$ FACS-sorted cells in co-culture with either lung stromal CD31$^+$ cells or MLg fibroblasts, alone or in the presence of non-labelling 4T1-GFP cells from metastatic lungs in the lower chamber; quantification (**b**) and representative bright-field images (**c**; scale bar, 150 μm) of organoids. **d**, **e**, Lung organoids with *Scgb1a1-Cre^{ERT2}* lineage cells with or without 4T1-GFP: quantification (**d**) and representative bright-field images (**e**; scale bar, 150 μm). **f**, Representative staining of lineage cells in metastatic lungs from *Scgb1a1-Cre^{ERT2}* mice injected with MMTV–PyMT cancer cells. Scale bars: top left, 200 μm; other panels, 50 μm; top middle inset, 25 μm. Data are generated with sorted EPCAM$^+$ (**b**) or club-lineage cells (**d**) and represented as cumulative percentage presented as mean ± s.d. of three co-cultures per sorting. Statistical analysis by two-tailed *t*-test on original non-cumulative values (**b**, **d**). Images are representative of three organoid cultures (**c**, **e**).

nature research

Corresponding author(s): Ilaria Malanchi and Joo-Hyeon Lee

Last updated by author(s): Jun 12, 2019

Reporting Summary

Nature Research wishes to improve the reproducibility of the work that we publish. This form provides structure for consistency and transparency in reporting. For further information on Nature Research policies, see Authors & Referees and the Editorial Policy Checklist .

Statistics

For all statistical analyses, confirm that the following items are present in the figure legend, table legend, main text, or Methods section.

n/a	Confirmed	
☐	☒	The exact sample size (*n*) for each experimental group/condition, given as a discrete number and unit of measurement
☐	☒	A statement on whether measurements were taken from distinct samples or whether the same sample was measured repeatedly
☐	☒	The statistical test(s) used AND whether they are one- or two-sided *Only common tests should be described solely by name; describe more complex techniques in the Methods section.*
☐	☒	A description of all covariates tested
☐	☒	A description of any assumptions or corrections, such as tests of normality and adjustment for multiple comparisons
☐	☒	A full description of the statistical parameters including central tendency (e.g. means) or other basic estimates (e.g. regression coefficient) AND variation (e.g. standard deviation) or associated estimates of uncertainty (e.g. confidence intervals)
☐	☒	For null hypothesis testing, the test statistic (e.g. *F*, *t*, *r*) with confidence intervals, effect sizes, degrees of freedom and *P* value noted *Give P values as exact values whenever suitable.*
☒	☐	For Bayesian analysis, information on the choice of priors and Markov chain Monte Carlo settings
☒	☐	For hierarchical and complex designs, identification of the appropriate level for tests and full reporting of outcomes
☒	☐	Estimates of effect sizes (e.g. Cohen's *d*, Pearson's *r*), indicating how they were calculated

Our web collection on statistics for biologists contains articles on many of the points above.

Software and code

Policy information about availability of computer code

Data collection	Flow cytometry: samples were run on a BD 671 LSR-Fortessa (BD Biosciences, USA) using the BD FACSDiva software v8.0.1.

Data analysis	Statistics: analyses were performed using Prism software (version 7.0c, GraphPad Software, USA) with the exception of the qRTPCR data, for which R was used. Fluorescence imaging: FiJi (version 2.0.0-rc-68/1.52g, ImageJ) and Adobe Photoshop CC 2018 (version 19.0, Adobe, USA) were used to analyse fluorescence images. Immunohistochemistry: images were acquired using NIS-elements software (version 4.51, Nikon, Japan) Flow cytometry: data analyses were carried out using FlowJo 10.4.2 (FlowJO, LCC 2006-2018, USA). ImageStream: analyisis were performed using IDEA software (version 6.2, IDEAS Amnis, Merck, USA) Proteomics: data analysis and differential protein expression was performed using Spectronaut Professional+. A detailed description of sample processing, data acquisition and processing are available on request. RNA sequencing: the RSEM package (version 1.2.29) and Bowtie2 were used to align reads to the mouse mm10 transcriptome. Differential expression analysis was carried out with DESeq2 package9 (version 1.12.4) within R version 3.3.1 (https://www.rproject.org/). Gene Set Enrichment Analysis, GSEA, (version 2.2.3) was carried out using ranked gene lists using the Wald statistic and the gene sets of C2 canonical pathways and C5 biological processes. Heatmaps of differentially expressed genes were generated using the gplots (Gregory et al., gplots: Various R Programming Tools for Plotting Data. R package version 3.0.1. (2016). https://CRAN.R-project.org/package=gplots) CRAN package (version 3.0.1). Single-cell RNA-sequencing: the Cell Ranger v2.1.1 pipeline was used to process raw reads, using STAR (v2.5.1b) to align to the mm10 transcriptome, deconvolve reads to their cell of origin using the UMI tags and report cell-specific gene expression count estimates. All subsequent analyses were performed in R-3.4.1 using the cellrangerRkit, monocle and pheatmap packages. See methods for further details

For manuscripts utilizing custom algorithms or software that are central to the research but not yet described in published literature, software must be made available to editors/reviewers. We strongly encourage code deposition in a community repository (e.g. GitHub). See the Nature Research guidelines for submitting code & software for further information.

Data

Policy information about availability of data

All manuscripts must include a data availability statement. This statement should provide the following information, where applicable:

- Accession codes, unique identifiers, or web links for publicly available datasets
- A list of figures that have associated raw data
- A description of any restrictions on data availability

The RNA sequencing datasets (GSE117930) and the single cell RNA sequencing datasets (GEO13150) are deposited in the Gene Expression Omnibus (GEO, NCBI) repository. The proteomic datasets are deposited in PRoteomics IDEntifications (PRIDE) repository (PXD010597).

Field-specific reporting

Please select the one below that is the best fit for your research. If you are not sure, read the appropriate sections before making your selection.

☒ Life sciences ☐ Behavioural & social sciences ☐ Ecological, evolutionary & environmental sciences

For a reference copy of the document with all sections, see nature.com/documents/nr-reporting-summary-flat.pdf

Life sciences study design

All studies must disclose on these points even when the disclosure is negative.

Sample size	Sample sizes were estimated based on previous experiments conducted in our laboratory, providing sufficient numbers of mice in each group to yield a two-sided statistical test, with the potential to reject the null hypothesis with a power (1 - beta) of 80%, subject to alpha = 0.05.
Data exclusions	No data was excluded
Replication	Unless otherwise specified in the figure legends, experiments were reproduced in at least two independent experiments.
Randomization	The majority of the in vivo data generated in this study involved analysis between different areas of the same tissue in each mouse, therefore both control and experiment cannot be randomized. The experiment involving a therapeutic treatment with the antibody was performed on litter mice all injected with tumour cells and then randomized for the antibody treatment.
Blinding	Investigators were not blinded for studies involving the analysis of the Niche versus distant lung cells as the cells were from the same samples and the two subsets could only be discriminated by FACS analysis itself. Experiments using sorted and stained cells (niche versus distant lung), scaffold assays and organoid assays were blinded at quantification. For the in vivo treatment experiment with antiWisp1, the quantification of metastatic burden between the two group was performed blinded.

Reporting for specific materials, systems and methods

We require information from authors about some types of materials, experimental systems and methods used in many studies. Here, indicate whether each material, system or method listed is relevant to your study. If you are not sure if a list item applies to your research, read the appropriate section before selecting a response.

Materials & experimental systems

n/a	Involved in the study
[ ]	[x] Antibodies
[ ]	[x] Eukaryotic cell lines
[x]	[ ] Palaeontology
[ ]	[x] Animals and other organisms
[x]	[ ] Human research participants
[x]	[ ] Clinical data

Methods

n/a	Involved in the study
[x]	[ ] ChIP-seq
[ ]	[x] Flow cytometry
[x]	[ ] MRI-based neuroimaging

Antibodies

Antibodies used

ANTIBODY_ COMPANY_ CATALOGUE No_ CLONAL_ (CLONE)_ DILUTION (Technique)
Acetylated-tubulin_ Sigma-Aldrich_ T7451_ Mouse monoclonal_ (6-11B-1)_ 1:1000 (IF)
CC10 (SCGB1A1)_ Santa Cruz_ sc-25555_ Rabbit polyclonal_ (FL-96)_ 1:200 (IF)
CD11b-APC_ Biolegend_ 10121_ Rat monoclonal_ (M1/70)_ 1:100 (FC)
CD11b-APCCy7_ Biolegend_ 101226_ Rat monoclonal_ (M1/70)_ 1:100 (FC)
CD45-BV421_ Biolegend_ 103133_ Rat monoclonal_ (30-F11)_ 1:200 (FC)
CD45-APC_ eBioscience_ 17-0451-83_ Rat monoclonal_ (30-F11)_ 1:200 (FC)
CD45-APC-eFluor780_ eBioscience_ 47-0451-82_ Rat monoclonal_ (30-F11)_ 1:200 (FC)
CD49f-PerCP-eFluor710_ eBioscience_ 46-0495-82_ Rat monoclonal_ (ebioGOH3)_ 1:200 (FC)
CD104-eFluor660_ eBioscience_ 50-1049-82_ Rat monoclonal_ (439-9b)_ 1:100 (FC; IF)
CD326(EPCAM)-APC_ eBioscience_ 17-5791-81_ Rat monoclonal_ (G8.8)_ 1:200 (FC)
CD326(EPCAM)-APC750Fire_ Biolegend_ 118230_ Rat monoclonal_ (G8.8)_ 1:200 (FC)
E-CADHERIN_ Abcam_ Ab11512_ Rat monoclonal_ (DECMA-1)_ 1:200 (IF)
GFP_ Abcam_ ab6673_ Goat polyclonal_ 1:300 (IF)
HOPX_ Santa Cruz_ sc-30216_ Rabbit polyclona_l (FL-73)_ 1:250 (IF)
Ki67_ Abcam_ Ab16667 _Rabbit monoclonal_ (SP6)_ 1:300 (IF)
Ly6A/E(SCA-1)-APC_ Biolegend_ 108111_ Rat monoclonal_ (D7)_ 1:200 (FC)
Ly6A/E(SCA-1)-APC750Fire_ Biolegend_ 127652_ Rat monoclonal_ (D7)_ 1:200 (FC)
Ly6A/E(SCA-1)-BV786_ BD Bioscience_ 563991_ Rat monoclonal_ (D7)_ 1:200 (FC)
Ly6G-APC_ BD Bioscience_ 560599_ Rat monoclonal_ (1A8)_ 1:150 (FC)
Ly6G-APC750Fire_ Biolegend_ 127652_ Rat monoclonal_ (1A8)_ 1:150 (FC)
Ly6G-V450_ BD Bioscience_ 560603_ Rat monoclonal_ (1A8)_ 1:150 (FC)
mCHERRY_ Abcam_ ab183628_ Rabbit polyclonal_ 1:750 (IF)
SOX2_ eBioscience_ 14-9811-80_ Rat monoclonal_ (Btjce)_ 1:500 (IF)
SP-C_ Santa Cruz_ sc-7706_ Goat polyclonal_ (M-20)_ 1:200 (IF)
TER-119_ Biolegend_ 116233_ Rat monoclonal_ (TER-119)_ 1:200 (FC)
TTF1_ DAKO_ M3575_ Mouse monoclonal_ (8G7G3/1)_ 1:50 (IF)
WISP1_ Abcam_ Ab178547_ Rabbit polyclonal_ 1:100 (IF)

Validation

The antibodies used have been validated accordingly to manufacturer's instructions. Mouse lung cell suspensions were used to validate FACS antibodies. Human or mouse lung sections were used to validates the antibodies for IF or IHC straining.

Eukaryotic cell lines

Policy information about cell lines

Cell line source(s)

MLg cells (murine normal lung fibroblasts) were purchased from ATCC (USA). CAF (cancer associated fibroblasts) isolated from MMTV-PyMT tumours and human normal fibroblast (hNLF) (FVB background) were a gift from E.Sahai. All other cell lines (4T1, EO771, HC11, RAW264.7, RENCAm CT26) were provided by the Cell Services Unit of The Francis Crick Institute. For primary cells, MMTV-PyMT cells were isolated from growing MMTV-PyMT tumours (FVB or C57/Blackl6 background).

Authentication

Short Tandem Repeat (STR) was used to identify all cell lines used while SPID was used to confirm the species of origin.

Mycoplasma contamination

All cells are routinely tested for Mycoplasma by the Cell Services Unit of The Francis Crick Institute.

Commonly misidentified lines
(See ICLAC register)

No commonly misidentified lines were used.

Animals and other organisms

Policy information about studies involving animals; ARRIVE guidelines recommended for reporting animal research

Laboratory animals	Mice used for this experiments were females of wild type Balb/cJ or C57BL/6 background or MMTV-PyMT/actin-GFP and RAG1 ko mice in FVB background, MMTV-PyMT, Sftpc-CreERT2, Rosa26R-YFP, Scgb1a1-CreERT2 and Rosa26R-fGFP mice in C57BL/6 background. All mice used were females between 4 and 10 weeks of age. All mice were bred in house at The Francis Crick Biological Research Facility or The Gurdon Institute of University of Cambridge, according to UK Home Office Regulations.
Wild animals	This study did not involve wild animals.
Field-collected samples	This study did not involve samples collected from the fields.
Ethics oversight	All experiments were approved by Francis Crick/Cambridge University ethical review committees and conducted according to UK Home Office Regulations (project license PPL/80/2531 and PC7F8AE82).

Note that full information on the approval of the study protocol must also be provided in the manuscript.

Flow Cytometry

Plots

Confirm that:

☒ The axis labels state the marker and fluorochrome used (e.g. CD4-FITC).

☒ The axis scales are clearly visible. Include numbers along axes only for bottom left plot of group (a 'group' is an analysis of identical markers).

☒ All plots are contour plots with outliers or pseudocolor plots.

☒ A numerical value for number of cells or percentage (with statistics) is provided.

Methodology

Sample preparation	Lungs were minced and digested for 30 min in a shaker at 37ºC with a mixture of DNase I (Merck Sigma-Aldrich, Germany) and Liberase TM and TH (Roche Diagnostics, Switzerland) in HBSS solution. Samples were then washed, passed through a 100 m filter and incubated in Red Blood Cell Lysis buffer (Miltenyi Biotec, Germany) for 3-5 min at room temperature. After a wash with MACS buffer (0.5% BSA and 250 mM EDTA in PBS), samples were passed subsequently through a 40 m filter and a 20 m strainercapped flow cytometry tube for single cell suspension to use for flow cytometric analysis or further purification. For ex vivo lineage tracing experiments: Lungs were cleared by perfusion, dissected, minced and dissociated with a collagenase/dispase solution containing DNase1 for 45 min at 37°C. Cells were then filtered sequentially through 100- and 40-µm strainers, centrifuged at 1000rpm for 5 min at 4°C and resuspended in 1ml of ACK lysis buffer (0.15 M NH4Cl, 10mM KHCO3, 0.1 mM EDTA) for 90 s at room temperature for red blood cell lysis. Cells were washed with basic F12 media containing FBS (ThermoFisher Scientific, USA), centrifuged and resuspended in PF10 buffer (PBS with 10% FBS) for further staining.
Instrument	Flow cytometry analyses were carried out on a BD LSR-Fortessa (BD Biosciences, USA). The majority of cell-sorting experiments were carried out on a BD Influx cell sorter (BD Biosciences, USA), with the exception of the ex vivo lineage tracing experiments which were performed on the MOFLO system (Beckman Coulter).
Software	FlowJo 10.4.2 (FlowJO, LCC 2006-2018, USA) was used for analysis.
Cell population abundance	Purity check was routinely performed after each sorting. Cells were used when purity was above 85%
Gating strategy	All gating strategy are described in the methods and two typical examples are provided.

☒ Tick this box to confirm that a figure exemplifying the gating strategy is provided in the Supplementary Information.

ARTICLE

https://doi.org/10.1038/s41586-019-1498-3

Identification of an ATP-sensitive potassium channel in mitochondria

Angela Paggio[1,4], Vanessa Checchetto[2,4], Antonio Campo[1], Roberta Menabò[3], Giulia Di Marco[1], Fabio Di Lisa[1,3], Ildiko Szabo[2,3], Rosario Rizzuto[1]* & Diego De Stefani[1]*

Mitochondria provide chemical energy for endoergonic reactions in the form of ATP, and their activity must meet cellular energy requirements, but the mechanisms that link organelle performance to ATP levels are poorly understood. Here we confirm the existence of a protein complex localized in mitochondria that mediates ATP-dependent potassium currents (that is, mitoK$_{ATP}$). We show that—similar to their plasma membrane counterparts—mitoK$_{ATP}$ channels are composed of pore-forming and ATP-binding subunits, which we term MITOK and MITOSUR, respectively. In vitro reconstitution of MITOK together with MITOSUR recapitulates the main properties of mitoK$_{ATP}$. Overexpression of MITOK triggers marked organelle swelling, whereas the genetic ablation of this subunit causes instability in the mitochondrial membrane potential, widening of the intracristal space and decreased oxidative phosphorylation. In a mouse model, the loss of MITOK suppresses the cardioprotection that is elicited by pharmacological preconditioning induced by diazoxide. Our results indicate that mitoK$_{ATP}$ channels respond to the cellular energetic status by regulating organelle volume and function, and thereby have a key role in mitochondrial physiology and potential effects on several pathological processes.

ATP-sensitive potassium (K_{ATP}) channels act as sensors of cellular metabolism. In the plasma membrane[1], they couple cell excitability with energy availability[2,3]. They have also been reported to be located in intracellular membranes—for example, in mitochondria (that is, mitoK$_{ATP}$)[4,5]—but, in this context, their existence is a matter of debate[6]. MitoK$_{ATP}$ mediates the electrophoretic uptake of potassium ions (K^+), which is driven by the negative mitochondrial membrane potential ($\Delta\Psi_m$), and it is inhibited by physiological levels of ATP. MitoK$_{ATP}$ was first described in the early 1990s, through patch clamp of mitoplasts[4] or by partial purification techniques[5]. MitoK$_{ATP}$ has been characterized from a pharmacological point of view, and both openers (diazoxide) and inhibitors (sulfonylureas and 5-hydroxydecanoate (5-HD)) have been described—some of them with proposed specific action on mitoK$_{ATP}$ versus plasma membrane K_{ATP} channels[7]. Drugs that target K_{ATP} channels are useful in the treatment of several pathologies. Importantly, some of their uses are due to the modulation of plasma membrane K_{ATP}[8] but others seem to depend on their effects on mitoK$_{ATP}$. For example, pharmacological preconditioning with diazoxide efficiently protects the heart from ischaemia–reperfusion injury[9,10] even in the absence of cardiac plasma membrane K_{ATP}[11,12]. However, the molecular identity and pharmacology of the mitoK$_{ATP}$ channel remain unknown[7,13,14].

MITOK is a cation channel

We screened a subset of mitochondrial proteins with unknown function and focused on a candidate protein that is encoded by the *CCDC51* gene (NCBI code 79714; we hereafter name the *CCDC51* gene *MITOK*), the overexpression of which markedly impaired mitochondrial physiology. The *MITOK* gene is conserved in vertebrates, in which it encodes a unique 45-kDa protein with a predicted N-terminal mitochondrial targeting sequence, one coiled-coil and two transmembrane domains. In humans, the *MITOK* gene encodes for two isoforms: isoform 1, which is full-length but has no predicted mitochondrial targeting sequence, and isoform 2, which is a splice variant that lacks the first 109 amino acids (34 kDa in size) and includes a supposed mitochondrial targeting sequence (Fig. 1a). Analyses of RNA and protein levels using existing datasets revealed that *MITOK* is expressed in all tissues in humans, as is *Ccdc51* (which we hereafter name *Mitok*) in mice[15,16]. First, we experimentally validated the mitochondrial localization of MITOK in humans and mice. Immunofluorescence showed a full co-localization of MITOK with a mitochondrial marker in HeLa cells (Fig. 1b), and subcellular fractionation of mouse liver revealed a progressive enrichment of MITOK in mitochondria and mitoplasts, and the absence of this protein on the outer membrane (Fig. 1c). Carbonate extraction confirmed membrane insertion (Extended Data Fig. 1a), which indicates that MITOK is in the inner mitochondrial membrane. To investigate the topology of MITOK, we used two antibodies—one against the N-terminal half, and the other covering the C-terminal half, of MITOK (Fig. 1d). Digestion of mouse mitoplasts using proteinase K caused the loss of full-length MITOK and the appearance of a smaller fragment that was recognized by the N-terminal antibody (Extended Data Fig. 1b), which indicates that a portion of the protein is protected inside the organelle. By contrast, no residual signal was detected with an antibody against the region between the two transmembrane domains, which indicates that this part is exposed to the intermembrane space. MITOK is a two-pass protein of the inner mitochondrial membrane with the N and C termini exposed towards the matrix. Next, we cloned and tagged (with Flag, V5 and GFP) mouse MITOK and investigated the effect of its overexpression. In terms of morphology, MITOK overexpression causes organelle fragmentation (Extended Data Fig. 1c) and swelling (Fig. 1e). At functional level, MITOK overexpression caused a drop in $\Delta\Psi_m$ (Extended Data Fig. 1d) and agonist-induced mitochondrial Ca^{2+} uptake (an additional readout for changes in $\Delta\Psi_m$) (Extended Data Fig. 1e). For the human isoforms, we designed both specific (isoform 1 versus isoform 2) and non-specific (pan-isoforms) primers for quantitative PCR. Both isoforms can be detected in HeLa cells at the transcript level, although isoform 2 is expressed one tenth the level of isoform 1 (Extended Data Fig. 1f). Despite this, only a

[1]Department of Biomedical Sciences, University of Padova, Padova, Italy. [2]Department of Biology, University of Padova, Padova, Italy. [3]CNR Institute of Neuroscience, Padova, Italy. [4]These authors contributed equally: Angela Paggio, Vanessa Checchetto. *e-mail: rosario.rizzuto@unipd.it; diego.destefani@gmail.com

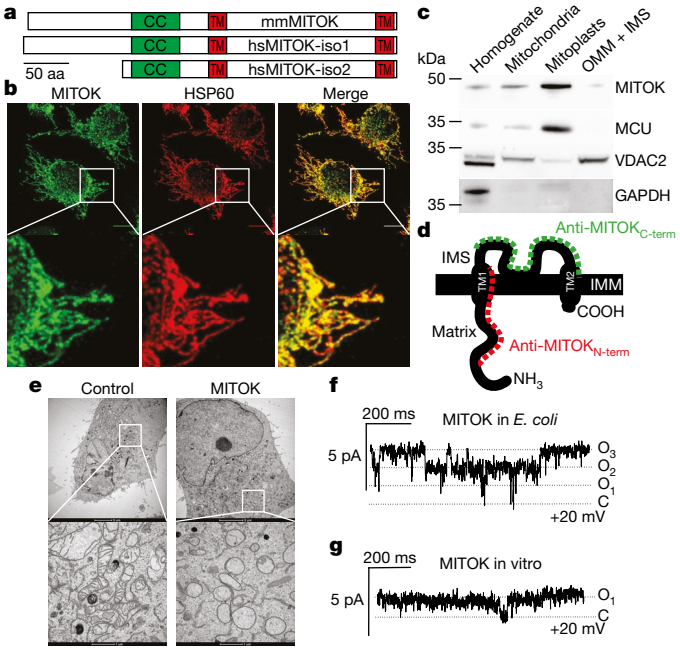

Fig. 1 | Biochemical and functional characterization of MITOK. **a**, Representation of human (hs) and mouse (mm) MITOK proteins. Transmembrane (TM) and coiled-coil (CC) domains are indicated. iso1, isoform 1; iso2, isoform 2. **b**, Immunolocalization of MITOK (green) and the mitochondrial marker HSP60 (red). Representative of four independent experiments. Scale bar, 10 μm. **c**, Subcellular fractionation of mouse liver (replicated twice). IMS, inter-membrane space; OMM, outer mitochondrial membrane. **d**, Representation of MITOK membrane topology. C-term, C terminus; IMM, inner mitochondrial membrane; N-term, N terminus; anti-MITOK, antibody raised against the indicated region of MITOK. **e**, Transmission electron microscopy images of control and MITOK-overexpressing HeLa cells (replicated three times). **f**, **g**, Representative current traces with MITOK purified from *E. coli* (**f**, $n = 5$ biological replicates from 2 independent preparations) or expressed in vitro (**g**, $n = 23$ biological replicates from 10 independent preparations).

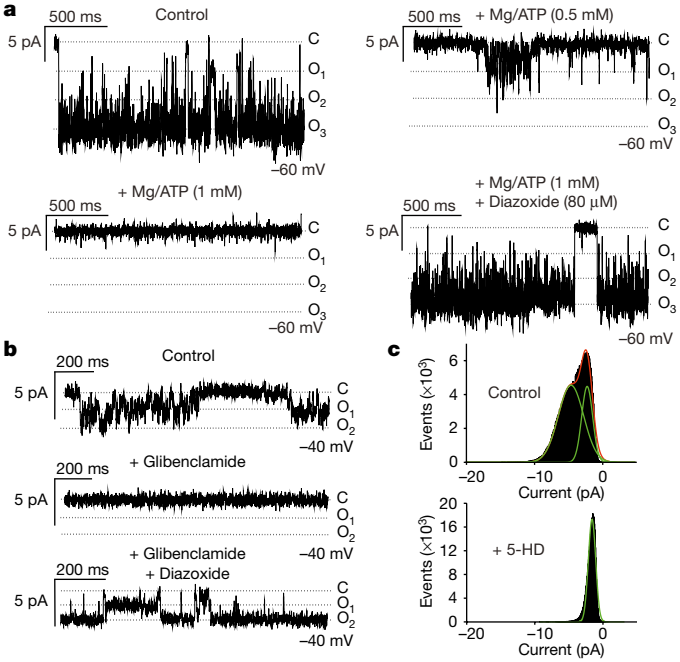

Fig. 2 | Electrophysiological characterization of recombinant MITOK co-expressed with MITOSUR. **a**, Current traces before (control) and after the first addition of 500 μM Mg and ATP, the second addition of 500 μM Mg and ATP and the third addition of 80 μM diazoxide. All traces were obtained from the same experiment, representative of four independent experiments. **b**, Current recordings before and after addition of 30 μM glibenclamide. The channel was re-activated by subsequent addition of 100 μM diazoxide ($n = 4$ for inhibition by glibenclamide, $n = 2$ for reactivation by diazoxide). **c**, Representative histograms before (top) and after (bottom) addition of 5-HD (100 μM, $n = 5$ independent experiments).

single band can be detected in western blots using HeLa cells (Extended Data Fig. 1g). In most human tissues, isoform 1 shows moderate levels of expression, whereas isoform 2 is barely detectable. This pattern is reversed in the case of the spleen, which shows substantial expression of isoform 2 and marginal expression of isoform 1 (Extended Data Fig. 1f). In terms of their roles, isoform 1 localizes to mitochondria and—similar to mouse MITOK—its overexpression induced morphological and functional organelle impairment (Extended Data Fig. 2a, b), which indicates that both mouse and human *MITOK* genes encode similar proteins (although some human cells express a shorter and less-active splicing variant). Overall, overexpression of MITOK causes a severe perturbation of mitochondrial structure and function. Although several mechanisms could account for these effects, we reasoned that MITOK could act as a cation channel, because valinomycin (a K^+ ionophore, a molecule that mediates K^+ influx into the matrix) closely mimics the phenotype observed on MITOK overexpression.

The unambiguous demonstration of channel activity necessarily requires a simplified reconstitution approach that uses recombinant proteins. We thus measured the channel activity of mouse MITOK in the planar lipid bilayer using MITOK from two systems (*Escherichia coli* and the wheat-germ cell-free transcription and translation tool), both of which express MITOK at high levels (Extended Data Fig. 3a, b). We observed channel activity in a medium that contained only K^+ as cation (Fig. 1g–h). Burst-like, flickering activity and cooperative transitions between dual- or multi-states were observed[4,17] (Extended Data Fig. 3c, d). The channel showed an ohmic behaviour (Extended Data Fig. 3e), was voltage-independent (Extended Data Fig. 3f) and was selective for K^+ over chloride (P_K:P_{Cl} = 1:0.02) (Extended Data Fig. 3g). Channel conductance was 57 ± 11 pS in both 100 mM KCl and K-gluconate media[18,19] (Fig. 1h, Extended Data Fig. 3e). Channel activity could be blocked by addition of barium, an inhibitor of K^+ channels (Extended Data Fig. 3h), but not by paxilline, an inhibitor of the BKCa channels (Extended Data Fig. 3i).

MITOK and MITOSUR form the mitoK$_{ATP}$ channel

On the basis of these data, we pursued the hypothesis that MITOK could be mitoK$_{ATP}$—despite the fact that (i), similar to the lysosomal K^+ channel TMEM175[20], MITOK does not contain the typical K^+ selectivity filter (and, accordingly, allows permeation of Na^+) (Extended Data Fig. 4a) and (ii) the purified protein per se did not respond to ATP (Extended Data Fig. 4b) or 5-HD (Extended Data Fig. 4c). However, we reasoned that ATP sensitivity could be conferred by a regulatory sulfonylurea-receptor (SUR)-like subunit. Ten ATP-binding cassette (ABC) proteins can be detected in mitochondria[15], most of which belong to ABCB subfamily[21]. We focused on ABCB8 (which we hereafter name MITOSUR) because (i), of the ten ABC proteins in mitochondria, the tissue expression of this protein best correlates with MITOK, and (ii) it has previously been suggested to be part of mitoK$_{ATP}$[22]. We expressed in vitro mouse MITOK together with MITOSUR; these were folded and incorporated into liposomes, as indicated by thermal stability assay (Extended Data Fig. 5a–c) and membrane extraction (Extended Data Fig. 5d), with a membrane orientation that resembled that in mitoplasts (Extended Data Figs. 5e, f, 6a). MITOK and MITOSUR were able to form a K^+ permeable channel (Fig. 2a, Extended Data Fig. 5g–i) that was (i) inhibited by millimolar concentrations of ATP, (ii) activated by diazoxide (Fig. 2a, Extended Data Fig. 5g, h) and (iii) blocked by both the sulfonylurea glibenclamide (Fig. 2b) and 5-HD (Fig. 2c). The channel conductance slightly decreased upon addition of 1 mM Mg^{2+} (Extended Data Fig. 5j). Activity was observed in

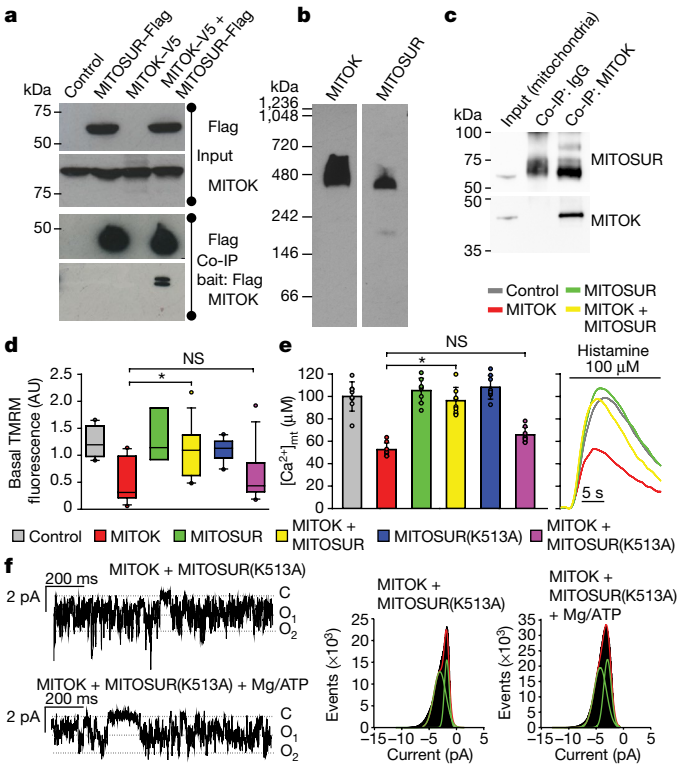

Fig. 3 | MITOK and MITOSUR form the mitoK$_{ATP}$ channel in situ. **a**, Co-immunoprecipitation (co-IP) between overexpressed MITOK and MITOSUR (representative of three independent experiments). **b**, Blue-native PAGE of digitonin-permeabilized mitochondria. Representative of two independent experiments. **c**, Co-immunoprecipitation of endogenous MITOK using liver mitochondria. Representative of two independent experiments. **d**, $\Delta\Psi_m$ measurements in HeLa cells transfected with the indicated constructs. $n \geq 9$ biological replicates from 3 independent experiments, $^*P \leq 0.01$ using two-way analysis of variance (ANOVA) with Holm–Sidak correction NS, not significant. AU, arbitrary units; TMRM, tetramethylrhodamine methyl ester. **e**, Measurements of Ca^{2+} concentration in mitochondria ($[Ca^{2+}]_{mt}$) (mean ± s.d.) in HeLa cells that express the indicated constructs; $n = 8$ biological replicates (representative of 3 independent experiments), $^*P < 0.001$ using two-way ANOVA with Holm–Sidak correction. **f**, Current traces (left) and histograms (right) of MITOK together with MITOSUR(K513A), before and after the addition of 2 mM Mg and ATP. Representative of three independent preparations.

the absence of divalent cations (Extended Data Fig. 5k) and the presence of Na^+ only (Extended Data Fig. 5l). Overall, all these features recapitulate the fundamental electrophysiological properties and the consensus pharmacological profile of mitoK$_{ATP}$[18,19], with MITOK forming the K^+-permeant channel and MITOSUR acting as a modulatory subunit that carries the ATP-binding site. We next investigated the membrane topology of MITOSUR by performing a protease protection assay using an antibody that covers the ATP-binding region (amino acids 394–693). Extended Data Figure 6a shows that proteinase K leads to the loss of the MITOSUR-specific band, which indicates that the ATP-binding cassette is exposed to the intermembrane space. Overall, the membrane orientations of both MITOK and MITOSUR are supported by previous bioenergetics studies[5] and independent proteomic approaches[23].

In light of this architecture, we reasoned that the unregulated K^+ uptake in cells that overexpress MITOK alone must be the cause of organelle impairment (Fig. 1). If this is true, the combined overexpression of human MITOSUR and mouse MITOK should reverse the mitochondrial dysfunction. To test this, we first verified the physical interaction between human MITOSUR and mouse MITOK through co-immunoprecipitation (Fig. 3a). In addition, immunoblot analysis of digitonin-solubilized mitochondrial complexes in native conditions revealed an approximately 500-kDa band that reacted with both MITOK and MITOSUR antibodies (Fig. 3b)—a size that is compatible with an octamer (four MITOK and four MITOSUR components). Accordingly, immunoprecipitation of endogenous MITOK could efficiently pull down MITOSUR using both mouse and human mitochondria (Fig. 3c, Extended Data Fig. 6b). In terms of function, the overexpression of mouse MITOK alone caused a decrease of both mitochondrial membrane potential and Ca^{2+} uptake (Fig. 3d, e), whereas the overexpression of the MITOSUR subunit alone did not affect these parameters. Most importantly, the combined overexpression of the two subunits fully rescued $\Delta\Psi_m$ and Ca^{2+} dynamics (which were impaired by mouse MITOK alone), suggesting the recovery of the proper channel gating. We also generated a MITOSUR mutant (MITOSUR(K513A)) that is unable to bind ATP. This mutant could interact with mouse MITOK (Extended Data Fig. 6c)—but did not respond to ATP in electrophysiological experiments (Fig. 3f) and did not rescue the loss of mitochondrial membrane potential and Ca^{2+} accumulation that is caused by the overexpression of mouse MITOK (Fig. 3d, e). This provides further confirmation that ATP acts as channel inhibitor. Overall, our data indicate that MITOK and MITOSUR form a complex that is responsible for the ATP-sensitive mitochondrial K^+ transport both in vitro and in situ.

MITOK controls mitochondrial volume

Despite consensus regarding the cytoprotective role of mitoK$_{ATP}$ opening in stress conditions (which is mainly based on pharmacological studies)[10], the constitutive physiological function of this channel remains obscure. We therefore generated HeLa cells that are knockout for *MITOK* by CRISPR–Cas9 DNA cleavage, using two different guides (Extended Data Fig. 7a, b). We first confirmed that MITOK is required for ATP-dependent K^+ fluxes in mitochondria, by measuring mitochondrial swelling rates in a K^+-based buffer[9,24]. In isolated wild-type mitochondria, ATP decreases, and diazoxide increases, the swelling rates (through the inhibition and activation of the mitoK$_{ATP}$ channel, respectively) (Fig. 4a). Accordingly, mitochondria isolated from *MITOK*-knockout cell lines swell at a constant rate, independently of either ATP or diazoxide (Fig. 4b).

MITOK-knockout cells were viable and showed a highly interconnected mitochondrial network by optical microscopy. Although the gross morphology appeared similar, ablation of *MITOK* led to the appearance of several doughnut-shaped (toroidal or ring-like) mitochondria (Extended Data Fig. 7c), a phenotype that is associated with impaired organelle K^+ homeostasis[25]. $\Delta\Psi_m$ was intact, but HeLa cells knockout for *MITOK* undergo asynchronous, rapid and transient depolarizations of single mitochondria (Extended Data Fig. 7d, e), a phenomenon known as mitochondrial 'flickering' or 'flashes'[26–29]. Importantly, this phenotype is specific, as shown by the fact that the reintroduction of human MITOSUR and mouse MITOK restored $\Delta\Psi_m$ stability (Fig. 4c). In terms of oxidative performance, the ablation of *MITOK* caused a decrease in the basal and maximal oxygen consumption rates, despite the similar levels of expression of components of the electron transport chain (Fig. 4d, Extended Data Fig. 7f). This could be partially rescued by (i) pharmacological treatment with a minimal dose of valinomycin (which has no effect in control cells) (Extended Data Fig. 8a) and (ii) the reintroduction of human MITOSUR and mouse MITOK (Extended Data Fig. 8b). To understand the causes of altered organelle function, we investigated mitochondrial ultrastructure by transmission electron microscopy. Although the gross mitochondrial morphology was preserved, *MITOK*-knockout cells show enlarged cristae (Fig. 4e), which is consistent with the effect of the inhibition of another inner mitochondrial membrane K^+ channel[30]. Normal morphology of cristae was readily restored by the re-expression of the mitoK$_{ATP}$ channel (Fig. 4e). Given that K^+ fluxes across the inner mitochondrial membrane are the main determinants of the water content of organelles[31], we speculated that cristae remodelling could be due to a dysregulation of matrix volume (as suggested by swelling experiments) (Fig. 4a, b). The inner mitochondrial membrane rapidly rearranges in

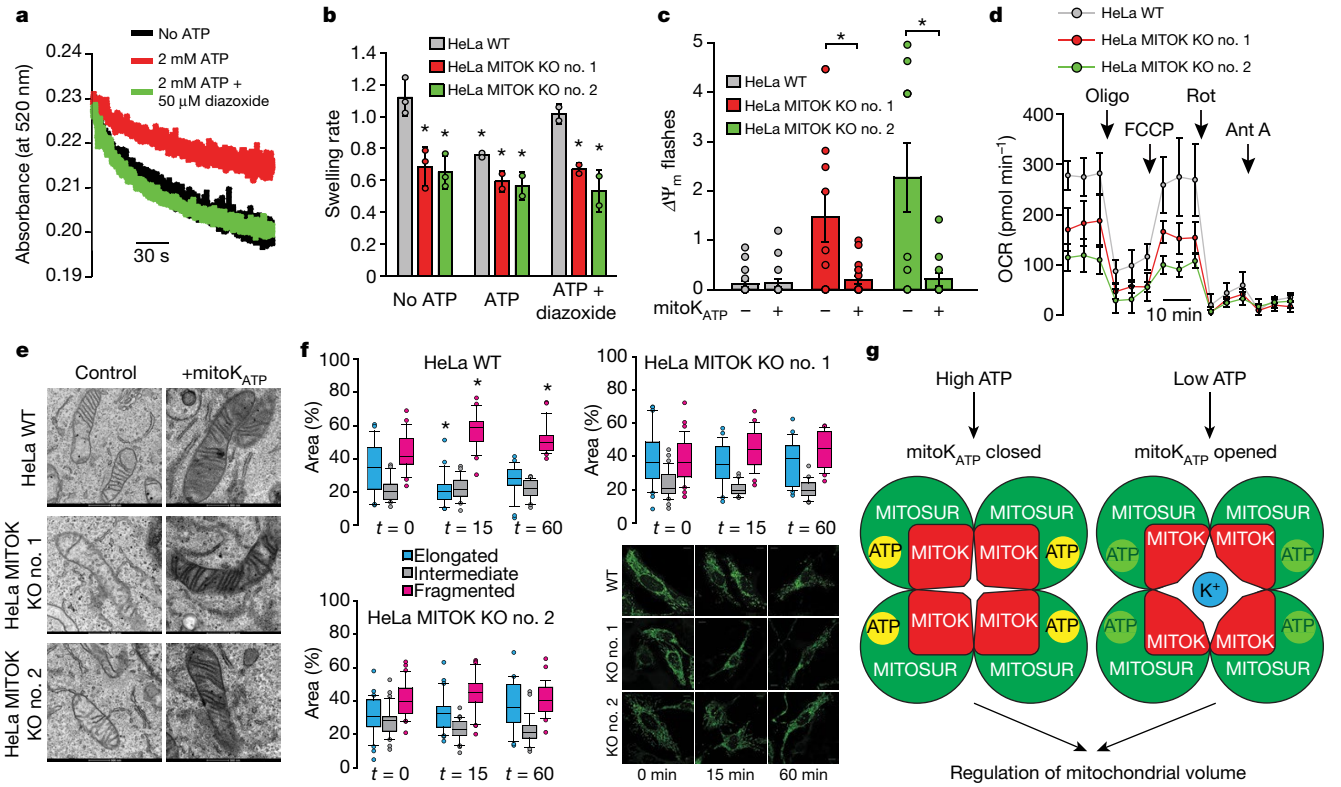

Fig. 4 | Loss of *MITOK* impairs mitochondrial structure and function. **a**, Swelling traces of wild-type mitochondria. Three independent experiments with similar results. **b**, Mitochondrial swelling rates in K^+-based medium. $n = 2$ independent experiments, $^*P \leq 0.009$ using two-way ANOVA with Holm–Sidak correction. KO, knockout; WT, wild type. **c**, Quantification of $\Delta\Psi_m$ flashes (number of depolarizations per cell per ten minutes). $n > 10$ independent experiments, $^*P \leq 0.001$ using two-way ANOVA with Holm–Sidak correction. **d**, Oxygen consumption rate (OCR) measurements. $n = 5$ biological replicates, representative of 3 independent experiments. Ant A, antimycin A; FCCP, carbonyl cyanide-4-(trifluoromethoxy)phenylhydrazone; oligo, oligomycin; rot, rotenone. **e**, Transmission electron microscopy images of mitochondrial ultrastructure, representative of two independent preparations. **f**, Analysis of mitochondrial morphology during energy stress. Box plots indicate the percentage of organelle area occupied by elongated (cyan), intermediate (grey) or fragmented (magenta) mitochondria. Scale bars, 10 µm. $n \geq 22$ individual cells from 3 independent experiments, $^*P < 0.01$ using one-way ANOVA with Holm–Sidak correction. *t*, time in minutes. **g**, Schematic of $mitoK_{ATP}$ channels.

response to osmotic changes: matrix contraction leads to expanded cristae and matrix swelling causes the collapse of the intracristae compartment. Genetic ablation of *MITOK* caused both a widening of the intracristae space (Extended Data Fig. 8c) and a lower oligomerization of OPA1 (an additional biochemical readout for cristae remodelling, for which higher multimerization correlates with tighter cristae[32]). Even in these cases, valinomycin partially recovered normal morphology of the cristae (Extended Data Fig. 8c, d).

We then considered how the $mitoK_{ATP}$ channel affects organelle adaptations to energy stress. We treated wild-type and *MITOK*-knockout cells with the glycolysis inhibitor 2-deoxyglucose, which rapidly decreases global cellular metabolism (Extended Data Fig. 8e, f). First, we tested how the mitochondrial morphology changes in response to ATP depletion. Wild-type HeLa cells rapidly underwent fragmentation of the mitochondrial network (Fig. 4f). By contrast, metabolic inhibition in *MITOK*-knockout cells caused no evident change of the overall mitochondrial morphology (Fig. 4f), which indicates that mitochondrial morphology adapts promptly to the energetic state of the cells through a $mitoK_{ATP}$-dependent mechanism. Then, we monitored the production of reactive oxygen species (ROS) during metabolic stress and/or pharmacological modulation of the $mitoK_{ATP}$ channel. Extended Data Figure 8g indicates that (i) loss of *MITOK* increases ROS production, notwithstanding the decreased oxygen consumption rate (which provides further support for the idea that this represents latent mitochondrial dysfunction); (ii) diazoxide increases ROS in wild-type but not in *MITOK*-knockout cells (which supports the idea of the $mitoK_{ATP}$ channel as a regulator of redox state); (iii) metabolic stress can increase ROS production in control cells; and (iv) ROS levels marginally increase when $mitoK_{ATP}$ is absent, thus indicating that mitochondria K^+ homeostasis impinges on the regulation of redox balance during metabolic stress. Overall, our data indicate that the $mitoK_{ATP}$ channel regulates mitochondrial adaptations to cellular stress, possibly through the regulation of matrix volume (Fig. 4g). In addition, as previously suggested[33], the loss of *MITOK* increases cell death triggered by oxidative stress (Extended Data Fig. 8h), which is consistent with cristae widening[34].

MITOK is required for pharmacological preconditioning

Finally, we generated *Mitok*-knockout mice through the specific deletion of exon 4, which contains most of the coding sequence. Overall, these mice show no overt phenotype (being born at the expected Mendelian ratio, with a similar aspect and weight gain) until at least four months of age. To demonstrate the lack of $mitoK_{ATP}$ activity, we measured organelle K^+ fluxes using $^{86}Rb^+$ as surrogate[18]. Energized mitochondria isolated from wild-type livers showed ATP- and diazoxide-sensitive K^+ uptake (Fig. 5a). By contrast, neither ATP nor diazoxide were able to alter K^+ fluxes when MITOK was absent (Fig. 5b, c). Finally, we performed ex vivo ischaemia–reperfusion experiments in wild-type and *Mitok*-knockout mice and evaluated the cardioprotective effect triggered by pharmacological preconditioning induced by diazoxide. As shown in Fig. 5d, the hearts of untreated *Mitok*-knockout mice are slightly more sensitive to the ischaemia–reperfusion protocol, which provides further confirmation of the cytoprotective role of MITOK. As previously shown[10,12,35,36], pharmacological preconditioning with diazoxide efficiently protects the heart from reperfusion damage. Most importantly, the effects of this pharmacological

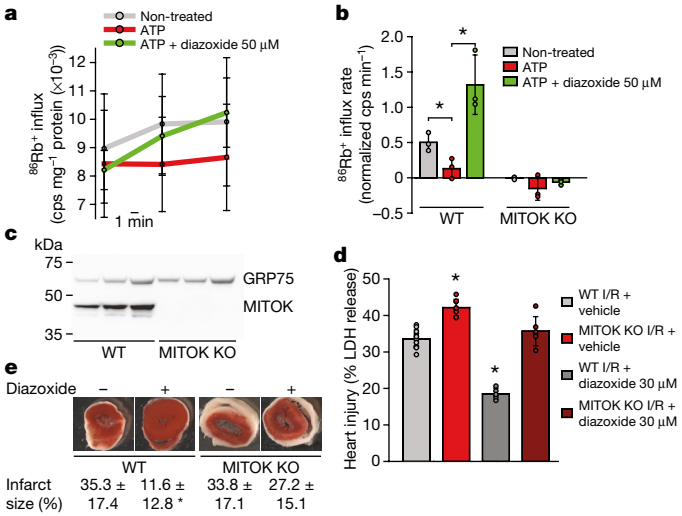

Fig. 5 | MITOK is required for diazoxide-induced cardioprotection. **a**, $^{86}Rb^+$ flux in isolated mitochondria. $n = 3$ independent experiments. **b**, $^{86}Rb^+$ uptake rate. $n = 3$ independent experiments, $^*P \leq 0.029$ using two-tailed Student's *t*-test. **c**, Western blot of wild-type and MITOK-knockout liver mitochondria. **d**, **e**, Heart injury after ischaemia–reperfusion (I/R), evaluated as percentage of lactate dehydrogenase (LDH) release (**d**, mean ± s.d., $n \geq 5$ independent mice, $^*P < 0.001$ using two-way ANOVA with Holm–Sidak correction) or percentage of infarct area after staining with 2,3,5-triphenyltetrazolium chloride (TTC) (**e**, mean ± s.d., $n \geq 7$ independent mice, $^*P = 0.008$). Single measurements are provided in Source Data.

preconditioning are nearly lost in the hearts of *Mitok*-knockout mice (as also shown by analysis of infarct size; Fig. 5e), which demonstrates that mitoK$_{ATP}$ is the molecular target of diazoxide—at least in this pathological setting.

In conclusion, we have identified a protein complex that accounts for ATP-sensitive K^+ transport across the inner mitochondrial membrane, composed of a channel-forming subunit (MITOK) and a regulatory subunit that carries the ATP-binding domain (MITOSUR). Although we do not exclude the possibility that other proteins could perform similar activities in specific tissues[37], the in vitro reconstitution of this complex is sufficient to reliably recapitulate the main electrophysiological properties and pharmacological profile of the long-sought mitoK$_{ATP}$ complex[13]. The mitoK$_{ATP}$ complex that we identify represents a potential mechanism for matching ATP availability to energy production, and thus contributing to the homeostatic control of cellular metabolism under stress conditions.

Online content

Any methods, additional references, Nature Research reporting summaries, source data, extended data, supplementary information, acknowledgements, peer review information; details of author contributions and competing interests; and statements of data and code availability are available at https://doi.org/10.1038/s41586-019-1498-3.

Received: 29 November 2017; Accepted: 25 July 2019;
Published online 21 August 2019.

1. Ashcroft, F. M., Harrison, D. E. & Ashcroft, S. J. Glucose induces closure of single potassium channels in isolated rat pancreatic β-cells. *Nature* **312**, 446–448 (1984).
2. Ashcroft, F. M. & Rorsman, P. K$_{ATP}$ channels and islet hormone secretion: new insights and controversies. *Nat. Rev. Endocrinol.* **9**, 660–669 (2013).
3. Nichols, C. G. K$_{ATP}$ channels as molecular sensors of cellular metabolism. *Nature* **440**, 470–476 (2006).
4. Inoue, I., Nagase, H., Kishi, K. & Higuti, T. ATP-sensitive K^+ channel in the mitochondrial inner membrane. *Nature* **352**, 244–247 (1991).
5. Paucek, P. et al. Reconstitution and partial purification of the glibenclamide-sensitive, ATP-dependent K^+ channel from rat liver and beef heart mitochondria. *J. Biol. Chem.* **267**, 26062–26069 (1992).
6. Garlid, K. D. & Halestrap, A. P. The mitochondrial K$_{ATP}$ channel—fact or fiction? *J. Mol. Cell. Cardiol.* **52**, 578–583 (2012).
7. Augustynek, B. B., Kunz, W. S. & Szewczyk, A. in *Pharmacology of Mitochondria (Handbook of Experimental Pharmacology vol. 240)* (eds Singh, H. & Sheu, S.S.) 103–127 (Springer, Cham, 2016).
8. Nessa, A., Rahman, S. A. & Hussain, K. Hyperinsulinemic hypoglycemia – the molecular mechanisms. *Front. Endocrinol. (Lausanne)* **7**, 29 (2016).
9. Garlid, K. D. et al. Cardioprotective effect of diazoxide and its interaction with mitochondrial ATP-sensitive K^+ channels. Possible mechanism of cardioprotection. *Circ. Res.* **81**, 1072–1082 (1997).
10. O'Rourke, B. Evidence for mitochondrial K^+ channels and their role in cardioprotection. *Circ. Res.* **94**, 420–432 (2004).
11. Sato, T., Sasaki, N., Seharaseyon, J., O'Rourke, B. & Marbán, E. Selective pharmacological agents implicate mitochondrial but not sarcolemmal K$_{ATP}$ channels in ischemic cardioprotection. *Circulation* **101**, 2418–2423 (2000).
12. Wojtovich, A. P. et al. Kir6.2 is not the mitochondrial K$_{ATP}$ channel but is required for cardioprotection by ischemic preconditioning. *Am. J. Physiol. Heart Circ. Physiol.* **304**, H1439–H1445 (2013).
13. Szabo, I. & Zoratti, M. Mitochondrial channels: ion fluxes and more. *Physiol. Rev.* **94**, 519–608 (2014).
14. Smith, C. O., Nehrke, K. & Brookes, P. S. The Slo(w) path to identifying the mitochondrial channels responsible for ischemic protection. *Biochem. J.* **474**, 2067–2094 (2017).
15. Calvo, S. E., Clauser, K. R. & Mootha, V. K. MitoCarta2.0: an updated inventory of mammalian mitochondrial proteins. *Nucleic Acids Res.* **44**, D1251–D1257 (2016).
16. The GTEx Consortium. The Genotype–Tissue Expression (GTEx) pilot analysis: Multitissue gene regulation in humans. *Science* **348**, 648–660 (2015).
17. Dahlem, Y. A. et al. The human mitochondrial K$_{ATP}$ channel is modulated by calcium and nitric oxide: a patch-clamp approach. *Biochim. Biophys. Acta* **1656**, 46–56 (2004).
18. Bednarczyk, P. et al. Quinine inhibits mitochondrial ATP-regulated potassium channel from bovine heart. *J. Membr. Biol.* **199**, 63–72 (2004).
19. Choma, K. et al. Single channel studies of the ATP-regulated potassium channel in brain mitochondria. *J. Bioenerg. Biomembr.* **41**, 323–334 (2009).
20. Cang, C., Aranda, K., Seo, Y. J., Gasnier, B. & Ren, D. TMEM175 is an organelle K^+ channel regulating lysosomal function. *Cell* **162**, 1101–1112 (2015).
21. Schaedler, T. A. et al. Structures and functions of mitochondrial ABC transporters. *Biochem. Soc. Trans.* **43**, 943–951 (2015).
22. Ardehali, H., Chen, Z., Ko, Y., Mejía-Alvarez, R. & Marbán, E. Multiprotein complex containing succinate dehydrogenase confers mitochondrial ATP-sensitive K^+ channel activity. *Proc. Natl Acad. Sci. USA* **101**, 11880–11885 (2004).
23. Lee, S.-Y. et al. Architecture mapping of the inner mitochondrial membrane proteome by chemical tools in live cells. *J. Am. Chem. Soc.* **139**, 3651–3662 (2017).
24. Bernardi, P. Mitochondrial transport of cations: channels, exchangers, and permeability transition. *Physiol. Rev.* **79**, 1127–1155 (1999).
25. Liu, X. & Hajnóczky, G. Altered fusion dynamics underlie unique morphological changes in mitochondria during hypoxia-reoxygenation stress. *Cell Death Differ.* **18**, 1561–1572 (2011).
26. Duchen, M. R., Leyssens, A. & Crompton, M. Transient mitochondrial depolarizations reflect focal sarcoplasmic reticular calcium release in single rat cardiomyocytes. *J. Cell Biol.* **142**, 975–988 (1998).
27. Schwarzländer, M. et al. Pulsing of membrane potential in individual mitochondria: a stress-induced mechanism to regulate respiratory bioenergetics in *Arabidopsis*. *Plant Cell* **24**, 1188–1201 (2012).
28. Wang, W. et al. Superoxide flashes in single mitochondria. *Cell* **134**, 279–290 (2008).
29. Rosselin, M., Santo-Domingo, J., Bermont, F., Giacomello, M. & Demaurex, N. L-OPA1 regulates mitoflash biogenesis independently from membrane fusion. *EMBO Rep.* **18**, 451–463 (2017).
30. Leanza, L. et al. Direct pharmacological targeting of a mitochondrial ion channel selectively kills tumor cells *in vivo*. *Cancer Cell* **31**, 516–531.e10 (2017).
31. Garlid, K. D. & Paucek, P. The mitochondrial potassium cycle. *IUBMB Life* **52**, 153–158 (2001).
32. Patten, D. A. et al. OPA1-dependent cristae modulation is essential for cellular adaptation to metabolic demand. *EMBO J.* **33**, 2676–2691 (2014).
33. Costa, A. D. T. & Garlid, K. D. Intramitochondrial signaling: interactions among mitoKATP, PKCε, ROS, and MPT. *Am. J. Physiol. Heart Circ. Physiol.* **295**, H874–H882 (2008).
34. Varanita, T. et al. The OPA1-dependent mitochondrial cristae remodeling pathway controls atrophic, apoptotic, and ischemic tissue damage. *Cell Metab.* **21**, 834–844 (2015).
35. Liu, Y., Sato, T., O'Rourke, B. & Marban, E. Mitochondrial ATP-dependent potassium channels: novel effectors of cardioprotection? *Circulation* **97**, 2463–2469 (1998).
36. Walters, A. M., Porter, G. A. Jr & Brookes, P. S. Mitochondria as a drug target in ischemic heart disease and cardiomyopathy. *Circ. Res.* **111**, 1222–1236 (2012).
37. Foster, D. B. et al. Mitochondrial ROMK channel is a molecular component of mitoK$_{ATP}$. *Circ. Res.* **111**, 446–454 (2012).

METHODS

No statistical methods were used to predetermine sample size. The experiments were not randomized and investigators were not blinded to allocation during experiments and outcome assessment.

Chemicals, cell culture and transfection. All chemicals were purchased from Sigma-Aldrich, unless otherwise specified. All the experiments were performed in HeLa cells (ATCC number CCL-2) cultured in Dulbecco's modified Eagle's medium (DMEM) (Gibco no. 41966052, Thermo Fisher Scientific), supplemented with 10% fetal bovine serum (FBS) (Thermo Fisher Scientific), containing penicillin (100 U/ml) and streptomycin (100 μg/ml) (Euroclone). When needed, cells were seeded onto 13- or 24-mm glass coverslips and allowed grow to 50% confluence before transfection. Transfection was performed with a standard Ca^{2+}-phosphate procedure.

Constructs. Mouse *Mitok* coding sequence (NCBI code NM_025689) was amplified from mouse skeletal-muscle cDNA library by PCR using the following primers.

For the cloning of *Mitok-gfp*: forward (fw), 5′-CTCGAGATGACAGGGTGCAGCCCCGT-3′; reverse (rv), 5′-GGATCCCGACTGGTCTTGAACAGCATGT-3′. The PCR fragment was cloned into pEGFP-N1 (Clontech) using XhoI and BamHI sites.

For the cloning of *Mitok-Flag* into pcDNA3.1: fw, 5′- AAGCTTATGACAGGGTGCAGCCCCGT-3′; rv, 5′-CTCGAGTTACTTATCGTCGTCATCCTTGTAATCACTGGTCTTGAACAGCATGT-3′. The PCR fragment was cloned into pcDNA3.1 (Thermo Fisher Scientific) using HindIII and XhoI sites.

For the cloning of *Mitok-V5* into pcDNA3.1: fw, 5′-AAGCTTATGACAGGGTGCAGCCCCGT-3′; rv, 5′-CTCGAGTTACGTAGAATCGAGGAGACCGAGAGGGTTAGGGATAGGCTTACCACTGGTCTTGAACAGCATGT-3′. The PCR fragment was cloned into pcDNA3.1 using HindIII and XhoI sites.

For the cloning of *Mitok-6×His* in pIVEX1.3WG: fw, 5′-CCATGGCAACAGGGTGCAGCCCCGTGTT-3′; rv, 5′- CTCGAGACTGGTCTTGAACAGCATGT-3′. The PCR fragment was cloned into pIVEX1.3WG (Roche) using NcoI and XhoI sites.

For the cloning of *Mitok-6×His* in pET-28A (+): fw, 5′-AAGCTTGCATGACAGGGTGCAGCCCCGT-3′; rv, 5′-CTCGAGTTAACTGGTCTTGAACAGCA-3′. The PCR fragment was cloned into pET-28A(+) (Novagen) using HindIII and XhoI sites.

Human *MITOK* coding sequences (NCBI codes NM_001256964 and NM_001256965) were amplified from human spleen cDNA library by PCR using the following primers.

For the cloning of *MITOK* isoform 1 (NM_001256964) into pcDNA3.1: fw, 5′- GGATCCATCTCAGGATGATGGGGC-3′; rv, 5′-GAATTCTTAGCTGGCTTTGAATAGCATGTAGAG-3′. The PCR fragment was cloned into pcDNA3.1 using BamHI and EcoRI sites.

For the cloning of *MITOK* isoform 1 tagged with haemagglutinin (HA) into pcDNA3.1: fw, 5′-GGATCCATCTCAGGATGATGGGGC-3′; rv, 5′-GAATTCTTAAGCGTAATCTGGAACATCGTATGGGTAGCTGGCTTTGAATAGCATGTAGAG-3′. The PCR fragment was cloned into pcDNA3.1 using BamHI and EcoRI sites.

For the cloning of *MITOK* isoform 2 (NM_001256965) into pcDNA3.1: fw, 5′-GGATCCGCCACCATGGTGGCTCGAGGGCTTG-3′; rv, 5′ GAATTCTTAGCTGGCTTTGAATAGCATGTAGAG-3′. The PCR fragment was cloned into pcDNA3.1 using BamHI and EcoRI sites.

For the cloning of *MITOK* isoform 2 tagged with HA into pcDNA3.1: fw, 5′-GGATCCGCCACCATGGTGGCTCGAGGGCTTG-3′; rv, 5′-GAATTCTTAAGCGTAATCTGGAACATCGTATGGGTAGCTGGCTTTGAATAGCATGTAGAG-3′. The PCR fragment was cloned into pcDNA3.1 using BamHI and EcoRI sites.

MITOSUR expression plasmid (pCMV6-ABCB8-myc-Flag) containing the NM_007188 reference sequence (and corresponding to ABCB8 transcript variant 2) was purchased from Origene (cat no RC224948).

For the cloning of *MITOSUR* in pIVEX1.3WG:c fw, 5′-GCGATCGCCCATATGCTGGTGCATTTA-3′; rv, 5′-CTACCGAGTACTTTAAACCTTATC-3′. The PCR fragment was cloned into pIVEX1.3WG using NdeI and ScaI sites.

The generation of the $MITOSUR^{K513A}$ mutant was performed by mutagenesis PCR using the wild-type *MITOSUR*-encoding vector as template and the mutagenesis primer: 5′- GGCCAGTCTGGCGGAGGAGCGACCACCGTGGCTTCCCTG-3′. The amino acid numbering refers to *ABCB8* isoform 1 (Uniprot code Q9NUT2).

For the generation of the construct MITOSUR-Myc-P2A-Mitok-Flag in pcDNA3.1, *MITOSUR-Myc* was amplified with following primers: fw, 5′-GGATCCATGCTGGTGCATTTATTTCG-3′; rv, 5′-GAATTCCGGTCCAGGATTCTCTTCGACATCTCCGGCTTGTTTCAGCAGAGAGAAGTTTGTTGCCAGATCCTCTTCTGAGATGAGTTTCTGCTCGGACTTGTGCTGGTGGCTCC-3′. The PCR fragment was cloned into pcDNA3.1 using BamHI and EcoRI sites.

Mitok-Flag was amplified with the following primers: fw, 5′-GAATTCATGACAGGGTGCAGCCCCGT-3′; rv, 5′-GCGGCCGCTTACTTATCGTCGTCATCCTTGTAATCACTGGTCTTGAACAGCATGT-3′. The PCR fragment was cloned into the above-mentioned plasmid using EcoRI and NotI sites.

For the generation of mitochondrial-targeted mEmerald, mEmerald was amplified from the mEmerald-Mito-7 plasmid (Addgene plasmid no. 54160), a kind gift of M. Davidson, with the following primers: fw, 5′-AAGCTTGTGAGCAAGGGCGAGG-3′; rv, 5′-GAATTCTTACTTGTACAGCTCGTCCATG-3′. The PCR fragment was cloned in a custom pcDNA3.1 plasmid containing four repeated mitochondrial targeting signals from human COX8A (pcDNA3.1-4mt) using HindIII and EcoRI sites.

All constructs were verified by Sanger sequencing.

RNA extraction, reverse transcription and quantitative real-time PCR. For quantitative (q)PCR analyses, HeLa cells were lysed in an appropriate volume of Trizol reagent (Thermo Fisher Scientific). For human tissues, a commercial mRNA library was used (Clontech Human Total RNA Master Panel II, cat no. 636643). The RNA was quantified with a NanoDrop (Thermo Fisher Scientific). Complementary DNA was generated with a cDNA synthesis kit (SuperScript II, Thermo Fisher Scientific) using the oligo(dT)12-18 primer (Thermo Fisher Scientific) and analysed by real-time PCR using the SYBR green chemistry (Thermo Fisher Scientific). Primers were designed using Primer-BLAST[38]. Real-time PCR standard curves were constructed by using serial dilutions of cDNA of the analysed samples, using at least 4 dilution points and the efficiency of all primer sets was between 80 and 120%. The housekeeping gene *ACTIN* was used as an internal control for cDNA quantification and normalization of the amplified products. All data are reported as mean ± s.d., from $n = 3$ experiments. In the case of HeLa cells, three independent RNA extractions and reverse transcription reactions were used. In the case of human tissues, three technical replicates were used. qPCR primer sequences were as follows. For *MITOK* both isoforms, fw GGATGCTGCAGGAGGAGAAG, and rv CTTGGTCCTCTCAGCCCTTG; for *MITOK* isoform 1, fw CGGAACCGTAGGAGGGGTACT, and rv CTCCGAACCAGTACGTGGGG; for *MITOK* isoform 2, fw CGGTTTTCTCTTTGCAGGCT, and rv TCTTGGTCCTCTCAGCCCTT; and for *ACTB*, fw CCTTTTATGGCTCGAGCGGC, and rv CATCATCCATGGTGAGCTGGC

The isoform-specific primers are not very efficient, as compared to non-specific ones (Extended Data Fig. 1d)—this is most probably due the fact that 5′ untranslated region region is under-represented when using oligo-dT for reverse transcription (all primers are, however, specific, as they do not detect substantial levels of transcript in HeLa cells that are knockout for *MITOK*).

Expression and purification of MITOK and of MITOSUR. C41(DE3) *E. coli* cells were transformed with the plasmid expressing mouse MITOK. Expression was achieved as previously described[39]. Five hours after induction with IPTG, cells were collected and sonicated in 250 mM NaCl and 25 mM TRIS, pH 8.0, with 1 μg/ml leupeptine and pepstatine. The samples were subsequently centrifuged 15000*g* for 30 min at 4 °C to separate the membrane fraction (pellet) from the soluble fraction (supernatant). Then, the pellet was solubilized in 2.5% decyl-β-D-maltopyranoside (Sigma-Aldrich) in the sonication buffer for 3 h, and the resulting soluble material was loaded onto Ni resin (HIS-Select Nickel Affinity Gel, Sigma-Aldrich). After 3 washes in equilibration buffer (50 mM sodium phosphate, pH 8.0, 300 mM sodium chloride), MITOK was eluted with a 250 mM imidazole solution in equilibration buffer. All fractions were collected and tested using standard SDS–PAGE and western blot analyses. Immuno-detection of the expressed channel was performed using anti-6×His tag antibody (Sigma-Aldrich) and anti-MITOK antibody. For in vitro expression and electrophysiology, a previously described protocol[40] was used. In brief, human MITOSUR and mouse MITOK proteins were expressed either separately or together in an in vitro wheat (*Triticum aestivum*) germ lysate system based on the continuous exchange cell-free technique, using the Wheat Germ CECF Kit (Biotechrabbit). Synthesis was achieved for 24 h at 24 °C under continuous mixing on a Thermomixer comfort unit (Eppendorf). After expression, the reaction mixture was either loaded on a Ni-chromatography column or directly solubilized for 30 min with either Triton X-100 or digitonin (1% w/v). No differences were observed in channel activity depending on the detergent used. Following centrifugation, the supernatant containing the solubilized proteins was diluted 1:10 in 10 mM HEPES, pH 7.4. For co-expression experiments, 1:1 ratio of DNA was used. After expression, MITOK alone or the MITOK and MITOSUR reaction mix were solubilized with 1% Triton X-100 or digitonin, and incorporated into liposomes. Purified soybean asolectin was used to produce liposomes at 2 mg/ml in 10 mM HEPES, 10 mM $CaCl_2$, pH 7.3. After solubilization, the reaction mix was incubated with liposomes for 15 minutes at room temperature. Liposomes were pelleted and suspended in the same volume and subjected to alkaline extraction by adding 1/10 volume of 2 M Na_2CO_3 to check for insertion of the proteins into the liposomes (data not shown). Liposomes containing the proteins were frozen in small aliquots and used up to 24 hours after thawing.

Electrophysiological recording of MITOK or MITOK and MITOSUR activities in planar lipid bilayer and data analysis. A Warner Instruments (Hamden) BC-525C electrophysiological planar bilayer apparatus was used. Bilayers with a

capacity of approximately 150 to 200 pF were prepared using partially purified (by precipitation with cold acetone from a chloroform solution) asolectin solution in decane:chloroform with a 100:1 ratio per mg of lipids (Sigma) across a 250-μm hole in a polystyrene cuvette. The contents of both chambers were stirred by magnetic bars when necessary. Voltages reported are those of the *cis* chamber, and current is considered positive when carried by cations flowing from the *cis* compartment to the *trans* compartment. Three ml of recording solution were added to both compartments. 100 mM K-gluconate, 10 mM HEPES/KOH, pH 7.4 or 100 mM KCl, 10 mM HEPES/KOH pH 7.4 medium ($[K^+]$ 117 mM) were used unless otherwise specified. Lack of activity in the membrane before addition of the protein was monitored for at least 5 min in each experiment and long-lasting (≥30 min) control experiments showed no activity without addition of the protein ($n = 50$) or following addition of the detergent only (at the same concentration that is added with the proteins, $n = 15$). Ten microlitres of the solubilized and diluted (1:10, see 'Expression and purification of MITOK and of MITOSUR') MITOK or MITOK and MITOSUR mixture incorporated into liposomes were added to the *cis* side. The final detergent concentration was between 0.0003% and 0.0006%. Channel modulators were added to both compartments to the required concentration for inhibition or activation. Electrical connections were made using Ag and AgCl electrodes and agar salt bridges to minimize liquid junction potentials. The current was digitized at a sampling rate of 10 kHz, the signals were filtered at 500 Hz and the data were analysed offline using pCLAMP8.0 (Molecular Devices). The channel recordings illustrated are representative of the most-frequently observed amplitudes of the opening channels under a given condition. The conductance values were calculated from the current–voltage relationship, averaged from at least three independent experiments. *P*(open) was calculated from segments of continuous recordings lasting 60 s. Amplitude histograms were obtained from ≥30-s gap-free current traces. The number of events in the amplitude histograms refers to the number of binned points at a given amplitude in the recordings. P_K:P_{Cl} ratios were calculated from the measured reversal potentials using the Goldman–Hodgkin–Katz equation taking into account the effective $[K^+]$ (117 mM *trans* versus 287 mM *cis*). All analysis was performed without leak subtraction and current trace idealization. Analysis and fitting of data was performed using Origin 6.1 programs (for Gaussian and linear fitting).

Thermal aggregation assay. The thermal aggregation profile of human MITOSUR and mouse MITOK proteins was been obtained by an adaptation of the cellular thermal shift assay to in vitro protein expression mixtures[41]. In brief, WGL lysate was solubilized in 0.8% digitonin then treated for 30 min at room temperature under shaking with 1 mM ATP and 2 mM $MgCl_2$ to avoid the interference of any chaperone or folding helper components in the wheat-germ extract used for protein expression. WGL lysate was aliquoted into PCR tubes in equal volumes (40 μl) and each sample was incubated at a different temperature, between 37 °C and 95 °C. A reference sample treated analogously was stored at 4 °C and was used for densitometry-value normalization. Each sample was exposed to the designed temperature for 10 min through an Eppendorf 96-well thermal cycler, vortexed and centrifuged 30,000*g* for 25 min at 4 °C to pellet aggregated and denatured proteins. Each supernatant containing the soluble proteins fraction was carefully removed and transferred into a new tube. The soluble fraction was analysed and quantified for each temperature using western blotting technique, loading an equivalent volume of each sample into the wells of the gel, and blotted using the indicated antibodies. The samples for each thermal shift assay were run on the same gel. All experiments were performed on four independent occasions, and data are given as the average from these experiments. The solid lines represent the best fits of the data using a Boltzmann sigmoidal fitting within the GraphPad Prism software.

Generation of MITOK-knockout cells. For the generation of MITOK-knockout cell lines, two Cas9 guides targeting different regions of the human *MITOK* gene were designed (GCCCCTCCGAACCAGTACGT and TCATGAGAAGGAGCGCACAA) using the MIT CRISPR design tool[42], and cloned into the BsmBI site of the pLentiCrisprV2 plasmid, a kind gift of F. Zhang (Addgene plasmid no. 52961)[43]. Lentiviral particles were produced by transfecting 293T cells with the transfer plasmids together with pRSV-Rev (Addgene plasmid no. 12253), pMDLg/pRRE (Addgene plasmid no. 12251) and pMD2.G (Addgene plasmid no. 12259) plasmids, kindly provided by D. Trono. Three days after transfection, the supernatants were collected, centrifuged and cleared through 0.45-μm cellulose acetate filters. Target cells were infected with viral particles and selected with one microgram per millilitre puromycin for one week. Dilution cloning was performed to obtain different monoclonal cell populations that were screened and validated for *MITOK* gene ablation through western blot.

Antibodies, SDS–PAGE and western blot. Cells were lysed in RIPA buffer (150 mM NaCl, 25 mM Tris-Cl pH 8, 1 mM EGTA-Tris, 1% Triton X-100, 0.5% sodium deoxycholate and 0.1% SDS) supplemented with complete EDTA-free protease inhibitor mixture (Roche Applied Science) and PhosStop (Roche Applied Science) for 30 min on ice. Crude extracts were centrifuged 15000*g* for 10 min to remove debris, and proteins in the supernatant were quantified using the BCA Protein Assay Kit (Pierce). Thirty micrograms of proteins were dissolved in LDS sample buffer (Life Technologies) supplemented with 100 mM dithiothreitol, heated for 5 min at 90 °C and loaded on 4–12% Bis-Tris NuPage gels (Thermo Fisher Scientific). After electrophoretic separation, proteins were transferred onto nitrocellulose membranes by wet (Thermo Fisher Scientific) or semidry (BioRad) transfer. Membranes were blocked for 1 h at room temperature with 5% non-fat dry milk (BioRad) in TBS-T (50 mM Trizma, 150 mM NaCl and 0.1% Tween) and probed with the indicated primary antibodies over night at 4 °C. Isotype-matched, horseradish-peroxidase-conjugated secondary antibodies (BioRad) were used, followed by detection by chemiluminescence (SuperSignal Pico, Pierce). The following primary antibodies were used: anti-$MITOK_{C\text{-}term}$ (1:1,000, Sigma HPA011408), anti-$MITOK_{N\text{-}term}$ (1:10,000, Sigma HPA010980), anti-MCU (1:1,000, Sigma HPA016480), anti-MICU1 (1:1,000, Sigma HPA037480), anti-HSP60 (1:5,000, Santa Cruz sc-1052), anti-OPA1 (1:1,000, BD biosciences 612606), anti-MITOSUR (1:1,000, Abcam ab182662), anti-OXPHOS (1:1,000, Abcam ab110413), anti-TOM20 (1:10,000, Santa Cruz sc-11415) and anti-Flag (1:1,000, Cell Signaling no. 2368). Western blots are representative of at least three independent preparations. Uncropped images of western blots used for the assembly of final figures are provided in Supplementary Fig. 1.

Blue Native PAGE. Mitochondrial fractions were lysed in the appropriate volume of NativePAGE Sample Buffer (Thermo Fisher Scientific) supplemented with 3% (w/w) digitonin. Crude extracts were centrifuged at 15000*g* for 10 minutes to remove debris, and proteins in the supernatant were quantified using the BCA Protein Assay Kit (Pierce). One hundred micrograms of proteins were dissolved in NativePAGE sample buffer supplemented with Coomassie G-250 (Thermo Fisher Scientific) and loaded on a 4–16% Novex NativePAGE Bis-Tris Gel System (Thermo Fisher Scientific). After electrophoretic separation, proteins were transferred onto PVDF membranes and probed with the indicated antibodies. As molecular mass marker, NativeMark Unstained Protein Standard (Thermo Fisher Scientific) was used and stained with Colloidal Blue Staining Kit (Thermo Fisher Scientific). Isotype-matched, horseradish-peroxidase-conjugated secondary antibodies (BioRad) were used, followed by detection by chemiluminescence (SuperSignal Pico, Pierce).

Mitochondrial isolation, proteinase K protection and swelling assays. Mitochondria were isolated from HeLa cells or mouse liver through differential centrifugation as previously described[44]. Mitoplasts were obtained through osmotic swelling by incubating mitochondrial fraction in 20 mM Tris-Cl pH 7.4 for 20 min on ice. The same amount of mitoplasts was treated with proteinase K (100 μg/ml) at 4 °C for the indicated time, and the proteolytic reaction was quenched by addition of PMSF. Samples were then loaded on SDS–PAGE and processed for western blot, as described in 'Antibodies, SDS–PAGE and western blot'. Results are representative of at least two different proteolytic reactions.

For the swelling assay, mitochondria were isolated using a slightly modified protocol to accelerate the procedure (as previously reported[6], $mitoK_{ATP}$ activity degrades quickly after organelle isolation). HeLa cells were initially disrupted through a brief (4-s) sonication (using a Braun Labsonic P at full cycle and 30% amplitude). After differential centrifugation, 0.25 mg of mitochondria was suspended in a cuvette containing 2 ml of swelling assay buffer (100mM KCl, 20 mM HEPES, 1 mM $MgCl_2$, 2 mM Pi, 1 mM EGTA, 0.1% BSA, 5mM succinate, 2.5mM glutamate, 2.5mM malate, 1μM oligomycin, pH 7.2). After 1 min of incubation, absorbance at 520 nm was recorded using an Agilent Cary 100 UV-Vis spectrophotometer. Swelling rate was calculated as the decrease in absorbance over 1 min of recording (using the SLOPE function of MS Excel). Two mitochondrial preparations were used.

Co-immunoprecipitation. For the interaction between human MITOSUR–Flag or MITOSUR(K513A)–Flag and mouse MITOK–V5, HeLa cells were transfected with the indicated plasmids. After 48 h, cells were lysed in co-immunoprecipitation buffer (150mM NaCl, 1% digitonin, 50mM Tris-Cl pH7.4, 1mM EGTA-Tris pH 7.4 and complete EDTA-free protease inhibitor mixture). Lysates were centrifuged at 15,000*g* for 10 min, and supernatant was transferred into new tubes. One milligram of proteins was precleared using a control agarose resin (Thermo Fisher Scientific) for 30 min at 4 °C. Precleared proteins were incubated with monoclonal anti-Flag-agarose-conjugated antibody (Sigma) for 3 h at 4 °C. After 3 washes (of 10 minutes each) in co-immunoprecipitation buffer, 50 μl of Laemmli buffer 2× was added to the resin and heated for 5 min at 95 °C. The precleared lysate (input) and the immunoprecipitated (co-immunoprecipitation) fractions were separated and blotted as described in 'Antibodies, SDS–PAGE and western blot'.

For the interaction between endogenous MITOK and MITOSUR, isolated mitochondria from mouse liver or HeLa cells were lysed in co-immunoprecipitation buffer and processed as indicated in 'Antibodies, SDS–PAGE and western blot'. One milligram of precleared proteins were incubated with 5 μg of anti-$MITOK_{N\text{-}term}$ (Sigma HPA010980) antibody for 3 h. Protein A-sepharose beads (GE Healthcare) were added for 1 h and washed 3 times with co-immunoprecipitation buffer. Fifty

microlitres of Laemmli buffer 2× was added to the resin and heated for 5 min at 95 °C. Results are representative of at least three independent transfections.

Analysis of OPA1 oligomers. HeLa cells were treated with 1 mM BMH (Thermo Fisher Scientific) for 30 min at 37 °C. After crosslinking reaction, cells were quenched and washed in PBS with 0.1% β-mercaptoethanol (BME) twice. Cells were then lysed in RIPA buffer supplemented with BME and subjected to western blot on NUPAGE Novex 3–8% Tris-acetate gradient gels (Thermo Fisher Scientific). The western blot provided in the figures is representative of three different crosslinking reactions.

Immunofluorescence and confocal imaging. HeLa cells were grown on 24-mm coverslips until 50% confluence. Cells were then washed with PBS, fixed in 4% formaldehyde for 10 min and quenched with 50 mM NH_4Cl in PBS. Cells were permeabilized for 10 min with 0.1% Triton X-100 in PBS and blocked in PBS containing 2% BSA for 1 h. Cells were then incubated with primary antibodies (anti-MITOK, anti-HSP60) for 3 h at room temperature and washed 3 times with 0.1% Triton X-100 in PBS. The appropriate isotype-matched Alexa-Fluor-conjugated secondary antibodies (Thermo Fisher Scientific) were incubated for 1 h at room temperature and coverslips were mounted with ProLong Gold Antifade reagent (Thermo Fisher Scientific). Alternatively, cells were transfected with mitochondrial-targeted DsRed or mEmerald. One day later, cells were fixed and mounted as described. Images were acquired on a Leica TCS-SP5-II-RS-WLL equipped with a 100×, 1.4 N.A. Plan-apochromat objective. Alexa Fluor 488 (or mEmerald) was excited by the 488-nm laser line and images were collected in the 495–535-nm range. Alexa Fluor 555 (or DsRed) was sequentially excited with the 543-nm laser line and signal was collected in the 555–600-nm range. Pixel size was set below 100 nm to meet the Nyquist criterion. For each image, a *z*-stack of the whole cell was acquired, with a step size of 130 nm. Images are presented as maximum projections of the whole stack using the Fiji image processing package based on ImageJ[45]. Images are representative of at least three independent transfections.

Analysis of mitochondrial morphology. HeLa cells were grown on 13-mm coverslips until 50% confluence and transfected with a plasmid encoding for a mitochondrially targeted mEmerald protein. After 36 h, cells were washed 3 times with PBS and treated with and incubated in a buffer based on Krebs–Ringer modified buffer (KRB) that contained 5.5 mM 2-deoxyglucose. After 0, 15 or 60 min, cells were fixed and processed for confocal imaging as described in 'Immunofluorescence and confocal imaging'. Images (single planes) were then analysed using a custom ImageJ script. In brief, background- and noise-corrected images were thresholded, and objects were counted with the 'Analyze particles' function (using 0.2 μm^2 as a lower cutoff). Objects were then classified as fragmented (circularity >0.8 or length <3 μm), elongated (circularity <0.2 or length >6 μm) or intermediate (all other cases). Finally, for each cell, the area occupied by elongated, intermediate and fragmented mitochondria was normalized on the global mitochondrial area and expressed as percentage. At least 20 cells were analysed per condition (more than 50 objects were counted in each cell) from 3 independent transfections.

Analysis of ROS production. HeLa cells were plated on 96-well black plates and grown until full confluency. Cells were then incubated for 45 min in a KRB-based buffer containing 5.5 mM glucose supplemented with 0.02% Pluronic F127 and 5 μM CM-H2DCFDA. Cells were washed twice with PBS and incubated in KRB-based buffer supplemented as indicated in 'Analysis of mitochondrial morphology'. Fluorescence (excitation 485/10 nm, emission 530/30 nm, recorded from the bottom of the plate) was monitored on a Perkin Elmer Envision multi-mode plate reader operating at 37 °C in well-scan mode. Blank was subtracted using two wells containing unstained cells. Fluorescence was recorded every 60 min over 16 h. Total fluorescence was calculated for each well at each time point and the rate of fluorescence increase was calculated using the SLOPE function in MS Excel. At least ten wells were analysed from three independent experiments.

$[Ca^{2+}]_{mt}$ measurements. HeLa cells were grown on 13-mm round glass coverslips at 50% confluence and cotransfected with a low-affinity mitochondrially targeted aequorin-based probe (mtAeqMut)[46] together with the indicated plasmid (the mock vector pcDNA3.1 was used as a control). Twenty-four or thirty-six hours after transfection, cells were incubated with 5 μM coelenterazine for 1–2 h in KRB (125 mM NaCl, 5 mM KCl, 1 mM Na_3PO_4, 1 mM $MgSO_4$, 5.5 mM glucose, 20 mM HEPES, pH 7.4) at 37 °C supplemented with 1 mM $CaCl_2$, and then transferred to the perfusion chamber. All aequorin measurements were carried out in KRB. Agonists and other drugs were added to the same medium as specified in text and figures. The experiments were terminated by lysing cells with 100 μM digitonin in a hypotonic Ca^{2+}-rich solution (10 mM $CaCl_2$ in H_2O), thus discharging the remaining aequorin pool. The light signal was collected and calibrated into $[Ca^{2+}]$ values by an algorithm based on the Ca^{2+} response curve of aequorin at physiological conditions of pH, $[Mg^{2+}]$ and ionic strength, as previously described[46]. Alternatively, $[Ca^{2+}]$ measurements were carried out on a Perkin Elmer Envision plate reader equipped with a two-injector unit. Cells were transfected as described in 'Chemicals, cell culture and transfection' in 24-well plates, and then replated into 96-well plates (1:5 dilution) the day before the experiment. After reconstitution with 5 μM coelenterazine, cells were placed in 70 μl of KRB and luminescence from each well was measured for 1 min. During the experiment, histamine was first injected at the desired concentration to activate calcium transients, and then a hypotonic, Ca^{2+}-rich digitonin-containing solution was added to discharge the remaining aequorin pool. Output data were analysed and calibrated with a custom-made macro-enabled Excel workbook. All the results are expressed as mean ± s.d. and are representative of at least three independent transfections.

$\Delta\Psi_m$ measurements. The measurement of $\Delta\Psi_m$ is based on the distribution of the mitochondrion-selective lipofilic cation dye TMRM (Thermo Fisher Scientific). Cells were loaded with 2 0 nM TMRM for 30 min at 37 °C and then transferred to the imaging system. Images were acquired on a Zeiss Axiovert 200 microscope equipped with a 40×, 1.3 N.A. PlanFluor objective. Excitation was performed with a Deltaram V high speed monochromator (Photon Technology International) equipped with a 75 W Xenon Arc lamp. Images were captured with a high-sensitivity Evolve 512 Delta EMCCD (Photometrics). The system is controlled by Metamorph 7.5 and was assembled by Crisel Instruments. TMRM excitation was performed at 560 nm and emission was collected through a 590–650-nm bandpass filter. Images were acquired every 5 s with a fixed 200-ms exposure time. At the end of each experiment, 10 μM CCCP was added to collapse $\Delta\Psi_m$. After background correction, the fluorescence value after addition of CCCP was subtracted for each cell. For the analysis of basal $\Delta\Psi_m$, data are presented as raw fluorescence values in resting conditions. For the analysis of $\Delta\Psi_m$ flashes, data are presented as time lapse of normalized fluorescence (F/F_0). Data were obtained from at least three independent preparations. All analyses were performed with the Fiji distribution of ImageJ.

Transmission electron microscopy. HeLa cells were grown in 24-well plates and fixed with 2.5% glutaraldehyde in 0.1 M sodium cacodylate buffer pH 7.4 for 1 h at 4 °C, post-fixed with a mixture of 1% osmium tetroxide and 1% potassium ferrocyanide in 0.1 M sodium cacodylate buffer for 1 h at 4 °C and incubated overnight in 0.25% uranyl acetate at 4 °C. After three water washes, samples were dehydrated in a graded ethanol series and embedded in an epoxy resin (Sigma). Ultrathin sections (60–70 nm) were obtained with an Ultrotome V (LKB) ultramicrotome, counterstained with uranyl acetate and lead citrate, and viewed with a Tecnai G2 (FEI) transmission electron microscope operating at 100 kV. Images were captured with a Veleta (Olympus Soft Imaging System) digital camera. For structural quantification, the cristae width was measured from all mitochondria from 15 cells for each condition.

OCR measurements. OCR measurements were performed in intact HeLa cells using the XF24 Extracellular Flux Analyzer platform (Agilent) according to manufacturer's instructions. Cells were counted and plated on XF24 cell-culture plates. The following day, growth medium was replaced with pre-warmed unbuffered DMEM (Sigma) and equilibrated for 1 h at 37 °C. Oligomycin (2 μM), FCCP (0.4 μM), rotenone (0.5 μM) and antimycin A (0.5 μM) were dissolved in assay medium and loaded on sensor cartridge ports. OC) was detected under basal conditions followed by the sequential addition of the indicated drugs[47].

Cell viability. HeLa cells of the indicated genotype were counted and plated in a 96-well plate. After 36 h, growth medium was replaced with KRB containing the indicated H_2O_2 concentration. After 2 h, PrestoBlue assay (Thermo Fisher Scientific) was performed according to manufacturer's instructions. Data are presented as percentage absorbance at 570 nm (600 nm was used as a reference wavelength) relative to untreated cells. Three independent experiments with 16 replicates each were performed.

Generation of MITOK-knockout mice. *Mitok*-knockout mice were generated by genOway on a C57BL/6N background. Two LoxP sites flanking exon 4 of the mouse *Mitok* gene were introduced by homologous recombination. The genotype was verified by PCR with the following primer: *Mitok* knockout, fw 1 GCACCTTGTCAGCACCATGACAACTC; *Mitok* knockout, fw 2 GAGGGA TCGCTGTGGAAGGCTGTAT; and *Mitok* knockout, rv GCGGACAAAGATTGT GTCACTGTTTGC.

The knockout allele yields an amplification product of 769 bp, whereas the wild-type allele generates a 278-bp fragment. All mouse experiments were performed in accordance with the Italian law D.L.vo n_26/2014 and approved by local (Organismo preposto al benessere degli animali, O.P.B.A.) and national (Ministry of Health) committees (376-2015PR).

$^{86}Rb^+$ uptake measurements. After isolation, 200 mg of mitochondria from wild-type and *Mitok*-knockout mouse liver were resuspended in swelling buffer (100 mM KCl, 20 mM HEPES, 1 mM $MgCl_2$, 2 mM Pi, 1 mM EGTA, 0.1% BSA, 5 mM succinate, 2.5 mM glutamate, 2.5 mM malate, 1 μM oligomycin, pH 7.2) containing trace amount (1–2 μCi) of $^{86}RbCl$. Where indicated, the buffer was supplemented with ATP (2 mM) and diazoxide (50 μM). After 1, 10, 20 and 30 min, mitochondria were rapidly centrifuged and washed. The amount of $^{86}Rb^+$ trapped within the organelle was estimated by scintillation counting and normalized on protein content. Rb^+

influx rate was calculated as the relative increase in isotope content over time (using the SLOPE function of MS Excel). Results are expressed as mean ± s.d. of three independent experiments.

Ischaemia–reperfusion experiments. Adult (4-month-old) wild-type and MITOK-knockout male mice were anaesthetized by intraperitoneal injection of Zoletil 100 (30 mg/kg). Hearts were perfused with bicarbonate buffer gassed with 95% O_2–5% CO2 at 37 °C (pH 7.4) at a constant flux of 5 ml/min. Perfusion was performed in the nonrecirculating Langendorff mode, as previously described[48]. The perfusion buffer contained (in mM) 118.5 NaCl, 3.1 KCl, 1.18 KH_2PO_4, 25.0 $NaHCO_3$, 1.2 $MgCl_2$, 1.4 $CaCl_2$ and 5.6 glucose. Hearts were treated as follows ($n \geq 5$ heart per group): after 10 min of normoxic stabilization, hearts were subjected to 40 min of global no-flow ischaemia followed by 15 min of reperfusion. Pharmacological preconditioning was carried out by perfusion in the presence of diazoxide (30 μM) for 10 min, followed by the ischaemia–reperfusion protocol in the absence of diazoxide. After reperfusion, hearts were quickly immersed into PBS containing 0.5% Triton X100 and homogenized for measurement of LDH. For TTC staining, hearts were subjected to the ischaemia–reperfusion protocol and frozen at −20 °C until used for quantification of myocardial infarct size. The hearts were cut into 5 transverse slices, incubated with TTC (1% w/v, pH 7.4) for 20 min at 37 °C and fixed overnight in 4% formaldehyde at 4 °C. The slices were digitally photographed. The infarcted tissue stains a characteristic white colour, whereas the viable tissue stains red. The infarct area was expressed as percentage of total area minus cavities, and was calculated using ImageJ. The whole heart is exposed to ischaemia in Langendorff mode, and thus there is no need to normalize on area-at-risk.

Measurement of LDH activity. To determine the amount of LDH released from the hearts exposed to ischaemia–reperfusion, coronary effluent was collected at 1-min intervals during the 15 min of reperfusion, as previously described[49]. At the end of reperfusion, hearts were homogenized for assessing the residual activity of LDH in the whole tissue. LDH activity was determined by means of a classic procedure. Because all values were normalized to heart weight, the amount of LDH released was expressed as the percentage of total (that is, effluent and homogenate) to rule out possible changes owing to variations in heart size[50].

Statistical analysis of data. In bar graphs, data are presented as mean ± s.d. unless specified. For box plots, the boundary of the box closest to zero indicates the 25th percentile, the line within the box marks the median, and the boundary of the box farthest from zero indicates the 75th percentile. Whiskers (error bars) above and below the box indicate the 90th and 10th percentiles, respectively. Dots represent outlying points. Variance was calculated by one-way, two-way or three-way ANOVA as indicated in the legends, and multiple comparisons were assessed using the Holm–Sidak post hoc test. Where applicable, data points and exact *P* values are indicated in Source Data. All analyses were performed with the SigmaPlot 12.0 (Systat Software) or Excel (Microsoft).

Reporting summary. Further information on research design is available in the Nature Research Reporting Summary linked to this paper.

Data availability

Source Data tables are provided for Fig. 3d, e, 4a–d, f, 5a, b, d and Extended Data Figs. 1d–f, 2b, g3, 5a, b, i, 7d, 8a–c, f–h. All other data supporting the findings of this study are available from the corresponding authors on request.

38. Ye, J. et al. Primer-BLAST: a tool to design target-specific primers for polymerase chain reaction. *BMC Bioinformatics* **13**, 134 (2012).
39. Carraretto, L. et al. A thylakoid-located two-pore K^+ channel controls photosynthetic light utilization in plants. *Science* **342**, 114–118 (2013).
40. Teardo, E. et al. Physiological characterization of a plant mitochondrial calcium uniporter in vitro and in vivo. *Plant Physiol.* **173**, 1355–1370 (2017).
41. Ashok, Y., Nanekar, R. & Jaakola, V.-P. Defining thermostability of membrane proteins by western blotting. *Protein Eng. Des. Sel.* **28**, 539–542 (2015).
42. Hsu, P. D. et al. DNA targeting specificity of RNA-guided Cas9 nucleases. *Nat. Biotechnol.* **31**, 827–832 (2013).
43. Sanjana, N. E., Shalem, O. & Zhang, F. Improved vectors and genome-wide libraries for CRISPR screening. *Nat. Methods* **11**, 783–784 (2014).
44. Frezza, C., Cipolat, S. & Scorrano, L. Organelle isolation: functional mitochondria from mouse liver, muscle and cultured fibroblasts. *Nat. Protocols* **2**, 287–295 (2007).
45. Schindelin, J. et al. Fiji: an open-source platform for biological-image analysis. *Nat. Methods* **9**, 676–682 (2012).
46. Granatiero, V., Patron, M., Tosatto, A., Merli, G. & Rizzuto, R. Using targeted variants of aequorin to measure Ca^{2+} levels in intracellular organelles. *Cold Spring Harb. Protoc.* **2014**, 86–93 (2014).
47. Nicholls, D. G. et al. Bioenergetic profile experiment using C2C12 myoblast cells. *J. Vis. Exp.* **3–7**, 2511 (2010).
48. Carpi, A. et al. The cardioprotective effects elicited by p66Shc ablation demonstrate the crucial role of mitochondrial ROS formation in ischemia/reperfusion injury. *Biochim. Biophys. Acta* **1787**, 774–780 (2009).
49. Di Lisa, F., Menabò, R., Canton, M., Barile, M. & Bernardi, P. Opening of the mitochondrial permeability transition pore causes depletion of mitochondrial and cytosolic NAD+ and is a causative event in the death of myocytes in postischemic reperfusion of the heart. *J. Biol. Chem.* **276**, 2571–2575 (2001).
50. Schlüter, K. D., Schwartz, P., Siegmund, B. & Piper, H. M. Prevention of the oxygen paradox in hypoxic-reoxygenated hearts. *Am. J. Physiol.* **261**, H416–H423 (1991).

Acknowledgements The authors are grateful to P. Bernardi, V. Petronilli, T. Pozzan, L. Scorrano and M. Zoratti for helpful discussion, to F. Caicci and F. Boldrin for electron microscopy, to A. Montagna for immunofluorescence, to L. Carraretto for help with expression of MITOK in *E. coli*, to L. Cendron for the help with thermal shift assay, and to M. Ruzzene and L. Cesaro for the help with the radioactive assay. This work was supported by grants from the University of Padova (Assegno junior 2015 and SID 2016 to D.D.S., STARS@UNIPD WiC grant 2017 to R.R. and UNIPD funds for research equipment 2015), the Italian Ministry of Education, University and Research (FIRB to R.R. PRIN no. 2015795S5W to I.S.), the European Union (ERC mitoCalcium, no. 294777 to R.R.), NIH (Grant no. 1P01AG025532-01A1 to R.R.), the Italian Association for Cancer Research (AIRC IG18633 to R.R. and IG20286 to I.S.), and Telethon-Italy (GGP16029 to R.R.).

Author contributions F.D.L. designed and discussed ischaemia–reperfusion experiments. R.M. and G.D.M. performed and analysed ischaemia–reperfusion experiments. I.S. designed the electrophysiological study. V.C. performed recordings, and I.S. and V.C. analysed biophysical data. R.R. and D.D.S designed and supervised all other experiments. A.P., A.C. and D.D.S. performed all other experiments and analysed data. I.S., R.R. and D.D.S conceived the study, discussed all the results and wrote the manuscript.

Competing interests : The authors declare no competing interests.

Additional information

Supplementary information is available for this paper at https://doi.org/10.1038/s41586-019-1498-3.

Correspondence and requests for materials should be addressed to R.R. or D.D.

Peer review information *Nature* thanks Diana Stojanovski and the other, anonymous, reviewer(s) for their contribution to the peer review of this work.

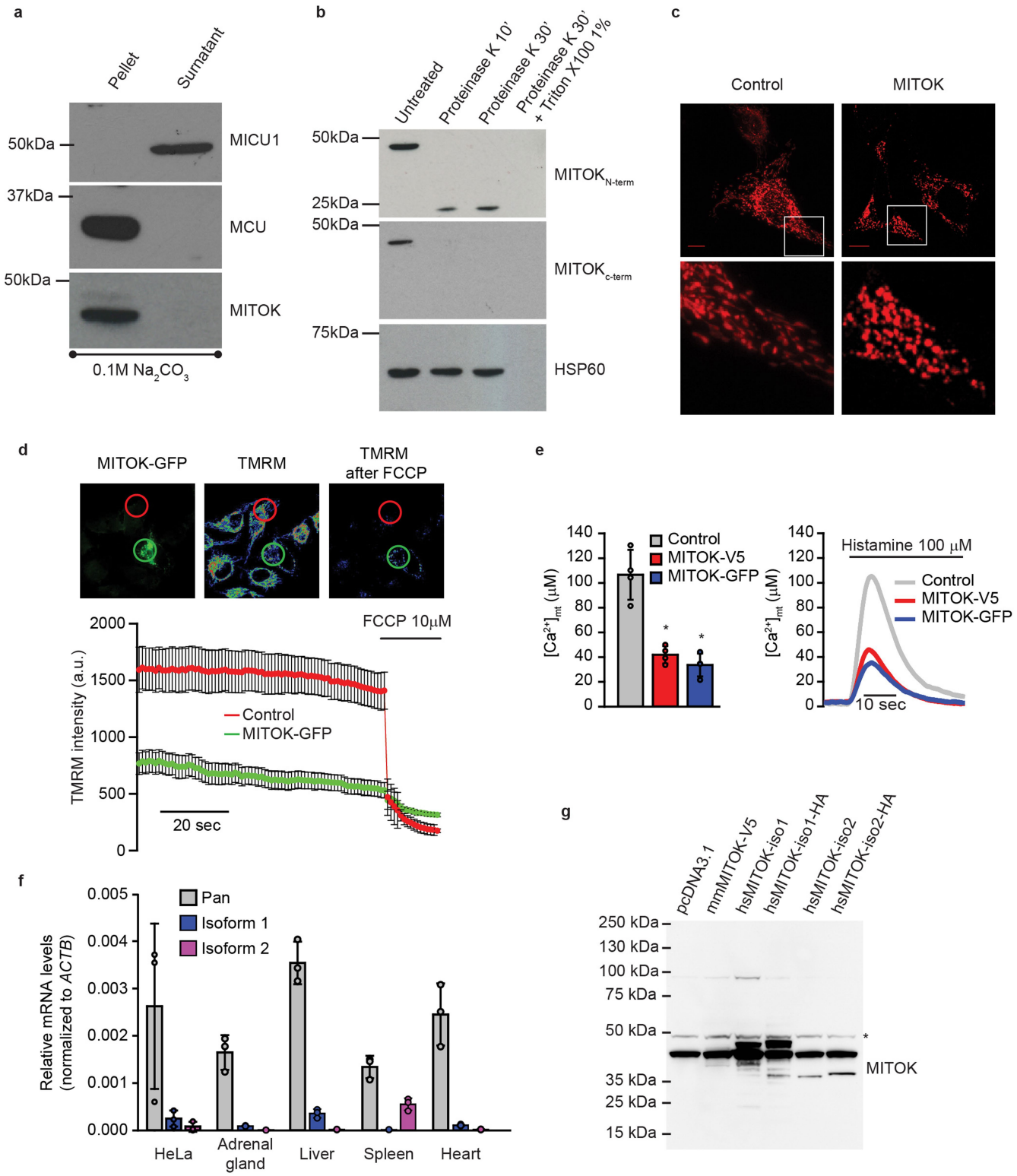

Extended Data Fig. 1 | Overexpression of mouse MITOK causes mitochondrial dysfunction. a, Membrane (pellet) and soluble (supernatant) proteins were separated from isolated liver mitochondria using ice-cold 0.1 M Na_2CO_3 (pH 11.5). Western blot is representative of three independent experiments. **b**, Proteinase K protection assay in isolated liver mitochondria. Similar results were obtained in three independent reactions. **c**, Mitochondrial morphology of control and MITOK-overexpressing HeLa cells. Representative of five independent experiments. Scale bar, 10 μm. **d**, Representative images and average ± s.d. traces of control and MITOK–GFP-expressing HeLa cells loaded with TMRM. $n = 9$ biologically replicates from 3 independent experiments. **e**, $[Ca^{2+}]_{mt}$ measurements (mean ± s.d.) in intact HeLa cells that express the indicated constructs. $n = 4$ biological replicates, representative of 3 independent experiments. $^*P < 0.001$ using one-way ANOVA with Holm–Sidak correction. **f**, qPCR analyses of transcripts from HeLa cells or the indicated human tissues using specific (isoform 1 and isoform 2) or non-specific (pan) primer pairs for *MITOK*. Data are normalized to *ACTB* and expressed as mean ± s.d. For HeLa cells, $n = 3$ biologically independent samples. For human tissues, $n = 3$ technical replicates. **g**, Protein expression of MITOK isoforms in HeLa cells transfected with the indicated constructs. Asterisk indicates a non-specific band. Image is representative of two independent experiments.

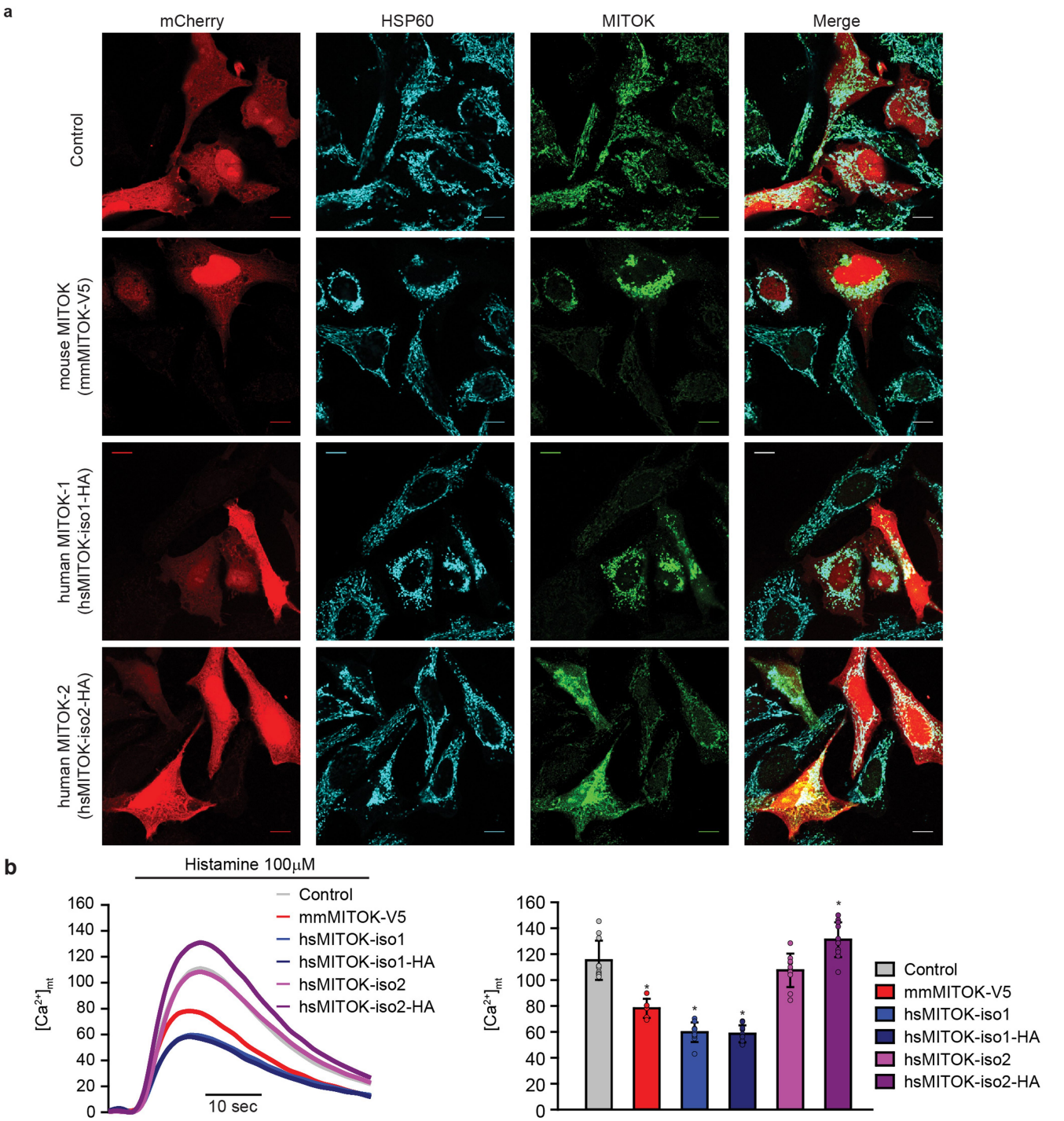

Extended Data Fig. 2 | Localization and function of human MITOK isoforms. a, Immunolocalization of MITOK (green) and the mitochondrial marker HSP60 (cyan) in HeLa cells transfected with the indicated constructs. Images are representative of two independent experiments. Scale bar, 10 μm. **b**, $[Ca^{2+}]_{mt}$ measurements (mean ± s.d.) in intact HeLa cells that express the indicated constructs. $n \geq 6$ independent samples, $^{*}P < 0.001$ using one-way ANOVA with Holm–Sidak correction.

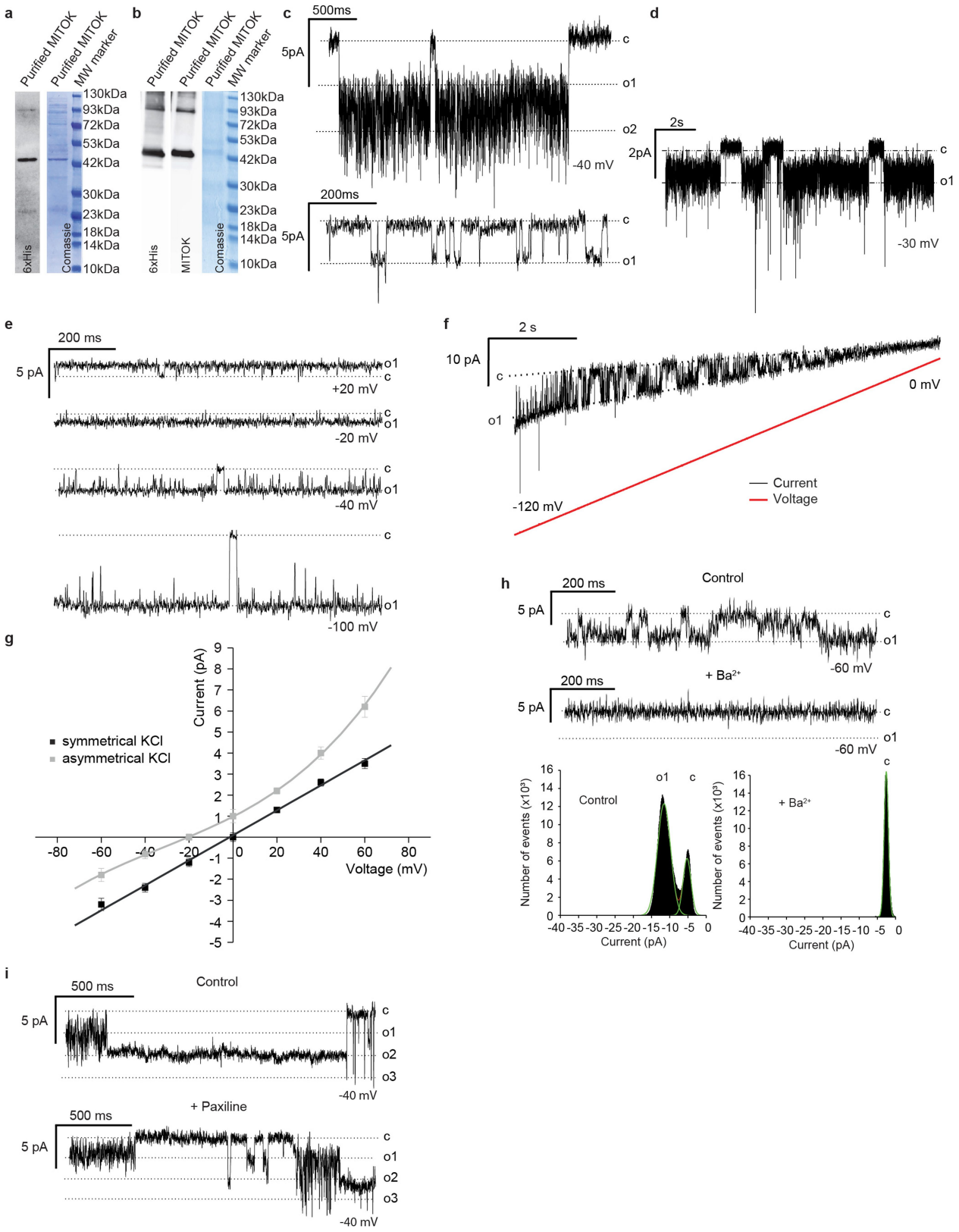

Extended Data Fig. 3 | See next page for caption.

Extended Data Fig. 3 | MITOK is a cation channel. a, **b**, Western blots and Coomassie staining of MITOK expressed and purified from *E. coli* (**a**) or WGL (**b**). Representative of three independent experiments. **c**, Current traces showing two channels gating together, resulting in flickering activity (top), or normal single-channel activity (bottom). The two traces were recorded in the same experiment, performed in 100 mM K-gluconate medium. Representative of five independent experiments. **d**, Current trace showing burst-like activity. Recording was performed in 100 mM K-gluconate medium. Similar activity was present in more than six recordings. **e**, Representative traces of MITOK channel activity at the indicated voltages. Similar results were obtained in three independent experiments. **f**, Voltage ramp (from -120 mV to 0 mV) of MITOK recorded in 100 mM K-gluconate symmetrical medium ($n = 3$ independent experiments). **g**, Single-channel *I–V* curves under symmetric (black) and asymmetric (grey) ionic conditions. Mean value ± s.d., $n = 50$ from 3–4 different experiments for each point. Fitting revealed an $E_{rev} = -21.6 \pm 1$ mV. $n = 4$ independent experiments. **h**, Representative traces (top) and amplitude histograms (bottom) before and after the addition of 2 mM Ba^{2+} ($n = 4$ independent experiments) in 100 mM KCl medium. **i**, Representative traces (top) and amplitude histograms (bottom) of MITOK activity before (control) and after addition of paxilline (40 μM). $n = 4$ independent experiments.

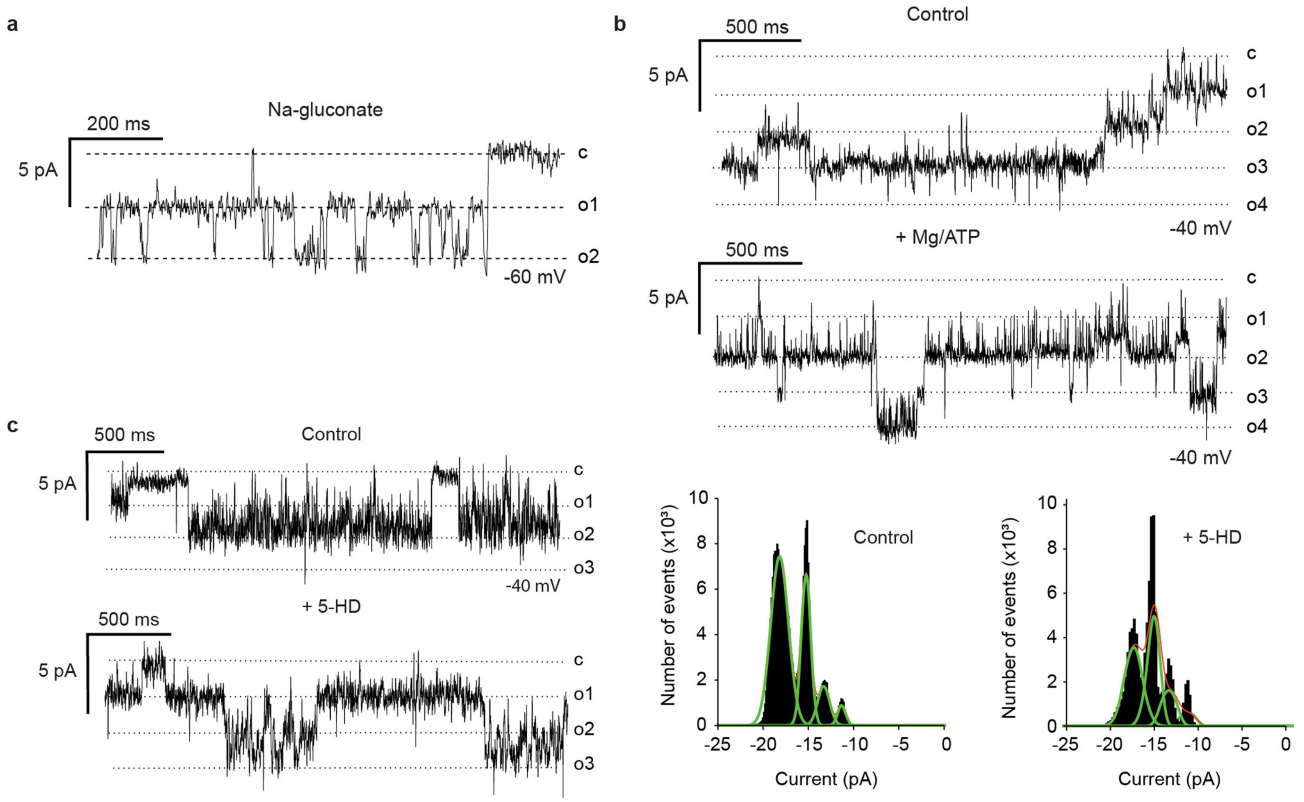

Extended Data Fig. 4 | MITOK alone is insensitive to ATP. a, Activity of MITOK in 100 mM Na-gluconate. $n = 5$ independent experiments. **b**, Current traces of MITOK channel activity obtained from 60-s recordings (in 100 mM K-gluconate) before (top) and after (bottom) addition of 2 mM Mg and ATP. Representative of eight independent experiments. Voltages of the *cis* side are reported. **c**, Representative traces (left) and amplitude histograms (right) of MITOK activity before (control) and after the addition of 5-HD (100 μM). $n = 5$ independent experiments.

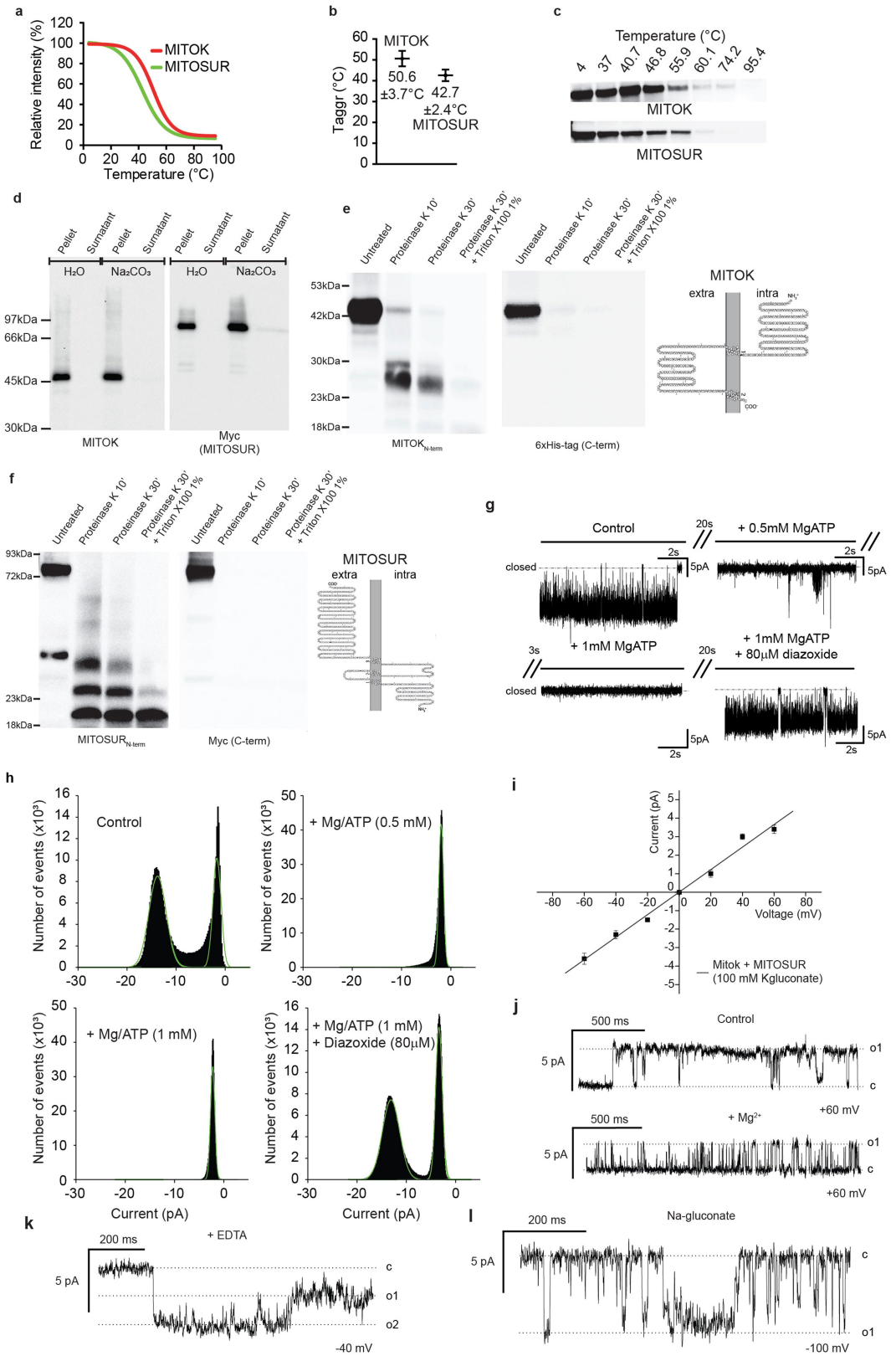

Extended Data Fig. 5 | See next page for caption.

Extended Data Fig. 5 | Biophysical characterization of recombinant human MITOSUR and mouse MITOK. a–c, Thermal shift assay analysis of human MITOSUR and mouse MITOK. Average curves (**a**), graphs of Taggr (**b**, expressed as mean ± s.d.) and western blot (**c**). Representative of four independent experiments. **d**, Membrane extraction and western blot (representative of two independent experiments) of in vitro co-expressed human MITOSUR and mouse MITOK incorporated into liposomes. **e**, **f**, Membrane topology assessed by proteinase K protection assay in reconstituted liposomes and probed for mouse MITOK (**e**) and human MITOSUR (**f**). **g**, The same experiment shown in Fig. 2a is here represented with a different time scale. **h**, Amplitude histograms of channel activity before (control) and after first addition of 500 μM Mg and ATP, the second addition of 500 μM Mg and ATP and the third addition of 80 μM diazoxide. Similar results were obtained with four independent preparations. Open probabilities over a period of 120 s were: control, 0.62; 0.5 mM Mg/ATP, 0.14; 1 mM Mg/ATP, 0; diazoxide, 0.75. **i**, Single-channel current (I)–voltage (V) relationship of human MITOSUR and mouse MITOK. Linear fitting revealed a chord conductance of 63 ± 3 pS. $n = 4$ independent experiments. **j**, Activity in the absence (control, top) and presence of 1 mM Mg^{2+} (bottom) in 100 mM K-gluconate medium. $n = 3$ independent experiments. **k**, Activity of human MITOSUR and mouse MITOK in 100 mM K-gluconate, 5 mM EDTA, 10 mM HEPES, pH 7.4 $n = 3$ independent experiments. **l**, Human MITOSUR and mouse MITOK channel activity in 100 mM Na-gluconate medium. $n = 4$ independent experiments.

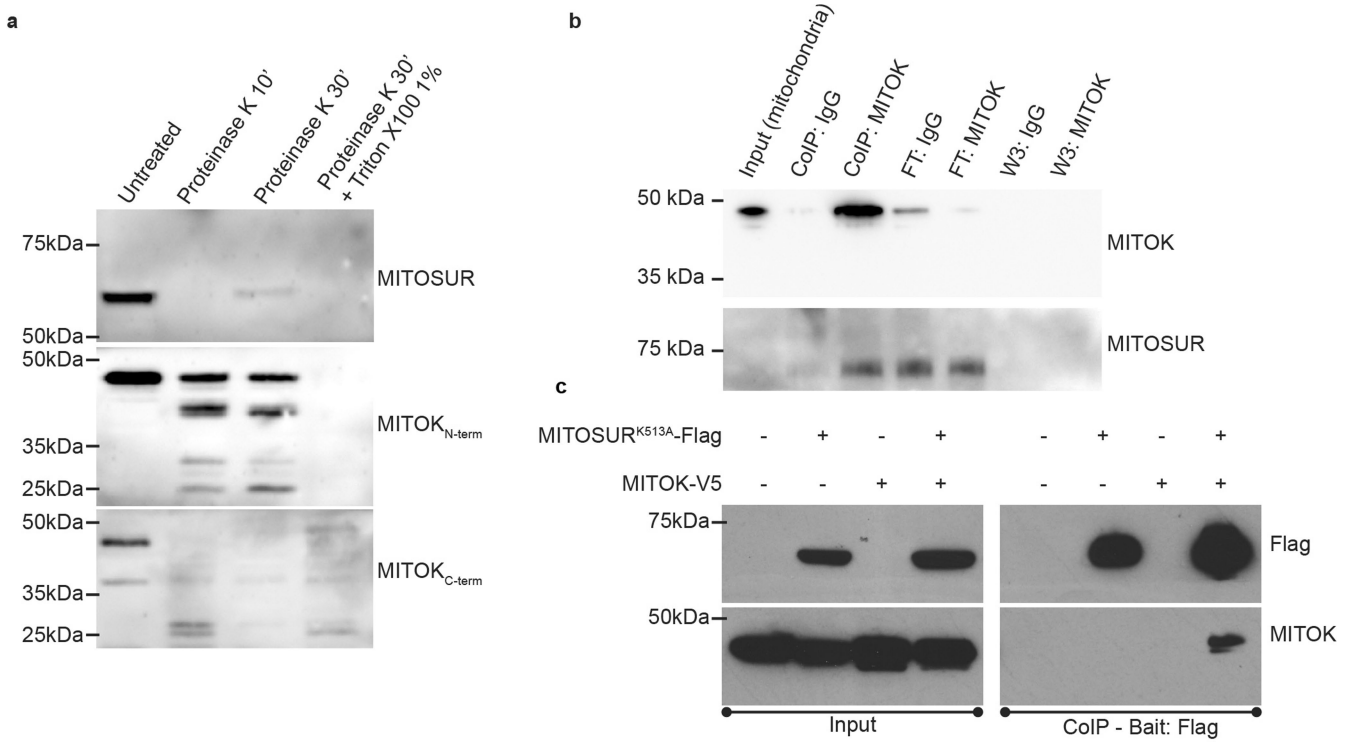

Extended Data Fig. 6 | MITOK and MITOSUR interact in situ. **a**, Proteinase K protection assay in isolated HeLa mitochondria. Similar results were obtained in two independent reactions. **b**, Co-immunoprecipitation of endogenous MITOK using mitochondria isolated from HeLa cells. FT, flow-through fraction; W3, third (last) co-immunoprecipitation wash. Representative of two independent experiments. **c**, Co-immunoprecipitation between overexpressed mouse MITOK and mutant human MITOSUR(K513A). Representative of two independent experiments.

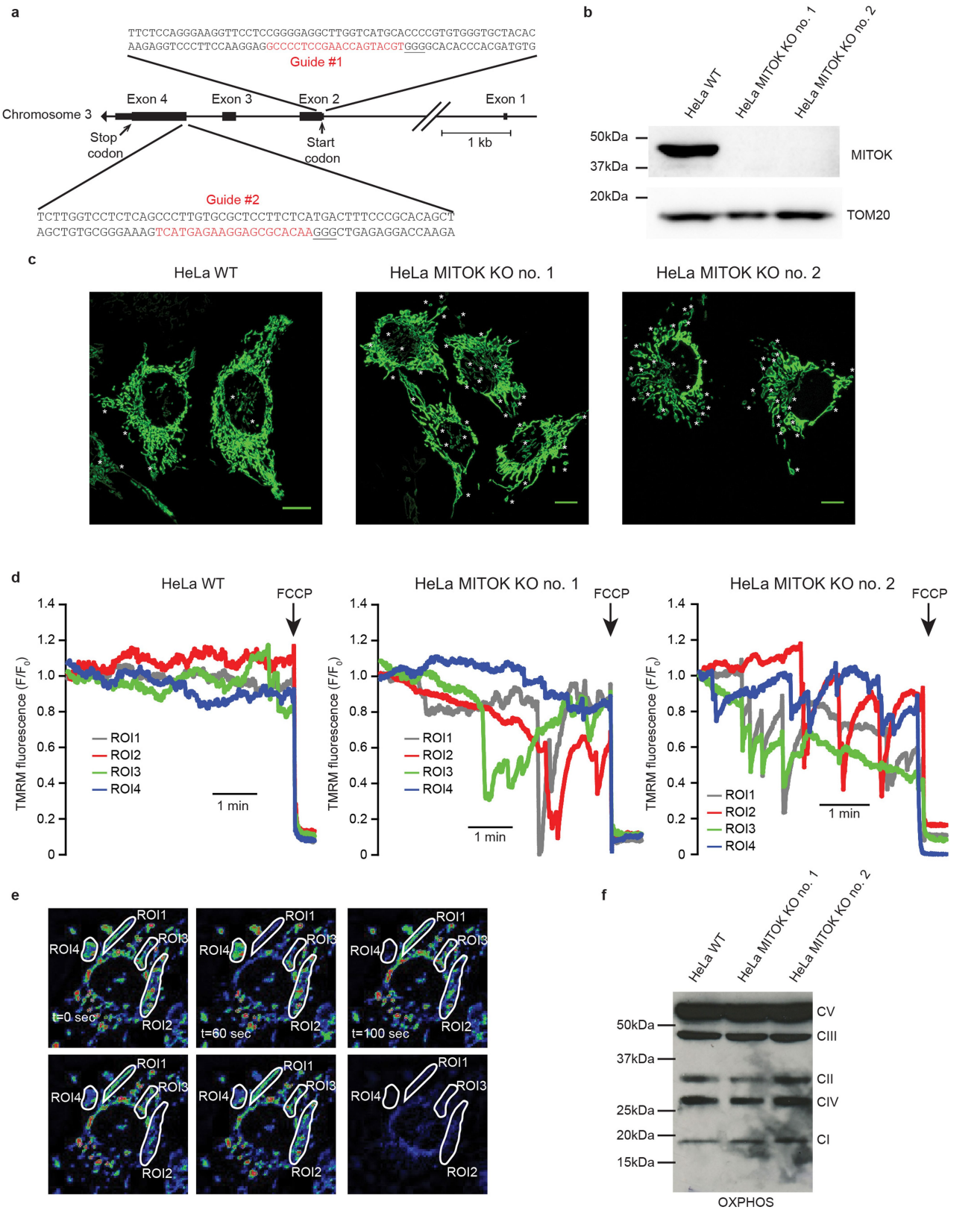

Extended Data Fig. 7 | Genetic ablation of *MITOK* in HeLa cells. **a**, Schematic of the *MITOK* gene. The expanded regions were used to design Cas9 guides (highlighted in red). **b**, Western blot of wild-type and MITOK-knockout HeLa cell lines. Representative of three independent experiments. **c**, Mitochondrial morphology in wild-type and MITOK-knockout HeLa cells. Scale bar, 10 μm. Asterisks are located near doughnut-shaped mitochondria. Similar results were obtained in five independent experiments. **d**, **e**, $\Delta\Psi_m$ measurements in control and MITOK-knockout cells. Cells were loaded with TMRM, and normalized fluorescence in different regions was monitored through time. **d**, Representative traces of single mitochondria. **e**, Pseudo-coloured representative images of a HeLa cell knockout for *MITOK*, loaded with TMRM at the indicated time points. Similar results were obtained in four independent experiments. **f**, Western blot in HeLa cells of the indicated genotype. Representative of two independent experiments.

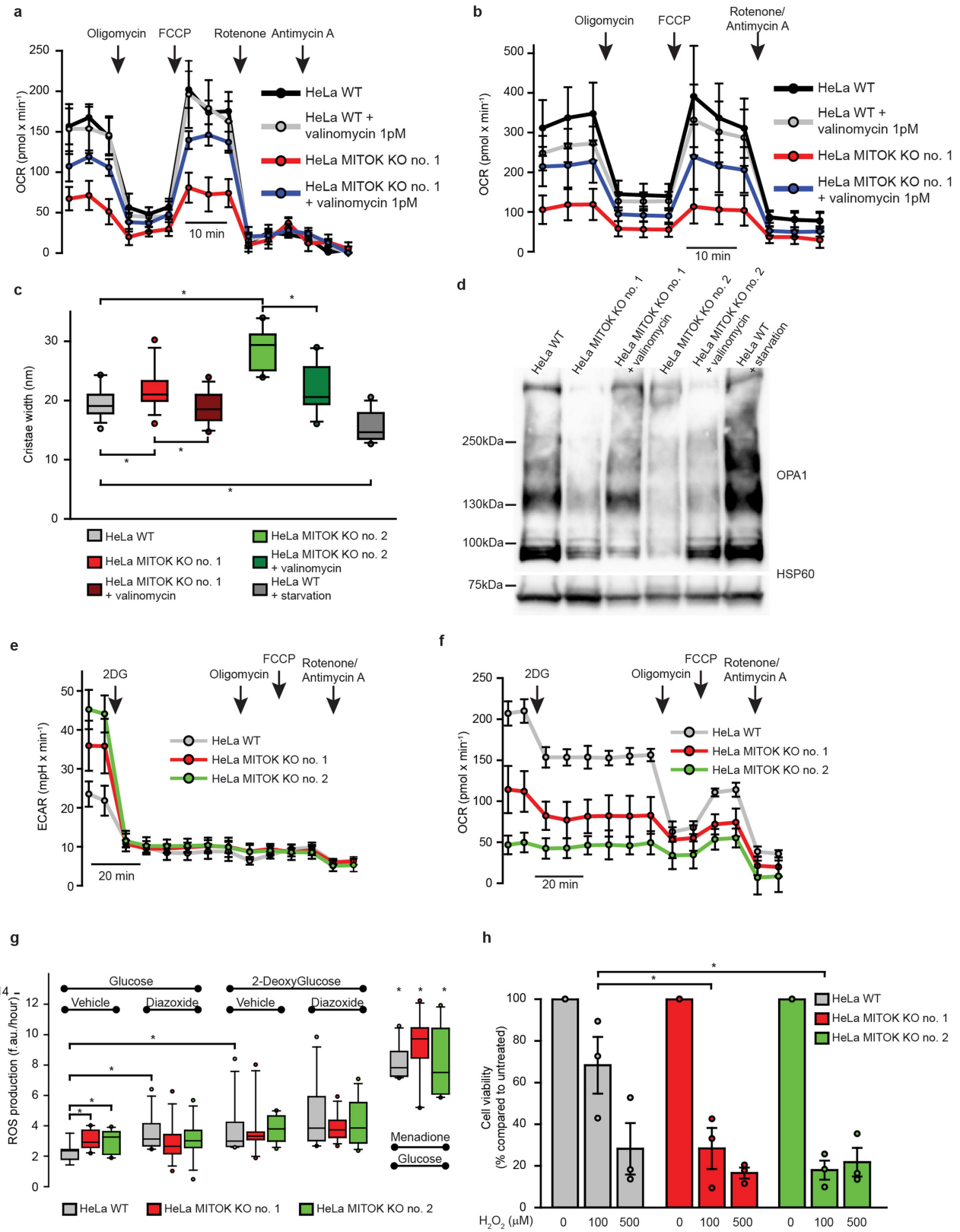

Extended Data Fig. 8 | See next page for caption.

Extended Data Fig. 8 | Loss of MITOK causes mitochondrial dysfunction. a, OCR measurements in wild-type and MITOK-knockout HeLa cells treated with either vehicle or 1 pM valinomycin for 1 h. Representative of three independent experiments. **b**, OCR measurements in wild-type and MITOK-knockout HeLa cells transfected with control or mitoK$_{ATP}$-expressing (MITOSUR-P2A-MITOK) plasmids. Representative of three independent experiments. **c**, Maximal cristae width in the indicated genotype. $n \geq 12$ individual cells (approximately 20 cristae per cell were measured) from 2 independent preparations. $^*P \leq 0.013$ using two-way ANOVA with Holm–Sidak correction. **d**, OPA1 crosslinking (using 1 mM BMH) in wild-type and MITOK-knockout cells. Similar results were obtained in three independent experiments. **e**, **f**, Extracellular acidification rate (ECAR) (**e**) and OCR (**f**) measurements in intact cells of the indicated genotype. $n = 5$ biological replicates, representative of 2 independent experiments. **g**, ROS production during energy stress. Cells were incubated in 5.5 mM of either glucose or 2-deoxyglucose in the presence or absence of 30 μM diazoxide, and fluorescence was monitored for 16 h. Box plots indicate the rate of ROS production over this time frame. $n \geq 10$ biological replicates from 3 independent experiments. $^*P < 0.05$ using three-way ANOVA with Holm–Sidak correction. **h**, Cell death analysis in HeLa cells treated with 0, 100 or 500 μM H_2O_2. Data are normalized to the untreated condition, and expressed as mean ± s.d. $n = 3$ independent experiments. $^*P < 0.003$ using two-way ANOVA with Holm–Sidak correction.

nature research

Corresponding author(s): Rosario Rizzuto
Diego De Stefani

Last updated by author(s): Jul 10, 2019

Reporting Summary

Nature Research wishes to improve the reproducibility of the work that we publish. This form provides structure for consistency and transparency in reporting. For further information on Nature Research policies, see Authors & Referees and the Editorial Policy Checklist.

Statistics

For all statistical analyses, confirm that the following items are present in the figure legend, table legend, main text, or Methods section.

n/a	Confirmed	
☐	☒	The exact sample size (*n*) for each experimental group/condition, given as a discrete number and unit of measurement
☐	☒	A statement on whether measurements were taken from distinct samples or whether the same sample was measured repeatedly
☐	☒	The statistical test(s) used AND whether they are one- or two-sided *Only common tests should be described solely by name; describe more complex techniques in the Methods section.*
☒	☐	A description of all covariates tested
☐	☒	A description of any assumptions or corrections, such as tests of normality and adjustment for multiple comparisons
☐	☒	A full description of the statistical parameters including central tendency (e.g. means) or other basic estimates (e.g. regression coefficient) AND variation (e.g. standard deviation) or associated estimates of uncertainty (e.g. confidence intervals)
☒	☐	For null hypothesis testing, the test statistic (e.g. *F*, *t*, *r*) with confidence intervals, effect sizes, degrees of freedom and *P* value noted *Give P values as exact values whenever suitable.*
☒	☐	For Bayesian analysis, information on the choice of priors and Markov chain Monte Carlo settings
☒	☐	For hierarchical and complex designs, identification of the appropriate level for tests and full reporting of outcomes
☒	☐	Estimates of effect sizes (e.g. Cohen's *d*, Pearson's *r*), indicating how they were calculated

Our web collection on statistics for biologists contains articles on many of the points above.

Software and code

Policy information about availability of computer code

Data collection	No software was used
Data analysis	Statistical analyses were performed with the SigmaPlot 12.0 (Systat) or Excel 365 (Microsoft).

For manuscripts utilizing custom algorithms or software that are central to the research but not yet described in published literature, software must be made available to editors/reviewers. We strongly encourage code deposition in a community repository (e.g. GitHub). See the Nature Research guidelines for submitting code & software for further information.

Data

Policy information about availability of data

All manuscripts must include a data availability statement. This statement should provide the following information, where applicable:

- Accession codes, unique identifiers, or web links for publicly available datasets
- A list of figures that have associated raw data
- A description of any restrictions on data availability

Source data for Figures 1g, 2a-b, 3d-e, 4a-d, 4f, 5a-b, 5d and Extended Data Figures 1c-d, 2b, 3g, 5g, 7d, 8a-c and 8f-h have been provided in Source Data Table. All other data supporting the findings of this study are available from the corresponding authors on request.

Field-specific reporting

Please select the one below that is the best fit for your research. If you are not sure, read the appropriate sections before making your selection.

☒ Life sciences ☐ Behavioural & social sciences ☐ Ecological, evolutionary & environmental sciences

Life sciences study design

All studies must disclose on these points even when the disclosure is negative.

Sample size	No a priori calculations were performed. Sample size was chosen based on previous experience with similar measurements.
Data exclusions	No data were excluded from the analyses.
Replication	Experiments were repeated multiple times, as detailed in the text, figure legends or Methods section.There were no attempts at replication that failed.
Randomization	Samples and animals were randomly divided into experimental groups.
Blinding	Analyses were not blinded because experiments were performed and analyzed by the same researchers.

Reporting for specific materials, systems and methods

We require information from authors about some types of materials, experimental systems and methods used in many studies. Here, indicate whether each material, system or method listed is relevant to your study. If you are not sure if a list item applies to your research, read the appropriate section before selecting a response.

Materials & experimental systems

n/a	Involved in the study
☐	☒ Antibodies
☐	☒ Eukaryotic cell lines
☒	☐ Palaeontology
☐	☒ Animals and other organisms
☒	☐ Human research participants
☒	☐ Clinical data

Methods

n/a	Involved in the study
☒	☐ ChIP-seq
☒	☐ Flow cytometry
☒	☐ MRI-based neuroimaging

Antibodies

Antibodies used	The following primary antibodies were used: anti-MITOK-C-term (1:1000, Sigma HPA011408), anti-MITOK-N-term (1:10000, Sigma HPA010980), anti-MCU (1:1000, Sigma HPA016480), anti-MICU1 (1:1000, Sigma HPA037480), anti-HSP60 (1:5000, Santa Cruz sc-1052), anti-OPA1 (1:1000, BD biosciences 612606), anti-MITOSUR (1:1000, Abcam ab182662), anti-OXPHOS (1:1000, Abcam ab110413), anti-TOM20 (1:10000, Santa Cruz sc-11415), anti-Flag (1:1000, Cell Signaling #2368).
Validation	MITOK antibodies are validate here: https://www.proteinatlas.org/ENSG00000164051-CCDC51/antibody MITOK antibodies were also validated in this study using overexpression and knock-out studies MCU antibody (Sigma HPA016480) validation data are here: https://www.proteinatlas.org/ENSG00000156026-MCU/antibody MICU1 antibody (igma HPA037480) validation data are here: https://www.proteinatlas.org/ENSG00000107745-MICU1/antibody HSP60 antibody (Santa Cruz sc-1052) validation data are here: https://www.scbt.com/scbt/product/hsp-60-antibody-n-20 Monoclonal OPA1 (Clone 18) antibody from BD (612606) has been used in many publications MITOSUR antibody (Abcam ab182662) was validated through overexpression experiments. This product is now discontinued. Total OXPHOS Rodent WB Antibody Cocktail (ab110413) validation data are here: https://www.abcam.com/total-oxphos-rodent-wb-antibody-cocktail-ab110413-references.html#top-0 TOM20 antibody (Santa Cruz sc-11415) validation data are here: https://www.scbt.com/scbt/product/tom20-antibody-fl-145 Flag antibody (Cell Signaling #2368) validation data can be found here: https://www.cellsignal.com/products/primary-antibodies/dykddddk-tag-antibody-binds-to-same-epitope-as-sigma-s-anti-flag-m2-antibody/2368

Eukaryotic cell lines

Policy information about cell lines

Cell line source(s)	HeLa cells were purchased from ATCC: http://www.lgcstandards-atcc.org/products/all/CCL-2.aspx
Authentication	Cells were authenticated by the commercial source
Mycoplasma contamination	Cell lines are tested for mycoplasma contamination every six months using MycoAlert Kit (Promega). Cell lines resulted "negative" or "bordeline".
Commonly misidentified lines (See ICLAC register)	No commonly misidentified cell lines were used.

Animals and other organisms

Policy information about studies involving animals; ARRIVE guidelines recommended for reporting animal research

Laboratory animals	Mus musculus on a C57BL/6N background. Adult (3 to 4 months-old) male mice were used.
Wild animals	This study did not involve wild animals
Field-collected samples	This study did not involve field-collected samples
Ethics oversight	Animal experiments were performed in accordance with the Italian law D. L.vo n_26/2014 and approved by local (O.P.B.A.) and national (Ministry of Health) committees (376-2015PR).

Note that full information on the approval of the study protocol must also be provided in the manuscript.

ARTICLE

https://doi.org/10.1038/s41586-019-1503-x

BCAA catabolism in brown fat controls energy homeostasis through SLC25A44

Takeshi Yoneshiro[1,2,3,14], Qiang Wang[1,2,3,14], Kazuki Tajima[1,2,3], Mami Matsushita[4], Hiroko Maki[5], Kaori Igarashi[5], Zhipeng Dai[6], Phillip J. White[7], Robert W. McGarrah[7], Olga R. Ilkayeva[7], Yann Deleye[7], Yasuo Oguri[1,2,3], Mito Kuroda[1,2,3], Kenji Ikeda[1,2,3,8], Huixia Li[1,2,3], Ayano Ueno[5], Maki Ohishi[5], Takamasa Ishikawa[5], Kyeongkyu Kim[1,2,3], Yong Chen[1,2,3], Carlos Henrique Sponton[1,2,3], Rachana N. Pradhan[1,2,3], Homa Majd[2], Vanille Juliette Greiner[1,9], Momoko Yoneshiro[1,2,3], Zachary Brown[1,2,3], Maria Chondronikola[10], Haruya Takahashi[11], Tsuyoshi Goto[11], Teruo Kawada[11], Labros Sidossis[12], Francis C. Szoka[6], Michael T. McManus[1,9], Masayuki Saito[13], Tomoyoshi Soga[5] & Shingo Kajimura[1,2,3]*

Branched-chain amino acid (BCAA; valine, leucine and isoleucine) supplementation is often beneficial to energy expenditure; however, increased circulating levels of BCAA are linked to obesity and diabetes. The mechanisms of this paradox remain unclear. Here we report that, on cold exposure, brown adipose tissue (BAT) actively utilizes BCAA in the mitochondria for thermogenesis and promotes systemic BCAA clearance in mice and humans. In turn, a BAT-specific defect in BCAA catabolism attenuates systemic BCAA clearance, BAT fuel oxidation and thermogenesis, leading to diet-induced obesity and glucose intolerance. Mechanistically, active BCAA catabolism in BAT is mediated by SLC25A44, which transports BCAAs into mitochondria. Our results suggest that BAT serves as a key metabolic filter that controls BCAA clearance via SLC25A44, thereby contributing to the improvement of metabolic health.

In addition to the well-known function of BAT as a thermogenic organ, studies using positron emission tomography–computed tomography (PET–CT) with ^{18}F-fluorodeoxyglucose (^{18}F-FDG) and fatty-acid tracers have demonstrated that BAT also serves as a metabolic sink for glucose and fatty acids[1–3]. This function is tightly coupled with the ability to improve metabolic health: cold acclimatization stimulates uptake of glucose, triglyceride-rich lipoproteins and fatty acids in BAT, thereby contributing to improved systemic lipid metabolism[4,5]. It remains unknown, however, whether BAT contributes to the clearance of any other metabolites and how such processes are regulated. Accordingly, we performed an unbiased metabolite analysis on sera from healthy human subjects (male, aged 23.4 ± 0.6 years old (all results are shown as mean ± s.e.m.), $n = 33$) with high BAT activity (standardized uptake value (SUV) > 4.03, $n = 17$) and low BAT activity (SUV ≤ 4.03, $n = 16$) at 27 °C (thermoneutral) and following cold exposure (19 °C) for 2 h (Supplementary Table1). Subjects with SUV > 4.03 were considered as the high-BAT group, on the basis of the median of the subjects in the study (Fig. 1a). The cold stimulus of 19 °C was selected on the basis that BAT thermogenesis is stimulated at 19 °C in adults without triggering skeletal muscle shivering (Extended Data Fig. 1a). Cold exposure stimulated lipolysis in adipose tissue, leading to a significant increase in circulating levels of non-esterified fatty acids in both groups, whereas cold exposure did not change blood glucose levels (Extended Data Fig. 1b, c).

Cold-activated BAT promotes systemic BCAA clearance

Unexpectedly, we found that serum concentration of Val was significantly reduced, preferentially in high-BAT subjects following cold exposure, whereas no significant change was seen in low-BAT subjects (Fig. 1b). The cold-induced reduction in serum Val concentrations showed a significant inverse correlation with BAT activity measured by ^{18}F-FDG-PET imaging (Fig. 1c). Similarly, cold-induced changes in Leu and total BCAA levels were inversely correlated with SUV, whereas no amino acids except Val and Leu showed a significant correlation (Fig. 1d, Extended Data Fig. 1d, Supplementary Table 2). Although skeletal muscle is a major organ that utilizes BCAA, there was no correlation of muscle mass with cold-induced changes in BCAA levels (Extended Data Fig. 1e). Consistent with the human study, plasma metabolomics in obese mice showed that cold exposure significantly reduced plasma Val, Leu and Ile levels (Fig. 1e, Extended Data Fig. 1f).

These observations caught our attention because epidemiological studies have demonstrated that increased circulating BCAA levels are strongly associated with obesity, insulin resistance and type 2 diabetes in humans and rodents[6–8], despite the fact that BCAA supplementation in healthy subjects is often associated with beneficial effects on muscle growth and energy expenditure[9]. Expression or activity of mitochondrial BCAA enzymes, such as the branched-chain α-keto acid dehydrogenase (BCKDH) complex, in the white adipose tissue (WAT) is reduced in obese and diabetic states[10–13], and transplantation of WAT from wild-type mice into branched-chain aminotransferase (BCAT2)-deficient mice reduces circulating BCAA levels[13], suggesting that adipose tissue contributes to the regulation of circulating BCAA levels. The extent to which cold acclimatization controls systemic BCAA homeostasis via BAT remains unknown.

Thus, we visualized Leu uptake in BAT using a PET–CT scan with ^{18}F-fluciclovine, a Leu-analogue tracer. Following cold acclimatization, ^{18}F-fluciclovine-PET–CT detected a robust increase in ^{18}F-fluciclovine uptake in the BAT and a modest increase in the inguinal WAT of mice

[1]UCSF Diabetes Center, San Francisco, CA, USA. [2]Eli and Edythe Broad Center of Regeneration Medicine and Stem Cell Research, San Francisco, CA, USA. [3]Department of Cell and Tissue Biology, University of California, San Francisco, San Francisco, CA, USA. [4]Department of Nutrition, Tenshi College, Sapporo, Japan. [5]Institute for Advanced Biosciences, Keio University, Yamagata, Japan. [6]Department of Bioengineering and Therapeutic Sciences, University of California, San Francisco, San Francisco, CA, USA. [7]Duke Molecular Physiology Institute, Duke University, Durham, NC, USA. [8]Department of Molecular Endocrinology and Metabolism, Tokyo Medical and Dental University, Tokyo, Japan. [9]Department of Microbiology and Immunology, University of California, San Francisco, San Francisco, CA, USA. [10]Center for Human Nutrition, Washington University in St Louis, St Louis, MO, USA. [11]Laboratory of Molecular Function of Food, Graduate School of Agriculture, Kyoto University, Uji, Japan. [12]Department of Kinesiology and Health, School of Arts and Sciences, Rutgers University, New Brunswick, NJ, USA. [13]Department of Biomedical Sciences, Graduate School of Veterinary Medicine, Hokkaido University, Sapporo, Japan. [14]These authors contributed equally: Takeshi Yoneshiro, Qiang Wang. *e-mail: shingo.kajimura@ucsf.edu

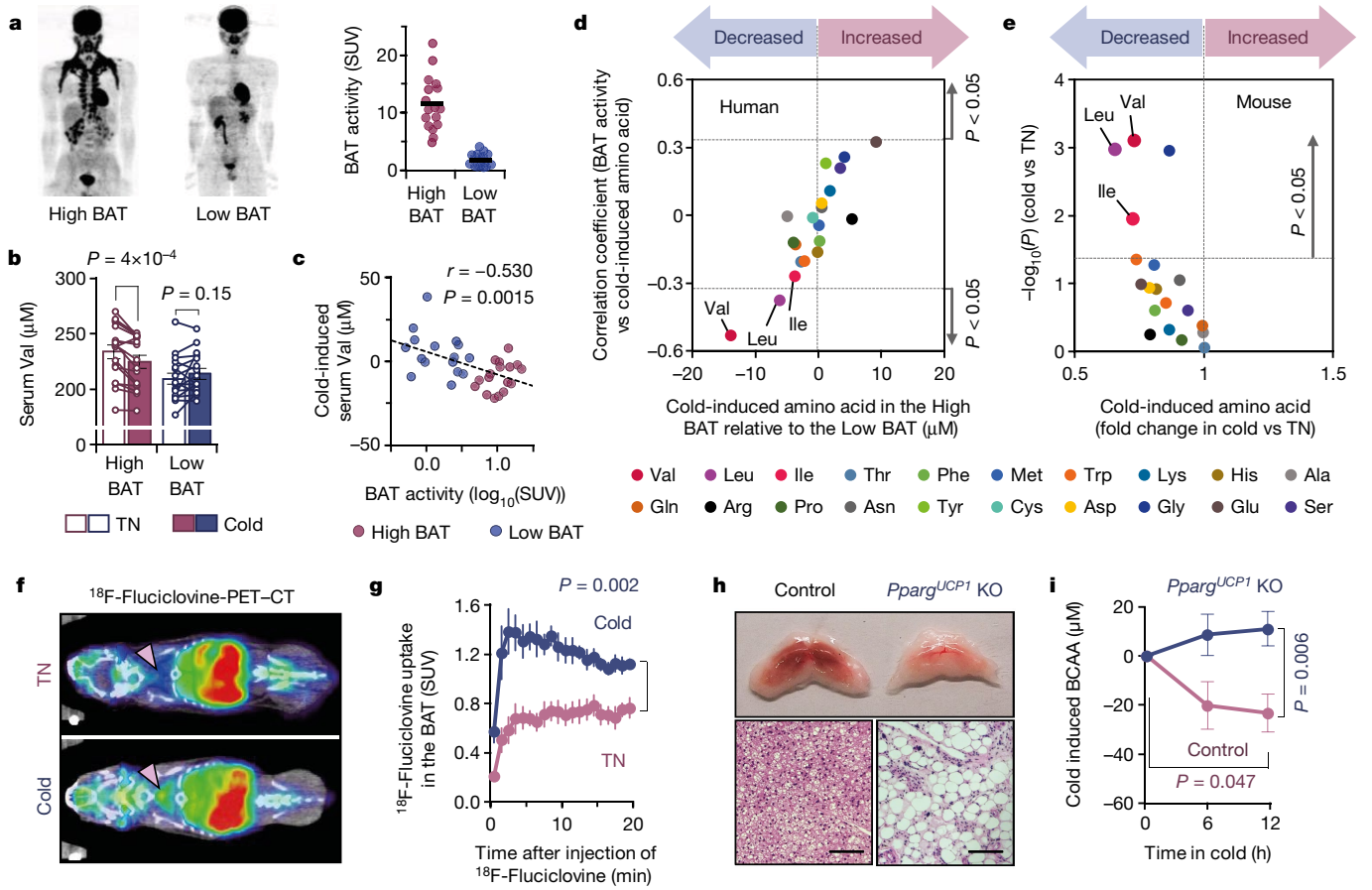

Fig. 1 | Cold-induced BAT thermogenesis promotes systemic BCAA clearance in mice and humans. a, Left, ^{18}F-FDG-PET–CT images of human experimental subjects following cold exposure. Right, SUV of ^{18}F-FDG in the BAT deposits. $n = 17$ (high BAT), $n = 16$ (low BAT). **b**, Circulating Val concentration in subjects in **a** at 27 °C (thermoneutral) and at 19 °C (cold). **c**, Correlation between BAT activity and cold-induced changes in serum Val concentration in **a**. **d**, Correlation between cold-induced amino acid changes and BAT activity (*y* axis) against the degree of BAT-dependent amino acid changes (*x* axis) in **a**. **e**, Cold-induced changes in plasma amino acids in diet-induced obese mice at 30 °C (thermoneutral (TN), $n = 5$) or 15 °C (cold, $n = 6$). **f**, ^{18}F-Fluciclovine-PET–CT images of mice acclimatized to 30 °C (TN) or 15 °C (cold) for two weeks. Arrows indicate interscapular BAT. **g**, SUV of ^{18}F-fluciclovine in BAT. $n = 5$ per group. **h**, Morphology and haematoxylin and eosin (H&E) staining of interscapular BAT of *Pparg*^{UCP1}-KO and control mice. Scale bars, 50 μm. Representative result from two independent experiments. **i**, Plasma levels of BCAA in **h** during cold temperature (12 °C). $n = 7$ per group. **a**–**i**, Biologically independent samples. Data are mean ± s.e.m.; two-sided *P* values by paired *t*-test (**b**), unpaired Student's *t*-test (**e**), or two-way repeated measures analysis of variance (ANOVA) (**g**) followed by post hoc paired or unpaired *t*-tests with Bonferroni's correction (**i**). Pearson's or Spearman's rank correlation coefficient was calculated, as appropriate (**c**, **d**).

(Fig. 1f, g). Whereas the basal SUV in the liver and heart was higher than in BAT, no significant change was seen in these organs following cold exposure (Extended Data Fig. 2a). Consistent with a recent study[14], we found that BAT displayed the highest Val oxidation on cold exposure, relative to other metabolic organs including inguinal WAT, epididymal WAT and gastrocnemius muscle of mice (Extended Data Fig. 2b, c). Furthermore, Val oxidation in differentiated human brown adipocytes was significantly higher than in white adipocytes and was further enhanced by noradrenaline (Extended Data Fig. 2d). Of note, transcriptomics and proteomics data from mice and humans[15–17] showed that more than 60% of genes encoding BCAA catabolic enzymes, including the gene for the rate-limiting enzyme BCAT2, were more highly expressed in brown adipocytes relative to white adipocytes (Extended Data Fig. 2e, f). Our previous analysis in humans[5] also found that the BCAA catabolic pathway was highly and selectively induced by cold exposure in the supraclavicular BAT but not in the abdominal WAT (Extended Data Fig. 2g). Notably, BCAA is oxidized primarily in the mitochondria of BAT; BAT predominantly expresses the mitochondria-localized form BCAT2, but not the cytosolic isoform BCAT1 (Extended Data Fig. 2h, i). Despite this knowledge, the mitochondrial transporter for BCAAs is unidentified, and it remains unknown how BCAAs are utilized in brown adipocytes.

To determine whether BAT contributes to systemic BCAA clearance, we generated a BAT-ablation mouse model in which peroxisome proliferator-activated receptor-γ (PPAR-γ) was deleted in uncoupling protein 1 (UCP1)-expressing thermogenic adipocytes (*Pparg*^{UCP1} knockout (KO), *Ucp1-cre*;*Pparg*$^{flox/flox}$). In contrast to littermate controls (*Pparg*$^{flox/flox}$), the presumptive BAT in *Pparg*^{UCP1}-KO mice was composed of unilocular adipocytes and fibrotic tissues (Fig. 1h). Following cold exposure, plasma BCAA concentration was significantly reduced in control mice but not in *Pparg*^{UCP1}-KO mice (Fig. 1i).

BAT-specific BCAA defect impairs energy homeostasis

To examine the extent to which BCAA catabolism in BAT regulates energy homeostasis, we next generated a mouse model in which BCAA oxidation is impaired specifically in the BAT (*Bckdha*^{UCP1}-KO mice, *Ucp1-cre*;*Bckdha*$^{flox/flox}$) (Fig. 2a, Extended Data Fig. 3a–c). Whereas no difference was seen in BAT mass and thermogenic gene expression between the genotypes on a regular diet (Extended Data Fig. 3d, e), the core-body temperature of *Bckdha*^{UCP1}-KO mice was significantly lower than that of controls after cold exposure without affecting muscle shivering (Fig. 2b, Extended Data Fig. 3f). Tissue-temperature recording also detected impaired thermogenesis in the BAT of *Bckdha*^{UCP1}-KO mice following treatment with noradrenaline, whereas no change was

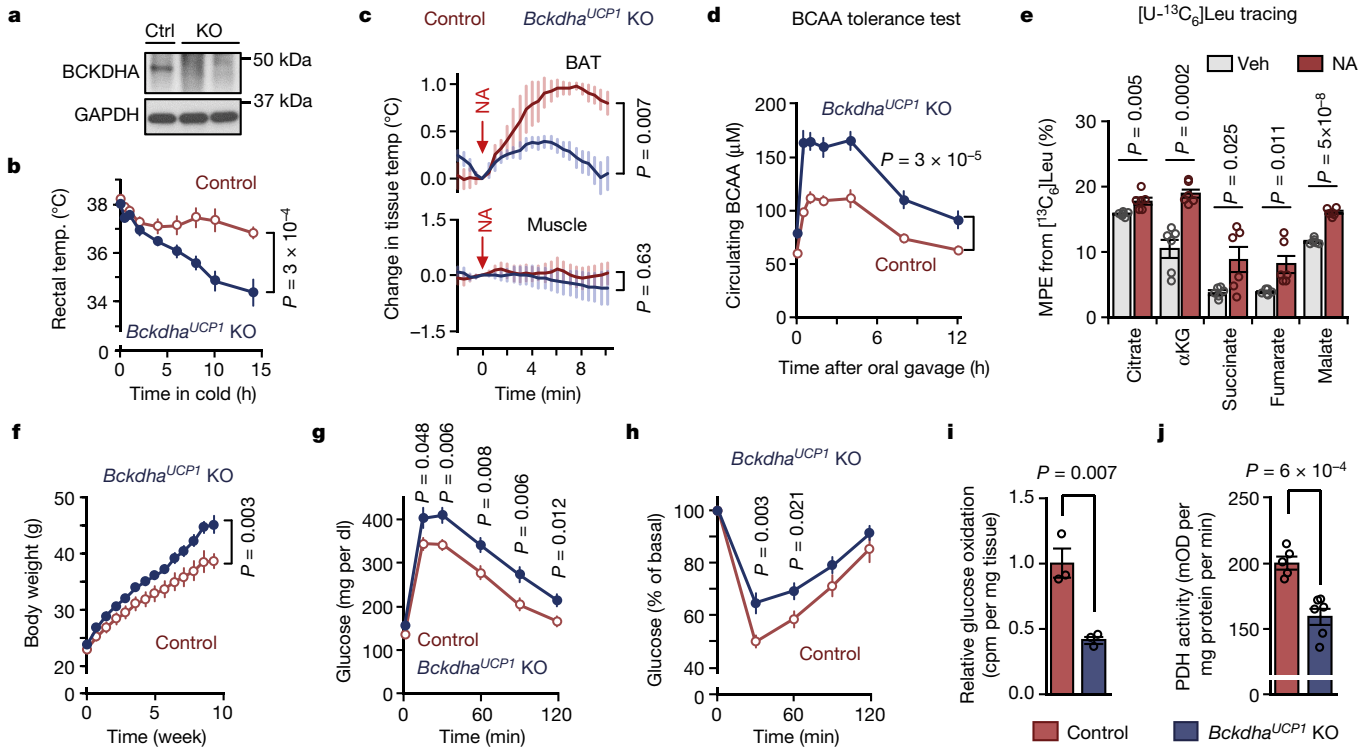

Fig. 2 | BCAA oxidation in BAT is required for BCAA clearance and energy homeostasis. a, Immunoblotting of BCKDHA in BAT of *Bckdha*^{UCP1}-KO and control (ctrl) mice. GAPDH was used as a loading control. Representative result from two independent experiments. Gel source data are presented in Supplementary Fig. 1. **b**, Rectal core body temperature following cold exposure at 8 °C. $n = 8$ (control), $n = 9$ (*Bckdha*^{UCP1}-KO). **c**, Change in tissue temperature (temp) in BAT and muscle following treatment with noradrenaline (NA). $n = 4$ per group. **d**, Plasma BCAA levels at indicated time points after a BCAA oral gavage at 12 °C. $n = 8$ per group. **e**, MPE of indicated metabolites derived from [U-^{13}C$_6$]Leu in human brown adipocytes. Cells were treated with vehicle (veh) or noradrenaline for 1 h. $n = 6$ per group. αKG, α-ketoglutarate. **f**, Body weight of *Bckdha*^{UCP1}-KO ($n = 15$) and control ($n = 13$) mice on high-fat diet at ambient temperature. **g**, Glucose tolerance test of mice in **f**. **h**, Insulin tolerance test of mice in **f**. **i**, Glucose oxidation in BAT normalized to tissue mass. $n = 3$ mice per group. **j**, PDH activity in BAT of mice maintained at 12 °C for one week. $n = 5$ (control), $n = 6$ (*Bckdha*^{UCP1}-KO). **b**–**j**, Biologically independent samples. Data are mean ± s.e.m.; two-sided *P* values by unpaired Student's *t*-test (**e**, **i**, **j**) or two-way repeated measures ANOVA (**b**–**d**, **f**) followed by post hoc unpaired *t*-test (**g**, **h**).

seen in muscle and liver temperature (Fig. 2c, Extended Data Fig. 3g). Notably, *Bckdha*^{UCP1}-KO mice were intolerant to oral BCAA challenge compared with control mice (Fig. 2d, Extended Data Fig. 3h). Similarly, *Bckdha*^{UCP1}-KO mice displayed higher plasma BCAA levels than controls following cold exposure (Extended Data Fig. 3i). These results indicate that BCAA oxidation is required for BAT thermogenesis and systemic BCAA clearance.

To examine how a cold stimulus alters BCAA utilization in brown fat, we next used capillary electrophoresis time-of-flight mass spectrometry (CE-TOFMS) and performed Leu stable-isotope tracing in differentiated human brown adipocytes. The mole percentage enrichment (MPE) of tricarboxylic acid (TCA) cycle intermediates derived from [U-^{13}C$_6$]Leu was quantified following noradrenaline treatment for 1 h (Extended Data Fig. 4a, Supplementary Table 3). We found that acute noradrenaline treatment significantly increased the MPE of TCA intermediates, including succinate (Fig. 2e, Extended Data Fig. 4b), although the fractional contribution of labelled Leu to the TCA cycle was relatively small. This rapid noradrenaline-stimulated BCAA oxidation was aligned with increased expression of many BCAA-oxidation enzymes in the BAT mitochondria within 8 h after cold exposure (Extended Data Fig. 4c, d) and the rapid oxidation of BCAA in BAT[14]. Of note, Val supplementation rapidly increased oxygen consumption rate (OCR) in human brown adipocytes stimulated with noradrenaline (Extended Data Fig. 4e). The stimulatory effect requires the generation of the TCA-cycle intermediate succinate: inhibition of succinyl coenzyme A synthetase or succinate dehydrogenase by vanadate or malonate, respectively, blunted the Val effect on OCR (Extended Data Fig. 4f, g). We also found that supplementation of Val, Leu or Ile significantly enhanced noradrenaline-stimulated thermogenesis in brown adipocytes in a UCP1-dependent fashion (Extended Data Fig. 4h, i). BCAA supplementation or pharmacological BCAT2 activation significantly increased brown fat respiration in a BCKDHA-dependent manner; the reduced respiration in *Bckdha*-deficient cells was not the result of a general mitochondrial defect, because succinate supplementation, but not α-ketoisovalerate (KIV), restored noradrenaline-stimulated thermogenesis in *Bckdha*-deficient brown adipocytes (Extended Data Fig. 4i, j). Previous studies report that BCAA catabolism fuels de novo lipogenesis by generating monomethyl branched-chain fatty acids (mmBCFAs), and that mmBCFA synthesis in BAT is activated after one month of cold acclimatization[18,19]. Consistent with these studies, proteomics data showed that the expression of mmBCFA synthesis enzymes, including carnitine acetyltransferase, were increased after three-week cold acclimatization, whereas many BCAA oxidative enzymes in the mitochondria were rapidly induced within 8 h of cold exposure and subsequently downregulated (Extended Data Fig. 4c, d). These data suggest a dynamic shift in BCAA utilization during cold acclimatization in BAT; that is, acute cold exposure activates BCAA oxidation in the TCA cycle, whereas chronic cold gradually promotes mmBCFA synthesis.

Next, we examined the degree to which a BAT-specific defect in BCAA catabolism influences whole-body metabolism. *Bckdha*^{UCP1}-KO mice on a high-fat diet gained significantly more body weight than littermate controls, owing to increased adipose tissue and liver mass, but not to changes in lean mass or food intake (Fig. 2f, Extended Data Fig. 5a–c). Consistent with previous studies showing that BAT thermogenesis controls hepatic triglyceride clearance[4,20], the livers

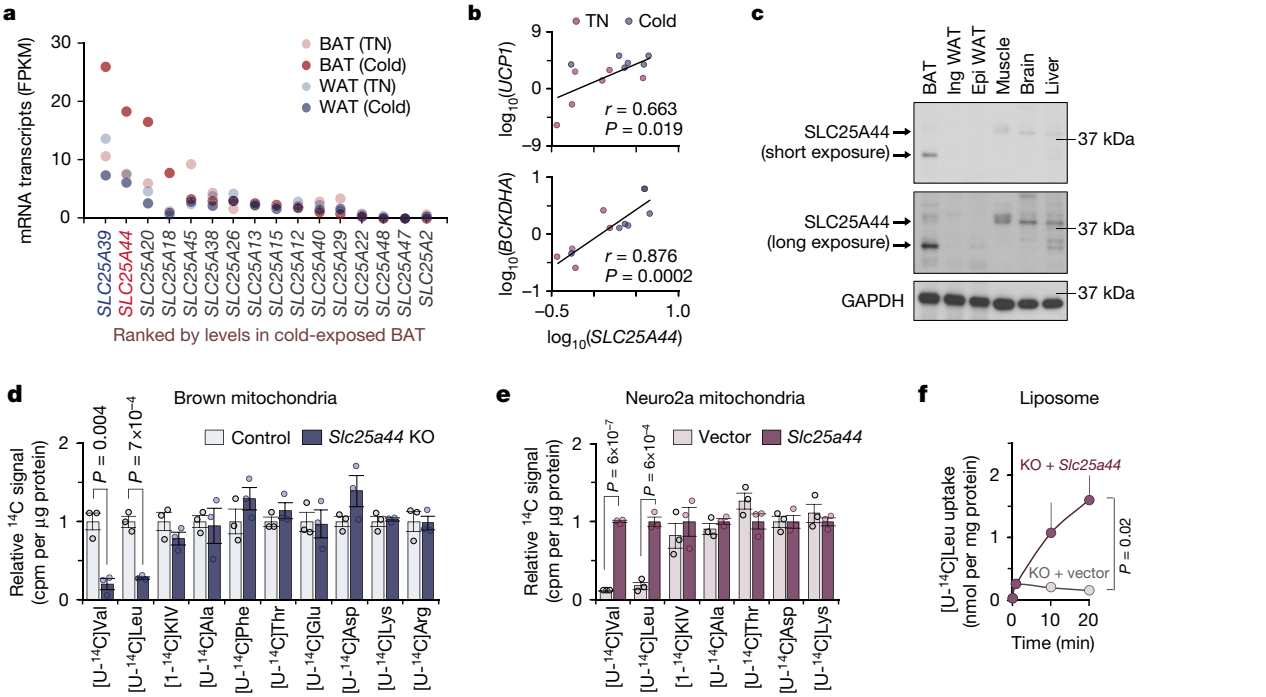

Fig. 3 | Identification of SLC25A44 as a mitochondrial BCAA transporter. a, Expression profile of SLC25A family members in human supraclavicular BAT and abdominal subcutaneous WAT from the same individual at 27 °C and 19 °C (ref. [5]). FPKM, fragments per kilobase of transcript per million mapped reads. **b**, Correlation of expression of *SLC25A44* mRNA with that of *UCP1* or *BCKDHA* in human BAT. Expression in thermoneutral (red) or cold (blue) conditions from six biologically independent subjects. *r*, Pearson's correlation coefficient. **c**, SLC25A44 protein expression in indicated tissues of mice. GAPDH was used as a loading control. Representative result from two independent experiments. Gel source data are presented in Supplementary Fig. 1. **d**, **e**, Mitochondrial uptake of indicated molecules in control and *Slc25a44*-KO brown adipocytes (**d**) or in Neuro2a cells expressing *Slc25a44* or an empty vector (**e**). $n = 3$ biologically independent samples per group. **f**, [U-$^{14}C_6$]Leu transport into mitochondrial liposomes from *Slc25a44*-KO brown adipocytes, expressing an empty vector (KO + vector) or *Slc25a44* (KO + *Slc25a44*). $n = 3$ technically independent samples per group. Representative result from two independent experiments. Data are mean ± s.e.m.; two-sided *P* values by unpaired Student's *t*-test (**d**, **e**) or two-way ANOVA (**f**).

of *Bckdha*^{UCP1} -KO mice contained significantly higher levels of triglycerides than those of controls (Extended Data Fig. 5d). Of note, *Bckdha*^{UCP1}-KO mice exhibited increased systemic glucose intolerance and insulin resistance compared with controls (Fig. 2g, h). Furthermore, glucose oxidation in the BAT of *Bckdha*^{UCP1}-KO mice was significantly reduced relative to controls (Fig. 2i). Fatty acid oxidation in the BAT of *Bckdha*^{UCP1}-KO mice was modestly reduced relative to controls (Extended Data Fig. 5e). The impaired glucose oxidation in *Bckdha*^{UCP1}-KO mice was associated with reduced pyruvate dehydrogenase (PDH) activity in the BAT and inguinal WAT, and with increased phosphorylation of the E1 subunit of PDH at S300 and, to a lesser degree, at S293 (Fig. 2j, Extended Data Fig. 5f–h).

SLC25A44 mediates mitochondrial BCAA transport

Recognizing the role of BCAA catabolism in BAT thermogenesis, we next sought to answer the long-standing question: how do cells take up BCAAs into the mitochondria? As described earlier, brown adipocytes in humans and mice predominantly express the mitochondria-localized isoform BCAT2 in preference to BCAT1, but the mitochondrial BCAA transporter remains uncharacterized. Therefore, we hypothesized that thermogenic adipocytes would express a mitochondrial BCAA transporter. Members of the SLC25A family are promising candidates for this role, because many of the mitochondrial amino acid transporters belong to this family of solute carrier transporter proteins[21]. In addition to the carnitine–acylcarnitine translocase SLC25A20 and the glutamate carrier SLC25A22, transcriptome analyses identified two uncharacterized SLC25A members, SLC25A39 and SLC25A44 that were abundantly expressed in mouse and human BAT (Fig. 3a, Extended Data Fig. 6a). Expression of *SLC25A44*, but not *SLC25A39* mRNA in the human supraclavicular BAT was significantly increased after cold exposure and showed a positive correlation with *UCP1* and *BCKDHA* mRNA expression (Fig. 3b, Extended Data Fig. 6b). SLC25A44 protein was localized to the mitochondria and more highly expressed in the BAT compared with other metabolic organs (Fig. 3c, Extended Data Fig. 6c, d). In addition, SLC25A44 expression was increased during brown adipogenesis (Extended Data Fig. 6e–g).

To determine the function of SLC25A44, we generated *Slc25a44*-KO brown adipocytes using CRISPR–Cas9 (Extended Data Fig. 7a). Mitochondrial BCAA uptake assays showed that Val and Leu uptake was selectively and significantly reduced in *Slc25a44*-KO cells, whereas *Slc25a44* deletion did not affect the mitochondrial uptake of other amino acids (Fig. 3d, Extended Data Fig. 7b, c). Similarly, depletion of *Slc25a44* by lentivirus short-hairpin RNAs (shRNAs) abrogated mitochondrial Val and Leu uptake, whereas *Slc25a39* depletion did not affect Val and Leu uptake (Extended Data Fig. 7d, e). Conversely, ectopic expression of SLC25A44 in a neuroblastoma cell line (Neuro2a cells) with undetectable endogenous SLC25A44 sufficiently and selectively restored mitochondrial Val and Leu uptake (Fig. 3e, Extended Data Fig. 7f).

To characterize SLC25A44 in a cell-free system, we prepared liposomes that were fused with the mitochondrial inner membrane from *Slc25a44*-KO brown adipocytes or *Slc25a44*-KO cells that ectopically expressed *Slc25a44* (Extended Data Fig. 7g, h). We observed robust and rapid Leu uptake in the mitochondrial liposomes from SLC25A44-expressing cells that were preloaded with Leu and Glu, whereas there was no detectable Leu uptake in the control group (Fig. 3f, Extended Data Fig. 7i). There was no difference in Glu uptake between the two groups (Extended Data Fig. 7j). As an alternative cell-free system, we reconstituted proteoliposomes by fusing liposomes with purified SLC25A44 protein (Extended Data Fig. 7k, l). Consistent with the results from mitochondrial liposomes, we detected active Leu uptake into the proteoliposomes with purified SLC25A44 (Extended Data Fig. 7m).

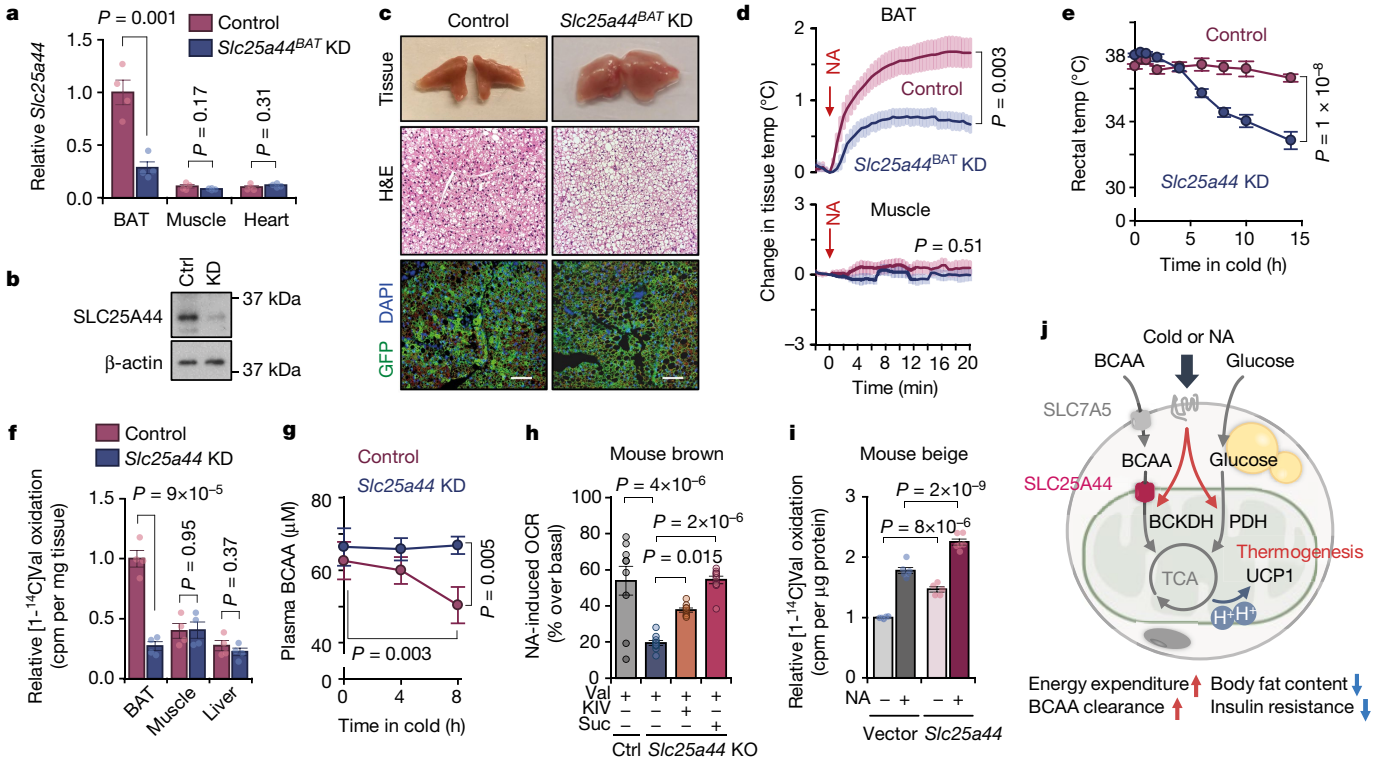

Fig. 4 | SLC25A44 is required for BAT thermogenesis and BCAA catabolism. a, Expression of *Slc25a44* mRNA in indicated tissues of *Slc25a44*^{BAT}-KD and control mice. $n = 4$ per group. **b**, Immunoblotting of SLC25A44 in BAT of mice in **a**. β-actin was used as a loading control. Representative result from two independent experiments. Gel source data are presented in Supplementary Fig. 1. **c**, Morphology (top), H&E staining (middle) and GFP immunofluorescence (bottom) in BAT from **a** (DAPI was used for counter staining). Scale bars, 100 μm. Representative result from two independent mice. **d**, Tissue temperature of BAT and muscle in **a** following treatment with noradrenaline (arrows). $n = 5$ (control), $n = 7$ (*Slc25a44*^{BAT}-KD). **e**, Rectal core body temperature of *Slc25a44*-KD ($n = 6$) and control ($n = 7$) mice following cold exposure at 8 °C. **f**, Val oxidation in indicated tissues normalized to tissue mass. $n = 4$ per group. **g**, Plasma BCAA levels in **e** following 8 h cold treatment at 8 °C. $n = 6$ per group. **h**, Noradrenaline-induced OCR normalized to total protein in control and *Slc25a44*-KO brown adipocytes. $n = 9$ per group (control + Val, *Slc25a44*-KO + Val + KIV), $n = 10$ per group (KO + Val, KO + Val + succinate). **i**, Val oxidation in inguinal WAT-derived white adipocytes expressing an empty vector or *Slc25a44* after noradrenaline treatment. $n = 5$ (vehicle), $n = 6$ (noradrenaline). **j**, A proposed model of BCAA catabolism in thermogenic adipose cells. Cold stimuli activate BCAA uptake and oxidation in the mitochondria of thermogenic adipocytes. Mitochondrial BCAA oxidation promotes BAT thermogenesis. This process requires SLC25A44, the mitochondrial BCAA transporter. SLC7A5, L-amino acid transporter 1. **a**, **d**–**i**, Biologically independent samples. Data are mean ± s.e.m.; two-sided *P* values by unpaired Student's *t*-test (**a**, **f**), one-way factorial (**h**) or two-way repeated measures ANOVA (**d**, **e**, **g**) followed by post hoc paired or unpaired *t*-test with Bonferroni's correction (**g**) or Tukey's test (**h**, **i**).

SLC25A44 is required for BCAA catabolism

To determine the role of SLC25A44 in vivo, we used a modified CRISPR system, using catalytically inactive Cas9 protein (dCas9) fused to Krüppel-associated box (KRAB) domain. Adeno-associated virus (AAV) expressing a guide RNA (gRNA) targeting *Slc25a44* or enhanced green fluorescent protein (eGFP; control) was injected into the interscapular BAT of dCas9-KRAB mice that were generated by the site-specific integrase-mediated approach[22] (Extended Data Fig. 8a–c). This system enabled BAT-selective knockdown of SLC25A44 (*Slc25a44*^{BAT}-KD) (Fig. 4a, b, Extended Data Fig. 8d, e). We found that brown adipocytes in *Slc25a44*^{BAT}-KD mice contained larger lipid droplets than those in control mice (Fig. 4c). Moreover, noradrenaline-induced BAT thermogenesis in *Slc25a44*^{BAT}-KD mice was significantly impaired relative to controls without affecting muscle thermogenesis (Fig. 4d). Next, we generated transgenic mice expressing gRNA-targeting *Slc25a44*, which were subsequently crossed with dCas9-KRAB mice to generate SLC25A44-deficient (*Slc25a44*-KD) mice (Extended Data Fig. 9a, b). Transcriptional analyses detected no compensatory change in other SLC25A members in *Slc25a44*-KD brown fat (Extended Data Fig. 9c, d). Similar to *Slc25a44*^{BAT}-KD mice, the BAT of *Slc25a44*-KD mice contained larger lipid droplets and higher levels of triglycerides compared with controls, whereas the morphology of WAT, liver, and muscle of *Slc25a44*-KD mice was normal (Extended Data Fig. 9e, f). Although we found no difference in the expression of *Ucp1* and genes associated with the fatty acid synthesis and oxidation pathway between the two groups, the core body temperature of *Slc25a44*-KD mice was significantly lower than in controls following cold exposure without affecting muscle shivering (Fig. 4e, Extended Data Fig. 9g–i). Tissue-temperature recording confirmed that noradrenaline-stimulated BAT thermogenesis was impaired in *Slc25a44*-KD mice (Extended Data Fig. 9j). Furthermore, Val oxidation in the BAT of *Slc25a44*-KD mice was lower than controls, indicating that SLC25A44 is the primary BCAA transporter in BAT (Fig. 4f). Of note, cold exposure failed to lower plasma BCAA concentration in *Slc25a44*-KD mice (Fig. 4g). These results indicate that SLC25A44 is required for cold-stimulated BAT thermogenesis and systemic BCAA clearance in vivo.

To determine the cell-autonomous function of SLC25A44 in brown adipocytes, we depleted *SLC25A44* in human brown preadipocytes using lentiviral shRNAs that target *SLC25A44* (Extended Data Fig. 10a, b). We found that *SLC25A44* depletion caused a significant reduction in noradrenaline-induced OCR in the presence of Val (Extended Data Fig. 10c, d). Supplementation with KIV or succinate, which bypasses mitochondrial BCAA transport, restored noradrenaline-induced OCR in *Slc25a44*-KO cells indicating that depletion of SLC25A44 did not cause a general mitochondrial defect (Fig. 4h, Extended Data Fig. 10e). In addition, SLC25A44-depleted brown adipocytes displayed active mitochondrial respiration (Extended Data Fig. 10f, g). Conversely,

overexpression of *Slc25a44* in mouse inguinal WAT-derived adipocytes or C2C12 myotubes significantly increased mitochondrial Val uptake and oxidation and cellular respiration (Fig. 4i, Extended Data Fig. 10h–m).

Discussion

The results of this study suggest the following model (Fig. 4j): in addition to glucose and fatty acids, cold stimuli potently increase mitochondrial BCAA uptake and oxidation in BAT, leading to enhanced BCAA clearance in the circulation. This process requires SLC25A44, a mitochondrial BCAA transporter in brown adipocytes. In turn, defective BCAA catabolism in BAT results in impaired BCAA clearance and thermogenesis, leading to the development of diet-induced obesity and glucose intolerance.

This model has important implications for the regulation of systemic BCAA metabolism in an obese or diabetic state, which results in impaired BAT activity and increased circulating BCAA in humans and rodents. It has been suggested that the accumulation of incompletely oxidized intermediates derived from BCAA oxidation, such as 3-hydroxyisobutyrate, causes insulin resistance[9,23,24]. Conversely, lowering circulating BCAA levels by inhibiting the kinase BDK or overexpression of the phosphatase PPM1K in the liver improves glucose tolerance independently for body-weight loss in rats[25]. Furthermore, reduced mitochondrial BCAA oxidation and subsequent intracellular accumulation of BCAA leads to constitutive activation of mTOR signalling, resulting in persistent IRS-1 phosphorylation by mTORC1 and inhibition of insulin signalling[6,23,26]. This study suggests a distinct yet non-mutually exclusive mechanism in which impaired BAT activity in conditions of obesity or diabetes reduces systemic BCAA clearance, whereas active BAT acts as a significant metabolic filter for circulating BCAA and protects against obesity and insulin resistance. Enhanced mitochondrial BCAA catabolism via SLC25A44 may serve as a promising strategy to improve systemic BCAA clearance and glucose homeostasis.

Online content

Any methods, additional references, Nature Research reporting summaries, source data, extended data, supplementary information, acknowledgements, peer review information; details of author contributions and competing interests; and statements of data and code availability are available at https://doi.org/10.1038/s41586-019-1503-x.

Received: 8 June 2018; Accepted: 22 July 2019;
Published online 21 August 2019.

1. Ouellet, V. et al. Brown adipose tissue oxidative metabolism contributes to energy expenditure during acute cold exposure in humans. *J. Clin. Invest.* **122**, 545–552 (2012).
2. Cypess, A. M. et al. Identification and importance of brown adipose tissue in adult humans. *N. Engl. J. Med.* **360**, 1509–1517 (2009).
3. Saito, M. et al. High incidence of metabolically active brown adipose tissue in healthy adult humans: effects of cold exposure and adiposity. *Diabetes* **58**, 1526–1531 (2009).
4. Bartelt, A. et al. Brown adipose tissue activity controls triglyceride clearance. *Nat. Med.* **17**, 200–205 (2011).
5. Chondronikola, M. et al. Brown adipose tissue activation is linked to distinct systemic effects on lipid metabolism in humans. *Cell Metab.* **23**, 1200–1206 (2016).
6. Newgard, C. B. et al. A branched-chain amino acid-related metabolic signature that differentiates obese and lean humans and contributes to insulin resistance. *Cell Metab.* **9**, 311–326 (2009).
7. Huffman, K. M. et al. Relationships between circulating metabolic intermediates and insulin action in overweight to obese, inactive men and women. *Diabetes Care* **32**, 1678–1683 (2009).
8. Wang, T. J. et al. Metabolite profiles and the risk of developing diabetes. *Nat. Med.* **17**, 448–453 (2011).
9. Lynch, C. J. & Adams, S. H. Branched-chain amino acids in metabolic signalling and insulin resistance. *Nat. Rev. Endocrinol.* **10**, 723–736 (2014).
10. Pietiläinen, K. H. et al. Global transcript profiles of fat in monozygotic twins discordant for BMI: pathways behind acquired obesity. *PLoS Med.* **5**, e51 (2008).
11. She, P. et al. Obesity-related elevations in plasma leucine are associated with alterations in enzymes involved in branched-chain amino acid metabolism. *Am. J. Physiol. Endocrinol. Metab.* **293**, E1552–E1563 (2007).
12. Lackey, D. E. et al. Regulation of adipose branched-chain amino acid catabolism enzyme expression and cross-adipose amino acid flux in human obesity. *Am. J. Physiol. Endocrinol. Metab.* **304**, E1175–E1187 (2013).
13. Herman, M. A., She, P., Peroni, O. D., Lynch, C. J. & Kahn, B. B. Adipose tissue branched chain amino acid (BCAA) metabolism modulates circulating BCAA levels. *J. Biol. Chem.* **285**, 11348–11356 (2010).
14. Neinast, M. D. et al. Quantitative analysis of the whole-body metabolic fate of branched-chain amino acids. *Cell Metab.* **29**, 417–429 (2019).
15. Shinoda, K. et al. Genetic and functional characterization of clonally derived adult human brown adipocytes. *Nat. Med.* **21**, 389–394 (2015).
16. Sustarsic, E. G. et al. Cardiolipin synthesis in brown and beige fat mitochondria is essential for systemic energy homeostasis. *Cell Metab.* **28**, 159–174 (2015).
17. Rosell, M. et al. Brown and white adipose tissues: intrinsic differences in gene expression and response to cold exposure in mice. *Am. J. Physiol. Endocrinol. Metab.* **306**, E945–E964 (2014).
18. Green, C. R. et al. Branched-chain amino acid catabolism fuels adipocyte differentiation and lipogenesis. *Nat. Chem. Biol.* **12**, 15–21 (2016).
19. Wallace, M. et al. Enzyme promiscuity drives branched-chain fatty acid synthesis in adipose tissues. *Nat. Chem. Biol.* **14**, 1021–1031 (2018).
20. Ohno, H., Shinoda, K., Ohyama, K., Sharp, L. Z. & Kajimura, S. EHMT1 controls brown adipose cell fate and thermogenesis through the PRDM16 complex. *Nature* **504**, 163–167 (2013).
21. Palmieri, F. The mitochondrial transporter family SLC25: identification, properties and physiopathology. *Mol. Aspects Med.* **34**, 465–484 (2013).
22. Tasic, B. et al. Site-specific integrase-mediated transgenesis in mice via pronuclear injection. *Proc. Natl Acad. Sci. USA* **108**, 7902–7907 (2011).
23. Newgard, C. B. Interplay between lipids and branched-chain amino acids in development of insulin resistance. *Cell Metab.* **15**, 606–614 (2012).
24. Jang, C. et al. A branched-chain amino acid metabolite drives vascular fatty acid transport and causes insulin resistance. *Nat. Med.* **22**, 421–426 (2016).
25. White, P. J. et al. The BCKDH kinase and phosphatase integrate BCAA and lipid metabolism via regulation of ATP-citrate lyase. *Cell Metab.* **27**, 1281–1293.e7 (2018).
26. Um, S. H., D'Alessio, D. & Thomas, G. Nutrient overload, insulin resistance, and ribosomal protein S6 kinase 1, S6K1. *Cell Metab.* **3**, 393–402 (2006).

METHODS

Human subjects. Thirty-three healthy young male volunteers were recruited in Sapporo, Japan to investigate the role of BAT in circulating BCAA clearance during cold exposure. All participants were carefully instructed regarding the study and provided written informed consent. The protocols were approved by the Institutional Research Ethics Review Board of Tenshi College (Sapporo, Japan) (UMIN000016361). Human BAT activity was assessed by ^{18}F-FDG-PET–CT scan (Aquiduo; Toshiba Medical Systems) after the standardized non-shivering cold exposure, as reported previously[27]. All the subjects have fasted for 12 h before ^{18}F-FDG-PET–CT scanning. Following cold exposure, the volunteers were given an intravenous injection of ^{18}F-FDG (1.66–5.18 MBq per kg (body weight)) and subsequently stayed in the same cold room for another 1 h. BAT activity was assessed by measuring the SUV of ^{18}F-FDG and Hounsfield Units from −300 to −10 in the supraclavicular region using Fusion software (Toshiba Medical Systems). On the basis of the median of BAT activity, subjects were divided into a high-BAT-activity group and a low-BAT-activity group. Arterialized blood samples were obtained from the same subject right before cold exposure and after 2 h cold exposure at 19 °C between 09:00 and 11:30. Sera were used for metabolite analysis. Amino acid levels were corrected for total amino acid levels by linear regression, since individual variation in the most of amino acids (85.3%) can be explained by total amino acids. To minimize possible effects of seasonal variation of BAT activities, the study was performed from January to March, during which the monthly average of ambient temperature in Sapporo was between −3.5 and 2.1 °C.

Animals. All the mouse experiments in this study were performed following the guidelines established by the UCSF Institutional Animal Care and Use Committee. Adult males and female mice aged 8–16 weeks had free access to food and water and were caged at 23 °C with 12-h light cycles and were used for the experiments. Mice were randomly assigned for the experimental groups at the time of purchase or weaning. For the generation of BAT-specific *Bckdha*-KO mice (*Bckdha*^{UCP1} mice), *Bckdha*-floxed mice were obtained from the European Mouse Mutant cell Repository (*Bckdha*$^{tm1a(EUCOMM)Hmgu}$) and crossed with *Ucp1-cre* mice[28]. For the generation of BAT-specific *Pparg*-KO mice, *Pparg*-floxed mice were obtained from the Jackson Laboratory (Stock #004584) and crossed with *Ucp1-cre* mice. Both knockout mice were on the C57BL/6 background.

For metabolic studies, male *Bckdha*^{UCP1}-KO and littermate control mice at eight weeks old were fed on a high-fat diet (HFD, 60% fat, D12492, Research Diets) at ambient temperature. Fat mass and lean mass were measured in mice on a high-fat diet for ten weeks by Body Composition Analyzer EchoMRI (Echo Medical Systems). For glucose tolerance test, the mice fed with high-fat diet for 10 weeks were fasted for 6 h (from 8:00 to 14:00) and injected intraperitoneally with glucose (1.5 g per kg (body weight)). For insulin tolerance test (ITT) experiments, the mice fed with high-fat diet for 11 weeks were fasted for 3 h (from 10:00 to 13:00) and injected intraperitoneally with insulin (0.875 U per kg (body weight)). Blood samples were collected at the indicated time points, and glucose levels were measured using blood glucose test strips (Abbott). BCAA tolerance test was performed in male *Bckdha*^{UCP1}-KO and control mice on a high-fat diet for ten weeks. For BCAA clearance test, mice were exposed to cold temperature under the fasting condition, and blood samples were obtained at the indicated time points. For BCAA tolerance test, mice were received a single bolus of BCAA oral gavage (500 mg per kg (body weight); weight ratio: Val:Leu:Ile, 1: 1.5: 0.8)[29] and were exposed to cold at 12 °C under the fasting condition. Blood was collected at the indicated time points and total plasma BCAA levels were measured by using a commercially available kit (ab83374, Abcam). Independently, plasma BCAA levels after 3 h oral BCAA gavage were quantified by flow-injection electrospray-ionization tandem mass spectrometry and quantified by isotope-dilution technique using a method described previously[30]. In brief, plasma samples were spiked with a cocktail of heavy-isotope internal standards (Cambridge Isotope Laboratories; CDN Isotopes), deproteinated with methanol, and esterified with butanol. Mass spectra for amino acid esters were obtained using neutral loss scanning methods. Ion ratios of analyte to the respective internal standard computed from centroided spectra were converted to concentrations using calibrators constructed from authentic amino acids (Sigma; Larodan) and dialysed fetal bovine serum (Sigma).

dCas9-KRAB mice were generated according to the method reported using a site-specific integrase-mediated approach as described[22]. In brief, transgenic mice dCas9-KRAB on the FVB background contain a CAG promoter within the *Hipp11* (H11) locus expressing the nuclease-deficient Cas9 fused to the zinc-finger protein 10 (ZNF10) Krüppel-associated box (KRAB) repressor domain[31], together with mCherry and the puromycin resistance cassette. dCas9-KRAB mice were backcrossed with wild-type C57BL/6J mice and subsequently crossed with gRNA-*Slc25a44* transgenic mice to generate *Slc25a44*-KD mice.

BAT-specific *Slc25a44*-KD (*Slc25a44*^{BAT}-KD) mice were generated by injecting adeno-associated virus (AAV) expressing gRNA-*Slc25a44* (AAV8-CAG-eGFP-U6-gRNA-long tracr; custom order, Vector Biolabs) or control GFP (AAV8-CAG-eGFP) into interscapular BAT following the published protocol[32]. In short, AAV was injected into the interscapular BAT of dCas9-KRAB adult mice at a viral titer of 6.0×10^{11} genomic copies (GC) per mouse. Fifty microlitres of AAV at a dose of 1.2×10^{10} GC μl^{-1} was injected in each BAT depot (5 μl per injection, 10 locations per depot). Efficacy of viral infection and knockdown was evaluated by immunohistochemistry for GFP and quantification of SLC25A44 expression level.

Chemicals and antibodies. All chemicals were obtained from Sigma-Aldrich unless otherwise specified. The following antibodies were used in this study: UCP1 antibody (ab-10983, Abcam), BCAT1 antibody (TA504360, OriGene), BCAT2 antibody (9432, Cell Signaling Tech), BCKDHA antibody (sc-271538, Santa Cruz), TOM20 antibody (11802-1-AP, Proteintech), COX-IV antibody (4850, Cell Signaling), OXPHOS cocktail (Abcam, ab110413), PDH-E1α antibody (sc-377092, Santa Cruz), PDH-E1α (pSer232) antibody (AP1063, Millipore), PDH-E1α (pSer293) antibody (ab177461, Abcam), PDH-E1α (pSer300) antibody (AP1064, Millipore), GAPDH antibody (sc-32233, Santa Cruz) and β-actin antibody (A3854, Sigma-Aldrich). Polyclonal antibody for SLC25A44 was generated by using the peptides (MEDKRNIQIIEWEHLDKKKC, MMQRKGEKMGRFQVC and CKKLSLRPELVDSRH) as epitopes for immunization in rabbit (GeneScript).

Cell culture. Brown adipocyte and beige adipocyte lines from C57BL/6 mice were established in our previous study[33]. Similarly, immortalized human brown adipocyte and white adipocyte lines were established previously[15]. Mouse adipocyte differentiation was induced by treating confluent preadipocytes with DMEM containing 10% FBS, 0.5 mM isobutylmethylxanthine, 125 nM indomethacin, 2 μg ml^{-1} dexamethasone, 850 nM insulin, 1 nM T3 and 0.5 μM rosiglitazone. Two days after induction, cells were switched to maintenance medium containing 10% FBS, 850 nM insulin, 1 nM T3 and 0.5 μM rosiglitazone. Mouse cells were fully differentiated 6–7 days after inducing differentiation. Immortalized human brown preadipocytes were cultured with animal component-free medium (Stem Cell Technologies; #05449). Brown adipocyte differentiation was induced by treating confluent preadipocytes with animal component free adipogenic differentiation medium (Stem Cell Technologies; #05412) supplemented with T3 (1 nM) and rosiglitazone (0.5 μM). Human cells were fully differentiated four weeks after induction. Mouse embryonic fibroblasts (MEF) were isolated from dCas9-KRAB mice and immortalized by infecting retrovirus expressing SV-Large T antigen. A mouse neuroblastoma line, Neuro2a (89121404, Sigma-Aldrich), was cultured in minimum essential medium Eagle (Sigma-Aldrich, M4655) containing 10% FBS, 1% non-essential amino acid solution (Sigma-Aldrich, M7145) and 1% penicillin–streptomycin solution on collagen-coated plates. C2C12 cells were differentiated into myotubes by culturing confluent cells with DMEM supplemented with 2% FBS and 850 nM insulin. HEK293S cells were infected with retrovirus expressing the C-terminal Flag-tagged *Slc25a44* or an empty vector and cultured in suspension with a FreeStyle 293 Expression Medium (Thermo Fisher; 12338018) supplemented with 2% FBS. HEK293 and C2C12 cells were purchased from ATCC. No commonly misidentified cell line was used in this study. All the cell lines were routinely tested negative for mycoplasma contamination.

Stable-isotope-labelled Leu metabolome analysis. To determine the metabolic fate and catabolic flux of Leu in brown adipocytes, we used [$^{13}C_6$, $^{15}N_1$]Leu tracing followed by CE-TOFMS (Agilent Technologies). Differentiated human brown adipocytes were incubated in the BCAA-free medium supplemented with 2 mM [$^{13}C_6$, $^{15}N_1$]Leu (608068, Sigma-Aldrich) and collected 1 h after the treatment with noradrenaline, washed twice with 10 ml of 5% mannitol aqueous solution, and subsequently incubated with 1 ml of methanol containing 25 μM internal standards (methionine sulfone, 2-(*N*-morpholino)-ethanesulfonic acid (MES) and D-camphor-10-sulfonic acid) for 10 min. Four hundred microlitres of the extracts were mixed with 200 μl Milli-Q water and 400 μl chloroform and centrifuged at 10,000*g* for 3 min at 4 °C. Subsequently, 400 μl of the aqueous solution was centrifugally filtered through a 5-kDa cut-off filter (Human Metabolome Technologies) to remove proteins. The filtrate was centrifugally concentrated and dissolved in 50 μl of Milli-Q water that contained reference compounds (200 μM each of 3-aminopyrrolidine and trimesate) immediately before metabolome analysis.

The concentrations of all the charged metabolites in samples were measured by CE-TOFMS, following the methods as previously reported[34]. In brief, a fused silica capillary (50 μm internal diameter × 100 cm) was used with 1 M formic acid as the electrolyte. Methanol:water (50% v/v) containing 0.1 μM hexakis (2,2-difluoroethoxy) phosphazene was delivered as the sheath liquid at 10 μl min^{-1}. Electrospray ionization (ESI)-TOFMS was performed in positive-ion mode, and the capillary voltage was set to 4 kV. Automatic recalibration of each acquired spectrum was achieved using the masses of the reference standards [(^{13}C isotopic ion of a protonated methanol dimer (2 MeOH + H)]$^+$, *m/z* 66.0632) and ([hexakis (2,2-difluoroethoxy) phosphazene + H]$^+$, *m/z* 622.0290). Quantification was performed by comparing peak areas to calibration curves generated using internal standardization techniques with methionine sulfone. The other conditions were identical to those described previously[34]. To analyse anionic metabolites, a commercially available COSMO(+) (chemically coated with cationic polymer) capillary (50 μm internal diameter × 105 cm) (Nacalai Tesque) was used with a

50 mM ammonium acetate solution (pH 8.5) as the electrolyte. Methanol–5 mM ammonium acetate (50% v/v) containing 0.1 μM hexakis (2,2-difluoroethoxy) phosphazene was delivered as the sheath liquid at 10 μl min^{-1}. ESI-TOFMS was performed in negative ion mode, and the capillary voltage was set to 3.5 kV. For anion analysis, trimesate and CAS were used as the reference and the internal standards, respectively. The other conditions were identical to those described previously[35]. MPE of isotopes, an index of isotopic enrichment of metabolites, was calculated as the percent of all atoms within the metabolite pool that are labelled according to the established formula[18,19]

DNA constructs for overexpression and knockdown studies. The lentiviral expression plasmid that encodes mouse *Slc25a44* open reading frame was obtained from GeneCopoeia (EX-Mm15289-Lv207-GS). The *Slc25a44* sequence was amplified from the lentiviral plasmid by PCR and cloned in-frame with a Flag sequence into the retroviral expression vector (Addgene, #75085). Lentiviral shRNA expression constructs targeting mouse *Slc25a44* and *Slc25a39* (sh*Slc25a44*, CS-MSH073484-LVRU6GH-01; sh*Slc25a39*, MSH034465-LVRU6GH; scrambled control, CSHCTR001-LVRU6GH), lentiviral shRNA expression constructs targeting human *SLC25A44* (sh*SLC25A44*, HSH057134-LVRH1H; scrambled control, CSHCTR001-LVRH1H), as well as lentiviral shRNA expression construct targeting mouse *Ucp1* were obtained from GeneCopoeia (sh*Ucp1*, MSH028473-LVRH1MH). For virus production, HEK293T packaging cells were transfected with 10 μg of lentiviral or retroviral plasmids and the packaging constructs (VSVg, pMDL, and Rev) using a calcium phosphate method. After 48 h, the viral supernatant was collected and filtered. Immortalized preadipocytes, Neuro2a or HEK293S cells were incubated overnight with the viral supernatant and supplemented with 10 μg ml^{-1} polybrene. Hygromycin at a dose of 50 or 200 μg ml^{-1} was used for selection of lentivirus-infected human cells and murine cells, respectively. Blasticidin at a dose of 10 μg ml^{-1} was used for selection of retrovirus-infected cells.

Generation of *Bckdha*-KO and *Slc25a44*-KO brown adipocytes. For generation of *Bckdha*-KO brown adipocytes, preadipocytes isolated from BAT of $Bckdha^{flox/flox}$ mice were immortalized by using the SV40 Large T antigen as described previously[15] and subsequently infected with retrovirus containing Cre (#34565, Addgene), followed by hygromycin selection at a dose of 200 μg ml^{-1}. For generation of *Slc25a44*-KO brown adipocytes, immortalized brown adipocyte cell line was infected with lentivirus packaged by lentiCRISPRv2 (#98291, Addgene) expressing Cas9 and gRNA for *Slc25a44* (5′-GGTGCTCCCACTCGATGATC-3′). After selection with 200 μg ml^{-1} hygromycin followed by isolating a monoclonal cell, we confirmed homozygous mutations in the *Slc25a44* genes by DNA sequencing.

RNA preparation, quantitative RT–PCR and RNA-sequencing. Total RNA was extracted from tissue or cells using RNeasy mini-kit (Qiagen) and cDNA was synthesized using iScript cDNA Synthesis kit (BioRad) according to the provided protocols. qRT–PCR was performed using an ABI ViiA7 PCR cycler. The primer sequences are listed in Supplementary Table 4. For RNA-sequencing, the libraries were constructed from total RNA and sequenced using a HiSeq 3000 instrument (Illumina) at the UCLA Technology Center for Genomics and Bioinformatics core by technical staff who were blinded to the experimental group. Sequenced tags were pseudo-aligned to mouse reference transcriptome. Transcript-levels estimated using Kallisto 0.44.0 were imported into R and expression levels per gene were estimated using the Bioconductor package tximport 1.10.0.

BCAA oxidation assay. Differentiated adipocytes in a six-well plate were washed with PBS and incubated in 1 ml Krebs–Ringer modified buffer (KRB)–HEPES buffer, containing 2% BSA, 15 mM glucose, 200 nM adenosine, and either 0.16 μCi ml^{-1} [1-^{14}C]Val together with 1 mM non-radioisotope (RI) Val or 0.16 μCi ml^{-1} [1-^{14}C]Leu together with non-RI 1 mM Leu, at 37 °C for 2 h. Subsequently, 350 μl 30% hydrogen peroxide was added in each well, and [^{14}C]CO_2 was trapped in the smears supplemented with 300 μl of 1 M benzethonium hydroxide solution at room temperature for 20 min. Similarly, isolated tissue (20–30 mg) was placed in a plypropylene round-bottom tube and incubated in the 1 ml KRB–HEPES buffer containing 0.16 μCi ml^{-1} [1-^{14}C]Val at 37 °C for 1 h. After adding 350 μl 30% hydrogen peroxide in the tube, [^{14}C]CO_2 was trapped in the centre well supplemented with 300 μl of 1 M benzethonium hydroxide solution for 20 min at room temperature. BCAA oxidation was quantified by counting radioactivity of trapped [^{14}C]CO_2 using a scintillation counter.

Mitochondrial amino acid uptake assay. Differentiated adipocytes in 10 cm culture plates were washed in cold PBS and incubated with KPBS at 4 °C for 10 min. Confluent Neuro2a cells were incubated with KPBS without washing in PBS to minimize cell loss. After removing KPBS, mitochondria were isolated by using a mitochondria isolation kit (Thermo Fisher; 89874) according to the provided protocol. Isolated mitochondria were incubated with KRB–HEPES buffer, containing 2% BSA, 15 mM glucose, 200 nM adenosine, and either 0.32 μCi ml^{-1} [U-^{14}C]Val, [U-^{14}C]Leu, [U-^{14}C]Ala, [U-^{14}C]Phe, [U-^{14}C]Thr, [U-^{14}C]Glu, [U-^{14}C]Asp, [U-^{14}C]Lys, [U-^{14}C]Arg (Moraveck), or [1-^{14}C]α-ketoisovalerate (American Radiolabelled Chemicals) at 37 °C for 1 h. After cooling down on ice, mitochondria were washed in chilled PBS three times and homogenized in 100 μl RIPA buffer. Mitochondrial amino acid uptake was quantified by counting radioactivity using a scintillation counter and normalized to protein content.

Liposome preparation. Egg phosphatidylcholine (1.280 ml, 25 mg ml^{-1} in $CHCl_3$, Avanti Polar Lipids, 840051), *E.coli* polar lipid (1.344 ml, 25 mg ml^{-1} in $CHCl_3$, Avanti Polar Lipids, 100600), and cardiolipin (0.640 ml, 10 mg m^{-1} in $CHCl_3$, Sigma-Aldrich, C0563) were mixed in round-bottomed flask. The solvent was removed by rotary evaporation under vacuum at room temperature to form a lipid film, and further dried under strong vacuum for at least 2 h to remove trace $CHCl_3$. Four millilitres of 10 mM PIPES buffer pH7.4, which contains 25 mM non-radioisotope Leu and Glu as internal substrates, was gently added to the dried lipid film. The flask was kept overnight at 4 °C to allow the formation of large unilamellar vesicles (LUVs), followed by incubating at 70 °C for 30 min. The LUVs were extruded seven times through an extruder (Avanti Polar Lipids, 610000), which was assembled with two drain disks separated with a 1.0-μm-pore polycarbonate membrane (GE Whatman, 889-78159). The extruded liposome was concentrated to 40 mg ml^{-1} lipid concentration in 10-kDa centrifugal filters (Millipore, UFC505024).

Mitochondrial liposome assay. Mitochondria were isolated from differentiated *Slc25a44*-KO brown adipocytes stably expressing either *Slc25a44* or an empty vector (90 plates per group). The mitochondrial membrane was obtained by mechanical disruption and sonication. Sonicated mitochondrial membranes (2 mg ml^{-1}) were fused with liposome (4 mg ml^{-1}) by incubating with 40 mM β-D-octyl glucoside (β-OG, Sigma-Aldrich, O8001) at 4 °C for 1 h in PIPES buffer containing non-radioactive Leu and Glu. After removal of β-OG by Bio-Beads SM-2 (Bio-Rad), mitochondrial liposomes were isolated on Sepharose 4B columns (Sigma-Aldrich, 4B-200) to remove the external substrates. Mitochondrial liposomes were trapped on 10-kDa centrifugal filters (Millipore, UFC505024), eluted in 1200 μl PIPES buffer without non-radioactive Leu or Glu, and then used for uptake assays. Transport of [$^{14}C_6$]Leu or [$^{14}C_5$]Glu was initiated by incubating mitochondrial liposomes with either 20 μM [$^{14}C_6$]Leu or 20 μM [$^{14}C_5$]Glu at 37 °C and stopped by filtering the reaction mixture with a vacuum manifold (0.45-μm pore size) at the indicated time points. Following six washes with 600 μl ice-cold PIPES buffer, uptake was quantified with a scintillation counter.

Proteoliposome assay. HEK293S cells stably expressing C-terminal Flag-tagged *Slc25a44* were cultured in 9 l suspension medium, collected and disrupted with a Dounce homogenizer in solubilization buffer (20 mM Tris-HCl, 100 mM NaCl, 10% glycerol, 1% DDM with 0.1% cholesteryl hemisuccinate (CHS, Anatrace, D310-CH210), EDTA-free protease inhibitor (Roche)), followed by solubilization at 4 °C for 1 h. After ultracentrifugation at 200,000*g* for 20 min, the supernatant was incubated with Flag M2 affinity gel (Sigma-Aldrich, A2220) at 4 °C for 2 h. The immunoprecipitates were washed five times with washing buffer (20 mM Tris-HCl, 500 mM NaCl, 10% glycerol, 0.1% DDM with 0.01% CHS), followed by competitive elution using Flag peptide (Sigma-Aldrich, F4799) in SEC buffer (20mM Tris-HCl, 100 mM NaCl, 10% glycerol, 0.1% DDM with 0.01% CHS). Purified SLC25A44–Flag (56 μg) was fused with liposome (8 mg) by incubating at 4 °C for 1 h in 2 ml PIPES buffer containing 25 mM non-radioactive Leu and Glu in the presence of 40 mM β-OG. Following removal of β-OG by Bio-Beads SM-2, proteoliposome was isolated on Sepharose 4B columns to remove the external substrates. Subsequently, the proteoliposomes were trapped on 10-kDa centrifugal filters, eluted in 1200 μl PIPES buffer without non-radioactive Leu or Glu, and then used for uptake assays. Transport of [$^{14}C_6$]Leu was initiated by incubating proteoliposomes with 20 μM [$^{14}C_6$]Leu at 37 °C and stopped by filtering the reaction mixture with vacuum manifold at the indicated time points. Following six washes with 600 μl ice-cold PIPES buffer, uptake was quantified by a scintillation counter.

Temperature recording. For core-body temperature recording experiments, rectal temperature of $Bckdha^{UCP1}$-KO and *Slc25a44*-KD mice was monitored using a TH-5 thermometer (Physitemp) up to 14 h after cold exposure. For tissue temperature recording, mice under anaesthesia were implanted with type T thermocouple probes in the interscapular BAT, inguinal WAT, liver, and skeletal muscle, according to the method that was described previously[33]. Tissue temperature was recorded by TC-2000 Meter (Sable Systems International). When tissue temperature was stable, mice were intraperitoneally administered noradrenaline at a dose of 1 mg per kg (body weight) to induce non-shivering thermogenesis.

Electromyography. Skeletal muscle shivering was assessed by using electromyography (EMG) recording, as reported in our previous study[33]. In brief, mice were placed in a restrainer to limit free movement, and 29-gauge needle electrodes were placed the back muscles of mice. The EMG signal was processed (low-pass filter, 3 kHz; high-pass filter,10 Hz; notch filter, 60 Hz) and amplified 1,000 × with Bio Amp (ADInstruments). EMG data were collected from the implanted electrodes at a sampling rate of 2 kHz using LabChart 8 Pro Software (ADInstruments). The raw signal was converted to root mean square (RMS) activity. RMS activity was analysed for shivering bursts in 10-s windows. For monitoring muscle shivering in humans, EMG at the pectoral muscle was recorded by using a surface EMG (Polymate II; TEAC). EMG was recorded for 10 min at 27 °C before cold exposure, and for another 10 min at 19 °C during the 2 h cold exposure.

^{18}F-Fluciclovine-PET–CT scan. ^{18}F-Fluciclovine (100 μCi) was administered to male wild-type mice (C57Bl6/J) at 14–15 weeks of age via a tail-vein injection under 2% isoflurane anaesthesia after 6 h fasting. Mice were acclimatized to either 30 °C or cold temperature at 15 °C for 2 weeks. ^{18}F-Fluciclovine-uptake (SUV) was measured every minute immediately after tail vein injection using micro-PET–CT imaging system at the UCSF PET–CT Imaging Core Facility. Changes in SUV were quantified starting from the first 60 s after ^{18}F-Fluciclovine injection by using software AMIDE 1.0.4 (Amide).

Oxygen consumption assays. OCR in cultured adipocytes was measured using the Seahorse XFe Extracellular Flux Analyzer (Agilent) in a 24-well plate. For measurement of noradrenaline-induced respiration in the presence and absence of BCAA, differentiated adipocytes were maintained in KRB–HEPES buffer containing 15 mM glucose, 200 nM adenosine, and 2% BSA. During OCR measurement, cells were treated with 2 mM BCAA (Val, Leu, or Ile), 2 mM KIV, 10 mM succinate, or vehicle, and subsequently treated with noradrenaline (1 μM) at the indicated time point. For the mitochondrial stress test, differentiated brown adipocytes in a 24-well plate were pretreated with 300 μM clofibrate, a BCAT2 activator, and subjected to respiratory assay. During OCR measurement, cells were treated with oligomycin (5 μM), carbonyl cyanide 4-(trifluoromethoxy) phenylhydrazone (FCCP, 5 μM) and antimycin (5 μM).

Mitochondrial electron transport activity. Mitochondrial electron transport (ETC) activity was assessed as reported previously[36]. In brief, mitochondria were isolated from BAT of mice using a Comitial Kit (Ab110168, Abcam) and were resuspended in 300 μl of isolation buffer provided by the kit. After protein quantification by the BCA method, the mitochondrial suspension was diluted with isolation buffer at concentration 0.1 mg ml^{-1}, seeded into a 24-well plate (5 μg per 50 μl per well), and adhered to the bottom of the plate by centrifugation 2,000*g* at 4 °C for 20 min using microplate rotor adaptor. Immediately before the measurement, 450 μl mitochondrial assay buffer and substrates supplemented with 10 mM pyruvate, 5 mM malate, 50 mM KCl, 4 mM KH_2PO_4, 5 mM HEPES, 1 mM EGTA and 4% fatty-acid-free BSA was added to each well. During OCR measurement by the Seahorse XFe Extracellular Flux Analyzer, mitochondria were treated with 2 μM rotenone, 10 mM succinate, 5 μM antimycin A and 100 μM *N*,*N*,*N*′,*N*′-tetramethyl-*p*-phenylenediamine (TMPD) with 10 mM ascorbate at the indicated time points.

PDH activity and BCKDH activity assays. Tissue lysate was prepared by homogenizing BAT in ice-cold PBS buffer containing cOmplete Protease Inhibitor Cocktail (Roche) and 5 mM NaF. Two hundred micrograms of BAT lysates were applied to measure PDH enzymatic activities by a commercially available kit (Abcam, ab109902). The BCKDH activity measurement was performed as previously described[37].

Glucose oxidation assay. Differentiated adipocytes in a six-well plate were incubated in DMEM containing 2% FBS for 2 h. After washing in PBS, cells were incubated in 1 ml of KRB–HEPES buffer containing 2% BSA, 15 mM glucose, 200 nM adenosine, and 0.5 μCi ml^{-1} [1-^{14}C]glucose, supplemented with or without 1 mM Val, at 37 °C for 2 h. Subsequently, 350 μl 30% hydrogen peroxide was added in each well, and [^{14}C]CO_2 was trapped in the smears supplemented with 300 μl 1 M benzethonium hydroxide solution at room temperature for 20 min. For the assay in tissues, mice were fasted for 6 h and euthanized. Isolated tissue (20–30 mg) was placed in a plypropylene round-bottom tube and incubated in the 1 ml KRB/HEPES buffer containing 1.0 μCi ml^{-1} [1-^{14}C]glucose at 37 °C for 1 h. After adding 350 μl 30% hydrogen peroxide in the tube, [^{14}C]CO_2 was trapped in the centre well supplemented with 300 μl of 1 M benzethonium hydroxide solution for 20 min at room temperature. Glucose oxidation was quantified by counting radioactivity of trapped [^{14}C]CO_2 using a scintillation counter.

Fatty acid oxidation assay. Differentiated adipocytes were plated in a six-well plate and incubated in medium containing 2% FBS for 4 h. After washing in PBS, the cells were incubated in 1 ml of KRB–HEPES buffer, containing 15 mM glucose, 0.1 mM oleic acid, and 0.5 μCi ml^{-1} [1-^{14}C]oleic acid bound to 2% BSA and 100 μM carnitine, supplemented with or without 1 mM Val, for 2 h at 37 °C. Then, 350 μl 30% hydrogen peroxide was added in each well to trap [^{14}C]CO_2 in the smears supplemented with 300 μl of 1 M benzethonium hydroxide solution. For the assay in tissues, mice were fasted for 4 h and euthanized. Isolated tissue (20–30 mg) was placed in a polypropylene round-bottom tube and incubated in the 1 ml KRB–HEPES buffer containing 1.0 μCi ml^{-1} [1-^{14}C]oleic acid at 37 °C for 1 h. After adding 350 μl 30% hydrogen peroxide in the tube, [^{14}C]CO_2 was trapped in the centre well supplemented with 300 μl of 1 M benzethonium hydroxide solution for 20 min at room temperature. Oleic acid oxidation was quantified by counting radioactivity of trapped [^{14}C]CO_2 using a scintillation counter.

Immunoblotting. Protein lysates from isolated tissues or cultured cells were extracted using Qiagen TissueLyzer LT and RIPA lysis and extraction buffer (Thermo Fisher) and cOmplete protease inhibitors (Roche). Tissue lysates were applied to immunoblot analysis using the UCP1 antibody (1:2,000), BCAT1 antibody (1:1,000), BCAT2 antibody (1:1,000), BCKDHA antibody (1:2,000), TOM20 antibody (1:2,000), COX-IV antibody (1:2,000), OXPHOS cocktail (1:2,000), PDH-E1α antibody (1:1,000), PDH-E1α (pSer232) antibody (1:1,000), PDH-E1α (pSer293) antibody (1:1,000), PDH-E1α (pSer300) antibody (1:1,000), and SLC25A44 antibody (1:1,000). β-actin (1:10,000) and GAPDH (1:2,000) were used as a loading control for each sample.

Tissue histology and immunostaining. For H&E staining, tissues of mice were fixed in 4% paraformaldehyde overnight at 4 °C, followed by dehydration in 70% ethanol. After the dehydration procedure, tissues were embedded in paraffin, sectioned at a thickness of 5 μm, and stained with H&E following the standard protocol. For immunostaining, paraffin-embedded tissues were deparaffinized twice in xylene and subsequently rehydrated. After incubating the slides for 20 min in boiling water, the tissues were blocked in PBS containing 2% BSA for 60 min. After washing in PBS, the slides were incubated with the primary antibody (chicken anti-mouse GFP, 1:200) overnight at 4 °C, followed by incubation with the fluorescence-conjugated second antibody (goat anti-chicken IgG Alexa Fluor 488 green, 1:500) for 1 h at room temperature. After washing, the sections were stained with DAPI and mounted with mounting medium (Cytoseal 60, Thermo-Scientific). Images of tissue samples were captured using the Inverted Microscope Leica DMi8.

Statistical analyses. All data were expressed as mean ± s.e.m. and analysed with statistical software (SPSS 25.0; IBM). The sample size was determined by the power analysis with $\alpha = 0.05$ and power of 0.8, and based on our experience with experimental models, anticipated biological variables and previous studies. The metabolite analyses in human sera and mouse plasma, the [$^{13}C_6$, $^{15}N^1$]Leu tracing in human brown adipocytes, the PET–CT examination using ^{18}F-FDG (in humans) or ^{18}F-fluciclovine (in mice), and GTT and ITT in mice fed high-fat diet were performed by researchers who were blinded to the experimental groups. RNA sequencing and library constructions were performed by technical staff at the UCLA genome core who were blinded to the experimental groups. RNA sequencing alignment were performed by researchers who were blinded to the experimental groups. Blinding was not relevant to the other experiments in mice or cells because mice or cells had to be genotyped by PCR. Comparisons between the two groups were analysed using the paired *t*-test or the Student's *t*-test, as appropriate. One-way or two-way ANOVA followed by Tukey's post hoc test or post hoc paired/unpaired *t*-tests with Bonferroni's correction was used for multiple group comparisons. One-way or two-way repeated measures ANOVA was used for the comparisons of repeated measurements. Pearson's and Spearman's correlation coefficients were used to determine normally distributed variables and non-normally distributed variables, respectively. One-tailed paired *t*-test was used to analyse qRT–PCR validation of human BAT biopsy RNA-seq data. For all other experiments, two-tailed *P* value was calculated; $P<0.05$ was considered statistically significant.

Reporting summary. Further information on research design is available in the Nature Research Reporting Summary linked to this paper.

Data availability

The RNA-seq data generated in this study are available at Array Express under the accession code E-MTAB-7987. ^{13}C-Leu tracing data are available in Supplementary Table 3. Uncropped immunoblot images are available in Supplementary Fig. 1. The other datasets that support the findings of this study are available in Supplementary Information and Source Data.

27. Yoneshiro, T. et al. Recruited brown adipose tissue as an antiobesity agent in humans. *J. Clin. Invest.* **123**, 3404–3408 (2013).
28. Kong, X. et al. IRF4 is a key thermogenic transcriptional partner of PGC-1α. *Cell* **158**, 69–83 (2014).
29. Li, T. et al. Defective branched-chain amino acid catabolism disrupts glucose metabolism and sensitizes the heart to ischemia–reperfusion injury. *Cell Metab.* **25**, 374–385 (2017).
30. Ferrara, C. T. et al. Genetic networks of liver metabolism revealed by integration of metabolic and transcriptional profiling. *PLoS Genet.* **4**, e1000034 (2008).
31. Gilbert, L. A. et al. CRISPR-mediated modular RNA-guided regulation of transcription in eukaryotes. *Cell* **154**, 442–451 (2013).
32. Balkow, A. et al. Direct lentivirus injection for fast and efficient gene transfer into brown and beige adipose tissue. *J. Biol. Methods* **3**, e48 (2016).
33. Ikeda, K. et al. UCP1-independent signaling involving SERCA2b-mediated calcium cycling regulates beige fat thermogenesis and systemic glucose homeostasis. *Nat. Med.* **23**, 1454–1465 (2017).
34. Soga, T. et al. Differential metabolomics reveals ophthalmic acid as an oxidative stress biomarker indicating hepatic glutathione consumption. *J. Biol. Chem.* **281**, 16768–16776 (2006).
35. Soga, T. et al. Metabolomic profiling of anionic metabolites by capillary electrophoresis mass spectrometry. *Anal. Chem.* **81**, 6165–6174 (2009).
36. Das, K. C. Hyperoxia decreases glycolytic capacity, glycolytic reserve and oxidative phosphorylation in MLE-12 cells and inhibits complex I and II function, but not complex IV in isolated mouse lung mitochondria. *PLoS One* **8**, e73358 (2013).
37. White, P. J. et al. Branched-chain amino acid restriction in Zucker-fatty rats improves muscle insulin sensitivity by enhancing efficiency of fatty acid oxidation and acyl-glycine export. *Mol. Metab.* **5**, 538–551 (2016).

Acknowledgements We thank C. B. Newgard for the initial metabolomics analysis, E. Kunji for liposome study, Y. Seo and T. Huynh for the PET–CT scan, Y. Cheng and E. Green for HEK293S cells, E. T. Chouchani and E. Mills for cell respiration studies, and X. Lu and K. Shinoda for technical help. This work was supported by the NIH (DK97441 and DK112268) and the Edward Mallinckrodt Jr. Foundation to S.K., the American Diabetes Association Pathways Award (1-16-INI-17) to P.J.W., the AMED–CREST from the Japan Agency for Medical Research and Development to T.S., and the NIH (U19CA179513 and P30 DK063720) to M.T.M. T.Y. and M.K. are supported by the JSPS Fellowships.

Author contributions T.Y. designed and carried out overall experiments and analysed data. Q.W. designed and performed cellular experiments and liposome assays and interpreted data. K.T. and C.H.S. performed mouse experiments. M.M. and M.C. carried out human studies and analysed the data with M.S. and L.S. H. Maki, K. Igarashi, A.U. and M.O. performed BCAA-tracing studies and analysed the data with T.S. Z.D., M.K., H.L. and H. Majd performed liposome assays and analysed the data with F.C.S. P.J.W., R.W.M., O.R.I. and Y.D. measured amino acids in mice and BCKDH activity. Y.O., K. Ikeda, K.K., Y.C., M.Y. and Z.B. assisted with mouse experiments and cultured cell studies. R.N.P. conducted RNA-sequencing analysis. V.J.G. and M.T.M. developed dCas9–KRAB mice. H.T., T.G. and T.K. assisted with quantification of metabolites in human sera. S.K. conceived the project and directed the research. S.K. and T.Y wrote the paper with input from all the authors.

Competing interests The authors declare no competing interests.

Additional information

Supplementary information is available for this paper at https://doi.org/10.1038/s41586-019-1503-x.
Correspondence and requests for materials should be addressed to S.K.
Peer review information *Nature* thanks Ferdinando Palmieri, Yibin Wang and the other, anonymous, reviewer(s) for their contribution to the peer review of this work.
Reprints and permissions information is available at http://www.nature.com/reprints.

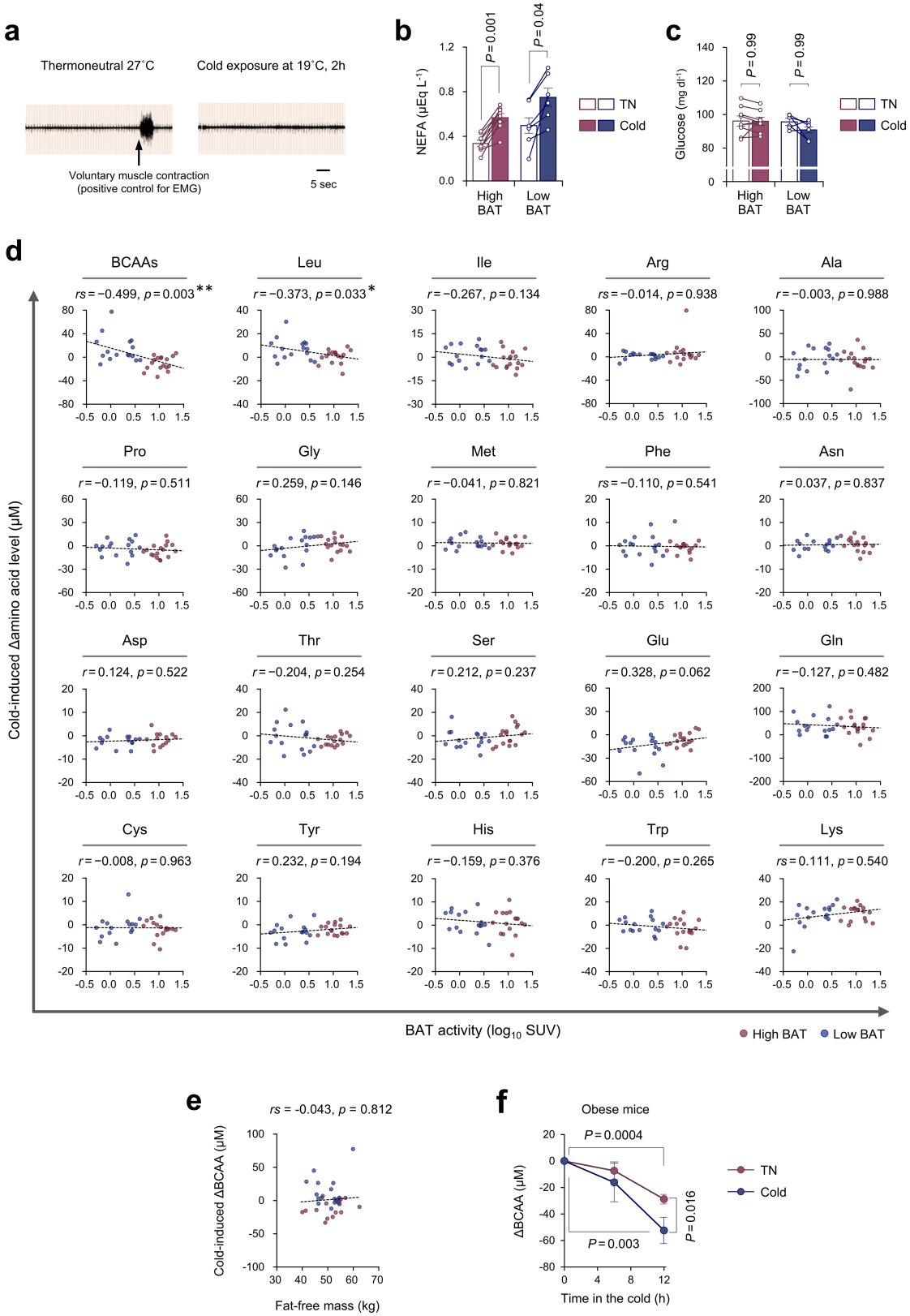

Extended Data Fig. 1 | Cold-induced changes in circulating metabolites in mice and humans. a, Representative EMG in adult humans at 27 °C and following cold exposure at 19 °C for 2 h. Voluntary muscle contraction as a positive control of EMG recording. **b**, **c**, Serum non-esterified fatty acids (NEFA) (**b**) and blood glucose (**c**) levels in high- ($n = 9$) and low-BAT subjects ($n = 6$) at thermoneutral 27 °C (TN) and following cold exposure at 19 °C. **d**, Correlation between BAT activity (SUV, $\log_{10}$) and cold-induced changes in serum amino acid levels of high- (red dots) and low-BAT subjects (blue dots). $n = 33$ per group (all amino acids) except $n = 29$ (Asp). **e**, Correlation between fat-free mass (kg) and changes in serum total BCAAs in **d**. $n = 33$. **f**, Changes in plasma BCAA levels at thermoneutral (30 °C) or cold exposure (15 °C) in diet-induced obese mice. $n = 8$ (TN), $n = 7$ (cold). **b**–**f**, Biologically independent samples. Data are mean ± s.e.m.; two-sided P values by paired t-test (**b**, **c**) or two-way repeated-measures ANOVA followed by post hoc paired or unpaired t-tests with Bonferroni's correction (**f**). Pearson's (r) or Spearman's rank correlation coefficient (rs) was calculated, as appropriate (**d**, **e**).

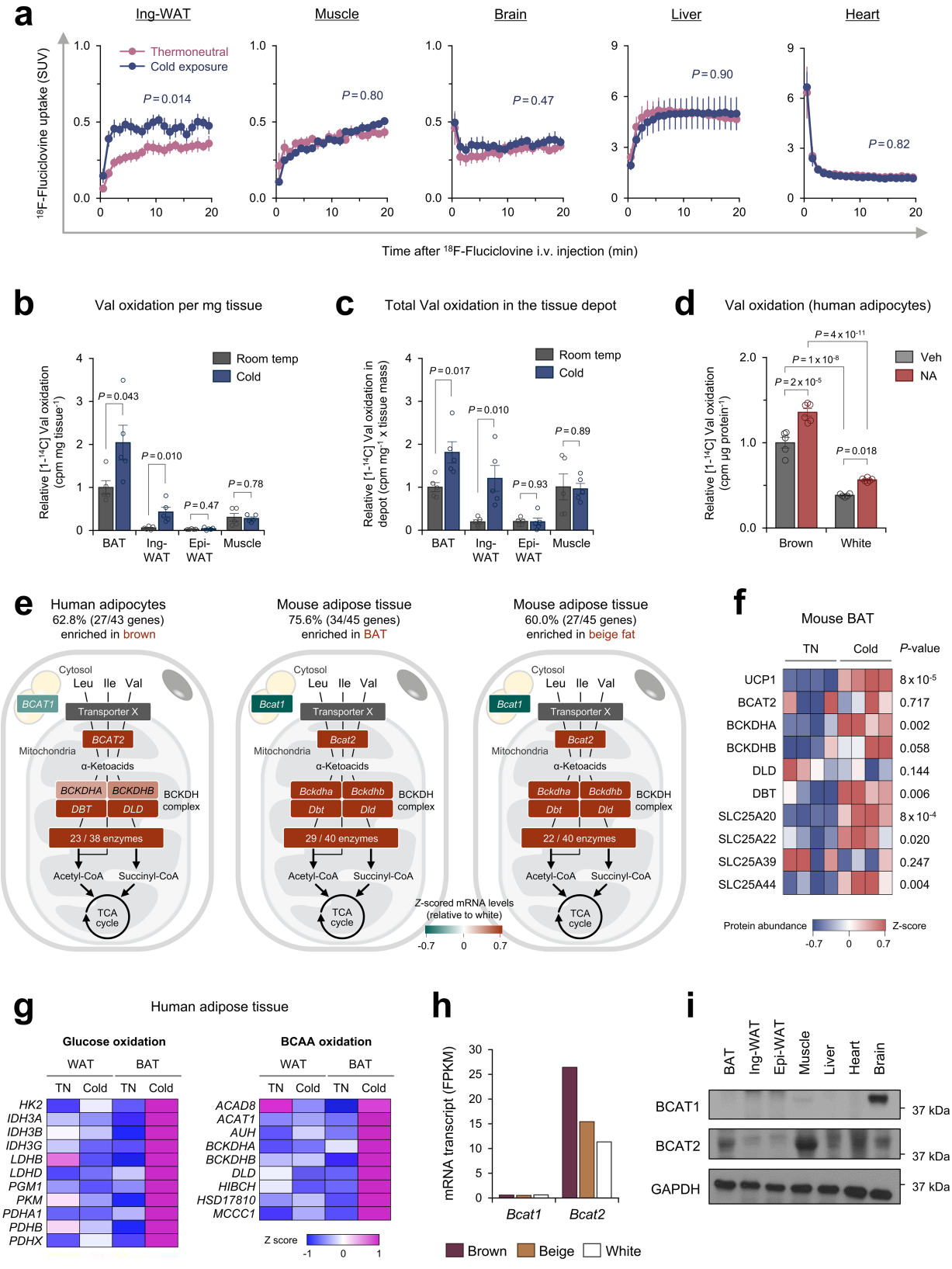

Extended Data Fig. 2 | See next page for caption.

Extended Data Fig. 2 | The BCAA catabolic pathway in human and mouse adipose tissues. a, ^{18}F-Fluciclovine-uptake into indicated organs determined by dynamic PET scanning. $n = 5$ per group. **b**, Val oxidation (per mg tissue) in indicated tissues of mice acclimatized to 23 °C or 12 °C for one week. $n = 5$ per group. **c**, Total Val oxidation in (**b**). Total Val oxidation was calculated by multiplying Val oxidation per mg tissue (cpm per mg tissue) and tissue mass of the depot (mg). **d**, Val oxidation normalized to total protein (μg) in human brown adipocytes and white adipocytes following 2-h treatment with noradrenaline or vehicle. $n = 5$ (Veh), $n = 6$ (noradrenaline). **e**, Expression profile of BCAA catabolic enzymes enriched in brown and beige fat relative to white fat of humans (left) and mouse (middle, right). Data were obtained from a previous RNA-seq dataset in humans[15] and a microarray dataset in mice[17]. The profiles were mapped onto the KEGG BCAA catabolic pathway. The number of brown and beige-enriched enzymes among total BCAA catabolic enzymes is shown. $n = 3$ per group. **f**, Proteomic profile of indicated enzymes in the BCAA oxidation pathway and mitochondrial carriers (SLC25A families) in interscapular BAT of mice at thermoneutrality (29 °C) or 5 °C for 3 weeks[16]. $n = 4$ per group. **g**, Transcriptional profile of indicated genes in the glucose oxidation pathway (left) and the BCAA oxidation pathway (right) in the supraclavicular BAT and abdominal WAT from the identical subject under a thermoneutral condition (27 °C) and after cold exposure at 19 °C (ref. [5]). The colour scale represents *Z*-scored FPKM (fragments per kilobase of exon per million fragments mapped). **h**, mRNA expression level (FPKM) of *Bcat1* and *Bcat2* in differentiated brown adipocytes, beige adipocytes and white adipocytes. The transcriptome data are from a previous RNA-seq dataset[15]. **I**, Immunoblotting of BCAT1 and BCAT2 in indicated tissues of mice kept at ambient temperature. GAPDH as a loading control. Representative result from two independent experiments. Gel source data are in Supplementary Fig. 1. **a**–**h**, biologically independent samples. Data are mean ± s.e.m.; two-sided *P* values by unpaired Student's *t*-test (**b**, **c**, **f**), two-way repeated measures ANOVA (**a**), or two-way factorial ANOVA followed by Tukey's post hoc test (**d**).

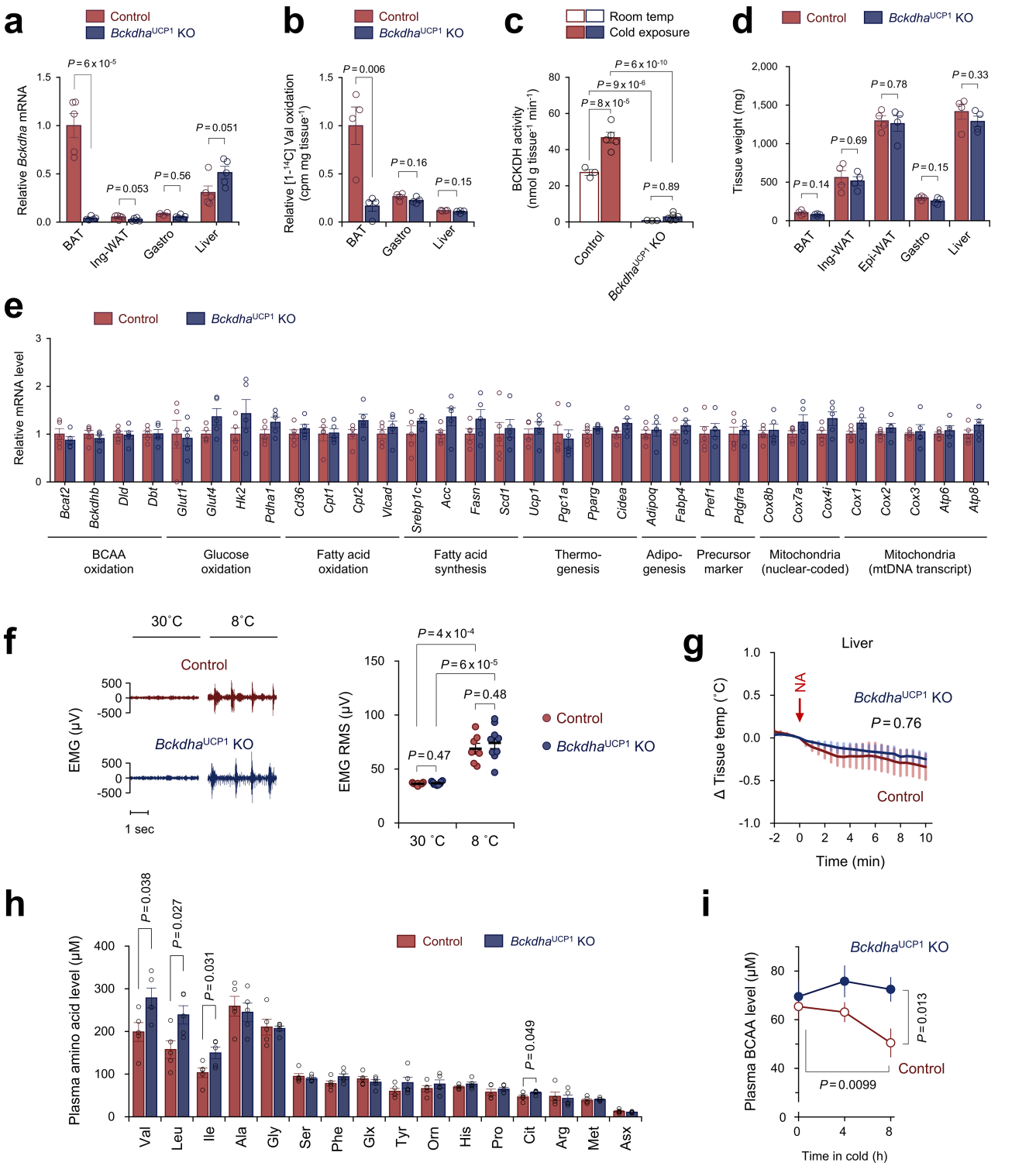

Extended Data Fig. 3 | Characterization of BAT-specific *Bckdha*-KO mice. a, mRNA expression of *Bckdha* in BAT of *Bckdha*^{UCP1}-KO and littermate control mice. $n = 5$ per group for all groups except $n = 3$ for control-gastrocnemius. **b**, Val oxidation normalized to tissue weight (in mg) in indicated tissues of mice in **a**. $n = 4$ per group. **c**, Enzymatic activity of BCKDH complex (KIV oxidation) in BAT of control and *Bckdha*^{UCP1}-KO mice acclimatized to 23 °C ($n = 3$ per group) or 12 °C (control $n = 5$, KO $n = 6$) for one week. **d**, Tissue weights of mice in (**a**) on a normal chow at ambient temperature. $n = 4$ per group. **e**, mRNA expression of indicated genes in BAT of mice in **a**. $n = 5$ per group. **f**, EMG of muscle shivering in control ($n = 7$) and *Bckdha*^{UCP1}-KO mice ($n = 9$) at 30 °C or 8 °C. The right graph shows quantitative root mean square (RMS) of EMG. **g**, Liver temperature of control and *Bckdha*^{UCP1}-KO mice following noradrenaline treatment. $n = 4$ per group. **h**, Plasma amino acid levels after 3 h BCAA oral gavage. $n = 5$ per group. **i**, Plasma BCAA concentration of control ($n = 7$) and *Bckdha*^{UCP1}-KO mice ($n = 9$) following cold exposure at 8 °C. **a**–**i**, Biologically independent samples. Data are mean ± s.e.m.; two-sided *P* values by unpaired Student's *t*-test (**a**, **b**, **d**, **e**, **h**), two-way factorial ANOVA followed by Tukey's post hoc test (**c**), or two-way repeated measures ANOVA (**f**, **g**, **i**) followed by post hoc paired or unpaired *t*-tests with Bonferroni's correction (**f**, **i**).

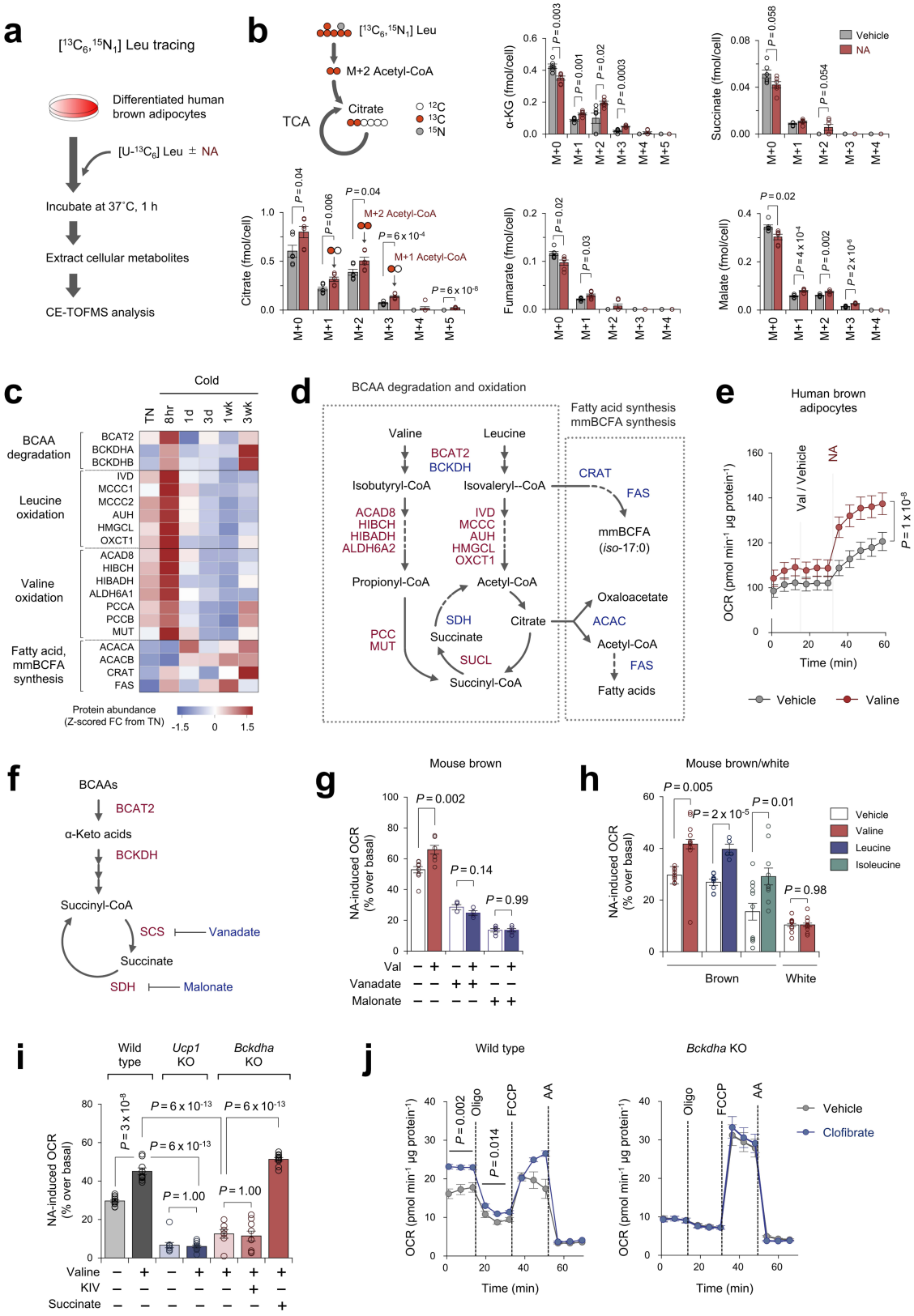

Extended Data Fig. 4 | See next page for caption.

Extended Data Fig. 4 | The effect of noradrenaline on BCAA metabolism in brown adipocytes. a, Scheme of the metabolic tracer experiment in human brown adipocytes. Cells were treated with vehicle or noradrenaline for 1 h in the presence of [$^{13}C_6$, $^{15}N_1$]Leu. **b**, Isotopologue distributions of TCA intermediates from [$^{13}C_6$, $^{15}N_1$]Leu in **a**. $n = 6$ per group. **c**, Protein expression of indicated BCAA catabolic enzymes at indicated time points of cold acclimatization. The expression profile is analysed in the proteomics dataset[16]. $n = 4$ (TN, cold 3 weeks), $n = 3$ (cold 8 h, 1 day, 3 days, 1 week). **d**, The BCAA catabolic pathway that indicates Val and Leu catabolic enzymes. Enzymes whose protein expression was transiently upregulated by acute cold exposure were highlighted in red on the basis of the results in **c**. Enzymes whose protein expression was gradually upregulated following chronic cold adaptation are highlighted in blue. **e**, OCR normalized to total protein (in μg) in human brown adipocytes. Differentiated adipocytes in the BCAA-free medium were supplemented with Val or vehicle, and subsequently stimulated with noradrenaline. $n = 10$ per group. **f**, Schematics of the mitochondrial Val catabolic pathway. Vanadate and malonate inhibit succinyl coenzyme A synthetase and succinate dehydrogenase, respectively. **g**, Noradrenaline-induced OCR in the presence and absence of Val in mouse brown adipocytes. Following pretreatment with vanadate (50 μM) or malonate (5 mM), differentiated cells in the BCAA-free medium were supplemented with Val or vehicle, and subsequently treated with noradrenaline. $n = 9$ (vehicle), $n = 8$ (Val), $n = 4$ (vehicle + vanadate, Val + vanadate), $n = 5$ (vehicle + malonate, Val + malonate). **h**, Noradrenaline-induced OCR in the presence and absence of BCAAs in mouse brown and white adipocytes. Differentiated cells were supplemented with indicated amino acids, and subsequently treated with 1 μM noradrenaline. Brown adipocytes: $n = 10$ (Val−, Val+, Ile+), 9 (Leu−), 5 (Leu+) and 11 (Ile−). White adipocytes: $n = 9$ (Val−) and 10 (Val+). **i**, Noradrenaline-induced OCR in the presence and absence of Val in wild-type, *Ucp1*-KO and *Bckdha*-KO brown adipocytes. *Bckdha*-KO brown adipocytes were treated with 2 mM KIV, 10 mM succinate or vehicle before noradrenaline stimulation. Wild type: $n = 10$ (Val−) and 9 (Val+). *Ucp1*-KO: $n = 10$ (Val−, Val+). *Bckdha* KO: $n = 7$ (Val+), 9 (Val+; KIV+) and 10 (Val+; succinate+). **j**, OCR normalized to total protein (μM) in wild-type (left) and *Bcdkha*-KO brown adipocytes (right). Differentiated adipocytes were pretreated with BCAT2 activator, clofibrate (300 μM), or vehicle. Following measurement of basal OCR, cells were treated with oligomycin (5 μM), FCCP (5 μM), and antimycin A (AA, 5 μM). Wild type: $n = 5$ per group. *Bckdha* KO: $n = 7$ per group. **b**, **c**, **e**, **g**–**j**, Biologically independent samples. Data are mean ± s.e.m.; two-sided *P* values by unpaired Student's *t*-test (**b**, **g**, **h**), one-way factorial ANOVA followed by Tukey's post hoc test (**i**) or two-way repeated measures ANOVA (**e**, **j**).

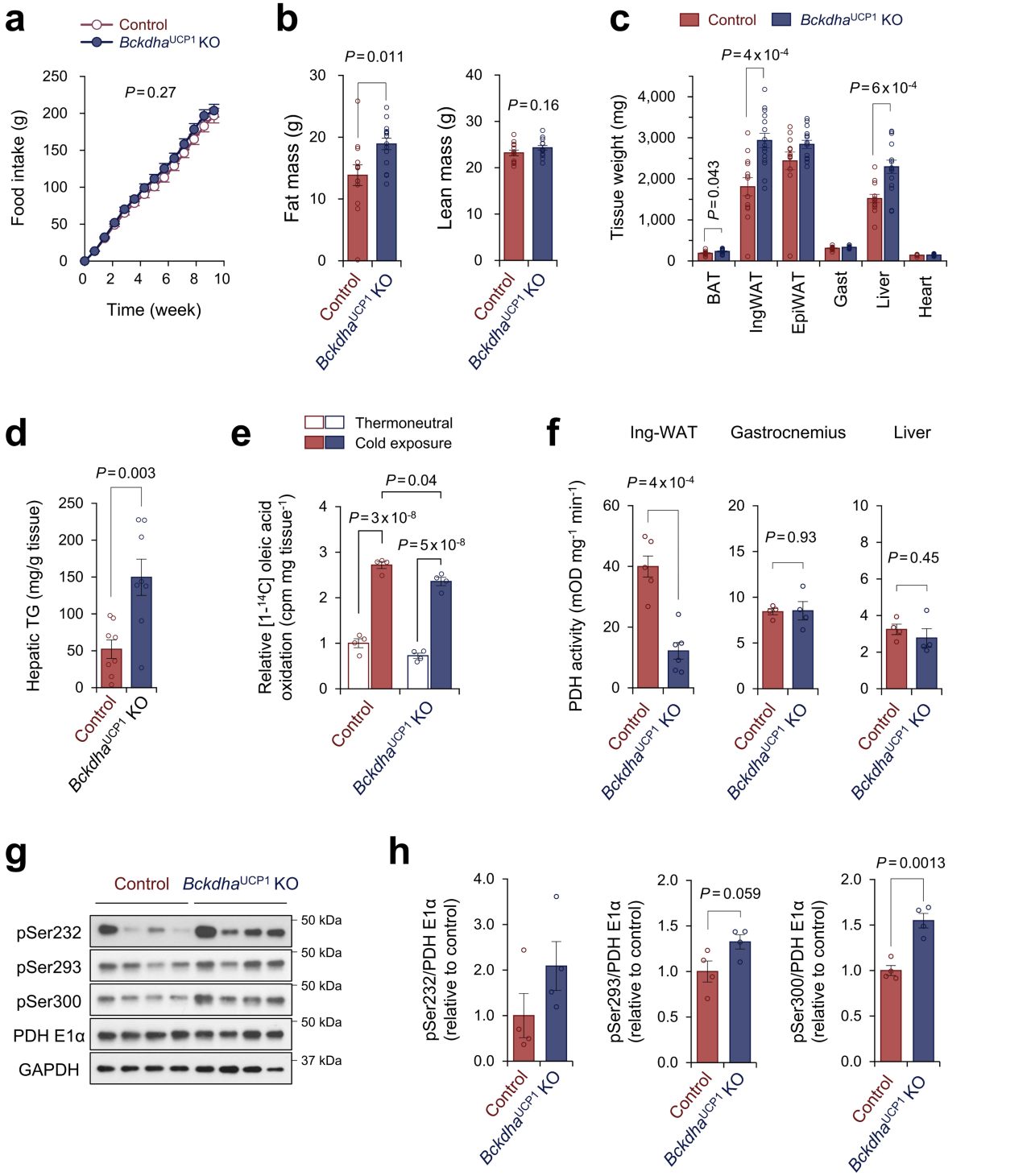

Extended Data Fig. 5 | Metabolic characterization of *Bckdha*^{UCP1}-KO mice. **a**, Cumulative food intake of *Bckdha*^{UCP1}-KO mice ($n = 15$) and littermate controls ($n = 13$) on high-fat diet. **b**, Fat mass and lean mass of mice in **a** at 10 weeks of high-fat diet. **c**, Tissue weights of mice in **a**. **d**, Triglyceride (TG) content in the liver of mice in **a**. $n = 8$ per group. **e**, Oleic acid oxidation normalized to tissue mass (mg) in the interscapular BAT of mice acclimatized to thermoneutral 30 °C or cold exposure at 12 °C. $n = 4$ per group. **f**, PDH activity in the inguinal WAT, gastrocnemius muscle and liver of *Bckdha*^{UCP1}-KO mice and littermate controls that were exposed to cold at 12 °C for 1 week. Inguinal WAT (Ing-WAT): $n = 5$ (control) and 6 (*Bckdha*^{UCP1}-KO). Gastrocnemius, liver: $n = 4$ per group. **g**, Immunoblotting for PDH-E1α(pSer232), PDH-E1α(pSer293), PDH-E1α(pSer300), and total PDH-E1α in the BAT of the control and *Bckdha*^{UCP1}-KO mice. GAPDH as a loading control. $n = 4$ per group. Uncropped immunoblot images of are available in Supplementary Fig. 1. **h**, Quantification of phosphorylated PDH-E1α normalized to total PDH-E1α protein level in **g**. **a**–**h**, Biologically independent samples. Data are mean ± s.e.m.; two-sided *P* values by unpaired Student's *t*-test (**b**-**d**, **f**, **h**), two-way repeated measures ANOVA (**a**) or two-way factorial ANOVA followed by Tukey's post hoc test (**e**).

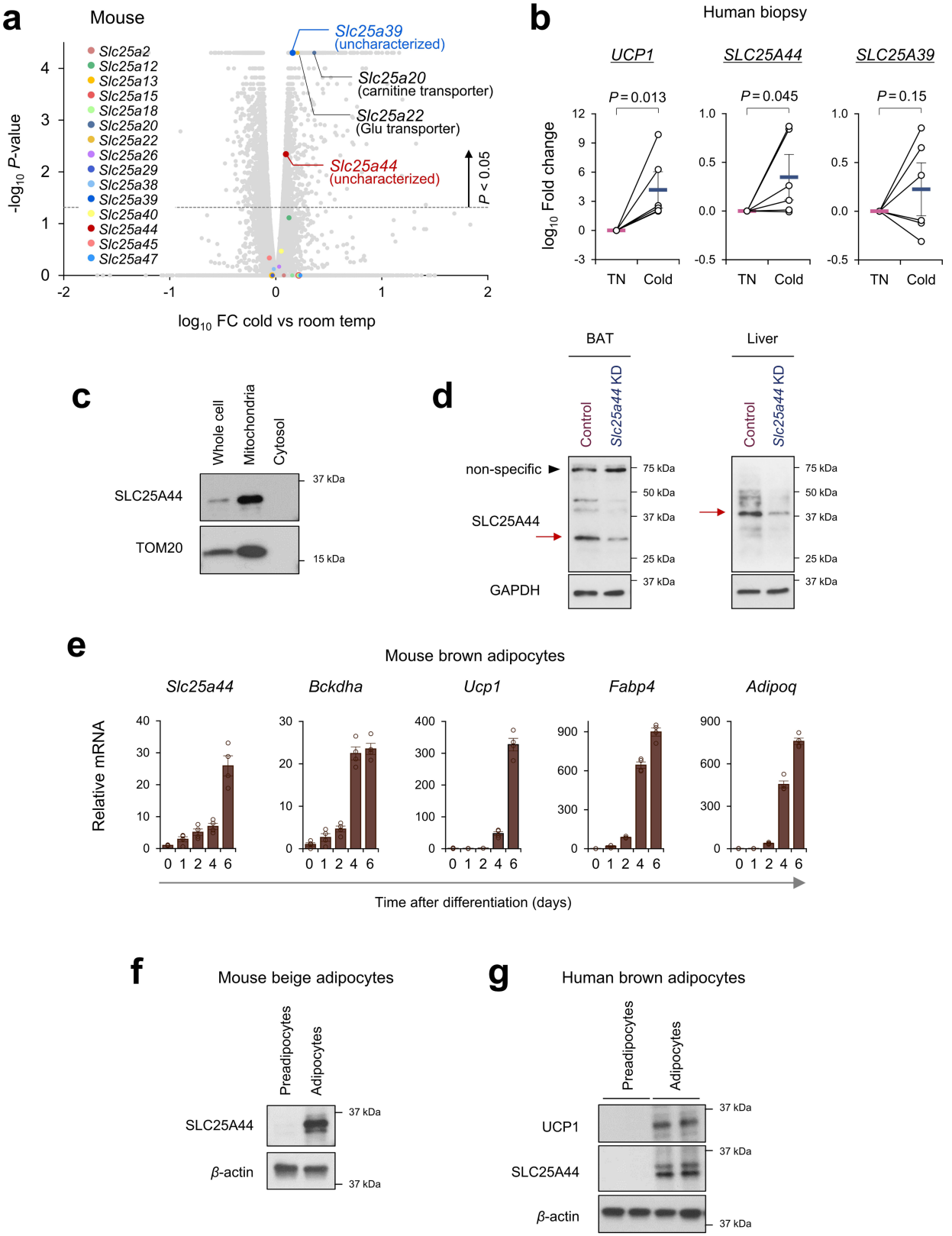

Extended Data Fig. 6 | See next page for caption.

Extended Data Fig. 6 | Characterization of SLC25A44 in thermogenic adipocytes. a, Expression profile of Slc25a family members in the inguinal WAT of mice acclimatized to 23 °C or 12 °C for 1 week. $n = 3$ per group. **b**, mRNA expression of *UCP1*, *SLC25A44* and *SLC25A39* normalized to *TBP* levels in the supraclavicular BAT from the same individuals (six pairs) at thermoneutrality (27 °C) and cold temperature (19 °C). **c**, Mitochondrial localization of SLC25A44 protein in differentiated mouse beige adipocytes. TOM20 was used as a mitochondrial marker. **d**, Immunoblotting for SLC25A44 in BAT and liver of control and *Slc25a44*-KD mice. GAPDH was used as a loading control. Red arrows indicate specific bands whose intensities were decreased in *Slc25a44*-KD mice. **e**, mRNA expression of *Slc25a44* and indicated genes normalized to levels of *36B4* (also known as *Rplp0*) during mouse brown adipogenesis. $n = 4$ per group. **f**, Protein expression of SLC25A44 in mouse beige preadipocytes and differentiated adipocytes. β-actin was used as a loading control. **g**, Protein expression of UCP1 and SLC25A44 in immortalized human brown preadipocytes and differentiated adipocytes. β-actin was used as a loading control. **a**, **b**, **e**, Biologically independent samples. Data are mean ± s.e.m.; one-sided *P* values by paired *t*-test (**b**) and two-sided *P* values by unpaired Student's *t*-test (**a**). **c**, **d**, **f**, **g**, Representative results from two independent experiments. Uncropped images are available in Supplementary Fig. 1.

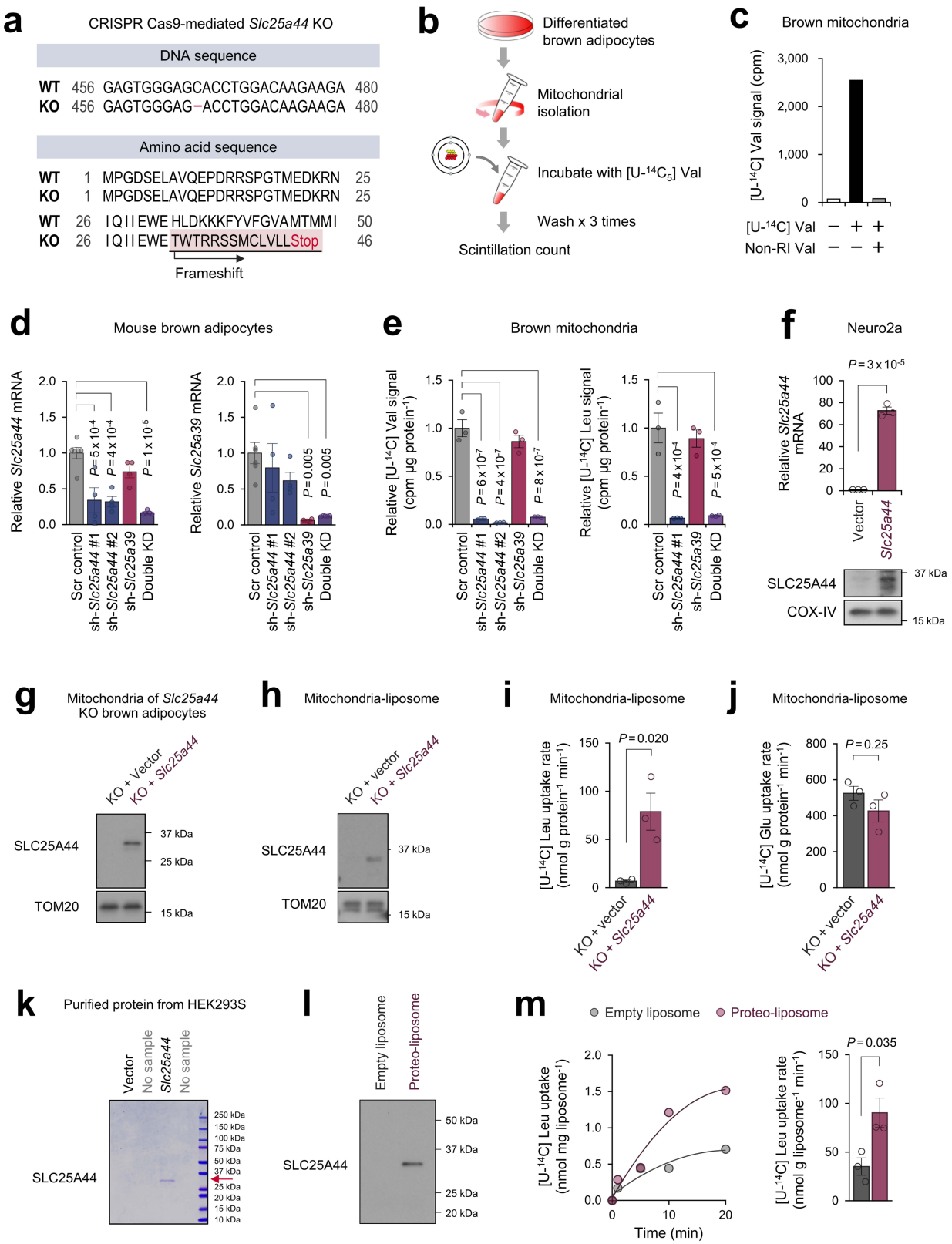

Extended Data Fig. 7 | See next page for caption.

Extended Data Fig. 7 | Biochemical characterization of SLC25A44. **a**, Genomic *Slc25a44* sequence of *Slc25a44*-KO brown cell line (upper panel). Predicted amino acid sequence of SLC25A44 is shown in lower panel. Homozygous mutation in the *Slc25a44* gene by CRISPR-Cas9 results in a premature stop codon in KO cells. **b**, Scheme of mitochondrial BCAA uptake assay. Isolated mitochondria from differentiated brown adipocytes were incubated with [U-$^{14}C_5$]Val. Mitochondrial uptake was quantified by a scintillation counter. **c**, Validation of mitochondrial Val uptake assay in differentiated brown adipocytes. Note that addition of excess non-labelled Val (20 mM) abolished [U-$^{14}C_5$]Val uptake into the mitochondria. **d**, mRNA expression of *Slc25a44* and *Slc25a39* in differentiated mouse brown adipocytes expressing a scrambled control shRNA (Scr, $n = 6$) and shRNAs targeting *Slc25a44* (shRNA #1, #2, $n =$ 4 per group), *Slc25a39* ($n = 4$) or both *Slc25a44* shRNA #1 and *Slc25a39* shRNA (double knockdown, $n = 5$). **e**, Mitochondrial uptake of [U-$^{14}C_5$] Val (left) and [U-$^{14}C_6$]Leu (right) in brown adipocytes in (**d**). $n = 3$ per group. **f**, mRNA and protein expression of *Slc25a44* in mitochondria of Neuro2a cells expressing an empty vector or *Slc25a44*. COX-IV was used as a loading control. $n = 3$ per group. **g**, Immunoblotting for SLC25A44 in the isolated mitochondria from differentiated *Slc25a44*-KO brown adipocytes expressing an empty vector or *Slc25a44*. TOM20 was used as a loading control. **h**, Immunoblotting of SLC25A44 in the mitochondria-fused liposome. Mitochondrial membrane isolated from *Slc25a44*-KO brown adipocytes expressing an empty vector or *Slc25a44* was fused with liposome. TOM20 was used as a loading control. **i**, [U-$^{14}C_6$]Leu uptake rate in the liposome in **h**. $n = 3$ per group. **j**, [U-$^{14}C_5$]Glu uptake rate in the liposome in **h**. $n = 3$ per group. **k**, Coomassie blue staining of purified SLC25A44 protein from HEK293S cells overexpressing *Slc25a44*. **l**, Immunoblotting of SLC25A44 in liposomes reconstituted with purified SLC25A44 (proteoliposome) and liposomes reconstituted without SLC25A44 (empty liposome). **m**, Left, [U-$^{14}C_6$]Leu transport into proteoliposomes in **l**. Right, Leu uptake rate. $n = 3$ per group. **d**–**f**, Biologically independent samples. **i**, **j**, **m**, Technically independent samples. **f**–**m**, Representative result from two independent experiments. Data are mean ± s.e.m.; two-sided *P* values by unpaired Student's *t*-test (**f**, **i**, **j**, **m**) or one-way ANOVA followed by Tukey's post hoc test (**d**, **e**). **f**–**h**, **k**, **l**, Uncropped images are available in Supplementary Fig. 1.

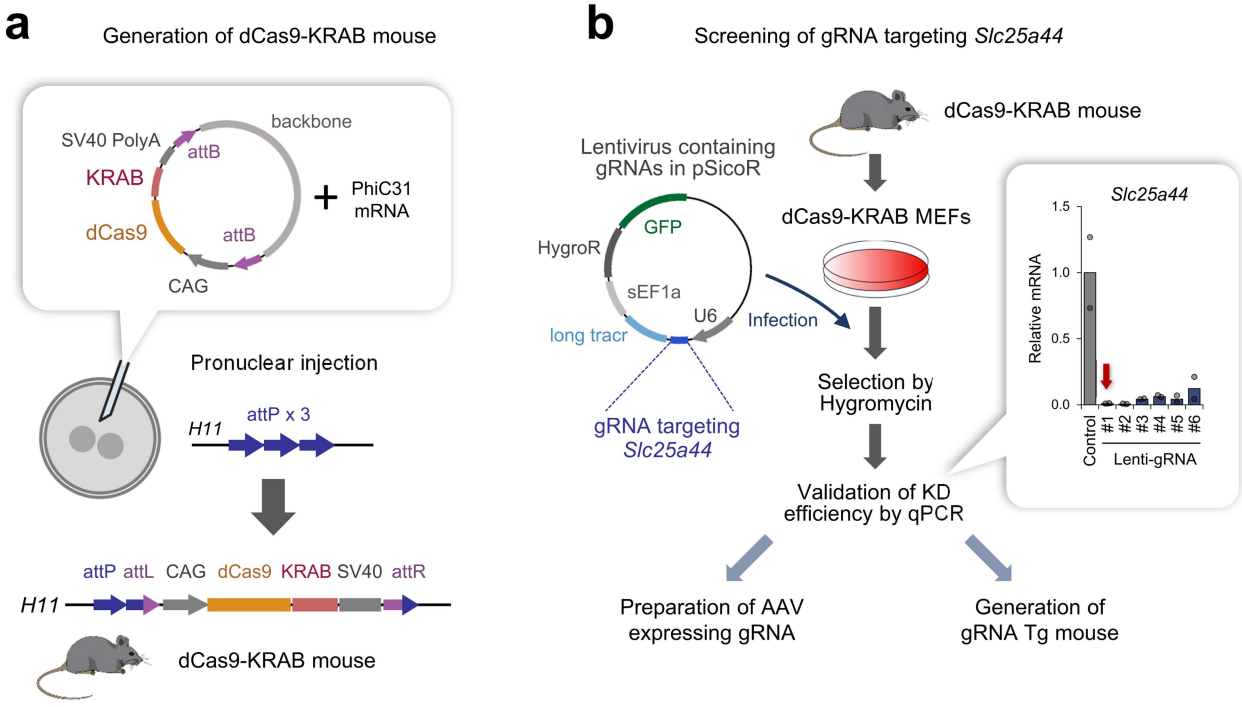

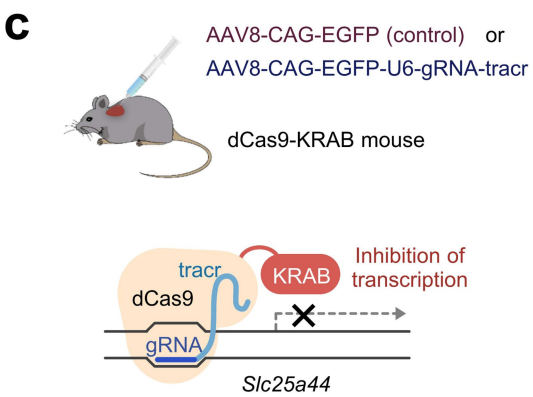

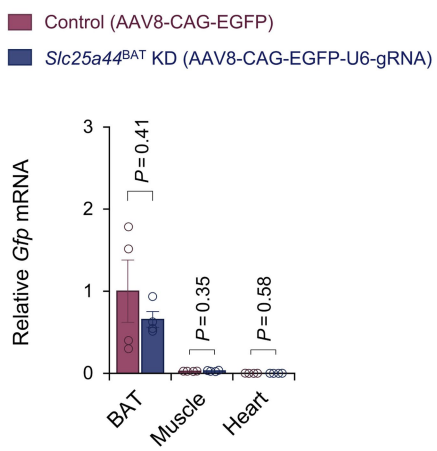

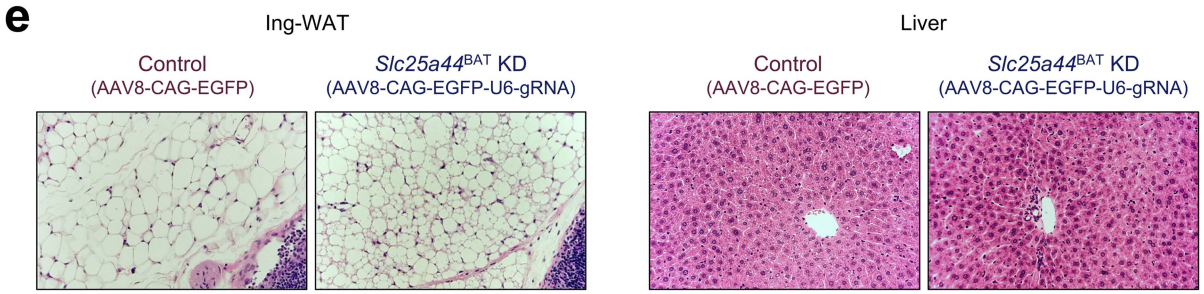

Extended Data Fig. 8 | Generation of *Slc25a44*^{BAT}-KD mice. a, DNA constructs used in the generation of dCas9-KRAB mice. The dCas9-KRAB construct was inserted into the *Hipp11* (H11) gene locus by the site-specific PhiC31 integrase. **b**, Experimental procedure of gRNA screening. MEFs from dCas9-KRAB mice were used to identify gRNA that effectively deplete *Slc25a44*. Graph shows *Slc25a44*-knockdown efficiency for six independent gRNAs in the dCas9-KRAB-derived MEFs ($n = 2$ per group). gRNA-*Slc25a44* #1 (indicated by a red arrow) was used for generation of gRNA Tg mouse. **c**, Schematics of BAT-specific *Slc25a44*-KD mice (*Slc25a44*^{BAT}-KD) by using the dCas9-KRAB system. AAV8-CAG-eGFP-U6-gRNA-tracr targeting *Slc25a44* was injected into the interscapular BAT of mice expressing dCas9-KRAB on the H11 locus (dCas9-KRAB mouse). AAV8-CAG-eGFP without gRNA was used as a control. **d**, mRNA expression of *Gfp* normalized to *36B4* in the indicated tissues of dCas9-KRAB mice in **c**. $n = 4$ per group. **e**, H&E staining of inguinal WAT and liver of control and *Slc25a44*^{BAT}-KD mice. **b**, **d**, biologically independent samples. Data are mean ± s.e.m.; two-sided *P* values by unpaired Student's *t*-test (**d**).

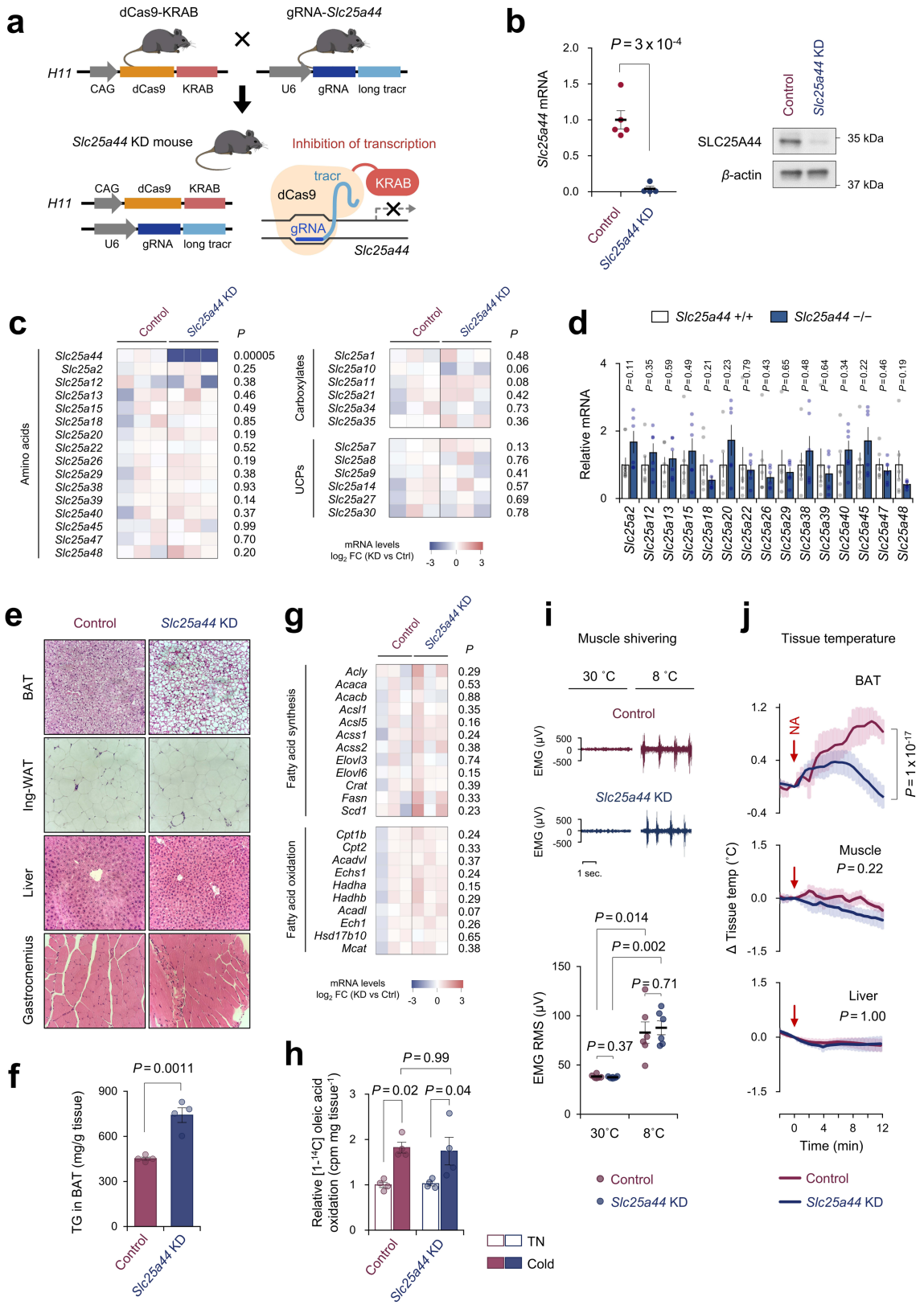

Extended Data Fig. 9 | See next page for caption.

Extended Data Fig. 9 | Characterization of *Slc25a44*-KD mice. **a**, Generation of *Slc25a44*-KD mice by the dCas9-KRAB system. The dCas9-KRAB mouse was crossed with transgenic mouse expressing gRNA targeting *Slc25a44* to generate SLC25A44 deficient mice. **b**, *Slc25a44* mRNA expression normalized to *36B4* levels and protein expression in the BAT of mice in **a**. β-actin was used as a loading control. $n = 5$ (control) and 4 (*Slc25a44*-KD). **c**, Expression profile of Slc25a family members in BAT in **a** by RNA-seq analysis. The colour scale shows $\log_2$-transformed fold change in TPM (*Slc25a44*-KD versus control). $n = 3$ per group. **d**, mRNA expression of *Slc25a* families normalized to *36B4* levels in *Slc25a44*-KO and control brown adipocytes. $n = 6$ per group. **e**, H&E staining of BAT, inguinal WAT, liver and gastrocnemius muscle from mice in **a**. **f**, Triglyceride content in the interscapular BAT of *Slc25a44*-KD and control mice. $n = 4$ per group. **g**, Expression profile of fatty acid synthesis- and oxidation-related genes in BAT of mice in **a** by RNA-seq analysis. The colour scale shows $\log_2$-transformed fold change in TPM (*Slc25a44*-KD versus control). $n = 3$ per group. **h**, Oleic acid oxidation normalized to tissue mass (mg) in BAT of *Slc25a44*-KD and control mice acclimatized to thermoneutral 30 °C or cold temperature (12 °C) for one week. $n = 4$ per group. **i**, EMG measurement of muscle shivering in control mice and *Slc25a44*-KD mice at 30 °C or 8 °C. The lower graph shows the RMS of the EMG. $n = 6$ per group. **j**, Tissue temperature in indicated tissues of control and *Slc25a44*-KD mice following noradrenaline treatment (indicated by red arrows). $n = 4$ per group. **b**–**d**, **f**–**j**, Biologically independent samples. Data are mean ± s.e.m.; two-sided *P* values by unpaired Student's *t*-test (**b**–**d**, **f**, **g**), two-way factorial ANOVA followed by Tukey's post hoc test (**h**), or two-way repeated measures ANOVA (**i**, **j**) followed by post hoc paired or unpaired *t*-test with Bonferroni's correction (**i**). **b**, **e**, Representative results from two independent experiments. Uncropped immunoblot images are available in Supplementary Fig. 1.

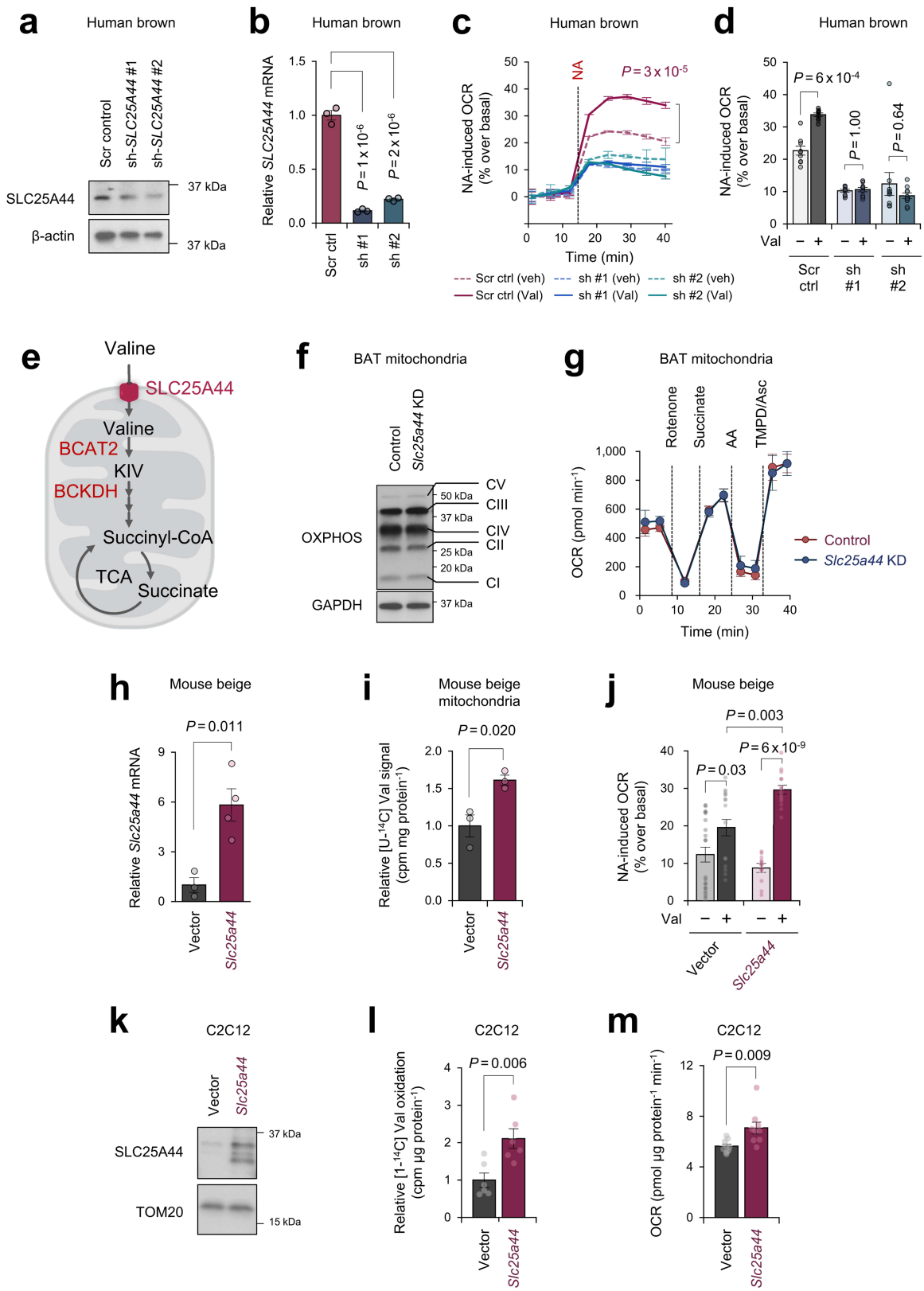

Extended Data Fig. 10 | See next page for caption.

Extended Data Fig. 10 | The cell-autonomous role of SLC25A44 in brown adipocytes. a, Immunoblotting of SLC25A44 in human brown adipocytes expressing a scrambled control shRNA (Scr) and shRNAs targeting *SLC25A44* (#1, #2). β-actin as a loading control. **b**, mRNA expression of *SLC25A44* normalized to *TBP* levels in **a**. $n = 3$ per group. **c**, Noradrenaline-induced OCR normalized to total protein (μg) in the presence and absence of Val supplementation in **a**. Differentiated human brown adipocytes in the BCAA-free medium were supplemented with Val or vehicle, and subsequently treated with noradrenaline. $n = 9$ per group (Scr control, sh-*Slc25a44* #1), $n = 10$ per group (sh-*Slc25a44* #2). **d**, Mean noradrenaline-induced OCR in **c**. **e**, Illustration of Val metabolism in the mitochondria. **f**, Immunoblotting of mitochondrial proteins (as indicated) in the interscapular BAT of control and *Slc25a44*-KD mice. GAPDH as a loading control. **g**, ETC activity of BAT mitochondria. Isolated mitochondria from BAT of control mice and *Slc25a44*-KD mice were treated with rotenone (2 μM), succinate (10 mM), antimycin A (5 μM) and TMPD (100 μM) with ascorbate (Asc, 10mM). $n = 5$ per group. **h**, mRNA expression of *Slc25a44* normalized to *36B4* in mouse beige adipocytes expressing an empty vector ($n = 3$) or *Slc25a44* ($n = 4$). **i**, Mitochondrial Val uptake in beige adipocytes in **h**. $n = 3$ per group. **j**, Noradrenaline-induced OCR in **h**. Differentiated adipocytes in the BCAA-free medium were supplemented with Val or vehicle and subsequently stimulated with noradrenaline. Vector: $n = 20$ (vehicle) and 16 (Val). *Slc25a44*: $n = 13$ (vehicle) and 16 (Val). **k**, Immunoblotting of SLC25A44 in C2C12 myotubes expressing an empty vector or *Slc25a44*. β-actin as a loading control. **l**, Val oxidation normalized to total protein (μg) in C2C12 myotubes in **k**. $n = 6$ per group. **m**, OCR normalized to total protein (μg) in C2C12 myotubes in **k**. $n = 9$ per group. **b**–**d**, **g**–**j**, **l**, **m**, Biologically independent samples. Data are mean ± s.e.m.; two-sided *P* values by unpaired Student's *t*-test (**h**, **i**, **l**, **m**), one-way (**b**) or two-way (**d**, **j**) factorial ANOVA followed by Tukey's post hoc test, or two-way repeated measures ANOVA (**c**, **g**). **a**, **f**, **k**, Representative results from two independent experiments. Uncropped immunoblot images are available in Supplementary Fig. 1.

nature research

Corresponding author(s): Shingo Kajimura

Reporting Summary

Nature Research wishes to improve the reproducibility of the work that we publish. This form provides structure for consistency and transparency in reporting. For further information on Nature Research policies, see Authors & Referees and the Editorial Policy Checklist.

Statistical parameters

When statistical analyses are reported, confirm that the following items are present in the relevant location (e.g. figure legend, table legend, main text, or Methods section).

n/a	Confirmed	
☐	☒	The exact sample size (*n*) for each experimental group/condition, given as a discrete number and unit of measurement
☐	☒	An indication of whether measurements were taken from distinct samples or whether the same sample was measured repeatedly
☐	☒	The statistical test(s) used AND whether they are one- or two-sided *Only common tests should be described solely by name; describe more complex techniques in the Methods section.*
☒	☐	A description of all covariates tested
☐	☒	A description of any assumptions or corrections, such as tests of normality and adjustment for multiple comparisons
☐	☒	A full description of the statistics including central tendency (e.g. means) or other basic estimates (e.g. regression coefficient) AND variation (e.g. standard deviation) or associated estimates of uncertainty (e.g. confidence intervals)
☐	☒	For null hypothesis testing, the test statistic (e.g. *F*, *t*, *r*) with confidence intervals, effect sizes, degrees of freedom and *P* value noted *Give P values as exact values whenever suitable.*
☒	☐	For Bayesian analysis, information on the choice of priors and Markov chain Monte Carlo settings
☐	☒	For hierarchical and complex designs, identification of the appropriate level for tests and full reporting of outcomes
☐	☒	Estimates of effect sizes (e.g. Cohen's *d*, Pearson's *r*), indicating how they were calculated
☐	☒	Clearly defined error bars *State explicitly what error bars represent (e.g. SD, SE, CI)*

Our web collection on statistics for biologists may be useful.

Software and code

Policy information about availability of computer code

Data collection	PET-CT image: VOX-BASE workstation (for humans), Amide 1.0.4 (for mice) RNAseq analysis: Kallisto 0.44.0; TopHat version 2.0.8; Cuffdiff 2.1.1; Metascape; Ingenuity Pathway Analysis; tximport 1.10.0. QPCR: QuantStudio Real-time PCR system 1.2v Seahorse: Wave 2.4 EMG: LabChart 8
Data analysis	Microsoft office Excel 2016; SPSS statistics version 25.0; R package version 3.6.1

For manuscripts utilizing custom algorithms or software that are central to the research but not yet described in published literature, software must be made available to editors/reviewers upon request. We strongly encourage code deposition in a community repository (e.g. GitHub). See the Nature Research guidelines for submitting code & software for further information.

Data

Policy information about availability of data

All manuscripts must include a data availability statement. This statement should provide the following information, where applicable:

- Accession codes, unique identifiers, or web links for publicly available datasets
- A list of figures that have associated raw data
- A description of any restrictions on data availability

RNA-seq dataset generated in this study (Extended Data Fig.9c, 9g) is available at Array Express under the accession code E-MTAB-7987 (For reviewers accession code: Username: Reviewer_E-MTAB-7987, Password: ww5qvwph). Publicly available array datasets used in this study are GSE51080 (Extended Data Figure 2e), ArrayExpress E-MTAB-2602 (Extended Data Figure 2e), ArrayExpress MTAB-4031 (Extended Data Figure 2g), ArrayExpress E-MTAB-2624 (Extended Data Figure 2h). RNA-seq analysis in Extended Data Figure 6a is available in Source Data Extended Data Figure 6. Publicly available proteomics analysis dataset (Sustarsic EG et al. Cell Metab 28: 159-174, 2018 doi: 10.1016/j.cmet.2018.05.003) was used in Extended Data Figures 2f, 4c. 13C-labeled Leu metabolic tracing data is available in Supplementary Table 3.

Field-specific reporting

Please select the best fit for your research. If you are not sure, read the appropriate sections before making your selection.

☒ Life sciences ☐ Behavioural & social sciences ☐ Ecological, evolutionary & environmental sciences

For a reference copy of the document with all sections, see nature.com/authors/policies/ReportingSummary-flat.pdf

Life sciences study design

All studies must disclose on these points even when the disclosure is negative.

Sample size	The sample size was determined by the power analysis with α = 0.05 and power of 0.8, developed by Cohen (1988), and based on our experience with experimental models, anticipated biological variables, and previous literatures. Sample numbers were described in the Figure legends.
Data exclusions	No data were excluded in the study.
Replication	All the biological experiments were repeated, at least, twice and reproduced. RNA-sequencing and metabolomics were performed once but three independent samples were analyzed and further validated by alternative approaches, such as qRT-PCR. Western blotting data were confirmed by two or three independent samples.
Randomization	Mice were randomly assigned at the time of purchase or weaning to minimize any potential bias. This is described in the Method (animals).
Blinding	The metabolite analyses in human sera and mouse plasma, the [13C6, 15N1] leucine tracing in human brown adipocytes, the PET/CT examination using 18F-FDG (in humans) or 18F-Fluciclovine (in mice), and GTT/ITT in mice fed high fat diet were performed by the authors who were blinded to the experimental groups. RNA sequencing and library constructions were performed by technical staffs at the UCLA genome core who were blinded to the experimental groups. RNA sequencing alignment were performed by the authors who were blinded to the experimental groups. Blinding was not relevant to the other experiments in mice or cells because mice or cells had to be genotyped by PCR.

Reporting for specific materials, systems and methods

Materials & experimental systems

n/a	Involved in the study
☐	☒ Unique biological materials
☐	☒ Antibodies
☐	☒ Eukaryotic cell lines
☒	☐ Palaeontology
☐	☒ Animals and other organisms
☐	☒ Human research participants

Methods

n/a	Involved in the study
☒	☐ ChIP-seq
☒	☐ Flow cytometry
☒	☐ MRI-based neuroimaging

Unique biological materials

Policy information about availability of materials

Obtaining unique materials

All unique materials used are available from the authors upon reasonable request.

Antibodies

Antibodies used

Following antibodies were used in this study:

- Anti-BCAT1 antibody, mouse monoclonal, 1:1000 (WB), OriGene (TA504360)
- Anti-BCAT2 antibody, rabbit polyclonal, 1:1000 (WB), Cell Signaling Tech (9432)
- Anti-BCKDHA antibody, mouse monoclonal, 1:2000 (WB), Santa Cruz (sc-271538)
- Anti-COX-IV antibody, rabbit monoclonal, 1:2000 (WB), Cell Signaling Tech (4850)
- Anti-Flag antibody, mouse monoclonal, 1:2000 (WB), Sigma (A8592)
- Anti-GAPDH antibody, mouse monoclonal, 1:2000 (WB), Santa Cruz (sc-32233)
- Anti-GFP antibody, chicken polyclonal, 1:200 (staining), Aves labs (GFP-1020)
- Anti-chicken IgG, Alexa Fluor 488, Goat polyclonal, 1:500 (staining), Life Technologies (A11039)
- Anti-OXPHOS antibody cocktail, mouse monoclonal, 1:2000 (WB), Abcam (ab110413)
- Anti-PDH-E1α antibody, mouse monoclonal, 1:1000 (WB), Santa Cruz (sc-377092)
- Anti-PDH-E1α (pSer232) antibody, rabbit polyclonal, 1:1000 (WB), Millipore (AP1063)
- Anti-PDH-E1α (pSer293) antibody, rabbit monoclonal, 1:1000 (WB), Abcam (ab177461)
- Anti-PDH-E1α (pSer300) antibody, rabbit polyclonal, 1:1000 (WB), Millipore (AP1064)
- Anti-SLC25A44 antibody, rabbit polyclonal, 1:1000 (WB), GeneScript (custom order; it was generated by using amino acids (MEDKRNIQIIEWEHLDKKKC, MMQRKGEKMGRFQVC, and CKKLSLRPELVDSRH) as epitopes for immunization in rabbit.
- Anti-TOM20 antibody, rabbit polyclonal, 1:2000 (WB), Proteintech (11802-1-AP)
- Anti-UCP1 antibody, rabbit polyclonal, 1:2000 (WB), Abcam (ab-10983)
- Anti-β-actin antibody, mouse monoclonal, 1:10000 (WB), Sigma (A3854)

Validation

All antibodies were validated for the application and species used in this study by their manufacturers and by the authors. Antibodies were validated based on the size of band in western blotting (molecular weight), specificity/selectivity assessed by using samples from knockout mouse/knockdown mouse/knockdown cells/over expression cells, and reproducibility of the results.

- Anti-BCAT1 antibody: https://www.origene.com/catalog/antibodies/primary-antibodies/ta504360/bcat1-mouse-monoclonal-antibody-clone-id-oti3f5
- Anti-BCAT2 antibody: https://www.cellsignal.com/products/primary-antibodies/bcat2-antibody/9432
- Anti-BCKDHA antibody: https://www.scbt.com/scbt/product/bckde1a-antibody-h-5?productCanUrl=bckde1a-antibody
- Anti-COX-IV antibody: https://www.cellsignal.com/products/primary-antibodies/cox-iv-3e11-rabbit-mab/4850
- Anti-Flag antibody: https://www.sigmaaldrich.com/catalog/product/sigma/a8592?lang=en&region=US
- Anti-GAPDH antibody: https://www.scbt.com/scbt/product/gapdh-antibody-g-9?gclid=Cj0KCQjw9pDpBRCkARIsAOzRzivPevMxfm1PECD4RaBDNpW5UMHHdAHUYTrRaPub43MCQxsOIJzk_zEaAlJlEALw_wcB
- Anti-GFP antibody: https://www.aveslabs.com/collections/epitope-tag-6xhis-beta-gal-actin-and-gfp-antibodies/products/green-fluorescent-protein-gfp-antibody
- Anti-chicken IgG, Alexa Fluor 488: https://www.thermofisher.com/antibody/product/Goat-anti-Chicken-IgY-H-L-Secondary-Antibody-Polyclonal/A-11039
- Anti-OXPHOS antibody cocktail: https://www.abcam.com/total-oxphos-rodent-wb-antibody-cocktail-ab110413.html?gclid=Cj0KCQjw9pDpBRCkARIsAOzRziujlUlTLatVARYKCilKliq1Wu_-hEZ13i6E0vQrr9vd03Z4rUF5CowaAhY9EALw_wcB&productWallTab=ShowAll
- Anti-PDH-E1α antibody: https://www.scbt.com/scbt/product/pdh-e1alpha-antibody-d-6
- Anti-PDH-E1α (pSer232) antibody: https://www.emdmillipore.com/US/en/product/PhosphoDetect-Anti-PDH-E1-pSer232-Rabbit-pAb,EMD_BIO-AP1063
- Anti-PDH-E1α (pSer293) antibody: https://www.abcam.com/pyruvate-dehydrogenase-e1-alpha-subunit-phospho-s293-antibody-epr12200-ab177461.html
- Anti-PDH-E1α (pSer300) antibody: https://www.emdmillipore.com/US/en/product/PhosphoDetect-Anti-PDH-E1-pSer300-Rabbit-pAb,EMD_BIO-AP1064
- Anti-SLC25A44 antibody: Fig 4b; Ext Fig 6d; Ext Fig 7f-h,l; Ext Fig 9b; Ext Fig 10a,k.
- Anti-TOM20 antibody: https://www.ptglab.com/products/TOM20-Antibody-11802-1-AP.htm
- Anti-UCP1 antibody: https://www.abcam.com/ucp1-antibody-ab10983.html
- Anti-β-actin antibody: https://www.sigmaaldrich.com/catalog/product/sigma/a3854?lang=en&region=US

Eukaryotic cell lines

Policy information about cell lines

Cell line source(s)

Preadipocytes were isolated from the interscapular BAT or the inguinal WAT of either wild type or Ucp1 -/- mice and immortalized by infecting retrovirus expressing SV-Large T antigen.
Mouse embryonic fibroblasts (MEF) were isolated from dCas9-KRAB mice and immortalized by infecting retrovirus expressing SV-Large T antigen.
Preadipocytes, isolated from either the supraclavicular BAT or subcutaneous WAT of healthy human participants, were immortalized, as reported previously (Shinoda et al. Nautre Medicine 2015).

	C2C12 (CRL-1772) and HEK293S (CRL-3022) were purchased from ATCC. Neuroblastoma cell line (Neuro2a) was purchased from Sigma-Aldrich (89121404).
Authentication	RNA-sequencing of the cell lines provide authentification.
Mycoplasma contamination	All the cell lines were routinely tested for mycoplasma infection and confirmed as negative for mycoplasma contamination.
Commonly misidentified lines (See ICLAC register)	No commonly misidentified cell line was used.

Animals and other organisms

Policy information about studies involving animals; ARRIVE guidelines recommended for reporting animal research

Laboratory animals	Mus musculus was used as an animal model. The strains were as followed: - C57BL/6J mice were obtained from the Jackson Laboratory. - Ucp1-Cre mice (Stock No. 024670) were obtained from the Jackson Laboratory. - Pparg flox mice (Stock No. 004584) were obtained from the Jackson Laboratory. - Bckdhatm1a(EUCOMM)Hmgu mice were obtained from EuMMCR and used for generation of Bckdha flox mice. - BAT-specific Bckdha-KO mice were generated by crossing Bckdha flox mouse and Ucp1-Cre mouse. - dCas9-KRAB mice were generated by a site-specific integrase-mediated approach (TARGATT system), in which a construct having dCas9-KRAB was integrated into H11 locus to express dCas9-KRAB ubiquitously. - Transgenic (Tg) mice of gRNA targeting Slc25a44 were generated by conventional transgenics. - Slc25a44 KD mice were generated by crossing dCas9-KRAB mouse and Slc25a44-gRNA mouse. Adult males and females aged 8-16 weeks were used for the experiments. Littermate controls with same sex were used. All the mice had free access to food and water, 12 hr light cycles, and were caged at 23 C.
Wild animals	This study did not involve wild animals
Field-collected samples	This study did not involve samples collected from the field.

Human research participants

Policy information about studies involving human research participants

Population characteristics	Thirty-three healthy young Japanese male volunteers participated in this study (23.4 ± 0.58 years old). BMI was within normal range (21.0 ± 0.30 kg/m2).
Recruitment	Volunteers were recruited by trial awareness-raising posters and consultant email-out. Potential selection biases were not detected/observed.

LETTER

https://doi.org/10.1038/s41586-019-1461-3

Non-line-of-sight imaging using phasor-field virtual wave optics

Xiaochun Liu[1], Ibón Guillén[2], Marco La Manna[3], Ji Hyun Nam[1], Syed Azer Reza[3], Toan Huu Le[1], Adrian Jarabo[2], Diego Gutierrez[2] & Andreas Velten[1,3]*

Non-line-of-sight imaging allows objects to be observed when partially or fully occluded from direct view, by analysing indirect diffuse reflections off a secondary relay surface. Despite many potential applications[1–9], existing methods lack practical usability because of limitations including the assumption of single scattering only, ideal diffuse reflectance and lack of occlusions within the hidden scene. By contrast, line-of-sight imaging systems do not impose any assumptions about the imaged scene, despite relying on the mathematically simple processes of linear diffractive wave propagation. Here we show that the problem of non-line-of-sight imaging can also be formulated as one of diffractive wave propagation, by introducing a virtual wave field that we term the phasor field. Non-line-of-sight scenes can be imaged from raw time-of-flight data by applying the mathematical operators that model wave propagation in a conventional line-of-sight imaging system. Our method yields a new class of imaging algorithms that mimic the capabilities of line-of-sight cameras. To demonstrate our technique, we derive three imaging algorithms, modelled after three different line-of-sight systems. These algorithms rely on solving a wave diffraction integral, namely the Rayleigh–Sommerfeld diffraction integral. Fast solutions to Rayleigh–Sommerfeld diffraction and its approximations are readily available, benefiting our method. We demonstrate non-line-of-sight imaging of complex scenes with strong multiple scattering and ambient light, arbitrary materials, large depth range and occlusions. Our method handles these challenging cases without explicitly inverting a light-transport model. We believe that our approach will help to unlock the potential of non-line-of-sight imaging and promote the development of relevant applications not restricted to laboratory conditions.

We have recently witnessed considerable advances in transient imaging techniques[10] that use streak cameras[11], gated sensors[6], amplitude-modulated continuous waves[12], single-photon avalanche diodes (SPADs)[13] or interferometry[14]. Access to time-resolved image information has led to advances in imaging of objects partially or fully hidden from direct view[1–3,5–7,15–18]: that is, non-line-of-sight (NLOS) imaging. Other methods are able to use information encoded in the phase of continuous light and do not use the time of flight[4]. In the basic configuration of an NLOS system, light bounces off a relay wall, travels to the hidden scene, then propagates back to the relay wall and finally reaches the sensor.

Recent NLOS reconstruction methods are based on heuristic filtered backprojection[2,3,6,7,19] or attempt to compute inverse operators of simplified forward light transport models[5,9,20]. These simplified models do not take into account multiple scattering, surfaces with anisotropic reflectance or, with a few exceptions[20], occlusions or clutter in the hidden scene. The depth range that can be recovered is also limited, partially owing to the difference in intensity between first- and higher-order reflections. Existing methods are thus limited to carefully controlled cases, imaging isolated objects of simple geometry with moderate or no occlusion. Whereas the goal of previous works has been limited to the reconstruction of hidden geometry, we develop a theoretical framework for general NLOS imaging, reconstructing the irradiance at a virtual sensor; this enables applications beyond geometric reconstruction.

Time-of-flight LOS imaging has used a phasor formalism (a phasor, or phase vector, is a complex number representing properties of a light wave) together with Fourier domain ranging[12] to describe the emitted modulated light signal. Kadambi et al.[21] extended this concept to reconstruct NLOS scenes by using a phasor model along with a non-line-of-sight capture system that uses intensity-modulated light sources and gain-modulated detection. We show that a similar description can be used to model the physics of light transport through the scene. The key insight is that propagation through a scene of intensity-modulated light can be modelled using a Rayleigh–Sommerfeld diffraction (RSD) operator acting on a quantity that we term the phasor field. This allows us to formulate any NLOS imaging problem as a wave imaging problem (Fig. 1) and to transfer well-established insights and techniques from classic optics into the NLOS domain. Given a captured time-resolved dataset of light transport through an NLOS scene, and a choice of a template LOS imaging system, our method provides a recipe that results in an NLOS imaging algorithm mimicking the capabilities of the corresponding LOS system. This template system can be any real or hypothetical wave imaging system that includes a set of light sources and detectors. The resulting algorithms can then be efficiently solved using diffraction integrals such as the RSD, for which various fast exact and approximate solvers exist[22]. Supplementary Information section A illustrates this.

We start by mathematically defining our phasor field $\mathcal{P}(\boldsymbol{x},t)$. Let $\mathcal{E}(\boldsymbol{x},t)$ (with units $\sqrt{\mathrm{W\,m^{-2}}}$) be a quasi-monochromatic scalar field at position $\boldsymbol{x}\in\mathcal{S}$ and time t, incident on (or reflected from) a Lambertian surface $\mathcal{S}$, with centre frequency Ω_0 and bandwidth $\Delta\Omega\ll\Omega_0$. We can then define

$$\mathcal{P}(\boldsymbol{x},t)\equiv\left\langle\frac{1}{\tau}\int_{t-\tau/2}^{t+\tau/2}|\mathcal{E}(\boldsymbol{x},t')|^2\,\mathrm{d}t'\right\rangle-\left\langle\frac{1}{T}\int_{t-T/2}^{t+T/2}|\mathcal{E}(\boldsymbol{x},t')|^2\,\mathrm{d}t'\right\rangle \quad (1)$$

as the mean subtracted irradiance (in watts per square metre) at point $\boldsymbol{x}$ and time t. The $\langle\cdot\rangle$ operator denotes spatial speckle averaging (for the reflected case) accounting for laser illumination, and τ represents the averaging of the intensity at a fast detector, with $\tau\ll 1/\Delta\Omega\ll T$. The second integral in equation (1) is a long-term average intensity over an interval $T\gg\tau$ of the signal as seen by a conventional non-transient photodetector. Now, let us define the Fourier component of $\mathcal{P}(\boldsymbol{x},t)$ for frequency ω as

$$\mathcal{P}_{0,\omega}(\boldsymbol{x})\equiv\int_{-\infty}^{+\infty}\mathcal{P}(\boldsymbol{x},t)\,\mathrm{e}^{-i\omega t}\mathrm{d}t \quad (2)$$

[1]Department of Electrical and Computer Engineering, University of Wisconsin Madison, Madison, WI, USA. [2]Graphics and Imaging Lab, Universidad de Zaragoza—I3A, Zaragoza, Spain. [3]Department of Biostatistics and Medical Informatics, University of Wisconsin Madison, Madison, WI, USA. *e-mail: velten@wisc.edu

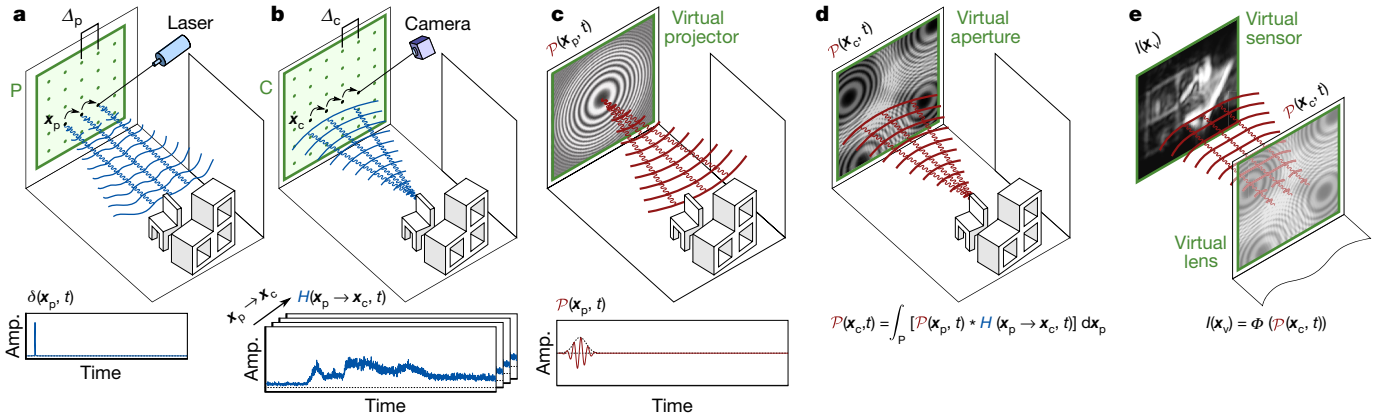

Fig. 1 | NLOS as a virtual LOS imaging system. a, **b**, Capturing scene data. **a**, A pulsed laser sequentially scans a relay wall (green); **b**, the light reflected back from the scene onto the wall is recorded at the sensor, yielding an impulse response H of the scene. **c**, Virtual light source. The phasor-field wave of a virtual light source $\mathcal{P}(\boldsymbol{x}_p, t)$ is modelled after the wavefront of the light source of the template LOS system. **d**, The scene response to this virtual illumination $\mathcal{P}(\boldsymbol{x}_c, t)$ is computed using H. **e**, The scene is reconstructed from the wavefront $\mathcal{P}(\boldsymbol{x}_c, t)$ using wave diffraction theory. The function $\Phi(\cdot)$ is also taken from the template LOS system. Amp., phasor-field amplitude.

from which we can define a monochromatic component of the phasor field $\mathcal{P}_\omega(\boldsymbol{x}, t)$ as

$$\mathcal{P}_\omega(\boldsymbol{x}, t) \equiv \mathcal{P}_{0,\omega}(\boldsymbol{x})\, e^{i\omega t} \tag{3}$$

Using the above, our phasor field $\mathcal{P}(\boldsymbol{x}, t)$ can be expressed as a superposition of monochromatic plane waves as $\mathcal{P}(\boldsymbol{x}, t) = \int_{-\infty}^{+\infty} \mathcal{P}_\omega(\boldsymbol{x}, t)\, \mathrm{d}\omega/2\pi$. Since $\mathcal{P}(\boldsymbol{x}, t)$ is a real quantity, the Fourier components $\mathcal{P}_{0,\omega}(\boldsymbol{x})$ are complex and symmetric about $\omega = 0$. Note that, in many places in this Letter, we assign $\mathcal{P}(\boldsymbol{x}, t)$ an explicitly complex value; in these cases, it is implied that the correct real representation is $\frac{1}{2}(\mathcal{P}(\boldsymbol{x}, t) + \mathcal{P}^*(\boldsymbol{x}, t))$. In practice, the complex conjugate can be safely ignored in our calculations. As can be seen in Supplementary Information section B, given an isotropic source plane S and a destination plane D, and assuming that the electric field at S is incoherent, the propagation of its monochromatic component $\mathcal{P}_\omega(\boldsymbol{x}, t)$ is defined by an RSD-like propagation integral:

$$\mathcal{P}_\omega(\boldsymbol{x}_d, t) = \gamma \int_S \mathcal{P}_\omega(\boldsymbol{x}_s, t) \frac{e^{ik|\boldsymbol{x}_d - \boldsymbol{x}_s|}}{|\boldsymbol{x}_d - \boldsymbol{x}_s|} \mathrm{d}\boldsymbol{x}_s \tag{4}$$

where γ is an attenuation factor, $k = 2\pi/\lambda$ is the wavenumber for wavelength $\lambda = 2\pi/\omega$, $\boldsymbol{x}_s \in \mathrm{S}$ and $\boldsymbol{x}_d \in \mathrm{D}$. Note that, as described in Supplementary Information section B, we approximate γ as a constant over the plane S as $\gamma \approx 1/|\langle \mathrm{S} \rangle - \boldsymbol{x}_d|$; this approximation has a minor effect on the signal amplitude at the sensor but does not change the phase of our phasor field. Although equation (4) is defined for monochromatic signals, it can be used to propagate broadband signals by propagating each monochromatic component independently; this can be efficiently done by time-shifting the phasor field (more details are provided in Supplementary Information section B.1).

The key insight of equation (4) is that, given the assumption that γ is a constant, the propagation of our phasor field is defined by the same RSD operator as any other physical wave. Therefore, to image a scene from a virtual camera with aperture on plane C, we can apply the image formation model of any wave-based LOS imaging system directly over the phasor field $\mathcal{P}(\boldsymbol{x}_c, t)$ at the aperture, with $\boldsymbol{x}_c \in \mathrm{C}$. The challenge is how to compute $\mathcal{P}(\boldsymbol{x}_c, t)$ from an illuminating input phasor field $\mathcal{P}(\boldsymbol{x}_p, t)$, where $\boldsymbol{x}_p$ is a point in the virtual projector aperture P, given a particular NLOS scene (see Fig. 1).

Because light transport is linear in space and time-invariant[23,24], we can characterize light transport through the scene as an impulse

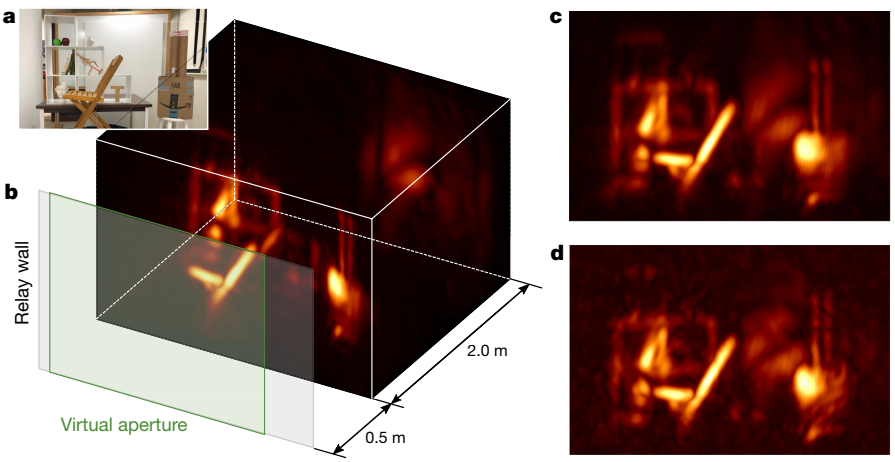

Fig. 2 | Reconstructions of a complex NLOS scene. a, Photograph of the scene as seen from the relay wall. The scene contains occluding geometries, with objects towards the front (such as the chair) partially occluding the objects further back; multiple anisotropic surface reflectances; large depth; and strong ambient and multiply scattered light. **b**, 3D visualization of the reconstruction with phasor fields ($\lambda = 6$ cm). We include the relay wall location and the coverage of the virtual aperture for illustrative purposes. **c**, Frontal view of the scene, captured with an exposure time of 10 ms per laser position. **d**, Frontal view captured with an exposure time of just 1 ms (24 s for the complete scan).

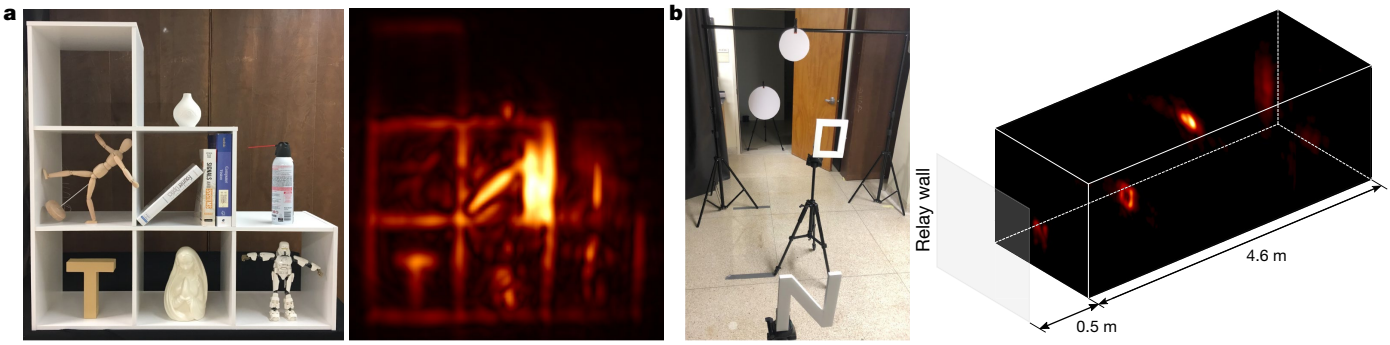

Fig. 3 | Robustness of our technique. a, Reconstruction in the presence of strong ambient illumination (all the lights on during capture). **b**, Hidden scene with a large depth range, leading to very weak signals from objects farther away.

response function $H(\boldsymbol{x}_\mathrm{p} \rightarrow \boldsymbol{x}_\mathrm{c}, t)$, where $\boldsymbol{x}_\mathrm{p}$ and $\boldsymbol{x}_\mathrm{c}$ are the positions of the emitter and detector, respectively. The phasor field at the virtual aperture $\mathcal{P}(\boldsymbol{x}_\mathrm{c}, t)$ can thus be expressed as a function of the input phasor field $\mathcal{P}(\boldsymbol{x}_\mathrm{p}, t)$ and $H(\boldsymbol{x}_\mathrm{p} \rightarrow \boldsymbol{x}_\mathrm{c}, t)$:

$$\mathcal{P}(\boldsymbol{x}_\mathrm{c}, t) = \int_\mathrm{P} [\mathcal{P}(\boldsymbol{x}_\mathrm{p}, t) * H(\boldsymbol{x}_\mathrm{p} \rightarrow \boldsymbol{x}_\mathrm{c}, t)] \mathrm{d}\boldsymbol{x}_\mathrm{p} \quad (5)$$

where $*$ denotes the convolution operator. Any imaging system can be characterized by its image formation function $\Phi(\cdot)$, which transduces the incoming field into an image

$$I(\boldsymbol{x}_\mathrm{v}) = \Phi(\mathcal{P}(\boldsymbol{x}_\mathrm{c}, t)) \quad (6)$$

where $\boldsymbol{x}_\mathrm{v}$ is the point being imaged (that is, the point at the virtual sensor). This, in turn, can be formulated as an RSD propagator, requiring a diffraction integral to be solved to generate the final image.

In an NLOS scenario, $H(\boldsymbol{x}_\mathrm{p} \rightarrow \boldsymbol{x}_\mathrm{c}, t)$ usually corresponds to five-dimensional transients acquired by an ultrafast sensor focused on $\boldsymbol{x}_\mathrm{c}$ and sequentially illuminating the relay wall with short pulses at different points $\boldsymbol{x}_\mathrm{p}$ (see Fig. 1 and Methods). Points $\boldsymbol{x}_\mathrm{p}$ and $\boldsymbol{x}_\mathrm{c}$ correspond to a virtual LOS imaging system projected on the relay wall. Once $H(\boldsymbol{x}_\mathrm{p} \rightarrow \boldsymbol{x}_\mathrm{c}, t)$ has been captured, both the wavefront $\mathcal{P}(\boldsymbol{x}_\mathrm{p}, t)$ and the imaging operator $\Phi(\cdot)$ can be implemented computationally, so they are not bounded by hardware limitations. We can leverage this to use different $\mathcal{P}(\boldsymbol{x}_\mathrm{p}, t)$ functions from any existing LOS imaging system[25] to emulate its characteristics in an NLOS setting.

We illustrate the robustness and versatility of our method by implementing three virtual NLOS imaging systems based on common LOS techniques: a conventional photography camera capable of imaging NLOS scenes without knowledge of the timing or location of the illumination source; a transient photography system capable of capturing transient videos of the hidden scene revealing higher-order interreflections (multiple light bounces between surface elements) beyond third bounce; and a confocal time-gated imaging system robust to interreflections. An in-depth description of these example imaging systems is provided in Supplementary Information section C, including their corresponding $\mathcal{P}(\boldsymbol{x}_\mathrm{p}, t)$ functions and imaging operators, and section D describes some examples of practical integral solvers.

The spatial resolution of our virtual camera is $\Delta_x = 0.61\lambda L/d$, where d is the virtual aperture diameter and L is the imaging distance. The distance Δ_p between sample points $\boldsymbol{x}_\mathrm{p}$ in P (see Fig. 1) has to be small enough to sample H at the phasor-field wavelength. We fix $\Delta_\mathrm{p} = 1$ cm and, unless stated otherwise, $\lambda = 4$ cm. The minimum sampling rate is $\Delta_\mathrm{p} < \lambda/2$; in practice, we found $\Delta_\mathrm{p} = \lambda/4$ to provide the best trade-off between reconstruction noise and resolution.

The computational cost of our algorithm is bounded by the RSD solver computing the image formation model $\Phi(\cdot)$. Fast diffraction integral solvers exist[22], with complexity $O(N^3 \log N)$. For the particular case of our confocal system, we formulate the algorithm as a backprojection (see Supplementary Information section D.2 for details), and so we are bounded by the computational cost of the backprojection algorithm used.

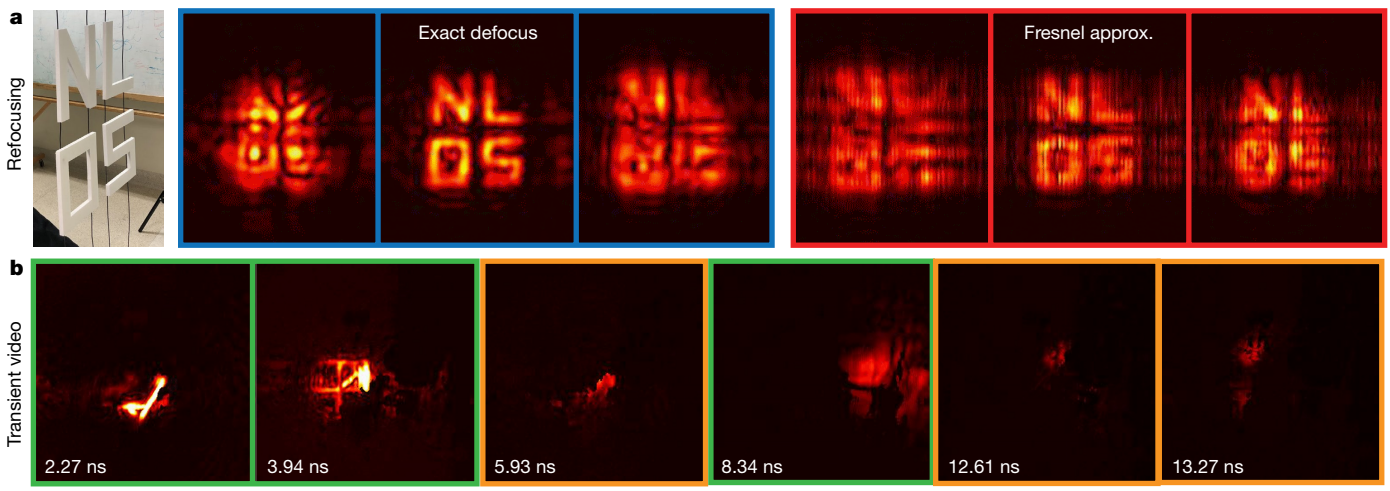

Fig. 4 | Additional NLOS imaging applications of our method. a, NLOS refocusing. The hidden letters (left) are progressively brought in and out of focus as seen from a virtual photography camera at the relay wall, using the exact lens integral (blue border), and the faster Fresnel approximation (red border). **b**, NLOS transient video. Example frames of light travelling through a hidden office scene when illuminated by a pulsed laser. Timestamps indicate the propagation time from the relay wall. Frames with a green border show third-bounce objects, frames with an orange border show fourth- and fifth-bounce effects.

One common application of NLOS imaging is the reconstruction of hidden geometry. Figure 2 shows the result for a complex scene imaged with our virtual confocal camera. This challenging scene contains multiple objects with occlusions distributed over a large depth, a wide range of surface reflectances and albedos, and strong interreflections. Our method is able to image many details of the scene, at the correct depths, even with an ultra-short (1 ms) exposure. More analysis on the robustness of our method to capture noise can be found in the Methods. For simpler scenes (no occlusions, limited depth, controlled reflectance and no interreflections), our method yields results on par with current techniques, which already approach theoretical limits for reconstruction quality (see Methods).

In Fig. 3, we demonstrate the robustness of our method when dealing with other challenging scenarios, including strong multiple scattering and ambient illumination (Fig. 3a), or a high dynamic range from objects spanning a large range of depths (Fig. 3b). Finally, our method allows new NLOS imaging systems and applications to be implemented, making use of the wealth of tools and processing methods available in LOS imaging. Figure 4a demonstrates NLOS refocusing with our virtual photography camera, computed using both the exact RSD operator and a faster Fresnel approximation, while Fig. 4b shows frames of NLOS femto-photography reconstructed using our virtual transient photography system, revealing fourth- and fifth-bounce components in the scene. The first, second and fourth frames, in green, show how light first illuminates the chair, then propagates to the shelf and finally hits the back wall 3 m away. The frames in orange show higher-order bounces. The third frame shows that the chair is illuminated again by light bouncing back from the relay wall, and the last two frames show how the pulse of light travels from the wall back to the scene (see Supplementary Video 1). A description of the Fresnel approximation to the RSD operator, as well as the LOS projector-camera functions used in these examples, appear in Supplementary Information sections D.1 and C.2.

In the Methods, we include comparisons against ground truth for two synthetic scenes, inside a corridor of 2 m × 2 m × 3 m to create interreflections, simulated using an open-source transient renderer[26]; these scenes are included in a publicly available database[27]. We analyse the robustness of our method with and without such interreflections; the reconstruction mean square error (MSE) does not increase, remaining below 5 mm. Finally, we progressively vary the specularity of the hidden geometry, from purely Lambertian to highly specular; again, the quality of the reconstructions does not vary significantly (MSE of about 2 mm).

The examples shown highlight the primary benefit of our approach. By turning NLOS into a virtual LOS system, the intrinsic limitations of previous approaches no longer apply, enabling a class of NLOS imaging methods that take advantage of existing wave-based imaging methods. Formulating NLOS light propagation as a wave does not impose limitations on the types of problems that can be addressed, nor the datasets that can be used. Any signal can be represented as a superposition of phasor-field waves; our formulation can thus be viewed as a choice of basis to represent any kind of NLOS data. Expressing the NLOS problem this way allows a direct analogy to LOS imaging, which can be exploited to derive suitable imaging algorithms and to implement them efficiently.

We have shown three imaging algorithms derived from our method. Our results include more complex scenes than in NLOS reconstructions shown so far in the literature, as well as new applications. In addition, our approach is flexible, fast, memory-efficient and lacks computational complexity since it does not require inverting a light transport model. We anticipate that it can be applied to other LOS imaging systems, for instance to separate light transport into direct and global components, or to use the phase of $\mathcal{P}_\omega$ for enhanced depth resolution. Our virtual imaging system could also be used to create a virtual imaging system to see around two corners, assuming the presence of a secondary relay Lambertian surface in the hidden scene, or to select and manipulate individual light paths to isolate specific aspects of the light transport in different NLOS scenes. In that context, combining our theory with light transport inversions, via, for example, an iterative approach, could potentially lead to better results and is an interesting avenue for future work.

Online content

Any methods, additional references, Nature Research reporting summaries, source data, extended data, supplementary information, acknowledgements, peer review information; details of author contributions and competing interests; and statements of data and code availability are available at https://doi.org/10.1038/s41586-019-1461-3.

Received: 18 October 2018; Accepted: 21 May 2019;
Published online 5 August 2019.

1. Kirmani, A., Hutchison, T., Davis, J. & Raskar, R. Looking around the corner using ultrafast transient imaging. *Int. J. Comput. Vis.* **95**, 13–28 (2011).
2. Gupta, O., Willwacher, T., Velten, A., Veeraraghavan, A. & Raskar, R. Reconstruction of hidden 3D shapes using diffuse reflections. *Opt. Express* **20**, 19096–19108 (2012).
3. Velten, A. et al. Recovering three-dimensional shape around a corner using ultrafast time-of-flight imaging. *Nat. Commun.* **3**, 745 (2012).
4. Katz, O., Small, E. & Silberberg, Y. Looking around corners and through thin turbid layers in real time with scattered incoherent light. *Nat. Photon.* **6**, 549–553 (2012).
5. Heide, F., Xiao, L., Heidrich, W. & Hullin, M. B. Diffuse mirrors: 3D reconstruction from diffuse indirect illumination using inexpensive time-of-flight sensors. In *IEEE Conf. Computer Vision and Pattern Recognition* (CVPR), 3222–3229 (IEEE, 2014).
6. Laurenzis, M. & Velten, A. Nonline-of-sight laser gated viewing of scattered photons. *Opt. Eng.* **53**, 023102 (2014).
7. Buttafava, M., Zeman, J., Tosi, A., Eliceiri, K. & Velten, A. Non-line-of-sight imaging using a time-gated single photon avalanche diode. *Opt. Express* **23**, 20997–21011 (2015).
8. Arellano, V., Gutierrez, D. & Jarabo, A. Fast back-projection for non-line of sight reconstruction. *Opt. Express* **25**, 11574–11583 (2017).
9. O'Toole, M., Lindell, D. B. & Wetzstein, G. Confocal non-line-of-sight imaging based on the light-cone transform. *Nature* **555**, 338–341 (2018).
10. Jarabo, A., Masia, B., Marco, J. & Gutierrez, D. Recent advances in transient imaging: a computer graphics and vision perspective. *Visual Informatics* **1**, 65–79 (2017).
11. Velten, A. et al. Femto-photography: capturing and visualizing the propagation of light. *ACM Trans. Graph.* **32**, 44 (2013).
12. Gupta, M., Nayar, S. K., Hullin, M. B. & Martin, J. Phasor imaging: a generalization of correlation-based time-of-flight imaging. *ACM Trans. Graph.* **34**, 156 (2015).
13. O'Toole, M. et al. Reconstructing transient images from single-photon sensors. In *2017 IEEE Int. Conf. Computational Photography (CVPR)*, 1539–1547 (IEEE, 2017).
14. Gkioulekas, I., Levin, A., Durand, F. & Zickler, T. Micron-scale light transport decomposition using interferometry. *ACM Trans. Graph.* **34**, 37 (2015).
15. Xin, S. et al. A theory of Fermat paths for non-line-of-sight shape reconstruction. In *IEEE Int. Conf. Computer Vision and Pattern Recognition (CVPR)*, 6800–6809 (IEEE, 2019).
16. Tsai, C., Sankaranarayanan, A. & Gkioulekas, I. Beyond volumetric albedo a surface optimization framework for non-line-of-sight imaging. In *IEEE Conf. Computer Vision and Pattern Recognition (CVPR)*, 1545–1555 (IEEE, 2019).
17. Liu, X., Bauer, S. & Velten, A. Analysis of feature visibility in non-line-of-sight measurements. In *IEEE Intl Conf. Computer Vision and Pattern Recognition (CVPR)* 10140–10148 (IEEE, 2019).
18. Wu, R. et al. Adaptive polarization-difference transient imaging for depth estimation in scattering media. *Opt. Lett.* **43**, 1299–1302 (2018).
19. Laurenzis, M. & Velten, A. Feature selection and back-projection algorithms for nonline-of-sight laser-gated viewing. *J. Electron. Imaging* **23**, 063003 (2014).
20. Heide, F. et al. Non-line-of-sight imaging with partial occluders and surface normals. *ACM Trans. Graph.* **38**, 22 (2019).
21. Kadambi, A., Zhao, H., Shi, B. & Raskar, R. Occluded imaging with time-of-flight sensors. *ACM Trans. Graph.* **35**, 15 (2016).
22. Shen, F. & Wang, A. Fast-Fourier-transform based numerical integration method for the Rayleigh–Sommerfeld diffraction formula. *Appl. Opt.* **45**, 1102–1110 (2006).
23. Sen, P. et al. Dual photography. *ACM Trans. Graph.* **24**, 745–755 (2005).
24. O'Toole, M. et al. Temporal frequency probing for 5D transient analysis of global light transport. *ACM Trans. Graph.* **33**, 87 (2014).
25. Goodman, J. *Introduction to Fourier Optics* 3rd edn (Roberts, 2005).
26. Jarabo, A. et al. A framework for transient rendering. *ACM Trans. Graph.* **33**, 177 (2014).
27. Galindo, M. et al. A dataset for benchmarking time-resolved non-line-of-sight imaging. In *IEEE Intl Conf Computational Photography* https://graphics.unizar.es/nlos (IEEE, 2019).

METHODS

Details on data acquisition. *Hardware configuration.* Our capture system, shown in Extended Data Fig. 1, consists of a Onefive Katana HP amplified diode laser (1 W at 532 nm, and a pulse width of about 35 ps used at a repetition rate of 10 MHz) and a gated SPAD detector processed by a time-correlated single-photon counter (PicoQuandt HydraHarp), with a time resolution of about 30 ps and a dead time of 100 ns. Two additional charge-coupled device (CCD) cameras are used to calibrate the laser's position. The measured time resolution of our system is approximately 65 ps, a combination of the pulse width of the laser and the time jitter of the system.

NLOS measurement geometry. We obtain an impulse response function $H(\boldsymbol{x}_p \rightarrow \boldsymbol{x}_c, t)$ of the scene by sequentially illuminating points $\boldsymbol{x}_p$ on the relay wall with a short pulse and detecting the signal returning at points $\boldsymbol{x}_c$.

Our hardware device is located 2.5 m from the relay wall, with the NLOS scenes hidden from direct view. The field of view is 25°. The walls are made of standard white styrofoam. The scanning area in the relay wall (virtual camera) is 1.8 m × 1.3 m, with laser points $\boldsymbol{x}_p$ spaced by $\Delta_p = 1$ cm in each direction. The SPAD is focused at a position near the centre of the grid. We avoid scanning a small square region around the SPAD focused position (the confocal position) because the signal becomes very noisy at this location. Figures 2, 3 provide additional details for the specific scenes shown.

Exposure time. Our capture set-up includes CCD cameras (Extended Data Fig. 1) to confirm the 3D position of every laser during the measurement; these are a limiting factor in the speed of our experiments. Because the capture process runs in parallel, we use a very long (1 s) exposure time per laser position for some datasets. They are used for all results unless otherwise specified. In addition, we capture scenes without the additional CCD photographs that can be collected much faster and with much shorter exposure times. In Fig. 2, we show datasets of an office scene captured with exposure times of 1 ms to 10 ms per laser position, which results in a total capture time as low as 24 s. Further reconstructions of a shelf dataset are shown later as additional results, showing that we can reduce exposure times at least down to 50 ms per data point without a significant loss in quality, even with ambient light. This results in less than 20 min of total capture time. In our current prototype, we capture data sequentially with a single SPAD. Prototype SPAD arrays are currently under development, and it seems likely that a 16 × 16 array will be available by the end of the year. We thus expect to be able to capture 256 data points in less than 0.1 s in the near future.

Collected data. In total (counting captures with different lighting and exposure times as different sets), we use 12 experimental and two simulated datasets. All experimental datasets use a single SPAD location and 180 by 130 laser positions. The datasets and exposure times are:

- An office scene collected with 1 s exposure per laser position. This dataset is used to create the video shown in Supplementary Video 1, frames of which are shown in Fig. 4b. A photograph and reconstruction of this scene is also shown in the Supplementary Video. The data are analysed in Extended Data Fig. 3 and Extended Data Table 1.
- An office scene collected with exposures of 10 ms, 5 ms and 1 ms, used in Fig. 2, Extended Data Figs. 6–8 and Extended Data Table 1.
- A scene of a bookshelf used in Fig. 3a and in Extended Data Table 1.
- A scene of a bookshelf captured with various exposure times and ambient light conditions, shown in Extended Data Fig. 2 and Extended Data Fig. 5.
- A scene with letters distributed over a large depth, used in Fig. 3b and Extended Data Table 1.
- A scene of the letters NLOS in a plane, used in Fig. 4a and Extended Data Table 1.

To provide further insight into the noise and artefacts present in our data, we go through an analysis of the raw data from our 1-s-exposure office scene. We compare the maximum and average number of photons per second and laser position $\boldsymbol{x}_p$ for our captured scenes in Extended Data Table 1. The dark count rate of our detector is 10 photons per second. We do not explicitly subtract dark counts nor ambient light or backgrounds. The high total photon numbers in the transient responses (Extended Data Table 1) are due to the long responses associated with the large depth and volume of the scenes, and not due to a particularly bright signal. Example data for a scene of a shelf are shown in Extended Data Fig. 2 (whose reconstruction can be found on Extended Data Fig. 5). In this scene, our longest (1 s) exposure time peaks at about 150 photons per second (such peaks are probably due to the presence of specular surfaces), and the captured signal is extremely noisy. In comparison, the recent method by O'Toole et al.[9] acquires a brighter, cleaner signal in 0.1 s, peaking at about 600 photons per second, owing to the use of retroreflective paint applied on the hidden objects (data from their data_resolution_chart_40cm dataset).

Let us further analyse the captured data. In Extended Data Fig. 3a, we show a visualization of our data matrix for the 1-s-exposure office scene using the Matlab function *imagesc*, in which each row is the data collected for a different location of the laser illumination spot, and each column contains a different time bin. The first time bin corresponds to the time when the illumination laser pulse leaves the relay wall. In the images, we do not show time bins 10,001 to 15,000 as they are mostly empty, owing to the closing of the gate. As can be seen, there are some sparse, very large peaks in the dataset that saturate the counting registers of our time-correlated single-photon counter ($2^{16} - 1$ counts). As we will see, these artefacts in the data are likely to be due to imperfections in the gating or optical set-up.

Let us focus on the first instants of the captured data shown in Extended Data Fig. 3a, which reveal features that look like straight diagonal lines in the first few time bins. The fact that there are straight lines in this plot indicates that they are likely related to a first-bounce signal, rather than the scene response. NLOS signals should show up as hyperbolas or sections of hyperbolas in this type of visualization, and the curvature of the hyperbolas should be highest at the earliest time bins. The image contains many more features that look like straight lines that do not appear to have the correct hyperbolic curvature to be NLOS signals. Many of them also appear identically in the other datasets, which is another hint that they are probably not real NLOS data but artefacts related to the measurement system. Our algorithm is completely agnostic to the presence of these artefacts. The brightest peaks also appear too early in the data to be associated with a NLOS object. To see this, consider that the closest object in any of our scenes is the chair in the office scene, and it is more than 50 cm away from the wall. Consequently, the first time response from an actual object cannot arrive at the SPAD earlier than 3.3 ns after the laser illuminates the relay wall. Time bins are 4 ps wide. Any data before time bin 833 therefore can only be an artefact. We will speculate more about the origin of these artefacts later.

If we ignore those first 833 time bins that contain no useful data, we obtain a dataset that can yield some meaningful statistics about the data. In this dataset, the largest photon count in all our over 200 million time bins is smaller than 1,400 photons. As we show below, this 1,400 maximum is probably still due to a gate artefact that happened to occur slightly later than 3 ns into the dataset. Statistics for all datasets are shown in Extended Data Table 1.

Maximum photon counts usually come from the objects in the scene closest to the wall. Considering the large depth and specularities of our scenes, most of the reconstructed scene volume is using signals much weaker than the maximum signal, as voxels are further from the wall. Signals from a given surface are expected to drop in magnitude with distance L as $1/L^4$. An object generating 100 photon peaks at 50 cm distance in the front of our scene would therefore only create 100/8 photons if placed at 1 m and $100/625 = 0.2$ photons at 2.5 m towards the end of our office scene. This ability to handle scenes with large dynamic range in the data is another advantage of our algorithm.

In Extended Data Fig. 3b, we show a plot of the photon counts over time bins for the laser position that received the most total photons. We again see the extreme peak of $2^{16} - 1$ counts in the beginning of the dataset. Again, this peak cannot be a real third-bounce signal as it would require the pulse to travel between the laser position and SPAD position much faster than the speed of light. The actual NLOS data start around time bin 1,000 and peak at just above 50 photons.

Finally, we show a plot of the laser position that received the total photon count closest to the median of all laser positions (Extended Data Fig. 3c). We can see that the count generally stays below 150 photons, with what are probably specular peaks reaching 200 photons and a large (450 photon) peak at the beginning of the dataset that is either a specular peak or another gate artefact. Note that as we illuminate only a grid of points at the wall, we do not capture all the specular peaks in our data. To see a specular reflection peak from a scene surface, we have to be lucky enough to illuminate the exact spot on the wall that results in the specular reflection that overlaps with the SPAD position (see Supplementary Fig. 2 for an illustration). Therefore, specular peaks in our measurements can vary greatly, depending on how close to the peak the laser sampled the wall. Again, we point out that this type of uncontrolled artefact does not affect our algorithm.

As we stated above, the time bin with the highest photon count when ignoring obvious early artefacts contains about 1,400 photons. Next we plot the laser position that contains this time bin (Extended Data Fig. 3d). Note that zero on the x axis here corresponds to time bin 834. As we see, the 1,400 photon peak appears very close to the beginning of the transient and may be a gating artefact that occurs in the data just after the opening of the gate. This type of data distortion is described further below. If not a gating artefact, the peak is probably a specular reflection, as it is very narrow and could only be caused by a small isolated diffuse patch or a specular surface in the scene. Peaks from extended diffuse surfaces are necessarily longer in duration.

We conclude that although our data contain artefacts, the photon counts useful for reconstructions are no higher or cleaner than in previous methods. Note that the removal of early artefacts is only done here to generate Extended Data Fig. 3b–d, to allow visualization. All reconstructions shown in the manuscript contain the full recorded data without the removal of any potential artefacts or time bins.

Even though an understanding of the origin of the artefacts is not needed for our method, we can speculate on the sources of some of them.

(1) Many of the early peaks in our data are likely to be related to imperfections in our gating method. When the SPAD gate opens just after the laser pulse has passed, photoelectrons in the SPAD may cause a detection event that is not due to a photon but to electrons excited by the first-bounce light and trapped in long-lived states in the SPAD. Even though these electrons are not amplified, they need to be transported off the SPAD junction or they can cause counts as soon as the gate opens.

(2) The gate may not block the pulse for some laser positions. The gate has to be positioned such that it blocks the laser in all laser positions while not blocking any signal. This is not always possible, and we do not re-adjust the gate for each position while scanning.

(3) Effects inside the imaging system can keep light trapped long enough to cause a peak at the time when the NLOS data arrive. This can be due to multiple reflections between lenses, multiphoton fluorescence in the glass or coating of the lenses, or stray light reflecting off a random surface at the right distance. We have confirmed some of these effects but suspect there are many more.

(4) In particular, we can see light that travels from the laser spot to the SPAD, reflects off the surface of the SPAD pixel, is imaged back to the relay wall and comes back to the SPAD. In confocal or near-confocal configurations, this can create a peak that is many times brighter than the data.

Retroreflective targets can be used to reduce many of these artefacts, most of which are created either by the laser or a first-bounce reflection of the laser. If the hidden target is retroreflecting, the ratios between the brightness of the laser and its first bounce and the brightness of the third-bounce NLOS data are reduced by multiple orders of magnitude.

Helmholtz reciprocity. Ideally, we would capture $H(\boldsymbol{x}_p \rightarrow \boldsymbol{x}_c, t)$ sampling points on both the projector aperture $\boldsymbol{x}_p \in P$ and the camera aperture $\boldsymbol{x}_c \in C$. In our current set-up with a single SPAD, we only sample a single point for $\boldsymbol{x}_c$. From Helmholtz reciprocity, we can interpret these datasets as having a single $\boldsymbol{x}_p$ and and array of $\boldsymbol{x}_c$. The choice of capture arrangement is made for convenience, as it is easier to calibrate the position of the laser spot on the wall. Improved results are anticipated once array sensors become available (currently under development).

Additional validation and discussion. *Resolution limits.* The resolution limit for NLOS imaging systems with an aperture diameter d at imaging distance L is closely related to the Rayleigh diffraction limit[7]: $\Delta_x = 1.22c\sigma L/d$, with c the speed of light in vacuum, for a pulse of full width at half maximum σ. O'Toole et al.[9] derive a criterion for a resolvable object based on the separability of the signal in the raw data, not in the reconstruction, resulting in a similar formula, $\Delta_x = 0.5c\sigma L/d \approx 0.5\lambda L/d$.

In our virtual LOS imaging system, we can formulate a resolution limit that ensures a minimum contrast in the reconstruction, based on the well-known resolution limits of wave-based imaging systems. The resolution limit therefore depends on the particular choice of virtual imaging system. For an imaging system that uses focusing only on the detection or illumination side, this limit is approximated by the Rayleigh criterion. For an imaging system that provides focusing on both the light source and the detector side, the resolution doubles (as it does, for example, in a confocal or structured illumination microscope) and the resolution limit becomes becomes $\Delta_x = 0.61\lambda L/d$.

Effect of strong interreflections. To confirm the presence and effect of strong interreflections in our captured data, we compare the data qualitatively with primary data from a synthetic bookshelf scene, with and without interreflections. The bookshelf is placed in a corridor of 2 m × 2 m × 3 m, with only a single lateral aperture of 1 m × 2 m to allow the hidden scene to be imaged. The shelf has a size of 1.4 m × 0.5 m, placed at 1.7 m from the relay wall and 0.3 m from the lateral walls. The virtual aperture has a size of 1.792 m × 1.792 m and a granularity of 256 × 256 laser points; we use $\lambda = 4\Delta_p$ and $\Delta_p = 0.7$ cm.

As can be seen in Extended Data Fig. 4, the synthetic data clearly show how the presence of interreflections adds, as expected, low-frequency information resembling echoes of light. The same behaviour can be seen in the real captured data, revealing the presence of strong interreflections.

Additionally, we evaluate the robustness of our method in the presence of such interreflections. Similar to recent work[9], we compare between a voxelization of the ground-truth geometry and a reconstructed voxel-grid obtained from our irradiance reconstructions, with and without including interreflections; the resulting MSE is as follows: without interreflections (Extended Data Fig. 4a), MSE 4.93 mm; with interreflections (Extended Data Fig. 4b), MSE = 4.66 mm.

Effect of exposure time. *Ambient light.* To analyse how well our technique works in ambient light and with much shorter exposure times, we perform several additional measurements using progressively shorter exposure times, showing that we can reduce exposure times at least down to 50 ms per data point without a significant loss in quality (see Extended Data Fig. 5). Extended Data Fig. 2 shows raw data for one of the laser positions. In particular, it shows the number of photons per second accumulated in each time bin (that is, the collected histogram divided by the integration time in seconds). As expected, all three curves appear to follow the same mean but have a larger variance for lower exposure times. The raw data thus become noisier as exposure time decreases. The effects on our reconstruction, however, are minor, as Extended Data Fig. 5 shows.

Short-exposure captured data. Extended Data Fig. 6 shows the reconstruction of the office scene (Fig. 2) for short exposure times of 10 ms, 5 ms and 1 ms for each of the roughly 24,000 laser positions. This leads to total capture times of about 4 min, 2 min and 24 s respectively. Plots showing raw data from those datasets are given in Extended Data Fig. 7.

We compare the results of our reconstructions on the 1 ms data against filtered backprojection with a Laplacian filter[3], as well as the Laplacian-of-Gaussian (LOG)-filtered backprojection[19], which generally achieves better results. We are not aware of any reconstruction method that consistently outperforms a LOG-filtered backprojection. Extended Data Fig. 8 shows the result of this comparison.

Non-Lambertian surfaces. To validate the robustness of our method in the presence of non-Lambertian materials in the hidden scene, we have created a synthetic scene made up of two letters, R and D, one partially occluding the other, placed in a corridor of 2 m × 2 m × 3 m, with only a single lateral aperture of 1 m × 2 m to allow imaging the hidden scene. The letters have a size of 0.75 m × 0.8 m, placed at 1.25 m and 1.7 m from the relay wall, respectively, and 0.5 m from the lateral walls (see Extended Data Fig. 9a). The virtual aperture has a size of 1.792 m × 1.792 m and a granularity of 128 × 128 laser points; we use $\lambda = 4\Delta_p$ with $\Delta_p = 1.4$ cm. We start with purely Lambertian targets and progressively increase their specularity. We use the Ward BRDF model[28], decreasing the surface roughness, using available transient rendering software[26]. The simulation includes up to the fifth indirect bounce.

Extended Data Fig. 9b shows the resulting irradiance reconstructions. Because our method does not make any assumption about the surface properties of the hidden scene, the changes in material appearance do not significantly affect our irradiance reconstructions. Similar to recent work[9], we compare a voxelization of the ground-truth geometry and the reconstructed voxel-grid; the resulting MSE for each of the different reflectances is as follows: for a surface roughness of 1 (perfect Lambertian), MSE = 2.1 mm; for a surface roughness of 0.4, 2.2 mm; for a surface roughness of 0.2, MSE = 2.2 mm.

Reconstruction comparison with other methods. Our imaging system allows hidden geometry to be reconstructed. For this application, we show a comparison using the publicly available confocal dataset[9]. This set can be reconstructed using different NLOS methods; we show results for confocal NLOS deconvolution[9], filtered backprojection[7] and our proposed method. For these confocal measurements, backprojection can be expressed as a convolution with a pre-calculated kernel, and thus all three methods are using the same backprojection operator. Neither our method nor filtered backprojection is limited to confocal data, and both can be acquired by making use of simpler devices and capture configurations. They can thus be applied to a broader set of configurations and considerably more complex scenes. For the confocal NLOS deconvolution method[9], we leave the optimal parameters unchanged. For our proposed virtual wave method, we use the aperture size and its spatial sampling grid (see Supplementary Information) to calculate the optimal phasor-field wavelength. For the filtered backprojection, it is important to choose a good discrete approximation of the Laplacian operator in the presence of noise. Previous works implicitly do the denoising step by adjusting the reconstruction grid size to approximately match the expected reconstruction quality[2,3,7], or by downsampling across the measurements[9]. If used correctly, all of these methods result in a high-quality reconstruction from a Laplacian filter. To provide a fair comparison without changing the reconstruction grid size, we convolve a Gaussian denoising kernel with the Laplacian kernel, resulting in a LOG filter, which we apply over the backprojected volume.

Note that a large improvement in reconstruction quality for the simple scenes included in the dataset (isolated objects with no interreflections) is not to be expected, since existing methods already deliver reconstructions approaching their resolution limits. We nevertheless achieve improved contrast and cleaner contours in our wave camera method, due to our better handling of multiply scattered light, which pollutes the reconstructions in the other methods (see Extended Data Fig. 10).

In the noisy datasets (Extended Data Fig. 11), filtered backprojection fails. confocal NLOS includes a Wiener filter that performs well at removing uniform background noise, although a noise level must be explicitly estimated. Our phasor-field virtual wave method, on the other hand, performs well automatically, without the need to explicitly estimate a noise level. This is important in complex scenes with interreflections, where the background is not uniform across the scene, and the noise level cannot be reliably estimated.

Nevertheless, our main contribution is not that of improving the reconstruction for simple, third-bounce scenes. Instead, our method allows a new class of NLOS algorithms to be derived, which can successfully handle scenes of much greater complexity.

Data availability

The measured data and the phasor-field NLOS code supporting the findings of this study are available in the figshare repository https://doi.org/10.6084/m9.figshare.8084987. Additional data and code are available from the corresponding authors upon request.

Code availability

Our data and reconstruction code can be found in the figshare repository https://doi.org/10.6084/m9.figshare.8084987.

28. Ward, G. J. Measuring and modeling anisotropic reflection. *Comput. Graph*. **26**, 265–272 (1992).

Acknowledgements This work was funded by DARPA through the DARPA REVEAL project (HR0011-16-C-0025), the NASA Innovative Advanced Concepts (NIAC) Program (NNX15AQ29G), the Air Force Office of Scientific Research (AFOSR) Young Investigator Program (FA9550-15-1-0208), the Office of Naval Research (ONR, N00014-15-1-2652), the European Research Council (ERC) under the EU's Horizon 2020 research and innovation programme (project CHAMELEON, grant no. 682080), the Spanish Ministerio de Economía y Competitividad (project TIN2016-78753-P) and the BBVA Foundation (Leonardo Grant for Researchers and Cultural Creators). We thank J. Teichman for insights and discussions in developing the phasor-field model. We also acknowledge M. Buttafava, A. Tosi and A. Ingle for help with the gated SPAD detector, and B. Masia, S. Malpica and M. Galindo for careful reading of the manuscript.

Author contributions X.L., S.A.R., M.L.M. and A.V. conceived the method. X.L., I.G., M.L.M. and J.H.N. implemented the reconstruction. M.L.M., X.L., J.H.N. and T.H.L. built and calibrated the system. I.G., D.G. and A.J. developed the simulation system. A.J., D.G. and A.V. coordinated the project. All authors contributed to writing the paper.

Competing interests The authors declare no competing interests.

Additional information
Supplementary information is available for this paper at https://doi.org/10.1038/s41586-019-1461-3.
Correspondence and requests for materials should be addressed to A.V.
Peer review information *Nature* thanks Jeffrey H. Shapiro, Ashok Veeraraghavan and the other, anonymous, reviewer(s) for their contribution to the peer review of this work.
Reprints and permissions information is available at http://www.nature.com/reprints.

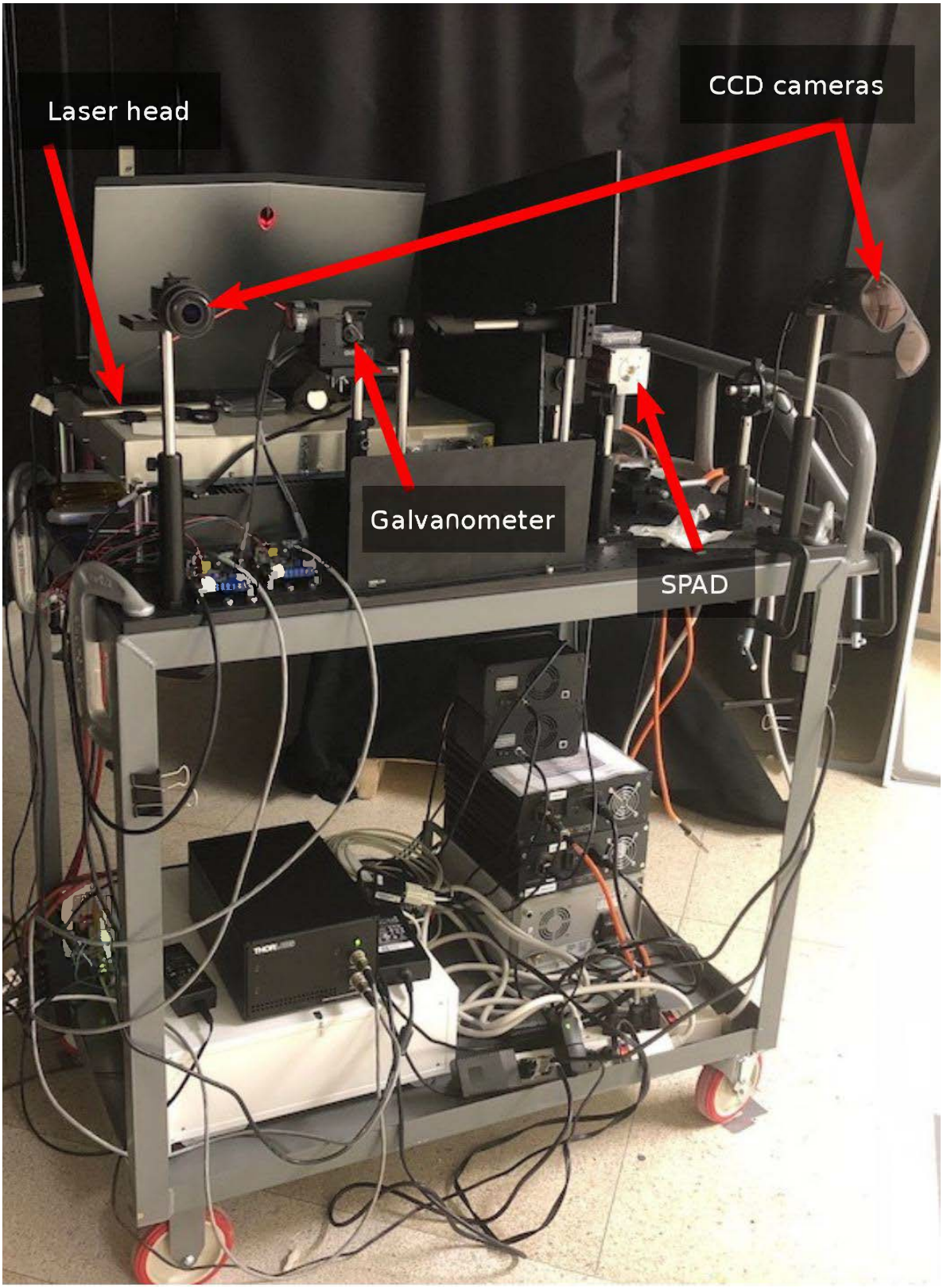

Extended Data Fig. 1 | Capture hardware used for the results shown in this Letter.

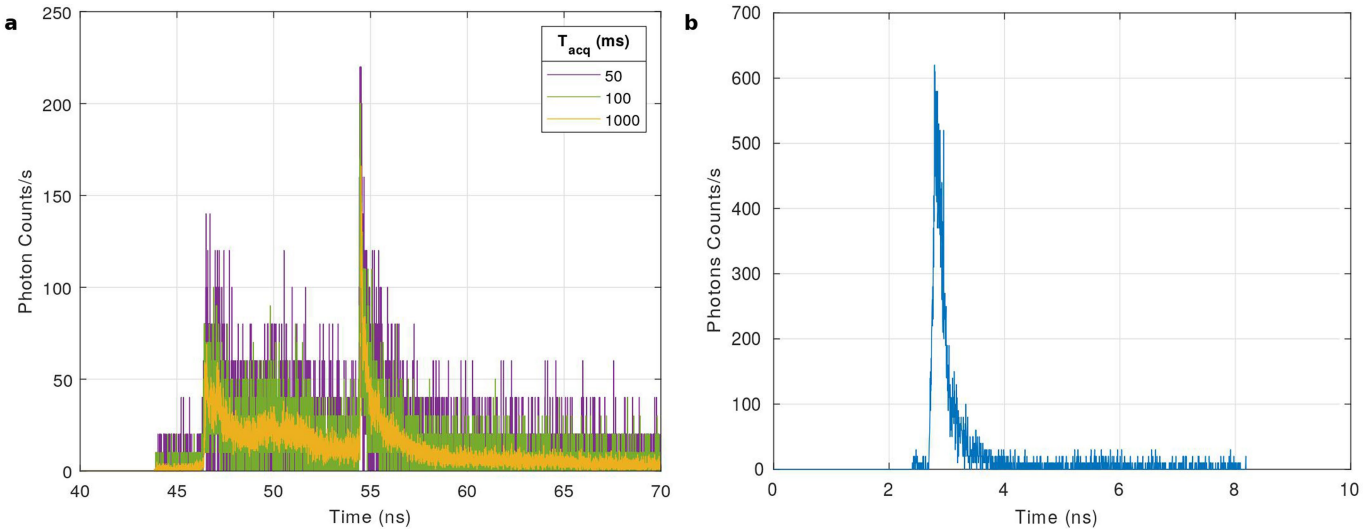

Extended Data Fig. 2 | Data comparison. a, Raw data for one of the laser positions $\boldsymbol{x}_p$. Shown is the number of photons per second accumulated in each time bin (that is, the collected histogram divided by the integration time in seconds). Time bins are 4 ps wide. As expected, all three curves appear to follow the same mean, but there is a larger variance for lower exposure times. The raw data thus become noisier as exposure time decreases. The effects on the reconstruction are minor, as Extended Data Fig. 4 shows. T_{acq}, acquisition time. **b**, Example dataset from ref. [9] for comparison.

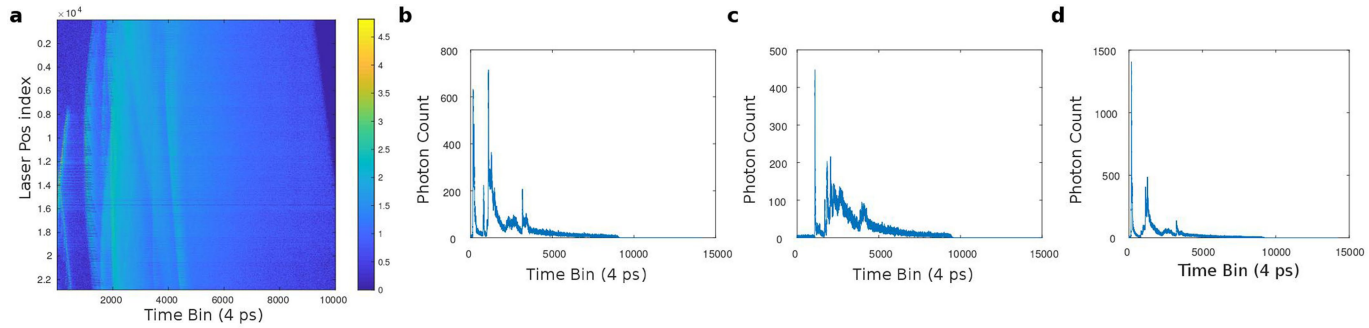

Extended Data Fig. 3 | Visualization of the raw data for our long-exposure office scene. a, Base-10 logarithm of the photon counts in all time bins. Pos index, laser position index; the 24,000 laser positions on the wall are labelled with these consecutive numbers. **b–d**, After removal of the first 833 time bins in each dataset, the plots show: the photon counts for the laser position that received the largest total number of photons in the dataset (**b**); the counts for the laser position that received the median number of photon counts (**c**); and the counts for the laser position that contains the time bin with the global maximum count in the entire set (**d**).

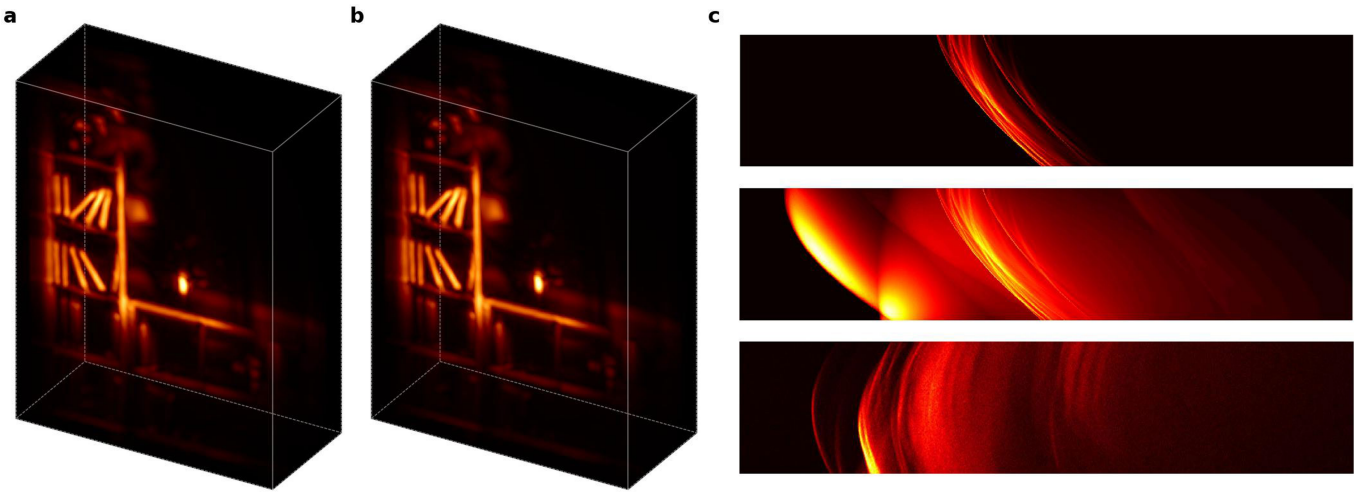

Extended Data Fig. 4 | Robustness to multiple reflections. Result for the synthetic bookshelf scene. **a**, Without interreflections. **b**, Including high-order interreflections. The quality of the results is very similar. **c**, Primary data (streak images) from the same scene without (top), and with interreflections (middle). The synthetic data clearly show how the presence of interreflections adds, as expected, low-frequency information resembling echoes of light. The bottom image shows primary data captured from the real office scene in Fig. 2. It follows the same behaviour as the middle image, revealing the presence of strong interreflections. Colours refer to numerical values from Matlab's 'fire colormap', in arbitrary units.

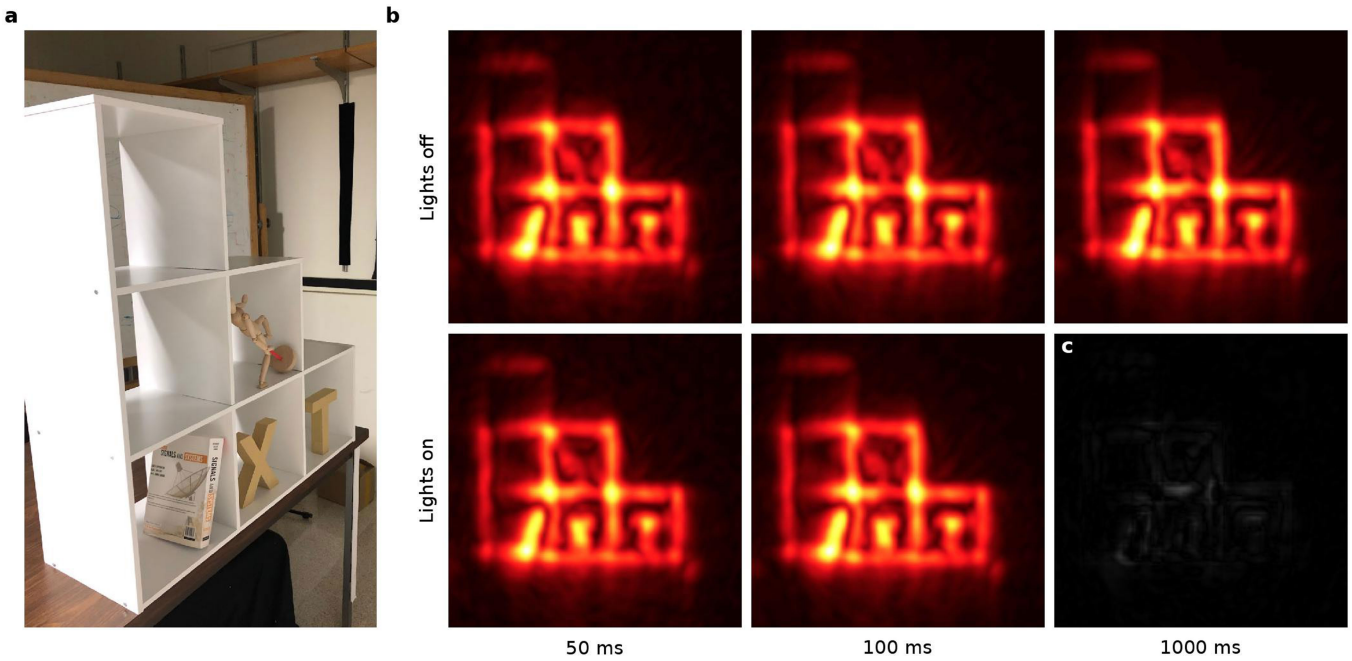

Extended Data Fig. 5 | Robustness to ambient light and noise. a, Hidden bookshelf. **b**, Imaging results with increasingly higher exposure times; even at 50 ms, there is no significant loss in quality. Top row, image using only the pulsed laser as illumination source. Bottom row, on adding a large amount of ambient light (same conditions as the photograph in **a**), the quality remains constant. **c**, Difference between the 50-ms- and 1,000-ms-exposure captures for the lights-off case.

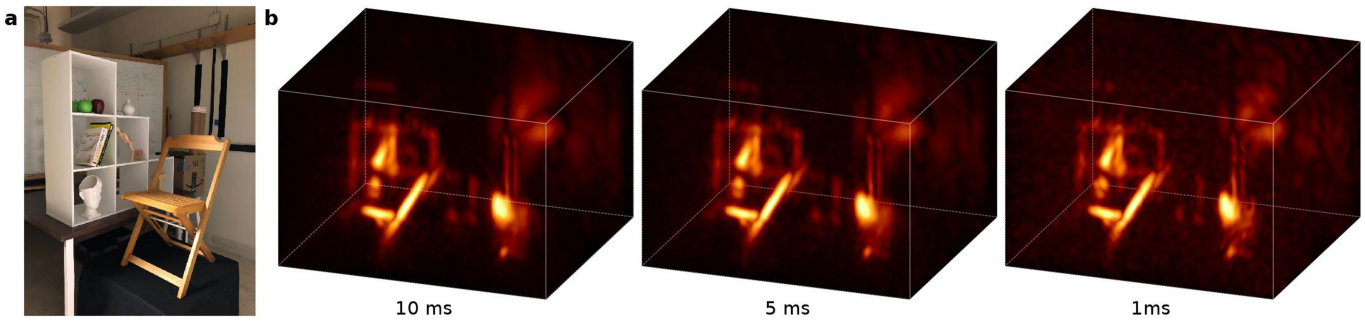

Extended Data Fig. 6 | Short-exposure reconstructions. Reconstruction of the office scene using very short capture times. **a**, Photograph of the captured scene. **b**, From left to right, reconstructions for data captured with 10 ms, 5 ms and 1 ms exposure time per laser. The total capture time was about 4 min, 2 min and 24 s, respectively.

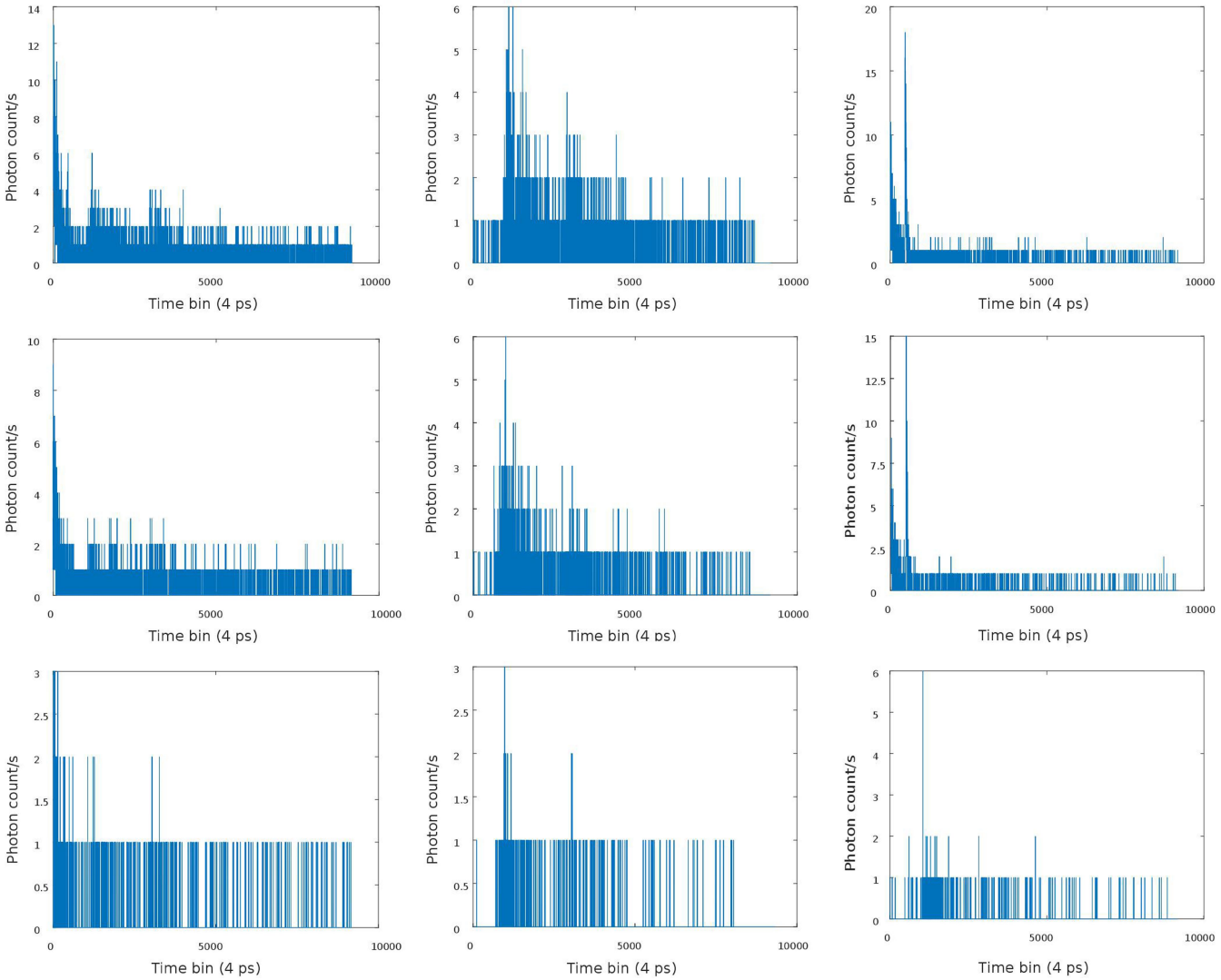

Extended Data Fig. 7 | Short-exposure data. Photon counts in the raw data for our office scene for 10 ms (top row), 5 ms (centre row) and 1 ms (bottom row) exposure times per laser position. After removing the first 833 time bins in each dataset, the columns show: the photon counts for the laser position that received the largest total number of photons in the dataset (left); the counts for the laser position that received the median number of photon counts (centre); and the laser position that contains the time bin with the global maximum count in the entire set (right).

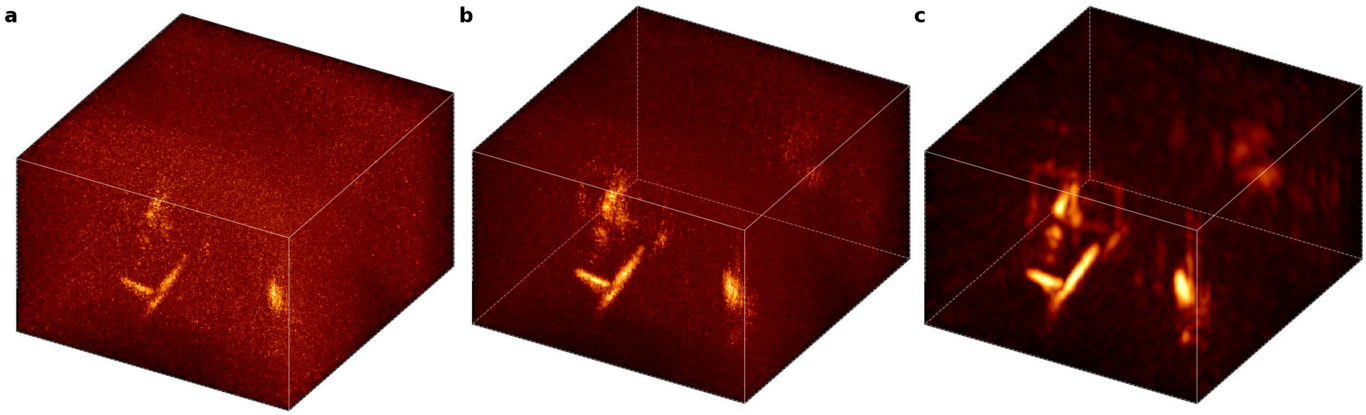

Extended Data Fig. 8 | Comparison to prior methods. Reconstruction of the office scene using very short capture times of 1 ms per laser (24 s in total). **a**, Filtered backprojection using the Laplacian filter. **b**, LOG-filtered backprojection. **c**, Our method.

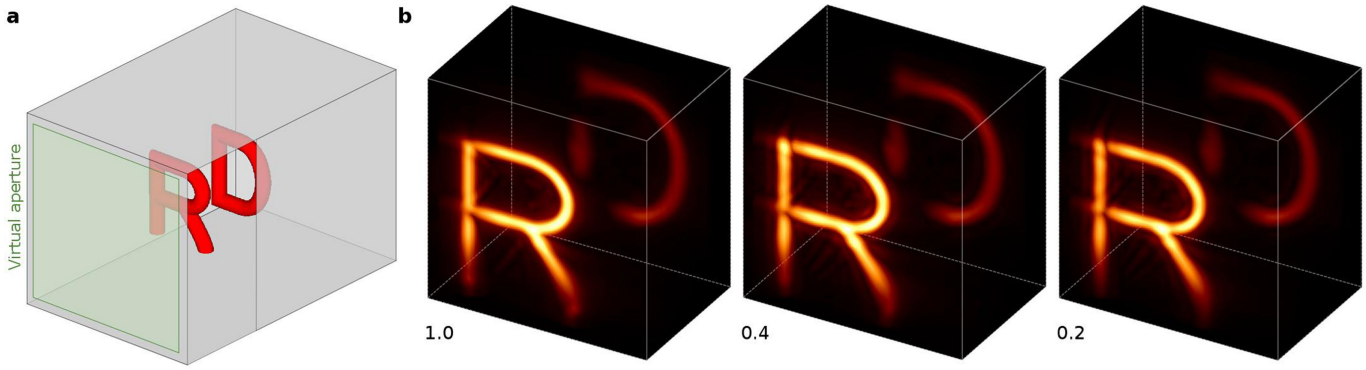

Extended Data Fig. 9 | Robustness to scene reflectance. a, Geometry of our experimental set-up. **b**, From left to right, imaging results for the Lambertian targets (roughness 1) and increasingly specular surfaces (roughness 0.4 and roughness 0.2). The reconstructed irradiance is essentially the same for all cases.

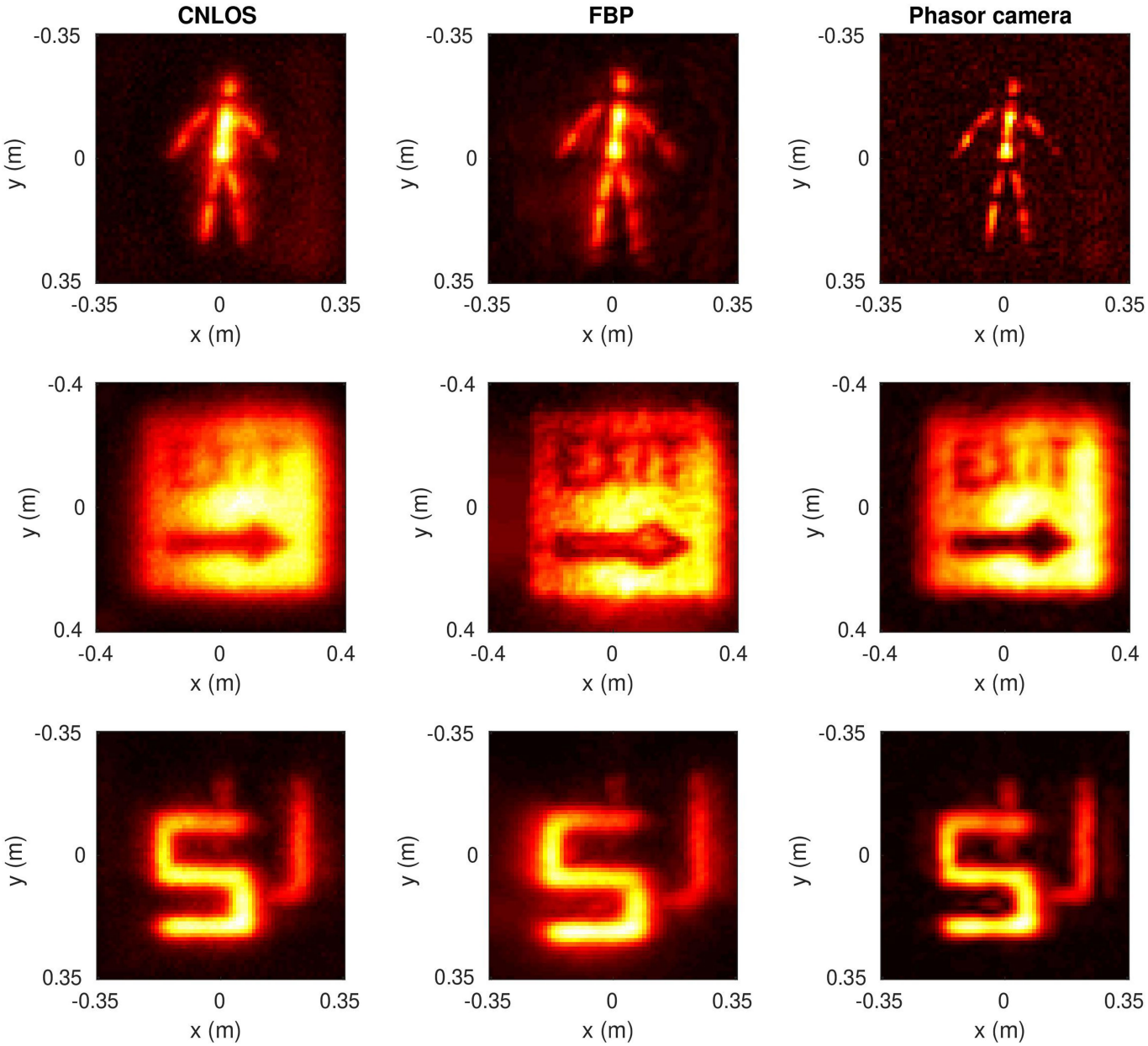

Extended Data Fig. 10 | Reconstruction comparison on a public dataset. From left to right: confocal NLOS deconvolution, filtered (LOG) backprojection (FBP) and our proposed method. A large improvement in reconstruction quality for the simple scenes included in the dataset (isolated objects with no interreflections) is not to be expected, as existing methods already deliver reconstructions approaching their resolution limits. Nevertheless, our method achieves improved contrast and cleaner contours, owing to better handling of multiply scattered light.

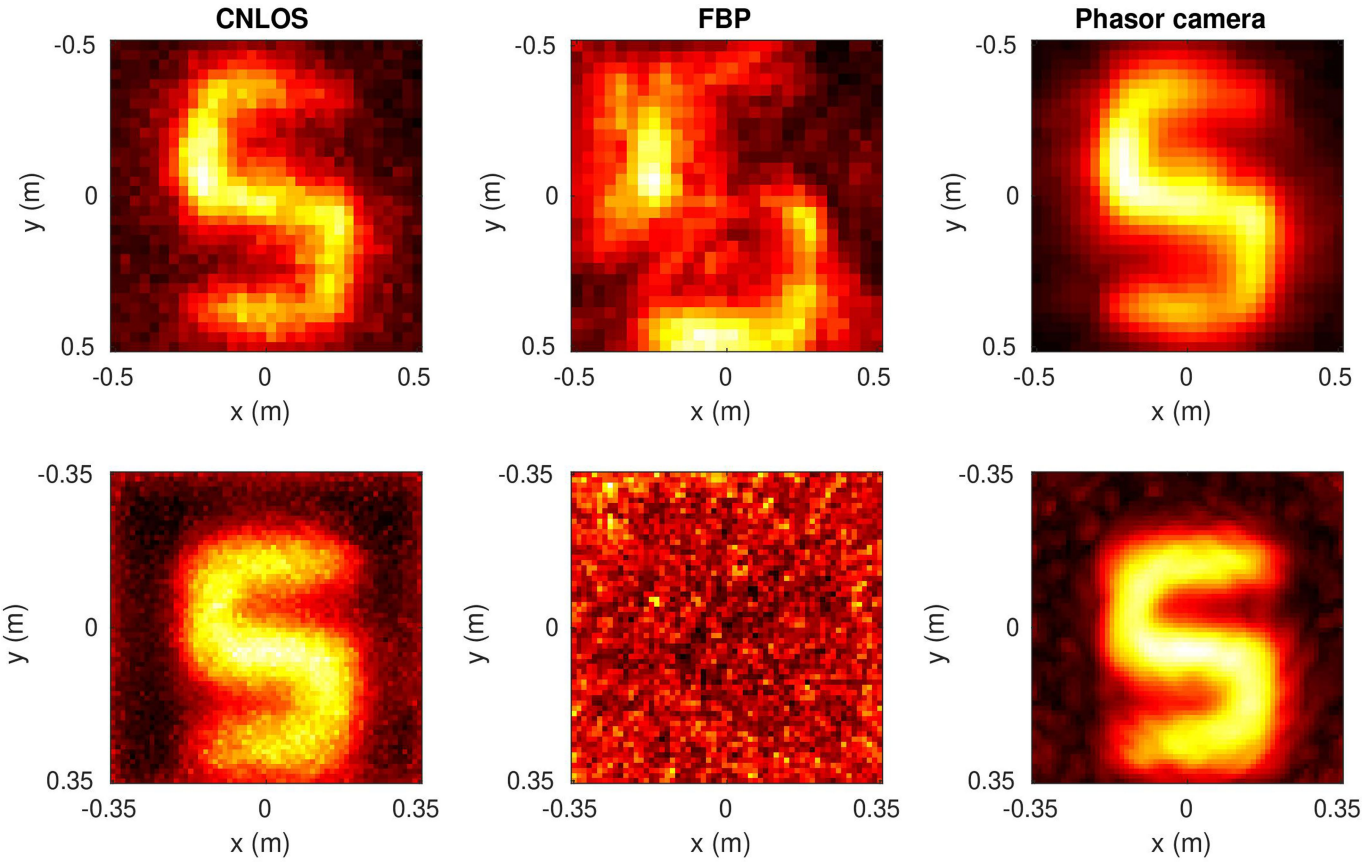

Extended Data Fig. 11 | Reconstruction comparison (noisy data). From left to right: confocal NLOS deconvolution, FBP and our proposed method. Top row represents a non-retroreflective object; bottom row represents a retroreflective object captured in sunlight. In the presence of noisy data, FBP fails. Confocal NLOS includes a Wiener filter that needs to be explicitly estimated. Our phasor-field virtual wave method yields better results automatically. This is particularly important in complex scenes with interreflections, where the background is not uniform across the scene, and the noise level cannot be reliably estimated.

Extended Data Table 1 | Photon statistics for captured data used in the paper and in Supplementary Information

	Total Photons	Photons/bin	Max. bin	Avg./ laser
Large depth scene	3215722952	9.7	552	13742
NLOS letters	6502986696	19.6	2889	27791
Shelf	6158590767	18.6	2074	26319
Office Scene	6201680972	18.7	1406	26503
Office Scene 10 ms	48017499	0.14	18	2716
Office Scene 5 ms	24012257	0.072	15	1026
Office Scene 1 ms	4801568	0.014	6	205

The first four scenes were captured with 1 s exposure time. The first column shows the total photons counted, the second shows the average photon count per time bin, the third is the maximum count over all time bins, and the last contains the average number of photons collected in each laser position in the dataset.

LETTER

https://doi.org/10.1038/s41586-019-1496-5

Superconductivity in an infinite-layer nickelate

Danfeng Li[1,2]*, Kyuho Lee[1,3], Bai Yang Wang[1,3], Motoki Osada[1,4], Samuel Crossley[1,2], Hye Ryoung Lee[1,4], Yi Cui[1,4], Yasuyuki Hikita[1] & Harold Y. Hwang[1,2]*

The discovery of unconventional superconductivity in $(La,Ba)_2CuO_4$ (ref. [1]) has motivated the study of compounds with similar crystal and electronic structure, with the aim of finding additional superconductors and understanding the origins of copper oxide superconductivity. Isostructural examples include bulk superconducting Sr_2RuO_4 (ref. [2]) and surface-electron-doped Sr_2IrO_4, which exhibits spectroscopic signatures consistent with a superconducting gap[3,4], although a zero-resistance state has not yet been observed. This approach has also led to the theoretical investigation of nickelates[5,6], as well as thin-film heterostructures designed to host superconductivity. One such structure is the $LaAlO_3/LaNiO_3$ superlattice[7–9], which has been recently proposed for the creation of an artificially layered nickelate heterostructure with a singly occupied $d_{x^2-y^2}$ band. The absence of superconductivity observed in previous related experiments has been attributed, at least in part, to incomplete polarization of the e_g orbitals[10]. Here we report the observation of superconductivity in an infinite-layer nickelate that is isostructural to infinite-layer copper oxides[11–13]. Using soft-chemistry topotactic reduction[14–20], $NdNiO_2$ and $Nd_{0.8}Sr_{0.2}NiO_2$ single-crystal thin films are synthesized by reducing the perovskite precursor phase. Whereas $NdNiO_2$ exhibits a resistive upturn at low temperature, measurements of the resistivity, critical current density and magnetic-field response of $Nd_{0.8}Sr_{0.2}NiO_2$ indicate a superconducting transition temperature of about 9 to 15 kelvin. Because this compound is a member of a series of reduced layered nickelate crystal structures[21–23], these results suggest the possibility of a family of nickelate superconductors analogous to copper oxides[24] and pnictides[25].

The most stable nickelates have a formal valence of Ni^{2+} and a d^8 electronic configuration, such as in NiO and La_2NiO_4, but they can also form with d^7 Ni^{3+}, as in $LaNiO_3$. Mimicking the d^9 configuration of undoped copper oxides requires the highly unusual valence Ni^{+}. Although this oxidation state cannot be reached by conventional high-temperature synthesis, it was found that low-temperature reduction of $LaNiO_3$ can induce a topochemical reaction to form $LaNiO_2$[14,15]. (In general, slight oxygen off-stoichiometry is possible, but for simplicity we use the stoichiometric formula throughout this manuscript.) Subsequently, it was shown that this oxygen deintercalation also occurs in epitaxial thin films, with the useful feature that the substrate can provide a template that preserves single-crystal *c*-axis-oriented $LaNiO_2$ (Fig. 1) in the vicinity of the substrate[17–19]. In this structure, nickel has square planar oxygen coordination in two-dimensional NiO_2 planes (alternating with planes of La), with a predicted d^9 configuration leaving one hole in the $d_{x^2-y^2}$ orbital and therefore a possible distinct orbital polarization[5]. Indeed such large preferential orbital occupancy near the Fermi level has been observed in the related trilayer reduced nickelate $La_4Ni_3O_8$ (nominally $Ni^{1.33+}$, $d^{8.67}$)[23].

In preliminary work, we first synthesized $LaNiO_3$ thin films on single-crystal $SrTiO_3$ (001) substrates by pulsed-laser deposition, followed by a reduction step using CaH_2 powder as a reagent (see Methods). Whereas $LaNiO_3$ was metallic down to low temperatures, $LaNiO_2$ was weakly insulating, consistent with previous reports[17,18]. Given that perovskite nickelates can be doped by chemical substitution on the rare-earth site[26,27], we then explored reduced $La_{1-x}Sr_xNiO_2$ thin films as an approach to hole-dope the parent compound. Although the conductivity was enhanced (maximally for $x \approx 0.2$; data not shown), in all cases the resistivity exhibited insulating temperature dependence below about 150 K. Although this result should not be considered definitive (it may depend on further optimization of the growth conditions and reduction process), we then turned to $NdNiO_2$ in an attempt to increase the electronic bandwidth via the smaller ionic radius of Nd with respect to La, which results in a smaller cell volume[15,16]. This tendency has been observed in trilayer reduced nickelates, where $La_4Ni_3O_8$ is insulating, whereas $Pr_4Ni_3O_8$ is metallic down to low temperature[23]. With these motivations, we focused our efforts on optimizing and investigating $NdNiO_2$ and $Nd_{0.8}Sr_{0.2}NiO_2$, which we present in detail here.

Bulk $NdNiO_3$ is orthorhombic with room-temperature lattice parameters $a = 5.39$ Å, $b = 5.38$ Å and $c = 7.61$ Å (a pseudocubic lattice parameter of about 3.81 Å), and doping with Sr has no substantial influence on its room-temperature structure and lattice constants[27]. $NdNiO_2$ reduced from $NdNiO_3$ has been previously synthesized in both polycrystalline[16] and thin-film form[20], and was reasonably straightforward to grow. By contrast, we found that the synthesis of thin-film $Nd_{0.8}Sr_{0.2}NiO_3$ is more challenging—presumably because of the high Ni oxidation state and reduced tolerance factor compared to $LaNiO_3$ (ref. [28]). Figure 2a shows an X-ray diffraction (XRD) θ–2θ symmetric scan of a $Nd_{0.8}Sr_{0.2}NiO_3$ film grown under conditions optimized using XRD, revealing only clear (001) and (002) perovskite peaks (see Methods; 2θ, diffraction angle). (Throughout much of this work we used a $SrTiO_3$ epitaxial capping layer to protect the reduced nickelate films from potential degradation, unless otherwise noted.) From their positions, the *c*-axis lattice constant was extracted to be 3.77 Å, in line with a film under epitaxial tensile strain imposed by the $SrTiO_3$ substrate. Figure 2a also shows the θ–2θ diffraction pattern of the film after reduction, showing peaks with 2θ values of 26.3° and 54.3° corresponding to the (001) and (002) peaks of the infinite-layer phase, respectively, confirming the transformation to $Nd_{0.8}Sr_{0.2}NiO_2$ (refs [16,17]). In measurements with diffraction angles up to $2\theta = 114°$ (not shown) the (003) film peak is not visible owing to its low intensity, whereas the (004) peak falls beyond the diffractometer limit, and no other peaks are observed. Both before and after reduction, the film was always clamped to the in-plane $SrTiO_3$ lattice (Fig. 2b, c).

In bulk undoped $NdNiO_3$, reducing the perovskite to the infinite-layer phase (reported for $NdNiO_{2.03}$) leads to an expansion of the in-plane lattice constants (about 3.92 Å), along with a shortened *c* axis (about 3.31 Å)[16], which is the distance between adjacent Ni–O planes. From the (00*l*) peak positions of the $Nd_{0.8}Sr_{0.2}NiO_2$ film, the *c*-axis lattice constant is found to be 3.37 Å, and it ranges from 3.34 Å to 3.38 Å in samples prepared in nominally similar conditions. The film experiences compressive strain on the $SrTiO_3$ (3.91 Å) substrate, as well as potential *c*-axis expansion due to the partial substitution of Nd by the larger Sr ion. We note, however, that the metallic nature of $Nd_{0.8}Sr_{0.2}NiO_2$ counteracts these trends. No signature of a fluorite defect phase[20] was observed in asymmetric θ–2θ XRD scans of our samples (both doped

[1]Stanford Institute for Materials and Energy Sciences, SLAC National Accelerator Laboratory, Menlo Park, CA, USA. [2]Department of Applied Physics, Stanford University, Stanford, CA, USA. [3]Department of Physics, Stanford University, Stanford, CA, USA. [4]Department of Materials Science and Engineering, Stanford University, Stanford, CA, USA. *e-mail: denverli@stanford.edu; hyhwang@stanford.edu

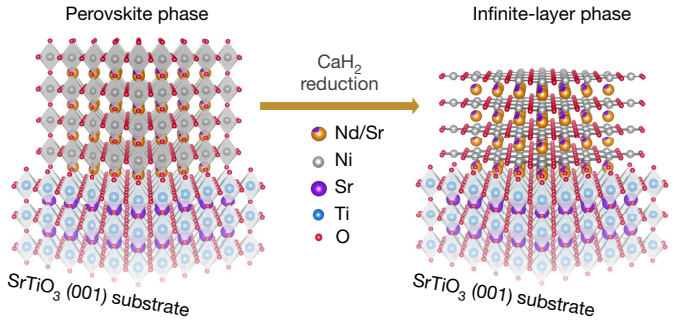

Fig. 1 | Topotactic reduction of nickelate thin films. Schematic crystal structures of $Nd_{0.8}Sr_{0.2}NiO_3$ (left) and $Nd_{0.8}Sr_{0.2}NiO_2$ (right) thin films on the TiO_2-terminated single-crystal $SrTiO_3$ (001) substrate. Upon low-temperature reduction, the films undergo a topotactic transition from the perovskite phase to the infinite-layer phase.

and undoped). For thin-film $LaNiO_3$, reduction induces a series of transformation steps: first to brownmillerite $LaNiO_{2.5}$, then to *c*-axis $LaNiO_2$, followed by a reorientation transition to *a*-axis $LaNiO_2$, before subsequent decomposition[29]. For $NdNiO_3$ and $Nd_{0.8}Sr_{0.2}NiO_3$, we only observe a direct transition to the *c*-axis infinite-layer structure (Fig. 1). Our annealing conditions (see Methods) are empirically optimized to maximize the XRD infinite-layer peak intensity and minimize the *c*-axis lattice constant (as a proxy for the removal of apical oxygen). The comparable (002) peak intensities for the perovskite and infinite-layer phases (Fig. 2a), as well as the thickness fringes observed near (002) after reduction, indicate a complete structural transformation of the film. Reduction for much longer times or at higher temperature induces decomposition of the film, and no XRD features are observed.

Figure 3a shows the temperature-dependent resistivity $\rho(T)$ of $NdNiO_3$ and $Nd_{0.8}Sr_{0.2}NiO_3$. $NdNiO_3$ shows the characteristic first-order phase transition from a high-temperature paramagnetic metal to a low-temperature charge-disproportionated antiferromagnetic insulator, which is suppressed with Sr doping[26,27]. After reduction (Fig. 3b), we find that $NdNiO_2$ displays metallic temperature dependence at high temperatures, with a resistive upturn below about 70 K. By contrast, $Nd_{0.8}Sr_{0.2}NiO_2$ exhibits metallic behaviour followed by a superconducting transition, with an onset at 14.9 K (point of maximum curvature), a midpoint at 13.6 K and zero resistance at 9.1 K (indistinguishable from the noise floor) for this sample. The temperature-dependent normal-state Hall coefficient $R_H(T)$ is given in Fig. 3c. R_H for $NdNiO_2$ is negative at all temperatures, whereas it undergoes a sign change at about 55 K for $Nd_{0.8}Sr_{0.2}NiO_2$. This feature, as well as the overall magnitude of R_H, are inconsistent with the expectations for simple hole doping of a single electronic band, and suggest a more complex Fermi surface. This may be consistent with calculations of the electronic band structure of $LaNiO_2$, which find multiple electron and hole pockets that have different orbital contributions[6] and that vary with the Coulomb interaction. We further note that the interface between the infinite-layer nickelate and the $SrTiO_3$ substrate (Fig. 1) hosts a strong polar discontinuity[30]. Depending on how this electrostatic boundary condition is resolved, there may be transport contributions from interface states. However, the comparison between $NdNiO_2$ and $Nd_{0.8}Sr_{0.2}NiO_2$ demonstrates that this alone does not lead to superconductivity here.

The observation of superconductivity is quite robust. In Fig. 3d, e we show a number of different samples of $Nd_{0.8}Sr_{0.2}NiO_2$ synthesized in nominally similar conditions. The origin of the variation in transition temperature (T_c) is unclear, but there are some indications that it correlates with the crystallinity of the parent perovskite phase and may also reflect slight variations in the oxygen stoichiometry. In Figs. 3f, 4 we focus on one sample (Fig. 3b) with a high transition temperature; all other samples showed similar behaviour as scaled by T_c. Figure 3f shows measurements of the temperature-dependent current–voltage characteristics for this sample. These features are linear in the normal state (outside nonlinearities due to Joule heating

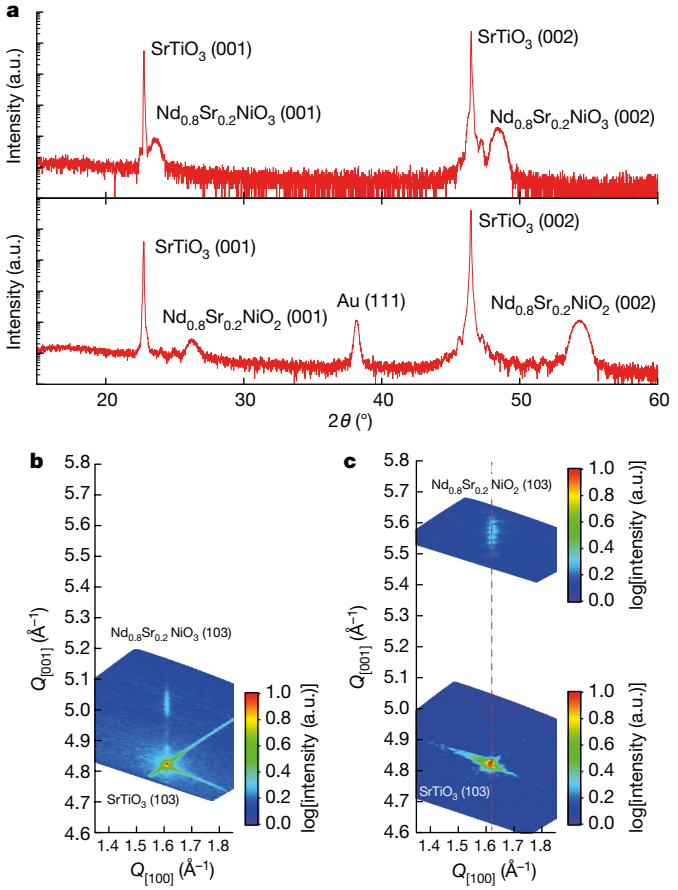

Fig. 2 | Structural characterization of the doped nickelate thin films. **a**, X-ray diffraction θ–2θ symmetric scans of 11-nm-thick $Nd_{0.8}Sr_{0.2}NiO_3$ (top) and $Nd_{0.8}Sr_{0.2}NiO_2$ (bottom; with contribution from gold contacts) films capped with 20-nm-thick $SrTiO_3$ layers grown on $SrTiO_3$ (001) substrates. **b, c**, Reciprocal space maps of $Nd_{0.8}Sr_{0.2}NiO_3$ (**b**) and $Nd_{0.8}Sr_{0.2}NiO_2$ (**c**) around the (103) $SrTiO_3$ diffraction peak. Both maps indicate that the films are fully strained to the $SrTiO_3$ substrates. a.u., arbitrary units.

at high bias) and increasingly nonlinear below the transition, and they are characteristic of superconductivity with a critical current density $J_c(2\,K) \approx 170\,kA\,cm^{-2}$.

Figure 4a displays the temperature-dependent magnetoresistance measured in magnetic fields perpendicular to the plane of the sample, up to 13 T. The normal state exhibits very little magnetoresistance, whereas superconductivity is suppressed with increasing field. As a proxy for the variation of the upper critical field $H_{c,\perp}$, we take the midpoint of the resistive transition to the normal state near T_c and fit it to the linearized Ginzburg–Landau form

$$H_{c,\perp}(T) = \frac{\Phi_0}{2\pi\xi_{GL}^2(0)}\left(1 - \frac{T}{T_c}\right)$$

where Φ_0 is the flux quantum and $\xi_{GL}(0)$ is the extrapolated zero-temperature Ginzburg–Landau coherence length, which we find to be 3.25 ± 0.01 nm. (This estimate does not consider potential contributions from vortex motion or variations due to sample inhomogeneity.) We further perform two-coil mutual-inductance measurements in the perpendicular geometry, as shown in Fig. 4b. Here we plot the real ($\mathrm{Re}(V_p)$) and imaginary ($\mathrm{Im}(V_p)$) components of the a.c. voltage signal detected by the pickup coil above the sample. As the sample is cooled through the transition, $\mathrm{Re}(V_p)$ decreases while $\mathrm{Im}(V_p)$ exhibits a peak, indicating an emergent diamagnetic response below the transition as the magnetic field generated from the drive coil becomes screened by the superconductor. The fact that $\mathrm{Re}(V_p)$ does not approach zero at low

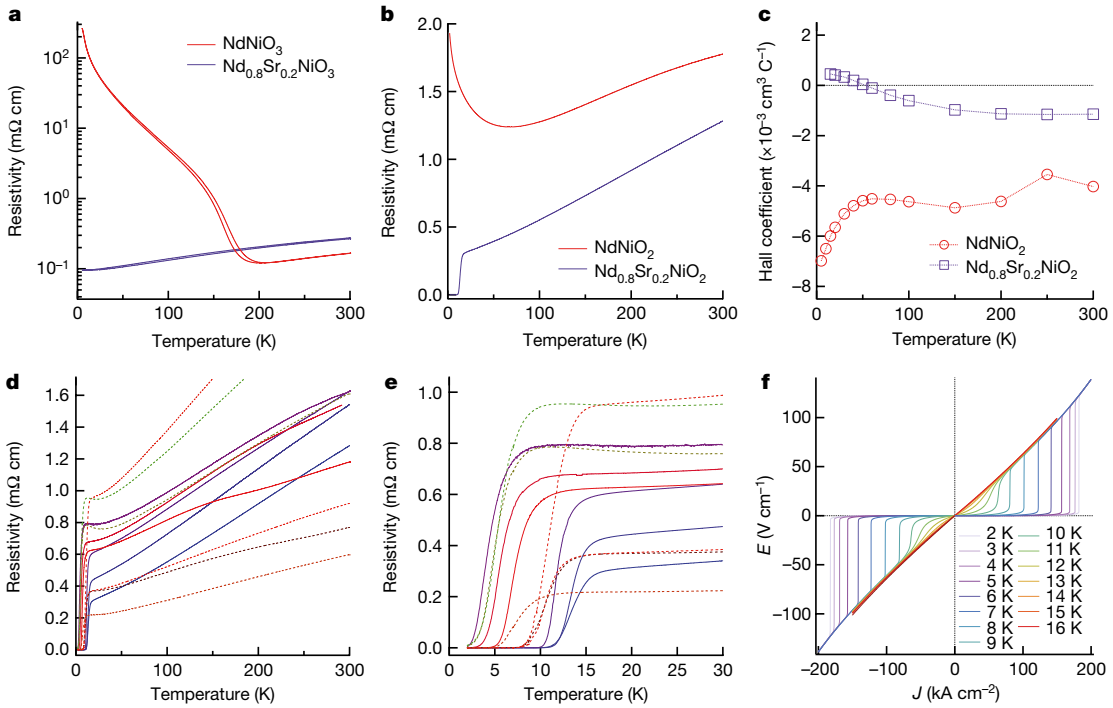

Fig. 3 | Transport properties and superconductivity of the nickelate thin films. a, Resistivity versus temperature $\rho(T)$ plots of the as-grown $NdNiO_3$ and $Nd_{0.8}Sr_{0.2}NiO_3$ films. **b, c**, Resistivity (**b**) and normal-state Hall coefficient (**c**) as a function of temperature for the corresponding reduced films ($NdNiO_2$ and $Nd_{0.8}Sr_{0.2}NiO_2$). **d, e**, $\rho(T)$ for multiple $Nd_{0.8}Sr_{0.2}NiO_2$ films, showing resistive superconducting transitions. Dotted lines indicate samples without a capping layer, for which the XRD Scherrer thickness was used to estimate the resistivity. **f**, Electric field (E) versus current density (J) characteristics for varying temperature.

temperatures resembles measurement results of a 40-nm-thick infinite-layer copper oxide film with $T_c \approx 10.8$ K and extrapolated London penetration depth $\lambda_L(T = 0) = 2.2$ μm (ref. [31]). This indicates that λ_L for $Nd_{0.8}Sr_{0.2}NiO_2$ is similarly large compared to the film thickness. Given the numerical uncertainties arising from the finite sample size (substantially wider films show indications of laterally inhomogeneous reduction), the order parameter symmetry and the scale of disorder, we did not attempt to extract λ_L (ref. [32]). Nevertheless, these data suggest that this is a type-II superconductor with second critical field $H_{c2,\perp}$ approximately given in the inset to Fig. 4a.

Clearly the analogy to copper oxides motivated this finding, and much remains to be explored in this new superconducting compound. However, several important dissimilarities between these two systems are apparent. One key difference is the energy level alignments in their orbital electronic structure. Holes in copper oxides are often discussed in terms of Zhang–Rice singlets with strong oxygen character, owing to the close spatial overlap and near-energetic degeneracy of the Cu $d_{x^2-y^2}$ orbitals and the O 2p orbitals[33]. This naturally leads to large in-plane antiferromagnetic coupling, which many consider to be central for superconducting pairing[24]. Because Ni^+ is one column to the left of Cu^{2+} on the periodic table and one oxidation state lower, the chemical potential in the infinite-layer nickelates is several electronvolts higher than that of comparable copper oxides; therefore, in hole-doped nickelates, much less hybridization with the O 2p band is expected[6]. Furthermore, powder neutron diffraction studies of $LaNiO_2$ and $NdNiO_2$ show no indication of magnetic order down to 5 K and 1.7 K, respectively[15,16], and the resistivity of $NdNiO_2$ (Fig. 3b) is inconsistent with a robust insulator (although interface effects may contribute to conductivity). Consequently, two features that are central to copper oxides—the Zhang–Rice singlet and large planar spin fluctuations—may be absent (or considerably diminished) in these nickelate superconductors.

On the materials side, one immediate question is the effect of the various substrates on the topotactic structural transition of this

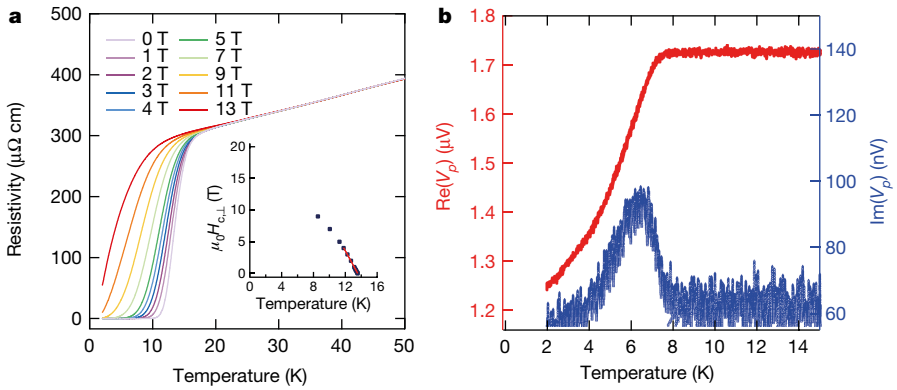

Fig. 4 | Magnetic-field response of superconducting $Nd_{0.8}Sr_{0.2}NiO_2$. **a**, $\rho(T)$ under a varying magnetic field perpendicular to the a–b plane. The inset shows the variation of the upper critical field $H_{c,\perp}$ (as estimated by the midpoint of the resistive transition) with a linear fit in the vicinity of T_c. **b**, The real ($\mathrm{Re}(V_p)$) and imaginary ($\mathrm{Im}(V_p)$) parts of the voltage as a function of temperature in the pickup coil on a $Nd_{0.8}Sr_{0.2}NiO_2$ film, measured using a two-coil mutual-inductance measurement. μ_0, magnetic constant.

system and the associated dependence of superconductivity on epitaxial strain. Here we have an unusual situation in which the substrate that stabilizes the phase also strains it. Another important question is whether there is a doping-dependent superconducting dome, as found in copper oxides[24]. We believe that our approach to chemical substitution is broadly applicable and can address this issue, but the central challenge will be whether complex reduction chemistry can be homogeneously controlled across a range of unconventional nickel oxidation states.

Online content

Any methods, additional references, Nature Research reporting summaries, source data, extended data, supplementary information, acknowledgements, peer review information; details of author contributions and competing interests; and statements of data and code availability are available at https://doi.org/10.1038/s41586-019-1496-5.

Received: 29 June 2019; Accepted: 30 July 2019;
Published online 28 August 2019.

1. Bednorz, J. G. & Müller, K. A. Possible high T_c superconductivity in the Ba-La-Cu-O system. *Z. Phys. B* **64**, 189–193 (1986).
2. Maeno, Y. et al. Superconductivity in a layered perovskite without copper. *Nature* **372**, 532–534 (1994).
3. Yan, Y. J. et al. Electron-doped Sr_2IrO_4: an analogue of hole-doped cuprate superconductors demonstrated by scanning tunneling microscopy. *Phys. Rev. X* **5**, 041018 (2015).
4. Kim, Y. K., Sung, N. H., Denlinger, J. D. & Kim, B. J. Observation of a *d*-wave gap in electron-doped Sr_2IrO_4. *Nat. Phys.* **12**, 37–41 (2016).
5. Anisimov, V. I., Bukhvalov, D. & Rice, T. M. Electronic structure of possible nickelate analogs to the cuprates. *Phys. Rev. B* **59**, 7901–7906 (1999).
6. Lee, K.-W. & Pickett, W. E. Infinite-layer $LaNiO_2$: Ni^{1+} is not Cu^{2+}. *Phys. Rev. B* **70**, 165109 (2004).
7. Chaloupka, J. & Khaliullin, G. Orbital order and possible superconductivity in $LaNiO_3/LaMO_3$ superlattices. *Phys. Rev. Lett.* **100**, 016404 (2008).
8. Hansmann, P. et al. Turning a nickelate Fermi surface into a cuprate-like one through heterostructuring. *Phys. Rev. Lett.* **103**, 016401 (2009).
9. Han, M. J., Wang, X., Marianetti, C. A. & Millis, A. J. Dynamical mean-field theory of nickelate superlattices. *Phys. Rev. Lett.* **107**, 206804 (2011); erratum **110**, 179904 (2013).
10. Disa, A. S. et al. Orbital engineering in symmetry-breaking polar heterostructures. *Phys. Rev. Lett.* **114**, 026801 (2015).
11. Siegrist, T., Zahurak, S. M., Murphy, D. W. & Roth, R. S. The parent structure of the layered high-temperature superconductors. *Nature* **334**, 231–232 (1988).
12. Smith, M. G., Manthiram, A., Zhou, J., Goodenough, J. B. & Markert, J. T. Electron-doped superconductivity at 40 K in the infinite-layer compound $Sr_{1-y}Nd_yCuO_2$. *Nature* **351**, 549–551 (1991).
13. Azuma, M., Hiroi, Z., Takano, M., Bando, Y. & Takeda, Y. Superconductivity at 110 K in the infinite-layer compound $(Sr_{1-x}Ca_x)_{1-y}CuO_2$. *Nature* **356**, 775–776 (1992).
14. Crespin, M., Levitz, P. & Gatineau, L. Reduced forms of $LaNiO_3$ perovskite. Part 1.—Evidence for new phases: $La_2Ni_2O_5$ and $LaNiO_2$. *J. Chem. Soc. Faraday Trans. II* **79**, 1181–1194 (1983).
15. Hayward, M. A., Green, M. A., Rosseinsky, M. J. & Sloan, J. Sodium hydride as a powerful reducing agent for topotactic oxide deintercalation: synthesis and characterization of the nickel(I) oxide $LaNiO_2$. *J. Am. Chem. Soc.* **121**, 8843–8854 (1999).
16. Hayward, M. A. & Rosseinsky, M. J. Synthesis of the infinite layer Ni(I) phase $NdNiO_{2+x}$ by low temperature reduction of $NdNiO_3$ with sodium hydride. *Solid State Sci.* **5**, 839–850 (2003).
17. Kawai, M. et al. Reversible changes of epitaxial thin films from perovskite $LaNiO_3$ to infinite-layer structure $LaNiO_2$. *Appl. Phys. Lett.* **94**, 082102 (2009).
18. Kaneko, D., Yamagishi, K., Tsukada, A., Manabe, T. & Naito, M. Synthesis of infinite-layer $LaNiO_2$ films by metal organic decomposition. *Physica C* **469**, 936–939 (2009).
19. Ikeda, A., Krockenberger, Y., Irie, H., Naito, M. & Yamamoto, H. Direct observation of infinite NiO_2 planes in $LaNiO_2$ films. *Appl. Phys. Express* **9**, 061101 (2016).
20. Onozuka, T., Chikamatsu, A., Katayama, T., Fukumura, T. & Hasegawa, T. Formation of defect-fluorite structured $NdNiO_xH_y$ epitaxial thin films via a soft chemical route from $NdNiO_3$ precursors. *Dalton Trans.* **45**, 12114–12118 (2016).
21. Lacorre, P. Passage from T-type to T′-type arrangement by reducing $R_4Ni_3O_{10}$ to $R_4Ni_3O_8$ (R = La, Pr, Nd). *J. Solid State Chem.* **97**, 495–500 (1992).
22. Poltavets, V. V. et al. $La_3Ni_2O_6$: a new double T′-type nickelate with infinite $Ni^{1+/2+}O_2$ layers. *J. Am. Chem. Soc.* **128**, 9050–9051 (2006).
23. Zhang, J. et al. Large orbital polarization in a metallic square-planar nickelate. *Nat. Phys.* **13**, 864–869 (2017).
24. Keimer, B., Kivelson, S. A., Norman, M. R., Uchida, S. & Zaanen, J. From quantum matter to high-temperature superconductivity in copper oxides. *Nature* **518**, 179–186 (2015).
25. Hosono, H. & Kuroki, K. Iron-based superconductors: current status of materials and pairing mechanism. *Physica C* **514**, 399–422 (2015).
26. Cheong, S.-W., Hwang, H. Y., Batlogg, B., Cooper, A. S. & Canfield, P. C. Electron-hole doping of the metal-insulator transition compound $RENiO_3$. *Physica B* **194–196**, 1087–1088 (1994).
27. García-Muñoz, J. L., Suaaidi, M., Martínez-Lope, M. J. & Alonso, J. A. Influence of carrier injection on the metal-insulator transition in electron- and hole-doped $R_{1-x}A_xNiO_3$ perovskite. *Phys. Rev. B* **52**, 13563–13569 (1995).
28. Torrance, J. B., Lacorre, P., Nazzal, A. I., Ansaldo, E. J. & Niedermayer, C. Systematic study of insulator-metal transitions in perovskites $RNiO_3$ (R=Pr, Nd, Sm, Eu) due to closing of charge-transfer gap. *Phys. Rev. B* **45**, 8209–8212 (1992).
29. Kawai, M. et al. Orientation change of an infinite-layer structure $LaNiO_2$ epitaxial thin film by annealing with CaH_2. *Cryst. Growth Des.* **10**, 2044–2046 (2010).
30. Nakagawa, N., Hwang, H. Y. & Muller, D. A. Why some interfaces cannot be sharp. *Nat. Mater.* **5**, 204–209 (2006).
31. Fruchter, L. et al. Penetration depth of electron-doped infinite-layer $Sr_{0.88}La_{0.12}CuO_{2+x}$ thin films. *Phys. Rev. B* **82**, 144529 (2010).
32. He, X., Gozar, A., Sundling, R. & Božović, I. High-precision measurement of magnetic penetration depth in superconducting films. *Rev. Sci. Instrum.* **87**, 113903 (2016).
33. Zhang, F. C. & Rice, T. M. Effective Hamiltonian for the superconducting Cu oxides. *Phys. Rev. B* **37**, 3759–3761 (1988).

METHODS

Film growth. TiO_2-terminated $SrTiO_3$ (001) substrates of size 5×5 mm^2 were pre-annealed at an oxygen partial pressure $P_{O2} = 5 \times 10^{-6}$ torr for 30 min at 950 °C to achieve sharp step-and-terrace surfaces. 9–11-nm-thick perovskite $NdNiO_3$ and $Nd_{0.8}Sr_{0.2}NiO_3$ films were grown on the annealed substrates by pulsed-laser deposition using a 248-nm KrF excimer laser. This thickness was chosen because it was approximately equal to the maximum thickness for which we could verify the formation of a uniform, single-phase infinite-layer film after reduction using XRD. $NdNiO_3$ ($Nd_{0.8}Sr_{0.2}NiO_3$) films were deposited at a substrate temperature of $T_g = 600$ °C and $P_{O2} = 150$ mtorr, using a laser fluence of 2 J cm^{-2} on the target. Subsequently, $SrTiO_3$ epitaxial capping layers (typically 20 nm thick) were deposited at $T_g = 570$ °C and the same P_{O2}, using a laser fluence of 0.8 J cm^{-2}. After growth, the samples were cooled to room temperature in the same oxygen environment. The nickelate targets were prepared by sintering mixtures of stoichiometric amounts of Nd_2O_3, $SrCO_3$ and NiO powder at 1,350 °C for 12 h, with two intermediate grinding and pelletizing steps after the initial decarbonation step at 1,200 °C for 12 h.

Reduction process. After growth, each sample was cut into two pieces of size 2.5×5 mm^2. Each piece (loosely wrapped in aluminium foil) was then vacuum-sealed together with about 0.1 g of CaH_2 powder in a Pyrex glass tube (pressure <0.1 mtorr). In this way, the pieces were not in direct contact with the CaH_2 powder[14–18], but underwent a gas-phase reaction with the powder upon annealing. The tube was heated to 260–280 °C at a rate of 10 °C min^{-1} and kept at this temperature for 4–6 h; then it was cooled to room temperature at a rate of 10 °C min^{-1}.

Characterization. The XRD data were taken using a monochromated Cu $K\alpha_1$ source. The resistivity, magnetotransport and current–voltage characteristic measurements were conducted in a six-point geometry using Au and Al wire-bonded contacts. In some cases, Au contact pads were first deposited using electron-beam evaporation. Critical-current density–voltage measurements were performed on a narrow channel defined by a diamond scribe, approximately 0.2 mm wide.

Mutual-inductance measurements. The $Nd_{0.8}Sr_{0.2}NiO_2$ samples were placed tightly between two collinear coils, the mutual inductance of which was sensitive to diamagnetic screening of the sample in the superconducting phase. The twin 80-turn coils had inner diameter of about 0.5 mm and outer diameter of around 1.5 mm, yielding a measured self-inductance of about 6 μH. The drive coil was driven with an alternating current of root-mean-square amplitude of 100 μA and frequency of 15 kHz. The in-phase and out-of-phase components of the voltage across the pickup coil (in the microvolt and submicrovolt range, respectively) were measured by lock-in amplification. The measured voltage was in a regime of linear response with respect to the amplitude of the drive current.

Data availability

The data presented in the figures and other findings of this study are available from the corresponding authors upon reasonable request.

Acknowledgements We thank A. Kapitulnik, S. A. Kivelson, W.-S. Lee, Y. Z. Li, S. Raghu and Z. X. Shen for discussions. This work was supported by the US Department of Energy, Office of Basic Energy Sciences, Division of Materials Sciences and Engineering, under contract number DE-AC02-76SF00515. D.L. acknowledges partial support by the Swiss National Science Foundation, and the Gordon and Betty Moore Foundation's Emergent Phenomena in Quantum Systems Initiative through grant number GBMF4415, which also supported S.C. and provided synthesis equipment. M.O. acknowledges partial financial support from the Takenaka Scholarship Foundation.

Author contributions D.L., Y.H. and H.Y.H. conceived the project. D.L. and M.O. grew the nickelate films and conducted the reduction experiments. K.L., D.L., M.O., H.R.L. and Y.C. conducted materials and structural characterization. B.Y.W., S.C. and D.L. performed the transport and mutual-inductance measurements. D.L. and H.Y.H. wrote the manuscript with contribution from all authors.

Competing interests The authors declare no competing interests.

Additional information

Correspondence and requests for materials should be addressed to D.L. or H.Y.H.

Peer review information *Nature* thanks George Sawatzky and the other, anonymous, reviewer(s) for their contribution to the peer review of this work.

LETTER

https://doi.org/10.1038/s41586-019-1420-z

Thermal conductance of single-molecule junctions

Longji Cui[1,6], Sunghoon Hur[1], Zico Alaia Akbar[2], Jan C. Klöckner[3,4], Wonho Jeong[1], Fabian Pauly[3,4]*, Sung-Yeon Jang[2,7]*, Pramod Reddy[1,5]* & Edgar Meyhofer[1]*

Single-molecule junctions have been extensively used to probe properties as diverse as electrical conduction[1–3], light emission[4], thermoelectric energy conversion[5,6], quantum interference[7,8], heat dissipation[9,10] and electronic noise[11] at atomic and molecular scales. However, a key quantity of current interest—the thermal conductance of single-molecule junctions—has not yet been directly experimentally determined, owing to the challenge of detecting minute heat currents at the picowatt level. Here we show that picowatt-resolution scanning probes previously developed to study the thermal conductance of single-metal-atom junctions[12], when used in conjunction with a time-averaging measurement scheme to increase the signal-to-noise ratio, also allow quantification of the much lower thermal conductance of single-molecule junctions. Our experiments on prototypical Au–alkanedithiol–Au junctions containing two to ten carbon atoms confirm that thermal conductance is to a first approximation independent of molecular length, consistent with detailed ab initio simulations. We anticipate that our approach will enable systematic exploration of thermal transport in many other one-dimensional systems, such as short molecules and polymer chains, for which computational predictions of thermal conductance[13–16] have remained experimentally inaccessible.

Studies of charge and heat transport in molecules are of great fundamental interest, and are of critical importance for the development of a variety of technologies, including molecular electronics[17], thermally conductive polymers[18] and thermoelectric energy-conversion devices[19]. Given this overall importance and the daunting experimental challenges, a number of initial studies explored charge transport in ensembles of molecules[20,21]. Although such measurements provided important insights, researchers gradually began to realize that it was

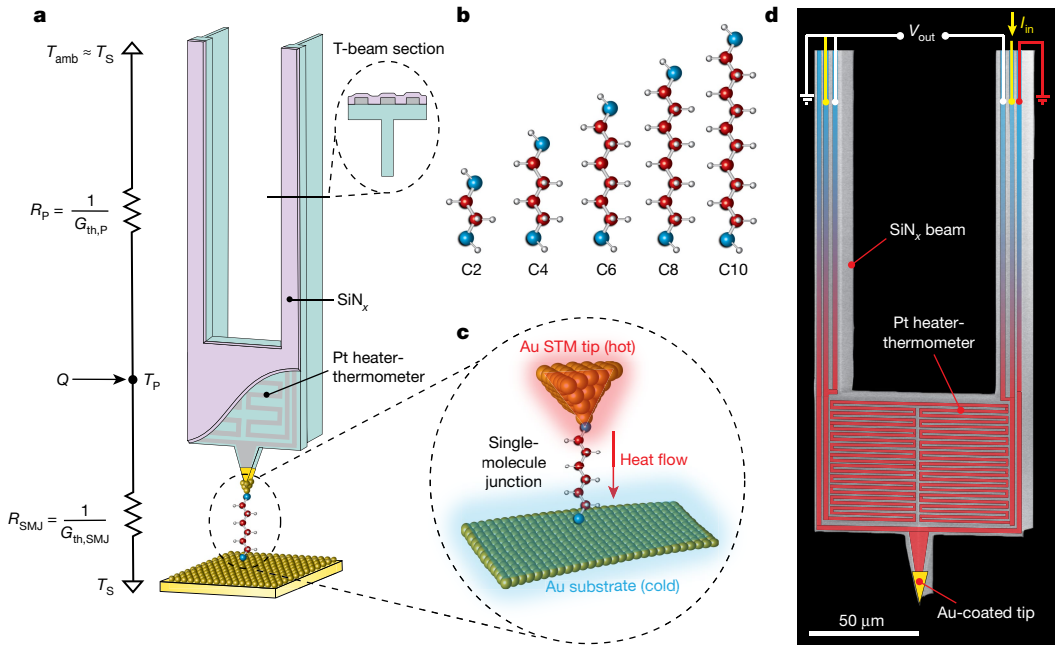

Fig. 1 | Experimental set-up and strategy for quantifying heat transport in single-molecule junctions. a, Schematic of the calorimetric scanning thermal microscopy (C-SThM) set-up. Right, a single molecule is trapped between an Au-coated tip of the C-SThM probe, which features 'T'-shaped silicon nitride (SiN_x) beams and is heated to temperature T_P by input of a heat current (Q) via an embedded serpentine Pt heater-thermometer, and an Au substrate at temperature T_S that is equal to ambient temperature (T_{amb}). The thermal conductance of single-molecule junctions is quantified by recording the temperature change of the Pt heater-thermometer when a single-molecule junction is broken. Left, resistance network capturing the thermal resistances of the molecular junction ($R_{SMJ} = 1/G_{th,SMJ}$) and the scanning probe ($R_P = 1/G_{th,P}$). **b**, Schematics of the alkanedithiol molecules (Cn) studied in this work; $n = 2, 4, 6, 8, 10$ denotes the number of carbon atoms in the molecules (red, carbon atom; grey, hydrogen atom; blue, sulphur atom). **c**, Magnified view of ringed area in **a**, describing the trapping of a single C6 molecule between the heated Au STM tip and the cold Au substrate. **d**, Scanning electron microscope image (false coloured to highlight the Pt heater-thermometer) of a custom-fabricated C-SThM probe (which shows the tip end), featuring two long 'T'-shaped SiN_x beams (see beam cross-section shown ringed in **a**) and a serpentine Pt heater-thermometer integrated on a suspended micro-island. The electrical resistance of the Pt heater-thermometer is monitored by measuring the voltage output (V_{out}) in the presence of an input d.c. current (I_{in}).

[1]Department of Mechanical Engineering, University of Michigan, Ann Arbor, MI, USA. [2]Department of Chemistry, Kookmin University, Seoul, South Korea. [3]Okinawa Institute of Science and Technology Graduate University, Onna-son, Okinawa, Japan. [4]Department of Physics, University of Konstanz, Konstanz, Germany. [5]Department of Materials Science and Engineering, University of Michigan, Ann Arbor, MI, USA. [6]Present address: Smalley-Curl Institute and Department of Physics and Astronomy, Rice University, Houston, TX, USA. [7]Present address: Department of Energy Engineering, Ulsan National Institute of Science and Technology (UNIST), Ulsan, South Korea. *e-mail: fabian.pauly@oist.jp; syjang@kookmin.ac.kr; pramodr@umich.edu; meyhofer@umich.edu

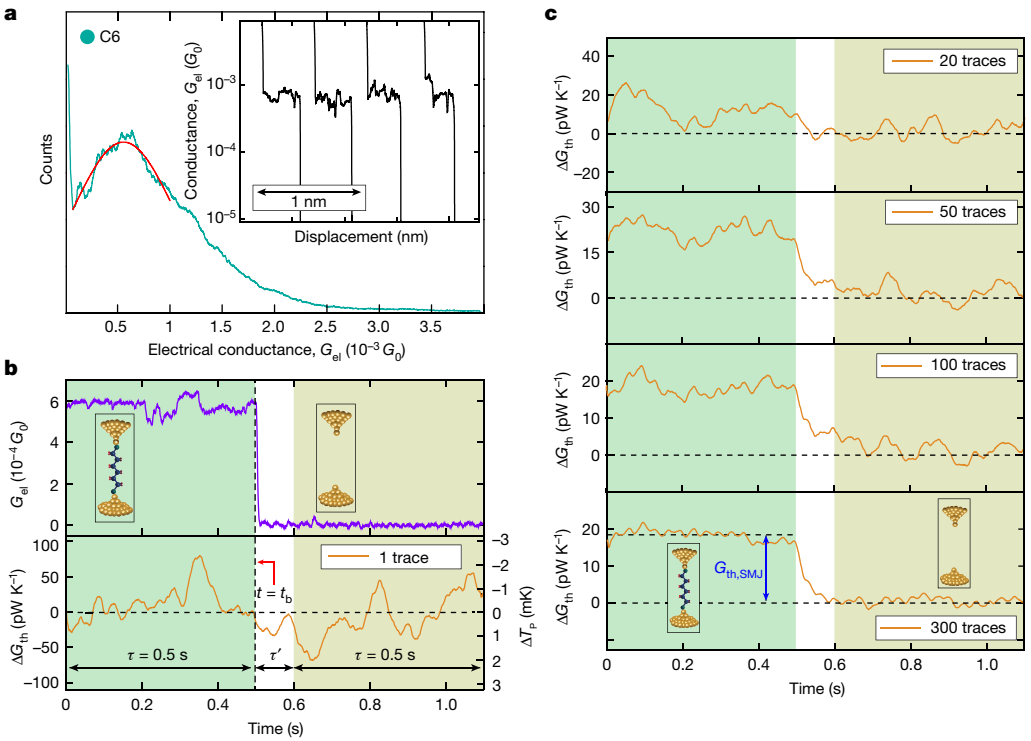

Fig. 2 | Measurement of electrical and thermal conductance of Au–C6–Au single-molecule junctions. a, Main panel, histogram (shown in teal) of the electrical conductance of Au–C6–Au junctions obtained from approximately 500 independent traces of electrical conductance versus displacement. Inset, representative traces of the electrical conductance for four independent measurements. A Gaussian fit to the histogram peak is represented by the solid red line. **b**, Experimental protocol for measuring the thermal conductance of a single-C6 junction (see Methods for details). Upper panel, the electrical conductance trace indicates rupture (at time $t = t_b$) of a single-molecule junction by a sudden drop of the measured G_{el} value. Lower panel, the coincident thermal conductance change (ΔG_{th}, left axis) and the related temperature change of the probe (ΔT_P, right axis), where the small effects of Joule heating are already accounted for (see Methods). It can be seen that, unlike the clearly identifiable electrical conductance change associated with the breaking of the junction, the corresponding thermal conductance change is not discernible in the noisy signal. **c**, An improved signal-to-noise ratio is obtained upon aligning via G_{el} and averaging multiple thermal conductance traces. $G_{th,SMJ}$, indicated by the drop in the thermal conductance signal after 0.5 s, can be seen after averaging 50 traces and is about 18 pW K^{-1} for Au–C6–Au single-molecule junctions. The coloured regions in **b** and **c** with their insets indicate the discernible pre- and post-rupture portions of the recorded and averaged traces.

necessary to develop single-molecule measurement techniques[1,3,5,7,9] to avoid the confounding effects of ensemble measurements—including uncertainties in the actual number of molecules contributing to transport through the junctions and the effects of intermolecular interactions—and to study systematically the electrical conduction properties of genuine single-molecule entities. Corresponding efforts over the past decade have been made to experimentally characterize heat transport in ensembles of molecules such as self-assembled monolayers[22–24] and polymer nanofibres[18,25]. Not surprisingly, these thermal ensemble measurements face challenges and uncertainties similar to those found in previous monolayer electrical measurements, and intermolecular interactions are expected to have an influence on the thermal transport properties of molecular junctions[16,26]. Although recent experimental advances[12,27] have enabled heat transport studies in metallic single-atom junctions (where thermal conductances are in the region of 500 pW K^{-1}), similar endeavours for single-molecule junctions—where contributions to heat transport by electrons are negligible and heat flow is instead dominated by phonons resulting in low thermal conductance values (tens of picowatts per kelvin)—have remained unattainable owing to experimental challenges in detecting such small conductances. This situation is especially frustrating as computations have predicted several interesting thermal transport properties in one-dimensional molecular and polymer junctions[13–16].

The first measurements of thermal transport in single-molecule junctions we report here are enabled by our custom-developed scanning probe technique, called calorimetric scanning thermal microscopy (C-SThM)[12], which has excellent mechanical stability and ultra-high thermal sensitivity. The nanofabricated C-SThM probes (see Extended Data Fig. 1 for the detailed fabrication process) feature a suspended micro-island supported by two thin, long 'T'-shaped silicon nitride (SiN_x) beams with both very high stiffness (>10^4 N m^{-1} in the normal direction, see Methods) and very small thermal conductance ($G_{th,P} \approx 800$ nW K^{-1}; here and elsewhere, subscript P indicates that a property of the probe is being given). A platinum (Pt) resistor of serpentine geometry is embedded into the micro-island and serves as both a heater and a highly sensitive resistance thermometer. When combined with the time-averaging scheme described below and in Methods, it reaches a temperature resolution of about 0.1 mK that enables us to detect heat currents with a resolution of approximately 80 pW, or thermal conductance with a resolution of about 2 pW K^{-1} root mean square (see Methods).

Figure 1a depicts the experimental set-up and the basic strategy for quantifying thermal conductance at the single-molecule level. The C-SThM probe, located in an ultra-high-vacuum (UHV) environment, is heated above ambient to a temperature T_P, typically 320–340 K, by supplying a constant electric current (about 30–40 μA) to the serpentine Pt resistor. The Au substrate, located in the same UHV environment, is connected to a thermal reservoir maintained at ambient room temperature $T_S = 295$ K (S indicates the Au substrate). The planar surface of the Au substrate is coated with a self-assembled monolayer of prototypical thiol-terminated alkane molecules that are widely regarded as a model system and have been extensively explored computationally[13,15]. We first create molecular junctions by displacing the Au-coated scanning probe tip at a constant speed via piezoelectric actuation towards the Au substrate until contact is made between the two Au electrodes. With a voltage bias applied between the Au tip and

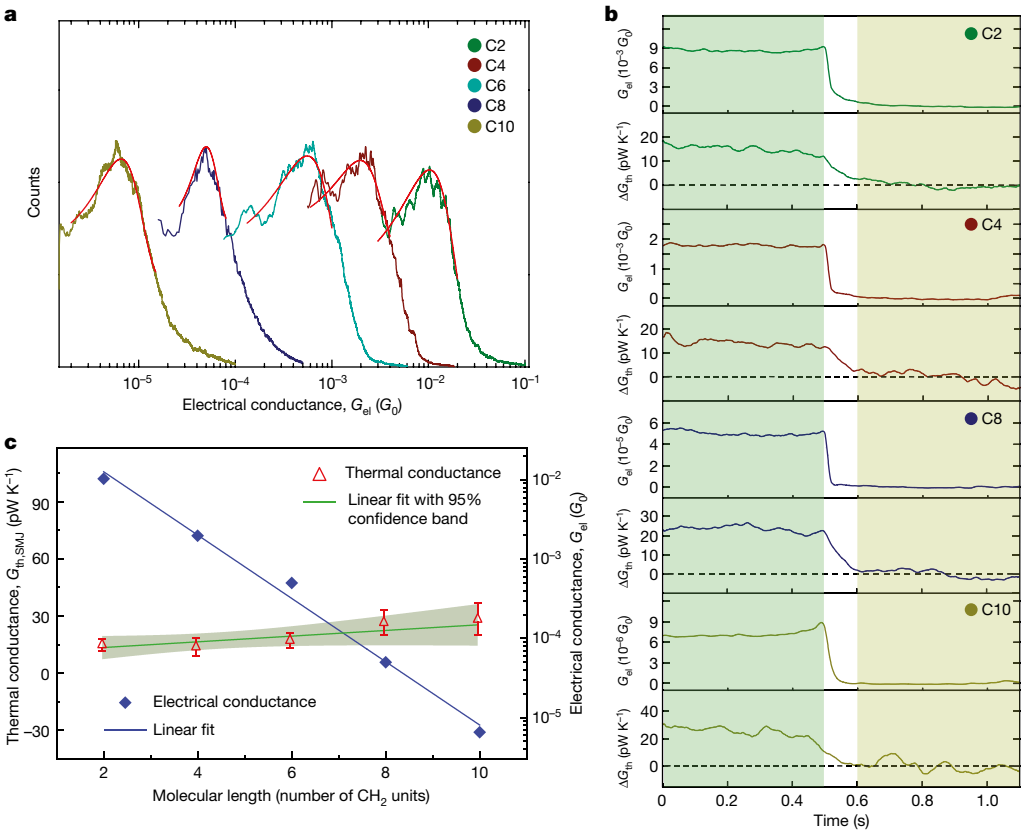

Fig. 3 | Length-dependent electrical and thermal transport in Au–alkanedithiol–Au single-molecule junctions. a, Measured electrical conductance histograms for different alkanedithiol junctions (C2 to C10; see key). Red lines represent the Gaussian fit of the histogram peaks. **b**, Electrical conductance and thermal conductance traces of single-alkanedithiol junctions obtained by averaging >100 traces for C2 (155 traces), C4 (133 traces), C8 (110 traces) and C10 (108 traces) junctions following the experimental protocol described in Fig. 2b. **c**, Measured electrical (blue diamonds, right axis) and thermal conductance (red triangles, left axis) as a function of the molecular length, as given by the number of CH_2 units in the alkanedithiol junctions. The solid blue line indicates a linear fit to the electrical conductance data on a logarithmic scale. The measured thermal conductance data are fitted by a linear curve (green line) on a linear scale, with the region shaded in light green representing the 95% confidence band. Error bars represent one standard deviation of the data obtained from three sets of measurements for each molecule.

the substrate, contact is signalled by a large, predictable increase in the recorded electrical conductance (see Methods) and the probe is then withdrawn slowly from the substrate at a speed of 0.05 nm s^{-1}. During withdrawal, molecules trapped between the tip of the scanning probe and the Au substrate break away from either the substrate or the tip until the last molecular junction is broken. Throughout the tip withdrawal from the substrate, we continuously monitor both the electrical current through the junction for a fixed voltage bias and the temperature of the probe. As detailed below, we use the measured electrical currents to determine the corresponding electrical conductance and thereby identify single-molecule trapping events, and infer from the measured temperature change of the probe (ΔT_P) the thermal conductance of single-molecule junctions ($G_{th,SMJ}$).

We first trap molecules of 1,6-hexanedithiol (C6) between the Au-coated tip of the C-SThM probe and the Au substrate. Figure 2a shows representative electrical conductance–distance traces obtained by repeatedly displacing the tip away from the substrate, and the electrical conductance histogram constructed from about 500 independently measured traces. The histogram features a pronounced conductance peak at about $5.1 \times 10^{-4} G_0$ (electrical conductance quantum, $G_0 = 2e^2/h \approx 77.5$ μS), indicating the most probable low-bias conductance of a single-molecule junction. This value is interpreted as the electrical conductance of a single C6 molecule bridging the Au electrodes, and is in good agreement with previous work[28].

To probe the thermal conductance of single-molecule junctions, we stop the tip withdrawal process when the electrical conductance of Au–C6–Au junctions is close to (within one standard deviation around the Gaussian-fitted histogram peak) the most probable low-bias conductance, and monitor the electrical current and temperature of the probe until the molecular junction spontaneously breaks. The top panel in Fig. 2b shows a typical electrical conductance trace measured for an Au–C6–Au single-molecule junction, showing how the electrical conductance suddenly drops within a few milliseconds (the time constant of the electrical measurements) when the molecular junction breaks. As the Joule heating is small for Au–C6–Au junctions (see Methods) and breaking removes the thermal conduction pathway through the molecular junction, we expect a small temperature rise in the probe (ΔT_P) immediately after the junction is broken. This temperature change can be related to the change in the thermal conductance of the junction (ΔG_{th}), that is, the thermal conductance of a single-molecule junction ($G_{th,SMJ}$), via $G_{th,SMJ} = -\Delta G_{th} \approx G_{th,P}\, \Delta T_P/(T_P - T_S)$ (see Methods), where $G_{th,P}$ is the thermal conductance of the probe and $T_P - T_S$ is the temperature difference between the probe and the substrate. The bottom panel of Fig. 2b presents the measured temperature change of the probe (right y-axis), from which the thermal conductance, ΔG_{th} (left y-axis), can be directly determined. (See Methods for a description of how the measured temperature change of the probe is processed and how the effects of Joule heating, which are small in this case but increase for shorter molecules, are systematically accounted for.)

Because the thermal conductance of the Au–C6–Au single-molecule junction is small relative to the noise present in ΔT_P, preventing reliable direct detection of changes in thermal conductance, we applied an averaging scheme to improve the signal-to-noise ratio of the thermal

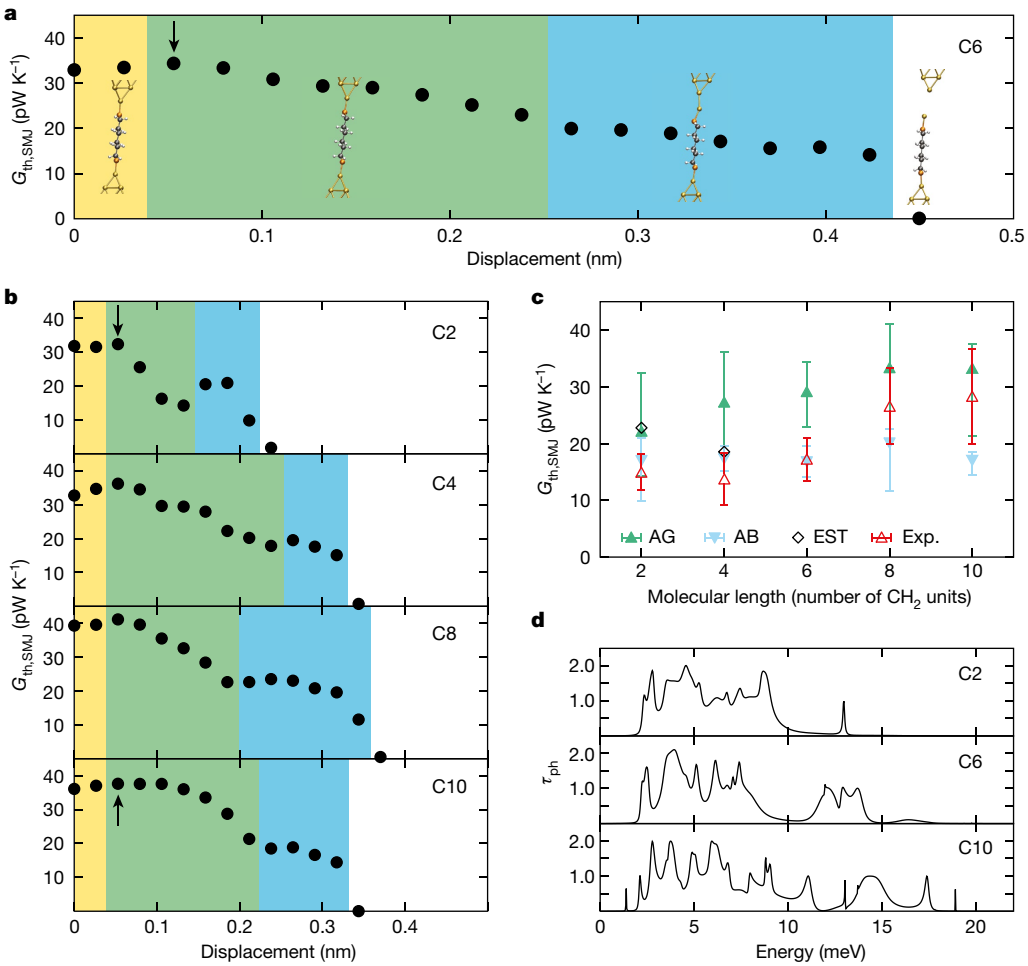

Fig. 4 | First-principles calculations of the thermal transport through alkanedithiol single-molecule junctions. a, Calculated thermal conductance as a function of electrode displacement for an Au–C6–Au single-molecule junction. Different regions of junction stretching are distinguished by differently coloured backgrounds, and characterized by the representative geometries shown as insets: plateau (yellow), decay (green), pulled-out gold atoms (blue) and broken junction (white). **b**, Thermal conductance as a function of electrode displacement for C2, C4, C8 and C10. **c**, Mean thermal conductance as calculated from the green area (AG, green triangles) and the blue area (AB, blue triangles). Error bars show maximum and minimum thermal conductances in the respective coloured regions. Estimates (EST, open diamonds) for the thermal conductance of C2 and C4 are obtained by taking the electronic contribution into account via the Wiedemann–Franz law and adding it to the corresponding average of the AB data points. The experimental data from Fig. 3c is also shown (red triangles and red error bars) to facilitate comparison between experiment and computations. **d**, Phonon transmission as a function of energy for C2, C6 and C10 junctions. The respective junction geometry, for which the transmission plot is performed, is indicated by an arrow in the corresponding trace in **a** or **b**. In each case the first geometry in the green region was selected.

measurements and resolve ΔG_{th}. In brief, we performed many measurements (hundreds) following the protocol described above, and first used the electrical conductance versus time traces to identify the time point t_b when the single-molecule junction breaks ($t_b = 0.5$ s in Fig. 2b). Using the electrical signal as a reference, thermal signals were then aligned and averaged (see Methods). As the averages over 20, 50, 100 and 300 traces in Fig. 2c illustrate, averaging suppresses noise and reveals a clear thermal conductance change (ΔG_{th}) that coincides with the electrical conductance change caused by the breaking of the single-molecule junction. This approach reveals a change in the conductance of about 18 pW K^{-1}, which represents the thermal conductance of the Au–C6–Au single-molecule junction ($G_{th,SMJ}$). In contrast to the rapid transition of the electrical signal on the breaking of the junction, the roll-off of the thermal conductance is much slower because it is limited by the thermal time constant of the scanning probe (about 25 ms).

The ability to resolve the thermal conductance at the single-molecule scale offers unique opportunities to address fundamental questions[13,15] with regard to how thermal transport in single-molecule junctions depends on molecular characteristics. We illustrate this with additional thermal transport measurements on a series of alkanedithiol molecules differing in the number of CH_2 units (from 2 to 10, with these molecules referred to as C2 to C10, respectively), to explore the influence of molecular length. Figure 3a shows the measured electrical conductance histograms for the studied molecules, with the Gaussian-fitted peak values summarized in Fig. 3c. The data document an exponential decay of the electrical conductance (G_{el}) of single-alkanedithiol junctions with increasing molecular length (L), indicating tunnelling-dominated electron transport. We extract a tunnelling decay constant (β, where $G_{el}/G_0 \propto e^{-\beta L}$) of 0.92 ± 0.05 per CH_2 unit, which agrees well with past work[3]. The measured thermal conductance of the single-molecule junctions containing C2 to C10 is shown in Fig. 3b, and the summary of the thermal conductance values is included in Fig. 3c. We note that, for all molecular junctions, the effect of Joule heating is systematically accounted for (see Methods). In strong contrast to the measured length-dependent electrical conductance, the thermal conductance of the single-alkanedithiol junctions exhibits a nearly length-independent behaviour with a value of approximately 20 pW K^{-1}, suggesting that thermal transport in single-molecule junctions is ballistic.

To elucidate the microscopic origin of our observations, we use the Landauer–Büttiker formalism for coherent transport[19,29] (see Methods).

Combining non-equilibrium Green's function techniques with density functional theory (DFT) in a custom-developed code[30,31], we compute, ab initio and thus without recourse to free parameters, the thermal conductance due to phonons for individual junction geometries matching the various alkane chain lengths and conditions used in our measurements. Figure 4a shows the computed thermal conductance data for a C6 single-molecule junction as a function of electrode displacement, with the conductance–distance trace divided into different stages. The first stage, shaded in yellow, corresponds to a plateau as the molecule rotates slightly upon stretching with little change to the thermal conductance. In the second stage, shaded in green, the thermal conductance decreases as the junction is elongated due to S–Au bond stretching and reconfigurations in the Au electrodes, which give rise to decreased metal–molecule coupling. Before the contact breaks, a third stage occurs, shaded in blue, where gold atoms are further pulled out of the electrodes and short atomic dimer chains form. This behaviour is well known in the context of atomic force studies[32] and typically leads to a small additional reduction of the phonon thermal conductance. In Fig. 4b we depict corresponding traces for C2, C4, C8 and C10 junctions, all of which feature similar regions. In all cases, the junction breaks owing to the rupture of an Au–Au bond (see also Extended Data Fig. 5).

The experimental data represent the thermal conductance at the point where the contact breaks, so we calculate for C2 to C10 the thermal conductance values AG and AB that are the average over the stretched junctions in the green- and blue-shaded regions in Fig. 4a, b, respectively, and compare these in Fig. 4c against the measured thermal conductance values. The computed AB and AG values lie in the range 16–21 pW K^{-1} and 22–33 pW K^{-1}, respectively, and agree well with the measured data. Further, we observe that the computed phononic contribution to the thermal conductance of the junctions is nearly independent of molecular length. For completeness, we also estimate the electronic contribution to the thermal conductance using the measured electrical conductance (Fig. 3a) and the Wiedemann–Franz law (see Methods for more details). We find that the electronic contribution is about 5.7 pW K^{-1} and 1.1 pW K^{-1} for C2 and C4, respectively, while it is negligible for all other molecules. We have added these values (indicated by open diamonds) to the AB data in Fig. 4c. On the whole, the theoretically determined thermal conductance values are in good agreement with the experimental data. We note that in contrast to previous studies[15], where thermal transport was calculated for single-molecule junctions under minimal tension, our analysis here includes the effect of stretching and reveals a lower thermal conductance when a junction is close to rupture.

To understand further how heat is transported through single-molecule junctions, we show in Fig. 4d the computed energy-dependent transmission function $\tau_{ph}(E)$ for C2, C6 and C10 junctions. The function quantifies the probability of elastic phonon transmission at a specific energy from one electrode to the other via the bridging molecule. Owing to coupling to the continuous modes of the metal electrodes, $\tau_{ph}(E)$ shows broad resonances with positions and widths that depend on the precise contact geometry (see Methods and Extended Data Fig. 6 for further discussions). We notice that the transmission functions in Fig. 4d are finite only in an energy range from 0 to $E_{max} \approx 20$ meV, where E_{max} represents the highest phonon energy of Au. At room temperature all the transmission resonances in this energy interval determine the actual value of the thermal conductance (see Methods section 'Computational methods', including equation (1), for further details), and they mainly arise from centre-of-mass motions of the molecule between the electrodes or low-energy molecular vibrations. For longer molecules more transmission resonances arise between 0 and E_{max}, since more molecular modes overlap with the phonon density of states of Au. In addition, we find that for all junctions the transmission values are below 3, which, as we have discussed before[29], is related to the linear, one-dimensional structure of the alkane molecules. Last, we note that anharmonic effects, which result in phonon–phonon scattering, could reduce heat flow. However, owing to the long wavelengths of the vibrational modes relevant for thermal transport we expect such anharmonic effects to be small[13].

Our experimental results illustrate a nearly length-independent thermal conductance in alkane-based single-molecule junctions, which is in strong contrast with the corresponding exponential length dependence of the electrical conductance. In contrast to work on monolayers and polymer bundles, our work realizes the long-sought goal of unambiguous identification of thermal conductance at the single-molecule level. Our ab initio computational analysis provides strong support for our experimental data regarding the length independence of thermal conductance, and offers mechanistic insights in terms of molecular vibrational properties. The experimental advances presented here will enable systematic studies of thermal transport through single-molecule junctions and other one-dimensional systems such as polymer chains, which are of great current interest but so far have remained experimentally inaccessible.

Online content

Any methods, additional references, Nature Research reporting summaries, source data, extended data, supplementary information, acknowledgements, peer review information; details of author contributions and competing interests; and statements of data and code availability are available at https://doi.org/10.1038/s41586-019-1420-z.

Received: 30 November 2018; Accepted: 26 June 2019;
Published online 17 July 2019.

1. Smit, R. H. M. et al. Measurement of the conductance of a hydrogen molecule. *Nature* **419**, 906–909 (2002).
2. Nitzan, A. & Ratner, M. A. Electron transport in molecular wire junctions. *Science* **300**, 1384–1389 (2003).
3. Xu, B. & Tao, N. J. Measurement of single-molecule resistance by repeated formation of molecular junctions. *Science* **301**, 1221–1223 (2003).
4. Reecht, G. et al. Electroluminescence of a polythiophene molecular wire suspended between a metallic surface and the tip of a scanning tunneling microscope. *Phys. Rev. Lett.* **112**, 047403 (2014).
5. Reddy, P., Jang, S. Y., Segalman, R. A. & Majumdar, A. Thermoelectricity in molecular junctions. *Science* **315**, 1568–1571 (2007).
6. Cui, L. et al. Peltier cooling in molecular junctions. *Nat. Nanotechnol.* **13**, 122–127 (2018).
7. Garner, M. H. et al. Comprehensive suppression of single-molecule conductance using destructive σ-interference. *Nature* **558**, 415–419 (2018).
8. Miao, R. et al. Influence of quantum interference on the thermoelectric properties of molecular junctions. *Nano Lett.* **18**, 5666–5672 (2018).
9. Lee, W. et al. Heat dissipation in atomic-scale junctions. *Nature* **498**, 209–212 (2013).
10. Ward, D. R., Corley, D. A., Tour, J. M. & Natelson, D. Vibrational and electronic heating in nanoscale junctions. *Nat. Nanotechnol.* **6**, 33–38 (2011).
11. Lumbroso, O. S., Simine, L., Nitzan, A., Segal, D. & Tal, O. Electronic noise due to temperature differences in atomic-scale junctions. *Nature* **562**, 240–244 (2018).
12. Cui, L. et al. Quantized thermal transport in single-atom junctions. *Science* **355**, 1192–1195 (2017).
13. Segal, D., Nitzan, A. & Hänggi, P. Thermal conductance through molecular wires. *J. Chem. Phys.* **119**, 6840–6855 (2003).
14. Sadeghi, H., Sangtarash, S. & Lambert, C. J. Oligoyne molecular junctions for efficient room temperature thermoelectric power generation. *Nano Lett.* **15**, 7467–7472 (2015).
15. Klöckner, J. C., Bürkle, M., Cuevas, J. C. & Pauly, F. Length dependence of the thermal conductance of alkane-based single-molecule junctions: an ab initio study. *Phys. Rev. B* **94**, 205425 (2016).
16. Henry, A. & Chen, G. High thermal conductivity of single polyethylene chains using molecular dynamics simulations. *Phys. Rev. Lett.* **101**, 235502 (2008).
17. Aradhya, S. V. & Venkataraman, L. Single-molecule junctions beyond electronic transport. *Nat. Nanotechnol.* **8**, 399–410 (2013).
18. Shen, S., Henry, A., Tong, J., Zheng, R. T. & Chen, G. Polyethylene nanofibres with very high thermal conductivities. *Nat. Nanotechnol.* **5**, 251–255 (2010).
19. Dubi, Y. & Di Ventra, M. Heat flow and thermoelectricity in atomic and molecular junctions. *Rev. Mod. Phys.* **83**, 131–155 (2011).
20. Xiang, D., Wang, X., Jia, C., Lee, T. & Guo, X. Molecular-scale electronics: from concept to function. *Chem. Rev.* **116**, 4318–4440 (2016).
21. Rincón-García, L., Evangeli, C., Rubio-Bollinger, G. & Agraït, N. Thermopower measurements in molecular junctions. *Chem. Soc. Rev.* **45**, 4285–4306 (2016).
22. Wang, R. Y., Segalman, R. A. & Majumdar, A. Room temperature thermal conductance of alkanedithiol self-assembled monolayers. *Appl. Phys. Lett.* **89**, 173113 (2006).
23. Wang, Z. et al. Ultrafast flash thermal conductance of molecular chains. *Science* **317**, 787–790 (2007).
24. Meier, T. et al. Length-dependent thermal transport along molecular chains. *Phys. Rev. Lett.* **113**, 060801 (2014).

25. Wang, X., Ho, V., Segalman, R. A. & Cahill, D. G. Thermal conductivity of high-modulus polymer fibers. *Macromolecules* **46**, 4937–4943 (2013).
26. Majumdar, S., Malen, J. A. & McGaughey, A. J. H. Cooperative molecular behavior enhances the thermal conductance of binary self-assembled monolayer junctions. *Nano Lett.* **17**, 220–227 (2017).
27. Mosso, N. et al. Heat transport through atomic contacts. *Nat. Nanotechnol.* **12**, 430–433 (2017).
28. Jang, S. Y., Reddy, P., Majumdar, A. & Segalman, R. A. Interpretation of stochastic events in single molecule conductance measurements. *Nano Lett.* **6**, 2362–2367 (2006).
29. Klöckner, J. C., Cuevas, J. C. & Pauly, F. Transmission eigenchannels for coherent phonon transport. *Phys. Rev. B* **97**, 155432 (2018).
30. Pauly, F. et al. Cluster-based density-functional approach to quantum transport through molecular and atomic contacts. *New J. Phys.* **10**, 125019 (2008).
31. Bürkle, M., Hellmuth, T. J., Pauly, F. & Asai, Y. First-principles calculation of the thermoelectric figure of merit for [2,2]paracyclophane-based single-molecule junctions. *Phys. Rev. B* **91**, 165419 (2015).
32. Krüger, D., Fuchs, H., Rousseau, R., Marx, D. & Parrinello, M. Pulling monatomic gold wires with single molecules: an ab initio simulation. *Phys. Rev. Lett.* **89**, 186402 (2002).

METHODS

Nanofabrication of scanning thermal probes. To fabricate the probes (Extended Data Fig. 1), we start with a 500-μm-thick double-sided silicon wafer and form an 18-μm-deep and 1-μm-wide trench on the silicon wafer via wet oxidation and deep reactive ion etching (DRIE). A 600-nm-thick silicon nitride (SiN_x) layer was deposited on both sides of the wafer via low pressure chemical vapour deposition (LPCVD) and the back side was patterned to facilitate etching using potassium hydroxide (KOH) for releasing the probe in the last step. A sensitive thermometer was defined by patterning a 30-nm-thick and 1-μm-wide platinum (Pt) serpentine line. The tip was fabricated by first depositing a 100-nm-thick platinum film. Subsequently, a 30-nm-thick SiN_x layer was deposited via plasma-enhanced chemical vapour deposition (PECVD) to protect the front side of the probe during KOH etching. Two shadow masks were introduced separately to deposit a sputtered 50-nm-thick SiN_x film on the serpentine-shaped Pt covered region and a 500-nm-thick gold (Au) layer on the tip.

Characterization of thermal, electrical and mechanical properties. *Temperature coefficient of resistance (TCR).* To measure the TCR of the Pt thermometer, a small a.c. current of amplitude $I_f = 1$ nA at frequency $f = 200$ Hz was supplied to the embedded Pt serpentine line on the probe, and the resultant 1*f* component of the voltage signal, V_f, was measured using a lock-in amplifier (SR830) in a four-probe configuration. The temperature-dependent electric resistance defined as $R(T) = V_f/I_f$ was evaluated by varying the temperature of the probe inside a cryostat (Janis ST-100). A representative plot of the measured resistance of a scanning thermal probe as a function of temperature is shown in Extended Data Fig. 2a. The TCR can be obtained by using the slope of the best-linear-fit curve of the measured data points. At room temperature, the TCR was found to be $(1.45 \pm 0.01) \times 10^{-3}\ K^{-1}$.

Thermal time constant of the probe. The thermal time constant of the calorimetric scanning thermal probes was determined by applying a sinusoidal electrical current with constant amplitude I_f at varying frequency *f* to the Pt resistor. This current enables sinusoidal Joule heating of the suspended island, Q_{2f}, with an associated temperature fluctuation at 2*f* and an amplitude of ΔT_{2f}. The 3*f* component of the output voltage across the Pt resistor V_{3f} was recorded using a lock-in amplifier (SRS 830). ΔT_{2f} can subsequently be determined according to the relation $\Delta T_{2f} = 2V_{3f}/(\alpha I_f R)$, where α is the measured TCR and *R* is the electrical resistance of the Pt serpentine line. The measured ΔT_{2f}, which was normalized by the amplitude at the lowest frequency, is shown as a function of the heating frequency in Extended Data Fig. 2b. Note that the −3 dB point (thermal cut-off frequency) is ~7 Hz, which can be used to determine the time constant of the probe from $\tau = (2\pi f_{-3\mathrm{dB}})^{-1} \approx 25$ ms.

Thermal conductance of the probe. This was measured by applying a sinusoidal electrical current with fixed frequency *f* and varying amplitude I_f to the embedded Pt serpentine line[12] of the probe, resulting in Joule heating. The magnitude of the heating power in the serpentine line can be calculated as $Q_{2f} = I_f^2 R/2$, resulting in a corresponding temperature increase ΔT_{2f} of the island (distal end of the probe). The heating frequency 2*f* was chosen to be 1 Hz to ensure a full thermal response of the probe. Similar to the characterization of the thermal time constant, ΔT_{2f} can be quantified by recording the 3*f* component of the output voltage across the Pt line. Extended Data Fig. 2c displays the relationship between the amplitude of the measured temperature increase ΔT_{2f} and the input heating power Q_{2f}. The thermal conductance of the probe can then be obtained via $G_{\mathrm{th,P}} = Q_{2f}/\Delta T_{2f}$, which is estimated to be about 800 nW K^{-1}.

Mechanical stiffness of the probe. Simulations with the finite element method (FEM) were carried out using COMSOL Multiphysics (Solid Mechanics module, COMSOL) to estimate the stiffness of the thermal probes using the following boundary conditions: a force of 50 nN, either in the normal or the transverse direction, was applied at the end of the probe tip, while the other end of the SiN_x cantilevers was fixed. From the computed resultant displacement field, the stiffness of the probe was estimated to be ~14,000 N m^{-1} in the normal direction, and ~275 N m^{-1} and ~12.5 N m^{-1} in the transverse directions, respectively (as shown in Extended Data Fig. 3a–c). In our experiments, the normal stiffness is found to be sufficiently large to form stable molecular junctions.

Temperature distribution on the probe. Temperature fields generated on the probe due to d.c. Joule heating or d.c. heat input to the tip were simulated using COMSOL (Joule Heating and Thermal Expansion module). A 10-μA d.c. electrical current (Extended Data Fig. 3d) was supplied to the Pt line or a 10-μW d.c. heat current was input at the tip (Extended Data Fig. 3e), while the ends of the SiN_x cantilevers were held at 300 K. We note that in both cases the Pt thermometer embedded in the island exhibits a uniform temperature distribution and the temperature drop occurs primarily along the beams.

Experimental set-up and measurement schemes. *Ultra-low-noise measurement environment.* All electrical and thermal measurements of single-molecule junctions were performed in a UHV (~10^{-9} torr) scanning probe instrument (RHK UHV 750), which is housed in a test chamber of a low-noise facility where the mechanical floor vibrations are maintained below the NIST-A standard. The temperature drift of the chamber was actively controlled to vary below 100 mK around a chosen set point at 295 K.

Molecular sample preparation and cleaning protocol for probes. To facilitate the formation of single-molecule junctions during the experiments, self-assembled monolayers of alkanedithiol molecules were prepared on an ultra-flat planar Au-coated substrate, which was prepared via template-stripping. The Au-coated substrate was immersed in 500-μM ethanol solutions of alkanedithiol molecules (C2, C4, C6, C8, C10, from Sigma Aldrich with purity >95%) to initiate the self-assembly process of the molecules on the Au surface. After ~12 h of incubation, the samples were thoroughly rinsed in ethanol and dried in a nitrogen-filled glove box before being transferred into the UHV measurement environment. Furthermore, in order to ensure high cleanliness of the Au-coated scanning thermal probes, which is critical for successful thermal transport measurements, we followed a protocol reported elsewhere[33]. We note that it is critical to avoid any direct contact of the probe with the ambient, and multiple cycles of wet and plasma cleaning are usually needed to eliminate any detectable contamination on the probe.

Formation of single-molecule junctions and transport measurement circuitry. All the single-molecule junctions were created between the scanning thermal probes and molecule-covered Au substrates. During the measurement, the probe was controllably displaced towards the substrate at a speed of 1 nm s^{-1}, and withdrawn from the substrate at 0.05 nm s^{-1} after making contact as indicated by a sufficiently large electrical conductance (compared to the single-molecule conductance). The withdrawal of the scanning probe was stopped once a single-molecule junction was formed, as indicated by an approximately constant electrical conductance that was within one standard deviation of the single-molecule conductance obtained from the conductance histogram. Simultaneous electrical and thermal conductance measurements were recorded for a constant electrode separation until the particular single-molecule junction spontaneously broke. The process of formation and breakdown of single-molecule junctions was repeated several hundred times for each type of molecule.

The electrical conductance was measured by supplying a d.c. voltage bias (30 mV, 50 mV, 100 mV, 100 mV and 200 mV for C2–C10 junctions, respectively) across the scanning thermal probe and the Au substrate, while monitoring the tunnelling current across the junctions via a current amplifier (SR570). We note that the filter settings of the current amplifier resulted in an electrical time constant of ~2 ms in all our experiments (see Figs. 2b and 3b). Smaller voltage biases were chosen for shorter molecular junctions, which feature larger electrical conductances, to minimize the effects of Joule heating.

In order to study the thermal conductance of the junctions, the temperature change of the scanning thermal probe was measured before and after the breakdown of the single-molecule junctions. For this purpose we monitored the change in the electric resistance of the embedded Pt resistance thermometer via a half-Wheatstone bridge. The output voltage signal of the bridge circuit in the presence of a d.c. electric current was first amplified by an instrumentation amplifier (AD524) with a gain of 100 and subsequently measured using a low-noise voltage amplifier (SR 560 with a gain of 100).

Selection criteria for single-molecule traces. To analyse the thermal conductance of single-molecule junctions, we identify single-molecule events via off-line analysis from our continuous recordings by applying the following criteria: (1) the electrical conductance drops in a clear last step from a constant, expected electrical conductance value (corresponding to the previously established values, see above), signalling the presence of a single-molecule junction before breakdown; (2) during formation and following breakdown of the junction, the thermal conductance from the probe to the monolayer sample is relatively stable (drift <100 pW K^{-1} in 0.5 s), signifying a thermal measurement that is not compromised by a large change of background conduction pathways. The first criterion ensures that we are only employing data from single-molecule junctions with well-defined electrical conductance corresponding to the most probable value, as identified from the analysis of the conductance histogram (Figs. 2a and 3a). The second criterion is principally informed by our past work[33], which suggests that the presence of organic contamination leads to parasitic conductances at the sub-nanowatt per K to nanowatt per K level. The variation in this background conductance as a function of time, if large, can limit the resolution of our time-averaging approach. In our analysis we found that drift values <100 pW K^{-1} in a 0.5-s period after rupture of contact are sufficient to achieve the desired signal-to-noise ratio. Rigorous application of the above criteria avoids artefacts and ensures reliable single-molecule thermal conductance measurements. A majority (>90%) of the curves that satisfy the first criterion were also found to satisfy the second. In the relatively rare events (<10%) where large background drift was observed, we deemed the experiment to have failed and excluded the curve from the thermal conductance analysis using a completely automated process.

Noise reduction due to the time-averaging scheme. The measured temperature change of the scanning thermal probe is associated with substantial noise contributions from electronics (amplifiers), Johnson noise, shot noise and temperature drift of the measurement environment. As shown in Fig. 2b, the unprocessed

thermal signals are featureless and buried in large noise ($\sim$100 pW K^{-1}). To improve the signal-to-noise ratio of the measurements, a time-averaging scheme is applied to the thermal conductance traces, which were acquired through independent measurements of many molecular junctions ($\sim$100). Briefly, the time at which a single-molecule junction breaks (t_b) was first detected by analysing the time series of electrical conductance traces. Subsequently the ΔG_{th} signal corresponding to the same electrical conductance trace was demarcated into a $\tau = 0.5$ s region (shaded in green in Fig. 2b, bottom panel) before t_b, and two intervals $\tau' = 0.1$ s (unshaded) and $\tau = 0.5$ s (shaded in brown) after t_b. We note that the $\tau' = 0.1$ s interval (around four times the thermal time constant of the probe) corresponds to the time required to achieve the full thermal response of the probe after the junction-breaking event. Further, the average value of the ΔG_{th} signal in the subsequent 0.5 s after breaking of the molecular junction is averaged and set to zero by suitably offsetting the curve. (This procedure ensures compliance with the physical expectation that the thermal conductance change after breaking of the junction is negligibly small.) Finally, the thermal conductance traces from each of the individual experiments were aligned using t_b as the reference point, and data from corresponding time points were averaged. Following a procedure described in detail in our previous work[9], we can estimate the smallest thermal conductance change ($\Delta G_{th,min}$) detectable using our time-averaging scheme to be:

$$\Delta G_{th,min} \approx \frac{G_{th,P}}{T_P - T_S}\frac{1}{IR_0\alpha} \times \left\{ \int_{-\infty}^{+\infty} G_{noise}(f)\left[\frac{2\tau+\tau'}{\tau}\frac{\sin(2\pi f\widetilde{T})}{2\pi f\widetilde{T}}\frac{2\sin[\pi f(\tau+\tau')]\sin(\pi f\tau)}{\sin[\pi f(2\tau+\tau')]}\right]^2 df \right\}^{1/2}$$

Here $G_{noise}(f)$ is the power spectral density at frequency f associated with the temperature noise that the probe is subject to, and $2\widetilde{T}$ is the total time over which the averaging is performed. For example, for 100 molecular junctions the total averaging time $2\widetilde{T}$ equals 110 s. By following the protocol that we have developed previously[34] to measure the noise spectrum of a Pt resistance thermometer, we can estimate the power spectral density. With this information and the above equation, we estimate $\Delta G_{th,min}$ to be $\sim$2 pW K^{-1}. Finally, we note that the electrical conductance traces show additional stepwise changes before rupture of the last junction (see Extended Data Fig. 4 top panels) that represent recordings during the withdrawal of the tip from multi-molecule junctions. These additional changes do not yield identifiable multiple conductance states in electrical conductance histograms (see, for example, Fig. 2a). Further, given the low thermal conductance of the studied molecular junctions, the thermal traces of multi-molecule junctions are, as expected, largely featureless (see Extended Data Fig. 4, bottom panels). An averaging approach analogous to the successful analysis of the thermal conductance of single-molecule junctions cannot yield the corresponding thermal conductances of these multiple-molecule junctions, as these states are not well correlated in time and step-size compared to the single-molecule junction states.

Effect of Joule heating on measurements of the thermal conductance. In addition to averaging the signals from many individual thermal conductance events as discussed above, we need to account for the heat dissipation that results from the applied electrical bias. Specifically, when a voltage bias (V) is supplied across a junction of resistance R, it results in a total heat dissipation of V^2/R. Since the Seebeck coefficient of alkanedithiol junctions is very small[35], the heat dissipation in the electrodes is symmetric to an excellent approximation[9]. Therefore, the heat dissipated in the probe due to the voltage bias is given by $V^2/2R$. When the single-molecule junction is broken, the probe not only heats up due to the loss of a thermal conduction pathway, but there is also a competing effect that attenuates the temperature drop as the heat dissipation in the probe decreases by $V^2/2R$. In order to systematically account for this effect, we add $\Delta T_{Joule} = V^2/(2RG_{th,P})$ to the measured data in the range 0 to t_b seconds (that is, for the region before the junction is broken) to obtain the ΔT_P plot in Fig. 2b and all other related ΔG_{th} plots shown in the manuscript (Figs. 2c, 3b). These corrections are modest for C6 ($\sim$20%), C8 ($<$2%) and C10 ($<$2%) junctions, but they are sizable for C2 ($\sim$60%) and C4 ($\sim$30%) junctions. Here, all the percentages represent how large ΔT_{Joule} is with respect to the observed temperature drop ΔT_P when the junction breaks.

Effect of intermolecular interactions on the measurements of the thermal conductance. Given the fact that all our experiments are performed in a UHV environment, the probability of interaction between the single-molecule junction of interest and other molecules is much smaller than that in experiments performed in a solution environment, where several surrounding molecules can potentially interact with the junction. Further, it is to be noted that in our experiments the single-molecule junction is expected to be isolated from surrounding molecules as the junction is created between elongated Au chains that protrude out from the electrodes. Therefore, the probability of interaction with surrounding molecules is expected to be very low.

Influence of near-field radiative heat transfer. Near-field radiative heat transfer has a negligible impact on our measurements. In particular, our strategy for determining the thermal conductance of a single-molecule junction relies on measuring the change of the thermal conductance when a single molecule that is bridging the calorimeter and the substrate breaks away. In the absence of any drift in the gap size, the near-field contribution before and after the junction-breaking event is identical. For this reason, near-field thermal radiation makes no contribution to the measurement, as we are determining the change in the thermal conductance upon the breakdown of the junction. The drift in the gap size of our system of $<$1 Å min^{-1} translates to $<$15 pm in a 1-s time interval. Given our past analysis[33], the near-field radiative conductance change is expected to be $\sim$2 pW K^{-1} when the gap size changes by $\sim$1 nm. Therefore, the change in the near-field contribution due to gap size drift of $\sim$15 pm is negligibly small ($<$0.03 pW K^{-1}) when compared to the thermal conductance of a single-molecule junction ($\sim$20 pW K^{-1}).

Computational methods. *Thermal conductance within the Landauer–Büttiker approach.* To calculate the thermal conductance of molecular junctions, we employ the Landauer–Büttiker formalism for coherent transport[19,29,36,37]. This theory describes phonon transport as phase-coherent and elastic. Since in this formalism transport is described as a scattering problem of waves, the key quantity is the probability $\tau_{ph}(E)$ of a phonon at a given energy E to be transmitted from one lead to the other, which is computed using the procedures developed in our past work[15,29,31]. The linear response coefficient ($G_{th,SMJ}$) can be calculated using:

$$G_{th,SMJ} = \frac{1}{h}\int_0^\infty E\tau_{ph}(E)\frac{\partial n(E,T)}{\partial T}dE \quad (1)$$

where $n(E, T) = [\exp(E/k_BT) - 1]^{-1}$ is the Bose function. The thermal conductance is given as an energy integral over the transmission function weighted by energy and the temperature derivative of the Bose function, which considers the energetic content of the transmitted phonons and the difference in phonon populations in the leads, respectively.

DFT modelling. In the calculation of the phononic transmission function, the dynamical matrix, which describes the mechanical coupling of individual atoms in the molecular junction at the microscopic scale, plays a key role. To obtain the dynamical matrix, we calculate the second derivative of the Born–Oppenheimer energy landscape[38,39] by using density functional perturbation theory, as implemented in the quantum chemistry software package TURBOMOLE, version 7.1[40]. Total energies are converged up to a precision of 10^{-9} a.u., and geometries are optimized until the change of the maximum norm of the Cartesian gradient is smaller than 10^{-5} a.u. We use the Perdew–Burke–Ernzerhof exchange-correlation functional[41,42] and the default2 basis set of split-valence-plus-polarization quality def2-SV(P)[43,44] in combination with the corresponding Coulomb fitting basis.

Junction geometries and pulling curves. All junction geometries studied in Fig. 4 are built up from two gold pyramids oriented in the crystallographic (111) direction: one end of the straight alkane chain is attached via a sulphur group to the tip atom of one of the pyramids, and the other end of the chain is attached via a sulphur atom to the other pyramid. The atomically sharp pyramids model probe and substrate metal electrodes close to the point of rupture, when they have been deformed by mechanical stress and gold atoms have been pulled out of the soft but initially flat substrate surface. The positions of the atoms in the central junction part, consisting of the molecule and the two metal layers closest to it, are optimized by energy minimization, while the Au atoms in the two outermost rows of the Au_{20} pyramids on each side, that is, those most distant from the molecule, are kept fixed. To generate the pulling curves of Fig. 4, the junctions are adiabatically stretched by displacing the frozen part of the gold atoms on one side of the molecular junction in the direction of the difference vector between the Au tip atoms with a step size of $d = 0.5$ a.u. $\approx$ 0.26 Å, and optimizing again all the atoms in the central junction part under the new boundary condition set by the fixed outermost Au layers. We note that in these simulations, we mimic the experiments and obtain contact geometries that correspond to those manifested in single-molecule junctions at breakdown[45].

Additional thermal conductance–distance traces. In Fig. 4 we present thermal conductance versus distance curves for molecular junctions of the five different molecules C2–C10. In each case a gold atom is pulled out from the Au electrodes to yield a short gold chain in the form of a dimer before the contact breaks. To inspect the robustness of the results, we performed further simulations of junction stretching processes and show in Extended Data Fig. 5 additional pulling curves for C2, C6 and C10. Here the gold atoms at the tips move from a three-fold hollow to a two-fold bridge position before the contact breaks, as is visible from the geometries displayed in the insets of Extended Data Fig. 5. We note that in this analysis the initial geometries differ from those shown in the main text with respect to the orientation of the molecule on the pyramidal leads, but the stretching protocol is otherwise identical. The computed thermal conductances at rupture are slightly higher than those shown in Fig. 4, since the blue region is missing, but they are

within the uncertainty of the measured thermal conductance values (Fig. 3c). As these examples show, the formation of gold chains in our simulations depends sensitively on the starting geometry and the details of the adiabatic stretching process. A faithful reproduction of the mechanical deformation of the macroscopically large gold electrodes will require a larger number of flexible gold atoms than what we can at present use in our computationally demanding ab initio simulations.

Influence of variations of the contact geometry. As for any mechanically controlled break-junction technique, junction geometries in the experiment are not well controlled at the atomic scale, and the space of possible configurations is huge. This leads to uncertainties with regard to molecular configuration, molecule–electrode coupling and electrode orientation. Assuming alkane molecules to be fully stretched before contact rupture, it is interesting to explore the variation of phonon thermal conductance as the geometry of the contacts is varied. In Extended Data Fig. 6 we show the computed changes in the energy-dependent phonon transmission for Au–C10–Au single-molecule junctions with different contact geometries. Specifically, we find that peak positions and peak widths in the transmission spectrum depend on the precise atomic geometries.

In Extended Data Table 1, we present the computed thermal conductances for the four Au–C10–Au junctions shown in Extended Data Fig. 6, but include also the data for corresponding junction types containing C2–C8. We also list the resulting standard deviations for each molecule that are found to be in the range of 3–7 pW K^{-1} and in close correspondence to the standard deviation of the measured thermal conductances (see Fig. 3c). We note that in this analysis we designed the different junction types such that stress is minimized, in order to concentrate on the effects of metal–molecule binding and electrode orientation. The molecular contacts are therefore located inside the yellow-shaded area of Fig. 4, which results in a somewhat larger thermal conductance than those obtained in our experiments.

Electronic contributions to the thermal conductance. In Fig. 4 of the main text we have estimated $G_{th,el}$ with the help of the Wiedemann–Franz law, based on the mean experimental single-molecule electrical conductance value. The Wiedemann–Franz law reads $G_{th,el} = L_0 T G_{el}$, where the Lorentz number $L_0 = \pi^2 k_B^2/3e^2 = 2.44 \times 10^{-8}\,W\,\Omega\,K^{-2}$, T is the temperature, and G_{el} the electrical conductance. Using the experimental values $G_{el} = 10^{-2} G_0$ for C2, and $G_{el} = 2 \times 10^{-3} G_0$ for C4, in addition to $T = 300$ K, we obtain the data for $G_{th,el}$ given in the text.

Transmission eigenchannels. To obtain further information about heat transport in nanosystems, we decomposed the phonon transmission function, $\tau_{ph}(E)$, into energy-dependent contributions $\tau_{ph,i}(E)$ of individual transmission eigenchannels i:

$$\tau_{ph}(E) = \sum_i \tau_{ph,i}(E) \quad (2)$$

These eigenchannels are scattering states, and the transmission coefficients $0 \leq \tau_{ph,i}(E) \leq 1$ are the eigenvalues of the transmission probability matrix[29].

In Extended Data Fig. 7 we display, along with $\tau_{ph,i}(E)$ for $i = 1, 2, 3$, the most transmissive eigenchannel $i = 1$ of C2, C6 and C10 at selected energies. These are the highest energies at which a transmission resonance occurs with a value close to 1. Note that we show here a static representation of the eigenchannels in terms of the real part at time $t = 0$, despite the general solution being complex or time-dependent. Similar to the discussion in our past work[29], a close relation of the molecular vibrations to the transmission eigenchannels often exists. We observe that for C2 junctions only the centre-of-mass motions of the molecule contribute to phonon transport due to the short molecular length. However, for C6 and C10, genuine molecular modes carry heat. This is evident from direction changes of the arrows in Extended Data Fig. 7 that indicate the atomic motion, when going from one end of the molecule in the junction to the other.

Data availability

The data that support the findings of this study are available from the corresponding authors on reasonable request.

Code availability

The DFT program used to analyse the electronic structure and vibrational properties is available from www.turbomole.com. The corresponding custom-developed code for the description of phonon transport implements the procedures outlined in ref. [31] and is available from F.P. on reasonable request.

33. Cui, L. et al. Study of radiative heat transfer in Ångström- and nanometre-sized gaps. *Nat. Commun.* **8**, 14479 (2017); correction **9**, 16225 (2018).
34. Sadat, S., Meyhofer, E. & Reddy, P. High resolution resistive thermometry for micro/nanoscale measurements. *Rev. Sci. Instrum.* **83**, 084902 (2012).
35. Malen, J. A. et al. Identifying the length dependence of orbital alignment and contact coupling in molecular heterojunctions. *Nano Lett.* **9**, 1164–1169 (2009).
36. Wang, J. S., Wang, J. & Lü, J. T. Quantum thermal transport in nanostructures. *Eur. Phys. J. B* **62**, 381–404 (2008).
37. Li, N. et al. Phononics: manipulating heat flow with electronic analogs and beyond. *Rev. Mod. Phys.* **84**, 1045–1066 (2012).
38. Deglmann, P., Furche, F. & Ahlrichs, R. An efficient implementation of second analytical derivatives for density functional methods. *Chem. Phys. Lett.* **362**, 511–518 (2002).
39. Deglmann, P., May, K., Furche, F. & Ahlrichs, R. Nuclear second analytical derivative calculations using auxiliary basis set expansions. *Chem. Phys. Lett.* **384**, 103–107 (2004).
40. TURBOMOLE version 7.1, http://www.turbomole.com (TURBOMOLE GmbH, Karlsruhe, 2016).
41. Perdew, J. P., Burke, K. & Ernzerhof, M. Generalized gradient approximation made simple. *Phys. Rev. Lett.* **77**, 3865–3868 (1996).
42. Perdew, J. P. & Wang, Y. Accurate and simple analytic representation of the electron-gas correlation energy. *Phys. Rev. B* **45**, 13244–13249 (1992).
43. Weigend, F. Accurate Coulomb-fitting basis sets for H to Rn. *Phys. Chem. Chem. Phys.* **8**, 1057–1065 (2006).
44. Weigend, F. & Ahlrichs, R. Balanced basis sets of split valence, triple zeta valence and quadruple zeta valence quality for H to Rn: design and assessment of accuracy. *Phys. Chem. Chem. Phys.* **7**, 3297–3305 (2005).
45. Paulsson, M., Krag, C., Frederiksen, T. & Brandbyge, M. Conductance of alkanedithiol single-molecule junctions: a molecular dynamics study. *Nano Lett.* **9**, 117–121 (2009).

Acknowledgements P.R. and E.M. acknowledge funding from the US Office of Naval Research (N00014-16-1-2672, instrumentation), the US Department of Energy (DE-SC0004871, scanning probe microscopy) and the US National Science Foundation (1803983). P.R. and E.M. acknowledge the Lurie Nanofabrication Facility and the Michigan Center for Materials Characterization for facilitating the fabrication and calibration of devices. S.-Y.J. gratefully acknowledges support from a National Research Foundation (NRF) grant funded by the Korean Government (no. 2016R1A5A1012966). J.C.K. and F.P. thank the Collaborative Research Center (SFB) 767 of the German Research Foundation (DFG) for financial support. A large part of the numerical modelling was carried out using the computational resources of the bwHPC programme, namely, the bwUniCluster and the JUSTUS HPC facility.

Author contributions The work was conceived by P.R. and E.M. The experiments were performed by L.C. The devices were fabricated by S.H. and W.J. The monolayer samples were prepared by Z.A.A. under the guidance of S.-Y.J. The calculations were performed by J.C.K. under the guidance of F.P. The manuscript was written by L.C., F.P., P.R. and E.M. with comments and inputs from all authors.

Competing interests The authors declare no competing interests.

Additional information

Correspondence and requests for materials should be addressed to F.P. (theory), S.-Y.J. (chemistry and sample preparation), P.R. and E.M. (transport experiments).

Peer review information *Nature* thanks Victor Manuel Garcia Suarez and the other, anonymous, reviewer(s) for their contribution to the peer review of this work.

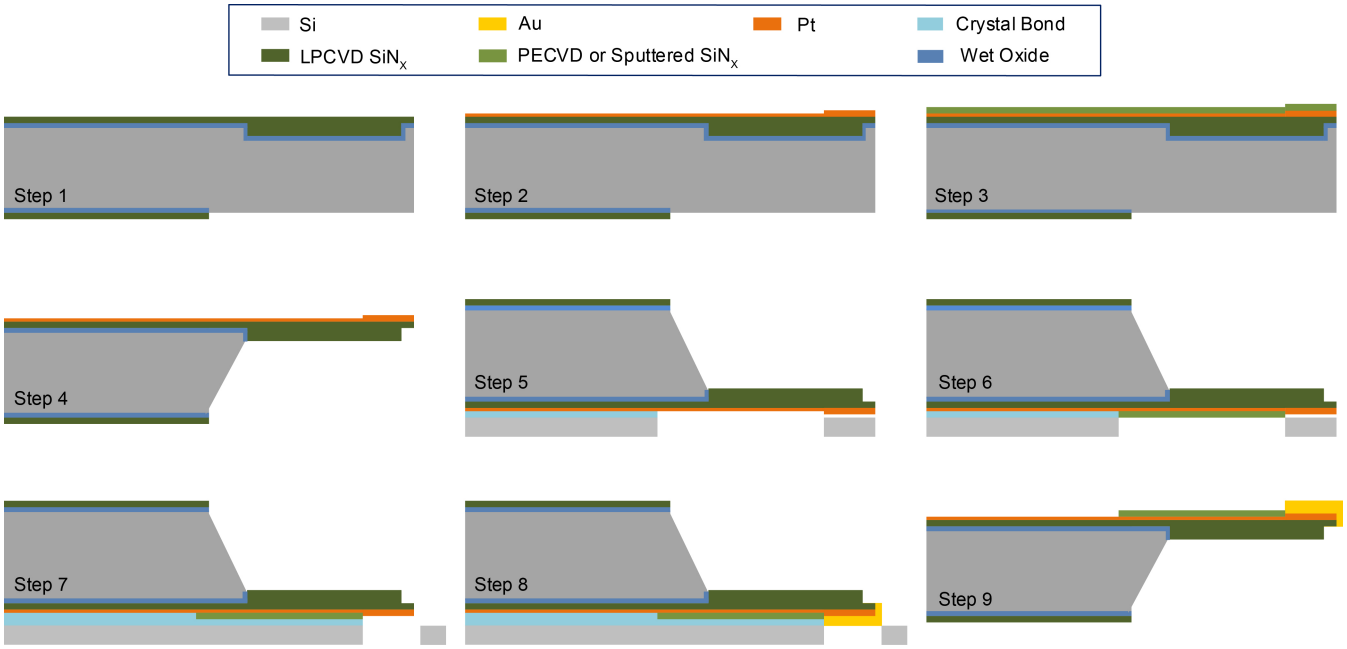

Extended Data Fig. 1 | Fabrication steps for thermal probes. Step 1, 'T'-shaped cantilever patterning. Step 2, deposition of Pt for the serpentine heater-thermometer, pads and the tip. Step 3, SiN_x layer deposition for front side KOH etching. Step 4, probe cantilever release. Step 5, aligning each probe on the first shadow mask using a thin low-temperature crystal bond layer. Step 6, SiN_x sputtering on the serpentine Pt heater-thermometer. Step 7, aligning each probe on the second shadow mask. Step 8, Au sputtering on the tip region. Step 9, detaching the scanning probe from the shadow mask and removing the residual crystal bond by 'piranha' cleaning.

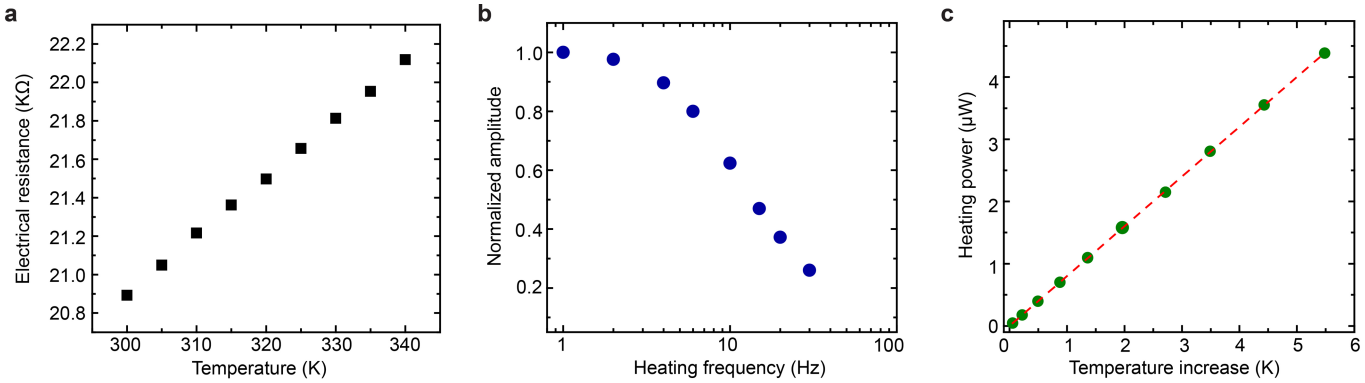

Extended Data Fig. 2 | Characterization of thermal and electrical properties of the scanning thermal probes. a, Measured electrical resistance of the Pt heater-thermometer as a function of temperature. **b**, Measured thermal response of the scanning probe as a function of the heating frequency. **c**, Calibration of the thermal conductance of the probe (input heating power provided to the Pt heater-thermometer plotted against the temperature rise of the probe). The slope of the dashed fitted line corresponds to the thermal conductance of the probe.

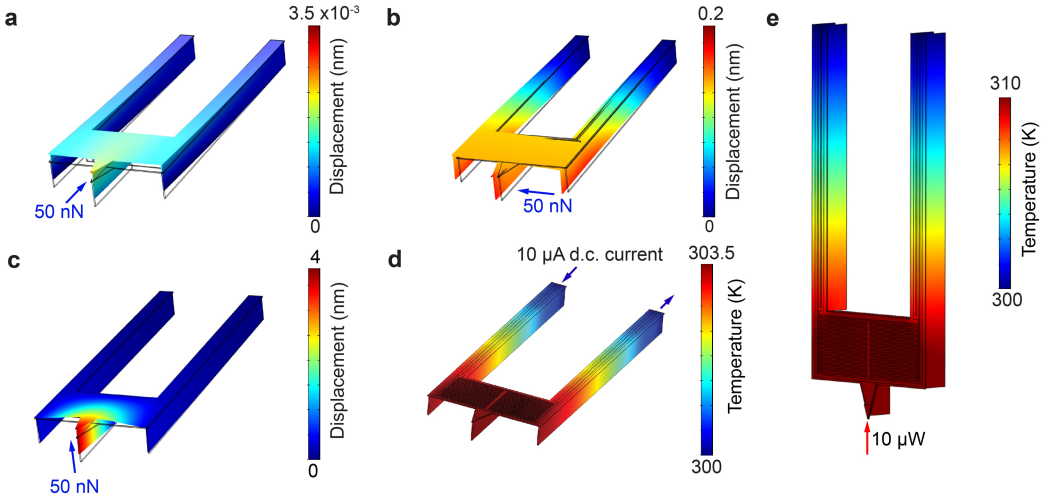

Extended Data Fig. 3 | Evaluation of mechanical properties and spatial temperature variation of the scanning thermal probes. a–c, A force of 50 nN was applied either in the normal or the transverse directions of the beams, and the deflection for each case was computed ('Displacement', colour key). The stiffness of the probe was calculated to be 14,000 N m^{-1} (**a**), 275 N m^{-1} (**b**) and 12.5 N m^{-1} (**c**), respectively, for the normal and two transverse directions. **d**, **e**, Calculated temperature field (colour key at right) of the scanning thermal probe when a 10-μA d.c. current was applied to the embedded serpentine Pt heater-thermometer (**d**) and a 10-μW heat current was input from the tip (**e**). The spatial temperature distribution on the island is very uniform (<5% change across locations), supporting the expectation that the distributed Pt heater-thermometer accurately measures the temperature of the suspended region.

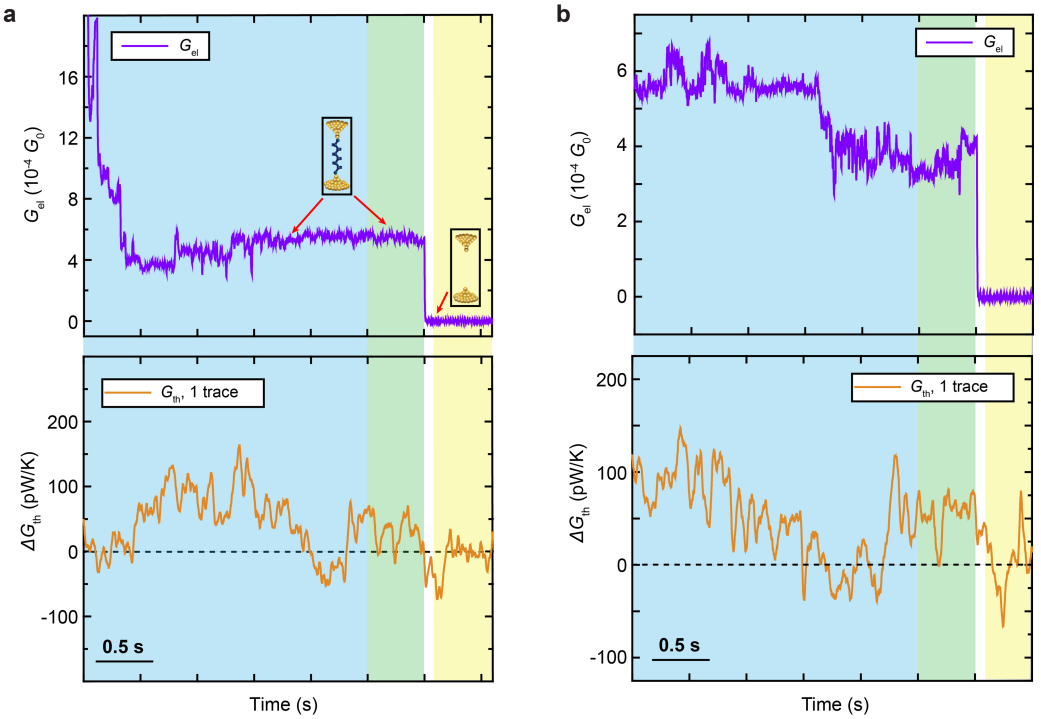

Extended Data Fig. 4 | Sample electrical and thermal conductance traces for Au–C6–Au molecular junctions. a, **b**, Two independent sample recordings. Top and bottom panels show electrical and thermal conductance, respectively. The green- and yellow-shaded regions mark portions of the recordings that capture the rupture of a single-molecule junction to which the time-averaging scheme is applied, while the blue-shaded regions during the earlier portions of the withdrawal cycle represent recordings that contain events involving multi-molecule junctions. A clear last step can be identified in the electrical conductance traces (green-yellow region), indicating the breakdown of a single-molecule junction. As can be seen, there are also additional steps before the last step in the blue-shaded region. The corresponding thermal conductance traces that are shown below each electrical conductance trace do not reveal any thermal conductance steps, owing to the low signal-to-noise ratio. Insets, schematics of single-molecule junctions before and after rupture.

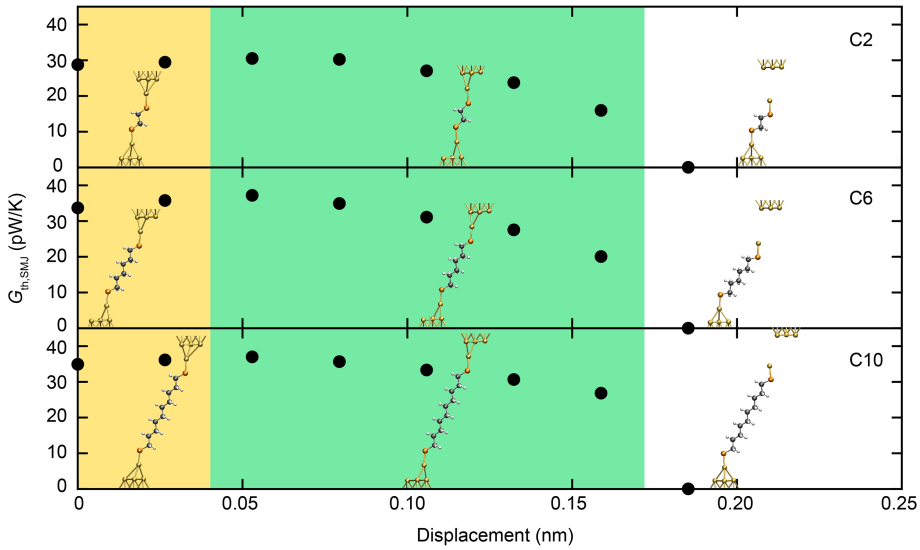

Extended Data Fig. 5 | Simulated thermal conductance as a function of electrode displacement for C2, C6 and C10 single-molecule junctions. The computed thermal conductance data are shown as black dots, coloured regions have the same meaning as in Fig. 4, and snapshots of junction structures are displayed as insets. The initial junction geometries before displacement of the electrodes differ from those used to generate the corresponding plots in Fig. 4, but the procedure employed for stretching the junctions is the same.

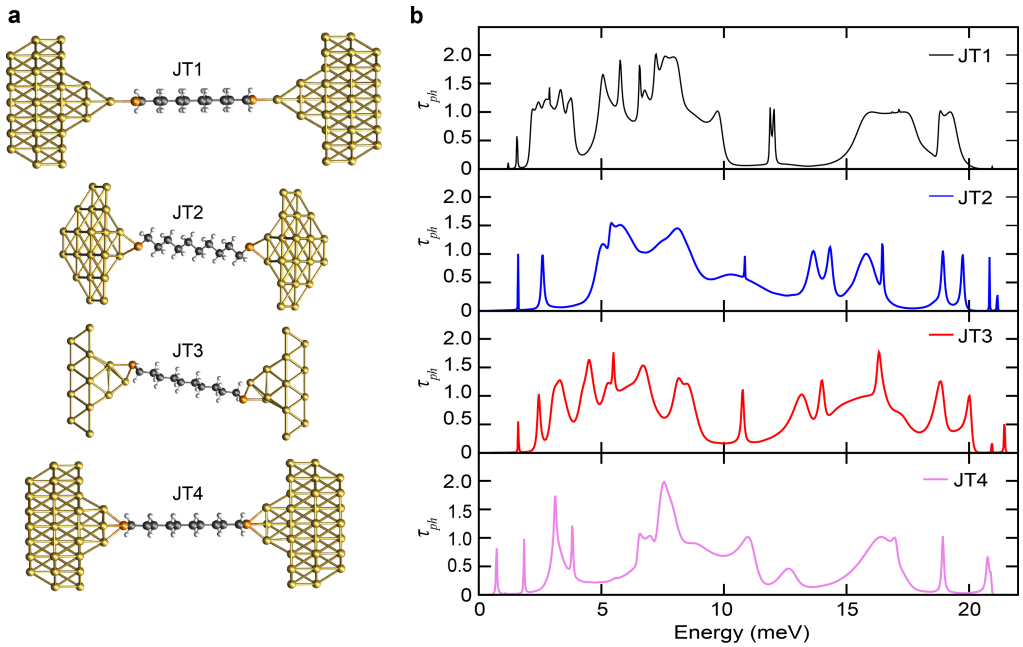

Extended Data Fig. 6 | Influence of the contact geometry on computed phonon transmission for Au–C10–Au single-molecule junctions. **a**, Different junction types that are used to evaluate the effect of contact geometry on the phonon transmission functions. Each terminal sulphur atom in the junction is attached to a single Au tip atom (JT1), to two Au tip atoms (JT2, JT3) or to three Au atoms (JT4). In these geometries, electrodes are oriented along the (111) crystallographic direction (JT1, JT4), the (110) direction (JT2) and the (100) direction (JT3). **b**, Phonon transmission as a function of energy for the different junction geometries illustrated in **a**.

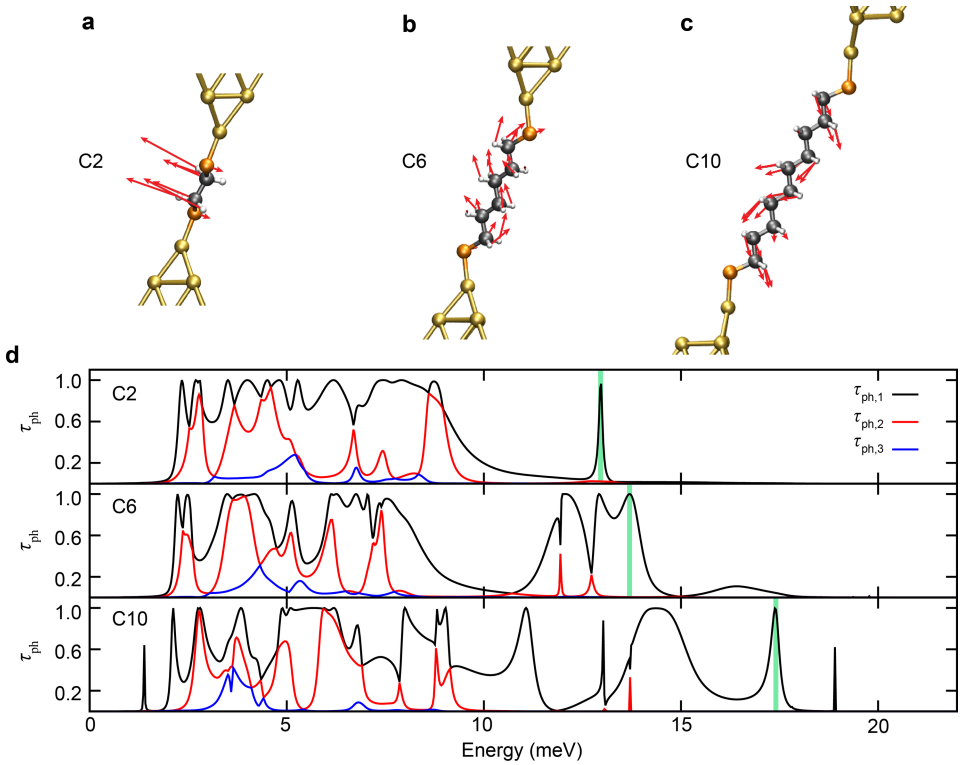

Extended Data Fig. 7 | Phonon transmission eigenchannels for C2, C6 and C10 junctions. a–c, Displacement patterns associated with the mode shapes of the most transmissive eigenchannel $i = 1$ for C2, C6 and C10, respectively, evaluated at energies of 13.5 meV, 14 meV and 18 meV. **d**, Phonon transmission associated with each of the three eigenchannels $i = 1, 2, 3$ for C2, C6 and C10 molecular junctions. A peak in the transmission of eigenchannel $i = 1$ is found to occur at energies of around 13.5 meV, 14 meV and 18 meV for C2, C6 and C10 junctions, respectively, and is indicated by the green bars. The displacement patterns of transmission eigenchannel $i = 1$ in **a–c** have been evaluated at these energies.

Extended Data Table 1 | Calculated thermal conductance

Molecule	$G_{th,JT1}$ (pW/K)	$G_{th,JT2}$ (pW/K)	$G_{th,JT3}$ (pW/K)	$G_{th,JT4}$ (pW/K)	Standard Deviation (pW/K)
C2	28.0	21.9	37.7	30.4	6.5
C4	29.7	30.9	41.4	41.0	6.3
C6	33.9	31.7	36.9	40.3	3.7
C8	35.5	35.5	42.2	32.0	4.2
C10	44.0	34.8	45.3	32.7	6.4

Columns 2–5 show the calculated thermal conductance of Au–alkanedithiol–Au single-molecule junctions for four types of junction geometries, respectively JT1, JT2, JT3 and JT4. The entry in column 1 shows the alkanedithiol molecule concerned. Junction geometries are either identical to those shown in Extended Data Fig. 6 (for C10) or similar to them (C2–C8). Each terminal sulphur atom attaches to a single Au tip atom for JT1, to two Au tip atoms for JT2 and JT3, or to three Au tip atoms for JT4, while the electrodes are oriented along the (111) crystallographic direction for JT1 and JT4, the (110) direction for JT2 or the (100) direction for JT3. The standard deviation (column 6) indicates the variability of the thermal conductance as determined for each molecule from the four different junctions types.

LETTER

https://doi.org/10.1038/s41586-019-1504-9

Efficient molecular doping of polymeric semiconductors driven by anion exchange

Yu Yamashita[1,2,3], Junto Tsurumi[1,2,3], Masahiro Ohno[1,2], Ryo Fujimoto[1,2], Shohei Kumagai[1,2], Tadanori Kurosawa[1,2], Toshihiro Okamoto[1,2,4,5], Jun Takeya[1,2,3,4] & Shun Watanabe[1,2,4,5]*

The efficiency with which polymeric semiconductors can be chemically doped—and the charge carrier densities that can thereby be achieved—is determined primarily by the electrochemical redox potential between the π-conjugated polymer and the dopant species[1,2]. Thus, matching the electron affinity of one with the ionization potential of the other can allow effective doping[3,4]. Here we describe a different process—which we term 'anion exchange'—that might offer improved doping levels. This process is mediated by an ionic liquid solvent and can be pictured as the effective instantaneous exchange of a conventional small p-type dopant anion with a second anion provided by an ionic liquid. The introduction of optimized ionic salt (the ionic liquid solvent) into a conventional binary donor–acceptor system can overcome the redox potential limitations described by Marcus theory[5], and allows an anion-exchange efficiency of nearly 100 per cent. As a result, doping levels of up to almost one charge per monomer unit can be achieved. This demonstration of increased doping levels, increased stability and excellent transport properties shows that anion-exchange doping, which can use an almost infinite selection of ionic salts, could be a powerful tool for the realization of advanced molecular electronics.

Chemical doping of π-conjugated materials necessarily involves redox reactions between the host and dopant[3]. In this process, an integer number of electrons is transferred from the host to the dopant via electron transfer in the ground state, which is well described by Marcus theory[5]. Because the driving force in donor–acceptor association is dominated primarily by the electrochemical redox potential between the π-conjugated material and the dopant, efficient doping occurs only when charge transfer is energetically favourable. To achieve higher doping efficiency (for example, p-type doping), the electron affinity of the acceptor (the dopant) should match or exceed the ionization potential of the host material[2].

Various dopants and processes have been used to achieve the efficient chemical doping of organic semiconductors. Despite the successful tuning of the electron affinity of various conjugated molecules to promote efficient doping, increasing the electron affinity often causes chemical instability. This represents a major challenge to extending the scope of potential molecular dopants, and there have been attempts to use photo-assisted doping to mitigate this problem[6]. In addition to charge-transfer interactions based on redox reactions, Coulomb interactions such as hole–hole and hole–counterion interactions in the case of p-type doping[4,7] are an important aspect of organic-semiconductor doping, suggesting the possibility of optimizing molecular doping by tuning Coulomb or ionic interactions[8,9].

Here we demonstrate a general strategy for overcoming charge-transfer limitations by using anion exchange. We focus on the chemical doping of the well-studied thiophene-based conjugated polymer poly(2,5-bis(3-tetradecylthiophen-2-yl)thieno[3,2-*b*]thiophene) (PBTTT)[10] in conjunction with tetrafluorotetracyanoquinodimethane (F4TCNQ)[11], as shown in Fig. 1a, introducing an additional anion to the host–guest system (see Extended Data Fig. 1 and Supplementary Information section 1.1). This combination of substances results in spontaneous exchange of the F4TCNQ radical anion and the newly introduced anion with near-unity exchange efficiency. The anion-exchange doping process used here results in remarkable improvements in both the doping level and the thermal durability of the doped material.

Our anion-exchange doping process involves a host–guest system that also includes a large excess of a salt (consisting of a cation, X^+, and an anion, Y^-; Fig. 1b). As an example, an ionic liquid in which X is 1-ethyl-3-methylimidazolium (EMIM) and Y is bis(trifluoromethylsulfonyl)imide (TFSI) can be used. Surprisingly, in this scenario, the TFSI anions are instantaneously exchanged with the F4TCNQ radical anions that form the intermediate ion pair [PBTTT$^{\bullet+}$ F4TCNQ$^{\bullet-}$] (Fig. 1b). Here, we realized anion-exchange doping by using the ionic liquid EMIM-TFSI instead of *n*-butylacetate as a solvent for F4TCNQ (details of this method are provided in Supplementary Information section 1.2). We confirmed hole doping of the polymer via charge transfer by observing bleaching of the neutral absorption of PBTTT at 553 nm (Fig. 1c). In contrast to a conventional binary system, a characteristic doublet originating from the F4TCNQ radical anion was not seen in the absorption spectrum of the doped film. We further verified the absence of F4TCNQ radical anions in the PBTTT by Fourier transform infrared (FTIR) spectroscopy (Fig. 1d and Extended Data Fig. 2). Specifically, the FTIR spectrum of the anion-exchanged film does not show the peak assigned to the C≡N stretching mode of the F4TCNQ radical anion (2,190 cm^{-1}; ref. [12]), indicating highly efficient anion exchange (F4TCNQ$^{\bullet-}$ → $TFSI^-$).

We also confirmed the absence of the F4TNQ radical anion in the PBTTT by Raman spectroscopy (Supplementary Information section 1.3) and electron spin resonance measurements. We estimated the Curie spin concentration resulting from the F4TCNQ radical anions to be 1.7×10^{19} cm^{-3} (Extended Data Fig. 3), which is very low compared with the actual doping level of roughly 1×10^{21} cm^{-3} derived from Hall effect measurements. Therefore, we conclude that the lower limit of the anion-exchange efficiency for this process (F4TCNQ$^{\bullet-}$ → $TFSI^-$) is 98%. This near-unity exchange efficiency suggests that the present anion exchange is driven by the host–guest hybrid system seeking to achieve a minimum free energy value. We note that hole doping is never observed when a PBTTT thin film is immersed in a pure ionic liquid (Extended Data Fig. 4), showing that the F4TCNQ has a vital role by producing the initial hole doping, following which the F4TCNQ radical anions are exchanged with Y^-. Note that because a large excess of $TFSI^-$ is introduced into the hybrid anion system, entropy gain according to $-k_B T \ln \frac{[TFSI^-]}{[F4TCNQ^{\bullet-}]}$ can be expected, and will be discussed below (here, k_B is the Boltzmann constant and T is temperature).

Ion exchange is applicable to various chemical processes, and operates not only on the principle of the binding preferences of ion pairs,

[1]Material Innovation Research Center (MIRC), University of Tokyo, Kashiwa, Japan. [2]Department of Advanced Materials Science, Graduate School of Frontier Sciences, University of Tokyo, Kashiwa, Japan. [3]International Center for Materials Nanoarchitectonics (WPI-MANA), National Institute for Materials Science (NIMS), Tsukuba, Japan. [4]AIST-UTokyo Advanced Operando-Measurement Technology Open Innovation Laboratory (OPERANDO-OIL), National Institute of Advanced Industrial Science and Technology (AIST), Kashiwa, Japan. [5]Japan Science and Technology Agency (JST), Precursory Research for Embryonic Science and Technology (PRESTO), Kawaguchi, Japan. *e-mail: swatanabe@edu.k.u-tokyo.ac.jp

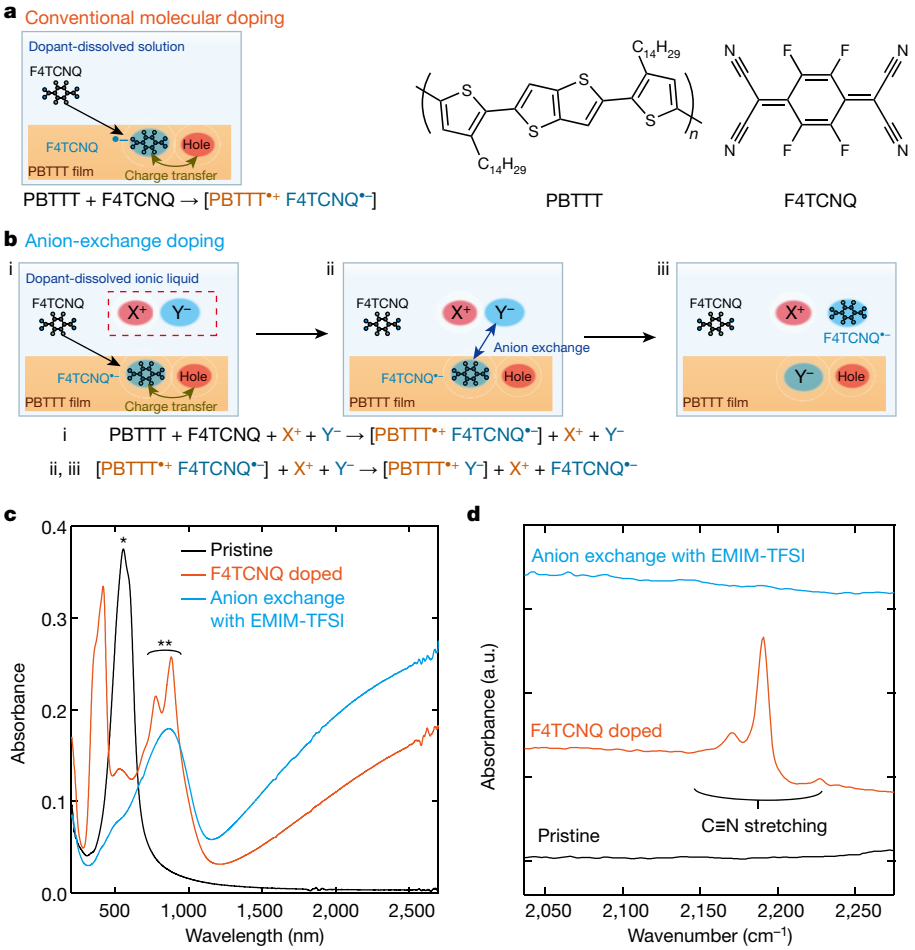

Fig. 1 | Summary of anion-exchange doping. a, **b**, Diagrams showing conventional molecular doping (**a**) and anion-exchange doping (**b**). The inset at the top right shows the chemical structures of PBTTT and F4TCNQ. In anion-exchange doping, a thin film of PBTTT is doped with the initiator molecule F4TCNQ (i) via a charge-transfer interaction. ii, The F4TCNQ radical anions are replaced by the Y^- anions (where Y is TFSI) of the ionic liquid. iii, This anion exchange ($F4TCNQ^{\bullet-} \rightarrow TFSI^-$) results in the formation of a solid-state donor–acceptor complex ([$PBTTT^{\bullet+}$ $TFSI^-$]). **c**, **d**, Optical absorbance (**c**) and FTIR spectra (**d**) of pristine PBTTT (black), F4TCNQ-doped PBTTT (orange), and PBTTT doped via anion exchange (blue). The centre value of the peak marked with a single asterisk is 553 nm. The centre values of the doublet peak (double asterisk) are 775 nm and 881 nm.

which in turn depends on ionic interactions, but also on statistics—that is, on entropy. Here, working under the assumption that the energetic gain via anion exchange is established to some extent by the entropy factor, we assessed the role of these ionic interactions by comparing combinations of eight cations, X^+, and six anions, Y^-, in conjunction with systematic variations in the effective ion radius, R_{eff}, that separates the charges. The correlation between the sizes of the molecular ions having unique shapes and the associated ionic interactions can be determined from spatial maps of the electrostatic potentials based on van der Waals surfaces (Fig. 2; see Supplementary Information section 1.4). The results of density functional theory (DFT) calculations show that smaller ions have higher electrostatic potentials on their surfaces. We discuss here the roles of ionic interactions on the basis of experimental observations, which demonstrate that the anion-exchange efficiency ($F4TCNQ^{\bullet-} \rightarrow Y^-$) and doping concentration both correlate with the strength of the ionic interaction. Specifically, the highest doping concentration and most efficient anion exchange are realized when using a salt composed of small cations and large anions, which possess high and low electrostatic surface potentials, respectively.

Initially, we assessed the manner in which the electrostatic potential of the ionic liquid anion Y^- affects the anion-exchange doping by considering ionic liquids with four different anions. These anions were tetrafluoroborate (BF_4^-), hexafluorophosphate (PF_6^-), tris(pentafluoroethyl)trifluorophosphate (FAP^-) and $TFSI^-$. In each case, the associated cation was 1-butyl-3-methylimidazolium ($BMIM^+$). Anion-exchange doping was performed by immersing PBTTT thin films in a solution of F4TCNQ dissolved in each ionic liquid for 10 min at 60 °C. Figure 3a presents the optical absorption spectra obtained from PBTTT thin films doped via anion exchange with the four different anions. The $F4TCNQ^{\bullet-}$ doublet at 775 nm and 881 nm is observed only for $Y^- = BF_4^-$ and PF_6^-, and this result is indicative of inefficient anion exchange. Interestingly, although smaller anions (such as BF_4^- and PF_6^-) should be more mobile than larger anions (FAP^- and $TFSI^-$), the anion-exchange efficiency shows the opposite trend. This clearly suggests that the present anion exchange proceeds only when the exchange lowers the free energy of the system, where the gain of Gibbs free energy is defined as Δ_{ex}. The results of DFT calculations also show that anion exchange with $TFSI^-$ is more energetically favourable than that with BF_4^- (see Supplementary Information section 1.5). This binding preference can be understood by considering both the size and the shape of the ions, because delocalized anions such as $TFSI^-$ will preferentially couple with the delocalized charges on the PBTTT.

We further assessed the mechanism associated with the anion-exchange doping here, which is based on the energetic gain Δ_{ex}, by investigating the effect of the cation. These trials used three different cations: Li^+, $EMIM^+$ and methyltributylphosphonium ($MtBPho^+$). In each case, Y^- was fixed as $TFSI^-$. The cation does not directly interact with the PBTTT, but rather can be considered as a spectator ion in the anion-exchange process that nevertheless affects the Δ_{ex} value by forming ion pairs. Assessing the disappearance of the $F4TCNQ^{\bullet-}$ doublet shows that only $MtBPho^+$ did not permit efficient anion exchange (Fig. 3b; see Extended Data Fig. 5 for additional data). One possible explanation for the beneficial effects of a small cation is that the initial ion pair must be composed of ions with poor affinity for one another (for example, a small cation and large anion) so as to produce a large Δ_{ex}. This explanation is in good agreement with the empirical hard and soft acid and base (HSAB) theory, which is often invoked to explain ion-exchange tendencies[13].

The optimization of X^+ and Y^- is of great importance, not only because it affects the anion-exchange efficiency, but also because of its effect on the doping level, as verified by conductivity measurements. During these analyses, we doped PBTTT thin films via anion

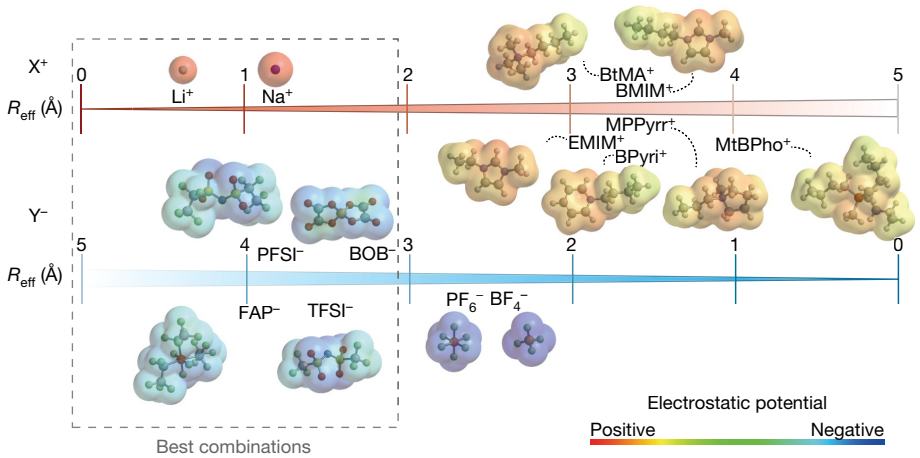

Fig. 2 | Molecular structures and electrostatic potential maps of the cations and anions used here. These molecular structures and calculated electrostatic potentials are based on van der Waals surfaces of the anions and cations. R_{eff} denotes the effective molecular radius, equal to the radius of a sphere with the same volume as the organic ion. Ionic radius values were used for Li^+ and Na^+. The spatial distributions of electrostatic potentials were calculated using DFT with the B3LYP functional and 6-311+G(d) basis set (Spartan'16 software). Detailed molecular structures are shown in Extended Data Fig. 1. BOB, bis(oxalato)borate; BPyri, 1-butylpyridinium; BtMA, butyltrimethylammonium; MPPyrr, 1-methyl-1-propylpyrrolidinium; PFSI, bis(pentafluoroethanesulfonyl)imide.

exchange using F4TCNQ together with either Li-TFSI or EMIM-TFSI. Surprisingly, the conductivity of the film anion-exchanged with EMIM-TFSI was increased by a factor of 1.7 compared with doping solely with F4TCNQ, while that of the Li-TFSI specimen was 2.4 times higher (Fig. 3c), which suggests that the doping level was improved as a result of the anion-exchange phenomenon when using an optimized combination of X^+ and Y^-. It could be argued that the concentration of F4TCNQ (F4TCNQ$^{\bullet-}$) and $TFSI^-$ affected the conductivity. We found

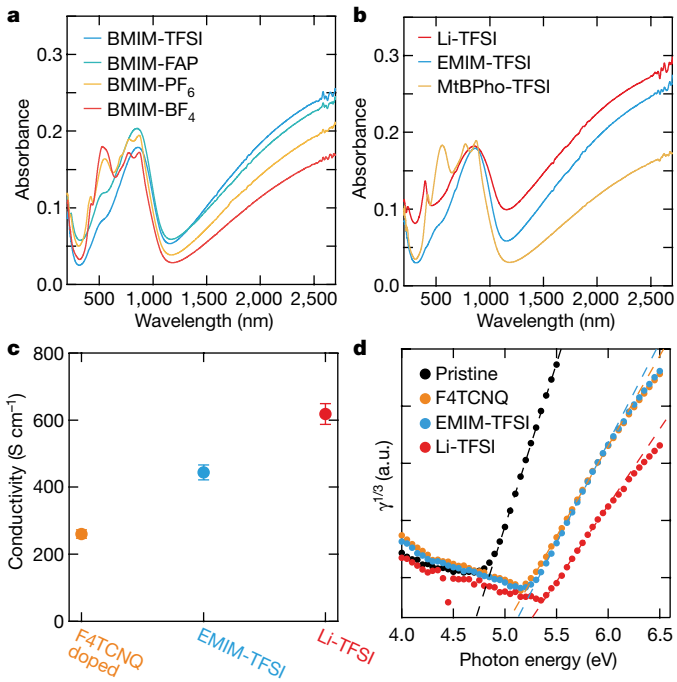

Fig. 3 | Variations in anion exchange and doping concentration with the strength of ionic interactions. a, Optical absorption spectra of anion-exchange-doped PBTTT thin films using various Y^- anions (blue, $TFSI^-$; green, FAP^-; orange, PF_6^-; and red, BF_4^-). **b**, Optical absorption spectra of anion-exchange-doped PBTTT thin films, using various spectator X^+ cations (red, Li^+; blue, $EMIM^+$; and orange, $MtBPho^+$). **c**, Variations in the conductivity of anion-exchange doped PBTTT thin films. The error bars in the conductivity show uncertainty in the thickness of PBTTT thin films, and represent one standard deviation. **d**, Photoelectron yield spectra acquired from doped PBTTT thin films.

that the doping efficiency (conductivity) becomes less when the supply of reactant, here $TFSI^-$, is lower (Extended Data Fig. 6). Indeed, at the concentrations of F4TCNQ$^{\bullet-}$ and $TFSI^-$ used here, the entropy gain is estimated to be approximately 200 meV, which is comparably large with respect to the ionic interactions. In considering the role of this entropy gain in our hybrid anion system, our focus is how the ionic interactions (binding preference) can have an effect on the doping efficiency (conductivity), and to what extent the doping level can be increased by tuning ionic compounds in anion-exchange doping. Specifically, the most efficient anion exchange, resulting in the highest conductivity of 620 S cm^{-1}, is realized when using Li-TFSI; this is one of the highest values yet reported for doped PBTTT thin films.

We also monitored the degree of doping with photoelectron yield spectroscopy. Figure 3d plots the photoemission yield, $\gamma^{1/3}$, as a function of the incident photon energy. From the threshold, we estimate the ionization potential, I_p, to be 4.83 eV for the pristine PBTTT thin film, which is identical to the energy level at the edge of the highest occupied molecular orbital (HOMO) band for this material, and close to the literature value (−4.7 eV; ref. [14]). Compared with F4TCNQ doping, a larger shift in the threshold photon energy is clearly obtained following anion-exchange doping with Li-TFSI. In this case, we estimate I_p to be 5.38 eV, exceeding the lowest unoccupied molecular orbital (LUMO) level of F4TCNQ and suggesting that anion-exchange doping energetically stabilized the final state by a factor of Δ_{ex} (Extended Data Fig. 7), which has a value of several hundred millielectronvolts. Thus, anion exchange is expected to be a driving force to overcome the redox potential limitations in molecular doping. We further verified this hypothesis through the successful anion-exchange doping of the donor–acceptor copolymer poly[2,5-(2-octyldodecyl)-3,6-diketopyrrolopyrrole-*alt*-5,5-(2,5-di(thien-2-yl)thieno[3,2-*b*]thiophene)] (PDPP-2T-TT-OD). We found anion-exchange doping to allow reasonably high doping levels even in donor–acceptor polymers that typically have a deep HOMO level (Extended Data Fig. 8). Another control experiment is shown in Extended Data Fig. 8, where a weak acceptor, tetracyanoquinodimethane (TCNQ), was used as an initiator instead of F4TCNQ. Even though the LUMO level of TCNQ does not exceed the I_p value of PBTTT, the introduction of Li-TFSI promotes doping (as shown by the bleaching of the neutral absorbance). Therefore, we conclude that anion exchange is indeed a driving force behind the doping level. Supplementary Information section 1.6 provides a summary of the kinetic mechanism responsible for the increased doping levels. The overall results show that introducing a salt into a conventional binary molecular doping system can overcome the redox potential limitations

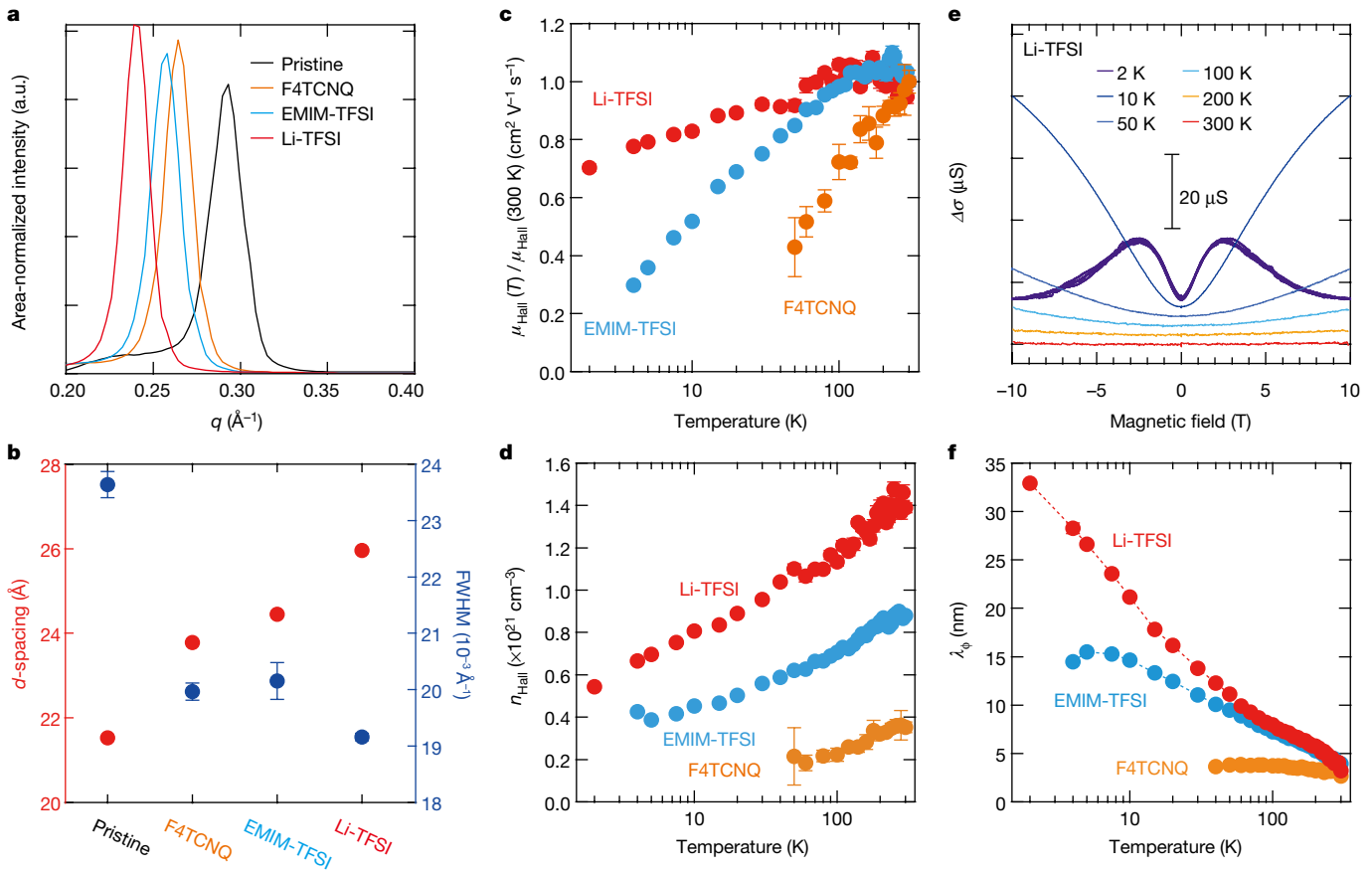

Fig. 4 | Highly ordered structures and coherent charge transport in doped PBTTT. a, Area-normalized X-ray diffraction profiles along the out-of-plane direction for PBTTT thin films (black, pristine; orange, F4TCNQ-doped; blue, anion-exchange-doped with EMIM-TFSI; and red, anion-exchange-doped with Li-TFSI). **b**, Variations in the *d*-spacing and FWHM values of (100) scattering peaks. The error bars in FWHM stem from compound errors that result from propagation of the uncertainties in fitting of the diffraction peak, and represent one standard deviation. **c**, Temperature dependence of the normalized Hall mobility μ_{Hall} (*T*)/ μ_{Hall} (300 K). From the Hall effect measurements in Extended Data Fig. 9, we determined the Hall mobilities at 300 K (μ_{Hall} (300 K)) to be 1.9, 2.4 and 2.0 cm^2 V^{-1} s^{-1} for F4TCNQ-doped PBTTT thin film (orange) and films anion-exchange-doped with EMIM-TFSI (blue) and with Li-TFSI (red), respectively. **d**, Temperature dependence of the Hall carrier density, n_{Hall}. **e**, Effects of the magnetic field (*B*) on differential sheet conductivity ($\Delta\sigma = \sigma(B) - \sigma(0)$) for Li-TFSI-doped film at various temperatures, with *B* applied perpendicular to the substrate plane. **f**, Effects of temperature on the phase-coherent length (λ_ϕ). The error bars in Hall mobility, Hall carrier density and λ_φ were determined from uncertainty in the extraction of electromotive force from the fitting, and represent one standard deviation.

described by Marcus theory, thus allowing further improvement of molecular doping levels through optimization of ionic interactions.

The remarkable enhancement in doping levels achieved by anion-exchange doping suggests that the additional anion (such as TFSI$^-$) is incorporated into the host polymer thin film to achieve charge neutrality. We verified this solid-state intercalation by X-ray diffraction (XRD) analyses. Figure 4a shows out-of-plane XRD profiles for various PBTTT thin-film specimens. Here, the first-order (*h*00) diffractions assigned to lamellar spacing (*d*-spacing) are plotted against the scattering vector, *q*. As in the conductivity measurements (Fig. 3c), the samples consisted of pristine PBTTT (black), PBTTT doped with F4TCNQ (orange), and PBTTT doped via anion exchange with EMIM-TFSI (light blue) or with Li-TFSI (red). We determined the *d*-spacing and full width at half maximum (FWHM) values by Gaussian peak fitting, with the results summarized in Fig. 4b. These data show that the conductivity of the doped PBTTT thin films increased (Fig. 3c) along with the *d*-spacing. The increases in the lamellar spacing suggest that the counteranions (F4TCNQ$^{\bullet-}$ or TFSI$^-$) were incorporated into the zones occupied by alkyl side chains, which is consistent with previous reports[11,15,16]. It is also evident that the FWHM values decrease as the doping level increases. Thus, it appears that the extent of lattice disorder decreases dramatically. We note here that the relaxation of torsion, tension and/or bending along the polymer backbones may result in crystal rearrangement (Supplementary Information section 1.3).

We assessed two-dimensional, coherent charge transport in the polymer thin film by magnetotransport analyses, in which we measured both the longitudinal and the transverse electromotive forces while applying an external magnetic field using a standard Hall bar geometry. The Hall voltage is observable only when the charge carriers are equivalent to a free electron—that is, when the wavenumber is definable in the charge-transport system[17–19]. Here, we observed a clear Hall voltage over a wide range of temperatures from 300 K down to 2 K, with the symmetry and sign of the voltage corresponding to the hole carrier conduction (Extended Data Fig. 9). Figure 4c, d plots Hall mobility, μ_{Hall}, and Hall carrier density, n_{Hall}, determined from a standard expression of the Hall effect. A remarkably high carrier concentration of more than 1×10^{21} cm^{-3} (Fig. 4d) was achieved, together with a reasonably high Hall mobility of 2 cm^2 V^{-1} s^{-1} (Fig. 4c). This concentration is equivalent to one hole per monomer unit (representing a half-filled state), and is also approximately three times larger than that obtained with conventional F4TCNQ doping[11]. Surprisingly, the Hall mobility was almost completely unaffected by temperature. Although a finite fraction of localized carriers hinders a truly metallic signature, the temperature-invariant Hall mobility indicates that the obtained half-filled state in highly conductive PBTTT thin films is close to the onset of metallicity[20].

Figure 4e summarizes the magnetic-field dependence of the differential sheet conductivity of a film ($\Delta\sigma = \sigma(B) - \sigma(0)$, where σ is the

electrical conductivity and B is the magnetic flux density) at various temperatures. The positive magnetoconductance displayed by the doped PBTTT thin film is attributed to weak localization[11,21], as both the magnitude and the curvature of the data can be fit using the well-established Hikami–Larkin–Nagaoka weak localization model[22]. This requires only the characteristic magnetic field at which the matrix element responsible for backscattering loses its phase as the fitting parameter. This fitting allows the phase-coherent length, λ_ϕ, to be determined at various temperatures (Fig. 4f; see also Supplementary Information section 1.7). Figure 4f compares the phase-coherent lengths of three doped PBTTT thin films (conventional F4TCNQ doping[11], orange; anion-exchange doping with EMIM-TFSI, light blue, and with Li-TFSI, red) and demonstrates that the phase-coherent length becomes longer as the doping level increases.

This approach to doping substantially increases the doping level, which in turn promotes two-dimensional, coherent carrier transport, and also imparts excellent thermal stability. Because the additional anions replace the initial dopant in the film and remain within the polymer network, they should have an effect on the physicochemical properties of the material[9,23]. Thus, we also assessed the thermal stability and durability of doped PBTTT thin films. To do so, we evaluated the thermal durability of the doped thin films through conductivity measurements, based on the proportion of the original conductivity retained after annealing in an argon-purged glove box for 10 min at 120 °C or 160 °C (Extended Data Fig. 10 and Supplementary Information section 1.8). The conductivity of an F4TCNQ-doped thin film was reduced by three orders of magnitude after heating at 160 °C, but this change was dramatically suppressed in the case of doping with hydrophobic closed-shell anions. We note that further improvements to thermal durability could therefore be achieved by tuning the physicochemical properties of the additional anion.

Our results show that the molecular doping of polymeric semiconductors via anion exchange increases both the doping level and the thermal durability of the polymer thin film. This process uses ionic interactions to build new host–guest structures and increase the doping levels, thus overcoming the limitations based on the redox potential, and could potentially be extended to electron doping—that is, to cation-exchange doping. This technique suggests opportunities for the storage, transport and conversion of functional molecules within solid-state conjugated materials. The remarkably high doping concentrations and enhanced conductivity demonstrated here should also improve our understanding of charge-transport physics, as the half-filled state in highly crystalline polymeric semiconductors is likely to trigger an electronic phase transition.

Data availability

The data that support the findings of this study are available within this Letter, its Extended Data and its Supplementary Information.

Online content

Any methods, additional references, Nature Research reporting summaries, source data, extended data, supplementary information, acknowledgements, peer review information; details of author contributions and competing interests; and statements of data and code availability are available at https://doi.org/10.1038/s41586-019-1504-9.

Received: 4 December 2018; Accepted: 20 June 2019;
Published online 28 August 2019.

1. Chiang, C. K. et al. Electrical conductivity in doped polyacetylene. *Phys. Rev. Lett.* **39**, 1098 (1977).
2. Jacobs, I. E. & Moulé, A. J. Controlling molecular doping in organic semiconductors. *Adv. Mater.* **29**, 1703063 (2017)
3. Lüssem, B. et al. Doped organic transistors. *Chem. Rev.* **116**, 13714–13751 (2016).
4. Salzmann, I., Heimel, G., Oehzelt, M., Winkler, S. & Koch, N. Molecular electrical doping of organic semiconductors: fundamental mechanisms and emerging dopant design rules. *Acc. Chem. Res.* **49**, 370–378 (2016).
5. Marcus, R. A. Electron transfer reactions in chemistry. Theory and experiment. *Rev. Mod. Phys.* **65**, 599 (1993).
6. Lin, X. et al. Beating the thermodynamic limit with photo-activation of n-doping in organic semiconductors. *Nat. Mater.* **16**, 1209 (2017); corrigendum **16**, 204 (2018).
7. Png, R.-Q. et al. Madelung and Hubbard interactions in polaron band model of doped organic semiconductors. *Nat. Commun.* **7**, 11948 (2016).
8. Chia, P.-J. et al. Direct evidence for the role of the Madelung potential in determining the work function of doped organic semiconductors. *Phys. Rev. Lett.* **102**, 096602 (2009).
9. Tang, C. G. et al. Doped polymer semiconductors with ultrahigh and ultralow work functions for ohmic contacts. *Nature* **539**, 536–540 (2016).
10. McCulloch, I. et al. Liquid-crystalline semiconducting polymers with high charge-carrier mobility. *Nat. Mater.* **5**, 328–333 (2006).
11. Kang, K. et al. 2D coherent charge transport in highly ordered conducting polymers doped by solid state diffusion. *Nat. Mater.* **15**, 896–902 (2016).
12. Le, T. H., Lu, J., Bond, A. M. & Martin, L. L. Identification of TCNQF4 redox levels using spectroscopic and electrochemical fingerprints (TCNQF4=2,3,5,6-tetrafluoro-7,7,8,8-tetracyanoquinodimethane). *Inorg. Chim. Acta* **395**, 252–254 (2013).
13. Pearson, R. G. Hard and soft acids and bases—the evolution of a chemical concept. *Coord. Chem. Rev.* **100**, 403–425 (1990).
14. Zhao, L.-H. et al. Polarization effects on energy-level alignment at the interfaces of polymer organic semiconductor films. *Appl. Phys. Lett.* **101**, 053304 (2012).
15. Fujimoto, R. et al. Molecular doping in organic semiconductors: fully solution-processed, vacuum-free doping with metal–organic complexes in an orthogonal solvent. *J. Mater. Chem. C* **5**, 12023–12030 (2017).
16. Guardado, J. O. & Salleo, A. Structural effects of gating poly(3-hexylthiophene) through an ionic liquid. *Adv. Funct. Mater.* **27**, 1701791 (2017).
17. Fukuyama, H., Ebisawa, H. & Wada, Y. Theory of Hall effect. I. Nearly free electron. *Prog. Theor. Phys.* **42**, 494–511 (1969).
18. Arnold, E. & Shannon, J. Anomalous Hall effect and carrier transport in bandtails at the Si/SiO_2 interface. *Solid State Commun.* **18**, 1153–1156 (1976).
19. Yamashita, Y. et al. Transition between band and hopping transport in polymer field-effect transistors. *Adv. Mater.* **26**, 8169–8173 (2014).
20. Ito, H., Harada, T., Tanaka, H. & Kuroda, S.-i. Critical regime for the insulator–metal transition in highly ordered conjugated polymers gated with ionic liquid. *Jpn. J. Appl. Phys.* **55**, 03DC08 (2016).
21. Farka, D. et al. Anderson-Localization and the Mott–Ioffe–Regel limit in glassy-metallic PEDOT. *Adv. Electron. Mater.* **3**, 1700050 (2017).
22. Hikami, S., Larkin, A. I. & Nagaoka, Y. Spin-orbit interaction and magnetoresistance in the two dimensional random system. *Prog. Theor. Phys.* **63**, 707–710 (1980).
23. Müller, L. et al. Electric-field-controlled dopant distribution in organic semiconductors. *Adv. Mater.* **29**, 1701466 (2017).
24. Holomb, R., Xu, W., Markusson, H., Johansson, P. & Jacobsson, P. Vibrational spectroscopy and ab initio studies of lithium bis (oxalato) borate (LiBOB) in different solvents. *J. Phys. Chem. A* **110**, 11467–11472 (2006).
25. Karpov, Y. et al. Molecular doping of a high mobility diketopyrrolopyrrole–dithienylthieno [3, 2-*b*] thiophene donor–acceptor copolymer with F6TCNNQ. *Macromolecules* **50**, 914–926 (2017).

Acknowledgements Y.Y. was supported by a Grant-in-Aid via a Japan Society for the Promotion of Science (JSPS) Research Fellowship. S.W. acknowledges support from PRESTO-JST through the Hyper-nanospace Design Toward Innovative Functionality project (JPMJPR151E) and from the Leading Initiative for Excellent Young Researchers of JSPS. This work was also supported in part by JSPS KAKENHI grants (JP17H06123 and JP17H06200).

Author contributions Y.Y. conceived, designed and performed the experiments and analysed the data. Y.Y. and S.W. wrote the manuscript. J. Tsurumi performed electron spin resonance analyses. M.O. assisted in performing the low-temperature magnetotransport measurements. R.F. assisted during the conductivity measurements. S.K., T.K. and T.O. contributed to interpretation of the anion-exchange phenomena. J. Takeya and S.W. supervised the work. All authors discussed the results and reviewed the manuscript.

Competing interests The authors declare no competing interests.

Additional information
Extended data is available for this paper at https://doi.org/10.1038/s41586-019-1504-9.
Supplementary information is available for this paper at https://doi.org/10.1038/s41586-019-1504-9.
Reprints and permissions information is available at http://www.nature.com/reprints.
Correspondence and requests for materials should be addressed to S.W.
Peer review information *Nature* thanks Antonio Facchetti and Peter Ho for their contribution to the peer review of this work.
Publisher's note: Springer Nature remains neutral with regard to jurisdictional claims in published maps and institutional affiliations.

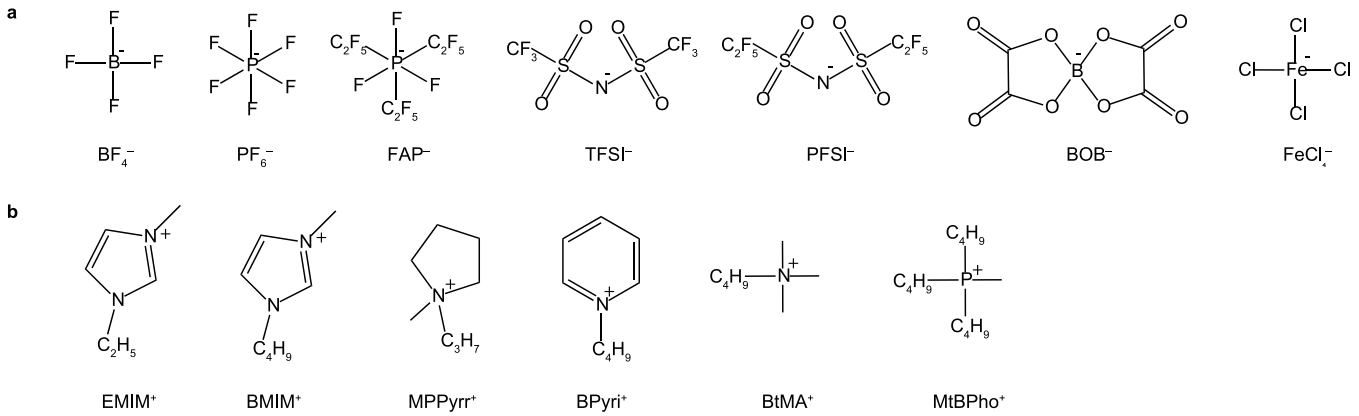

Extended Data Fig. 1 | Molecular structures of the compounds used here. a, The additional anions. **b**, The spectator cations. Further details regarding purities and suppliers are provided in the Supplementary Information

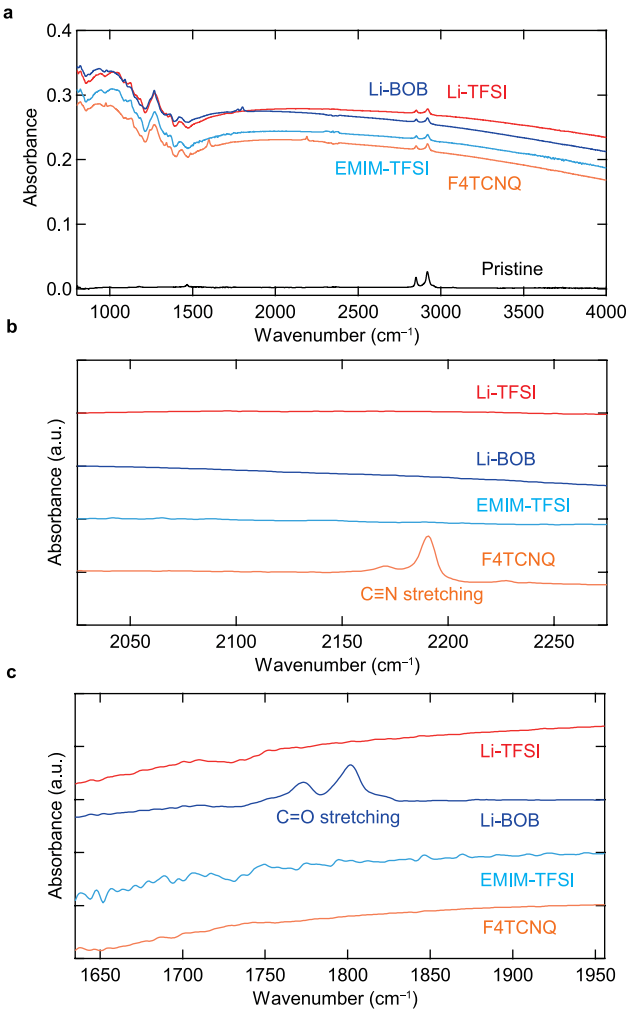

Extended Data Fig. 2 | FTIR spectroscopy to assess residual anions in PBTTT thin films. a, FTIR spectra of PBTTT-C14 thin films: black, pristine; orange, F4TCNQ-doped; light blue, anion-exchange-doped with EMIM-TFSI; red, anion-exchange-doped with Li-TFSI; and blue, anion-exchange-doped with Li-BOB. **b**, Magnified FTIR spectra from 2,050 cm^{-1} to 2,250 cm^{-1}. C≡N stretching (around 2,190 cm^{-1}) appears only in the case of the F4TCNQ-doped film. **c**, Magnified FTIR spectra from 1,650 cm^{-1} to 1,950 cm^{-1}. The doublet peak assigned to the C=O stretching mode (around 1,800 cm^{-1}) in carbonyl groups in BOB^- (ref. [24]) is generated only in PBTTT films anion-exchange-doped with Li-BOB. This suggests that the BOB^- anions were exchanged and incorporated into the PBTTT thin film.

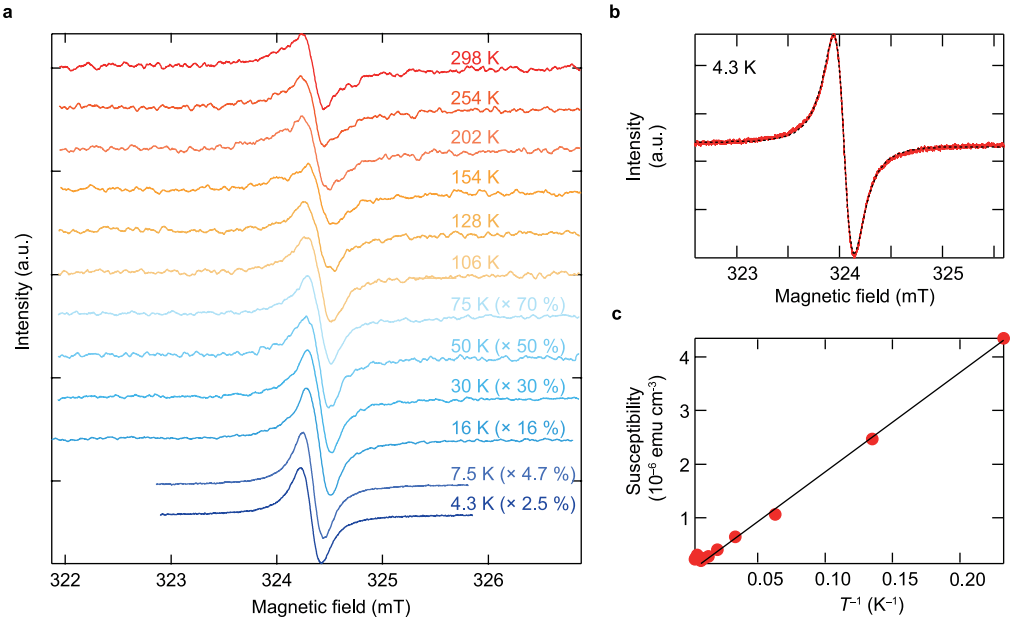

Extended Data Fig. 3 | The origin of Curie susceptibility in anion-exchange-doped PBTTT. a, Temperature-dependent electron spin resonance (ESR) spectra obtained from PBTTT thin film anion-exchange-doped with EMIM-TFSI. The single Lorentzian ESR spectra are observed to follow the Curie law. Note that Curie susceptibility is attributed to localized spins either on F4TCNQ radical anions or on PBTTT radical cations. Hall effect measurements indicate that carriers in the highly doped PBTTT are likely to undergo delocalized transport, thus producing Pauli paramagnetic susceptibility that is negligible compared with the Curie effect. Although the *g*-factors of the PBTTT radical cation and F4TCNQ radical anion are identical, it is reasonable to assume that the observed Curie susceptibility originates from localized F4TCNQ radical anions. We found the experimentally determined spin concentration to be much less than the actual carrier concentration in the PBTTT thin film, as discussed in the main text. **b**, ESR spectrum for anion-exchange-doped PBTTT, acquired at 4.3 K with the external magnetic field perpendicular to the film plane. The result of single Lorentzian fitting is plotted as a black curve. **c**, The effect of temperature (*T*) on spin susceptibility, as determined by double integration of the ESR spectra.

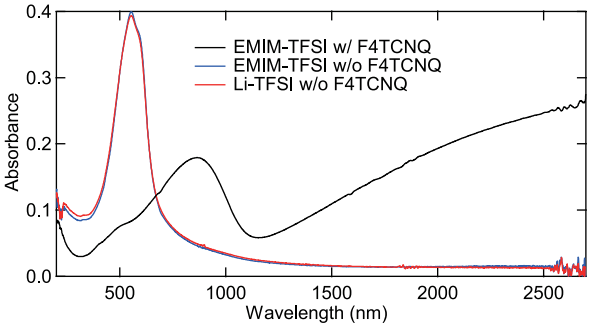

Extended Data Fig. 4 | Comparison of absorption spectra with and without an initiator dopant. Optical absorption spectra of PBTTT thin films after immersion in EMIM-TFSI, with and without F4TCNQ. The spectra show that doping occurs only when F4TCNQ is dissolved in the ionic liquid. Similarly, a PBTTT thin film immersed in a solution of Li-TFSI in *n*-butyl acetate without F4TCNQ shows no doping. These results demonstrate that F4TCNQ is necessary to initiate the doping reaction.

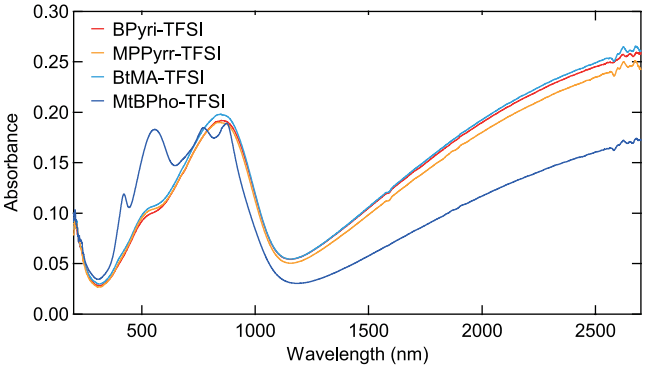

Extended Data Fig. 5 | Anion-exchange doping with a series of organic cations (X^+). Absorption spectra are shown following anion-exchange doping of PBTTT films with four different organic cations (with Y^- fixed as $TFSI^-$).

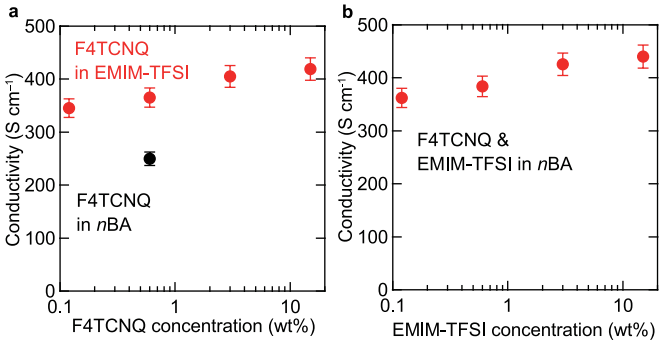

Extended Data Fig. 6 | Effects of the concentrations of the initiator dopant and additional anion. a, **b**, Changes in conductivity as a function of: initiator dopant (F4TCNQ) concentration (**a**; red); and additional anion ($TFSI^-$) concentration following anion-exchange doping (**b**; red). The conductivity of an F4TCNQ-doped PBTTT thin film in *n*-butyl acetate (*n*BA) is also shown as a reference (**a**; black). Concentration evidently has a limited effect by comparison with the salt species. The error bars in the conductivity stem from uncertainty in the thickness of PBTTT thin films, and represent one standard deviation.

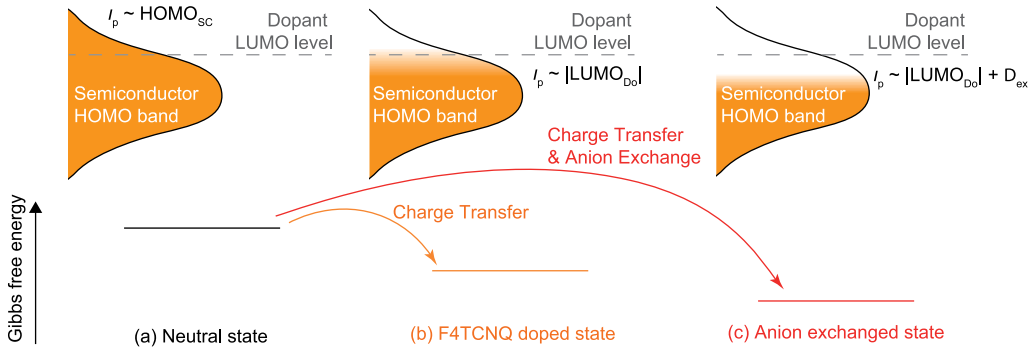

Extended Data Fig. 7 | Energy alignment diagram and change in Gibbs energy due to anion-exchange doping. a, In a neutral state, the ionization potential (I_P) of an organic semiconductor is equal to the edge of its semiconductor HOMO band (HOMO$_{SC}$). **b**, In conventional molecular doping with F4TCNQ, electrons within the HOMO band of the organic semiconductor are transferred to the LUMO level (dotted line) of the F4TCNQ, such that I_P is close to the LUMO level of the dopant (LUMO$_{Do}$). The resulting donor–acceptor association minimizes the Gibbs free energy at equilibrium (orange line) such that no further charge transfer occurs. **c**, In anion-exchange doping, additional energy gain reduces the Gibbs free energy of the final state (red line), thus promoting the charge-transfer reaction. In this case, the I_P of the organic semiconductor exceeds the LUMO level of the dopant approximately by the energy gain resulting from anion exchange (Δ_{ex}). We determined the resulting shift in I_P by photoelectron yield spectroscopy to be approximately 0.2 eV (Fig. 3d).

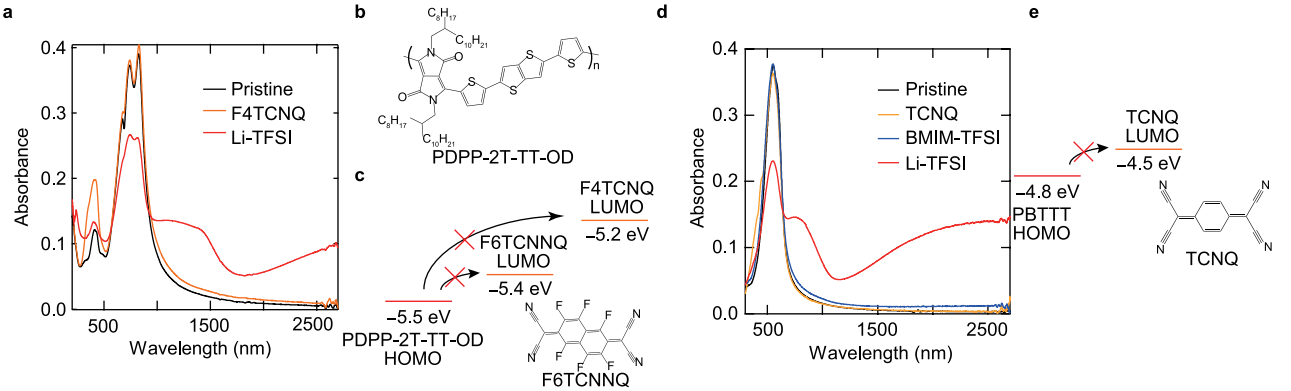

Extended Data Fig. 8 | An example of overcoming the limitation of redox potential by anion-exchange doping. a. Ultraviolet–visible–near-infrared (UV–vis–NIR) spectra of pristine, F4TCNQ-doped, and anion-exchange-doped (with Li-TFSI) donor–acceptor copolymer thin films based on PDPP-2T-TT-OD, which has a deep HOMO level (−5.5 eV). **b**, Molecular structure of PDPP-2T-TT-OD. **c**, Energy-level alignment diagram for PDPP-2T-TT-OD, F6TCNNQ and F4TCNQ, along with the molecular structure of F6TCNNQ. Because of the deep HOMO level of PDPP-2T-TT-OD, charge transfer is not expected following conventional molecular doping with F4TCNQ. Anion-exchange doping with Li-TFSI results in bleaching of the neutral peak and the appearance of PDPP-2T-TT-OD polaron peaks, using F4TCNQ as the initiator dopant. The doping level obtained from anion-exchange doping with Li-TFSI is high compared with that reported for F6TCNNQ doping[25], as determined from the intensity ratio of the neutral (815 nm) and polaron peaks (1,400 nm) (the polaron/neutral ratio is about 0.1 for F6TCNNQ molecular doping and about 0.5 for anion-exchange doping with Li-TFSI) **d**, UV–vis–NIR spectra of TCNQ-doped and anion-exchange-doped (with BMIM-TFSI or Li-TFSI) PBTTT thin films. A bleaching of neutral absorbance was observed only with Li-TFSI. **e**, Energy-level alignment diagram for PBTTT and TCNQ, along with the molecular structure of TCNQ. The LUMO level of TCNQ is too shallow (−4.5 eV) to produce ground-state charge transfer. Even so, introducing Li-TFSI (that is, anion-exchange doping) promotes efficient doping. This presumably occurs because a slight overlap of tail states between HOMO and LUMO levels could initiate charge transfer between PBTTT and TCNQ, and therefore $TCNQ^{\bullet-}$ is exchanged to $TFSI^{-}$. Overall, control experiments show that the initiator acceptor is not necessarily a powerful acceptor, and that efficient molecular doping is driven by anion exchange.

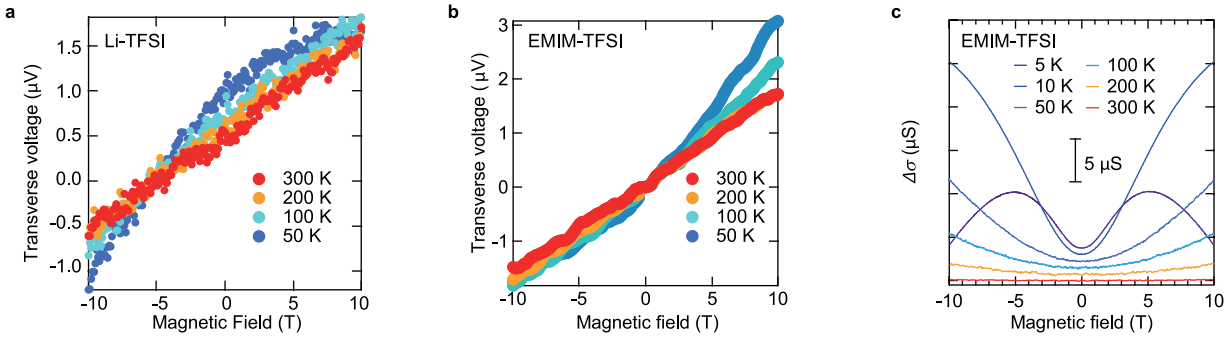

Extended Data Fig. 9 | Magnetotransport measurements of anion-exchange-doped PBTTT. a, **b**, Transverse (Hall) voltage values obtained from PBTTT thin films that have been anion-exchange-doped with Li-TFSI (**a**) and EMIM-TFSI (**b**) at various temperatures. **c**, Effect of magnetic field, *B*, on the differential sheet conductivity ($\Delta\sigma = \sigma(\mathrm{B}) - \sigma(0)$) at various temperatures, with *B* applied perpendicular to the substrate plane. See Supplementary Information for details on fitting of the magnetoconductance data.

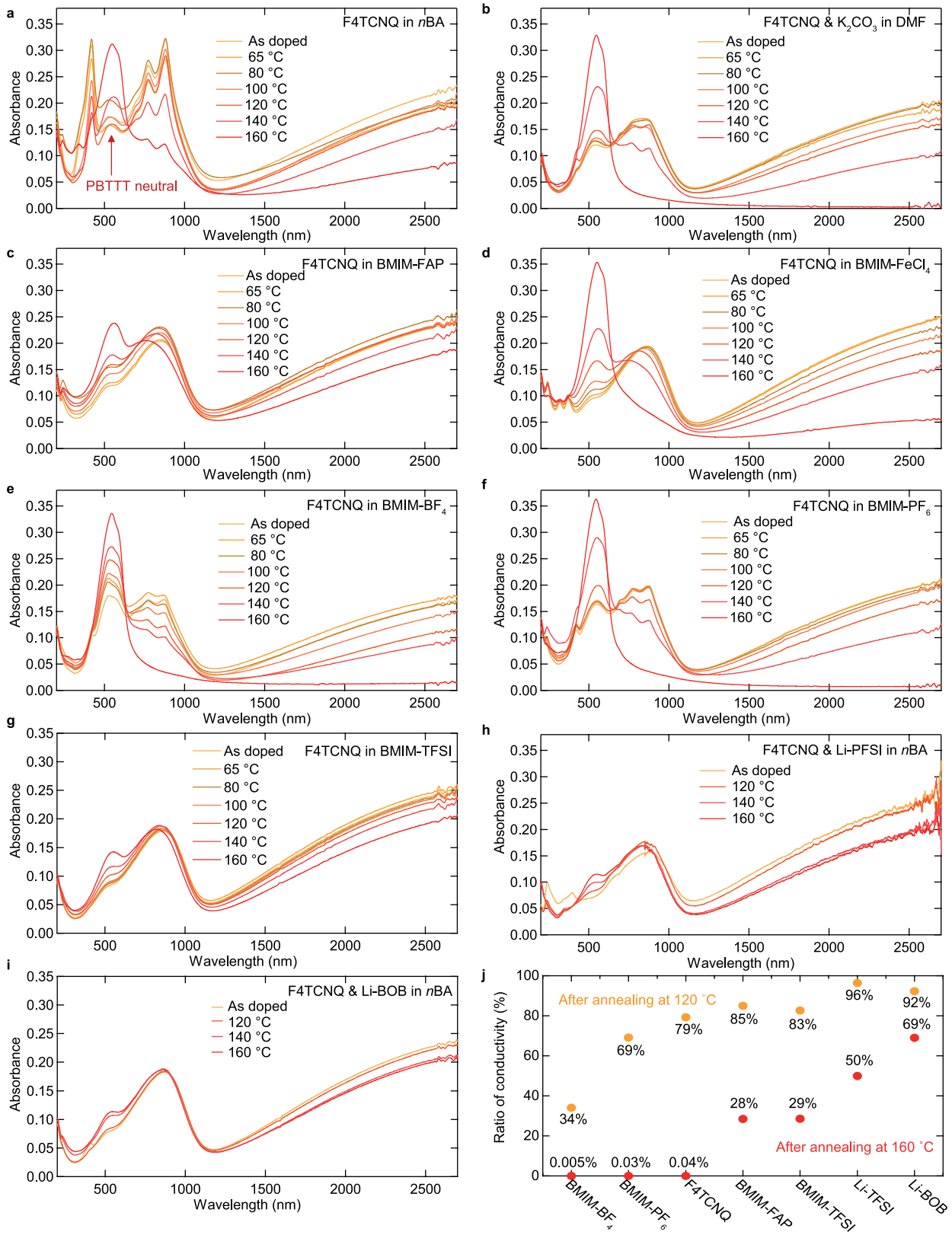

Extended Data Fig. 10 | Thermal durability of doped PBTTT thin films. These UV–vis–NIR spectra were obtained from doped PBTTT thin films before and after annealing at the indicated temperatures. **a**, An F4TCNQ-doped PBTTT thin film. **b**–**i**, Anion-exchange-doped films with: **b**, K_2CO_3; **c**, BMIM-FAP; **d**, BMIM-$FeCl_4$; **e**, BMIM-BF_4; **f**, BMIM-PF_6; **g**, BMIM-TFSI; **h**, Li-PFSI; and **i**, Li-BOB. **j**, Ratios of conductivity before and after annealing at 120 °C and 160 °C. Details of doping conditions are provided in the Supplementary Information.

LETTER

https://doi.org/10.1038/s41586-019-1465-z

Increased shear in the North Atlantic upper-level jet stream over the past four decades

Simon H. Lee[1], Paul D. Williams[1]* & Thomas H. A. Frame[1]

Earth's equator-to-pole temperature gradient drives westerly mid-latitude jet streams through thermal wind balance[1]. In the upper atmosphere, anthropogenic climate change is strengthening this meridional temperature gradient by cooling the polar lower stratosphere[2,3] and warming the tropical upper troposphere[4–6], acting to strengthen the upper-level jet stream[7]. In contrast, in the lower atmosphere, Arctic amplification of global warming is weakening the meridional temperature gradient[8–10], acting to weaken the upper-level jet stream. Therefore, trends in the speed of the upper-level jet stream[11–13] represent a closely balanced tug-of-war between two competing effects at different altitudes[14]. It is possible to isolate one of the competing effects by analysing the vertical shear—the change in wind speed with height—instead of the wind speed, but this approach has not previously been taken. Here we show that, although the zonal wind speed in the North Atlantic polar jet stream at 250 hectopascals has not changed since the start of the observational satellite era in 1979, the vertical shear has increased by 15 per cent (with a range of 11–17 per cent) according to three different reanalysis datasets[15–17]. We further show that this trend is attributable to the thermal wind response to the enhanced upper-level meridional temperature gradient. Our results indicate that climate change may be having a larger impact on the North Atlantic jet stream than previously thought. The increased vertical shear is consistent with the intensification of shear-driven clear-air turbulence expected from climate change[18–20], which will affect aviation in the busy transatlantic flight corridor by creating a more turbulent flying environment for aircraft. We conclude that the effects of climate change and variability on the upper-level jet stream are being partly obscured by the traditional focus on wind speed rather than wind shear.

In the Northern and Southern hemispheres, the mid-latitude baroclinic zone of the atmosphere is associated with a planetary-scale meridional temperature gradient between the equator and the pole. This temperature gradient generates westerly winds that strengthen with height—vertical wind shear—as a consequence of thermal wind balance[1]. Using pressure as a vertical coordinate, the vertical shear in the zonal wind, $-\partial u/\partial p$, is related to the meridional temperature gradient, $\partial T/\partial y$, by the thermal wind balance equation:

$$-\frac{\partial u}{\partial p} = -\frac{R}{fp}\frac{\partial T}{\partial y} \quad (1)$$

where R is the specific gas constant for dry air, f is the Coriolis parameter, p is pressure, and y is northward distance. Aloft, the strong westerly winds generated by thermal wind balance form the polar (or mid-latitude) jet stream, the speed of which is typically maximised near the tropopause, where the sign of the meridional temperature gradient (and thus the sign of the vertical shear) reverses. The polar jet stream is often described as eddy-driven, because eddies are required to support non-zero surface westerlies. It is distinct from the subtropical jet stream, which is primarily caused by poleward transport of angular momentum in the Hadley cell[21]. The polar jet stream influences mid-latitude weather systems, with the storm tracks being essentially a surface expression of the jet stream[22]. It also has an important role in commercial aircraft operations, partly because it creates strong headwinds and tailwinds on busy mid-latitude flight routes[23], but also because clear-air turbulence is generated by the associated intense vertical wind shear.

The mid-latitude meridional temperature gradients are being modified by anthropogenic climate change[24], and the jet streams are expected to adjust in response[23–25]. In the lower troposphere of the Northern Hemisphere, Arctic amplification caused primarily by

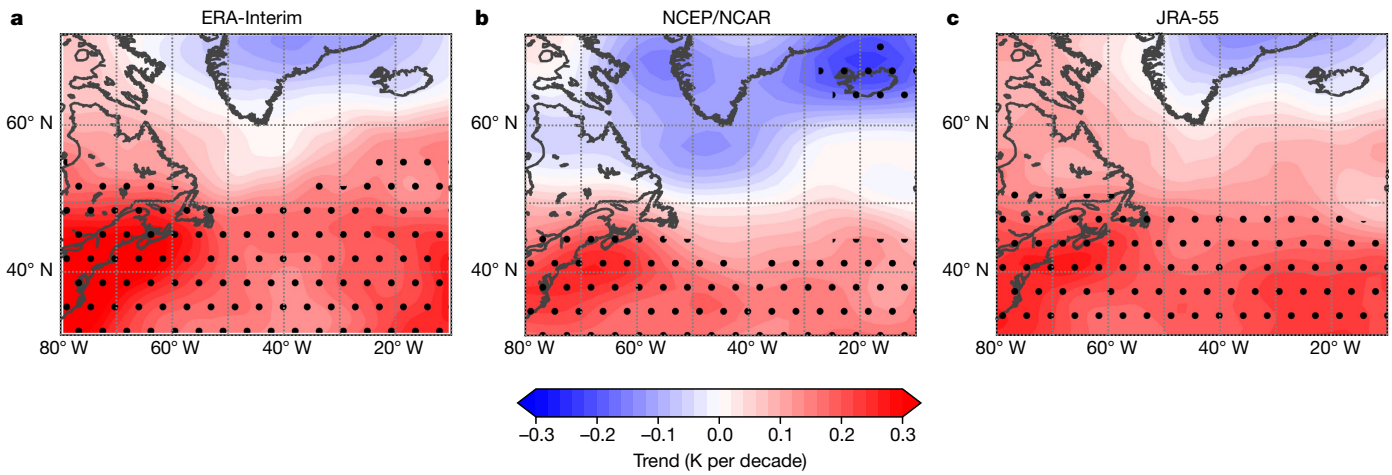

Fig. 1 | Annual-mean temperature trends in the North Atlantic at 250 hPa over the period 1979–2017. Linear trends are calculated using ordinary least-squares regression from the ERA-Interim (**a**), NCEP/NCAR (**b**) and JRA-55 (**c**) reanalysis datasets. Significant trends are indicated by stippling (two-tailed t-test; $P < 0.05$; $n = 39$).

[1]Department of Meteorology, University of Reading, Reading, UK. *e-mail: p.d.williams@reading.ac.uk

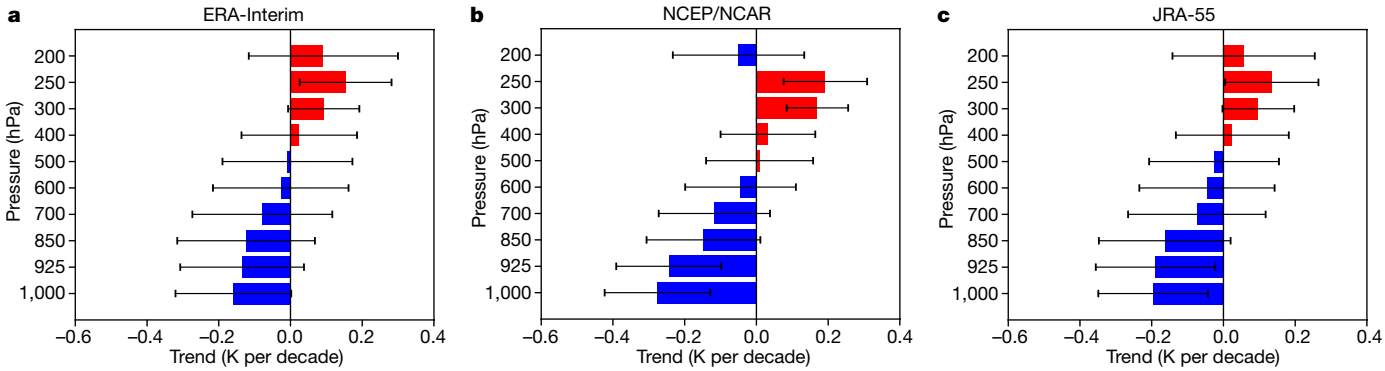

Fig. 2 | Vertical profiles of trends in the annual-mean north–south temperature difference across the North Atlantic over the period 1979–2017. Linear trends are calculated from the ERA-Interim (**a**), NCEP/NCAR (**b**) and JRA-55 (**c**) reanalysis datasets. Red and blue colours represent positive and negative trends, respectively. Error bars represent the 95% confidence intervals in the slope of the ordinary least-squares regression (two-tailed *t*-test; $n = 39$).

lapse-rate feedbacks[26] is weakening the meridional temperature gradient and polar jet stream[8–10]. In contrast, in the upper troposphere and lower stratosphere, the meridional temperature gradient is strengthening because of the combined effects of polar lower-stratospheric cooling and tropical upper-tropospheric warming, the latter caused by water vapour feedbacks releasing additional latent heat and reducing the lapse rate[7]. The vertically integrated thermal wind response is a tug-of-war between these two competing effects, with Arctic amplification acting to decrease the wind speed in the upper troposphere and lower stratosphere, but polar lower-stratospheric cooling and tropical upper-tropospheric warming acting to increase it. These competing influences suggest that upper-level trends in the jet stream may be better discerned through changes in vertical wind shear rather than absolute wind speed.

Here we analyse historic trends in the upper-level vertical wind shear in the North Atlantic region. In future climate projections, the prevalence of clear-air turbulence at typical aircraft cruising altitudes increases more here than anywhere else globally[20]. We use data from the ERA-Interim reanalysis at 0.75° horizontal resolution[16], the NCEP/NCAR reanalysis at 2.5° horizontal resolution[15], and the JRA-55 reanalysis at 1.25° horizontal resolution[17]. The use of three independently produced reanalysis datasets allows us to quantify the sensitivity of our results to uncertainties in the state of the atmosphere. We take six-hourly data from the years 1979–2017 inclusive. We restrict the temporal coverage to the satellite era, because the sparsity of upper-level wind observations over the North Atlantic before 1979 substantially increases uncertainty in reanalysis datasets[27]. We consider data within the region defined by 30–70° N and 10–80° W. This latitudinal range is chosen to include the polar jet stream (and the busy transatlantic flight corridor) while excluding the subtropical jet stream. We focus on the shear at a pressure altitude of 250 hPa (millibars), corresponding to the climatological core of the polar jet stream, and equating to a typical aircraft cruising altitude of around 34,000 feet.

We begin by analysing annual-mean upper-level temperature trends. As shown in Fig. 1, all three reanalysis datasets indicate a strengthening of the mid-latitude meridional temperature gradient at 250 hPa. The 250 hPa pressure surface evidently intersects the tropopause at around 50°–60° N, with lower-stratospheric cooling on the poleward side and upper-tropospheric warming on the equatorward side. The upper-tropospheric warming trend is slightly stronger in ERA-Interim and JRA-55, and the lower-stratospheric cooling trend is slightly stronger in NCEP/NCAR. Despite these minor differences, the spatial patterns and magnitudes of the temperature trends are broadly consistent across the datasets. Unlike the warming trends, the cooling trends are generally not statistically significant (except near Iceland in NCEP/NCAR), probably because of large inter-annual variability associated with the northern hemispheric circumpolar vortex[28].

To assess the vertical structure of the trends in the meridional temperature gradient, we calculate a bulk north–south temperature difference across the North Atlantic using a two-box method. On each pressure surface, annual-mean temperatures are averaged within a subpolar box (50°–70° N, 10°–80° W) and then subtracted from those averaged within a subtropical box (30°–50° N, 10°–80° W). This calculation yields a zonal-mean bulk meridional temperature difference, and the trends in this quantity are shown in Fig. 2. There is good agreement between the reanalysis datasets, with all three showing a statistically significant weakening of the meridional temperature gradient in the lower atmosphere and a statistically significant strengthening in the upper atmosphere. There is a transition between these two influences

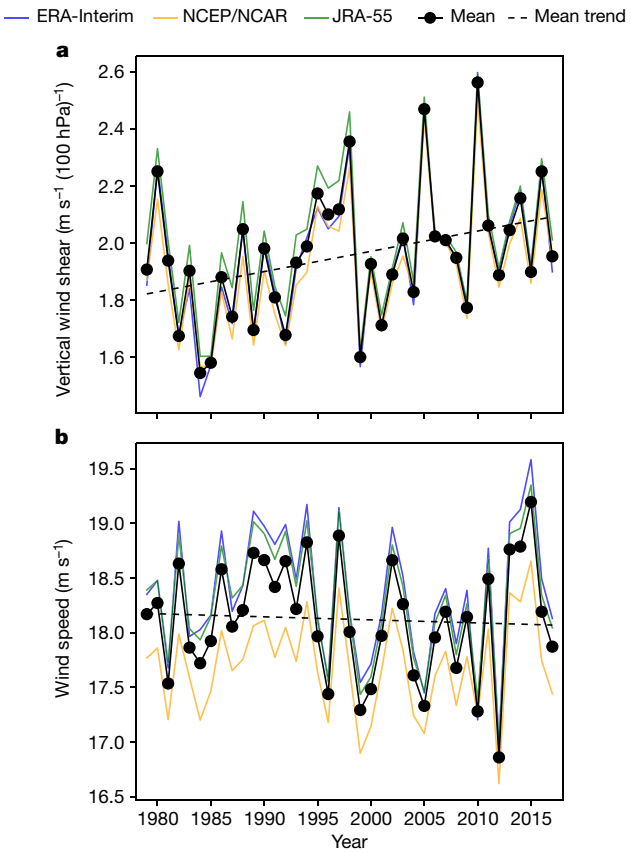

Fig. 3 | Time series of annual-mean wind characteristics in the North Atlantic at 250 hPa over the period 1979–2017. a, Vertical shear in the zonal wind. **b**, Zonal wind speed. Data are presented from the ERA-Interim, NCEP/NCAR and JRA-55 reanalysis datasets. Also shown are the mean of the three reanalysis datasets and the linear trend in the mean.

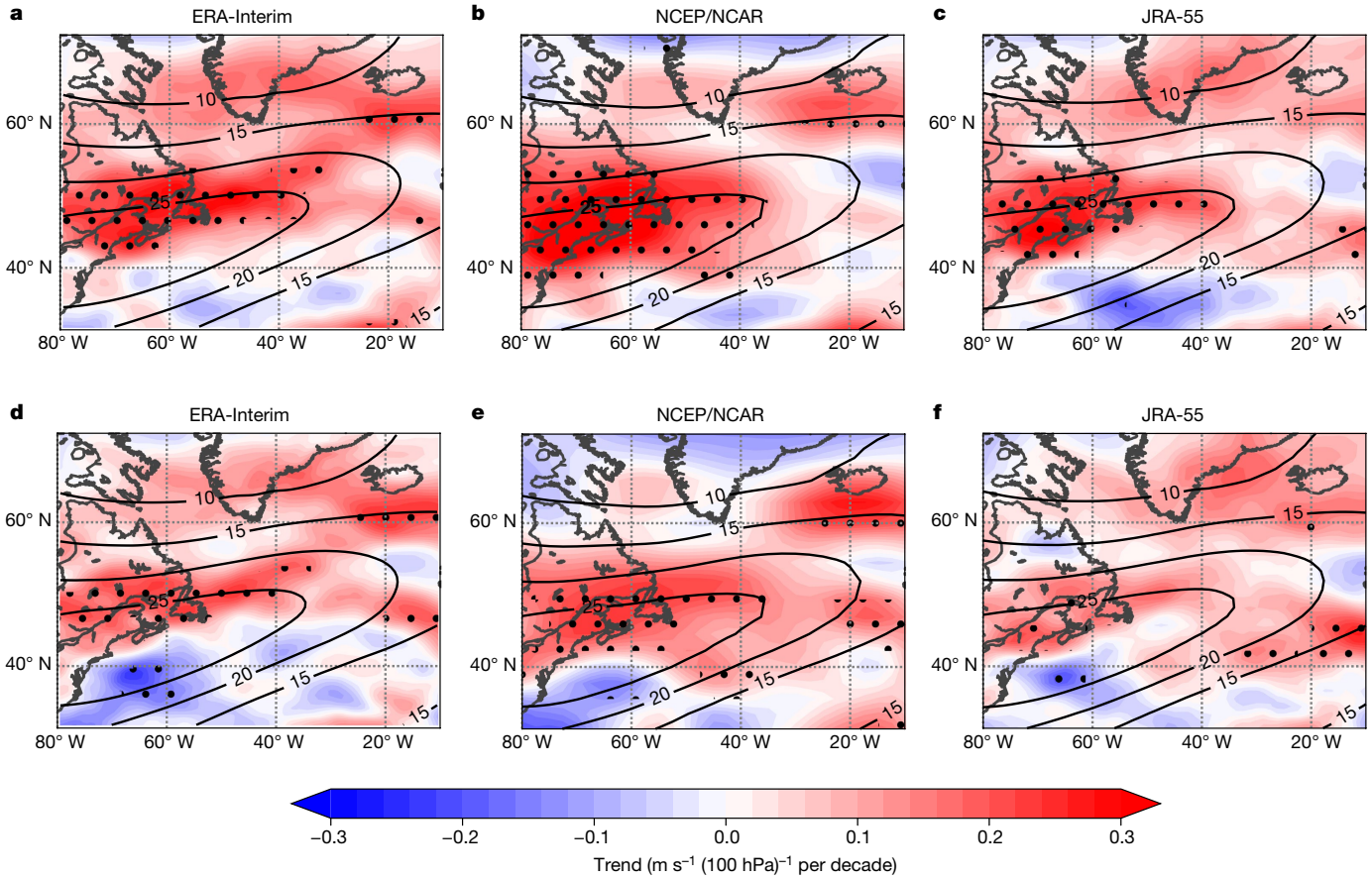

Fig. 4 | Annual-mean trends in vertical shear in zonal wind in the North Atlantic at 250 hPa over the period 1979–2017. a–c, Actual vertical wind shear trends calculated from the wind field. **d–f**, Expected vertical wind shear trends calculated from the temperature field using thermal wind balance. Linear trends are calculated using ordinary least-squares regression from the ERA-Interim (**a**, **d**), NCEP/NCAR (**b**, **e**) and JRA-55 (**c**, **f**) reanalysis datasets. Significant trends are indicated by stippling (two-tailed *t*-test; $P < 0.05$; $n = 39$). To indicate the climatological jet stream position, the 1979–2017 annual-mean zonal wind at 250 hPa in each reanalysis dataset is also shown (black contours every 5 m s^{-1}).

at around 450 hPa. There are some minor discrepancies, with NCEP/NCAR showing both a faster weakening of the meridional temperature gradient in the lower atmosphere and a faster strengthening aloft. At 250 hPa, however, all three reanalysis datasets show a statistically significant strengthening of the temperature difference by nearly 0.2 K per decade, consistent with Fig. 1.

To assess the impacts of the increasing meridional temperature gradient at 250 hPa on the atmospheric circulation, time series of the annual-mean vertical shear in zonal wind, averaged over the region 30°–70° N and 10°–80° W, are shown in Fig. 3a. All three reanalysis datasets are clearly in good agreement with respect to the inter-annual variability and the superimposed upward trend. The multi-reanalysis ensemble-mean vertical wind shear shows a statistically significant ($P = 0.03$) increase of 15% (0.07 m s^{-1} (100 hPa)$^{-1}$ per decade) over the 39-year period. The individual increases range from 11% in JRA-55 (0.06 m s^{-1} (100 hPa)$^{-1}$ per decade, $P = 0.09$) to 17% in ERA-Interim (0.08 m s^{-1} (100 hPa)$^{-1}$ per decade, $P = 0.02$) and 17% in NCEP/NCAR (0.08 m s^{-1} (100 hPa)$^{-1}$ per decade, $P = 0.01$). In contrast, as shown in Fig. 3b, the annual-mean zonal wind speed averaged over the same region at 250 hPa has not significantly changed in any of the three datasets ($P = 0.72$ for the slope of the ensemble-mean trend). It is notable that there is less spread between the three datasets for the shear than the speed; this may be because the speed is biased low in NCEP/NCAR because of the relatively coarse resolution compared to ERA-Interim and JRA-55, whereas this bias evidently disappears when vertical differences are taken to compute the shear.

The increased shear without increased speed shown for the upper atmosphere in Fig. 3 indicates that the weaker meridional temperature gradient (and weaker vertical wind shear) in the lower troposphere is masking the stronger meridional temperature gradient (and stronger vertical wind shear) in the upper troposphere and lower stratosphere, through a large degree of cancellation in the vertically integrated thermal wind. We illustrate this effect by showing vertical profiles of trends in shear and speed throughout the depth of the troposphere in Extended Data Fig. 1. The shear is strengthening within the jet core as well as throughout the broader region influenced by the jet stream (Extended Data Fig. 2) and the trends are not attributable to a shift in the annual-mean latitude of the jet core (Extended Data Fig. 3).

To relate trends in the meridional temperature gradient to trends in the vertical shear, we invoke the time derivative of the thermal wind balance equation (1):

$$-\frac{\partial}{\partial t}\frac{\partial u}{\partial p} = -\frac{R}{fp}\frac{\partial}{\partial t}\frac{\partial T}{\partial y} \quad (2)$$

We calculate both sides of this equation independently at each grid-point, as a measure of the extent to which the vertical wind shear changes are attributable to the local thermal wind response to the meridional temperature gradient changes. The time derivatives are evaluated as the linear trends over the period 1979–2017, calculated by applying ordinary least-squares regression to annual-mean values of $\partial u/\partial p$ and $\partial T/\partial y$ at each grid-point on the 250 hPa pressure surface. Maps of the left side of equation (2)—the directly calculated vertical wind shear trend, produced by differencing the wind fields at the two adjacent pressure levels—are shown in Fig. 4a–c. Maps of the right side of equation (2)—the expected vertical wind shear trend, produced by

using the temperature field and assuming thermal wind balance—are shown in Fig. 4d–f. There is a clear trend towards stronger vertical shear at 250 hPa over almost the entire North Atlantic domain in all three reanalysis datasets. The trend is statistically significant in the core of the climatological jet stream and on the poleward flank. We note the similarity in spatial patterns between these observed vertical wind shear increases and future projections of increased clear-air turbulence[18,19]. The good agreement between the left and right sides of equation (2), in terms of both the spatial patterns (the pattern correlation coefficients are $r > 0.70$ in all three datasets) and magnitudes, confirms that the vertical wind shear trends are indeed largely attributable to the response of the thermal wind to the meridional temperature gradient trends. The small discrepancies are presumably attributable to the numerical finite differences used to estimate the derivatives, as well as to weak ageostrophic and non-hydrostatic effects.

In summary, we have identified the first observationally based evidence of increased vertical wind shear in the North Atlantic upper-level jet stream over the satellite era (1979–2017). The increase of 15% (with a range of 11%–17%) is statistically significant, is present in three independently produced reanalysis datasets, and is attributable to the thermal wind response to the strengthening upper-level meridional temperature gradient. The stronger shear is consistent with the intensification of clear-air turbulence expected from climate change[18–20], because clear-air turbulence is generated by strong vertical wind shear (which means small Richardson number; we note that a 15% shear increase implies roughly a 30% Richardson number decrease, because of their inverse square relationship). In contrast to the large increase in vertical wind shear, we find that the zonal wind speed has not changed, consistent with previous studies[11,12]. The explanation for this effect is that, in the vertically integrated thermal wind balance equation, the weaker meridional temperature gradient and weaker vertical wind shear in the lower troposphere are mostly offsetting the stronger meridional temperature gradient and stronger vertical wind shear aloft. Increased vertical wind shear has important implications, not only for clear-air turbulence and its impacts on aviation, but also for the turbulent mixing of atmospheric constituents across the tropopause[29], with potentially important consequences for large-scale atmospheric thermodynamics and dynamics[30].

We conclude that the effects of climate change and variability on the upper-level jet stream are being partially obscured by the traditional focus on wind speed rather than wind shear. We suggest that climate-modelling studies into the response of the jet streams to climate change should therefore include consideration of the vertical shear as well as the speed. We anticipate that inter-model differences in upper-level vertical wind shear trends will have a clear interpretation in terms of different upper-level temperature trends. On the other hand, inter-model differences in upper-level wind speed trends may be more difficult to interpret, because of different balances in the competition between temperature trends at upper and lower levels.

Online content

Any methods, additional references, Nature Research reporting summaries, source data, extended data, supplementary information, acknowledgements, peer review information; details of author contributions and competing interests; and statements of data and code availability are available at https://doi.org/10.1038/s41586-019-1465-z.

Received: 9 August 2018; Accepted: 28 June 2019;
Published online 7 August 2019.

1. Wallace, J. M. & Hobbs, P. V. *Atmospheric Science: An Introductory Survey* (Academic Press, 2006).
2. Held, I. M. Large-scale dynamics and global warming. *Bull. Am. Meteorol. Soc.* **74**, 228–241 (1993).
3. Thompson, D. W. J. & Solomon, S. Recent stratospheric climate trends as evidenced in radiosonde data: global structure and tropospheric linkages. *J. Clim.* **18**, 4785–4795 (2005).
4. Allen, R. J. & Sherwood, S. C. Warming maximum in the tropical upper troposphere deduced from thermal winds. *Nat. Geosci.* **1**, 399–403 (2008).
5. Mitchell, D. M., Thorne, P. W., Stott, P. A. & Gray, L. J. Revisiting the controversial issue of tropical tropospheric temperature trends. *Geophys. Res. Lett.* **40**, 2801–2806 (2013).
6. Sherwood, S. C. & Nishant, N. Atmospheric changes through 2012 as shown by iteratively homogenized radiosonde temperature and wind data (IUKv2). *Environ. Res. Lett.* **10**, 054007 (2015).
7. Lorenz, D. J. & DeWeaver, E. T. Tropopause height and zonal wind response to global warming in the IPCC scenario integrations. *J. Geophys. Res. Atmos.* **112**, 1–11 (2007).
8. Francis, J. A. & Vavrus, S. J. Evidence linking Arctic amplification to extreme weather in mid-latitudes. *Geophys. Res. Lett.* **39**, L06801 (2012).
9. Haarsma, R. J., Selten, F. & van Oldenborgh, G. J. Anthropogenic changes of the thermal and zonal flow structure over Western Europe and Eastern North Atlantic in CMIP3 and CMIP5 models. *Clim. Dyn.* **41**, 2577–2588 (2013).
10. Francis, J. A. & Vavrus, S. J. Evidence for a wavier jet stream in response to rapid Arctic warming. *Environ. Res. Lett.* **10**, 014005 (2015).
11. Archer, C. L. & Caldeira, K. Historical trends in the jet streams. *Geophys. Res. Lett.* **35**, L08803 (2008).
12. Pena-Ortiz, C., Gallego, D., Ribera, P., Ordonez, P. & Del Carmen Alvarez-Castro, M. Observed trends in the global jet stream characteristics during the second half of the 20th century. *J. Geophys. Res. Atmos.* **118**, 2702–2713 (2013).
13. Manney, G. L. & Hegglin, M. I. Seasonal and regional variations of long-term changes in upper-tropospheric jets from reanalyses. *J. Clim.* **31**, 423–448 (2018).
14. Francis, J. A. Why are Arctic linkages to extreme weather still up in the air? *Bull. Am. Meteorol. Soc.* **98**, 2551–2557 (2017).
15. Kalnay, E. et al. The NCEP/NCAR 40-year reanalysis project. *Bull. Am. Meteorol. Soc.* **77**, 437–471 (1996).
16. Dee, D. P. et al. The ERA-Interim reanalysis: configuration and performance of the data assimilation system. *Q. J. R. Meteorol. Soc.* **137**, 553–597 (2011).
17. Kobayashi, S. et al. The JRA-55 reanalysis: general specifications and basic characteristics. *J. Meteorol. Soc. Jpn. Ser. II* **93**, 5–48 (2015).
18. Williams, P. D. & Joshi, M. M. Intensification of winter transatlantic aviation turbulence in response to climate change. *Nat. Clim. Chang.* **3**, 644–648 (2013).
19. Williams, P. D. Increased light, moderate, and severe clear-air turbulence in response to climate change. *Adv. Atmos. Sci.* **34**, 576–586 (2017).
20. Storer, L. N., Williams, P. D. & Joshi, M. M. Global response of clear-air turbulence to climate change. *Geophys. Res. Lett.* **44**, 9976–9984 (2017).
21. Lee, S. & Kim, H. The dynamical relationship between subtropical and eddy-driven jets. *J. Atmos. Sci.* **60**, 1490–1503 (2003).
22. Hannachi, A., Woollings, T. & Fraedrich, K. The North Atlantic jet stream: a look at preferred positions, paths and transitions. *Q. J. R. Meteorol. Soc.* **138**, 862–877 (2012).
23. Williams, P. D. Transatlantic flight times and climate change. *Environ. Res. Lett.* **11**, 024008 (2016).
24. Vallis, G. K., Zurita-Gotor, P., Cairns, C. & Kidston, J. Response of the large-scale structure of the atmosphere to global warming. *Q. J. R. Meteorol. Soc.* **141**, 1479–1501 (2015).
25. Woollings, T. & Blackburn, M. The North Atlantic jet stream under climate change and its relation to the NAO and EA patterns. *J. Clim.* **25**, 886–902 (2012).
26. Stuecker, M. F., Bitz, C. M., Armour, K. C., Proistosescu, C. & Kang, S. M. Polar amplification dominated by local forcing and feedbacks. *Nat. Clim. Chang.* **8**, 1076–1081 (2018).
27. Fujiwara, M. et al. Introduction to the SPARC Reanalysis Intercomparison Project (S-RIP) and overview of the reanalysis systems. *Atmos. Chem. Phys.* **17**, 1417–1452 (2017).
28. Waugh, D. W., Sobel, A. H. & Polvani, L. M. What is the polar vortex and how does it influence weather? *Bull. Am. Meteorol. Soc.* **98**, 37–44 (2017).
29. Shapiro, M. A. Turbulent mixing within tropopause folds as a mechanism for the exchange of chemical constituents between the stratosphere and troposphere. *J. Atmos. Sci.* **37**, 994–1004 (1980).
30. Maycock, A. C., Joshi, M. M., Shine, K. P. & Scaife, A. A. The circulation response to idealized changes in stratospheric water vapor. *J. Clim.* **26**, 545–561 (2013).

METHODS

The North Atlantic region was chosen for this study partly because it is the world's busiest oceanic flight corridor. Owing to the zonally extended nature of the polar jet stream in this region, transatlantic flights are typically affected by the strength and position of the jet stream throughout their entire flight paths. The effects of the jet stream on aircraft include headwinds, tailwinds and clear-air turbulence. A further reason for choosing the North Atlantic is that—unlike the North Pacific—it exhibits separate polar and subtropical jet streams, allowing an analysis of the polar jet stream exclusively.

We used pressure-level zonal wind and temperature data from the ERA-Interim, NCEP/NCAR and JRA-55 reanalysis datasets at six-hourly analysis intervals from 1 January 1979 to 31 December 2017 inclusive, giving 39 full years of data. All datasets were used on a standard latitude–longitude grid (0.75° for ERA-Interim, 2.5° for NCEP/NCAR and 1.25° for JRA-55). Trends were calculated using ordinary least-squares regression, and statistical significance was assessed at the 95% confidence level ($P < 0.05$) according to a two-tailed t-test. The effect of temporal autocorrelation on statistical significance was tested in the computed annual-mean data and found to be negligible. Percentage changes were calculated using the values of the fitted linear trend lines in 1979 and 2017.

To calculate the two-box zonal-mean bulk meridional temperature difference, we first averaged the annual-mean temperature in a subtropical box (30°–50° N, 10°–80° W) and a subpolar box (50°–70° N, 10°–80° W), with a cosine(latitude) weighting factor to account for the convergence of grid points at high latitudes. The latitudinal bounds of these boxes were chosen to be approximately either side of the climatological annual-mean jet stream latitude in the North Atlantic. We then found the meridional temperature difference across the North Atlantic by subtracting the subtropical box temperature from the subpolar box temperature.

The jet stream was analysed in the North Atlantic region (10°–80° W, 30°–70° N). The annual-mean regional-mean 250 hPa vertical shear in zonal wind was calculated by taking a centred vertical finite difference using the annual-mean zonal winds at 300 and 200 hPa:

$$-\left.\frac{\partial u}{\partial p}\right|_{250\,\mathrm{hPa}} \approx \frac{u(200\,\mathrm{hPa}) - u(300\,\mathrm{hPa})}{100\,\mathrm{hPa}} \tag{3}$$

We also calculated trends in the annual-mean regional-mean (area-weighted) zonal wind speed at 250 hPa over the North Atlantic region. Vertical profiles of vertical shear trends were calculated by taking centred finite differences at intervals of 50 hPa for ERA-Interim and JRA-55, and from neighbouring pressure levels in NCEP/NCAR (owing to the spacing of available pressure-level data).

The annual-mean regional-maximum vertical shear was calculated by a similar centred-difference method: we first subtracted the zonal wind at 300 hPa from the zonal wind at 200 hPa, and we then found the maximum value within the North Atlantic region at each six-hourly interval, before averaging the maximum values annually. For the annual-mean regional-maximum zonal wind speed, we found the maximum zonal wind speed at 250 hPa within the North Atlantic region at each six-hourly interval, before averaging annually. In both cases, the latitude at which the maximum occurred was stored.

When the calculations in Fig. 3 are repeated using the annual-mean regional-maximum vertical shear, instead of the annual-mean regional-mean vertical shear, a statistically significant ensemble-mean increase of 11% ($P < 0.01$) in the shear is found. The individual increases are 10% in ERA-Interim ($P < 0.01$), 18% in NCEP/NCAR ($P < 0.01$), and 7% in JRA-55 ($P < 0.01$) (Extended Data Fig. 2). These results confirm that the shear is strengthening within the jet core as well as throughout the broader region influenced by the jet stream. The trends are not attributable to a shift in the annual-mean latitude of the jet core, which shows no statistically significant trend over the period (Extended Data Fig. 3).

We used the time derivative of the thermal wind balance equation to relate linear trends in the meridional temperature gradient to linear trends in the vertical wind shear. At 250 hPa, we calculated trends in the annual-mean values of $\partial u/\partial p$ (using the centred finite difference method outlined above) and $\partial T/\partial y$. The agreement between the two was assessed through Pearson's correlation coefficient using an area-weighted pattern correlation.

According to thermal wind balance, the trend in the zonal wind speed in the upper troposphere and lower stratosphere is given by the vertical integral of equation (2). This vertical integral is performed throughout the depth of the free troposphere, starting from the top of the planetary boundary layer. Temperature gradients in the lower troposphere are included in the integral, and therefore Arctic amplification at low levels is able to influence the wind speed at upper levels. For example, written in equation form, we have:

$$\frac{\partial u(250\,\mathrm{hPa})}{\partial t} = \int_{p_0}^{450\,\mathrm{hPa}} \frac{R}{fp}\frac{\partial}{\partial t}\left(\frac{\partial T}{\partial y}\right)\mathrm{d}p + \int_{450\,\mathrm{hPa}}^{250\,\mathrm{hPa}} \frac{R}{fp}\frac{\partial}{\partial t}\left(\frac{\partial T}{\partial y}\right)\mathrm{d}p \approx 0 \tag{4}$$

where p_0 is the pressure at the top of the planetary boundary layer. Here, the free troposphere has been divided into two layers at 450 hPa, by reference to Fig. 2. The lower boundary term $\partial u(p_0)/\partial t$ arising from the vertical integration has been neglected in equation (4), because the zonal wind speed in the lower troposphere has no statistically significant trend in any of the reanalysis datasets, as shown in Extended Data Fig. 1d–f. Our study shows that, on the right-hand side of equation (4), the first integral (which includes the weakening low-level temperature gradient from Arctic amplification) and the second integral (which includes the strengthening upper-level temperature gradient) are essentially equal and opposite when averaged over the North Atlantic region, thus largely cancelling out and leaving no statistically significant trend in the upper-level speed.

Data availability

The NCEP/NCAR reanalysis data may be obtained from the National Oceanic and Atmospheric Administration (NOAA) Oceanic and Atmospheric Research (OAR) Earth System Research Laboratory (ESRL) Physical Sciences Division (PSD), Boulder, Colorado, USA (https://www.esrl.noaa.gov/psd/). The ERA-Interim and JRA-55 reanalysis data may be obtained from the Research Data Archive at the National Center for Atmospheric Research (NCAR), Computational and Information Systems Laboratory, Boulder, Colorado, USA (https://doi.org/10.5065/D6CR5RD9 and https://doi.org/10.5065/D6HH6H41, respectively).

Code availability

The analytical computer codes are publicly available at https://doi.org/10.5281/zenodo.3238842.

Acknowledgements S.H.L. acknowledges support through a PhD studentship from the Natural Environment Research Council SCENARIO Doctoral Training Partnership (reference NE/L002566/1).

Author contributions S.H.L. and P.D.W. jointly conceived the study. S.H.L. performed the data analysis and produced the figures with input from P.D.W. and T.H.A.F. All authors contributed to writing the manuscript. The authors discussed the results with each other at all stages.

Competing interests The authors declare no competing interests.

Additional information
Correspondence and requests for materials should be addressed to P.D.W.
Peer review information *Nature* thanks Darryn Waugh and Elizabeth A. Barnes for their contribution to the peer review of this work.
Reprints and permissions information is available at http://www.nature.com/reprints.

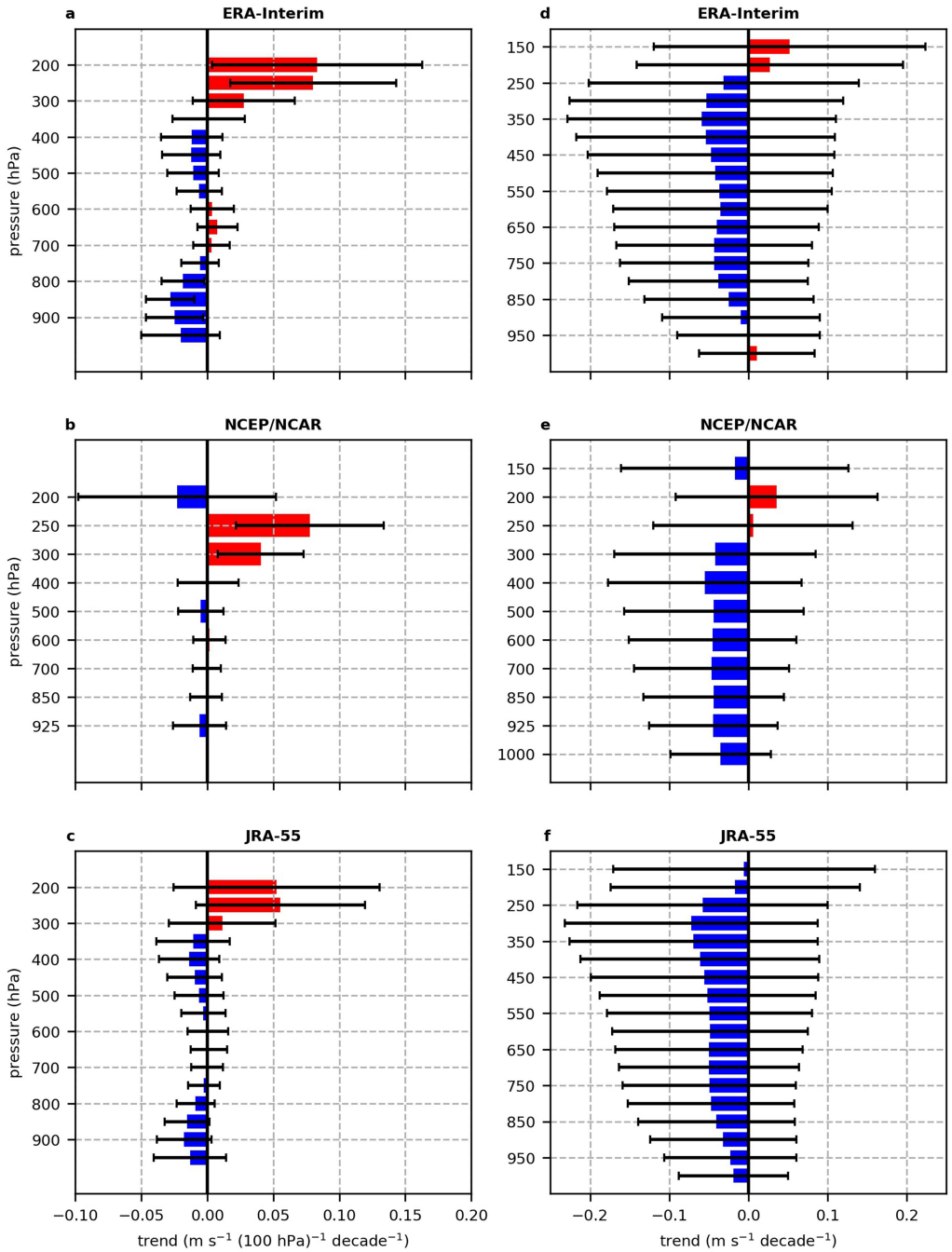

Extended Data Fig. 1 | Vertical profiles of annual-mean trends in wind characteristics in the North Atlantic over the period 1979–2017. **a**–**c**, Trends in the vertical shear in the zonal wind. **d**–**f**, Trends in the zonal wind speed. Linear trends are calculated from the ERA-Interim (**a**, **d**), NCEP/NCAR (**b**, **e**) and JRA-55 (**c**, **f**) reanalysis datasets. Red and blue colours represent positive and negative trends, respectively. Error bars represent the 95% confidence intervals in the slope of the ordinary least-squares regression (two-tailed *t*-test; $n = 39$).

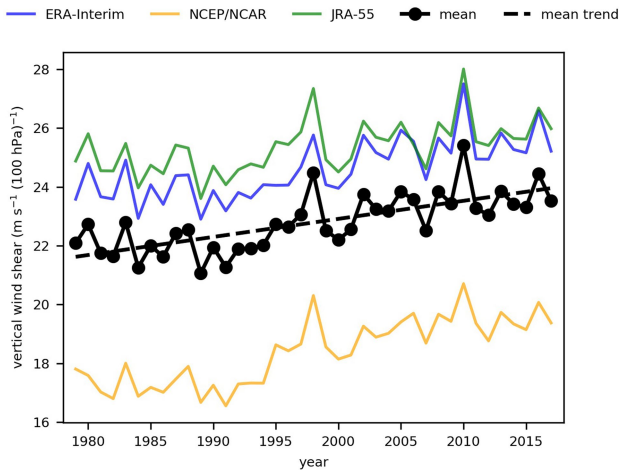

Extended Data Fig. 2 | Annual-mean regional-maximum six-hourly vertical shear in zonal wind in the North Atlantic at 250 hPa over the period 1979–2017. Data are presented from the ERA-Interim, NCEP/NCAR and JRA-55 reanalysis datasets. Also shown are the mean of the three reanalysis datasets and the linear trend in the mean.

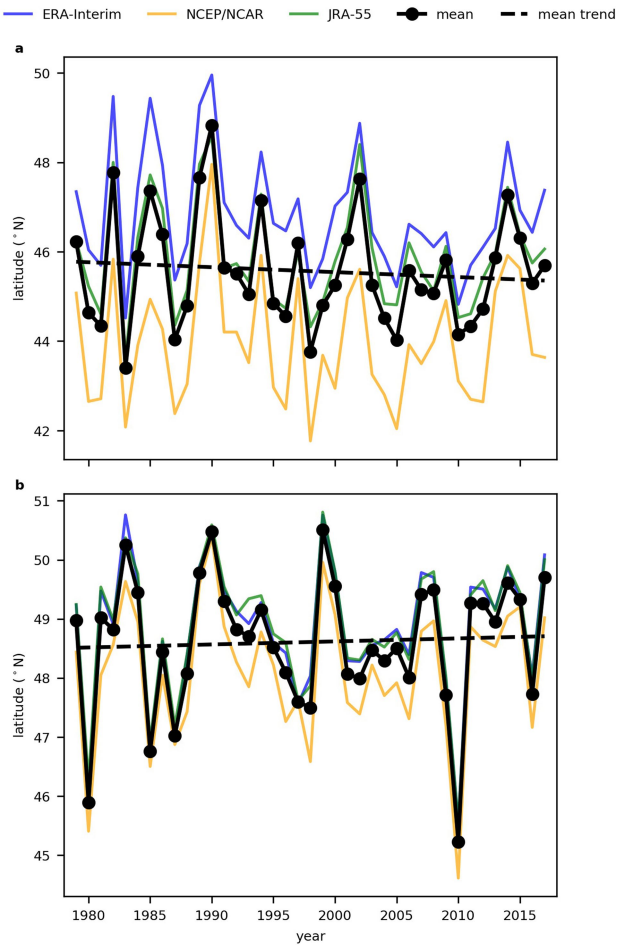

Extended Data Fig. 3 | Annual-mean latitude of the core of the polar jet stream in the North Atlantic at 250 hPa over the period 1979–2017. **a**, Annual-mean latitude of the regional-maximum six-hourly vertical shear in zonal wind. **b**, Annual-mean latitude of the regional-maximum six-hourly zonal wind speed. Data are presented from the ERA-Interim, NCEP/NCAR and JRA-55 reanalysis datasets. Also shown are the mean of the three reanalysis datasets and the linear trend in the mean, which has a statistically insignificant slope of –0.1° per decade (two-tailed *t*-test; $P = 0.54$; $n = 39$) (**a**) and 0.01° per decade (two-tailed *t*-test; $P = 0.76$; $n = 39$) (**b**).

LETTER

https://doi.org/10.1038/s41586-019-1483-x

Seismic velocities of $CaSiO_3$ perovskite can explain LLSVPs in Earth's lower mantle

A. R. Thomson[1,2]*, W. A. Crichton[2], J. P. Brodholt[1,3], I. G. Wood[1], N. C. Siersch[4], J. M. R. Muir[5], D. P. Dobson[1] & S. A. Hunt[1]

Seismology records the presence of various heterogeneities throughout the lower mantle[1,2], but the origins of these signals—whether thermal or chemical—remain uncertain, and therefore much of the information that they hold about the nature of the deep Earth is obscured. Accurate interpretation of observed seismic velocities requires knowledge of the seismic properties of all of Earth's possible mineral components. Calcium silicate ($CaSiO_3$) perovskite is believed to be the third most abundant mineral throughout the lower mantle. Here we simultaneously measure the crystal structure and the shear-wave and compressional-wave velocities of samples of $CaSiO_3$ perovskite, and provide direct constraints on the adiabatic bulk and shear moduli of this material. We observe that incorporation of titanium into $CaSiO_3$ perovskite stabilizes the tetragonal structure at higher temperatures, and that the material's shear modulus is substantially lower than is predicted by computations[3–5] or thermodynamic datasets[6]. When combined with literature data and extrapolated, our results suggest that subducted oceanic crust will be visible as low-seismic-velocity anomalies throughout the lower mantle. In particular, we show that large low-shear-velocity provinces (LLSVPs) are consistent with moderate enrichment of recycled oceanic crust, and mid-mantle discontinuities can be explained by a tetragonal–cubic phase transition in Ti-bearing $CaSiO_3$ perovskite.

The lower mantle is vast, extending from the seismic discontinuity observed at approximately 660 km depth to the core–mantle boundary (CMB) at a depth of about 2,890 km. Tomographic images demonstrate that despite a smooth variation of compressional-wave velocity, shear-wave velocity and density (respectively v_P, v_S and ρ) in 1D velocity models, the lower mantle is heterogeneous and regularly refertilized by subducting slabs[7,8]. Sluggish diffusive re-equilibration and incomplete mechanical mixing[9] mean that large-scale patterns of mantle convection may be directly observed via tomographic velocity anomalies and/or the distribution of seismic scatterers. Identifying the causes of heterogeneities requires accurate mineralogical models of Earth's mantle to facilitate comparisons between geophysical observations and predicted seismic velocities. However, a major uncertainty in many models[10,11] has been the influence of $CaSiO_3$ perovskite (Ca-Pv, here corresponding to $Ca[Si_xTi_{(1-x)}]O_3$) on velocity, despite the widespread expectation that it is the lower mantle's third most abundant phase, comprising 5–10 vol.% and 24–29 vol.% of peridotitic[12] and basaltic[13] assemblages, respectively.

Uncertainties stem from a sparsity of reliable measurements of Ca-Pv's physical properties, which are technically challenging because $CaSiO_3$ is unrecoverable[14], undergoing spontaneous amorphization at room temperature during decompression. The widely used thermodynamic model of Stixrude et al.[6] predicts that the seismic velocity of Ca-Pv is substantially higher than in average one-dimensional profiles such as the Preliminary Reference Earth Model (PREM)[15], and therefore low-velocity anomalies are difficult to explain using recycled crustal material. Although this is the widely adopted view, there is

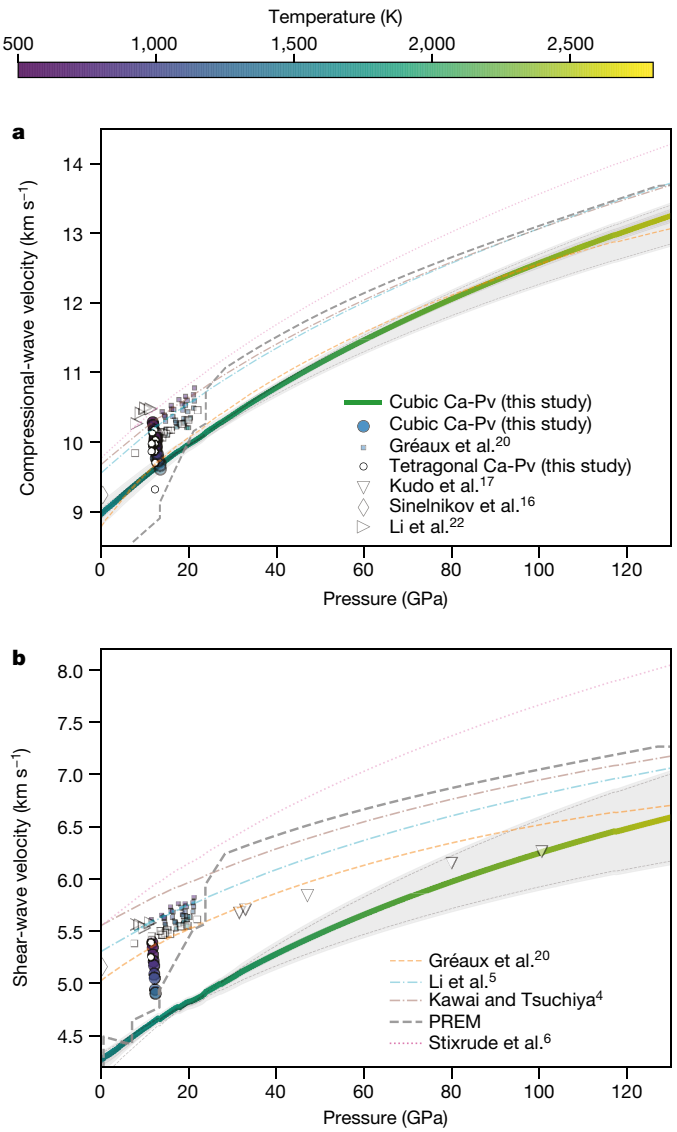

Fig. 1 | Compressional- and shear-wave velocities of cubic $CaSiO_3$ perovskite from this and previous studies. a, Compressional-wave velocity and **b**, shear-wave velocity of $CaSiO_3$ perovskite predicted in this and previous[4–6,16,17,20,22] studies throughout the mantle. Individual experimental measurements are shown with symbols, coloured by temperature (key at top; white symbols are data collected at 300 K). All velocity curves are extracted along a 1,500 K mantle adiabat. Thick coloured curve (and 95% confidence interval in grey) represents the velocity of cubic Ca-Pv based on finite-strain modelling (this study). Bold dashed line is the PREM velocity profile.

[1]Department of Earth Sciences, University College London, London, UK. [2]ESRF — The European Synchrotron, Grenoble, France. [3]Centre for Earth Evolution and Dynamics, University of Oslo, Oslo, Norway. [4]Bayeriches Geoinstitut, University of Bayreuth, Bayreuth, Germany. [5]School of Earth and Environment, University of Leeds, Leeds, UK. *e-mail: a.r.thomson@ucl.ac.uk

currently no consensus on the seismic properties of Ca-Pv. Existing high-temperature calculations[3–5] suggest that the velocity of Ca-Pv might be either slightly lower or much higher than in PREM[15] (Fig. 1). By contrast, room-temperature experiments[16,17] have measured a shear velocity of Ca-Pv that is at least 7% lower than the lowest computational estimates; however, there is difficulty extrapolating these to high-temperature conditions due to intervening phase transformations of the Ca-Pv structure[3,18,19]. Very recently, high-temperature experimental velocity measurements that are also lower than all computational values have been reported[20], although this study did not consider extrapolations of Ca-Pv's velocity throughout the deep mantle, leaving Ca-Pv's contribution in generating lower-mantle signatures unresolved. Here we report synchrotron-based high-pressure (P), high-temperature (T), experiments that simultaneously measure the crystal structure and seismic velocities (v_P and v_S) of $Ca[Si_xTi_{[1-x]}]O_3$ compositions ($x = 0.6$ and 1) that bracket the range of inclusions found in natural superdeep diamonds and are expected in lower-mantle assemblages[21]. Combining our new data with ab initio calculations and literature data, we directly address the influence of crystallographic phase transitions on the velocity of Ca-Pv and apply our results to provide a new understanding of Ca-Pv's geophysical signature throughout the lower mantle (see Methods)[16,17,22].

In line with expectations from previous experiments[18], in situ diffraction confirms that Ca-Pv is cubic at high temperature, and undergoes one or more structural distortions upon cooling to room temperature (Fig. 2a). Refinement and indexing of diffraction patterns reveals that endmember $CaSiO_3$ transforms on cooling from cubic ($Pm\bar{3}m$) at high temperatures into tetragonal ($I4/mcm$) perovskite between 380 K and 420 K at about 12 GPa (Fig. 2c). This phase transition is identified by the nonlinear splitting upon cooling (observed as broadening) of all diffraction peaks, except for those with indices hhh (that is, 111 and 222), from the cubic aristotype unit cell ($a \approx 3.5$ Å, Fig. 2b and Extended Data Fig. 1e). Additionally, weak superlattice reflections at d-spacings (in Å) of approximately 2.11, 1.61, 1.07 and 0.98 (Extended Data Fig. 2), which uniquely identify the $I4/mcm$ structure, were observed below about 420 K. Titanium incorporation (similarly to aluminium[23]) increases the upper stability limit of tetragonal Ca-Pv considerably, here by nearly 800 K. We find that $Ca[Si_{0.6}Ti_{0.4}]O_3$ takes the $Fm\bar{3}m$ space group at high temperature (Extended Data Figs. 1, 3, 4), possessing a double perovskite unit cell, with partial Si:Ti cation ordering that is apparently maintained throughout cooling. The cubic–tetragonal ($Fm\bar{3}m$–$I4/m$) transition in $Ca[Si_{0.6}Ti_{0.4}]O_3$ is observed at approximately 1,200 K (Extended Data Fig. 1). Upon further cooling, a subsequent symmetry distortion, thought to be to $P2_1/c$, is observed at about 700 K. These observations provide very strong evidence that Ca-Pv follows the same structural transitions on cooling as $CaTiO_3$ (see equations below[24]), with the apparent reductions in symmetry from $I4/mcm$ and $Pbnm$ to their $I4/m$ and $P2_1/c$ subgroups being a consequence of cation ordering:

$$Pm\bar{3}m \xrightarrow{\sim 420\,K} I4/mcm\text{–}CaSiO_3\ (\sim 12\ GPa)$$

$$Fm\bar{3}m \xrightarrow{\sim 1,200\,K} I4/m \xrightarrow{\sim 700\,K} P2_1/c\text{–}Ca[Si_{0.6}Ti_{0.4}]O_3\ (\sim 12\ GPa)$$

$$Pm\bar{3}m \xrightarrow{\sim 1,635\,K} I4/mcm \xrightarrow{\sim 1,512\,K} Pbnm\text{–}CaTiO_3\ (0\ GPa)$$

Acoustic velocities, determined simultaneously with synchrotron X-ray diffraction using pulse-echo ultrasonic interferometry, demonstrate that the observed phase transitions of Ca-Pv are associated with large elastic anomalies. $CaSiO_3$ and $Ca[Si_{0.6}Ti_{0.4}]O_3$ samples undergo v_P and v_S reductions of 4–14% and 8–20%, respectively, owing to their cubic–tetragonal transitions (Fig. 3). Continued cooling of $Ca[Si_{0.6}Ti_{0.4}]O_3$ into its presumed monoclinic structure sees the velocities increase near ambient temperature. The acoustic 'shear-strengthening' with temperature that we observe in tetragonal Ca-Pv is also reported for polycrystalline $BaTiO_3$ samples[25]. Such behaviour is thought to result from a temperature-activated twin-domain-wall process that also causes high

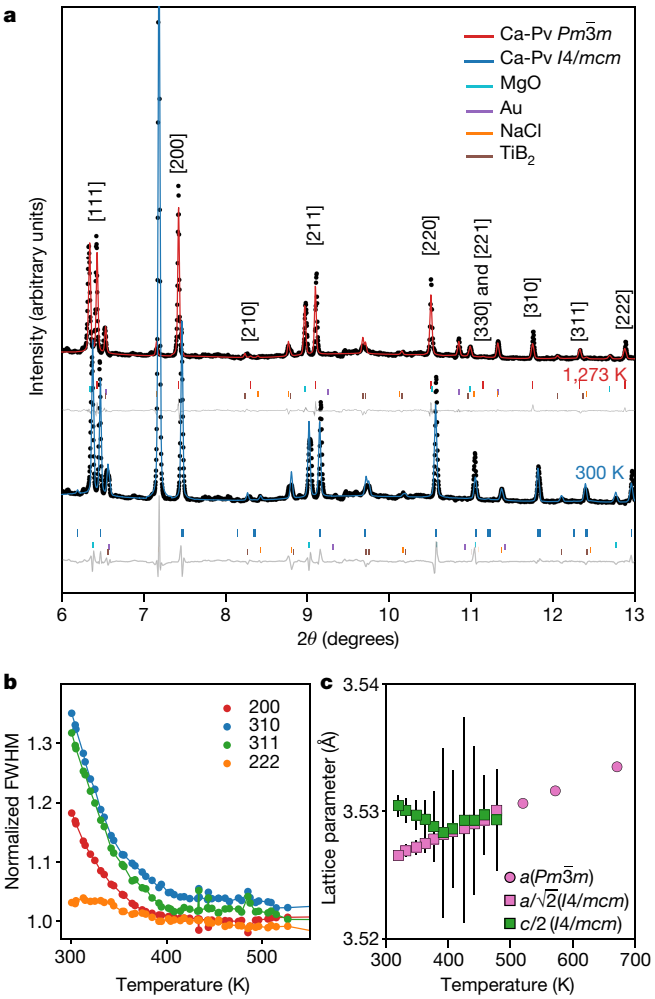

Fig. 2 | X-ray diffraction patterns demonstrating the cubic–tetragonal phase transition in $CaSiO_3$ perovskite. a, Rietveld refined X-ray diffraction patterns collected at about 12 GPa and 1,273 K (red, cubic) or 300 K (blue, tetragonal), with cubic $CaSiO_3$ peaks labelled by [hkl] and tick marks for other cell components. **b**, Normalized full-width at half-maximum (FWHM) of selected diffraction peaks (see key) of $CaSiO_3$ perovskite as a function of temperature. **c**, Refined lattice parameters of $CaSiO_3$ perovskite sample as a function of experimental temperature with 2σ uncertainties.

acoustic attenuation[26]. Although we cannot rigorously measure acoustic attenuation, we do observe a diminution in the intensity of reflected acoustic waves when samples are tetragonal. Experiments on endmember $CaSiO_3$ demonstrate a modest reduction in v_P and v_S across the cubic–tetragonal transition at $T < 450$ K; however, the relatively small decrease observed is likely to continue at sub-ambient temperatures that could not be examined in this study. We suggest that $CaSiO_3$, if cooled further, probably undergoes similar magnitudes of velocity reduction to those observed for $Ca[Si_{0.6}Ti_{0.4}]O_3$. Absolute acoustic velocities measured for $CaSiO_3$ are lower than computational predictions, but v_P and v_S in this study agree extremely well with previous experimental measurements made at room temperature[16,17,20]. It is only with increasing temperature that our results diverge from previous experimental data[20]. The excellent room-temperature agreement leads us to conclude that previous calculations must have overestimated the velocities, specifically the shear modulus (G), of Ca-Pv (as discussed below). We also observe that the temperature dependences of velocities $\left(\frac{1}{v}\frac{dv}{dT}\right)$ in cubic Ca-Pv are 1.5–3 times larger than those experimentally observed for other mantle silicates[27]. However, the temperature dependence of the elastic moduli in our experiments (dK_S/dT and dG/dT are both about -0.027 to -0.03 GPa K^{-1}) match those observed for cubic [Ca,Sr]TiO_3

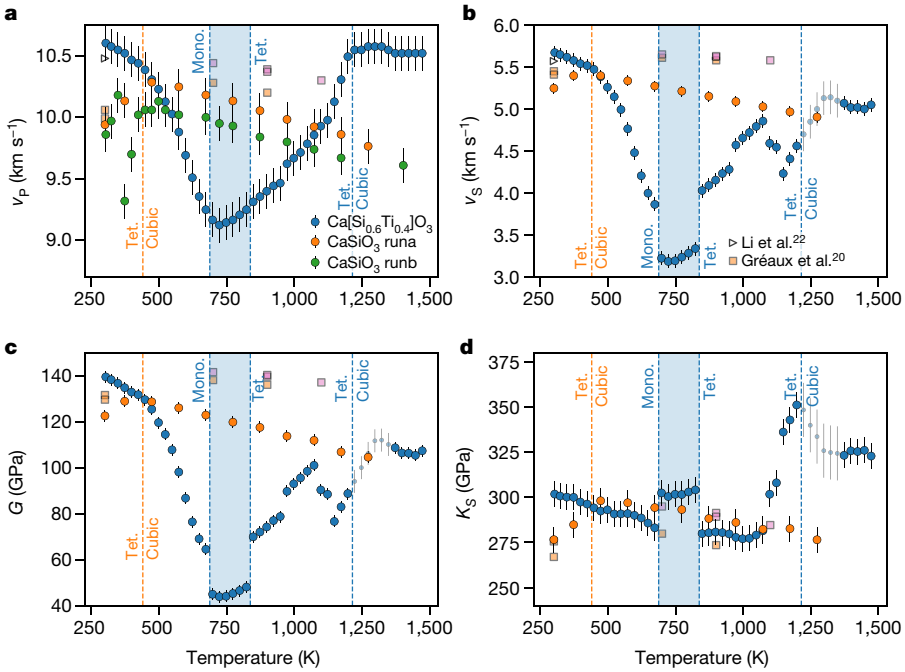

Fig. 3 | Acoustic velocities of Ca-Pv samples at high-*PT* conditions. **a–d**, Compressional-wave (v_P; **a**) and shear-wave (v_S; **b**) velocities, with derived shear modulus (G; **c**) and bulk modulus (K_S; **d**) of Ca-Pv samples measured as a function of temperature at constant press load (about 12 GPa), for Ca[Si$_{0.6}$Ti$_{0.4}$]O$_3$ (blue circles) and CaSiO$_3$ samples (orange and green circles). Data from "runa" and "runb" are results from two separate experiments on CaSiO$_3$ at slightly different pressure. Uncertainties are all 2σ. Small blue circles are data with a low signal-to-noise ratio, due to low amplitude of the buffer rod reflection, and have larger uncertainties. Experimental velocity measurements from previous studies are plotted as triangles[22] (about 12 GPa) and squares[20] (orange, 12 ± 1 GPa; purple, 15 ± 1 GPa). Dashed vertical lines indicate the temperatures of observed phase transitions for CaSiO$_3$ (orange) and Ca[Si$_{0.6}$Ti$_{0.4}$]O$_3$ (blue) to/from cubic (Cub.), tetragonal (Tet.) and/or monoclinic (Mono.) structure. The blue temperature interval represents the extent of the first-order $I4/m$ to $P2_1/c$ transition in Ca[Si$_{0.6}$Ti$_{0.4}$]O$_3$.

perovskites (-0.024 to -0.03 GPa K^{-1})[26] and the bulk (K_S), but not the shear, modulus in previous experiments on CaSiO$_3$ ($dK_S/dT \approx -0.036$ and $dG/dT \approx -0.015$ GPa K^{-1})[20].

Using ab initio molecular dynamics, we have calculated the *PT* slope of the $I4/mcm \rightarrow Pm\bar{3}m$ phase transition in CaSiO$_3$ perovskite (Methods, Extended Data Fig. 5) in order to apply our results to Earth's deep mantle. The calculated slope, approximately 15 K GPa^{-1}, is similar to results from previous calculations (about 10 K GPa^{-1})[3] and experiments on the $I4/mcm \rightarrow Pm\bar{3}m$ transition in SrTiO$_3$ (approximately 18.5 K GPa^{-1})[28]. However, it is much larger than, but still within uncertainty of, experimental estimates ($\leq$2 K GPa^{-1})[18,23] for CaSiO$_3$. Assuming our *PT* slope is only shifted in temperature by Ti-incorporation, average mid-ocean-ridge basalt (MORB) Ca-Pv (~Ca[Si$_{0.9}$Ti$_{0.1}$]O$_3$, ignoring other chemical components)[13], should undergo a cubic → tetragonal transformation at mid-mantle depths. In addition, Ca-Pv subducted within slab assemblages, particularly for Ti-rich Ca-Pv compositions, may in fact retain the tetragonal structure throughout the entire mantle at average temperatures (Extended Data Fig. 5). Pure CaSiO$_3$, which is similar to the composition stable in peridotitic and harzburgitic assemblages, is unlikely to become tetragonal in the ambient mantle, but could undergo a cubic–tetragonal transition in cold slab assemblages reaching pressures greater than about 90 GPa.

To evaluate our experimental results in the context of Earth's lower mantle, we have fitted finite-strain equations of state (EoS) for cubic and tetragonal CaSiO$_3$ perovskite, using the thermodynamically self-consistent Mie–Debye–Grüneisen Birch–Murnaghan formalism[29] commonly adopted in mineralogical models[6]. The narrow pressure range of our experiments means additional constraints from literature data are required for extrapolations where velocities remain experimentally unconstrained. All available literature data judged to reliably constrain Ca-Pv volume and/or acoustic velocities at high-*PT* conditions (Supplementary Table 1) were collated and converted to a common pressure scale for joint inversion with new data from this study (see Methods for full fitting procedure). We note that data from recent high-*PT* experiments[20] are not included, owing to inconsistencies within this dataset (Methods). Recovered EoS parameters (see Methods for nomenclature) for tetragonal Ca-Pv at 300 K are $V_0 = 46.10(6)$ Å^3 per formula unit, $K_0 = 224(4)$ GPa, $K_0' = 4$ (fixed), $G_0 = 107(6)$ GPa and $G_0 = 1.4(1)$ (Extended Data Fig. 6a). The EoS for cubic Ca-Pv, fitted using high-temperature data lying above the phase transition calculated by ab initio methods in this study (Fig. 1, Extended Data Fig. 6b, Supplementary Table 2) has the parameters: $V_0 = 45.57(2)$ Å^3, $K_0 = 248(3)$ GPa, $K_0' = 3.6(1)$, $G_0 = 107(1)$ GPa, $G_0' = 1.66$ (fixed, but manually varied by ± 0.22), $q_0 = 1.1(2)$, $\gamma_0 = 1.67(4)$, $\theta_0 = 771(90)$ K and $\eta_{s0} = 3.3$ (fixed to approximately $2\gamma_0$). Incorporation of our newly collected data, compared with only fitting literature data, improves estimations of G_0, γ_0, q_0 and α, owing to the high temperature resolution provided by this study, whereas the dominant constraints on K_0 and K_0' come from the highest-pressure literature data. The narrow pressure range of our velocity measurements mean they mainly constrain the shear modulus, but not its pressure derivative G_0'. However, literature values of G_0 from calculations and experiments[4,5,20] are highly consistent and it can be fixed with some confidence, although we have also varied it manually to assess its effect on extrapolations. Our approach relies on high-precision data from four previous diffraction studies on Ca-Pv at high-*PT* conditions and results in a single EoS that explains all data with no outliers at the 3σ level. This provides the best option to date to investigate Ca-Pv's velocity at deep mantle conditions and offers self-consistent EoS values without apparent reduction in predictive capacity throughout the pressures and temperatures relevant to Earth's mantle.

Our results imply that cubic Ca-Pv's compressional- and shear-velocity profiles are substantially lower than PREM[15] (see Fig. 1), whereas its bulk sound velocity is virtually indistinguishable from PREM[15] (Extended Data Fig. 7a). We observe Ca-Pv's velocities, especially v_S, to be much lower than those predicted from thermodynamic

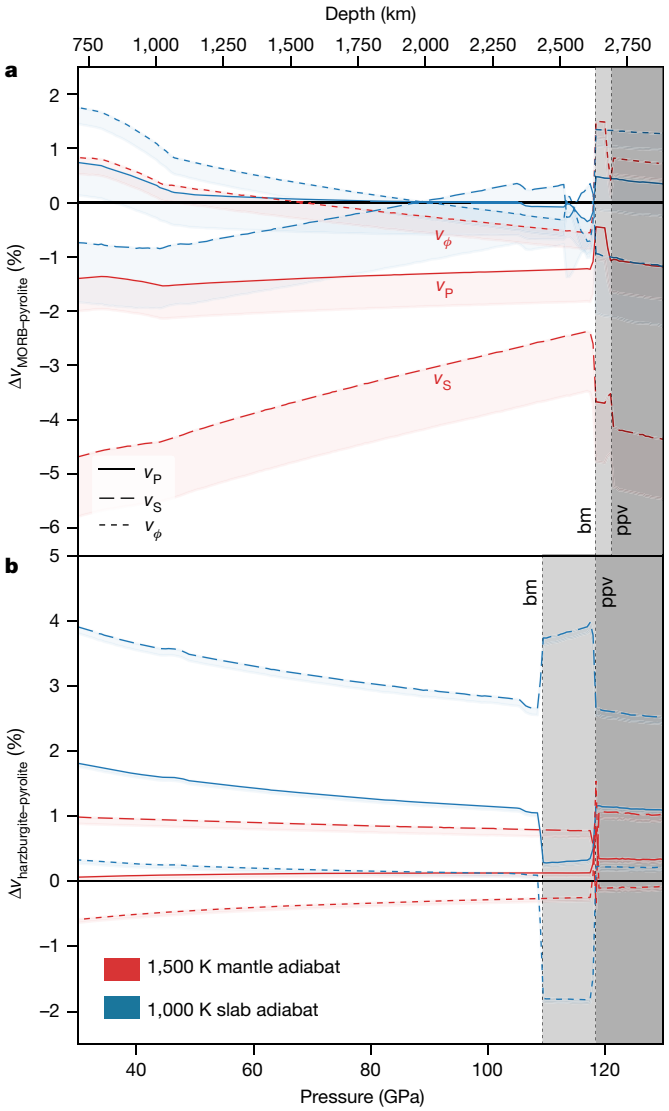

Fig. 4 | Modelled velocity profiles of lower-mantle phase assemblages incorporating Ca-Pv based on this study. a, **b**, Models of MORB (**a**) and harzburgite (**b**) phase assemblages relative to pyrolite throughout the lower mantle. Shown are profiles of compressional velocities, v_P (solid curves), shear velocities, v_S (long dashed curves) and bulk sound velocities, v_ϕ (short-dashed curves); red curves are calculated velocity profiles along a self-consistent 1,500 K adiabat, blue curves are calculated along a 1,000 K adiabat. The coloured lines are the velocity when Ca-Pv is cubic, whereas the lower bound of the coloured shading is indicative of the velocity expected if Ca-Pv forms a tetragonal structure. The vertical dashed lines, and corresponding grey shading, mark the depth of the bridgmanite (bm) to post-perovskite (ppv) transition in each assemblage.

datasets[6], by previous high-temperature calculations[3–5], or high-*PT* experiments[20]. In all cases the discrepancy is almost entirely due to the much lower shear modulus observed in this study. Indeed, it is evident that the shear modulus of Ca-Pv is one of the most critical parameters for accurately modelling the velocity of basaltic assemblages throughout the lower mantle. A full comparison with results from previous studies is provided in Methods. Although titanium-bearing Ca-Pv has not been included in finite-strain modelling, our experimental data demonstrate that titanium-incorporation will increase Ca-Pv's velocity by <1 km s^{-1} for v_P and <0.5 km s^{-1} for v_S for $Ca[Si_{0.6}Ti_{0.4}]O_3$. As MORB-derived Ca-Pv has[13] an approximate composition of $Ca[Si_{0.9}Ti_{0.1}]O_3$, the effect of this titanium content on mantle velocities is expected to be smaller.

Understanding the cause of the LLSVPs remains one of the most prominent questions currently pursued by the deep Earth research community[30]. Identifying whether they are purely thermal anomalies or are thermo-chemical piles of recycled or primordial material could have profound consequences for our understanding of mantle convection. In order to address the question of LLSVP composition, we have incorporated our new cubic Ca-Pv EoS in thermodynamic models (Methods, Fig. 4), extracting the acoustic velocities of recycled basalt and harzburgite assemblages, relative to pyrolite, throughout lower-mantle conditions (we are assuming pyrolite is representative of average lower-mantle composition). Along a 1,500 K mantle adiabat, recycled MORB is predicted to have distinctly lower compressional and shear velocities than pyrolite. This result is in stark contrast with published thermodynamic datasets, in which predicted MORB assemblages have a velocity 1%–2% higher than the average deep mantle[6]. Thus, despite geochemical observations implying a long-lived reservoir of recycled crust in the deep Earth[31] and the high density of MORB[32] favouring its accumulation in the LLSVPs[7], this was previously considered incompatible with observed low velocities unless temperatures were extremely hot[33]. However, our new results now imply LLSVPs are well explained by modest enrichments in recycled oceanic crust, without requiring excess temperature anomalies. Compared to the bulk mantle composition, which is assumed to be a mixture of approximately 80:20 harzburgite:MORB, the v_S anomalies of -1.5% and the v_S/v_P anomaly ratio >2 observed in LLSVPs[30] can be reproduced by a bimodal mixture of MORB + harzburgite consisting 64% MORB at about 100 GPa ($v_P = -0.77\%$) or 48% MORB at about 125 GPa ($v_P = -0.36\%$) if Ca-Pv is cubic. If the LLSVPs are hotter, or if Ca-Pv is tetragonal near the CMB, the proportion of basalt required to explain the LLSVPs would reduce. Our modelling further implies that the above-average velocities that surround the LLSVPs, lying beneath palaeo-subduction zones that are often considered to be slab graveyards[30], could potentially represent depleted assemblages. MORB-enriched LLSVPs, surrounded by depleted material, also provide an explanation for the anti- or non-correlation of v_S and v_ϕ (bulk sound velocity) just above the CMB if post-perovskite is stable[30]. Taken at face value, the predicted properties of $CaSiO_3$ suggest that pyrolite assemblages may be slightly slower than PREM[15]. However, although we are confident that our work robustly demonstrates that subducted MORB assemblages are slow, the amount of Ca-Pv in pyrolite is smaller and so further investigations on the effects of titanium and/or aluminium[32] in Ca-Pv are required to determine whether or not the average velocity of the lower mantle remains compatible with a pyrolitic bulk composition.

The properties of Ca-Pv also provide an explanation for observed seismic reflectors throughout the mid-mantle[2]. In very cold slabs following a 1,000 K adiabat, subducted basalts (if Ca-Pv is cubic) are predicted to have very similar velocities to pyrolitic assemblages on a 1,500 K adiabat and so may be seismically invisible. However, if stranded fragments are thermally equilibrated with surrounding depleted materials, impedance contrasts with magnitudes of up to about $\pm 2.8\%$ will be created, making them seismically visible as reflectors or as slow regions. Alternatively, if Ca-Pv undergoes the cubic–tetragonal phase transition, this may also generate mid-mantle anomalies (Extended Data Fig. 5). Although constraining the depth and compositional dependence of this phase transition requires further studies, it is expected that cold downwelling Ca-Pv is likely to experience the cubic to tetragonal transformation somewhere beyond 1,000 km depth. Stagnant or delaminated materials in the upper–lower mantle boundary region[8] may undergo the tetragonal–cubic transition during thermal equilibration, reducing MORB's shear velocity, which may be the origin of observed mid-mantle reflectors[2].

Online content

Any methods, additional references, Nature Research reporting summaries, source data, extended data, supplementary information, acknowledgements, peer review information; details of author contributions and competing interests; and statements of data and code availability are available at https://doi.org/10.1038/s41586-019-1483-x.

Received: 15 October 2018; Accepted: 6 June 2019;
Published online 15 August 2019.

1. Ritsema, J., Deuss, A., van Heijst, H. J. & Woodhouse, J. H. S40RTS: a degree-40 shear-velocity model for the mantle from new Rayleigh wave dispersion, teleseismic traveltime and normal-mode splitting function measurements. *Geophys. J. Int.* **184**, 1223–1236 (2011).
2. Waszek, L., Schmerr, N. C. & Ballmer, M. D. Global observations of reflectors in the mid-mantle with implications for mantle structure and dynamics. *Nat. Commun.* **9**, 385 (2018).
3. Stixrude, L., Lithgow-Bertelloni, C., Kiefer, B. & Fumagalli, P. Phase stability and shear softening in $CaSiO_3$ perovskite at high pressure. *Phys. Rev. B* **75**, 024108 (2007).
4. Kawai, K. & Tsuchiya, T. Small shear modulus of cubic $CaSiO_3$ perovskite. *Geophys. Res. Lett.* **42**, 2718–2726 (2015).
5. Li, L. et al. Elasticity of $CaSiO_3$ perovskite at high pressure and high temperature. *Phys. Earth Planet. Inter.* **155**, 249–259 (2006).
6. Stixrude, L. & Lithgow-Bertelloni, C. Thermodynamics of mantle minerals—II. Phase equilibria. *Geophys. J. Int.* **184**, 1180–1213 (2011).
7. Ballmer, M. D., Schmerr, N. C., Nakagawa, T. & Ritsema, J. Compositional mantle layering revealed by slab stagnation at 1000-km depth. *Sci. Adv.* **1**, e1500815 (2015).
8. Fukao, Y. & Obayashi, M. Subducted slabs stagnant above, penetrating through, and trapped below the 660 km discontinuity. *J. Geophys. Res.* **118**, 5920–5938 (2013).
9. Stixrude, L. & Lithgow-Bertelloni, C. Geophysics of chemical heterogeneity in the mantle. *Annu. Rev. Earth Planet. Sci.* **40**, 569–595 (2012).
10. Murakami, M., Ohishi, Y., Hirao, N. & Hirose, K. A perovskitic lower mantle inferred from high-pressure, high-temperature sound velocity data. *Nature* **485**, 90–94 (2012).
11. Cottaar, S., Heister, T., Rose, I. & Unterborn, C. BurnMan: a lower mantle mineral physics toolkit. *Geochem. Geophys. Geosyst.* **15**, 1164–1179 (2014).
12. Irifune, T. et al. Iron partitioning and density changes of pyrolite in Earth's lower mantle. *Science* **327**, 193–195 (2010).
13. Ricolleau, A. et al. Phase relations and equation of state of a natural MORB: implications for the density profile of subducted oceanic crust in the Earth's lower mantle. *J. Geophys. Res.* **115**, B08202 (2010).
14. Liu, L.-G. & Ringwood, A. E. Synthesis of a perovskite-type polymorph of $CaSiO_3$. *Earth Planet. Sci. Lett.* **28**, 209–211 (1975).
15. Dziewonski, A. M. & Anderson, D. L. Preliminary reference Earth model. *Phys. Earth Planet. Inter.* **25**, 297–356 (1981).
16. Sinelnikov, Y. D., Chen, G. & Liebermann, R. C. Elasticity of $CaTiO_3$-$CaSiO_3$ perovskites. *Phys. Chem. Miner.* **25**, 515–521 (1998).
17. Kudo, Y. et al. Sound velocity measurements of $CaSiO_3$ perovskite to 133 GPa and implications for lowermost mantle seismic anomalies. *Earth Planet. Sci. Lett.* **349–350**, 1–7 (2012).
18. Komabayashi, T., Hirose, K., Sata, N., Ohishi, Y. & Dubrovinsky, L. S. Phase transition in $CaSiO_3$ perovskite. *Earth Planet. Sci. Lett.* **260**, 564–569 (2007).
19. Chen, H. et al. Crystal structure of $CaSiO_3$ perovskite at 28–62 GPa and 300 K under quasi-hydrostatic stress conditions. *Am. Mineral.* **103**, 462–468 (2018).
20. Gréaux, S. et al. Sound velocity of $CaSiO_3$ perovskite suggests the presence of basaltic crust in the Earth's lower mantle. *Nature* **565**, 218–221 (2019).
21. Thomson, A. R., Walter, M. J., Kohn, S. C. & Brooker, R. A. Slab melting as a barrier to deep carbon subduction. *Nature* **529**, 76–79 (2016).
22. Li, B., Kung, J. & Liebermann, R. C. Modern techniques in measuring elasticity of Earth materials at high pressure and high temperature using ultrasonic interferometry in conjunction with synchrotron X-radiation in multi-anvil apparatus. *Phys. Earth Planet. Inter.* **143**, 559–574 (2004).
23. Kurashina, T., Hirose, K., Ono, S., Sata, N. & Ohishi, Y. Phase transition in Al-bearing $CaSiO_3$ perovskite: implications for seismic discontinuities in the lower mantle. *Phys. Earth Planet. Inter.* **145**, 67–74 (2004).
24. Yashima, M. & Ali, R. Structural phase transition and octahedral tilting in the calcium titanate perovskite $CaTiO_3$. *Solid State Ion.* **180**, 120–126 (2009).
25. Salje, E. K. H. et al. Elastic excitations in $BaTiO_3$ single crystals and ceramics: mobile domain boundaries and polar nanoregions observed by resonant ultrasonic spectroscopy. *Phys. Rev. B* **87**, 014106 (2013).
26. Perks, N. J., Zhang, Z., Harrison, R. J. & Carpenter, M. A. Strain relaxation mechanisms of elastic softening and twin wall freezing associated with structural phase transitions in (Ca,Sr)TiO_3 perovskites. *J. Phys. Condens. Matter* **26**, 505402 (2014).
27. Liu, Z. et al. Elastic wave velocity of polycrystalline $Mj_{80}Py_{20}$ garnet to 21 GPa and 2,000 K. *Phys. Chem. Miner.* **42**, 213–222 (2015).
28. Guennou, M., Bouvier, P., Kreisel, J. & Machon, D. Pressure-temperature phase diagram of $SrTiO_3$ up to 53 GPa. *Phys. Rev. B* **81**, 054115 (2010).
29. Stixrude, L. & Lithgow-Bertelloni, C. Thermodynamics of mantle minerals—I. Physical properties. *Geophys. J. Int.* **162**, 610–632 (2005).
30. Garnero, E. J., McNamara, A. K. & Shim, S.-H. Continent-sized anomalous zones with low seismic velocity at the base of Earth's mantle. *Nat. Geosci.* **9**, 481–489 (2016).
31. Hofmann, A. W. Mantle geochemistry: the message from oceanic volcanism. *Nature* **385**, 219–229 (1997).
32. Hirose, K., Fei, Y., Ma, Y. & Mao, H.-K. The fate of subducted basaltic crust in the Earth's lower mantle. *Nature* **397**, 53–56 (1999).
33. Deschamps, F., Cobden, L. & Tackley, P. J. The primitive nature of large low shear-wave velocity provinces. *Earth Planet. Sci. Lett.* **349–350**, 198–208 (2012).

METHODS

Starting materials. Starting materials of $CaSiO_3$ and $Ca[Si_{0.6}Ti_{0.4}]O_3$ compositions were initially prepared by grinding appropriate quantities of high purity $CaCO_3$, SiO_2 and TiO_2 together in an agate mortar before decarbonation and, in the case of $CaSiO_3$, sintering into crystalline wollastonite, or in the case of $Ca[Si_{0.6}Ti_{0.4}]O_3$, fusing to a glass. All materials were analysed with scanning electron microscopy with energy dispersive X-ray spectroscopy (SEM EDS) to check composition, and the $CaSiO_3$ was confirmed as pure wollastonite using X-ray powder diffraction ($\lambda = 1.7904$ Å). Ultrasonic experiments require fully dense cylindrical samples with parallel polished faces and an aspect ratio (length/diameter) <2. Thus, the $Ca[Si_{0.6}Ti_{0.4}]O_3$ glass was hot-pressed into Ca-Pv at ~14 GPa and 1,400 °C using a 10/5 multi anvil assembly, and the recovered products manipulated into suitable forms for subsequent acoustic experiments. Since $CaSiO_3$ perovskite is unrecoverable, undergoing a decomposition to amorphous 'glass' with pervasive fracturing at room temperature, it is not possible to prepare a similar sample of the endmember perovskite composition. Instead samples of walstromite were prepared, which is the highest-pressure recoverable polymorph of $CaSiO_3$, by sintering at ~7 GPa and 1,300 °C using a 14/8 multi-anvil assembly.

Diffraction and ultrasonic experimental methods. X-ray diffraction and pulse-echo ultrasonic experiments were performed on beamline ID06-LVP of the ESRF synchrotron, where modified 10/5 multi anvil assemblies were employed to allow simultaneous measurement of sample diffraction, length and acoustic velocity. Samples were placed adjacent to a polished polycrystalline alumina buffer rod on one side that reached the cube to which the ultrasonic transducer was attached, and an MgO + NaCl mixture serving as soft backing and (for the NaCl) as a pressure marker on the other. Thin Au foils were placed at each end of the sample to allow sample length to be observed with radiographic imaging, and also between the cube and buffer rod to assist with acoustic coupling. This acoustic column was encapsulated in a crushable MgO sleeve, and a Re or TiB_2 + BN furnace, which was contained within ZrO_2 insulation and a Cr:MgO octahedral pressure medium. A W-Re thermocouple was used, inserted from the opposite end of the cell assembly in an MgO sleeve to monitor temperature adjacent to the sample throughout the experiments (Extended Data Fig. 8c).

Along the path of the X-ray beam, the normal ceramic materials were replaced by high transparency amorphous SiBCN(O) windows. Monochromatic synchrotron X-rays ($\lambda = 0.22542$ Å or 0.2296 Å) were used to collect diffraction patterns from the sample and pressure markers throughout experiments using two different detectors available at ID06. In all experiments the standard Detection Technology X-scan 1D detector[34], which has a fixed 10-Hz integration rate, was used to record diffraction patterns every 3.2 s (continuous, with 32× rebin) and every 32 s (on increasing and decreasing pressure). Throughout one experiment on $CaSiO_3$ an additional Pixirad-8 detector was employed to assist with the identification of weak superlattice reflections from the sample. X-ray sample–detector geometry was calibrated using Si and/or LaB_6 NIST standards, and the collected diffraction patterns were suitably reduced and analysed using Fit2d[35] software. Rietveld refinement of selected diffraction patterns was performed using the GSAS software package[36] (Supplementary Tables 3 and 4). Experimental unit-cell volumes were also calculated and used to determine the pressure–volume–temperature (*PVT*) EoS by fitting the position and width of individual diffraction lines from the Ca-Pv samples and pressure markers. In this case Ca-Pv volumes are determined using the average volume calculated from the 200, 310, 321 and 222 diffraction peaks of the sample, while the volumes of NaCl and Au were determined using their 220 and 310 peaks, respectively (Supplementary Table 5).

Samples were compressed to target load and initially heated to $T > 1{,}000$ K to remove stress in the sample that might affect acoustic measurements. In the experiments on $CaSiO_3$, the starting material of walstromite was converted into Ca-Pv by annealing at constant load (initial pressure ~14 GPa) and 1,200–1,500 K for a period of 2–4 h, until all signs of walstromite diffraction peaks were lost. Pressure throughout the experiments was determined from the unit-cell volumes of NaCl-B1 and/or Au using cross-calibrated high-temperature EoSs[37], and the sample length was measured using the standard imaging system installed on ID06-LVP. Sample lengths determined with X-ray imaging were checked against those measured before and after (in the case of $Ca[Si_{0.6}Ti_{0.4}]O_3$) experiments with a digital gauge (1 μm accuracy). Uncertainties in sample lengths are estimated from images as ±5 pixels, corresponding to ±5.4 μm (<2% overall sample length), and it is this uncertainty that produces the reported uncertainties in velocities (Supplementary Table 6 and Fig. 3). Alongside ultrasonic measurements accompanied by diffraction and imaging, the crystallographic evolution of the samples was specifically investigated using continuous diffraction collected during constant rate cooling ramps (25–50 K min^{-1}) for $CaSiO_3$ and $Ca[Si_{0.6}Ti_{0.4}]O_3$ samples without collecting ultrasonic data.

Acoustic signals, always collected after sample annealing at high *T*, were transmitted into and received from the sample assembly using a 10° Y-cut dual mode $LiNbO_3$ piezoelectric transducer that was fixed to the corner of the 'acoustic cube' opposite to the sample using Epo-tek 353ND epoxy. A signal generator (Tektronix AFG3101C or Keysight 33622A) was used to create acoustic pulses composed of three consecutive periods of sine waves with 30–60 MHz frequency and 2.5 or 5 V peak-to-peak amplitude, which were passed to the transducer and oscilloscope. The resonant frequencies of v_P and v_S from the transducer crystal were ~50 MHz and ~30 MHz, respectively. Received echoes were measured using the same oscilloscope (Tektronix DPO5140 or Keysight DSOS104A) to record the delay between arrival times of compressional- and shear-wave signals at a rate of either 2.5×10^9 or 5×10^9 samples per s. In later experiments, a directional bridge (Keysight 86205A), preamplifier (LA020-OS) on the return signal, and external trigger (trigger rate 2 kHz) were variously used, as the system was continuously developed throughout this study. Collection times of individual acoustic spectra ranged from 5 s to 300 s with the various systems employed throughout this study. Two-way travel times of ultrasonic arrivals were converted into sample velocities using the 'pulse-echo overlap method' (for reflections from the near and far ends of the sample), which was implemented by maximizing absolute values of signal cross-correlation and sample lengths measured with X-ray imaging. Predicted reflection coefficients for both interfaces (based on $R = (Z_2 - Z_1)/(Z_1 + Z_2)$, with $Z_i = \rho_i v_i$) are both negative (approximately −0.025 and −0.25 for Al_2O_3–Ca-Pv and Ca-Pv–NaCl+MgO respectively) at the *PT* conditions of the experiments, suggesting that no phase shift is expected in the acoustic signals. The lack of observed phase shifts and measured pulse/echo amplitude ratios were found to be consistent with these expectations, which provides assurance that the phase of acoustic arrivals has been correctly identified. Measured velocities are reported in Supplementary Table 6. It should be noted that two independent experiments were performed to measure the velocity of $CaSiO_3$ samples (which agree within uncertainty for v_P) during separate visits to the ESRF, one employing a Re and the other a TiB_2:BN furnace. In the second of these experiments on $CaSiO_3$, the shear-wave signal from the sample was not observable above noise levels and thus the shear-wave velocity was not determined. These are labelled "runa" and "runb" in Fig. 3. Additionally, the ultrasonic data reported for $Ca[Si_{0.6}Ti_{0.4}]O_3$ above 975 K were collected on heating after annealing, while data below 975 K were subsequently collected upon cooling the sample. This results in a small pressure difference between the two sets of measurements and explains the discontinuity in Fig. 3.

Structure determination. Refined diffraction data from experiments on $CaSiO_3$ are consistent with a cubic crystal structure for Ca-Pv at high temperatures. All observed diffraction peaks have approximately constant widths at half maximum intensity, in line with expectations from the diffractometer geometry, and all observed diffraction peaks could be attributed to diffraction from the sample (in space group $Pm\bar{3}m$) or other cell components (MgO, Au, NaCl, TiB_2, Al_2O_3). Upon cooling, the diffraction peaks from the sample undergo substantial nonlinear *hkl*-dependent broadening below ~420 K (Fig. 2 and Extended Data Fig. 1e). Similarly to previous studies[18,23], we interpret this observation as the result of a cubic–tetragonal transition in $CaSiO_3$. Close inspection of diffraction data from the Pixirad-8 detector, which was employed during one experiment, reveals that weak superlattice peaks from $CaSiO_3$ (otherwise unexplained by other cell components) appear in data collected at 373 K and 300 K (Extended Data Fig. 2). The strongest of these is observed at $2\theta \approx 6.1°$ (indexed as 3/2 1/2 1/2 on the cubic sublattice) but additional peaks can also be observed at 2θ values of 8.05° (3/2 3/2 1/2), 12.1° (5/2 3/2 3/2) and 13.2° 2θ (5/2 5/2 1/2) (*d*-spacings of about 2.11, 1.61, 1.07 and 0.98 Å, respectively). Assuming that $CaSiO_3$'s initial distortion upon cooling is to a tetragonal phase, there are three likely candidate structures, with space groups *I*4/*mcm*, *P*4/*mbm* and *I*4/*mmm*. The predicted superlattice peak positions for the structure with *I*4/*mcm* symmetry exactly match the observed superlattice peak positions, explaining all four observed peaks, while $CaSiO_3$ structures with space groups *P*4/*mbm* or *I*4/*mmm* cannot account for the observations (Extended Data Fig. 2) as these should both produce many additional superlattice peaks (for example, those indexed as 1/2 0 3/2, 3/2 1/2 1, 1/2 0 5/2, 5/2 1 1/2 and so on, on the basis of the cubic subcell) that are not observed. Given that there are no additional unexplained diffraction peaks, the knowledge that the most obvious superlattice peak at $2\theta \approx 6.1°$ should indeed be the strongest in *I*4/*mcm* and that the same transition ($Pm\bar{3}m$ to *I*4/*mcm*) occurs[24] in $CaTiO_3$, we see no reason to doubt that the structure of $CaSiO_3$ at room temperature and at about 12 GPa is tetragonal with space group *I*4/*mcm*.

The observed behaviour of $Ca[Si_{0.6}Ti_{0.4}]O_3$ is similar to that of $CaSiO_3$, but the intensities of the superlattice peaks are much greater and the material is recoverable to ambient conditions. Diffraction patterns collected from the starting material $Ca[Si_{0.6}Ti_{0.4}]O_3$ (measured alongside LaB_6 as a calibrant at 300 K, Extended Data Fig. 3a) allow identification of superlattice peaks with odd and even Miller indices, which requires positive and negative octahedral tilts[38]. Thus, the highest possible symmetry of $Ca[Si_{0.6}Ti_{0.4}]O_3$ at ambient conditions is orthorhombic. Refining the diffraction data in three likely space groups (*Pbnm*, *Cmcm* and $P4_2/nmc$) demonstrates that both *Pbnm* and *Cmcm* can explain the patterns equally well, and so it is concluded that ambient $Ca[Si_{0.6}Ti_{0.4}]O_3$ is orthorhombic (actually monoclinic

when B-cation ordered, see below). We choose to assume the space group is *Pbnm*, as this is the known[24] structure of $CaTiO_3$. Since no phase transition is observed during decompression, the room-temperature structure at high pressure is also assumed to be *Pbnm*, or its B-cation ordered equivalent ($P2_1/c$). At high-*PT* conditions, $Ca[Si_{0.6}Ti_{0.4}]O_3$ is observed to undergo two structural phase transitions (Extended Data Fig. 4). At the highest temperatures, the diffraction pattern is well explained if the sample takes a cubic $Fm\bar{3}m$ structure. With respect to the cubic form of $CaSiO_3$, this has a double unit-cell edge length and partial B-cation ordering (assumed to follow a 1:1 B-site scheme[39]) of Si and Ti, a common ordering scheme in perovskites. On cooling, the $Ca[Si_{0.6}Ti_{0.4}]O_3$ first distorts to a tetragonal structure marked by the appearance of the same set of superlattice peaks that were observed for $CaSiO_3$. Since the cubic Ti-bearing Ca-Pv is B-cation ordered, it is assumed the tetragonal phase maintains this B-cation ordering, making the space group of the tetragonal phase $I4/m$. Continued cooling sees distortion into the room-temperature phase, which is assigned to be monoclinic $P2_1/c$ (the B-cation ordered variant of *Pbnm*). Between the tetragonal and monoclinic structures there is a temperature interval where the diffraction pattern cannot be indexed using a single structure model, and it is observed that this temperature interval corresponds to very low acoustic velocities. This may be indicative of a first-order phase transition, which further implies a preference for *Pbnm* or $P2_1/c$ over *Cmcm* or $C2/c$, based on the analysis of Glazer[38]. Alternative explanations for this behaviour are a temperature interval of phase coexistence, an additional perovskite structure or some other unexplained phenomena. Similar observations have been made for $CaTiO_3$ (ref. [40]), where there is a small temperature interval between the $I4/mcm$ and *Pbnm* structures where the behaviour is attributed to an interval of phase coexistence caused by the kinetic energy barrier of the first-order phase transition. A more detailed discussion of the crystallographic behaviour of Ca-Pv samples lies beyond the scope of the current study.

Ab initio calculations and the slope of the Ca-Pv tetragonal–cubic transition. Ab initio calculations were performed to constrain the conditions of the tetragonal–cubic transition of Ca-Pv throughout the Earth's mantle. All simulations were carried out with the density-functional-theory (DFT) code VASP[41] using the projector-augmented-wave (PAW) method[42] and the PBE formulation of the generalized gradient approximation[43]. Molecular dynamics (MD) calculations used the Nosé thermostat and were run at the gamma point with a cut-off of 600 eV and relaxed to within 10^{-5} eV and all forces to below 0.03 eV $Å^{-1}$. All computational runs were at least 20 ps in duration, although all measured properties were observed to be fully converged by 12 ps. Phonon calculations for calculating the force-constant matrix used an energy cut-off of 850 eV, $4 \times 4 \times 4$ K points and were relaxed to 10^{-8} eV with forces below 0.01 eV $Å^{-1}$. The finite difference method was used and processing was done with the phonopy code[44]. Ca atom semicore 3*s* and 3*p* states were treated as valence states. All static and molecular dynamics runs were spin-polarized and $CaSiO_3$ was always simulated with an 80-atom simulation box, based on a $2 \times 2 \times 4$ assemblage of the perovskite cubic aristotype cell containing 5 atoms. For cubic perovskite calculations, the subcells from which the simulation box was constructed were fixed to have a geometry of $a = b = c$, whereas for tetragonal $CaSiO_3$ the simulation geometry for was fixed such that $a = b \neq c$. Details of simulation cell volumes are provided in Supplementary Table 7. In each case the final stress on the crystal was correct to within 0.04 GPa for static calculations and to within 0.1 GPa (on average) for MD calculations. After the geometries were imposed at each *PT* condition the atoms were allowed to relax (within constraints maintaining cubic or tetragonal structure), before the simulations used to obtain free energies.

Free energy differences were calculated at 25, 75 and 125 GPa and at 0, 1,000, 2,000 and 3,000 K. To calculate the free energy of each state, we used an approximation of the thermodynamic integration represented by equation (1):

$$F - F_0 \cong \langle U - U_0 \rangle_0 + \frac{1}{2k_B T} \langle [U - U_0 - \langle U - U_0 \rangle_0]^2 \rangle_0 \quad (1)$$

where subscript 0 represents the reference state and other terms the state of interest. For a reference state we used a harmonic oscillator with free energy defined by equation (2):

$$U_0 = U + \sum_i \frac{p_i^2}{2m_i} + \frac{1}{2} \sum_{ij} u_i \Phi_{ij} u_j \quad (2)$$

where u_x is a displacement vector and Φ_{ij} is the force constant matrix. As cubic $CaSiO_3$ is unstable at low temperatures it has negative frequencies in its phonon spectrum, and the free energy cannot be calculated directly from its force constant matrix. Thus, we applied a small correction to eliminate these imaginary frequencies and allow free energy calculations. The correction matrix (Φ_{ij}^c) is formed by multiplying the onsite terms in the force constant matrix by kI (where I is the identity matrix and k is the smallest constant that eliminates all imaginary frequencies). The correction procedure then subtracts the correction matrix from the true force constant matrix ($\Phi_{ij} - \Phi_{ij}^c$) to produce a modified force constant matrix Φ_{ij}^*, which is used in equation (2). While this procedure cannot predict the correct absolute free energies, it should accurately calculate the free energy difference relative to a reference state that has had the same correction procedure applied. This procedure is repeated for both cubic (cub) and tetragonal (tet) $CaSiO_3$ structures at each *PT* condition, and finally the free energy difference between these states is determined using equation (3):

$$\Delta G_{\mathrm{cub-tet}} = \Delta G^{\mathrm{cub}}_{\mathrm{final-ref}} + G^{\mathrm{cub}}_{\mathrm{ref}} - (\Delta G^{\mathrm{tet}}_{\mathrm{final-ref}} + G^{\mathrm{tet}}_{\mathrm{ref}}) \quad (3)$$

The final calculated free energy differences between cubic and tetragonal states are reported in Supplementary Table 7. All free energy differences are subject to uncertainties, which are assumed to be 1 meV per formula unit (f.u.) at 0 K, and calculated to be <10 meV per f.u. at high temperatures, from the statistical uncertainty in the simulation energies. These uncertainties were incorporated in the weighted least-squares regression used to determine the conditions and uncertainty of the tetragonal–cubic transformation at each pressure (25, 75 and 125 GPa), as plotted in Extended Data Fig. 5.

Calcium perovskite EoS. *PVT*-velocity data from experiments in this, and literature, studies were combined to allow fitting of an EoS for both tetragonal and cubic $CaSiO_3$ perovskite. The pressures of all reported literature data were converted to a single pressure scale, which was used for pressure measurement in this study[37]. This ensures consistency of the pressure scale used throughout the dataset. The fitted EoS for tetragonal Ca-Pv uses only room-temperature data and all literature data collected on samples compressed in diamond anvil cells without use of a pressure-transmitting medium were discarded (small symbols in Extended Data Fig. 6a). The remaining *PV* data[19,45], including one-twentieth of the data collected during room-temperature decompression in this study before amorphization, were fitted to a second-order Birch–Murnaghan EoS for V_0 (volume at ambient conditions) and K_{T0} (isothermal bulk modulus at ambient conditions) using the BurnMan software package[11] (Supplementary Table 2). Only one-twentieth of the current data were used, to ensure that the final fitted model was not overly biased to the data collected in this study. Subsequently, room-temperature velocity measurements from this study were combined with literature data[17,20] to fit the shear modulus (G_0) and its pressure derivative (G_0') within the SLB2005[29] formalism, as provided in BurnMan. As the EoS is only calibrated at room temperature, estimates of velocity reductions for tetragonal Ca-Pv in Fig. 4 are qualitatively based on the magnitude of reductions observed in measurements from $Ca[Si_{0.6}Ti_{0.4}]O_3$, taken ~100 K below the phase transition, in this study, and are not calculated by using the tetragonal Ca-Pv EoS.

The EoS for cubic Ca-Pv (Supplementary Table 2) also fits data from this study and the literature[45–48] using the SLB2005[29] Mie–Grüneisen–Debye Birch–Murnaghan formalism implemented in BurnMan[11]. Only data falling above the calculated *P*–*T* curve of the tetragonal–cubic phase transition (Extended Data Fig. 5) were used, to ensure that no data from tetragonal-structured Ca-Pv were included (Extended Data Fig. 6b). *PVT* data were first used to fit V_0, K_0, K_0' (pressure derivative of the bulk modulus) and γ_0 (Grüneisen parameter). Subsequently, the complete *PVT*-velocity dataset was re-fitted for G_0, γ_0, q_0 (temperature dependence of the bulk moduli) and θ (Debye temperature) (V_0, K_{T0}, K_0' were unchanged) assuming $G_0' = 1.66$. G_0' was fixed to literature values[4,5,20] due to the small pressure range of velocity measurements in this study, a value consistent with literature scaling rules[29]. η_{s0} (temperature dependence of the shear moduli) was fixed at 3.3, based on the scaling rules ($\eta_{s0}/\gamma_0 \approx 2$) from Stixrude[29]. Alternatively, η_{s0} can also be a fitted parameter (Supplementary Table 2). However, since this second fit (with variable η_{s0}) results in slightly lower extrapolated velocities without drastically altering subsequent interpretation, fixing η_{s0} was viewed as a more conservative way to evaluate the influence of Ca-Pv. It is noted that the uncertainty bounds plotted in Fig. 1 account for variation of G_0' from 1.44 to 1.88 and Ca-Pv remains slower than PREM and ab initio estimates throughout this entire range. We recognize that, without using literature data, extrapolation throughout the mantle pressure range would be completely unrealistic—and are beholden to accepting the reliability of literature data; however we note that four previous studies on Ca-Pv at high-*PT* conditions, after conversion to a common pressure scale, can be combined and fitted to a single EoS without any outliers at the 3σ level. Readers are referred to Stixrude[29] for details of the SLB2005 formalism.

Thermodynamic modelling. The acoustic properties of MORB, peridotitic and harzburgitic assemblages have been calculated using the MMA-EoS software package[49]. Simplified bulk compositions for MORB (NCFMAS) and pyrolite/harzburgite (CFMAS) from the software's library were employed as typical of these assemblages throughout the lower mantle. Equilibrium phase assemblages were calculated across a 0.5 GPa by 25 K grid throughout the mantle for each system, and the elastic properties of each assemblage extracted along self-consistent adiabatic temperature profiles beginning at 1,000 K (representing slabs) and 1,500 K (average

mantle), which are plotted relative to one another in Fig. 4. The latter temperature profile is very similar to the geotherm of Brown and Shankland[50]. Thermoelastic data from Stixrude[6] were used for all phases except for the $MgSiO_3$ bridgmanite endmember (which used updated properties from Zhang[51]) and calcium perovskite which is defined in this study. We note that this database provides a somewhat simplified view of lower-mantle materials, as it does not include the effects of iron spin-transitions in ferropericlase or bridgmanite[52,53] or the ferroelastic phase transitions of stishovite[54]. We also highlight that the modelling in this study inherently assumes that the database from Stixrude et al.[6] accurately describes the elastic properties of all other lower-mantle phases.

Comparison with previous studies. As noted in the main text, the acoustic velocities of $CaSiO_3$ observed in this study are observed to be substantially slower than predicted in computational studies[3–5] and mineralogical databases[6]. Additionally, they are also observed to be slower than those found in previous high-*PT* experiments[20]. Although we cannot fully explain the reasons for all disagreements, we discuss some observations that may partially explain the mismatches. Database elastic properties[6] predict the fastest Ca-Pv velocities plotted in Fig. 1, and it is these that the Earth science community currently uses when interpreting seismic observations. Results from the two ab initio molecular dynamics (AIMD) computational studies[4,5] and experiments[20] all predict that Ca-Pv should be equal to (v_P) or slower (v_S) than PREM. If any of these results were adopted in mineralogical databases, slow velocity anomalies in the lower mantle could be interpreted as they are in this study, an indicator of MORB enrichment, although not to the extent implied here. We note that the other pseudo-high-temperature calculations[3] do not provide enough information in the paper to calculate acoustic properties at elevated temperatures, since the temperature effect on density is unquantified in the original publication.

Comparing our work in detail, first with previous experimental results, it is observed that the room-temperature velocities measured in this study are in excellent agreement with those of Gréaux et al.[20], Kudo et al.[17] and extrapolated estimates from Sinelnikov et al.[16]. Room-temperature velocities measured by Li et al.[22] are somewhat faster, but given the lack of details provided in that paper, which is a technical review, they are not considered further. It is observed that our reported velocities disagree with previous experimental data only at high temperature[20], appearing to diverge as the reported temperature increases. Given the similarities in methodology, it is most likely that temperature uncertainties are responsible for the differences. Based on published details, we believe Gréaux et al.[20] employed samples of 0.93–1.3 mm length (Fig. 2 and Extended Data Fig. 3 of Gréaux et al.[20]) and 2 mm diameter, with the thermocouple inserted radially (through the furnace) adjacent to the far end of the pressure marker that in their experiments is initially ~1 mm in length. This arrangement is substantially larger than the samples used in this study, which were 0.4–0.6 mm in length and 1.5 mm diameter, with the thermocouple inserted axially to the end of the pressure marker that had a maximum length of 0.5 mm. Thus, the maximum distance between the thermocouple and far end of the sample in our study is 1.1 mm, probably 0.75 mm at high pressure, approximately half of the equivalent distance in Gréaux et al.[20] (probably $\geq$1.5 mm at pressure). Additionally, by inserting the thermocouple axially we ensure the sample is centred in the cell at high pressure, whereas it is unclear whether or not this would be the case with a radial thermocouple, which could also have been affected by contacting the metal furnace. Given that, at 12–22 GPa, the sample column is likely to be 4–5 mm in length, the differences in geometry might have a very large influence on the temperature conditions experienced by samples. Thermal modelling using finite element code[55] suggests that the thermal gradient across samples at a measured temperature of 1,200 °C in our set-up should be <50–60 °C, with the measured temperature likely to be lower than peak conditions. By contrast, assuming the thermocouple is centred (as drawn by Gréaux et al.[20]) and measuring 1,200 °C, the range of temperatures experienced by a sample of 1 mm length × 2 mm diameter could very conceivably be 250–300 °C lower than that measured by the thermocouple. This implies that the apparent effect of temperature on velocities should be smaller using the geometry of Gréaux et al.[20], since portions of samples would be colder than believed. This is consistent with the observed differences in velocities between Gréaux et al.[20] and the present study, where the offset in reported velocities increases at higher temperatures. Additional evidence that the high-temperature velocities reported by Gréaux et al.[20] might be less reliable is demonstrated by comparing the independent estimates of bulk sound velocity (v_ϕ) expected for Ca-Pv from *PT*-volume systematics and acoustic measurements ($v_\phi = \sqrt{v_P^2 - \frac{4}{3}v_S^2} = \sqrt{K_S/\rho}$, where K_S is a function of K_{0T}, K', γ and α). We observe that the bulk sound velocity extracted from ultrasonic measurements in Gréaux et al.[20] are inconsistent with velocity extracted via a *PVT* EoS using their diffraction data (Extended Data Fig. 9). Ultrasonic v_ϕ values from Gréaux et al.[20] are offset to slower values and have a much larger reduction at high temperature than those predicted via an EoS fitted using density from their or compiled literature data[45–48]. In contrast, bulk sound velocities from data in this study are consistent with literature *PVT* EoS fitting. This inconsistency suggests that velocities reported in Gréaux et al.[20] might be affected by large temperature gradients.

Considering calculated properties of Ca-Pv, we observe that the database values[3] best reproduce the adiabatic bulk moduli of Ca-Pv (compared with that from the global experimental dataset, Extended Data Fig. 7b), while the two AIMD studies[4,5] predict a larger pressure effect on K_S than is observed in the experimental data. Other calculations employing mean-field and Landau theory[3] suggest that shear softening should be associated with the cubic–tetragonal transition, while AIMD approaches do not include this behaviour[4,5]. However, it has been proposed[4] that the choice of cubic unit cell employed by Stixrude et al.[3] prevented rotations of the SiO_6 octahedra, leading to an anomalously large shear modulus and explaining the high velocities. The AIMD results of Kawai and Tsuchiya[4] should be preferred to those from Li et al.[5], as the latter may not have fully converged and insufficiently sampled the Brillouin zone[4] to accurately predict crystal structure. Despite differences, all three computational studies predict a larger shear modulus than required by experimental data (from both this and previous studies[16,17]). It is possible that this discrepancy results from the strong anharmonicity of Ca-Pv, implying that extremely expensive calculations may be required to accurately describe Ca-Pv's elasticity using computational methods. Indeed, common first-principles methods inaccurately predict the elasticity or phonon temperature dependence of other anharmonic cubic perovskites ($SrTiO_3$, $BaTiO_3$ and $PbTiO_3$)[56–58]. DFT calculations that under/overestimate the cubic lattice parameter consistently over/underestimate the shear modulus in the opposite sense[56–58]. The local-density approximation, used by Kawai and Tsuchiya[4], has been observed to overestimate the shear modulus (c_{44}) of $SrTiO_3$, $BaTiO_3$ and $PbTiO_3$ by 8–18% for ~1% underestimate of unit cell volume[56]. Since we observe a similar mismatch between the volume of cubic $CaSiO_3$ at adiabatic conditions based on our fit to experimental data and the results of Kawai and Tsuchiya[4], which are ~1% too small, we expect that Ca-Pv's velocities predicted by Kawai and Tsuchiya[4] will be somewhat overestimated. However, it is unlikely this effect can explain the entirety of the disagreement between previous calculations and our experimental results. A second contributor to the mismatch could be the presence of crystallographic preferred orientation (CPO) within experimental samples, especially if the alignment of an acoustically slow direction coincided with the ultrasonic path. However, since refinement of X-ray diffraction patterns did not require CPO in the cubic $CaSiO_3$ field to fit the data, this seems unlikely. Additionally, the way crystal symmetry is stipulated and the lack of grain boundaries/defects in calculations may frustrate some phonon modes, further explaining the offset from experimental values. Finally, we re-iterate that the finite-strain model we report in this paper is subject to very large extrapolation from the experimental *PT* conditions (~12 GPa, 300–1,500 K) to those of the mantle (<130 GPa, 1,500–3,000 K) and we acknowledge additional experiments are now required to investigate in better detail the changes of Ca-Pv velocity at more extreme conditions.

Data availability

Raw data were collected at the European Synchrotron Radiation Facility in Grenoble and are available from https://doi.org/10.5285/6db95d87-365f-4018-abec-00e96e8fcf8d. Derived data from this study, which includes source data for Figs. 2 and 3 and Extended Data Figs. 1 and 5, are provided in the Supplementary Tables.

34. Guignard, J. & Crichton, W. A. The large volume press facility at ID06 beamline of the European synchrotron radiation facility as a high pressure-high temperature deformation apparatus. *Rev. Sci. Instrum.* **86**, 085112 (2015).
35. Hammersley, A. P. FIT2D: An Introduction and Overview. Technical Report ESRF-97-HA-02T (ESRF, 1997).
36. Larson, A. C. & von Dreele, R. B. General Structure Analysis System (GSAS). Los Alamos National Laboratory Report LAUR 86–748 (LANL, 2004).
37. Dorogokupets, P. I., Dewaele, A. & Dewaele, A. Equations of state of MgO, Au, Pt, NaCl-B1, and NaCl-B2: internally consistent high-temperature pressure scales. *High Press. Res.* **27**, 431–446 (2007).
38. Glazer, A. M. The classification of tilted octahedra in perovskites. *Acta Crystallogr. B* **28**, 3384–3392 (1972).
39. Woodward, P. M. Octahedral tilting in perovskites. I. Geometrical considerations. *Acta Crystallogr. A* **53**, 32–43 (1997).
40. Wood, I. G., Price, G. D., Street, J. N. & Knight, K. S. Equation of State and Structural Phase Transitions in CaTiO3 Perovskite. ISIS Experimental Report RB7844 (ISIS, 1997).
41. Kresse, G. & Furthmüller, J. Efficient iterative schemes for *ab initio* total-energy calculations using a plane-wave basis set. *Phys. Rev. B* **54**, 11169–11186 (1996).
42. Kresse, G. & Joubert, D. From ultrasoft pseudopotentials to the projector augmented-wave method. *Phys. Rev. B* **59**, 1758–1775 (1999).
43. Perdew, J. P. et al. Restoring the density-gradient expansion for exchange in solids and surfaces. *Phys. Rev. Lett.* **100**, 136406 (2008).
44. Togo, A. & Tanaka, I. First principles phonon calculations in materials science. *Scr. Mater.* **108**, 1–5 (2015).

45. Shim, S.-H., Duffy, T. S. & Shen, G. The stability and P–V–T equation of state of $CaSiO_3$ perovskite in the Earth's lower mantle. *J. Geophys. Res.* **105**, 25955–25968 (2000).
46. Sun, N. et al. Confirming a pyrolitic lower mantle using self-consistent pressure scales and new constraints on $CaSiO_3$ perovskite. *J. Geophys. Res.* **121**, 4876–4894 (2016).
47. Wang, Y., Weidner, D. J. & Guyot, F. Thermal equation of state of $CaSiO_3$ perovskite. *J. Geophys. Res.* **101**, 661–672 (1996).
48. Noguchi, M., Komabayashi, T., Hirose, K. & Ohishi, Y. High-temperature compression experiments of $CaSiO_3$ perovskite to lowermost mantle conditions and its thermal equation of state. *Phys. Chem. Miner.* **40**, 81–91 (2013).
49. Chust, T. C., Steinle-Neumann, G., Dolejš, D., Schuberth, B. S. A. & Bunge, H. P. MMA-EoS: a computational framework for mineralogical thermodynamics. *J. Geophys. Res.* **122**, 9881–9920 (2017).
50. Brown, J. M. & Shankland, T. J. Thermodynamic parameters in the Earth as determined from seismic profiles. *Geophys. J. R. Astron. Soc.* **66**, 579–596 (1981).
51. Zhang, Z., Stixrude, L. & Brodholt, J. Elastic properties of $MgSiO_3$-perovskite under lower mantle conditions and the composition of the deep Earth. *Earth Planet. Sci. Lett.* **379**, 1–12 (2013).
52. Wentzcovitch, R. M. et al. Anomalous compressibility of ferropericlase throughout the iron spin cross-over. *Proc. Natl Acad. Sci. USA* **106**, 8447–8452 (2009).
53. Badro, J. et al. Electronic transitions in perovskite: possible non-convecting layers in the lower mantle. *Science* **305**, 383–386 (2004).
54. Andrault, D., Fiquet, G., Guyot, F. & Hanfland, M. Pressure-induced Landau-type transition in stishovite. *Science* **282**, 720–724 (1998).
55. Hernlund, J., Leinenweber, K., Locke, D. & Tyburczy, J. A. A numerical model for steady-state temperature distributions in solid-medium high-pressure cell assemblies. *Am. Mineral.* **91**, 295–305 (2006).
56. Piskunov, S., Heifets, E., Eglitis, R. I. & Borstel, G. Bulk properties and electronic structure of $SrTiO_3$, $BaTiO_3$, $PbTiO_3$ perovskites: an ab initio HF/DFT study. *Comput. Mater. Sci.* **29**, 165–178 (2004).
57. Tadano, T. & Tsuneyuki, S. Self-consistent phonon calculations of lattice dynamical properties in cubic $SrTiO_3$ with first-principles anharmonic force constants. *Phys. Rev. B* **92**, 054301 (2015).
58. Hachemi, A., Hachemi, H., Ferhat-Hamida, A. & Louail, L. Elasticity of $SrTiO_3$ perovskite under high pressure in cubic, tetragonal and orthorhombic phases. *Phys. Scr.* **82**, 025602 (2010).
59. Caracas, R., Wentzcovitch, R., Price, G. D. & Brodholt, J. $CaSiO_3$ perovskite at lower mantle pressures. *Geophys. Res. Lett.* **32**, L06306 (2005).
60. Jung, D. Y. & Oganov, A. R. Ab initio study of the high-pressure behavior of $CaSiO_3$ perovskite. *Phys. Chem. Miner.* **32**, 146–153 (2005).
61. Mao, H. K. et al. Stability and equation of state of $CaSiO_3$-perovskite to 134 GPa. *J. Geophys. Res.* **94**, 17889–17894 (1989).
62. Yagi, T., Tsuchida, Y., Kusanagi, S. & Fukai, Y. Isothermal compression and stability of perovskite-type $CaSiO_3$. *Proc. Jpn. Acad. B* **65**, 129–132 (1989).
63. Tamai, H. & Yagi, T. High-pressure and high-temperature phase relations in $CaSiO_3$ and $CaMgSi_2O_6$ and elasticity of perovskite-type $CaSiO_3$. *Phys. Earth Planet. Inter.* **54**, 370–377 (1989).
64. Tarrida, M. & Richet, P. Equation of state of $CaSiO_3$ perovskite to 96 GPa. *Geophys. Res. Lett.* **16**, 1351–1354 (1989).

Acknowledgements We acknowledge the support of NERC grants NE/P017657/1 and NE/M00046X/1, and ESRF beamtime proposals ES-464 and ES-636. We thank G. Manthilake and D. Freitas for their assistance and for lending us ultrasonic equipment from Laboratoire Magmas et Volcans for use during the initial experiments of this study. Use of the Pixirad-8 detector was supported by the French Government via the 'Investissements d'Avenir' programme, under the reference ANR-10-AIRT-05.

Author contributions A.R.T. designed, performed and analysed the experiments, gathered data from the literature and wrote the manuscript. W.A.C. designed and developed the experimental procedure at ID06 of the ESRF. I.G.W. assisted with interpretation and refinement of diffraction data. J.P.B., D.P.D, W.A.C and N.C.S. helped perform experiments over two sessions at the ESRF. J.M.R.M. performed the computational simulations. S.A.H. assisted with data analysis. All authors contributed to the scientific discussion and preparation of the manuscript.

Competing interests The authors declare no competing interests.

Additional information
Supplementary information is available for this paper at https://doi.org/10.1038/s41586-019-1483-x.
Correspondence and requests for materials should be addressed to A.R.T.
Peer review information *Nature* thanks Ian Jackson and the other, anonymous, reviewer(s) for their contribution to the peer review of this work.
Reprints and permissions information is available at http://www.nature.com/reprints.

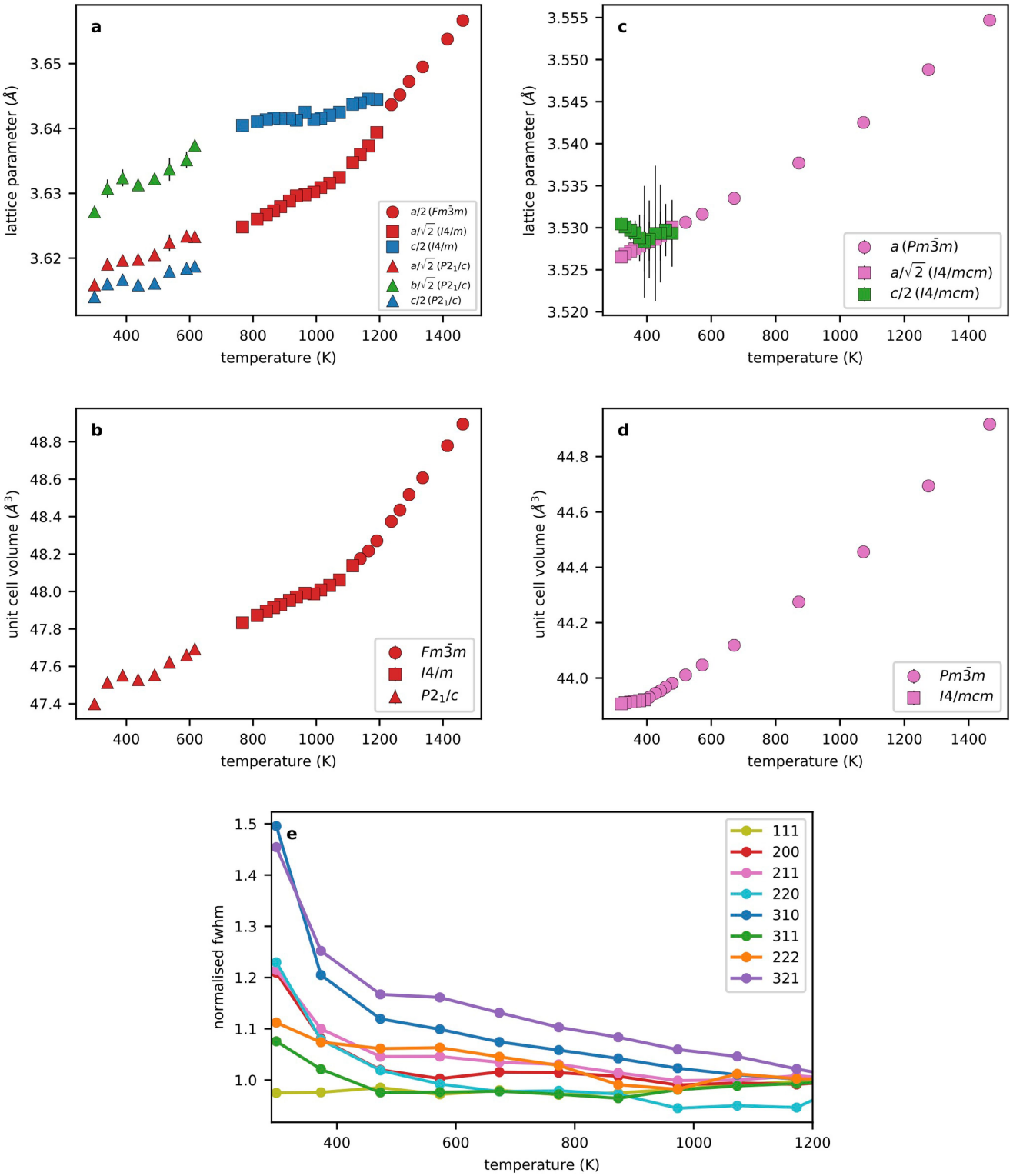

Extended Data Fig. 1 | Lattice and diffraction peak parameters for $CaSiO_3$ and $Ca[Si_{0.6}Ti_{0.4}]O_3$ perovskite. a–d, Refined lattice parameters and pseudo-cubic unit cell volumes from $Ca[Si_{0.6}Ti_{0.4}]O_3$ (**a**, **c**) and $CaSiO_3$ (**b**, **d**) plotted as a function of experimental temperature with 2σ uncertainties. **e**, Full-width at half-maximum (FWHM) of diffraction peaks (see key) of the $CaSiO_3$ perovskite sample, normalized to the FWHM at high temperature, measured at 100 K intervals in a separate experiment to that in Fig. 2.

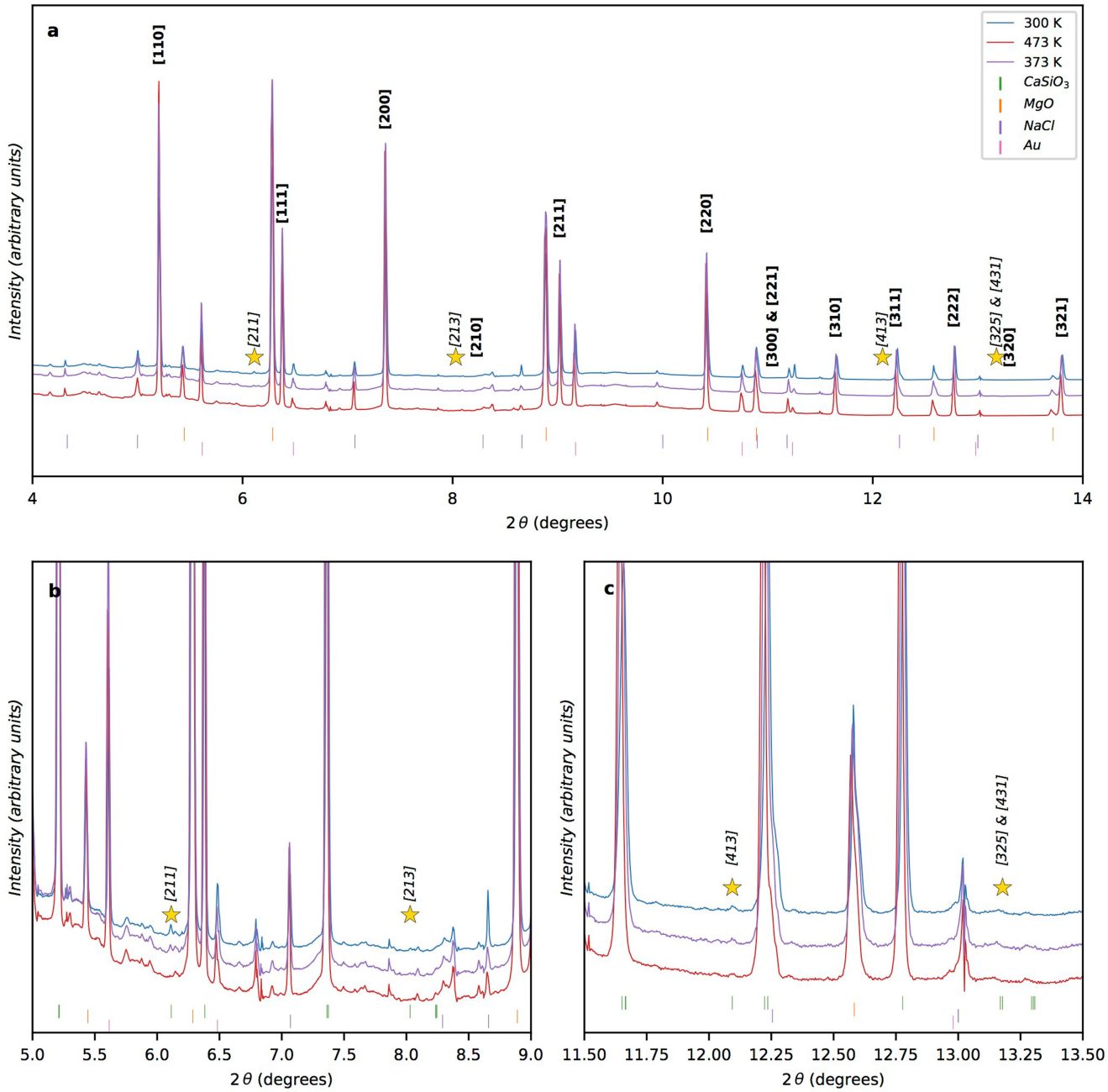

Extended Data Fig. 2 | X-ray diffraction patterns from $CaSiO_3$ perovskite. Shown are stacked diffraction patterns of $CaSiO_3$ perovskite; each panel shows data at 300 K, 373 K and 473 K (see key in **a**). **a**, Full patterns; **b**, **c**, patterns limited in the 2θ range to allow indication of weak superlattice peaks. The positions of the diffraction peaks from the Ca-Pv sample, MgO, NaCl and Au are indicated by markers—other small peaks are from boron epoxy and/or furnace components. Cubic Ca-Pv peaks are labelled with indices, *hkl*, in bold. The diffraction patterns reveal the appearance of small superlattice reflections at $T = 373$ K and 300 K at 2θ values of about 6.1°, 8.05°, 12.1° and 13.2° (we note there is believed to be an additional superlattice reflection obscured at $2\theta = 10.5°$) labelled with *hkl* indexed on the tetragonal ($I4/mcm$) unit cell and marked with gold stars.

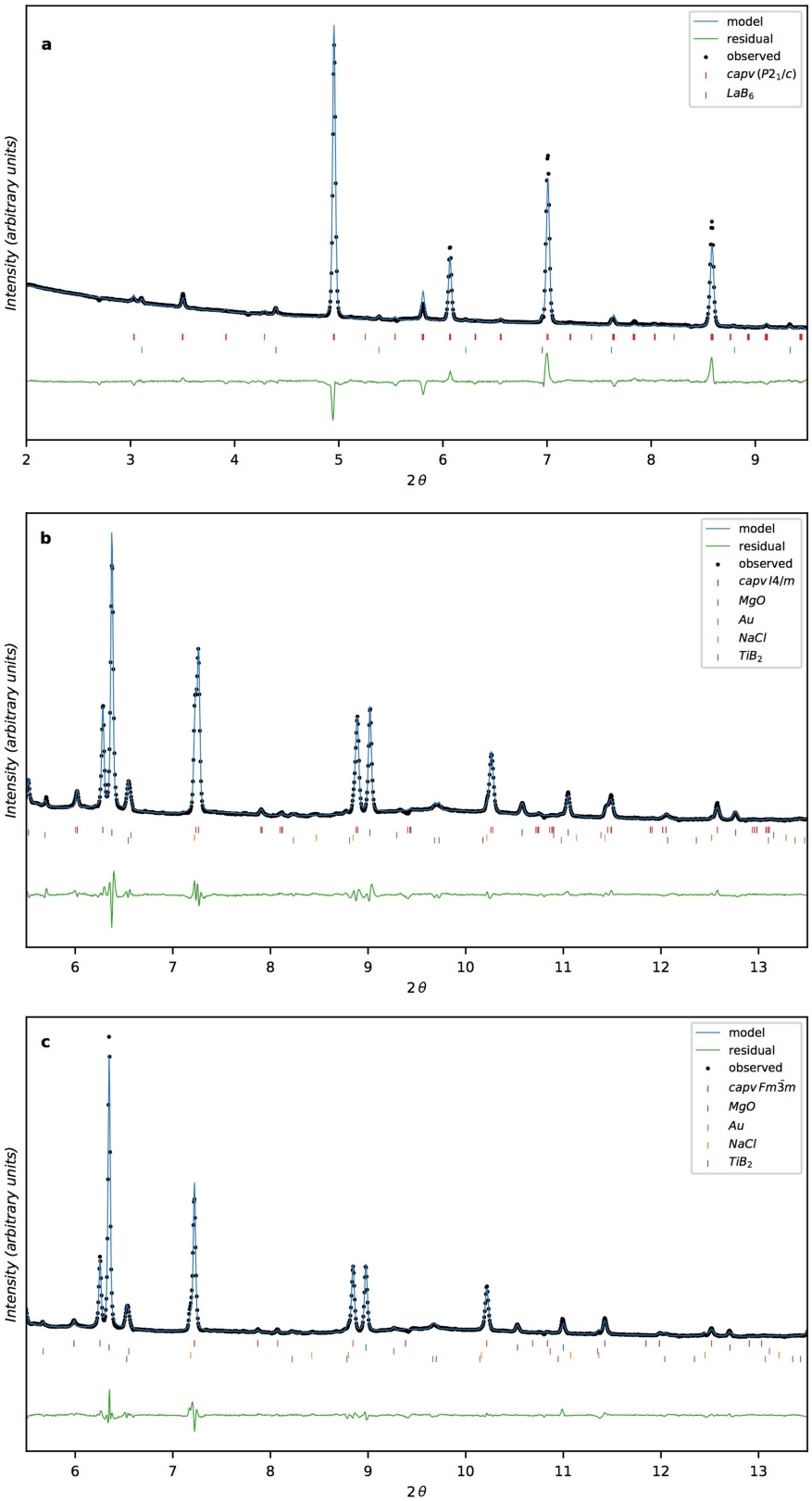

Extended Data Fig. 3 | Refined X-ray diffraction patterns from $Ca[Si_{0.6}Ti_{0.4}]O_3$ perovskite. **a**–**c**, Rietveld refinements of $Ca[Si_{0.6}Ti_{0.4}]O_3$ samples: **a**, in $P2_1/c$ with LaB_6 calibrant, at 300 K and ambient pressure; **b**, in the tetragonal $I4/m$ structure (with other cell components) at 890 K and high pressure (about 12 GPa); and **c**, in $Fm\bar{3}m$ at 1,336 K and high pressure (12 GPa). In each panel, the black dots are the collected data, the blue curve the model pattern and the green curve the residual. The coloured tick-marks indicate the positions of diffraction peaks of each phase.

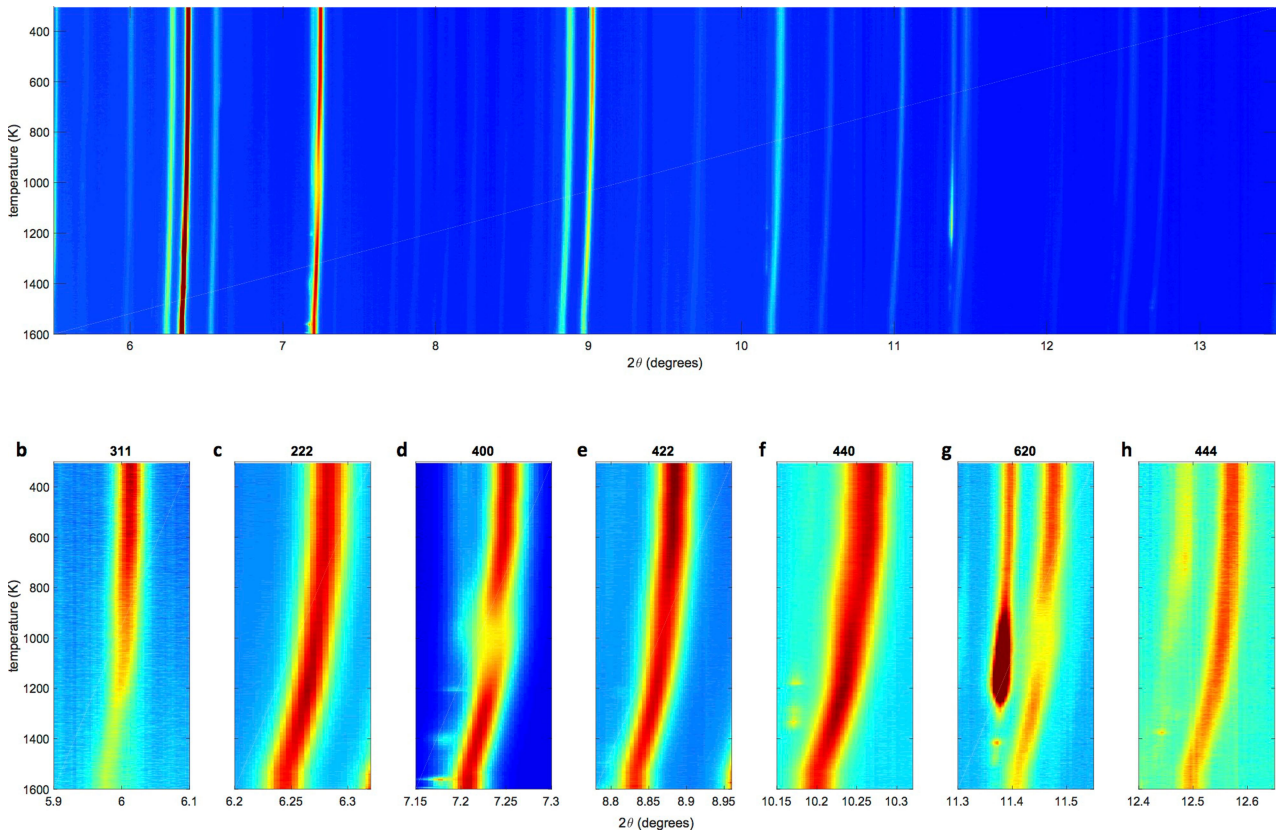

Extended Data Fig. 4 | X-ray diffraction patterns from $Ca[Si_{0.6}Ti_{0.4}]O_3$ perovskite. a, Complete diffraction pattern of the $Ca[Si_{0.6}Ti_{0.4}]O_3$ sample as a function of temperature at about 12 GPa, with diffraction intensity indicted by colour scaling. **b**–**h**, Magnified panels from **a** focusing on the temperature evolution of the 311, 222, 400, 422, 440, 620 and 444 diffraction peaks (**b**–**h**, respectively; indexed using a cubic lattice with $a \approx 7.3$ Å), demonstrating the change in thermal expansivity between cubic and tetragonal/monoclinic structures, and allowing visual identification of the observed phase transitions.

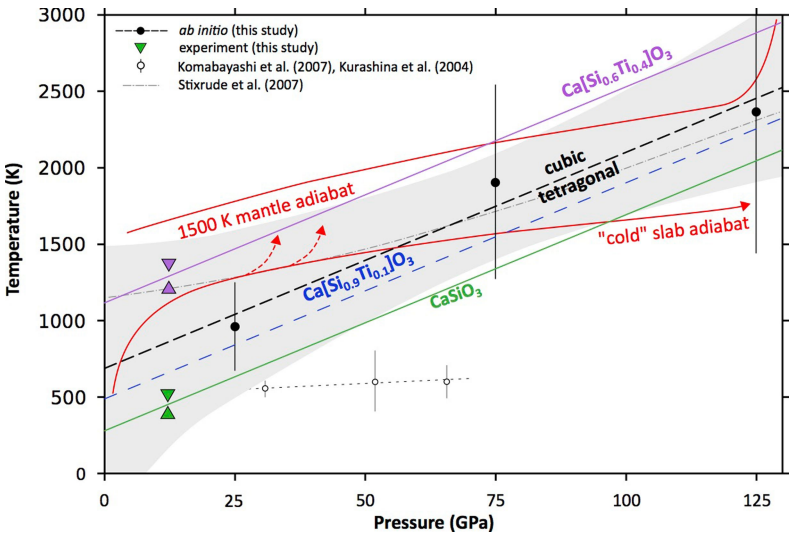

Extended Data Fig. 5 | Phase diagram of calcium perovskite throughout the mantle from ab initio simulations and experiments. Shown is the cubic–tetragonal transition extrapolated throughout the mantle based on ab initio (solid circles) and experimental (triangles) constraints from this study. Vertical error bars (1σ) and the grey envelope (80% confidence interval) represent the uncertainty in computational results from this study. A 1,500 K mantle adiabat and cold slab temperature profile are plotted as red curves, with dashed red arrows indicating the warming occurring during slab stagnation at 700–1,000 km depth. Results from previous experimental[18,23] and computational[3] studies are plotted as open symbols and grey curves, respectively.

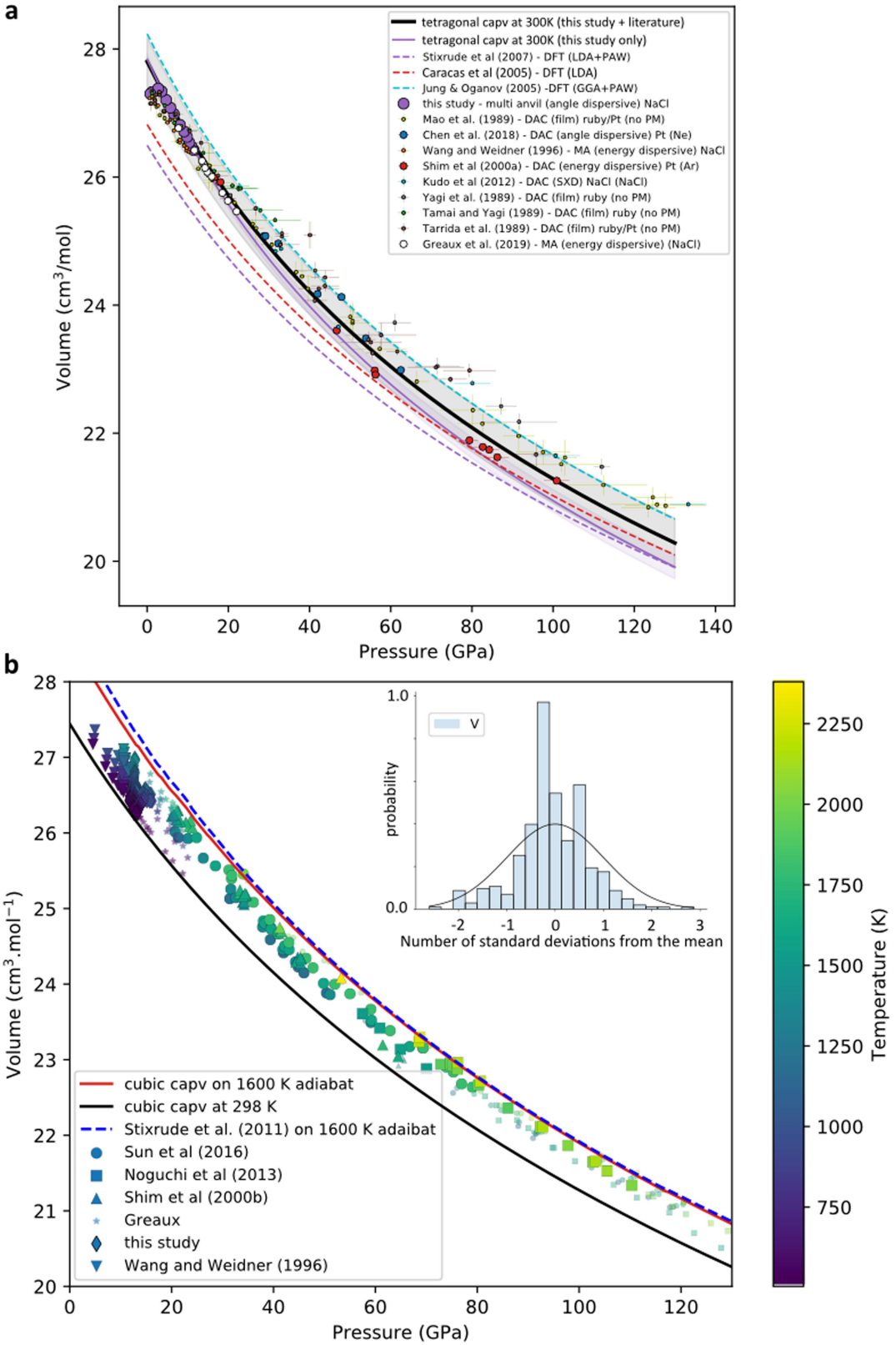

Extended Data Fig. 6 | Equations of state for $CaSiO_3$ perovskite. **a**, *PV* EoS for tetragonal $CaSiO_3$ at 300 K, fitted to data from this study only (purple line) and combined with data from previous studies (thick black curve). Only data with large symbols, those that used pressure transmitting media, have been included in fitting the EoS. All small symbols are from experiments that did not employ a pressure-transmitting medium so have been excluded as volumes are expected to be affected by residual sample stress. Additionally, data from Wang et al.[47] were excluded as they used energy dispersive diffraction in the large volume press, which can be subject to larger uncertainties in volume. Error bars represent pressure and volume uncertainties as reported in previous studies. Computational EoS for tetragonal Ca-Pv are plotted as dashed curves for comparison[3,17,19,45,47,59–64]. **b**, *PVT* EoS for cubic $CaSiO_3$ perovskite at 298 K and along a 1,600 K adiabat fitted to data from this and previous studies. Small, partially transparent symbols are literature data that were not included in the fitting, either due to falling below the calculated slope of the cubic–tetragonal transition (Methods) or due to concerns about data accuracy. The inset histogram shows the, approximately normal, distribution for the residuals for the fitted data compared with the best-fit model, demonstrating the lack of outliers[45–48].

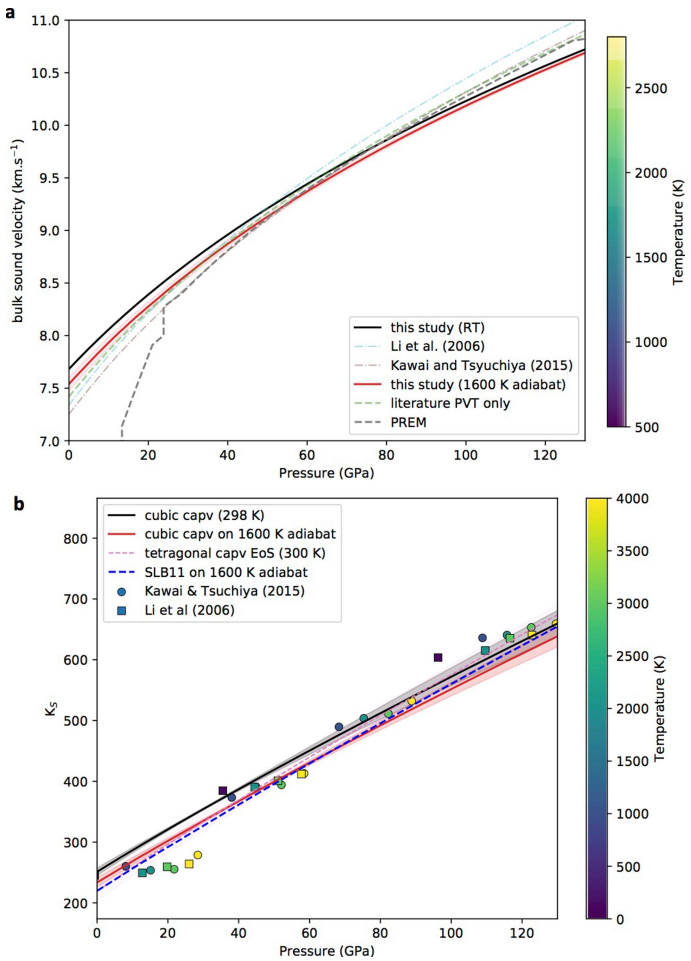

Extended Data Fig. 7 | Bulk sound velocity and bulk modulus of $CaSiO_3$ perovskite. a, Bulk sound velocity of Ca-Pv predicted from the EoS in this study along a 1,600 K mantle adiabat and at 300 K, compared with results from previous computational studies on a 1,600 K adiabat[4–6], a fit to previously published *PVT* diffraction data, and PREM[15]. **b**, The adiabatic bulk modulus of $CaSiO_3$ perovskite calculated at 300 K and along a 1,600 K mantle adiabat using the finite strain model from this study, compared with thermodynamic results in Stixrude et al.[6] and previous high-temperature computational studies[4,5].

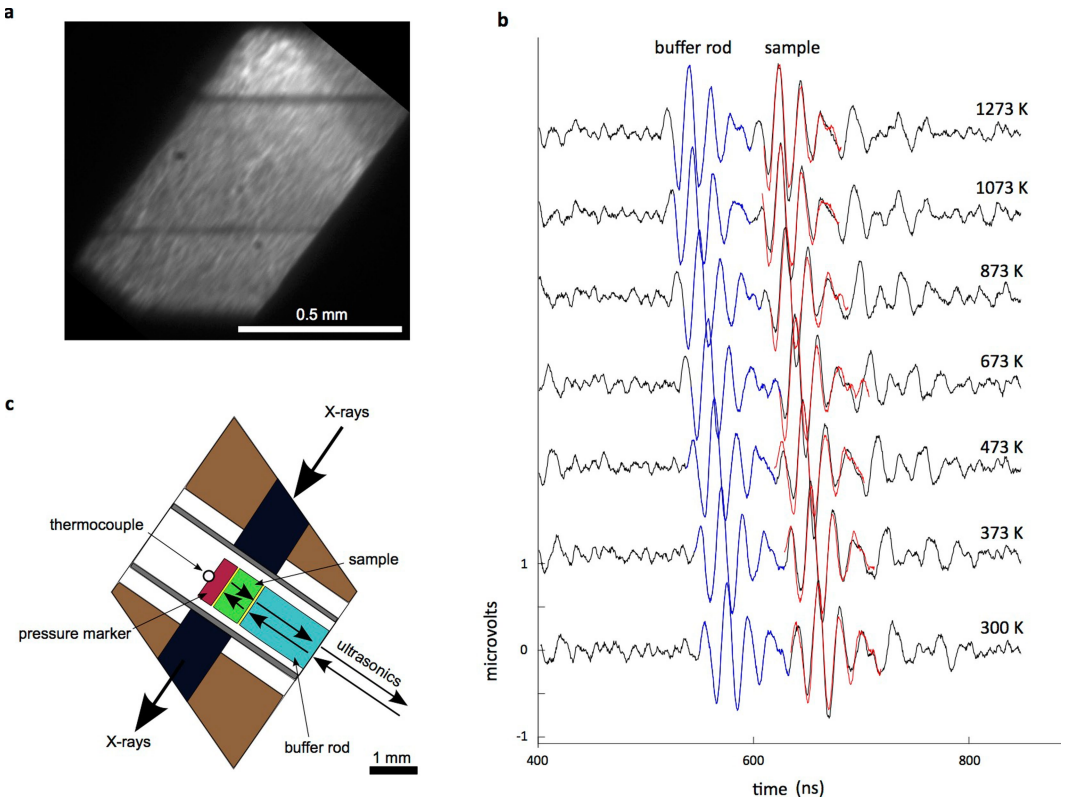

Extended Data Fig. 8 | Exemplar radiographic image, ultrasonic data and schematic of the experimental cell design. a, Example of synchrotron radiographic image in plan view used to measure sample length in a $Ca[Si_{0.6}Ti_{0.4}]O_3$ sample. **b**, Ultrasonic signals from the 'runa' experiment on a $CaSiO_3$ sample. **c**, Cross-section of the experimental assembly (to scale) used in ultrasonic experiments throughout this study.

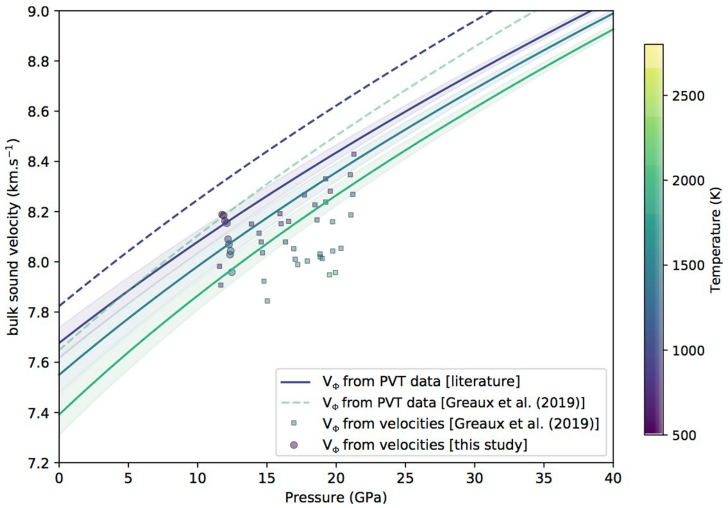

Extended Data Fig. 9 | Comparison of bulk sound velocity from diffraction and ultrasonic measurements. Shown is a comparison of bulk sound velocity calculated from *PVT* EoSs, fitted to literature diffraction data (solid curves) with 2σ uncertainties shown by shaded regions, and only to that reported by Gréaux et al.[20] (dashed curves), with bulk sound velocities calculated from ultrasonic measurements via $v_{bulk} = (v_P^2 - 4/3v_S^2)^{0.5}$ for data from Gréaux et al.[20] (squares) and this study (circles). All curves and symbols are coloured for temperature (colour scale at right).

LETTER

https://doi.org/10.1038/s41586-019-1468-9

Climate change and overfishing increase neurotoxicant in marine predators

Amina T. Schartup[1,2]*, Colin P. Thackray[1], Asif Qureshi[3], Clifton Dassuncao[1,2], Kyle Gillespie[4], Alex Hanke[4] & Elsie M. Sunderland[1,2]*

More than three billion people rely on seafood for nutrition. However, fish are the predominant source of human exposure to methylmercury (MeHg), a potent neurotoxic substance. In the United States, 82% of population-wide exposure to MeHg is from the consumption of marine seafood and almost 40% is from fresh and canned tuna alone[1]. Around 80% of the inorganic mercury (Hg) that is emitted to the atmosphere from natural and human sources is deposited in the ocean[2], where some is converted by microorganisms to MeHg. In predatory fish, environmental MeHg concentrations are amplified by a million times or more. Human exposure to MeHg has been associated with long-term neurocognitive deficits in children that persist into adulthood, with global costs to society that exceed US$20 billion[3]. The first global treaty on reductions in anthropogenic Hg emissions (the Minamata Convention on Mercury) entered into force in 2017. However, effects of ongoing changes in marine ecosystems on bioaccumulation of MeHg in marine predators that are frequently consumed by humans (for example, tuna, cod and swordfish) have not been considered when setting global policy targets. Here we use more than 30 years of data and ecosystem modelling to show that MeHg concentrations in Atlantic cod (*Gadus morhua*) increased by up to 23% between the 1970s and 2000s as a result of dietary shifts initiated by overfishing. Our model also predicts an estimated 56% increase in tissue MeHg concentrations in Atlantic bluefin tuna (*Thunnus thynnus*) due to increases in seawater temperature between a low point in 1969 and recent peak levels—which is consistent with 2017 observations. This estimated increase in tissue MeHg exceeds the modelled 22% reduction that was achieved in the late 1990s and 2000s as a result of decreased seawater MeHg concentrations. The recently reported plateau in global anthropogenic Hg emissions[4] suggests that ocean warming and fisheries management programmes will be major drivers of future MeHg concentrations in marine predators.

The exploitation of fisheries in the northwestern Atlantic Ocean for hundreds of years has led to large fluctuations in herring, lobster and cod stocks, which has altered the structure of food webs and the availability of prey for remaining species[5]. We synthesized more than three decades of ecosystem data and MeHg concentrations in seawater, sediment and biological species that represent five trophic levels from the Gulf of Maine, a marginal sea in the northwestern Atlantic Ocean that has been exploited for commercial fisheries for more than 200 years. These data were used to develop and evaluate a mechanistic model for MeHg bioaccumulation that is based on bioenergetics and predator–prey interactions (see Methods), to better understand the effects of ecosystem changes and overfishing[6].

A comparison of simulated MeHg concentrations based on extensive analysis of the stomach contents of two marine predators (Atlantic cod and spiny dogfish, *Squalus acanthias*) in the 1970s and 2000s reveals that the effects of shifts in trophic structures caused by overfishing differed between these two species (Fig. 1a, b). In the 1970s, cod consumed 8% more small clupeids than in the 2000s as a consequence of the overharvesting and reduced abundance of herring[7]. Simulated tissue MeHg concentrations in cod (larger than 10 kg) in the 1970s were 6–20% lower than for cod consuming a diet typical of the 2000s that relied more heavily on larger herring, lobster and other macroinvertebrates[7]. The 1970s diet for spiny dogfish when herring were limited included a higher proportion (around 20%) of squid and other cephalopods, which exhibit higher MeHg concentrations than many other prey fish. In contrast to cod, simulated MeHg concentrations in spiny dogfish were 33–61% higher in the 1970s than in the 2000s, when they consumed more herring and other clupeids[7]. These results illustrate that perturbations to the trophic structure of marine organisms from overfishing can have contrasting effects on MeHg concentrations across species. Such changes must therefore be assessed before concluding

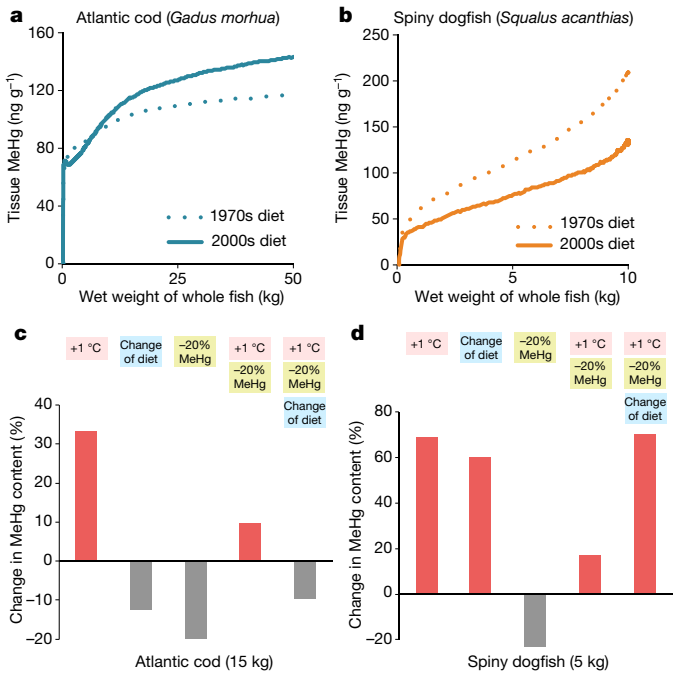

Fig. 1 | Modelled effects of ecosystem change on MeHg concentrations in Atlantic cod and spiny dogfish. a, **b**, Differences in modelled MeHg concentrations in Atlantic cod (**a**) and spiny dogfish (**b**) based on a diet typical of the 1970s (dotted line) and the 2000s (solid line). Prey preferences for each time period were derived from the stomach contents of more than 2,000 fish[7]. **c**, **d**, Modelled changes in fish MeHg concentrations (relative to a diet typical of the 2000s) that result from a temperature increase of 1 °C; a shift in diet composition driven by overfishing of herring (represented by 1970s prey preferences when this last occurred); an assumed 20% decline in seawater MeHg concentration; the combination of both an increase in temperature and a decrease in seawater MeHg; and the simultaneous combination of all three factors.

[1]Harvard John A. Paulson School of Engineering & Applied Sciences, Harvard University, Cambridge, MA, USA. [2]Department of Environmental Health, Harvard T. H. Chan School of Public Health, Harvard University, Boston, MA, USA. [3]Department of Civil Engineering, Indian Institute of Technology Hyderabad, Kandi, India. [4]Fisheries and Oceans Canada, St Andrews Biological Station, St Andrews, New Brunswick, Canada. *e-mail: aschartup@ucsd.edu; ems@seas.harvard.edu

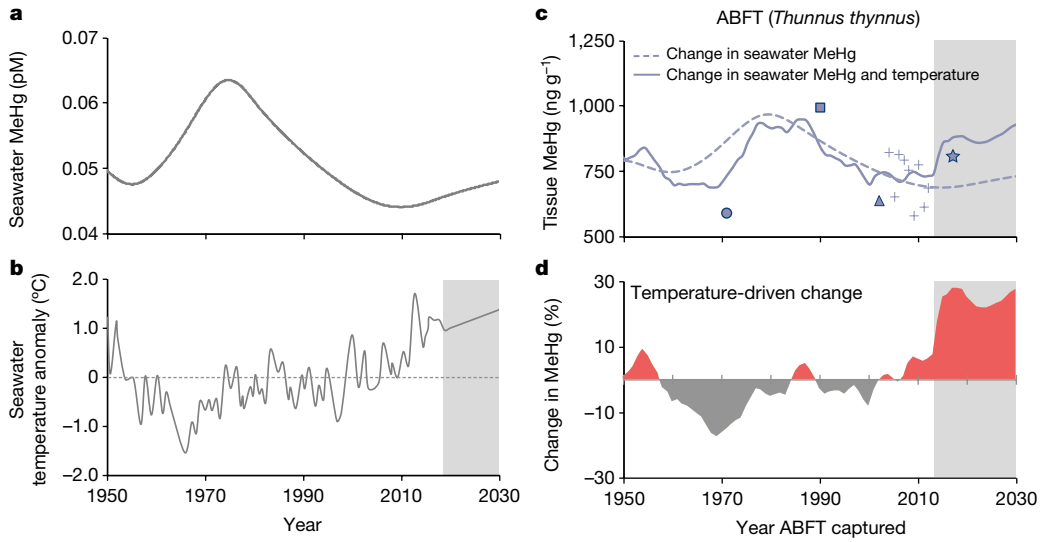

Fig. 2 | Effects of seawater warming in the Gulf of Maine on tissue MeHg concentrations in ABFT. a, Modelled seawater MeHg concentrations over time. The model is based on measured MeHg concentrations between 2008 and 2010[17] and scaled by modelled temporal changes in seawater Hg[12]. **b**, Measured temperature anomaly in seawater in the Gulf of Maine[8]. The shaded grey area indicates the projected future change. **c**, Modelled MeHg tissue concentrations in 14-year-old ABFT based on changes in seawater MeHg concentrations (dashed line), and based on the combined effect of changes in seawater MeHg concentrations and seawater temperature anomaly (solid line). The symbols indicate means of observed concentrations in multiple fish: new data for ABFT that were captured in 2017 ($n = 33$) are shown as a star; previously published data[16,18–20] are shown as crosses[16] ($n = 83$), a square[18] ($n = 14$), a triangle[19] ($n = 3$) and a circle[20] ($n = 5$). Sample size (n) represents the number of independent fish; s.d. and statistics are provided in Extended Data Table 3. **d**, Changes in MeHg concentrations in ABFT that are due to temperature only.

that temporal trends in biological MeHg concentrations reflect shifts in environmental Hg contamination.

Northward migration of the Gulf Stream and decadal oscillations in ocean circulation have led to unprecedented seawater warming in the Gulf of Maine between a low point in 1969 and 2015, which places this region in the top 1% of documented seawater temperature anomalies[8]. Both laboratory and field mesocosm data have demonstrated that rising temperatures lead to increases in MeHg concentrations in estuarine and freshwater fish[9,10], but the magnitudes of potential changes in wild species are poorly understood. The effects of seawater warming are complicated by the narrow temperature niches of many marine fish species, which we account for in our food web model (see Methods). Seawater warming of greater than 1–2 °C can lead to shifts in preferred foraging territory to higher latitudes or deeper in the water column, which alters the availability of prey for remaining species[11].

The effects of ecosystem changes on MeHg bioaccumulation vary across species and are not additive for predatory fish because of feeding relationships and bioenergetics at lower trophic levels. We modelled the changes in MeHg tissue concentrations in Atlantic cod and spiny dogfish that would result from increases in seawater temperature, declines in seawater MeHg concentrations and shifts in trophic structure due to overfishing (Fig. 1c, d). Experimental data indicate that MeHg uptake by most marine algae is not sensitive to variability in seawater temperature[6] and therefore our modelling analysis accounts for temperature-driven changes in MeHg at higher trophic levels, from zooplankton to predatory fish.

For a 15-kg Atlantic cod, our model predicts that an increase of 1 °C in seawater temperature relative to the year 2000 would lead to a 32% increase in simulated tissue MeHg concentrations. A shift in trophic structure characteristic of overexploited herring fisheries would result in a 12% decrease in fish MeHg. In the absence of ecosystem changes, simulated fish MeHg concentrations shift proportionally to seawater MeHg concentrations. If we assume that seawater MeHg concentrations decline by approximately 20% as a consequence of reductions in Hg loading, the combination of all three factors simultaneously results in a 10% decrease in tissue MeHg concentrations for Atlantic cod (Fig. 1c).

For a 5-kg spiny dogfish, our model estimates that a temperature increase of 1 °C would result in a 70% increase in tissue MeHg concentrations, and that switching to a diet that is characteristic of low herring abundance would lead to a 50% increase in fish MeHg. When combined with the assumed 20% decline in seawater MeHg concentrations, the model predicts a 70% increase in tissue MeHg concentrations for dogfish (Fig. 1d). Owing to a large reduction in Hg releases from wastewater and declines in atmospheric deposition of Hg in North America[12,13], seawater MeHg concentrations in the northwestern Atlantic Ocean are presumed to have declined since the 1970s (Fig. 2a). Our results help to explain why temporal changes in tissue MeHg concentrations in the Gulf of Maine have been mixed across species, despite declining inputs of Hg to the marine environment since the 1970s[12].

We used historical temperature records to further investigate the effects of recent temperature changes on MeHg bioaccumulation in Atlantic bluefin tuna (ABFT), another important marine predator (Fig. 2). No time-series data on seawater MeHg are available, so we extrapolated measured concentrations using information on emissions in North America and projected total Hg concentrations in seawater (see Methods). Increases in seawater temperature coincide with putative declines in seawater MeHg concentrations (Fig. 2b).

The implications of changes in seawater MeHg concentrations (Fig. 2a) and seawater temperature (Fig. 2b) in the Gulf of Maine for tissue MeHg concentrations in 14-year-old ABFT (250 ± 23 cm length[14] (mean ± s.d.)) are illustrated in Fig. 2. The dashed line in Fig. 2c shows the changes in MeHg in ABFT tissue that result from changing seawater MeHg only, and the solid line shows the combined influence of changes in seawater MeHg and temperature. Without including the effects of temperature, shifts in MeHg concentrations in ABFT lag peak seawater MeHg concentrations by five years, and the amplitude of the peak is dampened relative to seawater (Fig. 2c, dashed line). Historical temperature oscillations result in an additional lag of six years in maximum MeHg concentrations in ABFT (Fig. 2c, solid line), and reduce the standard error of the modelled tissue MeHg concentrations in ABFT compared to observations (Fig. 2c, symbols) from 120 ng g^{-1} (Fig. 2c, dashed line) to 95 ng g^{-1} (Fig. 2c, solid line).

Both the model and observations indicate that a large decline in MeHg concentrations in ABFT occurred after the late 1980s and early 1990s (Fig. 2c). The modelled decrease from peak to low concentrations is equivalent to a 23% decline in tissue MeHg concentrations (Fig. 2c).

Observed concentrations in 14-year-old ABFT from the Gulf of Maine show a 31% decrease between 1990 and 2012. Our model results suggest that 25–40% of tissue MeHg decreases in the 1990s are attributable to temperature decreases over this decade (Fig. 2d).

Modelled effects of continued warming in the Gulf of Maine suggest a reversal of previous declines, and projected increases of almost 30% in 2015 that are sustained into 2030 (Fig. 2d). Between 2012 and 2017, observations are consistent with model trends and show a statistically significant increase in MeHg (Fig. 2) of more than 3.5% per year in ABFT (one-way ANOVA, $P < 0.05$). These results illustrate the large effects on bioaccumulative toxicants in marine food webs that are expected as a result of climate-driven changes in marine ecosystems.

Global anthropogenic emissions of Hg have been relatively stable since approximately 2011[4]. In North America and Europe, aggressive Hg regulations that began in the 1970s have successfully reduced or phased out most large Hg sources, and global emissions are now driving atmospheric Hg trajectories in the Northern Hemisphere. This means that future changes in tissue concentrations of MeHg in pelagic marine predators such as ABFT and Atlantic cod in the Gulf of Maine will be strongly influenced by further shifts in seawater temperature and prey availability. Biotic MeHg concentrations in other marine regions are likely to be similarly affected by widespread shifts in trophic interactions and seawater temperature. A two-pronged regulatory effort that involves reductions in the emissions of both greenhouse gases and Hg is therefore needed to reduce MeHg concentrations in pelagic predators. Notably, regulations that aim to reduce air pollution caused by carbon-intensive fuel sources (such as coal-fired utilities) also have the co-benefit of bringing about large reductions in anthropogenic Hg releases[13].

Atmospheric Hg concentrations in the Northern Hemisphere declined by approximately 30% between the mid-1990s and 2000s, as a result of successful reductions in emissions from coal-fired utilities, industry and waste incinerators, and the phasing out of Hg in many commercial products in the United States and Europe[13]. Previous studies have suggested that these and other regulations have led to corresponding declines in tissue Hg concentrations in ABFT and bluefish (*Pomatomus saltatrix*) in the Atlantic Ocean[15,16]. Despite these benefits, recent regulatory proposals in the United States threaten to overturn rules that regulate mercury releases from coal-fired utilities and proposals to curb carbon emissions. Climate change is likely to exacerbate human exposure to MeHg through marine fish, suggesting that stronger rather than weaker regulations are needed to protect ecosystem and human health.

Online content

Any methods, additional references, Nature Research reporting summaries, source data, extended data, supplementary information, acknowledgements, peer review information; details of author contributions and competing interests; and statements of data and code availability are available at https://doi.org/10.1038/s41586-019-1468-9.

Received: 12 November 2018; Accepted: 3 July 2019;
Published online 7 August 2019.

1. Sunderland, E. M., Li, M. & Bullard, K. Decadal changes in the edible supply of seafood and methylmercury exposure in the United States. *Environ. Health Perspect.* **126**, 017006 (2018).
2. Horowitz, H. M. et al. A new mechanism for atmospheric mercury redox chemistry: implications for the global mercury budget. *Atmos. Chem. Phys.* **17**, 6353–6371 (2017).
3. Bellanger, M. et al. Economic benefits of methylmercury exposure control in Europe: monetary value of neurotoxicity prevention. *Environ. Health* **12**, 3 (2013).
4. Streets, D. et al. Global and regional trends in mercury emissions and concentrations. *Atmos. Environ.* **201**, 417–427 (2019).
5. Lotze, H. K. & Milewski, I. Two centuries of multiple human impacts and successive changes in a North Atlantic food web. *Ecol. Appl.* **14**, 1428–1447 (2004).
6. Schartup, A. T. et al. A model for methylmercury uptake and trophic transfer by marine plankton. *Environ. Sci. Technol.* **52**, 654–662 (2018).
7. Smith, B. E. & Link, J. S. *The Trophic Dynamics of 50 Finfish and 2 Squid Species on the Northeast US Continental Shelf.* NOAA Technical Memorandum NMFS-NE-21 (National Marine Fisheries Service, 2010).
8. Pershing, A. J. et al. Slow adaptation in the face of rapid warming leads to collapse of the Gulf of Maine cod fishery. *Science* **350**, 809–812 (2015).
9. Dijkstra, J. A. et al. Experimental and natural warming elevates mercury concentrations in estuarine fish. *PLoS ONE* **8**, e58401 (2013).
10. Maulvault, A. L. et al. Bioaccumulation and elimination of mercury in juvenile seabass (*Dicentrarchus labrax*) in a warmer environment. *Environ. Res.* **149**, 77–85 (2016).
11. Cheung, W. W. L. et al. Projecting global marine biodiversity impacts under climate change scenarios. *Fish Fish.* **10**, 235–251 (2009).
12. Sunderland, E. M. et al. Mercury sources and fate in the Gulf of Maine. *Environ. Res.* **119**, 27–41 (2012).
13. Zhang, Y. et al. Observed decrease in atmospheric mercury explained by global decline in anthropogenic emissions. *Proc. Natl Acad. Sci. USA* **113**, 526–531 (2016).
14. Restrepo, V. et al. Updated estimate of the growth curve of Western Atlantic bluefin tuna. *Aquat. Living Resour.* **23**, 335–342 (2010).
15. Cross, F. A., Evans, D. W. & Barber, R. T. Decadal declines of mercury in adult bluefish (1972–2011) from the Mid-Atlantic coast of the U.S.A. *Environ. Sci. Technol.* **49**, 9064–9072 (2015).
16. Lee, C.-S. et al. Declining mercury concentrations in bluefin tuna reflect reduced emissions to the North Atlantic Ocean. *Environ. Sci. Technol.* **50**, 12825–12830 (2016).
17. Hammerschmidt, C. R., Finiguerra, M. B., Weller, R. L. & Fitzgerald, W. F. Methylmercury accumulation in plankton on the continental margin of the northwest Atlantic Ocean. *Environ. Sci. Technol.* **47**, 3671–3677 (2013).
18. Hellou, J., Fancey, L. & Payne, J. Concentrations of twenty-four elements in bluefin tuna, *Thunnus thynnus* from the Northwest Atlantic. *Chemosphere* **24**, 211–218 (1992).
19. Harding, G., Dalziel, J. & Vass, P. Bioaccumulation of methylmercury within the marine food web of the outer Bay of Fundy, Gulf of Maine. *PLoS ONE* **13**, e0197220 (2018).
20. Peterson, C. L., Klawe, W. L. & Sharp, G. D. Mercury in tunas: a review. *Fish Bull.* **71**, 603–613 (1973).

METHODS

Mercury concentration data in fish. Many studies report total Hg rather than MeHg in fish tissue. Extensive data on total Hg and MeHg concentrations in pelagic, demersal and benthic food webs of the Gulf of Maine were collected between 2000 and 2002[19]. We used the measured MeHg fraction (90%) to scale total Hg values for ABFT. For lower trophic levels with variable MeHg concentrations we relied on direct MeHg measurements. Size-fractionated phytoplankton and zooplankton samples were obtained on research cruises and zooplankton species were identified and separated by a plankton ecologist. These data are shown in Extended Data Table 1. Fish and shellfish data are summarized in Extended Data Table 2. Trophic levels were determined from stable nitrogen isotopes ($\delta^{15}N$) measured in the same samples.

Mercury concentrations in apex predators were compiled from several sources. A previous study[21] reported total Hg in swordfish (*Xiphias gladius*) from the western Atlantic Ocean ($n = 192$) with corresponding weights. Another research team measured total Hg in $n = 1{,}279$ ABFT harvested from the Gulf of Maine[16]. Length (cm) and body weights (kg) were available for all tuna and used to estimate age, which ranged from 9 to 14 years. Data from this study[16] were converted from dressed weight to whole weight by multiplying dressed weight by 1.25.

Temporal data on MeHg concentrations in ABFT harvested from the Gulf of Maine were compiled from several sources, for fish lengths (250 ± 23 cm (mean ± s.d.)) and ages that correspond to approximately 14-year-old fish (Extended Data Table 3). For 1971 ($n = 5$)[20] and 2002 ($n = 3$)[19], 14-year old fish were identified based on reported length. For 1990, reported fish ages ($n = 14$) ranged between 8 and 15 years[18]. For 2004–2012, MeHg concentrations in 14-year-old ABFT harvested from the Gulf of Maine were reported in a comprehensive study[16]. ABFT tissue from individual fish harvested in 2017 from the Gulf of Maine were analysed for Hg in this study and are reported in Extended Data Table 3.

Food web bioaccumulation model. Measured MeHg concentrations in the northwestern Atlantic Ocean (Extended Data Fig. 1a) show characteristic increases across more than five trophic levels (derived from $\delta^{15}N$)[19]. However, MeHg concentrations in swordfish and ABFT are underpredicted by the linear relationship between log[MeHg] and $\delta^{15}N$. The slope of this relationship is known as the trophic magnification slope, and this parameter has been used to assess global patterns in biomagnification of MeHg in freshwater ecosystems[22]. However, the factors that govern variability in trophic magnification slopes across ecosystems are poorly understood, and their application to marine ecosystems is further complicated by potential shifts in baseline $\delta^{15}N$ for migratory species such as ABFT and swordfish[23]. We therefore developed a new mechanistic model for biomagnification of MeHg in marine food webs as a function of ecosystem properties[6].

We parameterized the mechanistic model for MeHg bioaccumulation to the food web that was characteristic of the Gulf of Maine in the early 2000s (Extended Data Fig. 2), and evaluated predicted tissue MeHg concentrations against measurements compiled previously for that period[19]. We then applied the evaluated model to simulate the effects of measured temperature anomalies and documented shifts in trophic structure on MeHg concentrations in predatory fish. The model can be run deterministically, using the central estimate of all parameter values, or stochastically, to capture variability in seawater MeHg, dissolved organic carbon (DOC), prey consumption and other parameters.

The food web model includes three size classes for phytoplankton (picoplankton (0.2–2.0 μm), nanoplankton (2–20 μm) and microplankton (20–200 μm)); small (herbivorous) and large (omnivorous) zooplankton; macroinvertebrates; and fish. The lower (plankton) food web model has been described in detail previously[6]. In brief, our model simulates changes in MeHg uptake by phytoplankton due to varying seawater MeHg concentrations, differences in the composition of phytoplankton communities and varying DOC concentrations. The relative abundance of different size classes of phytoplankton is based on empirical relationships with surface concentrations of chlorophyll *a*[6]. Monthly average concentrations of chlorophyll *a* for the Gulf of Maine were derived from measurements collected at eight stations between 1997 and 2001[6].

Phytoplankton MeHg concentrations are modelled based on passive uptake of MeHg from seawater (driven by cell surface-to-volume ratios and DOC concentrations), because experimental data show that MeHg uptake by most phytoplankton species is not sensitive to seawater temperature[6]. This parameterization has previously been used to explain phytoplankton MeHg concentrations across a range of ecosystems in the northwest Atlantic[6]. DOC concentrations measured in the Gulf of Maine ($n = 82$) are log-normally distributed (81 ± 15 μM (mean ± s.d.))[6]. Seawater MeHg concentrations are based on previous measurements[17] in the upper 60 m of the water column in the Gulf of Maine. Measured MeHg concentrations ranged between 0.015 and 0.055 pM and an average of 7% of the total Hg was present as MeHg. Sediment MeHg concentrations are based on those reported previously[12] in integrated 15–20-cm grab samples of surface sediment ($n = 95$) from the Gulf of Maine that were collected between 2000 and 2002 (0.44 ± 0.32 pmol g^{-1} (mean ± s.d.)).

Time-dependent simulations for ABFT are based on measured MeHg concentrations in seawater[17] between 2008 and 2010, scaled by the trajectory in total Hg concentrations in the surface ocean between 1950 and 2030. Total Hg concentrations in the North Atlantic surface ocean were modelled using historical data on atmospheric Hg emissions[24] and a global geochemical model with resolved ocean basins[24,25]. The annual concentrations (in pM) of MeHg in seawater that were used to force the time-dependent bioaccumulation simulation are shown in Extended Data Table 4. We used records of sea surface temperature (Extended Data Table 5) for the Gulf of Maine from 1950 to 2015[8] to simulate temperature-driven changes in MeHg in ABFT (Extended Data Table 6).

Evaluation and sensitivity analysis of the food web model. A comparison of modelled and observed MeHg concentrations in ABFT as a function of size revealed that measurements were substantially underestimated ($n = 1{,}195$ observations, 3% within the 67% model confidence interval) when standard bioenergetics algorithms for energy expenditure, prey consumption and growth were used (Extended Data Fig. 1b, dashed line). Most bioaccumulation models assume that fish activity levels are constant[26]. This results in a decreasing proportion of energy that is expended for respiration as fish weight increases. By contrast, migratory distance and energy expenditures for pelagic marine fish increase as they grow and swim more rapidly[27,28]. Wild activity, particularly for migratory fish, is difficult to measure and thus rarely incorporated into estimates of consumption rates. Accurate consumption rates for fish in the wild are needed to model bioaccumulative contaminants such as MeHg. To account for these factors, we used swimming speed-, mass- and species-dependent activity multipliers (see Supplementary Information).

Increasing the migratory energy expenditure of ABFT on the basis of established relationships with body size and swimming speed results in a shift in the expected mean of the model to match the central tendency of observations (Extended Data Fig. 1b, solid line). After accounting for migratory energy expenditure, the 95% confidence interval of probabilistically simulated MeHg concentrations in ABFT captures 90% of the observations. The probabilistic simulation includes distributions for variable seawater MeHg, DOC, MeHg assimilation efficiencies and prey selection (Extended Data Table 7, Supplementary Information). Electronic tagging data show that western ABFT and swordfish spend a large fraction of their lifespan in shallow waters (<200-m depth) near the eastern coastline of North America[29,30], where measured MeHg concentrations[17,31] range from 0.03 to 0.06 pM. The modelled upper and lower bounds for MeHg and DOC concentrations measured in the northwestern Atlantic Ocean capture 99% of the observed MeHg concentrations in ABFT. These results indicate a good model performance for ABFT when migratory energy expenditure is included.

Prey consumption by most species is restricted by their body size—specifically, by the width of their mouth gape. This constrains the predator-to-prey length ratio to approximately 9:1, which we use in our standard model[32]. For swordfish, observed MeHg concentrations ($n = 156$)[21] are underpredicted by both the standard bioenergetics model (Extended Data Fig. 1c, dashed line) and the model adjusted for increased migratory energy expenditure (Extended Data Fig. 1c, dotted line). Only 5% of observations fall within the 67% model confidence interval.

Swordfish are known to slash and knock out prey of a larger size than that predicted by their mouth-gape width[33]. The primary prey for swordfish at maturity are cephalopods, which catch larger prey using their tentacles and are thus also less constrained by body size. Better agreement between modelled MeHg concentrations and observations is achieved by adjusting allowable predator-to-prey length ratios[32,33] to account for the larger prey sizes consumed by swordfish and cephalopods (Extended Data Fig. 1c, solid line). Model results show that 29% of the observations fall within the 67% confidence interval of the probabilistic simulation (orange shaded region in Extended Data Fig. 1c; 57% within the 95% model confidence interval). Simulating the upper and lower envelope of predator-to-prey length ratios (ratios from 10:1 to 2:1; yellow region in Extended Data Fig. 1c) captures 98% of the observations. Following these adjustments for apex predators, our results indicate excellent performance ($R^2 = 0.92$) of the bioenergetics model for MeHg bioaccumulation[6] compared to observations[19] across five trophic levels in the Gulf of Maine food web (Extended Data Fig. 1d).

Reporting summary. Further information on research design is available in the Nature Research Reporting Summary linked to this paper.

Data availability

All data and model algorithms are available in the Extended Data and Supplementary Information.

Code availability

All model code is available at the following link: https://github.com/SunderlandLab/foodweb_bioaccumulation_model.

21. Mendez, E., Giudice, H., Pereira, A., Inocente, G. & Medina, D. Total mercury content—fish weight relationship in swordfish (*Xiphias gladius*) caught in the Southwest Atlantic Ocean. *J. Food Compos. Anal*. **14**, 453–460 (2001).
22. Lavoie, R. A., Jardine, T. D., Chumchal, M. M., Kidd, K. A. & Campbell, L. M. Biomagnification of mercury in aquatic food webs: a worldwide meta-analysis. *Environ. Sci. Technol*. **47**, 13385–13394 (2013).
23. Hoen, D. K. et al. Amino acid ^{15}N trophic enrichment factors of four large carnivorous fishes. *J. Exp. Mar. Biol. Ecol*. **453**, 76–83 (2014).
24. Streets, D. G. et al. Total mercury released to the environment by human activities. *Environ. Sci. Technol*. **51**, 5969–5977 (2017).
25. Sunderland, E. M. & Mason, R. P. Human impacts on open ocean mercury concentrations. *Glob. Biogeochem. Cycles* **21**, GB4022 (2007).
26. Kitchell, J. F., Stewart, D. J. & Weininger, D. Applications of a bioenergetics model to yellow perch (*Perca flavescens*) and walleye (*Stizostedion vitreum vitreum*). *J. Fish. Res. Board Can*. **34**, 1922–1935 (1977).
27. Nøttestad, L., Giske, J., Holst, J. C. & Huse, G. A length-based hypothesis for feeding migrations in pelagic fish. *Can. J. Fish. Aquat. Sci*. **56**, 26–34 (1999).
28. Rudstam, L. G. Exploring the dynamics of herring consumption in the Baltic: applications of an energetics model of fish growth. *Kieler Meeresforschungen Sonderheft* **6**, 312–322 (1988).
29. Block, B. A. et al. Migratory movements, depth preferences, and thermal biology of Atlantic bluefin tuna. *Science* **293**, 1310–1314 (2001).
30. Neilson, J. D. et al. Seasonal distributions and migrations of Northwest Atlantic swordfish: inferences from integration of pop-up satellite archival tagging studies. *PLoS ONE* **9**, e112736 (2014).
31. Bowman, K. L., Hammerschmidt, C. R., Lamborg, C. H. & Swarr, G. Mercury in the North Atlantic Ocean: the U.S. GEOTRACES zonal and meridional sections. *Deep Sea Res. Part II Top. Stud. Oceanogr*. **116**, 251–261 (2015).
32. Scharf, F. S., Juanes, F. & Rountree, R. Predator size–prey size relationships of marine fish predators: interspecific variation and effects of ontogeny and body size on trophic-niche breadth. *Mar. Ecol. Prog. Ser*. **208**, 229–248 (2000).
33. Young, J., Lansdell, M., Riddoch, S. & Revill, A. Feeding ecology of broadbill swordfish, *Xiphias gladius*, off eastern Australia in relation to physical and environmental variables. *Bull. Mar. Sci*. **79**, 793–809 (2006).

Acknowledgements We thank S. Durkee at the US Environmental Protection Agency (EPA) for discussion of this work; P. Balcom and P. Béziat for assistance in analysing fish Hg samples; and C. S. Lee, N. Fisher and G. Harding for biological data. Financial support for this study was provided by the US EPA (contract EP-H-11-001346); the US National Science Foundation (OCE 1260464); and the Nereus Program sponsored by the Nippon Foundation. Statements in this publication represent the professional views of the authors and should not be construed to represent any determination or policy of the US EPA.

Author contributions E.M.S. initiated the study; A.T.S. synthesized data and performed research; A.T.S., C.P.T., A.Q. and C.D. developed the model; K.G. and A.H. provided new data on ABFT; and A.T.S. and E.M.S. wrote the manuscript. All authors helped to interpret the results and provided comments.

Competing interests The authors declare no competing interests.

Additional information

Supplementary information is available for this paper at https://doi.org/10.1038/s41586-019-1468-9.

Correspondence and requests for materials should be addressed to A.T.S. or E.M.S.

Peer review information *Nature* thanks Richard T. Barber and the other, anonymous, reviewer(s) for their contribution to the peer review of this work.

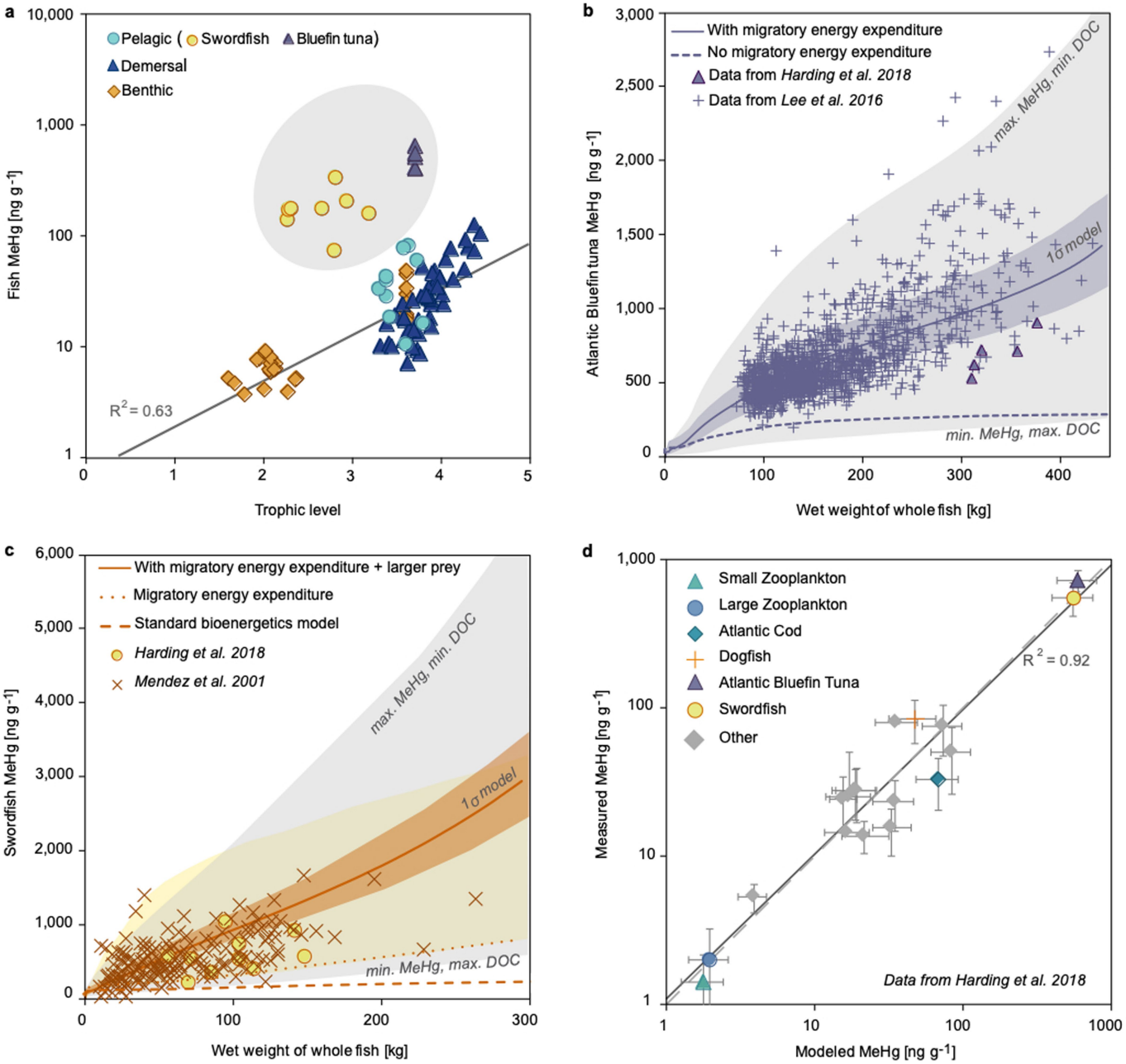

Extended Data Fig. 1 | Comparison of observed and modelled MeHg concentrations from a marine food web in the Gulf of Maine. **a**, Measured MeHg concentrations in biota and trophic positions based on nitrogen isotopes[19]. **b**, Measured (symbols) MeHg concentrations[16,19] in ABFT from the Gulf of Maine compared to modelled concentrations based on standard bioenergetics algorithms (dashed line) and based on bioenergetics algorithms adjusted for the energy consumption that is associated with migration and rapid swimming speeds (solid line). The blue shaded region shows the 67% confidence interval around the model and the grey shaded region represents the upper and lower bounds of modelled seawater MeHg and DOC concentrations. Each data point represents an individual fish; $n = 1,284$. **c**, Measured (symbols) MeHg concentrations[21] in swordfish and modelled MeHg concentrations based on standard bioenergetics algorithms (dashed line); algorithms adjusted for migratory energy expenditure and swimming speed (dotted line); and algorithms adjusted for energy expenditure and large prey consumption (solid line). The yellow shaded region indicates the upper and lower bounds of predator-to-prey length ratios (10:1 to 2:1), the orange shaded region shows the 67% confidence interval around the model and the grey shaded region represents the upper and lower bounds of modelled seawater MeHg and DOC. Each data point represents an individual fish; $n = 203$. **d**, Comparison of observed and modelled MeHg concentrations for the Gulf of Maine food web across five trophic levels[19]. The model is forced by seawater MeHg concentrations[17] ranging from 0.015 to 0.055 pM. Each data point represents the mean MeHg concentration in fish of a similar weight ($n = 119$); error bars represent s.d.

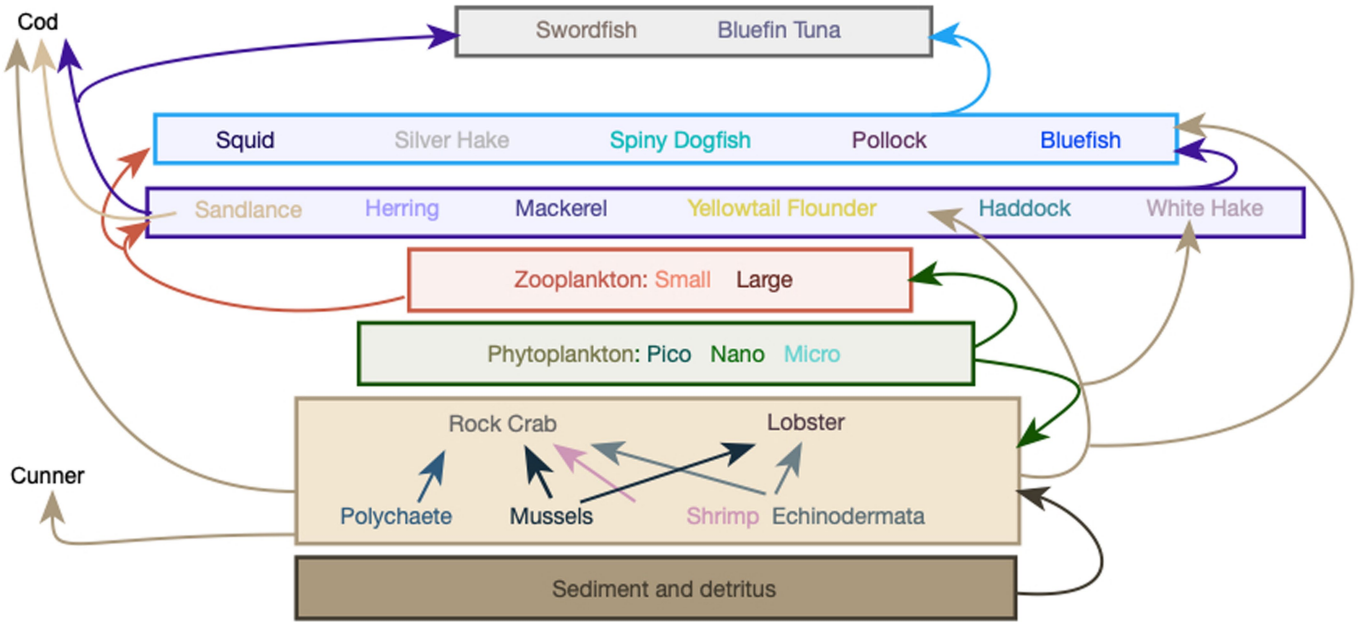

Extended Data Fig. 2 | Feeding relationships in the Gulf of Maine marine food web. Trophic interactions for the Gulf of Maine food web that are included in our MeHg bioaccumulation model.

Extended Data Table 1 | MeHg in Gulf of Maine plankton

Category	Dominant	Size [mm]	Mass [g]	MeHg [ng g^{-1}]	Trophic Level*
Microplankton	*Pleurosigma sp.* *Thalassionema nitschioides*	0.025-0.063	$6.5x10^{-8}$	0.13±0.10	1.0
	Streptotheca sp.	0.063-0.12	$1.1x10^{-6}$	0.17±0.13	1.0
	Rhizosolenia alata *Oithona sp.*	0.12-0.25	$8.2x10^{-6}$	0.32±0.16	2.6
Mesoplankton	*Calanus* sp.	0.25-0.50	$6.5x10^{-5}$	0.48±0.32	2.8
	Calanus finmarchicus (copepodites)	0.5-1.0	$5.2x10^{-4}$	0.58±0.19	2.7
Macroplankton	*Calanus finmarchicus* (adults)	1.0-2.0	$4.2x10^{-3}$	1.4±0.72	3.1
	Calanus hyperboreus	2.0-4.0	$3.4x10^{-2}$	2.0±1.2	3.4
Nekton	*Meganyctiphanes norvegica*	4.0-8.0	0.27	4.3±1.3	3.4
	Meganyctiphanes norvegica	8.0-16	2.1	5.5±1.9	3.4
	Pasiphaea multidentata	>16	17	14 ±11	3.9

MeHg concentrations (ng g^{-1}; mean ± s.d.) measured in Gulf of Maine plankton between 2000 and 2002[19]. Plankton were collected yearly with 3–5 tows and sieved for size fractions. Macroplankton, ichthyoplankton and nekton were collected yearly with 4–5 Vass–Tucker trawls[19].
*Trophic level (TL) was estimated previously[19] as $TL = 1 + (\delta^{15}N + 0.03)/3.4$.

Extended Data Table 2 | MeHg in Gulf of Maine fish and shellfish

Category	Species		Mass [kg]	MeHg [ng g^{-1}]	n	Trophic Level*
Invertebrates	Blue mussel	*Mytilus edulis*	0.005±0.001	5.3±1.1	12	3.1
	Sea scallop	*Placopecten magellanicus*	0.04±0.03	6.9±1.5	8	3.1
	American lobster	*Homarus americanus*	0.34±0.03	28±11	10	4.6
Benthic	Winter flounder	*Pseudopleuronectes*	0.22	15±7.8	14	4.4
	Yellowtail flounder	*Limanda ferruginea*	0.55±0.17	23±8.7	14	4.5
Benthopelagic	Pollock	*Pollachius virens*	0.41±0.48	15±5.4	10	4.6
	Haddock	*Melanogrammus anglefinus*	0.46±0.28	18±11	16	4.8
	Cod	*Gadus morhua*	1.5±1.2	27±14	19	4.7
	White hake	*Urophycis tenuis*	1.1±0.40	24±10	8	5.0
	Cunner	*Tautogolabrus adspersus*	0.12±0.02	75±28	9	5.2
	Spiny dogfish	*Squalus acanthias*	1.4±0.80	84±27	16	4.2
Pelagic	Atlantic Herring	*Clupea harengus*	0.15±0.050	40±25	15	4.5
	Atlantic Mackerel	*Scomber scombrus*	0.16±0.080	17±5.3	14	4.6
	Swordfish	*Xiphias gladius*	100±30	580±240	11	3.8
	Atlantic Bluefin Tuna	*Thunnus thynnus*	340±30	710±140	5	3.7
	Thresher Shark	*Alopias vulpinus*	560	1800	1	4.7

MeHg concentrations (ng g^{-1}; mean ± s.d.) measured in Gulf of Maine fish and shellfish between 2000 and 2002[19].
*Trophic level (TL) was estimated previously[19] as $TL = 1 + (\delta^{15}N + 0.03)/3.4$.

Extended Data Table 3 | MeHg in Gulf of Maine ABFT

Capture year	Mean MeHg† (ng g^{-1} wet weight)	Standard deviation	Pairwise Comparison‡	Sample size (*n*)	Data source
1971	593	144	a	5	[19]
1990	992	144	f	14	[18]
2002	637	96.1	ac	3	[16]
2004	822	254	de	15	[15]
2005	652	147	ac	9	[15]
2006	815	199	de	10	[15]
2007	792	182	de	7	[15]
2008	755	198	bcd	8	[15]
2009	580	--	a	1	[15]
2010	777	214	cde	9	[15]
2011	614	195	ab	12	[15]
2012	689	123	ad	13	[15]
2017	809	277	ef	33	This study§

MeHg concentrations (ng g^{-1}; mean ± s.d.) measured in ABFT that were captured in the Gulf of Maine between 1971 and 2017. All fish are approximately 14 years old or have a curved fork length of 250 ± 23 cm[14] (mean ± s.d.).

†MeHg was estimated as 90% of total Hg on the basis of previously published measurements[19].

‡A one-way ANOVA was used for each ABFT cohort to investigate the statistical significance of differences in fish MeHg concentrations between years ($P < 0.05$). Common letters indicate groups with no significant difference in between-group comparisons (post hoc analysis using Tukey's test). Statistical analysis was performed in R (v.3.4.3).

§Dorsal or cranial muscle tissue from ABFT that were captured in the Gulf of Maine in 2017 was freeze-dried and homogenized. Total Hg content was measured using a Nippon MA-3000 direct thermal decomposition Hg analyser at Harvard University. Average recoveries of certified reference materials were 104.0 ± 0.6% (mean ± s.d.) (TORT, $n = 5$) and 102.2 ± 1.7% (mean ± s.d.) (DORM-4, $n = 8$). The relative precision of duplicate samples (RPD) was 3.1%.

Extended Data Table 4 | Modelled changes in seawater MeHg in the Gulf of Maine

Year	MeHg (pM)	Year	MeHg (pM)	Year	MeHg (pM)	Year	MeHg (pM)
1950	0.049	**1970**	0.061	**1990**	0.052	**2010***	0.044
1951	0.049	**1971**	0.062	**1991**	0.052	**2011**	0.044
1952	0.048	**1972**	0.063	**1992**	0.051	**2012**	0.044
1953	0.048	**1973**	0.063	**1993**	0.050	**2013**	0.044
1954	0.048	**1974**	0.064	**1994**	0.050	**2014**	0.045
1955	0.048	**1975**	0.064	**1995**	0.049	**2015**	0.045
1956	0.048	**1976**	0.063	**1996**	0.049	**2016**	0.045
1957	0.048	**1977**	0.063	**1997**	0.048	**2017**	0.045
1958	0.049	**1978**	0.062	**1998**	0.048	**2018**	0.046
1959	0.049	**1979**	0.061	**1999**	0.047	**2019**	0.046
1960	0.050	**1980**	0.060	**2000**	0.047	**2020**	0.046
1961	0.051	**1981**	0.059	**2001**	0.046	**2021**	0.046
1962	0.052	**1982**	0.058	**2002**	0.046	**2022**	0.047
1963	0.053	**1983**	0.057	**2003**	0.045	**2023**	0.047
1964	0.054	**1984**	0.057	**2004**	0.045	**2024**	0.047
1965	0.055	**1985**	0.056	**2005**	0.045	**2025**	0.047
1966	0.056	**1986**	0.055	**2006**	0.045	**2026**	0.047
1967	0.057	**1987**	0.054	**2007**	0.044	**2027**	0.048
1968	0.059	**1988**	0.054	**2008***	0.044	**2028**	0.048
1969	0.060	**1989**	0.053	**2009***	0.044	**2029**	0.048

Seawater MeHg concentrations that were used to force modelled changes in MeHg tissue concentrations in ABFT.
*Time series is based on average measured concentrations[17] in the upper 60 m of the Gulf of Maine between 2008 and 2010 (grey shaded cells) and scaled by the trajectory in modelled total Hg in seawater between 1950 and 2030[24,25].

Extended Data Table 5 | Changes in seawater temperature in the Gulf of Maine

Year	***1981***	***1982***	***1983***	***1984***	***1985***	***1986***	***1987***	***1988***	***1989***
δT	-0.35	-0.08	0.43	0.29	0.06	-0.17	-0.65	-0.49	-0.24
Year	***1990***	***1991***	***1992***	***1993***	***1994***	***1995***	***1996***	***1997***	***1998***
δT	0.15	0.07	-0.73	-0.23	0.26	0.04	-0.83	-0.32	-0.37
Year	***1999***	***2000***	***2001***	***2002***	***2004***	***2004***	***2005***	***2006***	***2007***
δT	0.82	0.5	0.24	0.74	-0.14	-0.73	-0.04	0.58	-0.14
Year	***2008***	***2010***	***2011***	***2012***	***2013***	***2013***	***2014***	***2015***	***2016***
δT	0.2	0.29	0.89	0.81	2.11	1.23	1.16	1.17	1.23
Year	**2017**	**2018**	**2019**	**2020**	**2021**	**2022**	**2023**	**2024**	**2025**
δT	1.17	1.17	0.96	1.00	1.04	1.08	1.12	1.16	1.20
Year	**2026**	**2027**	**2028**	**2029**	**2030**				
δT	1.24	1.28	1.32	1.36	1.40				

Deviation (δT) from average seawater temperature (T,°C) in the Gulf of Maine. Grey shading indicates projected temperatures. Data are from a previous study[8].

Extended Data Table 6 | Food web model algorithms

Parameter	Unit	Description	Equation or Value
$\frac{dC_i}{dt}$	*ng g^{-1}*	Change in concentration of MeHg in predator species (i)	$\{k_D + k_V - (k_E + k_G)\} \cdot C_i$
k_D	*d^{-1}*	MeHg dietary uptake rate	$A_E \cdot X_j \cdot \frac{C_j}{C_i}$
k_V	*d^{-1}*	MeHg water/gill ventilation uptake rate	$\eta \cdot C_W \cdot \frac{G_V}{C_i \cdot M_i}$
k_E	*d^{-1}*	MeHg elimination rate	$a_E \cdot M^{b_E} \cdot e^{(c_E \cdot T)}$
k_G	*d^{-1}*	MeHg growth dilution rate	$\frac{G}{M_i}$
t	*d*	time	variable
M_i	*g*	wet weight of predator fish (i)	*Modeled based on bioenergetics equations*
A_E	*unitless*	dietary MeHg absorption efficiency	*Uniformly distributed between 0.75 and 0.95*
X_j	*d^{-1}*	Rate of consumption of prey (j)	*Species-specific model parameter*
C_j		concentration of MeHg in prey species (j)	*Modeled*
G_V	*L d^{-1}*	gill ventilation/ water filtration rate	$1400 \cdot \frac{(M_i \cdot 10^{-3})^{0.65}}{C_{OX}}$
η	*unitless*	absorption efficiency for MeHg from seawater	$\left(\Lambda + \frac{\Gamma}{K_{OW}}\right)^{-1}$
a_E	*d^{-1}*	MeHg elimination rate slope	0.00335
b_E	*unitless*	MeHg elimination rate intercept	-0.195
c_E	*unitless*	temperature coefficient	0.0066
G	*g d^{-1}*	growth rate	*Modeled based on bioenergetics equations*
T	*°C*	seawater temperature	**Extended Data Table 5**
C_{OX}	*mg O_2 L^{-1}*	dissolved oxygen concentration as a function of temperature	$(-0.24 \cdot T + 14.04) \cdot S_{OX}$
S_{OX}	*unitless*	oxygen saturation of the water column	0.9
Λ	*unitless*	constant	1.87
Γ	*unitless*	constant	155
K_{OW}	*unitless*	octanol-water partition coefficient for CH_3HgCl	1.7

Model algorithms for MeHg accumulation in marine predators. Additional background information is provided in the Supplementary Information and in our previous study[6].

Extended Data Table 7 | Trophic interactions in the food web model

	Prey																						
Predator	1-Picoplankton	2-Nanoplankton	3-Microplankton	4-Small zooplankton	5-Large Zooplankton	6-Mussels	7- Echinodermata	8-Polychaeta	9-Shrimp	10-Sand Lance	11-Mackerel	12-Rock Crab	13-Squid	13-Lobster	15-Herring	16-YT Flounder	17-Haddock	18-Silver Hake	19-Spiny Dogfish	20-Pollock	21-Bluefish	22-White Hake	23-Cunner	24-Cod
5	0.01	0.01	0.01	0.97	0	0	0	0	0	0	0	0	0	0	0	0	0	0	0	0	0	0	0	0
6	0	0	0	0	0	0	0	0	0	0	0	0	0	0	0	0	0	0	0	0	0	0	0	0
7	0.1	0.1	0.1	0	0	0.7	0	0	0	0	0	0	0	0	0	0	0	0	0	0	0	0	0	0
8	0	0	0	0	0	0	1	0	0	0	0	0	0	0	0	0	0	0	0	0	0	0	0	0
9	0	0.125	0.25	0.25	0.125	0.125	0	0.125	0	0	0	0	0	0	0	0	0	0	0	0	0	0	0	0
10	0	0	0	0.7	0.3	0	0	0	0	0	0	0	0	0	0	0	0	0	0	0	0	0	0	0
11	0	0	0	0.2	0.3	0	0	0	0.3	0.2	0	0	0	0	0	0	0	0	0	0	0	0	0	0
12	0	0	0	0	0	0.25	0.25	0.25	0.25	0	0	0	0	0	0	0	0	0	0	0	0	0	0	0
13	0	0	0	0	0.2	0	0	0	0.4	0.2	0.2	0	0	0	0	0	0	0	0	0	0	0	0	0
14	0	0	0	0	0.125	0.25	0.125	0	0	0	0	0.5	0	0	0	0	0	0	0	0	0	0	0	0
15	0	0	0	0.5	0.5	0	0	0	0	0	0	0	0	0	0	0	0	0	0	0	0	0	0	0
16	0	0	0	0	0.05	0	0.25	0.35	0.35	0	0	0	0	0	0	0	0	0	0	0	0	0	0	0
17	0	0	0	0	0.25	0.05	0.3	0.15	0.25	0	0	0	0	0	0	0	0	0	0	0	0	0	0	0
18	0	0	0	0	0.2	0	0	0	0.1	0.15	0.15	0	0.1	0	0.3	0	0	0	0	0	0	0	0	0
19	0	0	0	0	0	0.1	0	0	0.05	0.1	0.1	0.05	0.3	0.05	0.2	0.05	0	0	0	0	0	0	0	0
20	0	0	0	0	0.5	0	0	0	0	0.05	0	0	0.05	0	0.2	0	0	0.2	0	0	0	0	0	0
21	0	0	0	0	0	0	0	0.1	0.1	0	0	0	0.2	0	0.3	0	0.1	0.2	0	0	0	0	0	0
22	0	0	0	0	0.25	0.25	0.25	0.25	0	0	0	0	0	0	0	0	0	0	0	0	0	0	0	0
23	0	0	0	0	0	0.3	0	0	0.2	0	0	0	0	0.5	0	0	0	0	0	0	0	0	0	0
24	0	0	0	0	0	0	0	0	0.25	0.25	0	0.25	0	0.25	0	0	0	0	0	0	0	0	0	0
25*	0	0	0	0	0	0	0	0	0	0.25	0.05	0	0	0	0.5	0	0	0	0.05	0	0.1	0	0	0.05
26*	0	0	0	0	0	0	0	0	0	0	0.2	0	0.5	0	0.1	0	0	0.1	0	0	0.1	0	0	0

Feeding preferences of predator species in the Gulf of Maine. All feeding preferences are based on a synthesis of stomach-contents data by the Northeast Fisheries Science Center (NEFSC)[7].
*Predator no. 25 is ABFT and predator no. 26 is swordfish.

nature research

Corresponding author(s): Elsie Sunderland

Reporting Summary

Nature Research wishes to improve the reproducibility of the work that we publish. This form provides structure for consistency and transparency in reporting. For further information on Nature Research policies, see Authors & Referees and the Editorial Policy Checklist.

Statistical parameters

When statistical analyses are reported, confirm that the following items are present in the relevant location (e.g. figure legend, table legend, main text, or Methods section).

n/a	Confirmed	
☐	☒	The exact sample size (*n*) for each experimental group/condition, given as a discrete number and unit of measurement
☐	☒	An indication of whether measurements were taken from distinct samples or whether the same sample was measured repeatedly
☐	☒	The statistical test(s) used AND whether they are one- or two-sided *Only common tests should be described solely by name; describe more complex techniques in the Methods section.*
☐	☒	A description of all covariates tested
☐	☒	A description of any assumptions or corrections, such as tests of normality and adjustment for multiple comparisons
☐	☒	A full description of the statistics including central tendency (e.g. means) or other basic estimates (e.g. regression coefficient) AND variation (e.g. standard deviation) or associated estimates of uncertainty (e.g. confidence intervals)
☒	☐	For null hypothesis testing, the test statistic (e.g. *F*, *t*, *r*) with confidence intervals, effect sizes, degrees of freedom and *P* value noted *Give P values as exact values whenever suitable.*
☒	☐	For Bayesian analysis, information on the choice of priors and Markov chain Monte Carlo settings
☒	☐	For hierarchical and complex designs, identification of the appropriate level for tests and full reporting of outcomes
☒	☐	Estimates of effect sizes (e.g. Cohen's *d*, Pearson's *r*), indicating how they were calculated
☐	☒	Clearly defined error bars *State explicitly what error bars represent (e.g. SD, SE, CI)*

Our web collection on statistics for biologists may be useful.

Software and code

Policy information about availability of computer code

Data collection	We generated a new model for marine food web bioaccumulation of methylmercury in this study. All data and algorithms are provided in the SI and described in full.
Data analysis	All algorithms used in our study are provided in the supporting information and the code will be made available on request.

For manuscripts utilizing custom algorithms or software that are central to the research but not yet described in published literature, software must be made available to editors/reviewers upon request. We strongly encourage code deposition in a community repository (e.g. GitHub). See the Nature Research guidelines for submitting code & software for further information.

Data

Policy information about availability of data

All manuscripts must include a data availability statement. This statement should provide the following information, where applicable:

- Accession codes, unique identifiers, or web links for publicly available datasets
- A list of figures that have associated raw data
- A description of any restrictions on data availability

Data tables for data used in this study are provided in the extended and supporting information.

Field-specific reporting

Please select the best fit for your research. If you are not sure, read the appropriate sections before making your selection.

☐ Life sciences ☐ Behavioural & social sciences ☒ Ecological, evolutionary & environmental sciences

For a reference copy of the document with all sections, see nature.com/authors/policies/ReportingSummary-flat.pdf

Ecological, evolutionary & environmental sciences study design

All studies must disclose on these points even when the disclosure is negative.

Study description	This study presents a new model for the influence of ecosystem change on methylmercury bioaccumulation in marine food webs of the Northwestern Atlantic Ocean over the past 30 years. Empirical data were used to quantitatively evaluate a mechanistic simulation model for methylmercury bioaccumulation and evaluate changes over time.
Research sample	Data include concentrations of methymercury measured in a variety of marine species from the Northwestern Atlantic Ocean, stomach contents data from government databases, previously published data on seawater temperature anomalies, and seawater concentrations of dissolved organic carbon and methylmercury, and sediment concentrations of methylmercury.
Sampling strategy	This study was based on all available data/samples over the last 30 years. No new sampling was conducted.
Data collection	Data were collected from diverse sources in the peer-reviewed literature and government databases.
Timing and spatial scale	Study focuses on model evaluation for the 2000-2003 period and patterns in temperature and methylmercury accumulation between the 1970s to present in the Northwestern Atlantic Ocean.
Data exclusions	We present results for temporal changes in a single tuna age/length class of Atlantic bluefin tuna. Other ages/lengths would require additional simulations and are not included in this study.
Reproducibility	All results are reproducible with code provided in this study. This study does not include new experimental results. Code has been validated.
Randomization	Data on fish Hg concentrations were selected for similar length/age categories to ensure comparability. No randomization was needed.
Blinding	Blinding was not relevant to this study because it involved a synthesis of data on fish Hg concentrations and ecological shifts.

Did the study involve field work? ☐ Yes ☒ No

Reporting for specific materials, systems and methods

Materials & experimental systems

n/a	Involved in the study
☒	☐ Unique biological materials
☒	☐ Antibodies
☒	☐ Eukaryotic cell lines
☒	☐ Palaeontology
☒	☐ Animals and other organisms
☒	☐ Human research participants

Methods

n/a	Involved in the study
☒	☐ ChIP-seq
☒	☐ Flow cytometry
☒	☐ MRI-based neuroimaging

LETTER

https://doi.org/10.1038/s41586-019-1476-9

The decoupled nature of basal metabolic rate and body temperature in endotherm evolution

Jorge Avaria-Llautureo[1,2]*, Cristián E. Hernández[3], Enrique Rodríguez-Serrano[4] & Chris Venditti[1]*

The origins of endothermy in birds and mammals are important events in vertebrate evolution. Endotherms can maintain their body temperature (T_b) over a wide range of ambient temperatures primarily using the heat that is generated continuously by their high basal metabolic rate (BMR)[1]. There is also an important positive feedback loop as T_b influences BMR[1–3]. Owing to this interplay between BMRs and T_b, many ecologists and evolutionary physiologists posit that the evolution of BMR and T_b must have been coupled during the radiation of endotherms[3–5], changing with similar trends[6–8]. However, colder historical environments might have imposed strong selective pressures on BMR to compensate for increased rates of heat loss and to keep T_b constant[9–12]. Thus, adaptation to cold ambient temperatures through increases in BMR could have decoupled BMR from T_b and caused different evolutionary routes to the modern diversity in these traits. Here we show that BMR and T_b were decoupled in approximately 90% of mammalian phylogenetic branches and 36% of avian phylogenetic branches. Mammalian BMRs evolved with rapid bursts but without a long-term directional trend, whereas T_b evolved mostly at a constant rate and towards colder bodies from a warmer-bodied common ancestor. Avian BMRs evolved predominantly at a constant rate and without a long-term directional trend, whereas T_b evolved with much greater rate heterogeneity and with adaptive evolution towards colder bodies. Furthermore, rapid shifts that lead to both increases and decreases in BMRs were linked to abrupt changes towards colder ambient temperatures—although only in mammals. Our results suggest that natural selection effectively exploited the diversity in mammalian BMRs under diverse, often-adverse historical thermal environments.

Phylogenetic statistical methods[13,14] provide us with the opportunity to formally test whether BMR has been linked to T_b or ambient temperature (T_a) throughout the evolution of birds and mammals. By accommodating for and identifying heterogeneity in the rate of phenotypic evolution, these methods can detect and reconstruct accurate historical evolutionary processes[15]. Evaluation of the evolutionary coupling between BMR and T_b has direct consequences for several longstanding ecological and evolutionary theories[2–8] (including the metabolic theory of ecology) that assume coupling between BMR and T_b.

We first quantified and compared rates of evolution for BMR and T_b along each branch of the time-calibrated phylogenetic trees of birds and mammals (hereafter, branch-wise rates (r); Methods). r is a rate scalar by which the background rate of evolution (σ^2_b) is multiplied to increase or decrease the pace of evolution; it measures how fast a trait evolved along an individual phylogenetic branch (Methods). If BMR and T_b were coupled during the evolution of endotherms, the amount of change along phylogenetic branches for both traits should be positively associated—in cases in which r_{BMR} is high, we expect it to be high for r_{T_b} (Fig. 1 b). We tested this prediction against alternative evolutionary scenarios. First, we cannot make any inferences about coupling or decoupling in cases in which there is no rate heterogeneity for both BMR and T_b ($r = 1$ for all branches in the tree for both traits) (Fig. 1a). Second, we infer decoupled evolution if both traits show rate heterogeneity, for which the magnitudes of r values are negatively correlated (that is, branches that evolve at a high rate for BMR but a low rate for T_b, and vice versa) (Fig. 1c). We suggest this scenario indicates decoupled evolution because a negative correlation most probably indicates that one trait tends to be conserved while the other evolved rapidly. Third, we infer decoupled evolution if only one trait shows rate heterogeneity while the other evolved at a constant rate (Fig. 1d, e) or if both traits show heterogeneity but the branch-wise rates are not associated (Fig. 1f).

As BMR, body mass (M), T_b and T_a are—at least to some extent—correlated in extant birds and mammals, and such correlations may vary between orders[16], we estimated the branch-wise rates for BMR and T_b while accounting for their covariates across extant species using the phylogenetic variable-rate regression model[17] (Methods).

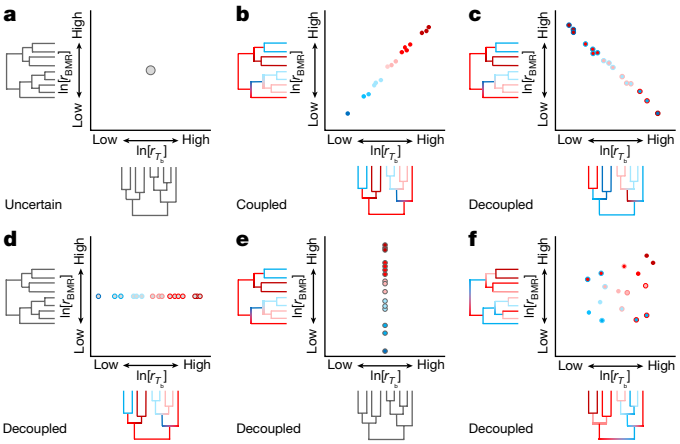

Fig. 1 | Possible evolutionary scenarios for BMR and T_b given their branch-wise rates in a bivariate space. a, Both traits evolve at a single constant rate across all branches of the tree ($r_{BMR} = 1$ and $r_{T_b} = 1$); in this case, we have no statistical power to evaluate an association between BMR and T_b. **b**, A positive correlation between r_{BMR} and r_{T_b} indicates that both traits are coupled—in cases in which BMR changed more, T_b also changed. **c**, A negative correlation between r_{BMR} and r_{T_b} implies that both traits are decoupled because when BMR changed more, T_b changed less. **d**–**f**, Correlations indicate that both traits are decoupled—when BMR evolved at a single constant rate, T_b evolved at a variable rate (**d**) or vice versa (**e**); or both traits evolved at variable rates ($r_{BMR} \neq 1$ and $r_{T_b} \neq 1$) but their magnitudes were not statistically correlated (**f**). Grey colour represents the constant background rate ($r = 1$). Red colours represent rates that are faster than the background rate ($r > 1$) and blue colours represent rates that are slower than the background rate ($r < 1$), which might be related to past events of positive[17] and stabilizing selection[24], respectively. Point fill colours represent the magnitudes of r_{BMR} and point outline colours represent magnitudes of r_{T_b}.

[1]School of Biological Sciences, University of Reading, Reading, UK. [2]Centro de Investigación en Biodiversidad y Ambientes Sustentables (CIBAS), Facultad de Ciencias, Universidad Católica de la Santísima Concepción (UCSC), Concepción, Chile. [3]Laboratorio de Ecología Evolutiva y Filoinformática, Departamento de Zoología, Facultad de Ciencias Naturales y Oceanográficas, Universidad de Concepción, Concepción, Chile. [4]Laboratorio de Mastozoología, Departamento de Zoología, Facultad de Ciencias Naturales y Oceanográficas, Universidad de Concepción, Concepción, Chile.
*e-mail: jorgeavariall@gmail.com; c.d.venditti@reading.ac.uk

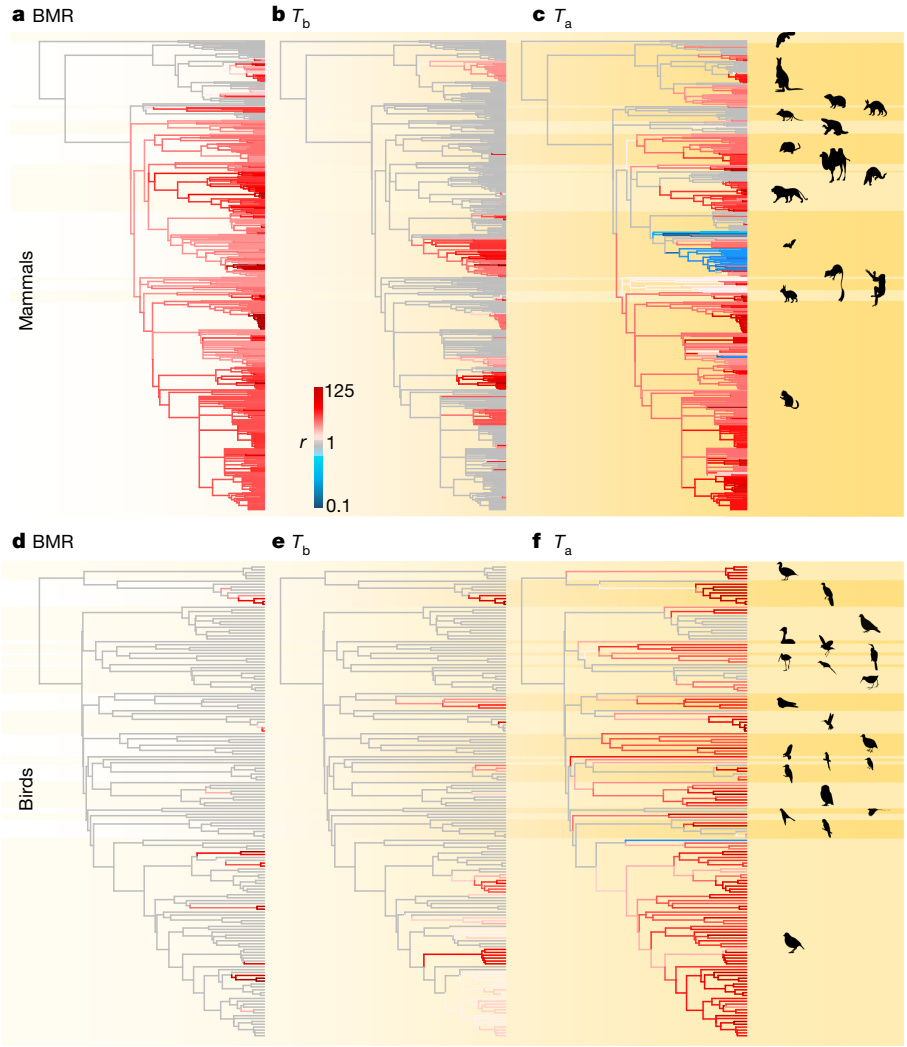

Fig. 2 | Branch-wise rates of BMR, T_b and T_a on the mammalian and avian phylogeny. a–c, Branch-wise rates for mammalian BMR (**a**), T_b (**b**) and T_a (**c**). **d–f**, Branch-wise rates for avian BMR (**d**), T_b (**e**) and T_a (**f**). The *r* values for each phylogenetic branch are shown in colours, and indicate whether the trait evolved at a constant background rate ($r = 1$, grey branches), at rates slower than the background rate ($r < 1$, blue-gradient branches) or at rates faster than the constant rate ($r > 1$, red-gradient branches). All silhouettes were obtained from http://phylopic.org/. Mammalian silhouettes were created by the following individuals (from top to bottom): Monotremata, S. Werning; Marsupialia, M. Callaghan; Hyracoidea, by S. Traver; Tubulidentata, P. Scott; Macroscelidea (uncredited); Pilosa, FunkMonk; Eulipotyphla, B. Barnes; Artiodactyla, nicubunu; Pholidota, S. Traver; Carnivora (uncredited); Chiroptera, Y. Wong; Scandentia, T. M. Keesey; Primates, T. M. Keesey; Lagomorpha, A. Caravaggi; and Rodentia (uncredited). Avian silhouettes were created by the following individuals from top to bottom: Anseriformes, M. Martyniuk; Galliformes (uncredited); Columbiformes, F. Sayol; Podicipediformes, D. Backlund; Procellariiformes, M. Hannaford; Suliformes, F. Sayol; Pelecaniformes, S. Traver; Cuculiformes, F. Sayol; Gruiformes, F. Sayol; Caprimulgiformes, F. Sayol; Apodiformes, F. Sayol; Charadriiformes (uncredited); Accipitriformes, S. Traver; Bucerotiformes, S. Traver; Coraciiformes, F. Sayol; Piciformes, S. Traver; Strigiformes, F. Sayol, Coliiformes, E. J. Wetsy; Falconiformes, R. Groom; Psittaciformes, F. Sayol; and Passeriformes, P. Pattawaro.

This approach enables the simultaneous estimation of both an overall relationship between—for instance—BMR as a function of *M* and T_b across extant species, and any shifts in branch-wise rates that apply to the phylogenetically structured residual variance in the relationship. In both birds and mammals, the phylogenetic variable-rate regression model fits the data significantly better than the constant-rate regression models, which assume a single constant rate ($r = 1$) across all branches (Methods and Supplementary Tables 1–8). The best-fitting phylogenetic variable-rate regression model for mammalian BMR includes both *M* and T_b with a single slope for each trait that is estimated across all orders (Supplementary Tables 1, 2). For mammalian T_b, the best-fitting model includes *M* and BMR as covariates, also with a single slope across all orders (Supplementary Tables 3, 7). In birds, the best model for BMR includes only *M*, with a single slope for all orders (Supplementary Table 4). Finally, the best-fitting model for avian T_b includes *M* only in Columbiformes (Supplementary Table 6).

The branch-wise rates estimated for the best-fitting models show that mammalian BMR evolved at a constant rate ($r = 1$) in only 11.2% of branches and at faster rates ($r > 1$) in 88.8% of branches (Fig. 2a). Mammalian T_b evolved at a constant rate in 70.3% of branches and faster rates in 29.7% of branches (Fig. 2b). In birds, BMR evolved at a constant rate in 90.5% of branches and at faster rates in 9.5% of branches (Fig. 2d). Avian T_b evolved at a constant rate in 69% of branches and at faster rates in 31% (Fig. 2e). When the branch-wise rates for BMR and T_b were compared, we found that in mammals both traits evolved at a constant rate in 10.6% of branches (Fig. 3a, consistent with Fig. 1a). In 60.2% of branches, only one trait evolved at faster rates while the other trait diverged at a constant rate. This indicates that BMR and T_b evolved in a decoupled manner along these branches (Fig. 3a, consistent with Fig. 1d, e). We found that 29.2% of branches had an increased rate for both BMR and T_b. However, the magnitudes of the branch-wise rates were not significantly correlated (the percentage of the posterior distribution crossing zero as assessed by Bayesian Markov

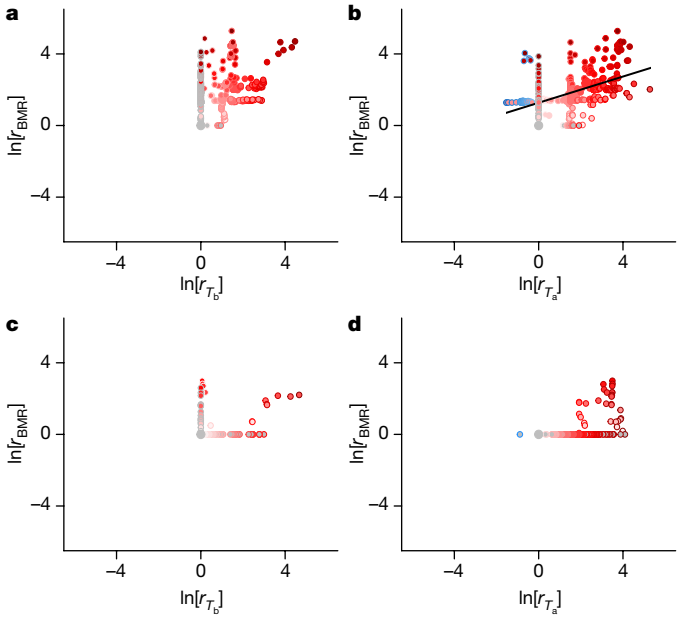

Fig. 3 | Branch-wise rates of BMR, T_b and T_a in bivariate space for mammals and birds. a, **b**, Bivariate space of mammals for r_{BMR} and r_{T_b} (**a**) or r_{T_a} (**b**). **c**, **d**, Bivariate space of birds for r_{BMR} and r_{T_b} (**c**) or r_{T_a} (**d**). **a**, In mammals, r_{BMR} was decoupled from r_{T_b} in 89.4% of branches because either only one trait showed rate heterogeneity while the other evolved a single constant rate (in 60.2% of branches; grey filled and red outlined dots, and grey outlined and red filled dots, consistent with Fig. 1d, e), or because both traits evolved at fast rates but the magnitudes of r_{BMR} and r_{T_b} were not correlated (in 29.2% of branches; red filled and outlined dots, consistent with Fig. 1f). In the remainder of the branches, 10.6%, (grey middle dot, consistent with Fig. 1a) there was no variation in either r_{BMR} or r_{T_b}. **b**, Bayesian generalized least squares analyses indicate that fast r_{BMR} and slow to fast r_{T_a} (red filled and blue and red outlined dots) were statistically correlated in 74.9% of mammalian branches ($P_{MCMC} = 0$; $n = 602$ branches; black line). In 18.2% of branches, the r_{BMR} was decoupled from r_{T_a} because only one trait shows rate heterogeneity (grey filled and red outlined dots and grey outlined and red filled dots). In the remainder of the branches, 6.9%, (grey middle dots), there was no variation in either r_{BMR} or r_{T_a}. **c**, In birds, r_{BMR} was decoupled from r_{T_b} in 36.2% of branches because either only 1 trait showed rate heterogeneity (in 32% of branches) or because the magnitude of fast rates in both traits were not correlated (in 4.2% of branches). There was no rate variation for either trait for the remaining 63.8% of branches. **d**, Avian r_{BMR} was decoupled from r_{T_a} in 77.9% of branches, because either only one trait showed rate heterogeneity (in 68.4% of branches) or because the magnitude of fast rates in both traits were not correlated (in 9.5% of branches). There was no variation in either trait for the remaining 22.1% of branches.

chain Monte Carlo (MCMC), $P_{MCMC} = 9\%$) (Fig. 3a, consistent with Fig. 1f; Supplementary Table 9). This also suggests that evolution was decoupled in those branches—probably because of distinct selection pressures that acted separately on BMR and T_b. On the other hand, both traits evolved at a constant rate in 63.8% of branches for birds (Fig. 3c, consistent with Fig. 1a). In 32% of branches, only one trait evolved at fast rates while the other trait diverged at a constant rate (Fig. 3c, consistent with Fig. 1d, e). In the remaining 4.2% of branches, both traits evolved at faster rates, but the magnitudes of r were not statistically correlated ($P_{MCMC} = 16.9\%$) (Fig. 3c, consistent with Fig. 1f; Supplementary Table 10).

As rapid bursts in the evolution of BMR were not coupled with the evolutionary changes in T_b, we evaluated the alternative hypothesis that postulates that BMR evolved in response to T_a. This hypothesis suggests that colder environments increase the rate of heat loss from organisms and that this loss is subsequently compensated for by increases in BMR[9–12]. These increases in BMR could have occurred over long periods of time because of global cooling[18]—generating a long-term directional trend in BMR during the radiation of mammals and birds. This expectation is consistent with the plesiomorphic–apomorphic endothermy model[6–8]. By assuming that BMR and T_b are coupled in endotherms and that they can both be used as a proxy for the degree of endothermy, the plesiomorphic–apomorphic endothermy model predicts a general tendency towards higher endothermic levels over time (from basoendothermic ancestors; Methods) associated with the global cooling during the Cenozoic era. However, global cooling is not the only source of variation in T_a. Long-term directional increases in BMR may have also been driven by historical dispersals of endotherms towards higher latitudes[19]. In either case, if a long-term decrease in T_a drove adaptation through increases in BMR, and T_b followed the same trajectory (as assumed by the plesiomorphic–apomorphic endothermy model), we expect to find a positive correlation between the branch-wise rates of BMR and the branch-wise rates of T_a. With this in mind, we also expect a positive trend towards higher values of BMR and T_b for basoendothermic ancestors and a negative trend towards lower T_a for warmer ancestral environments. We used the phylogenetic variable-rate regression model to estimate the branch-wise rates for T_a while accounting for latitude as, generally, T_a decreases from the equator to the poles (Methods and Supplementary Table 11).

The phylogenetic variable-rate regression model significantly improved the fit to the T_a data over the constant-rate regression model in both mammals and birds (Supplementary Table 11). T_a evolved at a constant rate in 21.2% of mammalian branches, and with rate heterogeneity in the remaining 78.8%—including 72.2% of branches with faster rates and 6.6% with slower rates ($r < 1$) (Fig. 2c). This indicates that most ancestral mammalian lineages (72.2%) faced abrupt historical changes in their T_a environment, while far fewer lineages (6.6%, most of which were bats) survived and continued to exist in similar thermal environments. In birds, 77.6% of branches show faster rates of change in T_a, 22.1% show changes at a constant rate and in only a single branch did the T_a change at a slower rate (Fig. 2f).

When branch-wise rates of mammalian BMR and T_a evolution were compared, we found that they were coupled in 74.9% of branches ($P_{MCMC} = 0\%$) (Fig. 3b, consistent with Fig. 1b; Supplementary Table 12). To evaluate further whether decreases in T_a were linked to increases in BMR in the 74.9% of mammals for which both traits were coupled (that is, to ascertain the direction of change), we evaluated the expected positive trend in BMR as a response to the long-term decrease in T_a. We conducted Bayesian phylogenetic regressions between extant values of these two variables (in turn) and the path-wise rates[15] (sum of rate-scaled branches along the path from the root of the tree to each terminal species; Methods). We found a negative effect of path-wise rates on T_a across all mammals (Fig. 4b and Supplementary Table 14), which supports a long-term directional trend towards habitats with lower T_a over time. However, we did not find evidence for any trend in mammalian BMR evolution—increases and decreases in BMR showed equal probabilities in our sample (Supplementary Table 14). Our results suggest that in colder environments, in which resources were available to fuel metabolic elevation, selection favoured higher mammalian BMR[20]. Another possibility might be that the increase in BMR was a correlated response to direct selection on other physiological traits, such as the maximum metabolic capacities for thermogenesis, for which the benefits outweigh the energetic cost of BMR elevation[20]. Otherwise, selection may have always favoured decreases in BMR in an ever-colder environment[20].

In contrast to mammals, most avian branches that experienced rapid shifts in T_a did not show evidence for coupled changes in BMR—68.4% of branches had fast rates of T_a evolution but a constant rate of BMR evolution (Fig. 3d, consistent with Fig. 1d, e). Moreover, the small fraction of branches for which BMR evolved at fast rates (9.5%) were not linked to rapid shifts in T_a (Fig. 3d, consistent with Fig. 1f; Supplementary Table 13). Avian BMR did not show a positive evolutionary trend despite the fact that birds also experienced colder environments over time (Fig. 4d and Supplementary Table 15). Birds might not have responded to colder temperatures by changes in their BMR

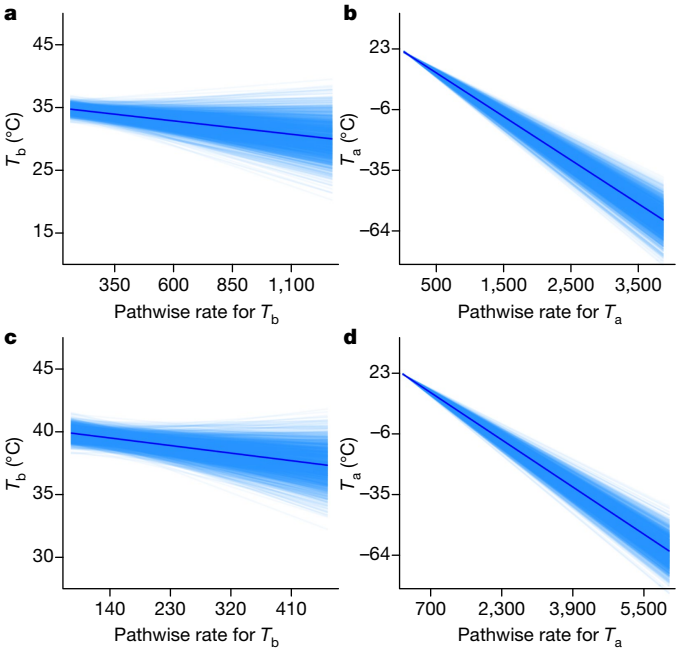

Fig. 4 | Mammals and birds evolved towards both colder T_b and T_a over their evolutionary history. a–d, Path-wise rates had a significant negative effect on mammalian T_b (**a**; $P_{MCMC} = 4\%$; $n = 502$ species) and avian T_b (**c**; $P_{MCMC} = 3\%$; $n = 367$ species) and on mammalian T_a (**b**; $P_{MCMC} = 0$; $n = 2{,}922$) and avian T_a (**d**; $P_{MCMC} = 0$; $n = 6{,}142$ species), supporting a negative macroevolutionary trend[15] for both T_b and T_a in mammals and birds. Lighter blue and dark blue lines indicate the posterior distribution of slopes and the mean slope, respectively, estimated from the Bayesian phylogenetic generalized least squares (Methods).

because their lower thermal conductance may have helped them to retain internal heat[9]. Alternatively, other physiological strategies, such as torpor, may have been selected for in colder environments[21].

Finally, we found a negative effect of path-wise rates on T_b in both mammals (Fig. 4a and Supplementary Table 14) and birds (Fig. 4c and Supplementary Table 15). This suggest that—on average—endotherms evolved towards colder bodies from warmer-bodied ancestors. These directional models predict a mean T_b of 35.3 °C and 40.4 °C for the most recent common ancestor (MRCA) of mammals and birds, respectively (Fig. 4a, c), suggesting that early birds and mammals were mesoendotherms rather than basoendotherms (Methods). This result does not support the idea that ancestral mammals could not attain $T_b > 30$ °C owing to the increased metabolic rates that would be necessary to compensate for heat loss in cold environments[22]. However, if the $T_b - T_a$ differential (ΔT) determines how hot early mammals were, we expect that a mammalian MRCA with a T_b of 35.3 °C could survive in an environment that was warm enough to have a low ΔT. Our model that describes the negative trend in T_a predicts that the MRCA of mammals lived in an environment that was 23 °C on average (Fig. 4b), resulting in a ΔT of 15.3 °C. This ancestral ΔT is very conservative compared with the ΔT values that have been observed in extant mammals. For example, there are small mammals that achieve a T_b higher than 39 °C (such as *Microdipodops pallidus*[16]) and that can survive in environments of 11 °C[19] ($\Delta T = 28$ °C). Furthermore, some larger mammals have a stable T_b even in extreme environmental conditions—the Arctic hare (*Lepus arcticus*) can maintain its T_b of 38 °C[16] in temperatures as low as −12 °C[19] ($\Delta T = 50$ °C).

Taken together, our results show that BMR was not coupled to T_b across the evolution of endothermic species. As environments became colder mammals survived by changing their BMR, while birds probably survived owing to their high thermal insulation. Evaluating the isolated and/or combined effects of environmental variables on physiological attributes has implications for evidence-based projections for the future[23]. In this sense, the previously unappreciated complexity, interplay and decoupled nature of the evolutionary history of BMR, T_b and T_a may point to the undetected resilience of endotherms in the face of modern global challenges.

Online content

Any methods, additional references, Nature Research reporting summaries, source data, extended data, supplementary information, acknowledgements, peer review information; details of author contributions and competing interests; and statements of data and code availability are available at https://doi.org/10.1038/s41586-019-1476-9.

Received: 5 November 2018; Accepted: 12 July 2019;
Published online 15 August 2019.

1. Clarke, A. *Principles of Thermal Ecology. Temperature, Energy and Life* (Oxford Univ. Press, 2017)
2. Gillooly, J. F., Brown, J. H., West, G. B., Savage, V. M. & Charnov, E. L. Effects of size and temperature on metabolic rate. *Science* **293**, 2248–2251 (2001).
3. Clarke, A. & Pörtner, H.-O. Temperature, metabolic power and the evolution of endothermy. *Biol. Rev. Camb. Philos. Soc.* **85**, 703–727 (2010).
4. Kemp, T. S. The origin of mammalian endothermy: a paradigm for the evolution of complex biological structure. *Zool. J. Linn. Soc.* **147**, 473–488 (2006).
5. Brown, J. H., Gillooly, J. F., Allen, A. P., Savage, V. M. & West, G. B. Towards a metabolic theory of ecology. *Ecology* **85**, 1771–1789 (2004).
6. Lovegrove, B. G. The evolution of endothermy in Cenozoic mammals: a plesiomorphic–apomorphic continuum. *Biol. Rev. Camb. Philos. Soc.* **87**, 128–162 (2012).
7. Lovegrove, B. G. The evolution of mammalian body temperature: the Cenozoic supraendothermic pulses. *J. Comp. Physiol. B* **182**, 579–589 (2012).
8. Lovegrove, B. G. A phenology of the evolution of endothermy in birds and mammals. *Biol. Rev. Camb. Philos. Soc.* **92**, 1213–1240 (2017).
9. Fristoe, T. S. et al. Metabolic heat production and thermal conductance are mass-independent adaptations to thermal environment in birds and mammals. *Proc. Natl Acad. Sci. USA* **112**, 15934–15939 (2015).
10. Naya, D. E., Naya, H. & White, C. R. On the interplay among ambient temperature, basal metabolic rate, and body mass. *Am. Nat.* **192**, 518–524 (2018).
11. White, C. R., Blackburn, T. M., Martin, G. R. & Butler, P. J. Basal metabolic rate of birds is associated with habitat temperature and precipitation, not primary productivity. *Proc. R. Soc. Lond. B* **274**, 287–293 (2007).
12. Jetz, W., Freckleton, R. P. & McKechnie, A. E. Environment, migratory tendency, phylogeny and basal metabolic rate in birds. *PLoS ONE* **3**, e3261 (2008).
13. Venditti, C., Meade, A. & Pagel, M. Multiple routes to mammalian diversity. *Nature* **479**, 393–396 (2011).
14. Rabosky, D. L. Automatic detection of key innovations, rate shifts, and diversity-dependence on phylogenetic trees. *PLoS ONE* **9**, e89543 (2014).
15. Baker, J., Meade, A., Pagel, M. & Venditti, C. Adaptive evolution toward larger size in mammals. *Proc. Natl Acad. Sci. USA* **112**, 5093–5098 (2015).
16. Clarke, A., Rothery, P. & Isaac, N. J. B. Scaling of basal metabolic rate with body mass and temperature in mammals. *J. Anim. Ecol.* **79**, 610–619 (2010).
17. Baker, J., Meade, A., Pagel, M. & Venditti, C. Positive phenotypic selection inferred from phylogenies. *Zool. J. Linn. Soc.* **118**, 95–115 (2016).
18. Zachos, J., Pagani, M., Sloan, L., Thomas, E. & Billups, K. Trends, rhythms, and aberrations in global climate 65 Ma to present. *Science* **292**, 686–693 (2001).
19. Rolland, J. et al. The impact of endothermy on the climatic niche evolution and the distribution of vertebrate diversity. *Nat. Ecol. Evol.* **2**, 459–464 (2018).
20. Swanson, D. L., McKechnie, A. E. & Vézina, F. How low can you go? An adaptive energetic framework for interpreting basal metabolic rate variation in endotherms. *J. Comp. Physiol. B* **187**, 1039–1056 (2017).
21. Körtner, G., Brigham, R. M. & Geiser, F. Winter torpor in a large bird. *Nature* **407**, 318 (2000).
22. Crompton, A. W., Taylor, C. R. & Jagger, J. A. Evolution of homeothermy in mammals. *Nature* **272**, 333–336 (1978).
23. Bozinovic, F. & Pörtner, H.-O. Physiological ecology meets climate change. *Ecol. Evol.* **5**, 1025–1030 (2015).
24. Lieberman, B. S. & Dudgeon, S. An evaluation of stabilizing selection as a mechanism for stasis. *Palaeogeogr. Palaeoclimatol. Palaeoecol.* **127**, 229–238 (1996).

METHODS

Data. We used a time-calibrated phylogenetic tree of extant mammals ($n = 3{,}321$)[25], and data for M, BMR and T_b were obtained from a previously published study[16] ($n = 632$). After identifying species in the tree that have trait information, we obtained a final mammalian dataset of 502 species, which includes representatives from 15 orders (Supplementary Information).

For birds, we used the consensus time-calibrated tree from a previous study[19]. This tree was inferred from the samples of trees that have previously been published[26]. Data for BMR, T_b and M were obtained from a previously published study[9]. After matching this database with the phylogenetic tree, we obtained a final sample of 164 species, which includes representatives from 21 orders (Supplementary Information). The dataset used to evaluate evolutionary trends in T_b (see below) has previously been published[27], and contains 367 species with phylogenetic information.

Data for T_a and latitude for extant mammals and birds were extracted from a previous publication[19]. These datasets include 2,922 species of mammals and 6,142 species of birds, which have phylogenetic information. The T_a for extant endothermic species is the temperature of the environments that birds and mammals inhabit today—measured as the mean ambient temperature for the mid-point latitude of each species distribution[19]. The T_a at which a species exists today may not be a heritable trait per se. However, the evolution of T_a can still be inferred using phylogenetic methods as habitat selection reflects adaptations of the species (traits) to some characteristics of the environment. This interrelationship should leave a phylogenetic signal in the T_a at which endothermic species live. Accordingly, we found a significant phylogenetic signal in the T_a of both mammals ($\lambda_{PosteriorMean} = 0.77$; Bayes factor = 665) and birds ($\lambda_{PosteriorMean} = 0.8$; Bayes factor = 1,404). Furthermore, the phylogenetic signal for T_a is very high ($\lambda = 1$) in birds and mammals when estimated using the median-r scaled tree.

Finally, to evaluate the endothermic levels for the MRCA of mammals and birds that have previously been proposed[7,8], we followed this categorization of endothermic species: as basoendotherms ($T_b^{Birds} < 40.4\,°C$; $T_b^{Mammals} < 35.0\,°C$), mesoendotherma ($40.4\,°C \leq T_b^{Birds} \leq 42.5\,°C$; $35\,°C \leq T_b^{Mammals} \leq 37.9\,°C$) and supraendotherms ($T_b^{Birds} > 42.5\,°C$; $T_b^{Mammals} > 37.9\,°C$).

Inferring the branch-wise rates of evolution. We identified heterogeneity in the rate of evolution along phylogenetic branches (branch-wise rates) by dividing the rate into two parameters: a background rate parameter (σ^2_b), which assumes that changes in the trait of interest (for example, BMR) are drawn from an underlying Brownian process, and a second parameter, r, which identifies a branch-specific rate shift. A full set of branch-wise rates are estimated by adjusting the lengths of each branch in a time-calibrated tree (stretching or compressing a branch is equivalent to increasing or decreasing the phenotypic rate of change relative to the underlying Brownian rate of evolution). Branch-wise rates are defined by a set of branch-specific scalars r ($0 < r < \infty$) that scale each branch to optimize the phenotypic rate of change to a Brownian process ($\sigma^2_b \times r$). If phenotypic change occurred at accelerated (faster) rates along a specific branch of the tree, then $r > 1$ and the branch is stretched. Decelerated (slower) rates of evolution are detected by $r < 1$ and the branch is compressed. If the trait evolves at a constant rate along a branch, then the branch will not be modified (that is, $r = 1$).

We estimated the r values of evolution for BMR, T_b, and T_a using the phylogenetic variable-rate regression model in a Bayesian framework[17]. This model is designed to automatically detect shifts in the rate of trait evolution across phylogenetic branches while accounting for a relationship with another trait or traits across values for extant species. This approach enables the simultaneous estimation of both an overall relationship between—for instance—BMR as a function of M and T_b across extant species, and any shifts in the rate r that apply to the phylogenetically structured residual variance in the relationship. As residual variance is explained by shifts in rate across phylogenetic branches (r) we can, for example, determine how much BMR has changed in the past after accounting for its covariation with M and T_b in the present (the relationship between the values across extant species). Thus, if the amounts of change in BMR along individual phylogenetic branches were coupled with the amounts of change of T_b, then we should find the r_{BMR} values to be positively associated with the r_{T_b} values. The branch-wise rates for T_b evolution can be estimated while accounting for its covariation with other traits or factor across extant species. Previous studies on the association between BMR and T_b that only used values for extant species have not evaluated the association in evolutionary terms, even when they use phylogenetic methods.

We evaluated 24 phylogenetic variable-rate regression models and 24 phylogenetic constant-rate regression models (Supplementary Tables 1–8). The selection of the regression model was conducted using Bayes factors (B) using marginal likelihoods estimated by stepping stone sampling. B is calculated as the double of the difference between the log marginal likelihood of the complex model and the simple model. By convention, $B > 2$ indicates positive evidence for the complex model, $B = 5$–10 indicates strong support and $B > 10$ is considered very strong support[28]. We inferred the r_{BMR} and r_{T_b} values with the phylogenetic variable-rate regression models that best fit the data for our samples of mammals and birds (Supplementary Tables 7, 8). We also estimated the r_{T_a} values after accounting for the effect of the latitude of the distribution of species (Supplementary Table 11) and, consequently, we accounted for the geographical variation of T_a across the distribution of extant species. We used BayesTraits v.3.0[29] to detect the magnitude and location of r in a Bayesian MCMC reversible-jump framework, which generates a posterior distribution of trees with scaled branches lengths according to the rate of evolution. There is no limit or prior expectation in the number of the r branch scalars, r numbers vary from zero (no branch is scaled) to n, in which n is the number of branches in the phylogenetic tree. Regarding the values of each r parameter, we used a gamma prior, with $\alpha = 1.1$ and a β parameter that is rescaled such that the median of the distribution is equal to 1. With this setting, the numbers of the rate increases and decreases that are proposed are balanced[13]. We ran 50,000,000 iterations sampling every 25,000 to ensure chain convergence and independence in model parameters in BMR and T_b analyses. We discarded the first 25,000 iterations as burn-in. For the T_a analysis in mammals, we ran 200,000,000 iterations sampling every 100,000, and we discarded the first 100,000 iterations as burn-in. For T_a analysis in birds, we ran 400,000,000 iterations discarding the first 100,000,000 as burn-in, and we sampled every 200,000. Regression coefficients were judged to be significant according to a calculated P_{MCMC} value for each posterior of regression coefficients for cases in which <5% of samples in the posterior distribution crossed zero; this indicates that the coefficient is significantly different from zero.

Testing the relationship between the branch-wise rates of evolution. We first estimated the consensus branch-scaled tree for BMR and T_b from the posterior sample of branch-scaled trees obtained with the phylogenetic variable-rate regression model. The consensus branch-scaled tree was generated by using the median r from the posterior distribution. We evaluated the correlation between the r_{BMR} and r_{T_b} values using a Bayesian generalized least squares regression in BayesTraits v.3.0. The same analyses were conducted to evaluate the correlation between r_{BMR} and r_{T_a}. We used a uniform prior for the β (slope coefficient), which ranged from -100 to 100. We ran 50,000,000 iterations sampling every 25,000 to ensure chain convergence and independence in model parameters. We discarded the first 25,000 iterations as burn-in. Significance of regression coefficients was determined as above.

Detecting trends. We evaluated the direction of change in BMR, T_b and T_a across all mammals and birds using the path-wise rates of these variables (Supplementary Tables 15, 16). The path-wise rate is the sum of all of the rate-scaled branches along the path of a species, which lead from the root (the MRCA) to the tips of the tree, and it accounts for the total amount of change that the species has experienced during its evolution[15]. If high path-wise rates have disproportionately been associated with trait increases or decreases, we expect to find that species with greater path-wise rates will have high or low trait values in the present. For instance, if ancestral mammals experienced progressively colder environmental temperatures owing to climate change or colonization of colder habitats as they were evolving from their MRCA, we expect a negative correlation between the path-wise rate of T_a and the T_a of extant species. We performed six Bayesian PGLS regressions in BayesTraits v.3.0 to evaluate the relationship between BMR, T_b, T_a and their path-wise rates (Supplementary Tables 15, 16). We used a uniform prior for the β (slope coefficients) that ranged from -100 to 100 to allow all possible values to have an equal probability. Finally, we ran 50,000,000 iterations sampling every 25,000 to ensure chain convergence and independence in model parameters. We discarded the first 25,000 iterations as burn-in. Significance of regression slopes was determined as above.

Reporting summary. Further information on research design is available in the Nature Research Reporting Summary linked to this paper.

Data availability

No new data were generated for this study. The data used for this paper are available from the original sources cited in the Methods and Supplementary Information.

25. Fritz, S. A., Bininda-Emonds, O. R. & Purvis, A. Geographical variation in predictors of mammalian extinction risk: big is bad, but only in the tropics. *Ecol. Lett.* **12**, 538–549 (2009).
26. Jetz, W., Thomas, G. H., Joy, J. B., Hartmann, K. & Mooers, A. O. The global diversity of birds in space and time. *Nature* **491**, 444–448 (2012).
27. Clarke, A. & Rothery, P. Scaling of body temperature in mammals and birds. *Funct. Ecol.* **22**, 58–67 (2008).
28. Raftery, A. E. in *Markov Chain Monte Carlo in Practice* (eds Gilks, W. R. et al.) 163–187 (Chapman & Hall, 1996).
29. Pagel, M., Meade, A. & Barker, D. Bayesian estimation of ancestral character states on phylogenies. *Syst. Biol.* **53**, 673–684 (2004).

Acknowledgements We thank C. O'Donovan, J. Baker, M. Sakamoto and A. N. Campoy for helpful discussion of the manuscript. A. Clarke supplied data for

mammals and birds. This work is part of the PhD thesis of J.A.-L., supported by the CONICYT Doctoral Fellowship 21130943. C.V. was supported by the Leverhulme Trust (RPG-2013-185 and RPG-2017-071). C.E.H. and E.R.-S. were supported by FONDECYT grants 1170815 and 1170486.

Author contributions J.A.-L., C.E.H., E.R.-S. and C.V. contributed to all aspects of this work.

Competing interests The authors declare no competing interests.

Additional information

Supplementary information is available for this paper at https://doi.org/10.1038/s41586-019-1476-9.

Correspondence and requests for materials should be addressed to J.A. or C.V.

Peer review information *Nature* thanks Olaf Bininda-Emonds, Isabella Capellini and the other, anonymous, reviewer(s) for their contribution to the peer review of this work.

nature research

Corresponding author(s): Chris Venditti

Reporting Summary

Nature Research wishes to improve the reproducibility of the work that we publish. This form provides structure for consistency and transparency in reporting. For further information on Nature Research policies, see Authors & Referees and the Editorial Policy Checklist.

Statistical parameters

When statistical analyses are reported, confirm that the following items are present in the relevant location (e.g. figure legend, table legend, main text, or Methods section).

n/a	Confirmed	
☐	☒	The exact sample size (*n*) for each experimental group/condition, given as a discrete number and unit of measurement
☒	☐	An indication of whether measurements were taken from distinct samples or whether the same sample was measured repeatedly
☐	☒	The statistical test(s) used AND whether they are one- or two-sided *Only common tests should be described solely by name; describe more complex techniques in the Methods section.*
☐	☒	A description of all covariates tested
☒	☐	A description of any assumptions or corrections, such as tests of normality and adjustment for multiple comparisons
☐	☒	A full description of the statistics including central tendency (e.g. means) or other basic estimates (e.g. regression coefficient) AND variation (e.g. standard deviation) or associated estimates of uncertainty (e.g. confidence intervals)
☒	☐	For null hypothesis testing, the test statistic (e.g. *F*, *t*, *r*) with confidence intervals, effect sizes, degrees of freedom and *P* value noted *Give P values as exact values whenever suitable.*
☐	☒	For Bayesian analysis, information on the choice of priors and Markov chain Monte Carlo settings
☒	☐	For hierarchical and complex designs, identification of the appropriate level for tests and full reporting of outcomes
☒	☐	Estimates of effect sizes (e.g. Cohen's *d*, Pearson's *r*), indicating how they were calculated
☒	☐	Clearly defined error bars *State explicitly what error bars represent (e.g. SD, SE, CI)*

Our web collection on statistics for biologists may be useful.

Software and code

Policy information about availability of computer code

Data collection	No software was used for data collection.
Data analysis	All analyses in this study were done using BayesTraits version 3 available at http://www.evolution.rdg.ac.uk/BayesTraitsV3/BayesTraitsV3.html

For manuscripts utilizing custom algorithms or software that are central to the research but not yet described in published literature, software must be made available to editors/reviewers upon request. We strongly encourage code deposition in a community repository (e.g. GitHub). See the Nature Research guidelines for submitting code & software for further information.

Data

Policy information about availability of data

All manuscripts must include a data availability statement. This statement should provide the following information, where applicable:

- Accession codes, unique identifiers, or web links for publicly available datasets
- A list of figures that have associated raw data
- A description of any restrictions on data availability

The authors declare that data supporting the finding of this study is available in previous studies listed in the references.

Field-specific reporting

Please select the best fit for your research. If you are not sure, read the appropriate sections before making your selection.

☒ Life sciences ☐ Behavioural & social sciences ☐ Ecological, evolutionary & environmental sciences

For a reference copy of the document with all sections, see nature.com/authors/policies/ReportingSummary-flat.pdf

Life sciences study design

All studies must disclose on these points even when the disclosure is negative.

Sample size	Sample size was determined by taxa present in the phylogeny which also had phenotypic, environmental, and geographic data. For mammals, 502 species had data for basal metabolic rate, body temperature, and body mass. 2922 species had data for ambient temperature and latitude. For birds, 164 species had data for basal metabolic rate. body temperature, and body mass. 6142 species had data for ambient temperature and latitude. The reversible-jump procedure we use in our analyses is specifically designed to identify significant shifts in the rate of evolution. Where statistical power is too low to detect a shift (e.g. n is low) no such shift will be identified.
Data exclusions	We excluded species that did not have data for all phenotypic variables or for ambient temperature and latitude.
Replication	Five replicates of rates of evolution inference, evolutionary trends, and correlation between rates, produced qualitatively the same results.
Randomization	This is not relevant to our study because it is not experimental in this way.
Blinding	Blinding is not relevant to our study as it is not experimental in this way.

Reporting for specific materials, systems and methods

Materials & experimental systems

n/a	Involved in the study
☒	☐ Unique biological materials
☒	☐ Antibodies
☒	☐ Eukaryotic cell lines
☒	☐ Palaeontology
☒	☐ Animals and other organisms
☒	☐ Human research participants

Methods

n/a	Involved in the study
☒	☐ ChIP-seq
☒	☐ Flow cytometry
☒	☐ MRI-based neuroimaging

LETTER

https://doi.org/10.1038/s41586-019-1478-7

Wnt and TGFβ coordinate growth and patterning to regulate size-dependent behaviour

Christopher P. Arnold[1,2,3], Blair W. Benham-Pyle[1,3], Jeffrey J. Lange[1], Christopher J. Wood[1] & Alejandro Sánchez Alvarado[1,2]*

Differential coordination of growth and patterning across metazoans gives rise to a diversity of sizes and shapes at tissue, organ and organismal levels. Although tissue size and tissue function can be interdependent[1–5], mechanisms that coordinate size and function remain poorly understood. Planarians are regenerative flatworms that bidirectionally scale their adult body size[6,7] and reproduce asexually, via transverse fission, in a size-dependent manner[8–10]. This model offers a robust context to address the gap in knowledge that underlies the link between size and function. Here, by generating an optimized planarian fission protocol in *Schmidtea mediterranea*, we show that progeny number and the frequency of fission initiation are correlated with parent size. Fission progeny size is fixed by previously unidentified mechanically vulnerable planes spaced at an absolute distance along the anterior–posterior axis. An RNA interference screen of genes for anterior–posterior patterning uncovered components of the TGFβ and Wnt signalling pathways as regulators of the frequency of fission initiation rather than the position of fission planes. Finally, inhibition of Wnt and TGFβ signalling during growth altered the patterning of mechanosensory neurons—a neural subpopulation that is distributed in accordance with worm size and modulates fission behaviour. Our study identifies a role for TGFβ and Wnt in regulating size-dependent behaviour, and uncovers an interdependence between patterning, growth and neurological function.

The infrequency of planarian fission behaviour has largely precluded its mechanistic dissection. However, recently optimized worm husbandry techniques augmented fission activity[11,12], and enabled us to study the integration of worm size with fission behaviour. Large planaria (*Schmidtea mediterranea*) from recirculation culture systems exhibited robust and reproducible increases in fission activity when transitioned to static culture systems and starved (Fig. 1a, Supplementary Video 1). Live imaging provided detailed characterization of the fission process. Planarians first elongate and adhere their posterior tissue to a substrate. Next, periodic body contractions concentrate body mass towards the head region while thinning out tissues immediately anterior to the adherent tail. After 20–40 minutes, progressive stretching ruptures connecting tissue with rapid recoil, which separates the anterior parent from the posterior fission progeny (Extended Data Fig. 1a, Supplementary Video 1).

Observation of fission behaviour in worms of increasing size showed that the length of first posterior fission fragments did not correlate with parent length (Fig. 1b, d). Instead, larger worms produced additional progeny, each approximately 1 mm in length, such that the number of progeny after 2 weeks linearly correlated with parent size (Fig. 1c, e, Extended Data Fig. 1b–d). Thus, the size of fission fragments is fixed independently of anterior–posterior position or parent length. The frequency of the production of fission fragments—that is, the fission rate—did correlate with worm length (Extended Data Fig. 1e, f), and both the time to the first fission event and the time between sequential fission events was inversely related to parent size (Extended Data Fig. 1g–1). Automated webcam imaging of individual worms allowed us to generate timelines chronicling successful (upward displacement) and unsuccessful (downward displacement) fission attempts (Fig. 1f, Supplementary Video 2). Fission attempts occurred only in worms above 4–5 mm in length, which indicates a minimal size required for fission (Fig. 1g, h, Extended Data Fig. 2a, b). Furthermore, larger worms produced fission progeny more frequently owing to more fission attempts (Fig. 1h, Extended Data Fig. 2c, d), rather than higher rates of success (Fig. 1i). Together, these results confirm that planarian fission is a size-dependent behaviour, with both progeny number and fission rate coupled to parent size.

We tested the hypothesis that patterning cues are required to coordinate worm size and planarian fission. Genes from the Wnt[13–16], TGFβ[17–19] and Hh[20] signalling pathways that regulate anterior–posterior identity were screened using RNA-dependent genetic interference (RNAi) techniques[21] (Fig. 2a, b, Extended Data Fig. 3a, b). Rescreening confirmed six presumptive activators of fission (*actR-1*, *smad2/3*, *β-catenin*, *dsh-B*, *tsh* and *wnt11-6*) and a presumptive inhibitor (*apc*) (Fig. 2c). The morphology of parent worms was observed at days 0 and 14 of the fission assay and in regenerating tissue fragments. RNAi knockdown reproduced published anterior–posterior patterning defects in regenerating tissue fragments (Extended Data Fig. 4a), but few morphological defects were observed in parent worms (Fig. 2d). On day 0, *β-catenin* RNAi worms exhibited morphological abnormalities, whereas other RNAi conditions were indistinguishable from controls. By day 14, RNAi of *actR-1* and *smad2/3* elicited motility defects, but RNAi of *dsh-B*, *wnt11-6*, *tsh* and *apc* significantly altered fission rates without changes in morphology. In situ staining of the central nervous system (CNS), intestine and muscle confirmed published anterior–posterior polarity regeneration phenotypes, but no gross morphological defects in parent RNAi worms (Extended Data Fig. 4b–d). Therefore, we conclude that Wnt and TGFβ signalling components modulate fission behaviour independently of overt body plan repolarization.

Serendipitously, we discovered that compression of planaria reveals cryptic mechanically vulnerable planes that divide the worm at regularly spaced intervals along the anterior–posterior axis (Fig. 3a, b, Supplementary Video 3). The number of these 'compression planes' scaled with worm size (Fig. 3b, c) and their position along the anterior–posterior axis overlapped with the position of fission planes (Fig. 3d). Furthermore, incomplete fission formed tears similar to those observed with compression (Extended Data Fig. 5a). Therefore, we conclude that compression planes are fission planes revealed by mechanical compression. Fission plane number and distribution correlated with worm length during tissue rescaling and regeneration. After starvation, worms reduced body length and lost fission planes to restore number and distribution (Extended Data Fig. 5b–d). To assay regeneration of the fission plane, we amputated worms around the pharynx such that 90% of fragments contained a single plane (Extended Data Fig. 5e–g). One week after amputation, worms remodelled, doubled in length and increased fission plane number (Extended Data Fig. 5f–j). Subsequent feeding increased worm length and fission plane number (Extended Data Fig. 5f–j). After starvation, worms exhibited little to no elongation

[1]Stowers Institute for Medical Research, Kansas City, MO, USA. [2]Howard Hughes Institute for Medical Research, Kansas City, MO, USA. [3]These authors contributed equally: Christopher P. Arnold, Blair W. Benham-Pyle. *e-mail: asa@stowers.org

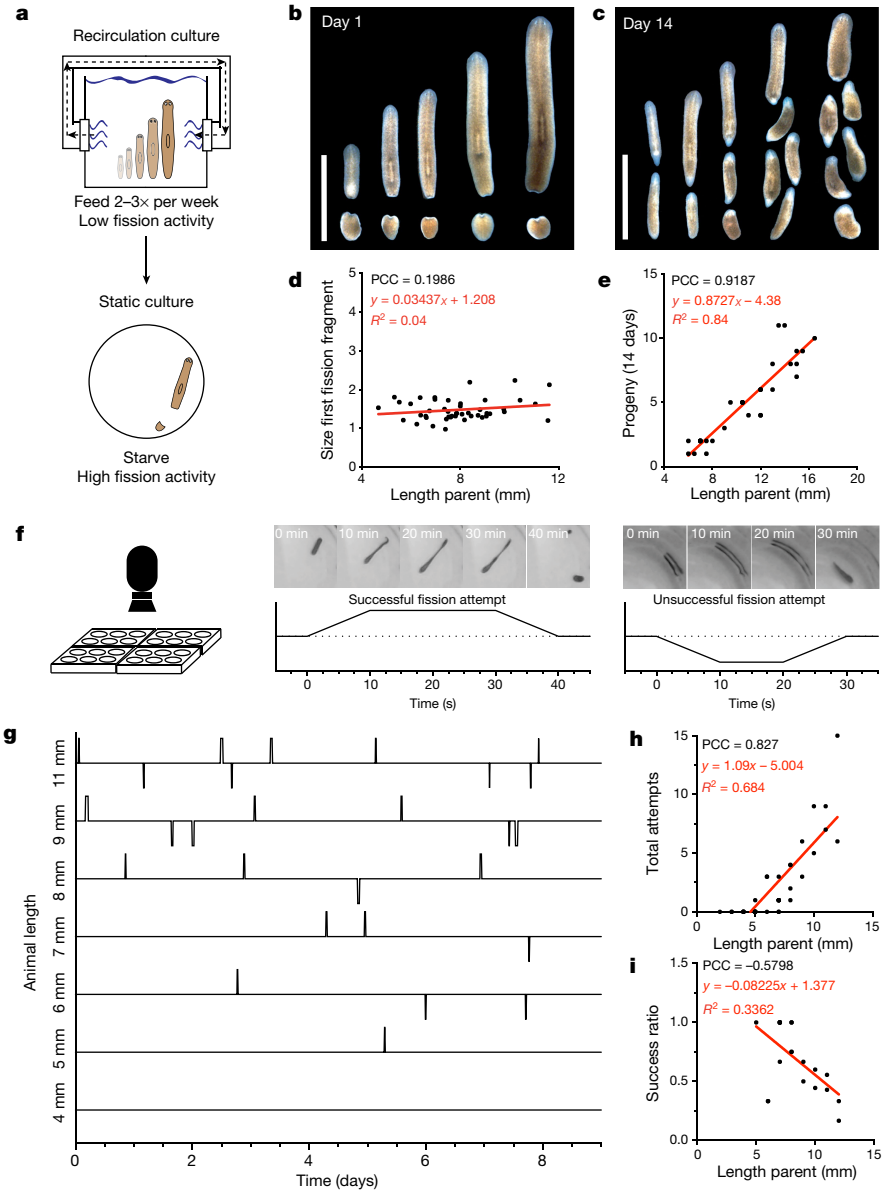

Fig. 1 | Planarian fission is a size-dependent behaviour. a, Optimized fission protocol. **b**, **c**, Representative images of 5–12-mm worms and fission fragments less than 24 h (**b**) and 14 days (**c**) after the first fission event ($n = 46$ worms from 1 experiment). Scale bars, 5 mm. **d**, **e**, Length of the first fission fragments (**d**) and progeny number (**e**) over 2 weeks relative to parent length ($n = 46$ (**d**) or 30 (**e**) worms from one experiment). **f**, Webcam live-imaging schematic (left) and example timeline depicting successful (middle) and unsuccessful (right) fission attempts. **g**, Representative fission behaviour timelines from a range of parent lengths. **h**, **i**, Total fission attempts (**h**) and successful attempts per total attempts (**i**) relative to parent length ($n = 39$ (**h**) and 21 (**i**) worms). Data are from a single experiment. Pearson correlation co-efficient (PCC), linear regression (red line), and R^2 values are provided.

or plane addition despite rescaling and regenerating their other tissues (Extended Data Fig. 5f–j). In summary, fission planes are pre-established in planarians and correlate dynamically with worm size and form.

Given the role of Wnt and TGFβ signalling in body patterning, we tested whether genes of these signalling pathways regulate fission planes. Worms treated with RNAi were mechanically compressed and the quantity and relative distribution of fission planes was measured (Fig. 3e–g). Notably, whereas RNAi of *actR-1* and *smad2/3* moderately reduced the number of fission planes, RNAi of Wnt signalling components had no effect on fission plane number or position (Fig. 3e, g, Extended Data Fig. 6a). Even knockdown of *wnt11-6* by three rounds of amputation and regeneration did not alter fission-plane patterning (Fig. 3f, g, Extended Data Fig. 6b). Hypomorphic RNAi knockdown of *β-catenin*, *actR-1* or *smad2/3* revealed little or no effect on the size of fission fragments (Extended Data Fig. 6c–e), which further supports the conclusion that neither Wnt nor TGFβ signalling regulate fission behaviour through the anterior–posterior patterning of fission planes.

We tested whether Wnt and TGFβ signalling instead regulated the frequency of fission attempts. Using the automated webcam image-capture system (Fig. 1f), we recorded fission behaviour in RNAi-treated worms (Fig. 4a). RNAi of *β-catenin*, *actR-1*, *smad2/3* and *wnt11-6* reduced fission attempts, whereas RNAi of *apc* increased fission attempts (Fig. 4b–d, Extended Data Fig. 7a–l, Supplementary Videos 4–6). RNAi of *β-catenin* and *smad2/3*, which resulted in observable morphological abnormalities, also significantly reduced the fission-success ratio (Figs. 2d, 4e, Extended Data Fig. 7k–n). *dsh-B* RNAi reduced the fission success ratio without altering the number or frequency of fission attempts (Fig. 4d, e, Extended Data Fig. 7k–n). Finally, *apc* RNAi reduced the time between fission attempts by approximately 50%, and worms initiated fission attempts independently of remaining tissue, markedly reducing their success ratio (Fig. 4e,

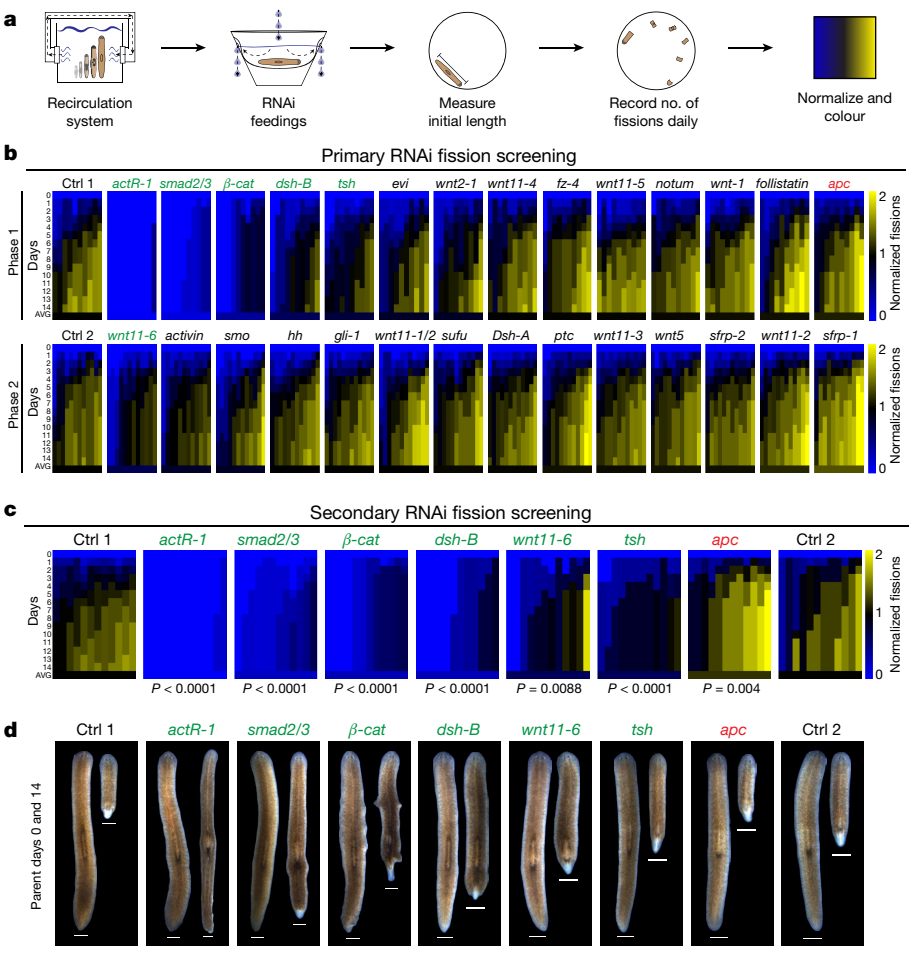

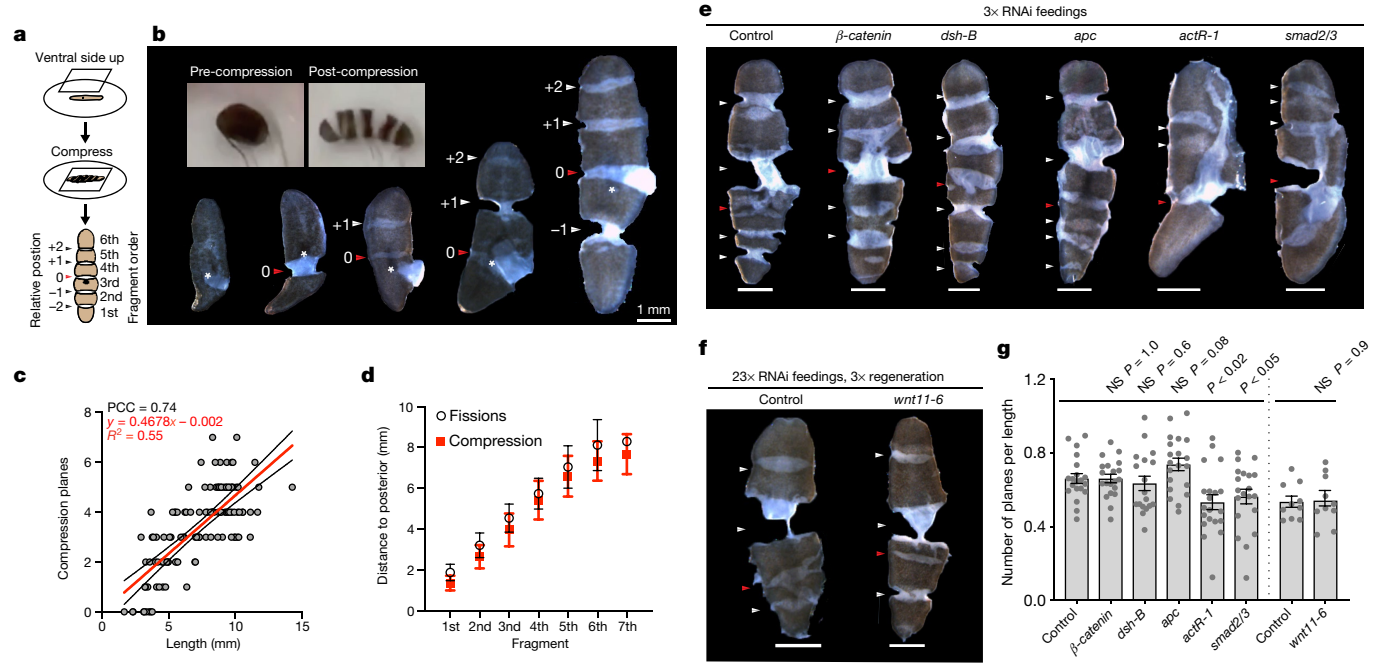

Fig. 2 | Wnt signalling and TGFβ signalling components modulate fission activity. **a**, RNAi screen workflow (see also Extended Data Fig. 3). **b**, **c**, Heat maps depicting fission activity after RNAi treatment for both the two-phase primary (**b**) and secondary (**c**) RNAi screens. Normalized cumulative fissions over time are displayed for individual worms from each RNAi condition ($n = 10$ worms for phase I, $n = 12$ worms for phase II and secondary screen). Targets in secondary screening (independently repeated three times) depicted in green (activators) and red (inhibitors). *P* values determined by two-way analysis of variance (ANOVA) interaction factor. Ctrl, control. **d**, Representative parent images on days 0 and 14 of the fission assay ($n = 10$–12, independently repeated 3 times). Scale bars, 1 mm.

Fig. 3 | Pre-established fission planes determine progeny size independently of Wnt and TGFβ signalling. **a**, Schematic of compression assay (Supplementary Video 3). **b**, Pre- and post-compression worm (inset) and compression planes revealed in 3–6-mm worms (independently repeated 5 times). **c**, Compression plane number relative to worm length ($n = 117$ worms). PCC, linear regression (red lines), R^2 values and 95% confidence interval (black lines) are shown. **d**, Fission ($n = 196$ fission progeny from 50 worms) and compression plane ($n = 173$ planes from 30 worms) overlap along the anterior–posterior axis of the worm. **e**, **f**, Representative images of post-compression worms after knockdown of Wnt and TGFβ signalling components using the specified number of RNAi feedings and rounds of regeneration (*n* depicted by dot plot quantification; experiment performed three times (**e**) or once (**f**)). Scale bars, 1 mm. **g**, Plot of the number of fission planes per worms length after RNAi treatment of 2 experiments ($n = 20$ and 10 worms to the left and right of the dotted line, respectively). *P* values determined by two-sided *t*-test. NS, not significant. Data are mean ± s.d. (**d**) or mean ± s.e.m. (**g**).

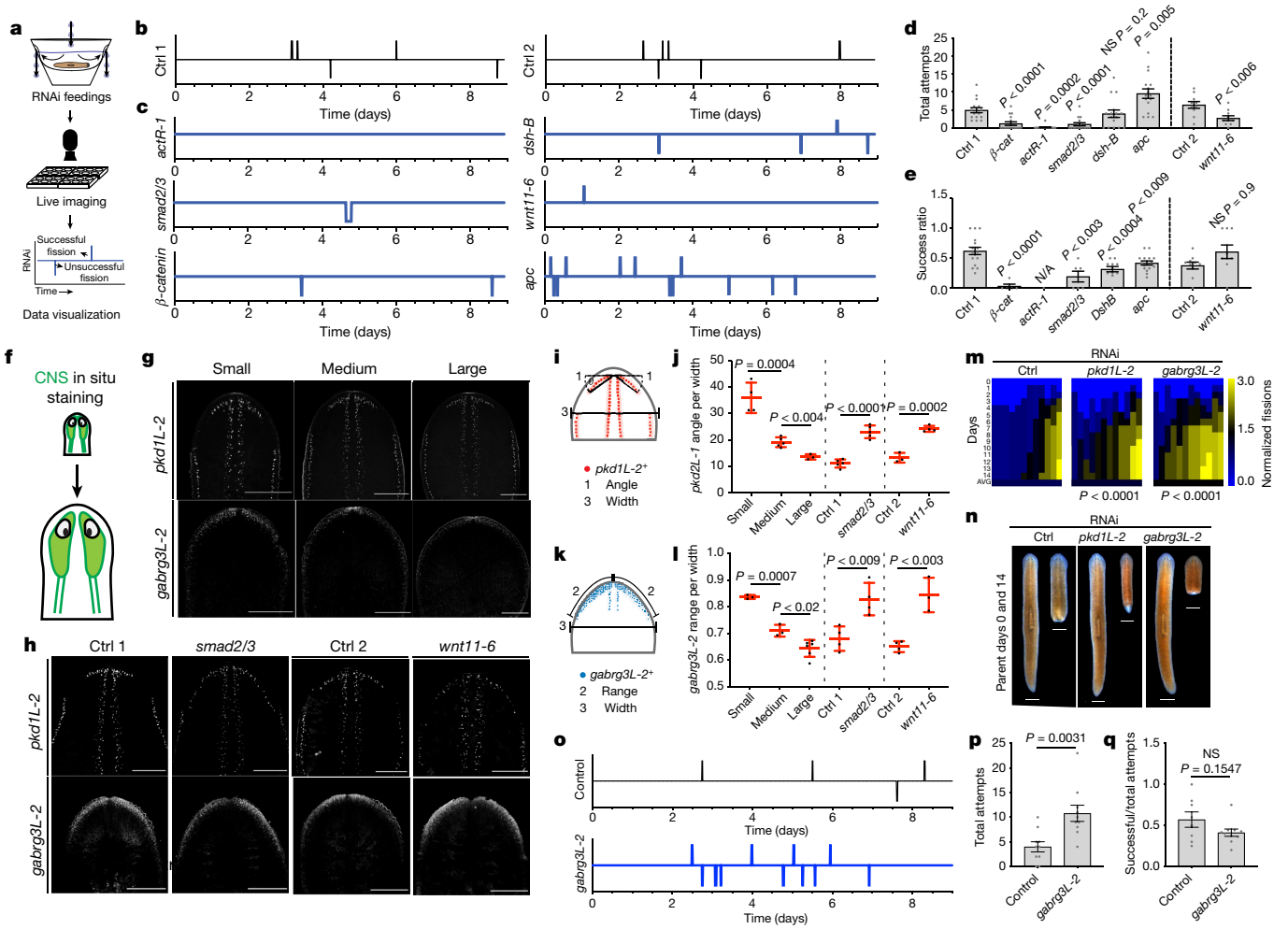

Fig. 4 | Wnt and TGFβ signalling regulates fission frequency by size-dependent patterning of mechanosensory neurons in the CNS. **a**, Schematic depicting RNAi treatment, live imaging and data analysis. **b**, **c**, Representative activity timelines. **d**, **e**, Total fission attempts (**d**) and successful attempts per total attempts (**e**) for RNAi-treated worms ($n = 16$ (**d**) and 10 (**e**) worms, from 1 (**d**) or 2 (**e**) independent experiments). **f**, Schematic depicting in situ staining strategy. **g**, **h**, Representative images of *pkd1L-2*$^+$ and *gabrg3L-2*$^+$ neurons in worms of increasing size (**g**), or after RNAi treatment (**h**). Scale bars, 0.5 mm. **i**, **k**, Diagrams depicting quantification of the angle of *pkd1L-2*$^+$ cells (**i**) or the range of *gabrg3L-2*$^+$ cells (**k**). **j**, **l**, Staining quantification of *pkd1L-2* (**j**) and *gabrg3L-2* (**l**) in worms of increasing size or after RNAi treatment ($n = 3$–6, exact n depicted in dot plot quantification). **m**, Fission activity heat maps after treatment with *pkd1L-2* and *gabrg3L-2* RNAi ($n = 12$; Fig. 2). **n**, Representative parent images on days 0 and 14 of fission assay ($n = 12$, 2 independent experiments). Scale bars, 1 mm. **o**, Representative fission activity timelines of worms treated with *gabrg3L-2* RNAi. **p**, **q**, Total fission attempts (**p**) and successful attempts per total attempts (**q**) for worms treated with *gabrg3L-2* RNAi ($n = 10$ worms). *P* values determined by two-sided *t*-test (**j**, **l**, **p**, **q**) or two-way ANOVA (**d**, **e**). Data are mean ± s.e.m. (**d**, **e**, **j**, **l**, **p**, **q**).

Extended Data Fig. 7i–n, Supplementary Video 6). These findings demonstrate that Wnt and TGFβ signalling regulate the frequency of fission behaviour.

We proposed that components of the Wnt and TGFβ signalling pathways might regulate fission behaviour through the planarian CNS. Double fluorescent in situ hybridization (FISH) with the CNS marker *pc2* confirmed that Wnt and TGFβ fission regulators were detected in *pc2*-positive cells in the anterior CNS (Extended Data Fig. 8a, b). Removal of anterior tissue that contains the cephalic ganglia delayed the onset of fission behaviour (Extended Data Fig. 8c–f). Restoration of fission activity coincided with regeneration and re-establishment of anterior, *pc2* co-localized, *tsh* expression (Extended Data Fig. 8g). Notably, removal of anterior tissue that contained just one cephalic ganglion did not alter the total number of fission progeny produced (Extended Data Fig. 8c–f), which indicates that half of the CNS is sufficient to initiate fission. Finally, RNAi against *coe*, a transcription factor essential for the patterning of the CNS[22,23], markedly reduced planarian fission (Extended Data Fig. 8h, i). Together, these data support a model in which an anterior CNS expressing Wnt and TGFβ signalling components regulates fission initiation.

We tested whether polarity genes could modulate size-dependent behaviour via size-dependent patterning of the CNS. To identify neuronal subpopulations that regulate fission downstream of Wnt and TGFβ, we analysed 17 neuronal markers[24–29] in small, medium and large planaria and 10 markers in worms treated with *smad2/3* RNAi (Fig. 4f, Extended Data Fig. 9a, b). Patterning of *pkd1L-2*$^+$, *gabrg3L-2*$^+$ and *sargasso-1*$^+$ mechanosensory neurons exhibited the clearest changes in worms of increasing size and after *smad2/3* RNAi treatment (Extended Data Fig. 9a, b). In large worms, mechanosensory neurons are tightly restricted to the anterior and knockdown of either *smad2/3* or *wnt11-6* broadened their distribution akin to that of smaller worms (Fig. 4g–l). RNAi against *pkd1L-2* and *gabrg3L-2* (homologous to cation and chloride channel genes, respectively) increased planarian fission activity (Fig. 4m, n), and live imaging of *gabrg3L-2* RNAi worms confirmed an increase in fission attempts without a reduction in fission success (Fig. 4o, p, Extended Data Fig. 10, Supplementary Video 7). These results indicate that mechanosensory neurons are differentially patterned during growth, inhibit fission behaviour and require Wnt and TGFβ for their appropriate patterning in accordance with worm size. Therefore, we conclude that Wnt and TGFβ signalling coordinates worm size and behaviour via size-dependent patterning in the adult CNS.

In conclusion, we used planaria as a model for the integration of size, patterning and function and established fission as a robust, reproducible and quantifiable size-dependent behaviour (Fig. 1, Supplementary Video 1). Although previous studies have generated physical models for the process of transverse fission[9], mechanisms that couple worm size and fission frequency have remained unknown. We discovered two independent mechanisms by which fission is coordinated with worm size in *S. mediterranea*. First, previously undescribed iterative structures patterned in accordance with anterior–posterior axis length couple worm size with the number of fission progeny produced (Fig. 3, Supplementary Video 3). Second, the Wnt and TGFβ signalling pathways mediate size-dependent patterning of mechanosensory neurons, which regulate fission frequency (Fig. 4, Extended Data Figs. 9, 10). Thus, we demonstrate that differential patterning of key cell populations in accordance with tissue size provides a mechanistic link between worm growth and the acquisition or modulation of tissue function. Together, our results identify a role for Wnt and TGFβ patterning genes in the regulation of size-dependent behaviour and show that developmental patterning cues coordinate tissue growth with size-dependent functions.

Online content

Any methods, additional references, Nature Research reporting summaries, source data, extended data, supplementary information, acknowledgements, peer review information; details of author contributions and competing interests; and statements of data and code availability are available at https://doi.org/10.1038/s41586-019-1478-7.

Received: 30 October 2018; Accepted: 15 July 2019;
Published online 15 August 2019.

1. Rinkevich, Y. et al. *In vivo* clonal analysis reveals lineage-restricted progenitor characteristics in mammalian kidney development, maintenance, and regeneration. *Cell Reports* **7**, 1270–1283 (2014).
2. Kaufman, J. M., Siegel, N. J. & Hayslett, J. P. Functional and hemodynamic adaptation to progressive renal ablation. *Circ. Res.* **36**, 286–293 (1975).
3. Fleming, S. et al. Normal ranges of heart rate and respiratory rate in children from birth to 18 years of age: a systematic review of observational studies. *Lancet* **377**, 1011–1018 (2011).
4. Bryant, P. J. & Simpson, P. Intrinsic and extrinsic control of growth in developing organs. *Q. Rev. Biol.* **59**, 387–415 (1984).
5. Hafen, E. & Stocker, H. How are the sizes of cells, organs, and bodies controlled? *PLoS Biol.* **1**, E86 (2003).
6. Oviedo, N. J., Newmark, P. A. & Sánchez Alvarado, A. Allometric scaling and proportion regulation in the freshwater planarian *Schmidtea mediterranea*. *Dev. Dyn.* **226**, 326–333 (2003).
7. Stückemann, T. et al. Antagonistic self-organizing patterning systems control maintenance and regeneration of the anteroposterior axis in planarians. *Dev. Cell* **40**, 248–263.e4 (2017).
8. Best, J. B., Goodman, A. B. & Pigon, A. Fissioning in planarians: control by the brain. *Science* **164**, 565–566 (1969).
9. Malinowski, P. T. et al. Mechanics dictate where and how freshwater planarians fission. *Proc. Natl Acad. Sci. USA* **114**, 10888–10893 (2017).
10. Thomas, M. A., Quinodoz, S. & Schotz, E.-M. Size matters! *J. Stat. Phys.* **148**, 664–676 (2012).
11. Arnold, C. P. et al. Pathogenic shifts in endogenous microbiota impede tissue regeneration via distinct activation of TAK1/MKK/p38. *eLife* **5**, 5 (2016).
12. Arnold, C., Benham-Pyle, B. & Alvarado, A. S. Planarian fission induction protocol. *Nat. Protoc.* https://doi.org/10.21203/rs.2.10324/v1 (2019).
13. Gurley, K. A., Rink, J. C. & Sánchez Alvarado, A. β-catenin defines head versus tail identity during planarian regeneration and homeostasis. *Science* **319**, 323–327 (2008).
14. Roberts-Galbraith, R. H. & Newmark, P. A. Follistatin antagonizes activin signaling and acts with notum to direct planarian head regeneration. *Proc. Natl Acad. Sci. USA* **110**, 1363–1368 (2013).
15. Hill, E. M. & Petersen, C. P. Wnt/Notum spatial feedback inhibition controls neoblast differentiation to regulate reversible growth of the planarian brain. *Development* **142**, 4217–4229 (2015).
16. Petersen, C. P. & Reddien, P. W. Wnt signaling and the polarity of the primary body axis. *Cell* **139**, 1056–1068 (2009).
17. Reddien, P. W., Bermange, A. L., Kicza, A. M. & Sánchez Alvarado, A. BMP signaling regulates the dorsal planarian midline and is needed for asymmetric regeneration. *Development* **134**, 4043–4051 (2007).
18. Gaviño, M. A. & Reddien, P. W. A Bmp/Admp regulatory circuit controls maintenance and regeneration of dorsal-ventral polarity in planarians. *Curr. Biol.* **21**, 294–299 (2011).
19. Molina, M. D., Saló, E. & Cebrià, F. The BMP pathway is essential for re-specification and maintenance of the dorsoventral axis in regenerating and intact planarians. *Dev. Biol.* **311**, 79–94 (2007).
20. Rink, J. C., Gurley, K. A., Elliott, S. A. & Sánchez Alvarado, A. Planarian Hh signaling regulates regeneration polarity and links Hh pathway evolution to cilia. *Science* **326**, 1406–1410 (2009).
21. Sánchez Alvarado, A. & Newmark, P. A. Double-stranded RNA specifically disrupts gene expression during planarian regeneration. *Proc. Natl Acad. Sci. USA* **96**, 5049–5054 (1999).
22. Cowles, M. W. et al. Genome-wide analysis of the bHLH gene family in planarians identifies factors required for adult neurogenesis and neuronal regeneration. *Development* **140**, 4691–4702 (2013).
23. Cowles, M. W., Omuro, K. C., Stanley, B. N., Quintanilla, C. G. & Zayas, R. M. COE loss-of-function analysis reveals a genetic program underlying maintenance and regeneration of the nervous system in planarians. *PLoS Genet.* **10**, e1004746 (2014).
24. Wenemoser, D., Lapan, S. W., Wilkinson, A. W., Bell, G. W. & Reddien, P. W. A molecular wound response program associated with regeneration initiation in planarians. *Genes Dev.* **26**, 988–1002 (2012).
25. Arenas, O. M. et al. Activation of planarian TRPA1 by reactive oxygen species reveals a conserved mechanism for animal nociception. *Nat. Neuroscience* **20**, 1686–1693 (2017).
26. Currie, K. W. & Pearson, B. J. Transcription factors *lhx1/5-1* and *pitx* are required for the maintenance and regeneration of serotonergic neurons in planarians. *Development* **140**, 3577–3588 (2013).
27. Collins, J. J. III et al. Genome-wide analyses reveal a role for peptide hormones in planarian germline development. *PLoS Biol.* **8**, e1000509 (2010).
28. Roberts-Galbraith, R. H., Brubacher, J. L. & Newmark, P. A. A functional genomics screen in planarians reveals regulators of whole-brain regeneration. *eLife* **5**, e17002 (2016).
29. Ross, K. G. et al. SoxB1 activity regulates sensory neuron regeneration, maintenance, and function in planarians. *Dev. Cell* **47**, 331–347.e5 (2018).
30. Pearson, B. J. et al. Formaldehyde-based whole-mount in situ hybridization method for planarians. *Dev. Dyn.* **238**, 443–450 (2009).
31. King, R. S. & Newmark, P. A. In situ hybridization protocol for enhanced detection of gene expression in the planarian Schmidtea mediterranea. *BMC Dev. Biol.* **13**, 8 (2013).

METHODS

Worm husbandry. Clonal CIW4 *S. mediterranea* were maintained in 1× Montjuic salts as previously described. CIW4 worms were sourced from a large recirculation culture as previously reported[11]. In brief, worms are housed in three culture trays (244 cm length × 61 cm width × 30.5 cm height) stacked vertically. Water is recirculated through the system by a sump pump, which moves water through a chiller, a canister filter, a UV sterilizer and the three housing trays. Water is then passed through two vertically stacked sieves and a set of filter/floss pads before being returned to the sump pump. Worms were pulled from this system and placed directly into fission assays, starved for at least seven days before tissue fixation for imaging, or transferred to a unidirectional flow system culture for controlled feeding or RNAi feeding experiments.

Gene cloning and RNAi feeding protocol. Candidate genes analysed in this study were cloned from a CIW4 cDNA library into a pPR-T4P vector as previously described[20] (Supplementary Table 1). These served as template for in vitro synthesis of dsRNA for RNAi feedings. *Unc22* dsRNA was used for control RNA treatment. RNAi food was prepared by mixing 1 volume of dsRNA at 1,600 ng ml^{-1} with 1.5 volumes of beef liver paste. For RNAi experiments that target neuronal genes, 1 volume of dsRNA at 1,400 ng μl^{-1} was mixed with 1 volume beef liver paste. The amount of food administered was 10 µl of food per 1 mm of worm length present in the worm flow container. Worms were allowed to feed for 6–10 h with 2 rounds of light stimulation to facilitate additional consumption. Worms were fed every three days for a total of three RNAi feedings, unless otherwise specified. After RNAi feedings, worms were transferred to the relevant biological assay.

Fission assay. A detailed protocol for fission induction has been made available through Protocol Exchange[10]. To induce fission, worms were removed from recirculation culture or unidirectional flow system culture and washed 5–10 times with fresh 1× Montjuic salts. Individual worms were placed in 15-cm tissue culture dishes with 50 ml 1× Montjuic salts and their body length was measured. Representative images of day-0 parents were captured using a Leica M205 microscope. Plates were stacked 6–12 dishes high and placed in a dark incubator at 20 °C. Daily, plates were removed from the incubator and fission fragments for each worm were counted and removed from the 15-cm dish. For some experiments, images of fission fragments were taken on the day they were collected to allow for quantification of fission fragment length. The 1× Montjuic salts in each individual dish was replaced weekly.

For data analysis, the number of daily cumulative fissions was divided by initial body length and then normalized to the average of the control RNAi fissions. This normalized fission score for each day was converted to a heat colour code. Daily scores for each individual worm were aligned in descending order along the *y* axis and the average score of each column was calculated and used to sort individual worms in ascending order along the *x* axis. The average fission score of each RNAi condition was then sorted in ascending order from left to right. This resulted in a heat map visualization ranking the effects of RNAi treatments on fission activity.

Fission plane compression assay. Fission planes were revealed by compression between a plastic tissue culture dish and a glass coverslip (Supplementary Video 3). Worms were inverted with their ventral side up, compressed using four fingertips, then imaged. To ensure that all compression/fission planes were revealed for every worm, images were acquired sequentially using a Leica M205 microscope as each fission plane was revealed by mechanical compression. Position of fission planes and distance between fission planes was quantified using Fiji (https://fiji.sc/). Video depicting compression assay was captured with an iPhone 6 (Apple).

Whole-mount FISH. For RNA expression analyses, FISH was performed as previously described[30,31]. Antibodies were used in MABT containing 5% horse serum for FISH (Roche anti-DIG-POD 1:1,000 and Roche anti-FLCN-POD 1:1,000) or NBT/BCIP in situ hybridization (Roche anti-DIG-AP 1:1,000). For double FISH, peroxidase activity was quenched between tyramide reactions using 100 mM sodium azide for at least 1 h at room temperature with agitation. Nuclear staining was performed using 1:1,000 Hoescht 33342 (Invitrogen) in PBST (1× PBS with 0.5% Triton-X-100).

Microscopy. Images of live worms and regenerating fission fragments were acquired using a Leica M205 microscope. Confocal images were acquired on an LSM-700-Vis and stitching was performed in Fiji using built-in grid collection plugins.

Live imaging of fission behaviour. Videos of worms from two orthogonal views were acquired using two webcams (Logitech C910/920). Webcams were mounted using a variety of ring stands and test tube clamps. The imaging chamber was a clear plastic square lid obtained from a box of coverslips. Lighting of the chamber was achieved using a Volpi illuminator (NCL-150). Each camera was connected to its own computer running micro-manager (https://micro-manager.org/). The cameras were set up in micro-manager using OpenCVgrabber to set the pixel density (1,920 × 1,080) and to acquire the images. The camera gain, exposure and all other settings were set using the Logitech Webcam Controller software (https://download01.logi.com/web/ftp/pub/video/lws/lws280.exe). Data were acquired using the Multi-Dimensional Acquisition mode of micro-manager. The two computers were synchronized for acquisition manually at the beginning of the experiment.

For the high-throughput screening of fission behaviour, worms were placed in six-well dishes with cameras mounted above the plates using optics components (Thor Labs). Illumination was obtained using four LED ring lights (AmScope) mounted upside down and above the cameras to provide diffuse light. Image acquisition was performed using two different camera configurations: four cameras connected to one computer via a USB hub or one 4K camera connected to a USB port. In the four-camera configuration, images where captured sequentially from the cameras every ten minutes. A script written in Python 3.6 (https://www.python.org/) was used as a wrapper for FFMPEG (https://www.ffmpeg.org/) to acquire images. The size of the images (1,920 × 1,080) and the pixel format (yuv420p) were set in the python script. The camera gain, exposure and other settings were controlled with the Logitech Webcam Controller software (https://download01.logi.com/web/ftp/pub/video/lws/lws280.exe). The DirectShow framework was used to interface between the cameras and FFMPEG. In the single 4k camera setup, a 4096 × 2160-pixel image was captured every ten minutes from a Logitech BRIO webcam. The same Python script was used as a wrapper for FFMPEG in this configuration.

Quantification of live imaging. Videos of individual worms were manually annotated. For each fission attempt, the start time and completion time were recorded and the success or failure of the attempt was recorded. To depict fission behaviour, a timeline was constructed and a numerical value was given to each frame of a video. A value of 0 was assigned to any frame in which no fission behaviour was observed; a positive value was given to any frame during a successful fission attempt; and a negative value was given to any frame during a failed fission attempt (see Fig. 1f). A prolonged diagonal line in a timeline indicates a period in which frames were not acquired owing to failed communication between the image acquisition software and the webcam.

Statistical tests. For all pairwise comparisons, significance was tested using an unpaired Student's *t*-test. GraphPad Prism was used to calculate PCC values with a two-tailed 95% confidence interval and to perform linear regression analyses. Two-way ANOVA analysis was performed in GraphPad Prism to determine the significance of RNAi treatment over time. No statistical methods were used to predetermine sample size. The experiments were not randomized, and investigators were not blinded to allocation during experiments and outcome assessment.

Reporting summary. Further information on research design is available in the Nature Research Reporting Summary linked to this paper.

Data availability

Source data and construct sequences can be accessed from the Stowers Original Data Repository at http://www.stowers.org/research/publications/libpb-1356. All other data are available from the corresponding author upon reasonable request.

Code availability

Code for the Python 3.6 (https://www.python.org/) script used for a wrapper for FFMPEG (https://www.ffmpeg.org/) for the high-throughput recording of fission behaviour is available at the Stowers Original Data Repository at http://www.stowers.org/research/publications/libpb-1356.

Acknowledgements We thank members of the A.S.A. laboratory for discussion and advice, F. Mann for providing unpublished reagents, and K. Si for comments. We are grateful to the Stowers Planarian and Microscopy core facilities for technical contributions and methods development. A.S.A. is an investigator of the Howard Hughes Medical Institute (HHMI) and the Stowers Institute for Medical Research. B.W.B.-P. is a Jane Coffin Childs Memorial Fund Postdoctoral Fellow. C.P.A. is a HHMI Postdoctoral Fellow. This work was supported in part by NIH R37GM057260 to A.S.A.

Authors contributions Conceptualization, data analysis and interpretation: C.P.A., B.W.B.-P. and A.S.A.; acquisition of data: C.P.A., B.W.B.-P. and J.J.L.; design and fabrication of planarian live-imaging systems: J.J.L.; software: C.J.W.; data curation: J.J.L. and C.J.W.; writing of the original manuscript: C.P.A., B.W.B.-P. and A.S.A.; supervision and funding acquisition: A.S.A.; and revision and editing of the manuscript: all authors.

Competing interests The authors declare no competing interests.

Additional information
Supplementary information is available for this paper at https://doi.org/10.1038/s41586-019-1478-7.
Correspondence and requests for materials should be addressed to A.S.
Peer review information *Nature* thanks Thomas Holstein and the other, anonymous, reviewer(s) for their contribution to the peer review of this work.
Reprints and permissions information is available at http://www.nature.com/reprints.

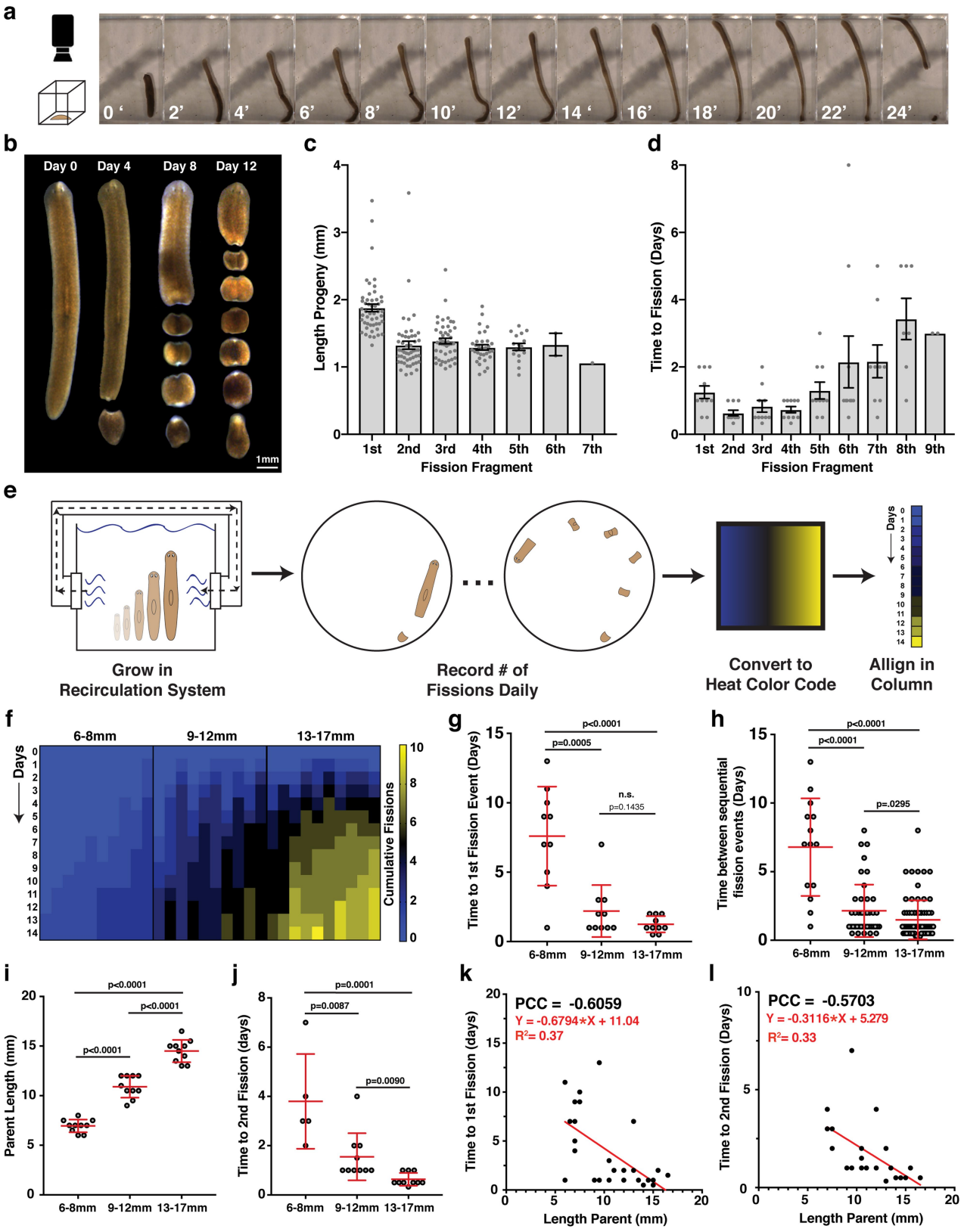

Extended Data Fig. 1 | See next page for caption.

Extended Data Fig. 1 | Characterization of planarian fission biology. **a**, Live imaging of large planarian worm during fission (representative of 12 experiments; see also Supplementary Video 1). **b**, Imaging of single individual large planarian and regenerating progeny 0, 4, 8 and 12 days after fission induction (experiment repeated 50 times). **c**, **d**, Anterior–posterior length of progeny (**c**) and time to fission event (**d**) since induction or the previous fission ($n = 50$ worms). Fission fragments binned by position along the anterior–posterior axis (the first fission is the most posterior). **e**, Schematic of fission induction and quantitative scoring system used to compare fission activity between different conditions. **f**, Cumulative fission fragments produced over 14 days by individual worms binned by parent size ($n = 10$ per bin). **g**, **h**, Time to first fission event (**g**) or time between sequential fission events (**h**) for worms 6–8 mm, 9–12 mm or 13–17 mm in length. **i**, Raw parent length measurement of planarian individuals 6–8 mm, 9–12 mm or 13–17 mm in length. **j**, Time between first and second fission events for worms 6–8 mm, 9–12 mm or 13–17 mm in length ($n = 139$ independent measurements from 30 worms). **k**, **l**, Time between induction and first fission (**k**) or between first and second fission (**l**) plotted relative to parent length ($n = 26$ and 21 independent measurements from 30 worms). PCC, linear regression and R^2 values are provided. *P* values determined by determined by two-sided *t*-test. Data are mean ± s.e.m. (**c**, **d**, **j**).

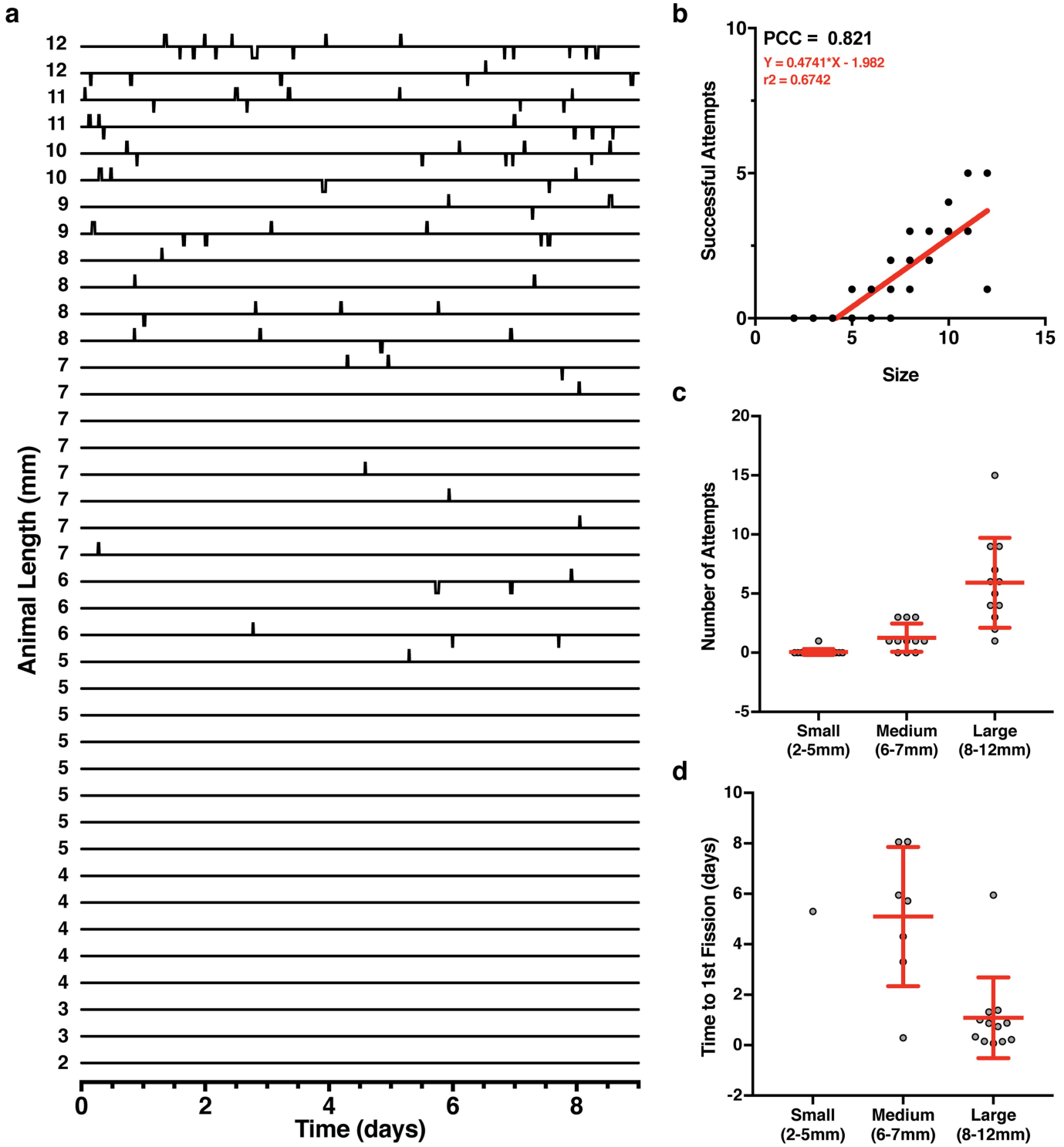

Extended Data Fig. 2 | Quantification of fission behaviour across a range of worm sizes. a, All individual timelines depicting fission activity over 9 days for worms ranging from 2 mm (bottom) to 12 mm (top) in length ($n = 39$ worms). **b**, Number of successful fission attempts per worm relative to parent length. **c**, **d**, Number of fission attempts (**c**) and time to first fission attempt (**d**) for worms binned into small (2–5 mm), medium (6–7 mm) and large (8–12 mm) groups ($n = 16$ small, 11 medium, 12 large worms). Data are mean ± s.e.m.

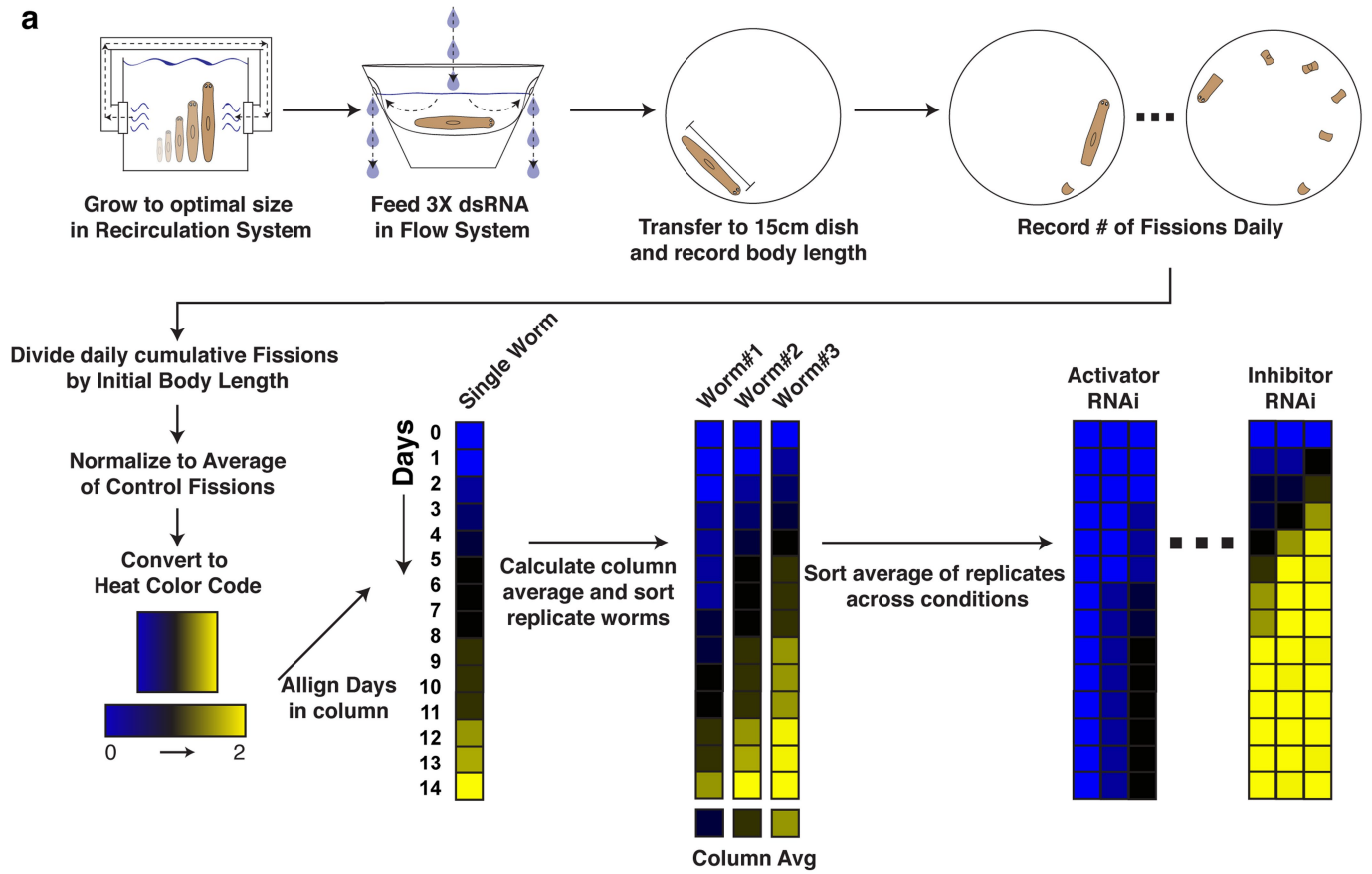

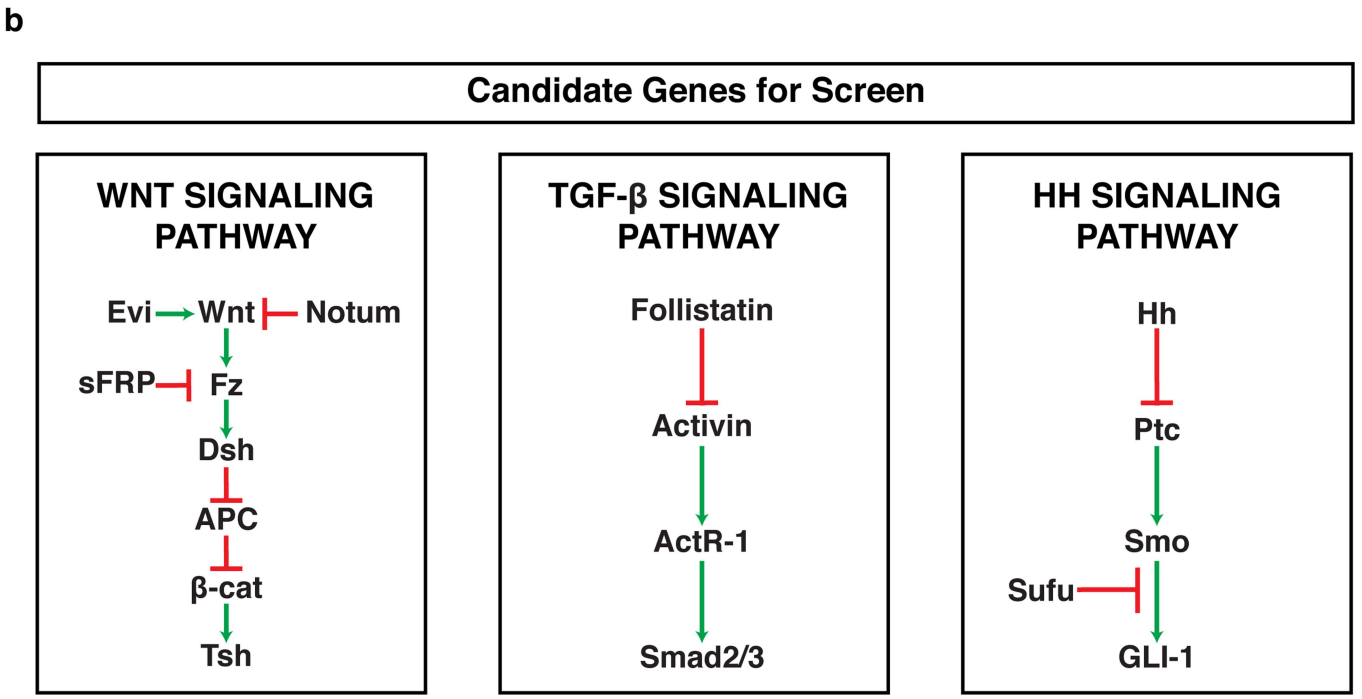

Extended Data Fig. 3 | Strategy for a targeted RNAi screen to identify regulators of fission. a, Detailed schematic of RNAi workflow. Worms are grown to an optimal size in the recirculation culture system and transferred to a flow system for RNAi feedings. After 3 RNAi feedings, worms were transferred to a 15-cm dish and worm length was recorded. The number of fissions were recorded daily for 14 days for each worm from each RNAi condition. For data analysis, the number of daily cumulative fissions were divided by initial body length and then normalized to the average of the control RNAi fissions. For data visualization, this normalized fission score for each day was converted to a heat colour code. Daily scores for each individual worm were aligned in ascending order along the *y* axis. The average score of each column is calculated and used to sort individual worms in ascending order along the *x* axis. The average fission score of each RNAi condition was then sorted in ascending order from left to right. The result is a heat-map visualization that ranks the effects of RNAi treatments on fission activity. **b**, Wnt, TGFβ and Hh signalling pathway diagrams focusing on components targeted for the RNAi screen. Green arrows indicate positive interactions; red arrows indicate inhibitory interactions.

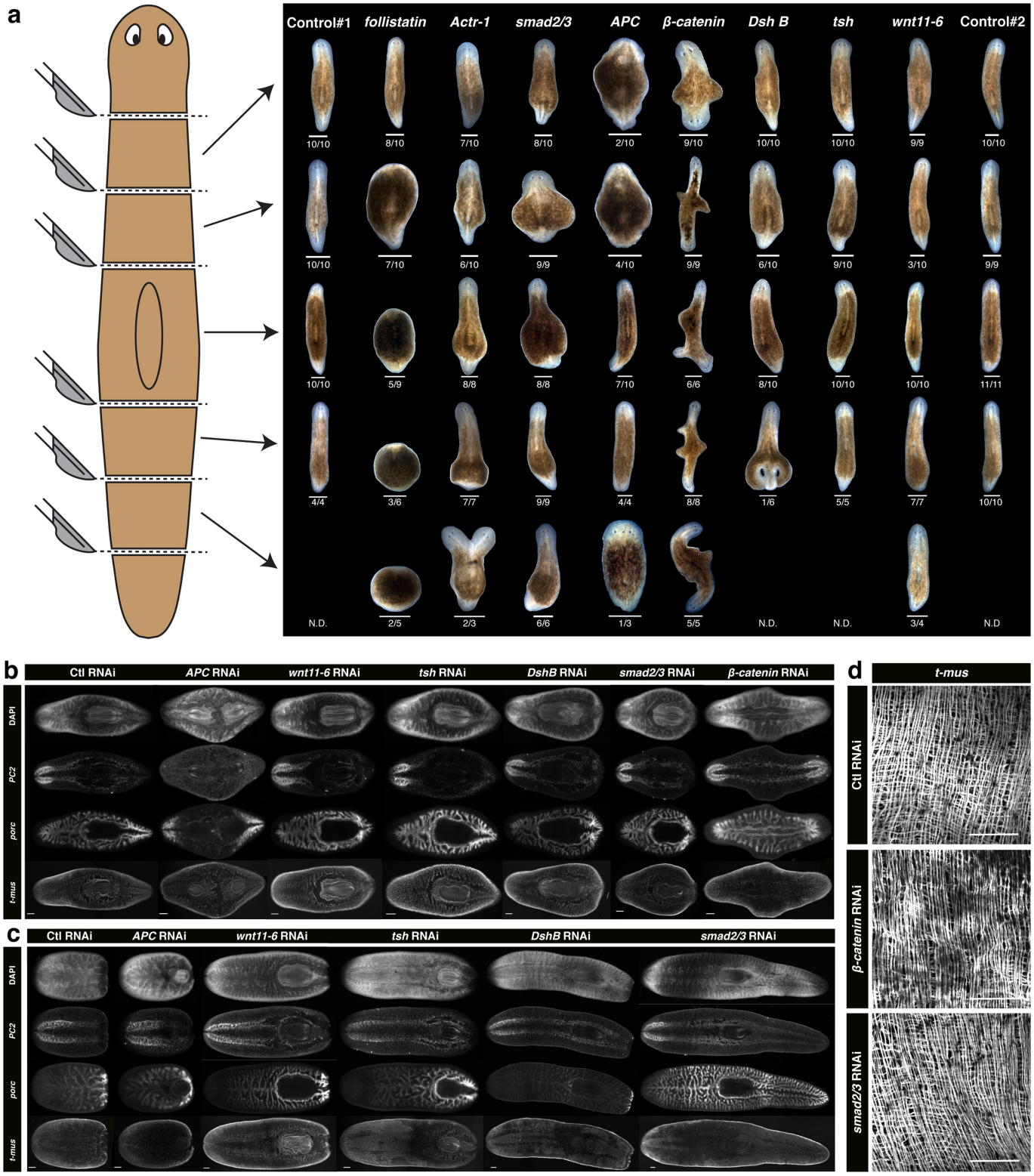

Extended Data Fig. 4 | Analysis of morphology and/or internal tissues in regenerating fragments and fissioning parents. a, Representative images of regenerating tissue fragments from different positions along the anterior–posterior axis at 15 days post-amputation (dpa). Fraction of worms with pictured phenotype along with 1-mm scale bar depicted below each image. **b**, **c**, In situ staining of CNS (*pc2*), intestine (*porc*) and muscle (*t-mus*) tissues at day 15 of regeneration (**b**) or the fission assay (**c**). **d**, High-resolution image of body wall musculature (*t-mus*) in control RNAi and *smad2/3* or *β-catenin* RNAi treated worms. Representative images ($n = 7–13$ worms) from a single experiment. All images are oriented ventral side up with anterior on the left side. Scale bars, 0.5 mm.

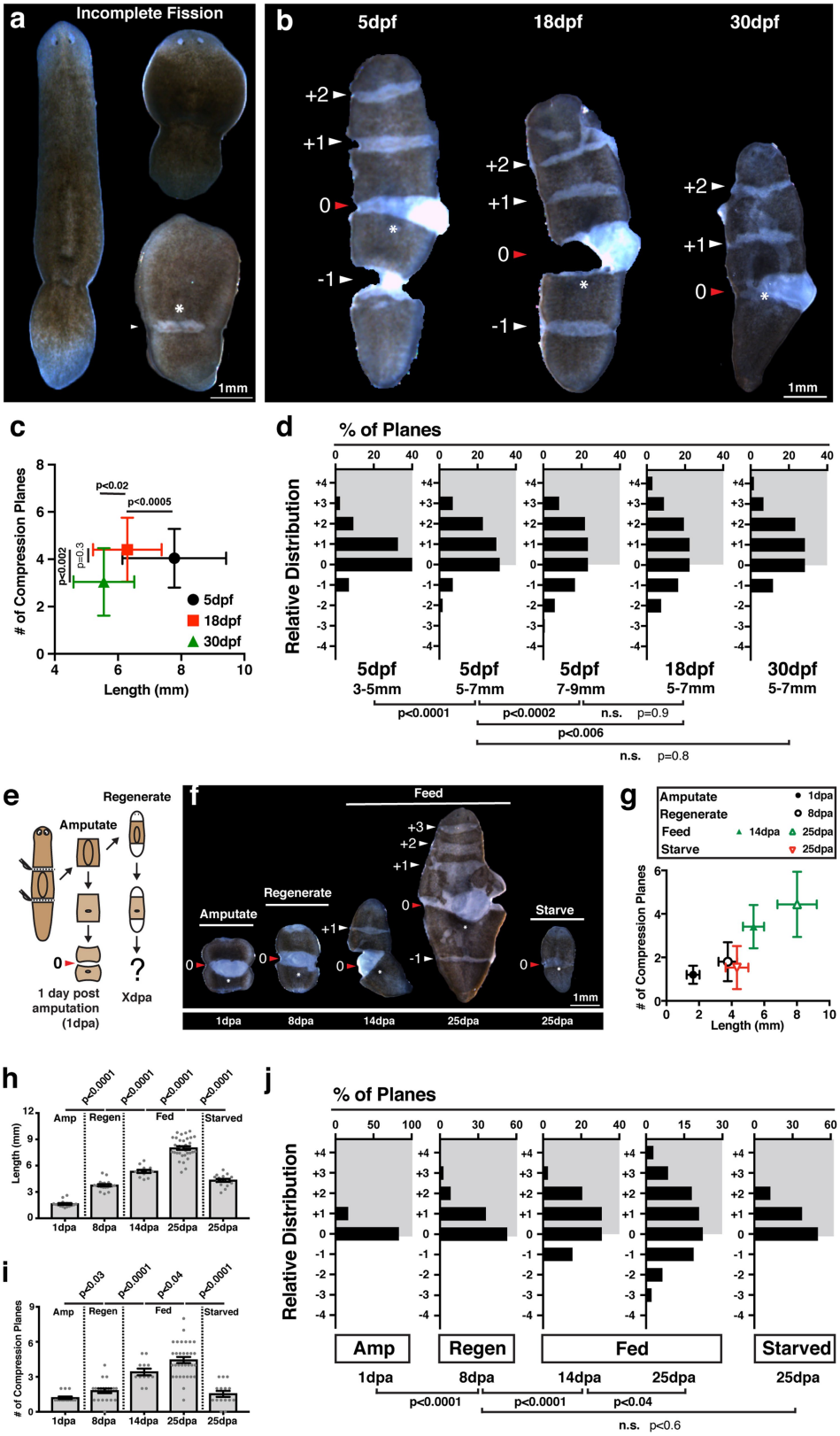

Extended Data Fig. 5 | See next page for caption.

Extended Data Fig. 5 | Effects of growth, starvation and regeneration on fission planes. a, Image of planaria after incomplete fission, revealing ventral tear identical to compression planes (observed more than five independent times). **b**, Post-compression worms at 5, 18 and 30 days post-fertilization (dpf) (5 dpf image from same experiment as Fig. 3b). Data are from a single experiment. **c**, **d**, Bidirectional plot of compression planes versus worm length ($n = 25$ worms) (**c**), and relative distribution of planes (**d**) at 5, 18 or 30 dpf ($n = 28$, 18, 31, 15 and 19 worms (left to right in **d**)). **e**, Schematic of experiment tracking establishment of fission planes during tissue regeneration. **f**, **g**, Representative images (**f**) and bidirectional plot of compression planes versus worm length (**g**) after amputation (1 dpa, $n = 15$ worms), regeneration (8 dpa, $n = 19$ worms) and growth (fed 14 dpa and 25 dpa, $n = 12$ and 32 worms) or de-growth (starved 25 dpa, $n = 15$ worms). Data from a single experiment. **h**–**j**, Worm length (**h**), number of compression planes (**i**) and relative distribution of planes (**j**) after amputation (1 dpa, $n = 15$ worms), regeneration (8 dpa, $n = 19$ worms) and growth (fed 14 dpa and 25 dpa, $n = 12$ and 32 worms) or de-growth (starved 25 dpa, $n = 15$ worms). Data are mean ± s.d. (**c**, **g**) or mean ± s.e.m (**h**–**j**).

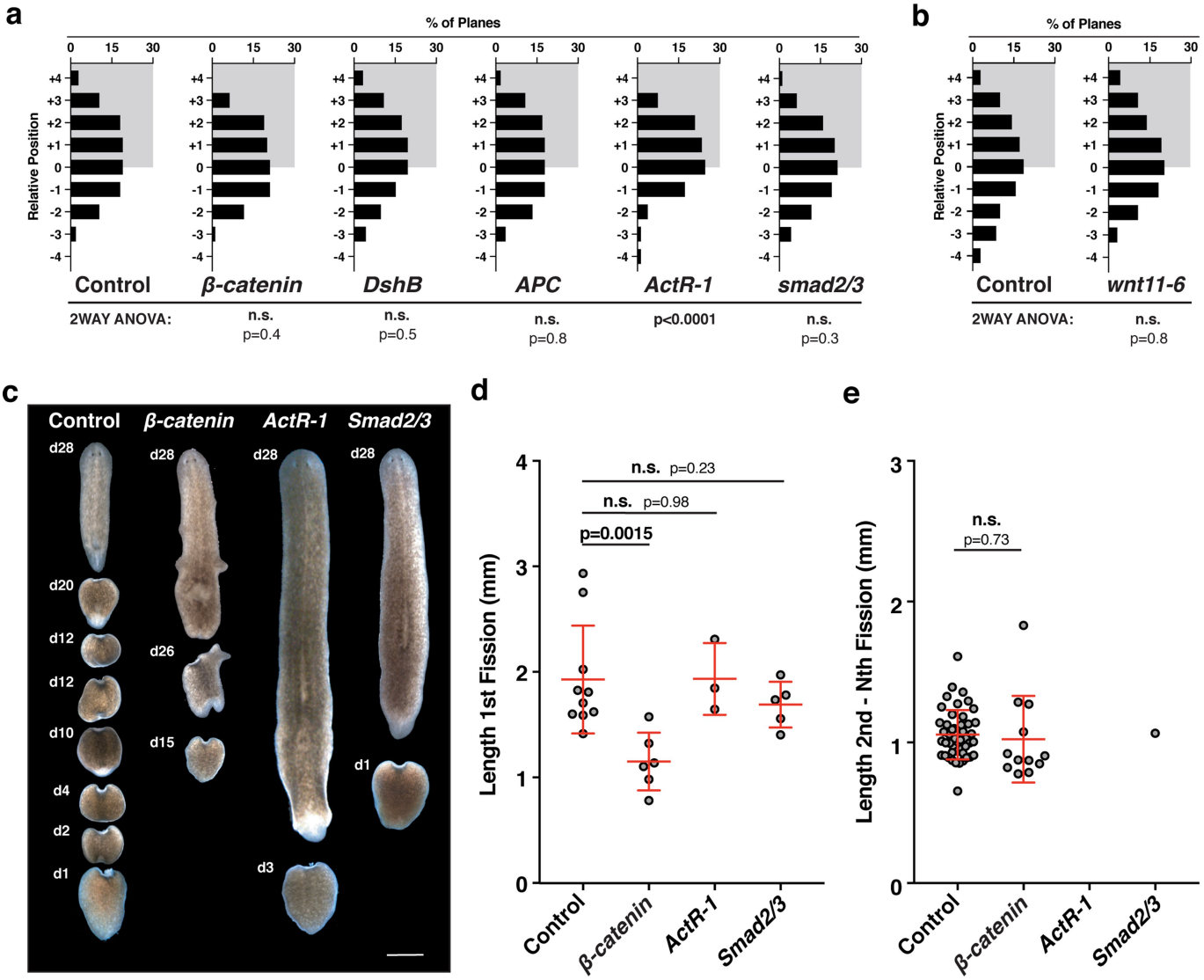

Extended Data Fig. 6 | Effects of RNAi of Wnt and TGFβ signalling components on fission planes. a, **b**, Relative plane distribution after RNAi treatment ($n = 20$ (**a**) and 10 (**b**) worms). **c**, Representative images of progeny within 24 h of fission and of remaining parent tissue at day 28 after fission induction for worms treated with control, *β-catenin*, *actR-1* or *smad2/3* RNAi (experiment independently performed twice). Scale bar, 1 mm. **d**, **e**, Length of the first fission progeny (**d**) or all subsequent progeny (**e**) in worms treated with control, *β-catenin*, *actR-1* or *smad2/3* RNAi ($n = 85$ fission fragments from 36 worms). *P* values determined by two-way ANOVA interaction factor (**a**, **b**) or two-sided *t*-test (**d**, **e**). Data are mean ± s.e.m.

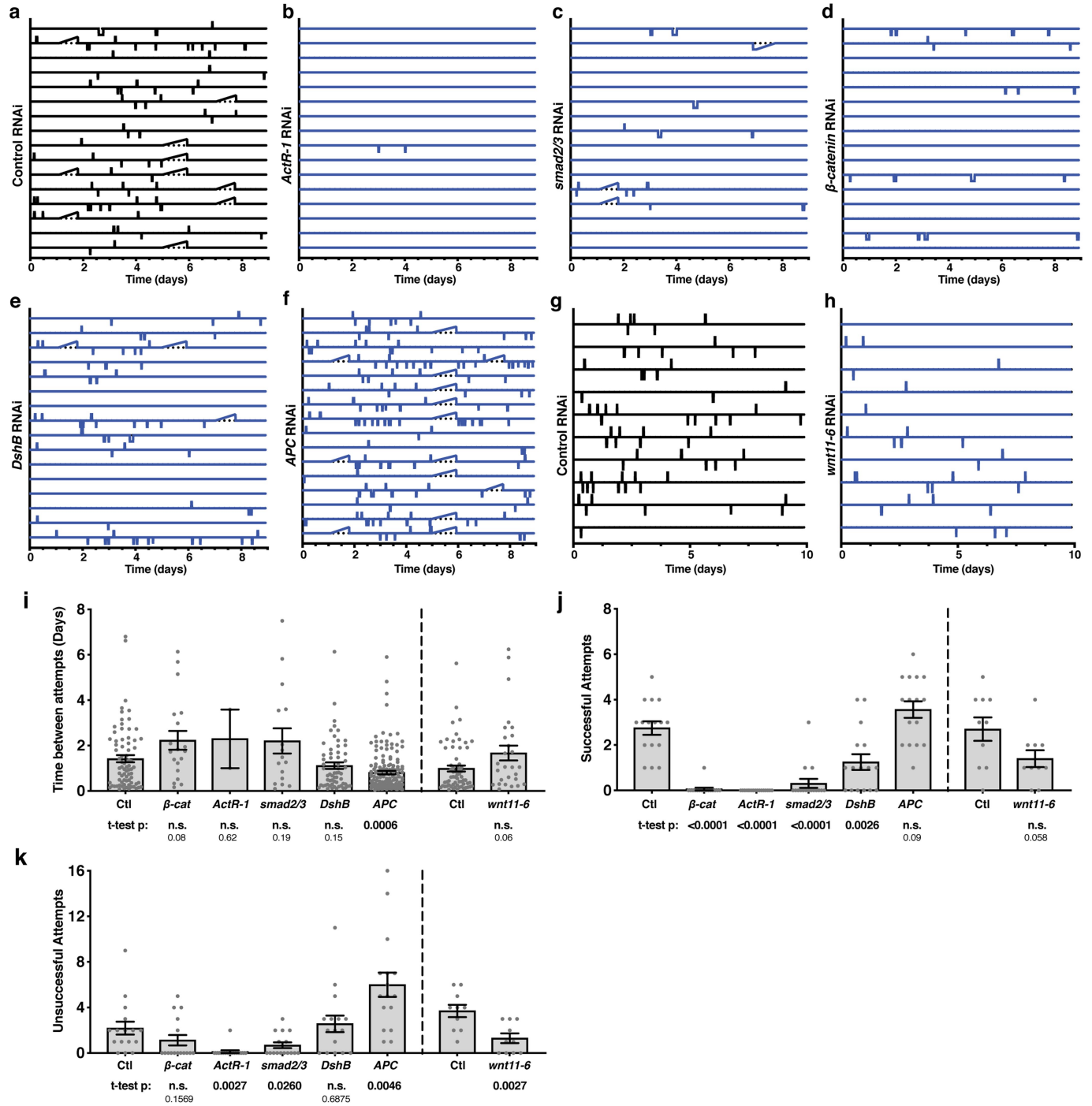

Extended Data Fig. 7 | Wnt and TGFβ signalling components regulate the frequency of fission initiation. a–h, All individual timelines depicting fission activity over 9–10 days for worms treated with control (**a**, **g**), *actR-1* (**b**), *smad2/3* (**c**), *β-catenin* (**d**), *dsh-B* (**e**), *apc* (**f**) or *wnt11-6* (**h**) RNAi. **i–n**, Graphs depicting the time between sequential fission attempts (**i**, **j**), the number of successful fission attempts (**k**, **l**) and the number of unsuccessful fission attempts (**m**, **n**) in worms fed double-stranded RNA (dsRNA) that targets regulators of fission ($n = 421$ fission events from 116 worms). Worms were given either 3 (**a–f**, **i**, **k**, **m**) or 18 (**g**, **h**, **j**, **l**, **n**) dsRNA feedings. Batched experiments are plotted separately. *P* values determined by two-sided *t*-test. Data are mean ± s.e.m.

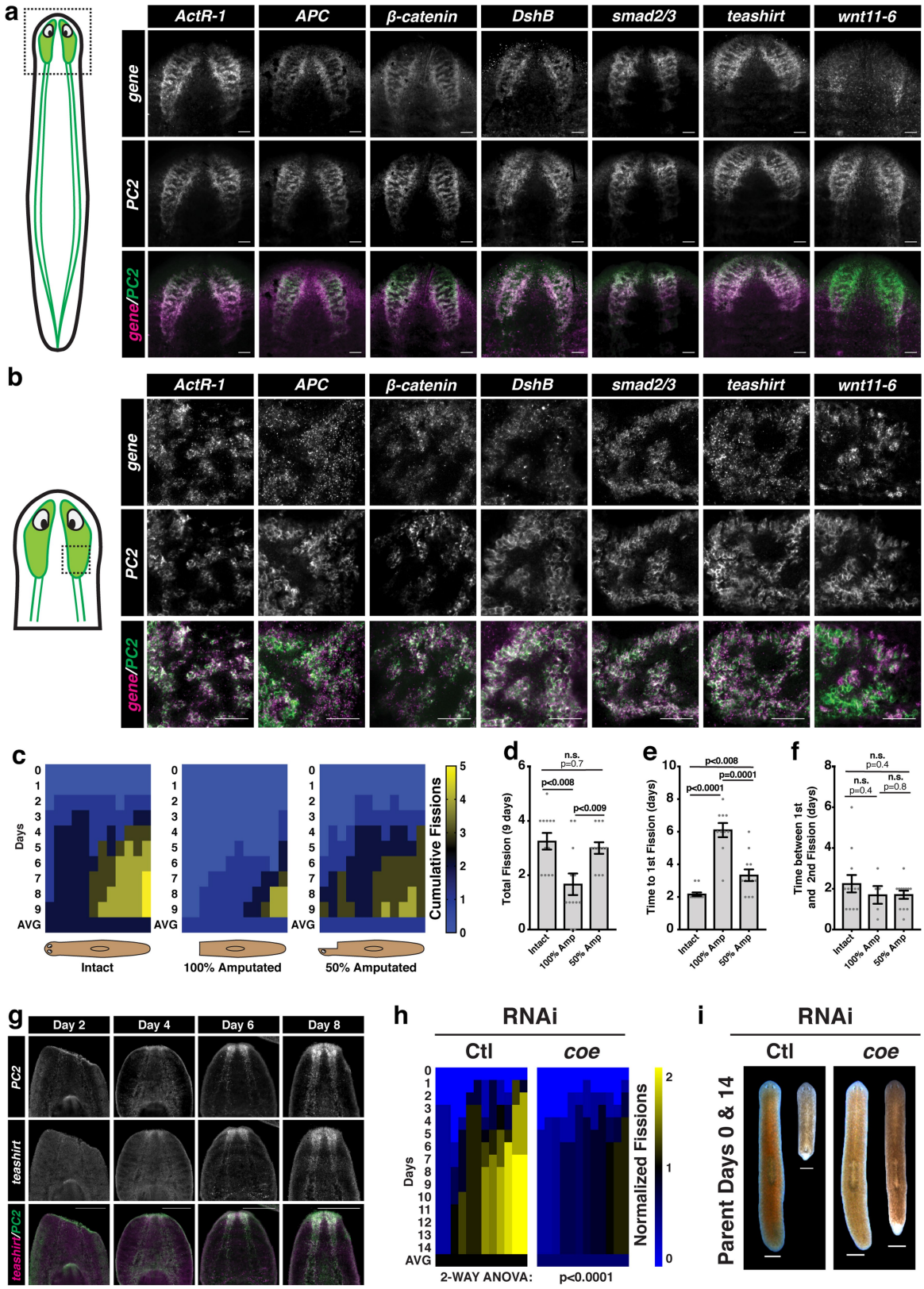

Extended Data Fig. 8 | See next page for caption.

Extended Data Fig. 8 | The planarian anterior CNS regulates fission. **a**, Whole-brain imaging of *pc2* and fission regulator gene expression detected by double FISH ($n = 2$–4 worms; experiment independently repeated). Scale bars, 100 μm. **b**, Single-cell co-expression of *pc2* and fission regulators in the posterior branches of the anterior CNS ($n = 3$–5 worms). Scale bar, 50 μm. **c**, Fission induction in intact, 100% head-amputated or 50% head-amputated worms over a 9-day observation period ($n = 12$ worms). **d**–**f**, Total number of fission progeny over 9 days (**d**), the time between fission induction and first fission (**e**), and the time between first and second fission (**f**) for intact, 100% head-amputated or 50% head-amputated worms ($n = 94$ fission events from 36 worms). **g**, Regeneration time course in 100% head-amputated worms showing recovery of anterior gene expression of *pc2* co-localized with *teashirt* ($n = 4$–5 worms; experiment performed once). Scale bar, 500 μm. **h**, Heat maps depicting fission activity after treatment with *coe* RNAi. Normalized cumulative fissions over time are displayed for individual worms from each RNAi condition ($n = 12$ worms). **i**, Representative parent images on days 0 and 14 of the fission assay ($n = 12$, experiment independently performed twice). Scale bars, 1 mm. *P* value determined by two-sided *t*-test (**d**–**f**) or two-way ANOVA (**h**). Data are mean ± s.e.m. (**d**–**f**).

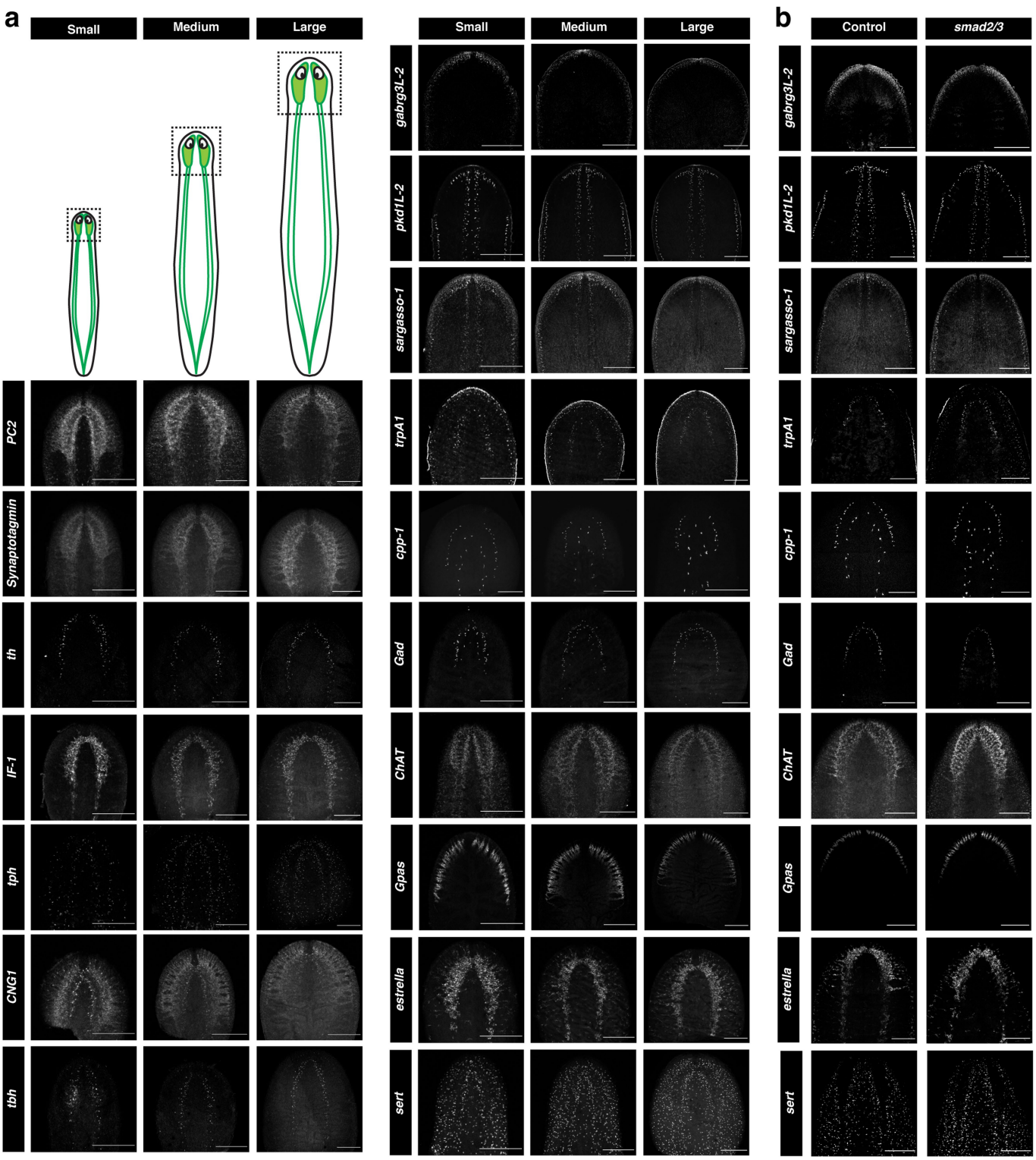

Extended Data Fig. 9 | Comparison of neuronal subpopulations in worms of increasing size and after *smad2/3* RNAi treatment. **a**, Representative images of neuronal marker staining in small, medium and large worms ($n = 3–5$ worms; 1 experiment). **b**, Representative images of a subset of neuronal markers analysed in worms treated with *smad2/3* RNAi ($n = 3–5$ worms; 1 experiment). Scale bars, 0.5 mm.

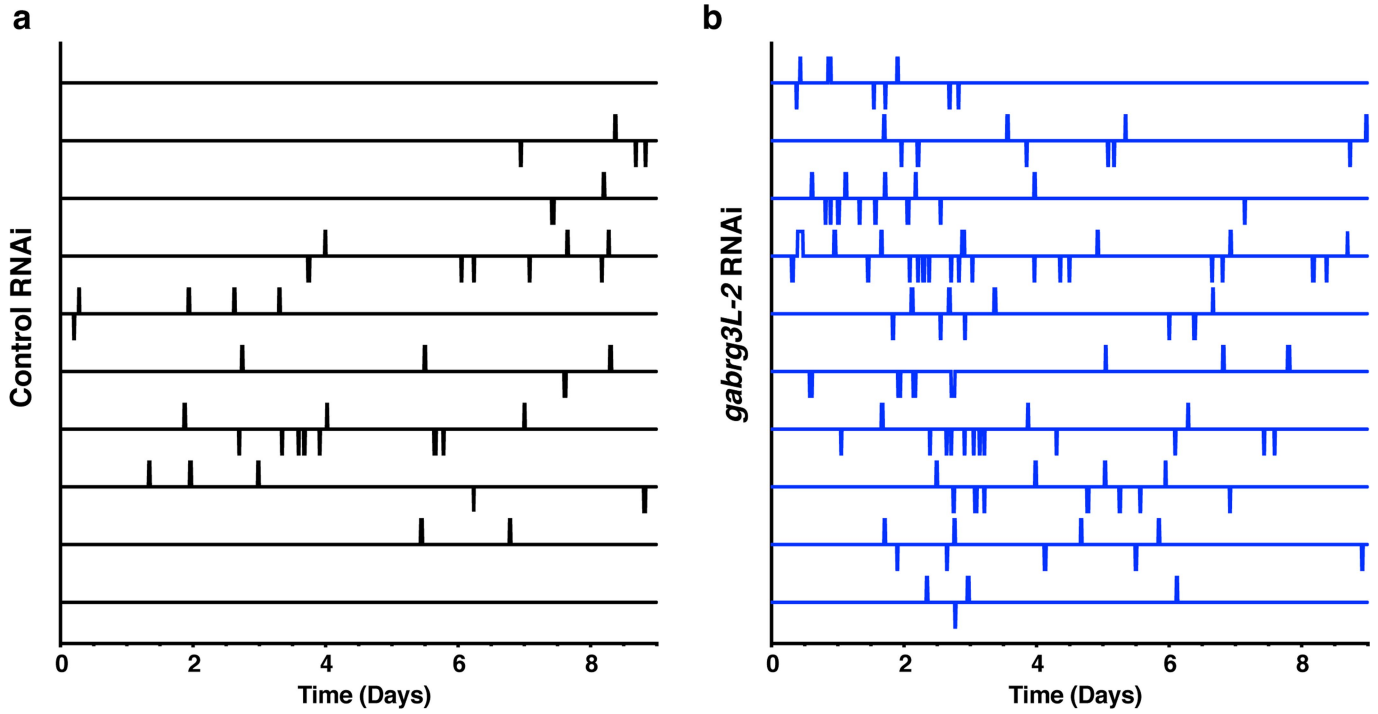

Extended Data Fig. 10 | *gabrg3L-2* negatively regulates the frequency of fission initiation. a, **b**, All individual timelines depicting fission activity over 9 days for worms treated with control (**a**) or *gabrg3L-2* (**b**) RNAi (n = recordings of 10 worms combined from 2 independent experiments).

LETTER

https://doi.org/10.1038/s41586-019-1500-0

Reconstituting the transcriptome and DNA methylome landscapes of human implantation

Fan Zhou[1,2,7], Rui Wang[1,2,7], Peng Yuan[1,3,7], Yixin Ren[1,3,7], Yunuo Mao[1,2,7], Rong Li[1,3], Ying Lian[1,3], Junsheng Li[1,3], Lu Wen[1,2], Liying Yan[1,2,3,4], Jie Qiao[1,2,3,4,5,6]* & Fuchou Tang[1,2,3,5,6]*

Implantation is a milestone event during mammalian embryogenesis. Implantation failure is a considerable cause of early pregnancy loss in humans[1]. Owing to the difficulty of obtaining human embryos early after implantation in vivo, it remains unclear how the gene regulatory network and epigenetic mechanisms control the implantation process. Here, by combining an in vitro culture system for the development human embryos after implantation and single-cell multi-omics sequencing technologies, more than 8,000 individual cells from 65 human peri-implantation embryos were systematically analysed. Unsupervised dimensionality reduction and clustering algorithms of the transcriptome data show stepwise implantation routes for the epiblast, primitive endoderm and trophectoderm lineages, suggesting robust preparation for the proper establishment of a mother-to-offspring connection during implantation. Female embryos showed initiation of random X chromosome inactivation based on analysis of parental allele-specific expression of X-chromosome-linked genes during implantation. Notably, using single-cell triple omics sequencing analysis, the re-methylation of the genome in cells from the primitive endoderm lineage was shown to be much slower than in cells of both epiblast and trophectoderm lineages during the implantation process, which indicates that there are distinct re-establishment features in the DNA methylome of the epiblast and primitive endoderm—even though both lineages are derived from the inner cell mass. Collectively, our work provides insights into the complex molecular mechanisms that regulate the implantation of human embryos, and helps to advance future efforts to understanding early embryonic development and reproductive medicine.

Human embryonic development starts from a fertilized egg, after which a free-floating blastocyst is formed, which consists of an outer trophectoderm (TE) and an inner cell mass. The mature inner cell mass is composed of the pluripotent epiblast (EPI) covered by a layer

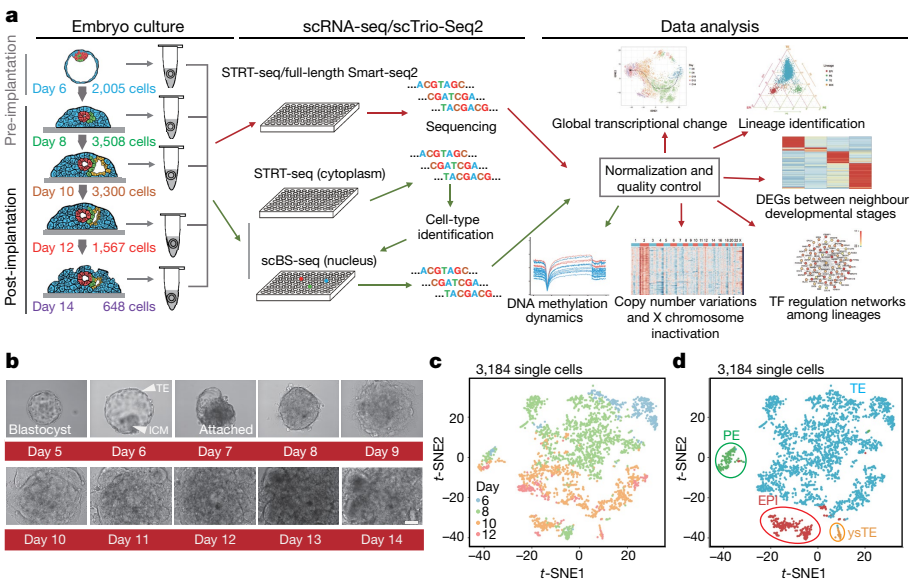

Fig. 1 | Single-cell RNA-sequencing transcriptome profiling of human post-implantation embryos. a, Schematic illustration of the strategy for the collection of single cells, and transcriptome and DNA methylome analyses used in this study. DEGs, differentially expressed genes; scBS-seq, single-cell bisulfite sequencing; scRNA-seq, single-cell RNA sequencing; STRT-seq, single-cell tagged reverse transcription sequencing; TF, transcription factor. **b**, Representative bright-field images of human in vitro cultured embryos until day 14. The blastocysts clearly attached to the bottom of the culture plate and formed a ring-like structure, with the EPI cells surrounded by TE cells, at approximately days 7–8. ICM, inner cell mass. All scale bars, 100 μm. All embryos used in this study are described in Supplementary Table 1. **c**, **d**, Cells from embryos containing all three major lineages at four representative stages were projected on to the *t*-SNE map, enabling the identification of the developmental path and cell lineage. Cells were identified as EPI, PE, TE and ysTE cells. Cells (dots) are coloured according to embryonic stages (**c**) and original lineage identities (**d**). **c**, **d**, In total, 3,184 single cells were included. **c**, Day 6, $n = 387$ cells; day 8, $n = 1{,}525$ cells; day 10, $n = 1{,}021$ cells; day 12, $n = 251$ cells. **d**, EPI, $n = 282$ cells; PE, $n = 138$ cells; TE, $n = 2{,}725$ cells; ysTE, $n = 39$ cells.

[1]Beijing Advanced Innovation Center for Genomics, Department of Obstetrics and Gynecology, Third Hospital, School of Life Sciences, Peking University, Beijing, China. [2]Biomedical Pioneering Innovation Center and Center for Reproductive Medicine, Third Hospital, Peking University, Beijing, China. [3]Key Laboratory of Assisted Reproduction and Key Laboratory of Cell Proliferation and Differentiation, Ministry of Education, Beijing, China. [4]Beijing Key Laboratory of Reproductive Endocrinology and Assisted Reproductive Technology, Beijing, China. [5]Academy for Advanced Interdisciplinary Studies, Peking University, Beijing, China. [6]Peking-Tsinghua Center for Life Sciences, Peking University, Beijing, China. [7]These authors contributed equally: Fan Zhou, Rui Wang, Peng Yuan, Yixin Ren, Yunuo Mao. *e-mail: jie.qiao@263.net; tangfuchou@pku.edu.cn

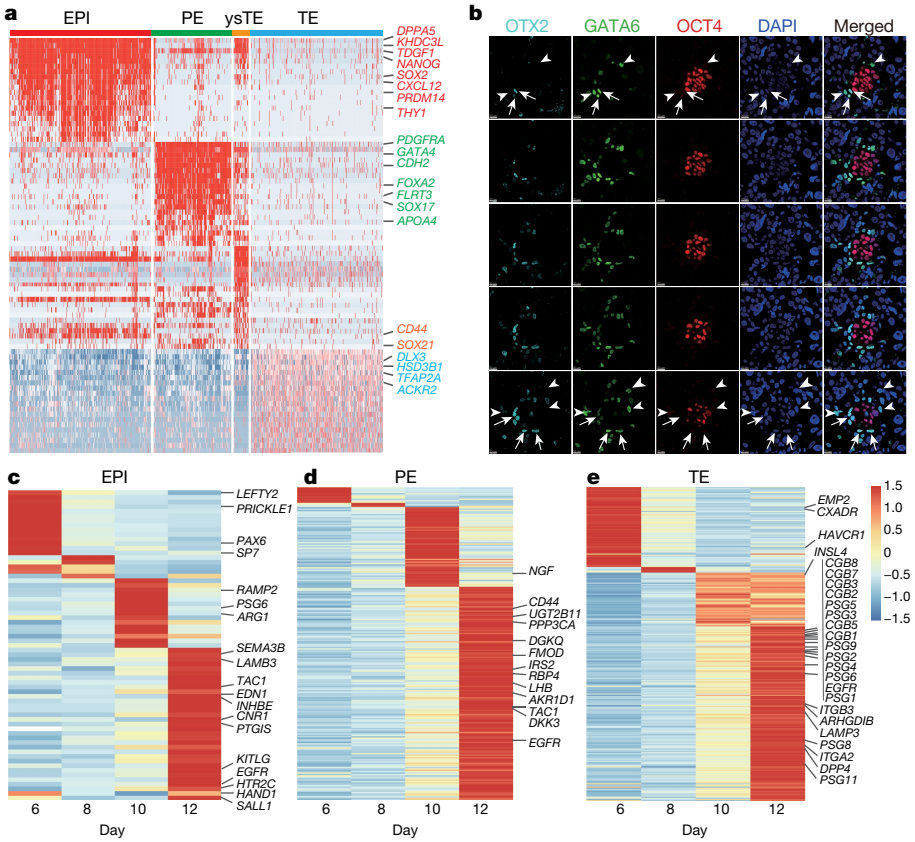

Fig. 2 | Transcriptome dynamics at post-implantation stages. **a**, The expression patterns of lineage signature genes. Among these genes, several genes were recognized as classical lineage-specific maker genes, such as *NANOG* for EPI, *GATA4* for PE and *TFAP2A* for TE. A marker that has been identified in the yolk sac of mice, *APOA4*, was identified as one of the signature markers in the PE lineage[25]. *ACKR2* was identified as a TE marker here, consistent with its known function for regulating placenta development in mice. The ysTE specifically expressed *CD44*, which has been reported as a critical gene for trophoblast cell invasion. On the basis of the signatures of each lineage, the EPI signatures were enriched in Gene Ontology (GO) terms related to embryonic morphogenesis, gastrulation and transcriptional regulation of pluripotent stem cells. The PE signatures were enriched in GO terms related to cell-fate specification, embryonic organ development and epithelial cell differentiation, and the TE signatures were enriched in response to steroid hormone, extracellular matrix organization and vasculature development (Supplementary Table 6). Such changes among lineages are probably to balance pluripotency maintenance/transition and lineage specification for different developmental potentials to support the continued development of the embryo after implantation. **b**, Morphological visualization of OTX2 expression in PE cells ($n = 3$). Series of confocal z-sections of the embryo stained for OCT4 (red), GATA6 (green) and OTX2 (cyan). Arrowheads, GATA6$^+$ but OTX2$^-$ cells. Arrows, GATA6$^+$ and OTX2$^+$ cells. All scale bars, 20 μm. **c**–**e**, Stage-specific gene-expression patterns for three major lineages. There were 67 (EPI), 224 (PE) and 282 (TE) genes that showed stage-specific expression features in each lineage (**c**–**e**; Supplementary Table 6). GO analysis showed that EPI stage-specific genes were clearly enriched in embryonic morphogenesis genes (such as *SALL1* and *HAND1*) between day 6 and day 12. Additionally, *PSG2*, a member of the pregnancy-specific glycoprotein (PSG) gene family, was upregulated from day 8 to day 10 in the TE lineage, which indicates that the embryo might be preparing for mother–fetal interactions during implantation. The colours from blue to red represent the expression levels from low to high.

of primitive endoderm (PE; also known as the hypoblast). The EPI, PE and TE then give rise to the embryo proper, yolk sac and placenta, respectively. By embryonic days 6–7 (after fertilization), the embryo will implant into the uterus to form a gastrula, followed by organogenesis. Owing to the limited access to embryos early after implantation in vivo, the lineage specification and corresponding patterns of the transcriptome and DNA methylome that are specific to the different lineages during human implantation are still poorly understood. In this study, with the help of donated human embryos and a robust in vitro culture system for post-implantation embryos and single-cell multi-omics sequencing technologies[2–5], we simultaneously analysed the gene-expression network and lineage-specific DNA methylation patterns of the human peri-implantation embryos at single-cell resolution.

First, we mimicked the implantation of human embryos as previously reported[2,3] (Fig. 1a, b, Extended Data Fig. 1a–d and Supplementary Videos 1–5). The culture of embryos was terminated at day 14 according to bioethical guidelines[6,7]. Next, we profiled 7,636 individual cells from 48 human pre/post-implantation embryos at 5 consecutive developmental stages, including the blastocyst stage (day 6, pre-implantation) and 4 later stages (days 8, 10, 12 and day14 after implantation) (Fig. 1c and Supplementary Tables 1, 2). In total, 5,911 single cells were retained for subsequent analyses following stringent filtering (Extended Data Fig. 1e–h). Unsupervised t-distributed stochastic neighbour embedding (t-SNE) analysis revealed that all of the cells were grouped by their developmental states (Extended Data Fig. 1i). Furthermore, t-SNE analyses partitioned the cells into four main clusters. The analysis of the expression of known markers and lineage scores identified these clusters as the EPI, PE, TE and yolk-sac trophectoderm (ysTE)[3,8,9] (Extended Data Figs. 1j, k, 2, Supplementary Methods and Supplementary Table 3). As there was only a limited number (only 39 cells in total) of ysTE cells and to avoid the potential influence of embryos that lacked lineage(s) on the outcome of the analysis, we next focused mainly on the features of the three major lineages in those embryos that contained all three of the major lineages (EPI, PE and TE); 3,184 individual cells were retained in the subsequent analyses (Fig. 1c, d and Extended Data Fig. 1g).

Next, we identified genes that were specifically expressed in the EPI, PE and TE cells, and defined these as lineage signature genes. In addition to the canonical lineage makers, the EPI expressed *KHDC3L*, *TDGF1*, *CXCL12* and *THY1*, which have previously been

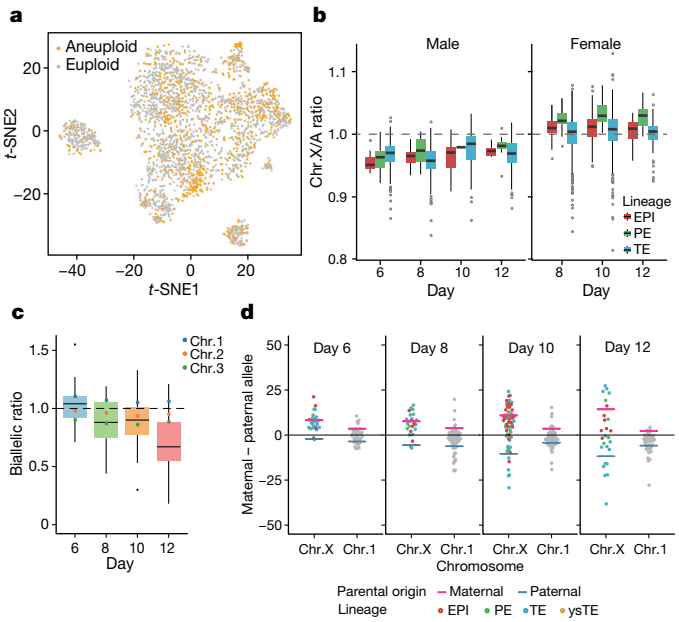

Fig. 3 | CNVs and unsynchronized X chromosome inactivation among different lineages during implantation. a, CNV information projected onto the *t*-SNE plot based on the transcription-factor regulatory network. In total, 3,184 single cells were included; 1,027 cells were aneuploid and 2,157 cells were euploid. **b**, The ratio of total expression levels of genes located on the X chromosome (Chr.X) and the same number of genes located on autosomes (A). In total, 3,184 cells were included; male, $n = 1{,}016$ cells; female, $n = 2{,}168$ cells (Supplementary Table 1). Black lines indicate median values, the boxes range from the 25th to 75th percentiles and the whiskers correspond to 1.5× the interquartile range (IQR; the distance between the first and third quantiles). **c**, The proportion of bi-allelic expression of chromosome-X-linked genes compared to the expression of autosome-linked genes (Supplementary Methods). In total, 150 cells were included; day 6, $n = 24$ cells; day 8, $n = 30$ cells; day 10, $n = 70$ cells; day 12, $n = 26$ cells. Black lines indicate median values, the boxes range from the 25th to 75th percentiles and the whiskers correspond to 1.5× the IQR. **d**, The percentage differences between maternal and paternal alleles (maternal allele (%) − paternal allele (%)) for each cell. According to the heterozygous single-nucleotide polymorphisms, reads were traced to their parental origins. For each chromosome, the ratio of reads from paternal or maternal alleles was calculated (Supplementary Methods). In total, 150 cells were included. For each developmental stage, the mean value for maternal or paternal alleles (maternal ($y > 0$), paternal ($y < 0$)) were calculated for chromosomes X and 1. Mean values are shown as pink and blue centre lines for maternal and paternal alleles, respectively.

reported to be signatures of EPI during the implantation process in monkeys[10] (Fig. 2a and Supplementary Tables 4–6). Immunostaining showed that OTX2, a pluripotency marker for EPI development during implantation[11], was expressed in a fraction of GATA6-expressing PE cells, but not in OCT4-expressing EPI cells, verifying our single-cell RNA-sequencing data (Fig. 2b and Extended Data Fig. 2d). Human and monkey embryos shared partial signatures of these three lineages and related derivatives[10], although human embryos also expressed several unique signature genes, such as *UTF1* in EPI, *GPC3* in PE and *CYP19A1* in TE (Extended Data Fig. 3).

Principal component analysis and pseudo-time analysis revealed that all three lineages presented their own developmental continuity, suggesting that there are stepwise implantation routes (Extended Data Fig. 4a, b). Further analysis of stage-specific gene-expression patterns for each lineage indicated that the embryo started preparing for mother–fetal interactions during implantation (for example, the expression of embryonic morphogenesis and pregnancy-associated genes; Fig. 2c–e and Extended Data Fig. 4c–f). Notably, the *t*-SNE results showed that TE gradually formed two separate subgroups around days 10–12. The differential expression of HCGB family genes corresponded to the subgrouping of TE by days 12–14 (Extended Data Fig. 4g). We determined that these subgroups consisted of cytotrophoblasts (which specifically expressed *ITGA6*) and syncytiotrophoblasts (which specifically expressed CGB family genes)[3,12]. Cytotrophoblasts also expressed regulators of the TE and placenta, such as *FABP5* and *FGFR1*, whereas syncytiotrophoblasts expressed hormone-related genes of the placenta (for example, *PSG3* and *PSG6*) and a number of newly identified genes (for example, *TCL6* and *TBX3*) (Extended Data Fig. 5). Furthermore, we found that both meiosis- and mitosis-derived copy number variations (CNVs) were widely present in the cultured embryos during implantation[13,14] (Extended Data Fig. 6 and Supplementary Methods). These aneuploid cells still clustered with the corresponding euploid cells in the *t*-SNE map, which suggests that the differentiation of the major lineages was generally not distorted by mild CNVs at the early stage of implantation (Fig. 3a).

Inactivation of the X chromosome is important for the dosage balance of X-linked genes between females (XX) and males (XY), whereas upregulation of the expression of genes on the X chromosome is critical for the dosage balance between X-linked genes and autosomal genes[15–19]. The expression of X-linked genes should be equivalent to that of autosomal genes, which is achieved through upregulation of genes on the X chromosome in both male and female cells[20]. Further measurements showed that the ratio of X chromosome to autosomes in male cells was near 2:2 (but not 1:2), indicating that the upregulation of the X chromosome had already started and the expression levels of genes on the only copy of the X chromosome in a male cell had already become comparable to those on two copies of the autosomes. Comparatively, the ratio of X chromosomes to autosomes in female cells appeared to be above 1 and slightly higher than the ratio found in male cells during implantation[21] (Fig. 3b and Extended Data Fig. 7). We therefore suggest that both the upregulation and inactivation of the X chromosome had started, but was not fully completed in female cells at day 12. That is, one of the X chromosomes had randomly been inactivated and expression of genes on this X chromosome had been downregulated, whereas the expression of genes on the other, active, X chromosome had increased by nearly twofold. Subsequently, 238 representative single cells for all three major lineages were selected for full-length cDNA high-depth sequencing to separate parental alleles within each individual cell (Supplementary Tables 1, 7). The genomes of the parental donors were also sequenced to call single-nucleotide polymorphisms (Supplementary Methods). At day 6, the majority of the cells still expressed X-linked genes in a balanced way from paternal and maternal alleles. However, at later stages many cells showed gradual accumulation of paternal- or maternal-allele-biased expression patterns, clearly indicating the initiation of random X chromosome inactivation during the early implantation period (Fig. 3c, d).

DNA methylation has critical roles in the epigenetic regulation of the development of mammalian embryos. Nevertheless, the lineage-specific DNA methylation dynamics around implantation remain largely unknown. Using the single-cell Trio-seq2 strategy[5] and another round of embryonic culture followed by the collection of single cells, 2,544 individual cells from 17 embryos were first analysed for lineage identification (Extended Data Fig. 8, Supplementary Methods and Supplementary Tables 8–10). We subsequently selected 371 lineage-specific individual cells for post-bisulfite adaptor-tagging DNA methylome sequencing (Extended Data Fig. 8b–d). Furthermore, 130 euploid cells were retained for subsequent analyses after removal of aneuploid cells (Extended Data Fig. 9). Principal component analysis of DNA methylome data showed that these 130 cells formed 4 major clusters (Extended Data Fig. 8g, h), with a combination of the EPI, PE and TE at the blastocyst stage (day 6) as a single cluster, and the EPI, PE and TE beyond the blastocyst stage as another 3 separate clusters, suggesting that all of the 3 lineages showed considerable changes in DNA methylation soon after implantation.

Next, we explored the dynamics of DNA methylation of each lineage. In general, EPI, PE and TE experienced strong genome re-methylation during implantation (Fig. 4a and Extended Data Fig. 10a). The median

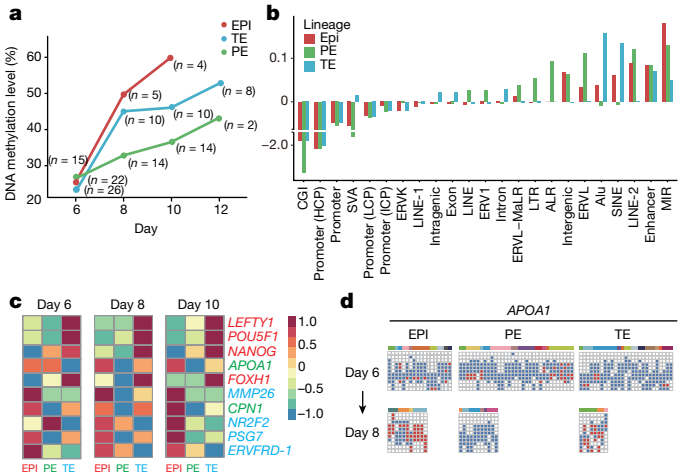

Fig. 4 | Lineage-specific dynamics of the DNA methylome in human peri-implantation embryos. a, The global DNA methylation levels across different developmental stages for each lineage. **b**, Distribution of the relative enrichment of increased methylation tiles from day 6 to day 8 at various genomic features, 1,512,276 (EPI), 310,255 (PE) and 1,140,524 (TE) tiles (300 bp) were de novo-methylated in each lineage. The re-methylated genomic regions were strongly enriched in enhancers and mammalian-wide interspersed repetitive (MIR) regions but depleted in the promoters and CpG islands (CGI) in all lineages. The EPI and PE lineages shared re-methylation enrichment of long interspersed nuclear element-2 (LINE-2) retroelements and intergenic regions. For PE, re-methylated genomic regions were strongly enriched for several families of repeat elements (for example, alpha satellites (ALR) and long terminal repeats (LTR)). For TE, re-methylated genomic regions were strongly enriched for intragenic regions—both exons and introns. This showed that DNA re-methylation has strong genomic-element-specific and clear developmental-lineage-specific features during implantation. Alu, Alu element; ERVs, endogenous retroviruses (ERVK, ERVL); HCP, high CpG density promoter; ICP, intermediate CpG density promoter; LCP, low CpG density promoter; MaLR, mammalian LTR; SINE, short interspersed nuclear elements; SVA, short interspersed element–variable number tandem repeat–Alu. **c**, The average DNA methylation levels for differentially methylated genes at promoter regions (transcription start sites included the upstream 250 bp and downstream 250 bp). **d**, DNA methylation levels of representative loci for lineage-specific genes at promoter regions. Each column represents one read. Red represents methylated CpG sites, blue represents unmethylated CpG sites and white represents undetected sites. Only reads that covered at least five CpG sites are shown in the heat map.

DNA methylation level of EPI markedly increased from 26.1% at day 6 to 60.0% at day 10. The median DNA methylation level of TE also increased from 23.5% at day 6 to 46.3% at day 10, an increase that is not as strong as that with the EPI (Fig. 4a). Notably, although the DNA methylation level of PE (27.0%) at day 6 is comparable to that of EPI (26.1%), it increased only to 33.2% at day 8 (compared to 49.9% in EPI), and 36.8% at day 10 (compared to 60.0% in EPI). The PE unexpectedly revealed much slower DNA re-methylation dynamics during implantation compared to the EPI, even though both cell lineages are derived from the inner cell mass. These results suggest that the embryos initiated considerable re-methylation of the DNA shortly after the blastocyst stage, and that the three major lineages not only had different gene-expression signatures but also showed markedly distinct and asynchronous DNA re-methylation patterns.

The patterns of hypermethylated gene body and hypomethylated promoter regions were shared in all of the three lineages (Extended Data Fig. 8i), which is similar to the patterns in pre-implantation embryos[22]. Further analysis of re-methylated genomic regions in all three lineages showed that DNA re-methylation has clear genomic element-specific and cell-lineage-specific features during implantation (Fig. 4b).

We found that 241 genes showed increased levels of methylation at their promoter regions, potentially silencing their expression during implantation (Extended Data Fig. 10b), and each lineage carried specifically methylated genes (Fig. 4c). For instance, the promoters of *POU5F1* (also known as *OCT4*) and *NANOG*, master regulators of pluripotency, were specifically methylated in TE cells, but not in EPI and PE cells at day 8 (Fig. 4c). By contrast, the promoters of development genes in the TE[23,24], such as *MMP26*, *PSG7* and *ELF5*, were specifically methylated in EPI and PE cells but not in TE cells at day 8 (Fig. 4c and Extended Data Fig. 10c). Similarly, the promoters of PE markers[25,26] such as *APOA1* and *CPN1* were specifically methylated in EPI and TE cells but not in PE cells at day 8 (Fig. 4c, d). These findings indicate that DNA methylation might have an important role in regulating the expression of lineage-specific genes and maintaining the segregated cell fates of different lineages.

We reconstituted the transcriptome and DNA methylome landscapes of human implantation at single-cell resolution and uncovered key developmental events, the molecular dynamics of which was previously unresolved. Although many potential differences may exist between in vivo and in vitro implantation systems, this study provides a potential basis for the development of better strategies to mimic this unique process in vitro. A better understanding of the implantation process will also provide valuable information—such as lineage-specific transcription-factor networks and signalling pathway characteristics (Supplementary Methods)—for the derivation and directed differentiation of pluripotent stem cells in vitro, which could be a potentially invaluable resource for reproductive and regenerative medicine.

Reporting summary

Further information on research design is available in the Nature Research Reporting Summary linked to this paper.

Data availability

The single-cell RNA-sequencing data have been deposited in the GEO (accession number GSE109555). The single-cell MALBAC whole-genome sequencing, full-length RNA-sequencing and Trio-seq2 data have been deposited in the European Genome-phenome Archive (EGA; https://www.ebi.ac.uk/ega/) with accession number EGAS00001003443. The whole-genome sequencing data of the paternal sperm and maternal peripheral blood were from a previous publication (EGAS00001002987). The data deposited and made public are compliant with the regulations of Ministry of Science and Technology of China.

Code availability

Scripts of the main steps of the analysis are provided at https://github.com/WRui/Post_Implantation. Other R scripts associated with graphic presentation are available from the corresponding authors on reasonable request.

Online content

Any methods, additional references, Nature Research reporting summaries, source data, extended data, supplementary information, acknowledgements, peer review information; and details of author contributions and competing interests are available at https://doi.org/10.1038/s41586-019-1500-0.

Received: 5 February 2018; Accepted: 15 July 2019;
Published online 21 August 2019.

1. Koot, Y. E., Teklenburg, G., Salker, M. S., Brosens, J. J. & Macklon, N. S. Molecular aspects of implantation failure. *Biochim. Biophys. Acta* **1822**, 1943–1950 (2012).
2. Shahbazi, M. N. et al. Self-organization of the human embryo in the absence of maternal tissues. *Nat. Cell Biol.* **18**, 700–708 (2016).
3. Deglincerti, A. et al. Self-organization of the *in vitro* attached human embryo. *Nature* **533**, 251–254 (2016).
4. Gao, S. et al. Tracing the temporal-spatial transcriptome landscapes of the human fetal digestive tract using single-cell RNA-sequencing. *Nat. Cell Biol.* **20**, 721–734 (2018).
5. Bian, S. et al. Single-cell multiomics sequencing and analyses of human colorectal cancer. *Science* **362**, 1060–1063 (2018).
6. Dickens, B. M. International Society for Stem Cell Research (ISSCR) Guidelines for the Conduct of Human Embryonic Stem Cell Research (December 2006). *Med. Law* **27**, 179–190 (2008).
7. National Research Council and Institute of Medicine of the National Acadamies. *Final Report of the National Academies' Human Embryonic Stem Cell Research Advisory Committee and 2010 Amendments to the National Academies'*

Guidelines for Human Embryonic Stem Cell Research (National Academies Press, 2010).
8. Stirparo, G. G. et al. Integrated analysis of single-cell embryo data yields a unified transcriptome signature for the human pre-implantation epiblast. *Development* **145**, dev158501 (2018).
9. Petropoulos, S. et al. Single-cell RNA-seq reveals lineage and X chromosome dynamics in human preimplantation embryos. *Cell* **165**, 1012–1026 (2016).
10. Nakamura, T. et al. A developmental coordinate of pluripotency among mice, monkeys and humans. *Nature* **537**, 57–62 (2016).
11. Shahbazi, M. N. et al. Pluripotent state transitions coordinate morphogenesis in mouse and human embryos. *Nature* **552**, 239–243 (2017).
12. Li, Y. et al. BMP4-directed trophoblast differentiation of human embryonic stem cells is mediated through a $\Delta Np63^{+}$ cytotrophoblast stem cell state. *Development* **140**, 3965–3976 (2013).
13. Patel, A. P. et al. Single-cell RNA-seq highlights intratumoral heterogeneity in primary glioblastoma. *Science* **344**, 1396–1401 (2014).
14. Hou, Y. et al. Single-cell triple omics sequencing reveals genetic, epigenetic, and transcriptomic heterogeneity in hepatocellular carcinomas. *Cell Res.* **26**, 304–319 (2016).
15. Lyon, M. F. Gene action in the X-chromosome of the mouse (*Mus musculus* L.). *Nature* **190**, 372–373 (1961).
16. Deng, X. et al. Evidence for compensatory upregulation of expressed X-linked genes in mammals, *Caenorhabditis elegans* and *Drosophila melanogaster*. *Nat. Genet.* **43**, 1179–1185 (2011).
17. Yildirim, E., Sadreyev, R. I., Pinter, S. F. & Lee, J. T. X-chromosome hyperactivation in mammals via nonlinear relationships between chromatin states and transcription. *Nat. Struct. Mol. Biol.* **19**, 56–61 (2012).
18. Giorgetti, L. et al. Predictive polymer modeling reveals coupled fluctuations in chromosome conformation and transcription. *Cell* **157**, 950–963 (2014).
19. Sangrithi, M. N. & Turner, J. M. A. Mammalian X chromosome dosage compensation: perspectives from the germ line. *BioEssays* **40**, 1800024 (2018).
20. Brockdorff, N. & Turner, B. M. Dosage compensation in mammals. *Cold Spring Harb. Perspect. Biol.* **7**, a019406 (2015).
21. Vallot, C. et al. *XACT* noncoding RNA competes with *XIST* in the control of X chromosome activity during human early development. *Cell Stem Cell* **20**, 102–111 (2017).
22. Guo, H. et al. The DNA methylation landscape of human early embryos. *Nature* **511**, 606–610 (2014).
23. Qiu, W. et al. Spatio-temporal expression of matrix metalloproteinase-26 in human placental trophoblasts and fetal red cells during normal placentation. *Biol. Reprod.* **72**, 954–959 (2005).
24. Camolotto, S. et al. Expression and transcriptional regulation of individual pregnancy-specific glycoprotein genes in differentiating trophoblast cells. *Placenta* **31**, 312–319 (2010).
25. Yadgary, L., Wong, E. A. & Uni, Z. Temporal transcriptome analysis of the chicken embryo yolk sac. *BMC Genomics* **15**, 690 (2014).
26. Gerovska, D. & Araúzo-Bravo, M. J. Does mouse embryo primordial germ cell activation start before implantation as suggested by single-cell transcriptomics dynamics? *Mol. Hum. Reprod.* **22**, 208–225 (2016).

Acknowledgements We thank D. Xie and J. Zhou for discussions and Y. Hu, X. Fan, D. Liu, Y. Yuan and Y. Cui for technical help in pilot experiments; C. Shan from National Center for Protein Sciences at Peking University for immunofluorescence imaging and analysis. This work was supported by grants from the Beijing Municipal Science and Technology Commission (Z181100001318001), the National Natural Science Foundation of China (81521002, 31625018 and 81730078) and National Basic Research Program of China (2017YFA0102702 and 2018YFA0107601). F.Z. was supported by Young Elite Scientists Sponsorship Program by China Association for Science and Technology (YESS20160129), the Postdoctoral Fellowship of Peking-Tsinghua Center for Life Sciences and the grant from China Postdoctoral Science Foundation (2017M610015 and 2017T100015). F.Z. was a Bayer Postdoc of the Bayer-Peking University Center for Translational Research. This work was supported by the Beijing Advanced Innovation Center for Genomics at Peking University. Part of the computational analyses was performed on the High Performance Computing Platform of the Center for Life Science.

Author contributions F.T. and J.Q. conceived the project. F.Z., P.Y., Y.R. and Y.M. performed the experiments including the collection and culture of embryos, collection of single cells and single-cell sequencing data generation with the help of L.W., L.Y., R.L., J.L. and Y.L. R.W. performed computational analyses. F.T., F.Z. and R.W. wrote the manuscript with feedback from all authors.

Competing interests The authors declare no competing interests.

Additional information

Supplementary information is available for this paper at https://doi.org/10.1038/s41586-019-1500-0.

Correspondence and requests for materials should be addressed to J.Q. or F.T.

Peer review information *Nature* thanks Ali H. Brivanlou, Gist Croft, Insoo Hyun, Celine Vallot and the other, anonymous, reviewer(s) for their contribution to the peer review of this work.

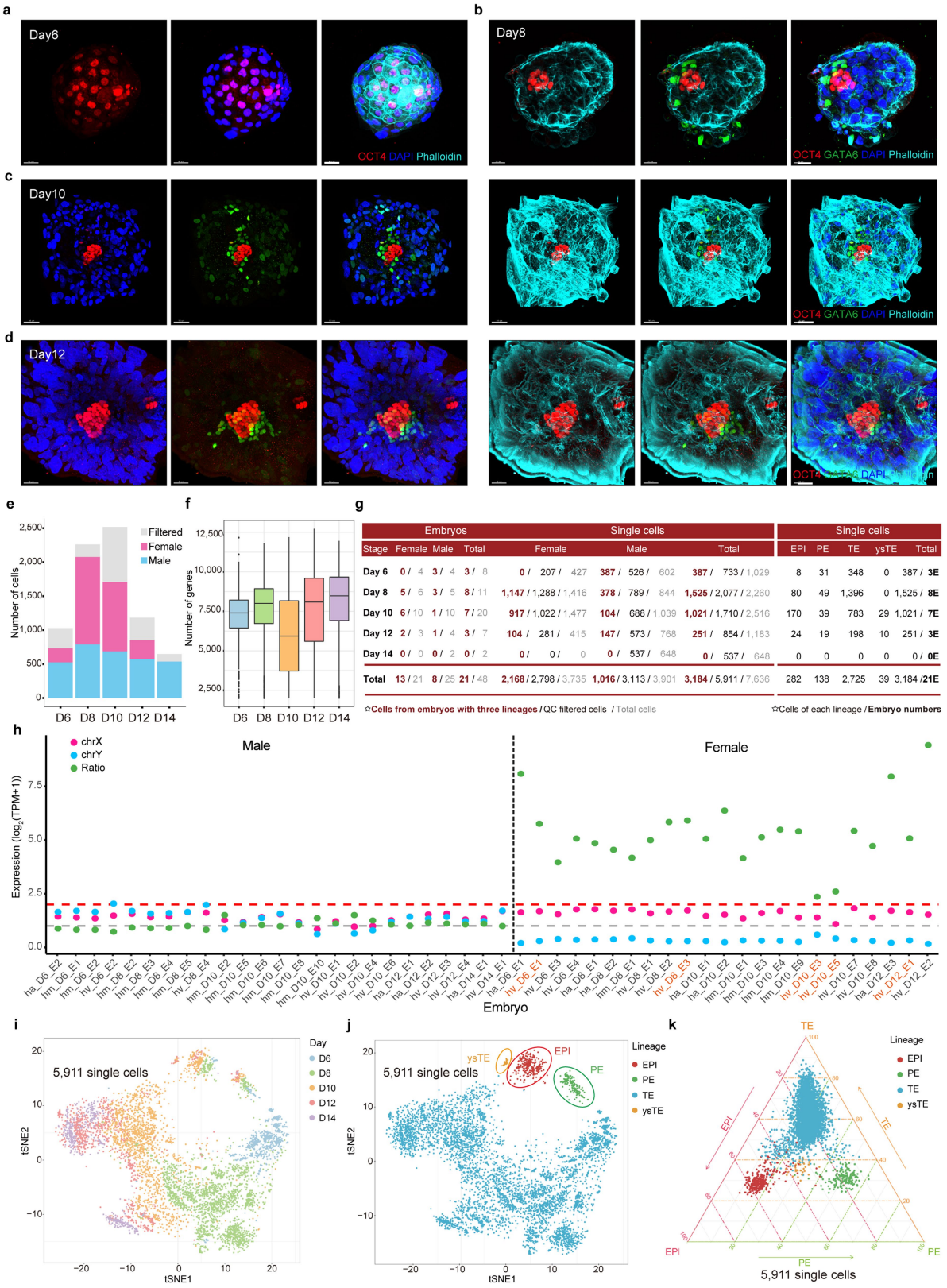

Extended Data Fig. 1 | See next page for caption.

Extended Data Fig. 1 | Lineage and sex identification of human pre- and post-implantation embryos. Related to Fig. 1. **a**–**d**, Immunofluorescence images of human embryos at different developmental stages ($n = 3$). Scale bars, 40 μm (**a**), 30 μm (**b**), 50 μm (**c**), 40 μm (**d**). **e**, Cell numbers of both sexes at each embryonic day. In total, 7,636 single cells were included. Day (D)6, $n = 1,029$ (filtered, $n = 296$; female, $n = 207$; male, $n = 526$). Day 8, $n = 2,260$ (filtered, $n = 183$; female, $n = 1,288$; male, $n = 789$). Day 10, $n = 2,516$ (filtered, $n = 806$; female, $n = 1,022$; male, $n = 688$). Day 12, $n = 1,183$ (filtered, $n = 329$; female, $n = 281$; male, $n = 573$). Day 14, $n = 648$ (filtered, $n = 111$; female, $n = 0$; male, $n = 537$). **f**, The number of expressed genes in each individual cell for different developmental stages. On average, 7,100 expressed genes and 139,792 transcripts were detected in each individual cell. Black lines indicate median values, the boxes range from the 25th to 75th percentiles and the whiskers correspond to 1.5× the IQR. In total, 5,911 single cells were included (day 6, $n = 733$; day 8, $n = 2,077$; day 10, $n = 1,710$; day 12, $n = 854$; day 14, $n = 537$). **g**, The number of cells and embryos of each cell lineage at distinct stages after filtering. E, embryo. **h**, The average mean levels of genes located on chromosome X (pink colour) and Y (blue colour) for each embryo. Mean expression ratios between X and Y are shown in green. Cells are ordered by sex and embryonic day. In total, 23 embryos with a sex expression ratio above two are defined as female embryos (2,798 cells from 4 stages), the remaining 25 embryos were male embryos (3,113 cells from 5 stages). The sex of the embryos highlighted in orange was confirmed by single-cell whole-genome sequencing. **i**, **j**, The unsupervised *t*-SNE plot of all cells at five representative stages, revealing a developmental path and cell lineage identification. **i**, In total, 5,911 cells were included (day 6, $n = 733$; day 8, $n = 2,077$; day 10, $n = 1,710$; day 12, $n = 854$; day 14, $n = 537$). **j**, Cells were identified as EPI, PE, TE and ysTE cells. Cells (dots) are coloured according to embryo stage and original lineage identity. EPI, $n = 330$; PE, $n = 179$; TE, $n = 5,363$; ysTE, $n = 39$. Clusters were assigned to indicate cell lineages using known lineage-specific markers. **k**, Lineage identification was further confirmed by lineage score analysis. The ggtern plot shows the lineage scores for each individual cell, calculated using previously published lineage-specific genes[9]. The cells are coloured according to their lineage identity.

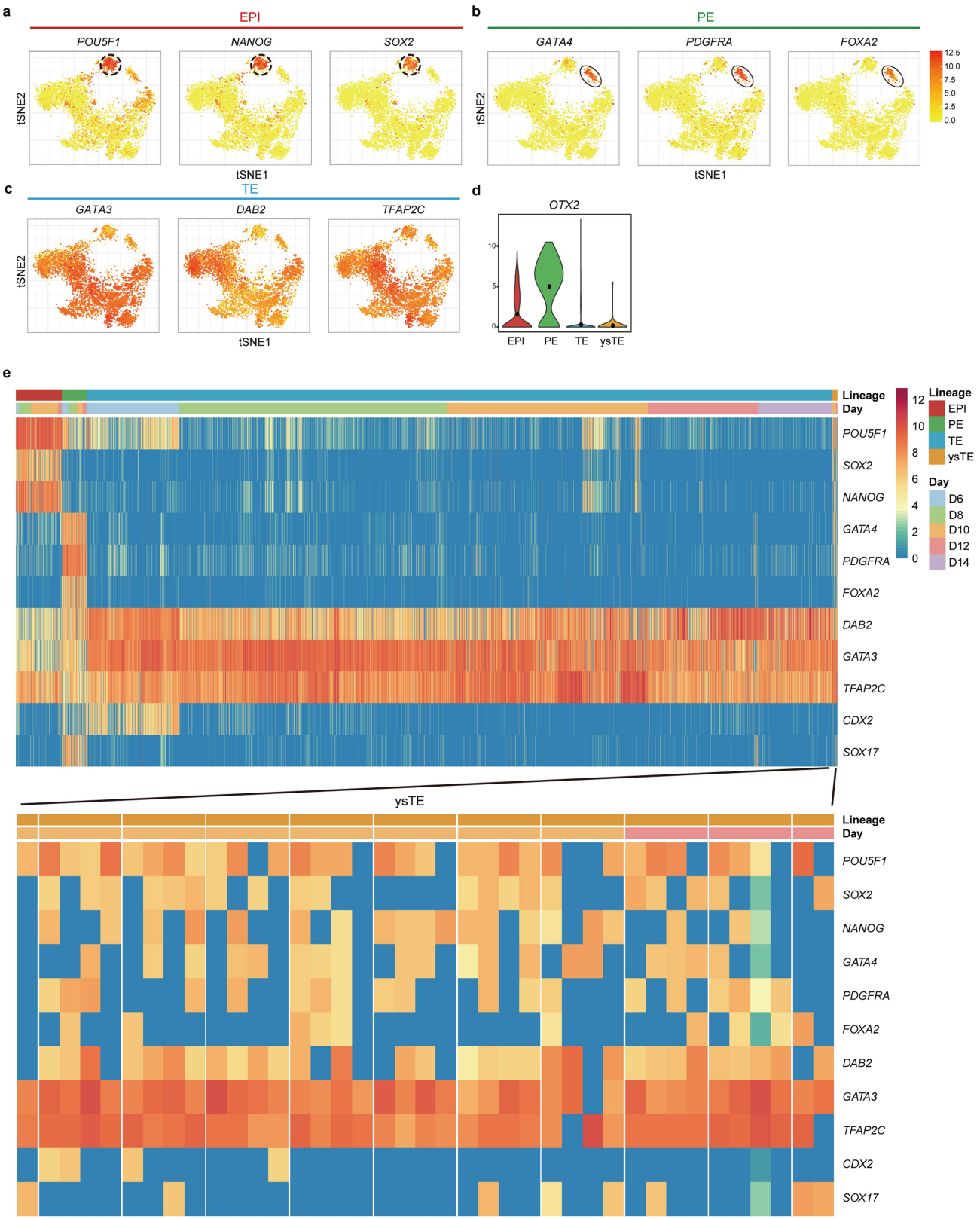

Extended Data Fig. 2 | Identification of gene-expression patterns during implantation. Related to Fig. 2. **a**–**d**, Cluster annotation based on the expression levels of conventional lineage markers. Each dot represents a single cell, and the cells are coloured based on the expression levels ($\log_2$(TPM + 1)) of several known gene markers for specific lineages. For example, the EPI population expressed the key pluripotency markers *POU5F1* (encoding OCT4), *NANOG* and *SOX2*. **a**–**c**, Colours from yellow to red represent expression levels from low to high. **d**, The violin plots show the expression of *OTX2* in three main lineages; by setting scale = width, all violins have the same maximum width. In total, 5,911 cells were included; EPI, $n = 330$; PE, $n = 179$; TE, $n = 5{,}363$; ysTE, $n = 39$. **e**, The expression levels of conventional lineage markers at single-cell levels. The cells that clustered away from the other three main cell clusters showed high expression of TE markers (for example, *GATA3*) and low expression of EPI (for example, *SOX2*) and PE (for example, *GATA4*) markers. Colours from blue to red represent expression levels from low to high.

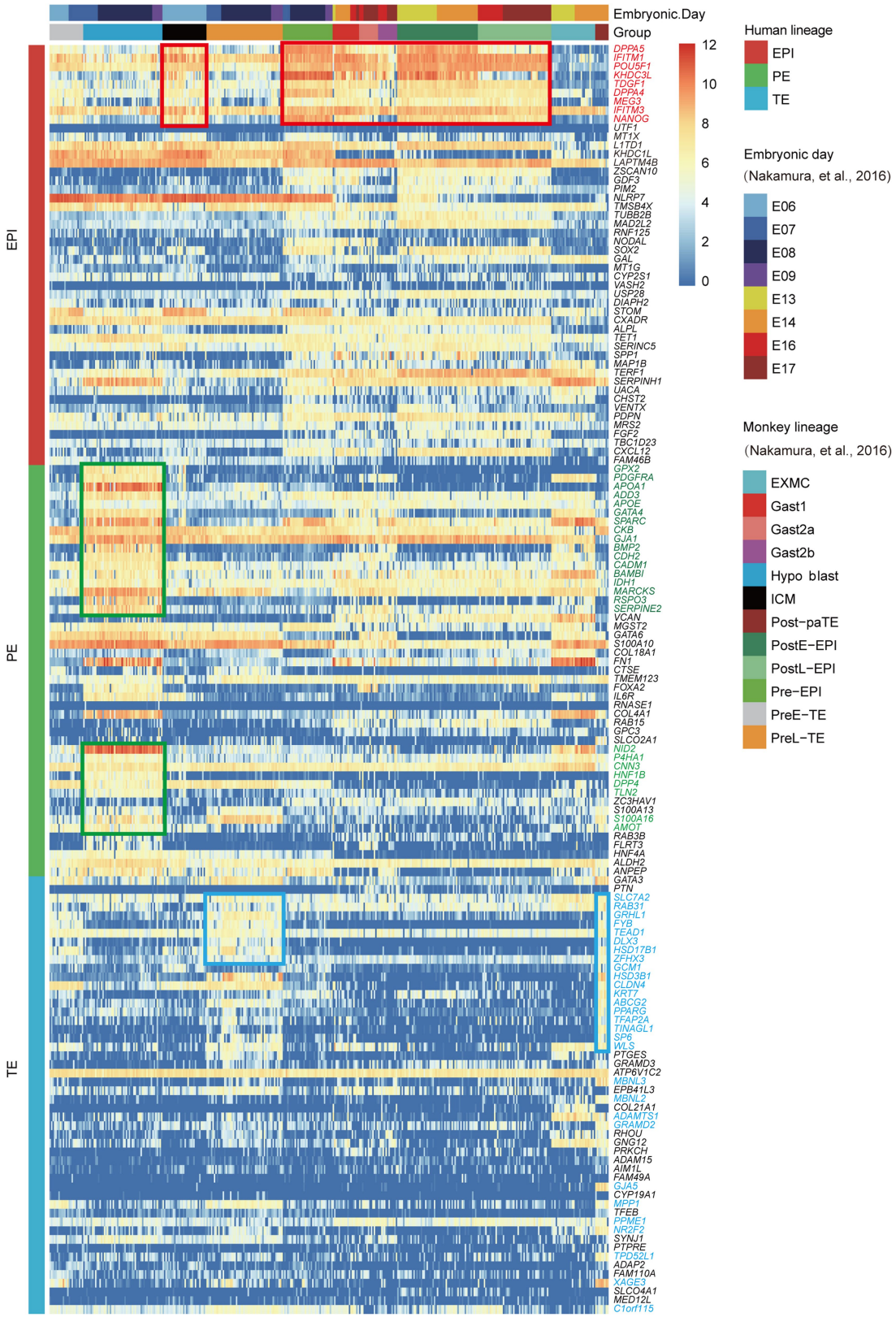

Extended Data Fig. 3 | Human lineage-specific gene-expression patterns on previously reported monkey data. The projection of signature genes for each lineage onto the monkey-related populations[10] around implantation stages, including *DPPA5*, *IFITM1* and *MEG3* in EPI and derivatives (Gast1, Gast2a and Gast2b), *GPX2*, *APOA1* and *APOE* in PE (also known as the hypoblast), and *SLC7A2*, *TEAD1* and *KRT7* in TE and derivatives (extra-embryonic mesenchyme, EXMC).

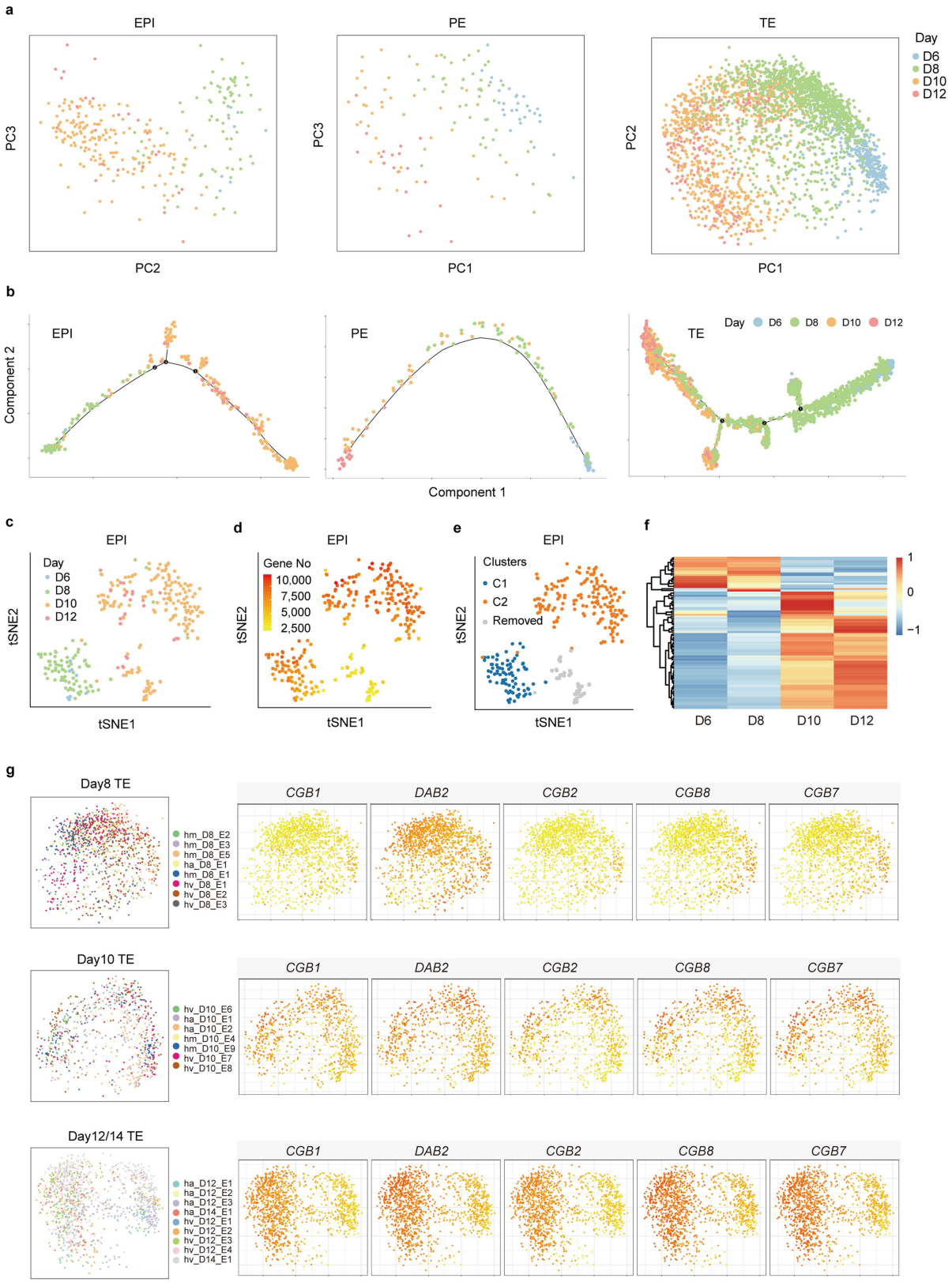

Extended Data Fig. 4 | See next page for caption.

Extended Data Fig. 4 | Lineage-specific gene-expression dynamics during implantation. a, Principal component analysis for each lineage. Only cells that came from embryos that contained all three major lineages were used. In total, 3,145 single cells were included: EPI, $n = 282$; PE, $n = 138$; TE, $n = 2,725$. **b**, The developmental trajectory of each lineage based on Monocle2. Only cells that came from embryos that contained all three major lineages were used. In total, 3,145 single cells were used. EPI, $n = 282$; PE, $n = 138$; TE, $n = 2,725$. **c**–**e**, *t*-SNE analysis of EPI cells at all four stages revealed three clusters. **c**, Clusters are shown for each of the days. **d**, We found that the main reason one minor cluster (in grey) of these three clusters was separated might be owing to the differences in the number of expressed genes, although all individual cells from these clusters passed our quality control in the first procedure of data processing. We could not exclude that this was caused by low transcriptional activity of this cluster of cells or technical limitations in our system. **e**, We therefore removed this cluster of cells and focused on the differentially expressed genes between those two main clusters (C1 and C2). **c**–**e**, In total, 282 single cells were included. **f**, The results showed that the differentially expressed genes in the population were basically consistent with that in the internal EPI stages, reflecting that the differences in gene-expression characteristics between the two clusters are mainly due to the diversity in developmental stages (days 6 and 8 compared with days 10 and 12), indicating that EPI subgroups mainly reflected the developmental stage-specific differences. The gene list related to **f** is provided in Supplementary Table 5. **g**, Principal component analysis for TE at different developmental stages. The sublineages of TE emerge around day 10. Day 6 TE, $n = 667$ cells; day 10 TE, $n = 1,443$ cells; days 12 and 14 TE, $n = 792$ cells (day 12) and 533 cells (day 14).

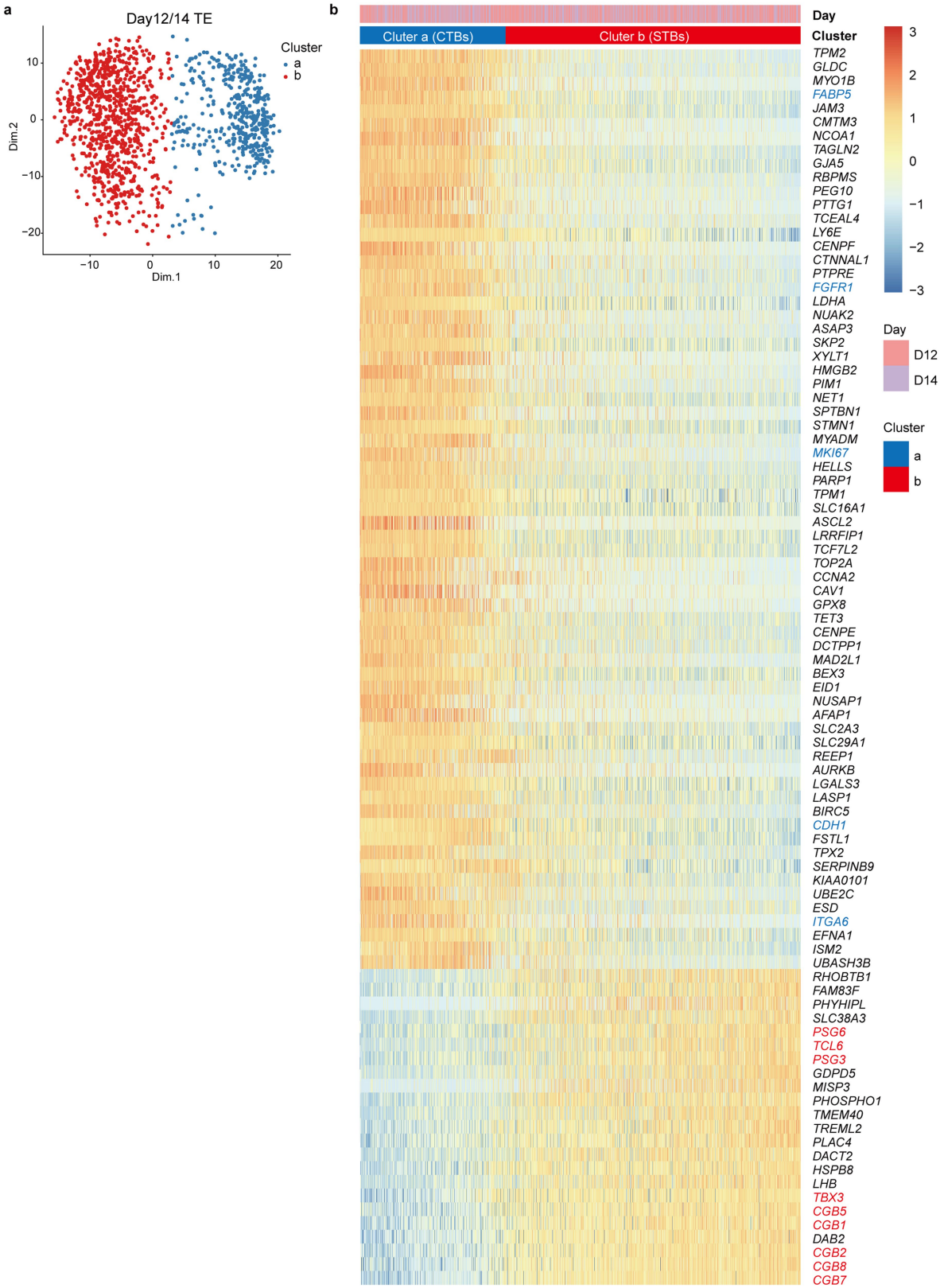

Extended Data Fig. 5 | Differential gene-expression features of the two TE clusters. a, TE cells from day-12 and day-14 embryos were divided into two clusters. In total, 1,325 single cells were included. Day 12, $n = 792$ cells; day 14, $n = 533$ cells. **b**, Differential gene-expression features of the two TE clusters.

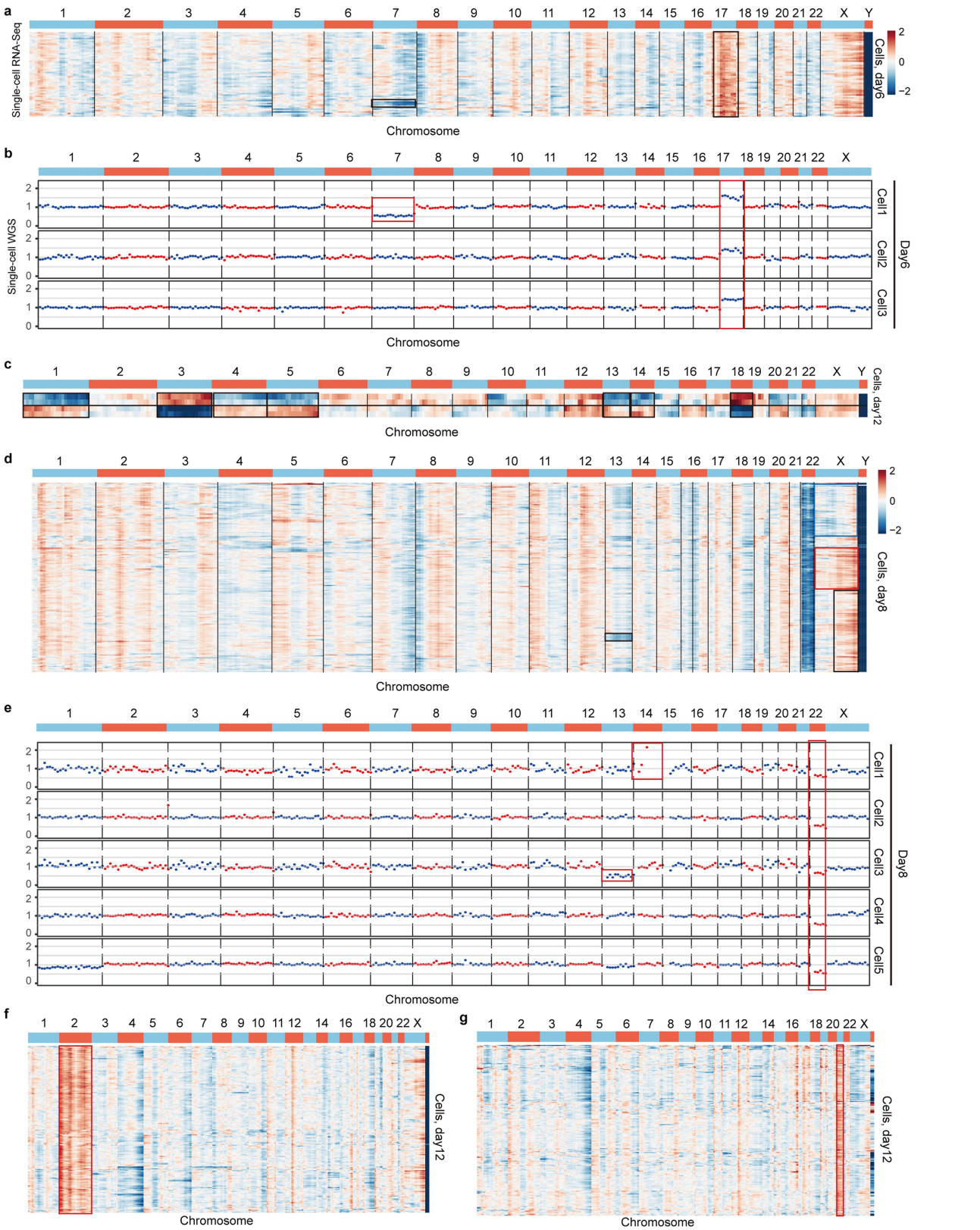

Extended Data Fig. 6 | Representative CNV patterns during implantation. a, Heat map shows large-scale CNVs in individual cells (rows) from a day-6 embryo based on single-cell RNA-sequencing data. The majority of cells from this embryo contained a whole-chromosomal duplication of chromosome 17, and a portion of the cells had a whole-chromosomal deletion of chromosome 7. **b**, CNVs confirmed by single-cell whole-genome sequencing. Related to **a**. **c**, Representative CNV-chimeric embryo. **d**, Heat map showing large-scale CNVs in individual cells (rows) from a day-8 embryo based on single-cell RNA-sequencing data. The majority of cells from this embryo contained a whole-chromosomal deletion of chromosome 22, and a portion of the cells had whole-chromosomal deletion of chromosome 13. Cells also show different chromosome X patterns at the transcriptome level. **e**, CNVs confirmed by single-cell whole-genome sequencing. Related to **d**. **f**, **g**, Heat maps show large-scale CNVs in individual cells (rows) from two day-12 embryos based on single-cell RNA-sequencing data.

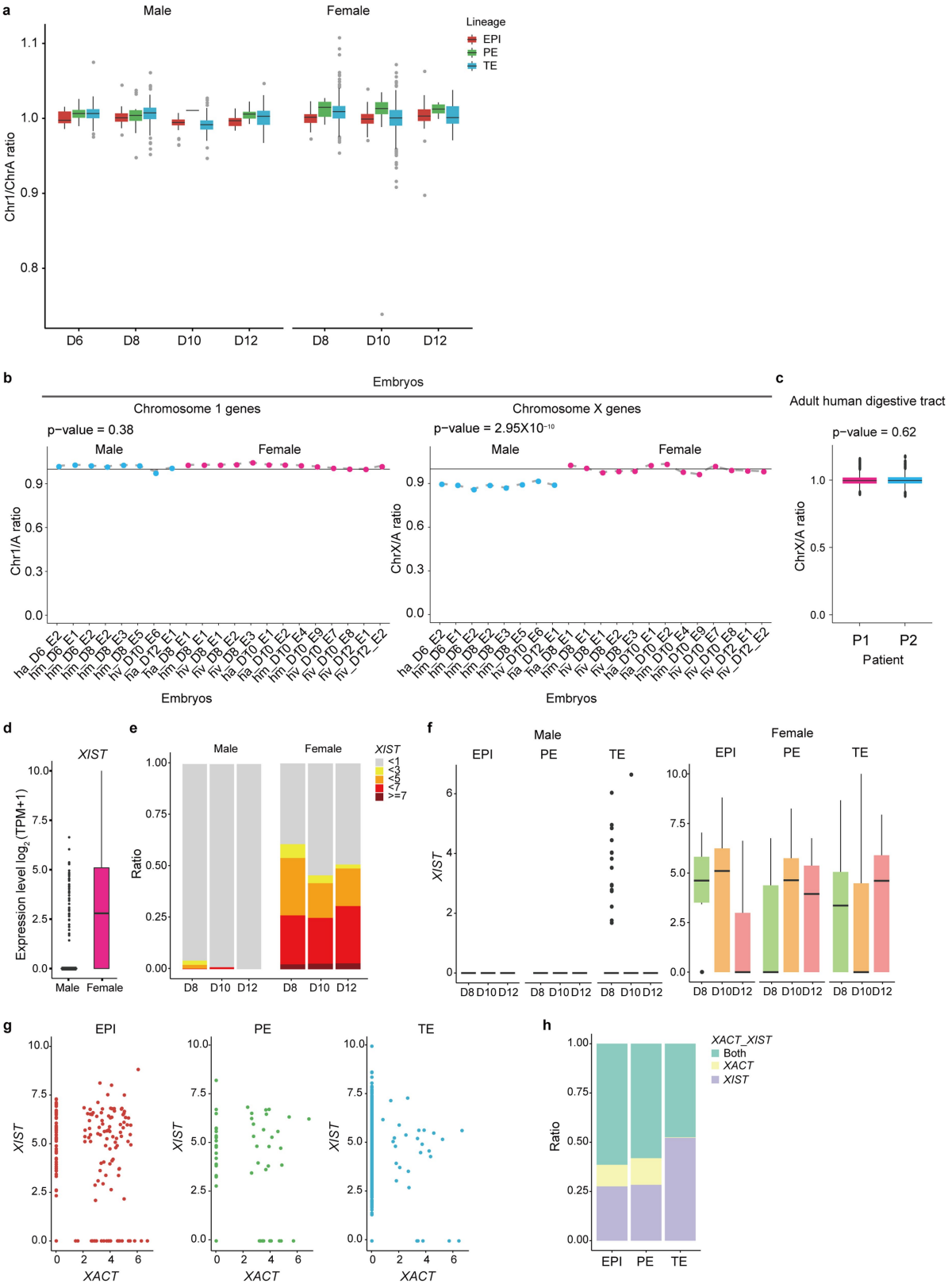

Extended Data Fig. 7 | See next page for caption.

Extended Data Fig. 7 | Dynamics of chromosome X dosage during implantation. Related to Fig. 3. **a**, The *y* axis represents the ratio of total expression levels of genes located on chromosome 1 and the same number of genes located on other autosomes (ChrA). Black lines indicate median values, the boxes range from the 25th to 75th percentiles and the whiskers correspond to 1.5× the IQR. In total, 3,184 single cells were included. Day 6, $n = 387$ (male); day 8, $n = 1,525$ (female, $n = 1,147$; male, $n = 378$); day 10, $n = 1,021$ (female, $n = 917$; male, $n = 104$); day 12, $n = 251$ (female, $n = 104$; male, $n = 147$) (Supplementary Table 1). **b**, The expression ratios of genes located on chromosome 1 or chromosome X to other autosomes in the different embryos that we sequenced. In total, 3,184 single cells were included: female, $n = 2,168$ single cells from 13 embryos; male, $n = 1,016$ single cells from 8 embryos. The statistical test was a two-sided *t*-test. **c**, The ratio of chromosome X to other autosomes in adult human digestive tract was used as a control. P, patient. P1, $n = 763$ cells; P2, $n = 700$ cells. The statistical test was a two-sided *t*-test. **d**, *XIST* expression in cells with different sexes. In total, 3,184 single cells were included; female, $n = 2,168$; male, $n = 1,016$. **e**, The distribution of *XIST* expression levels across different developmental stages for male and female embryos. In total, 3,184 single cells were included: day 6, $n = 387$ (male); day 8, $n = 1,525$ (female, $n = 1,147$; male, $n = 378$); day 10, $n = 1,021$ (female, $n = 917$; male, $n = 104$); day 12, $n = 251$ (female, $n = 104$; male, $n = 147$). **f**, *XIST* expression in different lineages for male and female embryos. In total, 3,184 single cells were included: female, $n = 2,168$; male, $n = 1,016$ (see details in Supplementary Table 1). **g**, The expression levels of *XIST* and *XACT* for different lineages. EPI, $n = 282$ cells; PE, $n = 138$ cells; TE, $n = 2,725$ cells. **h**, The distribution of *XIST* and *XACT* expression levels for different lineages. Both, cells that expressed *XIST* and *XACT*; *XIST*, cells that expressed only *XIST*; *XACT*, cells that expressed only *XACT*. EPI, $n = 282$ cells; PE, $n = 138$ cells; TE, $n = 2,725$ cells.

a

No. of single cells for scTrio-Seq									
		scRNA-seq				scBS-seq			
Day	Embryos	EPI	PE	TE	Total	EPI	PE	TE	Total
Day 6	7	41	38	681	760 / 976	22	15	26	65 / 126
Day 8	5	28	53	911	992 / 1,248	5	14	10	29 / 119
Day 10	3	10	40	546	596 / 784	4	14	10	30 / 99
Day 12	2	0	5	191	196 / 394	0	2	8	11 / 27
Total	17	79	136	2,329	2,544 / 3,392	31	45	54	130 / 371

☆QC filtered cells / All cells

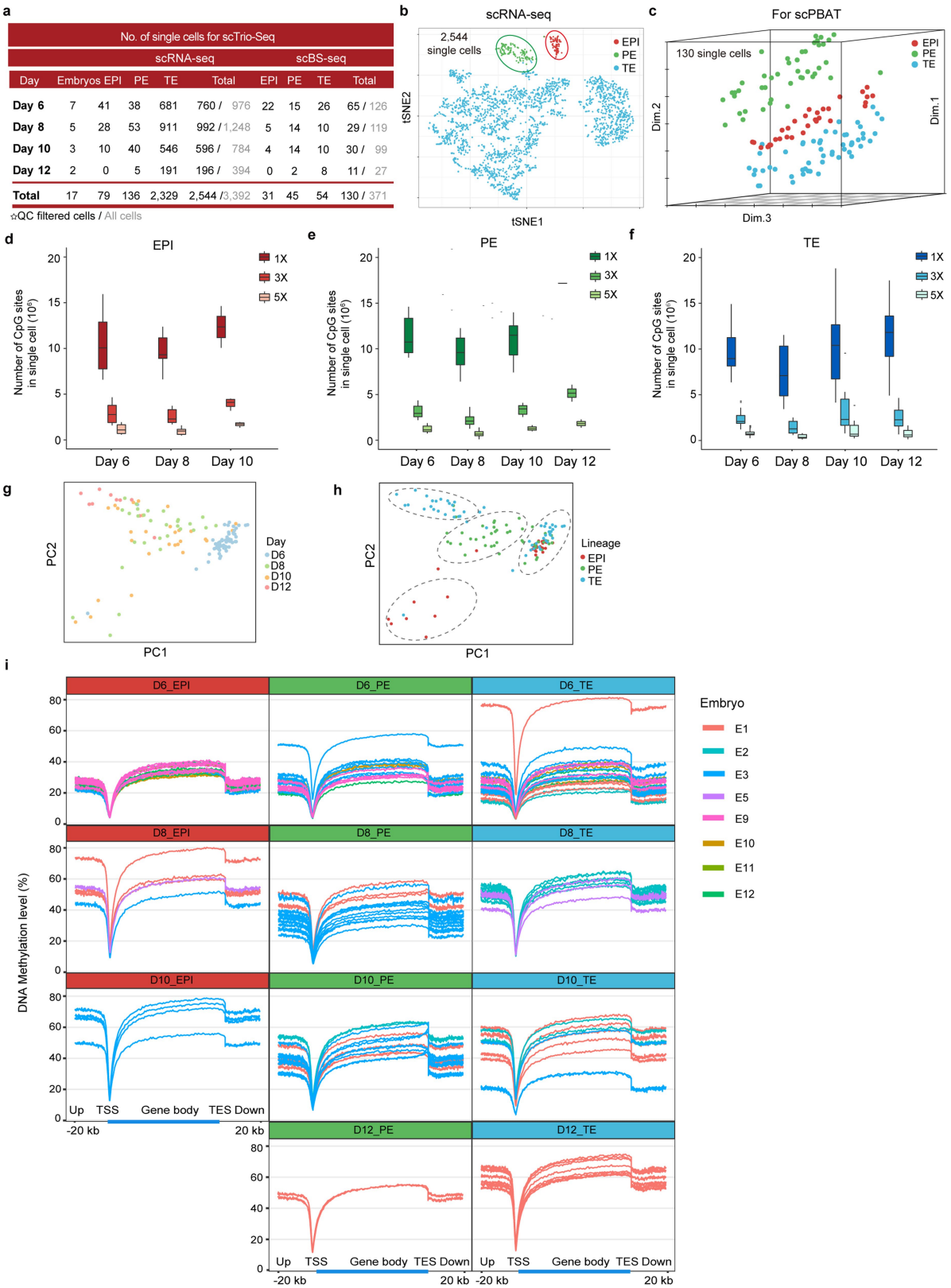

Extended Data Fig. 8 | See next page for caption.

Extended Data Fig. 8 | DNA methylation patterns during implantation. **a**, Total number of embryos and cells collected at each stage (days 6–12) for single-cell Trio-seq analysis. **b**, *t*-SNE plot of cells based on the expression matrix. Each dot represents one cell and colours represent lineage types. For each lineage, we selected several individual cells for bisulfite sequencing. In total, 2,544 cells were included: EPI, $n = 79$ cells; PE, $n = 136$ cells; TE, $n = 2{,}329$ cells. **c**, Principal component analysis of cells based on the expression matrix. Only cells that were also used for bisulfite sequencing were used for the analysis. In total, 130 cells were used: EPI, $n = 31$ cells; PE, $n = 45$ cells; TE, $n = 54$ cells. **d**–**f**, The number of CpG sites detected with at least one-, three- and fivefold coverage across the single-cell samples. In total 2.7 Tb of sequencing data was generated, and on average 10 million CpG sites per cell were covered. Black line, median value. EPI, $n = 31$ cells; PE, $n = 45$ cells; TE, $n = 54$ cells. **g**, **h**, *t*-SNE analysis based on promoter methylation levels of genes. Each dot represents one cell and cells were coloured by culture day and lineage identity. EPI, $n = 31$ cells; PE, $n = 45$ cells; TE, $n = 54$ cells. **i**, Single-cell DNA methylation levels across gene bodies (from transcription start site (TSS) to transcription end site (TES)) and the 20-kb flanking regions of the transcription start and end sites. We found shared distribution patterns: genes were hypomethylated around the transcription start sites, evenly hypermethylated in the gene body regions and significant decrease in methylation after the transcription end sites.

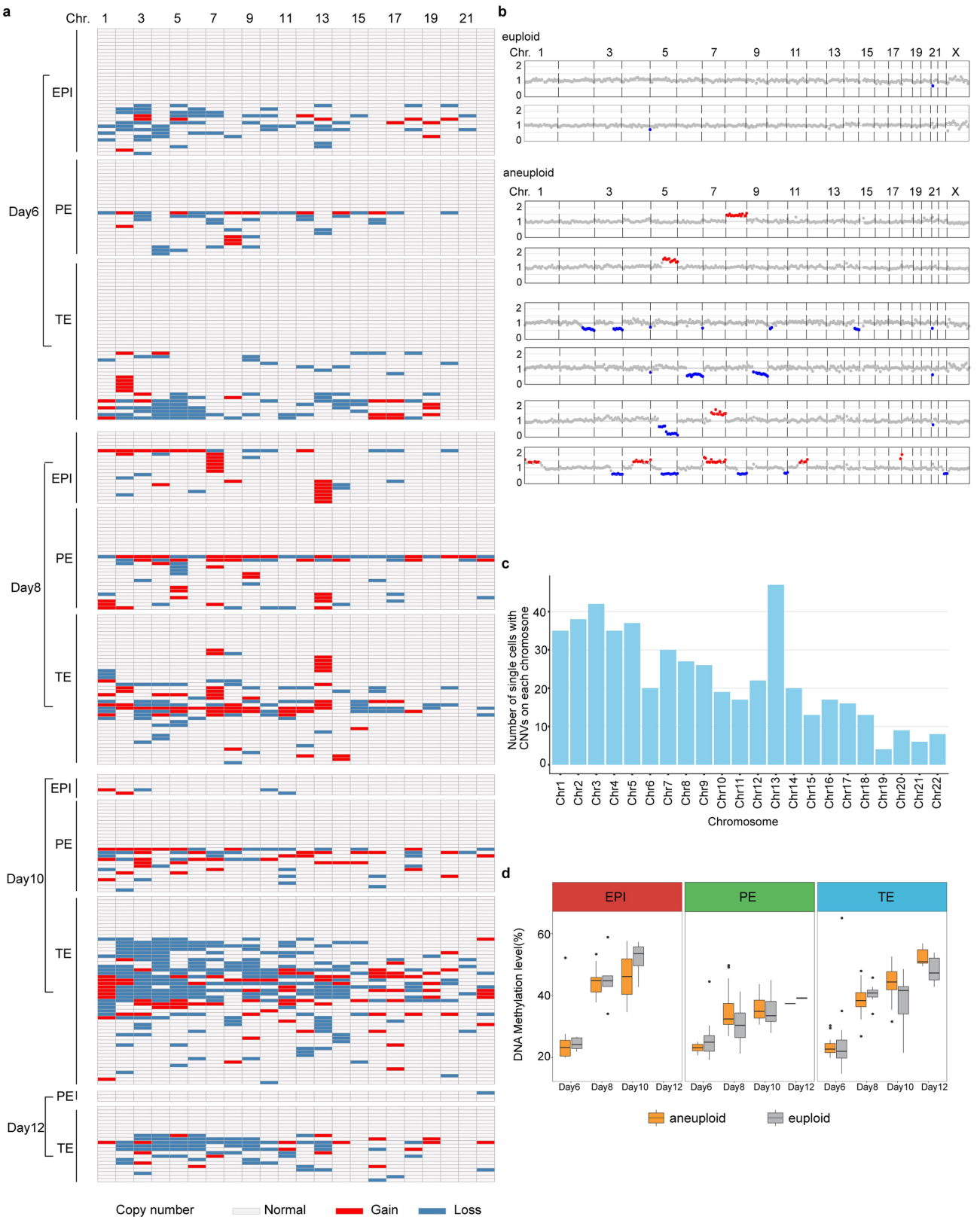

Extended Data Fig. 9 | The CNV landscapes of human early embryos by the DNA methylome dataset. a, The CNVs for each individual cell at different developmental stages. Red represents duplication, blue represents deletion and white represents diploid. **b**, Representative examples of euploid and aneuploid single-cell samples. Abnormal copy numbers are highlighted in red (duplication) or blue (deletion). **c**, The number of cells with CNVs for each chromosome. **d**, The global DNA methylation levels for euploid and aneuploid cells. Black lines indicate median values, the boxes range from the 25th to 75th percentiles and the whiskers correspond to 1.5× the IQR. EPI, $n = 61$ cells (euploid, $n = 31$; aneuploidy, $n = 30$); PE, $n = 84$ cells (euploid, $n = 45$; aneuploidy, $n = 39$); TE, $n = 141$ cells (euploid, $n = 54$; aneuploidy, $n = 87$) (see details in Supplementary Table 1).

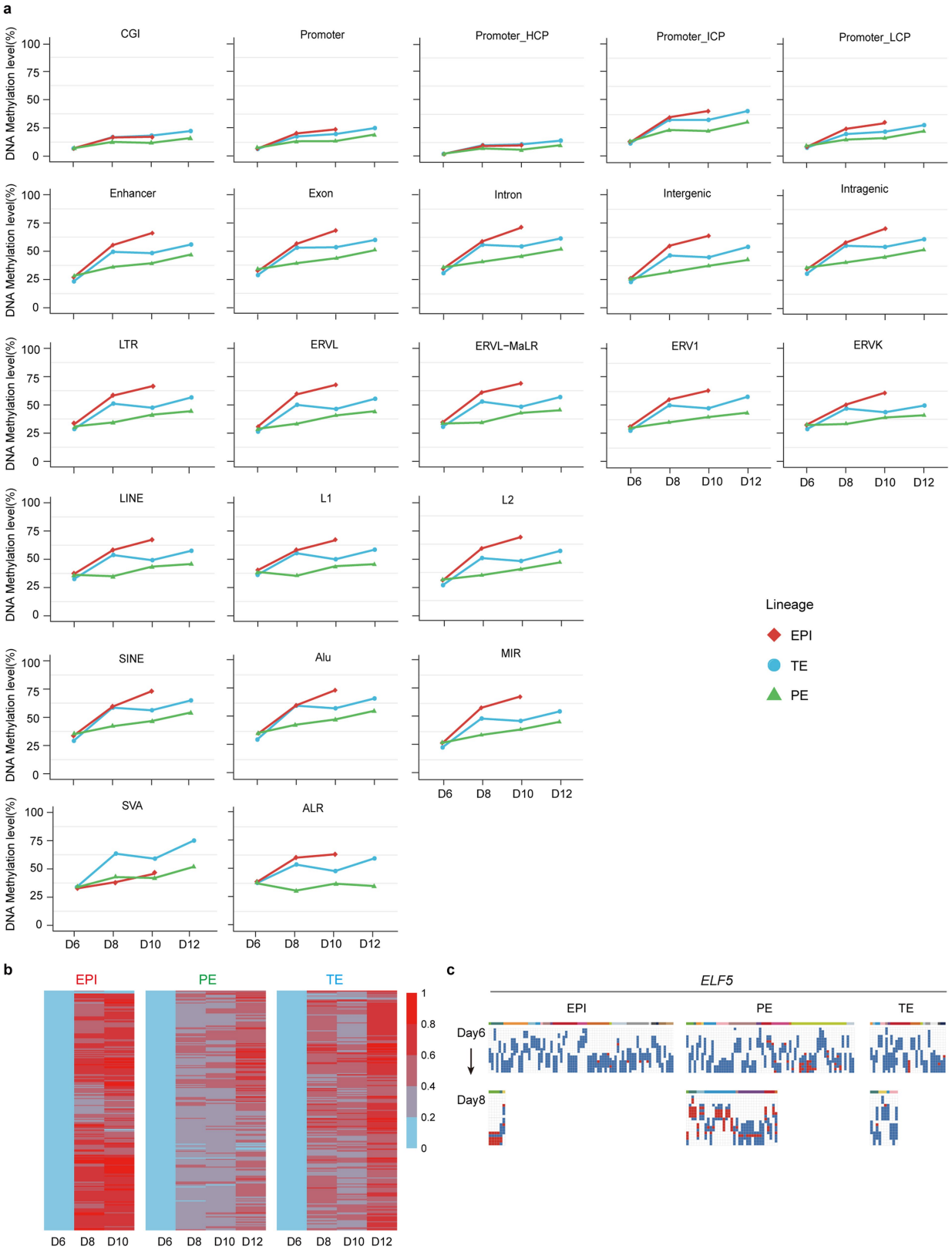

Extended Data Fig. 10 | The re-methylation levels of different genomic elements vary between the three lineages at the different developmental stages. a, Global methylation levels on different genomic elements for different cell lineages. EPI, $n = 31$ cells; PE, $n = 45$ cells; TE, $n = 54$ cells. **b**, The average DNA methylation levels of promoter regions (250 bp upstream to 250 bp downstream of the transcription start site) for each lineage at different developmental stages. Only promoters for which methylation levels were less than 0.1 at day 6 and more than 0.35 at days 10, 12 and 14 are shown in the heat map. Colours from blue to red represent methylation levels from low to high. EPI, $n = 31$ cells, PE, $n = 45$ cells; TE, $n = 54$ cells. **c**, DNA methylation levels of represent loci for lineage-specific genes at promoter regions. Each column represents one read. Red represents a methylated CpG site, blue represents an unmethylated CpG site and white represents an undetected site. Only reads that covered at least five CpG sites are shown in the heat map.

nature research

Corresponding author(s): Jie Qiao, Fuchou Tang

Last updated by author(s): Fan Zhou

Reporting Summary

Nature Research wishes to improve the reproducibility of the work that we publish. This form provides structure for consistency and transparency in reporting. For further information on Nature Research policies, see Authors & Referees and the Editorial Policy Checklist.

Statistics

For all statistical analyses, confirm that the following items are present in the figure legend, table legend, main text, or Methods section.

n/a	Confirmed
☐	☒ The exact sample size (*n*) for each experimental group/condition, given as a discrete number and unit of measurement
☐	☒ A statement on whether measurements were taken from distinct samples or whether the same sample was measured repeatedly
☐	☒ The statistical test(s) used AND whether they are one- or two-sided *Only common tests should be described solely by name; describe more complex techniques in the Methods section.*
☐	☒ A description of all covariates tested
☐	☒ A description of any assumptions or corrections, such as tests of normality and adjustment for multiple comparisons
☐	☒ A full description of the statistical parameters including central tendency (e.g. means) or other basic estimates (e.g. regression coefficient) AND variation (e.g. standard deviation) or associated estimates of uncertainty (e.g. confidence intervals)
☐	☒ For null hypothesis testing, the test statistic (e.g. *F*, *t*, *r*) with confidence intervals, effect sizes, degrees of freedom and *P* value noted *Give P values as exact values whenever suitable.*
☒	☐ For Bayesian analysis, information on the choice of priors and Markov chain Monte Carlo settings
☐	☒ For hierarchical and complex designs, identification of the appropriate level for tests and full reporting of outcomes
☐	☒ Estimates of effect sizes (e.g. Cohen's *d*, Pearson's *r*), indicating how they were calculated

Our web collection on statistics for biologists contains articles on many of the points above.

Software and code

Policy information about availability of computer code

Data collection	No special or proprietary software was used.
Data analysis	We used available pipelines and software to analyze single-cell RNA-Seq data and single-cell PBAT data. R Packages Version: R-3.5.1 scater_1.8.4 Seurat_2.3.4 ggplot2_3.1.0 FactoMineR_1.41 Rtsne_0.15 monocle_2.8.0 libpheatmap_1.0.10 reshape2_1.4.3 DDRTree_0.1.5 tsne_0.1-3 SingleCellExperiment_1.2.0 S4Vectors_0.20.1 IRanges_2.16.0 SummarizedExperiment_1.10.1 scales_1.0.0 beeswarm_0.2.3 ggbeeswarm_0.6.0 tsne_0.1-3 igraph_1.2.2 HSMMSingleCell_0.114.0 RColorBrewer_1.1-2 fastICA_1.2-1 gplots_3.0.1 SCENIC_1.0.0-03 ggtern_3.1.0 fpc_2.1-11.1 pheatmap_1.0.10 Other Packages: tophat-2.0.14.Linux_x86_64 samtools-1.2(RNA) & samtools-0.1.18(WGS & PBAT) python2.7 HTSeq-0.6.1 cufflinks-2.2.1 picard-tools-1.130 GenomeAnalysisTK.jar(3.4-46-gbc02625) snpEff_v4.3 TrimGalore-0.5.0 bwa-0.7.12 jdk1.8.0_151 bismark_v0.7.6 bowtie-1.0.0 methpipe-3.4.3 cgmaptools-0.1.1 pyscenic-0.8.9 See details in Supplementary information_Methods.

For manuscripts utilizing custom algorithms or software that are central to the research but not yet described in published literature, software must be made available to editors/reviewers. We strongly encourage code deposition in a community repository (e.g. GitHub). See the Nature Research guidelines for submitting code & software for further information.

Data

Policy information about availability of data

All manuscripts must include a data availability statement. This statement should provide the following information, where applicable:

- Accession codes, unique identifiers, or web links for publicly available datasets
- A list of figures that have associated raw data
- A description of any restrictions on data availability

Scripts of the main steps of the analysis are provided at GitHub website (https://github.com/WRui/Post_Implantation). Other R scripts associated with graphic presentation are available from the authors on reasonable request.

Field-specific reporting

Please select the one below that is the best fit for your research. If you are not sure, read the appropriate sections before making your selection.

☒ Life sciences ☐ Behavioural & social sciences ☐ Ecological, evolutionary & environmental sciences

For a reference copy of the document with all sections, see nature.com/documents/nr-reporting-summary-flat.pdf

Life sciences study design

All studies must disclose on these points even when the disclosure is negative.

Sample size	The sample size was determined when the main cell lineages at each developmental stages were captured. Related statistical analysis provides the rationale for sufficiency of the sample sizes.
Data exclusions	For sequencing data, we excluded low-quality cells according to the criteria in Supplementary information_Methods.
Replication	All attempts at replication were successful.
Randomization	Not applicable since all single cells were allocated into different groups according to their development stages.
Blinding	Not applicable since no specific grouping.

Behavioural & social sciences study design

All studies must disclose on these points even when the disclosure is negative.

Study description	*Briefly describe the study type including whether data are quantitative, qualitative, or mixed-methods (e.g. qualitative cross-sectional, quantitative experimental, mixed-methods case study).*
Research sample	*State the research sample (e.g. Harvard university undergraduates, villagers in rural India) and provide relevant demographic information (e.g. age, sex) and indicate whether the sample is representative. Provide a rationale for the study sample chosen. For studies involving existing datasets, please describe the dataset and source.*
Sampling strategy	*Describe the sampling procedure (e.g. random, snowball, stratified, convenience). Describe the statistical methods that were used to predetermine sample size OR if no sample-size calculation was performed, describe how sample sizes were chosen and provide a rationale for why these sample sizes are sufficient. For qualitative data, please indicate whether data saturation was considered, and what criteria were used to decide that no further sampling was needed.*
Data collection	*Provide details about the data collection procedure, including the instruments or devices used to record the data (e.g. pen and paper, computer, eye tracker, video or audio equipment) whether anyone was present besides the participant(s) and the researcher, and whether the researcher was blind to experimental condition and/or the study hypothesis during data collection.*
Timing	*Indicate the start and stop dates of data collection. If there is a gap between collection periods, state the dates for each sample cohort.*
Data exclusions	*If no data were excluded from the analyses, state so OR if data were excluded, provide the exact number of exclusions and the rationale behind them, indicating whether exclusion criteria were pre-established.*
Non-participation	*State how many participants dropped out/declined participation and the reason(s) given OR provide response rate OR state that no participants dropped out/declined participation.*
Randomization	*If participants were not allocated into experimental groups, state so OR describe how participants were allocated to groups, and if allocation was not random, describe how covariates were controlled.*

Ecological, evolutionary & environmental sciences study design

All studies must disclose on these points even when the disclosure is negative.

Study description	*Briefly describe the study. For quantitative data include treatment factors and interactions, design structure (e.g. factorial, nested, hierarchical), nature and number of experimental units and replicates.*
Research sample	*Describe the research sample (e.g. a group of tagged Passer domesticus, all Stenocereus thurberi within Organ Pipe Cactus National Monument), and provide a rationale for the sample choice. When relevant, describe the organism taxa, source, sex, age range and any manipulations. State what population the sample is meant to represent when applicable. For studies involving existing datasets, describe the data and its source.*
Sampling strategy	*Note the sampling procedure. Describe the statistical methods that were used to predetermine sample size OR if no sample-size calculation was performed, describe how sample sizes were chosen and provide a rationale for why these sample sizes are sufficient.*
Data collection	*Describe the data collection procedure, including who recorded the data and how.*
Timing and spatial scale	*Indicate the start and stop dates of data collection, noting the frequency and periodicity of sampling and providing a rationale for these choices. If there is a gap between collection periods, state the dates for each sample cohort. Specify the spatial scale from which the data are taken*
Data exclusions	*If no data were excluded from the analyses, state so OR if data were excluded, describe the exclusions and the rationale behind them, indicating whether exclusion criteria were pre-established.*
Reproducibility	*Describe the measures taken to verify the reproducibility of experimental findings. For each experiment, note whether any attempts to repeat the experiment failed OR state that all attempts to repeat the experiment were successful.*
Randomization	*Describe how samples/organisms/participants were allocated into groups. If allocation was not random, describe how covariates were controlled. If this is not relevant to your study, explain why.*
Blinding	*Describe the extent of blinding used during data acquisition and analysis. If blinding was not possible, describe why OR explain why blinding was not relevant to your study.*

Did the study involve field work? ☐ Yes ☐ No

Field work, collection and transport

Field conditions	*Describe the study conditions for field work, providing relevant parameters (e.g. temperature, rainfall).*
Location	*State the location of the sampling or experiment, providing relevant parameters (e.g. latitude and longitude, elevation, water depth).*
Access and import/export	*Describe the efforts you have made to access habitats and to collect and import/export your samples in a responsible manner and in compliance with local, national and international laws, noting any permits that were obtained (give the name of the issuing authority, the date of issue, and any identifying information).*
Disturbance	*Describe any disturbance caused by the study and how it was minimized.*

Reporting for specific materials, systems and methods

We require information from authors about some types of materials, experimental systems and methods used in many studies. Here, indicate whether each material, system or method listed is relevant to your study. If you are not sure if a list item applies to your research, read the appropriate section before selecting a response.

Materials & experimental systems

n/a	Involved in the study
☐	☒ Antibodies
☒	☐ Eukaryotic cell lines
☒	☐ Palaeontology
☒	☐ Animals and other organisms
☐	☒ Human research participants
☒	☐ Clinical data

Methods

n/a	Involved in the study
☒	☐ ChIP-seq
☒	☐ Flow cytometry
☒	☐ MRI-based neuroimaging

Antibodies

Antibodies used	Oct3/4 antibody (A1515, Santa Cruz Biotechnology, sc-5279, 1/200); OTX2 antibody (KNO0314101, AF199, 1/200) F-actin/AlexaFluor 488 phalloid (JLM0211061, Thermo Fisher Scientific, A12379); GATA6 antibody (JLM0211061, R&D Systems, mab1700). donkey anti-mouse AlexaFluor®568 (Thermo Fisher Scientific, A10037); donkey anti-rabbit AlexaFluor®647 (Thermo Fisher Scientific, A31573).
Validation	All the antibodies used in this study were commercial antibodies and were only used for applications, with validation procedures described on the following sites of the manufacturers: https://www.thermofisher.com; https://www.rndsystems.com; https://www.scbt.com/scbt/home

Eukaryotic cell lines

Policy information about cell lines

Cell line source(s)	*State the source of each cell line used.*
Authentication	*Describe the authentication procedures for each cell line used OR declare that none of the cell lines used were authenticated.*
Mycoplasma contamination	*Confirm that all cell lines tested negative for mycoplasma contamination OR describe the results of the testing for mycoplasma contamination OR declare that the cell lines were not tested for mycoplasma contamination.*
Commonly misidentified lines (See ICLAC register)	*Name any commonly misidentified cell lines used in the study and provide a rationale for their use.*

Palaeontology

Specimen provenance	*Provide provenance information for specimens and describe permits that were obtained for the work (including the name of the issuing authority, the date of issue, and any identifying information).*
Specimen deposition	*Indicate where the specimens have been deposited to permit free access by other researchers.*
Dating methods	*If new dates are provided, describe how they were obtained (e.g. collection, storage, sample pretreatment and measurement), where they were obtained (i.e. lab name), the calibration program and the protocol for quality assurance OR state that no new dates are provided.*

☐ Tick this box to confirm that the raw and calibrated dates are available in the paper or in Supplementary Information.

Animals and other organisms

Policy information about studies involving animals; ARRIVE guidelines recommended for reporting animal research

Laboratory animals	*For laboratory animals, report species, strain, sex and age OR state that the study did not involve laboratory animals.*
Wild animals	*Provide details on animals observed in or captured in the field; report species, sex and age where possible. Describe how animals were caught and transported and what happened to captive animals after the study (if killed, explain why and describe method; if released, say where and when) OR state that the study did not involve wild animals.*
Field-collected samples	*For laboratory work with field-collected samples, describe all relevant parameters such as housing, maintenance, temperature, photoperiod and end-of-experiment protocol OR state that the study did not involve samples collected from the field.*
Ethics oversight	*Identify the organization(s) that approved or provided guidance on the study protocol, OR state that no ethical approval or guidance was required and explain why not.*

Note that full information on the approval of the study protocol must also be provided in the manuscript.

Human research participants

Policy information about studies involving human research participants

Population characteristics	The average age of oocyte donors is 32 and the sperm donor is 41 years old. The oocyte donors involved in this study are fertile with at least one healthy baby. The oocyte donors with normal BMI are in good health. The healthy sperm donor with demonstrated fertility has normal semen parameters.
Recruitment	Research donors were recruited from Peking University Third Hospital. Before giving consent, donors have a suitable opportunity to receive proper counselling about the implications of the donation and potential risks. Gametes and embryos were collected with written informed consent from the donors in this study.

Ethics oversight	The Reproductive Medicine Ethics Committee of Peking University Third Hospital

Note that full information on the approval of the study protocol must also be provided in the manuscript.

Clinical data

Policy information about clinical studies

All manuscripts should comply with the ICMJE guidelines for publication of clinical research and a completed CONSORT checklist must be included with all submissions.

Clinical trial registration	*Provide the trial registration number from ClinicalTrials.gov or an equivalent agency.*
Study protocol	*Note where the full trial protocol can be accessed OR if not available, explain why.*
Data collection	*Describe the settings and locales of data collection, noting the time periods of recruitment and data collection.*
Outcomes	*Describe how you pre-defined primary and secondary outcome measures and how you assessed these measures.*

ChIP-seq

Data deposition

☐ Confirm that both raw and final processed data have been deposited in a public database such as GEO.

☐ Confirm that you have deposited or provided access to graph files (e.g. BED files) for the called peaks.

Data access links *May remain private before publication.*	*For "Initial submission" or "Revised version" documents, provide reviewer access links. For your "Final submission" document, provide a link to the deposited data.*
Files in database submission	*Provide a list of all files available in the database submission.*
Genome browser session (e.g. UCSC)	*Provide a link to an anonymized genome browser session for "Initial submission" and "Revised version" documents only, to enable peer review. Write "no longer applicable" for "Final submission" documents.*

Methodology

Replicates	*Describe the experimental replicates, specifying number, type and replicate agreement.*
Sequencing depth	*Describe the sequencing depth for each experiment, providing the total number of reads, uniquely mapped reads, length of reads and whether they were paired- or single-end.*
Antibodies	*Describe the antibodies used for the ChIP-seq experiments; as applicable, provide supplier name, catalog number, clone name, and lot number.*
Peak calling parameters	*Specify the command line program and parameters used for read mapping and peak calling, including the ChIP, control and index files used.*
Data quality	*Describe the methods used to ensure data quality in full detail, including how many peaks are at FDR 5% and above 5-fold enrichment.*
Software	*Describe the software used to collect and analyze the ChIP-seq data. For custom code that has been deposited into a community repository, provide accession details.*

Flow Cytometry

Plots

Confirm that:

☐ The axis labels state the marker and fluorochrome used (e.g. CD4-FITC).

☐ The axis scales are clearly visible. Include numbers along axes only for bottom left plot of group (a 'group' is an analysis of identical markers).

☐ All plots are contour plots with outliers or pseudocolor plots.

☐ A numerical value for number of cells or percentage (with statistics) is provided.

Methodology

Sample preparation	*Describe the sample preparation, detailing the biological source of the cells and any tissue processing steps used.*
Instrument	*Identify the instrument used for data collection, specifying make and model number.*

Software

Describe the software used to collect and analyze the flow cytometry data. For custom code that has been deposited into a community repository, provide accession details.

Cell population abundance

Describe the abundance of the relevant cell populations within post-sort fractions, providing details on the purity of the samples and how it was determined.

Gating strategy

Describe the gating strategy used for all relevant experiments, specifying the preliminary FSC/SSC gates of the starting cell population, indicating where boundaries between "positive" and "negative" staining cell populations are defined.

☐ Tick this box to confirm that a figure exemplifying the gating strategy is provided in the Supplementary Information.

Magnetic resonance imaging

Experimental design

Design type

Indicate task or resting state; event-related or block design.

Design specifications

Specify the number of blocks, trials or experimental units per session and/or subject, and specify the length of each trial or block (if trials are blocked) and interval between trials.

Behavioral performance measures

State number and/or type of variables recorded (e.g. correct button press, response time) and what statistics were used to establish that the subjects were performing the task as expected (e.g. mean, range, and/or standard deviation across subjects).

Acquisition

Imaging type(s)

Specify: functional, structural, diffusion, perfusion.

Field strength

Specify in Tesla

Sequence & imaging parameters

Specify the pulse sequence type (gradient echo, spin echo, etc.), imaging type (EPI, spiral, etc.), field of view, matrix size, slice thickness, orientation and TE/TR/flip angle.

Area of acquisition

State whether a whole brain scan was used OR define the area of acquisition, describing how the region was determined.

Diffusion MRI ☐ Used ☐ Not used

Preprocessing

Preprocessing software

Provide detail on software version and revision number and on specific parameters (model/functions, brain extraction, segmentation, smoothing kernel size, etc.).

Normalization

If data were normalized/standardized, describe the approach(es): specify linear or non-linear and define image types used for transformation OR indicate that data were not normalized and explain rationale for lack of normalization.

Normalization template

Describe the template used for normalization/transformation, specifying subject space or group standardized space (e.g. original Talairach, MNI305, ICBM152) OR indicate that the data were not normalized.

Noise and artifact removal

Describe your procedure(s) for artifact and structured noise removal, specifying motion parameters, tissue signals and physiological signals (heart rate, respiration).

Volume censoring

Define your software and/or method and criteria for volume censoring, and state the extent of such censoring.

Statistical modeling & inference

Model type and settings

Specify type (mass univariate, multivariate, RSA, predictive, etc.) and describe essential details of the model at the first and second levels (e.g. fixed, random or mixed effects; drift or auto-correlation).

Effect(s) tested

Define precise effect in terms of the task or stimulus conditions instead of psychological concepts and indicate whether ANOVA or factorial designs were used.

Specify type of analysis: ☐ Whole brain ☐ ROI-based ☐ Both

Statistic type for inference
(See Eklund et al. 2016)

Specify voxel-wise or cluster-wise and report all relevant parameters for cluster-wise methods.

Correction

Describe the type of correction and how it is obtained for multiple comparisons (e.g. FWE, FDR, permutation or Monte Carlo).

Models & analysis

n/a	Involved in the study
☐	☐ Functional and/or effective connectivity
☐	☐ Graph analysis
☐	☐ Multivariate modeling or predictive analysis

Functional and/or effective connectivity

Report the measures of dependence used and the model details (e.g. Pearson correlation, partial correlation, mutual information).

Graph analysis

Report the dependent variable and connectivity measure, specifying weighted graph or binarized graph, subject- or group-level, and the global and/or node summaries used (e.g. clustering coefficient, efficiency, etc.).

Multivariate modeling and predictive analysis

Specify independent variables, features extraction and dimension reduction, model, training and evaluation metrics.

LETTER

https://doi.org/10.1038/s41586-019-1501-z

Microbiota-derived lantibiotic restores resistance against vancomycin-resistant *Enterococcus*

Sohn G. Kim[1,2], Simone Becattini[1], Thomas U. Moody[1,3], Pavel V. Shliaha[4], Eric R. Littmann[3], Ruth Seok[1], Mergim Gjonbalaj[1], Vincent Eaton[1], Emily Fontana[3], Luigi Amoretti[3], Roberta Wright[3], Silvia Caballero[1,2], Zhong-Min X. Wang[1], Hea-Jin Jung[1], Sejal M. Morjaria[5], Ingrid M. Leiner[1,3], Weige Qin[6], Ruben J. J. F. Ramos[6], Justin R. Cross[6], Seiko Narushima[7], Kenya Honda[7,8,9], Jonathan U. Peled[2,10], Ronald C. Hendrickson[4,11], Ying Taur[5], Marcel R. M. van den Brink[1,2,10] & Eric G. Pamer[1,2,3,5]*

Intestinal commensal bacteria can inhibit dense colonization of the gut by vancomycin-resistant *Enterococcus faecium* (VRE), a leading cause of hospital-acquired infections[1,2]. A four-strained consortium of commensal bacteria that contains *Blautia producta* BP_{SCSK} can reverse antibiotic-induced susceptibility to VRE infection[3]. Here we show that BP_{SCSK} reduces growth of VRE by secreting a lantibiotic that is similar to the nisin-A produced by *Lactococcus lactis*. Although the growth of VRE is inhibited by BP_{SCSK} and *L. lactis* in vitro, only BP_{SCSK} colonizes the colon and reduces VRE density in vivo. In comparison to nisin-A, the BP_{SCSK} lantibiotic has reduced activity against intestinal commensal bacteria. In patients at high risk of VRE infection, high abundance of the lantibiotic gene is associated with reduced density of *E. faecium*. In germ-free mice transplanted with patient-derived faeces, resistance to VRE colonization correlates with abundance of the lantibiotic gene. Lantibiotic-producing commensal strains of the gastrointestinal tract reduce colonization by VRE and represent potential probiotic agents to re-establish resistance to VRE.

Preventing transmission of highly antibiotic-resistant pathogens in healthcare settings remains problematic[4]. A promising approach to reducing antibiotic-resistant infections involves enhancing microbiota-mediated colonization resistance of the host by administering protective commensal bacteria[5]. Although mechanisms of colonization resistance are being discovered, few bacterial strains that mediate resistance have been identified[6]. Faecal microbiota transplantation (FMT), although effective for recurrent *Clostridium difficile* infection[7], remains problematic because faecal compositions can be highly variable. Preclinical studies suggest that commensal bacterial strains that inhabit the lower gastrointestinal tract can be effective at providing resistance[3,8–11].

Enterococci colonize the human gastrointestinal tract and have developed resistance to antibiotics, including vancomycin[1,2]. Antibiotic-mediated depletion of the gut microbiota leads to expansion of VRE in the intestine, predisposing patients to bloodstream infections[6,12,13]. In mice, FMT can re-establish colonization resistance and reduce intestinal VRE density[14,15]. We recently described a four-strain-consortium named $CBBP_{SCSK}$, consisting of *Clostridium bolteae*, *Blautia producta* (BP_{SCSK}; SCSK refers to the *Blautia* strain, which was characterized by S.C. and S.G.K.), *Bacteroides sartorii* and *Parabacteroides distasonis*, that restored colonization resistance against VRE in antibiotic-treated mice[3].

To determine the mechanism of $CBBP_{SCSK}$-mediated VRE inhibition, we co-cultured each strain with VRE (Fig. 1a, Extended Data Fig. 1a–d). BP_{SCSK} inhibited VRE growth, as did BP_{SCSK}-conditioned media (Extended Data Fig. 1e–i), and dilution experiments demonstrated that BP_{SCSK}-mediated inhibition is not due to nutrient depletion. In contrast to BP_{SCSK}-conditioned media, culture supernatants of *B. producta* (Clostridiales VE202-06 ($BP_{control}$)) and other microbiota-derived *Blautia* species did not inhibit VRE growth (Extended Data Fig. 1j, Supplementary Tables 1, 2).

Previous studies demonstrated that BP_{SCSK} requires the other $CBBP_{SCSK}$ members to colonize the intestine[3]. $CBBP_{SCSK}$, but not a modified consortium in which BP_{SCSK} was replaced with $BP_{control}$ ($CBBP_{control}$), reduced VRE colonization (Fig. 1b), even though both consortia colonized mice (Extended Data Fig. 2a, b). $CBBP_{SCSK}$ also reduced VRE colonization in gnotobiotic mice (Extended Data Fig. 2c, d). $CBBP_{SCSK}$ reduced colonization by several VRE strains (Extended Data Fig. 2e–g, Supplementary Table 3) and fluorescence in situ hybridization analysis demonstrated BP_{SCSK} colonization throughout the large intestine (Extended Data Fig. 3).

To determine whether BP_{SCSK} produces an inhibitory factor, VRE was cultured in caecal contents from mice reconstituted with $CBBP_{SCSK}$ or $CBBP_{control}$ (Extended Data Fig. 4a). Only $CBBP_{SCSK}$ caecal contents inhibited VRE growth. Previous studies demonstrated that the commensal microbiota stimulates secretion of a host-derived antimicrobial peptide[16], such as RegIIIγ, which reduces intestinal VRE colonization[17]. CBBP colonization, however, did not induce *Reg3g* transcripts or RegIIIγ protein in the ileum of antibiotic-treated mice (Extended Data Fig. 4b, c). Host-derived antimicrobial peptides and inflammatory genes did not differ between mice treated with $CBBP_{SCSK}$ or PBS (Extended Data Fig. 4d–i). $CBBP_{SCSK}$ was effective at reducing VRE density in $Rag2^{-/-}Il2rg^{-/-}$ mice, indicating that T cells, B cells, natural killer cells and innate lymphoid cells do not contribute to $CBBP_{SCSK}$-mediated VRE inhibition (Extended Data Fig. 4j).

VRE was inhibited by proteins precipitated from BP_{SCSK}- but not $BP_{control}$-conditioned media (Extended Data Fig. 5a), which suggests that BP_{SCSK} secretes an inhibitor. We performed whole-genome sequencing of BP_{SCSK} and $BP_{control}$ and discovered that only BP_{SCSK} contains an operon for a lantibiotic, a lanthionine-containing antimicrobial peptide (Extended Data Fig. 5b–d, Supplementary Tables 4, 5). Lanthionines are formed by enzymatic dehydration of serine or threonine residues that cyclize with neighbouring cysteine residues[18,19]. Nisin-A, a lantibiotic expressed by *L. lactis*[20,21], binds lipid II and inhibits the synthesis of peptidoglycan and also forms a membrane pore complex[22]. Comparison of the lantibiotic operons from BP_{SCSK} and *L. lactis* (*lan* and *nis*, respectively) revealed homologous sequences for all genes except dissimilar signal peptidase sequences (Extended Data Fig. 5c, Supplementary Table 5). Although gene organization and number

[1]Immunology Program, Sloan Kettering Institute, Memorial Sloan Kettering Cancer Center, New York, NY, USA. [2]Weill Cornell Medical College, New York, NY, USA. [3]Lucille Castori Center for Microbes, Inflammation and Cancer, Memorial Sloan Kettering Cancer Center, New York, NY, USA. [4]Microchemistry and Proteomics Core Laboratory, Sloan Kettering Institute, Memorial Sloan Kettering Cancer Center, New York, NY, USA. [5]Infectious Diseases Service, Department of Medicine, Memorial Sloan Kettering Cancer Center, New York, NY, USA. [6]Donald B. and Catherine C. Marron Cancer Metabolism Center, Sloan Kettering Institute, Memorial Sloan Kettering Cancer Center, New York, NY, USA. [7]RIKEN Center for Integrative Medical Sciences, Yokohama, Japan. [8]JSR-Keio University Medical and Chemical Innovation Center, Tokyo, Japan. [9]RIKEN Center for Integrative Medical Sciences, Yokohama, Japan. [10]Adult Bone Marrow Transplant Service, Department of Medicine, Memorial Sloan Kettering Cancer Center, New York, NY, USA. [11]Molecular Pharmacology Program, Sloan Kettering Institute, Memorial Sloan Kettering Cancer Center, New York, NY, USA. *e-mail: egpamer@uchicago.edu

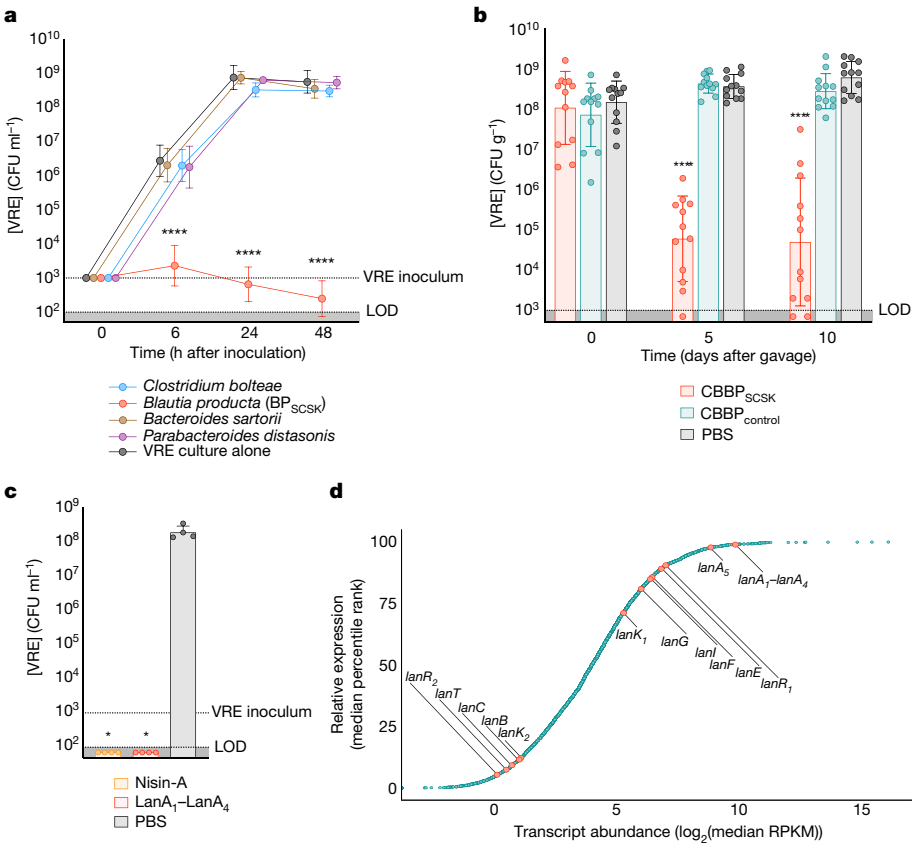

Fig. 1 | BP_{SCSK} expresses a lantibiotic in vivo that inhibits VRE. a, VRE was co-cultured in vitro with each $CBBP_{SCSK}$ isolate ($n = 15$ biologically independent samples from three independent experiments) and growth was monitored. CFU, colony-forming unit; LOD, limit of detection. **b**, Antibiotic-treated, VRE-dominated mice ($n = 12$ mice from three independent experiments) received treatment by oral gavage containing $CBBP_{SCSK}$, $CBBP_{control}$, or PBS. VRE colonization was monitored by CFU quantification in faecal samples. **c**, VRE was inoculated in culture broth with commercial nisin-A (100 μM), purified $LanA_1$–$LanA_4$ lantibiotic from BP_{SCSK} (100 μM), or PBS ($n = 4$ biologically independent samples from two independent experiments). VRE CFUs were enumerated 8 h after inoculation. **d**, RNA sequencing analysis was performed on caecal content from mice treated with CBBP ($n = 3$ mice from one independent experiment). RPKM, reads per kilobase of transcript per million mapped reads. VRE (ATCC 700221) was used in experiments in **a**–**c**. $^*P = 0.0286$, $^{****}P < 0.0001$, two-tailed Mann–Whitney *U*-test for comparisons with negative control (PBS, VRE culture alone). Data are mean ± s.d. (**a**, **c**), median ± range (**b**) and median values (**d**).

within the *lan* and *nis* operons differ, a lantibiotic operon recently characterized[23] in *Blautia obeum* is similar to that of BP_{SCSK}. Notably, BP_{SCSK} encodes five lantibiotic precursor genes ($lanA_1$–$lanA_5$), in contrast to one encoded by the Nis operon (*nisA*). The first four precursor sequences ($lanA_1$–$lanA_4$) are identical, whereas the fifth precursor ($lanA_5$) encodes a similar but non-identical sequence (Supplementary Table 4). $lanA_1$–$lanA_4$ and *nisA* belong to a lantibiotic subset that contains the gallidermin superfamily domain, which conserves two N-terminal lanthionine rings enabling lipid II binding[24] and inhibitory activity[22].

Nisin-A and other lantibiotics of the gallidermin superfamily carry a net positive charge, which enables electrostatic interactions with the cell membrane and lipid II[25]. The inhibitory factor of BP_{SCSK} and nisin-A elute similarly during cation exchange chromatography, which suggests that they both carry a positive charge (Extended Data Fig. 5e). In addition, the inhibitory factor of BP_{SCSK} and nisin-A are resistant to heat and proteases, a characteristic of lantibiotics (Extended Data Fig. 5f). Methods to edit the genome of *Blautia producta* are lacking, so we pursued a gain-of-function approach and heterologously expressed $lanA_1$–$lanA_4$ in *Escherichia coli* (Extended Data Fig. 6a, b, Supplementary Table 6), purified the lantibiotic to homogeneity, and validated it by mass spectrometry (Extended Data Fig. 6c). VRE was similarly inhibited by the addition of the purified BP_{SCSK} LanA or commercial nisin-A (Fig. 1c).

RNA sequencing of caecal contents from antibiotic-treated mice colonized with $CBBP_{SCSK}$ (Fig. 1d) demonstrated that, relative to the overall transcriptome of BP_{SCSK}, precursor lantibiotic transcripts and associated immunity genes were abundant (greater than the ninety-fifth percentile), whereas genes involved in post-translational modification of the precursor lantibiotic were expressed to a lesser degree. Oral administrations of proteins precipitated from BP_{SCSK} but not $BP_{control}$ cultures reduced VRE colonization in antibiotic-treated mice challenged with VRE (Extended Data Fig. 7), albeit to a lesser degree than $CBBP_{SCSK}$ administration. This probably reflects reduced concentrations of lantibiotic owing to intestinal absorption, metabolism and intermittent administration. These findings demonstrate that BP_{SCSK} encodes a lantibiotic that is highly expressed and inhibits VRE in vivo.

L. lactis is a lantibiotic-producing probiotic that, theoretically, could be used to reduce VRE colonization. VRE is inhibited after co-culture with BP_{SCSK} or *L. lactis* (Fig. 2a) and after exposure to precipitated proteins from either species (Extended Data Fig. 8a). By contrast, in vivo VRE colonization was inhibited by $CBBP_{SCSK}$ but not when BP_{SCSK} was replaced by *L. lactis* (CLBP) (Fig. 2b). Although BP_{SCSK} is prevalent in the microbiota after $CBBP_{SCSK}$ treatment (relative abundance > 25%), *L. lactis* was not detected after CLBP treatment (Fig. 2c). The failure of *L. lactis* to colonize the intestine probably explains its inability to reduce VRE density in vivo; *L. lactis* also does not colonize the porcine intestine or inhibit *Listeria monocytogenes* or *C. difficile* in a human distal-colon model[26].

To characterize the antibacterial spectrum of the BP_{SCSK} lantibiotic, we cultured 152 commensal strains obtained from human faeces (Supplementary Table 7) with protein precipitated from BP_{SCSK} or $BP_{control}$ cultures or broth spiked with nisin-A diluted to the same minimal inhibitory concentration (MIC) against VRE as BP_{SCSK}. The MIC was determined as the highest dilution that inhibited growth

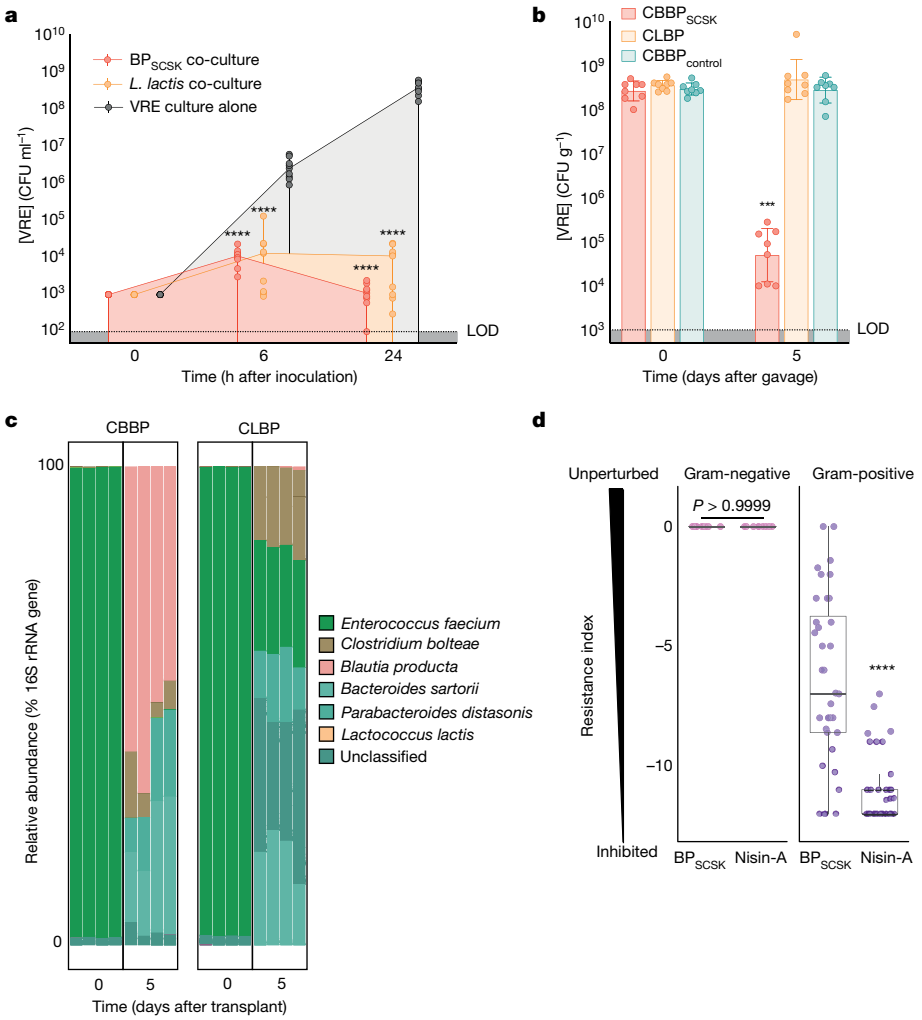

Fig. 2 | BP$_{SCSK}$ colonizes the gastrointestinal tract and broadly inhibits Gram-positive pathogens while preserving some commensal species. **a**, VRE was co-cultured in vitro with *L. lactis* or BP$_{SCSK}$ ($n = 9$ biologically independent samples from three independent experiments) and growth was monitored. **b**, Antibiotic-treated, VRE-dominated mice ($n = 12$ mice from three independent experiments) received an oral gavage that contained CBBP$_{SCSK}$, CLBP, or CBBP$_{control}$. VRE colonization was monitored by CFU quantification in faecal samples. **c**, The microbiota composition determined by metagenomic sequencing of 16S rRNA genes from faecal samples collected from mice treated with CBBP$_{SCSK}$ or CLBP. **d**, Culture broth was conditioned with proteins precipitated from BP$_{SCSK}$, BP$_{control}$ or commercial nisin-A and serially diluted. The MIC was determined for 158 strains from a commensal biobank by calculating the highest dilution factor that inhibited growth ($n = 2$ biologically independent samples from two independent experiments). The resistance index is a ratio between MIC of BP$_{control}$-conditioned media to the MIC of BP$_{SCSK}$ or nisin-A-conditioned media. VRE (ATCC 700221) was used for experiments in **a**–**c**. ***$P < 0.001$, ****$P < 0.0001$, two-tailed Mann–Whitney *U*-test for comparisons with negative control (**a**, **b**) or between experimental conditions (**d**). Data are median values (**a**) or mean ± s.d. (**b**). For the box plots in **d**, centre line denotes the median, box limits represent the upper and lower quartiles, and errors denote 1.5× the interquartile range.

over 24 h. Protein precipitates from BP$_{SCSK}$-conditioned or nisin-A-spiked media, but not BP$_{control}$-conditioned media, inhibited Gram-positive, but not Gram-negative, bacterial strains. A resistance index that compares the MIC values in conditioned media from BP$_{control}$ to that from BP$_{SCSK}$ or nisin-A was used to quantify the sensitivity of bacterial strains to both lantibiotics. The Gram-positive population demonstrated greater sensitivity to nisin-A-spiked media than BP$_{SCSK}$-conditioned media (Fig. 2d). Several VRE strains and other Gram-positive nosocomial pathogens (Extended Data Fig. 8b) demonstrate comparable sensitivity to either conditioned media, but many Gram-positive commensal strains were more resistant to the BP$_{SCSK}$ lantibiotic than nisin-A, including members implicated in resistance to intestinal infections, such as *Bifidobacterium longum* and *Pediococcus acidilactici*[27,28] (Extended Data Fig. 8c). Thus, the BP$_{SCSK}$ lantibiotic, relative to nisin-A, has a narrower spectrum of activity that targets VRE while preserving commensal bacteria.

Among 32 *Blautia* isolates cultured from faecal samples from healthy donors, BP$_{SCSK}$ was the only strain that encoded a lantibiotic and inhibited VRE in vitro (Fig. 3a, Supplementary Tables 1, 2). To determine the prevalence of lantibiotic genes in the human intestinal microbiome, we shotgun-sequenced faecal samples collected from 15 healthy donors and identified lantibiotic genes and homologues that contain the gallidermin superfamily domain (Extended Data Fig. 9a) in 7 of 15 samples, with different sequences within and between samples (Fig. 3b, Extended Data Fig. 9b).

We next mined the genomes of commensal biobank isolates for the gallidermin superfamily domain and identified one additional Clostridiales species, *Ruminococcus faecis*, which encodes a similar lantibiotic and inhibits VRE in vitro, whereas *R. faecis* strains that did not encode a lantibiotic did not inhibit VRE (Fig. 3c, Extended Data Fig. 9c, Supplementary Table 1). Although only a minority of cultured commensal bacteria encodes lantibiotics, it remains unclear whether this reflects their paucity in the microbiota or their relative resistance to in vitro culture.

Patients undergoing allogeneic haematopoietic cell transplantation frequently have intestinal domination by VRE[12,13,29]. From a biobank of longitudinally collected faecal samples, we identified 238 samples from

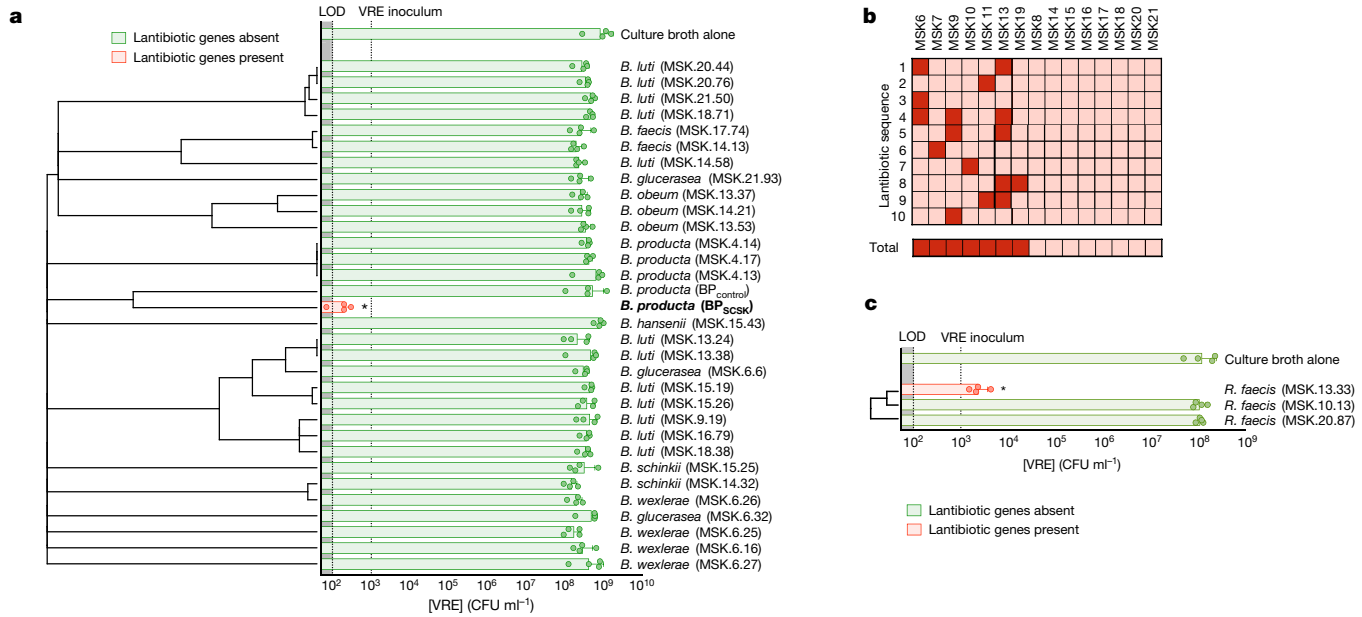

Fig. 3 | Lantibiotic genes are present in human microbiomes of healthy individuals and gut resident, lantibiotic-producing species inhibit VRE. a, Microbiota-derived *Blautia* species were whole-genome sequenced, assembled, annotated and mined for lantibiotic precursor sequences. VRE was inoculated in conditioned media from 39 strains ($n = 4$ biologically independent samples from four independent experiments) and monitored for growth. **b**, Lantibiotic detection from shotgun sequencing of human faecal samples ($n = 15$ faecal samples). **c**, In total 421 commensal biobank isolates were whole-genome sequenced, assembled, annotated and mined for lantibiotic precursor sequences to identify a strain of *R. faecis* that encoded a homologous lantibiotic. VRE was inoculated in conditioned media from three strains of *R. faecis* cultures ($n = 4$ biologically independent samples from four independent experiments) with or without detected lantibiotic genes, and VRE growth was monitored 8 h after inoculation. VRE (ATCC 700221) was used in experiments in **a** and **c**. $^*P = 0.0286$, two-tailed Mann–Whitney *U*-test for comparisons with negative control. Data are mean ± s.d. (**a**, **c**).

22 patients with a range of *E. faecium* densities and found lantibiotic gene abundance inversely correlated with the relative abundance of *E. faecium* (Spearman correlation coefficient $= -0.43$, $P = 2.08 \times 10^{-10}$) (Fig. 4a). Samples with high lantibiotic abundance (Lan^{high} > 85th percentile) consistently had low abundance of *E. faecium* (<10% 16S relative abundance), and were detected in half of patients (Extended Data Fig. 10). In Lan^{high} and Lan^{low} settings, 25% and 21%, respectively, had high microbiota diversity (inverse Simpson index ≥ 8)

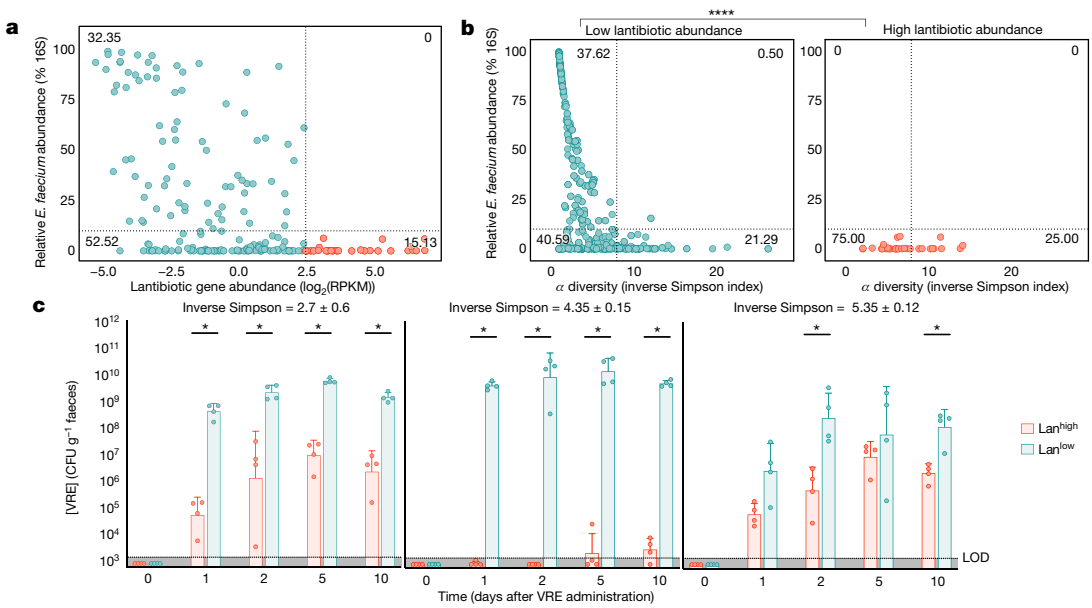

Fig. 4 | Enrichment of lantibiotic genes correlates with reduced *E. faecium* in patient faecal samples. a, **b**, Longitudinally collected faecal samples ($n = 238$ biologically independent samples) from 22 patients undergoing allogeneic haematopoietic cell transplantation were shotgun sequenced. **a**, The relative abundance of *E. faecium* determined by 16S rRNA was plotted against lantibiotic gene abundance (Spearman correlation coefficient $= -0.43$, $P = 2.08 \times 10^{-10}$). **b**, Samples were then stratified by abundance of the lantibiotic, and the relative abundance of *E. faecium* was plotted against microbiota α diversity. The percentage of sample distribution is shown in each quadrant. **c**, Faecal microbiota transplants were performed on germ-free mice using diversity-matched microbiomes containing either high or low lantibiotic gene abundance. One week after FMT administration, mice were orally gavaged with VRE and colonization was monitored by quantifying VRE from faecal samples. VRE (ATCC 700221) was used for experiments in **c**. Low lantibiotic abundance $\leq 2^{2.5}$ < high lantibiotic abundance (RPKM); low *E. faecium* abundance ≤ 10 < high *E. faecium* abundance (% relative 16S); low α diversity ≤ 8 < high α diversity (inverse Simpson index). $^*P < 0.05$, $^{****}P < 0.0001$, two-tailed Mann–Whitney *U*-test.

and low *E. faecium* abundance, which suggests that diversity compensates for low lantibiotic-gene abundance by parallel, lantibiotic-independent inhibitory mechanisms (Fig. 4b). However, nearly half of the Lan^{low} samples with low diversity (inverse Simpson index < 8) had high *E. faecium* abundance ($\geq$10% 16S relative abundance); low diversity decreases the likelihood, but some commensal species still provide lantibiotic-independent colonization resistance against *E. faecium*. By contrast, Lan^{high} samples had low *E. faecium* abundance ($P < 1 \times 10^{-6}$) despite low diversity, consistent with the notion that lantibiotic gene abundance in the microbiome contributes to colonization resistance against *E. faecium*.

To determine whether low-diversity Lan^{high} microbiomes can resist VRE colonization, we identified diversity-matched Lan^{high} and Lan^{low} samples and colonized germ-free mice before VRE challenge (Fig. 4c, Supplementary Table 8). Regardless of diversity, Lan^{high} samples consistently reduced VRE colonization compared with Lan^{low} samples, which suggests that lantibiotics in the gastrointestinal tract provide colonization resistance.

Microbiota-mediated colonization resistance remains incompletely defined and restoring resistance during antibiotic-induced dysbiosis remains an important goal. BP_{SCSK} belongs to a small subset of commensals that secrete lantibiotics, and therefore can influence the community structure of the microbiota. A potential clinical role for lantibiotics is supported by a previous report that uses lantibiotic-producing commensal *Staphylococcus* species on the skin to provide colonization resistance against *Staphylococcus aureus*[30]. Understanding the mechanisms by which the microbiota confers colonization resistance may lead to the development of therapies to repair dysbiosis, thereby reducing susceptible patients' risk of colonization by antibiotic-resistant pathogens.

Online content

Any methods, additional references, Nature Research reporting summaries, source data, extended data, supplementary information, acknowledgements, peer review information; details of author contributions and competing interests; and statements of data and code availability are available at https://doi.org/10.1038/s41586-019-1501-z.

Received: 22 October 2018; Accepted: 22 July 2019;
Published online 21 August 2019.

1. Lebreton, F. et al. Tracing the enterococci from Paleozoic origins to the hospital. *Cell* **169**, 849–861 (2017).
2. Gilmore, M., Clewell, D., Ike, Y. & Shankar, N. *Enterococci: From Commensals to Leading Causes of Drug Resistant Infection* (Massachusetts Eye and Ear Infirmary, 2014).
3. Caballero, S. et al. Cooperating commensals restore colonization resistance to vancomycin-resistant *Enterococcus faecium*. *Cell Host Microbe* **21**, 592–602. e594, (2017).
4. U.S. Department of Health and Human Services. *Antibiotic Resistance Threats in the United States, 2013* https://www.cdc.gov/drugresistance/biggest_threats.html (2013).
5. Pamer, E. G. Resurrecting the intestinal microbiota to combat antibiotic-resistant pathogens. *Science* **352**, 535–538 (2016).
6. Kim, S., Covington, A. & Pamer, E. G. The intestinal microbiota: antibiotics, colonization resistance, and enteric pathogens. *Immunol. Rev.* **279**, 90–105 (2017).
7. van Nood, E. et al. Duodenal infusion of donor feces for recurrent *Clostridium difficile*. *N. Engl. J. Med.* **368**, 407–415 (2013).
8. Lawley, T. D. et al. Targeted restoration of the intestinal microbiota with a simple, defined bacteriotherapy resolves relapsing *Clostridium difficile* disease in mice. *PLoS Pathog.* **8**, e1002995 (2012).
9. Buffie, C. G. et al. Precision microbiome reconstitution restores bile acid mediated resistance to *Clostridium difficile*. *Nature* **517**, 205–208 (2015).
10. Becattini, S. et al. Commensal microbes provide first line defense against *Listeria monocytogenes* infection. *J. Exp. Med.* **214**, 1973–1989 (2017).
11. Suez, J. et al. Post-antibiotic gut mucosal microbiome reconstitution is impaired by probiotics and improved by autologous FMT. *Cell* **174**, 1406–1423 (2018).
12. Ubeda, C. et al. Vancomycin-resistant *Enterococcus* domination of intestinal microbiota is enabled by antibiotic treatment in mice and precedes bloodstream invasion in humans. *J. Clin. Invest.* **120**, 4332–4341 (2010).
13. Taur, Y. et al. Intestinal domination and the risk of bacteremia in patients undergoing allogeneic hematopoietic stem cell transplantation. *Clin. Infect. Dis.* **55**, 905–914 (2012).
14. Ubeda, C. et al. Intestinal microbiota containing *Barnesiella* species cures vancomycin-resistant *Enterococcus faecium* colonization. *Infect. Immun.* **81**, 965–973 (2013).
15. Caballero, S. et al. Distinct but spatially overlapping intestinal niches for vancomycin-resistant *Enterococcus faecium* and carbapenem-resistant *Klebsiella pneumoniae*. *PLoS Pathog.* **11**, e1005132 (2015).
16. Cash, H. L., Whitham, C. V., Behrendt, C. L. & Hooper, L. V. Symbiotic bacteria direct expression of an intestinal bactericidal lectin. *Science* **313**, 1126–1130 (2006).
17. Brandl, K. et al. Vancomycin-resistant enterococci exploit antibiotic-induced innate immune deficits. *Nature* **455**, 804–807 (2008).
18. Chatterjee, C., Paul, M., Xie, L. & van der Donk, W. A. Biosynthesis and mode of action of lantibiotics. *Chem. Rev.* **105**, 633–684 (2005).
19. Knerr, P. J. & van der Donk, W. A. Discovery, biosynthesis, and engineering of lantipeptides. *Annu. Rev. Biochem.* **81**, 479–505 (2012).
20. Mattick, A. T. R. & Hirsch, A. A powerful inhibitory substance produced by Group *N* Streptococci. *Nature* **154**, 551 (1944).
21. Delves-Broughton, J., Blackburn, P., Evans, R. J. & Hugenholtz, J. Applications of the bacteriocin, nisin. *Antonie van Leeuwenhoek* **69**, 193–202 (1996).
22. Wiedemann, I. et al. Specific binding of nisin to the peptidoglycan precursor lipid II combines pore formation and inhibition of cell wall biosynthesis for potent antibiotic activity. *J. Biol. Chem.* **276**, 1772–1779 (2001).
23. Hatziioanou, D. et al. Discovery of a novel lantibiotic nisin O from *Blautia obeum* A2-162, isolated from the human gastrointestinal tract. *Microbiology* **163**, 1292–1305 (2017).
24. Hsu, S. T. et al. The nisin–lipid II complex reveals a pyrophosphate cage that provides a blueprint for novel antibiotics. *Nat. Struct. Mol. Biol.* **11**, 963–967 (2004).
25. Breukink, E. et al. The C-terminal region of nisin is responsible for the initial interaction of nisin with the target membrane. *Biochemistry* **36**, 6968–6976 (1997).
26. Dobson, A. et al. Fate and efficacy of lacticin 3147-producing *Lactococcus lactis* in the mammalian gastrointestinal tract. *FEMS Microbiol. Ecol.* **76**, 602–614 (2011).
27. Picard, C. et al. Review article: bifidobacteria as probiotic agents — physiological effects and clinical benefits. *Aliment. Pharmacol. Ther.* **22**, 495–512 (2005).
28. Kang, D. H. & Fung, D. Y. Reduction of *Escherichia coli* O157:H7 by stimulated *Pediococcus acidilactici*. *Lett. Appl. Microbiol.* **29**, 206–210 (1999).
29. Taur, Y., Jenq, R. R., Ubeda, C., van den Brink, M. & Pamer, E. G. Role of intestinal microbiota in transplantation outcomes. *Best Pract. Res. Clin. Haematol.* **28**, 155–161 (2015).
30. Nakatsuji, T. et al. Antimicrobials from human skin commensal bacteria protect against *Staphylococcus aureus* and are deficient in atopic dermatitis. *Sci. Transl. Med.* **9**, eaah4680 (2017).

METHODS

Bacterial strains. Vancomycin-resistant *E. faecium* purchased from ATCC (stock number 700221) was used for all experiments unless otherwise stated. Vancomycin-resistant *E. faecalis* strains used were V583 and MH.SK1. *Listeria monocytogenes* strains used were 10403S and 13932. *Salmonella Typhimurium* strains used were SL1344 and LT2. The following strains were isolated from patients at Memorial Sloan Kettering Cancer Center: vancomycin-resistant *E. faecium* strains MH.0139G, MH.0151F, MH.1107 and MH.1326H; vancomycin-resistant *E. faecalis* strain MH.SK1; *C. difficile* strain MH.BBL2; methicillin-resistant *S. aureus* strains MH.SK1 and MH.SK2; *Klebsiella pneumoniae* strains MH189 and MH258; *E. coli* strains MH.T18 and MH.X43; and *Proteus mirabilis* strains MH.42F and MH.43A. All gut commensal strains used were isolated from faecal samples of healthy donors and are listed in Supplementary Table 7.

Mouse husbandry. All experiments using wild-type mice were performed with C57BL/6J female mice that were 6–8 weeks old; mice were purchased from Jackson Laboratories. *Rag2*$^{-/-}$*Il2rg*$^{-/-}$ mice were purchased from Taconic Farms, and subsequently bred in-house. Germ-free mice were bred in-house in germ-free isolators. All mice were housed in sterile, autoclaved cages with irradiated food and acidified, autoclaved water. Mouse handling and weekly cage changes were performed by investigators wearing sterile gowns, masks and gloves in a sterile biosafety hood. All animals were maintained in a specific-pathogen-free facility at Memorial Sloan Kettering Cancer Center Animal Resource Center. After co-housing for at least two weeks, mice were individually housed and randomly assigned to experimental groups. All animal experiments were performed at least three times unless otherwise noted. Experiments were performed in compliance with Memorial Sloan-Kettering Cancer Center institutional guidelines and approved by the institution's Institutional Animal Care and Use Committee.

Mouse antibiotic administration. Mice were administered ampicillin (0.5 g l^{-1}; Fisher Scientific) in the drinking water for 5 days. Ampicillin was changed every 3 days. Antibiotic administration ceased after the initial administration of commensal bacteria (after 5 days) unless stated otherwise.

Bacterial in vitro broth culture conditions. The culture broth used for all cultures was pre-reduced brain heart infusion broth supplemented with yeast extract (5 g l^{-1}) and L-cysteine (1 g l^{-1}). The culture conditions were 37 °C and anaerobic unless otherwise stated.

VRE CFU enumeration. VRE CFUs were enumerated from samples by serial dilution in PBS and plating on BD Enterococcosel agar supplemented with vancomycin (8 μg ml^{-1}; Novagen) and streptomycin (100 μg ml^{-1}; Fisher Scientific).

VRE in vitro co-culture inhibition experiments. A frozen aliquot of each bacterial strain was inoculated and cultured in broth for 24 h. The resulting cultures were plated as lawns on pre-reduced Columbia agar supplemented with 5% sheep blood and cultured anaerobically at 37 °C for 24 h, collected and resuspended in pre-reduced PBS (10^8 CFUs ml^{-1}). Using these stocks, VRE (10^3 CFUs ml^{-1}) was co-cultured with each candidate bacterium (10^6 CFUs ml^{-1}) for 6, 24 and 48 h. VRE CFUs were enumerated at each time point. The co-cultured candidate bacterium CFUs were enumerated at each time point by anaerobically plating serial dilutions of the culture on pre-reduced Columbia agar supplemented with 5% sheep blood and calculating the difference from the enumerated VRE CFUs.

VRE in vitro supernatant inhibition experiments. A frozen aliquot of each bacterial strain was inoculated and cultured for 24 h. Culture supernatant was collected by centrifugation at 8,000*g* for 5 min and subsequent filtration (0.22 μm). Supernatants were diluted 1:2 with culture broth. VRE was subsequently inoculated (10^3 CFUs ml^{-1}) and cultured for 6, 24 and 48 h. VRE CFUs were enumerated at each time point.

Fluorescence in situ hybridization. Intestinal tissues with luminal contents were carefully excised and fixed in freshly made nonaqueous Methacarn solution (60% methanol, 30% chloroform and 10% glacial acetic acid) as previously described[31,32] for 6 h at 4 °C. Tissues were washed in 70% ethanol, processed with Leica ASP6025 processor (Leica Microsystems) and paraffin-embedded by standard techniques. Subsequently, 5-μm sections were baked at 56 °C for 1 h before staining. Tissue sections were deparaffinized with xylene (twice, 10 min each) and rehydrated through an ethanol gradient (95%, 10 min; 90%, 10 min) to water. Sections were incubated with a probe specific to BP_{SCSK} ([Alexa546]-TATAAGACTCAATCCGAAGAGATCAT-[Alexa546]) at 50 °C for 3 h. Probes were diluted to 5 ng μl^{-1} in 0.9 M NaCl, 20 mM Tris-HCl at pH 7.2 and 0.1% SDS before use. Sections were later washed twice in 0.9 M NaCl, 20 mM Tris-HCl at pH 7.2 (wash buffer) for 10 min and counterstained with Hoechst (1:3,000 in wash buffer) for nuclear staining.

VRE in vivo decolonization experiments. Antibiotic-treated mice or germ-free mice were orally gavaged with VRE (10^4 CFUs in 200 μl PBS). Three days after VRE inoculation, mice were orally gavaged with isolates from a candidate bacteria consortium (10^8 CFUs per isolate in 200 μl PBS) or vehicle (PBS). VRE colonization was monitored by enumerating VRE CFUs from faecal pellets at the stated time points. Faecal pellets were resuspended in PBS to a normalized concentration (100 mg ml^{-1}) for VRE CFU enumeration. Mice were screened for pre-existing VRE colonization by selective plating before proceeding forward with all experiments.

VRE ex vivo inhibition experiments. Antibiotic-treated mice were orally gavaged with isolates of a given bacteria consortium (10^8 CFUs per isolate), vehicle (PBS), or VRE (10^8 CFUs) in 200 μl PBS. Seven days after inoculation, the content from the caecum was obtained and resuspended in pre-reduced PBS to a normalized concentration (100 mg ml^{-1}). Supernatant from caecal content suspensions were collected by centrifugation at 8,000*g* for 5 min and subsequent filtration (0.22 μm). VRE (10^3 CFUs ml^{-1}) was inoculated and cultured anaerobically at 37 °C for 6 h, and VRE CFUs were enumerated.

Ammonium sulfate precipitation experiments. A frozen aliquot of each bacterium was inoculated and cultured to late log phase at 37 °C unless stated otherwise. *Lactococcus lactis* was cultured to late log phase at 25 °C. The resulting culture supernatants were collected by centrifugation at 8,000*g* for 5 min and subsequent filtration (0.22 μm). To collect 0–45% fractions, ammonium sulfate was added to 45% saturation and equilibrated overnight stirring at 4 °C. The precipitate was collected by centrifugation at 20,000*g* for 20 min, dissolved in PBS, and dialysed (molecular mass cut-off of= 3 kDa) against PBS overnight at 4 °C. To collect 45–90% fractions, ammonium sulfate was added to 90% saturation to the 0–45% fraction supernatants. The precipitate was collected as described for 0–45% fractions. Total protein concentrations were normalized (2 mg ml^{-1}) and diluted in culture broth (20 μg ml^{-1}). VRE was inoculated (10^3 CFUs ml^{-1}) and cultured for 6 and 24 h. VRE CFUs were enumerated at each time point.

Lantibiotic gene expression in vivo experiments. Antibiotic-treated mice were orally gavaged with CBBP (10^8 CFUs per isolate in 200 μl). Two weeks after inoculation, the content from the caecum was obtained and flash-frozen. The samples were subsequently RNA extracted, sequenced, and analysed as described below.

Construction of pRSFDuet-1/LanA+LanB and pCDF-1/LanC. Construction of expression vectors was based on previous methodology[33,34]. Custom gene synthesis of modified fragments of pRSFDuet-1 and pCDF-1 were generated (IDT) in which the precursor sequence LanA and the dehydratase LanB were inserted into multiple cloning site (MCS) 1 and MCS 2, respectively, in pRSFDuet-1; the cyclase LanC was inserted into MCS 2 in pCDF-1. The respective vector backbones, excluding the regions analogous to the modified gene fragments containing lantibiotic gene inserts described earlier, were linearized by inverse PCR amplification using linear_pDuet-1F (5′-CGAGTCTGGTAAAGAAACCGCTG-3′) and linear_pRSFDuet-1R (5′-GATCCTGGCTGTGGTGATGATGGT-3′) for pRSFDuet1, and linear_pDuet-1F and linear_pCDFDuet-1R (5′-TTCTTATACTTAACTAATATACTAA-3′) for pCDFDuet-1. The modified gene fragments containing the inserts were PCR amplified. For pRSFDuet-1 inserts, the first fragment, pRSFDuet-1.MCS1-gblock, was amplified using gblock_pRSFDuet-1.MCS1F (5′-ACCATCATCACCACAGCCAGGAT-3′) and gblock_pRSFDuet-1.MCS1R (5′-AAAAACTTTTGTAAATCGAATACTGATTTCTTCTGC-3′). The second fragment, pRSFDuet-1.MCS2-gblock, was amplified using gblock_pRSFDuet-1.MCS2F (5′-AGAAATCAGTATTCGAT-3′) and gblock_pDuet-1.MCS2R (5′-AGCAGCGGTTTCTTTACCAGACTCG-3′). For the pCDFDuet insert, the gene fragment was amplified using gblock_pCDFDuet-1.MCS2F (5′-TTAGTATATTAGTTAAGTAT-3′) and gblock_pDuet-1.MCS2R. The gene fragments were cloned into the linearized vector backbones using In-Fusion HD Cloning Plus (Takara). Stellar competent cells (Takara) were transformed with the fused vectors by heat shock and plated on selective plates at 37 °C for 16 h. The pRSFDuet-1/LanA+LanB transformants were selected on luria broth (LB) agar supplemented with kanamycin (30 μg ml^{-1}), and pCDFDuet-1 transformants were selected on LB agar supplemented with streptomycin (50 μg ml^{-1}) for pCDFDuet-1/LanC. Colonies containing each vector were inoculated in LB supplemented with the respective antibiotics for selection and cultured for 10 h at 37 °C, followed by isolation of the plasmids using a Qiaprep Spin Miniprep Kit (Qiagen). The sequences of the resulting plasmids were confirmed by DNA sequencing. The sequences of the lantibiotic genes are listed in Supplementary Table 4, and the custom gene fragment sequences are listed in Supplementary Table 6.

Overexpression and purification of lantibiotic. These were performed as previously described[33,34]. In brief, chemically competent BL21(DE3) cells were co-transformed with pRSFDuet-1/LanA+LanB and pCDFDuet-1/LanC. Overnight cultures grown from a single colony transformant were used as an inoculum for larger scale cultures in terrific broth medium containing 30 mg l^{-1} kanamycin and 50 mg l^{-1} streptomycin at 37 °C until the $OD_{600\,nm}$ reached between 0.6 and 0.8. The cultures were then induced with 1 mM IPTG and incubated at 18 °C for an additional 16 h. The cells were collected by centrifugation at 8,000*g* for 15 min. The cell pellets corresponding to 1.5 l of culture were resuspended in 45 ml of start buffer (20 mM Tris, 500 mM NaCl, 10% glycerol, protease inhibitor cocktail from Roche, pH 8.0). The suspensions were chilled on ice and lysed using a Branson ultrasonic homogenizer (35% amplitude, 10-s pulse, 10-s pause for total 10 min). The lysate supernatant was collected by centrifugation at 30,000*g* for 30 min at 4 °C. Chromatographic purification was performed using an AKTA pure

chromatography system at 4 °C. The lysate supernatant was loaded onto a HiTrap HP nickel affinity column. The column was washed with 75 ml (start buffer plus 30 mM imidazole) and recombinant product eluted in 25 ml (start buffer plus 1 M imidazole). The His-tagged lanthipeptide eluate was loaded on a Luna 10 μm C8(2) 100 Å, LC Column 250 × 4.6 mm and separated with 80 min linear gradient of 0–80%. Buffer A was 0.1% TFA in H_2O and buffer B was 90% acetonitrile, 20% buffer A. The $LanA_1$–$LanA_4$ peptide itself and its hydration + 18 Da series eluted in fractions 40–50 (Extended Data Fig. 6b) with the maximum for fully dehydrated product at 45%. Fractions 43–46 were lyophilized and the concentration of the solution was measured by BCA assay. We obtained approximately 1 mg of product from bacteria in 1.3 l of medium. The His tag and leader sequence were removed by trypsin digestion for 2 h at 25 °C. The digestion was stopped by adding formic acid to 1% and the product was separated by reverse phase chromatography on a 0–80% linear gradient as described above. The resulting product was checked by electrospray ionization–mass spectrometry and the spectrum was deisotoped and deconvoluted by Xtract algorithm in Xcalibur. The proteolytic fragment corresponding to mature $LanA_1$–$LanA_4$ was observed: 3,152.45. VRE was inoculated in culture broth supplemented with the purified lantibiotic (100 μM) and cultured for 24 h. VRE CFUs were subsequently enumerated.

DNA extraction. DNA was extracted using a phenol–chloroform extraction technique with mechanical disruption (bead beating). In brief, a frozen aliquot of approximately 100 mg per sample was suspended, while frozen, in a solution containing 500 μl of extraction buffer (200 mM Tris, pH 8.0; 200 mM NaCl; and 20 mM EDTA), 210 μl of 20% SDS, 500 μl of phenol:chloroform:isoamyl alcohol (25:24:1), and 500 μl of 0.1-mm-diameter zirconia/silica beads (BioSpec Products). Microbial cells were lysed by mechanical disruption with a bead beater (BioSpec Products) for 2 min, followed by two rounds of phenol:chloroform:isoamyl alcohol extraction. After extraction, DNA was precipitated in ethanol, resuspended in 200 μl of TE buffer with RNase (100 mg ml^{-1}), and further purified with QIAamp mini spin columns (Qiagen).

Microbial composition by 16S rRNA gene sequencing. Universal bacterial primers—563F (5′-nnnnnnnn-NNNNNNNNNNNN-AYTGGGYDTAAAGNG-3′) and 926R (5′-nnnnnnnn-NNNNNNNNNNNN-CCGTCAATTYHTTTRAGT-3), in which 'N' represents unique 12-base-pair Golay barcodes and 'n' represents additional nucleotides to offset the sequencing of the primers—were used to PCR-amplify the V4–V5 hypervariable region of the 16S rRNA gene. The V4–V5 amplicons were purified, quantified, and pooled at equimiolar concentrations before ligating Illumina barcodes and adaptors using the Illumina TruSeq Sample Preparation protocol. The completed library was sequenced using the MiSeq Illumina platform[35]. Paired-end reads were merged and demultiplexed. The UPARSE pipeline[36] was used for error filtering using the maximum expected error ($E_{max} = 1$)[37], clustering sequences into operational taxonomic units (OTUs) of 97% distance-based similarity, and identifying and removing potential chimeric sequences using both de novo and reference-based methods. Singleton sequences were removed before clustering. A custom Python script incorporating nucleotide BLAST, with NCBI RefSeq[38] as reference training set, was used to perform taxonomic assignment to the species level ($E \leq 1 \times 10^{-10}$) using representative sequences from each OTU.

Whole-genome sequencing, assembly and annotation. An overnight culture grown from a single colony in culture broth was DNA extracted and sequenced using the Illumina MiSeq platform. Purified DNA was sheared using a Covaris ultrasonicator and prepared for sequencing with a Kapa library preparation kit with Illumina TruSeq adaptors to create 300 × 300 bp nonoverlapping paired-end reads. Raw sequence reads were filtered (Phred score ≥ 30, 4 bp sliding window) using Trimmomatic[39] (v.0.36). Trimmed reads were assembled into contigs and annotated with putative open reading frames using the assembly and annotation services in PATRIC[40] (v.3.5.25).

Metagenomic sequencing. DNA was extracted, sheared, and libraries were prepared as described for whole-genome sequencing. Sequencing was performed using the Illumina HiSeq platform (Illumina) with a paired-end 100 × 100 bp kit in pools targeting 20–30 million reads per sample.

RNA extraction. Samples were extracted using an acidic phenol–chloroform protocol. In brief, approximately 100 mg per sample was suspended in 700 μl of RNA. The suspension was homogenized using a sterile RNase-free spatula and incubated at 4 °C overnight. Samples were pelleted by centrifugation at 13,000*g* for 10 min and resuspended in 200 μl of RNA extraction buffer supplemented with proteinase K (1 mg ml^{-1}) that was heat-activated at 50 °C for 10 min. Samples were incubated at room temperature for 10 min and vortexed every 2 min. Then, 300 μl of Qiagen RLT Plus Buffer (Qiagen) with β-mercaptoethanol (1%) was added to each sample, vortexed and incubated for 5 min at room temperature. Samples were then transferred to a sterile bead beating tube with 500 μl of 0.1 mm glass beads and 500 μl of acidic phenol:chloroform:isoamyl. Mechanical lysis was performed by bead beating the samples for 3 min (BioSpec Products), followed by one round of acidic phenol–chloroform extraction and one round of chloroform extraction. RNA was precipitated with 50 μl of 3 M ammonium acetate and 500 μl of 100% isopropanol and incubated at −20 °C overnight. RNA was pelleted by centrifugation at 13,000*g* for 20 min at 4 °C and washed with 450 μl of 70% ethanol. Ethanol wash was repeated, and the pellet was allowed to air dry at room temperature for 5 min. The pellet was then dissolved in 50 μl of RNase-free water. RNA samples were purified using RNAClean XP (Agencourt), DNA contaminants were removed using TURBO DNA-Free kit (Life Technologies), and ribosomal RNA removed using Ribo-Zero rRNA Removal Kit (Illumina). Following ribosomal RNA depletion, RNAClean XP purification was repeated.

RNA sequencing and analysis. RNA sample libraries were prepared using the TruSeq Stranded mRNA protocol (Illumina) and sequenced using the Illumina Miseq platform (Illumina). Raw sequence reads were filtered using Trimmomatic (v.0.36), aligned to the genome of BP_{SCSK} using bowtie2 (v.2.3.4.1), assigned to genes using featureCounts (v.1.6.1), and converted to normalized gene counts using DeSeq2 (v.1.20.0).

Oral administration of BP_{SCSK} protein precipitate. Antibiotic-treated mice were orally gavaged with BP_{SCSK} or $BP_{control}$ protein precipitate (400 μg). Three hours later, VRE (10^4 CFUs in 200 μl PBS) was orally gavaged, followed by oral administrations of BP_{SCSK} or $BP_{control}$ protein precipitate every 3 h for 12 h. VRE colonization was monitored by enumerating VRE CFUs from faecal pellets 12 h post-VRE-gavage. Faecal pellets were resuspended in PBS to a normalized concentration (100 mg ml^{-1}) for VRE CFU enumeration. Mice were screened for pre-existing VRE colonization by selective plating before proceeding forward with all experiments.

Healthy-donor faecal isolate collection. Faecal samples were collected from healthy human donors ($n = 15$) and transferred to an anaerobic chamber within 1 h of collection. All culture conditions were performed anaerobically on pre-reduced Columbia agar supplemented with 5% sheep blood at 37 °C. Samples were resuspended in pre-reduced PBS and serially diluted with three tenfold serial dilutions. The dilutions were streaked on plates and cultured for 72 h. Individual colonies were selected and streaked onto fresh plates and cultured for 48 h. Single colonies were then resuspended in 50 μl of pre-reduced PBS and 10 μl was streaked as a lawn onto a fresh plate and cultured for 48 h. Each isolate was obtained from culture and stocks were stored in pre-reduced PBS with 10% glycerol at 80 °C. Colony PCR was performed using 2 μl of the above 50 μl single-colony suspension in PBS as a template. The 16S rRNA gene was amplified with primers 8F (5′-AGAGTTTGATCCTGGCTCAG-3′) and 1492R (5′-GGTTACCTTGTTACGACTT-3′). Amplicons were purified with the Qiaquick PCR Purification Kit (Qiagen) and sanger sequenced (Eton Biosciences) with a panel of 6 primers: 8F (5′-AGAGTTTGATCCTGGCTCAG-3′), 533F (5′-GTGCCAGCAGCCGCGGTAA-3′), 16S.1100.F16 (5′-CAACGAGCGCAACCCT-3′), 1492R (5′-GGTTACCTTGTTACGACTT-3′), 907R (5′-CCGTCAATTCMTTTRAGTTT-3′), 519R (5′-GWATTACCGCGGCKGCTG-3′). Sanger sequences were quality filtered and assembled into a consensus sequence using custom Python scripts. Species identification was performed with nucleotide BLAST against the NCBI RefSeq database.

Patient stool collection. Patients were enrolled in a prospective faecal collection protocol, in which faecal samples were routinely collected during the initial transplant hospitalization and stored in a biospecimen bank, as described previously[13]. Patients were part of a study consisting of adult patients (≥18 years) undergoing allogeneic haematopoietic stem-cell transplantation at Memorial Sloan Kettering Cancer Center (MSKCC). The study was approved by the Institutional Review Board at MSKCC. All study patients provided written informed consent for IRB-approved biospecimen collection and analysis (protocols 09-141, 06-107). The study was conducted in accordance with the Declaration of Helsinki.

Lantibiotic gene mining. The lantibiotic genes were discovered in the genome of BP_{SCSK} using antiSMASH[41] and BAGEL3[42] and confirmed to be homologous to known lantibiotic gene sequences using BLASTp alignment (Supplementary Table 5). Lantibiotic sequences were identified from metagenomic sequences using DIAMOND (v.0.9.22)[43] to align reads ($E < 0.001$) to a custom database derived from the RefSeq nonredundant database (accessed August 2018), filtering only for lantibiotic genes containing the gallidermin superfamily domain. To identify RefSeq entries containing the gallidermin superfamily domain, a hidden Markov model profile was built according to the NCBI Conserved Protein Domain Family entry for the gallidermin superfamily domain (accession cl03420) by using pfam02052 and TIGR03731 hidden Markov model files and searching for RefSeq entries with these sequence patterns using HMMER (3.1b2)[44] ($E < 1 \times 10^{-5}$). Lantibiotic sequences were identified from whole-genome-sequenced genomes by assembling and annotating genomes as described previously. All open reading frames were searched for homology to the gallidermin superfamily domain using HMMER (3.1b2)[44].

Detected lantibiotic sequence assembly from metagenomic sequencing. Translated sequencing reads aligning to a RefSeq database entry were retrieved from the DIAMOND (v.0.9.22) alignment output and sorted by the RefSeq entry sequence they aligned. All sequencing reads within a sorted group were multiple sequence aligned to each other using MUSCLE (v.3.8.31) and the consensus sequence was used as the assembled, detected lantibiotic sequence.

Statistics. Statistical analyses were performed using R (v.3.3.1) and GraphPad Prism (v.7.0a) software packages. The two-tailed Mann–Whitney *U*-test was used for comparisons of continuous variables between two groups with similar variances. No statistical methods were used to predetermine sample size. When possible, investigators were blinded during group allocation and outcome assessment (16S and metagenomic shotgun sequence collection, extraction, quantification and analysis; enumeration of VRE in animal, ex vivo and in vitro experiments). Data were visualized using bar plots with centre values representing the geometric mean and error bars representing the geometric s.d.; line graphs with points representing the geometric mean and error bars representing the geometric s.d.; box plots with the centre line representing the median, box limits representing the upper and lower quartiles and whiskers representing 1.5× the interquartile range; and heat maps with individual values contained in a matrix representing the mean. Spearman rank correlation tests (two-tailed) were used to find significant correlations between two continuous variables.

Reporting summary. Further information on research design is available in the Nature Research Reporting Summary linked to this paper.

Data availability

Microbiome sequencing data are available from Bioproject with the accession number 394877.

31. Vaishnava, S. et al. The antibacterial lectin RegIIIγ promotes the spatial segregation of microbiota and host in the intestine. *Science* **334**, 255–258 (2011).
32. Swidsinski, A., Weber, J., Loening-Baucke, V., Hale, L. P. & Lochs, H. Spatial organization and composition of the mucosal flora in patients with inflammatory bowel disease. *J. Clin. Microbiol.* **43**, 3380–3389 (2005).
33. Shi, Y., Yang, X., Garg, N. & van der Donk, W. A. Production of lantipeptides in Escherichia coli. *J. Am. Chem. Soc.* **133**, 2338–2341 (2011).
34. Montalban-Lopez, M., Buivydas, A. & Kuipers, O. P. in *Hydrocarbon and Lipid Microbiology Protocols Springer Protocols Handbooks* (eds McGenity, T. et al.) (Springer, 2015).
35. Caporaso, J. G. et al. Ultra-high-throughput microbial community analysis on the Illumina HiSeq and MiSeq platforms. *ISME J.* **6**, 1621–1624 (2012).
36. Edgar, R. C. UPARSE: highly accurate OTU sequences from microbial amplicon reads. *Nat. Methods* **10**, 996–998 (2013).
37. Edgar, R. C. & Flyvbjerg, H. Error filtering, pair assembly and error correction for next-generation sequencing reads. *Bioinformatics* **31**, 3476–3482 (2015).
38. Tatusova, T., Ciufo, S., Fedorov, B., O'Neill, K. & Tolstoy, I. RefSeq microbial genomes database: new representation and annotation strategy. *Nucleic Acids Res.* **43**, 3872 (2015).
39. Bolger, A. M., Lohse, M. & Usadel, B. Trimmomatic: a flexible trimmer for Illumina sequence data. *Bioinformatics* **30**, 2114–2120 (2014).
40. Wattam, A. R. et al. Assembly, annotation, and comparative genomics in PATRIC, the All Bacterial Bioinformatics Resource Center. *Methods Mol. Biol.* **1704**, 79–101 (2018).
41. Medema, M. H. et al. antiSMASH: rapid identification, annotation and analysis of secondary metabolite biosynthesis gene clusters in bacterial and fungal genome sequences. *Nucleic Acids Res.* **39**, W339–W346 (2011).
42. de Jong, A., van Hijum, S. A., Bijlsma, J. J., Kok, J. & Kuipers, O. P. BAGEL: a web-based bacteriocin genome mining tool. *Nucleic Acids Res.* **34**, W273–W279 (2006).
43. Buchfink, B., Xie, C. & Huson, D. H. Fast and sensitive protein alignment using DIAMOND. *Nat. Methods* **12**, 59–60 (2015).
44. Eddy, S. R. Accelerated profile HMM searches. *PLOS Comput. Biol.* **7**, e1002195 (2011).

Acknowledgements This work was supported by grants RO1 AI42135, RO1 AI95706, UO1 AI124275, and P30 CA008748 from the US National Institutes of Health (NIH) and the Tow Foundation and Lucille Castori Center for Microbes, Inflammation and Cancer to E.G.P. S.G.K. is supported by a Medical Scientist Training Program grant from the National Institute of General Medical Sciences, NIH (award T32GM07739 to the Weill Cornell/Rockefeller/Sloan Kettering Tri-Institutional MD-PhD Program). S.B. was supported by an Early Postdoc Mobility Fellowship from the Swiss National Science Foundation and an Irvington Fellowship from the Cancer Research Institute. We thank members of the Pamer laboratory for discussions and comments on the manuscript.

Author contributions S.G.K. and E.G.P. designed the experiments and wrote the manuscript. S.G.K. performed and analysed most experiments. S.B. helped to design experiments, performed and analysed fluorescence in situ hybridization and RNA-sequencing analysis on caecal content. T.U.M., S.C. and V.E. cultured bacterial isolates from faecal samples and analysed whole-genome sequences of isolates. P.V.S. and R.C.H. performed peptide purifications and subsequent characterization by mass spectrometry. E.R.L. performed bioinformatic analyses and metagenomic sequence data. R.S. assisted in bacterial culturing and animal experiments. I.M.L. and R.S. maintained and screened mouse strains. M.G. generated and characterized bacterial isolates from faecal samples. W.Q., R.J.J.F.R. and J.R.C. contributed to the development of methods to purify bacterial lantibiotics for biochemical analyses. E.F., L.A. and R.W. performed DNA extractions, 16S MiSeq Illumina sequencing and analysed microbiome sequence data. Z.-M.X.W. assisted in ileal homogenization, western blot, and RT–qPCR analyses. H.-J.J. contributed to the cloning and expression of the lantibiotic gene. S.M.M. and Y.T. enrolled patients undergoing allogeneic haematopoietic cell transplantation in the prospective faecal collection protocol and contributed to the analysis of sequence data. S.N. and K.H. contributed human-derived commensal bacterial strains that were included in this study. J.U.P. and M.R.M.v.d.B. contributed to the analyses of patient-derived faecal samples.

Competing interests K.H. is co-founder and scientific advisor to Vedanta Biosciences. M.R.M.v.d.B. is on the advisory board of and has financial holdings in Seres Therapeutics Inc., serves on the DKMS medical council, has received speaker honoraria from Merck and Acute Leukemia Forum, holds patents that receive royalties from Seres Therapeutics Inc., has received honorarium and research support (1 January 2017 to present) from Seres Therapeutic Inc., and IP licensing with Seres Therapeutics Inc. and Juno. J.U.P. reports research funding, intellectual property fees, and travel reimbursement from Seres Therapeutics. E.G.P. has received speaker honoraria from Bristol-Myer Squibb, Celgene, Seres Therapeutics, MedImmune, Novartis, and Ferring Pharmaceuticals; is an inventor on patent application no. WPO2015179437A1, entitled 'Methods and compositions for reducing *Clostridium difficile* infection' and no. WPO2017091753A1, entitled 'Methods and compositions for reducing vancomycin-resistant *Enterococci* infection or colonization'; and holds patents that receive royalties from Seres Therapeutics Inc.

Additional information

Supplementary information is available for this paper at https://doi.org/10.1038/s41586-019-1501-z.

Correspondence and requests for materials should be addressed to E.G.P.

Peer review information *Nature* thanks Eran Elinav, Michael Gilmore, Barbara Murray and the other, anonymous, reviewer(s) for their contribution to the peer review of this work.

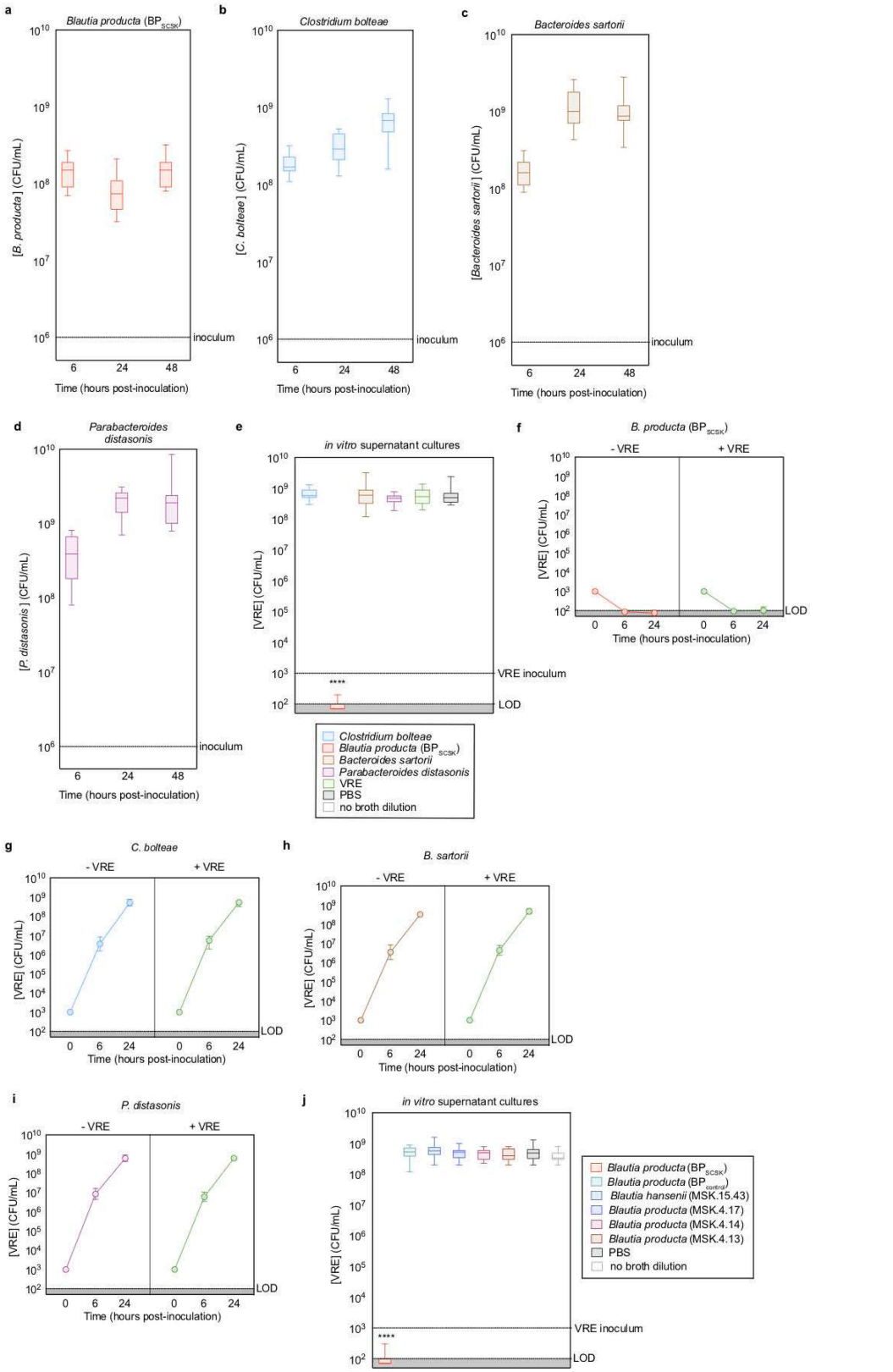

Extended Data Fig. 1 | BP$_{SCSK}$ directly inhibits VRE through a contact-independent mechanism. a–d, VRE was co-cultured with each CBBP$_{SCSK}$ isolate ($n = 15$ biologically independent samples from three independent experiments) and growth was monitored. **e**, VRE was inoculated in conditioned media from each CBBP$_{SCSK}$ isolate culture ($n = 15$ biologically independent samples from three independent experiments). **f–i**, VRE was inoculated in conditioned media from each CBBP$_{SCSK}$ isolate culture (−VRE), or each CBBP$_{SCSK}$ isolate co-cultured with VRE (+VRE) ($n = 5$ biologically independent samples from five independent experiments) and growth was monitored. **j**, VRE was inoculated in conditioned media from *Blautia* species cultures ($n = 6$ strains, 15 biologically independent samples from three independent experiments). VRE (ATCC 700221) was used in all experiments shown. Data are median ± range (**a–e**, **j**) or mean ± s.d. (**f–i**). ****$P < 0.0001$, two-tailed Mann–Whitney U-test for comparisons with a negative control.

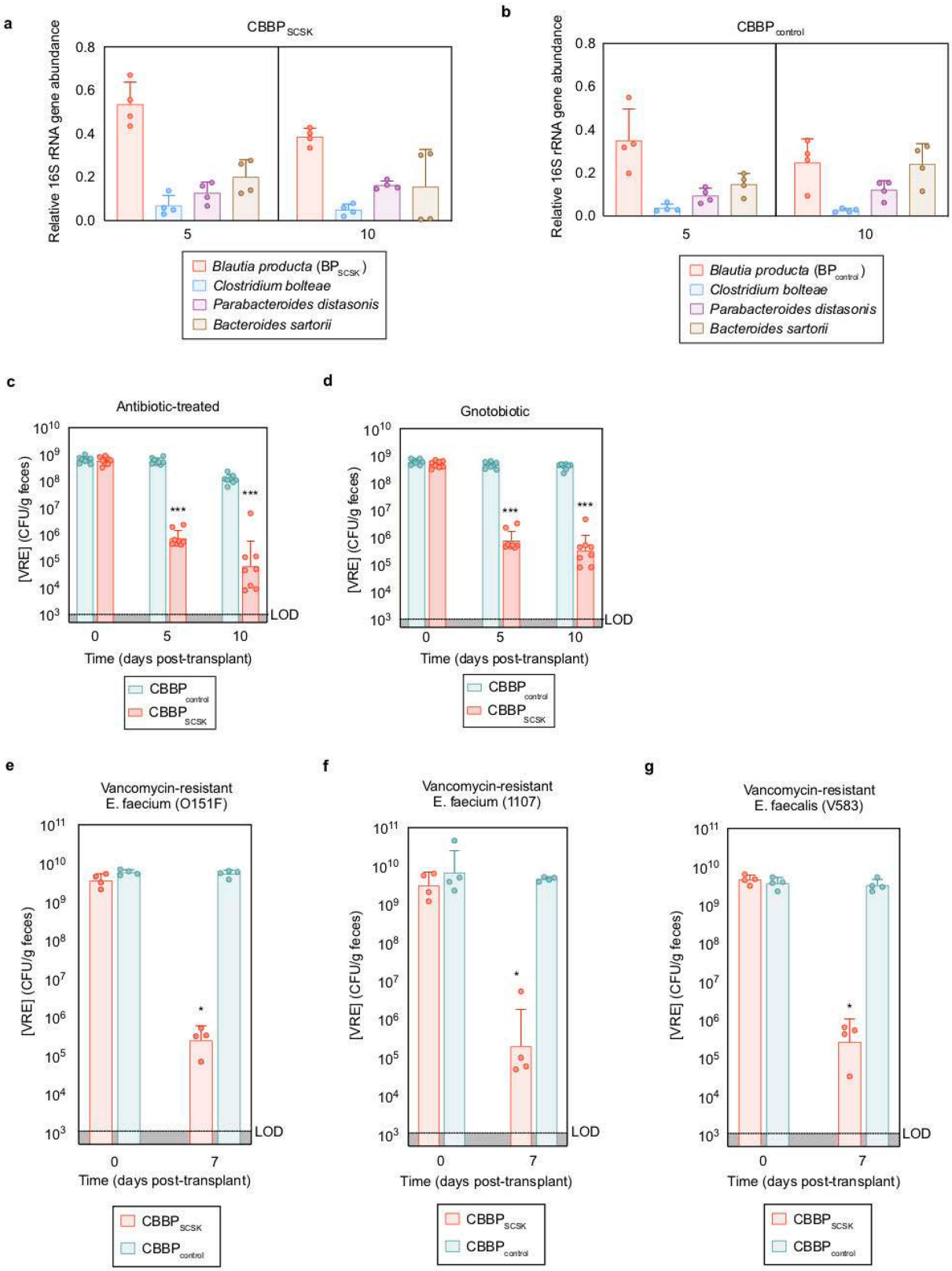

Extended Data Fig. 2 | See next page for caption.

Extended Data Fig. 2 | BP_{SCSK}, but not $BP_{control}$, reduces VRE colonization in vivo. a, **b**, Faecal samples collected from antibiotic-treated, VRE-dominated mice ($n = 4$ mice from one independent experiment) orally gavaged with $CBBP_{SCSK}$ (**a**) or $CBBP_{control}$ (**b**) were shotgun sequenced and the relative abundance of each species was determined by 16S rRNA. **c**, **d**, Antibiotic-treated (**c**) or germ-free (**d**) mice ($n = 8$ mice from two independent experiments) were orally gavaged with VRE. Three days later, VRE-dominated mice received an oral gavage of $CBBP_{SCSK}$ or $CBBP_{control}$ and VRE colonization was monitored by quantifying VRE in faecal samples. **e**–**g**, Antibiotic-treated mice ($n = 4$ mice from one independent experiment) were orally gavaged with different strains of clinical VRE isolates. Three days later, VRE-dominated mice received an oral gavage of $CBBP_{SCSK}$ or $CBBP_{control}$ and VRE colonization was monitored by quantifying VRE in faecal samples. The following VRE strains were used: strain 0151F is an *E. faecium* MLST type ST80 (**e**); strain 1107 is an *E. faceium* MLST type ST412 (**f**); strain V583 is an *E. faecalis* strain (**g**). VRE strains used were VRE (ATCC 700221) (**a**–**d**), VRE (0151F) (**e**), VRE (1107) (**f**), and VRE (V583) (**g**). Data are mean ± s.d. $*P < 0.05$, $***P < 0.001$, two-tailed Mann–Whitney *U*-test.

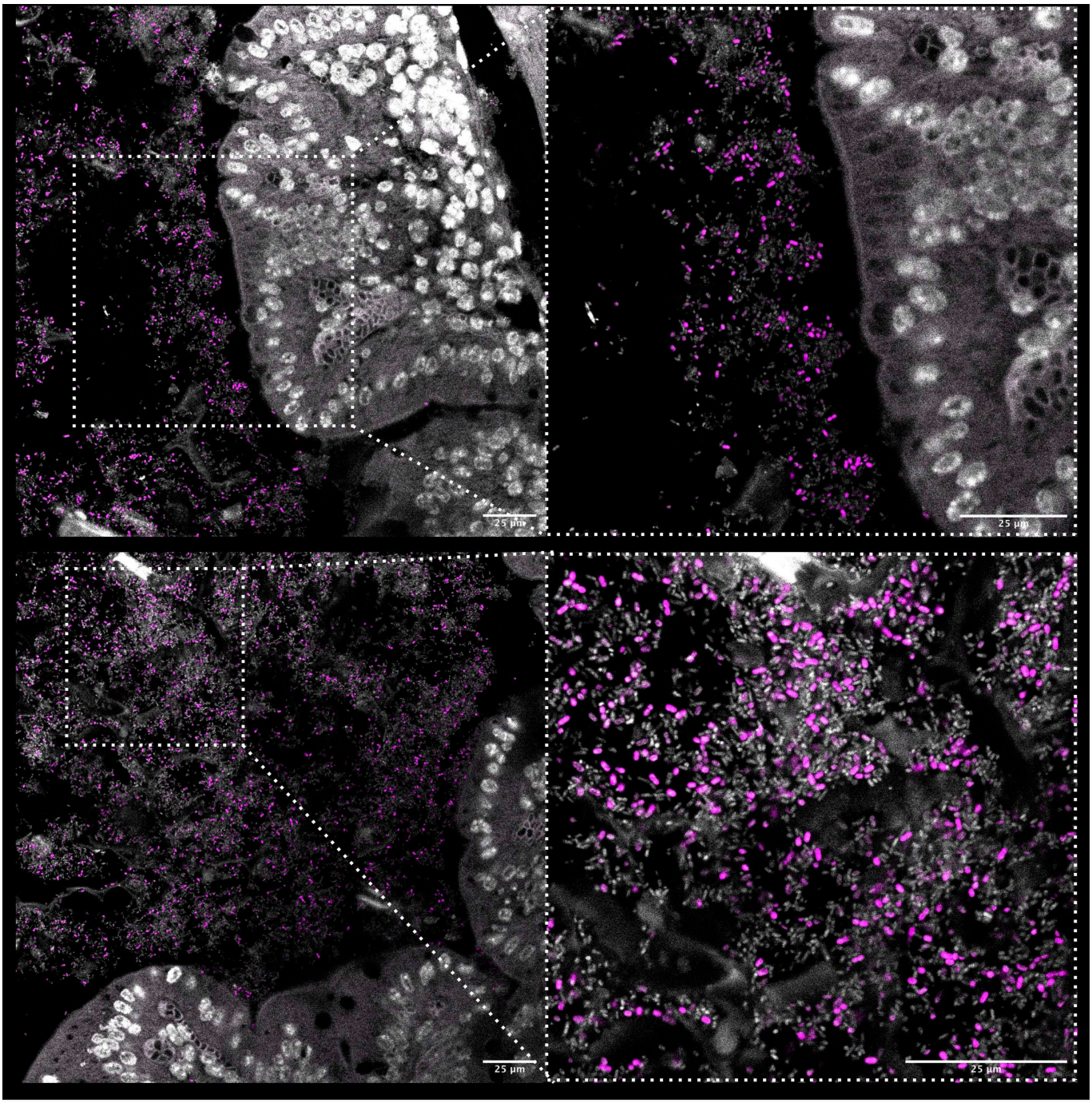

Extended Data Fig. 3 | BP_{SCSK} colonizes the large intestine. Antibiotic-treated mice ($n = 5$ mice from one independent experiment) were orally administered $CBBP_{SCSK}$. Two weeks later, BP_{SCSK} localization around the mucosal epithelium (top) and lumen (bottom) of the caecum were visualized by fluorescence in situ hybridization. Entire caecum cross-sections were hybridized with a probe specific for BP_{SCSK}. Sections were counterstained with Hoechst dye to visualize the nuclei. Representative images are shown. Scale bars, 25 µm.

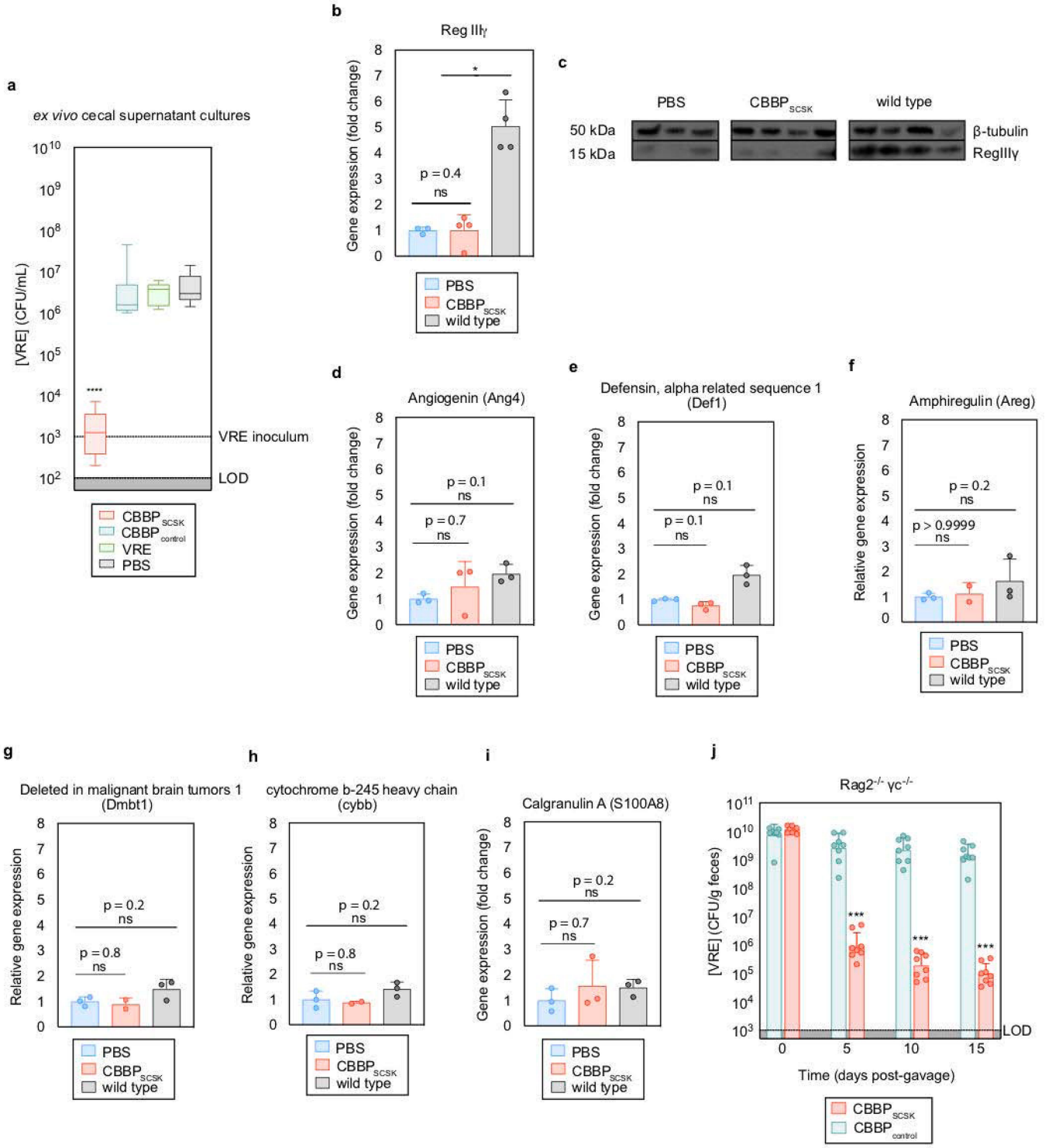

Extended Data Fig. 4 | CBBP$_{SCSK}$ mediates VRE colonization resistance by producing an inhibitor. a, Antibiotic-treated mice ($n = 8$ mice from two independent experiments) received treatment by oral gavage containing CBBP$_{SCSK}$, CBBP$_{control}$, PBS or VRE. One week later, VRE was inoculated into the caecal content and growth was monitored 6 h after inoculation. **b**–**i**, Antibiotic-treated mice received an oral gavage containing CBBP$_{SCSK}$ ($n = 4$ mice from one independent experiment) or PBS ($n = 3$ mice from one independent experiment). Wild-type mice ($n = 4$ mice from one independent experiment) were untreated and received no antibiotics. Four days later, RNA and proteins were extracted from the distal ileum, and RegIIIγ was measured by RT–qPCR (**b**) and western blot (**c**). Other genes involved in host-derived antimicrobial peptide production, including angiogenin-4 (*ang4*) (**d**), defensin-1 (*def1*) (**e**), amphiregulin (*areg*) (**f**), and deleted in malignant brain tumours 1 (*dmbt1*) (**g**); or inflammatory mediators including cytochrome *b* beta (*cybb*) (**h**) and calgranulin A (*s100a8*) (**i**) were measured by RT–qPCR. **j**, *Rag2*$^{-/-}$*Il2rg*$^{-/-}$ mice were treated with antibiotics, and orally gavaged with VRE. Three days later, VRE-dominated mice received CBBP$_{SCSK}$ or CBBP$_{control}$ by oral gavage and VRE colonization was monitored by quantifying VRE in faecal samples. VRE (ATCC 700221) was used in experiments in **a** and **j**. *$P < 0.05$ (0.0286), ***$P < 0.001$, ****$P < 0.0001$, two-tailed Mann–Whitney *U*-test. Data are median ± range (**a**) or mean ± s.d. (**b**, **d**–**i**).

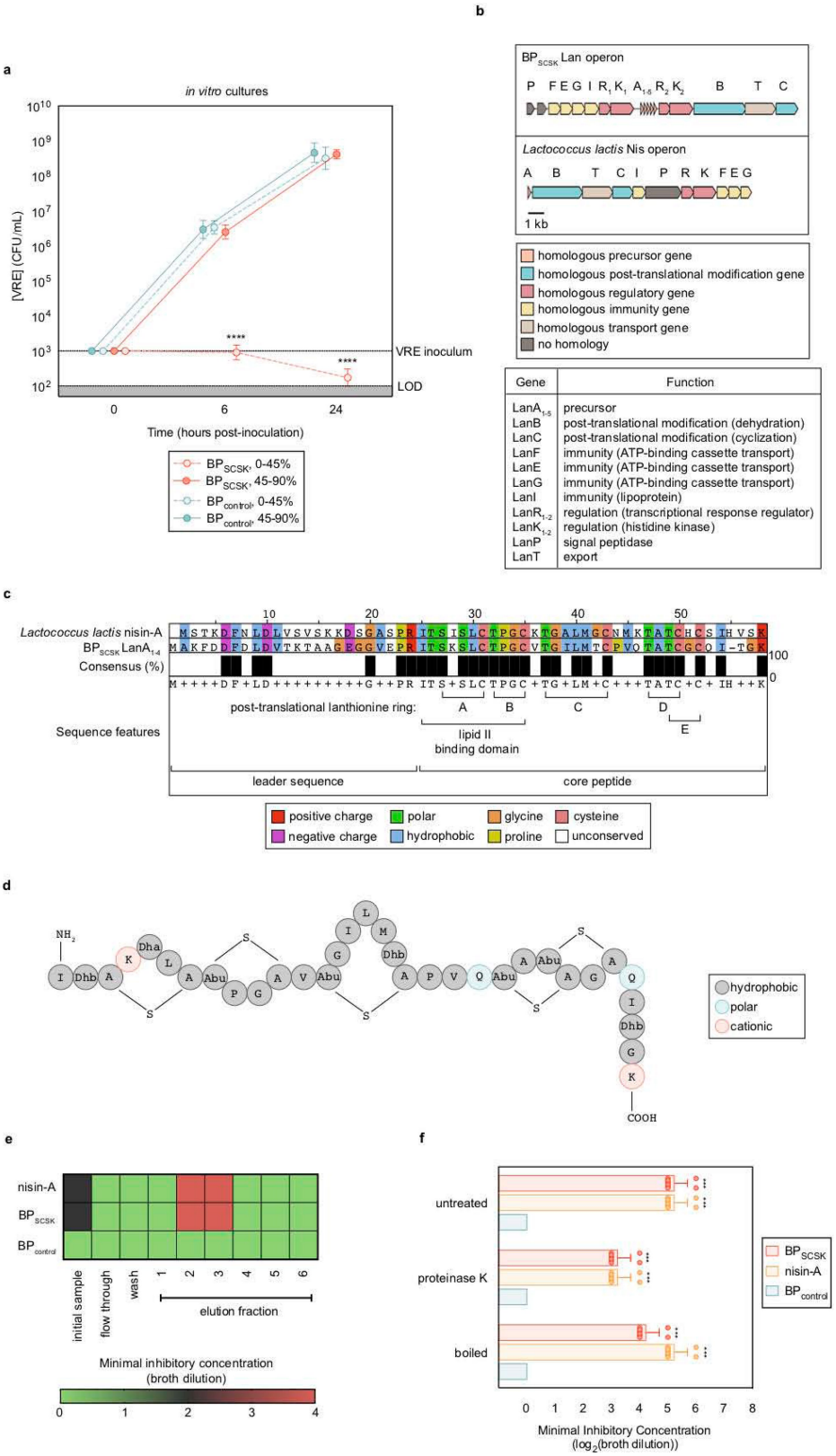

Extended Data Fig. 5 | See next page for caption.

Extended Data Fig. 5 | BP_{SCSK} encodes a lantibiotic. a, VRE was inoculated in media conditioned with BP_{SCSK} or $BP_{control}$ culture protein precipitate fractions ($n = 8$ biologically independent samples from two independent experiments), and monitored for growth. **b**, **c**, BP_{SCSK} was whole-genome sequenced, assembled and annotated. **b**, Schematic comparing the lantibiotic operon discovered in the genome of BP_{SCSK} to the *nisA* operon from *L. lactis*. Gene functions are based on the characterization of homologous genes in the *nis* operon. **c**, Amino acid sequence alignment comparing the BP_{SCSK} lantibiotic precursor ($LanA_1$–$LanA_4$) and the nisin-A precursor (NisA). Sequence features are based on the characterization of nisin. **d**, The molecular formula for the mature, post-translationally modified BP_{SCSK} $LanA_1$–$LanA_4$ lantibiotic with a predicted mass of 3152.45 Da. Abu, alpha-aminobutyric acid; Dha, dehydroalanine;Dhb, dehydrobutyrine. **e**, Media conditioned with BP_{SCSK} or $BP_{control}$ culture protein precipitates, or commercial nisin-A, were incubated with proteinase K for 3 h at 37 °C, boiled at 100 °C, or left untreated. The treated protein precipitate ($n = 8$ biologically independent samples from four independent experiments) was serially diluted and VRE was inoculated and cultured for 24 h. The MIC value was the highest mean dilution in which VRE inhibition was observed. **f**, Proteins were precipitated from BP_{SCSK} or $BP_{control}$, or nisin-A spiked cultures and applied to a SP sepharose column. Each fraction was serially diluted and VRE was inoculated and cultured for 24 h to determine the MIC ($n = 4$ biologically independent samples from four independent experiments). VRE (ATCC 700221) was used in experiments in **a**, **e** and **f**. $^{***}P < 0.001$, $^{****}P < 0.0001$, two-tailed Mann–Whitney *U*-test for comparisons with a negative control. Data are mean ± s.d. (**a**, **f**) or mean values (**e**).

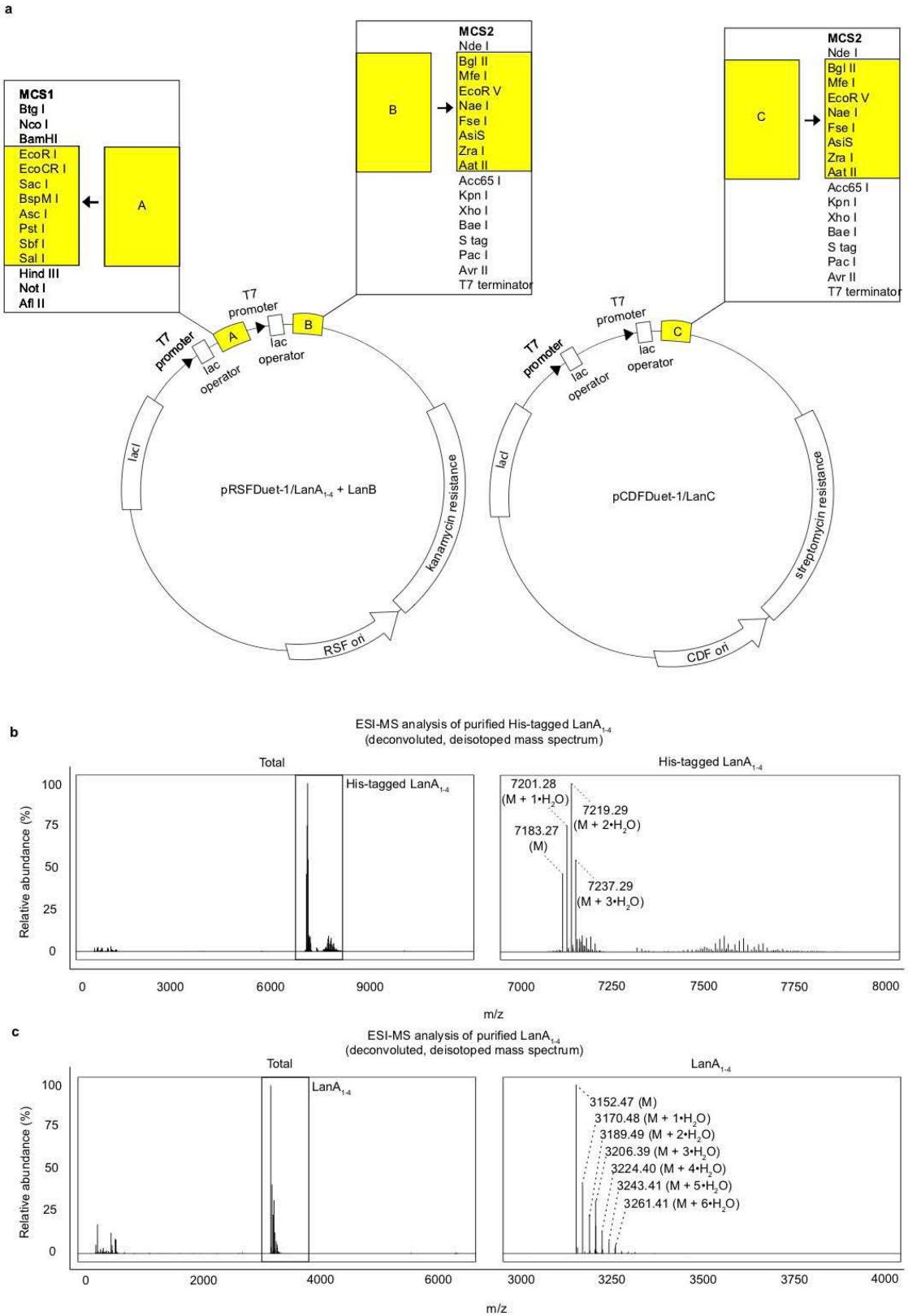

Extended Data Fig. 6 | Heterologous expression of BP_{SCSK} $LanA_1$–$LanA_4$ lantibiotic. a, Genes involved in biosynthesis of the BP_{SCSK} lantibiotic (His-tagged-LanA, LanB and LanC) were cloned into expression vectors (pRSFDuet-1/LanA+LanB, pCDFDuet-1/LanC) and heterologously expressed in *E. coli*. **a**, Schematic map indicating where each lantibiotic gene was inserted into the respective expression vectors. **b**, **c**, The His-tagged $LanA_1$–$LanA_4$ lantibiotic was purified from *E. coli* lysates by HiTrap HP nickel affinity chromatography and subsequently purified to homogeneity by reversed-phase high-performance liquid chromatography. The leader sequence and His tag were removed by trypsin digestion to yield the mature lantibiotic. The purified His-tag product (**b**) and the purified mature lantibiotic (**c**) were analysed by electrospray ionization–mass spectrometry (ESI–MS) and the spectrum was deisotoped and deconvoluted using the Xtract algorithm in Xcalibur. The signals with labels correspond to the predicted mass of the His-tagged lantibiotic (M) and its incomplete forms that did not dehydrate all nine residues (for example, $M + 1{\cdot}H_2O$ and $M + 2{\cdot}H_2O$).

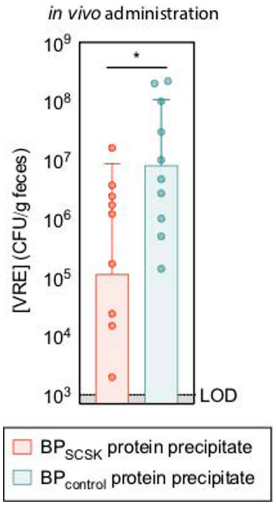

Extended Data Fig. 7 | Oral administrations of BP_{SCSK} protein precipitate reduce VRE colonization in vivo. Antibiotic-treated mice ($n = 9$ mice from three independent experiments) were administered BP_{SCSK} or $BP_{control}$ protein precipitate. Three hours later, VRE was orally gavaged, followed by oral administrations of BP_{SCSK} or $BP_{control}$ protein precipitate every 3 h for 12 h and VRE colonization was monitored by quantifying VRE in faecal samples. VRE (ATCC 700221) was used. $^*P = 0.0232$, two-tailed Mann–Whitney U-test. Data are mean ± s.d.

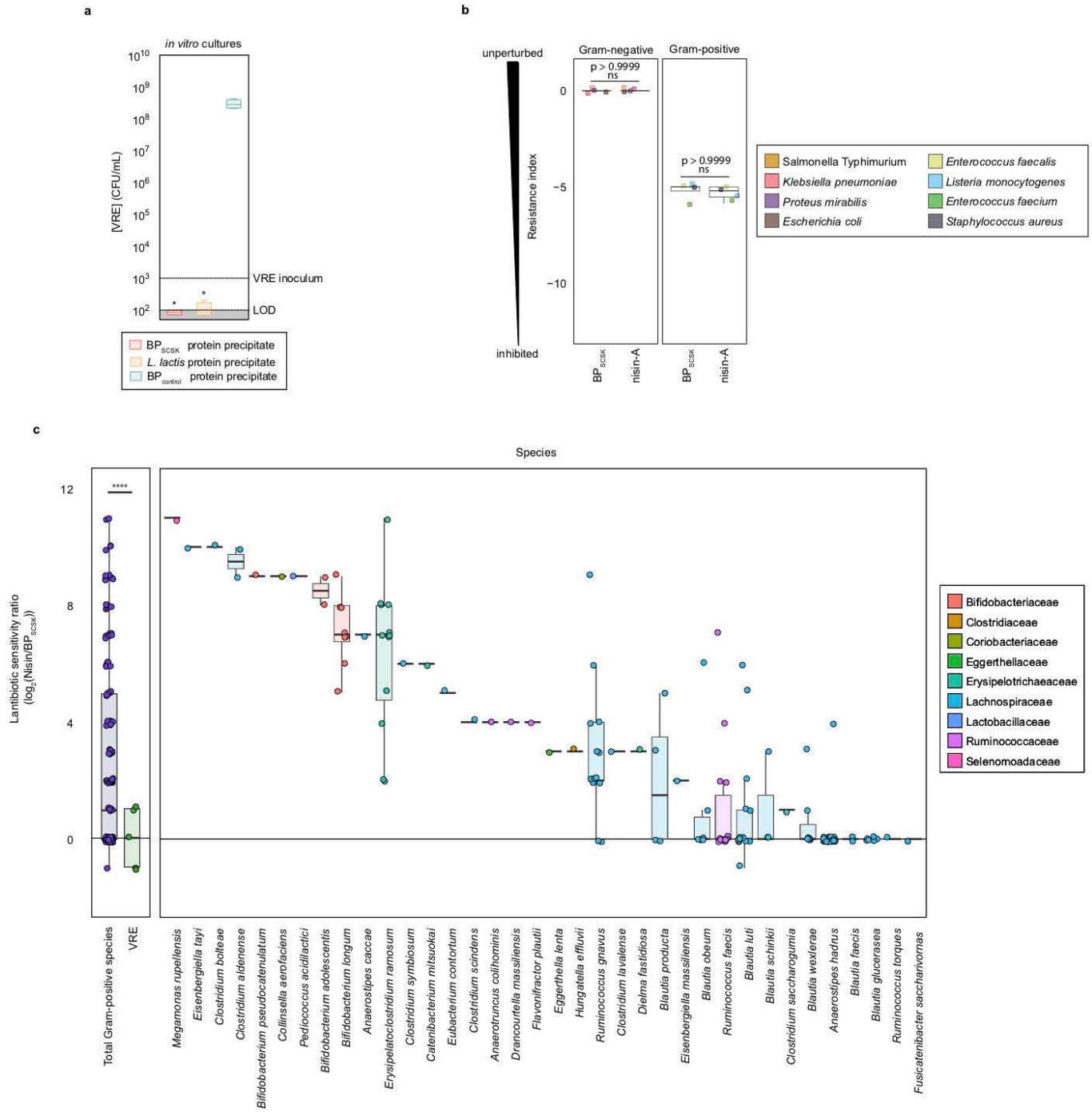

Extended Data Fig. 8 | The BP_{SCSK} lantibiotic has a narrower spectrum of activity against Gram-positive commensal strains. a, VRE was inoculated in media conditioned with BP_{SCSK}, *L. lactis* or $BP_{control}$ culture protein precipitate ($n = 4$ biologically independent samples from four independent experiments) and growth was monitored 24 h after inoculation. **b**, **c**, Culture broth was conditioned with proteins precipitated from BP_{SCSK}, $BP_{control}$ or commercial nisin-A and serially diluted. The MIC value was determined for common nosocomial pathogens (**b**) or 158 strains from a commensal biobank ($n = 2$ biologically independent samples from two independent experiments) (**c**) by calculating the highest dilution factor that inhibited growth. The resistance index is a ratio between MIC of $BP_{control}$-conditioned media over the MIC of BP_{SCSK} or nisin-A-conditioned media (**b**). The lantibiotic sensitivity ratio was calculated as the MIC of nisin-A to the MIC of the BP_{SCSK} lantibiotic for each strain (**c**). $^{*}P < 0.05$, $^{****}P < 0.0001$, two-tailed Mann–Whitney *U*-test for comparisons with a negative control (**a**) or between two experimental conditions (**b**, **c**). Box plots are as defined in Fig. 2.

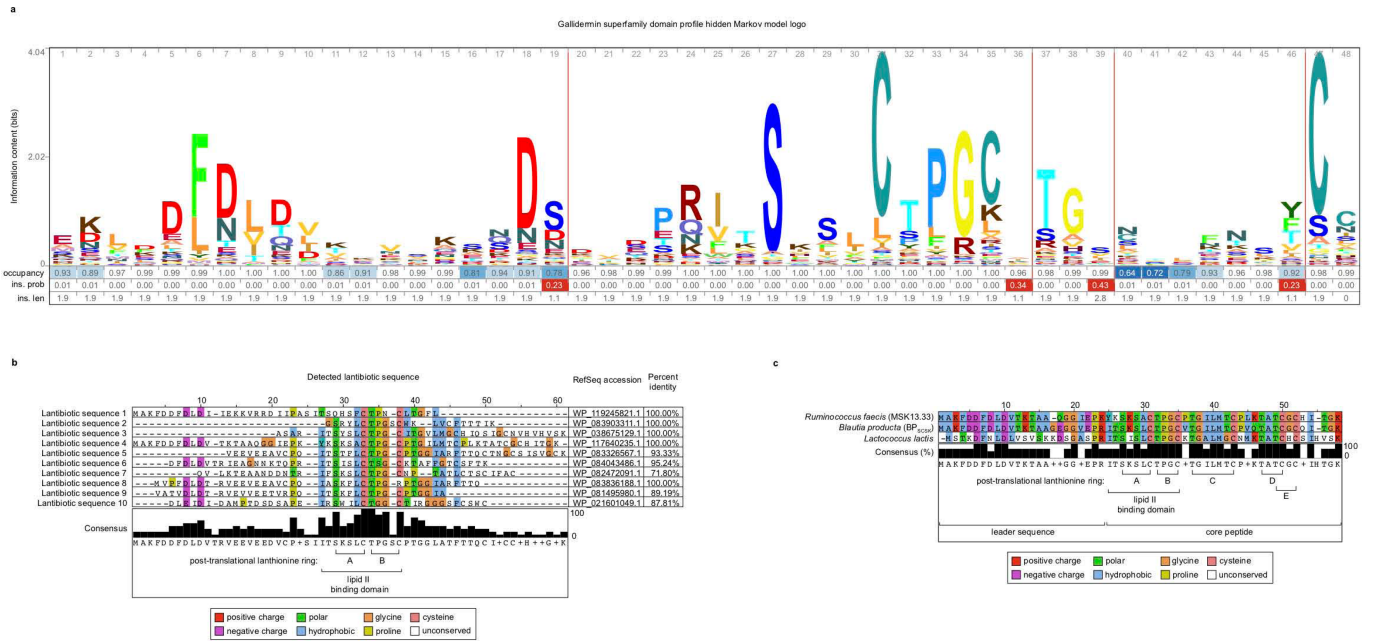

Extended Data Fig. 9 | Identification of lantibiotic sequences from metagenomic sequencing of healthy human faecal samples. a, The profile hidden Markov model used to identify the gallidermin superfamily domain, illustrated as a logo. **b**, Multiple sequence alignment of lantibiotic precursor sequences identified from shotgun sequencing of healthy-donor faecal samples. Detected lantibiotic sequences are the assembly of lantibiotic reads from shotgun metagenomic faecal samples. **c**, A total of 421 species were individually isolated from healthy human faecal samples, whole-genome sequenced, assembled, annotated and mined for lantibiotic precursor sequences to identify a strain of *R. faecis* encoding a homologous lantibiotic. The precursor lantibiotic sequence is compared to the sequences of BP_{SCSK} $LanA_1$–$LanA_4$ lantibiotic and nisin-A by multiple alignment.

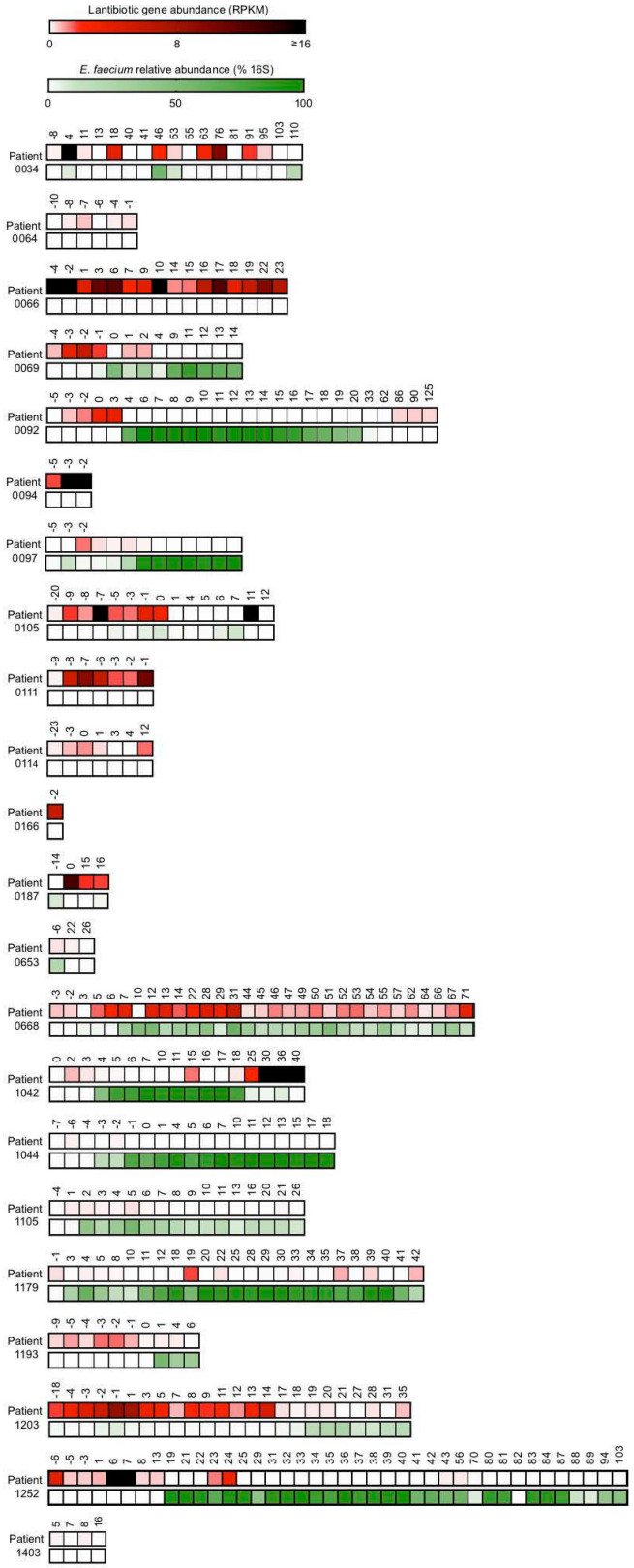

Extended Data Fig. 10 | Lantibiotic sequences identified from metagenomic sequencing of hospitalized patient faecal samples. **a**, Stacked heat map matrices represent a single patient. The top row illustrates abundance of the lantibiotic gene (RPKM). The bottom row illustrates relative abundance of *E. faecium* (percentage of 16S). Columns represent the sample collection day relative to transplant.

nature research

Corresponding author(s): Eric Pamer

Last updated by author(s): Jul 16, 2019

Reporting Summary

Nature Research wishes to improve the reproducibility of the work that we publish. This form provides structure for consistency and transparency in reporting. For further information on Nature Research policies, see Authors & Referees and the Editorial Policy Checklist.

Statistics

For all statistical analyses, confirm that the following items are present in the figure legend, table legend, main text, or Methods section.

n/a	Confirmed	
☐	☒	The exact sample size (*n*) for each experimental group/condition, given as a discrete number and unit of measurement
☐	☒	A statement on whether measurements were taken from distinct samples or whether the same sample was measured repeatedly
☐	☒	The statistical test(s) used AND whether they are one- or two-sided *Only common tests should be described solely by name; describe more complex techniques in the Methods section.*
☐	☒	A description of all covariates tested
☐	☒	A description of any assumptions or corrections, such as tests of normality and adjustment for multiple comparisons
☐	☒	A full description of the statistical parameters including central tendency (e.g. means) or other basic estimates (e.g. regression coefficient) AND variation (e.g. standard deviation) or associated estimates of uncertainty (e.g. confidence intervals)
☐	☒	For null hypothesis testing, the test statistic (e.g. *F*, *t*, *r*) with confidence intervals, effect sizes, degrees of freedom and *P* value noted *Give P values as exact values whenever suitable.*
☒	☐	For Bayesian analysis, information on the choice of priors and Markov chain Monte Carlo settings
☒	☐	For hierarchical and complex designs, identification of the appropriate level for tests and full reporting of outcomes
☒	☐	Estimates of effect sizes (e.g. Cohen's *d*, Pearson's *r*), indicating how they were calculated

Our web collection on statistics for biologists contains articles on many of the points above.

Software and code

Policy information about availability of computer code

Data collection	antiSMASH and BAGEL3 were used to screen for bacteriocin genes. To identify RefSeq entries containing the gallidermin superfamily domain, a hidden Markov model profile was built according to NCBI's Conserved Protein Domain Family entry for gallidermin superfamily domain (accession # cl03420) by using pfam02052 and TIGR03731 hidden Markov model files and searching for RefSeq entries with these sequence patterns using HMMER (3.1b2)(e-value <10-5). Translated sequencing reads were retrieved from the DIAMOND (v0.9.22) alignment output. Sequencing reads within a sorted group were multiple sequence aligned using MUSCLE 9v3.8.31).
Data analysis	R (v.3.3.1) and GraphPad Prism (version 7.0a) software packages were used for statistical analyses.

For manuscripts utilizing custom algorithms or software that are central to the research but not yet described in published literature, software must be made available to editors/reviewers. We strongly encourage code deposition in a community repository (e.g. GitHub). See the Nature Research guidelines for submitting code & software for further information.

Data

Policy information about availability of data

All manuscripts must include a data availability statement. This statement should provide the following information, where applicable:

- Accession codes, unique identifiers, or web links for publicly available datasets
- A list of figures that have associated raw data
- A description of any restrictions on data availability

Microbiome sequencing data are available from Bioproject with the accession number 394877.

Field-specific reporting

Please select the one below that is the best fit for your research. If you are not sure, read the appropriate sections before making your selection.

☒ Life sciences ☐ Behavioural & social sciences ☐ Ecological, evolutionary & environmental sciences

For a reference copy of the document with all sections, see nature.com/documents/nr-reporting-summary-flat.pdf

Life sciences study design

All studies must disclose on these points even when the disclosure is negative.

Sample size	Sample size for mouse experiments was determined by feasibility and the magnitude of the interventions impact. For the studies included in the letter, the impact of intestinal reconstitution with lantibiotic-producing Blautia producta was large, on the order of over 1000 fold reduction in VRE colonization, enabling comparison groups to consist of 3 or more mice. All experiments were repeated at least two times (for a total of at least 3 separate experiments).
Data exclusions	No data was excluded.
Replication	Experiments were repeated at least two times to demonstrate reproducibility.
Randomization	We selected samples for analyses by determining microbiota composition and also diversity. Thus, in germ free mice reconstituted with patient derived microbiota, samples differing in lantibiotic gene abundance were matched in terms of microbiota diversity.
Blinding	Blinding was not feasible for these experiments since mice receiving different treatments had to be clearly labeled and segregated during the course of the experiment.

Reporting for specific materials, systems and methods

We require information from authors about some types of materials, experimental systems and methods used in many studies. Here, indicate whether each material, system or method listed is relevant to your study. If you are not sure if a list item applies to your research, read the appropriate section before selecting a response.

Materials & experimental systems

n/a	Involved in the study
☒	☐ Antibodies
☒	☐ Eukaryotic cell lines
☒	☐ Palaeontology
☐	☒ Animals and other organisms
☐	☒ Human research participants
☒	☐ Clinical data

Methods

n/a	Involved in the study
☒	☐ ChIP-seq
☒	☐ Flow cytometry
☒	☐ MRI-based neuroimaging

Animals and other organisms

Policy information about studies involving animals; ARRIVE guidelines recommended for reporting animal research

Laboratory animals	We used C57BL/6 mice from Jackson laboratories. Mice were female and 6 to 8 weeks of age. Rag2-/-IL2rg-/- mice were purchased from Taconic Laboratories.
Wild animals	*Provide details on animals observed in or captured in the field; report species, sex and age where possible. Describe how animals were caught and transported and what happened to captive animals after the study (if killed, explain why and describe method; if released, say where and when) OR state that the study did not involve wild animals.*
Field-collected samples	*For laboratory work with field-collected samples, describe all relevant parameters such as housing, maintenance, temperature, photoperiod and end-of-experiment protocol OR state that the study did not involve samples collected from the field.*
Ethics oversight	*Identify the organization(s) that approved or provided guidance on the study protocol, OR state that no ethical approval or guidance was required and explain why not.*

Note that full information on the approval of the study protocol must also be provided in the manuscript.

Human research participants

Policy information about studies involving human research participants

Population characteristics	Patients undergoing allogeneic hematopoietic stem cell transplantation were receiving care at Memorial Hospital. Healthy human donors were employees of Memorial Sloan Kettering who consented to providing fecal samples for sequence analyses and for culture.
Recruitment	Patients were informed of the fecal collection study and consent was obtained prior to initiation of hematopoietic stem cell transplantation. Healthy donors were informed of the study and consent was obtained to perform sequencing studies of fecal samples and to culture bacterial species from the fecal sample.
Ethics oversight	The fecal collection protocol and the healthy human donor protocol were approved by the Memorial Sloan Kettering Institutional Review Board.

Note that full information on the approval of the study protocol must also be provided in the manuscript.

LETTER

https://doi.org/10.1038/s41586-019-1471-1

Locally renewing resident synovial macrophages provide a protective barrier for the joint

Stephan Culemann[1,2,11], Anika Grüneboom[1,2,11], José Ángel Nicolás-Ávila[3], Daniela Weidner[1,2], Katrin Franziska Lämmle[1,2], Tobias Rothe[1,2], Juan A. Quintana[3], Philipp Kirchner[4], Branislav Krljanac[5], Martin Eberhardt[6], Fulvia Ferrazzi[4], Elke Kretzschmar[7], Martin Schicht[7], Kim Fischer[1], Kolja Gelse[8], Maria Faas[1,2], René Pfeifle[1,2], Jochen A. Ackermann[1,2], Milena Pachowsky[8], Nina Renner[8], David Simon[1], Reiner F. Haseloff[9], Arif B. Ekici[4], Tobias Bäuerle[10], Ingolf E. Blasig[9], Julio Vera[6], David Voehringer[5], Arnd Kleyer[1], Friedrich Paulsen[7], Georg Schett[1], Andrés Hidalgo[3] & Gerhard Krönke[1,2]*

Macrophages are considered to contribute to chronic inflammatory diseases such as rheumatoid arthritis[1]. However, both the exact origin and the role of macrophages in inflammatory joint disease remain unclear. Here we use fate-mapping approaches in conjunction with three-dimensional light-sheet fluorescence microscopy and single-cell RNA sequencing to perform a comprehensive spatiotemporal analysis of the composition, origin and differentiation of subsets of macrophages within healthy and inflamed joints, and study the roles of these macrophages during arthritis. We find that dynamic membrane-like structures, consisting of a distinct population of CX_3CR1^+ tissue-resident macrophages, form an internal immunological barrier at the synovial lining and physically seclude the joint. These barrier-forming macrophages display features that are otherwise typical of epithelial cells, and maintain their numbers through a pool of locally proliferating CX_3CR1^- mononuclear cells that are embedded into the synovial tissue. Unlike recruited monocyte-derived macrophages, which actively contribute to joint inflammation, these epithelial-like CX_3CR1^+ lining macrophages restrict the inflammatory reaction by providing a tight-junction-mediated shield for intra-articular structures. Our data reveal an unexpected functional diversification among synovial macrophages and have important implications for the general role of macrophages in health and disease.

The healthy synovial cavity is a fluid-containing sterile space that lacks immune cell trafficking. During inflammatory joint diseases such as rheumatoid arthritis, increasing numbers of mononuclear phagocytes and synovial fibroblasts are thought to contribute to an expanding synovial pannus that drives the destruction of articular cartilage and bone[2–4]. Previous work that addressed the role of monocytes and macrophages during arthritis accordingly suggested that these cells promote both the onset and the progression of joint inflammation[1,5–8], a scenario that has substantially shaped our current view on the role of these cells during inflammatory disease in general.

More recent studies have questioned the concept that macrophages uniformly originate from blood monocytes, and have shown that certain subsets of macrophages populate organs during early development and subsequently self-sustain their numbers in a monocyte-independent manner[9–12]. Individual subsets of such resident macrophages have distinct transcriptional and epigenetic signatures, which suggests that they have highly specialized and tissue-specific functions[13–16]. These recent insights prompted us to question prevailing paradigms and to revisit the origin and function of synovial macrophages during homeostasis and inflammatory joint disease.

CX_3CR1 is a chemokine receptor that is specifically used by mononuclear phagocytes and their precursors[11]. To visualize the spatial distribution of CX_3CR1^+ macrophages and macrophages originating from CX_3CR1^+ precursors, respectively, we performed confocal immunofluorescence microscopy and three-dimensional light-sheet fluorescence microscopy of optically cleared knee joints in *Cx3cr1*^{cre}*Rosa26*(*R26*)-*tdTomato* mice (Fig. 1a, b, Supplementary Video 1). This approach revealed membrane-like structures of synovial $tdTomato^+$ macrophages that formed a dense physical barrier between the synovial capillary network and the intra-articular space, thereby secluding the joint space from the exterior (Fig. 1b, c, Supplementary Videos 2–4). Analysis of *ColVI*^{cre}*R26-tdTomato* reporter mice showed that these macrophages formed the uppermost cellular layer and covered the lining of collagen VI-expressing synovial fibroblasts (Extended Data Fig. 1a). In *Cx3cr1*^{GFP} mice, we confirmed that such membrane-forming lining macrophages selectively expressed CX_3CR1, stained positive for CD68 and F4/80, and constituted 40% of the total synovial macrophages under steady-state conditions. By contrast, interstitial synovial macrophages did not express CX_3CR1 (Extended Data Fig. 1a, b).

Next, we studied the response of macrophages during K/BxN serum-transfer arthritis (STA) and collagen-induced arthritis as mouse models of rheumatoid arthritis. The onset of inflammation resulted in a rapid change in the morphology and spatial orientation of CX_3CR1^+ macrophages that suddenly abrogated cell–cell contacts (Fig. 1d, Extended Data Fig. 1c–h, Supplementary Videos 5–7). Simultaneously, collagen VI-expressing fibroblasts started occupying the synovial surface (Extended Data Fig. 1f) and $Ly6G^+$ polymorphonuclear leucocytes (PMNs) appeared within the intra-articular space. Dying PMNs were subsequently removed by lining macrophages that had acquired a palisade-like shape (Fig. 1d, Extended Data Fig. 1c–e).

During embryonic development, we detected CX_3CR1^+ synovial lining macrophages by embryonic day (E)15.5 and E16.5, which indicates that synovial macrophage precursors derive from early embryonic haematopoiesis (Extended Data Fig. 2a). Adult parabiotic wild-type mice that shared circulation with *Cx3cr1*^{GFP} mice displayed chimeric myeloid cell populations within the peripheral blood, but no detectable chimerism among CX_3CR1^+ synovial lining macrophages (Fig. 2a). These data suggested that, in the adult mouse, this subset of macrophages maintained its numbers independent of blood monocytes. Analysis of Ki67 expression revealed no signs of proliferation within

[1]Department of Internal Medicine 3 - Rheumatology and Immunology, Universitätsklinikum Erlangen and Friedrich-Alexander University Erlangen-Nürnberg (FAU), Erlangen, Germany. [2]Nikolaus Fiebiger Center of Molecular Medicine, Universitätsklinikum Erlangen and Friedrich-Alexander University Erlangen-Nürnberg (FAU), Erlangen, Germany. [3]Area of Cell and Developmental Biology, Centro Nacional de Investigaciones Cardiovasculares Carlos III, Madrid, Spain. [4]Institute of Human Genetics, Universitätsklinikum Erlangen and Friedrich-Alexander University Erlangen-Nürnberg (FAU), Erlangen, Germany. [5]Department of Infection Biology, Universitätsklinikum Erlangen, Friedrich Alexander University Erlangen-Nürnberg (FAU), Erlangen, Germany. [6]Laboratory of Systems Tumor Immunology, Department of Dermatology, Universitätsklinikum Erlangen and Friedrich-Alexander University Erlangen-Nürnberg (FAU), Erlangen, Germany. [7]Department of Functional and Clinical Anatomy, Friedrich-Alexander University Erlangen-Nürnberg (FAU), Erlangen, Germany. [8]Department of Trauma Surgery, Universitätsklinikum Erlangen, Friedrich Alexander University Erlangen-Nürnberg (FAU), Erlangen, Germany. [9]Leibniz Research Institute of Molecular Pharmacology, Berlin, Germany. [10]Institute of Radiology, PIPE (Preclinical Imaging Platform Erlangen), Universitätsklinikum Erlangen and Friedrich-Alexander University Erlangen-Nürnberg (FAU), Erlangen, Germany. [11]These authors contributed equally: Stephan Culemann, Anika Grüneboom. *e-mail: gerhard.kroenke@uk-erlangen.de

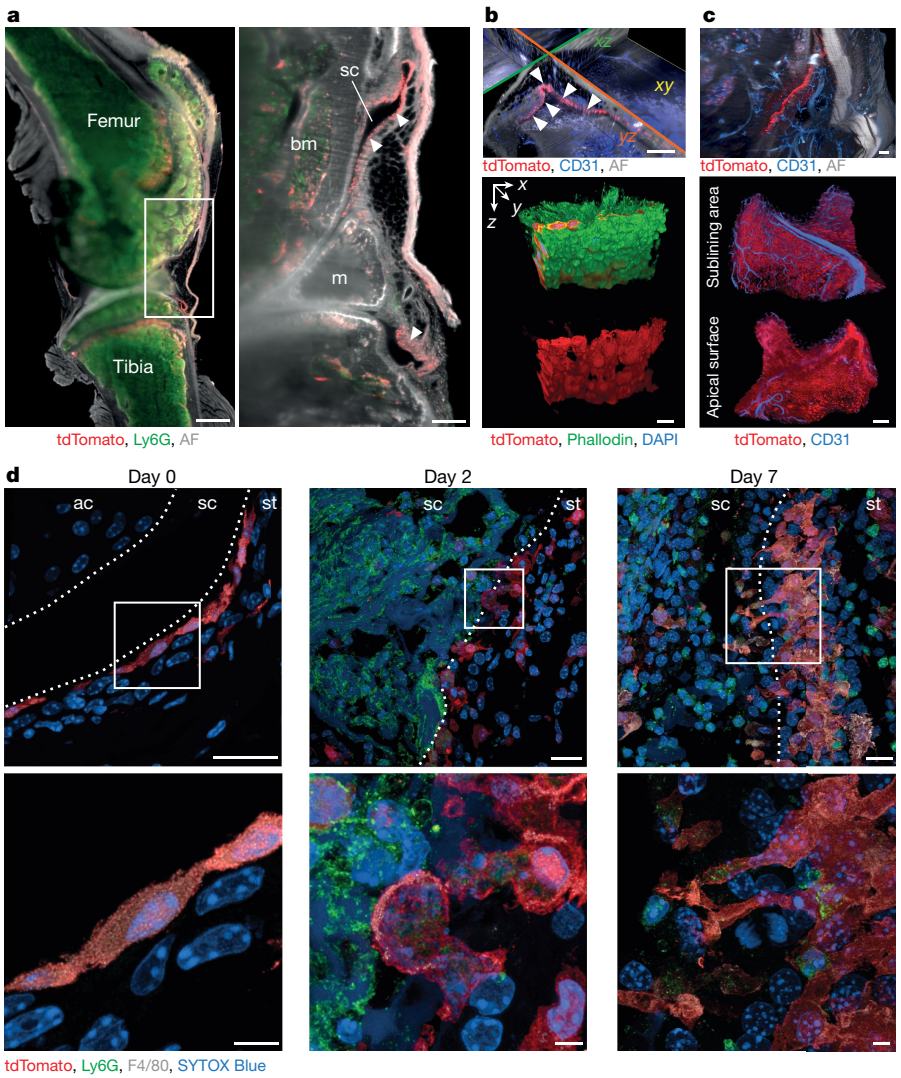

Fig. 1 | CX_3CR1^+ lining macrophages form a dynamic membrane-like structure around the synovial cavity. a–d, Representative 3D light-sheet fluorescence microscopy (LSFM) and confocal laser scanning microscopy (CLSM) of knee joints of *Cx3cr1*^{cre}*R26-tdTomato* mice (LSFM, $n = 10$; CLSM, $n = 3$). **a**, The spatial localization of synovial macrophages (tdTomato, red) and PMNs (Ly6G, green) are shown during steady state (autofluorescence (AF), grey). Arrowheads indicate the localization of the macrophage layer (tdTomato, red) at the border of the synovial cavity (sc). bm, bone marrow; m, meniscus. Scale bars, 500 μm (left), 100 μm (right). **b**, Top, LSFM analysis of the spatial arrangement of the synovial macrophage lining (tdTomato, red; arrowheads) and $CD31^+$ endothelial cells (blue) along the synovial cavity in three dimensions (AF, grey). Scale bars, 100 μm. Bottom, high-resolution 3D reconstruction of a processed CLSM scan of the synovial macrophage lining (tdTomato, red; Phalloidin, green; DAPI, blue). Scale bar, 10 μm. **c**, Three-dimensional reconstruction of LSFM data of the spatial orientation of synovial macrophages (tdTomato, red) and $CD31^+$ endothelial cells (blue) of the synovial capillary network (AF, grey). Scale bars, 100 μm. **d**, CLSM of the synovial membrane visualizing synovial macrophages (tdTomato, red) and PMNs (Ly6G, green) at the indicated time points upon the induction of K/BxN STA. Scale bars, 20 μm (top), 5 μm (bottom). ac, articular cartilage; st, synovial tissue.

the layer of CX_3CR1^+ lining macrophages (Fig. 2b), thus raising questions regarding their mechanism of repopulation and turnover. Notably, we detected clusters of proliferating $Ki67^+CX_3CR1^-$ interstitial cells within deeper layers of the synovial tissue (Fig. 2b). The Ki67 signal decreased in upper cellular layers in which CX_3CR1 expression simultaneously increased, suggestive of a pool of proliferating CX_3CR1^- interstitial macrophages that contributed to the pool of CX_3CR1^+ lining macrophages. Antibody-mediated staining of the M-CSF receptor (CSF1R) within the synovial tissue, as well as mice expressing a *Csf1r* promoter-driven GFP (*Csf1r*^{GFP} mice), showed that only CX_3CR1^- interstitial macrophages—and not CX_3CR1^+ lining macrophages—expressed CSF1R on their surface (Extended Data Fig. 2b, c). We therefore crossed *R26-tdTomato* mice with mice expressing a *Csf1r* promoter-driven and tamoxifen-dependent Cre recombinase (*Csf1r*^{creER}*R26-tdTomato*), an approach that enabled fate mapping of all cells that had expressed CSF1R at a certain developmental stage. After the start of tamoxifen treatment, lining CX_3CR1^+ macrophages acquired tdTomato expression only gradually over time, reaching 65% $tdTomato^+$ cells after 6 weeks. These data indicate that CX_3CR1^+ lining macrophages have a half-life of approximately five weeks and did indeed originate from local CSF1R-expressing CX_3CR1^- interstitial macrophages (Fig. 2c, d).

Additional characterization of parabiotic wild-type mice that shared circulation with *DsRed*-transgenic mice confirmed that, during steady state, both CX_3CR1^+ lining macrophages and CX_3CR1^- interstitial macrophages maintained their numbers independent of monocytes (Extended Data Fig. 2d–i). Although blood-derived monocytes contributed to the pool of synovial macrophages during STA, this influx only partially accounted for the inflammation-induced increase in macrophage numbers (Fig. 2e, f, Extended Data Fig. 2j, k), which indicates an increased proliferative response of tissue-resident synovial macrophages during arthritis. To differentiate between the proliferation of CX_3CR1^- interstitial macrophages and that of CX_3CR1^+ lining macrophages, we crossed *R26-tdTomato* mice with mice that express

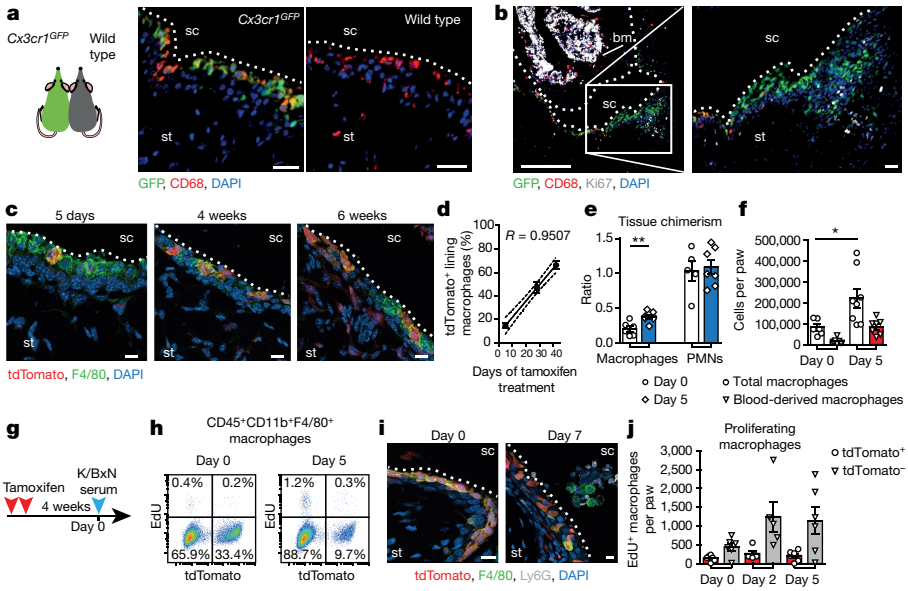

Fig. 2 | CX_3CR1^+ lining macrophages repopulate locally from CSF1R-expressing interstitial macrophages. a, Bright-field fluorescence microscopy of the synovial membrane of knees of *Cx3cr1*^{GFP} (left) and corresponding parabiotic wild-type mice (right) ($n = 3$) after 6 weeks of parabiosis (GFP, green; CD68, red; DAPI, blue). Scale bars, 25 μm. **b**, Bright-field fluorescence microscopy of the synovial membrane of knees of *Cx3cr1*^{GFP} mice ($n = 3$) determining proliferation among subsets of macrophages (GFP, green; Ki67, white; CD68, red; DAPI, blue). Scale bars, 250 μm (left), 25 μm (right). **c**, **d**, CLSM (**c**) and quantification (**d**) of tdTomato$^+$ macrophages within the synovial lining of *Csf1r*^{creER}*R26-tdTomato* mice at the indicated time points during tamoxifen treatment. $n = 3$ for each time point. In **c**, tdTomato, red; F4/80, green; DAPI, blue. Scale bars, 10 μm. In **d**, the dotted line represents the 95% confidence band of linear regression. **e**, Synovial tissue chimerism ratio of CD45$^+$CD11b$^+$F4/80$^+$ macrophages and Ly6G$^+$ PMNs of parabiotic *DsRed*/wild-type mice after 6 weeks of parabiosis under steady-state conditions (day 0: macrophage, $n = 6$; PMNs, $n = 5$) and 5 days after induction of K/BxN STA (macrophage, $n = 7$; PMNs, $n = 7$). Data are mean ± s.e.m.; two-tailed Student's *t*-test, $^{**}P = 0.004$. **f**, Absolute numbers of total and blood-derived CD45$^+$CD11b$^+$F4/80$^+$ macrophages under steady-state conditions (day 0: total macrophages, $n = 6$; blood-derived macrophages, $n = 6$) and at day 5 of STA (total macrophages, $n = 8$; blood-derived macrophages, $n = 7$). Data are mean ± s.e.m.; two-tailed Student's *t*-test, $^*P = 0.0261$. **g**–**j**, Synovial tissue of *Cx3cr1*^{creER}*R26-tdTomato* mice was analysed 4 weeks after tamoxifen pulse to determine EdU incorporation (EdU pulse 4 h before collection) into CD45$^+$CD11b$^+$F4/80$^+$ macrophages (**h**) and tdTomato expression within the synovial lining at indicated time points upon the induction of STA (F4/80, white; Ly6G, green; tdTomato, red; DAPI, blue) (**i**). Scale bars, 10 μm. **j**, Quantification of total proliferating EdU$^+$ tdTomato$^+$ and tdTomato$^-$ macrophages from the paws of tamoxifen-pulsed *Cx3cr1*^{creER}*R26-tdTomato* mice at day 0 ($n = 6$), 2 ($n = 5$), and 5 ($n = 6$) after the induction of STA. Data are mean ± s.e.m.

a gene encoding a tamoxifen-dependent Cre recombinase within the *Cx3cr1* locus (*Cx3cr1*^{creER}*R26-tdTomato* mice). Tamoxifen treatment resulted in selective and continuous expression of tdTomato in the layer of CX_3CR1^+ synovial lining macrophages. A proportion of CX_3CR1^+ blood monocytes was initially marked after systemic tamoxifen treatment, but became rapidly replaced by newly generated tdTomato$^-$ monocytes. Induction of arthritis four weeks after a systemic tamoxifen pulse or a local tamoxifen injection enabled selective fate mapping of tissue-resident CX_3CR1^+ lining macrophages during steady state and inflammation, and therefore enabled discrimination from interstitial or monocyte-derived macrophages (Fig. 2g–i, Extended Data Fig. 3a–f). In conjunction with 5-ethynyl-2′-deoxyuridine (EdU) labelling, this approach confirmed that—at the onset of arthritis—CX_3CR1^+ lining macrophages changed their spatial orientation and morphology but maintained their position, and neither proliferated nor changed in number. By contrast, CX_3CR1^- macrophages rapidly proliferated and accordingly increased in number (Fig. 2h–j, Extended Data Fig. 3f–h).

Bulk RNA sequencing of sorted steady-state CX_3CR1^+ lining macrophages and CX_3CR1^- interstitial synovial macrophages showed that they did indeed represent distinct macrophage populations, both of which are only distantly related to bone-marrow-derived macrophages (Fig. 3a, b, Extended Data Fig. 4a–e). In addition, unbiased molecular profiling of total synovial CD45$^+$CD11b$^+$Ly6G$^-$ mononuclear phagocytes by single-cell RNA sequencing (scRNA-seq) confirmed the presence of the defined cluster of differentiated CX3CR1$^+$ lining macrophages, which co-expressed immune-genes such as *Trem2* or *Vsig4* (Fig. 3c, d, Supplementary Table 1). However, scRNA-seq also revealed an additional degree of heterogeneity among CX_3CR1^- interstitial macrophages. A large number of interstitial CX_3CR1^- macrophages expressed relatively high levels mRNAs encoding MHCII and aquaporin (AQP1), whereas another population of interstitial CX_3CR1^- macrophages was characterized by the expression of *Retnla* (which encodes RELM-α) and additional genes—such as *Mrc1* or *Cd163*—that have previously been implicated in the alternative activation of macrophages (Fig. 3c, d). There was also a smaller population of interstitial *Stmn1*-expressing CX_3CR1^- macrophages that were clustered primarily as a result of their high expression of cell-cycle-associated genes such as *Cdk1*; this suggests that they were not a distinct cellular population but instead were proliferating interstitial MHCII$^+$ and AQP1$^+$$CX_3CR1^-$ macrophages (Fig. 3c, d, Extended Data Fig. 4f, g). Pseudotime analyses indicated that both RELM-α$^+$ macrophages and CX_3CR1^+ lining macrophages were differentiated macrophages that originated from the cluster of proliferating MHCII$^+$$CX_3CR1^-$ interstitial macrophages (Extended Data Fig. 4h–j). This analysis additionally suggested that the initial proliferation of interstitial MHCII$^+$$CX_3CR1^-$ macrophages was followed by an upregulation of mRNAs encoding the transcription factors MAFB and MAF, which have previously been shown to interfere with macrophage proliferation[17] (Extended Data Fig. 4j). Fate mapping in tamoxifen-treated *Csf1r*^{creER}*R26-tdTomato* mice confirmed that—in accordance with this pseudotime model—interstitial MHCII$^+$ macrophages immediately responded with the expression of tdTomato, whereas interstitial RELM-α$^+$ macrophages and CX_3CR1^+ lining macrophages only gradually acquired tdTomato expression over time (Extended Data Fig. 4k–m). Analysis of *Retnla*^{cre}*R26-tdTomato* mice and *Cx3cr1*^{creER}*R26-tdTomato* mice indicated that both subsets of macrophages represented the end stages of synovial macrophage differentiation, because we detected very few

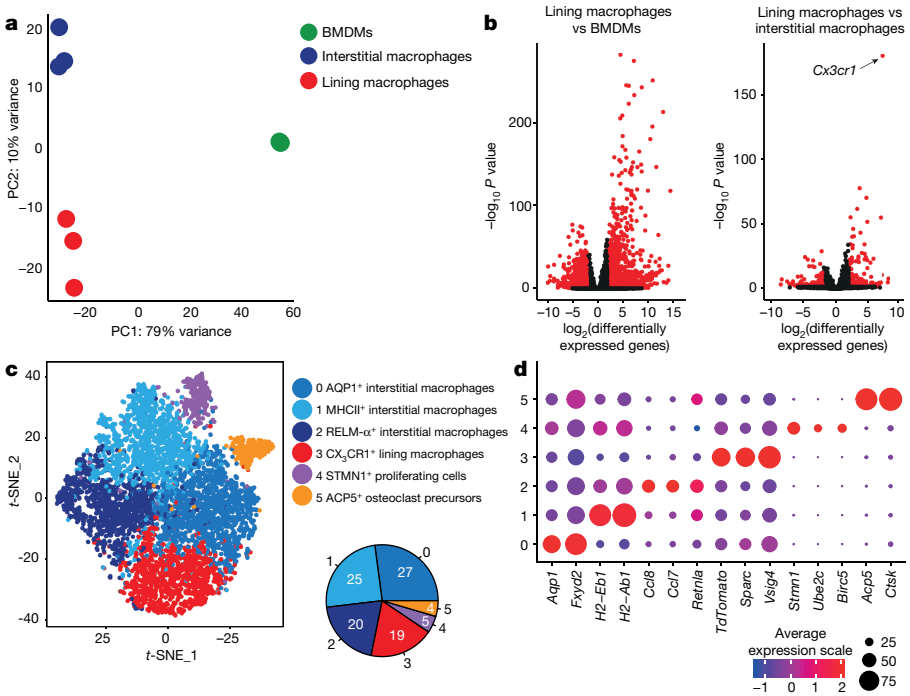

Fig. 3 | Transcriptional profiling of synovial macrophage subsets. **a**, **b**, Principal component (PC) analysis (**a**) and differential gene expression (**b**) of sorted synovial CD45$^+$CD11b$^+$F4/80$^+$GFP$^+$ lining macrophages and CD45$^+$CD11b$^+$F4/80$^+$GFP$^-$ interstitial macrophages of *Cx3cr1*^{GFP} mice, and in vitro-cultured bone-marrow-derived macrophages (BMDMs) of C57BL/6 mice during steady state ($n = 3$) after bulk RNA sequencing. Differential expression analysis was performed with DESeq2. The Wald test was used to calculate two-sided *P* values; adjustment for multiple comparisons was performed with the Benjamini–Hochberg method. **c**, **d**, *t*-distributed stochastic neighbour embedding (*t*-SNE) scRNA-seq profiles (**c**) and dot plot (**d**) showing the average expression level of selected marker genes of the respective clusters of sorted synovial CD45$^+$CD11b$^+$Ly6G$^-$ mononuclear phagocytes of *Cx3cr1*^{creER}*R26-tdTomato* mice analysed 4 weeks after tamoxifen pulse during steady-state conditions ($n = 7{,}362$ cells). The average expression level corresponds to all cells expressing the certain gene. The size of the dots represents the percentage of cells expressing a gene.

cells that had expressed RELM-α within the synovial lining (Extended Data Fig. 4n) or cells that had expressed CX$_3$CR1 within the interstitial synovial tissue (Fig. 2i). As expected, continuous diphtheria toxin (DT)-mediated depletion of CSF1R-expressing synovial macrophages in *Lysm*^{cre}*CD115DTR* mice resulted in the complete depletion of interstitial MHCII$^+$ macrophages, whereas the density of CX$_3$CR1$^+$ lining macrophages decreased only slowly with time. Cessation of DT treatment led to rapid repopulation of the pool of proliferating interstitial MHCII$^+$ macrophages, whereas the repopulation of CX$_3$CR1$^+$ lining macrophages was delayed (Extended Data Fig. 4o, p). Together, these experimental datasets supported the scRNA-seq-based pseudotime model of a dynamic continuum within resident synovial macrophages, in which proliferating MHCII$^+$CX$_3$CR1$^-$ interstitial macrophages further differentiate either into CX$_3$CR1$^+$ lining macrophages or RELM-α$^+$ interstitial macrophages (Extended Data Fig. 5q).

scRNA-seq confirmed that the onset of STA resulted in the appearance of additional clusters of mononuclear phagocytes that displayed the signature of monocyte-derived macrophages; these clusters expanded during the progression of arthritis. These mostly *Ccr2*- and *Ly6c2*-expressing cells displayed a pro-inflammatory activation profile, including the expression of *Il1b* (Extended Data Fig. 5a, b and Supplementary Table 2). Tamoxifen-pulsed *Cx3cr1*^{creER}*R26-tdTomato* mice enabled us to fate map tdTomato-expressing CX$_3$CR1$^+$ lining macrophages within the generated scRNA-seq datasets throughout the course of STA. This analysis showed that—despite their increasingly inflammatory microenvironment—lining macrophages stably maintained their immune-regulatory phenotype, including the expression of *Trem2* and of high levels of receptors that mediate the clearance of apoptotic cells, such as *Axl* and *Mfge8* (Extended Data Fig. 5b, c). A comparison of available scRNA-seq datasets from human rheumatoid arthritis synovium[8] showed that the expression profiles of two of four recently described subsets of human synovial monocytes (SC-M2 and SC-M3) matched the profiles of mouse resident synovial macrophages, whereas the other two subsets of human synovial monocytes (SC-M1 and SC-M4) resembled mouse monocyte-derived synovial macrophages (Extended Data Fig. 5d).

Notably, CX$_3$CR1$^+$ lining macrophages also displayed features that are otherwise typical of barrier-forming epithelial cells, and expressed mRNAs encoding tight-junction proteins such as JAM1 (*F11r*), ZO-1 (*Tjp1*) and claudin 5 (*Cldn5*), as well as genes involved in planar cell polarity, including *Fat4* and *Vangl2* (Extended Data Figs. 4a–e, 5b). Consistent with this, confocal immunofluorescence microscopy and transmission electron microscopy images showed the expression of tight-junction and gap-junction proteins, as well as the presence of definite tight junctions, adherens junctions, desmosomes and prominent cellular interdigitations at the cell–cell border of CX$_3$CR1$^+$ lining macrophages (Extended Data Figs. 6, 7a–d). The results of confocal immunofluorescence microscopy and flow cytometry of human synovial tissue confirmed a dense macrophage lining, consisting of closely associated TREM2$^+$ macrophages that also expressed tight-junction proteins (Extended Data Fig. 8a–c). These TREM2$^+$MHCII$^-$ macrophages comprised 10–30% of the total human synovial macrophages during steady state in samples derived from patients with osteoarthritis, but were seemingly outnumbered by TREM2$^-$ mononuclear phagocytes that dominated the disrupted synovial lining of patients with rheumatoid arthritis (Extended Data Fig. 8b–e).

Tight junctions between synovial lining macrophages rapidly disintegrated both during STA and during human rheumatoid arthritis, correlating with the changing physical density of this macrophage network during the onset and resolution of inflammation (Fig. 4a, b, Extended Data Figs. 6, 7e–i, 8a–e, 9a). Magnetic resonance imaging confirmed that this disintegration of the tight-junction-mediated barrier of macrophages was accompanied by an increased intra-articular influx of contrast agent during the initiation of STA (Fig. 4c, Extended Data

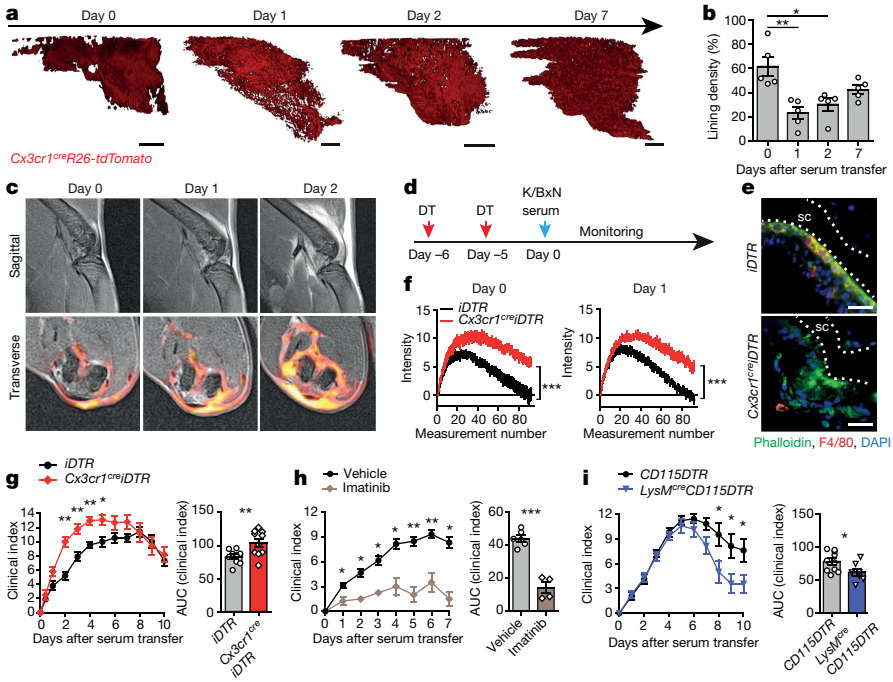

Fig. 4 | CX_3CR1^+ synovial lining macrophages provide a tight junction-mediated anti-inflammatory barrier for the joint. a, **b**, LSFM-derived 3D reconstruction of spatiotemporal changes (**a**) and calculated lining density (**b**) of tdTomato$^+$ macrophages from the knees of *Cx3cr1^{cre}R26-tdTomato* mice ($n = 5$) at the indicated days (0–7) after the induction of K/BxN STA. Data are mean ± s.e.m.; Kruskal–Wallis *H*-test with Dunn's multiple comparison test, $^{**}P = 0.0025$, $^{*}P = 0.034$. Scale bars, 100 μm. **c**, Representative magnetic resonance imaging analysis of knee joints at the indicated days ($n = 4$ each day) of STA showing sagittal T1-weighted images after the application of contrast agent (top) and transverse T1-weighted images after the application of contrast agent and merged with T1-weighted dynamic-contrast-enhanced colour maps (bottom). The merged magnetic resonance images include a colour-coded map of the area under the curve (AUC) of contrast-agent accumulation over 12 min (bottom), ranging from yellow (high AUC values) to red (low AUC values). **d**, Depletion strategy for CX_3CR1^+ lining macrophages. *Cx3cr1^{cre}iDTR* and *iDTR* control mice received 2 × 500 ng DT intraperitoneally 5 days before the administration of K/BxN serum. **e**, Representative bright-field fluorescence microscopy of the synovial lining on day 5 after the application of DT (phalloidin, green; F4/80, red; DAPI, blue). **f**, Normalized signal intensity curves from the dynamic-contrast-enhanced magnetic resonance imaging of synovial tissue from the knee joints of DT-treated mice at the indicated days of STA, over 90 measurements with intervals of 7 s in *Cx3cr1^{cre}iDTR* ($n = 8$ knee joints) and *iDTR* control mice ($n = 10$ knee joints). Data are mean ± s.e.m. of AUC, two-tailed Student's *t*-test; day 0, $^{***}P = 0.0003$; day 1, $^{***}P = 0.0001$. **g**, Clinical course of STA, including AUC of the corresponding clinical index, in *Cx3cr1^{cre}iDTR* ($n = 10$) and *iDTR* control ($n = 9$) of DT-treated mice. Data are mean ± s.e.m.; two-tailed Mann–Whitney *U*-test for clinical index with $^{*}P \leq 0.05$ and $^{**}P \leq 0.01$; two-tailed Student's *t*-test for AUC, $^{**}P = 0.0093$. **h**, Clinical course of STA, including AUC of the corresponding clinical index, in C57BL/6 wild-type mice treated with imatinib (80 μg kg^{-1}, oral gavage, twice daily, $n = 4$) or vehicle ($n = 6$) starting one day before the induction of STA. Mean ± s.e.m.; Mann–Whitney *U*-test for clinical index with $^{*}P \leq 0.05$ and $^{**}P \leq 0.01$; two-tailed Student's *t*-test for AUC with $^{***}P = 0.0001$. **i**, Clinical course of STA, including AUC of the corresponding clinical index, in *LysM^{cre}CD115DTR* ($n = 7$) and *CD115DTR* control mice ($n = 10$) treated with DT (500 ng per mouse intraperitoneally) starting one day before STA induction followed by a daily intraperitoneal injection of 100 ng DT. Mean ± s.e.m.; Mann–Whitney *U*-test for clinical index with $^{*}P \leq 0.05$; two-tailed Student's *t*-test for AUC, $^{*}P = 0.0417$.

Fig. 9b). This inflammation-associated barrier breakdown occurred after the deposition of autoantibody-containing immune complexes, which were immediately ingested by CX_3CR1^+ lining macrophages (Extended Data Fig. 9c, d). Depletion of PMNs and Ly6C^{high} inflammatory monocytes did not interfere with barrier breakdown, indicating that disintegration of tight junctions within the synovial macrophage lining resulted from an initial immune-complex-mediated activation of CX_3CR1^+ lining macrophages and was independent of the recruitment of inflammatory myeloid cells (Extended Data Fig. 9e, f). To investigate the role of tight-junction-expressing CX_3CR1^+ macrophages during arthritis, we crossed *Cx3cr1^{cre}* mice with mice containing a Cre-inducible DT receptor (*Cx3cr1^{cre}R26-iDTR* mice), allowing for the DT-mediated depletion of CX_3CR1^+ resident synovial lining macrophages. This protocol resulted in the additional depletion of a proportion of blood monocytes; however, with the exception of tissue-resident macrophages, they repopulated within 48 h (Fig. 4d, e, Extended Data Fig. 9g). Magnetic resonance imaging on day 5 after DT injection confirmed that the selective absence of CX_3CR1^+ macrophages indeed abolished the synovial barrier in healthy mice, which corresponded to the barrier breakdown observed during the onset of arthritis (Fig. 4f). Both systemic and local depletion of CX_3CR1^+ lining macrophages—as well as forced disintegration of tight junctions upon the injection of claudin 5 peptidomimetics—resulted in a disrupted barrier function, an early and exacerbated onset of arthritis and accelerated PMN influx (Fig. 4g, Extended Data Fig. 9h–k). Together, these data suggest that this subset of macrophages exerts an important immune-regulatory function by maintaining a physical and functional tight-junction-mediated barrier that secludes and protects intra-articular structures and thereby controls the onset of inflammation. Consistent with this, the tyrosine kinase inhibitor imatinib—which has been shown to stabilize the formation of tight junctions at the blood–brain barrier[18]—was found to interfere with the onset of arthritis (Fig. 4h). During STA in *Lysm^{cre}CD115DTR* mice, DT-mediated depletion of CSF1R$^+$ monocytes and macrophages occurred without directly targeting CSF1R$^-$$CX_3CR1^+$ lining macrophages—an intervention that did not affect the onset of arthritis but, in accordance with a pro-inflammatory role of monocyte-derived macrophages, accelerated the resolution of inflammation (Fig. 4i, Extended Data Fig. 9l).

Our data reveal a complex functional specialization within synovial macrophage subsets and demonstrate the divergent roles of different tissue-resident and monocyte-derived macrophages during homeostasis and inflammation. The identification of an internal, locally

renewing and protective tight-junction-mediated macrophage barrier has important implications for our general understanding of the role of macrophages in health and disease (Extended Data Fig. 10). Other tissue-resident macrophages might use similar mechanisms to fulfil related gatekeeping functions, thereby determining the onset and resolution of inflammation, modulating host defence[19], preventing neutrophil-driven inflammatory tissue damage[20] or potentially interfering with an anti-tumour immune response.

Online content

Any methods, additional references, Nature Research reporting summaries, source data, extended data, supplementary information, acknowledgements, peer review information; details of author contributions and competing interests; and statements of data and code availability are available at https://doi.org/10.1038/s41586-019-1471-1.

Received: 4 October 2018; Accepted: 5 July 2019;
Published online 7 August 2019.

1. Udalova, I. A., Mantovani, A. & Feldmann, M. Macrophage heterogeneity in the context of rheumatoid arthritis. *Nat. Rev. Rheumatol.* **12**, 472–485 (2016).
2. Firestein, G. S. & McInnes, I. B. Immunopathogenesis of rheumatoid arthritis. *Immunity* **46**, 183–196 (2017).
3. Orr, C. et al. Synovial tissue research: a state-of-the-art review. *Nat. Rev. Rheumatol.* **13**, 463–475 (2017).
4. Croft, A. P. et al. Distinct fibroblast subsets drive inflammation and damage in arthritis. *Nature* **570**, 246–251 (2019).
5. Barrera, P. et al. Synovial macrophage depletion with clodronate-containing liposomes in rheumatoid arthritis. *Arthritis Rheum.* **43**, 1951–1959 (2000).
6. Haringman, J. J. et al. Synovial tissue macrophages: a sensitive biomarker for response to treatment in patients with rheumatoid arthritis. *Ann. Rheum. Dis.* **64**, 834–838 (2005).
7. Misharin, A. V. et al. Nonclassical Ly6C$^-$ monocytes drive the development of inflammatory arthritis in mice. *Cell Rep.* **9**, 591–604 (2014).
8. Zhang, F. et al. Defining inflammatory cell states in rheumatoid arthritis joint synovial tissues by integrating single-cell transcriptomics and mass cytometry. *Nat. Immunol.* **20**, 928–942 (2019).
9. Ginhoux, F. et al. Fate mapping analysis reveals that adult microglia derive from primitive macrophages. *Science* **330**, 841–845 (2010).
10. Schulz, C. et al. A lineage of myeloid cells independent of Myb and hematopoietic stem cells. *Science* **336**, 86–90 (2012).
11. Yona, S. et al. Fate mapping reveals origins and dynamics of monocytes and tissue macrophages under homeostasis. *Immunity* **38**, 79–91 2013).
12. Hashimoto, D. et al. Tissue-resident macrophages self-maintain locally throughout adult life with minimal contribution from circulating monocytes. *Immunity* **38**, 792–804 (2013).
13. Rosas, M. et al. The transcription factor Gata6 links tissue macrophage phenotype and proliferative renewal. *Science* **344**, 645–648 (2014).
14. Okabe, Y. & Medzhitov, R. Tissue-specific signals control reversible program of localization and functional polarization of macrophages. *Cell* **157**, 832–844 (2014).
15. Lavin, Y. et al. Tissue-resident macrophage enhancer landscapes are shaped by the local microenvironment. *Cell* **159**, 1312–1326 (2014).
16. Chakarov, S. et al. Two distinct interstitial macrophage populations coexist across tissues in specific subtissular niches. *Science* **363**, eaau0964 (2019).
17. Aziz, A., Soucie, E., Sarrazin, S. & Sieweke, M. H. MafB/c-Maf deficiency enables self-renewal of differentiated functional macrophages. *Science* **326**, 867–871 (2009).
18. Armulik, A. et al. Pericytes regulate the blood–brain barrier. *Nature* **468**, 557–561 (2010).
19. Cronan, M. R. et al. Macrophage epithelial reprogramming underlies mycobacterial granuloma formation and promotes infection. *Immunity* **45**, 861–876 (2016).
20. Uderhardt, S., Martins, A. J., Tsang, J. S., Lämmermann, T. & Germain, R. N. Resident macrophages cloak tissue microlesions to prevent neutrophil-driven inflammatory damage. *Cell* **177**, 541–555.e17 (2019).

METHODS

For additional information on materials used, see Supplementary Table 3.

Ethical compliance. We complied with all relevant ethical regulations in terms of animal experiments and human samples in this study. All animal experiments conducted at the University of Erlangen were performed in accordance with German guidelines and laws, were approved by local animal ethic committees of the Regierung von Mittelfranken and were conducted according to the guidelines of the Federation of European Laboratory Animal Science Associations. Parabiosis experiments were approved by the Animal Care and Ethics Committee of the Centro Nacional de Investigaciones Cardiovasculares and local authorities.

Synovial biopsies were obtained from knee joints of patients diagnosed with osteoarthritis or rheumatoid arthritis. Patients with rheumatoid arthritis fulfilled the 2010 EULAR/ACR criteria of rheumatoid arthritis. All patients were ≥18 years of age. Patients with osteoarthritis were recruited at the Department of Trauma Surgery, University Hospital Erlangen and patients with rheumatoid arthritis were recruited at the Department of Internal Medicine 3 - Rheumatology and Immunology, University Hospital Erlangen. All patients signed an informed consent form, which was approved by the local ethics committee of the University Hospital Erlangen.

Mice. For all experiments, mice of both sexes were used. For details regarding mouse strains, see Supplementary Table 3. All mice used were aged between 8 and 18 weeks, unless stated otherwise. No statistical methods were used to predetermine sample size.

To generate *Cx3cr1^{cre}R26-tdTomato* mice, STOCK Tg(Cx3cr1^{cre})MW126Gsat/Mmucd mice (identification number 036395-UCD) were obtained from the Mutant Mouse Regional Resource Center (MMRC), a National Institutes of Health (NIH)-funded strain repository, and were donated to the MMRRC by the National Institute of Neurological Disorders and Stroke (NINDS)-funded GENSAT BAC transgenic project. B6.129P2(C)-*Cx3cr1$^{tm2.1(cre/ERT2)Jung}$*/J (*Cx3cr1^{ERcre}*), FVB-Tg(Csf1r-cre/Esr1*)1Jwp/J (*CSF1R^{ERcre}*), C57BL/6-Gt(ROSA)26Sortm1(HBEGF)Awai/J (*iDTR*), B6;129S6-*Gt(ROSA)26Sor$^{tm9(CAG-tdTomato)Hze}$*/J (*tdTomato*), C57BL/6-Tg(Csf1r-HBEGF/mCherry)1Mnz/J (*CD115DTR*) and B6.129P-Cx3cr1tm1Litt/J (*Cx3cr1^{GFP}*) mice were purchased from Jackson Laboratories. These mice were bred and housed at the animal facilities of the University of Erlangen under specific-pathogen-free conditions. *ColVI^{cre}* mice were generated in the laboratory of G. Kollias and have previously been described[21]. *Retnla^{cre}R26-tdTomato* mice were generated in the laboratory of D. Vöhringer[22].

In vivo treatments and arthritis induction. K/BxN STA was induced by the injection of K/BxN serum collected from arthritic K/BxN mice. Clinical development of arthritis was evaluated using a clinical index ranging from 0 (minimum) to 16 (maximum), which represents a cumulative score of 0 to 4 for each paw, with 0 = no signs of inflammation; 1 = minor swelling and reddening of a paw, or affecting only single digits; 2 = moderate swelling and erythema, or affecting multiple digits per paw; 3 = severe swelling and erythema affecting the whole paw; 4 = maximum swelling and erythema. Measurements of hind-paw swelling were conducted using dial thickness gauges (Peacock).

Cx3cr1^{creER}tdTomato mice were treated systemically with 4 mg tamoxifen dissolved in peanut oil intraperitoneally (i.p.) twice within 48 h. *Csf1r^{creER}R26-tdTomato* mice were fed with tamoxifen-containing food (400 mg kg^{-1} tamoxifen citrate, Envigo) for 5 days, 4 weeks or 6 weeks. Local administration of (*Z*)-4-hydroxytamoxifen (Sigma-Aldrich, H7904) was performed by intra-articular injection of 25 µl of (*Z*)-4-hydroxytamoxifen (2 mM) dissolved in PBS/4% ethanol into the right knee joint. Five days after injection, K/BxN serum transfer arthritis was induced. Mice were analysed seven days after the induction of arthritis.

For systemic administration of DT, *Cx3cr1^{cre}iDTR* mice received 500 ng DT per mouse i.p. on 2 consecutive days, beginning 6 days before the induction of STA. Local depletion of macrophages in *Cx3cr1^{cre}iDTR* mice was induced by the injection of 50 ng DT in 50 µl PBS directly into the hind paw 3 days before the induction of STA. The contralateral hind paw was injected with PBS and served as a control.

LysM^{cre}CD115DTR mice received a single dose of 500 ng DT per mouse (i.p.) 1 day before the induction of arthritis followed by daily injections of 100 ng DT per mouse (i.p.). To study the depletion of synovial macrophages in *LysM^{cre}CD115DTR* mice under healthy conditions, 500 ng DT per mouse was injected intraperitoneally 3 times a week until day 10.

The claudin peptidomimetics[23] (C5C2, sequence SSVVQSTGHMQSKV YESVLALSAEVQAAR-NH2) and scrambled variant (C5C2scr, AHLVRSVSD VMQSQTGKTSESYSAVQLVA-NH2) were dissolved in PBS and injected intravenously (i.v.) (3.5 µmol kg^{-1}) one day before and one day after the induction of STA for clinical evaluation, with a single injection one day before the induction of STA for the magnetic resonance imaging experiments.

Imatinib (80 µg kg^{-1}) was given orally twice a day, starting one day before the induction of STA. Imatinib was dissolved in aqueous vehicle solution containing 0.5% (hydroxypropyl)cellulose and 0.05% TWEEN 80.

K/BxN serum IgG was isolated with protein-G Gravi-Trap (GE Healthcare, 28-9852-55) and labelled using SAIVI Alexa Fluor 647 Antibody/Protein 1 mg-Labelling Kit. Labelled IgGs were injected i.v. with K/BxN serum at a ratio of 1:4.

Collagen-induced arthritis was induced as previously described[24]. In brief, C67BL/6 mice were immunized by intradermal injection of an emulsion of 200 µg of chicken type II collagen (Sigma-Aldrich, C-930) with 250 µg heat-inactivated *Mycobacterium tuberculosis* H37RA in incomplete Freund's adjuvant (Sigma-Aldrich, F5506) at day 0 and day 21.

Depletion of neutrophils and Ly6C$^+$ monocytes was performed by i.v. injection of 200 µg InVivoPlus anti-mouse Ly6G/Ly6C (Gr-1) (clone: RB6-8C5, Bio X Cell, BP0075) one day before K/BxN serum transfer. InVivoPlus rat IgG2b isotype control, anti-keyhole limpet haemocyanin (200 µg, i.v., clone: LTF-2, Bio X Cell, BP0090) served as control.

The severity of both K/BxN STA and collagen-induced arthritis was scored in a blinded manner. Mice were not randomized before the experiment.

Parabiosis. Parabiosis was performed following a previously described procedure[25]. Mice were shaved under anaesthesia at the corresponding lateral region and incisions were made from the olecranon to the knee joint of each mouse. Olecranons and knee joints of partner mice were tied together by a single 5-0 polypropylene suture. Dorsal and ventral skins were stitched up forming a continuous suture. Finally, each mouse received a single injection of buprenorphine subcutaneously. Analysis was performed as indicated six or nine weeks after surgery. The tissue chimerism was calculated as the quotient of the ratios of partner-derived macrophages of synovial joints and the ratio of partner-derived monocytes in the blood as quantified by flow cytometry. A tissue-to-blood chimerism of one thus represents an equal ratio between blood and tissue.

Flow cytometry and fluorescence-activated cell sorting. For isolation of synovial macrophages, hind paws were dissected by removing skin, muscle and tendons. Cells were dissociated by incubation for 45 min in a digestion medium consisting of RPMI medium, 10% heat-inactivated fetal calf serum (FCS), collagenase (2 mg ml^{-1}) from *Clostridium histolyticum* (Sigma-Aldrich, C5138-1G) and 0.03 mg ml^{-1} DNase (Sigma-Aldrich, 9003-98-9). After washing with PBS containing 2% heat-inactivated FCS and 2 mM EDTA, cells were blocked with 10% rat serum in PBS for 10 min at room temperature and stained with fluorophore-conjugated antibodies for 20 min at 4 °C. After washing with PBS, cells were resuspended in FACS buffer (PBS, 2% FCS). EdU, which was injected intraperitoneally (50 mg kg^{-1}) 4 h before collecting the cells, was detected using the EdU base click EdU-Flow Cytometry Kit 488 (BCK-FC488-100).

Human synovial tissue was dissociated in digestion medium containing RPMI medium, 10% heat-inactivated fetal calf serum (FCS), collagenase (2 mg ml^{-1}) from *C. histolyticum* (Sigma, C5138-1G) and 0.03 mg ml^{-1} DNase (Sigma, 9003-98-9) at 37 °C for 45 min. After washing with PBS, cells were incubated with Zombie Aqua (1:1,000, BioLegend) for 15 min at room temperature. Dissociated cells were fixed with 4% PFA/PBS, incubating for 15 min at room temperature. After washing with 1% BSA/PBS, cells were resuspended in saponin-based permeabilization buffer containing the following antibodies: CD11b-AF488, MHC II-PE, CD14-PeCy7, CD45-AF700, CD1c-PerCP/Cy5.5, CD20-BV421, CD15-BV421 and TREM2-APC, overnight at 4–8 °C.

Flow cytometry was performed with a CytoFLEX S, Beckman Coulter. Sorting of cells was performed with a MoFlo XDP, Beckman Coulter and the Summit Software System. Data were analysed with Kaluza (Beckman Coulter, v.1.5a), CytExpert (Beckman Coulter, v.2.2.0.97) or FlowJo (v.7.6.5).

Bulk RNA sequencing of sorted CX_3CR1^+ and CX_3CR1^- macrophages and bone-marrow-derived macrophages. Tissues from *Cx3cr1^{GFP}* mice were prepared for sorting of synovial macrophages as described in the section 'Flow cytometry and fluorescence-activated cell sorting'. Macrophages were defined as CD45$^+$CD11b$^+$F4/80$^+$. Expression of enhanced GFP discriminated CX_3CR1^+ lining and CX_3CR1^- macrophages. For generating BMDMs, bone marrow cells were isolated from femurs of C57BL/6 mice and cultured for one day in DMEM (10% FCS, 1% penicillin–streptomycin). Non-adherent macrophage precursors were cultivated and differentiated to macrophages for 5 days in M-CSF-conditioned DMEM medium (10% FCS, 1% penicillin–streptomycin). Isolation of RNA was performed using the RNeasy Mini kit (Qiagen, 74104). Libraries were subjected to single-end sequencing (101 bp) on a HiSeq-2500 platform (Illumina). The obtained reads were converted to .fastq format and demultiplexed using bcl2fastq v2.17.1.14. Quality filtering was performed using cutadapt v. 1.15; then reads were mapped against the mouse reference genome (Ensembl GRCm38, release 91) using the STAR aligner v.2.5.4a[26], and a STAR genome directory created by supplying the Ensembl gtf annotation file (release 91). Read counts per gene were obtained using featureCounts program v.1.6.1[27] and the Ensembl gtf annotation file. The subsequent analyses were performed using R v.3.5.0. In particular, differential expression analysis was performed with the DESeq2 package v.1.20.0[28] and plots were generated with the ggplot2_2.2.1 package.

Quantitative real-time PCR of sorted CX_3CR1^+ macrophages and BMDMs. RNA of sorted GFP^+ macrophages from *Cx3cr1*^{GFP} mice and BMDMs was isolated using the RNeasy Mini kit (Qiagen, 74104). Reverse transcription of total RNA was performed with human leukaemia virus reverse transcriptase using the Gene Amp RNA PCR kit (Applied Biosystems) and oligo$(dT)_{16}$ primers (Invitrogen). Quantification of gene expression was performed as previously described[29]. The following primer sequences were used: β-actin: TGT CCA CCT TCC AGC AGA TGT (sense), AGC TCA GTA ACA GTC CGC CTA GA (antisense); ZO-1: GCT AAG AGC ACA GCA ATG GA (sense), GCA TGT TCA ACG TTA TCC AT (antisense); claudin 5: TTA AGG CAC GGG TAG CAC TCA CG (sense), TTA AGG CAC GGG TAG CAC TCA CG (antisense), claudin 10: TGG TGT GTG GTG TTG GAG GGT TTG G (sense), TGG AAG GAG CCC AGA GCG TTA CCT G (antisense)[30,31].

Single-cell sequencing of sorted myeloid cells of different stages of arthritis. Sorted $CD45^+CD11b^+Ly6G^-$ synovial cells of hind paws of mice at steady state (day 0) and at different stages of K/BxN STA (day 1, day 2 and day 5 after serum transfer) were subjected to 10x Chromium Single Cell 3′ Solution v2 library preparation according to the manufacturer's instructions. Library sequencing was performed on an Illumina HiSeq 2500 sequencer to a depth of 100 million reads each. Reads were converted to .fastq format using mkfastq from cellranger 2.1.0 (10x Genomics). Reads were then aligned to the mouse reference genome (mm10, Ensembl annotation release 91) including the additional sequence and feature annotation for tdTomato. Alignment was performed using the count command from cellranger 2.1.0 (10x Genomics). Primary analysis, quality control filtering (gene count per cell, unique molecular identifier count per cell, percentage of mitochondrial transcripts), clustering, cell-cycle phase scoring based on canonical markers and regression, identification of cluster markers and visualization of gene expression were performed using the Seurat (v.2.3)[32] package for R.

Construction of single-cell trajectories, identification of genes changing as a function of pseudotime and clustering of genes by pseudotemporal expression patterns were performed using the Monocle 2 package for R. Pseudotime calculations were performed on the top 1,000 differentially expressed genes between clusters[33,34]. For gene ontology enrichment analysis of biological processes, the PANTHER Statistical Overrepresentation Test (http://www.pantherdb.org) was used.

Cryo-sectioning of mouse knee joints. Mouse long bones were fixed in 4% PFA/PBS (pH 7.4) for 12 h at 4–8 °C, incubated for 10 days in decalcification buffer (14% EDTA free acid, NH_4OH, pH 7.2) and embedded in OCT Compound (Sakura Finetek). A Leica CM 3050 S cryostat and Cryofilm Type 2C(9) (C-MK001-A2, Section-Laboratory) were used for the generation of 7-μm-thick histological sections.

Histological immunofluorescence staining. For staining cryo-sections of mouse knee joints, samples were blocked with rat serum or 0.2% BSA and permeabilized with 0.1% saponin in PBS for 1 h at room temperature. For immunofluorescence staining, the antibodies listed in Supplementary Table 3 were used. Staining was performed for 4 h at room temperature or overnight at 4 °C using the indicated antibodies diluted in blocking solution. Unbound primary antibodies were washed off with DPBS and unlabelled primary antibodies were counterstained with donkey anti-Rabbit IgG AF488 or AF647 antibody in blocking solution for 4 h at room temperature and washed with DPBS. Joint sections were stained with DAPI or SYTOX Blue by incubating samples for 10 min (DAPI) or 1 h (SYTOX Blue) at room temperature. Samples were washed three times with DPBS, once with water for injection, and embedded onto a coverslip with Dako Fluorescence Mounting Medium.

Bright-field fluorescence microscopy of histological samples. Histological joint samples were imaged with an upright Nikon Eclipse Ni-U microscope, using a 10× (numerical aperture (NA) 0.30), 20× (NA 0.50) or 40× (NA 0.75) CFI Plan Fluor objective for varying magnifications. The halogen lamp excitation light (of wavelength λ_{ex}) as well as the emitted light (λ_{em}) was filtered specifically according to individual excitation/emission profiles: DAPI λ_{ex}: 390/18 nm and λ_{em}: 460/60 nm, fluorescein isothiocyanate (FITC)/AF488 λ_{ex}: 475/35 nm and λ_{em}: 530/43 nm, tdTomato/AF594 λ_{ex}: 542/20 nm and λ_{em}: 620/52 nm, AF647 λ_{ex}: 628/40 nm and λ_{em}: 692/40 nm. The generated data were processed with Imaris software.

Confocal laser scanning microscopy of histological samples. For high-magnification imaging of histological joint sections, a Leica TCS SP 5 II confocal microscope with acousto-optic tunable filter and acousto-optical beam splitter, and hybrid detector (HyD) on a DMI6000 CS frame was used. Imaging of coverslip-embedded samples was performed using an HCX PL APO 100× oil objective with a NA of 1.44. Fluorescence signals were generated via sequential scans, exciting tdTomato using a diode-pumped solid-state laser at 561 nm and detecting with a HyD at 600–650 nm. The second sequence for visualizing Alexa Fluor 488 or FITC-labelled staining included an argon laser at 488 nm for excitation and a HyD detector at 500–550 nm. A third imaging sequence involved a simultaneous excitation of SYTOX Blue with a 458-nm argon laser and of Alexa Fluor 647 staining with a 633-nm helium-neon laser. SYTOX Blue was detected by HyD at 470–520 nm and Alexa Fluor signals were detected by HyD at 650–700 nm. Generated images were deconvoluted with Huygens Professional and 3D-reconstructed with Imaris software.

Spinning disk confocal microscopy of histological samples. For spinning disk confocal microscopy of histological joint sections, an inverted Zeiss Spinning Disc Axio Observer.Z1 with a Yokogawa CSU-X1M 5000 spinning disk unit, a LD C-Apochromat 63× water immersion objective (NA 1.15) and an Evolve 512 EMCCD camera was used. Fluorescence signals were excited and detected as follows: DAPI λ_{ex}: 405 nm DPSS laser and λ_{em}: 445/50 nm BP filter, AF488 λ_{ex}: 488 nm DPSS laser and λ_{em}: 525/50 nm BP filter, tdTomato λ_{ex}: 561 nm DPSS laser and λ_{em}: 605/70 nm BP filter. Acquired images were processed via Zen Blue 2.3 image acquisition software.

Optical clearing of mouse joint samples. Optically cleared samples for light-sheet fluorescence microscopy were generated as previously described[35]. In detail, mice received 2.5 μg Ly6G-AF647 or CD31-AF647 in PBS i.v. and were euthanized after 1 h. Mice were perfused with 5 mM EDTA/PBS and perfusion-fixed with 4% PFA/PBS (pH 7.4). Knee joints were relieved from muscle tissue and post-fixed in 4% PFA/PBS (pH 7.4) for 4 h at 4–8 °C with gentle shaking. Tissue fixation was followed by dehydration. Tissue dehydration was performed by increasing the proportion of ethanol according to the following series: 50%, 70% and two consecutive incubations with 100% ethanol each. The 50% and 70% ethanol solutions were generated by diluting 100% ethanol with water for injection, and their pH values were adjusted to 9.0 using NaOH. All tissue dehydration steps were performed at 4–8 °C in gently shaking 5 ml tubes. After tissue dehydration, joint samples were transferred to ethyl cinnamate and incubated at room temperature for 6 h.

LSFM of optically cleared samples. LSFM of optically cleared mouse knee joints was performed with a LaVison BioTec Ultramicroscope II including an Olympus MVX10 zoom body (Olympus), a LaVision BioTec Laser Module, and an Andor Neo sCMOS Camera with a pixel size of 6.5 μm. Detection optics with an optical magnification range from 1.263 to 12.63 and a NA of 0.5 were used.

For visualization of general tissue morphology, a 488-nm optically pumped semiconductor laser (OPSL) was used to generate autofluorescent signals. For tdTomato excitation, a 561-nm OPSL and for CD31-AF647 or Ly6G-AF647 excitation, a 647-nm diode laser was used. Emitted wavelengths were detected with specific detection filters: 525/50 nm for autofluorescence, 620/60 nm for tdTomato, and 680/30 nm for CD31-AF647 or Ly6G-AF647. The optical zoom factor of the measurements varied from 1.26 to 8 and the light-sheet thickness ranged from 5 to 10 μm.

Three-dimensional lining density analysis. The density of the synovial lining was analysed by a volumetric ratio of $tdTomato^+$ lining macrophages to synovial tissue.

Three-dimensional reconstruction of LSFM-scanned mouse knee joints was performed using Imaris software. The synovial lining was optically separated from the joint tissue by manual surface rendering. Volumes of the isolated synovial lining tissue and $tdTomato^+$ lining cells were fully automatically rendered by the Imaris volume rendering tool with a size threshold of 5 μm for $tdTomato^+$ cells and 10 μm for synovial tissue. The percentage lining density was calculated from the ratio of cell and tissue volumes.

Magnetic resonance imaging. Magnetic resonance imaging (MRI) data were acquired using the ClinScan 70/30 7 T MRI System (Bruker) and a RatBrain 1H-Surface Coil (Bruker). Before measurement, mice were anaesthetized and a tail-vein catheter was placed for the injection of contrast agent during measurement. The body temperature was kept constant with a heating blanket and the respiration rate was monitored constantly. Anaesthesia was maintained with isoflurane. Dynamic contrast-enhanced (DCE) MRI was conducted using a fast low angle shot (FLASH) sequence with repetition time (TR)/echo time (TE): 2.92 ms/0.88 ms, flip angle: 25°, voxel size: 0.182 × 0.182 × 0.7 mm, matrix 192 × 192, acquisition time of 12 min and 100 measurements. The contrast agent (0.1 mmol kg^{-1} Gadovist, Bayer) was injected after 40 s over a time period of 10 s. Sagittal and transverse T1-weighted images were acquired after running the DCE sequence with the following specifications: voxel size: 0.078 × 0.078 × 0.7 mm, TR/TE: 500 ms/9 ms, matrix 448 × 448. The mean contrast agent enrichment over time in the synovial tissue set as region of interest was analysed using Horos software (https://horosproject.org/).

Transmission electron microscopy. Mouse knee joints were fixed in ITO fixation solution containing 2.5% glutaraldehyde (Roth, 4157.1), 2.5% paraformaldehyde (Roth, 0335.3), 0.1 M cacodylate buffer (Roth, 5169.2) and 0.3% picric acid dissolved in phosphate-buffered saline (pH 7.3) for two days, decalcified in cacodylate buffer (0.1 M) containing 14% EDTA for two weeks and finally embedded in Epon. Ultra-thin sections (Microtome, Reichert Ultracut S) of 50 nm were contrasted with uranyl acetate and lead(II) acetate trihydrate and finally imaged with a transmission electron microscope (JEM 1400 Plus, Jeol).

Statistics and reproducibility. For calculations of statistical significance, GraphPad Prism 5 was used. Data are presented as mean ± s.e.m. and were analysed using the two-sided Student's *t*-test, the Mann–Whitney *U*-test or the Kruskal–Wallis *H*-test with Dunn's multiple comparisons test as post hoc procedure unless stated otherwise. *P* values less than 0.05 were considered significant. LSFM of Fig. 1a is representative of ten individual mice. Experiments in Fig. 1b, c were performed three times. Bright-field microscopy (BFM), CLSM and LSFM images of Fig. 1d and Extended Data Fig. 1c–e are representative images of three experiments with three mice each per day. Extended Data Fig. 1a, f are representative images of three individual mice. Flow cytometry experiments in Extended Data Fig. 1a were performed three times. Images in Extended Data Fig. 1g, h are representative of at least three individual mice. Parabiosis experiments and analysis of Fig. 2a, e, f and Extended Data Fig. 2d–k were performed once each per parabiotic combination and time points and images were representative of at least three mice. Images in Fig. 2b and Extended Data Fig. 2b, c are representative of three individual mice. Images in Extended Data Fig. 2a are representative of three individual mice. Flow cytometry experiments in Fig. 2h, j and Extended Data Fig. 3f–h were performed once. Images in Fig. 2i and Extended Data Fig. 3e are representative of three mice per group. Experiments in Extended Data Fig. 3a–c were performed twice. Experiments in Extended Data Fig. 3e are representative of three individual mice per day. Bulk RNA-seq analysis of Fig. 3a, b and Extended Data Fig. 4a–c was performed once. RNA quantification experiments in Extended Data Fig. 4d using the sorting strategy in Extended Data Fig. 4a was performed once. Single-cell RNA profiling experiments of sorted cells of Fig. 3c, d and Extended Data Figs. 4f–j, 5a–c comprise four different datasets of four individual mice at steady state, day 1, day 2 and day 5 after K/BxN serum transfer. Images in Extended Data Fig. 4k are representative of three individual mice of experiments that are shown in Extended Data Fig. 4l, m that were performed once. Images in Extended Data Fig. 4n are representative of two individual mice. The experiments in Extended Data Fig. 4o, p were performed once and show representative images of one mouse per group and the corresponding statistics for each mouse. Extended Data Fig. 6 shows representative images of four individual mice. Images in Extended Data Fig. 7a are representative of four individual mice. Transmission electron micrographs in Extended Data Fig. 7 are representative of three mice per time point. CLSM images in Extended Data Fig. 8a are representative of six mice per time point. CLSM of Extended Data Fig. 8b, c and the corresponding lining density analysis are representative of two patients with osteoarthritis and three patients with rheumatoid arthritis. Flow cytometry analyses are representative of three patients with osteoarthritis and two patients with rheumatoid arthritis. Experiments in Fig. 4a, b and Extended Data Fig. 9a were performed twice. MRI experiments of Fig. 4c, f and Extended Data Fig. 9k were performed once. BFM images of Fig. 4e are representative of 3 mice per group. Mouse experiments of Fig. 4g and Extended Data Fig. 9j were performed twice. Mouse experiments of Fig. 4h, i and Extended Data Fig. 9i were performed once. Images in Extended Data Fig. 9c, d are representative of three individual mice per time point. Images in Extended Data Fig. 9h are representative of three individual mice per group. Flow cytometry experiments in Extended Data Fig. 9g, l were performed once and confirmed the depletion efficiency. Experiments shown in Supplementary Videos 1, 3 and 4 were performed three times, that in Supplementary Video 2 was performed once, and those in Supplementary Videos 5, 6 and 7 were each performed five times.

Reporting summary. Further information on research design is available in the Nature Research Reporting Summary linked to this paper.

Data availability

The data that support the plots within this paper and other findings of this study are available from the corresponding author upon request. The bulk and single-cell RNA-seq data are available as part of the Gene Expression Omnibus (GEO) SuperSeries GSE134691.

21. Armaka, M. et al. Mesenchymal cell targeting by TNF as a common pathogenic principle in chronic inflammatory joint and intestinal diseases. *J. Exp. Med.* **205**, 331–337 (2008).
22. Krljanac, B. et al. RELMα-expressing macrophages protect against fatal lung damage and reduce parasite burden during helminth infection. *Sci. Immunol.* **4**, eaau3814 (2019).
23. Dithmer, S. et al. Claudin peptidomimetics modulate tissue barriers for enhanced drug delivery. *Ann. NY Acad. Sci.* **1397**, 169–184 (2017).
24. Pfeifle, R. et al. Regulation of autoantibody activity by the IL-23–T_H17 axis determines the onset of autoimmune disease. *Nat. Immunol.* **18**, 104–113 (2017).
25. Casanova-Acebes, M. et al. Rhythmic modulation of the hematopoietic niche through neutrophil clearance. *Cell* **153**, 1025–1035 (2013).
26. Dobin, A. et al. STAR: ultrafast universal RNA-seq aligner. *Bioinformatics* **29**, 15–21 (2013).
27. Liao, Y., Smyth, G. K. & Shi, W. featureCounts: an efficient general purpose program for assigning sequence reads to genomic features. *Bioinformatics* **30**, 923–930 (2014).
28. Love, M. I., Huber, W. & Anders, S. Moderated estimation of fold change and dispersion for RNA-seq data with DESeq2. *Genome Biol.* **15**, 550 (2014).
29. Ipseiz, N. et al. The nuclear receptor Nr4a1 mediates anti-inflammatory effects of apoptotic cells. *J. Immunol.* **192**, 4852–4858 (2014).
30. Katsuno, T. et al. Deficiency of zonula occludens-1 causes embryonic lethal phenotype associated with defected yolk sac angiogenesis and apoptosis of embryonic cells. *Mol. Biol. Cell* **19**, 2465–2475 (2008).
31. Ohtsuki, S., Yamaguchi, H., Katsukura, Y., Asashima, T. & Terasaki, T. mRNA expression levels of tight junction protein genes in mouse brain capillary endothelial cells highly purified by magnetic cell sorting. *J. Neurochem.* **104**, 147–154 (2008).
32. Butler, A., Hoffman, P., Smibert, P., Papalexi, E. & Satija, R. Integrating single-cell transcriptomic data across different conditions, technologies, and species. *Nat. Biotechnol.* **36**, 411–420 (2018).
33. Trapnell, C. et al. The dynamics and regulators of cell fate decisions are revealed by pseudotemporal ordering of single cells. *Nat. Biotechnol.* **32**, 381–386 (2014).
34. Qiu, X. et al. Single-cell mRNA quantification and differential analysis with Census. *Nat. Methods* **14**, 309–315 (2017).
35. Klingberg, A. et al. Fully automated evaluation of total glomerular number and capillary tuft size in nephritic kidneys using lightsheet microscopy. *J. Am. Soc. Nephrol.* **28**, 452–459 (2017).

Acknowledgements We thank C. Stoll, A. Klej, L. Seyler, R. Palmisano and the Optical Imaging Center Erlangen for technical assistance. M. Mroz and U. Appelt provided help during cell sorting and W. Baum and U. Baschant helped to generate K/BxN serum. This work was supported by the Deutsche Forschungsgemeinschaft (DFG – FG 2886 "PANDORA" - B01/A03 to G.K. and G.S., the CRC1181-A03/A01/A02/Z2 to G.K., G.S., D.V. and T.B. and the GK 1660 to G.K.), the Emerging Field Initiative (EFI) of the Friedrich-Alexander University Erlangen-Nürnberg (FAU) and the STAEDTLER Stiftung (EFI_Verbund_Med_05_MIRACLE to G.K. and T.B.), the Bundesministerium für Bildung und Forschung (BMBF) (METARTHROS to G.K. and G.S.) and the European Union (Horizon 2020 ERC-2014-StG 640087 - SOS to G.K and Horizon 2020 ERC-2018-SyG nanoSCOPE and RTCure to G.S.). J.Á.N.-Á. was supported by fellowship SVP-2014-068595 and A.H. by grant SAF2015-65607-R from Ministerio de Ciencia, Investigacion y Universidades (MCIU), and co-funding by Fondo Europeo de Desarrollo Regional (FEDER). The CNIC is supported by the MCIU and the Pro CNIC Foundation, and is a Severo Ochoa Center of Excellence (MCIU award SEV-2015-0505). *Col1*^{cre} mice were provided by G. Kollias.

Author contributions S.C. and A.G. designed the study, performed experiments, interpreted results and wrote the manuscript. J.Á.N.-Á. designed the study and experiments and interpreted data. D.W., K.F., J.A.Q., K.F.L., T.R., M.F., J.A.A. and R.P. performed experiments and collected and interpreted data. A.K., D.S., M.P., K.G. and N.R. provided expertise, patient material and input and wrote the manuscript. T.B. designed, performed and interpreted the MRI measurements. B.K. and D.V. were involved in the generation of *Retnla*^{cre} mice and provided input. P.K., M.E., A.B.E., F.F. and J.V. performed bioinformatics analysis and interpreted the data. E.K. and M.S. performed electron microscopy experiments and interpreted the results. R.F.H. and I.E.B. designed and tested the claudin peptidomimetics, designed experiments and wrote the manuscript. F.P., G.S., A.H. and G.K. designed the study and experiments and wrote the manuscript. All authors read and commented on the manuscript.

Competing interests The authors declare no competing interests.

Additional information

Supplementary information is available for this paper at https://doi.org/10.1038/s41586-019-1471-1.

Correspondence and requests for materials should be addressed to G.K.

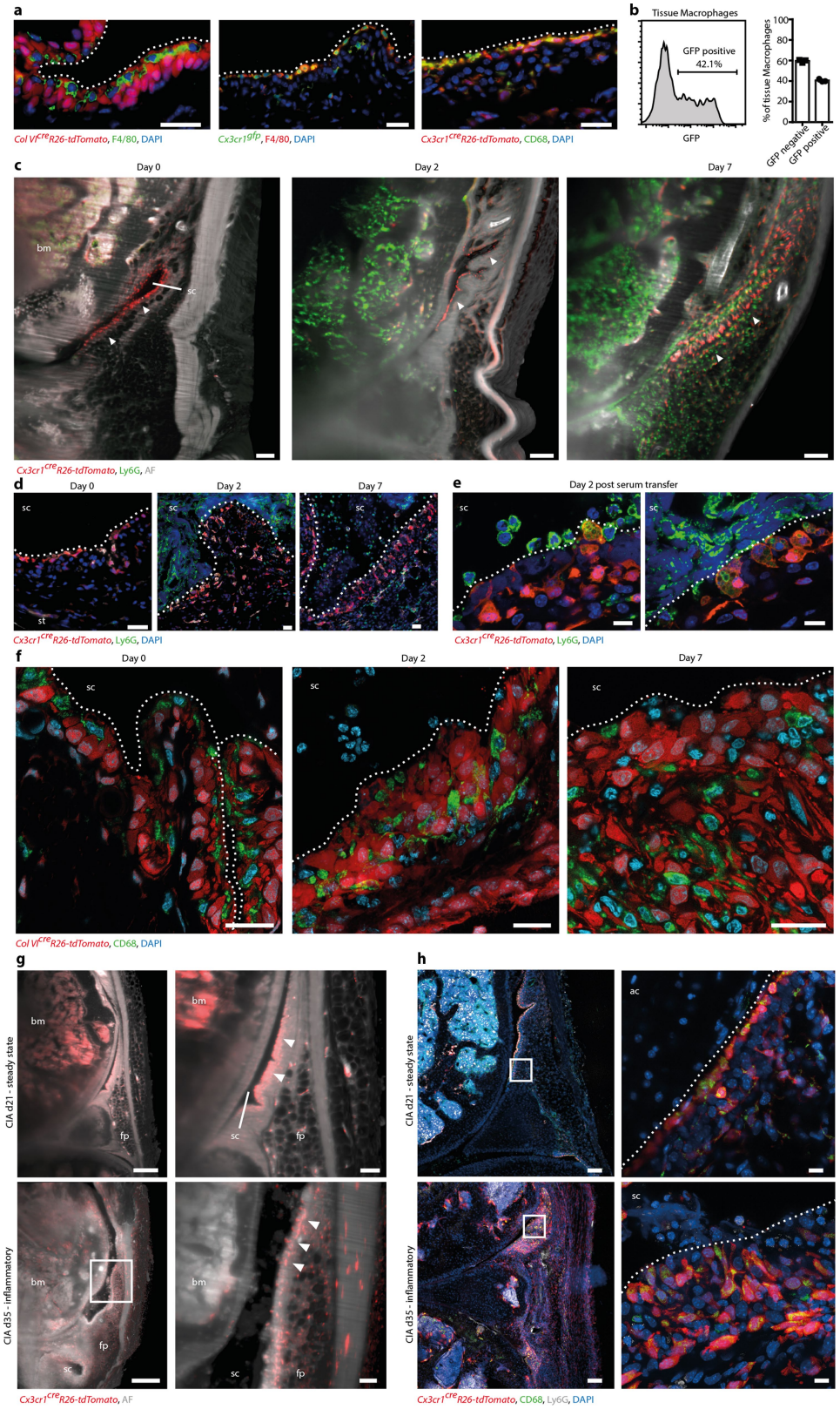

Extended Data Fig. 1 | See next page for caption.

Extended Data Fig. 1 | Spatiotemporal profiling of synovial CX_3CR1^+ macrophages. a, BFM of macrophages within the synovial tissue using the macrophage markers F4/80 (left and middle; colour as indicated) and CD68 (right; green) in *ColVI^{cre}R26-tdTomato* reporter mice (left; tdTomato$^+$, red), *Cx3cr1^{GFP}* mice (middle; GFP$^+$, green), and *Cx3cr1^{cre}R26-tdTomato*, mice (right; tdTomato$^+$, red). Scale bars, 25 μm. **b**, Flow cytometry analysis of macrophages of dissociated hind-paw joints of *Cx3cr1^{gfp}* mice ($n = 3$) gated for CD45$^+$, CD11b$^+$, F4/80$^+$ and GFP. Data are mean ± s.e.m. **c**, Representative 3D LSFM showing the spatial distribution of PMNs (Ly6G, green) and mononuclear phagocytes (tdTomato$^+$, red) in knee joints of *Cx3cr1^{cre}R26-tdTomato* mice at indicated time points upon induction of K/BxN STA (AF, grey). Filled arrowheads point towards the macrophage lining layer to highlight changes in its morphology upon induction of STA. Scale bars, 100 μm. **d**, Exemplary BFM images of the synovial membrane of knee joints of *Cx3cr1^{cre}R26-tdTomato* mice at day 0, day 2 and 7 after induction of STA. Macrophages are defined as tdTomato$^+$ (red) and F4/80$^+$ (white) and infiltrating neutrophils as Ly6G$^+$ (green) cells. Scale bars, 25 μm. **e**, Spinning disk confocal microscopy images of the synovial membrane of *Cx3cr1^{cre}R26-tdTomato* mice at day 2 after induction of K/BxN STA visualizing macrophages (tdTomato$^+$, red) and neutrophils (Ly6G, green). Scale bars, 10 μm. **f**, CLSM scans of the synovial membrane in knee joints of *ColVI^{cre}R26-tdTomato* reporter mice at the indicated time points after the induction of STA, enabling the visualization of synovial fibroblasts (tdTomato, red) and macrophages (CD68, green) along the synovial cavity (sc). Scale bars, 20 μm. **g**, LSFM of knee joints of *Cx3cr1^{cre}R26-tdTomato* mice showing the spatial distribution of macrophages (tdTomato, red) along the synovial cavity at day 21 after the first immunization during collagen-induced arthritis before the onset of arthritis (steady state) (top) and at day 35 after the first immunization after onset of joint inflammation, identifying rearrangement of macrophages in the form of palisade-like structures (filled arrowheads). Scale bars, 500 μm (left), 100 μm (right). AF, grey. **h**, CLSM images of knee joints of *Cx3cr1^{cre}R26-tdTomato* mice at day 21 (top; steady state before onset of arthritis) and day 35 (bottom; during active arthritis) of collagen-induced arthritis, illustrating reorganization of lining macrophages (tdTomato, red; CD68, green). Scale bars, 100 μm; scale bar of magnified view, 10 μm.

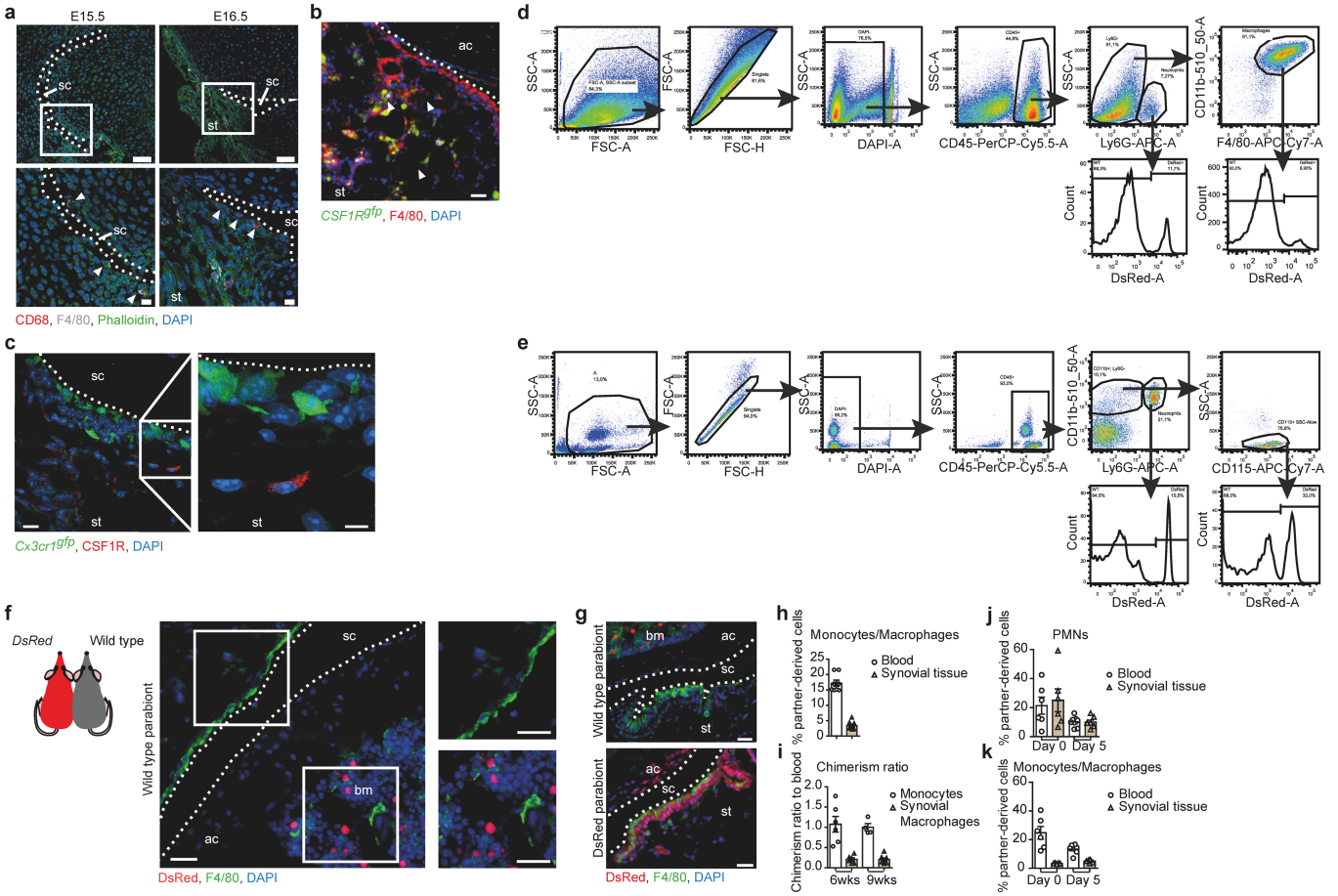

Extended Data Fig. 2 | Developmental origin of synovial lining macrophages. a, Histological CLSM analysis of embryonic mouse knee joints at E15.5 and E16.5 visualizing CD68 (red) and F4/80 (white) expressing embryonic macrophages (filled arrowheads) within the newly formed synovial lining. Scale bars, 50 μm (top), 10 μm (bottom). **b**, BFM showing expression of CSF1R and the distribution of macrophages (F4/80, red) within the synovial tissue of *CSF1R*^{GFP} mice (GFP, green; left). **c**, Representative CLSM scans of *Cx3cr1*^{GFP} (green) knee joints confirming the expression of CSF1R (red) by antibody-mediated staining on interstitial CX_3CR1^- macrophages. Scale bars, 25 μm, scale bar of magnified view, 10 μm. **d**, Gating strategy for analysis of synovial macrophages isolated from hind paws of parabiotic *DsRed*/wild-type mice. Synovial macrophages were defined as $DAPI^-$ living, $CD45^+$, $Ly6G^-$, $CD11b^+$, $F4/80^+$ cells. DsRed expression discriminates the origin. **e**, Gating strategy for blood monocytes of parabiotic *DsRed*/wild-type mice. Blood monocytes were defined as $DAPI^-$ living, $CD45^+$, $CD11b^+$, $Ly6G^-$, $CD115^+$ and SSC^{low}. DsRed expression discriminates the origin. **f**, Representative BFM of the synovial membrane of knee joints of a wild-type mouse sharing circulation with a *DsRed* mouse, six weeks after establishment of parabiosis ($n = 3$; DsRed, red; F4/80, green). Scale bars, 25 μm. **g**, BFM images of parabiotic wild-type (top) and *DsRed* (bottom) mice after nine weeks of parabiosis. In the wild-type mice, $DsRed^+$ partner-derived macrophages are visible in the bone marrow (bm), but not detected in the macrophage (F4/80, green) lining layer. Scale bars, 25 μm. **h**, Flow-cytometric analysis of the percentage of partner-derived blood monocytes and synovial macrophages of *DsRed*/wild-type parabionts after 9 weeks of parabiosis. Mean ± s.e.m. Blood, $n = 8$; synovial joint, $n = 8$. **i**, Chimerism ratio of blood monocytes and synovial macrophages in *DsRed*/wild-type parabionts after six weeks and nine weeks of parabiosis, calculated as the quotient of content of partner-derived tissue macrophages to partner-derived blood monocytes. A chimerism ratio of one represents the chimerism observed in blood monocytes. Mean ± s.e.m. Monocytes 6 weeks, $n = 6$; synovial macrophages 6 weeks, $n = 6$; monocytes 9 weeks, $n = 4$; synovial macrophages 9 weeks, $n = 8$. **j**, **k**, Flow-cytometric analysis of parabiotic hind paws of *DsRed*/wild-type parabionts at the indicated time points of K/BxN serum transfer arthritis. Data presented show the percentage of partner-derived PMNs (**k**) and monocytes/macrophages (**l**) within the blood circulation and the synovial tissue and are used to calculate the individual chimerism of tissue- and blood-derived cells. Mean ± s.e.m. For **j**, blood day 0 $n = 6$; synovial tissue day 0, $n = 6$; blood day 5, $n = 8$; synovial tissue day 5, $n = 7$. For **k**, blood day 0, $n = 6$; synovial tissue day 0, $n = 5$; blood day 5, $n = 7$; synovial tissue day 5, $n = 8$.

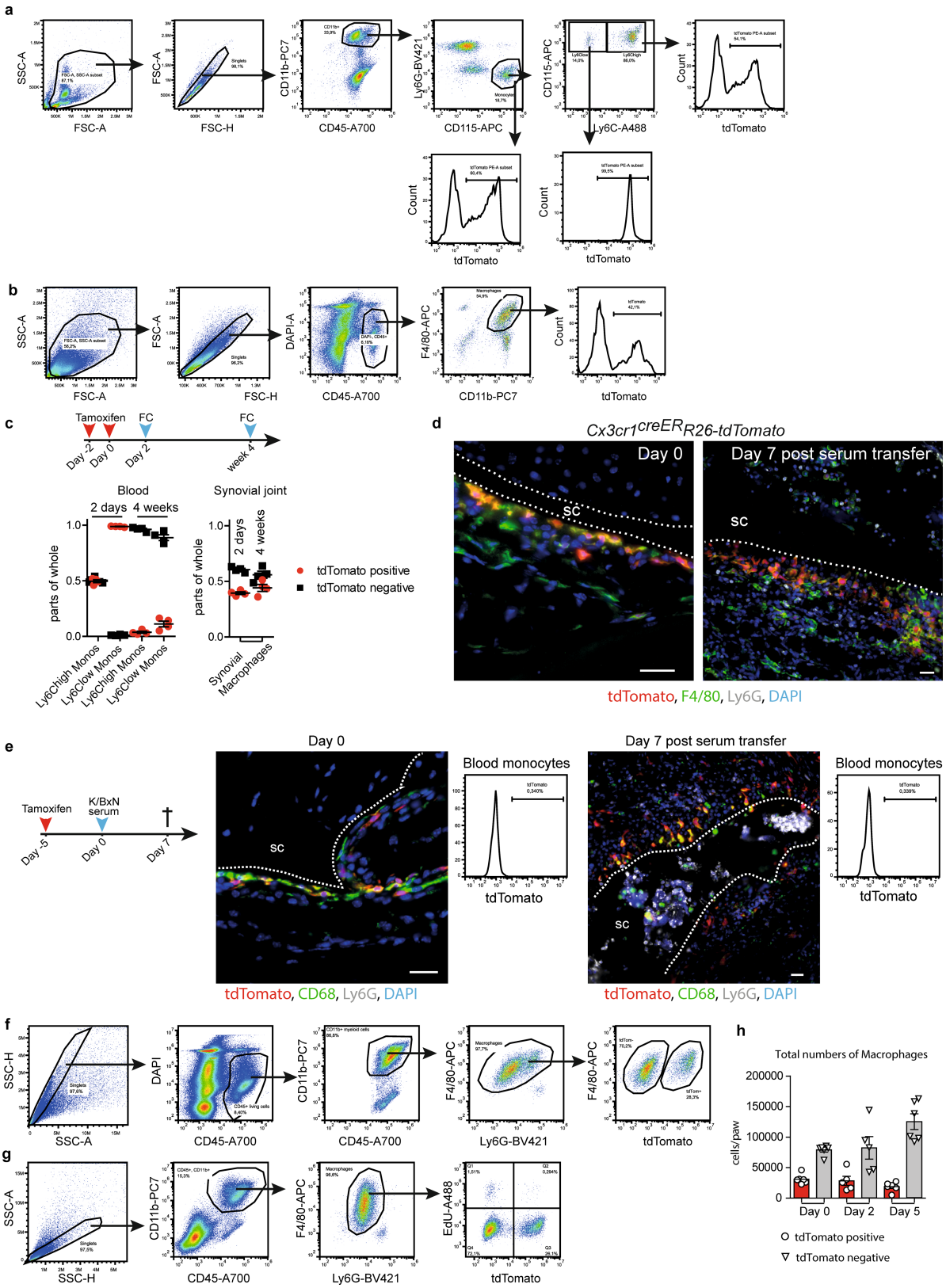

Extended Data Fig. 3 | See next page for caption.

Extended Data Fig. 3 | Fate mapping of synovial lining macrophages during arthritis. a, Gating strategy for $CD45^+CD11b^+Ly6G^-CD115^+$ classical $Ly6C^{high}$ and non-classical $Ly6C^{low}$ monocytes of *Cx3cr1*^{creER}*R26-tdTomato* mice. **b**, Gating strategy for $DAPI^-$ living, $CD45^+CD11b^+Ly6G^-F4/80^+$ macrophages of *Cx3cr1*^{creER}*R26-tdTomato* mice. **c**, Evaluation of tdTomato expression in blood monocytes and synovial macrophages two days and four weeks after tamoxifen pulse. Mean ± s.e.m.; $n = 4$ per group. **d**, **e**, BFM images of knee joint synovial membranes of *Cx3cr1*^{creER}*tdTomato* mice four weeks after systemic tamoxifen pulse (**d**) and five days after local injection of (*Z*)-4-hydroxytamoxifen (**e**) at day 0 and day 7 after the induction of K/BxN STA showing selective tdTomato (red) expression in synovial lining macrophages. The smaller graphs to the right in **e** show the absence of tdTomato expression in blood monocytes after local (Z)-4-hydroxytamoxifen injection. Scale bars, 25 μm. **f**, Gating strategy for $DAPI^-$ living, $CD45^+CD11b^+Ly6G^-F4/80^+$ macrophages of *Cx3cr1*^{creER}*R26-tdTomato* mice four weeks after tamoxifen pulse, used to calculate the absolute numbers of $tdTomato^+$ macrophages during steady state and K/BxN STA. **g**, Gating strategy after EdU labelling of proliferating macrophages ($CD45^+CD11b^+Ly6G^-$ $F4/80^+$) of *Cx3cr1*^{creER}*R26-tdTomato* mice. **h**, Quantification of total $tdTomato^+$ and $tdTomato^-$ macrophages in paws of *Cx3cr1*^{creER}*R26-tdTomato* mice 4 weeks upon tamoxifen pulse at day 0, 2 and 5 after induction of STA. Mean ± s.e.m. Day 0, $n = 6$; day 2, $n = 5$; day 5, $n = 6$.

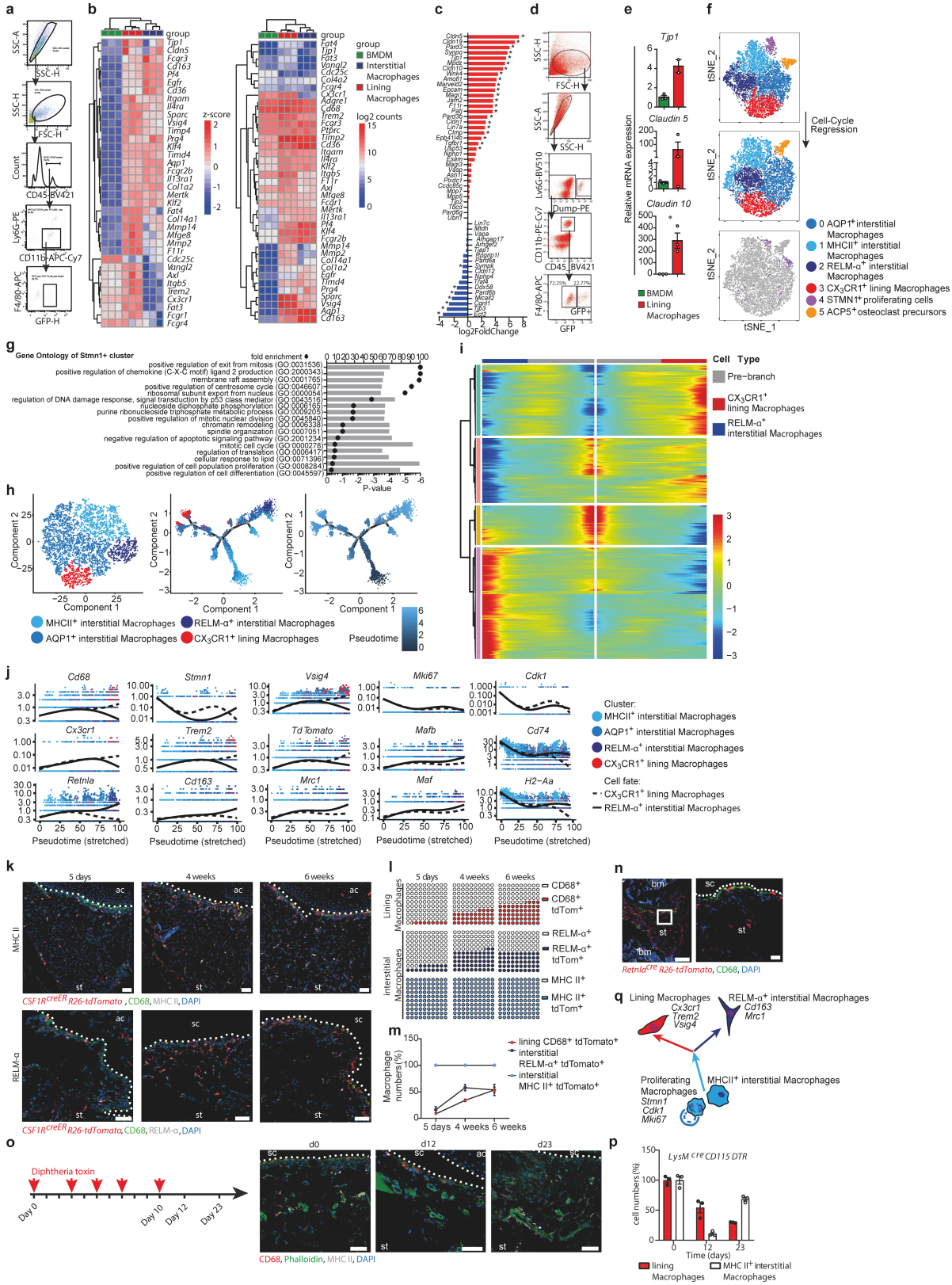

Extended Data Fig. 4 | See next page for caption.

Extended Data Fig. 4 | Transcriptional profiling of steady-state synovial macrophage subsets. a, Sorting strategy for bulk RNA sequencing analysis of synovial macrophages of *Cx3cr1*^{GFP} mice. Macrophages were defined as CD45$^+$, Ly6G$^-$, CD11$^+$ and F4/80$^+$. GFP discriminated GFP$^+$ lining macrophages and GFP$^-$ interstitial macrophages. **b**, Hierarchical clustering of *z*-score (left) and $\log_2$ counts (right) of selected genes of sorted GFP$^+$ lining macrophages, GFP$^-$ interstitial macrophages and BMDMs generated from bulk RNA sequencing. **c**, Differential gene expression (mean fold change, $\log_2$(differentially expressed genes) ($n = 3$ per group) of tight-junction-associated genes comparing CX_3CR1^+ lining macrophages and BMDMs. Differential expression was performed with DESeq2. A Wald test was used to calculate two-sided *P* values; adjustment for multiple comparisons was performed with the Benjamini–Hochberg method. $^*P \leq 0.05$. **d**, Sorting strategy for synovial macrophages of *Cx3cr1*^{GFP} mice for confirmatory quantitative analysis by PCR with reverse transcription (RT–PCR). Macrophages were defined as CD45$^+$, Ly6G$^-$, CD11$^+$ and F4/80$^+$. GFP discriminated GFP$^+$ lining macrophages and GFP$^-$ interstitial macrophages. A dump channel using anti-CD31 and anti-E-cadherin was integrated to avoid endothelial cell or epithelial cell contaminations. **e**, Confirmatory quantitative RT–PCR analysis in synovial macrophage subsets determining expression of mRNAs encoding TJP1 (BMDM, $n = 3$; lining macrophage, $n = 2$), claudin 5 ($n = 3$ per group) and claudin 10 ($n = 3$ per group) in sorted GFP$^+$ lining macrophages and in vitro cultured BMDMs, mean ± s.e.m.; two-tailed Student's *t*-test, $^*P = 0.012$. **f**, *t*-SNE profile of sorted synovial CD45$^+$CD11b$^+$Ly6G$^-$ mononuclear phagocytes of *Cx3cr1*^{creER}*R26-tdTomato* mice analysed four weeks after tamoxifen pulse during steady-state conditions (top). After clustering, cell-cycle phase scoring based on canonical markers and regression was performed to determine clustering independent of cell cycle phase (middle and bottom). $n = 7{,}362$ cells. **g**, Gene ontology enrichment analysis of biological processes in cells of the proliferating *Stmn1*$^+$ cluster of sorted CD45$^+$CD11b$^+$Ly6G$^-$ mononuclear phagocytes of a healthy tamoxifen-pulsed *Cx3cr1*^{creER}*R26-tdTomato* mouse. The top 51 cluster marker genes determined with Seurat were used to perform a PANTHER overrepresentation test. The list of markers for the *Stmn1*$^+$ cluster was compared to the reference list using Fisher's exact test with false discovery rate correction. **h**, *t*-SNE profile of sorted synovial CD45$^+$CD11b$^+$Ly6G$^-$ mononuclear phagocytes of a healthy tamoxifen-pulsed *Cx3cr1*^{creER}*R26-tdTomato* mouse after excluding *Acp5*$^+$ osteoclast precursors revealing four remaining clusters (left). Single-cell trajectory analysis integrating cluster information (middle) and pseudotime (right) show a branch point of cellular differentiation into lining macrophages (red) or interstitial *Retnla*$^+$ macrophages (dark blue) starting from proliferating MHCII$^+$ macrophages (light blue). $n = 7{,}028$ cells. **i**, Differential gene expression analysis as a function of pseudotime in a branch-dependent manner showing a common gene signature of a pre-branch precursor cell population choosing two main cell fates: either *Cx3cr1*$^+$ lining macrophage or interstitial *Retnla*$^+$ macrophage. **j**, Gene expression changes of selected marker genes as a function of pseudotime reflecting the cellular differentiation into *Retnla*$^+$ interstitial macrophages (solid line) and *Cx3cr1*$^+$ lining macrophages (dashed line). $n = 7{,}028$ cells. **k**, BFM images of knee joints of *Csf1r*^{creER}*R26-tdTomato* mice (tdTomato, red) determining tdTomato expression in CD68$^+$ (green) lining macrophages, MHCII$^+$ interstitial macrophages (MHCII, white; top) and RELM-α$^+$ interstitial macrophages (RELM-α, white; bottom) at indicated times after the start of tamoxifen treatment. Scale bars, 50 μm. **l**, **m**, Quantification of relative changes in tdTomato$^+$ cells among CD68$^+$ lining macrophages, RELM-α$^+$ interstitial macrophages and MHCII$^+$ interstitial macrophages in *Csf1r*^{creER}*R26-tdTomato* mice at indicated times after the start of tamoxifen treatment. $n = 3$ mice per group. Data are mean ± s.e.m. **n**, tdTomato (red) expression in CD68$^+$ (green) macrophages in synovial tissue of the knee joint of *Retnla*^{cre}*R26-tdTomato* mice. Scale bars, 250 μm (left), 25 μm (right). **o**, **p**, BFM images (**o**) and quantification of changes (**p**) in CD68$^+$ (red) lining macrophages and MHCII$^+$ (white) interstitial macrophages in *LysM*^{cre}*CD115DTR* mice after 10 days of DT treatment, at the indicated time points after the beginning of DT treatment. Scale bars, 50 μm. $n = 3$ technical replicates. Data are mean ± s.e.m. **q**, Scheme of the postulated dynamic continuum of differentiating tissue-resident macrophages within the synovial tissue.

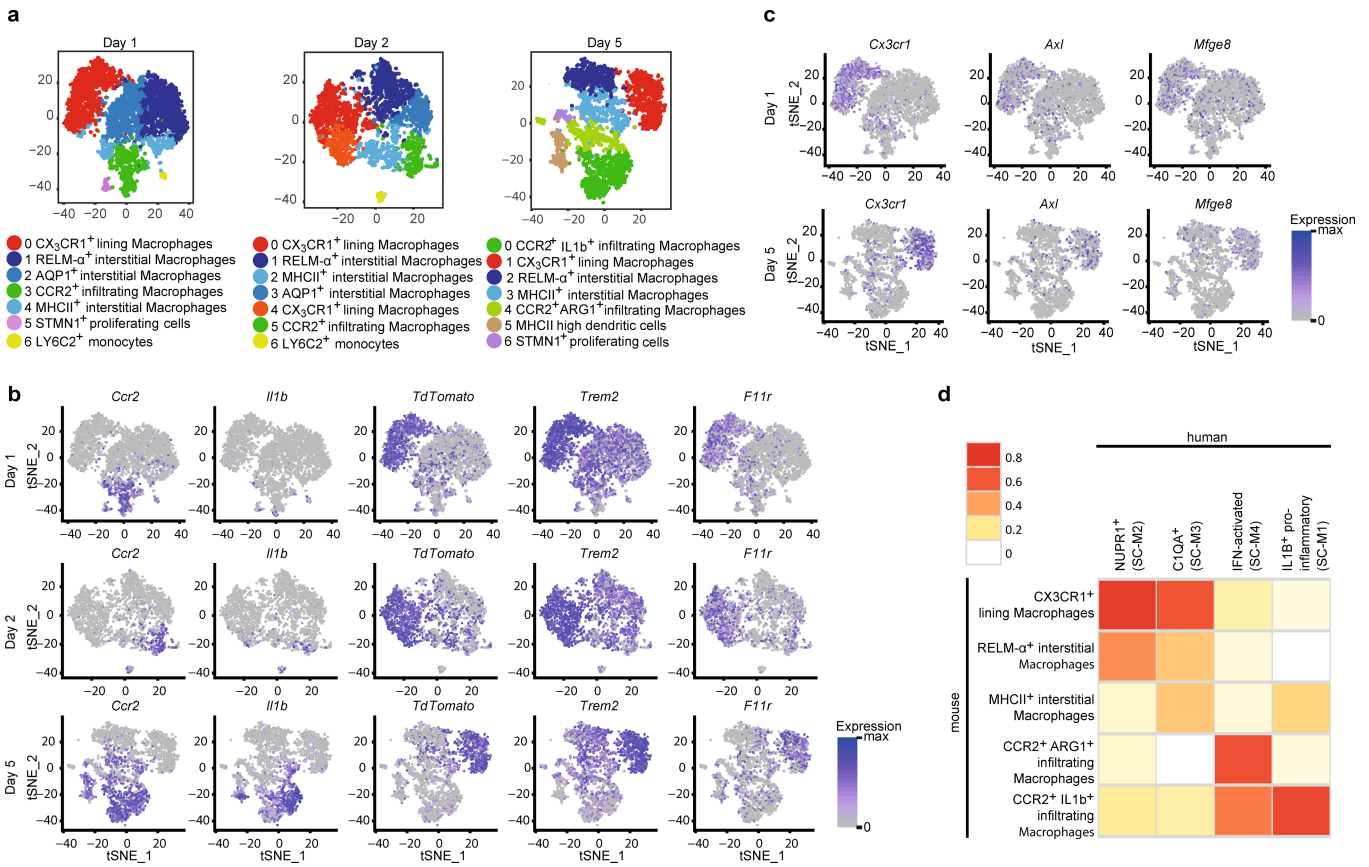

Extended Data Fig. 5 | Transcriptional profiling of mononuclear phagocytes during arthritis. a, *t*-SNE scRNA-seq profiles of sorted synovial CD45$^+$CD11b$^+$Ly6G$^-$ mononuclear phagocytes of *Cx3cr1*^{creER}*R26-tdTomato* mice analysed four weeks after tamoxifen pulse at the indicated time points after the induction of K/BxN STA, coloured by cluster assignment and annotated post hoc. Day 1, $n = 4{,}640$ cells; day 2, $n = 2{,}722$ cells; day 5, $n = 3{,}237$ cells. **b**, scRNA-seq-derived expression patterns of indicated genes within synovial mononuclear phagocytes at indicated time points after the induction of STA. Day 1, $n = 4{,}640$ cells; day 2, $n = 2{,}722$ cells; day 5, $n = 3{,}237$ cells. **c**, *t*-SNE plots of sorted CD45$^+$CD11b$^+$Ly6G$^-$ cells from arthritic hind paws at day 1 and day 5 after K/BxN serum transfer, showing the expression of *Cx3cr1*, *Axl* and *Mfge8* within the cluster of lining macrophages. **d**, Comparison of available scRNA-seq datasets from monocytes of human synovial tissue derived from patients suffering from rheumatoid arthritis and osteoarthritis[8] with scRNA-seq profiles of mouse CD45$^+$CD11b$^+$Ly6G$^-$ cells on day 5 after the induction of STA. Values represent the quotient of the numbers of all co-expressed marker genes of the 5 macrophage clusters at day 5 to the top 20 provided human marker genes of the 4 described subpopulations of human monocytes SC-M1, SC-M2, SC-M3 and SC-M4.

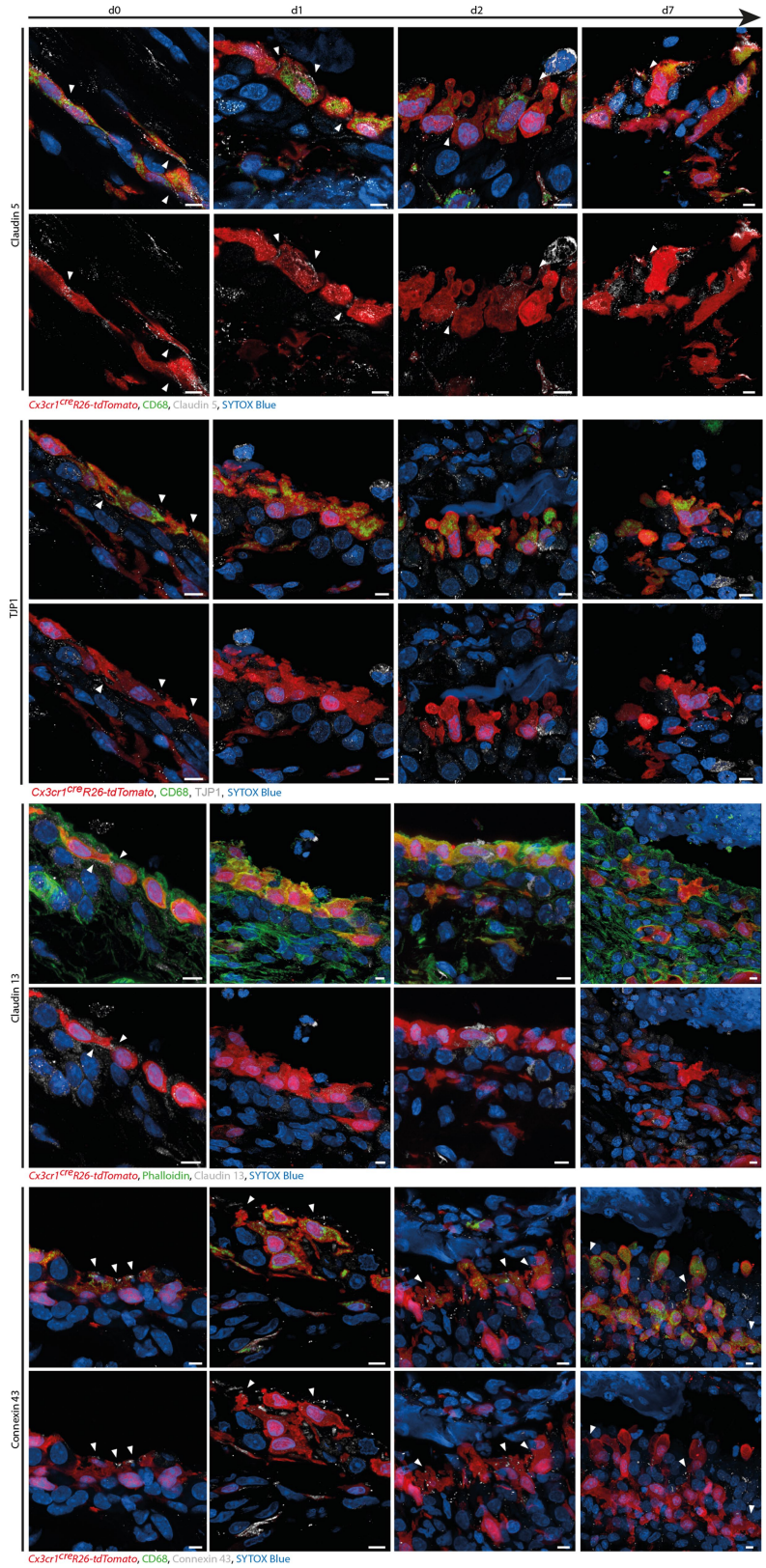

Extended Data Fig. 6 | Expression patterns of tight-junction proteins and gap-junction proteins in tdTomato^{+} lining macrophages. Expression of claudin 5, TJP1/ZO-1 and claudin 13 as well as that of connexin 43 (grey, filled arrowheads) in synovial lining tdTomato^{+} (red) macrophages of *Cx3cr1^{cre}R26-tdTomato* mice during steady state and on days 1, 2 and 7 after the induction of K/BxN STA. Scale bars, 5 μm.

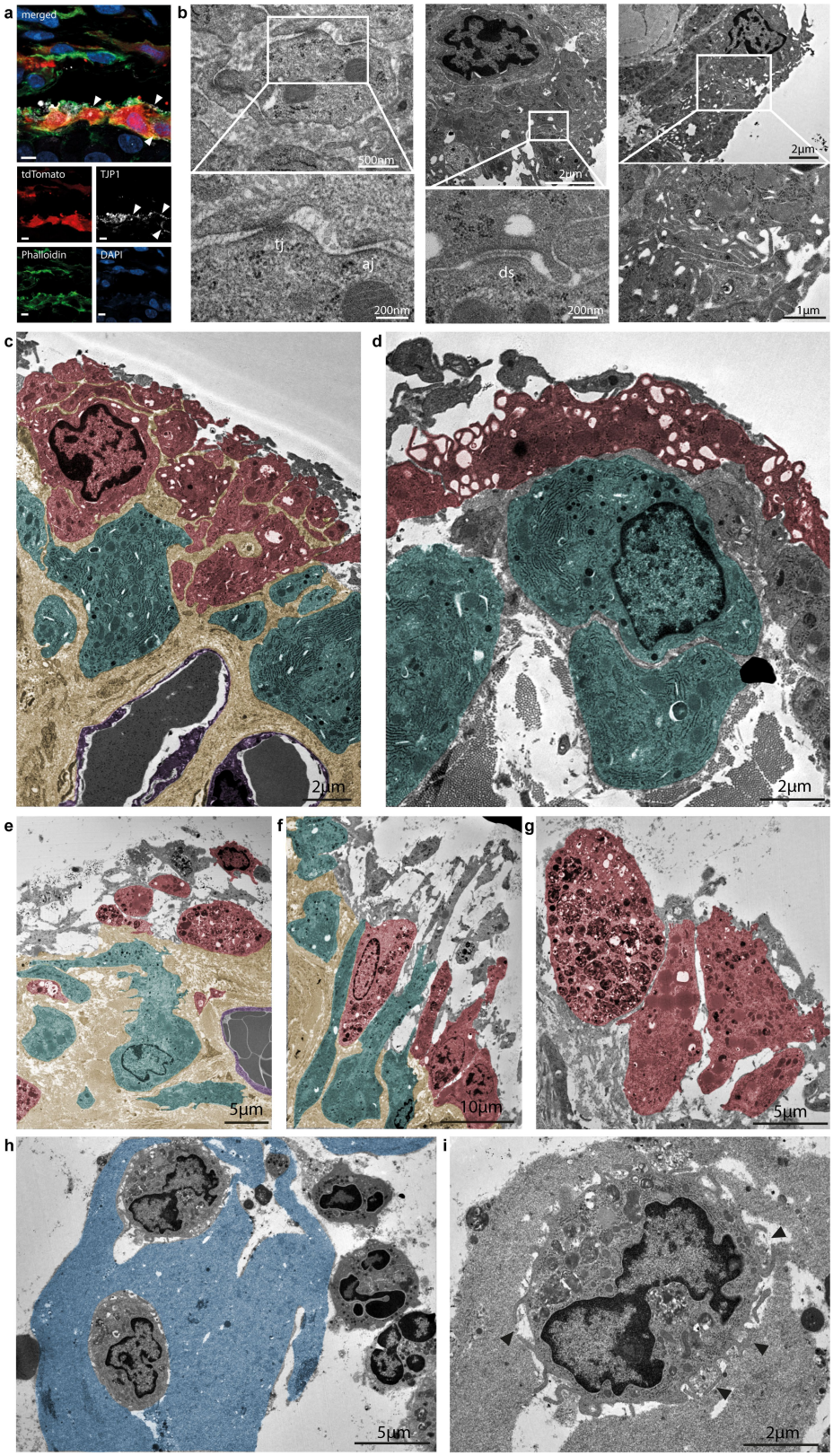

Extended Data Fig. 7 | See next page for caption.

Extended Data Fig. 7 | Ultrastructural characterization of cell–cell contacts between lining macrophages. a, Representative CLSM of macrophages (tdTomato, red) within the synovial membrane of knee joints of *Cx3cr1*^{creER}*R26-tdTomato* mice, visualizing the tight-junction protein ZO-1/TJP1 (white). Phalloidin, green; DAPI, blue. Scale bars, 5 μm. **b**, Transmission electron microscopy (TEM) images of the synovial membrane of a healthy knee joint showing tight junctions (tj), adherens junctions (aj), desmosomes (ds) and interdigitations connecting synovial lining macrophages. **c**, TEM micrograph showing synovial lining macrophages (red) constituting a dense physical barrier segregating the synovial fluid from sublining interstitial tissue containing synovial fibroblasts (cyan), endothelial cells (purple) embedded into the extracellular matrix (beige). **d**, TEM micrograph demonstrating synovial macrophages (red) forming the uppermost cell layer covering the layer of synovial fibroblasts (cyan). **e**, **f**, TEM micrographs of an inflamed synovial membrane two days after induction of K/BxN STA, showing the disruption of the covering synovial macrophage (red) layer and a reorientation of synovial macrophages (red) and synovial fibroblasts (cyan) directed to the synovial cavity. **g**, A TEM micrograph of an inflamed synovial membrane two days after the induction of STA reveals the emergence of macrophages containing large amounts of vacuoles filled with phagocytosed material. **h**, **i**, Recruited monocytes and granulocytes as well as free DNA of neutrophil extracellular traps (blue) within the synovial cavity of knee joints two days after the induction of STA. Filled arrowheads point at an exemplary monocyte engulfing free DNA.

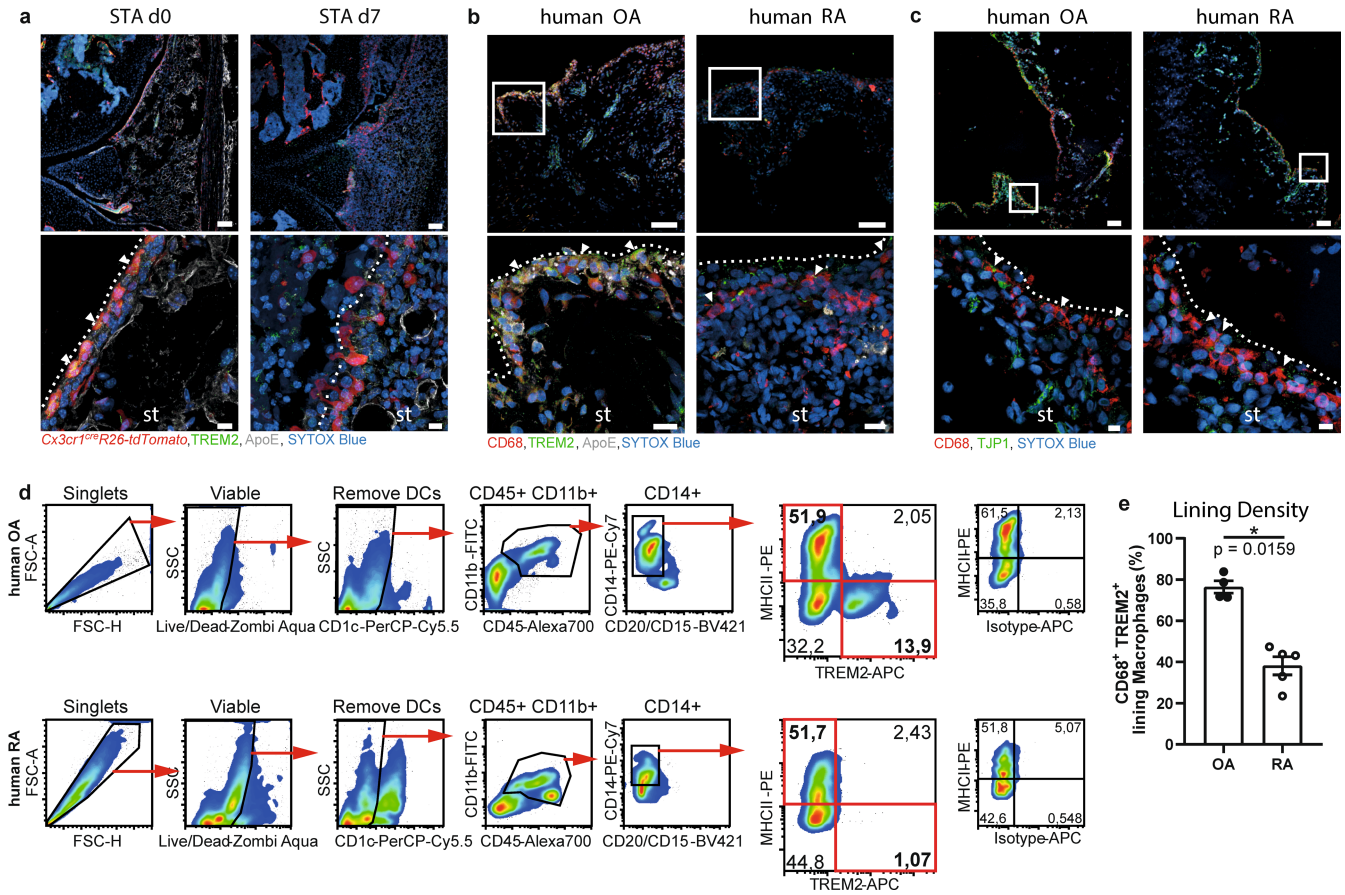

Extended Data Fig. 8 | Comparison of mouse and human synovial lining macrophages. a, Histological sections of healthy (STA day 0, left) and inflamed (STA day 7, right) mouse knee joints of *Cx3cr1*^{cre}*R26-tdTomato* mice, showing the expression of TREM2 (green; filled arrowheads) in lining macrophages (tdTomato, red). Scale bars, 100 μm (top), 10 μm (bottom). **b**, **c**, Histological sections of synovial tissue of human knee joints isolated from patients diagnosed with osteoarthritis (OA) and rheumatoid arthritis (RA) determining expression of TREM2 (green; filled arrowheads) (**b**) and TJP1 (green; filled arrowheads) (**c**) in synovial macrophages (CD68, red). Scale bars, 100 μm (top), 10 μm (bottom). **d**, Flow-cytometric analysis of the composition and frequencies of MHCII^{+}TREM2^{-} and MHCII^{-}TREM2^{+} mononuclear phagocytes in synovial tissue samples isolated from human knee joints of patients diagnosed with osteoarthritis and rheumatoid arthritis. **e**, Histology-based quantification of the density of the synovial macrophage lining (defined as percentage of CD68^{+}TREM2^{+} macrophages among total lining cells) in synovial tissue sections of patients diagnosed with osteoarthritis ($n = 4$) and rheumatoid arthritis ($n = 5$), respectively. Data are mean ± s.e.m., two-tailed Student's *t*-test.

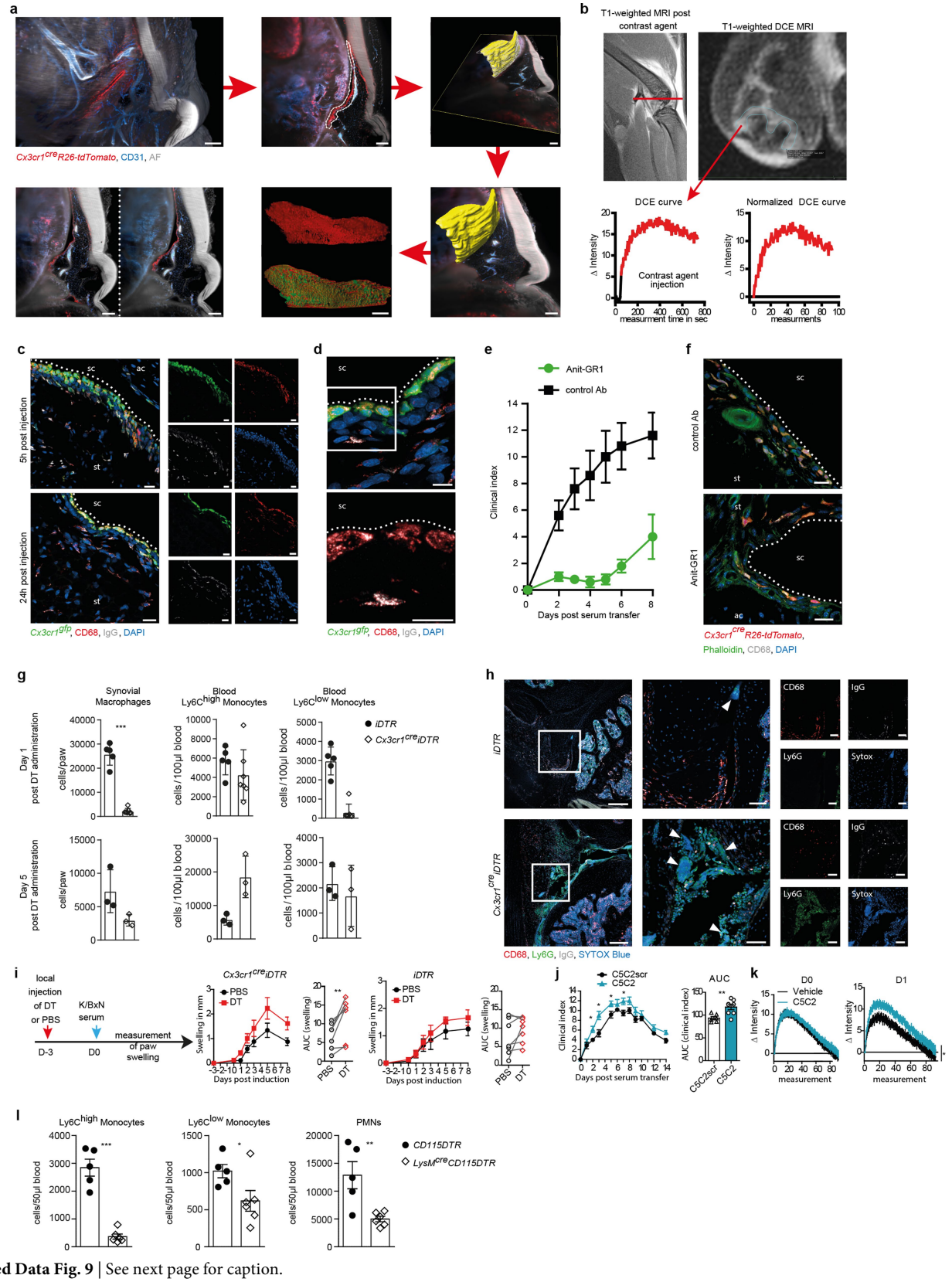

Extended Data Fig. 9 | See next page for caption.

Extended Data Fig. 9 | Role of CX_3CR1^+ macrophages during arthritis. **a**, To quantify lining density, tdTomato$^+$ macrophages (red) were manually isolated from 3D reconstructions of optically cleared and LSFM-imaged *Cx3cr1^{cre}R26-tdTomato* knee joints (autofluorescence, grey; CD31, blue) using Imaris software. Isolated surfaces (yellow) were volume-rendered for tdTomato$^+$ macrophages (red) and whole-area volume (green). Lining density was calculated from the ratio of whole-area volume to macrophage volume. An exemplary image of the same knee joint before and after isolation of lining macrophages is shown. Scale bars, 200 μm. **b**, Dynamic-contrast-enhanced magnetic resonance imaging (DCE-MRI) data analysis. The red line drawn in the sagittal T1-weighted image after administration of contrast agent marks the transverse plane used for T1-weighted DCE-MRI analysis. The DCE curve generated from the region of interest (synovial tissue) was normalized to the measurement time point after complete injection of contrast agent, and the time of measurements was converted to distinctive measurements. **c**, CLSM images of knee joints of *Cx3cr1^{GFP}* mice injected with protein-G-purified and Alexa-Fluor-647-labelled K/BxN serum IgG (grey) at the indicated time points after IgG injection, determining the uptake of labelled IgG by macrophages (GFP, green; CD68, red) in the synovial tissue and the synovial lining (synovial cavity, sc). Scale bars, 10 μm. **d**, CLSM scan with higher magnification showing localization of labelled IgG (grey) inside the vacuoles of CD68$^+$ (red) lining and interstitial synovial macrophages 24 h after injection. Scale bars, 10 μm. **e**, Clinical course of K/BxN STA in wild-type mice that were treated with an anti-GR1 antibody to deplete PMNs and inflammatory Ly6C^{high} monocytes and a control antibody (LTF-2), one day before induction of STA. Mean ± s.e.m.; $n = 5$ per group. **f**, Histological CLSM analysis of lining morphology after anti-GR1 antibody-mediated neutrophil/monocyte depletion one day after induction of STA. Lining macrophages (tdTomato, red). Scale bars, 20 μm. **g**, Flow cytometry analysis of synovial macrophages and blood Ly6C^{high} or Ly6C^{low} monocytes of *Cx3cr1^{cre}iDTR* mice and *iDTR* control mice one day and five days after two injections of DT (500 ng per mouse per day, i.p.). Mean ± s.e.m; For day 1: *iDTR*, $n = 5$; *Cx3cr1^{cre}iDTR*, $n = 7$; for day 5, $n = 3$ per group. Two-tailed Student's *t*-test, $***P < 0.0001$. **h**, Representative BFM images of the infiltration of PMNs (Ly6G, green) and neutrophil extracellular trap formation (filled arrowheads, DAPI, blue) within the synovial cavity of knee joints of *Cx3cr1^{cre}iDTR* ($n = 3$) and *iDTR* control ($n = 3$) mice 6 days after injection of DT and 24 h after induction of STA (CD68, red). Scale bars, 200 μm and for magnified view, 50 μm. **i**, Treatment scheme and clinical course of STA in *Cx3cr1^{cre}iDTR* and *iDTR* control mice that had received a unilateral local injection of DT ($n = 7$) and PBS ($n = 7$), respectively. *P* values calculated using two-tailed paired *t*-test, $**P = 0.008$. **j**, Clinical course of STA including AUC of the corresponding clinical index in C57BL/6 wild-type mice treated with C5C2 claudin peptidomimetics (3.5 μmol kg^{-1}, i.v., $n = 8$) or scrambled C5C2 control peptide (C5C2scr; 3.5 μmol kg^{-1}, i.v., $n = 6$) one day before and after the induction of STA. Data are mean ± s.e.m. Mann–Whitney *U*-test for clinical index with $*P \leq 0.05$, and two-tailed Student's *t*-test for AUC with $**P = 0.0062$. **k**, Normalized signal intensity curves of DCE-MRI of synovial tissue of knee joints over 90 measurements with intervals of 7 s at the indicated days after STA in C57BL/6 wild-type mice treated with C5C2 claudin peptidomimetics (3.5 μmol kg^{-1}, i.v.) or vehicle one day before the induction of STA. Data are mean ± s.e.m. Day 0: vehicle, $n = 10$ knee joints; C5C2, $n = 10$ knee joints; day 1: vehicle, $n = 9$ knee joints; C5C2, $n = 10$ knee joints. *P* values for AUC were calculated using two-tailed Student's *t*-test, $*P = 0{,}0256$. **l**, Flow cytometry of blood monocytes and neutrophils of *LysM^{cre}CD115DTR* mice ($n = 6$) and *CD115DTR* control mice ($n = 5$) one day after two injections of DT (500 ng per mouse per day, i.p.). Mean ± s.e.m.; two-tailed Student's *t*-test, $*P = 0.0467$, $**P \leq 0.0069$, $***P = 0.0001$.

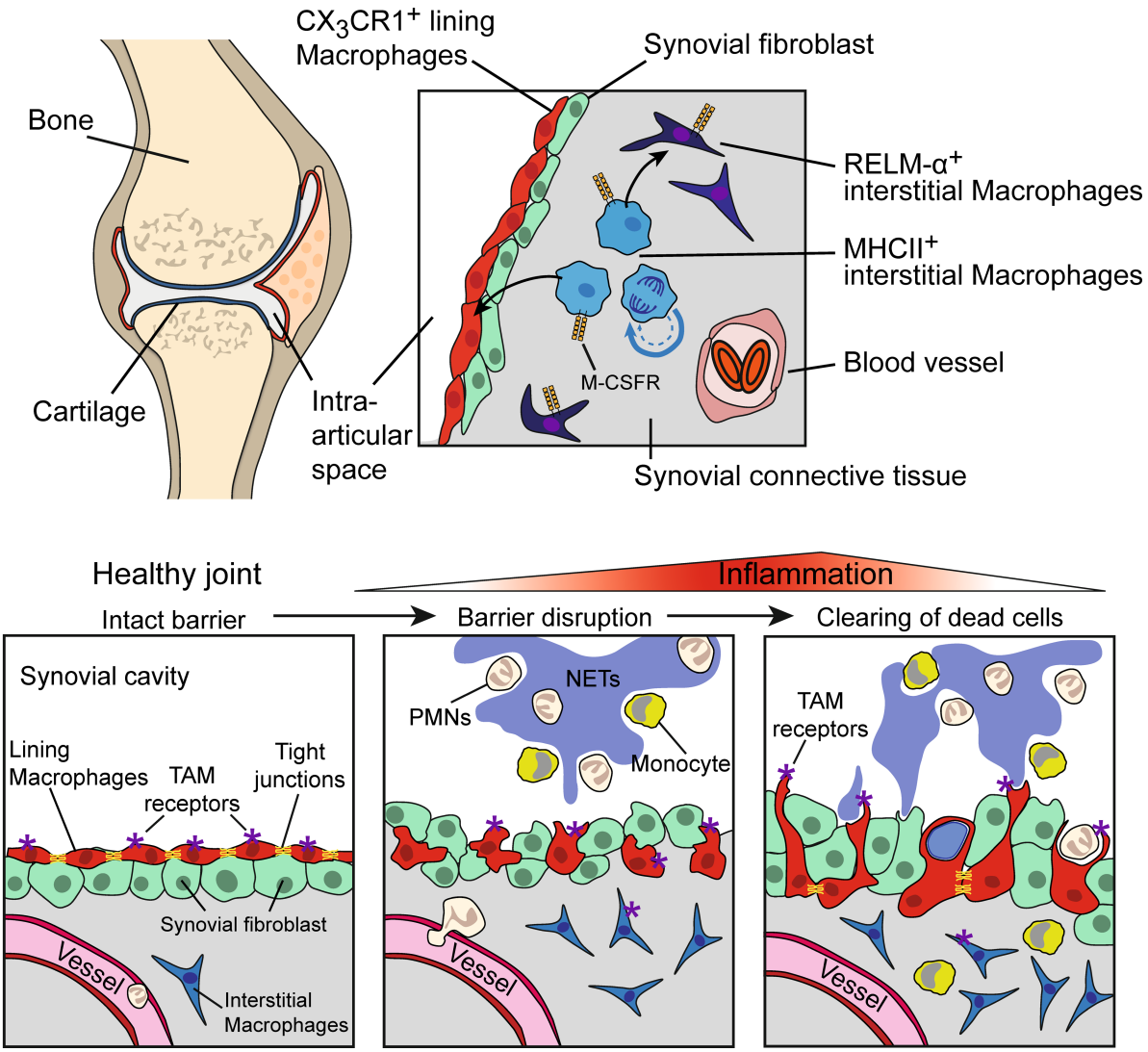

Extended Data Fig. 10 | Schematic summary. Top, scheme of the postulated origin of resident synovial CX_3CR1^+ lining macrophages that constantly repopulate from proliferating tissue resident $CX_3CR1^-MHCII^+$ interstitial macrophages. Bottom, tight-junction-forming resident lining macrophages form a protective barrier for joint structures that disintegrates during arthritis, enabling infiltration of inflammatory myeloid cells.

nature research

Corresponding author(s): G. Krönke, S. Culemann, A. Grüneboom

Reporting Summary

Nature Research wishes to improve the reproducibility of the work that we publish. This form provides structure for consistency and transparency in reporting. For further information on Nature Research policies, see Authors & Referees and the Editorial Policy Checklist.

Statistical parameters

When statistical analyses are reported, confirm that the following items are present in the relevant location (e.g. figure legend, table legend, main text, or Methods section).

n/a	Confirmed	
☐	☒	The exact sample size (*n*) for each experimental group/condition, given as a discrete number and unit of measurement
☐	☒	An indication of whether measurements were taken from distinct samples or whether the same sample was measured repeatedly
☐	☒	The statistical test(s) used AND whether they are one- or two-sided *Only common tests should be described solely by name; describe more complex techniques in the Methods section.*
☒	☐	A description of all covariates tested
☐	☒	A description of any assumptions or corrections, such as tests of normality and adjustment for multiple comparisons
☐	☒	A full description of the statistics including central tendency (e.g. means) or other basic estimates (e.g. regression coefficient) AND variation (e.g. standard deviation) or associated estimates of uncertainty (e.g. confidence intervals)
☒	☐	For null hypothesis testing, the test statistic (e.g. *F*, *t*, *r*) with confidence intervals, effect sizes, degrees of freedom and *P* value noted *Give P values as exact values whenever suitable.*
☒	☐	For Bayesian analysis, information on the choice of priors and Markov chain Monte Carlo settings
☒	☐	For hierarchical and complex designs, identification of the appropriate level for tests and full reporting of outcomes
☒	☐	Estimates of effect sizes (e.g. Cohen's *d*, Pearson's *r*), indicating how they were calculated
☐	☒	Clearly defined error bars *State explicitly what error bars represent (e.g. SD, SE, CI)*

Our web collection on statistics for biologists may be useful.

Software and code

Policy information about availability of computer code

Data collection	Leica TCS SP 5 II CLSM data were collected using Las AF software version 2.7.3.9723. Spinning Disc Confocal Microscopy (SDCM) was eprfomred by using a Zeiss Spinning Disc Axio Observer.Z1 and images were collected via the Zen Blue image aquisition software Version 2.3. Light sheet fluorescence microscopy (LSFM) data were generated using an Ultramicrospe II (LaVision BioTech GmbH) and collected with Imspector software Version 5.1.304. MRI scans were performed using a ClinScan 70/30 7 Tesla MRI System (Bruker). Flow cytometry data and cell sorting data were aquired by using a CytoFLex S (Beckman Coulter) and a MoFlo XDP (Beckman Coulter) system. Individual settings for data acquisitions via the systems listed above are described in detail in the experimental procedures.
Data analysis	CLSM and SDCM data were processed and analysed using huygens professional software Version 17.10 (Scientific Volume Imaging), Imaris software Version 9.1 (Bitplane) and Image J software Version 1.8.0_112. LSFM data were processed using Imaris software Version 9.1 (Bitplane) and Image J software version 1.8.0_112. MRI data were processed via Horos LGPL Version 3.0. Flow cytometry data and cell sorting data were analyzed via the Summit Software System, MacsQuantify (Miltenyi Biotec, Version 2.5), CytExpert (Beckman Coulter, Version 2.2.0.97), FlowJo (FlowJo, Version 7.6.5), and Kaluza software (Beckman Coulter, Version 1.5a). Statistical data analysis was performed with GraphPad Prism 5.

Differential expression analysis was performed with the DESeq2 package v.1.20.0 and volcano plots were generated with ggplot2 package in R software.
For single cell RNA sequencing analysis CellRanger 2.1.0, FastQC v0.11.7, the Seurat (Version 2.3) package for R and Monocle 2 package were used.

All data analysis strategies and softwares are described prescisely in the experimental procedures and supplementary table 3.

For manuscripts utilizing custom algorithms or software that are central to the research but not yet described in published literature, software must be made available to editors/reviewers upon request. We strongly encourage code deposition in a community repository (e.g. GitHub). See the Nature Research guidelines for submitting code & software for further information.

Data

Policy information about availability of data

All manuscripts must include a data availability statement. This statement should provide the following information, where applicable:

- Accession codes, unique identifiers, or web links for publicly available datasets
- A list of figures that have associated raw data
- A description of any restrictions on data availability

The data that support the findings of this study are available on reasonable request from the corresponding author [G.K, S.C., A.G.]. The data are not publicly available due to comprised information that could compromise research participant privacy.

Field-specific reporting

Please select the best fit for your research. If you are not sure, read the appropriate sections before making your selection.

☒ Life sciences ☐ Behavioural & social sciences ☐ Ecological, evolutionary & environmental sciences

For a reference copy of the document with all sections, see nature.com/authors/policies/ReportingSummary-flat.pdf

Life sciences study design

All studies must disclose on these points even when the disclosure is negative.

Sample size	Sample size was determined by statistical power analysis including high signficance levels ($p < 0.05$). For calculation of statistical significance GraphPad Prism 5 was used. Data are presented as mean ± SEM and were analyzed using Student's t-test, Mann-Whitney U-Test, or Kruskal-Wallis H-Test with Dunn's multiple comparisons test as post hoc procedure. P values less than 0.05 were considered significant. Differential expression analysis for Bulk RNA sequencing has been performed with DESeq2. Wald test was used to calculate two-sided p-values; adjustment for multiple comparisons was performed with the Benjamini-Hochberg method. For PANTHER Overrepresentation Test Fisher's exact Test with False Discovery Rate correction. Cluster markers of SingleCell Sequencing data sets were identified using the Wilcoxon Rank Sum test. Adjusted p-values based on Bonferroni correction using all genes in the dataset.
Data exclusions	No data were excluded from analysis.
Replication	Minimum three independent measurements per experiment were performed and successfully confirmed results.
Randomization	Experimental groups were randomly allocated. Treated groups were housed together with control groups.
Blinding	Data analysis was performed in a blinded fashion. The results were confirmed by two investigators, who analyzed the blindet data independently.

Reporting for specific materials, systems and methods

Materials & experimental systems

n/a	Involved in the study
[ ]	[x] Unique biological materials
[ ]	[x] Antibodies
[x]	[ ] Eukaryotic cell lines
[x]	[ ] Palaeontology
[ ]	[x] Animals and other organisms
[ ]	[x] Human research participants

Methods

n/a	Involved in the study
[x]	[ ] ChIP-seq
[ ]	[x] Flow cytometry
[x]	[ ] MRI-based neuroimaging

Unique biological materials

Policy information about availability of materials

Obtaining unique materials

All unique biological materials (genetically modified mouse strains) are available from standard commercial sources:

- C57BL/6J
Charles River
632

- C57BL/6Rj
Janvier Labs

- Tg(Cx3cr1-cre)MW126Gsat/Mmucd MMRRC
036395-UCD

- B6;129S6-Gt(ROSA)26Sortm9(CAG-tdTomato)Hze/J The Jackson Laboratory
007905

- STOCK Tg(ACTB-DsRed*MST)1Nagy/J, DsRed.T3 The Jackson Laboratory
005441

- B6.129P2(C)-Cx3cr1tm2.1(cre/ERT2)Jung/J The Jackson Laboratory
020940

- FVB-Tg(Csf1r-cre/Esr1*)1Jwp/J The Jackson Laboratory
019098

- C57BL/6-Gt(ROSA)26Sortm1(HBEGF)Awai/J
The Jackson Laboratory
007900

- B6;129S6-Gt(ROSA)26Sortm9(CAG-tdTomato)Hze/J The Jackson Laboratory
007905

- C57BL/6-Tg(Csf1r-HBEGF/mCherry)1Mnz/J The Jackson Laboratory
024046

- B6.129P-Cx3cr1tm1Litt/J The Jackson Laboratory
005582

All used mouse strains are additionally listed in supplementary table 1.

Antibodies

Antibodies used

Antibodies used in this study are:

- ApoE
unconjugated, Thermo Fisher, Cat: 701241, Lot: 1984882, Clone: 16H22L18, Dilution: 1:200

- CD1c-PerCP/Cy5.5
BioLegend, Cat: 331513, Lot: B267879, Clone: L161, Dilution: 1:500

- CD11b-PE/Cy7
BioLegend, Cat: 101216, Lot: B185646, Clone: M1/70, Dilution: 1:500

- CD11b-Alexa Fluor 488

BioLegend, Cat: 393107, Lot: B261594, Clone: LM2, Dilution: 1:500

- CD 14 PE-Cy7
BioLegend, Cat: 367111, Lot: B252403, Clone: 63D3, Dilution: 1:500

- CD15-Brilliant Violet 421
BioLegend, Cat: 232039, Lot: B263781, Clone: W6D3, Dilution: 1:500

- CD20-Brilliant Violet 421
BioLegend, Cat: 302329, Lot: B257594, Clone: 2H7, Dilution: 1:500

- CD31-PE
Biolegend, Cat:102507, Lot: B129965, Clone: MEC13.3, Dilution: 1:500

- CD31-Alexa Fluor 647
Biolegend, Cat: 102516, Lot: B234197, Clone: MEC13.3, Dilution: 2.5µg/mouse

- CD45-BrilliantViolet 421,
Biolegend, Cat:103133, Lot: B263588, Clone: 30-F11, Dilution: 1:500

- CD45-Alexa Fluor 700,
Biolegend, Cat: 368513, Lot: B248833, Clone: 2D1, Dilution: 1:500

- CD45.2-Alexa Flour 700
BioLegend, Cat: 109822, Lot: B202497, Clone: 104, Dilution: 1:500

- CD68-Alexa Fluor 594
BioLegend, Cat: 137020, Lot: B239125, Clone: FA-11, Dilution: 1:400

- CD68-Alexa Fluor 647
BioLegend, Cat: 137004, Lot: B153907, Clone: FA-11, Dilution: 1:400

- CD68 unconjugated
BioLegend, Cat: 333801, Lot: B200949, Clone: Y1/82A, Dilution: 1:200

- CD68 unconjugated
Abcam, Cat: ab955, Lot: GR3230929-1, Clone: KP1, Dilution: 1:200

- CD68 -Alexa Fluor 594
R&D systems, Cat: IC20401T, Lot: 1471045, Clone: 298807, Dilution: 1:200

- CSF1R-APC
Biolegend, Cat: 135510, Lot: B183456, Clone: AFS98, Dilution: 1:500

- CSF1R-Alexa Fluor 647
Biolegend, Cat: 135530, Lot: , Clone: AFS98, Dilution: 1:200

- Claudin 2 unconjugated
Abcam, Cat: ab53032, Lot: GR314368-11, Clone: polyclonal, Dilution: 1:200

- Claudin 5 unconjugated
Abcam, Cat: ab15106, Lot: GR3182385, Clone: polyclonal, Dilution: 1:200

- Claudin 13 unconjugated
Invitrogen, Cat: PA1-24420, Lot: TA2507851, Clone: polyclonal, Dilution: 1:200

- Connexin 43 unconjugated
Sigma Aldrich, Cat: C6219, Lot: 027144804V, Clone: polyclonal, Dilution: 1:200

- Donkey anti-Rabbit IgG Alexa Fluor 647
Life Technologies, Cat: A-31573, Lot: 1563697, Clone: polyclonal, Dilution: 1:200

- Donkey anti-Rabbit IgG Alexa Fluor 488
Life Technologies, Cat: A-21206, Lot: 1644644, Clone: polyclonal, Dilution: 1:200

- E-Cadherin-PE,
Biolegend, Cat: 147303, Lot: B260705, Clone: DECMA-1, Dilution: 1:500

- F4/80-Alexa Fluor 647,
BioLegend, Cat: 123122, Lot: B212680, Clone: BM8, Dilution: 1:400

- F4/80-FITC,
BioLegend, Cat: 123108, Lot: B177257, Clone: BM8, Dilution: 1:400

- HLA-DR PE,

BioLegend, Cat: 361605, Lot: B261328, Clone: Tü36, Dilution: 1:500

- Ki67-Af647,
BioLegend, Cat: 652407, Lot: B238782, Clone: 16A8, Dilution: 1:200

- Ly6C-Alexa Flour 488,
BioLegend, Cat: 128022, Lot: B248739, Clone: HK1.4, Dilution: 1:400

- Ly6G-Brilliant Violet,
BioLegend, Cat: 127627, Lot: B193096, Clone: 1A8, Dilution: 1:400

- Ly6G-FITC,
BioLegend, Cat: 127606, Lot: B175677, Clone: 1A8, Dilution: 1:400

- Ly6G-Alexa Fluor 488,
BioLegend, Cat: 127626, Lot: B240194, Clone: 1A8, Dilution: 1:400

- Ly6G-Alexa Fluor 647,
BioLegend, Cat: 127610, Lot: B204928, Clone: 1A8, Dilution: 1:200

- MHC II-PE,
Biolegend, Cat: 107608, Lot: B130064, Clone: M5/114.15.2, Dilution: 1:200

- Relm alpha
Abcam, Cat: ab39626, Lot: GR1287151, Clone: polyclonal, 1:200

- Trem 2 unconjugated
Abcam, Cat: ab86491, Lot: GR3207091-11, Clone: RM0139-5J46, Dilution: 1:200

- Trem2-APC,
R&D systems, Cat: FAB17291A, Lot: AADSO17111, Clone: 237920, Dilution: 1:500

- ZO-1 unconjugated, EMD Millipore, Cat: AB2272, Lot: 2905383, Clone: polyclonal, Dilution: 1:100

All used antibodies are listed in more detail in supplementary table 2, including information regarding antigen, conjugation, concentration, isotype, host reactivity, clone, source, Cat#, Lot#, dilution, and application.

Validation

Exclusively comercially available antibodies were used. Antibody specivicity, concentration and quality validation were performed by the manufacturers. Validation statements of the manufacturers can be found on their webpages:

- Abcam: https://www.abcam.com/primary-antibodies/improving-reproducibility-with-better-antibodies
- Biolegend: https://www.biolegend.com/reproducibility
- Invitrogen: https://www.thermofisher.com/de/de/home/life-science/antibodies/invitrogen-antibody-validation.html
- LifeTechnologies: https://www.thermofisher.com/de/de/home/life-science/antibodies/invitrogen-antibody-validation/independent-antibody-validation.html
- R&D Systems: https://www.rndsystems.com/tags/antibody-validation
- Sigma-Aldrich: https://www.sigmaaldrich.com/technical-documents/articles/biology/antibody-standard-validation.html

- ApoE, unconjugated, Thermo Fisher, Cat: 701241
https://assets.thermofisher.com/TFS-Assets/LSG/certificate/Certificates-of-Analysis/701241_1984882.PDF

- CD1c-PerCP/Cy5.5, BioLegend, Cat: 331513
https://www.biolegend.com/en-us/global-elements/pdf-popup/percp-cyanine5-5-anti-human-cd1c-antibody-5182?filename=PerCPCyanine55%20anti-human%20CD1c%20Antibody.pdf&pdfgen=true

- CD11b-PE/Cy7, BioLegend, Cat: 101216
https://www.biolegend.com/en-us/global-elements/pdf-popup/pe-cy7-anti-mouse-human-cd11b-antibody-1921?filename=PECy7%20anti-mousehuman%20CD11b%20Antibody.pdf&pdfgen=true

- CD11b-Alexa Fluor 488, BioLegend, Cat: 393107
https://www.biolegend.com/en-us/global-elements/pdf-popup/alexa-fluor-488-anti-human-cd11b-antibody-16010?filename=Alexa%20Fluor%20488%20anti-human%20CD11b%20Antibody.pdf&pdfgen=true

- CD 14 PE-Cy7, BioLegend, Cat: 367111
https://www.biolegend.com/en-us/global-elements/pdf-popup/pe-cy7-anti-human-cd14-antibody-12794?filename=PECy7%20anti-human%20CD14%20Antibody.pdf&pdfgen=true

- CD15-Brilliant Violet 421, BioLegend, Cat: 232039 falsch! ? 323039
https://www.biolegend.com/en-us/global-elements/pdf-popup/brilliant-violet-421-anti-human-cd15-ssea-1-antibody-12371?filename=Brilliant%20Violet%20421%20anti-human%20CD15%20SSEA-1%20Antibody.pdf&pdfgen=true

- CD20-Brilliant Violet 421, BioLegend, Cat: 302329
https://www.biolegend.com/en-us/global-elements/pdf-popup/brilliant-violet-421-anti-human-cd20-antibody-7192?filename=Brilliant%20Violet%20421%20anti-human%20CD20%20Antibody.pdf&pdfgen=true

- CD31-PE, Biolegend, Cat:102507
https://www.biolegend.com/en-us/global-elements/pdf-popup/pe-anti-mouse-cd31-antibody-379?filename=PE%20anti-mouse%20CD31%20Antibody.pdf&pdfgen=true

- CD31-Alexa Fluor 647, Biolegend, Cat: 102516
https://www.biolegend.com/en-us/global-elements/pdf-popup/alexa-fluor-647-anti-mouse-cd31-antibody-3094?filename=Alexa%20Fluor%20647%20anti-mouse%20CD31%20Antibody.pdf&pdfgen=true

- CD45-BrilliantViolet 421, Biolegend, Cat:103133
https://www.biolegend.com/en-us/global-elements/pdf-popup/brilliant-violet-421-anti-mouse-cd45-antibody-7253?filename=Brilliant%20Violet%20421%20anti-mouse%20CD45%20Antibody.pdf&pdfgen=true

- CD45-Alexa Fluor 700, Biolegend, Cat: 368513
https://www.biolegend.com/en-us/global-elements/pdf-popup/alexa-fluor-700-anti-human-cd45-antibody-12399?filename=Alexa%20Fluor%20700%20anti-human%20CD45%20Antibody.pdf&pdfgen=true

- CD45.2-Alexa Flour 700, BioLegend, Cat: 109822
https://www.biolegend.com/en-us/global-elements/pdf-popup/alexa-fluor-700-anti-mouse-cd45-2-antibody-3393?filename=Alexa%20Fluor%20700%20anti-mouse%20CD452%20Antibody.pdf&pdfgen=true
- CD68-Alexa Fluor 594, BioLegend, Cat: 137020
https://www.biolegend.com/en-us/global-elements/pdf-popup/alexa-fluor-594-anti-mouse-cd68-antibody-9671?filename=Alexa%20Fluor%20594%20anti-mouse%20CD68%20Antibody.pdf&pdfgen=true

- CD68-Alexa Fluor 647, BioLegend, Cat: 137004
https://www.biolegend.com/en-us/global-elements/pdf-popup/alexa-fluor-647-anti-mouse-cd68-antibody-6422?filename=Alexa%20Fluor%20647%20anti-mouse%20CD68%20Antibody.pdf&pdfgen=true
- CD68 unconjugated, BioLegend, Cat: 333801
https://www.biolegend.com/en-us/global-elements/pdf-popup/purified-anti-human-cd68-antibody-4835?filename=Purified%20anti-human%20CD68%20Antibody.pdf&pdfgen=true

- CD68 unconjugated, Abcam, Cat: ab955
https://www.abcam.com/cd68-antibody-kp1-ab955.html?productWallTab=Questions

- CD68 -Alexa Fluor 594, R&D systems, Cat: IC20401T https://resources.rndsystems.com/pdfs/datasheets/ic20401t.pdf

- CD115-APC, BioLegend, Cat: 135510

- Claudin 2 unconjugated, Abcam, Cat: ab53032 https://www.abcam.com/claudin-2-antibody-ab53032.html

- Claudin 5 unconjugated, Abcam, Cat: ab15106 https://www.abcam.com/claudin-5-antibody-ab15106.html

- Claudin 13 unconjugated, Invitrogen, Cat: PA1-24420
https://www.thermofisher.com/document-connect/document-connect.html?url=https%3A%2F%2Fassets.thermofisher.com%2FTFS-Assets%2FLSG%2Fcertificate%2FCertificates-of-Analysis%2FMA191114_TA2507851.PDF&title=TG9zLU5yLiZuYnNwO1RBMjUwNzg1MQ==

- Connexin 43 unconjugated, Sigma Aldrich, Cat: C6219 https://www.sigmaaldrich.com/content/dam/sigma-aldrich/docs/Sigma/Datasheet/3/c6219dat.pdf

- CSF1R-APC, Biolegend, Cat: 135510
https://www.biolegend.com/en-us/global-elements/pdf-popup/apc-anti-mouse-cd115-csf-1r-antibody-6336?filename=APC%20anti-mouse%20CD115%20CSF-1R%20Antibody.pdf&pdfgen=true

- CSF1R-Alexa Fluor 647, Biolegend, Cat: 135530
https://www.biolegend.com/en-us/global-elements/pdf-popup/alexa-fluor-647-anti-mouse-cd115-csf-1r-antibody-12485?filename=Alexa%20Fluor%20647%20anti-mouse%20CD115%20CSF-1R%20Antibody.pdf&pdfgen=true

- Donkey anti-Rabbit IgG Alexa Fluor 647, Life Technologies, Cat: A-31573
https://assets.thermofisher.com/TFS-Assets/LSG/certificate/Certificates%20of%20Analysis/1563697_A31573.pdf

- Donkey anti-Rabbit IgG Alexa Fluor 488, Life Technologies, Cat: A-21206
https://www.thermofisher.com/document-connect/document-connect.html?url=https%3A%2F%2Fassets.thermofisher.com%2FTFS-Assets%2FLSG%2Fcertificate%2FCertificates-of-Analysis%2F1644644_A21202.pdf&title=TG9zLU5yLiZuYnNwOzE2NDQ2NDQ=

-E-Cadherin-PE, Biolegend, Cat: 147303
https://www.biolegend.com/en-us/global-elements/pdf-popup/pe-anti-mouse-human-cd324-e-cadherin-antibody-9276?filename=PE%20anti-mousehuman%20CD324%20E-Cadherin%20Antibody.pdf&pdfgen=true

- F4/80-Alexa Fluor 647, BioLegend, Cat: 123122
https://www.biolegend.com/en-us/global-elements/pdf-popup/alexa-fluor-647-anti-mouse-f4-80-antibody-4074?filename=Alexa%20Fluor%20647%20anti-mouse%20F480%20Antibody.pdf&pdfgen=true

- F4/80-FITC, BioLegend, Cat: 123108
https://www.biolegend.com/en-us/global-elements/pdf-popup/fitc-anti-mouse-f4-80-antibody-4067?filename=FITC%20anti-

mouse%20F480%20Antibody.pdf&pdfgen=true
- HLA-DR PE, BioLegend, Cat: 361605
https://www.biolegend.com/en-us/global-elements/pdf-popup/pe-anti-human-hla-dr-antibody-9390?filename=PE%20anti-human%20HLA-DR%20Antibody.pdf&pdfgen=true

- Ki67-AF647, BioLegend, Cat: 652407 https://www.biolegend.com/Default.aspx?Id=18921

- Ly6C-Alexa Flour 488, BioLegend, Cat: 128022
https://www.biolegend.com/en-us/global-elements/pdf-popup/alexa-fluor-488-anti-mouse-ly-6c-antibody-6756?filename=Alexa%20Fluor%20488%20anti-mouse%20Ly-6C%20Antibody.pdf&pdfgen=true
- Ly6G-Brilliant Violet, BioLegend, Cat: 127627
https://www.biolegend.com/en-us/global-elements/pdf-popup/brilliant-violet-421-anti-mouse-ly-6g-antibody-7161?filename=Brilliant%20Violet%20421%20anti-mouse%20Ly-6G%20Antibody.pdf&pdfgen=true

- Ly6G-FITC, BioLegend, Cat: 127606
https://www.biolegend.com/en-us/global-elements/pdf-popup/fitc-anti-mouse-ly-6g-antibody-4775?filename=FITC%20anti-mouse%20Ly-6G%20Antibody.pdf&pdfgen=true

- Ly6G-Alexa Fluor 488, BioLegend, Cat: 127626
https://www.biolegend.com/en-us/global-elements/pdf-popup/alexa-fluor-488-anti-mouse-ly-6g-antibody-7085?filename=Alexa%20Fluor%20488%20anti-mouse%20Ly-6G%20Antibody.pdf&pdfgen=true

- Ly6G-Alexa Fluor 647, BioLegend, Cat: 127610
https://www.biolegend.com/en-us/global-elements/pdf-popup/alexa-fluor-647-anti-mouse-ly-6g-antibody-4780?filename=Alexa%20Fluor%20647%20anti-mouse%20Ly-6G%20Antibody.pdf&pdfgen=true

- MHC II-PE, Biolegend, Cat: 107608
https://www.biolegend.com/en-us/global-elements/pdf-popup/pe-anti-mouse-i-a-i-e-antibody-367?filename=PE%20anti-mouse%20I-AI-E%20Antibody.pdf&pdfgen=true

- Trem 2 unconjugated, Abcam, Cat: ab86491 https://www.abcam.com/trem2-antibody-rm0139-5j46-ab86491.html

- Trem2-APC, R&D systems, Cat: FAB17291A https://resources.rndsystems.com/pdfs/datasheets/fab17291a.pdf

- ZO-1 unconjugated, EMD Millipore, Cat: AB2272
http://www.merckmillipore.com/DE/de/product/Anti-ZO-1-Antibody,MM_NF-AB2272?ReferrerURL=https%3A%2F%2Fwww.google.com%2F#documentation

Animals and other organisms

Policy information about studies involving animals; ARRIVE guidelines recommended for reporting animal research

Laboratory animals

In this study the following mouse lines were used:

- C57BL/6
Strain: C57BL/6J, Source: Charles River, Identifier: 632

- C57BL/6
Strain: C57BL/6JRj, Source: Janvier Labs

- Cx3cr1cre:R26-tdTomato
Strain: Tg(Cx3cr1-cre)MW126Gsat/Mmucd, Source: MMRRC, Identifier: 036395-UCD

- DsRed
Strain: STOCK Tg(ACTB-DsRed*MST)1Nagy/J, DsRed.T3, Source: The Jackson Laboratory, Identifier: 005441

- Cx3cr1creER
Strain: B6.129P2(C)-Cx3cr1tm2.1(cre/ERT2)Jung/J, Source: The Jackson Laboratory, Identifier: 020940

- CSF1RcreER
Strain: FVB-Tg(Csf1r-cre/Esr1*)1Jwp/J, Source: The Jackson Laboratory, Identifier: 019098

- iDTR
Strain: C57BL/6-Gt(ROSA)26Sortm1(HBEGF)Awai/J, Source: The Jackson Laboratory, Idnetifier: 007900

- tdTomato
Strain: B6;129S6-Gt(ROSA)26Sortm9(CAG-tdTomato)Hze/J, Source: The Jackson Laboratory, Identifier: 007905

- CD115DTR
Strain: C57BL/6-Tg(Csf1r-HBEGF/mCherry)1Mnz/J, Source: The Jackson Laboratory, Identifier: 024046

- Cx3cr1gfp
Strain: B6.129P-Cx3cr1tm1Litt/J, Source: The Jackson Laboratory, Identifier: 005582

	All mice were housed under "specific pathogen-free" (SPF) conditions at the animal facilities of the University of Erlangen, Germany. Male and female mice at an age of 8-18 weeks were used.
Wild animals	This study does not include wild animals.
Field-collected samples	This study does not include field-collected samples.

Human research participants

Policy information about studies involving human research participants

Population characteristics	Synovial biopsies were obtained from knee joints of patients diagnosed with osteoarthritis (OA) and rheumatoid arthritis (RA), respectively. RA patients fulfilled the 2010 EULAR/ACR criteria of RA. All patients were ≥ 18years of age.
Recruitment	OA patients were recruited at the Department of Trauma Surgery, Universitätsklinikum Erlangen and RA patients were recruited at the Department of Internal Medicine 3 - Rheumatology and Immunology, Universitätsklinikum Erlangen. All patients signed an informed consent.

Flow Cytometry

Plots

Confirm that:

☒ The axis labels state the marker and fluorochrome used (e.g. CD4-FITC).

☒ The axis scales are clearly visible. Include numbers along axes only for bottom left plot of group (a 'group' is an analysis of identical markers).

☒ All plots are contour plots with outliers or pseudocolor plots.

☒ A numerical value for number of cells or percentage (with statistics) is provided.

Methodology

Sample preparation	Sample preparation is described in detail in the supplemental experimental procedures.
Instrument	Flow cytometry was performed with a CytoFLex S, Beckman Coulter. Sorting of cells was performed with a MoFlo XDP, Beckman Coulter.
Software	Flow cytometry data and cell sorting data were analyzed via the Summit Software System, CytExpert, FlowJo, and Kaluza software.
Cell population abundance	Purity of sorted cells was confirmed by flow cytometry analysis.
Gating strategy	FACS strategies are provided in detail in the extended data and supplementary experimental procedures.

☒ Tick this box to confirm that a figure exemplifying the gating strategy is provided in the Supplementary Information.

LETTER

https://doi.org/10.1038/s41586-019-1472-0

BORIS promotes chromatin regulatory interactions in treatment-resistant cancer cells

David N. Debruyne[1,2,15], Ruben Dries[1,2,3,15], Satyaki Sengupta[1,2], Davide Seruggia[1,4,5,6], Yang Gao[1,2], Bandana Sharma[1,2], Hao Huang[1,2], Lisa Moreau[7], Michael McLane[1,2], Daniel S. Day[8,9], Eugenio Marco[3,10], Ting Chen[11], Nathanael S. Gray[12,13], Kwok-Kin Wong[14], Stuart H. Orkin[1,4,5,6], Guo-Cheng Yuan[3,10], Richard A. Young[8,9] & Rani E. George[1,2,4]*

The CCCTC-binding factor (CTCF), which anchors DNA loops that organize the genome into structural domains, has a central role in gene control by facilitating or constraining interactions between genes and their regulatory elements[1,2]. In cancer cells, the disruption of CTCF binding at specific loci by somatic mutation[3,4] or DNA hypermethylation[5] results in the loss of loop anchors and consequent activation of oncogenes. By contrast, the germ-cell-specific paralogue of *CTCF*, *BORIS* (brother of the regulator of imprinted sites, also known as *CTCFL*)[6], is overexpressed in several cancers[7–9], but its contributions to the malignant phenotype remain unclear. Here we show that aberrant upregulation of *BORIS* promotes chromatin interactions in *ALK*-mutated, *MYCN*-amplified neuroblastoma[10] cells that develop resistance to ALK inhibition. These cells are reprogrammed to a distinct phenotypic state during the acquisition of resistance, a process defined by the initial loss of *MYCN* expression followed by subsequent overexpression of *BORIS* and a concomitant switch in cellular dependence from MYCN to BORIS. The resultant BORIS-regulated alterations in chromatin looping lead to the formation of super-enhancers that drive the ectopic expression of a subset of proneural transcription factors that ultimately define the resistance phenotype. These results identify a previously unrecognized role of BORIS—to promote regulatory chromatin interactions that support specific cancer phenotypes.

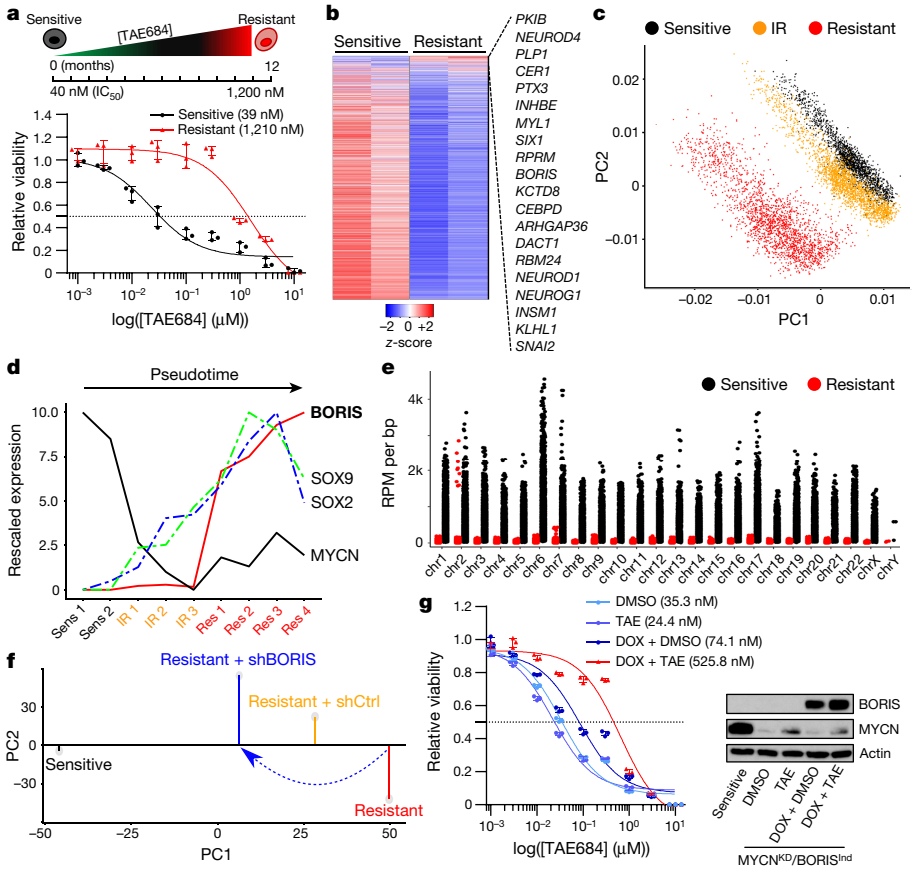

Fig. 1 | Targeted therapy resistance in neuroblastoma is associated with transcriptional reprogramming and a switch in dependency from amplified MYCN to BORIS. a, Top, schematic representation of the development of resistance. Bottom, dose–response curves of TAE684-sensitive and -resistant Kelly neuroblastoma cells incubated in increasing concentrations of TAE684 for 72 h. Data are mean ± s.d., $n = 3$ biological replicates. **b**, Heat map of gene expression values in sensitive versus resistant cells ($n = 2$ biological replicates). Rows are z-scores calculated for each gene in both cell types. **c**, PCA of scRNA-seq data of sensitive ($n = 5{,}432$), intermediate resistant (IR; $n = 6{,}376$) and resistant ($n = 6{,}379$) cells showing the first two principal components (PCs). **d**, Pseudotime analysis of transcription factor expression during the development of resistance. **e**, ChIP–seq signals of genome-wide MYCN binding in sensitive and resistant cells, reported as reads per million (RPM) per base pair (bp) for each chromosome (chr). **f**, PCA of gene expression profiles showing the first two principal components ($n = 2$ biological replicates). **g**, Dose–response curves for TAE684 (half-maximum inhibitory concentration (IC_{50}) values in parenthesis) and immunoblot analysis (representative of two independent experiments) of BORIS and MYCN expression in sensitive cells expressing short hairpin RNA (shRNA) against *MYCN* ($MYCN^{KD}$) and doxycycline-inducible *BORIS* ($BORIS^{Ind}$), treated with dimethylsulfoxide (DMSO) or 1 μM TAE684, with or without doxycycline (DOX). Data are mean ± s.d., $n = 3$ biological replicates.

[1]Department of Pediatric Oncology, Dana-Farber Cancer Institute, Boston, MA, USA. [2]Department of Pediatrics, Harvard Medical School, Boston, MA, USA. [3]Department of Biostatistics and Computational Biology, Dana-Farber Cancer Institute, Boston, MA, USA. [4]Division of Hematology/Oncology, Boston Children's Hospital, Boston, MA, USA. [5]Harvard Stem Cell Institute, Harvard Medical School, Boston, MA, USA. [6]Howard Hughes Medical Institute, Boston, MA, USA. [7]Department of Radiation Oncology, Dana-Farber Cancer Institute, Boston, MA, USA. [8]Whitehead Institute for Biomedical Research, Cambridge, MA, USA. [9]MIT Department of Biology, Cambridge, MA, USA. [10]Department of Biostatistics, Harvard TC Chan School of Public Health, Boston, MA, USA. [11]Department of Medical Oncology, Dana-Farber Cancer Institute, Boston, MA, USA. [12]Department of Cancer Biology, Dana-Farber Cancer Institute, Boston, MA, USA. [13]Department of Biological Chemistry and Molecular Pharmacology, Harvard Medical School, Boston, MA, USA. [14]Division of Hematology and Medical Oncology, Laura and Isaac Perlmutter Cancer Center, New York University Langone Medical Center, New York, NY, USA. [15]These authors contributed equally: David N. Debruyne, Ruben Dries.. *e-mail: rani_george@dfci.harvard.edu

Unlike *CTCF*, which is uniformly expressed in healthy tissues and cancer cells, the expression of *BORIS* is typically restricted to the testis[6] and embryonic stem cells[11] (Extended Data Fig. 1a). However, when aberrantly expressed in cancer[7–9], it is associated with high-risk features that include resistance to treatment (Extended Data Fig. 1b, c). We identified *BORIS* as one of the most differentially expressed genes in neuroblastoma cells driven by amplified *MYCN*[12] and ALK(F1174L)[13] and rendered resistant to ALK inhibition. Kelly human neuroblastoma cells were exposed to increasing concentrations of the ALK inhibitor TAE684[14] until stable resistance was achieved (Fig. 1a, Extended Data Fig. 2a–d). The acquisition of stable resistance coincided not only with the loss of ALK phosphorylation—which indicates that the cells no longer required activation of this receptor tyrosine kinase to maintain their oncogenic properties—but also with the absence of other common instigators of resistance (Extended Data Fig. 2a, e–h; Supplementary Note 1). However, comparison of the gene expression profiles of the TAE684-sensitive and resistant cells showed generalized downregulation of transcription in the resistant cells, but with marked upregulation of a subset of transcription factors not typically associated with neuroblastoma cells[15,16] (Fig. 1b).

We therefore proposed that the resistant cells had probably undergone transcriptional reprogramming during the development of resistance. To determine the dynamics of resistance development, we performed single-cell RNA sequencing (scRNA-seq) analysis on sensitive, intermediate and fully resistant cell states (Extended Data Fig. 3a). Principal component analysis (PCA) indicated a stepwise transition as cells progressed from the sensitive to the fully resistant state (Fig. 1c). This transition was confirmed by distributed stochastic neighbour embedding (*t*-SNE)[17], which clustered the cells into three non-overlapping categories (Extended Data Fig. 3b, c). Pseudotime analysis based on the transcription factors that were differentially expressed throughout the development of resistance revealed that the initial major alteration was loss of *MYCN* expression, which persisted in stably resistant cells (Fig. 1d, Extended Data Fig. 3d, e). To understand this unexpected result, we analysed the status of *MYCN* in these cells, and found that although genomic amplification was retained, the *MYCN* locus was epigenetically repressed (Extended Data Fig. 3f, g). This state was accompanied by a genome-wide reduction of MYCN binding to DNA and a consequent revision of associated downstream transcription outcomes[15,18,19] (Fig. 1e, Extended Data Fig. 3h). Coincident with this loss of transcriptional activity, the resistant cells were no longer dependent on MYCN for survival, unlike their sensitive controls, which underwent apoptosis after depletion of MYCN (Extended Data Fig. 3i). Subsequent resistance stages were defined by a gradual increase in the expression of the neural developmental markers *SOX2* and *SOX9*[20], followed by upregulation of *BORIS*, ultimately leading to a fully resistant state in which *BORIS* expression was highest and detectable in essentially all cells (Fig. 1d, Extended Data Fig. 3j, k). Overexpression of *BORIS*, which coincided with promoter hypomethylation (Extended Data Fig. 4a, b), was also observed in additional neuroblastoma cell lines rendered resistant to TAE684 (SK-N-SH) or the CDK12 inhibitor E9[21] (SK-N-BE(2)) (Extended Data Fig. 4c, d), which suggests that our findings are not restricted to a single cell line or kinase inhibitor. Indeed, overexpression of *BORIS* in tumours was significantly associated with high-risk disease and a poor outcome in patients with neuroblastoma treated with a variety of regimens (Extended Data Fig. 4e–g).

To clarify the role of BORIS in the resistance phenotype, we depleted its expression in resistant cells, and observed a partial reversal to the sensitive-cell state with re-emergence of MYCN and ALK expression (Fig. 1f, Extended Data Fig. 5a–c). However, this outcome was insufficient to maintain cell growth, as depletion of BORIS in resistant cells ultimately decreased cell viability (Extended Data Fig. 5d, e), which indicates a switch from MYCN to BORIS dependency with stable resistance. This transition was associated with changes in cellular growth kinetics—from a highly proliferative, *MYCN*-overexpressing sensitive state to an intermediate, slow-cycling phenotype that was partially reversed in fully resistant cells, coincident with overexpression of

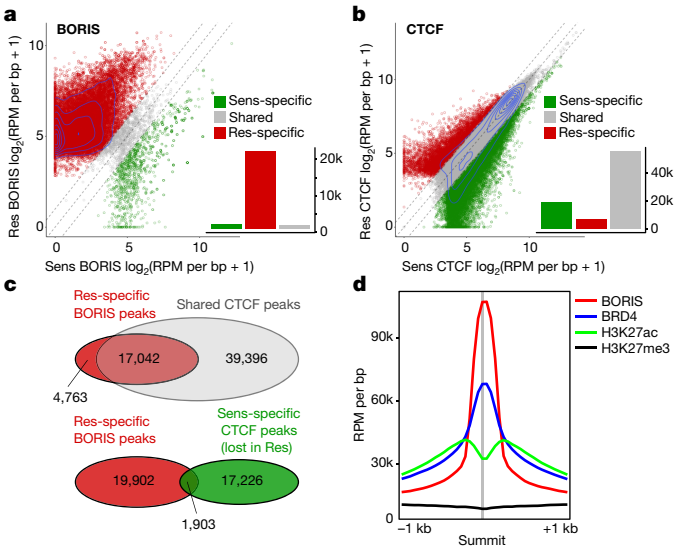

Fig. 2 | *BORIS* overexpression is associated with its increased chromatin occupancy in resistant cells, whereas CTCF binding is unchanged. **a**, Scatter plot of BORIS binding in sensitive (Sens) and resistant (Res) cells for all detected BORIS-binding sites. BORIS peaks unique to resistant cells ($n = 21,805$; 91%), sensitive cells ($n = 1,125$; 4.7%) and shared between the two cell types ($n = 1,086$; 4.5%) are shown. **b**, Scatter plot of CTCF binding in sensitive and resistant cells for all detected CTCF-binding sites. CTCF peaks unique to resistant cells ($n = 6,808$; 8.3%), sensitive cells ($n = 19,129$; 23.2%) and shared between the two cell types ($n = 56,438$; 68.5%) are shown. **c**, Overlap between BORIS peaks that are unique to resistant cells and CTCF peaks shared between resistant and sensitive cells (top), and between resistant cell-specific BORIS peaks and sensitive cell-specific CTCF peaks (bottom). **d**, Meta-analysis of average ChIP–seq signals at resistant cell-specific BORIS-binding sites. All panels, $n = 2$ biological replicates.

BORIS (Extended Data Fig. 5f–h). Given the many sequential steps involved in the evolution of resistance, overexpression of *BORIS* alone was not adequate to induce this phenotype (data not shown). Instead, concomitant downregulation of *MYCN* expression and *BORIS* overexpression in the presence of ALK inhibition were required to generate resistance in sensitive cells (Fig. 1g). This combination of factors also led to increased expression of the transcription factors that were upregulated in the original TAE684-resistant cells, including *SOX2* and *SOX9* (Extended Data Figs. 3d, 5i). Thus, resistance to inhibition of ALK in neuroblastoma cells evolves through a multistep process that promotes a dependency switch from a dominant oncogenic stimulus—amplified *MYCN*—to a phenotypically distinct state characterized by overexpression of *BORIS*. In this context, the resistant cells ultimately become dependent on BORIS for survival, which supports a key role for this protein in maintenance of the resistance state.

We next asked whether the aberrant expression of BORIS, a DNA-binding protein[6], affected its genome-wide occupancy in resistant cells. We observed a large (tenfold) gain in BORIS-bound peaks after chromatin immunoprecipitation followed by high-throughput sequencing (ChIP–seq) analysis in resistant cells: 22,891 versus 2,211 in sensitive cells (Fig. 2a, Extended Data Fig. 6a, b). By contrast, CTCF binding did not change substantially between sensitive and resistant cells (75,567 versus 63,246 peaks) (Fig. 2b). A considerable portion ($n = 17,042$; 78%) of the BORIS peaks unique to resistant cells overlapped with CTCF peaks shared by both cell types (Fig. 2c), consistent with their heterodimerization[22] (Extended Data Fig. 6c). However, only a small proportion ($n = 1,903$; 8.7%) overlapped with CTCF peaks unique to sensitive cells, which suggests that BORIS does not replace CTCF in resistant cells. BORIS preferentially occupied gene regulatory regions—enhancers and promoters (60%)—in resistant cells (Extended Data Fig. 6d, e), which is consistent with its propensity to bind to open chromatin regions[23] (Fig. 2d). Such differential chromatin

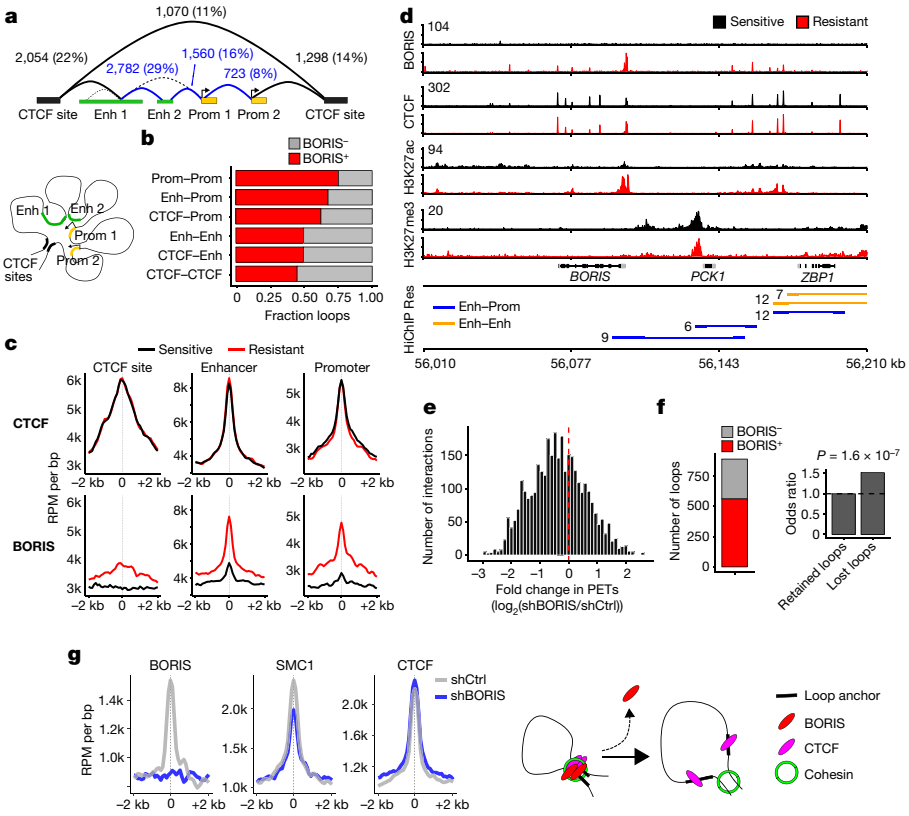

Fig. 3 | BORIS promotes new chromatin interactions in resistant cells. a, DNA interactions gained in resistant cells based on SMC1A HiChIP analysis. Interaction classes were determined from the genomic locations of the associated anchors (overlapping promoter (Prom) regions (transcription start site (TSS) ± 2 kb), active enhancer (Enh) regions, or CTCF sites only, in that order). Absolute numbers and percentages for each loop type (structural (black), regulatory (blue)) are shown. Cartoon illustrates the spatial proximity induced by DNA looping between these regions. **b**, Fractions of loops bound by BORIS within each interaction class. **c**, Meta-analysis of average CTCF and BORIS ChIP–seq signals in sensitive and resistant cells at the three main anchor types normalized by the number of interactions ($n = 2$ biological replicates). Anchor sites were centred and extended in both directions (± 2 kb). **d**, ChIP–seq tracks of the indicated proteins in sensitive and resistant cells at the *BORIS* locus (representative of two independent experiments), with resistant cell-specific regulatory interactions shown below (HiChIP resistant: paired-end tag (PET) numbers, next to each interaction). Signal intensity is given in the top left corner for each track. **e**, PET interactions in BORIS-depleted (shBORIS) versus control (shCtrl) cells. **f**, Resistant cell-specific loops lost after depletion of BORIS based on loops negative or positive for BORIS binding in shCtrl cells (left), and the odds ratio of losing a loop previously bound by BORIS (right). *P* value determined by two-sided Fisher's exact test. **g**, Meta-analysis of average BORIS, SMC1A and CTCF ChIP–seq signals at resistant cell-specific loop anchors that were lost after depletion of BORIS ($n = 2$ biological replicates). BORIS depletion at loop anchors inhibits retention of the cohesin complex, and thus prevents the formation of new loops (loop extrusion model). In **a**, **b**, **e** and **f**, $n = 3$ biological replicates.

binding at distinct highly expressed genes in resistant versus sensitive cells was commensurate with the MYCN-to-BORIS dependency switch (Extended Data Fig. 6f, g).

The proclivity of aberrantly expressed BORIS for genomic regions associated with active chromatin features in resistant cells suggested that it may, like CTCF and cohesin, regulate gene expression through chromatin looping. Thus, we examined the chromatin looping profiles of sensitive and resistant cells, using cohesin (SMC1A)-based high-throughput chromosome conformation capture followed by chromatin immunoprecipitation (HiChIP)[24] (Extended Data Fig. 7a). On the basis of the genomic locations of the associated loop anchors, six classes of interactions were identified[25]: three longer average interaction loops with a CTCF site on at least one anchor; and three smaller connecting regulatory regions (Fig. 3a, Extended Data Fig. 7b). The overlap of BORIS binding with loop anchors revealed that most (56%) of the 9,487 interactions gained in resistant cells were positive for BORIS ($\log_2$-transformed fold change > 1; false discovery rate (FDR) < 0.01) (Fig. 3b, Extended Data Fig. 7c). Notably, BORIS was enriched at anchors that were associated with regulatory regions, whereas CTCF binding remained constant, as seen at the BORIS locus itself (Fig. 3c, d). In fact, BORIS binding alone at CTCF-negative loop anchors was sufficient to generate new interactions in resistant cells (Extended Data Fig. 7d).

To test whether the newly formed interactions in resistant cells were mediated by BORIS binding, we analysed the consequences of BORIS depletion on loop architecture (Extended Data Fig. 7e). Regulatory interactions specific to resistant cells displayed a global shift towards loss after knockdown of BORIS (Fig. 3e), with more than one-quarter of the total interactions lost, of which 63% were positive for BORIS at their anchors (Fig. 3f). Interactions in which anchors were bound by BORIS (especially enhancer–promoter and promoter–promoter interactions) were more likely to be lost after BORIS depletion than those that were not BORIS-bound (Fig. 3f, Extended Data Fig. 7f, g). These results agree with the loop extrusion model[26], as BORIS loss resulted in decreased SMC1A binding, preferentially at lost interactions, whereas CTCF binding did not change significantly (Fig. 3g, Extended Data Fig. 7h–j). These data confirm that BORIS is a crucial factor in the looping landscape of resistant cells.

Genes associated with new BORIS-positive regulatory interactions were expressed at higher levels than those associated with BORIS-negative regulatory interactions or genes not associated with new regulatory interactions (Fig. 4a). Because genes that define cell identity are often regulated by super-enhancers in both healthy and cancer cells[15,27,28], we characterized the super-enhancer landscape of our cells, observing that the super-enhancers unique to resistant cells were enriched at BORIS-positive regulatory loops (Extended Data Fig. 8a–c).

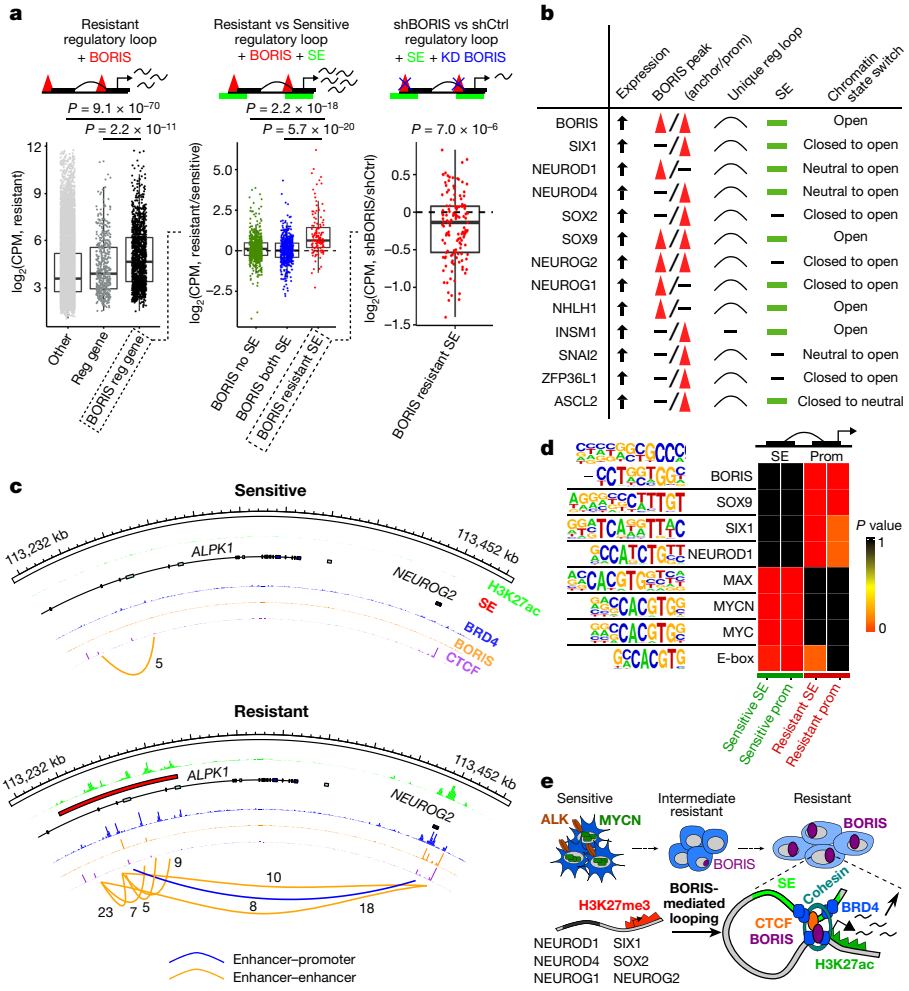

Fig. 4 | BORIS-regulated chromatin remodelling supports a phenotypic switch that maintains the resistant state. a, Left, fold change in expression in counts per million (CPM) of genes involved in resistant cell-specific regulatory interactions that are positive for BORIS binding ($n = 1{,}368$) versus those involved in regulatory interactions that are negative for BORIS binding ($n = 519$) or not associated with a new regulatory interaction (other) ($n = 16{,}151$). Centre, fold change in expression of genes involved in resistant cell-specific regulatory interactions positive for BORIS binding and associated with super-enhancers (SEs) specific to resistant cells ($n = 134$) versus those with super-enhancers shared by both cell types ($n = 514$) or not associated with super-enhancers ($n = 720$). Right, fold change in expression of genes involved in resistant cell-specific regulatory interactions positive for BORIS binding and associated with resistant cell-specific super-enhancers before and after BORIS knockdown (KD) ($n = 134$) (P values determined by two-sided Wilcoxon rank-sum test). For all box plots, centre lines denote medians; box limits denote twenty-fifth and seventy-fifth percentiles; whiskers denote minima and maxima (1.5× the interquartile range). **b**, Highest-ranked transcription factors associated with the resistance phenotype selected based on the presence of at least four of the five indicated features. **c**, ChIP–seq tracks of the indicated proteins in sensitive and resistant cells at the *NEUROG2* locus; regulatory interactions with PET numbers indicated below. **d**, Transcription factor recognition motifs at super-enhancers and promoters (± 2 kb) of the 1,000 highest-expressed genes in resistant and sensitive cells ($n = 2$ biological replicates) (P values determined by hypergeometric enrichment test). Panels **a**–**c** integrate data of biological replicates from expression microarrays ($n = 2$), ChIP–seq ($n = 2$) and HiChIP ($n = 3$). **e**, Proposed role of BORIS in resistant cells.

The presence of such super-enhancers correlated significantly with higher expression of their associated genes in resistant versus sensitive cells (Fig. 4a). These BORIS-positive super-enhancer-associated genes were also enriched for genes that underwent a chromatin state switch from a closed or neutral to an open configuration in resistant cells (Extended Data Fig. 8d, e). Depletion of BORIS resulted in the decreased expression of genes associated with BORIS-positive interactions, especially genes associated with resistant cell-specific super-enhancers (Fig. 4a, Extended Data Fig. 8f). These observations suggest that BORIS-mediated alterations in chromatin looping lead to interactions of newly formed super-enhancers with their target genes, which results in their increased expression.

We next sought to identify BORIS-regulated genes that are functionally linked to the resistance phenotype by integrating gene expression, BORIS-mediated looping, super-enhancer landscape and chromatin state. This analysis revealed 89 genes (Supplementary Table), including 13 transcription factors, that are highly expressed during early neural development and are crucial to cell fate decisions[20,29,30] (Fig. 4b, c, Extended Data Fig. 8g). The expression of these proneural transcription factors paralleled that of BORIS in resistant cells, and was dependent on BORIS-mediated looping, as BORIS depletion led to their downregulation (Extended Data Fig. 8h, i). Moreover, analysis of transcription factor binding sites revealed enrichment of BORIS and several of these proneural transcription factors at the regulatory regions of the highest-expressed genes in resistant cells, whereas sensitive cells were dominated by MYC, MYCN and MAX E-box and E-box-like motifs (Fig. 4d). Similar increased expression of proneural transcription factors with increased BORIS occupancy at their promoters was seen in *BORIS*-overexpressing E9-resistant SK-N-BE(2) neuroblastoma cells compared with their sensitive counterparts (Extended Data Fig. 8j, k). The high transcriptional activity of these BORIS-regulated genes was also associated with increased binding of the transcriptional activator

BRD4, which rendered the resistant cells more sensitive to BET inhibition (Extended Data Fig. 9; Supplementary Note 2). Together, these results indicate the establishment of an alternative transcription factor regulatory network controlled by BORIS-induced chromatin remodelling to support the resistant cell state.

Thus, using a pair of isogenic ALK-inhibitor sensitive and resistant neuroblastoma cell lines, we show that the CTCF paralogue BORIS can promote regulatory DNA interactions that support a phenotypic switch in the context of treatment resistance (Fig. 4e). This mechanism appears relevant to different neuroblastoma cell lines and kinase inhibitors and may extend to other cancers. In Ewing sarcoma, in which overexpression of *BORIS* is associated with metastasis and relapse (Extended Data Fig. 1c), we observed increased BORIS occupancy at regulatory regions in chemotherapy-resistant cell lines (Extended Data Fig. 10; Supplementary Note 3). Further work will establish whether BORIS-mediated alteration of chromatin looping is a general mechanism by which tumour cells co-opt developmental networks to sustain alternative cell states in response to targeted or conventional therapies.

Online content

Any methods, additional references, Nature Research reporting summaries, source data, extended data, supplementary information, acknowledgements, peer review information; details of author contributions and competing interests; and statements of data and code availability are available at https://doi.org/10.1038/s41586-019-1472-0.

Received: 21 July 2017; Accepted: 11 July 2019;
Published online 7 August 2019.

1. Dixon, J. R. et al. Topological domains in mammalian genomes identified by analysis of chromatin interactions. *Nature* **485**, 376–380 (2012).
2. Phillips-Cremins, J. E. et al. Architectural protein subclasses shape 3D organization of genomes during lineage commitment. *Cell* **153**, 1281–1295 (2013).
3. Hnisz, D. et al. Activation of proto-oncogenes by disruption of chromosome neighborhoods. *Science* **351**, 1454–1458 (2016).
4. Katainen, R. et al. CTCF/cohesin-binding sites are frequently mutated in cancer. *Nat. Genet.* **47**, 818–821 (2015).
5. Flavahan, W. A. et al. Insulator dysfunction and oncogene activation in *IDH* mutant gliomas. *Nature* **529**, 110–114 (2016).
6. Loukinov, D. I. et al. BORIS, a novel male germ-line-specific protein associated with epigenetic reprogramming events, shares the same 11-zinc-finger domain with CTCF, the insulator protein involved in reading imprinting marks in the soma. *Proc. Natl Acad. Sci. USA* **99**, 6806–6811 (2002).
7. Klenova, E. M., Morse, H. C. III, Ohlsson, R. & Lobanenkov, V. V. The novel *BORIS + CTCF* gene family is uniquely involved in the epigenetics of normal biology and cancer. *Semin. Cancer Biol.* **12**, 399–414 (2002).
8. Martin-Kleiner, I. BORIS in human cancers — a review. *Eur. J. Cancer* **48**, 929–935 (2012).
9. Garikapati, K. R. et al. Down-regulation of BORIS/CTCFL efficiently regulates cancer stemness and metastasis in *MYCN* amplified neuroblastoma cell line by modulating Wnt/β-catenin signaling pathway. *Biochem. Biophys. Res. Commun.* **484**, 93–99 (2017).
10. Cheung, N. K. & Dyer, M. A. Neuroblastoma: developmental biology, cancer genomics and immunotherapy. *Nat. Rev. Cancer* **13**, 397–411 (2013).
11. Monk, M., Hitchins, M. & Hawes, S. Differential expression of the embryo/cancer gene *ECSA*(*DPPA2*), the cancer/testis gene *BORIS* and the pluripotency structural gene *OCT4*, in human preimplantation development. *Mol. Hum. Reprod.* **14**, 347–355 (2008).
12. Brodeur, G. M., Seeger, R. C., Schwab, M., Varmus, H. E. & Bishop, J. M. Amplification of N-myc in untreated human neuroblastomas correlates with advanced disease stage. *Science* **224**, 1121–1124 (1984).
13. George, R. E. et al. Activating mutations in ALK provide a therapeutic target in neuroblastoma. *Nature* **455**, 975–978 (2008).
14. Galkin, A. V. et al. Identification of NVP-TAE684, a potent, selective, and efficacious inhibitor of NPM-ALK. *Proc. Natl Acad. Sci. USA* **104**, 270–275 (2007).
15. Chipumuro, E. et al. CDK7 inhibition suppresses super-enhancer-linked oncogenic transcription in MYCN-driven cancer. *Cell* **159**, 1126–1139 (2014).
16. Durbin, A. D. et al. Selective gene dependencies in *MYCN*-amplified neuroblastoma include the core transcriptional regulatory circuitry. *Nat. Genet.* **50**, 1240–1246 (2018).
17. van der Maaten, L. & Hinton, G. Visualizing data using t-SNE. *J. Mach. Learn. Res.* **9**, 2579–2605 (2008).
18. Zeid, R. et al. Enhancer invasion shapes MYCN-dependent transcriptional amplification in neuroblastoma. *Nat. Genet.* **50**, 515–523 (2018).
19. Muhar, M. et al. SLAM-seq defines direct gene-regulatory functions of the BRD4-MYC axis. *Science* **360**, 800–805 (2018).
20. Wegner, M. & Stolt, C. C. From stem cells to neurons and glia: a Soxist's view of neural development. *Trends Neurosci.* **28**, 583–588 (2005).
21. Gao, Y. et al. Overcoming resistance to the THZ series of covalent transcriptional CDK inhibitors. *Cell Chem. Biol.* **25**, 135–142 (2018).
22. Pugacheva, E. M. et al. Comparative analyses of CTCF and BORIS occupancies uncover two distinct classes of CTCF binding genomic regions. *Genome Biol.* **16**, 161 (2015).
23. Bergmaier, P. et al. Choice of binding sites for CTCFL compared to CTCF is driven by chromatin and by sequence preference. *Nucleic Acids Res.* **46**, 7097–7107 (2018).
24. Mumbach, M. R. et al. HiChIP: efficient and sensitive analysis of protein-directed genome architecture. *Nat. Methods* **13**, 919–922 (2016).
25. Dowen, J. M. et al. Control of cell identity genes occurs in insulated neighborhoods in mammalian chromosomes. *Cell* **159**, 374–387 (2014).
26. Sanborn, A. L. et al. Chromatin extrusion explains key features of loop and domain formation in wild-type and engineered genomes. *Proc. Natl Acad. Sci. USA* **112**, E6456–E6465 (2015).
27. Whyte, W. A. et al. Master transcription factors and mediator establish super-enhancers at key cell identity genes. *Cell* **153**, 307–319 (2013).
28. Hnisz, D. et al. Super-enhancers in the control of cell identity and disease. *Cell* **155**, 934–947 (2013).
29. Kumar, J. P. The sine oculis homeobox (SIX) family of transcription factors as regulators of development and disease. *Cell. Mol. Life Sci.* **66**, 565–583 (2009).
30. Dennis, D. J., Han, S. & Schuurmans, C. bHLH transcription factors in neural development, disease, and reprogramming. *Brain Res.* **1705**, 48–65 (2019).

METHODS

Cell lines. Human neuroblastoma cell lines Kelly and SK-N-BE(2) and human Ewing sarcoma cell lines TC-32, TC-71 and CHLA-10[31,32] were obtained from the Children's Oncology Group cell line bank. Human neuroblastoma cell line SK-N-SH and human embryonic kidney cell line HEK293T were obtained from the American Type Culture Collection. Cell line authenticity was confirmed by genotyping, and cells were tested negative for mycoplasma contamination every 3 months. All cells except HEK293T were grown in RPMI-1640 medium supplemented with 10% fetal bovine serum (FBS) and 1% penicillin/streptomycin (Life Technologies). HEK293T cells were grown in DMEM medium supplemented with 10% FBS and 1% penicillin/streptomycin (Life Technologies). Resistant cells were grown in the presence of either the ALK inhibitor, TAE684[14] (Kelly and SK-N-SH) or the CDK12 inhibitor, E9[21] (SK-N-BE(2)).

Compounds. TAE684 and E9 were synthesized in-house in the Gray laboratory and JQ1[33] was obtained from J.Qi's laboratory at the Dana-Farber Cancer Institute (DFCI). Ceritinib[34], lorlatinib[35] and I-BET726[36] were purchased from Selleck Chemicals.

Synthetic RNA spike-in and microarray analysis. Total RNA and sample preparation was performed as previously described[37]. In brief, cells were either incubated in medium containing DMSO, TAE684 (1 μM) or JQ1 (2.5 μM), or infected with shRNA (Ctrl or BORIS) for 24 h. Cell numbers were determined using a Countess II cell counter (Life Technologies) before lysis and RNA extraction. Biological duplicates (equivalent to 5×10^6 cells per replicate) were collected and homogenized in 1 ml of TRIzol Reagent (Ambion), purified using the mirVANA miRNA isolation kit (Ambion) following the manufacturer's instructions and re-suspended in 50 μl nuclease-free water (Ambion). Total RNA was spiked-in with ERCC RNA Spike-In Mix (Ambion), treated with DNA-free DNase I (Ambion) and analysed on an Agilent 2100 Bioanalyzer (Agilent Technologies) for integrity. RNA with the RNA Integrity Number above 9.8 was hybridized to Affymetrix GeneChip PrimeView Human Gene Expression arrays (Affymetrix).

Antibodies. The following antibodies were used: N-MYC (9405), N-MYC (51705), cleaved PARP (9541), cleaved caspase 3 (9661), ALK (3333), AKT (4691), pAKT-T308 (9275), pAKT-S473 (#9271), ERK (4695), pERK (4377), S6 (2217), pS6 (4857), STAT3 (4904), pSTAT3 (9131), ABCB1 (12683), SOX2 (3579), β-actin (4967), CTCF (3417), normal rabbit IgG (2729) and HRP anti-mouse IgG (7076) from Cell Signaling Technology; HRP anti-rabbit IgG (sc-2357) from Santa Cruz Biotechnology; BRD4 (A301-985A100) and SMC1A (A300-055A) from Bethyl Laboratories; CTCF (07-729), SOX9 (AB5535) and H3K27me3 (07-449) from Millipore; pALK-Y1507 (ab73996), BORIS (ab187163) and H3K27ac (ab2729) from Abcam; BORIS (NBP2-52405) from NOVUS Biologicals; BORIS (39851) from Active Motif; SIX1 (HPA001893) from Sigma-Aldrich; and Vysis LSI N-MYC (2p24) SpectrumGreen/Vysis CEP 2 SpectrumOrange Probe (07J72-001) from Abbott.

Cell viability and growth curve assays. Viability and growth experiments were performed using the CellTiter-Glo Luminescent Cell Viability Assay (Promega) according to the manufacturer's instructions, as previously described[38]. Cells were plated in 96-well plates at a seeding density of 4×10^3 cells per well. For growth assays, the cells were analysed each day until day 5. For viability, after 24 h, the cells were treated with various concentrations of the indicated drug (ranging from 1 nM to 10 μM except for I-BET726: 2 nM to 20 μM). DMSO without drug served as a negative control. After 72 h of incubation, cells were analysed for cell viability and IC_{50} values were determined using a nonlinear regression curve fit with GraphPad Prism 6 software.

Cell-cycle analysis. Cell-cycle analysis was performed 24 h after cell plating using propidium iodide staining, as previously described[15]. Cells fixed with 80% ethanol overnight at 4 °C were resuspended in PBS supplemented with 0.1% Triton X-100 (Sigma-Aldrich), 25 mg ml^{-1} propidium iodide (BD Biosciences) and 0.2 mg ml^{-1} RNase A (Sigma-Aldrich). After 45 min at 37 °C in the dark, analysis was performed on a FACSCalibur flow cytometer (BD Biosciences). Cell-cycle profiles were plotted as histograms generated using FlowJo software (FLOWJO).

Western blotting. Cell or tumour tissue was lysed in NP-40 buffer (Invitrogen) containing a 1× complete protease inhibitor tablet (Roche) per 10 ml buffer and a cocktail of phosphatase inhibitors (Roche). Protein concentration was measured using the DC Protein Assay (Bio-Rad); protein (50 μg) was denatured in LDS sample buffer with reducing agent (Invitrogen), separated on precast 4–12% Bis-Tris gels (Life Technologies) and transferred to nitrocellulose membranes (Bio-Rad). Membranes were incubated in blocking buffer (5% dry milk in TBS with 0.2% Tween-20) for 1 h, and then incubated in the primary antibody in blocking buffer overnight at 4 °C. Chemiluminescent detection was performed with the appropriate secondary antibodies and developed using Genemate Blue ultra-autoradiography film (VWR). The actin loading controls for the protein samples shown in the immunoblots of the following panels (two independent mouse tumour samples, and cell lines representative of two independent experiments) are the same because the samples were run on a single gel but probed for pALK, ALK (Extended Data Fig. 2a), MYCN (Extended Data Fig. 3e) and BORIS (Extended Data Fig. 4a), respectively.

Co-immunoprecipitation. Cells were collected in immunoprecipitation lysis buffer (50 mM Tris-HCl buffer (pH 7.4), 100 mM NaCl, 1% Triton-100, 1 mM PMSF), containing a 1× complete protease inhibitor tablet (Roche) per 10 ml buffer and a cocktail of phosphatase inhibitors (Roche). Homogenates were centrifuged at 20,000*g* for 10 min at 4 °C to obtain supernatants. DNase I (approximately 1 U ml^{-1}) was used to degrade DNA in supernatants by incubation for 1 h at room temperature. Co-immunoprecipitation of endogenously expressed proteins was performed using protein A Dynabeads (Invitrogen), according to the manufacturer's instructions. In brief, antibody-conjugated Dynabeads were incubated with purified cell lysates to immunoprecipitate the target antigen. Antibodies used for immunoprecipitation were CTCF (3417, Cell Signaling Technology) and BORIS (NBP2-52405, NOVUS Biologicals). The elution step was conducted by heating the beads for 10 min at 95 °C in lithium dodecyl sulfate (LDS) sample buffer with reducing agent (Invitrogen), after which western blotting was performed using the following antibodies: CTCF (3417, Cell Signaling Technology) and BORIS (9851, Active Motif).

Plasmids, shRNA knockdown and overexpression systems. pLKO.1 shRNA constructs (control: SHC007; MYCN: 1-TRCN0000020694 and 2-TRCN0000363425; BORIS: 3-TRCN0000370229 and 4-TRCN0000365141; BRD4: A-TRCN0000318771 and B-TRCN0000196576) were purchased from Sigma-Aldrich and pLKO.1 GFP shRNA was a gift from D. Sabatini (Addgene plasmid 30323)[39]. Overexpression constructs were generated by cloning *BORIS* cDNA into the Tet-inducible pInducer20 vector, provided by S. Elledge (Addgene plasmid 44012)[40]. Production of lentiviral particles and subsequent infection were performed as previously described[38]. The lentivirus was packaged by co-transfection of either pLKO.1 or pInducer20 plasmid with the helper plasmids, pCMV-deltaR8.91 and pMD2.G-VSV-G into HEK293T cells using TransIT-LT1 Transfection Reagent (Mirus Bio LLC). Virus-containing supernatants were collected 48 h after transfection. Cells were infected with 8 μg ml^{-1} polybrene (Sigma-Aldrich) and 24–48 h later selected with puromycin (pLKO.1) (Sigma-Aldrich) and then collected at appropriate time points. When using the Tet-inducible system for *BORIS* overexpression, induction of gene expression was achieved by treating cells every 2–3 days with doxycycline (0.2 μg ml^{-1}) for a total duration of 37 days.

qRT–PCR. RNA isolation and PCR amplification were performed as previously described[38], except that the RT–PCR was performed using the SuperScript III First-Strand system (Life Technologies). Total RNA was isolated from cell lines with the RNeasy kit (Qiagen). One microgram of purified RNA was reverse transcribed using Superscript III First-Strand (Invitrogen) according to the manufacturer's protocol, and quantitative PCR was performed using SYBR Green on a Viia7 Real-Time PCR system (Thermo Fisher Scientific). All experiments were performed in biological triplicates unless stated otherwise. Each individual biological sample was amplified by qPCR in technical replicates and normalized to actin as an internal control. Amplification was carried out with primers specific to the genes to be quantified (sequences available on request).

Sequence analysis. The kinase domain of ALK was amplified from cDNA extracted from sensitive and resistant cells using the HotStar HiFidelity Polymerase Kit (Qiagen). The PCR products were cloned into the pGEM-T vector (Promega) and confirmed by sequencing.

RTK array. The Human Phospho-RTK Array Kit (R&D Systems) was used as previously described[38]. Cell lysate (500 μg) was incubated on a phospho-RTK membrane array (ARY001B) according to the manufacturer's instructions. Target proteins were captured with their respective antibodies. After washing, the proteins were incubated with a phosphotyrosine antibody conjugated to horseradish peroxidase to allow the detection of captured phosphorylated RTKs.

Fluorescent in situ hybridization. Fluorescent in situ hybridization (FISH) analyses were performed using a Vysis LSI N-MYC (2p24) SpectrumGreen/Vysis CEP 2 SpectrumOrange Probe (Vysis), in accordance with the manufacturer's instructions.

Immunohistochemistry. All human tumour specimens (formalin-fixed paraffin-embedded slides) were obtained under an Institutional Review Board (IRB)-approved protocol of the Dana-Farber/Boston Children's Cancer and Blood Disorders Center, and informed consent was obtained from all subjects. Staining was performed by Applied Pathology Systems using the ImmPRESS Excel Amplified HRP Polymer Staining Kit (MP-7601, Vector Laboratories) on a Dako Autostainer (Agilent Technologies). Sections were deparaffinized, rehydrated, and subjected to antigen retrieval in citrate-based buffer on a steamer for 25 min. Slides were blocked with BLOXALL blocking solution and 2.5% horse serum sequentially before a 1-h incubation with BORIS antibody at 1:50 dilution (ab187163, Abcam). Sections were then incubated with anti-rabbit amplifier antibody and ImmPRESS Excel Amplified HRP Polymer Reagent sequentially before incubation with ImmPACT DAB EqV Substrate. Finally, slides were counterstained with haematoxylin, followed by dehydration and the addition of coverslips.

Bisulfite sequencing. Methylation analysis of *BORIS* (NCBI RefSeq NC_000020.11, spanning nucleotides chr20: 57,524,203–57,525,234 on GRCh38.p7 assembly) was performed using a bisulfite sequencing assay. Genomic DNA (500 ng) was treated with the EZ DNA Methylation-Lightning Kit (Zymo Research), followed by PCR using ZymoTaq Polymerase premix (Zymo Research) and specific primers designed using the Zymo bisulfite primer seeker (http://www.zymoresearch.com/tools/bisulfite-primer-seeker/; sequences available on request). PCR products were then sequenced for the assessment of CpG site-specific DNA methylation in the *BORIS* promoter region.

Growth assay. After shRNA-mediated knockdown of BORIS, cells were reseeded at a density of 4×10^5 cells per well in 6-well plates. At 48 and 120 h of incubation, cells were stained with trypan blue (Sigma-Aldrich) and counted on a Countess II cell counter (Life Technologies).

Mouse experiments. All mouse experiments were performed with approval from the Institutional Animal Care and Use Committee (IACUC) of the DFCI. Three mouse experiments were performed: (i) to assess the tumorigenic potential of resistant cells in vivo; (ii) to assess that resistance to TAE684 was maintained in vivo; and (iii) to assess the effect of JQ1 on resistant cells in vivo. All experiments were performed using subcutaneous cell xenograft models generated by injecting 2×10^6 sensitive or resistant Kelly neuroblastoma cells into the flanks of NU/NU (Crl:NU-*Foxn1*^{nu}) (Charles River Laboratories) or NU/NU (CrTac:NCr-*Foxn1*^{nu}) (Taconic) 7-week-old female mice. Mice were randomized into groups of equal average volumes, and investigators were not blinded to group allocation during data collection. (i) To assess the tumorigenic potential of resistant cells in absence of treatment, mice with established disease (mean tumour volume of 200 mm^3) were monitored for up to 23 days ($n = 4$ per group). Tumours were obtained, dissociated and used to establish cell lines and for assessment of mRNA levels, protein expression and sensitivity to TAE684. (ii) To ensure that the in vitro resistance to TAE684 was maintained in vivo, mice with established disease were divided into two cohorts and were treated with either TAE684 (10 mg kg^{-1}) or vehicle control by oral gavage once daily ($n = 8$ per group), and were monitored for up to 56 days from start of treatment. (iii) To assess the sensitivity of resistant cells to BRD4 inhibition, mice with established disease were divided into two cohorts and treated with either JQ1 (50 mg kg^{-1}) or vehicle control intraperitoneally (i.p.) once daily ($n = 6$ per group), and were monitored for up to 87 days from start of treatment. For all experiments, disease burden was quantified using electronic caliper measurements (2–3 times a week) and mouse weights were monitored at least twice a week. Tumour volumes were calculated using the modified ellipsoid formula[41]: ½(length × width^2). Animals were euthanized when tumour volumes reached 1,500–2,000 mm^3 based on institutional IACUC criteria for maximum tumour volumes. In none of the experiments were the institutional limits for tumour volumes (<2,000 mm^3 measurement preceding the day of euthanization) exceeded.

ChIP–seq. ChIP was carried out as previously described[15] with minor changes as described. Approximately 1×10^7 cells were crosslinked for 10 min at room temperature with 1% formaldehyde (Thermo Scientific) in PBS followed by quenching with 0.125 M glycine for 5 min. The cells were then washed twice in ice-cold PBS, and the cell pellets flash frozen and stored at −80 °C. Fifty microlitres of protein G Dynabeads per sample (Invitrogen) were blocked with 0.02% Tween20 (w/v) in PBS. Magnetic beads were loaded with 10 μg each of antibody and incubated overnight at 4 °C. Crosslinked cells were lysed, placed in sonication buffer with 0.2% SDS, placed on ice and chromatin was sheared using a Misonix 3000 sonicator (Misonix) at the following settings: 10 cycles, each for 30 s on, followed by 1 min off, at a power of approximately 20 W. The lysates were then centrifuged for 10 min at 4 °C, supernatants collected and diluted with an equal amount of sonication buffer to reach a final concentration of 0.1% SDS. The sonicated lysates were incubated overnight at 4 °C with the antibody-bound magnetic beads, washed with low-salt buffer (50 mM HEPES-KOH (pH 7.5), 0.1% SDS, 1% Triton X-100, 0.1% sodium deoxycholate, 1 mM EGTA, 1 mM EDTA, 140 mM NaCl and 1× complete protease inhibitor), high-salt buffer (50 mM HEPES-KOH (pH 7.5), 0.1% SDS, 1% Triton X-100, 0.1% sodium deoxycholate, 1 mM EGTA, 1 mM EDTA, 500 mM NaCl and 1× complete protease inhibitor), LiCl buffer (20 mM Tris-HCl (pH 8), 0.5% NP-40, 0.5% sodium deoxycholate, 1 mM EDTA, 250 mM LiCl and 1× complete protease inhibitor) and Tris-EDTA buffer. DNA was then eluted in elution buffer (50 mM Tris-HCl (pH 8.0), 10 mM EDTA, 1% SDS), and high-speed centrifugation was performed to pellet the magnetic beads and collect the supernatants. The crosslinking was reversed overnight at 65 °C. RNA and protein were digested using RNase A and proteinase K, respectively, and DNA was purified with phenol chloroform extraction and ethanol precipitation. Purified ChIP DNA was used to prepare Illumina multiplexed sequencing libraries using the NEBNext Ultra II DNA Library Prep kit and the NEBNext Multiplex Oligos for Illumina (New England Biolabs) according to the manufacturer's protocol. Libraries with distinct indexes were multiplexed and run together on the Illumina NextSeq 500 (SY-415-1001, Illumina) for 75 bases in single-read mode.

HiChIP. HiChIP was performed as previously described[24] with a few modifications. Approximately 1×10^7 cells were crosslinked for 10 min at room temperature with 1% formaldehyde in growth medium and quenched in 0.125 M glycine. After washing twice with ice-cold PBS, the supernatant was aspirated and the cell pellet flash frozen in liquid nitrogen. Crosslinked cell pellets were thawed on ice, resuspended in 1 ml of ice-cold Hi-C lysis buffer (10 mM Tris-HCl (pH 8.0), 10 mM NaCl, 0.2% NP-40 and 1× complete protease inhibitor) and incubated at 4 °C for 30 min with rotation. Nuclei were pelleted by centrifugation for 5 min at 4 °C and washed once with 500 μl of ice-cold Hi-C lysis buffer. After removing the supernatant, nuclei were resuspended in 100 μl of 0.5% SDS and incubated at 62 °C for 10 min. SDS was quenched by adding 335 μl of 1.5% Triton X-100 and incubating for 15 min at 37 °C. After the addition of 50 μl of 10× NEB Buffer 2 (New England Biolabs, B7002) and 375 U of MboI restriction enzyme (New England Biolabs, R0147), chromatin was digested at 37 °C for 2 h with rotation. After digestion, MboI enzyme was heat-inactivated by incubating the nuclei at 62 °C for 20 min. To fill in the restriction fragment overhangs and mark the DNA ends with biotin, 52 μl of fill-in master mix, containing 37.5 μl of 0.4 mM biotin-dATP (Invitrogen, 19524016), 1.5 μl of 10 mM dCTP (Invitrogen, 18253013), 1.5 μl of 10 mM dGTP (Invitrogen, 18254011), 1.5 μl of 10 mM dTTP (Invitrogen, 18255018), and 10 μl of 5 U μl^{-1} DNA Polymerase I, Large (Klenow) Fragment (New England Biolabs, M0210), were added and the tubes were incubated at 37 °C for 1 h with rotation. Proximity ligation was performed by the addition of 948 μl of ligation master mix, containing 150 μl of 10× NEB T4 DNA ligase buffer (New England Biolabs, B0202), 125 μl of 10% Triton X-100, 7.5 μl of 20 mg ml^{-1} BSA (New England Biolabs, B9000), 10 μl of 400 U μl^{-1} T4 DNA ligase (New England Biolabs, M0202), and 655.5 μl of water, and incubation at room temperature for 4 h with rotation. After proximity ligation, nuclei were pelleted by centrifugation for 5 min and resuspended in 1 ml of ChIP sonication buffer (50 mM HEPES-KOH (pH 7.5), 140 mM NaCl, 1 mM EDTA pH 8.0, 1 mM EGTA (pH 8.0), 1% Triton X-100, 0.1% sodium deoxycholate, 0.1% SDS and 1× complete protease inhibitor). Nuclei were sonicated using a Misonix 3000 sonicator (Misonix) at the following settings: 12 cycles, each for 30 s on, followed by 1 min off, at a power of approximately 20 W. Sonicated chromatin was clarified by centrifugation for 15 min at 4 °C and the supernatant was transferred to a tube. Sixty microlitres of protein G Dynabeads (Invitrogen) were washed three times and resuspended in 50 μl sonication buffer. Washed beads were then added to the sonicated chromatin and incubated for 1 h at 4 °C with rotation. Beads were then separated on a magnetic stand and the supernatant was transferred to a new tube. Seventy-five microlitres of protein G Dynabeads pre-incubated overnight at 4 °C with 10 μg of anti-SMC1A antibody (Bethyl A300-055A) or 10 μg of BORIS antibody (Abcam, ab187163) were added to the tube and incubated overnight at 4 °C with rotation. Beads were then separated on a magnetic stand and washed twice with 1 ml of sonication buffer, followed by once with 1 ml high-salt sonication buffer (50 mM HEPES-KOH (pH 7.5), 500 mM NaCl, 1 mM EDTA pH 8.0, 1 mM EGTA (pH 8.0), 1% Triton X-100, 0.1% sodium deoxycholate, 0.1% SDS), once with 1 ml of LiCl wash buffer (20 mM Tris-HCl (pH 8.0), 1 mM EDTA pH 8.0, 250 mM LiCl, 0.5% NP-40, 0.5% sodium deoxycholate, 0.1% SDS) and once with 1 ml of TE buffer with salt (10 mM Tris-HCl (pH 8.0), 1 mM EDTA pH 8.0, 50 mM NaCl). Beads were then resuspended in 200 μl of elution buffer (50 mM Tris-HCl (pH 8.0), 10 mM EDTA pH 8.0, 1% SDS) and incubated at 65 °C for 15 min. To purify the eluted DNA, RNA was degraded by the addition of 8.5 μl of 10 mg ml^{-1} RNase A and incubation at 37 °C for 2 h. Protein was degraded by the addition of 20 μl of 10 mg ml^{-1} proteinase K and incubation at 55 °C for 45 min. Samples were then incubated at 65 °C overnight to reverse crosslink protein–DNA complexes. DNA was then purified using Zymo ChIP DNA Clean and Concentrator columns (Zymo, D5205) according to the manufacturer's protocol and eluted in 14 μl water. The amount of eluted DNA was quantified by Qubit dsDNA HS kit (Invitrogen, Q32854). Tagmentation of ChIP DNA was performed using the Illumina Nextera DNA Library Prep Kit (Illumina, FC-121-1030). First, 5 μl of MyOne Streptavidin C1 Dynabeads (Invitrogen, 65001) was washed with 1 ml of Tween wash buffer (5 mM Tris-HCl (pH 7.5), 0.5 mM EDTA (pH 8.0), 1 M NaCl, 0.05% Tween-20) and resuspended in 10 μl of 2× biotin binding buffer (10 mM Tris-HCl (pH 7.5), 1 mM EDTA pH 8.0, 2 M NaCl). Then, 25 ng of purified DNA was added in a total volume of 10 μl water to the beads and incubated at room temperature for 15 min with agitation every 5 min. After capture, beads were separated with a magnet and the supernatant was discarded. Beads were then washed twice with 500 μl of Tween wash buffer, incubating at 55 °C for 2 min with shaking for each wash. Beads were resuspended in 25 μl of Nextera Tagment DNA buffer. To tagment the captured DNA, 1 μl of Nextera Tagment DNA Enzyme 1 was added with 24 μl of Nextera Resuspension Buffer and samples were incubated at 55 °C for 10 min with shaking. Beads were separated on a magnet and supernatant was discarded. Beads were

washed twice with 500 μl of 50 mM EDTA at 50 °C for 30 min, washed twice with 500 μl of Tween wash buffer at 55 °C for 2 min each, and finally washed once with 500 μl of 10 mM Tris-HCl (pH 7.5) for 1 min at room temperature. Beads were separated on a magnet and supernatant was discarded. To generate the sequencing library, PCR amplification of the tagmented DNA was performed while the DNA was still bound to the beads. Beads were resuspended in 15 μl of Nextera PCR Master Mix, 5 μl of Nextera PCR Primer Cocktail, 5 μl of Nextera Index Primer 1, 5 μl of Nextera Index Primer 2 and 20 μl water. DNA was amplified with 9–10 cycles of PCR. After PCR, beads were separated on a magnet and the supernatant containing the PCR-amplified library was transferred to a new tube, purified using Zymo DNA Clean and Concentrator columns (Zymo, D5205) according to the manufacturer's protocol, and eluted in 14 μl water. Purified HiChIP libraries were size-selected to 300–700 bp using a Sage Science Pippin Prep instrument according to the manufacturer's protocol and subjected to 2 × 100 paired-end sequencing using an Illumina HiSeq 2500 system (SY–401–2501, Illumina).

scRNA-seq. Kelly cells (sensitive, intermediate and resistant states) were grown to 70% confluence in T75 culture flasks. In brief, growth medium was aspirated and cells were treated with 0.25% Trypsin/EDTA for 3 min at 37 °C, after which cells were washed twice with 1× PBS. Cells were then resuspended into single cells at a concentration of 1×10^6 per ml in 1× PBS with 0.4% BSA for 10x Genomics processing. The sorted cell suspensions were loaded onto a 10x Genomics Chromium instrument to generate single-cell gel beads in emulsion (GEMs). Approximately 5,000 cells were loaded per channel. scRNA-seq libraries were prepared using the following Single Cell 3′ Reagent Kits: Chromium Single Cell 3′ Library & Gel Bead Kit v2 (PN-120237), Single Cell 3′ Chip Kit v2 (PN-120236) and i7 Multiplex Kit (PN-120262) (10x Genomics) as previously described[42], and following the Single Cell 3′ Reagent Kits v2 User Guide (Manual Part CG00052 Rev A). Libraries were run on an Illumina HiSeq 4000 system (SY-401-4001, Illumina) as 2 × 150 paired-end reads, one full lane per sample, for approximately >90% sequencing saturation.

Genomics analysis: direct comparison of *CTCF* and *BORIS* expression in healthy and tumour samples. To assess the expression levels and range of *BORIS* and *CTCF* in healthy and tumour cells all GTEx, TCGA and TARGET datasets were downloaded and converted to FPKM values and displayed as [$\log_2$(FPKM + 1)] (Extended Data Fig. 1a, b).

Association of BORIS with prognostic features. For each dataset, processed values were extracted from the Gene Expression Omnibus (GEO) and scaled values were created by normalizing the expression levels by the minimum mean value of the conditions that were compared, Esi,j = Ei,j/min(average(Ej)). The two-sided Wilcoxon rank-sum test on the original values was used to determine statistical differences between the compared conditions (Extended Data Fig. 1c and Extended Data Fig. 4f).

Microarray data analysis. Microarray data were analysed using a custom CDF file (GPL16043) that contained the mapping information of the ERCC probes used in the spike-in RNAs. The arrays were normalized as previously described[37]. In brief, all microarray chip data were imported in R (https://www.r-project.org/, v.3.1.3) using the affy package[43] (v.1.44.0), converted into expression values using the expresso command, normalized to take into account the different numbers of cells and spike-ins used in the different experiments and renormalized using loess regression fitted to the spike-in probes. Sets of differentially expressed genes were obtained using the limma package[44] (v.3.22.7) and a FDR value of 0.05. Spike-in normalized absolute expression values (counts) were normalized to CPM as a measurement of relative gene expression concentrations per condition. Total number of transcripts per sample was determined as the total number of counts after spike-in normalization and the *BORIS* shRNA sample was first normalized to the control shRNA sample to account for technical effects that originated from the transfection protocol.

ChIP–seq analysis. For all ChIP–seq samples, high-quality data were confirmed using the Fastqc tool (v.0.11.5) and samples were aligned to the human genome (build hg19, GRCh37.75) with STAR (v.2.5.1b_modified) and the parameters '–alignIntronMax 1–alignEndsType EndToEnd–outFilterMultimapNmax 1–outFilterMismatchMax 5'. Next, non-duplicate reads that mapped to the reference chromosomes were retained using Samtools (v.1.3.1) and MarkDuplicates (v.2.1.1) from Picard tools. For each experimental replicate, antibody enrichment was assessed using the plotFingerprint command from deepTools (v.2.2.4). Peaks were identified with MACS2 (v.2.1.1) for narrow peaks (BORIS, CTCF, BRD4, Pol2, MYCN) with the parameters '–q 0.01–call-summits' and for broad peaks (H3K27ac, H3K27me3) with the parameters '–broad-cutoff 0.01'. Peaks overlapping regions with known artefact regions (http://mitra.stanford.edu/kundaje/akundaje/release/blacklists/) were blacklisted out. Input normalized bedgraph tracks were created with the deepTools command bamCompare and the parameters '–scaleFactorsMethod=readCount–ratio=subtract–binSize=50–numberOfProcessors=4–extendReads=200'. Subsequently, negative values were set to zero and counts were scaled to RPM per bp to account for differences in library size. Bigwig files were created with bedGraphToBigWig (v.4). ChIP–seq replicates ($n = 2$) were merged at the BAM level after assessment of strong correlation with the deepTools command 'multiBigwigSummary BED-file' using all replicate bigwigs and identified peaks as input. Identification of peaks and generation of tracks were then repeated for these merged files and used for further analyses. Downstream analyses for ChIP–seq and other genomic interval data was performed in R (https://www.r-project.org/) (v.3.5.1) using the data.table (v.1.12.2) package.

Gencode annotation and isoform selection. Gencode (http://www.gencodegenes.org/, release 19) annotation was used and for each gene the most likely isoform was selected based on data-driven criteria. In brief, only genes that were part of the Refseq transcriptome annotation and with a minimum length of 1 kb were considered. Next, isoforms were prioritized according to increased deposition of Pol2 and H3K27ac reads on the TSS, transcript length and alphabet rank, in that order, until only one transcript was selected for each gene.

Cell-type-specific binding patterns. To determine the cell specificities of BORIS and CTCF peaks, we first combined all peaks identified by MACS2 and merged the peak regions that overlapped by at least 50%. A 50% threshold was empirically selected to avoid merging peaks that had clear and distinct summits. Next, normalized BORIS or CTCF read densities were calculated for each region and a ratio [$\log_2$(resistant/sensitive)] was calculated. Peak regions with a twofold density increase or decrease were classified as resistant or sensitive cell-specific peaks, respectively, whereas other regions were denoted as 'shared' to indicate that these peaks had similar BORIS or CTCF deposition in both cell types (Fig. 2a, b and Extended Data Fig. 6a). To explore the proximity of BORIS and CTCF peaks and how they were altered during the transition from sensitive to resistant cells, we overlapped all shared and cell-type-specific peaks from both cell types in the least stringent way (minimum 1-bp overlap) (Fig. 2c and Extended Data Fig. 6a).

Genomic enrichment of peak-binding sites. To identify genomic locations with BORIS or CTCF binding we determined the number of peaks that overlapped with at least 25% of known functional regions in the following order: (i) broad promoter (±2 kb TSS); (ii) $BRD4^+$ $H3K27ac^+$ (active) enhancers; (iii) $BRD4^-$ $H3K27ac^+$ enhancers; (iv) exons; (v) introns; (vi) repressed chromatin represented by H3K27me3 broad peaks; or (vii) other (if the peak was outside the aforementioned regions) (Extended Data Fig. 6d). Enrichment of ChIP–seq binding at resistant cell BORIS peaks was performed by extending BORIS summits by 1 kb in both directions and calculating the normalized read densities in 50-bp bins (Fig. 2d).

Genomic enrichment of regulatory regions. To visualize the enrichment of CTCF and BORIS at regulatory regions (enhancers and promoters) and the differences between sensitive and resistant cells, a metagene analysis for CTCF and BORIS occupancies was performed for all H3K27ac enhancer regions and gene promoters. All TSSs were extended in both directions by 2 kb and binned in 50-bp bins, and each enhancer (start–end) was divided into 40 equally sized bins and extended with 2 kb in both directions and these extended regions were binned in 50-bp bins. Normalized bedgraph files were used to calculate read density (RPM per bp). An aggregated summary profile was created for each cell type. To account for different numbers of identified enhancers in both cells types we calculated a normalization factor (*N* resistant enhancers/*N* sensitive enhancers) to divide each aggregated read density (Extended Data Fig. 6e).

HiChIP processing and quality control. For all SMC1A-based HiChIP datasets, raw reads were first trimmed to a uniform length of 50 bp using trimmomatic[45](v.0.36) and were then processed using the HiC-Pro (v.2.10.0) pipeline[46] with default settings for the human genome (build hg19, GRCh37.75) and corresponding MboI cut sites. To perform intra- and inter-correlation analysis for biological replicates, forward and reverse reads from the HiC-Pro output were merged together to generate one-dimensional SMC1A BAM profiles. Genome-wide Spearman correlation in 5-kb bins was computed for all merged genomic anchor regions on those merged BAMs for all replicates using the 'multiBamSummary BED-file' command from deepTools (Extended Data Fig. 7a, e).

HiChIP loop calling and differential looping analysis. Loops were directly called from the HiC-Pro output using hichipper[47] (v.0.7.3), with parameter 'peaks = combined, all', and subsequently diffloop[47] (v.1.10.0) with default settings. Only loops that were detected in all three biological replicates of a sample (sensitive, resistant, shCtrl or shBORIS) with a minimum of five paired-end tags in total and an FDR ≤ 0.01 were retained for further analysis. To call differential loops between samples, the quickAssocVoom function was used and significantly different loops were either considered reinforced (mango.FDR < 0.01 and $\log_2$-transformed fold change > 1) or lost (mango.FDR < 0.01 and $\log_2$-transformed fold change < −1).

Classification of HiChIP interactions. SMC1A-based HiChIP interactions (loops) were classified as previously described[48] with minor adaptations. Associated anchors of loops were overlapped with our ChIP-seq peaks (CTCF, BORIS, H3K27ac, BRD4) and promoter regions (TSS ± 2 kb), requiring a minimum 1-bp overlap. Each anchor was then independently classified according to its overlap profile, following a hierarchical tree. If an anchor overlapped a promoter, an enhancer (BRD4 + H3K27ac), or a CTCF peak, it was classified as

promoter-, enhancer- or CTCF-anchor, in that order. If there was no overlap, the anchor was considered 'other'. By combining these four anchor classes we discriminated 10 different interaction classes. We excluded from further analyses any interaction that contained an anchor classified as other, which also represented on average much shorter interactions (data not shown), and which were hence more likely to have occurred due to linear proximity on the DNA. This resulted in the identification of 6 main interaction classes (Fig. 3a and Extended Data Fig. 7b).

Association of BORIS with lost loops. Only loops that were detected in both the original (sensitive versus resistant) and BORIS depletion (shBORIS versus shCtrl) samples were used for this analysis. First, loops were divided into lost and retained loops upon BORIS depletion, and an odds ratio (two-sided Fisher's exact test) was calculated for the initial presence of BORIS binding on the anchors of these two groups (Fig. 3f). An analogous strategy was followed after first stratifying loops according to the different identified loop classes (Extended Data Fig. 7f, g).

Identification of super-enhancer regions. Super-enhancers were identified using the ROSE algorithm (v.1) (https://bitbucket.org/young_computation/rose). In short, H3K27ac enriched regions were identified with MACS2 and termed typical enhancers. These regions were stitched together if they were within 12.5 kb of each other. Stitched regions were ranked by H3K27ac signal therein and the inclination point at which the two classes of enhancers separated was determined by ROSE. Stitched enhancers above this threshold were considered super-enhancers and the others, typical enhancers. To compare different samples, we used the same maximum threshold between the conditions considered (Extended Data Fig. 8a).

Identification of cell-type-specific super-enhancers. Cell-type-specific and active super-enhancers were identified by merging both sensitive- and resistant-cell super-enhancers and determining cell-type specificity based on the differential normalized read density of both H3K27ac and BRD4. In brief, ratios [$\log_2$ (resistant/sensitive)] were calculated for H3K27ac and BRD4. A combined threshold of 2.5 was required to identify a cell-type-specific super-enhancer with at least a minimum 0.75 change for each individual mark. Super-enhancers that did not meet these criteria were classed as shared (neutral) between cell types (Extended Data Fig. 8b).

Correlation analysis of looping with gene expression and enhancer landscape. Regulatory interactions were associated to target genes and super-enhancers based on proximity to the TSS and minimal overlap (1 bp) with its anchors, respectively (Fig. 4a and Extended Data Fig. 8f).

Chromatin-based gene classification. Genes were classified as having an 'open', 'neutral' or 'closed' chromatin state based on unsupervised clustering of a metagene representation of ChIP–seq occupancy of H3K27ac and H3K27me3. Each gene (from TSS to TES, and 2 kb up- and downstream of this region) was divided into 20 equally sized bins; the extended regions were binned in regions of 50 bp. Normalized bedgraph files were used to calculate read density (RPM per bp) and *k*-means clustering was applied to group each extended gene region in one of three clusters (Extended Data Fig. 8d, e). An aggregated summary profile was created for each group of genes. The open and closed clusters were classified based on predominantly H3K27ac and H3K27me3 accumulation, respectively, and the 'neutral' cluster displayed on average equal levels of both.

Integrated genomic data analysis. An ensemble analysis was performed to identify the set of genes that showed characteristics of reactivation in resistant cells. For each gene, five features were examined: (i) creation of a unique regulatory interaction; (ii) deposition of BORIS on its promoter or looped enhancer; (iii) association with a resistant cell-specific super-enhancer through overlap with either its promoter or looped anchor; (iv) increased mRNA expression; and (v) transition from a closed or neutral state to an open chromatin state. A unique set of 89 genes (Supplementary Table) that exhibited four out of five features were identified as the top reactivated genes in resistant cells. Within these 89 genes, 13 were identified as transcription factors by the TcoF database (http://www.cbrc.kaust.edu.sa/tcof/) (Fig. 4b).

Allen Brain atlas gene signature. Expression data and metadata for human brain development were downloaded from the Allen Brain atlas (http://www.brainspan.org). Row-normalized *z*-scores of [$\log_2$(RPKM + 1)] values were used to create a heat map. Values greater than 3.5 were set to 3.5 to reduce the effect of extreme outliers on the visualization. Samples were ordered according to developmental time points (Extended Data Fig. 8g).

BORIS and BRD4 correlation at promoter regions. BORIS and BRD4 colocalization and correlation were assessed for the promoter regions of the 89 top-ranked genes. The TSS was extended in both directions by 2 kb and binned in 100-bp regions. Normalized read densities for BORIS and BRD4 were calculated and a Spearman's rank correlation coefficient calculated for sensitive and resistant cells. An aggregated density plot of all 89 genes was created to visualize the increased deposition and correlation of BRD4 and BORIS in resistant cells (Extended Data Fig. 9a).

Gene expression and DNA-binding analysis. To examine the association between gene expression and overlapping targets of MYCN and BORIS in sensitive and resistant cells, respectively, the percentage of gene promoters (±2 kb TSS) that overlapped with ChIP–seq peaks in 10 equally sized bins based on the expression distribution was calculated (Extended Data Fig. 6f). To visualize and correlate gene expression with DNA binding of MYCN or BORIS, genes were ranked based on expression and plotted against the total rescaled (0–100) binding intensities calculated for each gene promoter (±2 kb TSS). For each ChIP–seq mark a loess regression curve was computed using a span of 0.1 (Extended Data Fig. 6g).

Transcription factor motif enrichment analysis. Statistically overrepresented motifs were identified with HOMER[49] (v.2) using the command findMotifs.pl providing both target and background fasta sequences for regions of interest. For promoter regions we selected the top 1,000 up- and downregulated genes in resistant cells and extended the TSS of each gene by 2 kb in both directions. The genomic coordinates were used to extract fasta sequences with the Biostrings package (v.2.50.1) in R and used as target or background to identify motifs associated with promoter regions of genes within each cell type. A similar strategy was followed to identify overrepresented motifs associated with cell-type-specific super-enhancers. Target and background fasta sequences were extracted from the summits of BRD4 peaks located on cell-type-specific super-enhancers and extended by 500 bp in both directions. For a selection of enriched sequences, the associated transcription factor motif and significance level (*P*) was visualized using a heat map (Fig. 4d).

scRNA-seq analysis. The Cell Ranger Single Cell Software Suite, v.1.3 was used to perform sample de-multiplexing, barcode and unique molecular identifier (UMI) processing, and single-cell 3′ gene counting. A detailed description of the pipeline and specific instructions to run it can be found at: https://support.10xgenomics.com/single-cell-gene-expression/software/pipelines/latest/what-is-cell-ranger. A high-quality gene expression matrix was created in sequential preprocessing steps. First UMI-based counts were converted to relative expression concentrations by rescaling each cell to a library size of 10,000. Genes were considered detected if rescaled count $> \log_2(0.1 + 1)$ and retained for further analysis if present in at least 0.5% of the cells from the sample with the lowest cell count. Cells were removed if fewer than 1,000 genes were detected. To remove low-quality cells, we calculated five technical indicators (ratio of detected genes/UMI, percentage of mitochondrial genes, percentage of ribosomal genes, average GC content of library and library complexity measured by Shannon Entropy) and performed PCA on indicators with a coefficient of variation $> 5\%$. Next, density-based clustering was performed on the first and second principal component using an epsilon determined by a *k*-nearest neighbour plot. All cells that were located outside the main cluster were considered low quality and removed from further analysis. Next, we used the R package 'scater' (v.1.10.0) to confirm that there were no technical or experimental confounding effects and the R package 'Seurat' (v.2.3.4) to analyse and visualize the data. In brief, UMI counts were log-normalized with a scale factor of 10,000 and subsequently centre-scaled. To visualize cells in a reduced dimensionality, PCA was performed on the most variable genes, which were identified as genes with higher-than-expected variability in consecutive ranked expression bins. Higher complexity clustering was performed with *t*-SNE using the first 10 principal components, which were deemed most informative based on heat map and elbow plot observation. To identify homogeneous subpopulations, we performed iterative clustering using the network-based clustering algorithm (shared nearest neighbour) with different resolutions as input until each sample was at least separated in two groups. A simple pseudotime analysis was performed by calculating an average expression profile for each identified subpopulation and ordering them according to the summarized expression of transcription factors that displayed variable expression between sensitive and intermediate or intermediate and resistant cells. Variable expression was defined as showing at least a 33% change in the rank of expression between two samples with a minimal normalized expression level > 0.2. For each sample comparison, at least the top 10 most variable transcription factors were included. In total this resulted in 32 transcription factors. Gene expression values were then linearly rescaled between 0 and 10 to jointly visualize relative expression changes during this pseudotime. To examine co-detection or mutual exclusivity between genes of interest, a two-sided Fisher's exact test was performed for all cells in a given sample. A score combining both the odds ratio and the $-\log_{10}(P \text{ value})$ was calculated to visualize both the strength and direction between genes in pairwise co-expression tests.

Statistical analysis. Analysis for each plot is listed in the figure legend and/or in the corresponding Methods. In brief, all grouped data are presented as mean ± s.d. unless stated otherwise. All box and whisker plots of expression data are presented as: centre lines, medians; box limits, twenty-fifth and seventy-fifth percentiles; whiskers, minima and maxima (1.5× the interquartile range). Statistical significance for pairwise comparisons was determined using the two-sided Wilcoxon rank-sum test or two-sided unpaired *t*-test, unless stated otherwise. Survival analysis was performed using the Kaplan–Meier method and differences between groups calculated by the two-sided log-rank test and the Bonferroni correction method. Tumour volume comparisons for the xenograft studies were analysed by Mann–Whitney *U* test. $*P < 0.05$; $**P < 0.01$. Statistical comparisons of distributions of

fold changes for the expression microarrays were done using the Mann–Whitney *U* test. All quantitative analyses are expressed as the mean ± s.d. of three biological replicates, unless stated otherwise. Microarray and ChIP–seq data are based on at least two independent experiments. For all experiments, no statistical methods were used to predetermine sample size. Unless stated otherwise, experiments were not randomized and investigators were not blinded to allocation during experiments and outcome assessment.

Track visualizations. Peaks, (super-) enhancers and HiChIP interactions were visualized with a custom build tool (github.com/RubD/GeTrackViz2) or with the circlize package (v.0.4.5) in R.

Retrospective analysis of gene expression in human samples. Gene expression levels or correlations across primary tumours, healthy tissues or experimental data and patient survival were determined through analysis of the TCGA and TARGET (https://cancergenome.nih.gov/), GTEx (https://www.gtexportal.org/home/), R2 (https://hgserver1.amc.nl/cgi-bin/r2/main.cgi), Allen Brain atlas (http://www.brain-map.org/) and selected datasets representing distinct tumour types with poor prognosis feature annotations (GSE49710 (Neuroblastoma)[50], GSE17679 (Mixed Ewing Sarcoma)[51], GSE63074 (Non-small cell lung carcinoma)[52], GSE15709 (ovarian cancer)[53], GSE16179 (breast cancer)[54] and GSE7181 (Glioblastoma)[55]).

Reporting summary. Further information on research design is available in the Nature Research Reporting Summary linked to this paper.

Data availability

The microarray, ChIP–seq, HiChIP and scRNA-seq datasets generated and analysed during the current study are available in the Gene Expression Omnibus (GEO) repository under accession number GSE103084. The authors declare that all other data supporting the findings of this study are available within the paper and its Supplementary Information files.

Code availability

Custom code is available upon reasonable request.

31. Batra, S., Reynolds, C. P. & Maurer, B. J. Fenretinide cytotoxicity for Ewing's sarcoma and primitive neuroectodermal tumor cell lines is decreased by hypoxia and synergistically enhanced by ceramide modulators. *Cancer Res.* **64**, 5415–5424 (2004).
32. Whang-Peng, J. et al. Cytogenetic characterization of selected small round cell tumors of childhood. *Cancer Genet. Cytogenet.* **21**, 185–208 (1986).
33. Filippakopoulos, P. et al. Selective inhibition of BET bromodomains. *Nature* **468**, 1067–1073 (2010).
34. Marsilje, T. H. et al. Synthesis, structure–activity relationships, and in vivo efficacy of the novel potent and selective anaplastic lymphoma kinase (ALK) inhibitor 5-chloro-*N*2-(2-isopropoxy-5-methyl-4-(piperidin-4-yl)phenyl)-*N*4-(2-(isopropylsulfonyl)phenyl)pyrimidine-2,4-diamine (LDK378) currently in phase 1 and phase 2 clinical trials. *J. Med. Chem.* **56**, 5675–5690 (2013).
35. Johnson, T. W. et al. Discovery of (10*R*)-7-amino-12-fluoro-2,10,16-trimethyl-15-oxo-10,15,16,17-tetrahydro-2*H*-8,4-(metheno)pyrazolo[4,3-*h*][2,5,11]-benzoxadiazacyclotetradecine-3-carbonitrile (PF-06463922), a macrocyclic inhibitor of anaplastic lymphoma kinase (ALK) and c-ros oncogene 1 (ROS1) with preclinical brain exposure and broad-spectrum potency against ALK-resistant mutations. *J. Med. Chem.* **57**, 4720–4744 (2014).
36. Gosmini, R. et al. The discovery of I-BET726 (GSK1324726A), a potent tetrahydroquinoline ApoA1 up-regulator and selective BET bromodomain inhibitor. *J. Med. Chem.* **57**, 8111–8131 (2014).
37. Lovén, J. et al. Revisiting global gene expression analysis. *Cell* **151**, 476–482 (2012).
38. Debruyne, D. N. et al. ALK inhibitor resistance in ALK(F1174L)-driven neuroblastoma is associated with AXL activation and induction of EMT. *Oncogene* **35**, 3681–3691 (2016).
39. Sancak, Y. et al. The Rag GTPases bind Raptor and mediate amino acid signaling to mTORC1. *Science* **320**, 1496–1501 (2008).
40. Meerbrey, K. L. et al. The pINDUCER lentiviral toolkit for inducible RNA interference in vitro and in vivo. *Proc. Natl Acad. Sci. USA* **108**, 3665–3670 (2011).
41. Tomayko, M. M. & Reynolds, C. P. Determination of subcutaneous tumor size in athymic (nude) mice. *Cancer Chemother. Pharmacol.* **24**, 148–154 (1989).
42. Zheng, G. X. et al. Massively parallel digital transcriptional profiling of single cells. *Nat. Commun.* **8**, 14049 (2017).
43. Gautier, L., Cope, L., Bolstad, B. M. & Irizarry, R. A. affy—analysis of Affymetrix GeneChip data at the probe level. *Bioinformatics* **20**, 307–315 (2004).
44. Smyth, G. K., Yang, Y. H. & Speed, T. Statistical issues in cDNA microarray data analysis. *Methods Mol. Biol.* **224**, 111–136 (2003).
45. Bolger, A. M., Lohse, M. & Usadel, B. Trimmomatic: a flexible trimmer for Illumina sequence data. *Bioinformatics* **30**, 2114–2120 (2014).
46. Servant, N. et al. HiC-Pro: an optimized and flexible pipeline for Hi-C data processing. *Genome Biol.* **16**, 259 (2015).
47. Lareau, C. A. & Aryee, M. J. diffloop: a computational framework for identifying and analyzing differential DNA loops from sequencing data. *Bioinformatics* **34**, 672–674 (2018).
48. Ji, X. et al. 3D chromosome regulatory landscape of human pluripotent cells. *Cell Stem Cell* **18**, 262–275 (2016).
49. Heinz, S. et al. Simple combinations of lineage-determining transcription factors prime *cis*-regulatory elements required for macrophage and B cell identities. *Mol. Cell* **38**, 576–589 (2010).
50. SEQC/MAQC-III Consortium. A comprehensive assessment of RNA-seq accuracy, reproducibility and information content by the Sequencing Quality Control Consortium. *Nat. Biotechnol.* **32**, 903–914 (2014).
51. Savola, S. et al. High expression of complement component 5 (*C5*) at tumor site associates with superior survival in Ewing's sarcoma family of tumour patients. *ISRN Oncol.* **2011**, 168712 (2011).
52. Huang, S. et al. Analytical performance of a 15-gene prognostic assay for early-stage non-small-cell lung carcinoma using RNA-stabilized tissue. *JMD* **17**, 438–445 (2015).
53. Li, M. et al. Integrated analysis of DNA methylation and gene expression reveals specific signaling pathways associated with platinum resistance in ovarian cancer. *BMC Med. Genomics* **2**, 34 (2009).
54. Liu, L. et al. Novel mechanism of lapatinib resistance in HER2-positive breast tumor cells: activation of AXL. *Cancer Res.* **69**, 6871–6878 (2009).
55. Beier, D. et al. $CD133^+$ and $CD133^-$ glioblastoma-derived cancer stem cells show differential growth characteristics and molecular profiles. *Cancer Res.* **67**, 4010–4015 (2007).

Acknowledgements We thank the George, Young and Gray laboratories and J. R. Gilbert for discussions, and C. Li for assistance with the HiChIP experiments. We thank J. Qi for providing JQ1, and D. Sabatini and S. Elledge for sharing plasmids, pLKO.1 GFP shRNA and pInducer20, respectively. We thank A. Ward and C. Clinton at DFCI Pediatric Oncology and J. Chan and the Clark Smith Tumor Bank, Charbonneau Cancer Institute, Calgary, Canada, for the human tumour samples. We thank Applied Pathology Systems, the DFCI Molecular Biology Core, the Whitehead Genome Technology Core, D. Adeegbe and the NYULH Genome Technology Center for technical support. The results shown here are in part based on data generated by the TCGA Research Network: http://cancergenome.nih.gov/, the R2: Genomics Analysis and Visualization Platform: http://r2.amc.nl/ and the Allan Brain Map Data Portal: http://www.brain-map.org/. This work was supported by NIH grants R01CA197336 (R.E.G. and R.A.Y.), R01CA148688 (R.E.G. and N.S.G.) and a Hyundai Hope on Wheels Scholar Grant (R.E.G.). D.N.D. is a recipient of a Young Investigator Grant from the Alex's Lemonade Stand Foundation/Northwestern Mutual Foundation. D.S.D. is supported by an American Cancer Society fellowship PF-16-146-01-DMC. The NYULH Genome Technology Center is partially supported by the Cancer Center Support Grant P30CA016087 at the Laura and Isaac Perlmutter Cancer Center.

Author contributions D.N.D. and R.E.G. conceived the project and designed the experiments. D.N.D. planned and performed the molecular, cellular and genomic studies. R.D. performed computational analyses with input from D.S.D. and E.M. S.S. contributed to the ChIP–seq and HiChIP experiments. D.S. and S.H.O. contributed to the HiChIP experiment. D.N.D., Y.G. and T.C. performed the mouse experiments. B.S. and M.M. provided technical assistance. H.H. performed the co-immunoprecipitation experiments. L.M. performed the FISH analysis. N.S.G. provided TAE684 and E9. G.-C.Y. supervised the bioinformatics analyses. K.-K.W. enabled the mouse and scRNA-seq studies. D.N.D., R.D., R.A.Y. and R.E.G. interpreted the data. D.N.D., R.D. and R.E.G. wrote the manuscript with input from R.A.Y. R.E.G. supervised the research. All authors edited the manuscript.

Competing interests N.S.G. is a founder, SAB member and equity holder of Gatekeeper, Syros Pharmaceuticals, Petra, C4, B2S and Soltego. The Gray laboratory receives or has received research funding from Novartis, Takeda, Astellas, Taiho, Janssen, Kinogen, Voronoi, Her2llc, Deerfield and Sanofi. S.H.O. is a SAB member of Syros. R.A.Y. is a founder and shareholder of Syros, Camp4 Therapeutics, Omega Therapeutics and Dewpoint Therapeutics. R.E.G. is a SAB member of Global Gene Corp.

Additional information

Supplementary information is available for this paper at https://doi.org/10.1038/s41586-019-1472-0.

Correspondence and requests for materials should be addressed to R.E.G.

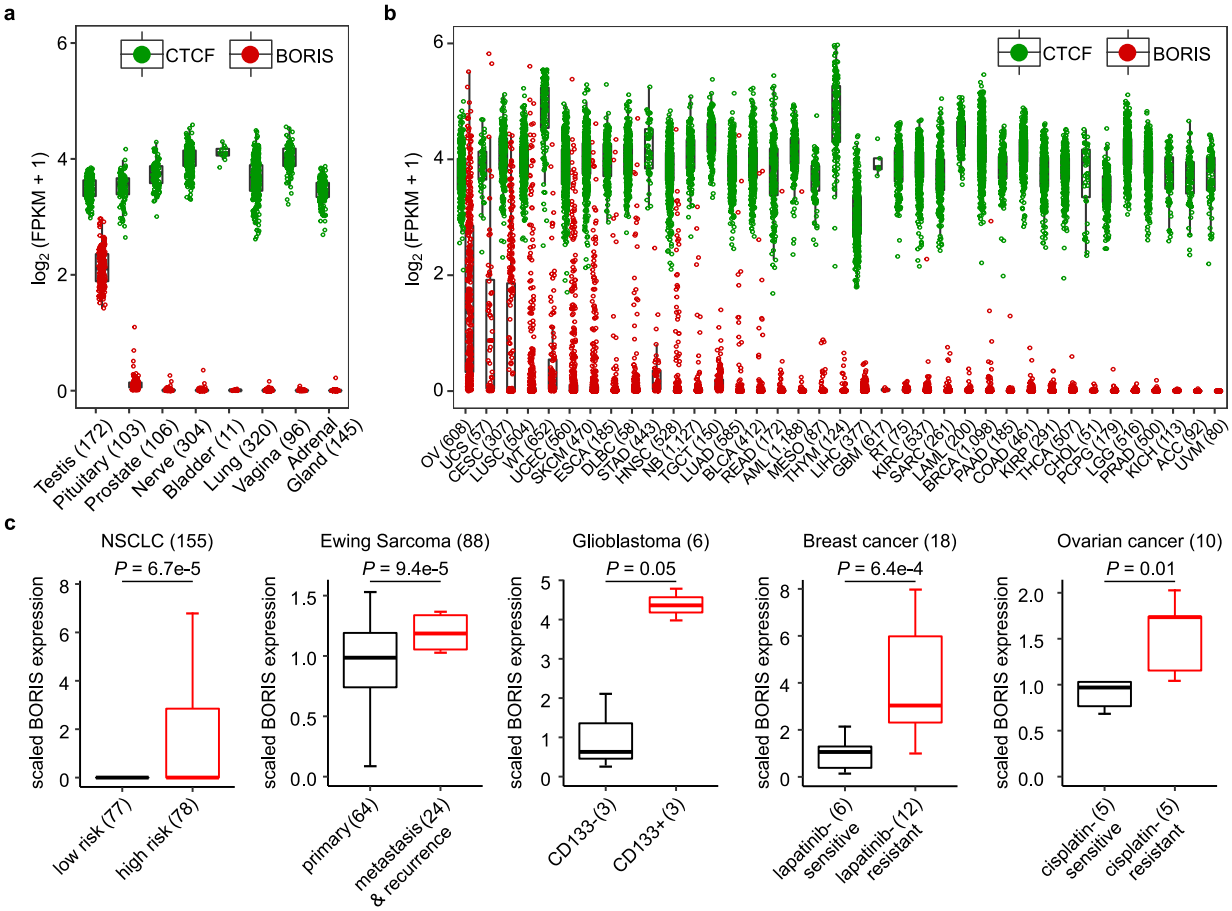

Extended Data Fig. 1 | BORIS is expressed in several cancers and associated with high-risk features. a, **b**, Relative mRNA expression [$\log_2$(FPKM + 1)] of *CTCF* and *BORIS* in normal tissues (**a**) and in various cancer types based on TCGA datasets (**b**). FPKM, fragments per kilobase of transcript per million mapped reads. Keys to cancer types: ACC, adrenocortical carcinoma; AML, acute myeloid leukaemia; BLCA, bladder urothelial carcinoma; BRCA, breast invasive carcinoma; CESC, cervical squamous cell carcinoma and endocervical adenocarcinoma; CHOL, cholangiocarcinoma; COAD, colon adenocarcinoma; DLBC, diffuse large B-cell lymphoma; ESCA, oesophageal carcinoma; GBM, glioblastoma multiforme; HNSC, head and neck squamous cell carcinoma; LGG, low-grade glioma; KICH, kidney chromophobe; KIRC, renal clear cell carcinoma; KIRP, kidney renal papillary cell carcinoma; LAML, acute myeloid leukaemia; LIHC, hepatocellular carcinoma; LUAD, lung adenocarcinoma; LUSC, lung squamous cell carcinoma; MESO, mesothelioma; NB, neuroblastoma; OV, serous ovarian cystadenocarcinoma; PAAD, pancreatic adenocarcinoma; PCPG, pheochromocytoma and paraganglioma; PRAD, prostate adenocarcinoma; READ, rectum adenocarcinoma; RT, rhabdoid tumour; SARC, sarcoma; SKCM, skin cutaneous melanoma; STAD, stomach adenocarcinoma; TGCT, testicular germ cell tumour; THCA, thyroid carcinoma; THYM, thymoma; UCEC, uterine corpus endometrial carcinoma; UCS, uterine carcinosarcoma; UVM, uveal melanoma; WT, Wilms tumour. **c**, Box plots showing the correlation of BORIS expression with risk status, tumour stage (primary versus metastasis/recurrence), presence of cancer stem cells (CD133 positivity) and response to targeted (lapatinib) or cytotoxic (cisplatin) therapy in the tumour types depicted. NSCLC, non-small cell lung cancer. Datasets (Mixed Ewing Sarcoma-Savola-117 and NSCLC-Plamadeala-410) were extracted from the R2: Genomics Analysis and Visualization Platform (http://r2.amc.nl). GSE7181 (glioblastoma); GSE16179 (breast cancer); GSE15372 (ovarian cancer). *P* values determined by two-sided Wilcoxon rank-sum test. For all panels, sample sizes (*n*) are depicted in parenthesis and box plots are as defined in Fig. 4.

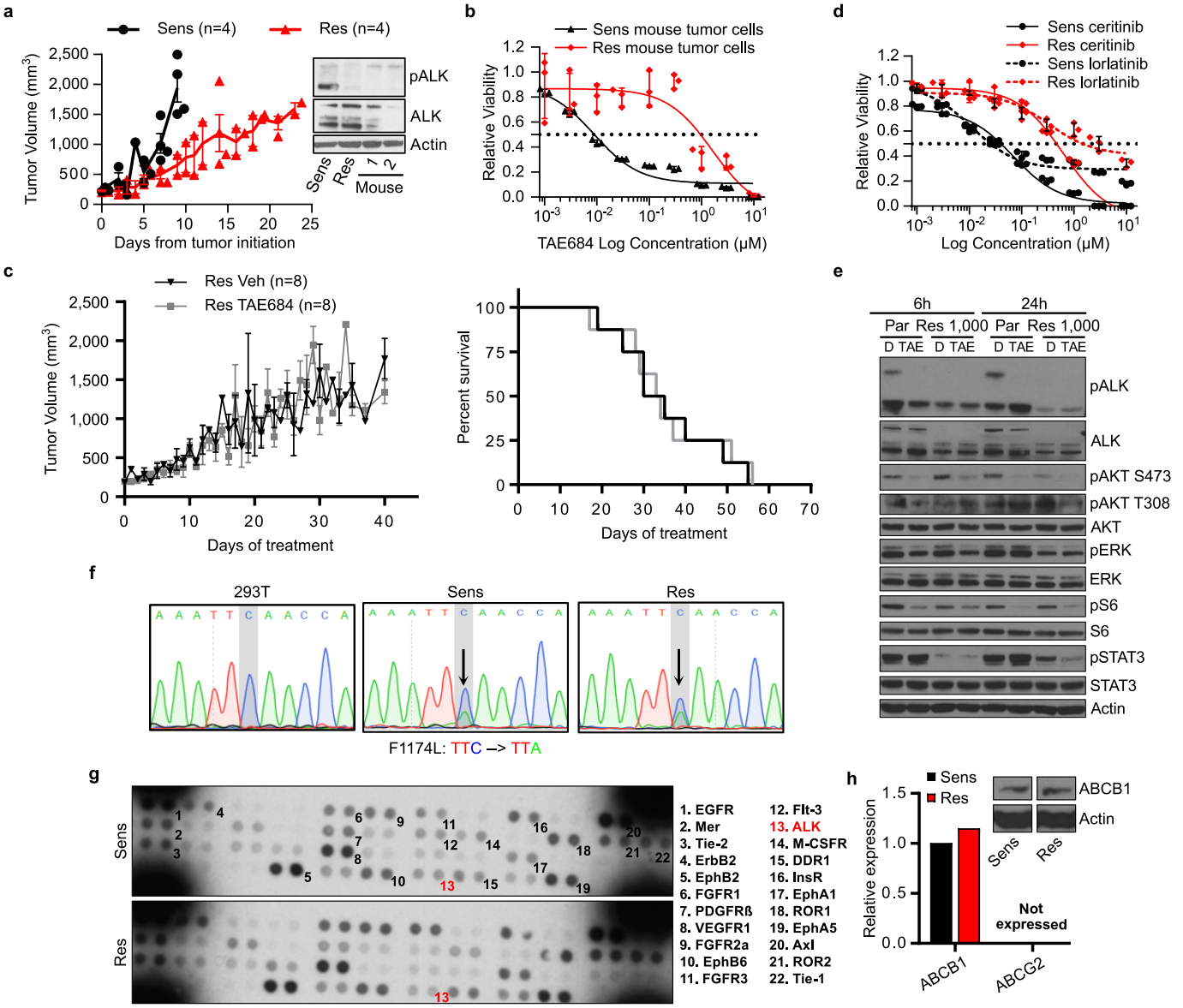

Extended Data Fig. 2 | ALK inhibitor-resistant cells exhibit stable resistance in vivo and no longer rely on ALK signalling. a, Left, tumour volumes of sensitive and resistant cell xenografts in untreated NU/NU (Crl:NU-*Foxn1*^{nu}) mice established by subcutaneous injection of 2×10^6 cells into both flanks. Animals were euthanized when tumours reached 1,500–2,000 mm^3. Data are mean ± s.e.m., $n = 4$ per arm. Right, immunoblot analysis of total and phosphorylated ALK in TAE-resistant xenograft tumours (1 and 2) and sensitive and resistant cells in culture. **b**, Dose–response curves for TAE684 in sensitive and resistant cell lines established from the same tumour xenografts as in **a** (IC_{50} values: sensitive, 7.9 nM; resistant, 878.6 nM). Data are mean ± s.d., $n = 3$ biological replicates. **c**, Tumour volumes (left) and Kaplan–Meier survival curves (right) of resistant cell xenografts in NU/NU (CrTac:NCr-*Foxn1*^{nu}) mice treated with TAE684 (10 mg kg^{-1} by oral gavage once daily) or vehicle control for up to 56 days. Data are mean ± s.e.m., $n = 8$ per arm. *P* values determined by Mann–Whitney *U* test for tumour volumes ($P = 0.8404$) and by log-rank test for Kaplan–Meier survival analysis ($P = 0.8076$), both two-sided. **d**, Dose–response curves for TAE684-sensitive and -resistant cells treated with ceritinib (IC_{50} values: sensitive, 33.8 nM; resistant, 446.5 nM) or lorlatinib (IC_{50} values: sensitive, 47.5 nM; resistant, 2,318 nM). Data are mean ± s.d., $n = 3$ biological replicates. **e**, Immunoblot analysis of the indicated proteins in sensitive and resistant cells treated with DMSO or 1 μM TAE684 for 6 or 24 h. **f**, Electropherograms of ALK kinase domain sequencing in sensitive and resistant cells. Arrows show the F1174L mutation characteristic of Kelly cells. HEK293T cells were used as a control for sequencing wild-type ALK. **g**, Phosphoproteomic analysis of a panel of receptor tyrosine kinases (RTKs) in sensitive and resistant cells. Each RTK is shown in duplicate and the pairs in the corners of each array are positive controls. Numbered RTKs with corresponding names listed on the right represent the highest-phosphorylated proteins. ALK is depicted in red. **h**, Quantitative reverse transcription PCR (qRT–PCR) and immunoblot analysis of ABCB1 and ABCG2 multidrug transporter expression in sensitive and resistant cells. The qRT–PCR data are means of $n = 2$ biological replicates. In **a** (immunoblot), **d**, **f** and **g**, data are representative of two independent experiments (see Supplementary Note 1 for details; for gel source data, see Supplementary Fig. 1).

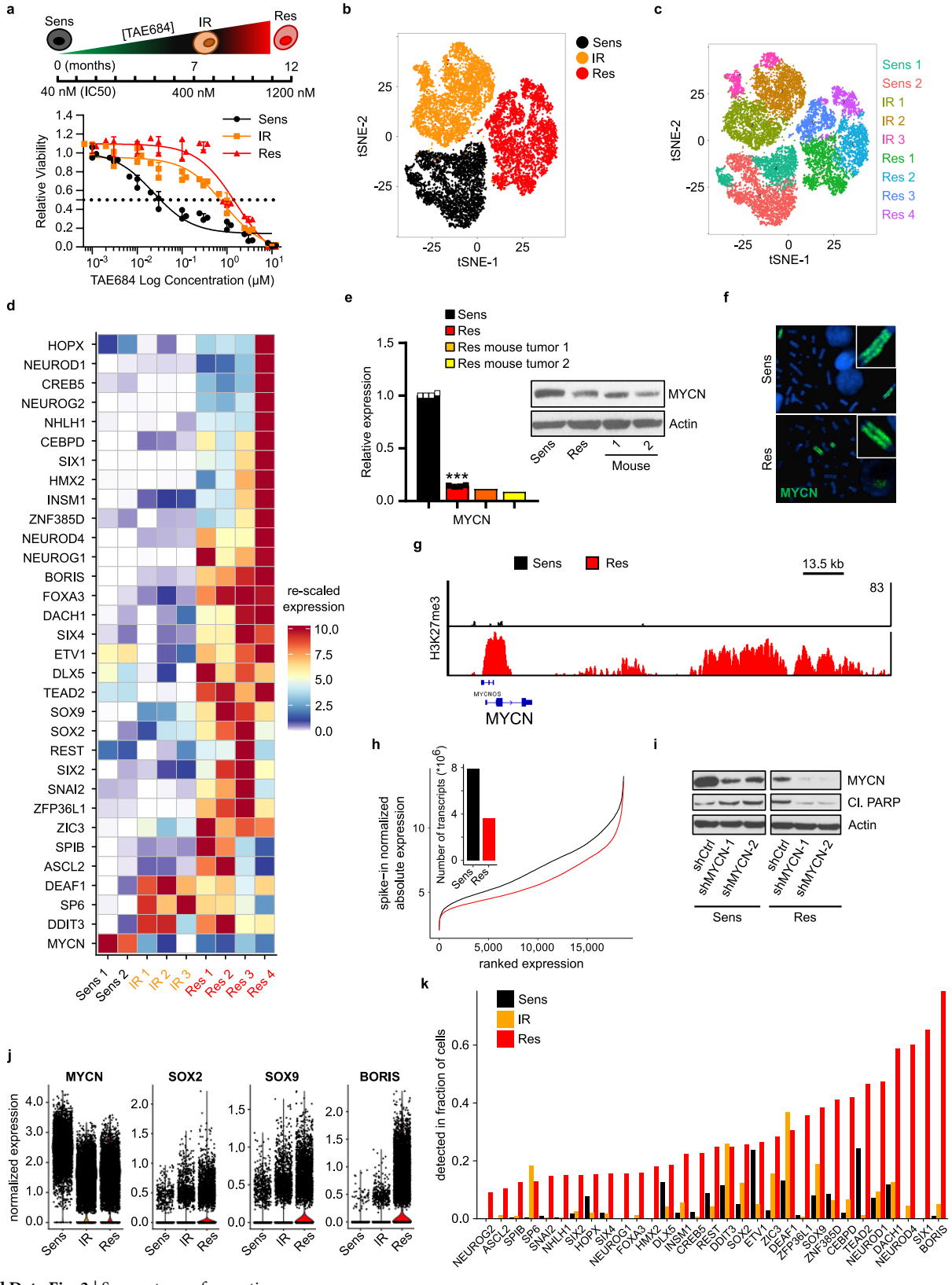

Extended Data Fig. 3 | See next page for caption.

Extended Data Fig. 3 | Development of resistance is associated with loss of MYCN followed by gradual induction of proneural transcription factors. a, TAE684 dose–response curves of Kelly neuroblastoma cells during resistance establishment (IC_{50} values: sensitive, 39.4 nM; intermediate, 618 nM; resistant, 1,739 nM). Data are mean ± s.d., $n = 3$ biological replicates. Schematic representation of development of resistance is shown above. **b**, *t*-SNE plot of scRNA-seq data showing the segregation of sensitive ($n = 5{,}432$), intermediate ($n = 6{,}376$) and resistant ($n = 6{,}379$) cells. **c**, *t*-SNE plot depicting unsupervised clusters for the individual subpopulations that underlie the pseudotime analysis. **d**, Heat map of rescaled gene expression values of the most variable ranked transcription factors in the three cell states. **e**, qRT–PCR and immunoblot analysis of MYCN expression in TAE684-resistant xenograft tumours (1 and 2) and sensitive and resistant cells in culture. The qRT–PCR data are mean ± s.d., $n = 4$ biological replicates for sensitive and resistant cells ($^{***}P = 1.396 \times 10^{-11}$; unpaired two-sided *t*-test) and $n = 3$ technical replicates for each tumour. **f**, Fluorescence in situ hybridization of MYCN in sensitive and resistant cells (representative of 20 nuclei per condition). **g**, ChIP–seq track of H3K27me3 binding at the *MYCN* locus in sensitive and resistant cells. Signal intensity is given in the top right corner. **h**, Line plot showing the association between genes ordered by expression (*x* axis) and changes in absolute gene expression levels (*y* axis) in sensitive versus resistant cells. Bar plot, total transcriptional yield in sensitive or resistant cells. **i**, Immunoblot analysis of the indicated proteins in sensitive and resistant cells expressing control (shCtrl) or MYCN (shMYCN-1 and -2) shRNAs. **j**, Violin plots representing the expression distribution of selected genes in the same cells as in **a** (centre line, median). **k**, Bar plot showing the fractions of cells with detectable mRNA levels of the same genes as in **d**. In **e** (immunoblot) and **f**–**i**, data are representative of two independent experiments (for gel source data, see Supplementary Fig. 1).

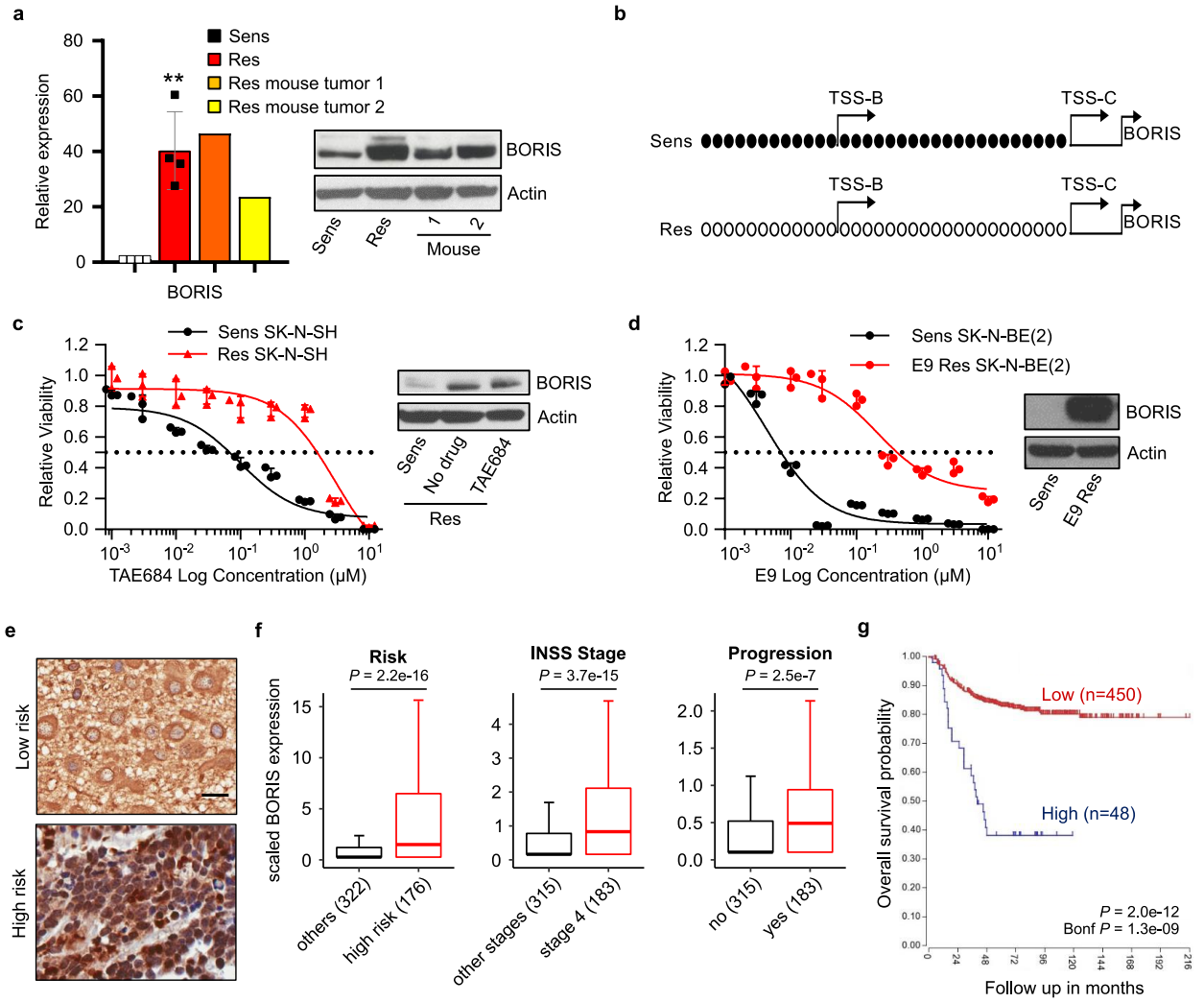

Extended Data Fig. 4 | Overexpression of *BORIS* is seen in resistance models of neuroblastoma and correlates with high-risk disease and a poor outcome. a, qRT–PCR and immunoblot analysis of BORIS expression in TAE684-resistant Kelly cell xenograft tumours (1 and 2) and sensitive and resistant cells in culture. The qRT–PCR data are mean ± s.d., $n = 4$ biological replicates for sensitive and resistant cells (**$P = 0.0014$; unpaired two-sided t-test) and $n = 3$ technical replicates for each tumour. **b**, Bisulfite sequencing of the *BORIS* promoter in sensitive and resistant cells. Black circles represent methylated cytosine residues in a CpG dinucleotide, empty circles are unmethylated cytosines. The B and C TSSs are indicated by arrows. **c**, Dose–response curves to TAE684 (left) and immunoblot analysis of BORIS expression (right) in TAE684-sensitive and -resistant SK-N-SH neuroblastoma cells (IC_{50} values: sensitive, 47.9 nM; resistant, 1,739 nM). **d**, Dose–response curves to the CDK12 inhibitor, E9 (left) and immunoblot analysis of BORIS expression (right) in sensitive and resistant SK-N-BE(2) neuroblastoma cells (IC_{50} values: sensitive, 9.5 nM; resistant, 638 nM). Data are mean ± s.d., $n = 3$ biological replicates for **c** (left) and **d** (left). **e**, Immunohistochemical staining of BORIS expression in primary neuroblastoma tumour samples (representative of four independent experiments). Scale bar, 20 μm. **f**, Box plots showing correlation of BORIS expression with the indicated parameters in a human neuroblastoma dataset ($n = 498$; Tumour Neuroblastoma-SEQC-498; R2: Genomics Analysis and Visualization Platform (http://r2.amc.nl)). Box plots are as defined in Fig. 4. P values were determined by two-sided Wilcoxon rank-sum test. **g**, Kaplan–Meier analysis of overall survival based on BORIS expression in the same dataset as in **f** ($n = 498$; two-sided log-rank test with Bonferroni correction). In **a**, **c**, **d** (immunoblots) and **b**, data are representative of two independent experiments. Sample sizes (n) are depicted in parenthesis for **f** and **g** (for gel source data, see Supplementary Fig. 1).

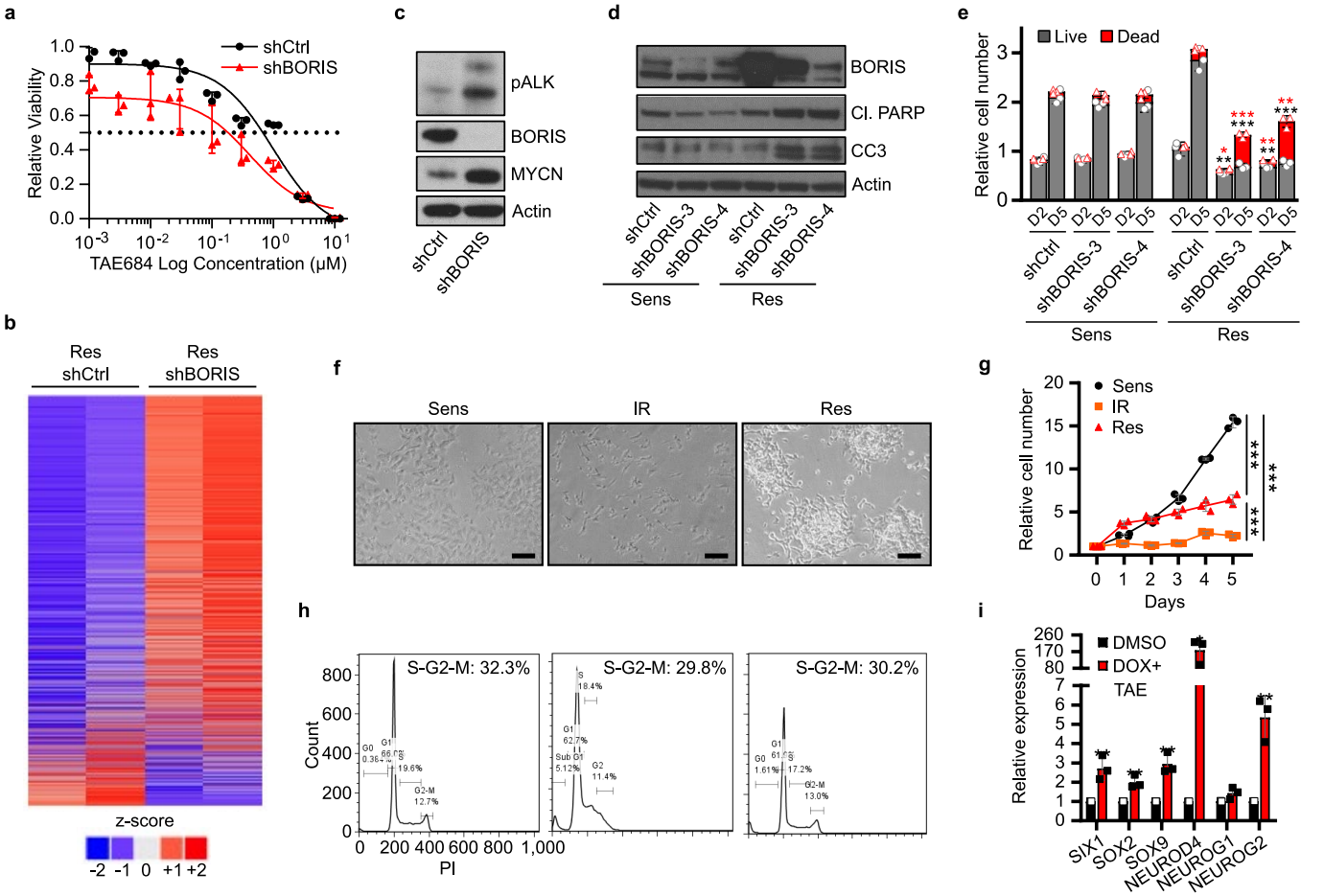

Extended Data Fig. 5 | Resistant cells are dependent on BORIS for survival. a, Dose–response curves to TAE684 in resistant cells expressing control (shCtrl) or BORIS (shBORIS) shRNAs (IC_{50} values: shCtrl, 537.7 nM; shBORIS, 141.2 nM). Data are mean ± s.d., $n = 3$ biological replicates. **b**, Heat map of gene expression values in the same cells as in **a** ($n = 2$ biological replicates). Rows are z-scores calculated for each gene in both conditions. **c**, Immunoblot analysis of the indicated proteins in the same cells as in **a**. **d**, **e**, Immunoblot analysis of the indicated proteins (Cl., cleaved; CC3, cleaved caspase 3) (**d**), and quantification of trypan blue staining (**e**) in sensitive and resistant cells expressing control (shCtrl) or BORIS (shBORIS-3 and -4) shRNAs. Data are mean ± s.d., $n = 3$ biological replicates ($^*P < 0.05$; $^{**}P < 0.01$; $^{***}P < 0.001$; unpaired two-sided t-tests). **f**–**h**, Phase-contrast microscopy images (scale bars, 150 μm) (**f**), growth curves (**g**) and flow cytometry analyses (**h**) of propidium iodide (PI) staining in sensitive, intermediate and resistant cells. Data are mean ± s.d., $n = 3$ biological replicates ($^{***}P < 0.0001$ for all comparisons; two-way ANOVA). **i**, qRT–PCR analysis of the expression of the indicated proneural transcription factors in the same sensitive (DMSO) versus $MYCN^{KD}$ and $BORIS^{Ind}$ (DOX + TAE) cells as in Fig. 1g. Data are mean ± SD, $n = 3$ biological replicates ($^*P < 0.05$; $^{**}P < 0.01$; unpaired two-sided t-tests). In **c**, **d**, **f** and **h**, data are representative of two independent experiments (for gel source data, see Supplementary Fig. 1).

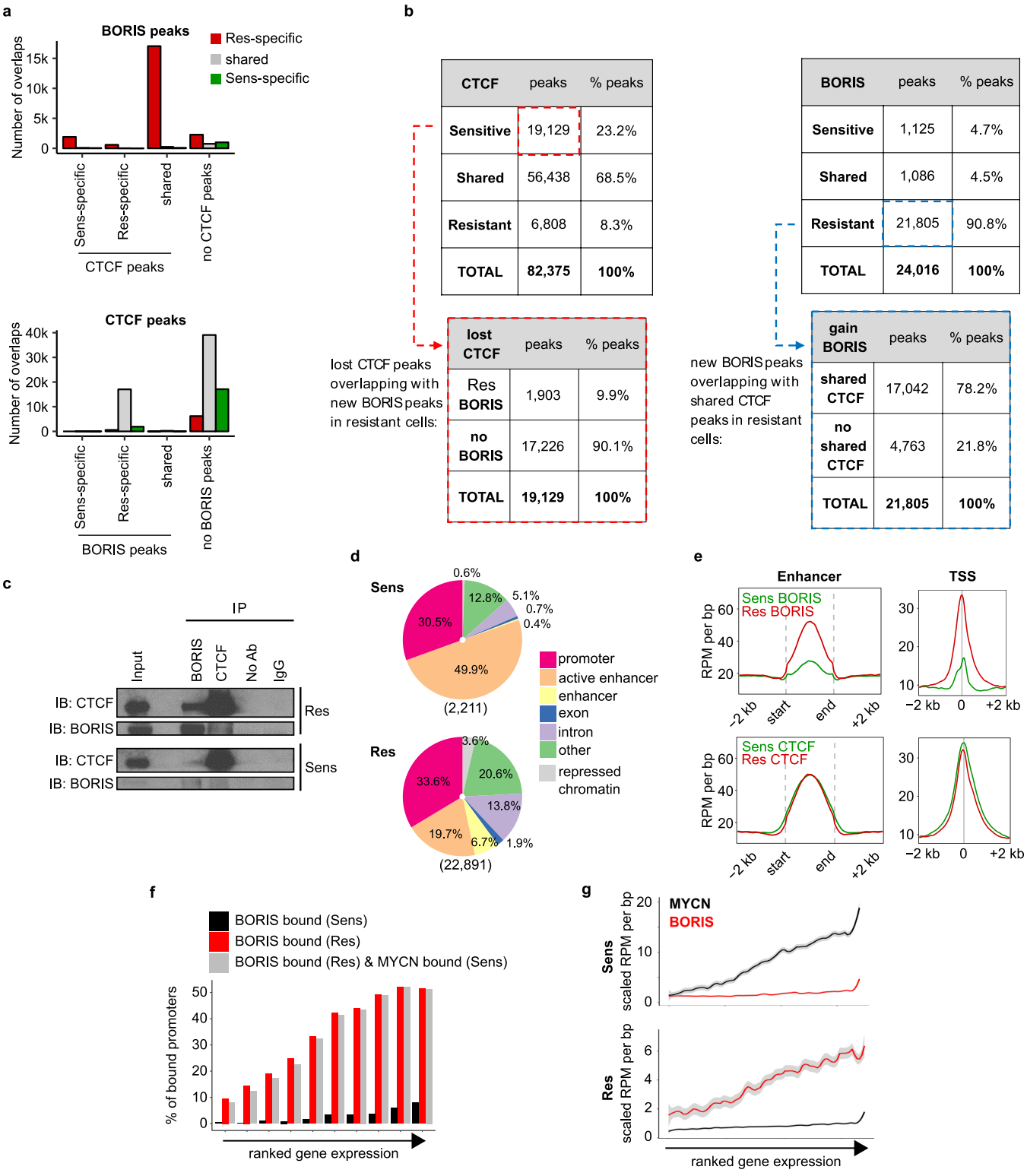

Extended Data Fig. 6 | See next page for caption.

Extended Data Fig. 6 | BORIS colocalizes with CTCF and open chromatin. a, Bar graphs illustrating the overlap of shared and specific BORIS and CTCF-binding sites in sensitive and resistant cells. Most resistant cell-specific BORIS peaks (red) colocalize with CTCF peaks that are shared between the two cell types. The markedly lower number of BORIS peaks that are unique to sensitive cells (green) or shared between sensitive and resistant cells (grey) typically do not overlap with CTCF peaks that are shared or specific to any cell type (top). Most CTCF peaks are shared (grey) between sensitive and resistant cells and either do not overlap with BORIS peaks, or overlap only with those restricted to resistant cells (bottom). **b**, Comparison of CTCF and BORIS peaks identified in sensitive and resistant cells. **c**, Co-immunoprecipitation of BORIS with CTCF in sensitive and resistant cells (representative of two independent experiments). IgG and sample without antibody (Ab) serve as controls. **d**, Pie charts depicting the percentages of genomic regions bound by BORIS in sensitive (top) and resistant (bottom) cells. Numbers of BORIS-binding peaks in each cell type are given below each pie chart. The regions shown are promoters (TSS ± 2 kb), typical enhancers (H3K27ac), active enhancers (H3K27ac + BRD4), repressed chromatin (H3K27me3), exons, introns, and other (peaks not assigned to any of the previous categories). **e**, Meta-analysis of average CTCF and BORIS ChIP–seq signals in RPM per bp at enhancer and TSS regions in sensitive and resistant cells. **f**, Percentage of gene promoters bound by BORIS in sensitive (black) and resistant (red) cells for 10 equal-sized groups ordered based on absolute gene expression levels in resistant cells. Percentage of promoters bound by BORIS in resistant cells that were also originally bound by MYCN in sensitive cells is shown in grey. **g**, Loess regression analysis of ranked gene expression against BORIS and MYCN occupancies at gene promoters in sensitive and resistant cells. Shaded regions represent 95% confidence intervals. All panels except **c** depict data from $n = 2$ biological replicates (for gel source data, see Supplementary Fig. 1).

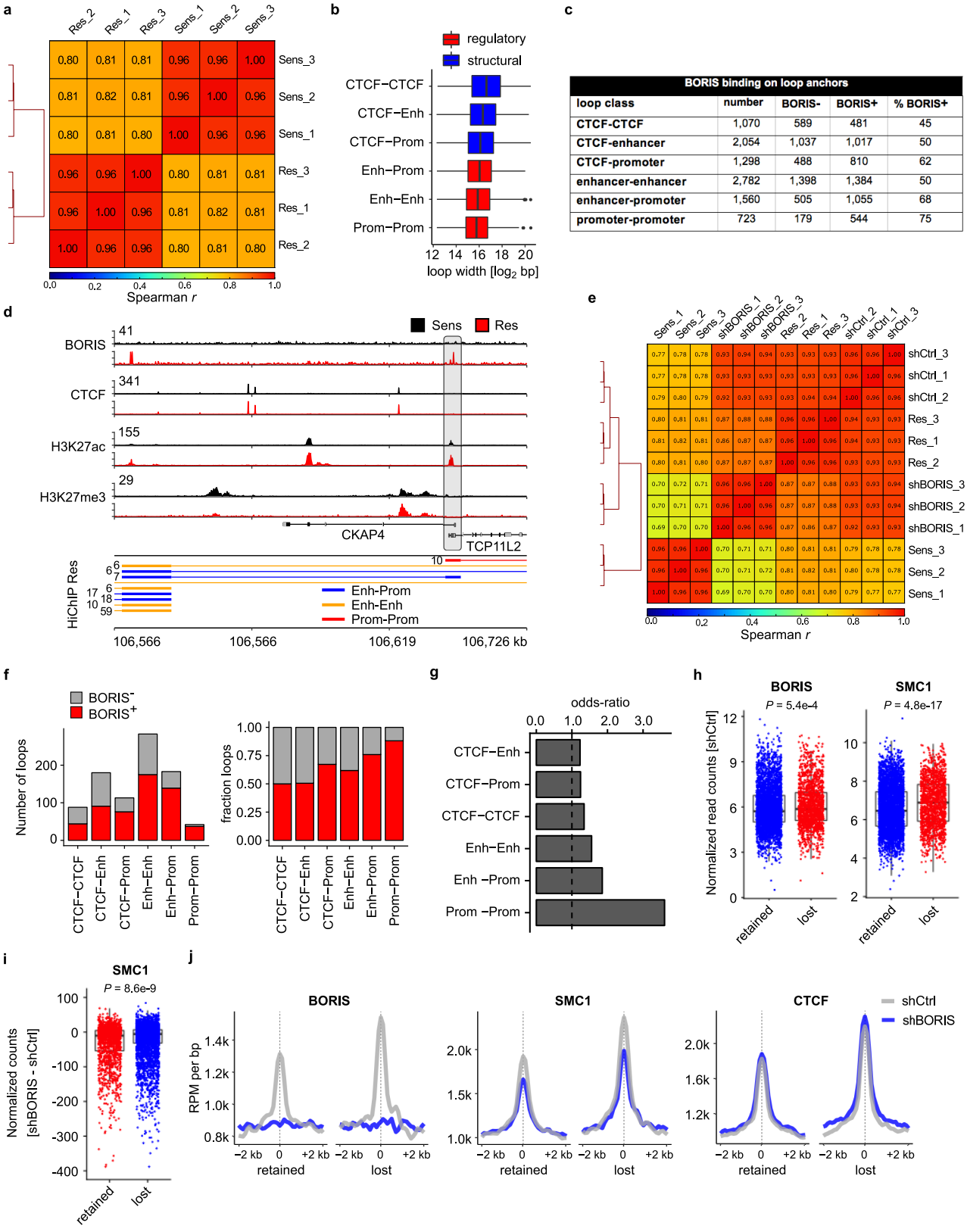

Extended Data Fig. 7 | See next page for caption.

Extended Data Fig. 7 | Regulatory loops in resistant cells are more vulnerable to BORIS depletion. a, Heat map depicting the Spearman correlation between HiChIP biological replicates of sensitive and resistant cells in genome-wide bins of 5 kb for all merged anchor regions. **b**, Box plots showing the genomic length distribution (in $\log_2$(bp)) for interaction classes that are specific to resistant cells. **c**, Table depicting HiChIP loop class statistics in resistant cells, including their association with BORIS binding. **d**, ChIP-seq tracks of the indicated proteins in sensitive and resistant cells at the *TCP11L2* locus (representative of two independent experiments), with resistant cell-specific regulatory interactions shown below (HiChIP Res: PET numbers, next to each interaction). Signal intensity is given in the top left corner for each track. **e**, Heat map depicting the Spearman correlation between HiChIP biological replicates of sensitive, resistant, shCtrl and shBORIS cells in genome-wide bins of 5 kb for all merged anchor regions. **f**, Bar plots showing the number and fraction of resistant cell-specific loops for all interaction classes that were BORIS negative and positive in resistant cells, and that were lost after BORIS depletion. **g**, Bar plots showing the odds ratio (two-sided Fisher's exact test) of losing loops that were previously bound by BORIS for all interaction classes. **h**, Box plots showing the initial intensities (in normalized read counts) of BORIS and SMC1A binding in the shRNA control cells at the anchors of the resistant cell-specific loops that were significantly lost versus those that were retained in shBORIS cells (two-sided Wilcoxon rank-sum test). **i**, Box plot showing the difference in SMC1A loss (shBORIS versus shCtrl) on the same anchors as in **h**. *P* value determined by two-sided Wilcoxon rank-sum test. All box plots are as defined in Fig. 4. **j**, Metaplots depicting BORIS, SMC1A and CTCF binding at the anchors of the resistant cell-specific loops that were lost or retained after BORIS depletion. In **a**–**c** and **e**–**g**, data are from $n = 3$ biological replicates. In **h**–**j**, data are from $n = 2$ biological replicates.

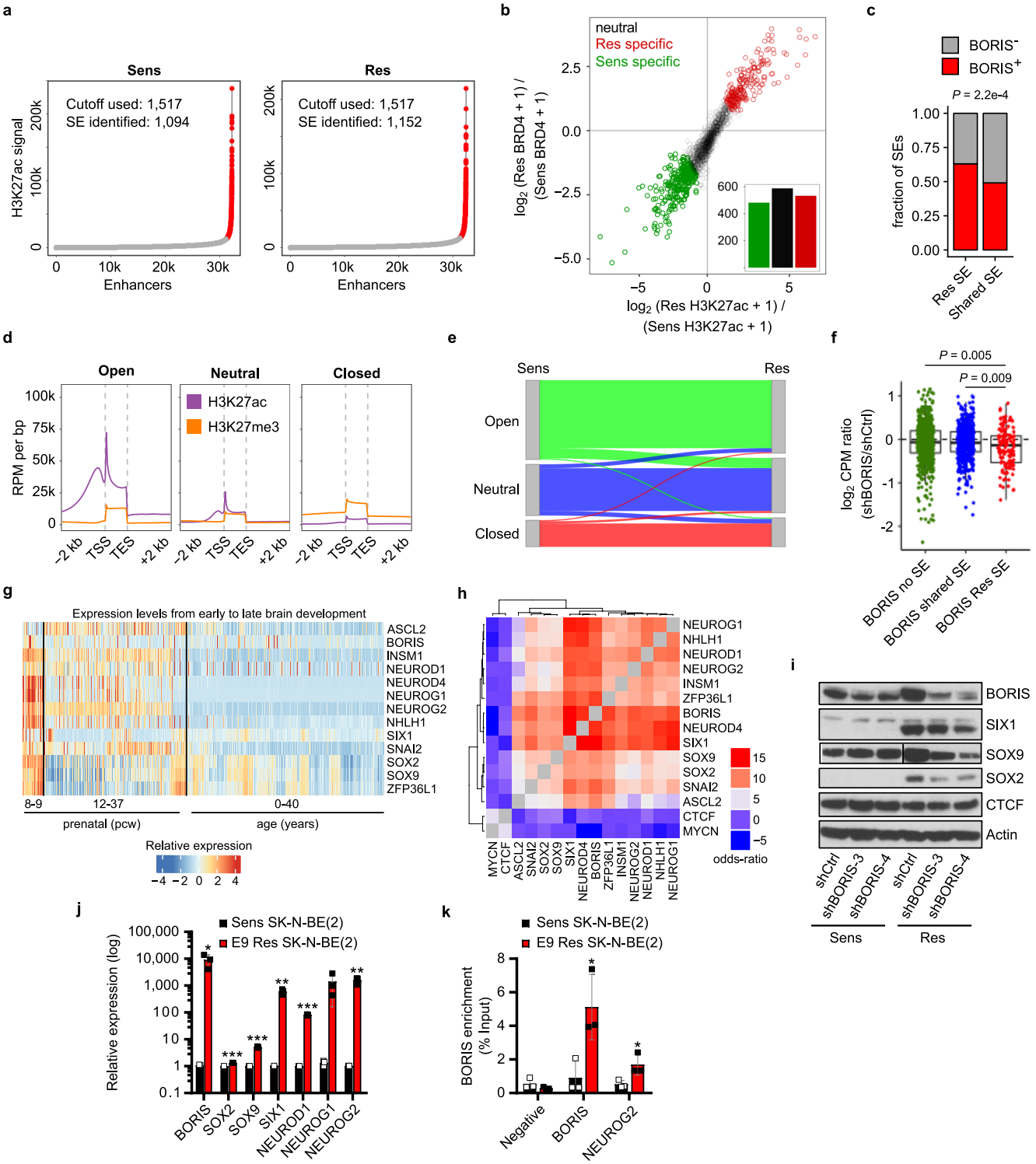

Extended Data Fig. 8 | See next page for caption.

Extended Data Fig. 8 | Redistribution of the super-enhancer landscape with subsequent expression of a BORIS-dependent proneural network in resistant cells. a, Accumulation of H3K27ac signal at enhancer regions. Typical enhancers (grey) are plotted according to increasing levels of normalized H3K27ac signal (length × density) in sensitive and resistant cells. The highest cut-off based on the inclination point in both sensitive and resistant cells was used to delineate super-enhancers (red). **b**, Scatter plot showing differential binding of H3K27ac [$\log_2$(RPM per bp + 1)] and BRD4 [$\log_2$(RPM per bp + 1)] for all detected super-enhancers in both sensitive and resistant cells. Cell-specific super-enhancers were identified based on the combined increase in H3K27ac and BRD4 binding. For each individual histone mark, a 0.75 $\log_2$-transformed fold change threshold was applied and a minimum summed 2.5 $\log_2$-transformed fold change was used as the final cut-off. **c**, Bar plot depicting the enrichment (two-sided Fisher's exact test) and fractions of resistant cell-specific and shared super-enhancers that were located at resistant cell-specific regulatory loop anchors in resistant cells. **d**, Density plots showing the aggregated accumulation of H3K27ac and H3K27me3 at gene regions, defined as 2 kb upstream of the TSS and 2 kb downstream of the transcription end site (TES). *k*-means clustering ($k = 3$) analysis resulted in the separation of genes associated with 'open', 'neutral' or 'closed' chromatin in both sensitive and resistant cells. **e**, Sankey diagram of the distribution of genes in distinct chromatin states and the switches between sensitive and resistant cells. **f**, Box plots showing the expression level changes upon BORIS depletion for genes that had a resistant cell-specific and BORIS-positive regulatory interaction and were not associated with a super-enhancer ($n = 720$), associated with a super-enhancer in both cell types ($n = 514$) or associated with a super-enhancer seen only in the resistant cells ($n = 134$) (two-sided Wilcoxon rank-sum test). Box plots are as defined in Fig. 4. **g**, Heat map of the expression levels of the indicated proneural transcription factor genes during brain development (http://www.brain-map.org/). Gene expression levels are represented as *z*-scores for different developmental time points ($n = 413$; pcw, post-conceptional weeks). **h**, Heat map showing the odds ratios (two-sided Fisher's exact test) for co-detection of the indicated transcription factors based on the scRNA-seq data in resistant cells ($n = 6{,}379$). **i**, Immunoblot analysis of the indicated proteins in sensitive and resistant cells expressing control (shCtrl) or BORIS (shBORIS-3 and -4) shRNAs. **j**, **k**, qRT–PCR analysis of the indicated genes (**j**) and ChIP–qPCR analysis of BORIS binding at the promoter regions of *BORIS* and *NEUROG2* (**k**) in sensitive and resistant SK-N-BE(2) neuroblastoma cells. Data are mean ± s.d., $n = 3$ biological replicates in **j** and **k** (*$P < 0.05$; **$P < 0.01$; ***$P < 0.001$; unpaired two-sided *t*-tests). All other panels except **g** and **h** depict data from $n = 2$ biological replicates (for gel source data, see Supplementary Fig. 1).

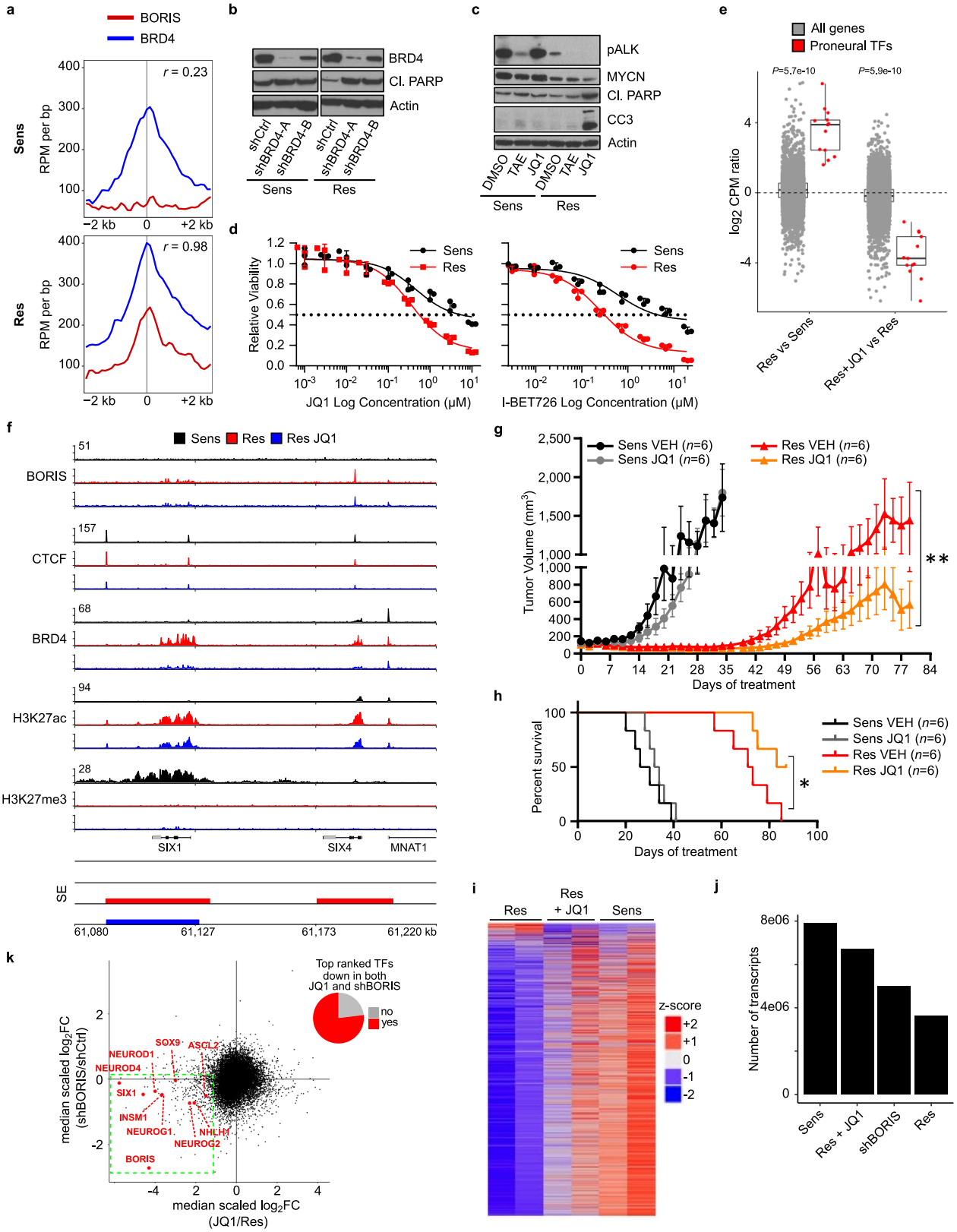

Extended Data Fig. 9 | See next page for caption.

Extended Data Fig. 9 | The proneural transcription factor network in resistant cells is sensitive to BRD4 inhibition. a, Metaplots showing the correlation between BRD4 and BORIS co-occupancies at the promoter regions (± 2 kb) of the 89 top-ranked genes in resistant versus sensitive cells based on the features in Fig. 4b (*r*, Spearman correlation coefficient). **b**, Immunoblot analysis of BRD4 and cleaved PARP expression in sensitive and resistant cells expressing control (shCtrl) or BRD4 (shBRD4-A and -B) shRNAs. **c**, Immunoblot analysis of the indicated proteins in sensitive and resistant cells treated with DMSO, TAE684 (1 μM) or JQ1 (2.5 μM) for 48 h. **d**, Dose–response curves for sensitive and resistant cells treated with JQ1 or I-BET726 (JQ1 (IC_{50} values: sensitive, 4,798 nM; resistant, 645 nM); I-BET726 (IC_{50} values: sensitive, 6,203 nM; resistant, 347 nM)). Data are mean ± s.d., $n = 3$ biological replicates. **e**, Box plots comparing the expression of the transcription factors listed in Fig. 4b ($n = 13$) with that of all genes ($n = 18{,}038$) in sensitive versus resistant cells (left), and between DMSO and JQ1-treated resistant cells (right) (*P* values determined by two-sided Wilcoxon rank-sum test). **f**, ChIP–seq tracks of the indicated proteins at the *SIX1* or *SIX4* locus in sensitive, resistant and JQ1-treated resistant cells (2.5 μM for 48 h). Super-enhancers are depicted as coloured rectangles below the tracks. Signal intensity is shown in the top left corner for each track. **g**, **h**, Tumour volumes (**g**) and survival curves (**h**) in sensitive- and resistant-cell xenografts in NU/NU (Crl:NU-*Foxn1*^{nu}) mice treated with JQ1 (50 mg kg^{-1} i.p. once daily) and vehicle control for up to 87 days. Data are mean ± s.e.m., $n = 6$ per arm. Significance was calculated by Mann–Whitney *U* test for tumour volumes (sensitive: $P = 0.3231$; resistant: $P = 0.0023$) and by log-rank test for Kaplan–Meier survival analysis (sensitive: $P = 0.3047$; resistant: 0.0348), both two-sided. **i**, Heat map of gene expression values in sensitive, resistant and JQ1-treated resistant cells. Rows are *z*-scores calculated for each gene in each condition. **j**, Number of transcripts in sensitive, JQ1-treated resistant, shBORIS-expressing resistant and resistant cells based on expression array data after spike-in normalization. **k**, Scatter plot displaying the median-scaled fold-change gene expression values for shBORIS and JQ1-treated resistant cells. The top-ranked transcription factors that show decreased expression levels after both *BORIS* knockdown and JQ1 treatment are listed in red (bottom left quadrant). The pie chart represents the fraction of all top-ranked transcription factors that are located in the left lower quadrant of the scatter plot. All box plots are as defined in Fig. 4. In **b**, **c** and **f**, data are representative of two independent experiments. In **a**, **e** and **i**–**k**, data are from $n = 2$ biological replicates (see Supplementary Note 2 for further details; for gel source data, see Supplementary Fig. 1).

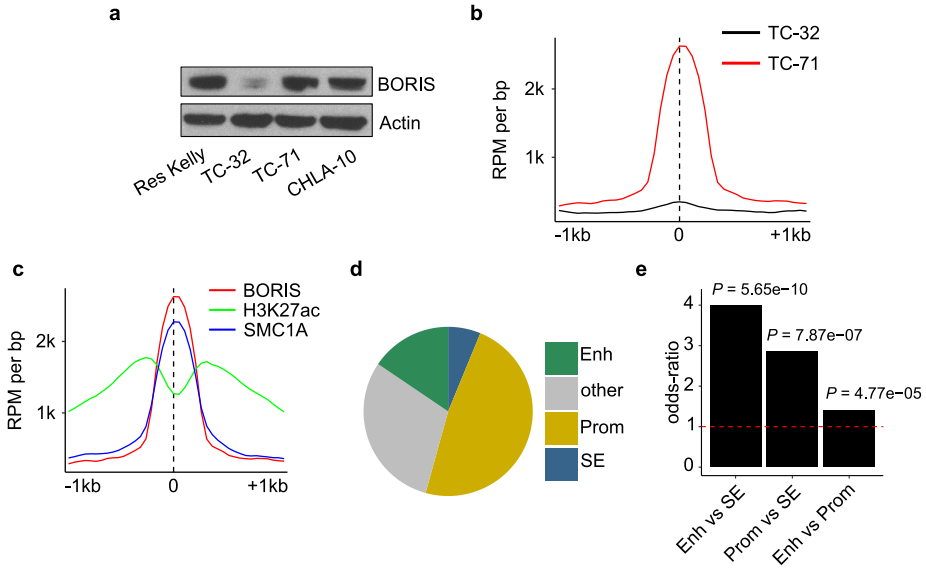

Extended Data Fig. 10 | Aberrantly expressed BORIS binds to regulatory regions and is associated with new super-enhancers in Ewing sarcoma cells. a, Immunoblot analysis of BORIS expression in TC-32 (pre-chemotherapy), TC-71 and CHLA-10 (relapsed, post-chemotherapy) Ewing sarcoma cells, compared with BORIS expression in resistant (Kelly) neuroblastoma cells. **b**, Meta-analysis of average BORIS ChIP–seq signals in RPM per bp at all combined BORIS-binding sites for TC-32 and TC-71 cells. **c**, Meta-analysis of average BORIS, H3K27ac and SMC1A ChIP–seq signals in RPM per bp at TC-71-specific BORIS-binding sites. **d**, Pie chart depicting the proportions of genomic regions bound by BORIS in TC-71 cells. The regions shown are promoters (TSS ± 2 kb), typical and super-enhancers (H3K27ac), and other (if peaks were not assigned to any of the previous categories). **e**, Bar plot showing the odds ratios (two-sided Fisher's exact test) of BORIS localization to regulatory genomic regions in TC-71 cells. All panels are representative of two independent experiments (see Supplementary Note 3 for further details; for gel source data, see Supplementary Fig. 1).

nature research

Corresponding author(s): Rani E. George

Last updated by author(s): Jun 13, 2019

Reporting Summary

Nature Research wishes to improve the reproducibility of the work that we publish. This form provides structure for consistency and transparency in reporting. For further information on Nature Research policies, see Authors & Referees and the Editorial Policy Checklist.

Statistics

For all statistical analyses, confirm that the following items are present in the figure legend, table legend, main text, or Methods section.

n/a	Confirmed
☐	☒ The exact sample size (*n*) for each experimental group/condition, given as a discrete number and unit of measurement
☐	☒ A statement on whether measurements were taken from distinct samples or whether the same sample was measured repeatedly
☐	☒ The statistical test(s) used AND whether they are one- or two-sided *Only common tests should be described solely by name; describe more complex techniques in the Methods section.*
☒	☐ A description of all covariates tested
☐	☒ A description of any assumptions or corrections, such as tests of normality and adjustment for multiple comparisons
☐	☒ A full description of the statistical parameters including central tendency (e.g. means) or other basic estimates (e.g. regression coefficient) AND variation (e.g. standard deviation) or associated estimates of uncertainty (e.g. confidence intervals)
☐	☒ For null hypothesis testing, the test statistic (e.g. *F*, *t*, *r*) with confidence intervals, effect sizes, degrees of freedom and *P* value noted *Give P values as exact values whenever suitable.*
☒	☐ For Bayesian analysis, information on the choice of priors and Markov chain Monte Carlo settings
☒	☐ For hierarchical and complex designs, identification of the appropriate level for tests and full reporting of outcomes
☐	☒ Estimates of effect sizes (e.g. Cohen's *d*, Pearson's *r*), indicating how they were calculated

Our web collection on statistics for biologists contains articles on many of the points above.

Software and code

Policy information about availability of computer code

Data collection	Data collection was done with BD CellQuest Pro software (BD Biosciences) for the flow cytometry experiment. The Cell Ranger Single Cell Software Suite (v1.3) was used to perform sample de-multiplexing, barcode and UMI processing, and singlecell 3′ gene counting for the single cell RNA-sequencing experiment.
Data analysis	R (v3.1.3), affy (v1.44.0), limma (v3.22.7), Fastqc (v0.11.5), STAR (v2.5.1b_modified), Samtools (v1.3.1), MarkDuplicates (v2.1.1), deepTools (v2.2.4), MACS2 (v2.1.1), bedGraphToBigWig (v4), R (v3.5.1), Rstudio (v1.1.463), data.table (v1.12.2), trimmomatic (v0.36), HiC-Pro (v2.10.0), hichipper (v0.7.3), diffloop (v1.10.0), ROSE (v1), HOMER (v2) (http://homer.ucsd.edu/homer/motif/), Biostrings (v2.50.1),Cell Ranger (v1.3), Scater (v1.10.0), Seurat (v2.3.4), Circlize (v0.4.5), IGV (v2.3.74), FlowJo (v10.0.5) and GraphPad Prism (v7.02). Custom code is available upon reasonable request.

For manuscripts utilizing custom algorithms or software that are central to the research but not yet described in published literature, software must be made available to editors/reviewers. We strongly encourage code deposition in a community repository (e.g. GitHub). See the Nature Research guidelines for submitting code & software for further information.

Data

Policy information about availability of data

All manuscripts must include a data availability statement. This statement should provide the following information, where applicable:

- Accession codes, unique identifiers, or web links for publicly available datasets
- A list of figures that have associated raw data
- A description of any restrictions on data availability

The microarray, ChIP-seq, HiChIP and scRNA-seq datasets generated and analyzed during the current study are available in the Gene Expression Omnibus repository under accession number GSE103084. The authors declare that all other data supporting the findings of this study are available within the paper and its Supplementary Information files.

Field-specific reporting

Please select the one below that is the best fit for your research. If you are not sure, read the appropriate sections before making your selection.

☒ Life sciences ☐ Behavioural & social sciences ☐ Ecological, evolutionary & environmental sciences

For a reference copy of the document with all sections, see nature.com/documents/nr-reporting-summary-flat.pdf

Life sciences study design

All studies must disclose on these points even when the disclosure is negative.

Sample size	No statistical methods were used to predetermine sample sizes. Sample sizes were chosen in order to be able to perform statistical analyses, as is standard in the field
Data exclusions	No data were excluded from the analyses.
Replication	To verify the reproducibility of our findings, experiments were performed using at least three biological replicates, unless clearly stated otherwise in the figure legends. All attempts at replication were successful.
Randomization	For in vivo mice experiments, mice were randomized into groups of equal average volumes.
Blinding	For experiments involving human research participants, investigators were blinded to group allocation during data collection. For in vivo mice experiments, investigators were not blinded to group allocation during data collection. For experiments involving cell culture, blinding did not apply.

Reporting for specific materials, systems and methods

We require information from authors about some types of materials, experimental systems and methods used in many studies. Here, indicate whether each material, system or method listed is relevant to your study. If you are not sure if a list item applies to your research, read the appropriate section before selecting a response.

Materials & experimental systems

n/a	Involved in the study
☐	☒ Antibodies
☐	☒ Eukaryotic cell lines
☒	☐ Palaeontology
☐	☒ Animals and other organisms
☐	☒ Human research participants
☒	☐ Clinical data

Methods

n/a	Involved in the study
☐	☒ ChIP-seq
☐	☒ Flow cytometry
☒	☐ MRI-based neuroimaging

Antibodies

Antibodies used

The following antibodies were used (all commercially available):

From Cell Signaling Technology (Danvers, MA, USA):
1. N-Myc (#9405, lot 2, 1:1,000);
2. N-Myc (#51705, Clone D4B2Y, lot 1);
3. Cleaved PARP Asp214 (#9541, lot 15, 1:4,000);
4. Cleaved caspase 3 Asp175 (#9661, lot 45, 1:500);
5. ALK (#3333, Clone C26G7, lot 7, 1:1,000);
6. Akt (pan) (#4691, Clone C67E7, lot 20, 1:4,000);
7. Phospho-Akt Thr308 (#9275, lot 26, 1:1,000);
8. Phospho-Akt Ser473 (#9271, lot 14, 1:2,000);
9. p44/42 MAPK (ERK1/2) (#4695, Clone 137F5, lot 21, 1:4,000);
10. Phospho- p44/42 MAPK (ERK1/2) (Thr202/Tyr204) (#4377, Clone 197G2, lot 10, 1:4,000);
11. S6 Ribosomal Protein (#2217, Clone 5G10, lot 5, 1:8,000);
12. Phospho-S6 Ribosomal Protein (Ser235/236) (#4857, Clone 91B2, lot 2, 1:8,000);
13. Stat3 (#4904, Clone 79D7, lot 7, 1:2,000);
14. Phospho-Stat3 (Tyr705) (#9131, lot 30, 1:1,000);
15. MDR1/ABCB1 (#12683, Clone D3H1Q, lot 2, 1:5,000);
16. Sox2 (#3579, Clone D6D9, lot 8, 1:2,000);
17. β-Actin (#4967, multiple lots, 1:5,000);
18. CTCF (#3417, Clone D1A7, lot 1);
19. Normal Rabbit IgG (#2729, lot 7)

20. Anti-mouse IgG, HRP-linked (#7076, lot 33, 1:2,000).

From Santa Cruz Biotechnology (Santa Cruz, CA, USA):
21. Anti-rabbit IgG-HRP (sc-2357, multiple lots, 1:5,000).

From Bethyl Laboratories (Montgomery, TX, USA):
22. BRD4 (A301-985A100, lot 6, 1:30,000);
23. SMC1A (A300-055A, lot 6).

From Millipore (Billerica, MA, USA):
24. CTCF (#07-729, lot 2887267, 1:5,000);
25. SOX9 (#AB5535, lot 2847051, 1:10,000);
26. H3K27me3 (#07-449, lot 2972864).

From Abcam (Cambridge, MA, USA):
27. ALK (phospho Y1507) (ab73996, lot GR57100-14, 1:1,000);
28. BORIS (ab187163, Clone EP12204, lot GR228943-6);
29. H3K27ac (ab2729, lot GR3198866-1).

From NOVUS Biologicals (Littleton, CO, USA):
30. BORIS (NBP2-52405, Clone 20B11, lot CRT/17/124).

From Active Motif (Carlsbad, CA, USA):
31. BORIS (#39851, lot 18916002, 1:3,000).

From Sigma-Aldrich (Saint Louis, MO, USA):
32. SIX1 (HPA001893, lot I114662, 1:4,000).

From Abbott (Abbott Park, IL, USA):
33. Vysis LSI N-MYC (2p24) SpectrumGreen/Vysis CEP 2 SpectrumOrange Probe (07J72-001).

Validation

Validation for commercially available antibodies can be found using the links below:

1. https://www.cellsignal.com/products/primary-antibodies/n-myc-antibody/9405
2. https://www.cellsignal.com/products/primary-antibodies/n-myc-d4b2y-rabbit-mab/51705
3. https://www.cellsignal.com/products/primary-antibodies/cleaved-parp-asp214-antibody-human-specific/9541
4. https://www.cellsignal.com/products/primary-antibodies/cleaved-caspase-3-asp175-antibody/9661
5. https://www.cellsignal.com/products/primary-antibodies/alk-c26g7-rabbit-mab/3333
6. https://www.cellsignal.com/products/primary-antibodies/akt-pan-c67e7-rabbit-mab/4691
7. https://www.cellsignal.com/products/primary-antibodies/phospho-akt-thr308-antibody/9275
8. https://www.cellsignal.com/products/primary-antibodies/phospho-akt-ser473-antibody/9271
9. https://www.cellsignal.com/products/primary-antibodies/p44-42-mapk-erk1-2-137f5-rabbit-mab/4695
10. https://www.cellsignal.com/products/primary-antibodies/phospho-p44-42-mapk-erk1-2-thr202-tyr204-197g2-rabbit-mab/4377
11. https://www.cellsignal.com/products/primary-antibodies/s6-ribosomal-protein-5g10-rabbit-mab/2217
12. https://www.cellsignal.com/products/primary-antibodies/phospho-s6-ribosomal-protein-ser235-236-91b2-rabbit-mab/4857
13. https://www.cellsignal.com/products/primary-antibodies/stat3-79d7-rabbit-mab/4904
14. https://www.cellsignal.com/products/primary-antibodies/phospho-stat3-tyr705-antibody/9131
15. https://www.cellsignal.com/products/primary-antibodies/mdr1-abcb1-d3h1q-rabbit-mab/12683
16. https://www.cellsignal.com/products/primary-antibodies/sox2-d6d9-xp-rabbit-mab/3579
17. https://www.cellsignal.com/products/primary-antibodies/b-actin-antibody/4967
18. https://www.cellsignal.com/products/primary-antibodies/ctcf-d1a7-xp-rabbit-mab/3417
19. https://www.cellsignal.com/products/primary-antibodies/normal-rabbit-igg/2729
20. https://www.cellsignal.com/products/secondary-antibodies/anti-mouse-igg-hrp-linked-antibody/7076
21. https://www.scbt.com/scbt/product/mouse-anti-rabbit-igg-hrp
22. https://www.bethyl.com/product/A301-985A100/BRD4+Antibody
23. https://www.bethyl.com/product/A300-055A/SMC1+Antibody
24. http://www.emdmillipore.com/US/en/product/Anti-CTCF-Antibody,MM_NF-07-729
25. http://www.emdmillipore.com/US/en/product/Anti-Sox9-Antibody,MM_NF-AB5535
26. http://www.emdmillipore.com/US/en/product/Anti-trimethyl-Histone-H3-Lys27-Antibody,MM_NF-07-449
27. https://www.abcam.com/alk-phospho-y1507-antibody-ab73996.html
28. https://www.abcam.com/boris-antibody-ep12204-ab187163.html
29. https://www.abcam.com/histone-h3-acetyl-k27-antibody-chip-grade-ab4729.html
30. https://www.novusbio.com/products/boris-antibody-20b11_nbp2-52405
31. https://www.activemotif.com/catalog/details/39851/boris-ctcfl-antibody-pab
32. https://www.sigmaaldrich.com/catalog/product/sigma/hpa001893?lang=en&region=US
33. https://www.molecular.abbott/sal/en-us/staticAssets/AMD-US-Oncology-and-Genetics-Catalog.pdf

Eukaryotic cell lines

Policy information about cell lines

Cell line source(s)	Human NB cell lines Kelly and SK-N-BE(2) and human Ewing sarcoma cell lines TC-32, TC-71 and CHLA-10 were obtained from the Children's Oncology Group cell line bank (Lubbock, TX, USA). Human NB cell line SK-N-SH and human embryonic kidney cell line HEK293T were obtained from the American Type Culture Collection (Manassas, VA, USA).
Authentication	All cell lines have been authenticated by short tandem repeat analysis.
Mycoplasma contamination	All cell lines tested negative for mycoplasma.
Commonly misidentified lines (See ICLAC register)	No commonly misidentified cell lines were used.

Animals and other organisms

Policy information about studies involving animals; ARRIVE guidelines recommended for reporting animal research

Laboratory animals	NU/NU (Crl:NU-Foxn1nu) mice (6-8 weeks old female) were purchased from Charles River Laboratories. NU/NU (CrTac:NCr-Foxn1nu) mice (6-8 weeks old female) were purchased from Taconic.
Wild animals	The study did not involve wild animals.
Field-collected samples	The study did not involve samples collected from the field.
Ethics oversight	All animal experiments were performed with approval from the Institutional Animal Care and Use Committee of the DFCI.

Note that full information on the approval of the study protocol must also be provided in the manuscript.

Human research participants

Policy information about studies involving human research participants

Population characteristics	Data involving human research participants pertain to immunohistochemistry of formalin-fixed paraffin-embedded tumor tissue slides, and were de-identified prior to analysis.
Recruitment	Data involving human research participants pertain to immunohistochemistry of formalin-fixed paraffin-embedded tumor tissue slides, and were de-identified prior to analysis.
Ethics oversight	All human tumor specimens (formalin-fixed paraffin-embedded slides) were obtained under an Institutional Review Board-approved protocol of the Dana-Farber/Boston Children's Cancer and Blood Disorders Center.

Note that full information on the approval of the study protocol must also be provided in the manuscript.

ChIP-seq

Data deposition

☒ Confirm that both raw and final processed data have been deposited in a public database such as GEO.

☒ Confirm that you have deposited or provided access to graph files (e.g. BED files) for the called peaks.

Data access links *May remain private before publication.*	https://www.ncbi.nlm.nih.gov/geo/query/acc.cgi?acc=GSE103084
Files in database submission	ChIPseq_Original_Submission_sens_res Raw files: Par_BORIS_1.fastq.gz Par_BORIS_2.fastq.gz Par_BRD4_1.fastq.gz Par_BRD4_2.fastq.gz Par_CTCF_1.fastq.gz Par_CTCF_2.fastq.gz Par_H3K27ac_1.fastq.gz Par_H3K27ac_2.fastq.gz Par_H3K27me3_1.fastq.gz Par_H3K27me3_2.fastq.gz Par_input_1.fastq.gz Par_input_2.fastq.gz Par_Pol2_1.fastq.gz Par_Pol2_2.fastq.gz

Res_BORIS_1.fastq.gz
Res_BORIS_2.fastq.gz
Res_BRD4_1.fastq.gz
Res_BRD4_2.fastq.gz
Res_CTCF_1.fastq.gz
Res_CTCF_2.fastq.gz
Res_H3K27ac_1.fastq.gz
Res_H3K27ac_2.fastq.gz
Res_H3K27me3_1.fastq.gz
Res_H3K27me3_2.fastq.gz
Res_input_1.fastq.gz
Res_input_2.fastq.gz
Res_Pol2_1.fastq.gz
Res_Pol2_2.fastq.gz
Res_JQ1_BORIS_1.fastq.gz
Res_JQ1_BORIS_2.fastq.gz
Res_JQ1_BRD4_1.fastq.gz
Res_JQ1_BRD4_2.fastq.gz
Res_JQ1_CTCF_1.fastq.gz
Hi2.fastq.gz
Res_JQ1_H3K27ac_1.fastq.gz
Res_JQ1_H3K27ac_2.fastq.gz
Res_JQ1_H3K27me3_1.fastq.gz
Res_JQ1_H3K27me3_2.fastq.gz
Res_JQ1_input_1.fastq.gz
Res_JQ1_input_2.fastq.gz
Processed files:
norm_Par_BORIS_merged.noNeg.sorted.bw
norm_Par_BRD4_merged.noNeg.sorted.bw
norm_Par_CTCF_merged.noNeg.sorted.bw
norm_Par_H3K27ac_merged.noNeg.sorted.bw
norm_Par_H3K27me3_merged.noNeg.sorted.bw
norm_Par_Pol2_2.noNeg.sorted.bw
norm_Res_BORIS_merged.noNeg.sorted.bw
norm_Res_BRD4_merged.noNeg.sorted.bw
norm_Res_CTCF_merged.noNeg.sorted.bw
norm_Res_H3K27ac_merged.noNeg.sorted.bw
norm_Res_H3K27me3_merged.noNeg.sorted.bw
norm_Res_Pol2_2.noNeg.sorted.bw
norm_Res_JQ1_BORIS_merged.noNeg.sorted.bw
norm_Res_JQ1_BRD4_merged.noNeg.sorted.bw
norm_Res_JQ1_CTCF_merged.noNeg.sorted.bw
norm_Res_JQ1_H3K27ac_merged.noNeg.sorted.bw
norm_Res_JQ1_H3K27me3_merged.noNeg.sorted.bw
Par_BORIS_vs_Par_input_peaks.narrowPeak
Par_BRD4_vs_Par_input_peaks.narrowPeak
Par_CTCF_vs_Par_input_peaks.narrowPeak
Par_narrow_Pol2_vs_Par_input_peaks.narrowPeak
Res_BORIS_vs_Res_input_peaks.narrowPeak
Res_BRD4_vs_Par_input_peaks.narrowPeak
Res_CTCF_vs_Res_input_peaks.narrowPeak
Res_narrow_Pol2_vs_Res_input_peaks.narrowPeak
Res_JQ1_BORIS_vs_Res_JQ1_input_peaks.narrowPeak
Res_JQ1_BRD4_vs_Res_JQ1_input_peaks.narrowPeak
Res_JQ1_CTCF_vs_Res_JQ1_input_peaks.narrowPeak
Par_H3K27ac_vs_Par_input_peaks.broadPeak
Par_H3K27me3_vs_Par_input_peaks.broadPeak
Res_H3K27ac_vs_Res_input_peaks.broadPeak
Res_H3K27me3_vs_Res_input_peaks.broadPeak
Res_JQ1_H3K27ac_vs_Res_JQ1_input_peaks.broadPeak
Res_JQ1_H3K27me3_vs_Res_JQ1_input_peaks.broadPeak
ChIPseq_MYCN
Raw files:
Kelly_input_MYCN_1.fastq.gz
Kelly_MYCN_CS_1.fastq.gz
Kelly_MYCN_CS_2.fastq.gz
Res_Kelly_input_MYCN_CS_1.fastq.gz
Res_Kelly_input_MYCN_CS_2.fastq.gz
Res_Kelly_MYCN_CS_1.fastq.gz
Res_Kelly_MYCN_CS_2.fastq.gz
Processed files:
Par_Kelly_MYCN.noNeg.sorted.bw
Res_Kelly_MYCN.noNeg.sorted.bw
Par_Kelly_MYCN_vs_Par_Kelly_MYCN_INPUT_peaks.narrowPeak
Res_Kelly_MYCN_vs_Res_Kelly_MYCN_INPUT_peaks.narrowPeak

ChIPseq_KD_Boris
Raw files:
shB4_Res_Kelly_BORIS_1.fastq.gz
shB4_Res_Kelly_BORIS_2.fastq.gz
shB4_Res_Kelly_CTCF_1.fastq.gz
shB4_Res_Kelly_CTCF_2.fastq.gz
shB4_Res_Kelly_H3K27ac_1.fastq.gz
shB4_Res_Kelly_H3K27ac_2.fastq.gz
shB4_Res_Kelly_INPUT_1.fastq.gz
shB4_Res_Kelly_INPUT_2.fastq.gz
shB4_Res_Kelly_INPUT_BORIS_1.fastq.gz
shB4_Res_Kelly_INPUT_BORIS_2.fastq.gz
shB4_Res_Kelly_SMC1_1.fastq.gz
shB4_Res_Kelly_SMC1_2.fastq.gz
shLUC_Res_Kelly_BORIS_1.fastq.gz
shLUC_Res_Kelly_BORIS_2.fastq.gz
shLUC_Res_Kelly_CTCF_1.fastq.gz
shLUC_Res_Kelly_CTCF_2.fastq.gz
shLUC_Res_Kelly_H3K27ac_1.fastq.gz
shLUC_Res_Kelly_H3K27ac_2.fastq.gz
shLUC_Res_Kelly_INPUT_1.fastq.gz
shLUC_Res_Kelly_INPUT_2.fastq.gz
shLUC_Res_Kelly_SMC1_1.fastq.gz
shLUC_Res_Kelly_SMC1_2.fastq.gz
Processed files:
shB4_Res_Kelly_BORIS.noNeg.sorted.bw
shB4_Res_Kelly_CTCF.noNeg.sorted.bw
shB4_Res_Kelly_H3K27ac.noNeg.sorted.bw
shB4_Res_Kelly_SMC1.noNeg.sorted.bw
shLUC_Res_Kelly_BORIS.noNeg.sorted.bw
shLUC_Res_Kelly_CTCF.noNeg.sorted.bw
shLUC_Res_Kelly_H3K27ac.noNeg.sorted.bw
shLUC_Res_Kelly_SMC1.noNeg.sorted.bw
shB4_Res_Kelly_BORIS_vs_shB4_Res_Kelly_INPUT_peaks.narrowPeak
shB4_Res_Kelly_CTCF_vs_shB4_Res_Kelly_INPUT_peaks.narrowPeak
shB4_Res_Kelly_H3K27ac_vs_shB4_Res_Kelly_INPUT_peaks.broadPeak
shB4_Res_Kelly_SMC1_vs_shB4_Res_Kelly_INPUT_peaks.narrowPeak
shLUC_Res_Kelly_BORIS_vs_shLUC_Res_Kelly_INPUT_peaks.narrowPeak
shLUC_Res_Kelly_CTCF_vs_shLUC_Res_Kelly_INPUT_peaks.narrowPeak
shLUC_Res_Kelly_H3K27ac_vs_shLUC_Res_Kelly_INPUT_peaks.broadPeak
shLUC_Res_Kelly_SMC1_vs_shLUC_Res_Kelly_INPUT_peaks.narrowPeak
ChIPseq_Ewing_Sarcoma
Raw files:
TC32_BORIS_1.fastq.gz
TC32_BORIS_2.fastq.gz
TC32_H3K27ac_1.fastq.gz
TC32_H3K27ac_2.fastq.gz
TC32_input_1.fastq.gz
TC32_input_2.fastq.gz
TC32_SMC1_1.fastq.gz
TC32_SMC1_2.fastq.gz
TC71_BORIS_1.fastq.gz
TC71_BORIS_2.fastq.gz
TC71_H3K27ac_1.fastq.gz
TC71_H3K27ac_2.fastq.gz
TC71_input_1.fastq.gz
TC71_input_2.fastq.gz
TC71_SMC1_1.fastq.gz
TC71_SMC1_2.fastq.gz
Processed files:
Ewings_TC32_BORIS.noNeg.sorted.bw
Ewings_TC32_H3K27ac.noNeg.sorted.bw
Ewings_TC32_SMC1.noNeg.sorted.bw
Ewings_TC71_BORIS.noNeg.sorted.bw
Ewings_TC71_H3K27ac.noNeg.sorted.bw
Ewings_TC71_SMC1.noNeg.sorted.bw
Ewings_TC32_BORIS_vs_David_Ewings_TC32_INPUT_peaks.narrowPeak
Ewings_TC32_H3K27ac_vs_David_Ewings_TC32_INPUT_peaks.broadPeak
Ewings_TC32_SMC1_vs_David_Ewings_TC32_INPUT_peaks.narrowPeak
Ewings_TC71_BORIS_vs_David_Ewings_TC71_INPUT_peaks.narrowPeak
Ewings_TC71_H3K27ac_vs_David_Ewings_TC71_INPUT_peaks.broadPeak
Ewings_TC71_SMC1_vs_David_Ewings_TC71_INPUT_peaks.narrowPeak
Microarray_ Original_Submission_sens_res_res-JQ1
Raw files:
DD_1_PrimeView_par_Kelly_DMSO.CEL

DD_2_PrimeView_par_Kelly_DMSO.CEL
DD_5_PrimeView_Res_Kelly_TAE.CEL
DD_6_PrimeView_Res_Kelly_TAE.CEL
DD_7_PrimeView_Res_Kelly_JQ1.CEL
DD_8_PrimeView_Res_Kelly_JQ1.CEL
Microarray_KD_Boris
Raw files:
Res_Kelly_shBORIS_1.CEL
Res_Kelly_shBORIS_2.CEL
Res_Kelly_shLUC_1.CEL
Res_Kelly_shLUC_2.CEL
10X_sens_IR_Res
Raw files:
Sens.possorted_genome_bam.bam
Intermediate_Res.possorted_genome_bam.bam
Full_Res.possorted_genome_bam.bam
Processed files:
Sens_matrix.mtx
Intermediate_Res_matrix.mtx
Full_Res_matrix.mtx
barcodes.tsv
genes.tsv
HiChIP_sens_res
Raw files:
KellyRes1_1.fastq.tar.gz
KellyRes1_2.fastq.tar.gz
KellyRes2_1.fastq.tar.gz
KellyRes2_2.fastq.tar.gz
KellyRes3_1.fastq.tar.gz
KellyRes3_2.fastq.tar.gz
KellyWTrep1_1.fastq.bz2
KellyWTrep1_2.fastq.bz2
KellyWTrep2_1.fastq.bz2
KellyWTrep2_2.fastq.bz2
KellyWTrep3_1.fastq.bz2
KellyWTrep3_2.fastq.bz2
Processed files:
Kelly-Res-SMC1.bedpe
Kelly-Res-SMC1-petcount.bedpe
Kelly-SMC1.bedpe
Kelly-SMC1-petcount.bedpe
HiChIP_KD_Boris
Raw files:
Kelly_shBORIS1_1.fastq.tar.gz
Kelly_shBORIS1_2.fastq.tar.gz
Kelly_shBORIS2_1.fastq.tar.gz
Kelly_shBORIS2_2.fastq.tar.gz
Kelly_shBORIS3_1.fastq.tar.gz
Kelly_shBORIS3_2.fastq.tar.gz
Kelly_shLUC1_1.fastq.tar.gz
Kelly_shLUC1_2.fastq.tar.gz
Kelly_shLUC2_1.fastq.tar.gz
Kelly_shLUC2_2.fastq.tar.gz
Kelly_shLUC3_1.fastq.tar.gz
Kelly_shLUC3_2.fastq.tar.gz
Processed files:
shBORIS-results.csv
shLUC-results.csv

Genome browser session
(e.g. UCSC)

No longer applicable.

Methodology

Replicates

For each mark assessed, two biological replicates were performed. All ChIP-seq data are derived from the analysis of both replicates.

Sequencing depth

ChIP-seq libraries were generated using the NEBNext Ultra II DNA Library Prep kit (E7645), following the manufacturer's instructions. Starting DNA material ranged from 2.5 to 10ng, and PCR amplification (8 to 10 cycles) was performed using NEBNext Multiplex Oligos for Illumina (E7335 and E7500) with distinct indices to allow for multiplexing of up to 12 samples to be run on the Illumina NextSeq 500 for 75 bases in single-read mode.
Sample Total_reads Uniquely_mapped_reads
Par_BORIS_1.fastq.gZ 52592735 39434783
Par_BORIS_2.fastq.gz 54031826 40040869

Par_BRD4_1.fastq.gz 32913499 24145172
Par_BRD4_2.fastq.gz 34899996 25050068
Par_CTCF_1.fastq.gz 32357383 21742074
Par_CTCF_2.fastq.gz 38048050 25570483
Par_H3K27ac_1.fastq.gz 34652785 31481286
Par_H3K27ac_2.fastq.gz 36652655 33723955
Par_H3K27me3_1.fastq.gz 35375006 28384362
Par_H3K27me3_2.fastq.gz 33791944 27655558
Par_Pol2_1.fastq.gz 24373861 6139176
Par_Pol2_2.fastq.gz 41084548 2685056
Kelly_MYCN_CS_1.fastq.gz 22544426 19447997
Kelly_MYCN_CS_2.fastq.gz 43975115 38012488
Par_input_1.fastq.gz 74638885 66630061
Par_input_2.fastq.gz 40772400 36361135
Kelly_input_MYCN_1.fastq.gz 43184072 34957425
Res_BORIS_1.fastq.gz 43137736 32555678
Res_BORIS_2.fastq.gz 47143635 35144692
Res_BRD4_1.fastq.gz 32159271 24332339
Res_BRD4_2.fastq.gz 36755542 30051197
Res_CTCF_1.fastq.gz 40911369 28372298
Res_CTCF_2.fastq.gz 36878692 25628082
Res_H3K27ac_1.fastq.gz 33542051 30727706
Res_H3K27ac_2.fastq.gz 37596270 34409319
Res_H3K27me3_1.fastq.gz 35238601 29098617
Res_H3K27me3_2.fastq.gz 35026938 28826263
Res_Pol2_1.fastq.gz 35817388 6953374
Res_Pol2_2.fastq.gz 48429363 2674818
Res_Kelly_MYCN_CS_1.fastq.gz 18821385 14198653
Res_Kelly_MYCN_CS_2.fastq.gz 30543884 24497611
Res_Kelly_input_MYCN_CS_1.fastq.gz 77322913 68513199
Res_Kelly_input_MYCN_CS_2.fastq.gz 53883106 47951287
Res_input_1.fastq.gz 45072526 40107804
Res_input_2.fastq.gz 49535965 44608902
Res_JQ1_BORIS_1.fastq.gz 81479030 61882578
Res_JQ1_BORIS_2.fastq.gz 64057634 49039377
Res_JQ1_BRD4_1.fastq.gz 32714245 25430455
Res_JQ1_BRD4_2.fastq.gz 33031805 25335103
Res_JQ1_CTCF_1.fastq.gz 33287924 24508642
Res_JQ1_CTCF_2.fastq.gz 39674176 29154183
Res_JQ1_H3K27ac_1.fastq.gz 40677082 37149902
Res_JQ1_H3K27ac_2.fastq.gz 32078957 29293906
Res_JQ1_H3K27me3_1.fastq.gz 36342163 30007069
Res_JQ1_H3K27me3_2.fastq.gz 37930668 31338450
Res_JQ1_input_1.fastq.gz 49313027 43993392
Res_JQ1_input_2.fastq.gz 43284562 38433644

Antibodies

The following antibodies were used: MYCN (#51705, Cell Signaling Technology), BRD4 (A301-985A100, lot 6, Bethyl Laboratories), CTCF (#07-729, lot 2887267, Millipore), H3K27me3 (#07-449, lot 2972864, Millipore), H3K27ac (ab2729, lot GR3198866-1, Abcam), and BORIS (#39851, lot 18916002, Active Motif).
All antibodies were previously validated by their manufacturers.

Peak calling parameters

Samples were aligned to the human genome (build hg19, GRCh37.75) with STAR (v2.5.1b_modified) and the parameters "--alignIntronMax 1 --alignEndsType EndToEnd--outFilterMultimapNmax 1 --outFilterMismatchMax 5". Next, non-duplicate reads that mapped to the reference chromosomes were retained using Samtools (v1.3.1) and MarkDuplicates (v2.1.1) from Picard tools. Peaks were identified with MACS2 (2.1.1) for narrow peaks with the parameters "--q 0.01--call-summits" and for broad peaks with the parameters "--broad-cutoff 0.01".

Data quality

1) Peaks overlapping regions with known artefact regions (http://mitra.stanford.edu/kundaje/akundaje/release/blacklists/) were blacklisted out.
2) Antibody enrichment was assessed using the plotFingerprint command from deepTools (v2.2.4).
3) Correlation of replicates was assessed with the deepTools command "multiBigwigSummary BED-file" using all bigwigs and identified peaks as input.
4) broad peaks with 5-fold enrichment, 5% FDR and after blacklisting
Par_H3K27ac_vs_Par_input_peaks.broadPeak.blacklisted 15626
Par_H3K27me3_vs_Par_input_peaks.broadPeak.blacklisted 3946
Res_H3K27ac_vs_Res_input_peaks.broadPeak.blacklisted 16725
Res_H3K27me3_vs_Res_input_peaks.broadPeak.blacklisted 2293
Res_JQ1_H3K27ac_vs_Res_JQ1_input_peaks.broadPeak.blacklisted 15942
Res_JQ1_H3K27me3_vs_Res_JQ1_input_peaks.broadPeak.blacklisted 1819
5) narrow peaks with 5-fold enrichment, 5% FDR and after blacklisting
Par_BORIS_vs_Par_input_peaks_blacklisted.narrowPeak 1055
Par_BRD4_vs_Par_input_peaks_blacklisted.narrowPeak 52158
Par_CTCF_vs_Par_input_peaks_blacklisted.narrowPeak 69566
Par_narrow_Pol2_vs_Par_input_peaks_blacklisted.narrowPeak 19193
Par_MYCN_vs_Par_input_peaks_blacklisted.narrowPeak 36047

Res_BORIS_vs_Res_input_peaks_blacklisted.narrowPeak 17035
Res_BRD4_vs_Res_input_peaks_blacklisted.narrowPeak 26297
Res_CTCF_vs_Res_input_peaks_blacklisted.narrowPeak 58724
Res_JQ1_BORIS_vs_Res_JQ1_input_peaks_blacklisted.narrowPeak 12674
Res_JQ1_BRD4_vs_Res_JQ1_input_peaks_blacklisted.narrowPeak 9702
Res_JQ1_CTCF_vs_Res_JQ1_input_peaks_blacklisted.narrowPeak 37791
Res_narrow_Pol2_vs_Res_input_peaks_blacklisted.narrowPeak 54174
Res_MYCN_vs_Res_input_peaks_blacklisted.narrowPeak 6500

Software

Fastqc (v0.11.5), STAR (v2.5.1b_modified), Samtools (v1.3.1), MarkDuplicates (v2.1.1), deepTools (v2.2.4), MACS2 (v2.1.1), bedGraphToBigWig (v4), R (v3.5.1), Rstudio (v1.1.463), data.table (v1.12.2), trimmomatic (v0.36), HiC-Pro (v2.10.0), hichipper (v0.7.3), diffloop (v1.10.0), ROSE (v1), Circlize (v0.4.5), IGV (v2.3.74). Custom code is available upon reasonable request.

Flow Cytometry

Plots

Confirm that:

☒ The axis labels state the marker and fluorochrome used (e.g. CD4-FITC).

☒ The axis scales are clearly visible. Include numbers along axes only for bottom left plot of group (a 'group' is an analysis of identical markers).

☐ All plots are contour plots with outliers or pseudocolor plots.

☐ A numerical value for number of cells or percentage (with statistics) is provided.

Methodology

Sample preparation

Flow cytometry was used for cell cycle analysis in both parental and resistant cells using propidium iodide (PI) staining. After fixation of 1x10e6 cells overnight at 4C with 80% ethanol, cells were resuspended in PBS supplemented with 0.1% Triton X-100, 25 mg/ml PI, and 0.2 mg/ml RNase A, and incubated for 45 min at 37C in the dark before analysis.

Instrument

Samples were run on a FACSCalibur flow cytometer (BD Biosciences).

Software

Data collection was done with BD CellQuest Pro software (BD Biosciences), and analysis was performed using FlowJo software (v10.0.5).

Cell population abundance

No FACS sorting was performed for this work.

Gating strategy

Cell debris as well as non-singlets were excluded by a gate based on FSC-H and SSC-H.

☐ Tick this box to confirm that a figure exemplifying the gating strategy is provided in the Supplementary Information.

CORRECTION
https://doi.org/10.1038/s41586-019-1378-x

Author Correction: Diverse and robust molecular algorithms using reprogrammable DNA self-assembly

Damien Woods, David Doty, Cameron Myhrvold, Joy Hui, Felix Zhou, Peng Yin & Erik Winfree

Correction to: *Nature* https://doi.org/10.1038/s41586-019-1014-9, published online 20 March 2019.

In Fig. 1 of this Letter, prime symbols were erroneously included in some labels in panels **c** and **d**. In the bottom section of panel **c**, in the diagram beneath 'SST self-assembly', the labels w2a′, w3a′, w4a′ and w5a′ should read w2a, w3a, w4a and w5a, respectively. Similarly, in panel **d**, the labels w2a′ and w3a′ should read w2a and w3a, respectively. Additionally, there were some omissions in the Acknowledgements: R. Schulman should have been thanked for experimental advice, and R. Hariadi for contributing to preliminary designs for algorithmic self-assembly by SST. Finally, in Supplementary Figs. 8 and 9, the rightmost labels s should read s′, and on page 64 of the Supplementary Information a citation to Telser et al. (1989) was missing and has been added as ref. 89; the subsequent citations have been renumbered. The Supplementary Information has been updated accordingly, and minor changes have also been made to the phrasing throughout to improve clarity. The original, incorrect version of the Supplementary Information is included as Supplementary Information to this Amendment, for transparency. The original Letter has been corrected online.

Supplementary Information is available in the online version of this Amendment.

CORRECTION

https://doi.org/10.1038/s41586-019-1454-2

Publisher Correction: Heterochromatin drives compartmentalization of inverted and conventional nuclei

Martin Falk, Yana Feodorova, Natalia Naumova, Maxim Imakaev, Bryan R. Lajoie, Heinrich Leonhardt, Boris Joffe, Job Dekker, Geoffrey Fudenberg, Irina Solovei & Leonid A. Mirny

Correction to: *Nature* https://doi.org/10.1038/s41586-019-1275-3, published online 05 June 2019.

In this Letter, the *x*-axis labels of Fig. 3b were inadvertently shifted to the left. The original Letter has been corrected online, and Fig. 1 of this Amendment shows the original panel, for transparency.

In addition, in panels b1 and c1 of Extended Data Fig. 9, the word 'week' should have been 'weak'. The original Letter has been corrected online.

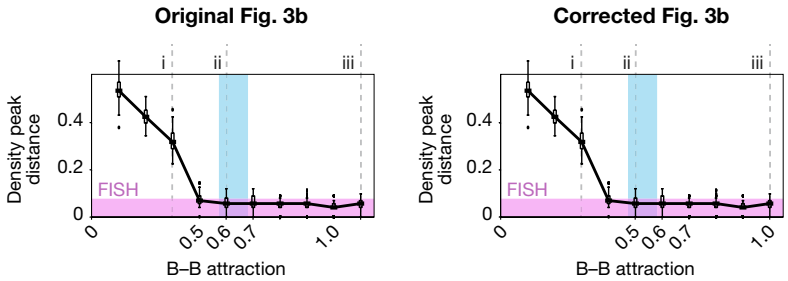

Fig. 1 | This figure displays the corrected and the incorrect published Fig. 3b of the original Letter.

CAREERS

Q&A How to communicate science at a music festival **p.683**

ONLINE Learning to fail can lead to success in science **go.nature.com/fail**

JOBS For the latest career listings **www.naturecareers.com**

LEON NEAL/GETTY

Greta Thunberg, an environmental activist from Sweden, speaks about the climate to politicians, the media and guests at the UK Houses of Parliament.

COLUMN

How to bring science into politics

Six ways to gain traction with policymakers, from **Hannah Safford** and **Austin Brown**.

No matter how hard scientists work, our impact will almost always be limited to our immediate academic circles if our results never catch the attention of those who have the power to act on them. These people are often policymakers — local, state or central-government officials who write laws and regulations, craft budgets and govern communities.

But effective collaboration requires strong communication. The policy world can be tricky to navigate. Institutions can seem impenetrable, and decision-making is often opaque. Fortunately, simple strategies can help scientists to communicate effectively with policymakers.

STRATEGIES FOR SUCCESS

Know who you want to reach. Communicating with top-ranking officials — such as a state governor or a US senator — isn't always the most effective way to spur change. Perhaps your research shows that overflowing storm drains are harming a nearby ecosystem. Such a local issue isn't likely to rise high on the priority list of a senator, but does fall within the remit of your state environmental protection agency or county board of supervisors.

Your best partners might even be outside the government. Non-profit organizations, industry groups, advocacy organizations and private-sector companies don't implement public policy as such, but certainly shape the debate. If you aren't sure who you need to reach, ask around! Your university's government-relations office and colleagues in your field might be able to point you in the right direction.

Have clear and actionable recommendations. Providing specific recommendations makes it easier for your audience to act. Pointing out that more charging stations ▶

JONATHAN ERNST/REUTERS

Former US president Barack Obama met with traditional fishers near Dillingham, Alaska, as part of a trip in 2015 to call attention to climate change.

would support a growing demand for electric vehicles is a good start, but it's even more helpful to explain exactly where and how many are needed. Specificity also prepares you to defend your recommendations by forcing you to think through the details.

Your suggestions should be feasible. Every government body is constrained by its mission and budget. Do your best to propose actions that fall within your target agency's authority.

Finally, remember that making recommendations is not the same as advocacy. One of the most valuable roles a scientist can have is laying out the likely pros and cons of different policy options. Whereas an advocate typically exhorts a policymaker to 'do *Y*', a scientist can marshal the best available research to explain that, "If you do *Y*, chances are good that *Z* will result."

Repackage your work. The peer-reviewed article is the currency of the scientific realm, but it's not going to get you far in policy. A new audience demands a new format — one that is accessible and understandable.

Consider synthesizing your key findings and recommendations into a two-page policy brief that can be distributed easily in person or online. Repackaging your work into a publishable blog or opinion piece is also useful when you're trying to reach a broader audience.

Write well. Conversations and presentations are great ways to introduce a topic, but policymakers will want a written product to react to or to share with colleagues.

Organization, brevity and clarity are more important than wit or style when it comes to policy writing. State your key points first, then provide more explanation. Make sure there is a clear one-sentence takeaway in the first paragraph. Add headings to separate sections, and use visual cues, such as bullets, to draw attention to key points. Define technical terms and spell out acronyms.

Above all, get someone else to read your work. Communicating your science to friends (especially non-experts) is the best way to get better at communicating your science to policymakers.

Pick your moment. Strategically selecting when to engage increases the chance that your idea will fall on receptive ears. Electoral and legislative calendars can help you to choose a good time. Meetings with elected officials tend to be much more effective towards the beginning of a term (when policy priorities are being set) than towards the end.

"Providing specific recommendations makes it easier for your audience to act."

When in doubt, engage early. By the time a bill comes up for a vote, or a rule is in its final stages, most policymakers will have been discussing it for months or longer. Even highly credible input will be unlikely to change minds. Look for newsletters and podcasts that can help you stay aware of when topics you care about are coming up for debate — and talk to legislators before this happens. Submit comments on draft rules and participate in stakeholder workshops when those are offered.

Current events can yield extra opportunities to advance your work. The value of news-generated 'policy windows' has been well documented. Stay aware of what's going on in the world and link your research to it.

Sustain and amplify your engagement. Building support takes time and ongoing effort. Partnering with people and institutions who have an agenda similar to yours is a great way to strengthen your collective case.

It's also crucial to follow up. Policy proposals evolve as they undergo review, debate and public comment. Once you've established a relationship with a key player, check in periodically to stay abreast of changes and update your recommendations accordingly. As a bonus, staying in touch demonstrates a level of investment that sets you apart from the crowd. This, in turn, increases the odds that a policymaker will reach out proactively with questions, making it even easier for you to stay in the loop as policies move forward. ■

Hannah Safford *is a PhD student in environmental engineering at the University of California, Davis, and a researcher with the UC Davis Policy Institute for Energy, Environment, and the Economy.* **Austin Brown** *is executive director of the UC Davis Policy Institute for Energy, Environment, and the Economy.*

Q&A

Bringing fish research to festivals

In February 2017, Helen Currie joined a team of researchers on a tour of UK festivals to share the impact of her work with people outside her field. Currie studies how sound affects migratory-fish behaviour, and is in the fourth year of a doctoral programme at the University of Southampton, UK.

IAN GAVAN/GETTY

Festivals are a place to celebrate not only music and art — but also science.

How did you break into science communication?
Some of the events I took part in during the first year of my PhD lacked the impact I was hoping for. When we just set up under a gazebo in a park with a poster, nobody stopped to talk to us, which was discouraging. At an ecology festival in Southampton, however, my team and I found our groove. We received feedback from environment-conscious visitors who thought that our research into how dams, weirs and other structures can damage migratory-fish ecosystems would have a real impact on assisting the development of river infrastructure that is more sustainable.

How do you engage people with your research?
After our first few events, we learnt that our activities needed to be hands-on and interactive, so with the help of others at the University of Southampton, we created a marble run consisting of a custom-built sloped structure on which people place several marbles. These roll down past a series of barriers, such as gates, gaps, side channels and plastic pins. The marbles represent fish, and the run itself is a river, with barriers representing things that are dangerous to the fish, such as hydropower turbines or locations where water is purposely removed from the river to control flooding or for irrigation use. Participants can alter the river system to make it more friendly or hostile for the fish. We challenge participants to get as many fish through the marble run as possible while we explain our research.

We then joined our university's public-engagement 'roadshow'. This is an ongoing project that encourages researchers to share their work with the public. Every summer, the roadshow travels to several events in the United Kingdom, including music festivals.

Which festivals have you attended?
The biggest one was Glastonbury 2017, a 5-day event that drew 135,000 attendees. For the past few years, festival organizers have invited UK universities to showcase some of their research in the science tent. Our team shared the tent with a number of other universities. I also presented my work at the Green Man, an arts festival in Crickhowell, Wales, which welcomes researchers and universities to apply for a space in a dedicated science area.

What is it like to be a science presenter at these events?
It can be logistically challenging because you're in a field, not a building. You really need to think about what activity you're bringing with you. How heavy is it? Do you need a power source? But it's also great fun. All the presenters at Glastonbury had prepared a key message about their project to share with visitors, which was simple enough for any other presenters to take over and explain the concept. So if we wanted to see a band play, we could briefly hand over responsibility to another presenter and experience some of the festival for ourselves. There were a number of great bands there that year, but my favourite was Royal Blood.

Are people surprised to find science at a music festival?
People these days tend to expect more than just music. Glastonbury has comedy, poetry readings and art installations, so a science tent fits in well. People come to get an experience, and learning just happens to be a secondary outcome. And science probably isn't the strangest thing you will find at a music festival. A couple of people did ask us why we were there, so we explained what we did and the importance of giving back. A lot of public funding goes into science research. It's good to get out and tell people what their taxes are being spent on and why.

Who visits the science area?
It's so varied. Some people hear there's a science tent and actively seek it out. Others wander around the festival and just come across it. There is a wide range of ages as well, from families with young kids to groups of friends, older couples and lone travellers.

How do you switch your message between these different visitors?
People will tell you when they know more about your topic. Even when talking to kids, you'd be surprised what they're already aware of. But you don't want to pitch too high and risk confusing or boring someone, so it's best to start lower and increase the level as the conversation goes. You can have really long conversations this way. Sometimes I walked away having learnt something myself. For example, a fisherman I was speaking to referred to a three-spined stickleback fish as a 'bramstickle', a term I had never heard before. I have since found out that in the British Isles, there are at least 70 dialectical terms for the same species of fish.

What have you learnt about science communication from your festival experience?
It really helped me to see the big picture of my research. I think we sometimes get caught up in the 'nicheness' of what we do, but talking to people at music festivals really helped me to break it back down to the key research question.

What is your advice to colleagues who want to share their research at a similar event?
Just give it a go. You get so much out of it in terms of feedback from people. It makes you realize that you're having an impact, and the conversations you have with people make you think about your research in a different way. So if you have the opportunity, get involved. ■

INTERVIEW BY EVA AMSEN

This interview has been edited for length and clarity.

SEEDS TRAVEL

Plotting a route.

BY BETH GODER

Hajar piloted the mech over vast mountains, through meadows lush with grasses that were almost like those of Earth, except for their orange tips. She travelled through dense forests and snowscapes heavy with wind.

The mech was like an extension of her body, never tiring, wrapping around her like a seed pod protecting its cargo.

Hajar reviewed the data from the soil samples gathered by the mech's feet. A rich composition of minerals in this region, but not enough nitrogen for farming.

In her pocket rested a blue stone.

When Hajar was six, back on Earth, she brought her father a seed. "What's this?" she asked.

He scooped her onto the kitchen counter and kissed her nose. "That's a boxelder maple seed. Look at how it's held within this thin layer, like a paper coat."

"How did it get here?"

Her father told her that seeds travel by wind and water, in the hard shells of nuts and blankets of fruit, carried on the coats of animals or mashed within their digestive tracts, pulled underground by insects, buried by squirrels, scattered by the dual forces of pressure and gravity.

Blackberry plants stretch their creeping vines, plunging spines into the earth. Coconuts embark on sea journeys, carrying the weight of meat and milk, to germinate on the sands of far beaches. Dandelion seeds dance in the air, and the boxelder maple encases its seeds in thin wings, to glide gently down.

Hajar triggered the wings on the mech and leapt from a cliff, gliding in large loops until she touched down. The hands of the mech tested the air for breathability and temperature, and searched for spores.

Forward went the mech. Hajar read messages from the others. Nathaniel was heading north from a desert in the western hemisphere, while Denisa had found a promising sector near the equator. Arwa had done a fascinating preliminary survey of insects in a grassland biome. No one had heard from Suraya, aside from a terse message that she had touched down and was exploring, but she tended to go quiet on bad days.

They all carried their own secret griefs, ready to bloom. Nathaniel refused to listen to Debussy, except for days when he would listen to nothing else, and the melody of 'Clair De Lune' floated across the ship. Arwa had a singular teacup, light green and decorated with fish, which she hid away in her quarters. Every member of the crew had left someone behind. They carried their grief in different ways: in photographs and letters, in knitted scarves and handwritten recipes, in ordinary objects

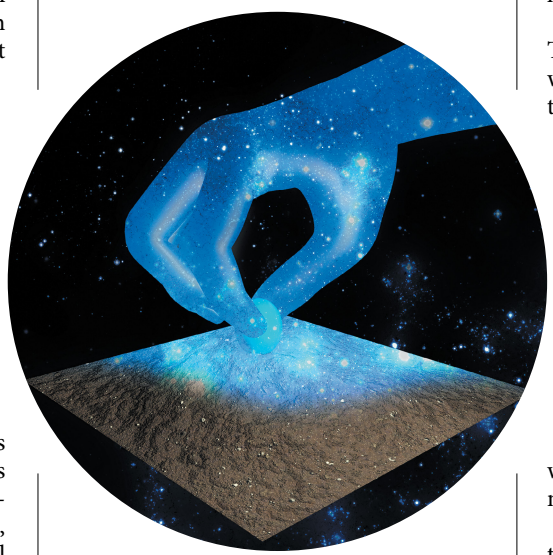

such as teacups and brooms, chipped pots and blue stones.

The mech marched onward under an alien sunset. When it grew too dark to see, Hajar halted the machine. She took the blue stone out of her pocket and turned it over. Before she left Earth, her father had folded the stone into her hands, his faded green hat tipped back, his hands smelling of cinnamon from baking. The stone had come from his garden, prised up from the mud. "Find a new place for it," he'd said, planting those words in the space meant for goodbyes. This was what she brought from Earth, what she carried.

Today, the stone felt rough against her fingers. She thought of her father, imagined the sound of the blender churning his breakfast, the worn leather of his hiking boots, his collection of rocks scattered over geology books on the kitchen counter.

Eventually, she slept, the stone clutched in her hand.

NATURE.COM
Follow Futures:
@NatureFutures
go.nature.com/mtoodm

For her thesis, Hajar studied seed-dispersal strategies of *Oenothera deltoides*, the bird-cage plant of Californian deserts.

The plant travels like this: as dunes shift, the roots are exposed. Shade melts away, leaving the plant under the light of an intolerable sun. The plant dies, curling its roots over itself: a bird cage, a wicker ball. Wind pulls the plant kilometres from its home. When the plant finds shelter from wind, seeds spill out from the lattice.

New plants rise, phoenix-like, from the husk.

The mech emerged in a clearing blanketed with grass. Three-petalled flowers bent in the wind.

The soil readings were good. A river rushed by to the east, the water potable.

Hajar sent a message to the others. A habitable zone to add to the list. She imagined all of them out in the meadow, tilling the soil, constructing houses from the durable bio-plastic they'd brought.

Hajar emerged from the mech. For the first time, she felt the planet's air on her face. The wind carried the smell of sun-simmered grass and wet soil.

Next to her, a tree thick with seeds wrapped in flexible coating, like a boxelder maple.

Once, her father had told her how seeds travel — to arid deserts and rich soil, through woodland and tundra, across oceans and rivers. By centimetres or kilometres, they go.

Not all of them survive.

Seeds travel, tumbling, falling, swept along until they cannot travel farther.

Where they land is home. They put down roots, they grow.

She wished her father was there. Seeds, she would tell him, are designed to travel, to seek out habitable spaces, leaving behind their progenitors, pushing forward into the wide future.

Hajar slipped the blue stone from her pocket. This place felt right, already full of life. How many seeds were even now under the soil, waiting to grow?

She clutched the stone close, then buried it in the soft earth. ■

ILLUSTRATION BY JACEY

Beth Goder *works as an archivist, processing the papers of economists, scientists and other interesting folk. Her fiction has appeared in venues such as* Escape Pod, Fireside *and an anthology from Flame Tree Press. You can find her online at http://www.bethgoder.com.*